MC 2019 BERLIN
MICROSCOPY CONFERENCE

01–05 September 2019
Berlin | Germany

ABSTRACTS

Organized by

DGE DEUTSCHE GESELLSCHAFT FÜR ELEKTRONENMIKROSKOPIE

www.microscopy-conference.de

Content

PL.01
Proteins in whole cells studied with liquid-phase electron microscopy

N. de Jonge[1,2], D. B. Peckys[3], I. N. Dahmke[1], S. Keskin[1]

[1]INM-Leibniz Institute for New Materials, Saarbrücken, Germany
[2]Saarland University, Physics Department, Saarbrücken, Germany
[3]Saarland University, Department of Biophysics, Homburg, Germany

Transmission electron microscopy (TEM) has traditionally been associated with the study of thin solid samples in vacuum. With the availability of reliable thin membranes of silicon nitride, TEM of liquid specimens has become accessible (1). The usage of liquid-phase scanning transmission electron microscopy (STEM) presents a novel concept to study membrane proteins within whole mammalian cells in their native liquid environment (2). The cells in liquid are placed in a microfluidic chamber enclosing the sample in the vacuum of the electron microscope, and are then imaged with STEM. It is not always necessary to enclose the cells in the microfluidic chamber. For many studies, it is sufficient to obtain information from the thin outer regions of the cells, and those can be imaged with high resolution using environmental scanning electron microscopy (ESEM) with STEM detector (3). A third option is to cover a liquid specimen under a thin membrane of graphene providing the thinnest possible layer (4). The obtained spatial resolution is typically limited by ration damage (5). An advantage in liquid is that the electron dose tolerance of the sample is improved by an order of magnitude in liquid compared to samples in ice under the right conditions (6).

Liquid-phase STEM was used to explore the formation of HER2 homodimers at the single-molecule level within intact SKBR3 breast cancer cells in liquid (3). HER2 is a membrane protein and plays an important role in breast cancer aggressiveness and progression. Data analysis based on calculating the pair correlation function from individual HER2 positions (Figure 1) revealed remarkable differences in its functional state between rare- and bulk cancer cells with relevance for studying the role of cancer cell heterogeneity in drug response. We discovered a small sub-population of cancer cells with a different response to a therapeutic drug (7). The same approach to study the spatial distribution of HER2 is now also available for the study of biopsy samples from patients.

Other membrane proteins have been studied as well, such as calcium channels. Here, we aimed to determine the composition of the protein complex from its subunits, and monitor differences with location in the plasma membrane and with functional state.

References:

(1) de Jonge, N. and Ross, F.M.*Nat. Nanotechnol.* 6, 695-704 (2011)

(2) de Jonge, N., et al. *Proc. Natl. Acad. Sci.* 106, 2159-2164 (2009)

(3) Peckys, D.B., et al. *Sci. Adv.* 1, e1500165 (2015)

(4) Dahmke, I.N., et al. *ACS Nano* 11**,** 11108-11117 (2017)

(5) de Jonge, N., et al. *Nat. Rev. Mater.* **4**, 61-78 (2019)

(6) Keskin, S. and de Jonge, N. *Nano Lett.* 18, 7435-7440 (2018)

(7) Peckys, D.B., et al. *Mol. Biol. Cell* 28, 3193-3202 (2017)

This work is supported by DFG under SFB1027 and by the Else Kröner-Fresenius-Stiftung.

Fig: 1: Liquid-phase STEM of HER2 proteins in SKBR3 breast cancer cells. A) Overview STEM-Image at 800 x magnification. B) STEM image recorded at the position of the yellow square in A, at 60.000x magnification, showing the abundance of quantum dot labeled HER2 molecules; the labels in B were automatically detected and outlined in yellow. C) Pair correlation function $g(r)$ analysis of all label positions in B indicating HER2 homodimer formation at a distance of r= 20 nm.

Fig. 1

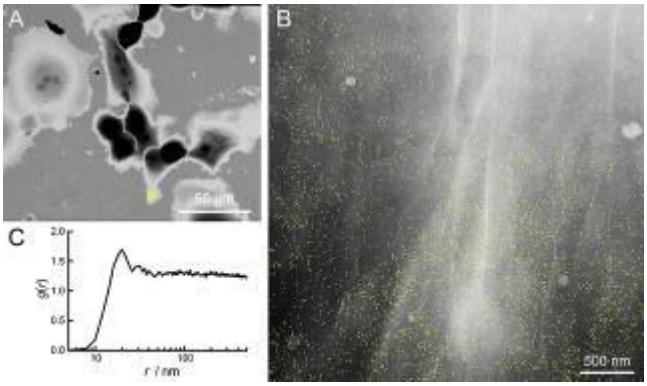

PL.03
Visualizing membrane dynamics with electron microscopyVisualizing membrane dynamics with electron microscopy

S. Watanabe[1]

[1]John Hopkins School of Medicine, Department of Cell Biology, Baltimore, MD, United States

Cell membranes undergo constant remodeling, and these morphological changes must be visualized to study processes such as synaptic transmission. However, it is difficult to capture these changes with precise temporal and spatial resolution. To address this problem we have combined optogenetics with electron microscopy to develop a high-resolution, time-resolved technique called flash-and-freeze. Using flash-and-freeze we have discovered a fast endocytic process in neurons called ultrafast endocytosis.

Neurons communicate via neurotransmitter release. Upon stimulation, synaptic vesicles fuse with the synaptic plasma membrane and release their contents. However, the number of synaptic vesicles is limited in the mammalian neurons and vesicles must be regenerated quickly. Based on 40 years of work, clathrin-mediated endocytosis is thought to be responsible for synaptic vesicle regeneration. However, clathrin-mediated endocytosis is too slow to match the speed of fast synaptic transmission. To directly capture fast membrane remodeling events during synaptic transmission, we used flash-and-freeze. We expressed channelrhodopsin, a light-gated cation channel, in mouse hippocampal neurons. A brief flash of blue light triggers sodium influx and generates an action potential, leading to synaptic activity. Neurons are then fixed by high-pressure freezing at defined time points after the action potential, ranging from 15 ms to 10 s, to capture morphological changes by electron microscopy. Using this approach, we found that membranes are internalized within 50-300 ms. Owing to its unmatched speed, we termed this process ultrafast endocytosis.

This new electron microscopy technique, flash-and-freeze, combines optogenetics and high-pressure freezing to generate time-resolved, high-resolution images of any cellular process. Using this approach, we have discovered ultrafast endocytosis, a mechanism for rapid membrane recycling at chemical synapses, and probed the underlying molecular mechanisms. However, flash-and-freeze could be applied to study other fast cellular events with combined spatial and temporal resolution unmatched by any other technique.

MS1.001
Ultra low voltage DELTA-SEM – beam energy-dependent surface charging identifies defects in organic thin film transistors

W. S. Zhang[1], M. Matthiesen[2], J. Zaumseil[2], L. Gade[3], R. R. Schröder[1,4]

[1]Universität Heidelberg, Centre for Advanced Materials, Heidelberg, Germany
[2]Universität Heidelberg, Institute of Physical Chemistry, Heidelberg, Germany
[3]Universität Heidelberg, Institute of Inorganic Chemistry, Heidelberg, Germany
[4]Universität Heidelberg, Cryo Electron Microscopy, Heidelberg, Germany

Surface charging of non-conductive or very low conductive materials resulting from the incident beam is normally unfavorable for the imaging process in a SEM. It generates an extra electric field, which changes the kinetic energy of the emitted electrons and their trajectory, resulting in image artifacts. However, this side-effect can be utilized advantageously when investigating semiconducting materials, if one carefully chooses the primary energy (PE) of the e-beam.

In this work, we show a novel way for a quick exploration of fabrication defects in solution-processed organic field effect transistors (OFET).

The OFET device examined in this work is built with the n-type (electron-transporting) small-molecule material TAPP[1], which is zone-cast on top of a dielectric polymer layer. It is first imaged in an epi-illumination light microscope (LM) and then at different, rather low voltages in a novel prototype SEM, the DELTA (Carl Zeiss Microscopy) which has spatial and chromatic aberration correction.[2]

In the LM the TAPP layer shows a feather-like pattern, incomplete coverage of the area between source and drain, and inhomogeneity in thickness.

To examine its electron-transporting ability, a negatively charged surface layer on TAPP is created by PE=50 eV. Several places between source and drain, where charges cannot quickly dissipate, are found (Fig. 1, left). Although an e-beam with a higher energy (PE=1000 eV) can also generate negative charging (Fig. 1, right), no defects can be visualized, probably due to the much larger interaction volumes of the incident electrons. A weak positive charging is achieved at PE=100 eV, which may allow investigation of hole-transporting. The critical energy point E_2 (no charging/charge equilibrium[3]) for this crystalline TAPP layer is found at PE=200 eV. Here a well-resolved image using a slow scan rate is obtained. Islands and narrow passes (Figure 2), which lead to a charge accumulation or a slow dissipation, are easily detected.

Dynamic imaging of a semi-conductor layer at different landing energies around the charge-neutral E_2 point allows easy detection of defects within the layer. By image processing, e.g. binary thresholding, the effective area of the TAPP layer that actually contributes to OFET performance may be calculated. Thus, the measured electron-transport mobility can be corrected. Electron-microscopic investigation in terms of charge transport mobility is underway.

References:

(1) C. Martens, U. Zschieschang, H. Wadepohl, H. Klauk, L.H. Gade,*Chem. Eur. J.* 2012, *18*, 3498

(2) Steigerwald, *Frontiers of Characterization and Metrology for Nanoelectronics* 2013

(3) Reimer, *Image Formation in Low-voltage Scanning Electron Microscopy*. SPIE Optical Engineering Press 1993

The authors thank the DFG for funding (SFB 1249)

Fig. 1: Surface charging of the TAPP layer in an OFET device under different PEs: negative charging at PE=50 eV and 1000 eV, positive charging at PE=100 eV and free of charging at PE=200 eV, scale bar 10 µm.

Fig. 2: Fabrication defects exposed at PE=50 eV (left) and imaged at PE=200 eV (right), scale bar 10 µm.

Fig. 1

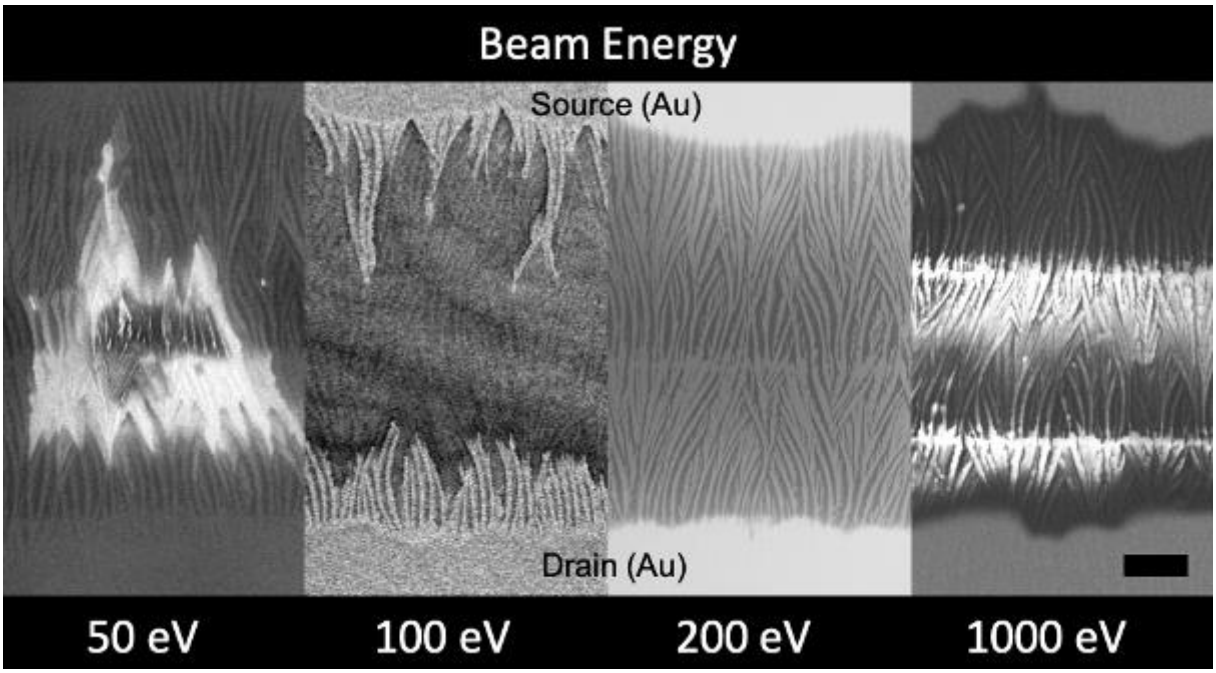
Beam Energy
Source (Au)
Drain (Au)
50 eV
100 eV
200 eV
1000 eV

Fig. 2

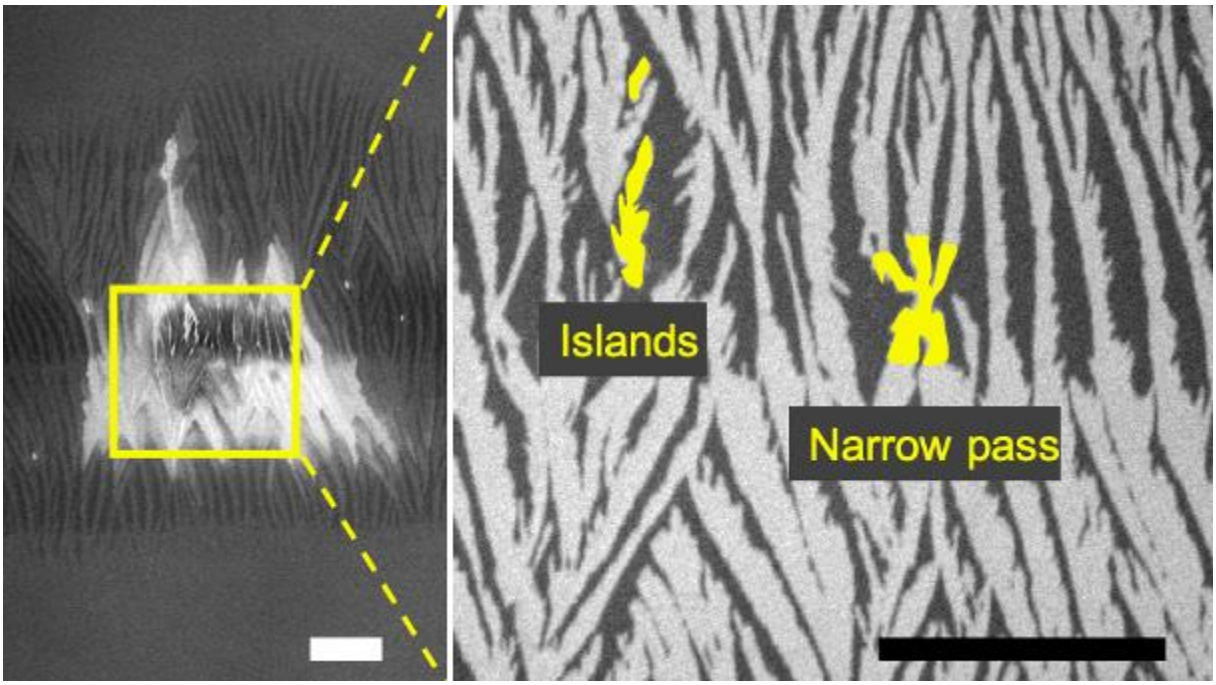
Islands
Narrow pass

MS1.002
In situ STEM differential phase contrast magnetic imaging of FeRh thin gilm

S. Gorji[1,2], X. Mu[2], R. Witte[2], D. Wang[2,3], R. Kruk[2], T. Scherer[2,3], H. Hahn[1,2], C. Kübel[1,2,3]

[1]Technische Universität Darmstadt, KIT-TUD-Joint Research Laboratory Nanomaterials, Darmstadt, Germany
[2]Karlsruhe Institute of Technology, Institute of Nanotechnology, Eggenstein-Leopoldshafen, Germany
[3]Karlsruhe Institute of Technology, Karlsruhe Nano Micro Facility, Eggenstein-Leopoldshafen, Germany

FeRh with nearly equiatomic composition is an intriguing magnetic material exhibiting a first-order magnetic transition a little bit above room temperature (~78-87 ºC) from antiferromagnetic (AF) to ferromagnetic (FM) (1, 2). The AF-FM magnetic phase transition in FeRh is reversible and accompanied by an isotropic lattice expansion. This makes FeRh a interesting choice for a variety of applications such as room-temperature AF memory resistors and heat assisted magnetic recording devices (1). However, the underlying fundamental dynamics of the FeRh AF-FM transition are yet to be fully understood. We have previously shown qualitative *in situ* Lorentz transmission electron microscopy (TEM) images of FeRh thin film where the magnetic domain walls are identified during the AF-FM transition (3). In this work, we have used differential phase contrast (DPC) for quantitative magnetic imaging of a FeRh thin film, with local Rh-rich precipitates, where the local magnetization intensity and orientation is determined. To investigate the dynamics of the AF-FM transition, *in situ* heating was carried out using a Gatan heating holder inside an aberration-corrected TEM in zero magnetic field by turning off the objective lens of the TEM; with a measured stray field value of 0.01 mT. DPC images were obtained in scanning TEM (STEM) mode with a pixelated detector (4). Fig.1a shows a DPC image of a relatively large area of the thin film. A HAADF STEM image (Fig.1b) was subsequently obtained, with the objective lens back on, from the same area to correlate the formation and the final orientation of magnetic domains to the local distribution of Rh-rich precipitates. Our results give new perspective in correlating the magnetic domain evolution and stabilization with the crystallographic structure and coherent inhomogeneities of the FeRh thin film.

References:

(1) Ralf Witte *et al.*, *Physical Review B,* (2016) 93, 104416.

(2) Ralf Witte *et al.*, *Journal of Physics D,* (2017) 50, 025007.

(3) Saleh Gorji *et al*, *Microscopy and Microanalysis,* (2018) 24 (S1), 934-935.

(4) Matus Krajnak *et al.*, Ultramicroscopy, (2016) 165, 42–50.

Fig. 1:a) a DPC magnetic image of FeRh thin film after transition from antiferromagnetic to ferromagnetic at around 130 °C. Color wheel and arrows indicate the magnetization orientation. b) a HAADF-STEM image of the same area at room temperature.

Fig. 1

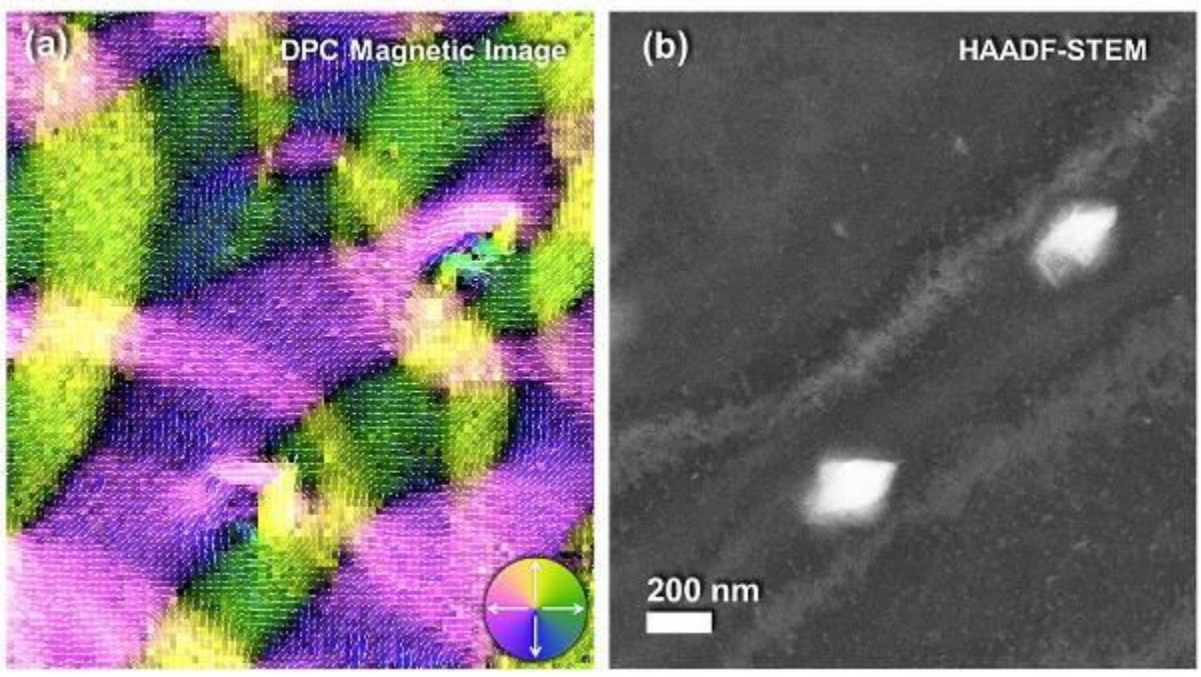

MS1.003
Strain measurement of finFET device using moiré fringes by scanning transmission electron microscopy

Y. Kondo[1], N. Endo[1], Y. Aoyama[1], C. C. Lin[2], K. Hsu[2]

[1]JEOL Ltd., EM business unit, Tokyo, Japan
[2]IST Inc., Material analysis division, Hsinchu, Taiwan

Recently, a device structure has become three dimensional (3D). A typical 3D structure in modern device is a finFET, which has a tri-gate structure (1). In other aspects, strained silicon is used to enhance the mobility of carriers. Typically, channel strain in pMOS of the finFET is arisen by pinching the channel with stressors made of typically Si/Ge. Measurement of the channel strain is important because it relates to device performance. However, we have difficulties in measuring the strain due to the structure of finFET. First, the channel is sandwiched with gate electrodes. The channel strain must be measured in such a direction that the electron beam scans across these layers. Second, the sample thickness must be more than 100 nm to avoid strain release (2). This paper reports how we measure the strain of the finFET by scanning transmission electron microscopy (STEM). We measured the strain by a method that utilizes moiré fringes of STEM, (3,4,5), which arise as a result of undersampled lattice fringes with the raster of STEM.

Sample made by focused ion beam was 150 nm thick. The pitch of fins in this sample was ~ 50 nm, so three fins were included in the thickness. The lamella was cut along the channel direction so that we can observe the strained channel pinched between Si/Ge stressors. The measured moiré fringe was arisen as a result of undersampling of lattice (0.192 nm, Si [220]). The moiré fringes of the targeted lattice was selectively extracted, since it works as a real space frequency filter and filters out the other lattices having different spacing and directions.

Figure 1 (a) shows a bright field STEM image of the sample observed at 200 kV. The black area is overlapped with the W electrode, and the grey area is a sandwiched with double-layer of the TiN_x gate electrode of and an SiO_xN_y insulator. These elements were confirmed from 3D elemental volume map by 3D EDS (energy dispersive X-ray spectroscopy) tomography. We could not observe the moiré fringe under the W electrode due to its heavy absorbance of electrons. Thus, we measured the channel strain from the area surrounding the W wire, which is indicated by a pink square in Fig. 1(b). Figure 1(b) shows a strain map of the (220) lattice, which is along the channel direction (*X*-direction). The line profile of the strain along the pink square is shown in Fig. 1(c). Finally, the compressive strain of the channel pinched between Si/Ge stressors was measured to be - 0.7 - 0.9%.

The STEM moiré method can be applicable to measure the strain of finFET, since the STEM moiré fringes act as a spatial filter in real space and extract only the target lattice. This method can be applied to measure the strain of the target volume surrounded by other materials. In addition to this, the nature of the real space filter leads the capability to detect dislocations that are intrinsically fatal for device manufacturing.

References:

(1) D. Hisamoto et al., Int. Electron Devices Meeting, (IEEE, 1989), p. 833.

(2) S. Kim et al., AIP Advances 3, 092110 (2013).

(3) N. Endo and Y. Kondo, Proc. 32th LSI Testing Symposium, (2012), p73.

(4) S. Kim et al., Appl. Phys. Lett. 102 (16), 161604 (2013).

(5) N. Endo and Y. Kondo, Microsc. Microanal. 20 (S3), 1068 (2014).

Fig. 1: Results of strain analysis by STEM moiré method. a) X-cut view of a finFET device. The gate and W wire overlap the Si channel. b) Strain map along channel of finFET. c) Profile of strain map along the pink square shown in (b).

Fig. 1

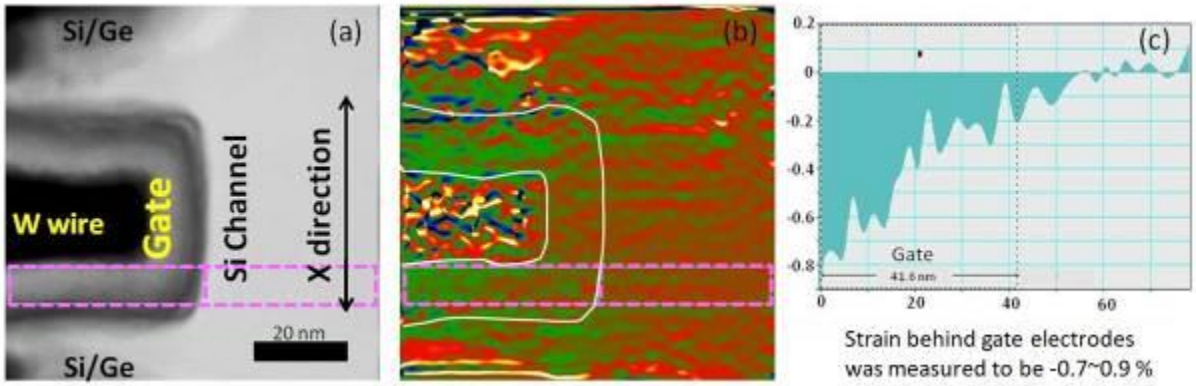
Si/Ge
(a)
W wire
Gate
Si Channel
X direction
20 nm
Si/Ge
(b)
(c)
0.2
0
-0.2
-0.4
-0.6
-0.8
Gate
41.6 nm
0
20
40
60
Strain behind gate electrodes
was measured to be -0.7~0.9 %

MS1.005
Atomic resolution differential phase contrast imaging of defect structures in heteroepitaxial GaAs grown on Si_3N_4 nanohole-masked Si(001)

J. Bürger[1,2], T. Riedl[1,2], T. Langer[1,2], A. Trapp[1,2], D. Reuter[1,2], J. K. N. Lindner[1,2]

[1]Paderborn University, Department of Physics, Paderborn, Germany
[2]Center for Optoelectronics and Photonics Paderborn (CeOPP), Paderborn, Germany

Differential phase contrast (DPC) imaging is a promising technique in scanning transmission electron microscopy allowing for the visualization of electric and magnetic fields. With a probe Cs-corrected microscope equipped with a DPC detector electric fields in the vicinity of defects or at interfaces of polar mismatched materials are measurable at atomic resolution. III-V semiconductors like GaAs form a variety of defects when grown on a silicon substrate due to a high lattice, thermal expansion and polarity mismatch. In the optimization of GaAs-based optoelectronic devices DPC opens a whole new field of defect detection and characterization possibilities.

Heteroepitaxial GaAs grown on Si(001) forms defects like dislocations, stacking faults, nano-twins and even anti-phase boundaries close to the GaAs-Si heterointerface. Some of the above mentioned defects exhibit polar terminations allowing differential phase contrast imaging for the detection of their extension and position as well as their electronic properties. Therefore, DPC images of nano-twins, stacking faults bounded by partial dislocations and anti-phase boundaries are captured. By comparison with HAADF-STEM, BF- and DF-TEM the nature of these defects can be analyzed and the influence of Bragg contrasts on the DPC signal can estimated. In addition, electric fields at the Si(001)/GaAs heterointerface are analyzed and quantified.

A nanohole-patterned Si_3N_4 film acts as a trap for threading defects in the heteroepitaxial GaAs grown on Si(001) substrate. The patterning is accomplished by nanosphere lithography in combination with reactive ion etching and wet-chemical cleaning, leaving nanoholes with diameters of about 70 nm in Si_3N_4. The removal of surface oxides prior to solid source MBE growth of GaAs is achieved by an in-situ atomic hydrogen treatment. A 30 nm thin cross-section specimen, which is prepared by mechanical dimple grinding and argon ion polishing, is analyzed with a probe Cs-corrected JEOL JEM-ARM200F microscope equipped with an 8-fold segmented annular detector for DPC imaging. For the characterization and determination of the defects BF-/DF-TEM, EFTEM, STEM-HAADF and STEM-DPC images with a resolution down to 70 pm are employed.

The above mentioned misfit-related defects concentrate close to the GaAs/Si(001) heterointerface. Nano-twins, stacking faults and anti-phase boundaries are analyzed by DPC imaging revealing the electric field and charge distributions in vicinity of the defects (Fig. 1). At the Si(001)/GaAs interface a shift of the beam perpendicular to the interface is seen, which can be ascribed to the polar/non-polar transition and related charge redistribution at the interface.

Differential phase contrast STEM imaging is well suited to analyze defect structures in polar semiconductors and at heterointerfaces. At medium resolutions defects can be elegantly visualized but care must be taken on the influence of Bragg contrasts. DPC images at atomic resolution show characteristic features for each analyzed type of defect.

Fig. 1: (a) Cross-section DPC image of GaAs grown selectively in the opening of a Si_3N_4 mask on Si(001). Nanotwins are marked with dotted white lines, while white arrows highlight fields at the heterointerface.(b) A DPC image of a stacking fault is shown in the inset. Atomic column positions are determined from the corresponding HAADF-STEM image and marked by white dots.

Fig. 1

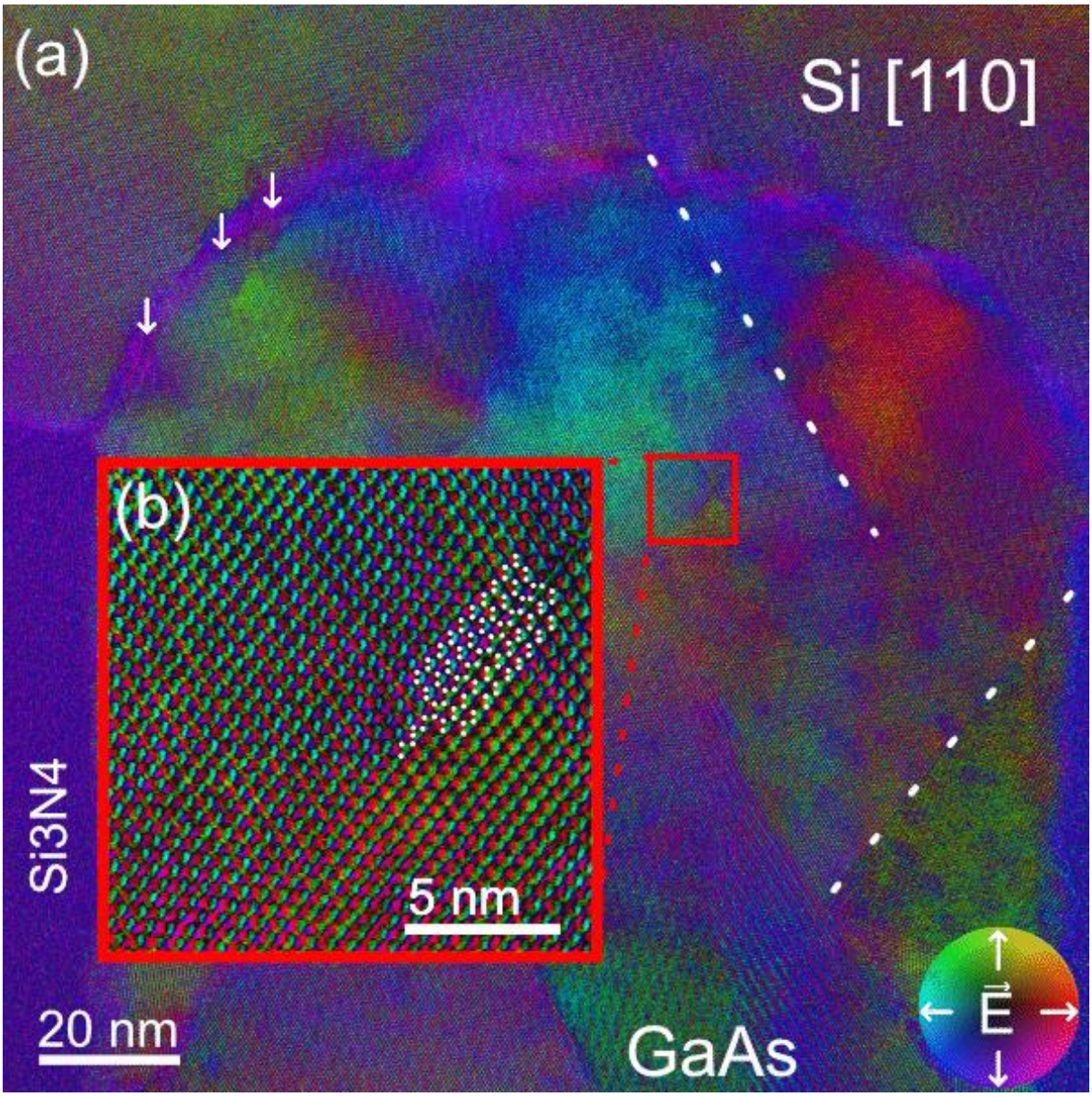

MS1.006
Correlation of structural modifications and switching characteristics by multiscale phase mapping in filamentary type HfO_2-based RRAM

A. Zintler[1], R. Eilhardt[1], S. Petzold[1], N. Kaiser[1], S. Ulhas[1], L. Alff[1], L. Molina-Luna[1]

[1]Technische Universität Darmstadt, Materials- and Earth Science, Darmstadt, Germany

Hafnia based resistive random access memories (RRAM) are candidates for next generation nonvolatile memory due to their potential for fast, dense and energy efficient data storage and proven compatibility to CMOS technology (1). According to the current state of understanding, the resistive switching (RS) behavior relies on the electric field driven formation and dissolution of oxygen deficient nanoscale conducting paths, so called "filaments" (2). The effects behind this mechanism includes accelerated diffusivity and inter band-gap states located at possible grain boundaries (GBs) as well as interfacial redox processes.

By using HR-STEM imaging and Automated Crystal Orientation Mapping (ACOM) we were able to analyze the nanoscale grain structure of the multilayer and the arrangement of the m-HfO_2 grains in the TiN/HfO_2/Pt stack which is deposited on a *c*-cut Al_2O_3 substrate.

In an attempt to achieve a forming free RRAM device, the texture of the HfO_2 thin film was controlled by a reactive molecular beam epitaxy synthesis routine. The proposed methods allow characterization of the texture transfer of the substrate texture to the TiN electrode thin film and finally to the dielectric layer.

EBSD and XRD data (not shown) indicates the TiN grains grow with the (111) axis parallel to the surface normal (001) of the c-cut Al2O3 and the HfO2 layer exhibit (11-1) as their out-of-plane axis. High-resolution ACOM (Fig.1b) allows a detailed analysis of the set of existing in-plane rotations for the m-HfO_2 phase. For a single grain of the TiN bottom electrode a set of three HfO2 grains is observed (Fig.1c-d). Fig.2b shows GBs in the dielectric layer which connect top and bottom electrode. The importance of the GBs also arises due to localized electronic inter-bandgap states (3) and the reduced defect formation energies at GBs (4). Due to preferable diffusivity at GBs, the proposed interface reactions (5) were also accessible by EELS mappings (not shown).

These physical properties strongly suggest that the initial dielectric breakdown and consequent conducting path formation occurs at the grain boundary. In our electric field dependent in situ TEM studies (6), we demonstrated for the first time how to electrically contact and operate a device fabricated in a FIB. The RS behaviour of the electron-transparent lamella were comparable to a conventional reference device (Fig.2c).

References:

(1) S.U. Sharath *et al.*, *Adv. Funct. Mater*, 27 (2017).

(2) R. Waser *et al.*, *Adv. Mater.*, 21 (2009).

(3) K.-H. Xue *et al.*, *Appl. Phys. Lett.*, 102 (2013).

(4) K. McKenna and A. Shluger, *Appl. Phys. Lett.*, 95 (2009).

(5) G. Niu *et al.*, *Mater. Res. Lett.*, 7 (2019).

(6) A. Zintler *et al.*, *Ultramicroscopy*, 181 (2017).

The authors acknowledge financial support from the Deutsche Forschungsgemeinschaft (DFG) under research grant MO 3010/3-1 and the European Research Council (ERC) "Horizon 2020" program under grant No. 805359-FOXON.

Fig. 1: a. TEM image of the MIM stack. b. ACOM phase and orientation mapping of a. c-d. PFs derived from the ACOM dataset.

Fig. 2: a. SEM image of a FIB prepared HfO_2 device on a MEMS based chip used for in situ biasing TEM experiments, 1: contact for bottom TiN electrode, 2: top Pt electrode. b. Corresponding HAADF-STEM image of the stack. c. Unipolar RS behavior of a bulk device (purple/black dotted curve), unipolar reset of the prepared lamella device (blue curves).

Fig. 1

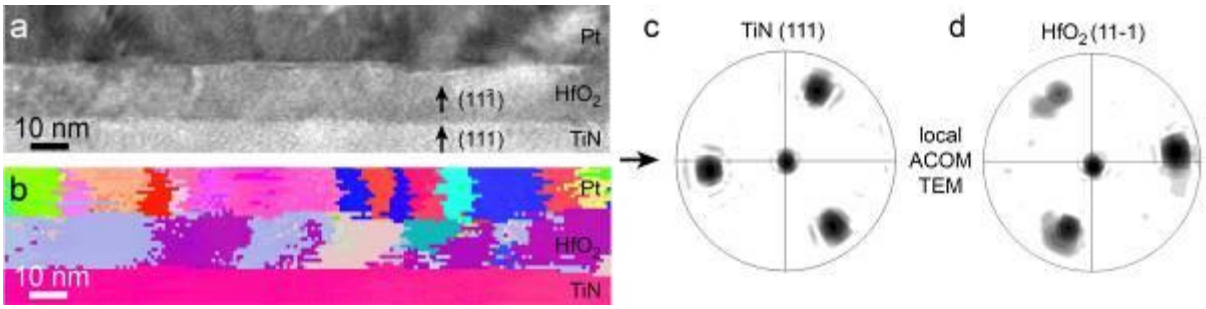
a
Pt
(111)
HfO2
10 nm
(111)
TiN
b
Pt
HfO2
10 nm
TiN
c
TiN (111)
d
HfO2 (11-1)
local
ACOM
TEM

Fig. 2

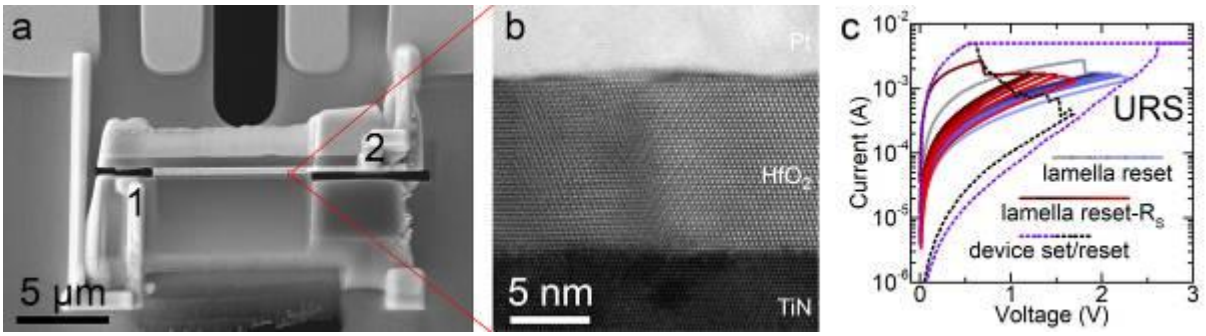
a
2
1
5 μm
b
Pt
HfO2
5 nm
TiN
c
Current (A)
Voltage (V)
URS
lamella reset
lamella reset-Rs
device set/reset

MS1.008
Hollow-cone Foucault imaging of magnetic microstructures in large magnetostrictive FeGa alloy

A. Kawaguchi[1], A. Kotani[1], K. Harada[1,2], H. Numakura[1], Y. Ishii[1], S. Mori[1]

[1]Osaka Prefecture University, Department of Materials Science, Naka-ku, Sakai, Osaka, Japan
[2]RIKEN, Hatoyama, Saitama, Japan

Magnetostrictive materials exhibit external form changes by applying an external magnetic field. Recently, FeGa alloys has attracted much attention as a practical magnetostrictive material because they exhibit a large magnetostriction at low magnetic field (1). It is suggested that the magnetostriction of FeGa alloy should originate from the reorientation of magnetoelastically and magnetostatically autarkic rigid micro-"cells", and thus, dynamical behaviors of the magnetic domain structures by applying external magnetic fields should have strong relationship with the large magnetostriction in FeGa alloys. In this study, we have investigated the magnetic microstructures of large magnetostrictive FeGa alloys by using Lorentz microscopy, hollow-cone Foucault imaging (2) and small-angle electron diffraction techniques (3).

Figure 1(a) shows magnetic microstructures obtained using Fresnel method in the (001) plane of the FeGa thin film without external magnetic fields. In the Fresnel image, bright and dark lines identified as magnetic domain walls can be clearly seen. Thus, we determined spatial distribution of magnetization in each magnetic domains by SmAED and Foucault images. In Fig. 1(a), yellow arrows indicate the direction of the magnetizations in each magnetic domains. The 180° and 90° magnetic domains are formed at room temperature without external magnetic field. Note that magnetic moments are oriented along the (100) direction. When a magnetic field of 400 Oe is applied perpendicular to the film, it is found that the magnetic moments should rotate in the in-plane direction toward the (010) direction and the magnetic domains with magnetization along the (100) direction are dominant at the expense of magnetic domains with the magnetic moments along the (001) direction. In addition, SmAED experiments revealed that the magnitude of the magnetization remains intact. These unusual magnetic responses of magnetic domains to the external magnetic field should be important for better understanding of the large magnetostrictive effect in FeGa alloys. In this presentation, we will also report the development of hollow-cone Foucault imaging method.

References:

(1) C. Harsh, *et al., Nature* 521, 340–343 (2015).

(2) K. Harada *et al.*, *Applie Physics Express* (in press).

(3) H. Nakajima *et al.*, Microscopy, 67, 207–213 (2018).

Fig. 1:

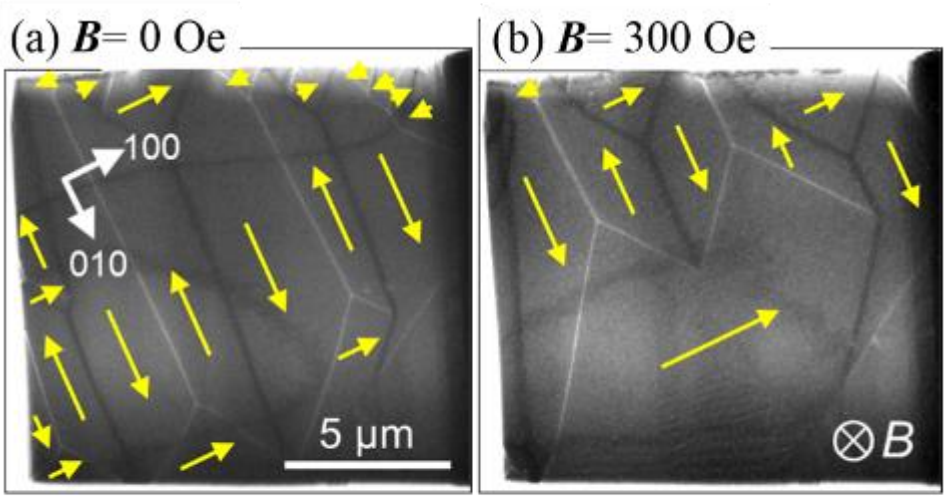

Fig.1 Changes of magnetic domain structures by applying the strength of magnetic fields of (a) 0 Oe and (b) 300 Oe.

MS1.P001
Growth feature characterization of laser annealed GeSn films on insulators by EBSD method

R. Matsumura[1], W. Jevasuwan[1], N. Fukata[1]

[1]National Institute for Materials Science, International Center for Materials Nanoarchitectonics, Tsukuba, Japan

Thanks to their high carrier mobility and direct band structure, germanium tin alloys (GeSn) attract much attention to realize next generation electronics (1,2). To apply such significant properties to thin-film devices, we have investigated continuous-wave (CW) laser annealing (LA) method to grow polycrystalline GeSn film on insulating substrates.

In the experiment, amorphous Ge (a-Ge) or a-GeSn films with Sn concentration of 17% (thickness: 100 nm) were firstly deposited on quartz substrates by molecular beam deposition. Laser lights (wavelength: 532 nm, energy density: 1.6 x 10^9 W/m^2) were irradiated on the samples. Here, laser irradiation time (t_{irr}) was varied from 0.67 to 3.0 μs. Samples were characterized by microscopic Raman spectroscopy (facility designed by PHOTON Design corp.), and electron back scattered diffraction (EBSD) method (JEOL JSM-7000F with EBSD detector designed by TSL solutions corp.).

Fig. 1(a) shows Raman signals measured at surface of GeSn thin film before and after LA (t_{irr}: 1.5 μs). We can see clear peak around 300 cm^{-1} due to Ge-Ge atomic bond after LA, which supports that GeSn film has been successfully crystallized by LA. Peak intensity and full width at half maximum (FWHM) of Raman signals are summarized as a function of tirr in Fig. 1(b). Interestingly, we can clearly see that the peak intensity of Raman signal measured from GeSn film increases with increasing t_{irr}, while that of Ge film shows little dependence on t_{irr}. Moreover, we can also say that FWHM of the Raman peak measured from GeSn samples decreases with increasing t_{irr}, while that of Ge film showed little dependence. From these results, we can say that crystallization of GeSn film proceeds with increasing t_{irr}, while that of Ge film has little dependence on t_{irr}.

To discuss the growth feature of GeSn films, EBSD measurements were carried out. Mapping images of Ge and Sn signals are summarized in Fig. 2 as a function of t_{irr}. Here, we can clearly see the Sn crystal signals for all $t_{irr,}$ while Ge crystal signal does not appear for short t_{irr}. These results strongly suggest that crystallization of GeSn occurs following to Sn precipitation, due to the low solid solubility of Sn in Ge (~1%), and that such Sn precipitation triggers the crystallization of GeSn. This is a very interesting finding in the field of GeSn crystal growth. Detailed physics will be discussed with more supporting data during the presentation.

References:

(1) D.W. Jenkins and J.D. Dow, Phys. Rev. B 36, 7994 (1987).

(2) S. Gupta, Y.-C. Huang, Y. Kim, E. Sanchez, and K.C. Saraswat, IEEE Electron Device Lett. 34, 831 (2013).

Fig. 1

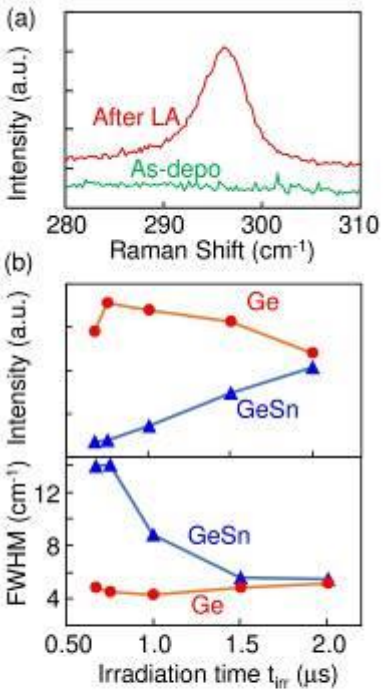

Fig. 1 (a) Raman signals of GeSn sample before and after LA for 1.5 μs. (b) Intensity and FWHM of Ge-Ge bonding peak of samples after LA as a function of laser irradiation time.

Fig. 2

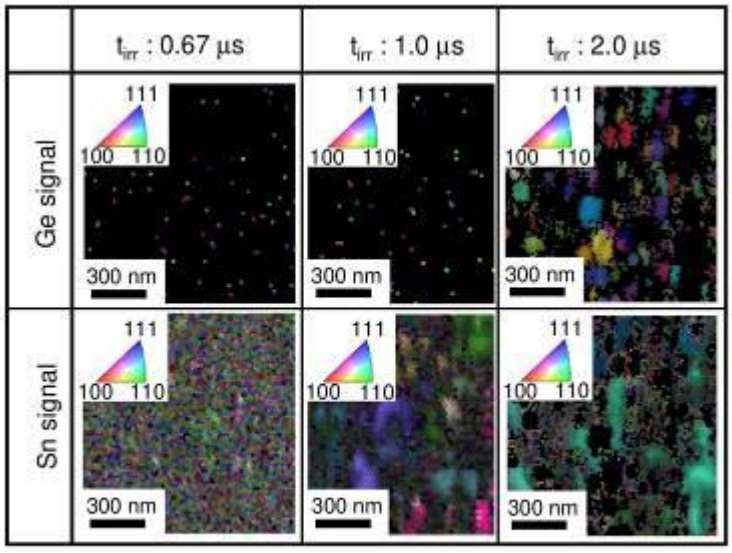

Fig. 2 EBSD images of GeSn samples after LA with various irradiation times.

MS1.P002
Characterization of Selective-area Growth (SAG) hetero-structures for quantum computing devices

E. M. Fiordaliso[1], J. H. Kang[2], M. Rajpalke Krishnappa[2], P. Krogstrup[2]

[1]DTU Nanolab, Lyngby, Denmark
[2]Niels Bohr Institute and Microsoft Quantum Materials Lab, University of Copenhagen, Copenhagen, Denmark, Copenhagen, Denmark

III–V semiconductor nanowires have shown great potential in various quantum transport experiments. However, realizing a scalable high-quality nanowire-based platform that could lead to quantum information applications is challenging. Selective-area growth (SAG) is a promising technique for enabling of the fabrication of the scalable III−V nanowire (NW) networks required to test proposals for Majorana-based quantum computing devices. By using the SAG approach, high quality semiconductor-superconductor hybrids can be grown and patterning of topological superconducting networks can be fabricated. Compared to traditional methods for NWs growth, such as vapor−liquid−solid (VLS), SAG allows a change of geometry from vertical nanowires to an in-plane growth of NW networks, with a large number of NW interconnections (1-3).

SAG was realized on a (100) GaAs substrate. PECVD grown SiOx was patterned using electron beam lithography and wet etching. A GaAs(Sb) buffer was grown on the substrate and a second InGaAs buffer was grown on top of the first one. The buffered geometry allows for substantial elastic strain relaxation and a strong enhancement of field effect mobility. InAs wires with triangular cross-sections were grown by molecular beam epitaxy (MBE). The Al was grown in-situ by MBE using angled deposition covering one of the facets.

Figure 1 shows the morphology of the SAG NWs. Figure 1 (a) is a SEM image of four NWs grown in-plan on the GaAs substrate. Figure 1 (b) is a magnified SEM image of one of the NWs, acquired at 52°, showing the truncated central (1-10) facet surrounded by the three (111) facets of InAs. Figure 1 (c) and (d) are an illustration of the NW cross section and the corresponding FIB cut, showing the buffered layer structure and the triangular InAs NW.

The quantum device performance of the individual SAG NWs are affected by the atomic arrangement in the heterostructures and particularly at the interface between the individual NWs and their buffer. The interface is therefore investigated at the atomic level using HAADF-STEM images acquired from a FIB lamella containing the NWs. The composition of the different layers is measured by STEM-EDX and EELS, while the strain is measured from atomic resolved images using Geometrical Phase Analysis (GPA).

Atomic resolved STEM images of the InGaAs/InAs interface are shown in Figure 2, corresponding to a FIB cut from a (100) oriented in-plane NW. In this segment, we observe an epitaxial interface with no defects. This is the ideal case, however, the overall structure contains a low density of defects and dislocations, which affect the device performance and reduces the conductivity.

In order to improve the device performance, the growth of the InGaAs second buffer has to be optimized in terms of growth rate and temperature, with the aim of eliminating atomic defects and achieve the best quantized conductance.

References:

(1) Krizek, Filip, et al. *Physical Review Materials*2.9 (2018): 093401.

(2) Aseev, Pavel, et al. *Nano letters*19.1 (2018): 218-227.

(3) Vaitiekėnas, S., et al. *Physical review letters*121.14 (2018): 147701.

Fig. 1: (a) SEM image of four in-plane SAG NWs acquired at 0° and (b) of a magnified NW acquired at 52°. (c) Illustration of the SAG NW cross section. (d) FIB cross section.

Fig. 2: HAADF STEM images of InGaAs/InAs interface at increasing magnification, showing an epitaxial interface.

Fig. 1

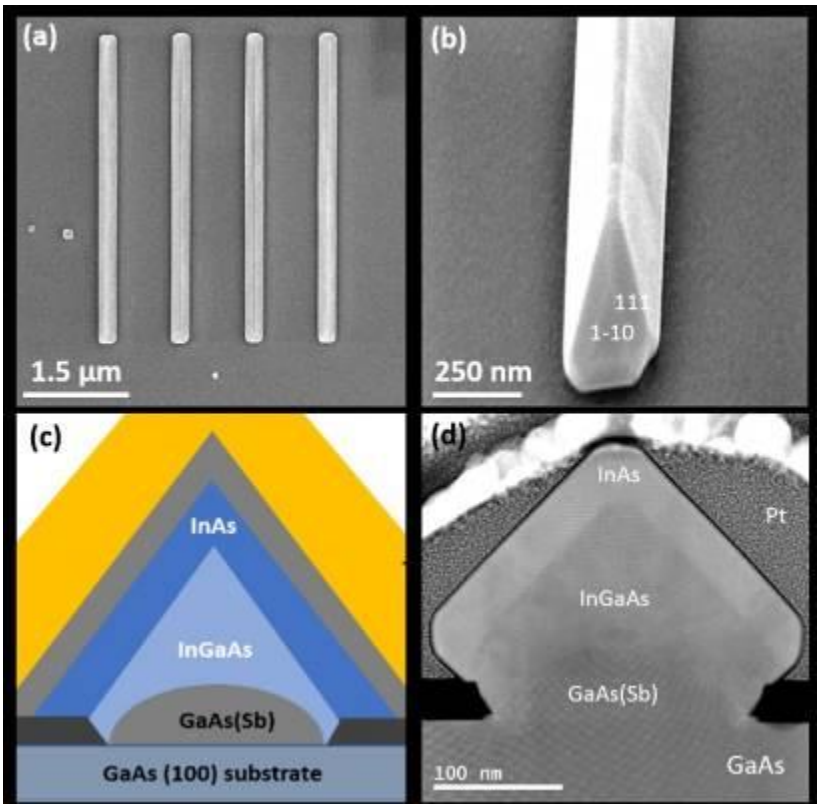
(a)
1.5 µm
(b)
111
1-10
250 nm
(c)
InAs
InGaAs
GaAs(Sb)
GaAs (100) substrate
(d)
InAs
Pt
InGaAs
GaAs(Sb)
100 nm
GaAs

Fig. 2

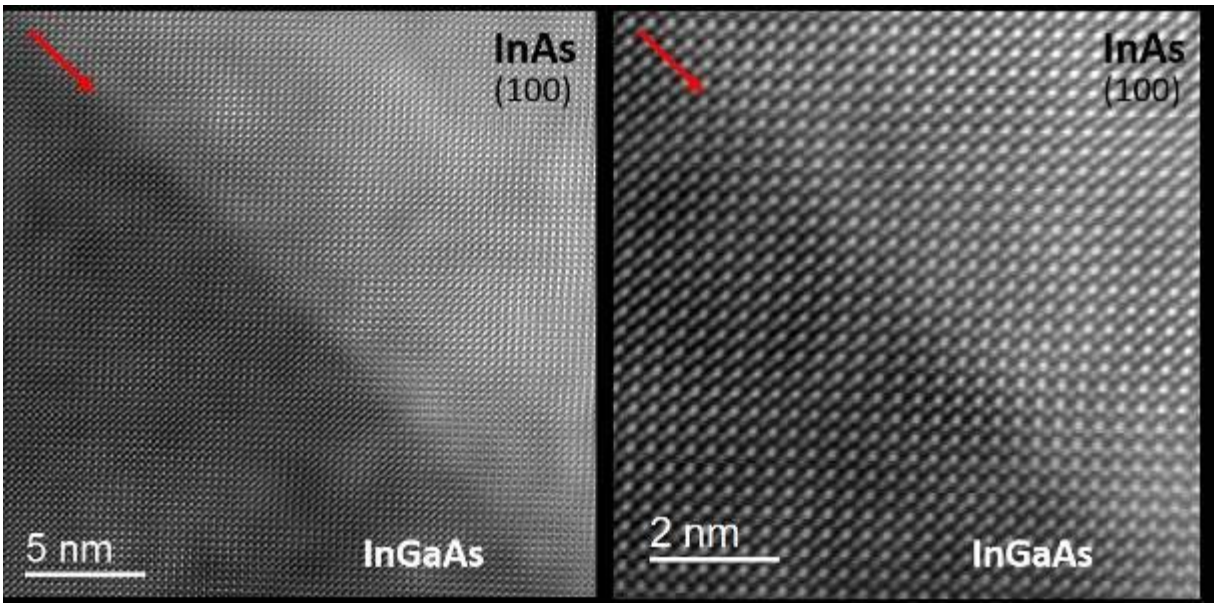
InAs
(100)
5 nm
InGaAs
InAs
(100)
2 nm
InGaAs

MS1.P003
On the dislocation inclination and strain in Si-doped GaN

J. Weinrich[1,2], A. Mogilatenko[1,2], F. Brunner[1], M. Weyers[1], C. T. Koch[2]

[1]Ferdinand-Braun-Institut, Leibniz-Institut für Höchstfrequenztechnik, Berlin, Germany
[2]Humboldt University of Berlin, Institute of Physics, Berlin, Germany

The (Al,Ga)N material system is widely used for applications like LEDs, lasers and high power transistors. Heteroepitaxial growth by metalorganic vapour-phase epitaxy (MOVPE) on sapphire or SiC substrates leads to a high density of threading dislocations (TDs) of about 109 cm-2 limiting the device efficiencies. The incorporation of silicon for n-doping induces tensile strain and an inclination of TDs into <1-100> directions (1,2,3) in GaN. Several studies presume different origins for these effects. Two different approaches are considered as the most important ones. The so called surface mediated climb model assumes that TD movement (inclination) is always a process to minimize lattice energy by strain release (1,2). The other approach is that Si hinders the growth of the dislocation half plane for edge and mixed type TDs (3). As the GaN growth on sapphire takes place under tensile strain these two models lead to opposite directions of TD inclination with respect to the half plane position as shown in Fig. 1 (b,c).

The goal of our experiment was to find the correlation between the inclination direction and the half plane position of TDs in Si-doped GaN layers in order to clarify the origin of the inclination. A Si-doped and an undoped GaN layer grown by MOVPE on a sapphire substrate were examined. Scanning transmission electron microscopy (STEM) analysis showed a broad distribution of inclination directions of the TD lines around the reported <1-100>-direction in the Si doped GaN layer (Fig. 2). However, in undoped GaN the TDs incline mainly into <11-20>-directions. Using tilting series in low magnification STEM and high resolution STEM we show for the first time that the half plane size is decreased by the inclination due to Si-doping. This indicates a hindering of the half plane growth and favours the inclination model shown in Fig. 1c. It further explains the increase of tensile strain in GaN as well as the reduction of compressive strain in AlGaN on AlN by Si introduction. Additional inclination into the <11-20>-directions in doped and undoped GaN takes place simultaneously. This explains the distribution of the inclination directions in Si-doped GaN.

References:

(1) M. A. Moram, *Journal of Applied Physics* 109 (2011), 073509

(2) K. Forghani et al., *Journal of Applied Physics* 112 (2012), 093102

(3) A. Dadgar et al., *Applied Physics Express* 4 (2011), 011001

Fig. 1: Different models for TD inclination and the resulting inclination direction. Strain driven, surface mediated climb in a) compressively and b) tensely strained layers. c) Model of TD inclination caused by SixN masking.

Fig. 2: a) Distribution of TD inclination directions in doped and undoped GaN grown on sapphire (m and a correspond to <1-100> and <11-20> directions). b) Cross-section ADF STEM image showing TD inclination in Si-doped and undoped GaN.

Fig. 1

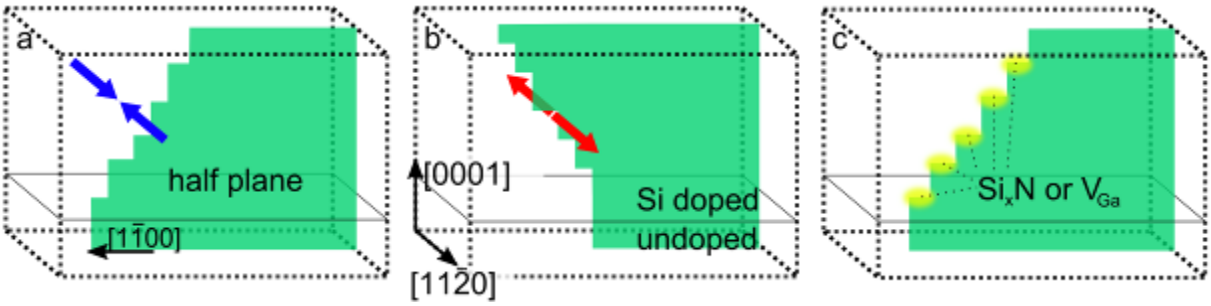

Fig. 2

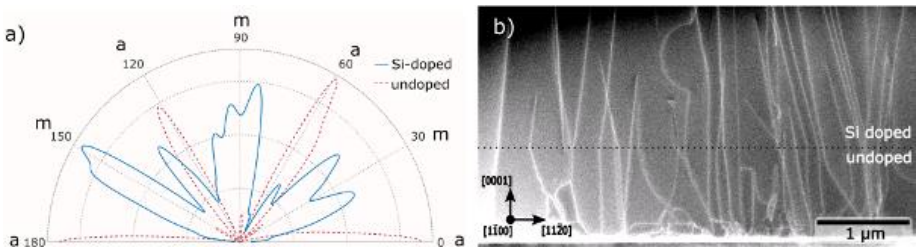
a)
m
90
a
120
a
60
m
150
30
m
a
180
0
a
Si-doped
undoped
b)
Si doped
undoped
[0001]
[1$\bar{1}$00]
[11$\bar{2}$0]
1 µm

MS1.P004
In situ heating experiments: Structural changes and their relation to electrical properties for $Ge_6Sn_2Sb_2Te_{11}$

T. Dankwort[1], C. Koch[2], A. L. Hansen[3], D. C. Johnson[4], M. Wuttig[5], W. Bensch[1], L. Kienle[1]

[1]University of Kiel, Kiel, Germany
[2]University of Applied Sciences Bremerhaven, Bremerhaven, Germany
[3]Karlsruhe Institute of Technology, Karlsruhe, Germany
[4]University of Oregon, Eugene, OR, United States
[5]RWTH Aachen, Aachen, Germany

Thin films of Ge-Sb-Te materials are known for their unique properties which make them ideal candidates for non-volatile data storage applications. The reversible phase change between the amorphous and the crystalline structure represents high and low resistive states. However, micro and nanostructural changes, especially those which are connected to structural vacancies, play a decisive role in multilevel data storage applications

Our study focuses on the micro- and nanostructural changes occurring by heating an amorphous $Ge_6Sn_2Sb_2Te_{11}$ thin film. Therefore *in situ* TEM and XRD studies were performed to reveal nano- and microstructural changes. These structural changes are correlated to changes in the electrical properties of the material.

$Ge_6Sn_2Sb_2Te_{11}$ represents Sn substituted $Ge_8Sb_2Te_{11}$ which is used as storage medium in blue-ray discs. Thin amorphous films of $Ge_6Sn_2Sb_2Te_{11}$ were deposited by sputtering and phase changes were investigated by in situ XRD and TEM measurements. Further temperature dependent resistivity measurements were performed ex situ using the van der Pauw method.

Besides the amorphous phase three different crystalline phases were observed which can be separated by their unique distribution of structural vacancies on cationic sites.

At 112 °C the films started to crystallize. In the temperature range of 112 °C – 130 °C a so far for $Ge_8Sb_2Te_{11}$ unreported (pseudo) cubic phase with statistically distributed structural vacancies was observed.

At ~ 130 °C structural vacancies start to order and form vacancies layers. It could be demonstrated for the first time that these ordering processes are associated with a domain growth/coalescence process.

At ~ 260 °C a gradual transition to a trigonal phase with van der Waals gaps is observed. It could be demonstrated that an in plane movement of defects, so called bi-layer defects, largely increases the structural order of the materials. This mechanism was recently proposed but so far could not be observed directly by means of *in situ* observations.

The temperature dependent resistivity measurements revealed an extra intermediate resistive state which appears in the same temperature region with sole presence of the strongly disordered (pseudo) cubic phase.

In summary, micro and nanostructural changes in amorphous $Ge_6Sn_2Sb_2Te_{11}$, were studied in detail by *in situ* XRD and TEM heating experiments. The formation of a pseudo cubic phase lead to the presence of an extra intermediate resistivity state.

References:

(1) C.Koch, T.Dankwort et al., Acta Materialia, 152, 2018

MS1.P005
Characterisation of Crystalline Defects in As-Transformed and Hot-Deformed τ-MnAl Alloys using Weak-Beam Dark Field Imaging

P. Zhao[1,2], K. Nielsch[1,2], T. G. Woodcock[1]

[1]IFW Dresden, Institute for Metallic Materials, Dresden, Germany
[2]TU Dresden, Dresden, Germany

The L10-ordered, thermodynamically metastable phase τ-MnAl exhibits a high uniaxial magnetic anisotropy, high magnetisation and contains no critical elements, making it a highly promising rare-earth free permanent magnetic material. The thermal stability of the τ-phase at high temperatures could be improved through the addition of carbon, however, the low coercivity currently achieved (<10% of the anisotropy field) is still the main obstacle for the real application of MnAl magnets. Studies have found that the extrinsic magnetic properties (remanence, coercivity and energy density) could be greatly improved through hot deformation compared to the as-transformed state. If detailed knowledge about defects in both as-transformed and deformed τ-MnAl-C alloys is obtained, further improvements, particularly in coercivity, could be made, as defects interact with magnetic domain walls. In this study, various defects including dislocations, stacking faults, twin boundaries and grain boundaries have been characterized in both as-transformed and deformed τ-MnAl-C alloys by transmission electron microscopy (TEM) using weak-beam dark-field analysis or bright/dark field image analysis. The results revealed that the density of these defects are very sensitive to the sample state, stacking faults and dislocations decreased greatly in the deformed samples. In addition, the decreased grain size in the deformed τ-MnAl-C sample may be the main reason for the improvement of coercivity due to pinning of domain walls at grain boundaries. Further studies about the atomistic structure and elementary segregation at these defects should be investigated in order to deep our understanding about the interaction of magnetic domain walls and these defects.

MS1.P006
LTEM and DPC measurements on room temperature magnetic skyrmions in Pt/Co/W and Pt/Co/Tb multilayers

S. Pöllath[1], T. Lin[2], H. Liu[3], Y. Zhang[4], B. Ji[2], N. Lei[2], J. J. Yun[5], L. Xi[5], D. Z. Yang[5], T. Xing[2], Z. L. Wang[2], L. Sun[3,6], Y. Z. Wu[3], L. F. Yin[3], W. B. Wang[3], J. Shen[3], J. Zweck[1], C. H. Back[1,7], Y. G. Zhang[2], W. S. Zhao[2]

[1]University of Regensburg, Institute for experimental and applied physics, Regensburg, Germany
[2]Beihang University, Beijing, China
[3]Fudan University, Shanghai, China
[4]Chinese Academy of Sciences, Beijing, China
[5]Lanzhou University, Lanzhou, China
[6]Shanghai Technology University, Shanghai, China
[7]Technische Universität München, Garching, Germany

Magnetic Skyrmions are a potential candidate for future data storage and spintronics applications. The first experimental discovery was done with Small Angle Neutron Scattering (SANS) from the bulk chiral B20 material MnSi at temperatures below 30K, where a hexagonal lattice of skyrmions was evidenced (1). With a Transmission Electron Microscope (TEM), magnetic skyrmions can be conveniently observed in real space using phase related techniques like Lorentz-TEM (LTEM), electron holography or Differential Phase Contrast (DPC) microscopy (2,3,4).

To approach a technological application, skyrmion hosting materials with a T_c well above room temperature need to be investigated (5). Microscopic classification includes the skyrmion size, magnetic phase diagram with respect to temperature and applied magnetic field as well as topological charge density determination.

In this work multilayer systems of Pt/Co/W and Pt/Co/Tb stacks are investigated. Due to the interfacial Dzyaloshinskii-Moriya interaction, Neel-type skyrmions are present in these systems. Therefore, a sample tilt is required to image the skyrmions. LTEM and DPC is used to characterize the skyrmion size in combination with magnetic phase simulations. The magnetic phase diagram and topological charge map is studied with LTEM using a liquid nitrogen holder.

The magnetic phase diagram is retrieved and for the case of field increase from zero field, the skyrmions are generated as topological remnants of the stripe phase (Fig. 1 (a)-(d)). The magnetic contrast is shown for DPC and LTEM and is in agreement with contrast simulations. Using those the actual skyrmion size is related to the observed contrast. As an example for LTEM, the contrast for a single skyrmion is shown for three different sample tilt angles in Fig. 1 (e)-(g). The contrast profile along the tilt axis is taken and compared to simulations in Fig. 1(h).

LTEM and DPC are suitable methods to characterize Room Temperature skyrmion samples. The size is best evaluated using the in-focus technique DPC. The increased contrast of LTEM compared to DPC makes it the best tool to quickly sample the magnetic phase diagram.

References:

(1) Mühlbauer S., et al., *Science* 323, 915 (2009)

(2) Yu X. Z., et al., *Nature* 465, 901 (2010)

(3) Park H., et al., *Nat. nanotechnol.* 9, 337 (2014)

(4) Schneider S., et al. *Phys. Rev. let.* 120, 217201 (2018)

(5) Pollard S. D., et al., *Nature commun. 8*, 14761 (2017)

Fig 1: LTEM image of (a) the magnetic labyrinth domains at zero field, (b) extended domains with residual stripe domains and skyrmions, (c) magnetic skyrmions and (d) reduced number of magnetic skyrmions due to increased field. (e)-(g) Sample tilt series for a single magnetic skyrmion. (h) Image profile along skyrmion contrast and included contrast simulations.

Fig. 1

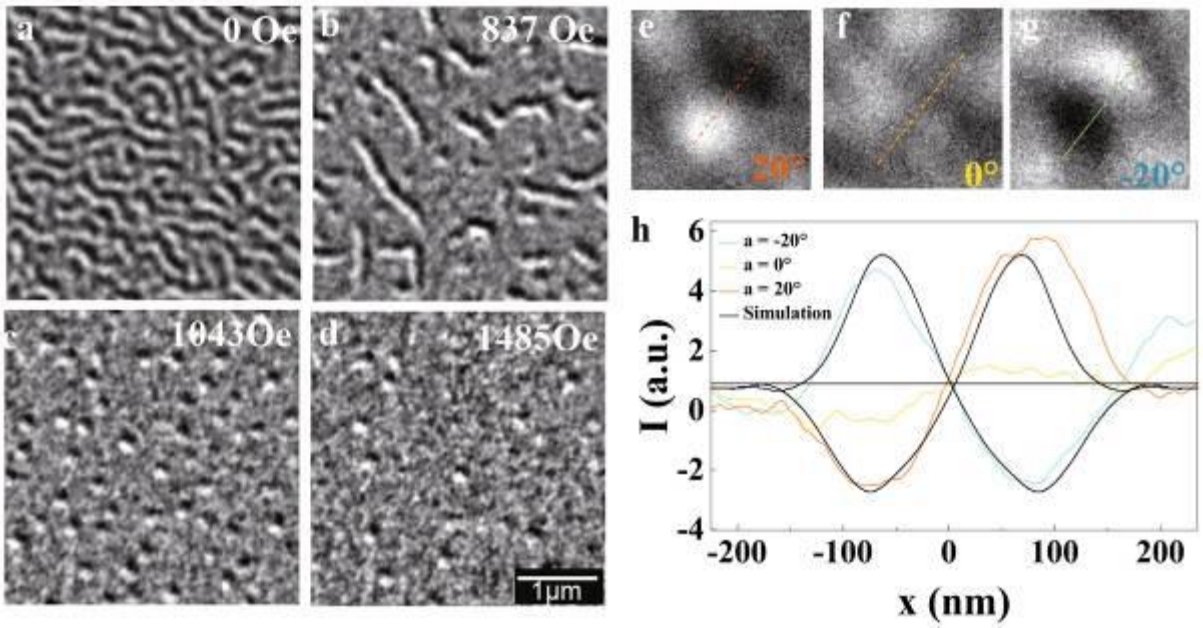
a
0 Oe
b
837 Oe
c
1043Oe
d
1485Oe
1μm
e
20°
f
0°
g
-20°
h
a = -20°
a = 0°
a = 20°
Simulation
I (a.u.)
x (nm)
6
4
2
0
-2
-4
-200
-100
0
100
200

MS1.P007
Analysis of Polar Structures in Relaxor Ferroelectrics with Wide Temperature Ranges of Stability

T. Roncal-Herrero[1], R. Brydson[1], A. Zeb[1,2], S. Milne[1], A. P. Brown[1]

[1]University of Leeds, School of Chemical and Process Engineering, Leeds, United Kingdom
[2]Islamia College, Peshawar, Pakistan

In the search for Class II capacitor materials with stable relative permittivity, εr, to temperatures exceeding 200°C for renewable energy and harsh environment applications, a number of relaxor ferroelectric ceramics, all of which contain Bi, have attracted attention. There is uncertainty as to the mechanism responsible for the suppression of the dielectric relaxation peak and the near-flat εr response across wide temperature ranges, extending to limiting temperatures >300°C.

Investigations as to the cause of stable relative permittivity are presented, based on analytical scanning transmission electron microscopy (STEM) analyses of the relaxor solid solution systems: $(1-x)BaTiO_3$ - $xBi(M_{0.5}Ti_{0.5})O_3$;M= Mg or Sc. Nanoscale compositional segregation is revealed within the perovskite phase at high levels of Mg or Sc substitution, close to the limiting compositions that give near-flat εr(T)responses. The possibility that changes in bulk polarisation in the ergodic region are supressed because of this compositional immiscibility is discussed. The STEM data, in association with εr(T) trends, imply that segregated, weakly polar Bi and Mg/Sc rich nanoregions inhibit the increase in polar order that normally occurs in a relaxor ferroelectric as it cools below the Burns temperature. Based on these findings, a final overview of options for developing Bi-free materials with similar levels of performance, but which are compatible with industrial processes for manufacturing multilayer capacitors will be presented.

MS1.P008
Interface effects on the ferroelectric polarization in ultrathin $PbTiO_3$ films investigated by ISHG and HAADF imaging

A. Vogel[1,2], N. Strkalj[2], M. Campanini[1], C. Gattinoni[2], N. Spaldin[2], M. Rossell[1], M. Fiebig[2], M. Trassin[2]

[1]Empa Dübendorf, Electron Microscopy Center, Dübendorf, Switzerland
[2]ETH Zürich, Department of Materials, Zürich, Switzerland

During the last decade, a strong focus in condensed-matter physics and material science has been on the construction of atomically sharp perovskite oxide heterointerfaces. This has led to the deterministic control of ultrathin functional oxide interfaces at the atomic level, revealing novel interfacial properties, such as two-dimensional electron gases, superconductivity, ferromagnetism, and multiferroicity, which are not inherent to the individual constituents.

In ferroelectric heterostructures, atomic-scale interface engineering leads to the control of bulk properties, namely the domain state and polarization orientation. Taking uniaxial ferroelectric PbTiO3 ferroelectric thin films as model system, we investigate the emergence of the polarization in the ultrathin regime for different interfacial atomic terminations. Using a combination of in-situ optical second harmonic generation (ISHG)(1) and aberration-corrected scanning transmission electron microscopy (STEM), we reveal the different interface contributions of the atomically controlled bottom interface and the free surface of the ferroelectric layers in the enforcement of the polarization orientation.

Specifically, two PbTiO3 thin films are grown by pulsed laser deposition on either MnO2 or LaO terminated LaSrMnO3 buffered SrTiO3 substrates. The polarization dynamics of the corresponding downwards and upwards enforced polarized films is monitored ISGH. Further, differences in the atomic structure of the PbTiO3 layers depending on the termination-sequence at the PbTiO3 - LaSrMnO3 interface are investigated by quantitative analysis of high-angle annular dark-field (HAADF) STEM images. Figure 1 shows a HAADF-STEM image of a PbTiO3 thin film along the [010] zone axis. The structural information is obtained by fitting the atomic positions using the python library atomap (2). The overlaid yellow arrows point to the polarization vector resulting from the off-centering of the Ti cation from the center of its four Pb neighbors; they are plotted opposite to the polar atomic displacements. Besides, the analysis of the strain state (tetragonality) of the two films reveals clear differences between the two PbTiO3 films.

We show that the macroscopic polarization dynamics during the film synthesis alters drastically depending on the polarization orientation of the films. The interaction of the ferroelectric surface with the growth environment results in either a strong enhancement or suppression of the macroscopic polarization of the thin films, which is driven by the choice of atomic terminations and polarization orientation. Post growth measurements of the polar atomic displacements and of the tetragonality distribution using HAADF-STEM confirm the interface impact on the internal polarization state. Our results demonstrate the interface competition in the onset of the ferroelectric state in PTO thin films in the ultrathin regime and identify routes to enhance the polarization of ultrathin films.

References:

(1) G. De Luca, N. Strkalj, S. Manz, C. Bouillet, M. Fiebig, and M. Trassin, Nat. Commun. 8, 1419 (2017)

(2) M. Nord et al., Advanced Structural and Chemical Imaging 2017, 3:9

Fig. 1: (a) Polarization map calculated from the atomic displacement superimposed on a HAADF image. (b) Average atomic displacement of B-site atoms. (c) Average tetragonality of the A-site atoms.

Fig. 1

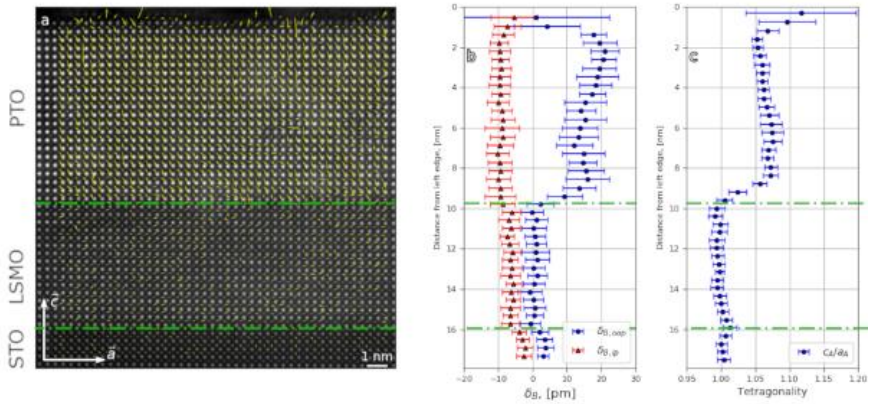

MS1.P009
Electron tomography of InGaN/GaN dot-in-a-nanowire structure

L. Nicolai[1], Z. Gačević[2], E. Calleja[2], A. Trampert[1]

[1]Paul-Drude-Institut für Festkörperelektronik, Berlin, Germany
[2]Universidad Politécnica de Madrid, ISOM-ETSIT, Madrid, Spain

The ongoing process of miniaturization of optoelectronic devices has given rise to the development of complex, three-dimensional (3D) nanostructures. In this respect, nanowires (NWs) in core-shell geometry are promising candidates due to the large surface-to-volume ratio. A detailed microstructural analysis of the 3D heterostructures is necessary to understand the influence of NW morphology, shell thicknesses and local chemical composition on the optical emission characteristics.

However, the lower symmetry of these 3D nanostructures compared to e.g. planar systems makes the interpretation of transmission electron microscope (TEM) images far more difficult. This work presents the use of electron tomography to circumvent the challenging interpretation of single projections of core-shell NWs.

The goal of this work is to apply electron tomography method for detecting and analyzing the morphology and chemical composition of complex 3D dot-in-a-nanowire structures based on InGaN/GaN core-shell NWs.

GaN/InGaN/GaN core-shell-shell NWs were grown on a GaN-on-sapphire (0001) template by plasma-assisted molecular beam epitaxy using a Ti nano-hole mask produced by colloidal lithography. A sophisticated focused ion-beam preparation was applied to fabricate needle-shaped specimens containing only a single NW. A tilt series of high-angle annular dark-field (HAADF) scanning TEM (STEM) micrographs with steps of 2° was recorded and used for the tomographic reconstruction. Subsequently, slices of different orientations and isosurface representations were extracted out of the 3D data to visualize and analyze the NW core-shell structure.

The isosurface representation (cf. Fig. 1) of the GaN outer shell reveals the crystal shape und surface faceting of the NW. As expected, the lower section of the NW consists of six energetically favored m-plane facets whereby the NW tip reflects a pyramidal shape being composed of s- and r-plane facets, which are, however, not perfect symmetrically positioned to each other. This asymmetry in the pyramidal tip shape is associated with the presence of an inversion domain.

Longitudinal and transversal slices (cf. Fig. 2) through the reconstruction reveal the internal (In,Ga)N shell structure. The slices allow the complete determination of shell thicknesses and verify variations of the (In,Ga)N shell composition. The overall development of the (In,Ga)N shell morphology deviates to some extent from the expected 6-fold symmetry, which is not the case for the outer GaN shell. Moreover, the dot-in-a-nanowire structure is clearly resolved inside the NW tip by sharp increase in the indium content. The 3D form of the dot resembles an inverse truncated pyramid with distorted hexagonal base. Energy dispersive x-ray (EDX) spectroscopy is applied to compare the intensities of the tomographic slices based on HAADF contrast with EDX maps in order to discuss the sensitivity of chemical concentration in the tomographic reconstruction.

An InGaN/GaN core-shell NW has been investigated by electron tomography. The faceting and spatial distribution of the chemical composition of the NW core, shell and dot-in-a-nanowire structure is revealed unambiguously. It has been shown that the symmetry of the NW is disturbed by defect interactions. The results demonstrate that electron tomography allows insights into the evolution of the core-shell structure formation during growth.

Fig. 1

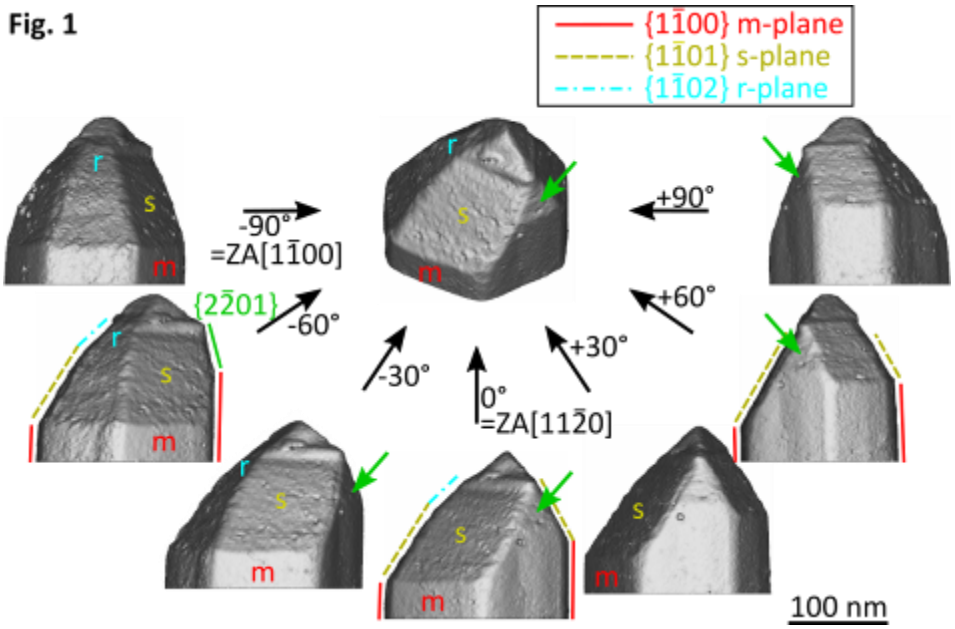
Fig. 1
{1$\bar{1}$00} m-plane
{1$\bar{1}$01} s-plane
{1$\bar{1}$02} r-plane
r
s
m
-90°
=ZA[1$\bar{1}$00]
+90°
{2$\bar{2}$01}
-60°
+60°
-30°
+30°
0°
=ZA[11$\bar{2}$0]
100 nm

Fig. 2

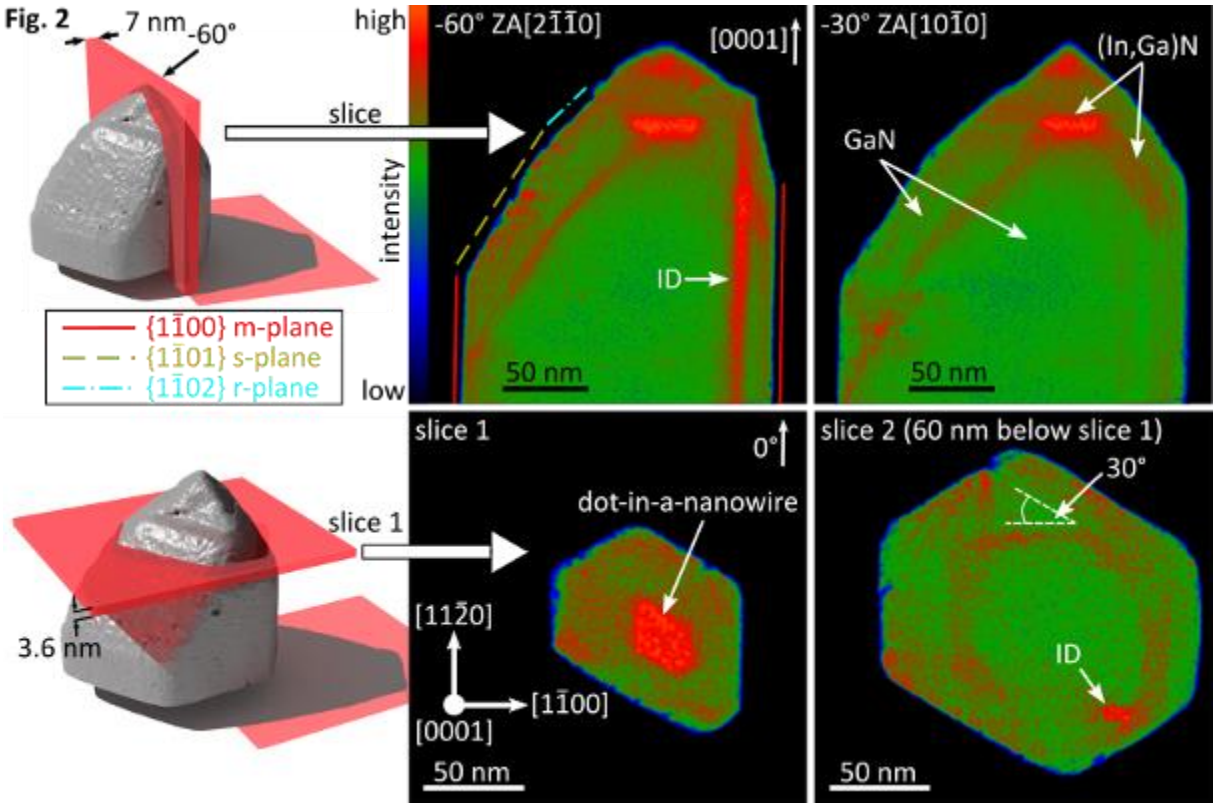
Fig. 2
7 nm
-60°
high
low
slice
intensity
{1$\bar{1}$00} m-plane
{1$\bar{1}$01} s-plane
{1$\bar{1}$02} r-plane
-60° ZA[2$\bar{1}\bar{1}$0]
[0001]
ID
50 nm
-30° ZA[10$\bar{1}$0]
(In,Ga)N
GaN
50 nm
slice 1
3.6 nm
slice 1
0°
dot-in-a-nanowire
[11$\bar{2}$0]
[1$\bar{1}$00]
[0001]
50 nm
slice 2 (60 nm below slice 1)
30°
ID
50 nm

MS1.P010
A Spectroscopic Study on the Nature of Electron-Beam-Induced Damage in Transition Metal Thiophosphates

J. Köster[1], M. K. Kinyanjui[1], U. Kaiser[1]

[1]Electron Microscopy Group of Materials Science, Ulm University, Ulm, Germany

Transmission electron microscopy (TEM) methods offer excellent probes to study the structural and electron properties of low dimensional materials at high spatial resolution. However, the high energy electrons can cause physical damage accompanied with electronic and chemical changes in the sample. This may include creation of atomic vacancies, extended defects, phase transitions, as well as amorphisation. These damage processes are dependent on experimental factors such as the accelerating voltage of the microscope, electron dose, as well as specimen chemistry and thickness. The mechanisms of electron-beam-induced damage are not well understood and are a topic of intense research. Here we use electron energy loss spectroscopy (EELS) to study electron-beam-induced changes in transition metal thiophosphates (TMTPs) $MnPS_3$ and $FePS_3$. The choice of these materials is dictated by the fact that they show both ionic and covalent bonding character (1).

$FePS_3$ and $MnPS_3$ layers were prepared from bulk through mechanical exfoliation. EELS spectra were acquired at 80 kV using GIF attached to a Titan 80-300. The energy resolution was determined to be 0.6 eV. We used core-loss EELS spectroscopy obtained at the S $L_{2,3}$, Fe/Mn, $M_{2,3}$ (2), Fe $L_{2,3}$ and P $L_{2,3}$ edges (3) in order to study the effects of the beam-induced damage in these two systems. In the experiments, the peak positions and the fine structures (ELNES) of these edges were monitored as a function of electron dose and exposure time. These experimental investigations were supported by density functional theory (DFT) electronic structure and EELS spectra calculations.

Figure 1 shows the changes observed at the Fe $M_{2,3}$ edge of $FePS_3$ with prolonged exposure to the electron beam. In the spectra, both shift in the peak positions as well as the changes in the peak intensity ratios are observed as a result of prolonged exposure to the electron beam. These spectral changes point towards the changes in Fe valency as a result of the beam-induced damage on the structure. Similar spectral changes are also observed at the S and P-$L_{2,3}$ edges. Based on these experimental results as well as DFT calculations, we show that this is due to electron-beam-induced changes in S-S and P-S bonds.

In conclusion we have used electron energy loss spectroscopy to understand the interaction between the incident electron-beam and $MnPS_3$ respectively $FePS_3$ thin layers. Our EELS results point towards electron-beam-induced changes in the bonding character in these transition metal thiophosphates.

References:

(1) Brec, Solid State Ionics 22, 3 (1986).

(2) Van Aken, P. A., et al. *Physics and Chemistry of Minerals*7 (1999): 584-590.

(3) Laffont, L., et al. *Chemistry of Materials*23 (2006): 5520-5529.

Fig. 1: Fe M2,3 electron energy-loss near-edge structure in FePS3 during electron irradiation. The experiment was executed in an 80 kV Titan TEM with an energy resolution of 0.6 eV.

Fig. 1

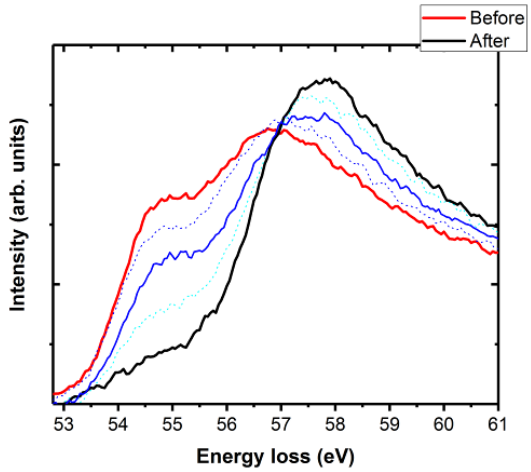
Before
After
Intensity (arb. units)
53
54
55
56
57
58
59
60
61
Energy loss (eV)

MS1.P011
Microstructural modifications in Josephson junctions created by focused helium ion beam irradiation of $YBa_2Cu_3O_7$

M. Becker[1,2], B. Schröppel[1], C. J. Burkhardt[1], B. Müller[2], M. Karrer[2], F. Limberger[2], R. Kleiner[2], E. Goldobin[2], D. Kölle[2]

[1]NMI Reutlingen, Center of Nanoanalytics, Reutlingen, Germany
[2]Universitiy of Tübingen, Physikalisches Institut, Tübingen, Germany

The invention of the He ion microscope (HIM) offers unprecedented spatial resolution in ion beam microscopy, not only for imaging, but also for modification of material properties on the nanoscale. Recently, the creation of Josephson barriers by focused He ion beam (He-FIB) irradiation of the cuprate superconductor $YBa_2Cu_3O_7$ (YBCO) has been demonstrated (1).

To get a deeper understanding of the microstructure-property relationship in He-FIB Josephson junctions, the local microstructural modifications caused by He ion irradiation, as a function of irradiation dose *D,* has to be investigated. This can be achieved by transmission electron microscopy (TEM), which requires the site-specific preparation of a TEM-lamella from the Josephson barrier region.

Epitaxial c-axis oriented YBCO thin films were grown by pulsed laser deposition (PLD) on (001)-oriented $SrTiO_3$ (STO), single crystal substrates. For electric transport measurements, Au layers were deposited in-situ after the PLD process, and we used photolithography and Ar ion milling to prepattern 4 µm wide YBCO microbridges. Subsequently, focused ion beam irradiation was done in a Zeiss Orion NanoFab He/Ne ion microscope (HIM) with 30 keV He^+ ions to fabricate the Josephson barriers. To image possible structural modifications in our YBCO films, we used scanning transmission electron microscopy (STEM). For the STEM studies, we irradiated a YBCO bridge with a series of parallel lines, using increasing doses from D = 50 to 10^5 ions/nm, with well-defined spacing between adjacent lines. Subsequently we prepared a cross-sectional TEM-lamella containing all irradiated lines, by in-situ lift-out using a Ga-FIB microscope together with a micromanipulator.

We found that the critical current density j_c of the He-FIB Josephson barriers decays exponentially with irradiation dose D (2). A simple explanation of the exponential decay of j_c with increasing D would be a linear increase of the junction barrier thickness. The STEM analysis showed that for doses higher than D = 1000 ions/nm, highly resistive amorphous tracks appeared and their width increases roughly linear up to the highest dose D=10^5 ions/nm. For D = 1000 ions/nm and below, we could not identify any change in the structure of the irradiated sections.

Our STEM analysis indicates that medium doses do not induce significant structural damage of the YBCO crystal lattice, which is consistent with the assumption that the He-FIB easily moves oxygen ions from the Cu-O chains to interstitial sites (3) and thereby altering the local electric transport properties of YBCO on the nanometer scale. This observation indicates that He-FIB is a promising tool for nanopatterning (without removal of material) of YBCO films with ultra-high spatial resolution.

References:

(1) S.A. Cybart *et al.*, Nature Nanotechnology 10, 598-602 (2015).

(2) B. Müller *et al.*, arXiv1901.08039 (2019).

(3) E.Y. Cho *et al.*, Appl. Phys. Lett 113, 022604 (2018)

MS1.P012
Analytical TEM investigation of structural changes in electrical stressed 0.25 µm AlGaN/GaN HEMTs

A. Graff[1], P. Diehle[1], M. Simon-Najasek[1], F. Altmann[1], M. Rzin[2], F. Rampazzo[2], M. Meneghini[2], G. Meneghesso[2], E. Zanoni[2], J. Grünenpütt[3], H. Jung[3], K. Riepe[3], H. Blanck[3], B. Lambert[4]

[1]FraunhoferInstitute for Microstructure of Materials and Systems IMWS , Electronic Materials and Components, Halle, Germany
[2]University of Padova, Information Engineering, Padova, Italy
[3]United Monolithic Semiconductors GmbH, Ulm, Germany
[4]United Monolithic Semiconductors S.A.S., Villebon sur Yvette, France

High electron mobility transistors (HEMTs) based on AlGaN/GaN heterostructure improved over the last two decades and moved into industrial use for RF power amplifiers in space and defense applications.

The stability and reliability under high dissipated power and high junction temperature should be ensured. Therefore a better understanding of degradation mechanisms limiting performance and electrical reliability is needed. In this work, we are focusing on structural failure modes of AlGaN/GaN HEMTs, related to the gate metallization, that are reducing the reliability of the devices.

The tested technology is based on GaN/AlGaN/GaN epitaxy grown by metal-organic chemical vapor deposition (MOCVD) on a SiC substrate. The studied AlGaN/GaN HEMTs are characterized by a 2x40 µm gate finger topology with a gate length of 0.25 µm. The devices have a Ni/Pt/Au Schottky gate metallization. Hot-electron characterization was carried out by means of electroluminescence (EL) microscopy where differences in the EL signal could be detected between center and rim of the transistor structures. These results are used to determine reasonable positions for the TEM cross section preparation. Three HEMTs (Samples A, B, C) were selected to investigate the structural changes at the Schottky gate after a 24h electrical test under different DC conditions (Table 1). Two TEM cross sections were prepared by FIB (Zeiss, NVision) out of each HEMT, one at the rim and one near the center of a gate finger. The cross sections were investigated in detail by means of TEM, STEM and EDX (FEI, Titan XFEG and SuperX system).

Table 1: DC 24h electrical test scenario for the three selected devices.

TEM investigations of the HEMT cross sections show structural changes in the semiconductor mainly in the barrier layer in the Schottky gate region. Here pitting into the AlGaN barrier layer could be observed at the dielectric / semiconductor interface. It is assumed that these pits are formed at position of high electrical fields. The pit formation gets more pronounced for the higher loaded HEMT structures (Fig. 1). Oxygen diffuses into the Pits during the 24h test (Fig.2).

Beside the pit formation structural changes at the metal / semiconductor interface can be observed where Ga is missing in the AlGaN layer and oxygen gets into the barrier. This Ga deficit is correlated with gold diffusion through the Pt and Ni gate metal layers to the Schottky barrier. These significant structural changes explain the measured reduction in transconductance.

The investigated AlGaN/GaN HEMTs show different level of degradation after 24 hours stress test depending on the dissipated power. The failure modes seemed to be thermally activated and enhanced by the electric field. The test results led to an improved technology qualified for space applications.

Fig. 1: HRTEM detail images of the Schottky gate edges in direction of the drain contact for sample A, B and C. Structural changes in the AlGaN barrier layer and the metal / semiconductor interface are highlighted by red circles.

Fig. 2: Normalized distributions of selected elements out of EDX mappings after 24h DC test (Sample A, B, C). Direction to the drain contact marked by D.

Fig. 1

W_G = 2x40 µm L_G = 0.25 µm	V_{GS} (V)	V_{DS} (V)	Dissipated power (W/mm)
A	0	30	22.6
B	1	38	31.5
C	0	60	36.7

Fig. 2

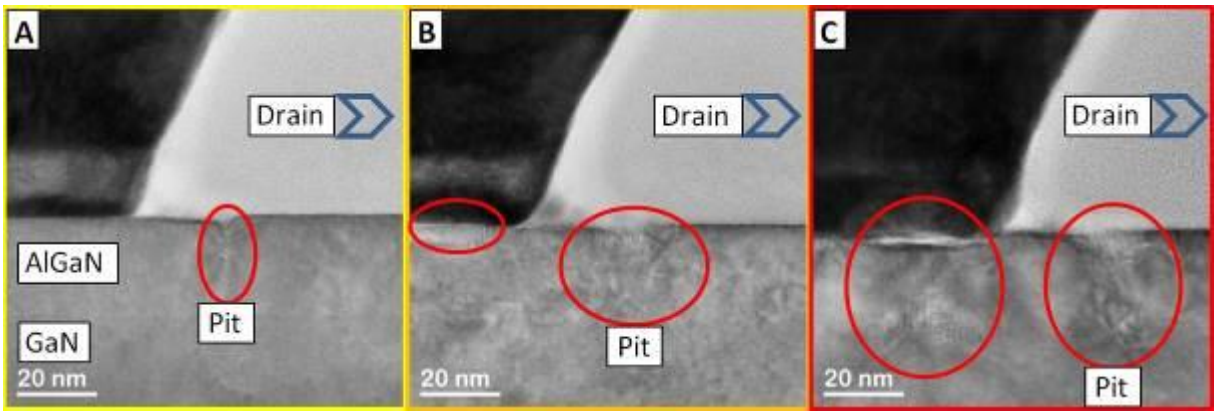

Fig. 3

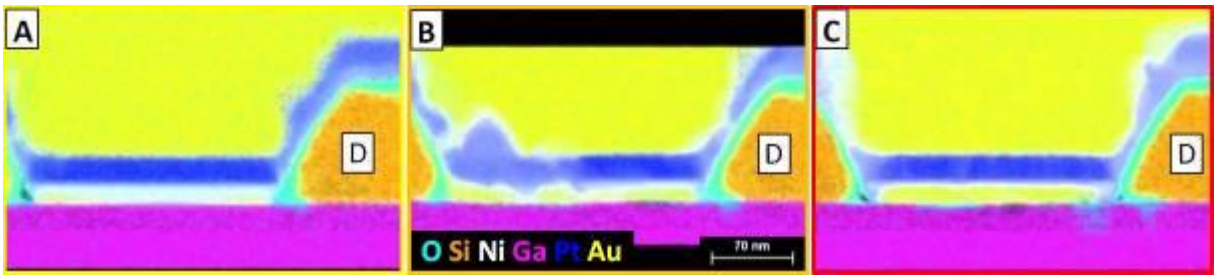

MS1.P013
Characterization of Solution-grown and Sputtered Inx(O,S)y Buffer Layers in Cu(In,Ga)Se2-based Solar Cells by Analytical TEM

X. Jin[1], R. Schneider[1], D. Hariskos[2], W. Witte[2], M. Powalla[2], D. Gerthsen[1]

[1]Karlsruhe Institute of Technology (KIT), Laboratory for Electron Microscopy, Karlsruhe, Germany
[2]Zentrum für Sonnenenergie- und Wasserstoff-Forschung Baden-Württemberg (ZSW), Stuttgart, Germany

Nowadays, solar cells with thin-film absorbers of Cu(In,Ga)Se2 (CIGS) are widely used and show power conversion efficiencies above 22%. For such CIGS-based cells, Cd-free materials with wider bandgap energies are required to replace the commonly used CdS buffer layer, and Inx(O,S)y has become a promising candidate among other possible materials.

In this work, TEM results are reported on CIGS-based solar cells with CdS and Inx(O,S)y buffer layers, which were prepared by either chemical-bath deposition (CBD) or sputtering. In each case, the cell has a ~2 µm thick CIGS absorber deposited on a Mo-coated soda-lime glass substrate by in-line co-evaporation of the elements. In addition, after deposition of the buffer layers the cell setup was completed by sputtering of ZnO/ZnO:Al window layers. The data obtained from the cells with Inx(O,S)y buffers are compared with those of a standard CIGS solar cell with a CBD-CdS buffer with an efficiency of ~17.8%. Moreover, the influence of the deposition temperature on the layer properties was analyzed.

In detail, the microstructure of the different buffer layers was studied by diffraction-contrast and high-resolution TEM imaging, nanobeam electron diffraction, and energy-dispersive X-ray spectroscopy was performed for chemical analysis. Both the CBD-grown and sputtered Inx(O,S)y layers show a nanocrystalline structure in contrast to larger grains in the standard CdS buffer. There are differences in the chemical composition of the Inx(O,S)y layers, i.e. the oxygen content in CBD-Inx(O,S)y is considerably higher than the applied oxygen concentration in sputtered-Inx(O,S)y. The difference in crystalline quality of the buffers and CIGS/buffer interfaces might contribute to the different performance of the investigated CIGS-based thin-film solar cells.

MS1.P014
Structure–Composition Interplay in Vanadate Perovskite Superlattices

D. T. L. Alexander[1], H. Meley[2], B. Mundet[1,2], J. M. Triscone[2], S. Gariglio[2]

[1]Ecole Polytechnique Fédérale de Lausanne (EPFL), Institute of Physics (IPHYS), Lausanne, Switzerland
[2]University of Geneva, Department of Quantum Matter Physics (DQMP), Geneva, Switzerland

Recently, a strategy for creating magnetic materials with improper hybrid ferroelectricity was devised by *ab-initio* theory (1). The working principle rests on the stacking of odd numbers of orthorhombic distorted ABO_3 and $A'BO_3$ perovskite unit cells, in order to generate a macroscopic polarization out of the uncompensated displacements of the *A*-site cations in the superlattice. These displacements are the result of the strong coupling between chemistry and structure in perovskite oxides.

Towards this goal, we investigate vanadate superlattices composed of $(LaVO_3)n/(PrVO_3)n$ repetitions, where *n* is in terms of psuedo-cubic (PC) unit cells, using aberration-corrected scanning transmission electron microscopy (STEM). These atomic scale studies are vital to identify changes in *A*-site cation ordering between the layers that could lead to improper ferroelectricity.

We study $(LaVO_3)n/(PrVO_3)n$ films ~20 nm thick, for $3 \leq n \leq 8$ and grown by pulsed laser deposition on $SrTiO_3$, using a double aberration-corrected FEI Titan Themis 60-300 operated at 300 kV. High angle annular dark field (HAADF) image series are acquired and effects of scan drift and other distortions compensated (2). Chemical analyses are made with electron energy-loss spectroscopy (EELS), using a Gatan GIF Quantum ERS.

Figure 1 presents analyses of the $n = 6$ film. The *A*-site cations in its HAADF image (a) show the antipolar displacements of an in-plane X_5^- mode, as seen in all the films. Their displacements are plotted as a virtual strain in (b), whose average per row is shown in (c). By correlating to EELS data (d, e), it can be seen that the displacements are greater in the Pr-rich layers than the La-rich layers. Moreover, the contents of La and Pr cations modulate sinusoidally between the $LaVO_3$ and $PrVO_3$ repetitions (rather than being chemically abrupt), and the antipolar displacements vary in coincidence with these compositional fluctuations. While this result supports the working hypothesis for obtaining improper ferroelectricity, remarkably, the films with n = odd – which are also the candidates for improper hybrid ferroelectricity – systematically show a different behavior. Their layers are chemically indistinct, with strong intermixing of La and Pr cations; accompanying this, their *A*-site cation displacements are much more uniform across the film thickness.

The results suggest a strong interplay between the structure and composition of the vanadate superlattices. We hypothesize that the n = odd films are structurally "inhibited", pushing them to intermix. Equally, a proportional relationship is seen between *A*-site cation ordering and composition. We are pursuing further studies to understand these phenomena, which could have strong implications for this field.

References:

(1) J M Rondinelli and C J Fennie, Adv. Mater. 24 (2012), p. 1961.

(2) L Jones et al., Adv. Struct. Chem. Imaging 1 (2015), 8.

This work was supported by the Swiss National Science Foundation, Sinergia Project No. 154410. We acknowledge the CIME, EPFL for access to its facilities; at the CIME we thank Colette Vallotton and Danièle Laub for TEM specimen preparation.

Fig. 1: (a) HAADF image of $(LaVO_3)6/(PrVO_3)6$ film on $[110]_{PC}$ zone axis (substrate plane vertical); (b) corresponding ε_{xy} virtual strain map of displacements of *A*-site cation positions; and (c) average strain per atomic row. (d) STEM-EELS map (from another film region); (e) normalized compositional line-profile.

Fig. 1

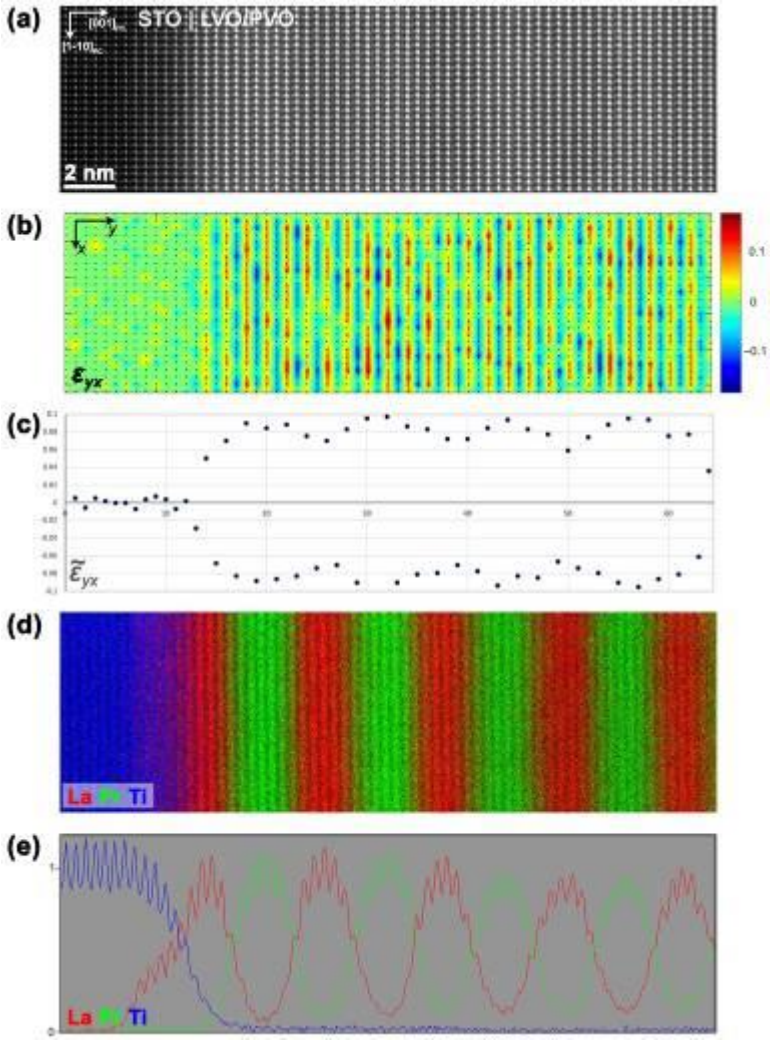

MS1.P015
Optimization of sample preparation procedure for correlative SEM-CL and TEM study of the luminescence and core structure of freshly introduced dislocations in GaN

S. Shapenkov [1], O. Vyvenko[1], O. Medvedev[1], E. Ubyivovk[1], M. Seibt[2]

[1]SPbSU, Physics, Saint-Petersburg, Russian Federation
[2]Georg-August-Universität Göttingen, Physics, Göttingen, Germany

GaN, along with other III-nitrides, is a direct wide bandgap semiconductor that is used for the production of light-emitting devices and high-electron-mobility transistors. Growing of crystal films on a sapphire, silicon and other substrates is the most profitable way to produce GaN. Unfortunately, significant differences both in lattice constants and in thermal expansion coefficients between semiconductor and substrate lead to a very high density of threading dislocations, which commonly are considered to act detrimentally on GaN-based device parameters.

Nevertheless, recently it has been discovered in Cathodoluminiscence (CL) experiments that straight segments of freshly introduced dislocations in the basal plane of a wurzite-type GaN are effective UV light emission centers with intense spectral band with a doublet-like structure at around 3.1-3.2 eV at 70K, which persisted at room and even higher temperature. In addition, the luminous dots at the intersections of the dislocations with spectral luminescence band at around 3.3 eV were observed at temperatures below 100 K. Following TEM and scanning TEM (STEM) studies revealed dissociated character of a-screw dislocations and extended structure of the nodes (1). However, previous CL and TEM experiments were performed not on the same samples or their areas making, thus, not possible to establish one-to-one correlation between luminescent and structural properties of the dislocations.

To establish a direct correlation between dislocation structure revealed by TEM and dislocation related luminiscence (DRL) detected by CL in SEM the foil thickness has to be optimized. It has to be thin enough to make possible TEM/STEM structural study and to be thick enough to have sufficient electron-hole pair generation volume for the excitation of detectable intensity at room temperature. One of the way is to perform step-by-step subsequent ion milling but such procedure is tedious and poorly reproducible. Thus, was utilized the fact that by proper choice of the distance between multiple indentations procedure one can find one of them where such conditions are fulfilled.

In this research Zeiss Supra 40VP with Gatan MonoCL3+ extension was applied for conducting CL experiments and TEM and STEM studies of the core structure of dislocations were performed on Zeiss Libra 200FE.

Small square piece (2 µm x 2 µm) of undoped low-ohmic n-GaN 10 µm crystal film grown by HVPE technique on the sapphire substrate was used for the experiment. It was mechanically thinned to ~100 µm from sapphire side. Then grid of pricks 6x6 was introduced in a basal plane of GaN by indenting with Nanoindentor G200. Thin area was acquired by ion milling and polishing via Gatan PIPS (Figure 1a).

Detailed STEM (Figure 1b) and CL (Figure 1c,d) experiments revealed that there are two types of linear dislocation structures. First ones were a-screw dislocation lines perpendicular to indenter pyramid sides, they exhibited bright contrast on monochromatic CL map for energy 3.12 eV (Figure 1d). Second ones were tangled bands crossing indenter pyramid sides at an acute angle, they exhibited strong dark contrast in CL panchromatic map, overlaying intensity of first ones (Figure 1c).

References:

(1) O.S. Medvedev et al. JAP 123(16), 161427, 2018

Fig. 1

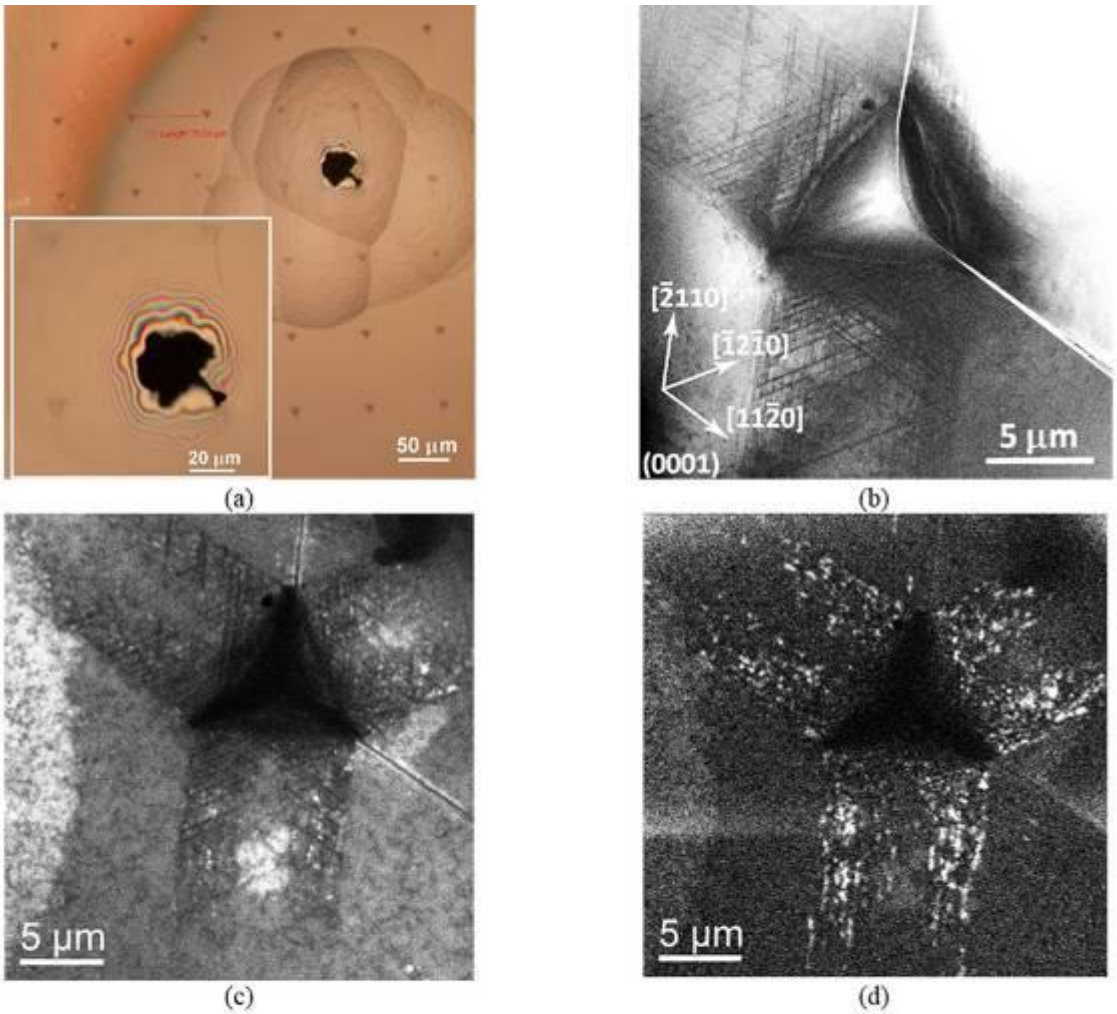

FIGURE 1. (a) – Optical image of TEM foil of GaN sample with a net of pricks on basal plane; (b) – BF STEM image of the prick on c-plane of GaN; (c) – panchromatic CL map; (d) – monochromatic CL map with a photon energy corresponded with DRL emission energy (3.12 eV at 300 K). V_{ac} = 3 kV

MS1.P016
Synthesis and characterization of $BaCo_2Ti_2Fe_8O_{19}$ hexagonal ferrite

J. W. Sandino del Busto[1,2], W. Salazar González[2], L. C. Moreno Aldana[3]

[1]Universidad Nacional de Colombia, Physics, Bogotá, Colombia
[2]Universidad Nacional de Colombia, Physics - electron microscopy group, Bogotá, Colombia
[3]Universidad Nacional de Colombia, Chemistry, Bogotá, Colombia

The M Hexaferrite BaCo2Ti2Fe8O19 is a material member of the ferrites" family, presenting multiferroic properties at room temperature due to its crystalline structure (1). Because of their properties, this hexaferrite has become potentially important for technological applications, e.g. microwave communication, microwave dark room, electromagnetic wave radiation, non-volatile memories, among others (2). In this work, this M ferrite is synthesized by citrate method (3). This procedure has as stages: formation of ion chelates by using citric acid ($C_6H_8O_7$); formation of a foam by heating. This last one produces the precursor material to obtain the searched phase for posteriors successive annealing temperatures. Annealing at 1200°C was employed in order to obtain the M single-phase. Phase characterization was carried out by XRD using CuKα radiation. Figure 1 shows results of XRD, there was found coexistence of several phases of ferrites.

EDX analyses and SEM micrographs of secondary and backscattering electrons allowed to identify the grains correspondent to the BaCo2Ti2Fe8O19 ferrite and revealed homogeneous size and shape as well as a uniform material contrast in those grains.

From this information FIB lamella were milled trying of cut in specific crystallographic grain orientations. Large field of view micrographs of electron holography were acquired and reconstructed allowing to access to the amplitude and phase of the electron wave. These phase images sensitive to magnetics structure of the material were correlated with SAED indicating the induced magnetization dependent on the crystal orientation (Figure 2). Additionally, characterization by Vibrant Sample Magnetisation technique was applied to correlate the last results with the magnetic behaviour.

The present study shows the synthesis process of the M hexaferrite by citrate method and the implementation of several characterization techniques to study in detail the relationship between the crystalline structure and the magnetic properties.

References:

(1) C.A. Triana, « Investigación Teórico-Experimental de Propiedades Físicas de los Nuevos Materiales Multifuncionales AMXFe8O19 (A:Sr-Ba-Ca; M:Co-Mn; X:Ti-Zr)»,Master's thesis, Universidad Nacional de Colombia 2013.

(2) R. C. Pullar, «Hexagonal ferrites: A review of the synthesis, properties and applications of hexaferrite ceramics», Prog. Mater. Sci., vol. 57, n.o 7, pp. 1191-1334, sep. 2012.

(3) Pechini M. P. US Patent 3,3306,97. 1967. www.google.com/patents/about?id=D3sfAAAAEBAJ&dq=3,330,697 (reference date: 30.03.2015).

Fig. 1: XRD pattern for the sample synthetized.

Fig. 2: Holographic phase micrograph showing the magnetic induction.

Fig. 1

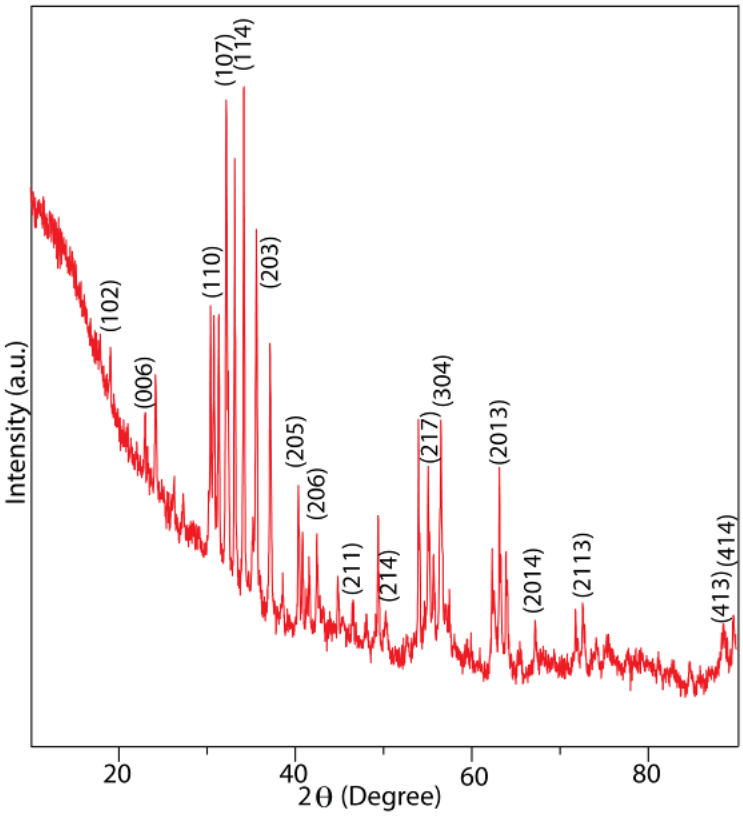
Intensity (a.u.)
(102)
(006)
(110)
(107)
(114)
(203)
(205)
(206)
(211)
(214)
(217)
(304)
(2013)
(2014)
(2113)
(413)
(414)
20
40
60
80
2θ (Degree)

Fig. 2

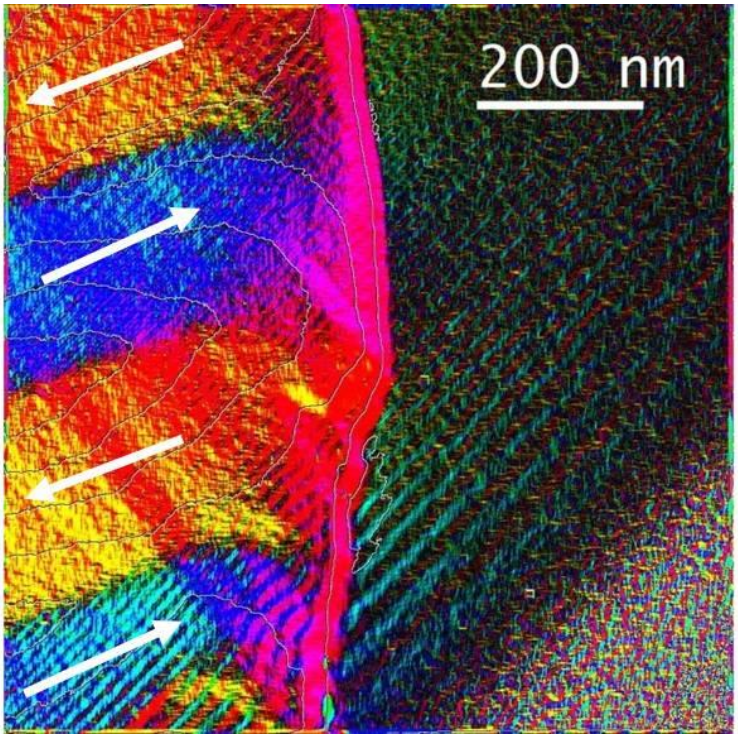
200 nm

MS1.P017
Defect structure, optical and structural properties of epitaxial layers of gallium oxide of different polytypes (alpha, betta, epsilon)

E. Ubyivovk[1], O. Medvedev[1], S. Shapenkov[1], O. Vyvenko[1], V. Nikolaev[2,3], A. Pechnikov[2,3], V. Nikolaev[2], A. Chikiryaka[3], S. Stepanov[2,3]

[1]Saint Petersburg State University, solid state electronics, St. Petersburg, Russian Federation
[2]Perfect Crystals LLC, St. Petersburg, Russian Federation
[3]Ioffe Institute, RAS, St. Petersburg, Russian Federation

In the recent years, gallium oxide has acquired a rapidly growing interest of the global community of scientists engaged in wide-gap materials, which is associated with its unique properties such as high optical transparency up to wavelengths of about 250 nm, the possibility of varying electronic conductivity over a wide range, high breakdown voltage and economically reasonable cost of crystal and epitaxial layer growth. These advantages open up prospects for its wide applications in power and high-voltage electronics, as well as optoelectronics, for example, in photodetectors, the so-called "solar blind" detector for solar radiation (UV-C range).

Most of the research on this material today is focused on monoclinic beta-Ga2O3 due to its thermal stability and the possibility to obtain large single crystals from the melt for the manufacture of substrates. At the same time, there are other polytypes, which have recently been paid attention to due to some unique properties not found in the beta phase. This is an alpha-Ga2O3 with a corundum lattice and a hexagonal epsilon-phase, the lattice parameter of which is close to sapphire. It has recently been demonstrated that in the epitaxial layers obtained by gas transport deposition on sapphire substrates, the semiconductor quality of both these polytypes can be achieved. In addition, the epsilon phase is of interest due to internal polarization, which can lead to the formation of a high-density two-dimensional electron gas (2DEG) at the (AlGa)2O3/Ga2O3 interface, similar to AlGaN/GaN-based heterostructures.

Here we report on the growth and characterisation of Ga 2 O 3 epitaxial films deposited by halide vapour phase epitaxy (HVPE) on sapphire substrates. Ga 2 O 3 films were synthesized through a reaction of gaseous gallium chloride GaCl and oxygen. The GaCl vapour was synthesised in situ upstream in the reactor by the reaction of metallic gallium (99.9999%) and gaseous hydrogen chloride (99.999%). The growth was conducted at atmospheric pressure and at the temperature of about 500 o C. Patterned sapphire substrates with regular cone-like features and plain c-face sapphire substrates were placed in the same growth run. After the deposition the samples were studied by x-ray diffraction (XRD), scanning electron microscopy (SEM), transmission electron microscopy (TEM), optical transmission spectroscopy (OTS) and cathodoluminescence (CL). The growth on plain sapphire substrate produced an 11 μm thick continuous α-Ga 2 O 3 layer. The full width at half maximum (FWHM) of the (0006) XRD rocking curve is 180 arcsec, which indicates a good crystallinity of the layer. In contrast, growth on the patterned sapphire substrate resulted in a very different structure. XRD analysis revealed the presence of both α- and ε-phases in Ga 2 O 3 grown on patterned sapphire substrate. The presence of the ε-Ga 2 O 3 phase, which has narrower bandgap, was also confirmed by OTS. SEM, TEM observations revealed that α-Ga 2 O 3 phase forms columnar structures on top of cone-shaped bumps while ε-Ga 2 O 3 phase fills the valleys between the columns. Intense broad luminescent bands were found by CL study on microscale for both phases that were shifted spectrally by 0.5 eV with respect to each other in accordance with OTS data.

MS2.002
In situ TEM study of phase separation in Ni-Au alloy nanoparticles produced by solid-state dewetting

J. Schubert[1], M. Landes[1], M. Wu[1], C. Wiktor[2], J. Will[1], S. Kraschewski[1], E. Spiecker[1]

[1]Institute of Micro- and Nanostructure Research, Erlangen, Germany
[2]Universität Siegen, Siegen, Germany

Ni-Au alloy nanoparticles produced by solid-state dewetting of multilayer metal thin films can be tailored in size, shape and orientation (1,2), and serve as an ideal model system for studying fundamental aspects of phase transformation in confined volumes (3). By dewetting Ni/Au bilayer films on a SiNx membrane *in situ* in the transmission electron microscope alloy nanoparticles with distinct (111) texture have been produced (Figure 1a-c). Making use of the ultrafast quenching rate (~ 1000 K/s) achievable with chip-based TEM heating devices [4] the Ni-Au nanoparticles are kept in the solid solution state down to room temperature, despite the large miscibility gap. Local phase separation is only observed at dislocations forming small angle grain boundaries (not shown). A subsequent annealing step at temperatures inside the miscibility gap initiates phase separation, yielding particles with either Au-rich phases on the outer facets or with lamellar structure of altering Ni- and Au-rich phases (Figure 1d). Figure 2a,b show a HAADF-STEM image and EDXS map of a particle with lamellar structure in cross section geometry. The particle reveals characteristic Au segregation to the (111) surface and lower interface (to the SiNx substrate). The interfaces between Au- and Ni-rich lamellae are mostly inclined to the electron beam and therefore appear blurred. In fact, they are almost atomically sharp as revealed by high resolution STEM imaging (Figure 2c). A closer analysis shows that the lattice misfit of > 10 % is almost completely accommodated by closely spaced ½[110]-type misfit dislocations located at the interface.

References:

(1) Niekiel, F.; Kraschewski, S.M.; Schweizer, P.; Butz, B.; Spiecker, E. *Acta Mater.* 2016 *115*, 230-241.

(2) Herz, A.; Wang, D.; Müller, R.; Schaaf, P. *Materials Letters* 2013 *102-103*, 22-25.

(3) Herz, A.; Friák, M.; Rossberg, D.; Hentschel, M.; Theska, F.; Wang, D.; Holec, D.; Sob, M.; Schneeweiss, O.; Schaaf, P. *Appl. Phys. Lett.* 2015 *107*, 073109.

(4) Niekiel, F.; Kraschewski, S.; Müller, J.; Butz, B.; Spiecker, E. Ultramicroscopy 2017 *176*, 161-169

Fig. 1: a-c) HAADF-STEM images taken during *in situ* solid-state dewetting of a Ni/Au bilayer thin film at 970°C. d) Phase separation into Au-rich and Ni-rich phases upon annealing at 650°C for 600 s.

Fig. 2: a, b) HAADF-STEM image and EDXS map of cross section taken from a Ni-Au nanoparticle after phase separation into lamellar structure; in b) the Ni K line is depicted in red, the Au L line in green. c) High-resolution STEM image of interface between Ni-rich and Au-rich phase marked in a).

Fig. 1

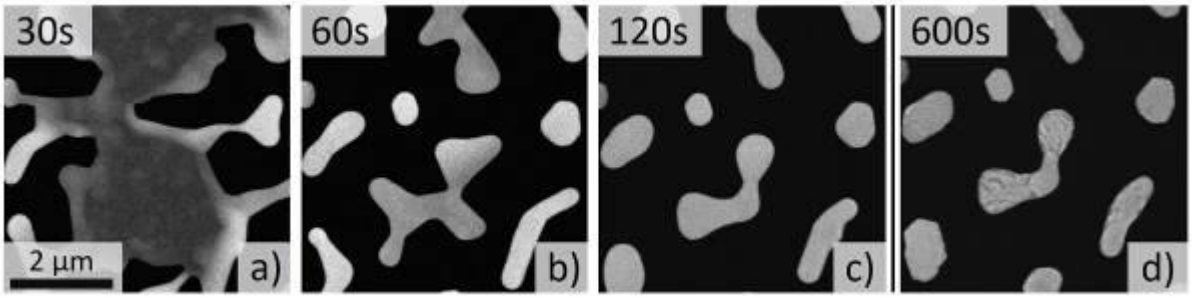

Fig. 2

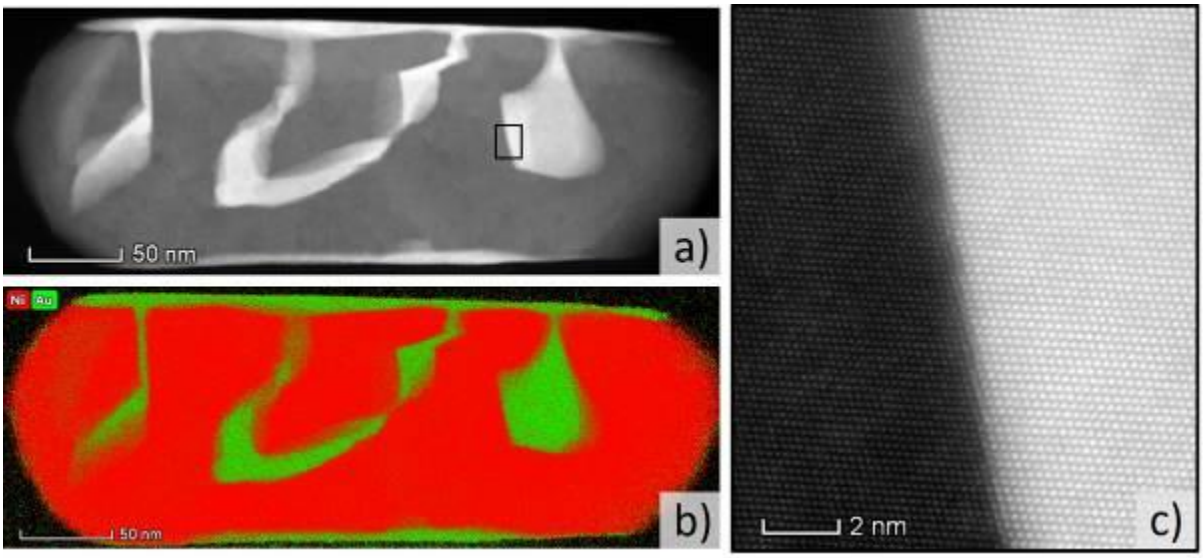

MS2.003
Atomic structure of covalently bond diamond-graphite interfaces studied by aberration corrected transmission electron microscopy

S. Tulić[1], T. Waitz[1], M. Čaplovičová[2], G. Habler[3], M. Varga[4], M. Kotlár[2], V. Vretenár[2], O. Romanyuk[4], A. Kromka[4], B. Rezek[4], V. Skákalová[1]

[1]University of Vienna, Faculty of Physics, Physics of nanostructured materials, Vienna, Austria
[2]Slovak University of Technology, Centre for Nanodiagnostics, Bratislava, Slovakia
[3]University of Vienna, Department of Lithospheric Research, Vienna, Austria
[4]Czech Academy of Sciences, Institute of Physics, Prague, Czech Republic

Placing graphene on a diamond surface can result in electronic devices with superior performance. Direct conversion of diamond to graphene can be mediated by Ni catalysts. However, a clear understanding of the catalytic mechanisms forming graphene or graphite from solid carbon sources has not yet been provided.

Atomic structures formed by a Ni-mediated transformation from nanocrystalline diamond (NCD) to graphite are studied to elucidate the transformation mechanisms and type of bonding at graphite-diamond interfaces.

NCD films grown on Si substrates were covered by thin Ni films and annealed. Specimens for transmission electron microscopy (TEM) were prepared in cross-sectional geometry by focused ion beam sputtering using protective Au and Pt layers. High resolution TEM (HRTEM) and scanning TEM (STEM) with a high angle annular dark field (HAADF) detector was carried out at 200 kV with aberration corrected instruments (JEOL JEM ARM200-F, FEI Titan 80-300).

Fig. 1 shows a HAADF STEM image of graphite channels in NCD terminated by hemispherical Ni nanoparticles (Ni appears bright, graphite with a density more than 30% less than that of diamond is darker than diamond). Via a Ni-mediated catalytic reaction C is released at the Ni-diamond interface, diffuses along the surfaces of the Ni particles and is reconstructed as graphite at their backsides. This causes Ni particles to move forward drilling channels into diamond. Fig. 2 shows a low-magnification HRTEM image of a channel. Basal planes of graphite attached to Ni exactly follow its slightly concave backside curvature. With increasing distance the curvature decreases and becomes increasingly convex. At a distance of ~30 nm, flat basal planes run almost perpendicular to the channel walls. The flat or even concave backside and significant bending of graphite planes are caused by uniaxial strain due to the volume increase of the transformation exerting stress at the backside of the Ni particle and activating mechanisms of plasticity in the channel. Fig. 3 shows a HRTEM image of a graphite-diamond interface with vertically orientated basal planes of graphite. While the interface is incoherent, a well-defined diamond-graphite orientation relationship allows to resolve atomic structures indicated by a superimposed model. Directly at the interface the atoms tend to relax, minimizing their distances to obtain atop positions. Such local relaxations at incoherent interfaces were found by first-principles calculations to favor covalent bonding (1).

A catalytically driven diamond to graphite transformation was studied by TEM. Channels drilled by Ni in diamond are filled with graphite. The bending of graphite planes and the hemispherical morphology of Ni particles is caused by stress arising by the volume increase of the transformation. Incoherent graphite-diamond interfaces occur with basal planes of graphite orientated perpendicular to them. At the interfaces, atomic positions relax to form covalent bonds.

References:

(1) K. Matsunaga et al. *Phys. Rev. B* (2006) 74, 125423.

Fig. 1: HAADF STEM image of channels of graphite drilled into NCD.

Fig. 2: HRTEM image showing the basal planes of graphite (indicated by white lines).

Fig. 3: Fourier-filtered HRTEM image showing the atomic structures of diamond and graphite.

Fig. 1

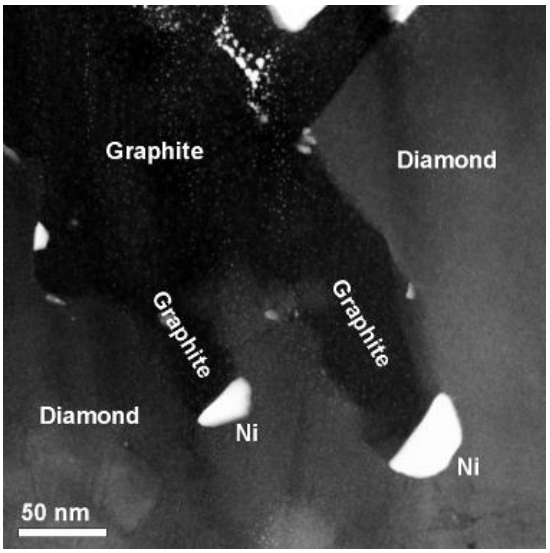

Fig. 2

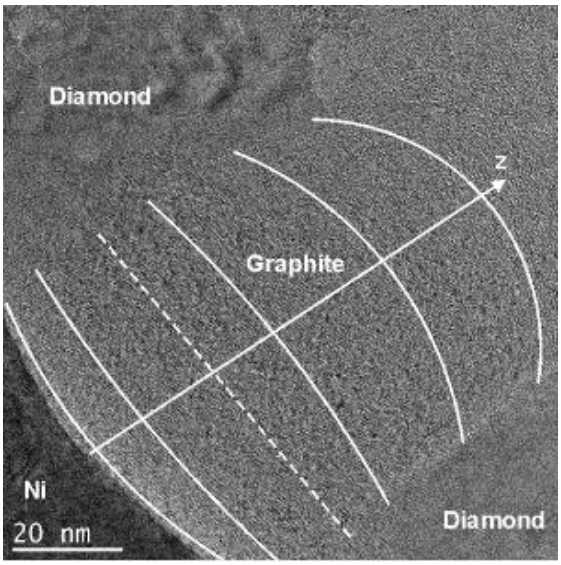

Fig. 3

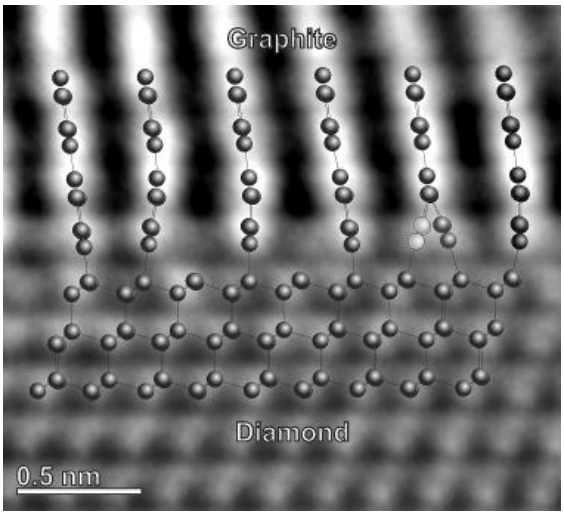

MS2.004
Quantifying Grain Growth and Confirming Growth Laws in Nanocrystalline ZnO Thin Films

A. B. Aebersold[1], L. Fanni[2], A. Hessler-Wyser[2], S. Nicolay[3], C. Ballif[2], C. Hébert[4,1], D. T. L. Alexander[4,1]

[1]Ecole Polytechnique Fédérale de Lausanne (EPFL), Interdisciplinary Centre for Electron Microscopy (CIME), Lausanne, Switzerland
[2]Ecole Polytechnique Fédérale de Lausanne (EPFL), Institute of Microengineering (IMT), Neuchâtel, Switzerland
[3]CSEM, PV-Center, Neuchâtel, Switzerland
[4]Ecole Polytechnique Fédérale de Lausanne (EPFL), Institute of Physics (IPHYS), Lausanne, Switzerland

Non-epitaxial polycrystalline thin films are often understood to grow by a process of competitive overgrowth, in which favorably-oriented grains overgrow other grains. This "evolutionary selection", first proposed by van der Drift (1), leads to grain coarsening and self-texturing as the film becomes thicker. According to analytical models and simulations, this principle should lead to a power-law scaling of the average grain size d with film height h, i.e. $d \propto h^{\alpha}$, where the growth exponent $\alpha = 0.4$ for 3-D growth (2). However, until now, experimental studies have failed to confirm this value, e.g. (3,4).

We study the applicability of this model for polycrystalline ZnO thin films grown, by metal–organic chemical vapor deposition, for use as transparent conductive oxide layers in solar and optoelectronic devices. To tackle the challenge of making quantitative measurements of the nano-scale grains, we apply a methodology in which we combine a "double wedge" specimen geometry developed by Spiecker et al. (3,5) with TEM nanobeam diffraction-based automated crystal orientation mapping (6). This allows the measurement of the size, shape and orientation of >10"000 grains across defined heights within a film, giving unprecedented statistics for quantifying their growth evolution (7).

The measurements are made using the NanoMEGAS ASTAR system, installed on a JEOL JEM 2200FS. Three *a*-textured ZnO films are analyzed and compared, deposited using different ratios of H_2O/diethyl zinc (DEZ) precursor gases.

For the first time, our experimental data confirm the predicted power-law growth exponent, with films grown with H_2O/DEZ ratios of 0.25, 1 and 4 showing $\alpha = 0.38$, 0.39 and 0.40 respectively. A predicted self-similarity in grain size distributions is also found. Because the grain size and orientation data are spatially-resolved, a deeper understanding is also obtained. In the H_2O/DEZ = 1 and 4 films, the majority of grains are found to grow as twinned pairs, while the H_2O/DEZ = 0.25 and 1 films are subject to strong renucleation during their growth. Indeed, by careful data analysis, and comparison to growth simulations for this hexagonal system, it is concluded that only the H_2O/DEZ = 4 film properly obeys the van der Drift model. In the other two films, opposing factors of an initial nucleation orientation biased away from late-stage growth, and renucleation during growth, compensate to give a similar growth exponent.

Compared to previous studies, the methodology used here gives a more "forensic" capability for analyzing the growth of complex and "messy" nano-grained polycrystalline films; e.g. its application could be able to confirm proposed growth mechanisms for 3C-SiC films (3,4). Further analytical strength is shown by its ability to give insights into mechanisms such as twinning, renucleation and elongated grains shapes that can affect the microstructural evolution during thin film growth (8).

References:

(1) A. van der Drift, Philips Res. Reports 22 (1967) 267.

(2) P. Smereka et al., Acta Mater. 53 (2005) 1191.

(3) E. Spiecker et al., Acta Mater. 55 (2007) 3521.

(4) S. Zhang et al., J. Am. Ceram. Soc. 98 (2015) 236.

(5) E. Spiecker, Philos. Mag. 86 **(**2006) 4941.

(6) E.F. Rauch et al., Zeitschrift für Krist. 225 (2010) 103.

(7) A.B. Aebersold et al., Ultramicrosc. 159 (2015) 112.

(8) A.B. Aebersold et al., Acta Mater. 130 (2017) 240.

The authors acknowledge funding from the SNSF, Grant Number 200021_137833 (*ZONEM* project).

MS2.005
Impact of crystallinity on resistive switching properties of HfO2 based Memristive Devices

R. Eilhardt[1], A. Zintler[1], S. Petzold[1], L. Alff[1], L. Molina-Luna[1]

[1]Technische Universität Darmstadt, Department of Material- and Earth sciences, Darmstadt, Germany

In filament-type resistive random access memory (RRAM), resistive switching (RS) is mediated by growth/rupture of a conductive filament being possibly locally constricted along grain boundaries (GBs) across a polycrystalline insulating layer, as suggested by conductive AFM (1). These predefined pathways (GBs) should lower the electrical stress required for CF formation thus minimizing the risk of formation damage and ensuring CMOS compatibility (2).

In this work, the influence of the texture of HfO2 in Pt/HfO2/TiN memristive devices and the effect on the RS properties is investigated to reveal whether all types of GBs are favourable for CF formation.

By using reactive molecular beam epitaxy (RMBE), 50 nm thick TiN films have been grown on *c*-cut sapphire followed by *in situ* growing 10 nm thick HfO2 thin films being highly textured in [11-1] and in [010], respectively, as shown by the XRD patterns in Fig. 1(b). The MIM structure has been complemented by *ex situ* sputter deposition of 100 nm Pt after a photolithographic patterning step resulting in devices being 35x35 µm² in size. Information about the forming voltages have been obtained by applying compliant current dc voltage sweeps on the Pt top electrode with the TiN bottom electrode grounded.

As shown by the BF-STEM images in Fig. 2, the microstructure of both hafnia films is similar, with vertically oriented grain boundaries interconnecting top and bottom electrode. Hence, it is expected that both devices exhibit low forming voltages. As shown in Fig. 1(a), this is only true for devices with hafnia oriented in [11-1] (black distribution), whereas for the other textured hafnia most of the devices exhibit comparably high forming voltages (magenta distribution). This might be related to less thermodynamically favourable segregation of vacancies (3) and/or hampered ionic movement due to strain. Here, ab initio calculations and 4D-STEM could provide further information about the bonding states of different textured hafnia.

Forming voltages and device to device variability can be optimized through precise GB engineering of the insulating layer in hafnia based memristive devices.

References:

(1) M. Lanza *et al.*, "Grain boundaries as preferential sites for resistive switching in the HfO2 resistive random access memory structures", *Appl. Phys. Lett.*, vol. 100, no. 12, p. 123508, Mar. 2012.

(2) J. S. Lee, S. Lee, and T. W. Noh, "Resistive switching phenomena: A review of statistical physics approaches", *Appl. Phys. Rev.*, vol. 2, no. 3, p. 031303, Sep. 2015.

(3) G. Bersuker *et al.*, "Grain boundary-driven leakage path formation in HfO2 dielectrics", *Solid-State Electron.*, vol. 65–66, pp. 146–150, Nov. 2011.

The authors acknowledge funding from DFG grant MO 3010/3-1 and the European Research Council (ERC) "Horizon 2020" Program under Grant No. 805359-FOXON.

Fig. 1: (a) Cumulative probability distributions of the forming voltage measured for different textured 10 nm thick hafnium oxide thin films. (b) X-ray patterns of the corresponding hafnium oxide films (colour indicates correspondence). The rhombus indicate the reflex positions of monoclinic HfO2 and the cross the reflex position of TiN(111).

Fig. 2: Bright-field scanning transmission electron microscopy (BF-STEM) images of two TiN/HfO2/Pt memristive devices with HfO2 grown in [010] (a) and [11-1] (b).

Fig. 1

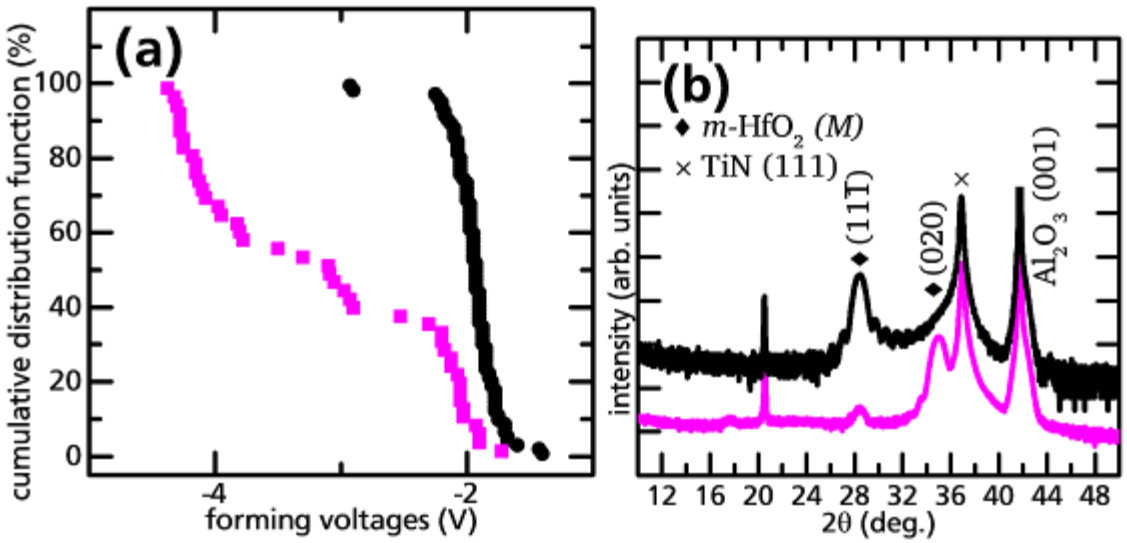
(a)
cumulative distribution function (%)
100
80
60
40
20
0
-4
-2
forming voltages (V)
(b)
◆ m-HfO2 (M)
× TiN (111)
(11T)
(020)
×
Al2O3 (001)
intensity (arb. units)
12 16 20 24 28 32 36 40 44 48
2θ (deg.)

Fig. 2

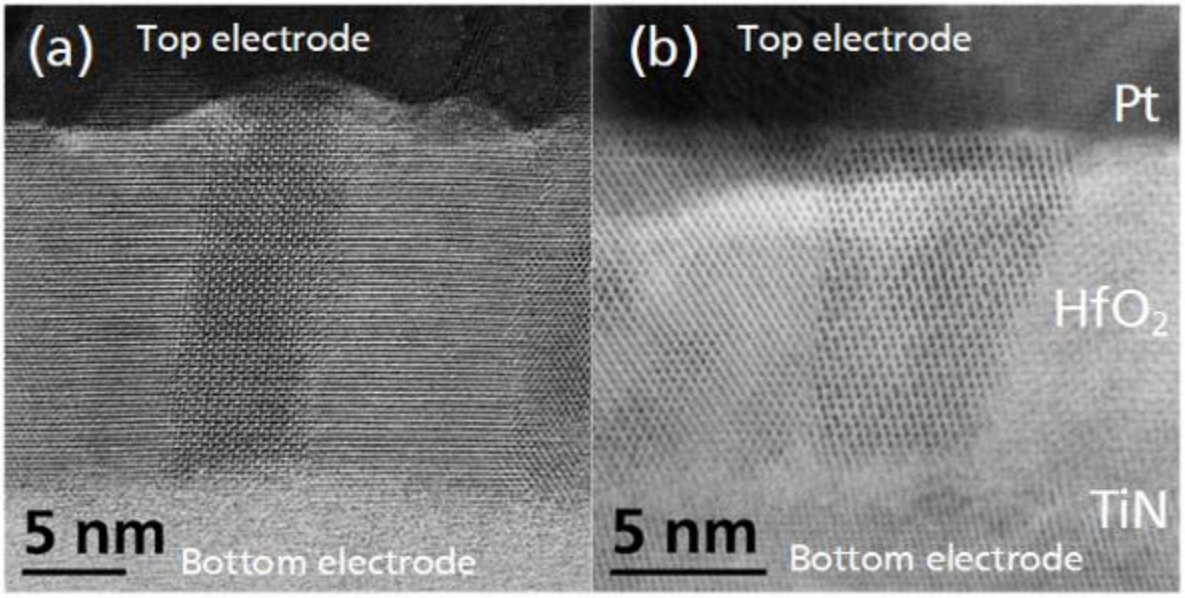
(a)
Top electrode
5 nm
Bottom electrode
(b)
Top electrode
Pt
HfO2
TiN
5 nm
Bottom electrode

MS2.006
Atomic-scale imaging of [201] extended mixed dislocations of $SrTiO_3$ using scanning transmission electron microscopy and spectroscopy

H. Du[1,2], C. L. Jia[1,3,4], J. Mayer[1,2]

[1]Forschungszentrum Juelich GmbH, Ernst Ruska-Centre for Microscopy and Spectroscopy with Electrons, Jülich, Germany
[2]RWTH Aachen University, Central Facility for Electron Microscopy, Aachen, Germany
[3]Forschungszentrum Juelich GmbH, Peter Grünberg Institute, Jülich, Germany
[4]Xi'an Jiaotong University, School of Electronic and Information Engineering, Xi'an, China

Dislocations strongly influence many properties of materials. To better understand the nature and properties of dislocations, biycrstals are often used as model systems since the type and the density of dislocations along the low-angle grain boundaries can be controlled to a large extent by adjusting the boundary plane and the misorientation between the two crystal parts. Strontium titanate ($SrTiO_3$) is a representative perovskite oxide and is the best-known prototype material for resistive switching.(1) At low-angle symmetrical tilt grain boundaries of $SrTiO_3$, edge dislocations appear to be spaced uniformly along the boundary.(2) Besides, faceting and extended mixed dislocations may also occur at the low-angle tilt grain boundaries in real bicrystals due to unavoidable deviations of the boundary plane and the misorientation angle from their ideal values. In order to establish unambiguous microstructure-property relationships, knowledge on atomistic structures of different types of dislocations is a prerequisite.

Recently, extended mixed dislocations were observed at a [001]/(100) low-angle tilt grain boundary of $SrTiO_3$ because of the presence of a small amount of twist between the two crystal parts.(3) In this case, the dislocations at the grain boundary disassociate into three dislocations with Burgers vector $\boldsymbol{b}$ of 1/2 [011], [010], and 1/2 [011], respectively. A structure model has been proposed in particular for the two $\boldsymbol{b}$ = 1/2 [011] dislocation cores based on the results obtained from high angle annular dark field (HAADF) scanning transmission electron microscopy (STEM). However, the details of the atomic structure and the chemical composition at the dislocation cores remains unexplored. In this work,(4) we study the atomic structure and the chemical information of the extended mixed dislocations in a $SrTiO_3$ bicrystal using STEM, electron energy loss spectroscopy (EELS), and energy dispersive X-ray (EDX) spectroscopy techniques. By these atomic-scale imaging techniques, we determine a rock salt FCC type TiO phase segregated at the extended mixed dislocations of the grain boundary.

Fig. 1 Atomic structure of the $\boldsymbol{b} = \boldsymbol{a}/2[101]$ mixed partial dislocation core. (a) Structural model of the mixed partial dislocation core projected against the [001] direction. The TiO_6 octahedra in red at the dislocation core share edges with three adjacent TiO_6. The TiO_6 octahedra in blue and yellow at the antiphase boundary can be considered to belong to the respective left and right sides of the perovskite lattice. The yellow and blue marks indicate the respective parts shown in (b) and (c), wherein the arrows indicate the viewing direction. The images at the right sides show the experimental HAADF-STEM image (left-up), the image overlaid with the structural model (left-down), simulated image (right-up), and the EDX composite map (right-down, Sr: green, Ti: red).

References:

(1) R. Waser, R. Dittmann, G. Staikov and K. Szot, *Adv. Mater.*, 2009, 21, 2632–2663.

(2) H. Du, C.-L. Jia, L. Houben, V. Metlenko, R. A. De Souza, R. Waser and J. Mayer, *Acta Mater.*, 2015, 89, 344–351.

(3) Y. Furushima, Y. Arakawa, A. Nakamura, E. Tochigi and K. Matsunaga, Acta Mater., 2017, 135, 103–111.

(4) H. Du, C.-L. Jia, J. Mayer, *Faraday Discussions*, 2018, doi:10.1039/C8FD00102B.

This work is supported by DFG under SFB 917.

Fig. 1

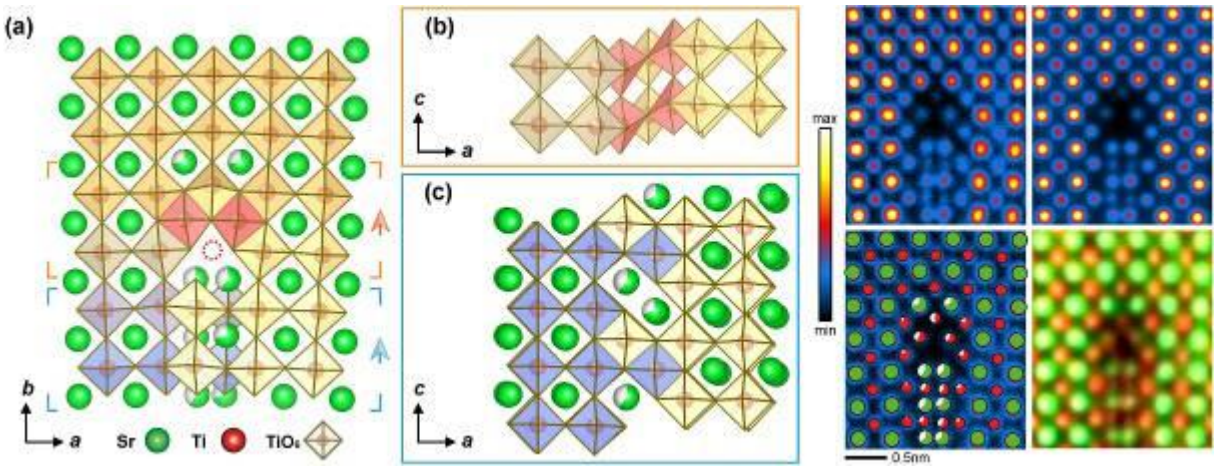

MS2.007
Customizing high-temperature superconductivity at La_2CuO_4-based heterostructure interfaces

Y. E. Suyolcu[1], F. Baiutti[1], Y. Wang[1], W. Sigle[1], G. Gregori[1], G. Cristiani[1], G. Logvenov[1], P. A. van Aken[1], J. Maier[1]

[1]Max Planck Institute for Solid State Research, Stuttgart, Germany

Transition-metal-oxide thin films and heterostructures host novel functionalities and have stimulated large interest recently due to the ability to tailor physical properties at the atomic layer scale. It is the complex interactions at the interfaces of epitaxial oxide systems, which contribute to intriguing physical effects. (1) In this work, we focus on space-charge induced high-temperature superconductivity (HTSC) (2,3) of iso- and hetero-structural La_2CuO_4-based interfaces. In particular, we fabricate (i) $La_{1.6}A_{0.4}CuO_4$–La_2CuO_4 (A = Ca, Sr, Ba) metallic–insulating (M–I) bilayers and (ii) La_2CuO_4–$La_{2-x}Sr_xNiO4$ multilayers using atomic-layer-by-layer oxide molecular beam epitaxy (ALL-oxide MBE). We extensively have characterized these interfaces using aberration-corrected analytical scanning transmission electron microscopy (STEM) techniques, such as electron energy-loss spectroscopy (EELS), energy-dispersive X-ray spectroscopy (EDXS), high-angle annular dark-field (HAADF) and annular bright-field (ABF) imaging in order to correlate structural and functional properties. A JEOL JEM-ARM200F equipped with a cold field-emission electron source, a probe Cs-corrector (DCOR, CEOS GmbH), and a Gatan GIF Quantum ERS spectrometer is used for the STEM investigations.

In the case of M–I bilayers, the choice of the dopants remarkably influences the superconducting mechanisms (i.e. bulk vs interface) as a consequence of dopant distribution near the interfaces (4). For Ca- and Sr-doped bilayers, the interfaces are sharp and thus present striking interface effects, i.e. electronic redistribution is predominant. In the case of Ba-doping, the HTSC is rather ascribed to "classical" homogeneous doping determined by cationic intermixing and a wide redistribution of Ba (5). For the first time, we demonstrate the occurrence of HTSC by the heteroepitaxial contact of La_2CuO_4 with $La_{2-x}Sr_xNiO_4$ (6), where the STEM-HAADF image presented in Figure 1 reveals the high epitaxial quality of the $La_2CuO_4/La_{1.2}Sr_{0.8}NiO_4/La_2CuO_4$ trilayer. The final superconducting properties of the La_2CuO_4–$La_{2-x}Sr_xNiO_4$ interface can be tuned by changing the structural parameters and HTSC is characterized by the accumulation of holes at the interfaces due to the local cationic intermixing and the presence of space-charges (7).

References:

(1) H. Y. Hwang, Y. Iwasa, M. Kawasaki, B. Keimer, N. Nagaosa, Y. Tokura, Nat. Mater. 2012, 11, 103.

(2) A. Gozar, G. Logvenov, L. F. Kourkoutis, A. T. Bollinger, L. A. Giannuzzi, D. A. Muller, I. Bozovic, Nature 2008, 455, 782.

(3) F. Baiutti, G. Logvenov, G. Gregori, G. Cristiani, Y. Wang, W. Sigle, P. A. van Aken, J. Maier, Nat. Commun. 2015, 6, 8586.

(4) Y. E. Suyolcu, Y. Wang, F. Baiutti, A. Al-Temimy, G. Gregori, G. Cristiani, W. Sigle, J. Maier, P. A. van Aken, G. Logvenov, Sci. Rep. 2017, 7, 453.

(5) Y. E. Suyolcu, Y. Wang, W. Sigle, F. Baiutti, G. Cristiani, G. Logvenov, J. Maier, P. A. van Aken, Adv. Mater. Interfaces 2017, 4, 1700737.

(6) F. Baiutti, G. Gregori, Y. E. Suyolcu, Y. Wang, G. Cristiani, W. Sigle, P. A. van Aken, G. Logvenov, J. Maier, Nanoscale 2018, 10, 8712.

This project has received funding from the European Union"s Horizon 2020 research and innovation programme under grant agreement No. 823717 – ESTEEM3.

Fig. 1

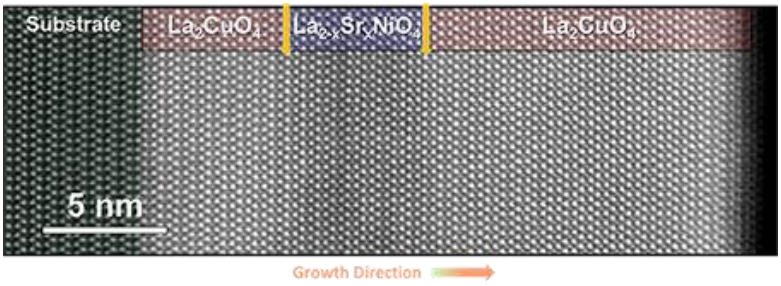
Substrate
La_2CuO_4
$La_{2-x}Sr_xNiO_4$
La_2CuO_4
5 nm
Growth Direction

MS2.LB.P01
3D check board pattern formation in a NiCoMnAl shape memory Heusler alloy thin film system

D. Ramermann[1,2], A. Becker[1,2], I. Ennen[1,2], B. Büker[1,2], M. Gottschalk[1,2], A. Hütten[1,2]

[1]Bielefeld University, Physics, Bielefeld, Germany
[2]Center for Spinelectronic Materials and Devices, Physics, Bielefeld, Germany

Magnetic shape memory Heusler alloys as NiMnX (X=Al, Ga, Sn, In) are promising candidates for thin film devices as well as magnetocaloric applications (1) because of their strong magnetism and their magnetoelastic coupling near room temperature. One limiting factor for cooling applications is their large thermal hysteresis, giving the need for a mechanism changing the martensitic transition (2). Inserting martensitic intercalation layers in the austenitic film is proposed to reduce the formation energy of the martensitic nucleation and thus reducing the width of the hysteresis. With a rising number of intercalations the layer thickness of the austenite approaches that of the martensite layers. In this specimen investigation via TEM shows the formation of a 3D checkboard pattern.

References:

(1) Tino Gottschall et al., Phys. Rev. B 93, 184431

(2) Jian Liu et al., Nature Materials vol. 11, p. 620–626

The crystallographic and chemical properties of the checkboard pattern are investigated by TEM methods to gain insights on the reasons for the formation of the checkboard.

Via magnetron co-sputter deposition from pure Al, Ni, Co, Mn targets a series of systems have been prepared on a 30nm Vanadium layer on MgO substrate, where the active austenitic layer of 600nm thickness is divided by 0, 2, 3 4, 7 and 13 martensitic intercalations of 30nm thickness by slightly varying the composition and therefore varying the transition temperature of the layer below or above room temperature. The active layer consists of $Ni_{43}Co_7Mn_{31}Al_{19}$ (T_M=232K, T_A=248K) and the intercalation of $Ni_{47}Co_3Mn_{33}Al_{17}$ (T_M=308K, T_A=343K).

Fig. 1: Schematic illustration of the multilayer systems with 4, 7 and 13 martensitic intercalations

TEM specimen have been prepared by cutting a FIB grating. Only the specimen with 13 intercalations shows the checkerboard behavior. It has been investigated via HRTEM, Diffraction, Dark field, EDX, EELS, STEM BF/DF and EMCD to reveal the structure and the chemical composition as well as get an idea of the magnetism. Used were the JEOL FS-2200 (200kV) equipped with an in-column energy filter end EDX in Bielefeld and the Cs-corrected JEOL ARM200F (200kV) with cold FEG and post-column energy filter in Paderborn.

Fig. 2: TEM overview BF image of the specimen

Fig. 3: FFTs of HRTEM images help revealing the crystal structure

Fig. 4: Overlay of BF and DF TEM image

The checkerboard pattern shows up at an angle of 45° to the substrate, with fields in the size of 55x55nm (big dark), 40x40nm (small dark), and brighter fields in between of 40x55nm size. Diffraction studies resolve both martensitic and austenitic structure in the darker fields and at least two austenitic cells at an angle to each other in the bright fields. Dark field TEM imaging resolves clearly the fields to the corresponding crystal structure, showing the checkerboard pattern is a 3D crystallographic structure. EDX mappings show the composition varying in a layered structure as intended by the sputter deposition process. The amount of Ni and Co varies layer by layer, showing no checkerboard-like pattern in the composition. First EMCD measurements show magnetic moments on both Mn and Ni, a dependence on the crystal structure can slightly be seen.

TEM measurements reveal an overall crystallographic reordering resulting in a 3D checkerboard pattern, which is presumably caused by the presence of long-range interactions.

Fig. 1

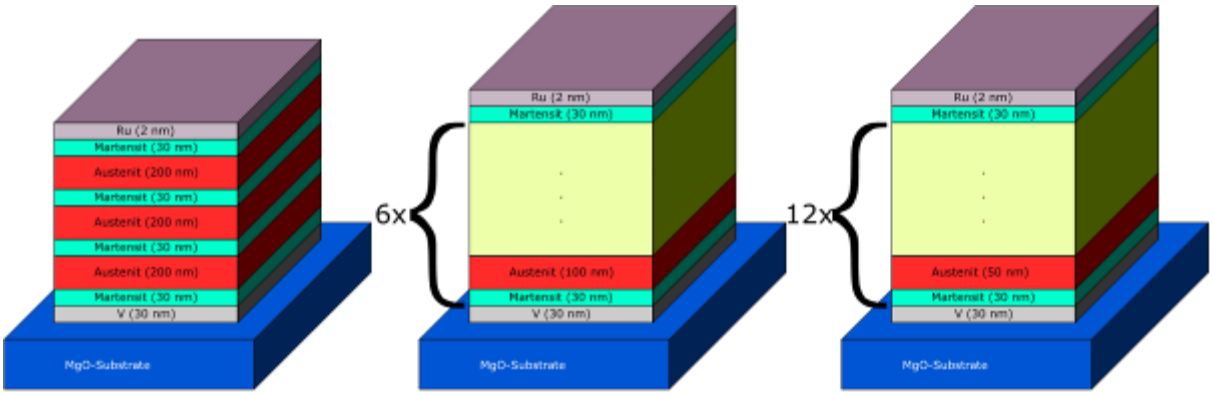
Ru (2 nm)
Martensit (30 nm)
Austenit (200 nm)
Martensit (30 nm)
Austenit (200 nm)
Martensit (30 nm)
Austenit (200 nm)
Martensit (30 nm)
V (30 nm)
MgO-Substrate
6x
Ru (2 nm)
Martensit (30 nm)
Austenit (100 nm)
Martensit (30 nm)
V (30 nm)
MgO-Substrate
12x
Ru (2 nm)
Martensit (30 nm)
Austenit (50 nm)
Martensit (30 nm)
V (30 nm)
MgO-Substrate

Fig. 2

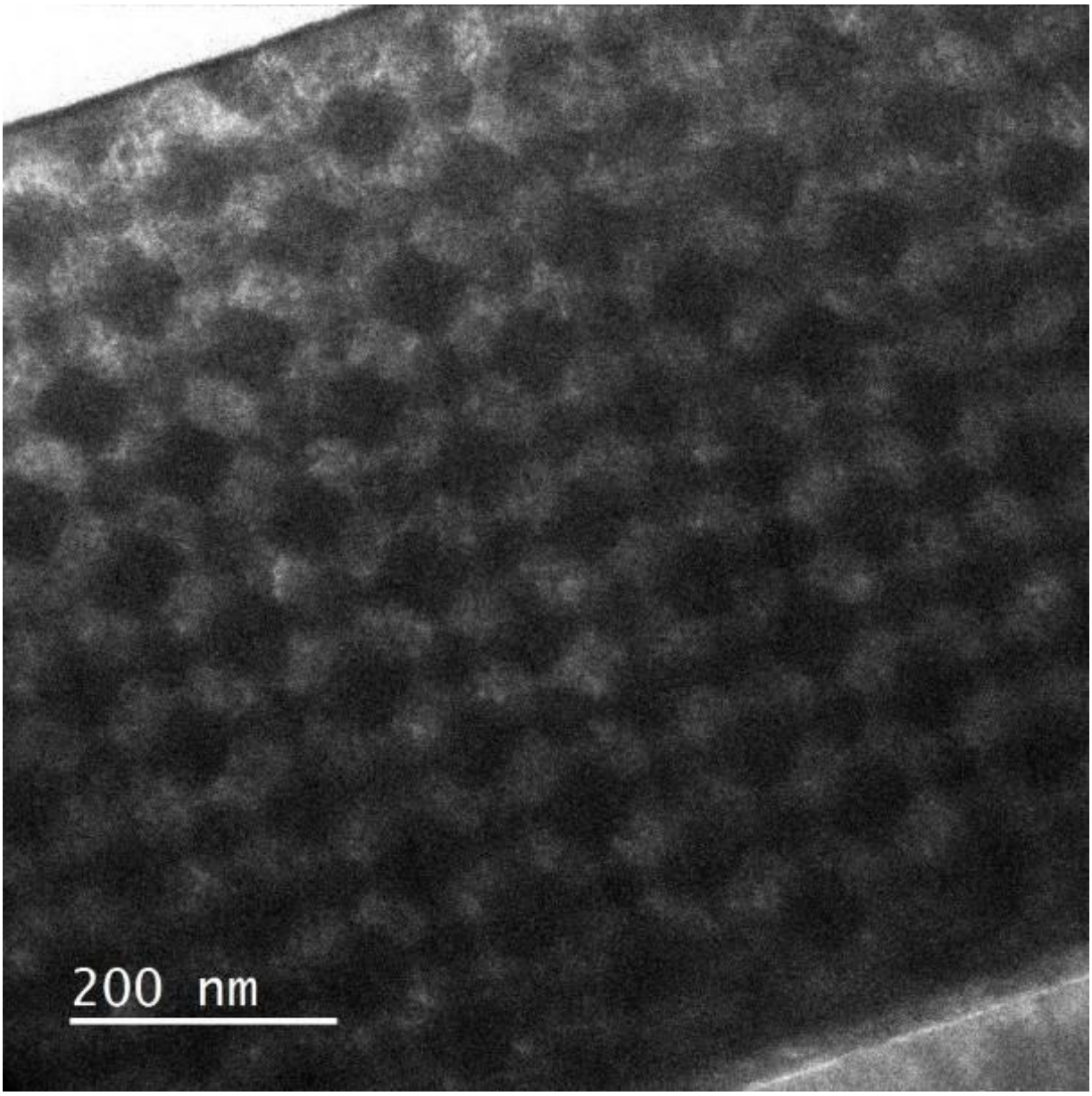
200 nm

Fig. 3

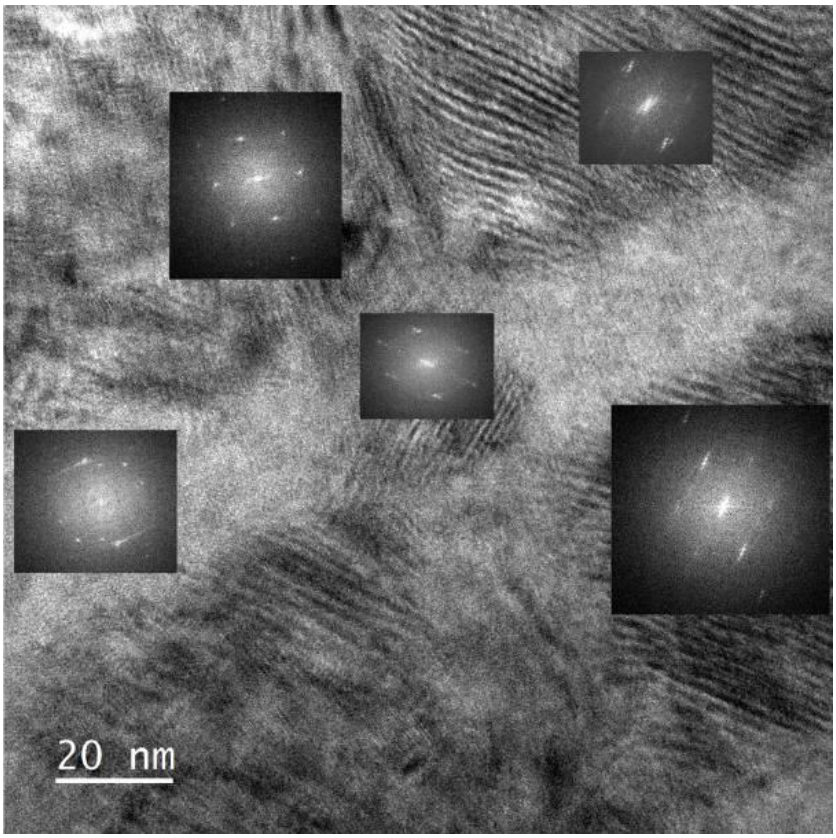

Fig. 4

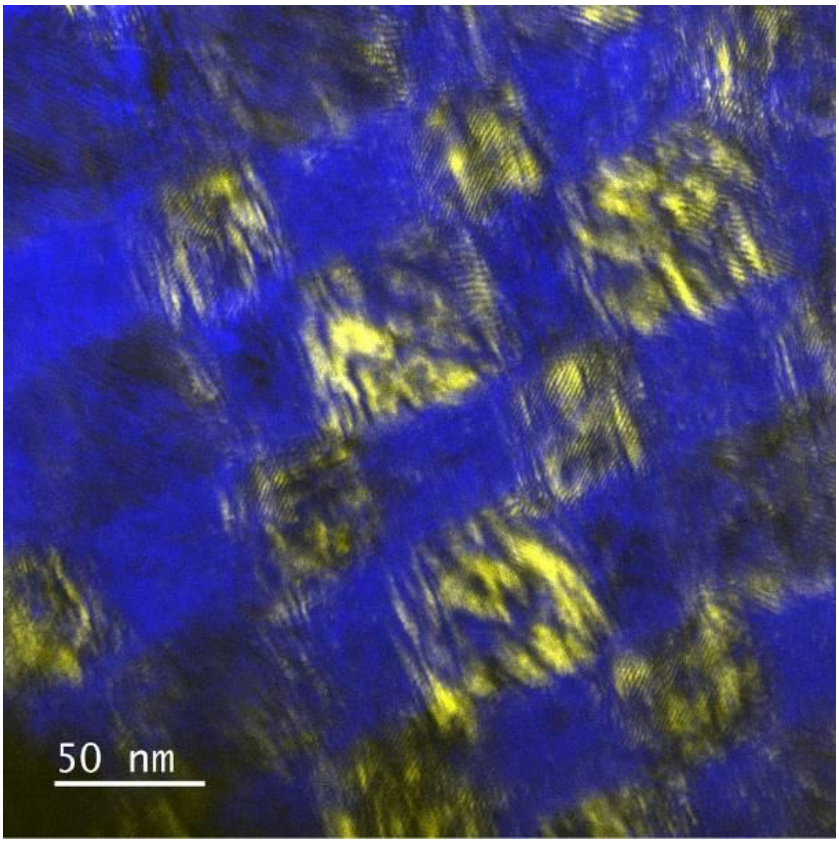

MS2.LB.P03
Fracture surfaces of nano-reinforced CFRP-specimens

L. Ploszczanski[1], G. Sinn[1], H. Rennhofer[1], H. Lichtenegger[1]

[1]Universität für Bodenkultur, Institut für Physik und Materialwissenschaften, Wien, Austria

Carbon fibre reinforced sheet materials show excellent strength properties, high stiffness and toughness, when the composites are loaded in-plane, whereas the out-of-plane properties are much lower and the properties of the composite in this direction are dominated by the matrix. Therefore, it is of great technological interest to reinforce the matrix and the attachment of the fibres to the matrix. Especially mode I or mode II fracture toughness are interesting in this context.

One promising approach to reinforce the matrix is to use nanofillers. Several kind of fillers, nano-particles and fibres are reported in the literature to increase the toughness (Domun, Hadavinia et al. 2015). For this study, nano-reinforced CFRPs where produced with single wall carbon-nanotubes SWCNT, multiwall carbon-nanotubes MWCNT and carbon-nano-fibers CNF.

Mode I fracture experiments in a double cantilever beam DCB configuration were performed to measure the mode I fracture toughness (ASTM D5529-13). Following the fracture experiments images of the fracture surfaces were taken using a Quanta FEG 250. Images were analysed and size and number of air-bubbles quantified with ImageJ (Schneider et al. 2012).

Different sizes and numbers of air-bubbles were found and representative for the kind of filler. The lowest amount of bubbles was found for the single wall carbon-nanotubes reinforced material. This material also performed best in fracture testing and gave the highest specific fracture energy.

References:

(1) ASTM D5528-13, Standard Test Method for Mode I Interlaminar Fracture Toughness of Unidirectional Fiber-Reinforced Polymer Matrix Composites, ASTM International, West Conshohocken, PA, 2013, www.astm.org Domun, N., H. Hadavinia, T. Zhang, T. Sainsbury, G. H. Liaghat and S. Vahid (2015). "Improving the fracture toughness and the strength of epoxy using nanomaterials – a review of the current status." Nanoscale 7(23): 10294-10329.

(2) Schneider, C. A.; Rasband, W. S. & Eliceiri, K. W. (2012), "NIH Image to ImageJ: 25 years of image analysis", Nature methods 9(7): 671-675, PMID 22930834 (on Google Scholar)

MS2.P001
Atomic interfacial characterization of quantum wells by using aberration-corrected STEM

C. N. Hsiao[1], P. K. Chiu[1], Y. W. Lin[1], F. Z. Chen[1]

[1]National Applied Research Laboratories, Hsinchu, Taiwan

The atomic structure of epitaxial Si0.81Ge0.19/Si multiple quantum wells grown via molecular beam epitaxy on a single crystal silicon (100) substrate was investigated using an aberration-corrected scanning transmission electron microscope with energy distribution spectrometer. Also, the influence of various aberration coefficients such as defocus, astigmatism, coma, spherical aberration and star aberration on the shape of the probe and more importantly on the electron intensity distribution within the probe was calculated. The accuracy required for compensation of the various aberration coefficients to achieve subangstrom resolution with the electron optics system was evaluated by the calculation of phase shift. It was found that the interfacial layer was composed of a single silicon crystal coherently connected to an epitaxial Si0.81Ge0.19 layer. Moreover, the distance between the dumbbell structures of the Si and Ge atoms was revealed at the SiGe/Si interface along the (111) [110] orientation (Figure 1). The corresponding fast Fourier transform exhibited a subangstrom scale point resolution. Furthermore, the higher point resolution provided much improved signal sensitivity for the atomic arrangements at interfaces. The atomic EDS chemical mapping simultaneously interpreted with the dumbbell epitaxial SiGe/Si structure. The relative positions of the atom columns at interfaces in the X-ray chemical composition image could be directly interpreted from the corresponding incoherent high-angle annular dar k-field image. Qualitative agreement was observed, and there was a one-to-one correspondence with the known projected atomic structure.

Fig. 1

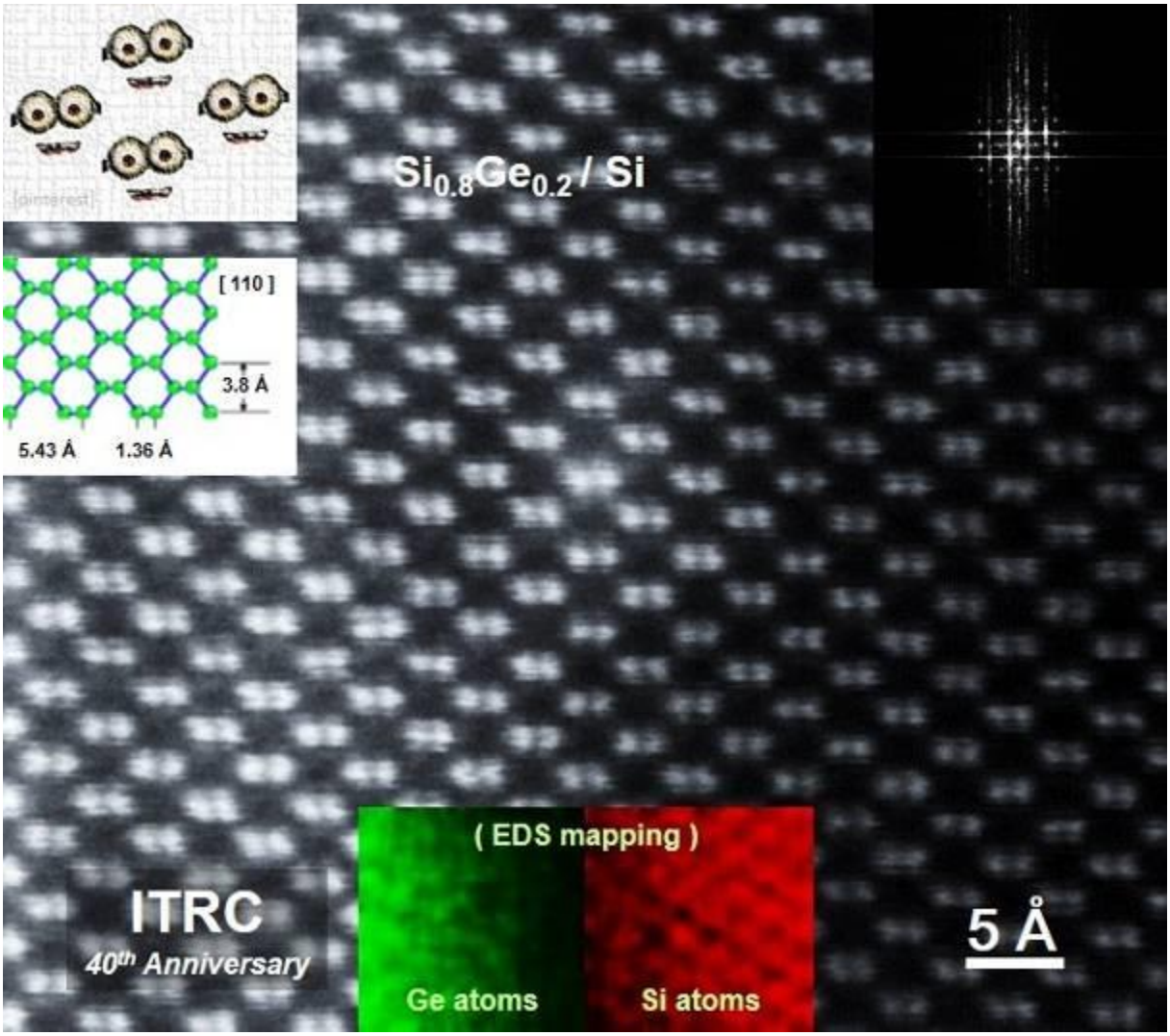

MS2.P002
TEM of PLD-obtained BaSn/ZrO3-GdBaCuO nanocomposites

A. Kamenev[1], V. Chepikov[1], A. Molodyk[1]

[1]SuperOx, Moscow, Russian Federation

External magnetic field gradually diminishes critical current of high temperature superconductors due to creep of magnetic vortices. Many of coated conductors" applications suffer from it. The mainstream way to solve this problem is introduction of artificial pinning centers (APC) to fix the vortices. As magnetic field perpendicular to film surface affects the HTS performance much more significantly than other field orientations specific attention is paid to obtaining APC in shape of nanocolumns perpendicular to HTS film.

We deposited GdBaCuO films with BaSnO3 (BSO) and BaZrO3 (BZO) inclusions in our semi-industrial PLD system on CeO2/LaMnO3/IBAD_MgO/a-Y2O3/a-Al2O3/Hastelloy tapes and characterized shape, number density and orientation of nanocolumns obtained. BSO/BZO were admixed to the target for doped HTS deposition. Transmission electron microscopy (TEM) studies were performed on a S/TEM Titan 80-300 (Thermo Fisher Scientific, USA) equipped with a spherical aberration probe corrector, energy dispersive X-ray spectrometer (EDAX, USA), Gatan imaging filter system (Gatan, USA) and high angle annular dark field detector (HAADF) (Fischione, USA). The microscope was operated at 300 kV. The JEMS software developed by P. Stadelman was used for electron diffraction patterns and images simulations. Vertical cross-sectional foils were prepared using focused Ga+ ion beam (FIB) in a Helios Nanolab 600i (Thermo Fisher Scientific, USA) FIB/scanning electron microscope (SEM) equipped with a Pt, W, C gas injection systems (GIS) and an Omniprobe 200 micromanipulator (Omniprobe, USA). To obtain planar cross-sections of the samples, a FIB-SEMs Versa 3D DualBeam FIB/SEM (Thermo Fisher Scientific, USA), equipped with a Pt and W GIS, and EasyLift micromanipulator (Thermo Fisher Scientific, USA), was used in high vacuum mode.

We have tried 6% molar of BaZrO3 and 6, 12 and 18% molar of BaSnO3. BSO and BZO inclusions were well observed by TEM as moiré patterns caused by superposition of GdBa2Cu3O7 and BaZrO3/BaSnO3 lattices. It was clear that BZO/BSO forms vertical nanoinclusions almost perpendicular to the HTS film surface but several degrees tilt. The average tilt angles were ~ 4.5˚ and ~11˚ for BSO and BZO samples, respectively.

The number density of defects was measured on both vertical and horizontal cross-sections and results correspond each other well. 6% molar BZO-doped sample contains 500±100 nanocolumns per square micrometer of HTS film. BSO-doped films contain 400±100, 700±200, 1100±300 nanocolumns/mkm2 for 6, 12 and 18% of dopant, respectively.

Observation of both types of cross-section also shows quiet the same results about size of perovskite inclusions: BSO and BZO nanocolumns are formed in the doped samples with the typical diameter of ~8 nm and ~6.5 nm, respectively.

It is hard to evaluate vertical size of nanocolumns obtained as we can not distinguish the locations where the nanocolumn terminates from the locations where the nanocolumn goes out of the cross-section plane. Anyway, observed by TEM average nanocolumn length is not less than 100 nm for BSO and 50 nm for BZO and such relation between them corresponds well with the fact that BZO nanocolumns are more inclined than BSO ones.

SuperOx acknowledges the support from Ministry of Science and Higher Education of the Russian Federation, Grant 075-11-2018-176.

MS2.P003
Structural properties of superconducting $Ba(Fe,Co)_2As_2$ thin films

L. Grünewald[1], M. Langer[2], S. Meyer[2], J. Hänisch[2], B. Holzapfel[2], D. Gerthsen[1]

[1]Karlsruhe Institute of Technology, Laboratory for Electron Microscopy, Karlsruhe, Germany
[2]Karlsruhe Institute of Technology, Institute for Technical Physics, Eggenstein-Leopoldshafen, Germany

Iron-based superconductors are a recently discovered type of high-temperature superconductors with transition temperatures as high as 58 K and large, nearly isotropic upper critical fields at low temperatures (1). Besides for fundamental investigations, iron-based superconducting thin films (2) are of interest for, e.g., superconducting tapes (3). In particular, Co-doped $BaFe_2As_2$ (Ba122) is a widely studied material system. However, the growth mechanisms of Ba122 thin films are still not fully understood due to various fabrication parameters and possible interactions with the substrate (4). In this work, we address the characterization of Ba122 by preparing thin films on different substrates with varying fabrication parameters and investigating the microstructure with electron microscopy. $Ba(Fe_xCo_{1-x})_2As_2$ thin films with nominal doping of x = 0.08 and varying thickness (20 to 300 nm) are deposited on single-crystalline substrates ($LaAlO_3$, CaF_2, MgO) by pulsed laser deposition. Cross-section samples are prepared by focused ion beam (FIB) using the *in-situ* lift-out technique. The microstructure is analyzed by (high-resolution) transmission electron microscopy ((HR)TEM) and scanning TEM (STEM) (FEI Titan^3 80-300). Energy-dispersive X-ray spectroscopy (EDXS) gives information about the elemental distribution (FEI Tecnai Osiris). In general, epitaxial growth of Ba122 thin films is observed. However, crystalline precipitates are visible in Ba122 layers (Fig. 1). In layers up to 20 nm, they often occur in a diamond-like morphology (Fig. 1a) but also with distorted symmetry (Fig. 1b, 2a). STEM-EDXS (Fig. 1b) and HRTEM analyses (Fig. 1c) suggest that they consist of Fe (or Fe-Co). An amorphous region at the substrate interface is visible in almost all inspected samples which is most likely a result of the FIB preparation. In thicker layers, the precipitates are elongated and the surrounding Ba122 layers are strained (Fig. 2a). HRTEM reveals that the bright contrast lines in Fig. 2a correspond to stacking faults at the Ba planes, i.e. missing FeAs layers (Fig. 2b). On other substrates, e.g. CaF_2, similar features in the microstructure are observed (Fig. 2c) and are currently investigated in more detail. To conclude, Ba122 thin films show deviations from the homogeneous Ba122 phase in the form of defects and precipitates. Further analysis will show how different fabrication parameters will affect the microstructure and superconducting properties.

References:

(1) H. Hosono *et al.*, *Mater. Today* 21 (2018), 278–302

(2) M. Sakoda *et al*., *Supercond. Sci. Technol*. 31 (2018), 093001

(3) K. Iida *et al*., *Appl. Phys. Rev.* 5 (2018), 031304

(4) M. Langer *et al*., *J. Phys. Conf. Ser*. (2019) in press

Fig. 1: (a) HRTEM image of a diamond-shaped precipitate embedded in a 20 nm Ba122 layer on $LaAlO_3$ substrate. (b) Bright-field STEM image and corresponding Fe K_α EDXS map qualitatively shows an enhanced Fe content in such precipitates. (c) FFT of a HRTEM image shows good agreement with the simulated diffraction pattern of Fe in [101] zone axis.

Fig. 2: (a) Bright-field TEM image of a 100 nm Ba122 layer showing bending of lattice planes around a precipitate and defects with bright contrast. (b) The defects visible in (a) are resolved in the HRTEM image of Ba122 in [100] zone axis (red arrows) and correspond to stacking faults on the Ba planes. (c) High-angle annular dark-field STEM image showing that precipitates and defects also form in Ba122 layers grown on CaF_2.

Fig. 1

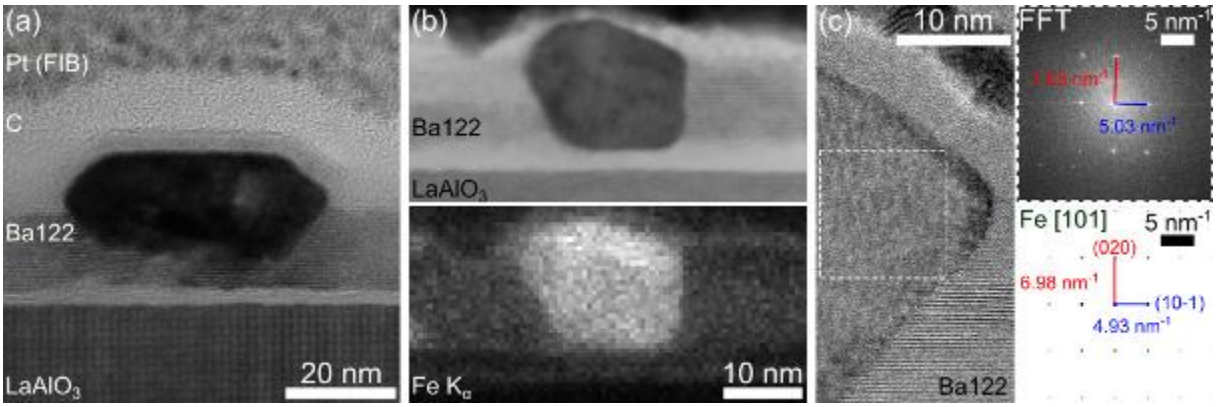
(a)
Pt (FIB)
C
Ba122
LaAlO3
20 nm
(b)
Ba122
LaAlO3
Fe Kα
10 nm
(c)
10 nm
Ba122
FFT
5 nm-1
5.03 nm-1
Fe [101]
5 nm-1
(020)
6.98 nm-1
(10-1)
4.93 nm-1

Fig. 2

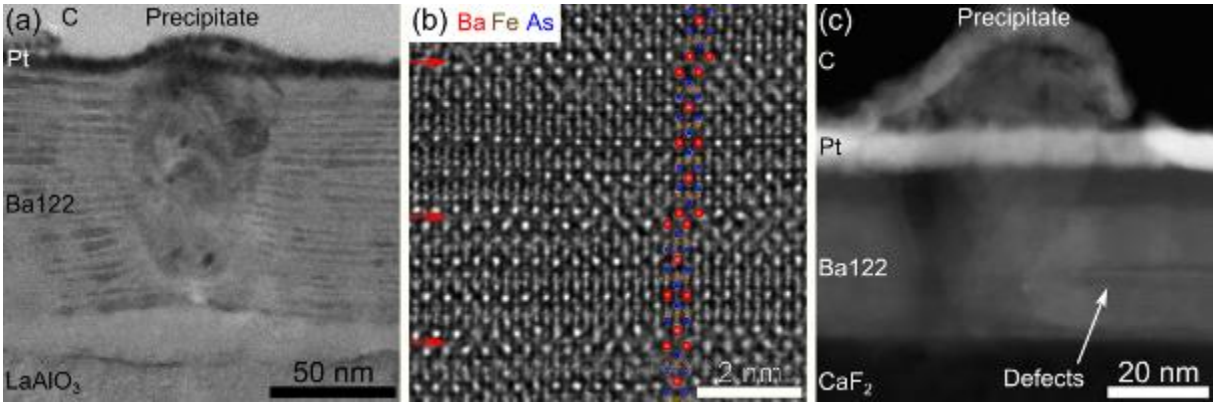
(a) C
Precipitate
Pt
Ba122
LaAlO3
50 nm
(b) Ba Fe As
2 nm
(c)
Precipitate
C
Pt
Ba122
CaF2
Defects
20 nm

MS2.P004
High-temperature behavior of RuAl-Pt thin films

M. Seifert[1], S. Menzel[1], T. Gemming[1]

[1]Leibniz Insitute for Solid State and Materials Research, Dresden, Germany

Sensors working at high temperatures (above 600 °C) are interesting for many industrial applications to enable monitoring and control of high temperature processes. To realize such devices, a high temperature metallization is required which is oxidation and creep resistant at the operation temperatures. A promising metallization is the RuAl alloy with its high melting temperature of about 2300 K (1-3). For the application in wireless sensors based on the surface acoustic wave (SAW) principle an electrical connection of the RuAl electrodes with an antenna, which is in general based on Pt, has to be established. One possibility to use the known Pt wire bonding for this interconnection is the utilization of Pt-RuAl bilayer contact pads.

The aim of this work is to analyze the high temperature stability of Pt-RuAl bilayers as a reference for the contact pads in SAW devices.

Pt-RuAl bilayers are deposited on $Ca_3TaGa_3Si_2O_{14}$ (CTGS) substrates with a 20 nm SiO_2 barrier layer by magnetron co-sputtering (RuAl) and e-beam evaporation (Pt). The thickness of the RuAl layer is 110 nm, the covering Pt layer is 100 nm thick. The films are annealed at temperatures up to 900 °C under HV and in air for 10 h. The phase formation is controlled by XRD. Auger electron spectroscopy is applied to determine the chemical composition across the film thickness by measuring depth profiles. TEM in combination with EDX is used to reveal the local morphology and local chemical composition.

The analyses show a strong interdiffusion between the Pt and RuAl layer during the heat treatment. After annealing at 600 °C in air the former bilayer structure is still visible (Fig. 1(a)). However, Al has diffused out of the RuAl film into the Pt layer and up to the film surface where a 20 nm thick Al_2O_3 film has formed. The former RuAl layer changed its composition to $Ru_{50}Al_{25}Pt_{25}$ and the Pt layer contains about 30 at% of Al. A heat treatment at 800 °C in air results in a complete oxidation of the Al and the formation of an 80 nm thick Al_2O_3 film at the film surface (Fig. 1(b)) Locally, also Ru starts to oxidize and RuO_2 grains appear.

During annealing at 900 °C in air Ru is oxidized almost completely to volatile RuO_3 or RuO_4 and the film consists of Pt grains and pores in the region of the former Pt-RuAl bilayer covered by an Al_2O_3 layer (Fig. 1(c)).

Annealing under HV at 900 °C leads to a reaction between the layer system and the CTGS substrate. There is no flat interface to the substrate anymore and Al_2O_3 is found in addition to the SiO_2 barrier. Al diffused into the former Pt film and locally Al_2O_3 has formed at the film surface (Fig. 1(d)).

The results show that Pt-RuAl bilayers show only a limited applicability for high temperature devices due to the strong interdiffusion and oxidation of Al starting at 600 °C. To use these systems in high temperature sensors, additional cover layers have to be applied to protect the film.

References:

(1) M. Seifert et al., J. Alloy Compd. 688 (2016) 228-240

(2) M. Seifert et al., Materials 10 (2017) 277

(3) M. Seifert et al., J. Alloy Compd. 776 (2019) 819-825

Financial support by BMBF IPT 03IPT610Y is gratefully acknowledged.

Fig. 1: STEM images (predominant orientation contrast) of a Pt-RuAl bilayer on CTGS after annealing in air at (a) 600 °C, (b) 800 °C, (c) 900 °C and (d) under HV at 900 °C.

Fig. 1

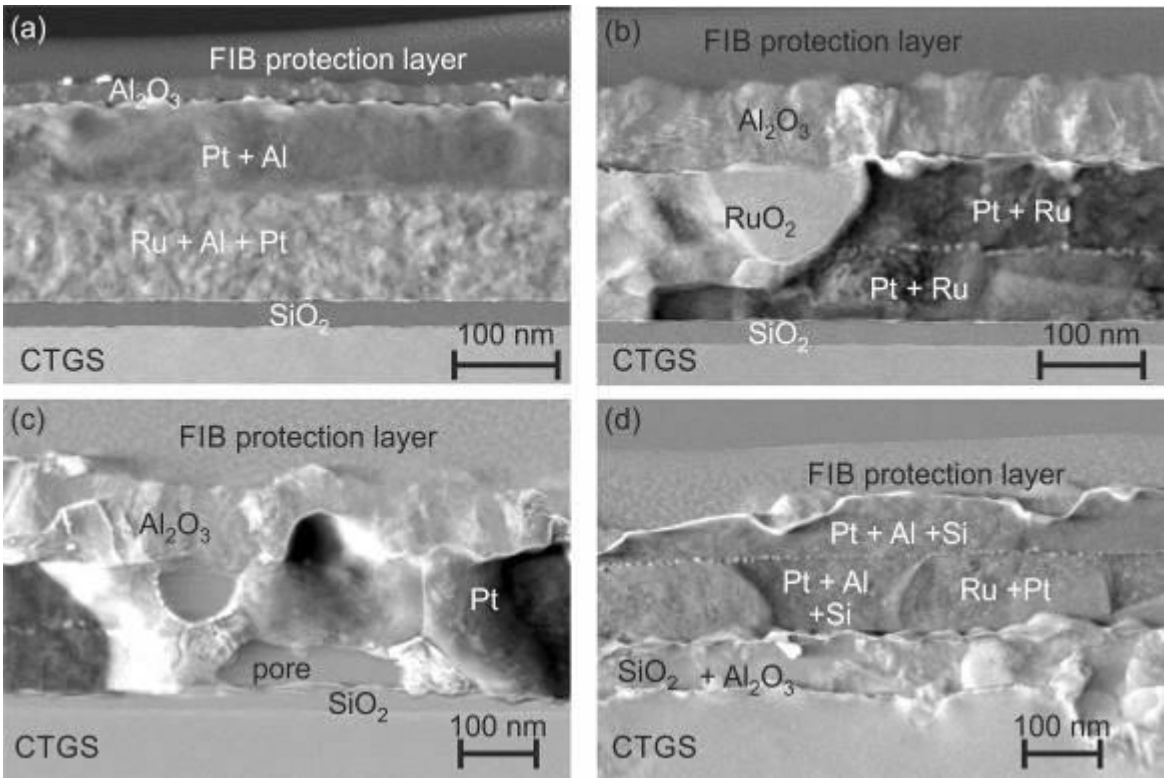
(a)
FIB protection layer
Al_2O_3
Pt + Al
Ru + Al + Pt
SiO_2
CTGS
100 nm
(b)
FIB protection layer
Al_2O_3
RuO_2
Pt + Ru
Pt + Ru
SiO_2
CTGS
100 nm
(c)
FIB protection layer
Al_2O_3
Pt
pore
SiO_2
CTGS
100 nm
(d)
FIB protection layer
Pt + Al +Si
Pt + Al +Si
Ru +Pt
SiO_2 + Al_2O_3
CTGS
100 nm

MS2.P005
TEM investigation of Compact Tellurium Thin Films with Bismut Atomic Doping

C. Damm[1], L. Guodong[1], R. Hübner[2], K. Nielsch[1]

[1]IFW Dresden, Dresden, Germany
[2]Helmholtz-Zentrum Dresden-Rossendorf, Dresden, Germany

Compact tellurium (Te) thin films show important applications in micro-thermoelectric modules, which are able to convert waste heat to electrical energy (µTEG) or vice versa to use electricity to generate cooling (µTEC). The as-fabricated µTECs, which are based on electrochemically deposited n-type Bi2(TexSe1-x)3 (in short BiTeSe) and p-type tellurium, demonstrate a rapid response time of 1 ms, a high cycling reliability of up to 10 million cycles and a long term cooling stability of more than 1 month at constant electric current [Fig.1].(1) However, a mismatch of electrical conductivity between pure Te and BiTeSe often leads to some difficulties in the geometry design of micro-thermoelectric modules. In order to enhance the electrical property of Te, we have introduced an atomic bismuth (Bi) doping.

In this report, we have performed transmission electron microscopy (TEM, FEI Tecnai G2/ 200 kV) analysis to observe the presence and distribution of Bi within Te. To this end, cross-sectional TEM specimens were prepared using the Focused Ion Beam technique (FIB, FEI Helios NanoLab 600i). The Bi-doped Te samples have a columnar grain structure. Selected-area electron diffraction [A1] proves the presence of crystalline Te. Results of Nanodiffraction in numerous areas also suggest Te (hexagonal, space group 152, a = b = 0,4458 nm, c = 0,5925 nm, α = ß = 90°, γ = 120°) but could be explained with Bi (rhomboedral, space group 166, a = b = 0,4550 nm, c = 1,1850nm, α = ß = 90°, λ[A2] = 120°), too. Unfortunately, the geometry of the Bi and Te unit cells differ only in the length of the c-axis. In addition, HRTEM images show lattice fringes, which could belong to Bi or Te. To unambiguously distinguish between both elements, chemical analysis is necessary.

Performing energy-dispersive X-ray spectroscopy (EDXS) analysis with a conventional Si(Li) detector, no Bi counts appear in the EDX spectra during reasonable measuring times of several minutes. To finally get the distribution of Bi in the Te matrix was, we employed a FEI Talos F200X microscope operated at 200 kV and equipped with an X-FEG electron source and a Super-X EDX detector system and performed spectrum imaging analysis based on EDXS [Fig.2].

References:

(1) Li, G. *et al.* Integrated microthermoelectric coolers with rapid response time and high device reliability. *Nat. Electron.* 1**,** 555–561 (2018).

Fig. 1: View of an integrated µ- TEC with six leg pairs, demonstrating the four- layer structure

Fig. 2: Superimposed element distributions (in particular Bi (brown) and Te (blue)) obtained by spectrum imaging analysis based on EDXS in scanning TEM mode.

Fig. 1

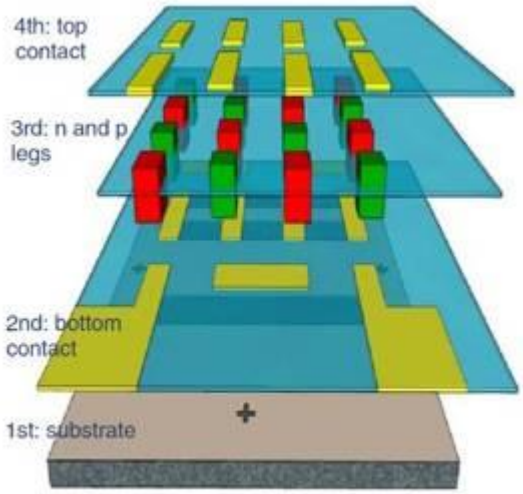

Fig. 2

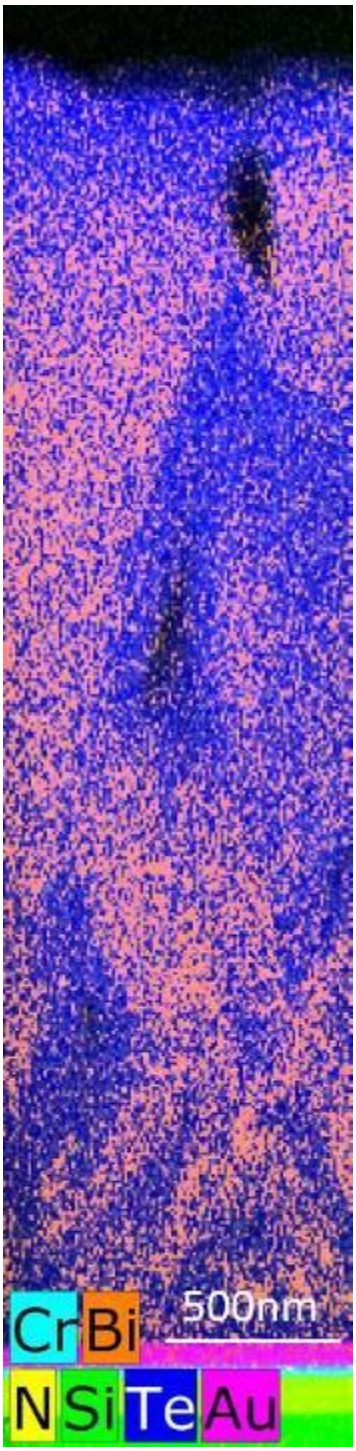

MS2.P006
Scale-bridging and correlative *in situ* study of functional thin films throughout their full life-cycle

L. Vogl[1], P. Schweizer[1], P. Denninger[1], J. Kauth[1], M. Moninger[1], A. Hutzler[2], T. Zech[3], F. Niekiel[1], M. Wu[1], J. Will[1], J. Schubert [1], T. Unruh[3], E. Spiecker[1]

[1]Friedrich-Alexander University Erlangen-Nuremberg, Institue of Micro-and Nanostructure Research, Erlangen, Germany
[2]Friedrich-Alexander University Erlangen-Nuremberg, Lehrstuhl für elektronische Bauelemente, Erlangen, Germany
[3]Friedrich-Alexander University Erlangen-Nuremberg, Institute of Condensed Matter Physics, Erlangen, Germany

Metallic thin films find a broad range of applications in functional electronic devices. However, failure mechanism like solid- state dewetting are still not totally understood. With the focus on even thinner films in the range of few nanometers, *in situ* microscopy is increasingly used to gain insights into the dynamic processes even on the atomic scale.

While recent studies focused on individual aspects of the structural evolution of thin films using *in situ* microscopy, a complete *in situ* life cycle monitoring of the interplay between structural and functional properties has not been achieved so far.

Here we present an all-encompassing study of the structure-property relationship of metallic thin films, stating from their formation until heat-induced degradation by solid-state dewetting.

Noble metals (Au,Pt,Cu) are chosen for this study, due to their widespread application in electronics. By measuring the conductivity during PVD based deposition (see figure 1b), a direct feedback control allows for *in situ* optimization of processing parameters, drastically reducing process development times. A Comparison between sputtered and electron beam evaporated films is conducted with respect to morphology, crystallography and electrical conductivity. Different film thicknesses (see figure 1a) are compared looking for the "sweet-spot" of electrical percolation and optical properties. The prepared films are characterized by light and electron microcopy as well as X-ray diffraction and UV-Vis spectroscopy.

Heat treatment of metallic films can be used on the one hand to increase grain size and conductivity, but on the other hand lead to degradation via solid-state dewetting. To fine-tune this heat treatment, *in situ* light and electron microscopy is combined with *in situ* electrical measurements (see figure 1c). The electrical resistance of thin films stays at a steady state for a prolonged period of time during heating, until de-percolation sets in (figure 1 d). The initial increase can be attributed to thermal effects and is partially counteracted by recrystallization.

To understand the early stages of degradation continous, ultrathin films are heated *in situ* in TEM (see Figure 2a). Before Void formation starts the degradation process, grain growth and texture formation is observed. The interface between thin film and substrate plays a crucial role in all of those processes. Epitaxial growth and lattice mismatch can be tailored to produce desired properties.

On an amorphous substrate, the void formation occurs randomly, while a single crystalline substrate (MoS2) leads to highly ordered voids. These voids act as a template for the further degradation process of the thin film (see Figure 2b). Finally, simultaneously acquired low energy electron diffraction patterns and secondary electron images during the dewetting process help to elucidate the temporal interplay between morphology and crystallography (see Figure 2c).

Fig. 1

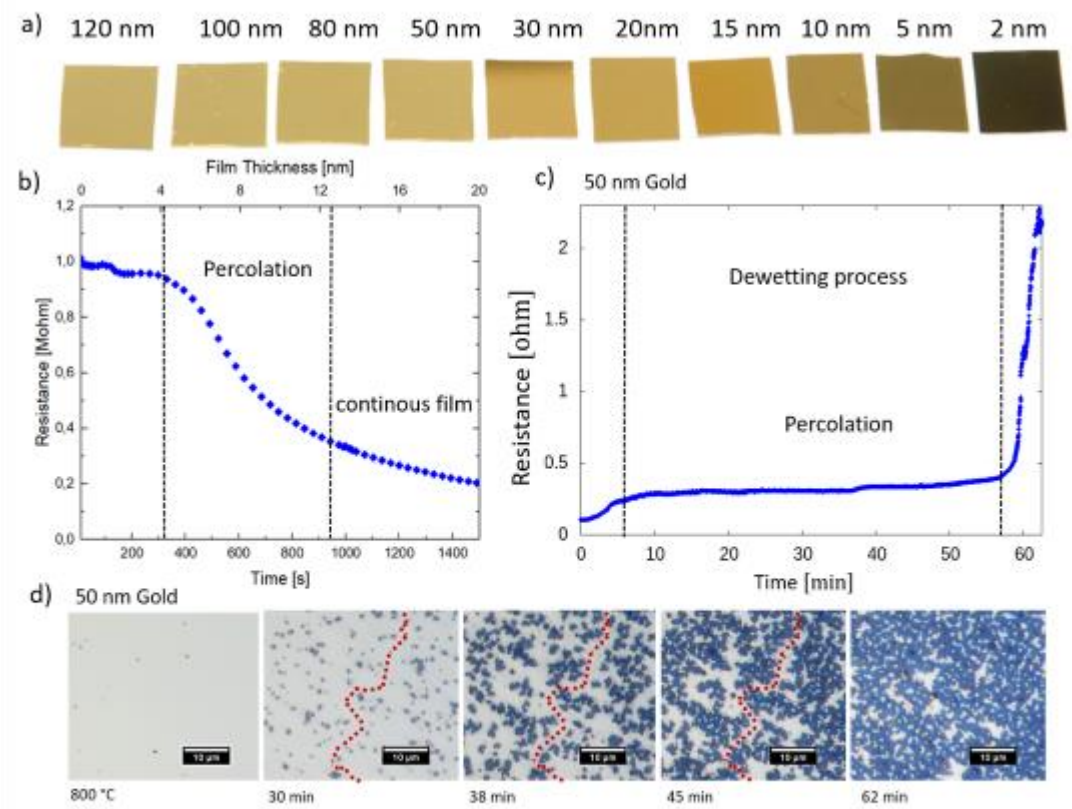

Figure 1: a) Optical image of Gold thin films of different thickness. In situ electrical measurement during sputtering b) and heating c). d) in situ light microscopy during heating showing dewetting and depercolation.

Fig. 2

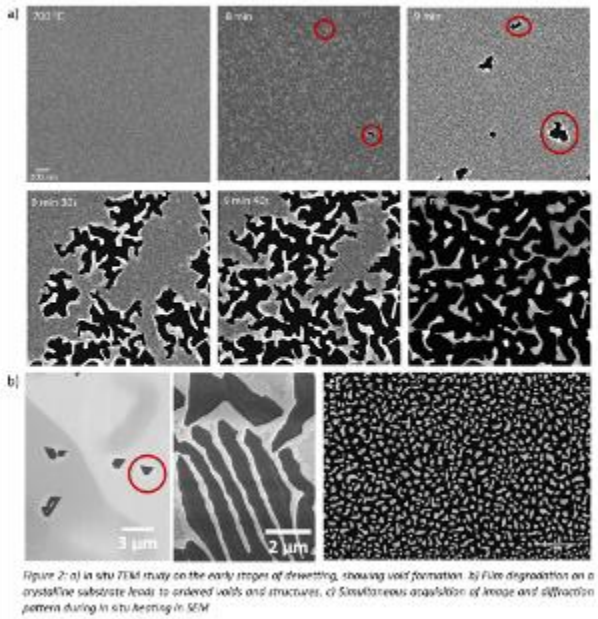

Figure 2: a) in situ TEM study on the early stages of dewetting, showing void formation. b) Film degradation on a crystalline substrate leads to ordered voids and structures. c) Simultaneous acquisition of image and diffraction pattern during in situ heating in SEM

MS2.P007
Atomic-scale investigation of nickelate-based perovskite superlattice interfaces

F. Misjak[1], D. Geiger[1], H. Qi[1], R. Ortiz[2], E. Benckiser[2], U. Kaiser[1]

[1]Ulm University, Electron Microscopy Group of Materials Science, Ulm, Germany
[2]Max Plank Institute for Solid State Research, Stuttgart, Germany

Superconductors have great potential for applications, but can be used widespread only when critical temperatures (T_c) of the superconducting phase can be substantially raised. Therefore the search for new high-Tc materials is ongoing. It has been shown that oxide heterostructures and superlattices composed of rear-earth nickel oxide and a wide bandgap insulator may host similar physics to that of the high-T_c cuprates (1). For tailoring this kind of materials, the precise control of interfaces between two different materials become crucial.

In this work, we investigated $LaNiO_3/LaGaO_3$ superlattices grown on (001) $SrTiO_3$ substrate. The superlattice films were prepared by pulsed laser deposition with four unit cell thick layers of $LaNiO_3$ and different number of unit-cell-layers of $LaGaO_3$.

Negative-spherical-aberration (C_s) imaging was used to resolve the oxygen atomic columns and the interface structures using 300kV aberration-corrected (AC)-HRTEM. 300kV AC scanning (S)TEM equipped with an energy-dispersive X-ray spectrometer was used to map the chemical composition across the heterointerfaces.

The results show that the superlattice films had atomic flat (001) planes without lattice defects (Fig. 1a), while the chemical distribution of the elements shows waviness resembling closely the surface roughness. Slight intermixing of the constituent cations across the heterointerfaces was also found (2). The cation intermixing can be attributed to cation interdiffusion to avoid polar discontinuity at the interfaces, while incomplete monolayer coverage during epitaxial growth can also play a role. The atomic steps referring to the incomplete coverage of the sublayers can be clearly seen in Fig 1a. The projected structure and the image simulations corresponding to $LaNiO_3$ and $LaGaO_3$ are shown in Fig 1b.

We propose a model for the possible mechanisms affecting the chemical abruptness of the heterointerfaces which may help understanding the growth mechanism.

References:

(1) J. Chaloupka, G. Khaliullin, Phys. Rev. Lett. 100, 016404, 2008

(2) H.Y. Qi, M.K. Kinyanju, X.D. Chen, J. Biskupek, D. Geiger, E. Benkiser, H.-U. Habermeier, B. Keimer, U. Kaiser, J Mater Sci 51, 8186, 2016

We are grateful for financial support from the IQST project-between the University of Ulm and University of Stuttgart. We gratefully acknowledge Sabine Grözinger for cross-sectional TEM sample preparation.

Fig. 1: Experimental and calculated 300kV TEM image of the $LaNiO_3/LaGaO_3$ heterointerface in [110] projection. (a) Experimental image under negative Cs condition. (b) Atomic arrangement and calculated image along [110] direction.

Fig. 1

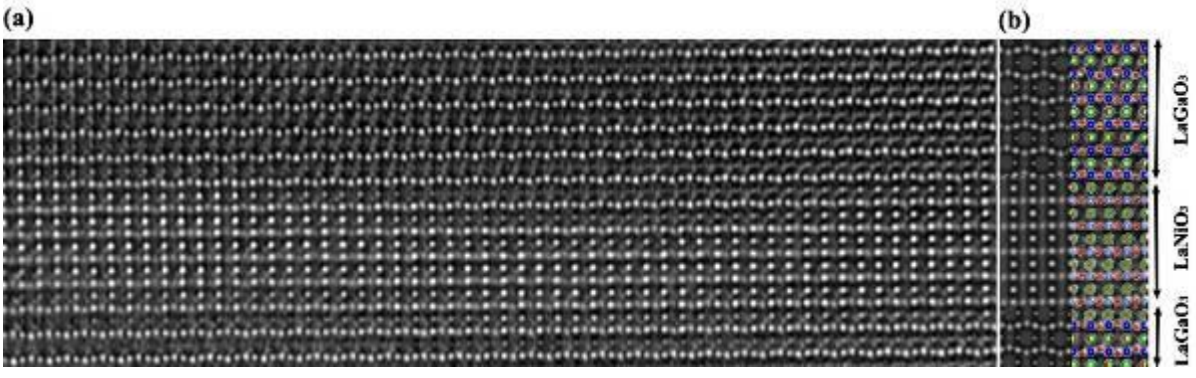

MS2.P008
FIB lamella characterization containing NaNbO3 nanostructure grown up over metallic niobium.

B. Rodrigues Canabarro[1], P. M Jardim[1], M. J. Rodrigues Marim[1]

[1]UFRJ, PEMM, Rio de Janeiro, Brazil

Sodium niobate has gained scientific attention due to its properties as semiconductivity, piezoelectricity, and photoactivity. To improve their efficiency and combine these properties, they need to be synthesized in the nanoscale (1). A cheap and efficient way to obtain oriented anisotropic oxide crystals is by alkali hydrothermal route, forming nanowires naturally, without the addition of any help to orient their growth (2). In this study, we used metallic niobium as a substrate and also as a precursor to obtain the oriented growth of the nanocrystals. In order to use this system composed by a nanostructured layer of NaNbO3 supported on metallic niobium as a possible piezo-phototronic device, it is necessary to understand the nanostructure organization.

Characterize the nanostructure morphology formed over niobium plate and their interface.

The NaNbO3 nanostructures were synthesized by alkali hydrothermal route from metallic niobium in plate form. In order to do that, we added the niobium plates with NaOH 0.75M inside an autoclave, at 40°C for 36h. The sample was washed with distilled water and dried at 100°C for 3h. Lastly, they were thermally treated in a vacuum furnace at 550°C for 15 minutes.

We have milled one sample lamella, cut perpendicularly to surface, with a focused ion beam (FIB) at the scanning electron microscopy (SEM), in order to analyze its interface. The sample was analyzed by transmission electron microscopy (TEM), combined with the techniques of selected area electron diffraction (SAED) and energy dispersive spectroscopy (EDS).

Analyzing the FIB lamella TEM images (Figure 1 - TEM image from lamella), it is possible to observe that nanowires present a layer width of 1,19µm. It is also possible to observe that nanowires do not grow in a perpendicular way regarding the surface of metallic niobium, but they connect each other along the layer, forming a porous nanostructure. They present much smaller diameters in the region near interface NaNbO3/Nb, and they grow along the niobate layer, presenting bigger diameters in the top of the layer.

FIB lamella EDS mapping analysis (Figure 2 - EDS mapping showing chemical elements), allows us to observe the localization of the chemical elements that compose the sample, mainly Na, O, and Nb. With the EDS maps, it was possible to identify a Nb2O5 layer in the NaNbO3/Nb interface, with 50nm of width. The intensity of the Na is bigger in nanowires region, and in the interface region near nanowires, reducing its intensity in the interface region near Nb. Oxygen, in its turn, shows great intensity in nanowires region and interface region, both near nanowire, and near Nb. Whereas Nb shows bigger intensity in niobium plate region, and its intensity decreases in the interface region, in which oxide intensity increases.

It was possible to characterize the NaNbO3 nanostructure and the interface by TEM image analysis obtained from a cut FIB lamella. It was possible to identify the presence of Nb2O5 layer in the interface and quantify its width.

We acknowledge the LNNano/CNPEM, the CENANO/INT, and the Electron *Microscopy Nucleus* of UFRJ, for their support with the use of equipments Titan Cubed Themis – FEI, HELIOS NanoLab DualBeam G3 CX – FEI and Versa 3D – FEI.

References:

(1) R. Grange, *et al*. *Nanowires - Implementations and Applications* (InTech, 2011).

(2) M.-A. Einarsrud, *et al*. *Chem. Soc. Rev.* 43**,** 2187–2199 (2014).

Fig. 1

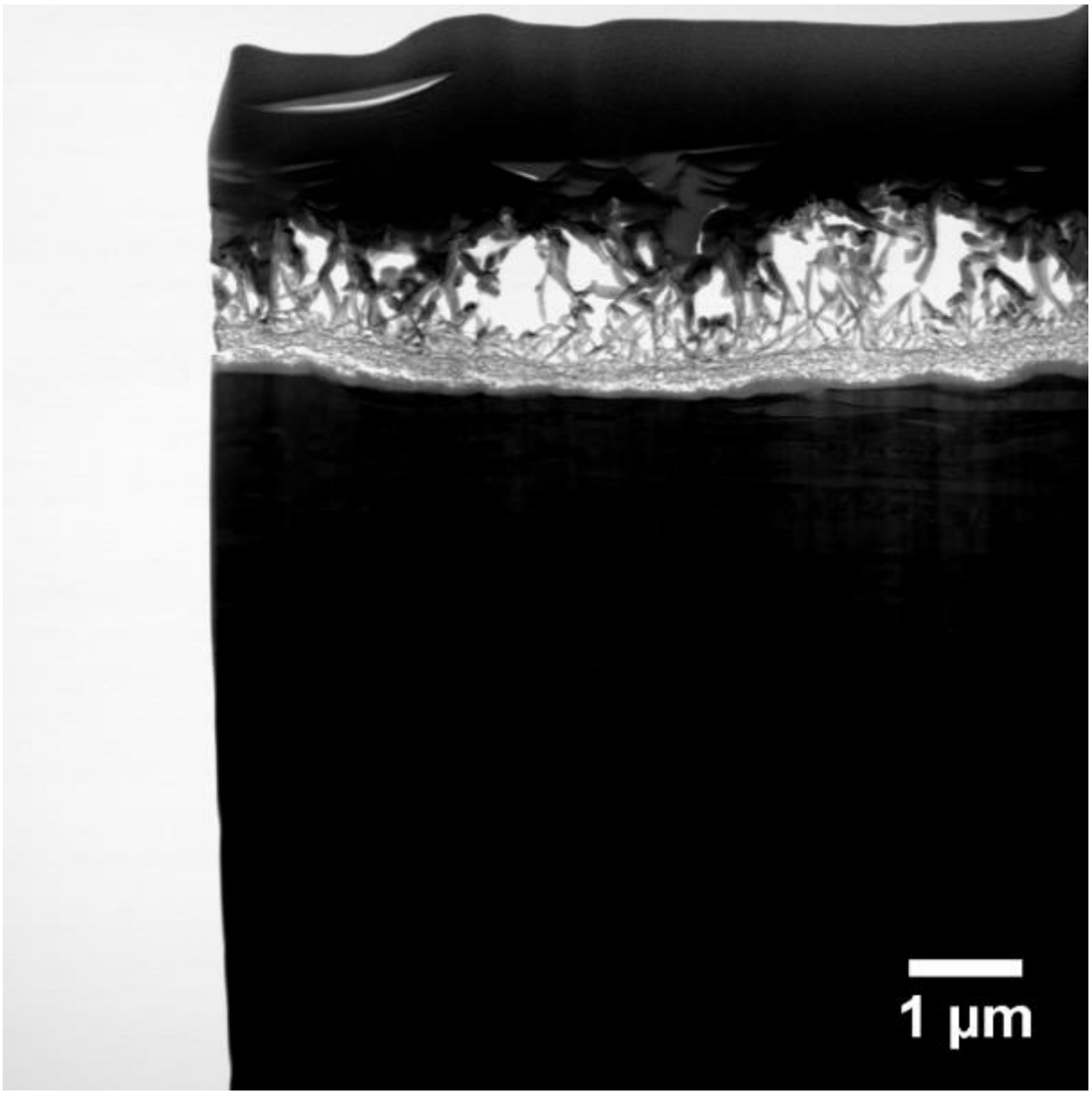

Fig. 2

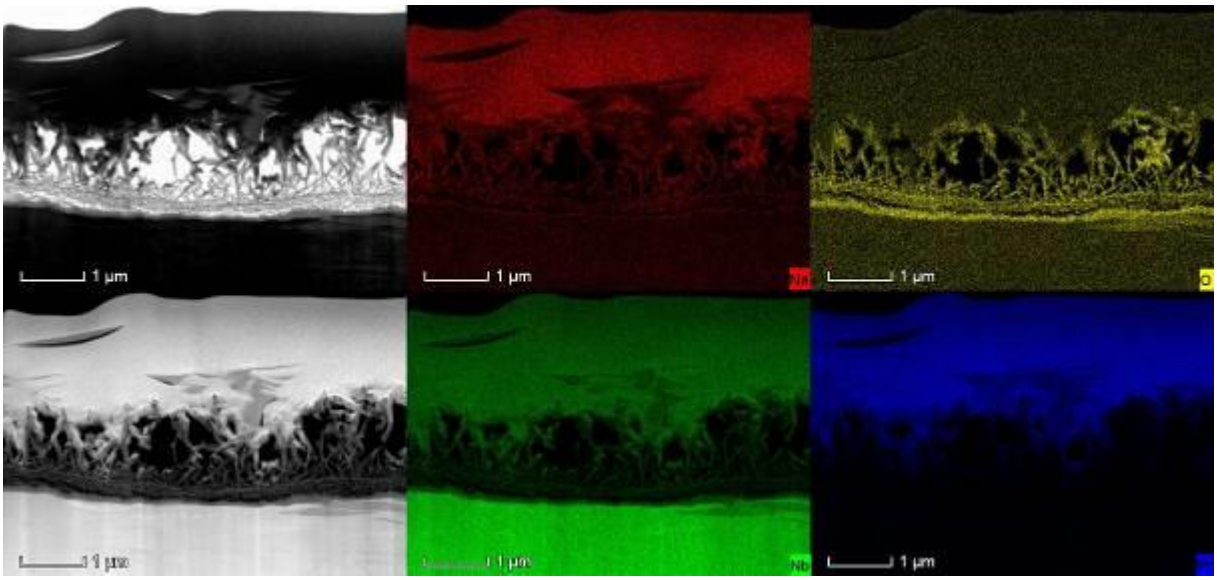

MS2.P009
Correlative scanning electron microscopy on cross-section of high efficient $Cu(In,Ga)Se_2$ thin-film solar cell

M. Krause[1], A. Nikolaeva[1], P. Jackson[2], D. Hariskos[2], W. Witte[2], D. Abou-Ras[1]

[1]Helmholtz-Zentrum Berlin für Materialien und Energie, Berlin, Germany
[2]Zentrum für Sonnenenergie- und Wasserstoff-Forschung , Stuttgart, Germany

In order to quantify limitations on the device performance several scanning electron microscope (SEM) characterization techniques were performed on the same position of a cross-sectional prepared high efficiency (21% without anti-reflective coating) $Cu(In,Ga)Se_2$ (CIGSe) thin-film solar cell. In spite of highest conversion efficiencies of 22 - 23% the photovoltaic performance of CIGS solar cells is still limited by open-circuit voltage (V_{oc}) and short-circuit current (j_{sc}) losses in terms of the theoretical limit. The present work reports an insight into the microstructure and reveals potential limitations caused by enhanced nonradiative recombination at grain boundaries (GBs) and by electronic potential fluctuations. The stacking sequence of the CIGSe solar cell studied in the present work is ZnO:Al/(Zn,Mg)O/CdS/CIGSe/Mo/glass, of which the coevaporated CIGSe absorber underwent a RbF postdeposition treatment (PDT). Specimens were prepared by careful mechanical polishing the cross-section and coated with a thin carbon layer. Microscopic investigations on the microstructural, compositional, electrical and optoelectronic properties were carried out using Zeiss UltraPlus and Merlin scanning electrion microscopes. Electron backscatter diffraction (EBSD), energy dispersive X-ray spectrometry (EDX), electron-beam induced current (EBIC) and cathodoluminescence (CL) were performed on a cross-sectional specimen. All characterization techniques were performed on the same position of the cross-section expect of EBSD, Figure 1. By means of EBSD, an average grain size of 0.5 µm was determined as well as a weak preferred orientation in <110>/<201> crystal directions. From the EBIC results, the width of the space-charge region (w_{SCR}) and the minority-carrier diffusion length in the quasi-neutral region (L_D) were extracted by modeling profiles (1) perpendicular to the *p*-*n*-junction. EDX elemental distribution analysis did not show any substantial, spatial variations in composition, except for the Ga/In gradient perpendicular to the substrate, which can be also correlated to the detected spectral shift in the CL peak in the same perpendicular direction. Extracted elemental profiles reveals the band-gap energy minimum is located in vicinity to CdS/CIGSe interface. Recombination velocities at GBs were determined to be on the order of 10^3 cm/s from CL profiles across GBs [2]. Thus, they are on the same order of magnitude as GBs in various Na-containing CIGSe thin films without any PDT. In conclusion, the acquisition of several SEM characterization techniques on a CIGSe cross-section can be correlated and their results pointed out electrostatic potential fluctuations seems to be negligible in terms of performance limitations. In contrast enhanced nonradiative recombination at GBs is one origin of a significant limitation on the *V*oc of a high-efficient CIGSe solar cell.

References:

(1) M. Nichterwitz *et al.*, "Influence of grain boundaries on current collection in Cu(In,Ga)Se2 thin-film solar cells," *Thin Solid Films*, vol. 517, no. 7, pp. 2554–2557, 2009.

(2) B. G. Mendis *et al.*, "A contactless method for measuring the recombination velocity of an individual grain boundary in thin-film photovoltaics," *Appl. Phys. Lett.*, vol. 97, no. 9, pp. 1–3, 2010.

Fig. 1

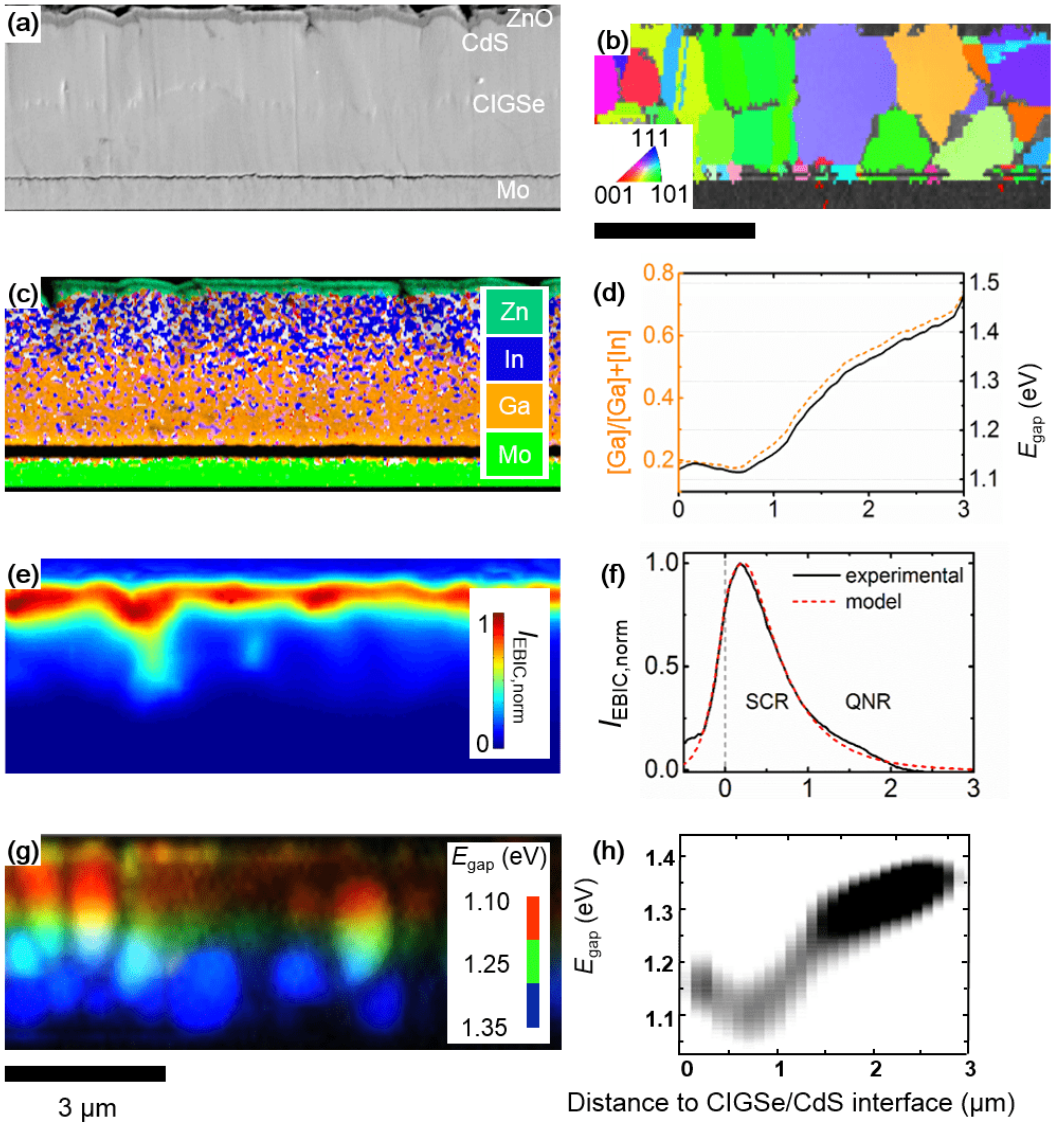
(a)
ZnO
CdS
CIGSe
Mo
(b)
111
001
101
(c)
Zn
In
Ga
Mo
(d)
[Ga]/([Ga]+[In])
E_{gap} (eV)
(e)
$I_{EBIC,norm}$
(f)
experimental
model
SCR
QNR
$I_{EBIC,norm}$
(g)
E_{gap} (eV)
1.10
1.25
1.35
3 µm
(h)
E_{gap} (eV)
Distance to CIGSe/CdS interface (µm)

MS2.P010
Microscopic study of a low temperature synthesized MoAlB coating by combinatorial direct current magnetron sputtering

R. Sahu[1], B. Völker[1,2], J. O. Achenbach[2], M. Hans[2], D. Primetzhofer[3], D. Miljanovic[2], J. M. Schneider[1,2], C. Scheu[1,2]

[1]Max-Planck-Institut für Eisenforschung, Independent Research Groups, Düsseldorf, Germany
[2]RWTH Aachen University, Materials Chemistry, Aachen, Germany
[3]Uppsala University, 3Department of Physics and Astronomy, Uppsala, Sweden

MoAlB belonging to a family of ternary borides known as MAB phases exhibits an interesting combination of properties such as high melting point, good electrical and thermal conductivities. MAB phase materials are transition metal borides (TMB), where M is an early transition metal, A is a group A element and B represents borides. These TMB's are potential candidates for technological applications such as structural high temperature materials (1), solar absorbers (2), wear resistant coating (3), battery electrodes (4) as well as chemical coating (5). While the synthesis of orthorhombic MoAlB in bulk form has been communicated in 2016 (6), no thin film synthesis reports have been published to date. Here, we report the atomic level characterization of MoAlB thin films synthesized at a 500 °C lower temperature as during bulk processing.

MoAlB thin films were synthesized on single crystalline Al_2O_3 (0001) by DC magnetron sputtering using MoB and Al target at 700 °C. Bruker D8 Discovery general area detector diffraction system (GADDS) was used for XRD measurements and the chemical composition was determined by time-of-flight elastic recoil detection analysis (ToF-ERDA) based energy-dispersive X-ray spectroscopy (EDS). Atomic level structural characterizations were done utilizing several transmission microscopy methods, e.g. conventional transmission electron microscopy (TEM), high resolution TEM (HRTEM), scanning TEM (STEM), energy dispersive X-ray spectroscopy mapping (EDS), and electron energy loss spectroscopy (EELS). HRTEM of a lamella, prepared by focused ion beam (FIB) lift-out technique, was performed at 300 kV using a FEI image-side Cs corrected FEI Titan Themis. For spectral analysis, STEM EELS and STEM EDS mappings were conducted with a FEI Titan equipped with a probe-side Cs corrector and a high energy resolution Gatan image filter (Quantum) operating at 300 kV. During acquisition of STEM-EELS spectra, the energy resolution was measured to be 1 eV at the full width half maxima of zero loss. The spectra were collected with the 5 nm aperture at an energy dispersion of 0.10 eV/C.

Macroscopic structural analysis based on XRD revealed phase pure MoAlB having a lattice parameter less than 0.4% deviating from theoretical calculations. The microscopic study reports MoAlB as major phase with two other minor phase components. MoAlB growth is in two different orientations in [001] and [010] perpendicular to the substrate surface. The atomic arrangement of Mo and Al layers in the high resolution images confirm the MAB phase formation. STEM-EDS and STEM-EELS confirmed elemental composition of MoAlB. Elemental transition of Mo $M_{4,5}$, Al L_1, Al $L_{2,3}$, and B K edges are detected with an edge onset at 228.8, 119.4, 73.5, and 192.2 eV respectively from an integrated EELS spectrum. Apart from the major MoAlB phase EDS shows two other minor phase components, which are rich in O and Al. These two minor phases have been analyzed further using the MATLAB code developed by Zhang and Scheu (7).

In summary, we report the formation of orthorhombic MoAlB thin films. In addition to the majority phase MoAlB the formation of O and Al rich impurity phases was observed.

References:

(1) Polymer International 1986. 18(6):p.359-363

(2) Renewable Energy 2016. 91:p.340-346

(3) Wear 2004. 256(6):p.608-613

(4) Journal of Power Sources 2008. 179(1):p.407-411

(5) Angewandte Chemie 2012. 124(51):p.12875-12878

(6) Scientific reports 2016. 6:p.1-9

(7) Microscopy 2018. 67:p.i133-141

MS2.P011
Correlative scanning microscopy approach for detecting potential fluctuations is Cu(In,Ga)Se_2 solar cells

A. Nikolaeva[1], M. Krause[1], J. Marquez[1], S. Levcenko[1], T. Unold[1], W. Witte[2], D. Hariskos[2], D. Abou-Ras[1]

[1]Helmholtz-Zentrum Berlin, Berlin, Germany
[2]Zentrum für Sonnenenergie- und Wasserstoff-Forschung Baden-Württemberg (ZSW), Stuttgart, Germany

Although Cu(In,Ga)Se_2 (CIGS) thin-film solar cells exhibit power conversion efficiencies of up to more than 23%, even the record devices are limited by the open-circuit voltage (V_{oc}), when compare with theoretical values. The band gap and electrostatic potential fluctuations can be addressed as a possible reason of deteriorated photovoltaic performance (1). In the present work we investigated the possible origins of potential fluctuations in CIGS solar cells varying [Ga] content and buffer layer. Besides, light soaking procedure was carried out to study its impact on the detected fluctuations. By applying scanning electron microscopy (SEM) techniques in a correlative manner we investigated the spatial distribution and relevance of present fluctuations. Cathodoluminescence (CL), energy dispersive X-ray spectrometry (EDX), and electron-beam induced current (EBIC) measurements were performed on the cross-sectional samples with CdS or Zn(O,S) solution-grown buffer layers. The flat cross-sections of solar cells for the SEM measurements were prepared by mechanical polishing. EBIC images and EDX compositional maps were acquired using a Zeiss UltraPlus scanning electron microscope, equipped with beam blanker. CL intensity and peak-wavelength distribution maps were obtained at Zeiss Merlin SEM at room temperature. The maximum amplitude of band-gap fluctuations determined from CL measurements is located near the CIGS/buffer interface. However, it does not exceed 25 meV, which is negligible for the device performance. These results are in a good agreement with EDX elemental distribution maps, which did not show significant variations in the composition in CIGS absorbers parallel to the substrate. By evaluating EBIC profiles, perpendicular to the *p-n* junction, the values for the width of the space-charge region (w_{SCR}) were extracted. It was revealed that cells with Zn(O,S) buffer layer exhibit significant fluctuations in the w_{SCR} independently of the [Ga] content of the CIGS absorber. As the w_{SCR} is a function of doping densities N_A of the absorber, N_D of the buffer/window part and the interface-charge density N_{IF} (2), the contribution of each variable to electrostatic fluctuations was estimated. It was shown that the dominant effect for these fluctuations is linked to the local variations in N_D and N_{IF} introduced via the buffer layer deposition. Light illumination of cells with Zn(O,S) buffer layer for 30 min resulted in a significant reduction of fluctuations in the w_{SCR} (Fig. 1).

References:

(1) J. H. Werner, J. Mattheis, and U. Rau, "Efficiency limitations of polycrystalline thin film solar cells: Case of Cu(In,Ga)Se2," *Thin Solid Films*, vol. 480–481, pp. 399–409, 2005.

(2) R. Scheer and H.-W. Schock, *Chalcogenide Photovoltaics*. Weinheim, Germany: Wiley-VCH, 2011.

Fig. 1: SEM image (a) for CIGS solar cell with solution-grown Zn(O,S) buffer and EBIC images before (b) and after light-soaking (c) for 30 min

Fig. 1

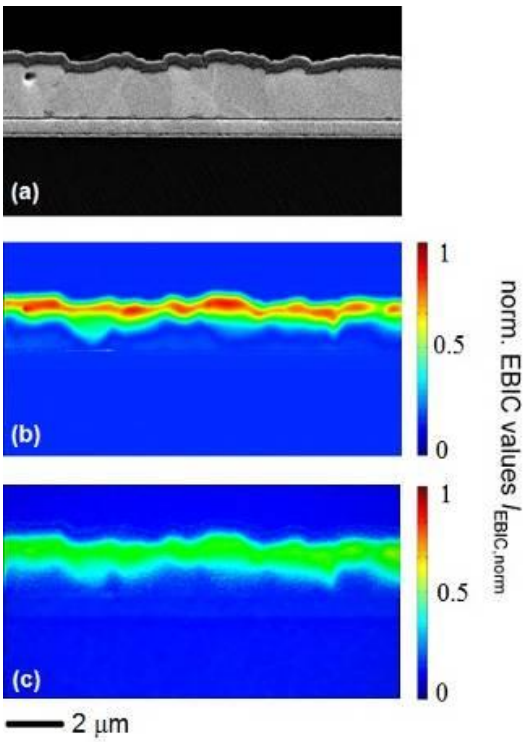

MS2.P013
Correlative electron microscopy for advanced characterization of halide perovskite thin films and devices

S. Caicedo-Dávila[1], H. Funk[1], R. Lovrinčić[2], C. Müller[2], M. Sendner[3], C. Rehermann[4], V. Schroeder[4], P. Caprioglio[5,6], S. D. Cruz[7], E. Unger[4], M. Antonietti[7], S. Albrecht[6], D. Neher[5], D. Abou-Ras[1]

[1]Helmholtz-Zentrum Berlin, Department Structure and Dynamics of Energy Materials, Berlin, Germany
[2]InnovationLab GmbH, Heidelberg, Germany
[3]Heidelberg University, Kirchhoff Institute for Physics, Heidelberg, Germany
[4]Helmholtz-Zentrum Berlin, Young Investigator Group Hybrid Materials Formation and Scaling, Berlin, Germany
[5]University of Potsdam, Institut für Physik und Astronomie, Potsdam, Germany
[6]Helmholtz-Zentrum Berlin, Young Investigator Group Perowskite Tandem Solar Cells, Berlin, Germany
[7]Max Planck Institute of Colloids and Interfaces, Potsdam, Germany

Lead halide perovskites (Pb-HP) are highly efficient optoelectronic materials that have raised great interest among the research community for photovoltaics, photodetection, light-emitting diodes (LEDs) and laser applications. (1) Despite the outstanding optoelectronic properties, such as sharp optical absorption edges and low nonradiative recombination, some unusual attributes of these materials remain unexplained. (2) Some of these attributes, such as the high defect tolerance and the apparent benign character of grain boundaries, are linked to the microstructure of the material. Therefore, advanced microscopic characterization is crucial to fully comprehend the phenomena in halide perovskites. In the present contribution we show how correlative scanning electron microscopy and spectroscopy aid to identify the microscopic phase distribution and the localized optoelectronic properties in both inorganic and hybrid halide perovskite thin films. We show how the microscopic properties can then be linked to macroscopic film and device characteristics.

Using energy-dispersive X-ray spectroscopy (EDX), cathodoluminescence (CL), we investigated thin films of $CsPbBr_3$, triple-cation-lead-bromide (3CatPbBr$_3$) for LEDs, and a triple-cation mixed-halide perovskite (3CatPb(I_xBr_{1-x})$_3$) treated with a poly(ionic-liquid) (PIL) for solar cell devices.

The $CsPbBr_3$ films contain additional Cs_4PbBr_6 and CPb_2Br_5 ternary phases (Figure 1), consistent with what is reported in the literature. (3) We found that these phases exhibit different spatial distribution inside the film depending on the deposition method and synthesis parameters. Furthermore, in films deposited by coevaporation we investigated the effect of post-deposition annealing and found that $CsPb_2Br_5$ can be transformed into green-luminescent $CsPbBr_3$.

On the 3CatPbBr$_3$ films we found that, depending on the concentration of the precursor solution, the resulting film"s surface has different degrees of wrinkling. Such wrinkles were found to be formed by worm-like precipitates covered by a perovskite film. The precipitates exhibit Pb and Br enhancement, as well as strong N and C depletion on their EDX signals (Figure 2a). In addition, CL on the same position revealed that the precipitates do not emit in the visible spectral range. These results suggest the formation of $PbBr_2$ precipitates beneath the surface of the films.

On the 3CatPb(I_xBr_{1-x})$_3$ films we found that, although the PIL aggregates on the surface of the perovskite in very localized islands, it enhances the CL emission overall the surface of the film (Figure 2b), which correlates well with the enhancement of the photoluminescence quantum yield and V_{OC} on full devices subjected to the same treatment.

In summary, phases and optoelectronic properties at the microscale correlate with macroscopic device characteristics, and help understanding the unusual properties of Pb-HPs. Additionally, we discuss the challenges of SEM characterization on these beam-sensitive materials.

References:

(1) Brenner, T. M. *et al. Nat. Rev. Mater.* 1, 15007 (2016).

(2) Cahen, D. *et al. Adv. Mater.* 30, 1800691 (2018).

(3) Nikl, M. *et al. Chem. Phys. Lett.* 306, 280–284 (1999).

Fig. 1: a) CL map superimposed on SEM image, and ternary phases in Cs-Pb-Br film. b) CL spectra of the phases in a)

Fig. 2: a) SEM image, N and Br EDX maps of 3CatPbBr film. b) SEM images and CL maps of 3CatPb(I_xBr_{1-x})$_3$ with and without PIL treatment

Fig. 1

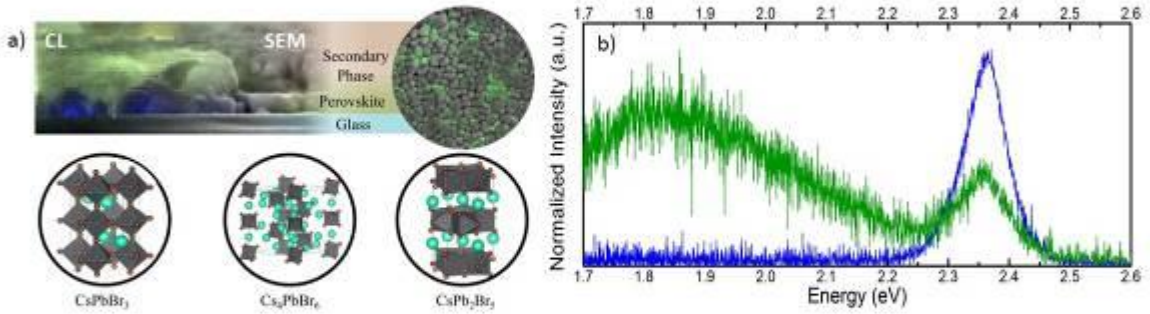
a)
CL
SEM
Secondary Phase
Perovskite
Glass
CsPbBr3
Cs4PbBr6
CsPb2Br5
b)
Normalized Intensity (a.u.)
Energy (eV)
1.7
1.8
1.9
2.0
2.1
2.2
2.3
2.4
2.5
2.6

Fig. 2

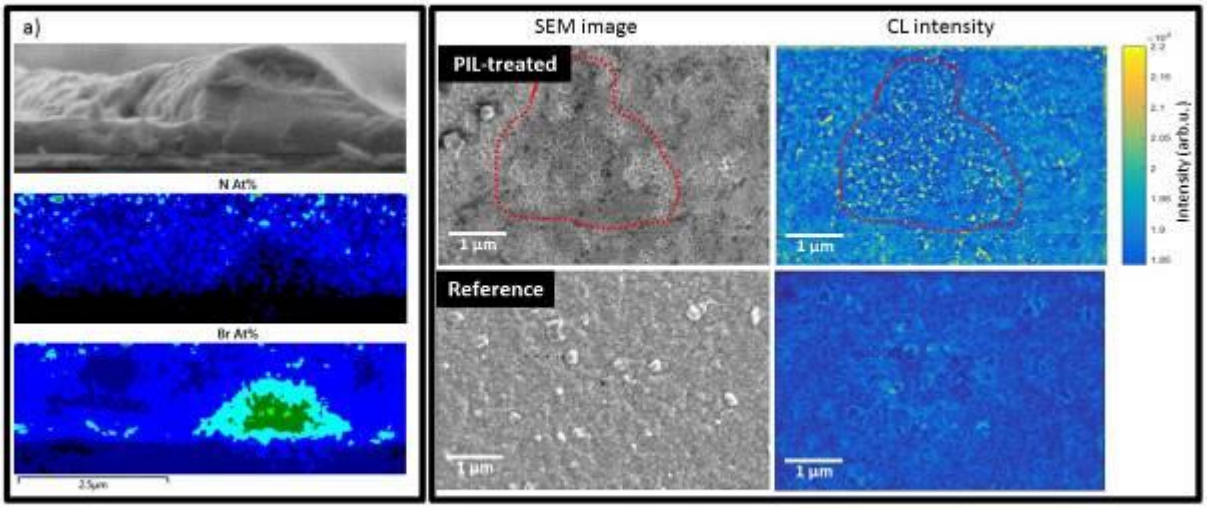
a)
N At%
Br At%
SEM image
CL intensity
PIL-treated
Reference
1 µm
Intensity (arb.u.)

MS2.P015
InAs selective area heteroepitaxy on SiN_x-masked nanopillar-patterned GaAs (111)A

V. Kunnathully[1,2], T. Riedl[1,2], T. Langer[1,2], A. Trapp[1,2], D. Reuter[1,2], M. Schaper[3], J. K. N. Lindner[1,2]

[1]Paderborn University, Physics, Paderborn, Germany
[2]Center for Optoelectronics and Photonics Paderborn (CeOPP), Paderborn, Germany
[3]Paderborn University, Mechanical Engineering, Paderborn, Germany

As is known for its high electron mobility and narrow band gap making it a versatile candidate for optoelectronic applications. However, its high lattice mismatch with respect to Si and GaAs substrates hinders the effective exploitation of these properties in devices due to the formation of extended defects. A feasible approach towards defect density reduction relies on substrate compliance and elastic strain accommodation resulting from heteroepitaxial growth on nanoscale substrate areas (1). However, site-selective growth is essential for effective realization of such advantages.

The aim of this study is to investigate the site-selective molecular beam epitaxy (MBE) growth of InAs on nanopillar-patterned GaAs (111)A with the help of an appropriate dielectric mask. Previous experiments revealed preferential InAs growth at GaAs pillar bottoms. Hence, there is a need for development of a dielectric mask to explore the possibility of confining the InAs growth to the pillar tops.

GaAs (111)A substrates patterned with pillars approximately 25 and 40 nm in diameter and 90 nm in height were fabricated by employing a combination of cost-effective polystyrene nanosphere lithography and reactive ion etching (RIE). The patterned substrate was overgrown by a partially plasma densified, amorphous silicon nitride (SiN_x) film using plasma enhanced chemical vapor deposition. The pillar tops were released by a combination of controlled vibratory polishing in colloidal silica medium and RIE of the SiN_x film. After that, InAs layers with thicknesses of 5 – 15 nm were grown using MBE at temperatures in the range 150 – 300°C. For the morphological and structural characterization of SiN_x films and InAs growths imaging in a Raith field-emission SEM as well as bright-field TEM and HAADF-STEM imaging in a Jeol JEM-ARM200F microscope were employed.

SEM examination of the SiN_x films reveals the presence of triangularly shaped growth fronts, which are bounded by nanoscale voids (Fig. 1). Controlled removal of SiN_x leads to exposed GaAs pillar tops (Fig. 2). MBE growth of InAs on such substrates results in the formation of InAs islands atop GaAs pillars and at SiN_x mask deepenings between the pillars. HAADF-STEM investigations of the InAs/GaAs heterointerface reveals the presence of misfit dislocations and stacking faults, the density of which declines with decreasing island size.

SiNx template assisted selective growth of InAs on GaAs (111) A pillars has been achieved by appropriately tuning process parameters. The mechanism of SiN_x film growth on nano-patterned GaAs pillar arrays and strain relaxation at the InAs/GaAs heterointerfaces has been studied by TEM and STEM.

References:

(1) D. Zubia, S. D. Hersee: J. Appl. Phys. 85 (1999) 6492

Fig. 1: Top-view SEM image of SiN_x covered nanopillar-patterned GaAs after vibratory polishing. A triangular network of voids between adjacent SiN_x growth fronts is faintly visible (dark spots).

Fig. 2: Top-view SEM image of SiN_x covered nanopillar-patterned GaAs after vibratory polishing and RIE, showing exposed GaAs pillar tops and elongated voids in the SiN_x film (dark streaks).

Fig. 1

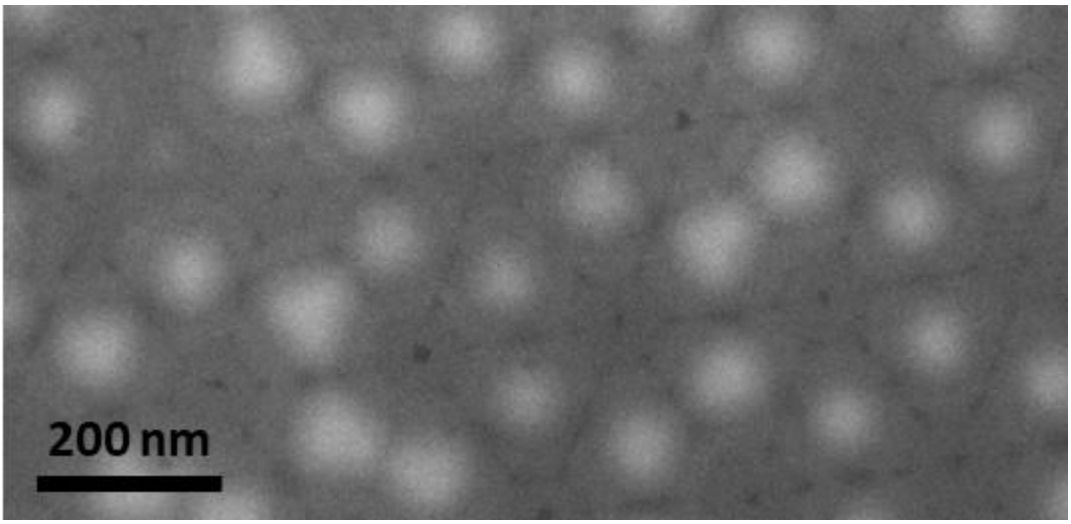

Fig. 2

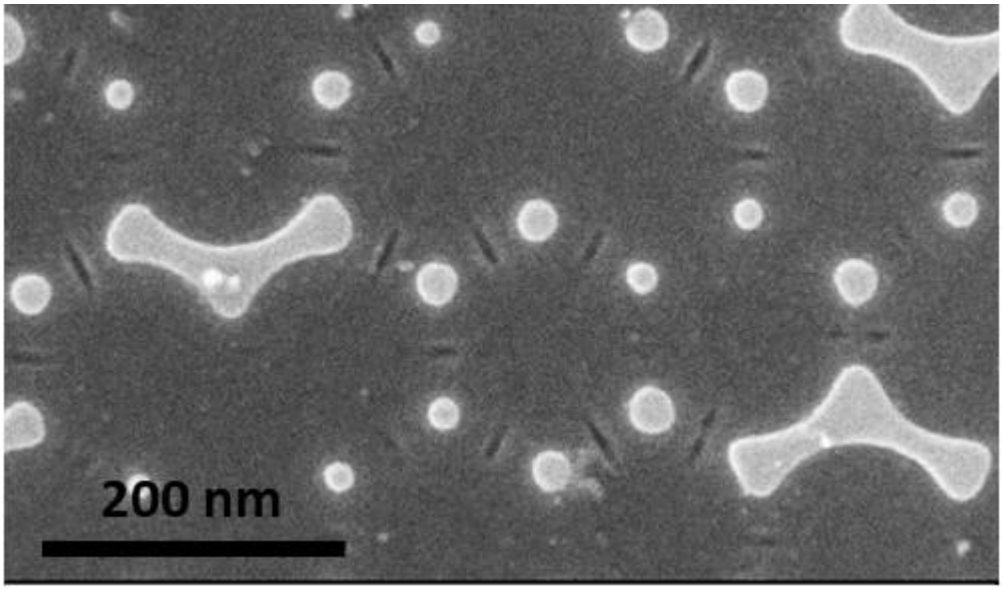

MS2.P016
Influence of film morphology tailored by solid state dewetting on phase decomposition of NiAu thin films

M. Landes[1], J. Schubert[1], J. Will[1], E. Spiecker[1]

[1]Institute of Micro- and Nanostructure Research, Department of Materials Science and Engineering, Erlangen, Germany

The NiAu system is an ideal system to study phase decomposition due to its large miscibility gap extending over the whole concentration range. Solid-state dewetting allows tailoring the morphology of the NiAu thin film to the point of complete separation into nanoparticles, enabling investigation of the impact of surfaces and interfaces on the decomposition behavior.

Monolayers are deposited by electron beam co-evaporation of Ni and Au onto a sapphire substrate and subsequently annealed in a rapid thermal annealing (RTA) furnace. The evolution of dewetting and decomposition in the thin film after various heat treatments are observed by scanning electron microscopy using the Phenom table top SEM. Heating the samples to a temperature slightly above the miscibility gap allows to control the degree of dewetting and thus the particle size and morphology as shown in Figure 1 with a) fingerlike structures of the dewetted film after short dewetting times and b) faceted particles after longer dewetting times. A subsequent annealing step at a temperature inside the miscibility gap causes phase decomposition and results in a lamellar structure of alternating Ni and Au enriched phases (Fig 2). The decomposition is directly revealed by material contrast in SEM images taken with back scattered electrons and can be further analyzed by energy dispersive x-ray spectroscopy (not shown). Fig 2a shows the nucleation stage of decomposition in a hardly dewetted NiAu film after short annealing time. Phase decomposition starts at grain boundaries where it results in an altering structure of Ni-rich (dark) and Au-rich (bright) phases. Fig. 2b shows decomposition of a NiAu film after dewetting into fingerlike structures and nanoparticles. Also here, decomposition starts at grain boundaries but is also influenced by the surfaces of the nanoparticles. Further investigations address the growth direction in respect to the grain orientation. Moreover, the interface between Ni-rich and Au-rich phases have been studied by cross-section TEM (not shown).

Fig. 1: Dewetting of NiAu thin film: a) formation of fingerlike structures, b) isolated particles after longer dewetting time.

Fig. 2: Decomposition of partially dewetted thin NiAu films: a) Nucleation of Ni-rich (dark) and Au-rich (bright) phases at grain boundaries in still continuous film, b) Formation of lamellar structures extending across nanoparticles.

Fig. 1

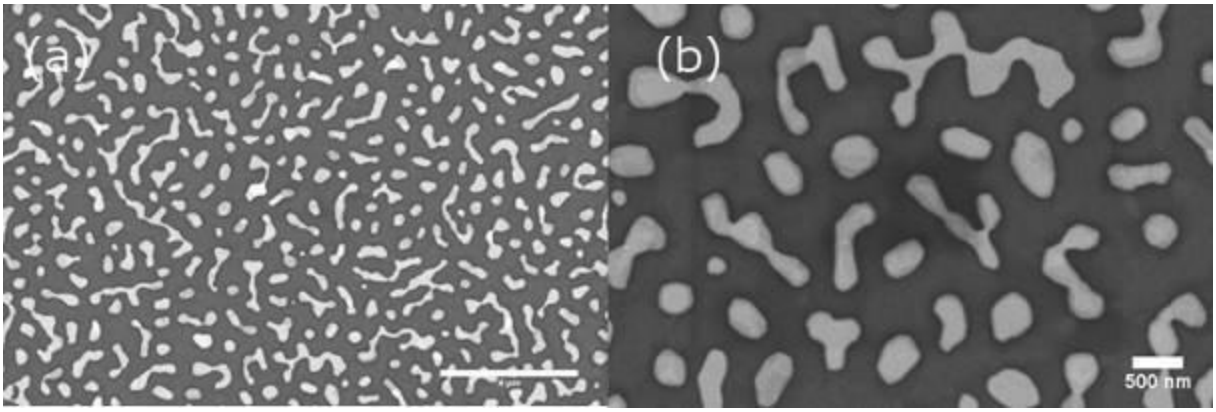

Fig. 2

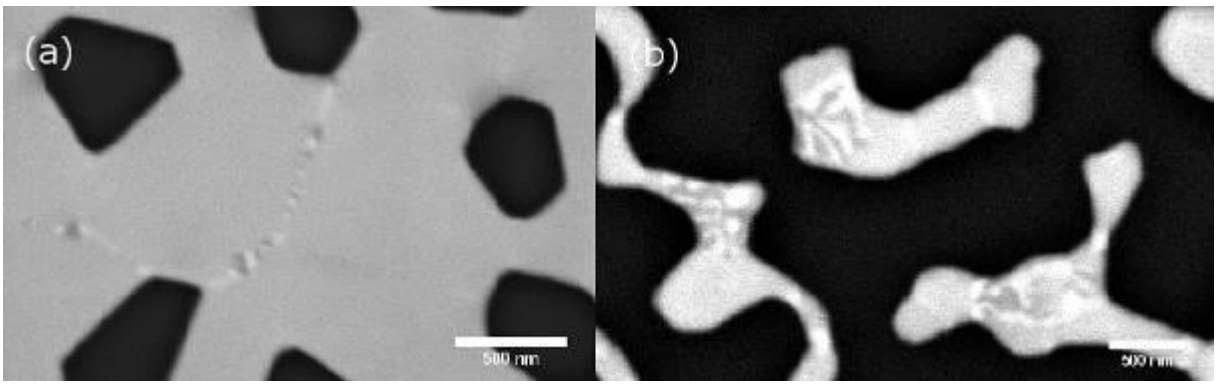

MS2.P017
Metal-induced crystallization of amorphous semiconductor films: Nucleation Phenomena in Ag-Ge couples

A. Kryshtal[1], S. Bogatyrenko[2], P. Ferreira[3,4,5]

[1]AGH University of Science and Technology, International Centre of Electron Microscopy for Material Science and Faculty of Metals Engineering and Industrial Computer Science, Krakow, Poland
[2]Karazin National University, Department of Physics and Technology, Kharkiv, Ukraine
[3]Iberian International Nanotechnology Laboratory, Braga, Portugal
[4]The University of Texas at Austin, Materials Science & Engineering Program, Austin, United States
[5]University of Lisbon, Instituto Superior Técnico, Mechanical Engineering Department and IDMEC, Lisboa, Portugal

Thin crystalline Ge and Si films are key materials for innovative electronics. However, Si or Ge films grown from the vapor phase are usually amorphous. The crystallization of such films requires annealing temperatures above 500°C, which are often incompatible with the fabrication processes used industrially. Yet, when a thin film of amorphous germanium (a-Ge) or amorphous silicon (a-Si) is in contact with a metal (e.g, Au, Ag, Al, Bi, Pd), such that a eutectic couple is formed, the crystallization temperature of the amorphous film is reduced significantly. This effect was found almost 50 years ago and is commonly referred to as "metal-induced crystallization (MIC)". Despite numerous studies of the MIC effect, a fundamental mechanism of the reaction remains unknown (1).

In this work, the goal is to provide a fundamental understanding of this reaction using advanced electron microscopy techniques. We have used silver-germanium (Ag-Ge) films, formed by the sequential condensation of components in high vacuum, as a model system. The bimodal ensemble of Ag particles (ca. 7 and 40 nm in size) was formed on an amorphous and continuous Ge film (10 nm thick) grown on KCl crystals. Synthesized Ag-Ge samples were separated from the substrate and were transferred onto through-hole MEMS-based chips for *in situ* TEM investigation. In this fashion, we got freestanding Ag/Ge samples for TEM observation.

The nucleation and growth of the crystalline Ge phase was observed at the atomic scale in real time by heating the system in a double corrected FEI Titan G3 Themis 60-300 operated at 200 kV and fitted with NanoEx-i/v MEMS-based heating holder. *In situ* monochromated STEM-EELS spectral imaging was performed in the 350-450°C temperature range using a probe Cs-corrected FEI Titan G2 60-300 TEM equipped with Wildfire D6 heating holder (DENSsolutions) at 80 kV and probe current of 8 pa. A surface plasmon resonance peak of Ag and a bulk Ge plasmon peak were used for mapping the interphase boundaries and chemical elements at different stages of the reaction without substantial radiation damage of the area under study. HAADF-STEM tomography was used for 3D reconstruction of post-annealed Ag/Ge film structure.

We found that the eutectic/contact melting at the metal-semiconductor interface and at temperatures well below the eutectic temperature of the bulk alloy triggers the crystallization of the amorphous Ge film. The excess energy of the amorphous Ge drives the formation of liquid and the propagation of the reaction front through the Ge film, which results in crystallization of the entire Ge film. Two intermediate solid phases were detected at the reaction front, namely, intermetallic Ag-Ge hcp compound (Fig. 1) and fcc Ge phase (2). Both phases were metastable, and we believe they are the product of non-equilibrium solidification of the liquid eutectic alloy at the reaction zone.

This work was supported by the National Science Centre, Poland under project No. 2016/23/B/ST8/00537.

References:

(1) A. Kryshtal, A. Minenkov, S. Bogatyrenko, A. Gruszczyński, Journal of Alloys and Compounds 786 (2019) 817-825

(2) A.P. Kryshtal, A.A. Minenkov, P.J. Ferreira, Applied Surface Science, 409 (2017) 343-349

Fig. 1: Phase contrast TEM images (a, b) and FFT (c) of a Ag-Ge hcp nucleus at 450°C.

Fig. 1

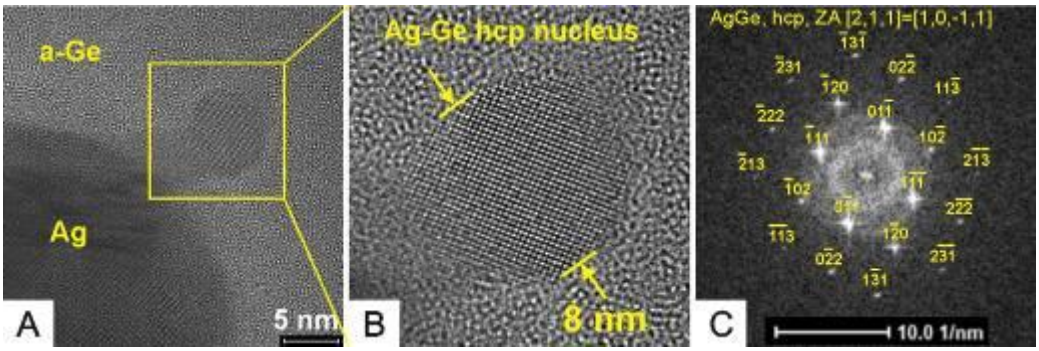
a-Ge
Ag
5 nm
A
Ag-Ge hcp nucleus
8 nm
B
AgGe, hcp, ZA [2,1,1]=[1,0,-1,1]
10.0 1/nm
C

MS2.P018
Strain relaxation in nanoscale GaAs/InAs heterojunctions analysed by high-resolution TEM/STEM and atomistic simulations

T. Riedl[1,2], V. Kunnathully[1,2], T. Langer[1,2], A. Trapp[1,2], D. Reuter[1,2], J. K. N. Lindner[1,2]

[1]Paderborn University, Physics, Paderborn, Germany
[2]Center for Optoelectronics and Photonics Paderborn (CeOPP), Paderborn, Germany

Semiconductor heterostructures are widely employed for opto- and nanoelectronic devices, since they enhance device performance and functionality by exploiting carrier confinement, tunneling or strain engineering. In contrast to their planar counterparts, heterostructures with nanoscale lateral dimensions of both substrate and layer offer the advantage of larger critical dimensions for misfit defect formation (1).

The present study aims at evaluating the size-dependent strain distribution as well as the critical dimensions for misfit defect formation in axial GaAs/InAs nanoheterojunctions, revealing the operating strain relaxation mechanisms. Moreover, the misfit defect configuration is studied as a function of structure size.

Nanopillar arrays were patterned on GaAs(111)A wafers by using nanosphere lithography and anisotropic reactive ion etching of the substrate. Next, InAs heteroepitaxy was performed by solid-source molecular beam epitaxy at a low temperature of 150°C for obtaining island-like InAs growth atop the pillars. Structural characterization at high resolution was accomplished by HRTEM and aberration-corrected HAADF-STEM imaging, where the strain was mapped by geometrical phase analysis (GPA). In addition, simulations of strain distributions and misfit defect stability were carried out by energetic relaxation of atomistic models using an optimized parametrization of the empirical bond-order Tersoff potential (2).

According to cross-sectional HRTEM and HAADF-STEM images plastic relaxation of the misfit in the InAs island on GaAs pillar nanostructures is observed for InAs diameters above around 8-10 nm, while purely elastic accommodation occurs for smaller sizes, in fair agreement with the atomistic calculations of dislocation stability. The dominating misfit defects are 60° dislocations located at the GaAs/InAs heterointerface, where the number of dislocations augments with increasing InAs diameter. Moreover, experimental and simulated strain maps reveal that the lattice parameter transition between GaAs and InAs occurs in a 1.0 - 1.5 nm narrow region at the heterointerface (Fig. 1).

In conclusion, the strain and defect state of axial GaAs/InAs nanoheterojunctions shows a considerable dependence on the structure size. Thus, control of the dimensions of nanoheterostructures is of paramount importance for realizing electronic properties required for advanced applications.

References:

(1) H. Ye et al.: Nano Lett. 9 (2009) 1921

(2) T. Hammerschmidt et al.: Phys. Rev. B 77 (2008) 235303

Fig. 1: (a) Schematic of an InAs island atop a GaAs nanopillar. (b,c) Maps of the [2-1-1] Lagrange strain in the plane marked in (a) for an InAs diameter of around 12 nm with one interfacial 60 misfit dislocation (arrow): (b) GPA of experimental HAADF-STEM and (c) atomistic simulation.

Fig. 1

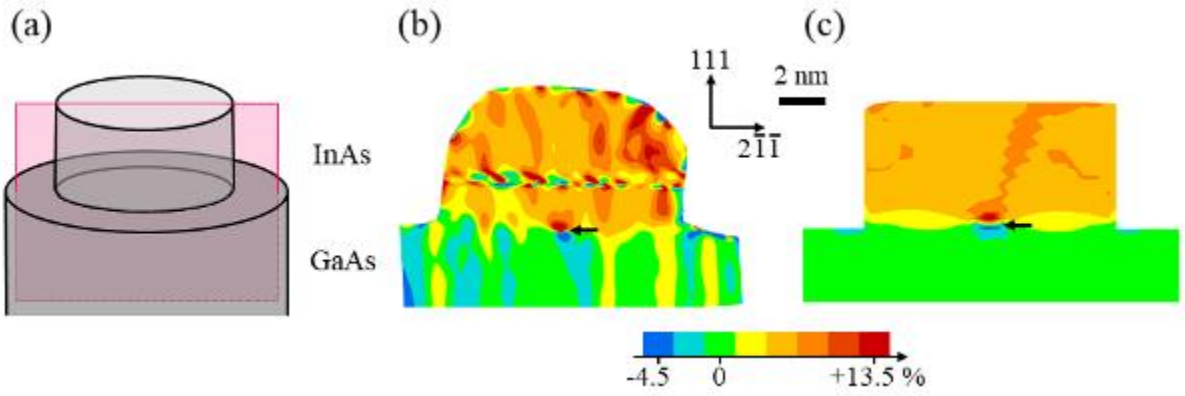

MS2.P021
Microstructure and defect structure of Zr-1Nb alloy deep surface modified by high Intensity Ti Ion implantation

A. Obrosov[1], E. Kashkarov[1,2], A. Sharma[1,2,3], S. Weiß[1]

[1]BTU Cottbus-Senftenberg, Department of Physical Metallurgy and Materials Technology, Cottbus, Germany
[2]National Research Tomsk Polytechnic University, School of Nuclear Science and Engineering, Tomsk, Russian Federation
[3]Indian Institute of Technology (Banaras Hindu University) Varanasi, Department of Metallurgical Engineering, Varanasi, India

A deep surface modified TiZr layer was fabricated by high-intensity low-energy titanium ion implantation into zirconium alloy Zr-1Nb alloy with the various dose in the range of (5.4–9.56) × 1020 ion/cm2. The gradient distribution of titanium as well as vacancy type defects were analysed. The effects of ion implantation on microstructure, phase composition and elemental distribution of TiZr layer were analysed by scanning electron microscopy, transmission electron microscopy, X-ray diffraction, and glow-discharge optical emission spectroscopy, respectively. The results show the appearance of Zr-Ti intermetallic phases of different stoichiometry after Ti implantation. The intermetallic phases are transformed from both Zr0.7Ti0.3and Zr0.5Ti0.5 to single Zr0.6Ti0.4 phase with the increase in the implantation dose. The depth of Ti penetration into the bulk of Zr increases from 6 to 13 μm with the implantation dose. The higher current density (170 mA/cm2) leads to the increase in the grain size and surface roughness. It was revealed that TiZr layer (~10 μm thickness) is represented by α′ + α(TiZr) lamellar microstructure with gradient distribution of Ti through the layer depth. Transmission electron microscopy was used for investigation of the physical basis of Ti diffusion and its influence on the evolution of the defect structure after surface modification. Furthermore, it was found that on the surface between substrate and implanted layer was found an amorphous layer, which occur as a result of further stress accumulations from the higher implantation doses.

MS2.P022
Microstructure and recrystallization studies of thin Bi films using electron microscopy

V. Y. Kolosov[1], A. A. Yushkov[1], A. O. Bokuniaeva[1]

[1]Ural Federal University, Ekaterinburg, Russian Federation

Thin bismuth films are actively investigated in connection with their unusual thermoelectric, magnetic, and transport properties but are rarely studied by transmission electron microscopy (TEM) (1). We evaporated Bi nanothin film in vacuum on a carbon sublayer over mica substrate with subsequent separation of the film in the distilled water. Besides TEM studies we probed electron beam (e-beam) irradiation of free-standing Bi film (placed on TEM grids) in the column of 2 different microscopes: JEM-2100 (LaB6, 200Kv) in TEM mode and LVEM-5 (FEG, 5Kv) in TEM, STEM and SEM modes. The last mode resulted in phase and structure transformations that we were seeking for. The irradiation time was from several seconds to about 10 seconds and more. The studies of initial film and irradiated area were performed with the use of JEM-2100 operated primarily in transmission mode with correlative studies in SEM mode (using additional BS&SE detector our microscope is equipped with). The bend-contour technique we developed earlier (2) was used for the analyses of the crystals with individual bend contours and crossed bend contours (zone-axis patterns) on the TEM images.

Polycrystalline bismuth film has grain sizes ranging from 10 to 250 nm, Fig. 1 a, with essential part of faceted grains above the film surface inclined at different angles with respect the film plane, Fig. 1 e, f. It is the evidence of at least 2 concurrent processes associated with film growth.

Films are subject to recrystallization under a beam of an electron microscope with FEG at low accelerating voltage 5Kv, Fig. 1 b-d. In this case, assorted different single-crystal and amorphous structures are formed: more or less faceted single crystals (size 10 - 100 nm), single-crystalline areas (1 – 10 µm), round-shaped particles (50 nm – 1 µm) exceeding essentially the initial film thickness and net of amorphous material in strongly irradiated regions.

In thin crystallized bismuth films, bending of the crystal lattice is observed, varying from ~10 deg/µm, to high magnitudes, exceeding 100 deg/µm. Previously it was made known (3) that amorphous films often crystallize with specific internal lattice bending rather than crystal (foil) bending as a whole.

Probably it can be the case for Bi films studied.

References:

(1) M. Neklyudova, C. Sabater et al., Appl. Phys. Lett., 110, 103101 (2017).

(2) I. E. Bolotov, V. Yu. Kolosov, Phys. Stat. Sol. (a), V. 69, p. 85-96 (1982)

(3) V. Yu. Kolosov, A. R. Thölen, Acta Mater., V. 48, p. 1829-1840 (2000)

Partial support of project 3.6121.2017/8.9 (The Ministry of Education and Science of the Russian Federation) and Agreement No 02.A03.21.0006 (Act 211 Government of the Russian Federation) is acknowledged.

Fig.1: TEM images of initial area with corresponding SAED (a), irradiated by electron beam area (b) with large nontransparent particles ant the net of amorphous material with fine crystals (some of these crystals encircled), large single crystal (with broad bend contours) formed at the boundary of melted area (c), single crystalline recrystallized area (d); STEM (e) and SEM (f) images of the same initial film area (some faceted grains above the film surface are circled).

Fig. 2: TEM of crystals with pairs of bright bend contours in bright field (a), with some pairs (hkl, -h-k-l) shown by arrows in black color, and in dark field (c) of corresponding diffraction spot shown by white arrow at SAED (b) of the area.

Fig. 1

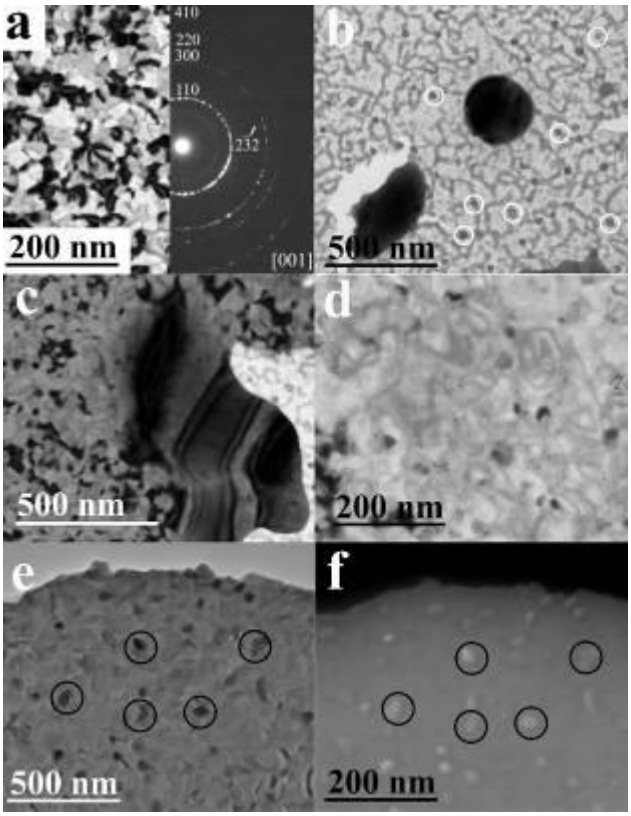
a
410
220
300
110
232
[001]
200 nm
b
500 nm
c
500 nm
d
200 nm
e
500 nm
f
200 nm

Fig. 2

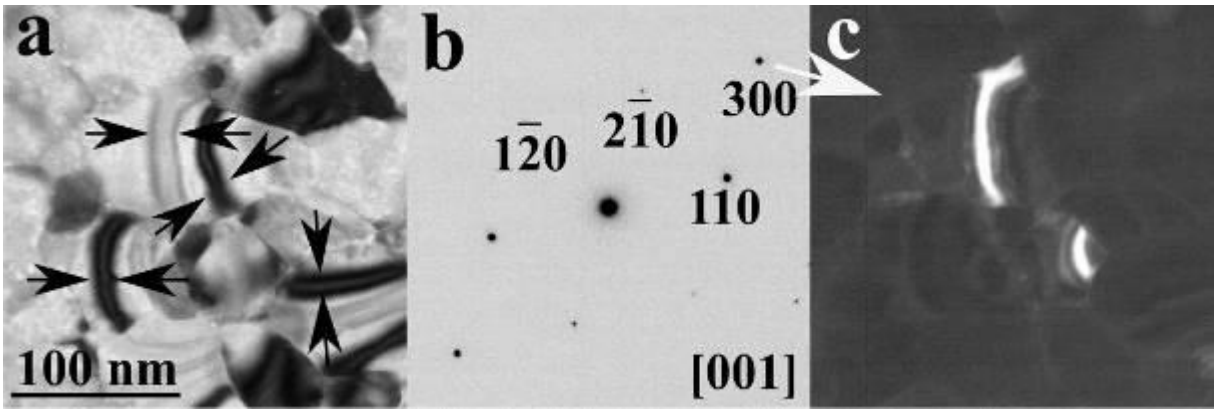
a
100 nm
b
$1\bar{2}0$
$2\bar{1}0$
300
$1\dot{1}0$
[001]
c

MS3.001 invited
Correlating performance with microstructure for metal halide perovskite solar cells by TEM

Q. Jeangros[1], F. Sahli[1], P. Fiala[1], R. A. Z. Razera[1], F. Fu[1], M. Bräuninger[1], T. C. Yang[1], A. Hessler-Wyser[1], C. Ballif[1]

[1]EPFL PV-LAB, Neuchâtel, Switzerland

Photovoltaics (PV) is driving the progression of renewable electricity generation technologies. Crystalline Si (c-Si) technologies dominate the PV market but are likely only a first step in the "solarization" of energy systems as they fail to convert high-energy photons efficiently. Additional power output can be achieved by stacking a top cell with a higher bandgap onto c-Si to form a tandem device. Solar cells based on a ABX3 perovskite absorber, where A is a monovalent, often organic, cation (methylammonium, formamidinium and/or Cs), B a metal (lead and/or tin) and X an halide (iodide, bromide and/or chloride), are promising top cell candidates thanks to their high single-junction efficiency, tunable bandgap, potential low fabrication costs and soft processing conditions.

A perovskite/c-Si tandem consists of a <1 mm-thick perovskite cell deposited onto a ~200 mm-thick c-Si solar cell and contains multiple layers, some as thin as 1 nm, each with its own functionality. c-Si wafers are often etched to reveal pyramids of a few mm in height, a texture that reduces reflection losses and promotes light trapping. Optimal control of the layer formation from the nanometer (crystallinity, chemistry, microstructure of each layer) to the micrometer scale (conformity of the layers on the pyramids) is thus essential to maximize the optoelectronic properties of the device. During operation, this nano-/microstructure may then evolve due to mechanisms that are still debated, often leading to a performance loss.

Analytical transmission electron microscopy (TEM) can shed light on this nanostructure and help the understanding of the solar cell performance depending on processing/operation conditions. However, the fragile nature of perovskite solar cells complicates their preparation into thin cross-sections and analysis with high-energy electrons. The perovskite degrades when immersed in water, exposed to air, heated to temperatures >80°C, and undergoes a phase transition when cooled to liquid nitrogen temperatures. By default, the focused ion beam (FIB) lift-off approach has become the main sample preparation method, as it leads to the lowest impact on the overall morphology of the device stack. Nevertheless, bombardment with gallium ions and electrons in the FIB/SEM still damage the absorber. In addition, the scanning TEM electron doses typically required to achieve a sufficient signal-to-noise ratio in energy-dispersive X-ray spectroscopy may also lead to severe damages.

This presentation will review the possible artifacts that may occur during TEM sample preparation and observation and discuss several strategies to identify and mitigate them. As these effects cannot be completely avoided with today's perovskite compositions, TEM data of FIB-prepared perovskite cross-sections must be carefully cross-checked with results retrieved from other characterization methods to avoid false interpretations. Following this methodology, this contribution will present how TEM could guide the development of high-efficiency (>25%) perovskite/c-Si tandems, notably by identifying shunts running through the absorber, dewetting of charge-selective layers (1), microstructural features that enable the recombination junction to quench shunts (2), degradation pathways triggered by high voltages (by in situ experiments) (3) or long-term operation.

References:

(1) Sahli et al., Nat. Mater. 17 (2018)

(2) Sahli et al., Adv. Energy Mater. 8 (2018)

(3) Jeangros *et al.*, Nano Lett. 16 (2016)

MS3.002
Microstructural study of octahedral Pt-alloy nanoparticle fuel cell catalysts

M. Heggen[1], P. Strasser[2], R. Dunin-Borkowski[1]

[1]Forschungszentrum Jülich GmbH, Jülich, Germany
[2]TU Berlin, Department of Chemistry, Berlin, Germany

Pt-alloy nanoparticles (NPs) with octahedral shapes are attractive as fuel cell catalysts for the oxygen reduction reaction (ORR). A deep understanding of their atomic-scale structure, degradation and formation is a prerequisite for their use as rationally-designed NP catalysts with high activity and long-term stability (1). Here, we present results from a comprehensive microstructural study of the growth and degradation of various octahedral Pt-alloy NPs performed using *ex situ*, *in situ* and identical location high-resolution transmission electron microscopy (TEM) and high-angle annular dark-field scanning TEM (STEM), combined with electron energy-loss spectroscopy and energy-dispersive X-ray spectroscopy (EDX). We show that the NPs often show compositional anisotropy and form Ni-rich {111} facets, leading to complex structural degradation during ORR electrocatalysis. The Ni-rich {111} facets are etched preferentially, resulting in the formation of first concave octahedra and then Pt-rich skeletons that have less active facets (2). We also reveal element-specific anisotropic growth as the reason for their compositional anisotropy and limited stability. During solvothermal synthesis, a Pt-rich nucleus evolves into precursor nanohexapods, followed by the slower step-induced deposition of Ni on the concave hexapod surface to form octahedral facets (Fig. 1) (3). *In situ* thermal annealing of phase-segregated octahedral Pt-Ni alloy NPs was performed to study their morphological stability and surface compositional evolution. Pristine octahedral Pt-Ni NPs show Pt-rich corners/edges and concave Ni-rich {111} facets. Time-resolved image series reveal that, on being annealed up to 800 C, the Pt-rich surface atoms at the corners/edges diffuse onto and subsequently cover the concave Ni-rich {111} surfaces, leading to the formation of perfectly flat Pt-rich {111} surfaces with Ni-rich subsurface layers. These results suggest a feasible approach for the synthesis of shaped Pt-alloy NPs with Pt-rich {111} surfaces and Ni-rich subsurface layers that are catalytically active and stable for the ORR, with important implications for the rational synthesis of durable highly-active shaped Pt-alloy fuel cell electrocatalysts (4). Surface doping of octahedral Pt-Ni NPs with a third element such as Mo or Rh is found to be an effective method for stabilization of the octahedral shapes of the NPs thereby improving their long-term stability during electrochemical cycling (5,6). We present results from a systematic comparison of Rh-doped and undoped Pt-Ni NPs by STEM EDX before and after 4k and 8k electrochemical cycles. Whereas undoped NPs are observed to lose their octahedral shapes and to become nearly spherical after 8k cycles as a result of Pt surface diffusion, Rh-doped Pt-Ni NPs have more stables after 4k, 8k and even 30k cycles.

References:

(1) Heggen M, Gocyla M, Dunin-Borkowski RE, Advances in Physics X 2017; 2: 281.

(2) Gan L, Cui CH, Heggen M, Dionigi F, Rudi S, Strasser P, Science 2014; 346: 1502.

(3) Cui CH, Gan L, Heggen M, Rudi S, Strasser P, Nature Materials 2013; 12: 765.

(4) Gan L, Heggen M, Cui CH, Strasser P, ACS Catalysis 2016; 6: 692.

5) Huang X et.al. Science 2015 ; 348: 1230.

(6) Beermann V, Gocyla M, Willinger E, Rudi S, Heggen M, Dunin-Borkowski RE, Willinger MG, Strasser P, Nano Letters 2016; 16: 1719.

Fig. 1

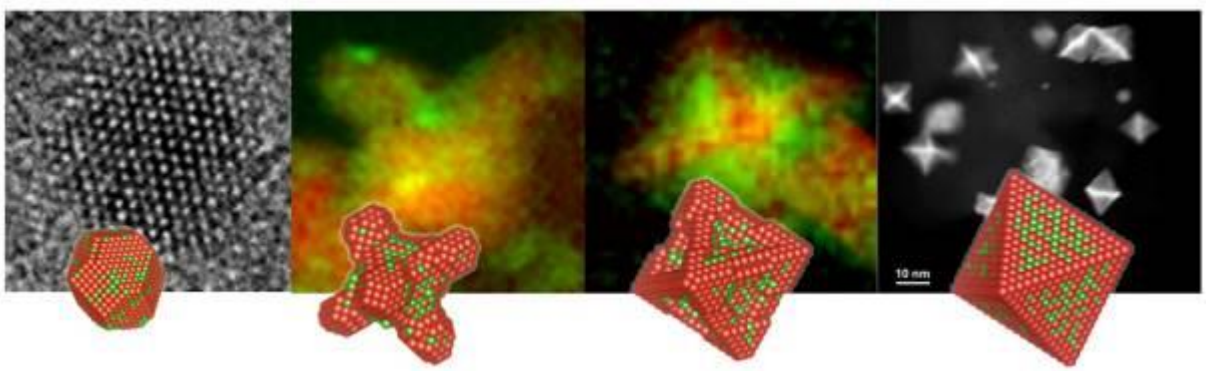

MS3.003
In situ 2D and fast 3D Environmental TEM study of the conditioning of Pd/δ-alumina nanocatalysts

T. Epicier[1], L. Roiban[1], A. S. Gay[2]

[1]University of Lyon, INSA-Lyon, MATEIS, umr5510 CNRS, Villeurbanne Cedex, France
[2]IFPen, Solaize, France

Preparing compounds for heterogeneous catalysis generally proceeds by impregnating a support with nanoparticles (NPs), drying, calcination and reduction. Environmental Transmission Electron Microscopy (ETEM) enables today to perform many of these steps in situ, which brings precious insights in the phenomena involved during phase between the oxide and metallic phases.

We present the study of a classical system, e.g. palladium NPs on δ-alumina powders (1). A first objective is to compare the NP size after ex situ and in situ calcination (CAL) treatments. A second objective concerns the chemical nature of Pd-based NPs, introduced as a 2nm PdO colloidal solution; they may experience an undesired reduction due to irradiation effects and/or pressure conditions in the TEM. Finally, a third ambitious objective is to quantify in 3D the distribution of NPs during calcination by following the same area for consistency (so-called 'identification location' approach).

STEM and BF TEM images were obtained at 300 kV in a FEI TITAN ETEM instrument. Drying, calcination and reduction (RED) treatments of 2 hours each were performed under conditions similar to industrial conditions, respectively in air (or O_2) at 120 and 400-450°C, and in H_2 at 200°C. However, an important difference is the gas pressure in the microscope, between 1 and 15 mbar instead of atmospheric pressure. TEM samples were classically prepared (1) and deposited onto Si/SiN_x nanochips mounted on a Wildfire heating holder (DENSsolutions). Tomographic tilt series were acquired over a tilting amplitude of 140° in less than 3 minutes according to our fast BF method (2,1).

Figure 1a-d) shows a typical area followed from the initial impregnated state to the RED state. Size histograms (not shown here) confirm the increase of size during calcination and their subsequent decrease due to the variation of atomic densities when reducing the oxide into the metallic phase. These data agree with TEM results from samples treated ex situ.

Figure 2 shows the unambiguous crystallographic identification of the chemical nature of NPs in both HRSTEM (2a-b) and HRTEM (2c-d) during the reduction of oxide NPs, either under the effect of H_2 or as induced by the instability of oxides under a low O_2 pressure at high temperature.

The present work demonstrates the interest of ETEM in following quantitatively and in situ the preparation of nanocatalysts with major advantages vs conventional high vacuum and ex situ TEM observations. More details will be given on fast tomography successfully performed in a few minutes under gas and in temperature. Such performances, or even faster acquisitions within a few seconds as already reported (3), open the way to more complete investigation of 3D features such as the distribution of NPs at various stages, or to kinetic studies during phase transformations (4).

References:

(1) T. Epicier et al., *Catal. Today* (2019), doi: 10.1016/j.cattod.2019.01.061.

(2) L. Roiban et al., *J. of Microsc.* 269 (2018) 117.

(3) H. Banjak et al., *Utramicr.* 189 (2018) 109.

We thank the support of the French National Research Agency through the 3DCLEAN project and CLYM for the access to the ETEM.

Fig. 1: Evolution of Pd NPs on δ-Al_2O_3: in situ STEM-ADF imaging in ETEM. Coalescence and size effects will be discussed.

Fig. 2: In situ HR imaging of the PdO_x reduction: a-b) from CAL to RED states (STEM), c-d): under O_2 but due to the oxide instability when increasing the temperature (TEM).

Fig. 1

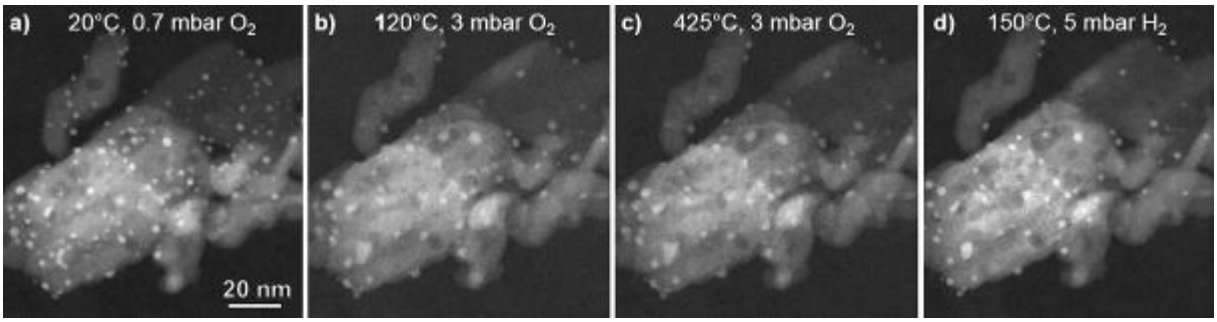
a) 20°C, 0.7 mbar O_2
b) 120°C, 3 mbar O_2
c) 425°C, 3 mbar O_2
d) 150°C, 5 mbar H_2
20 nm

Fig. 2

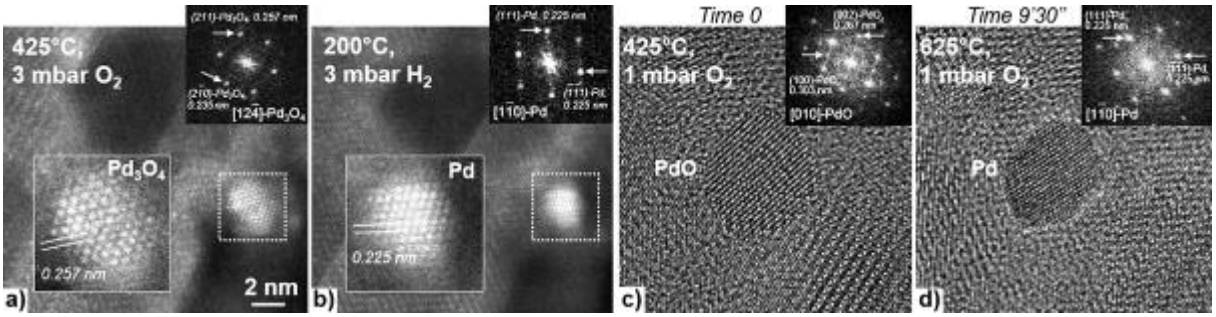
425°C,
3 mbar O_2
Pd_3O_4
0.257 nm
2 nm
a)
200°C,
3 mbar H_2
Pd
0.225 nm
b)
Time 0
425°C,
1 mbar O_2
PdO
c)
Time 9'30"
625°C,
1 mbar O_2
Pd
d)

MS3.004 invited
Novel *operando* approaches for combined low voltage STEM and synchrotron spectroscopy

R. Ciancio[1]

[1]CNR-IOM, Trieste, Italy

Understanding the function of materials in reactive environments is a crucial issue to advancing several of the world"s most pressing energy needs, specifically in the areas of catalysis, energy conversion and energy storage. In most of the cases, much of the current knowledge has been obtained under conditions that largely deviate from those of practical applications of these materials. There is common agreement that information have to be acquired on different lengh scales and that, to this aim, multiple techniques need to be intelligently combined. Much of effort has been made lately in designing new instruments and adapting existing ones to investigate catalysts under *operando* conditions. Another approach has been the use of micro- or nanoreactors that separatethe high-pressure volume from the (ultra)high vacuum part via ultrathin walls of an inert material. Very recently, microreactor cells have been developed to integrate the capabilities of ensemble-averaging synchrotron techniques with local probe ones as TEM to analyze the same catalytic process with different instruments (1,2).

We propose here the development of a novel multifunctional microreactor for *operando* low voltage Scanning TEM in a SEM compatible with a broad range of synchrotron techniques. The microreactor is a sealed chamber consisting of two facing membranes with SiN semi-transparent windows allowing transmission of both electrons and X-rays. It allows operation at atmospheric pressure, in presence of reactive gases and at elevated temperatures. The device is designed to be compatible with Grazing Incident Small Angle X-ray Scattering (GISAXS) and Wide-Angle X-ray Scattering (GIWAXS) where extended beam footprint (about 1x10 mm2) and small penetration of the beam are involved due to the grazing incidence geometry. The entire fabrication protocol has been designed to ensure optimal electron transparency for STEM imaging and to preserve the mechanical resistance of the membranes for GISAXS experiments.

We successfully demonstrated the feasibility of our approach by studying the stability, shape and size evolution of PVP-capped Pd nanocrystals under oxidation/reaction conditions. Information on size, morphology of the nanocrystals obtained at the nanoscale by STEM have been coupled with that concerning their collective behaviour over extended areas such as size, aggregation and cristalline structure by GISAXS/GIWAXS, all in one portable microreactor and under identical reaction conditions.

References:

(1) J.F. Creemer Ultramicroscopy 2008, 108, 993– 998

(2) Shen Zhao ChemCatChem 2015, 7, 3683 – 3691

MS3.005
Operando transmission electron microscopy study of catalysts at work during the industrially relevant reaction of dehydrogenation of propane

H. C. Nerl[1], M. Plodinec[1], R. Schlögl[1,2], A. Trunschke[1], T. Lunkenbein[1]

[1]Fritz Haber Institute of the Max Plack Society, Inorganic chemistry, Berlin, Germany
[2]Max Planck Institute for Chemical Energy Conversion, Mülheim an der Ruhr, Germany

Many questions remain unanswered about the fundamental factors influencing the activity, deactivation and regeneration of catalysts at work. Improved understanding of structure-activity correlations and coke formation are crucial to develop better, more efficient industrial processes including for dehydrogenation of propane (DHP).(1) However, to date most electron microscopy (EM) studies of catalysts have been done not in relevant conditions (mostly in vacuum, low pressure and RT).(2) Recent developments in operando EM techniques have opened exciting horizons for studying catalysts under relevant conditions.(3)

In this study, we show for the first time using operando EM that we can visualize the structure of Platinum (Pt) catalysts at high magnification and track coke formation at the different stages of the industrially relevant reaction of DHP. We also show that we can correlate the EM findings with catalyst function by identifying the different states of the catalysts using mass spectrometry and calorimetry data. To achieve this we used a similar but modified set-up as described by Willinger *et al.* (4), consisting of an aberration-corrected FEI Titan with an in-house developed gas feeding, heating set-up where the gas outlet is directly connected to a QMS mass spectrometer (with a response time of 20s) to analyse the total flow of outgoing gas. Thereby we can correlate imaging in different gas environments with possible heating up to 1000°C, achievable pressures up to 1bar with mass spectrometry data. Particular focus has also been paid to study the effects of the electron beam on the sample.

With this approach we were able to obtain proof of conversion of propane to propylene. We also found that catalysts undergo changes in size and shape at different stages of the reaction (shown in fig a&b regions 1-4). Many of the small Pt NPs were found to be present prior to the reaction only (fig a) but not after 3 days in reaction conditions (fig b). We also investigated the formation of coke since it is known to play a major role in the deactivation of the Pt catalysts. We observed coke formation in DHP for the first time operando and found that both, hard and soft coke, are present from the early stages of the reaction. Graphitic coke build-up was found to occur via initial formation of individual layers of graphene on the surface of the Pt NPs followed by the progressive addition of layers of carbon with time of reaction to ultimately form graphitic carbon nanosheets and carbon nanotubes.

To summarize, in this work we show for the first time that using operando EM techniques we can gain meaningful insights into the industrially relevant process of DHP by studying the catalysts at work during the reaction. Furthermore, we observed for the first time the changes in shape and size of the Pt catalysts as well as the progressive formation of coke on the Pt NPs in real time during the reaction of DHP.

Figure: Operando transmission EM study of dehydrogenation of propane. a) Pt catalyst nanoparticles prior to the reaction and b) after 3 days exposed to propane at 700 C. c) High magnification image (from blue box in b) shows how layers of carbon (arrows) form operando.

References:

(1) Bartholomew, CH, Applied Catalysis a-General, 2001. 212(1-2): p. 17-60.

(2) Su, DS, B Zhang, and R Schlogl, Chem Rev, 2015. 115(8): p. 2818-82.

(3) Vendelbo, SB, et al. Nat Mater, 2014. 13(9): p. 884-90.

(4) Willinger, MG et al. Micr. Microanal. 22 (Supl 3), 2016.

Fig. 1

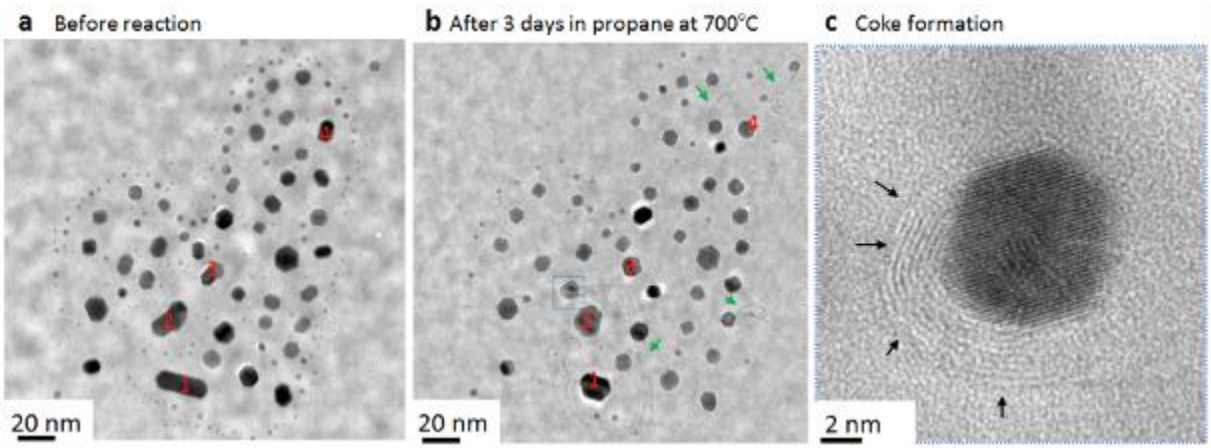
a Before reaction
b After 3 days in propane at 700°C
c Coke formation
20 nm
20 nm
2 nm

MS3.006
Electron tomographic studies on all-ceramic solid oxide fuel cells

H. Störmer[1], M. Meffert[1], F. Wankmüller[2], J. Schmieg[1], A. Weber[2], J. C. Njodzefon[3], P. Lupetin[3], E. Ivers-Tiffée[2], D. Gerthsen[1]

[1]Karlsruhe Institute of Technology (KIT), Laboratory for Elektron Microscopy (LEM), Karlsruhe, Germany
[2]Karlsruhe Institute of Technology (KIT), Institute for Applied Materials (IAM-WET), Karlsruhe, Germany
[3]Robert Bosch GmbH, Renningen, Germany

Energy related materials like intermediate-temperature solid oxide fuel cells (SOFCs) are considered a key device to address global environmental challenges. However, a detailed understanding of the complex relationship between manufacturing parameters, choice of materials and resulting microstructure is challenging. Alternative design concepts like co-sintering of inert substrate supported cells offer opportunities to study the interplay between different cell components and improve methodological aspects which then can be transferred to different cell concepts. In order to correlate manufacturing parameters, potential aging mechanisms and cell performance one cannot rely on 2D imaging methods alone without acknowledging the 3D nature energy-related materials. For example, SOFCs require layered cell geometries with suitable 3D porous networks of ionic and electronic conducting electrode materials to efficiently convert chemical into electrical energy. To improve the correlation of fabrication parameters and cell performance and consequently identify aging mechanisms, sophisticated 3D chemical and microstructural analysis of all cell components is necessary. This analysis task covers several orders of magnitude ranging from (i) large-scale parameters like layer uniformity, large pores or macroscopic cracks, down to (ii) formation of nanoscale secondary phases and (iii) corresponding modeling of ionic/electronic transport pathways.

Combining several tomographic techniques in a correlative way provides the key to a complete set of relevant 3D microstructural data. The use of X-ray computed tomography (micro-CT) for example allows reconstructions of large sample volumes with moderate resolution providing information about gas transport pathways and large scale inhomogeneities within the cell geometry. Serial sectioning tomography using a focused ion beam (FIB) to remove the material slice-by-slice and imaging in a scanning electron microscope (SEM) (1) gives complementary information due to access to smaller features. Within this study, a state-of-the-art Thermo Scientific Helios G4 FX instrument equipped with numerous detectors allowing simultaneous readout of up to four detectors was used. Imaging parameters and the combination of multiple detector signals were systematically investigated to improve segmentation accuracy. Figure 1 shows a FIB-SEM tomography reconstruction which visualizes the (La,Sr)MnO3 (LSM) cathode - Y2O3-doped ZrO2 (YSZ) electrolyte interface in a SOFC. Moreover, pore size, tortuosity and distribution of secondary phases were extracted from 3D reconstructions to model the impact on cell performance. Additionally, electrochemical impedance spectroscopy was used to correlate microstructural findings with their corresponding contributions to the overall cell performance.

References:

(1) F. Wankmüller et al., Journal of Power Sources 360 (2017 399-408.

We acknowledge funding by the German Ministry for Economic Affairs and Energy (BMWi)

Fig. 1

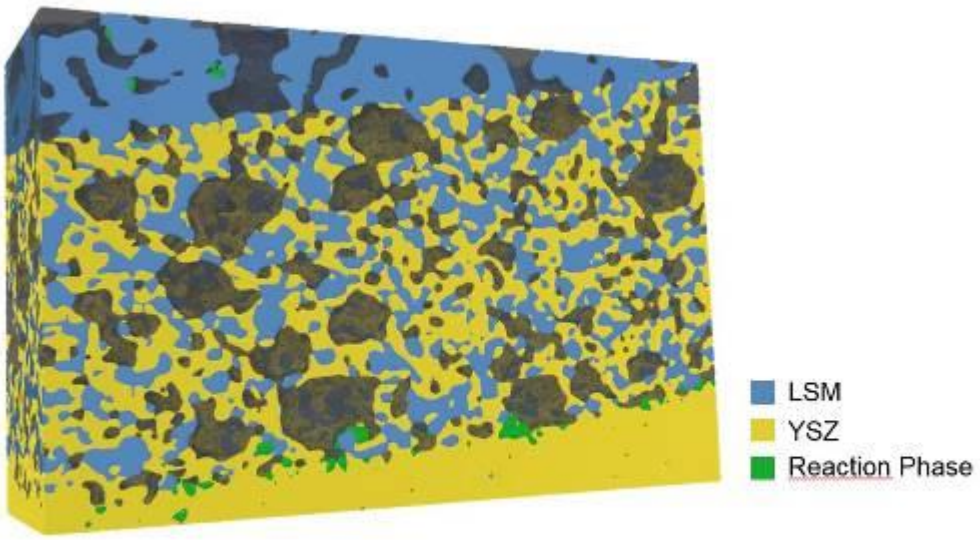

Fig. 1. FIB-SEM reconstruction of Y_2O_3-doped ZrO_2 (YSZ) electrolyte –(La,Sr)MnO_3 (LSM) cathode interface with grains of $ZnMn_2O_4$ spinel reaction phase at the electrolyte/cathode interface.

MS3.LB.P01
Rational Design of Two-Dimensional Hybrid Co/N-Doped Carbon Nanosheet Arrays for Efficient Bi-Functional Electrocatalysis

N. Cheng[1], L. Ren[1], G. Casillas[1], S. Zhou[1], J. Zhuang[1,2], L. Wang[2], X. Xu[1,2,3,4], S. Dou[1,2,3,4], Y. Du[1,2,3,4]

[1]University of Wollongong, Institute for superconducting and electronic materials, WOLLONGONG, Australia
[2]Beihang University, Beijing, China
[3]University of Melbourne, Melbourne, Australia
[4]University of Wollongong, Wollongong, Australia

3*d* transition-metals are regarded as the most promising substitutes for noble metals in electrocatalysis. (1-3) Most 3*d* TMs possess various valence states arising from their *d*-orbitals, which enables the they to be used as electrocatalysts for both the HER and the OER. Besides variable valence states, the distribution of TM-based particles on conductive supports also significantly affects their electrocatalytic activities. (4) Using an annealing process is the general approach to achieve 3*d* TM-based electrocatalysts with variable valence states. Nevertheless, it is hard to avoid particle aggregation in annealing, which decreases the density of active surface sites. (5) Wet-chemical routes, such as the hydrothermal method, on the other hand, can suppress the aggregation by controlling particle dispersion, but face difficulties in modulating valence states. Thus, it is still extremely challenging to synthesize well-distributed TM particles with controllable mixed valence states on conductive supports for electrocatalysis, which is very much in demand for the development of multi-functional TM-based electrocatalysts.

Try to use bimetallic leaf-like zeolitic imidazolate framework nanosheet arrays as the precursor to design and synthesize size and valence-state controllable Co based nanoparticles in 2D nitrogen-doped leaf-like carbon matrix arrays on conductive carbon cloth. Moreover, we want to find out the relationship between the particle size and valence-state of Co based nanoparticles with the electrocatalytic properties.

BMZIF-x/CC were synthesized using different ratio of $Co(NO_3)_2 \cdot 6H_2O$ and $Zn(NO_3)2 \cdot H_2O$ using hydrothermal method. CoNC-x/CC was prepared by calcining the corresponded BMZIF-x/CC**.**

In this work, 2Dnitrogen-doped leaf-like carbon matrix arrays functionalized with multi-valence-state transition metal (cobalt) hybrids were successfully prepared by *in-situ* calcination of the corresponding bimetallic leaf-like zeolitic imidazolate framework (ZIF-L) in inert atmosphere. The 2D morphology of the matrix along with the particle size and surface valence state of the anchored particles has been successfully controlled via precise adjusting the Co^{2+} ratio in the bimetallic ZIF-L precursor. Electrochemical measurements show that the kinetics and stability towards the hydrogen evolution reaction (HER) and oxygen evolution reaction (OER) are highly dependent on the particle size as well as their valence states. It was found that the particles with sizes less than 60 nm exhibit mixed Co^0/Co^{+2} valence states, which demonstrate a bi-functional electrocatalytic performance. The theoretical simulations revealed that the bi-functional electrocatalytic activity should be attributed to the synergic effect of mixed Co^0/Co^{+2} and electronic coupling in the hybrids, which are of benefit to the catalytic kinetics and dynamics. High HER and OER activities of the hybrids have been verified, in which an overpotential of 171 and 280 mV to deliver the current density of 10 mA/cm^2 for the HER and OER, respectively, were achieved. The obtained correlation between non-noble-metal-based carbon composites and HER/OER activities may be exploited as a rational guideline in the design and engineering of electrocatalysts.

References:

(1) *Adv. Mater.,* 2016, 28, 9266;

(2) *Nano Research,* 2016, 9, 28;

(3) *Small,* 2017, 13, 1701931;

(4) *Energy Environ. Sci.,* 2013, 6, 3693;

(5) *Nat. Commun.*, 2014, 5, 4695.

MS3.LB.P02
Investigation of Solid State Electrolytes using (Scanning) Transmission Electron Microscopy

M. Malaki[1], A. Pokle[1], A. Beyer[1], E. Trevisanello[1], T. Krauskopf[2], F. H. Richter[2], J. Janek[2], K. Volz[1]

[1]Material Science Center and Faculty of Physics, Philipps University Marburg, Marburg, Germany
[2]Physikalisch-Chemisches Institut, Justus-Liebig-Universität Gießen, Gießen, Germany

Conventional lithium-ion batteries (LIBs) make use of liquid electrolytes (LEs) to facilitate ion transport between the electrodes. However, the LEs present a significant challenge to ensure overall safety and limits the achievable energy density in combination with the separator. Solid electrolytes (SEs) can circumvent these issues by playing the dual-role of electrolyte and separator in combination with a lithium metal anode. The ionic conductivity of the SE is mostly limited by grain boundaries and the electrode-electrolyte interface. Despite the availability of bulk crystallographic information, the local structure of the grain boundaries and interfaces with the electrodes (< 10 nm thickness) has not been sufficiently investigated due to the radiation-sensitive nature of many SEs.

The requirement of high Li-ion conductivity and chemical stability of SEs led to the development of several types of SEs such as the NASICON type $Li_{1+x}Al_xTi_{2-x}(PO_4)_3$ -LATP and garnet type $Li_7La_3Zr_2O_{12}$ (LLZO) compounds. Both are usually synthesized in powder form and sintered to get densely packed poly-crystalline pellets. Previously, it was found with the aid of high-resolution transmission electron microscopy (HRTEM) that the interface between the grain boundaries in LATP consisted of either amorphous or intermediate-transition layers although precise and detailed information was not made available (1). For the LLZO, it was initially reported that they are extremely unstable under imaging conditions used for HRTEM leading to loss of structural ordering (2), however, high resolution (scanning) transmission electron microscopy (HR (S)TEM) analysis were reported later (3,4). This reveals a lack of understanding of the damage mechanism in radiation-sensitive SEs.

Here, we report the possibility of probing local structures of radiation sensitive SEs by employing conventional and Focused Ion Beam preparation techniques. Using Aberration-Corrected (AC) (S)TEM to directly visualize the light elements, we have also investigated the effect of beam damage both in the preparation and imaging stages. The AC-STEM, coupled with a fast, pixelated detector (PN detector), is used to investigate the grain boundaries and the possible orientation relation between the grains is evaluated.

References:

(1) Gellert, M. et al. Grain Boundaries in a Lithium Aluminum Titanium Phosphate-Type Fast Lithium Ion Conducting Glass Ceramic: Microstructure and Nonlinear Ion Transport Properties. *The Journal of Physical Chemistry C* 116, 22675-22678 (2012).

(2) Buschmann, H. et al. Structure and dynamics of the fast lithium ion conductor "Li7La3Zr2O12". *Physical Chemistry Chemical Physics* 13, 19378 (2011).

(3) Ma, C. et al. Excellent Stability of a Lithium-Ion-Conducting Solid Electrolyte upon Reversible Li+/H+Exchange in Aqueous Solutions. *Angewandte Chemie International Edition* 54, 129-133 (2014).

(4) Ma, C. et al. Interfacial Stability of Li Metal–Solid Electrolyte Elucidated via in Situ Electron Microscopy. *Nano Letters* 16, 7030-7036 (2016).

MS3.P001
Exothermic behavior and microstructures of the electrode materials for lithium-ion batteries

H. Tsukasaki[1]

[1]Osaka Prefecture University, Sakai, Japan

In terms of safe use for electric vehicles and accumulators, all-solid-state lithium secondary batteries, in which incombustible inorganic solid electrolytes replace flammable organic solvents, have recently received significant attention. Among the inorganic solid electrolytes, sulfide-based inorganic solid electrolytes are a candidate material to produce all-solid-state batteries because of their high ionic conductivity and wide electrochemical window (1, 2). To develop reliable all-solid-state cells, the suppression of heat generation during exposure to the operating environment is a mandatory step. Therefore, evaluating the exothermal behavior of battery materials and understanding the origin of exothermic reactions is quite important.

A composite comprising LiNi1/3Mn1/3Co1/3O2 (NMC) and 75Li2S·25P2S5 (LPS) glass electrolytes are used as a positive electrode material, which exhibits excellent charge–discharge cycle characteristics (3). In this study, to understand the origin of exothermal reactions during heating, we investigated structural changes in the NMC–LPS composites mainly by *ex situ* TEM observations, combined with X-ray diffraction measurements and *ex situ* SEM observations. Figure 1 shows the *ex situ* TEM observation results for the initially charged NMC–LPS composites after heating at 500 °C. The electron diffraction (ED) pattern and its intensity profile are shown in (a). Based on the analysis of the intensity profile, main crystalline phases precipitated were identified as Li3PO4, CoNi2S4 and MnS. The hollow-cone dark filed (DF) image in (b) shows these crystalline phases are randomly present as a nanocrystellite, as indicated by the arrows. These results suggest that LPS and NMC yield a chemical reaction by heat treatment, which leads to the exothermal reactions. In the presentation, we will discuss the detailed exothermal mechanism of the NMC–LPS composites, including *ex situ* SEM observation and XRD measurement results.

References:

(1) Tatsumisago, *et al., J. Asian. Ceram. Soc.* 1, 17–25 (2013).

(2) Kato, *et al., Nature Energy* 1, 16030 (2016).

(3) Tsukasaki, *et al., J. Power Sources* 367, 42–48 (2017).

(4) H. Tsukasaki, *et al., Sci. Rep.* 8, 6214 (2018).

Fig. 1: (a) The ED pattern and the intensity profile of initially charged NMC–LPS composites after heating at 500 °C. (b) The corresponding hollow-cone DF image.

Fig. 1

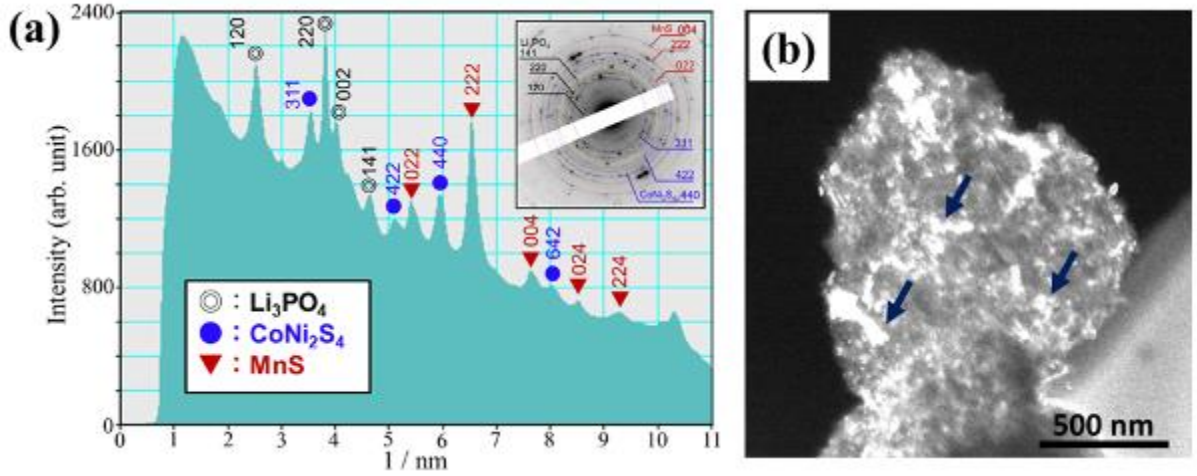

MS3.P002
In Situ Studies for Understanding Intragranular Nanopore Evolution in Ni-rich Layered Oxide Cathode Material

A. Pokle[1], S. Ahmed[1], A. Beyer[1], S. Schweidler[2], M. Bianchini[3], P. Hartmann[2], T. Brezesinski[2], J. Janek[2], K. Volz[1]

[1]Philipps University Marburg, Materials Science Center and Faculty of Physics (WZMW), Marburg, Germany
[2]KIT/BASF Battery and Electrochemistry Laboratory (BELLA), Karlsruhe, Germany
[3]KIT/BASF-Joint Laboratory BELLA, Karlsruhe, Germany

Understanding the electrode material behavior under various conditions is critical for developing next-generation battery technologies. Dynamic conditions inside the working battery cell have been recently explored using advanced in-situ characterization techniques. Despite widespread applications and research investments, energy storage materials still face a lack of complete understanding. Performing real-time electron microscopy is one of the significant developments, which has enabled us to probe local chemo-mechanical changes under dynamic conditions.

The requirement for higher energy densities within lithium ion batteries lead to the development of Ni-rich NCMs. Within this class we investigated a material with 85% Ni: Li1+x(Ni0.85Co0.10Mn0.05)1-xO2. Typically, NCMs are synthesized as secondary particles made from densely packed primary particles. Strain is induced within the primary particles during charging/discharging cycles due to volume change, which can result in cracking of the secondary particles. Previously, surface reconstruction from a layered structure to a rock salt structure (refer figure 1), the formation of inter/intragranular cracks, and pores (or voids) have been reported. Among these, the pore formation in cycled materials is not well characterized, and its presence in pristine samples is usually neglected (1,2). Pore formation has been attributed to the release of oxygen in work carried out by Linqin Mu et al. (3).

Here, we report the origin of nanopores and investigate the heating and biasing effects using in-situ heating/biasing holder. Intragranular nanopores are observed in a wide variety of layered oxide cathode materials, but so far it is not clear if and how they affect the performance of the materials. By employing Focussed Ion Beam, Aberration-Corrected STEM (AC-STEM) and Electron Energy Loss Spectroscopy with 4DSTEM capabilities, we study the effect of nanopores on the intragranular structure of the primary particles during cycling. In addition to observing phase transformation (leading to metal segregation) and inter/intragranular cracks, we have also investigated cation disordering within the nanopore at sub-angstrom resolution.

References:

(1) P. Yan, J. Zheng, M. Gu, J. Xiao, J.-G. Zhang, and C.-M. Wang, "Intragranular cracking as a critical barrier for high-voltage usage of layer-structured cathode for lithium-ion batteries," *Nat Commun*, vol. 8, Jan. 2017.

(2) J. Zheng *et al.*, "Suppressed oxygen evolution induced degradation at high charge cut-off voltages in LiNixMnyCozO2 cathodes," *Nano Research*, no. Tsinghua University Press and Springer-Verlag, p. 20.

(3) L. Mu *et al.*, "Oxygen Release Induced Chemomechanical Breakdown of Layered Cathode Materials," *Nano Lett.*, vol. 18, no. 5, pp. 3241–3249, May 2018.

Fig. 1: HAADF micrographs using AC-STEM of NCM851005. (a) showing layered structure, the green arrow marks the undetected Li position (O atomic columns exhibiting diffused contrast) between the TM rows in uncycled sample, (b) 200-cycled displaying TM replacing Li positions (blue arrow exhibiting sharp contrast), (c) high-resolution image from region (d) showing rock salt (cubic) structure. (d) surface appearance at low magnification of the region that has been transformed into rock salt structure in 500-cycled sample.

Fig. 1

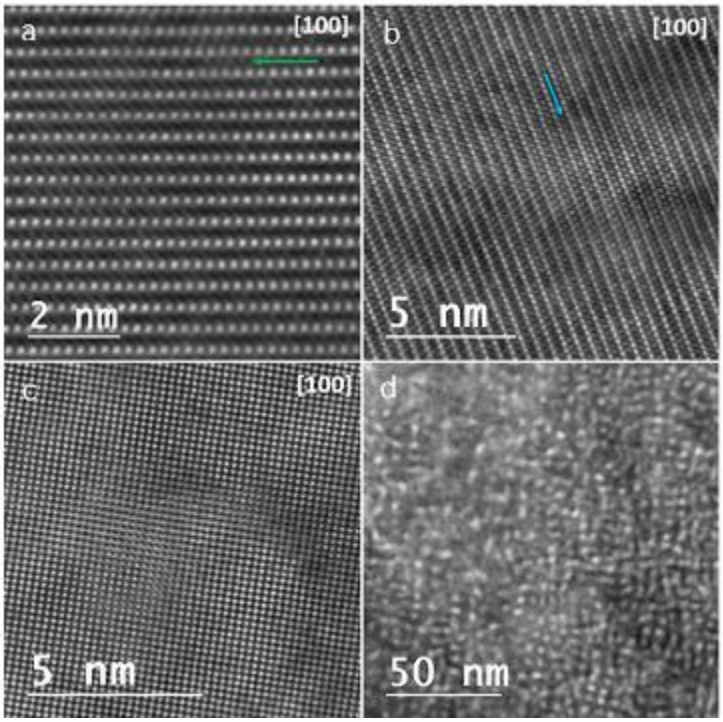

MS3.P003
Advanced and *in situ* electron microscopy investigation of phase composition and phase transformation in Ga-Rh liquid metal catalysts

M. Wu[1], M. Grabau[2], N. Taccardi[3], C. Papp[2], H. P. Steinrück[2], P. Wasserscheid[3,4], E. Spiecker[1]

[1]University of Erlangen-Nürnberg, Materials Science, Erlangen, Germany
[2]University of Erlangen-Nürnberg, Physical Chemistry, Erlangen, Germany
[3] University of Erlangen-Nürnberg, Institute of Chemical Reaction (CRT), Erlangen, Germany
[4]Forschungszentrum Jülich, Helmholtz-Institute Erlangen-Nuremberg for Renewable Energy (IEK-11), Erlangen, Germany

Supported Catalytic Active Liquid Metal Solutions (SCALMS) have been recently demonstrated to be a highly promising class of heterogeneous catalysts, which show superior activity, robust performance and selectivity in dehydrogenation reactions (1,2). At typical dehydrogenation temperatures of 500 °C, it is conceived that the large surface to volume ratio of the nano-droplets of the liquid metals, supported in the open meso- or macroporous scaffold, provide huge number of catalytically active sites which are intrinsically robust to coke formation and degradation due to the highly dynamic nature of the liquid metal alloy. Such liquid metal nanoalloys are intermetallic compounds of low-melting host elements (e.g., Ga, In) with small amount of catalytically active transition metal elements. These intermetallic compounds typically have complex stable crystal phases in solid state. The structural information, particularly the phase stability of the nanoalloys, is indispensable to render the full picture of their catalytic performance, which is however hardly accessible with catalytic tests and require a combination of *in situ* surface science, scattering and high-resolution imaging and spectroscopy techniques.

In this work, we study the structure, composition and phase stability of model Ga-Rh systems with advanced transmission electron microscopy (TEM), both static at room temperature and *in situ* during heating/cooling. The Ga-Rh nanoparticles are deposited on a SiOx membrane via physical vapor deposition with Rh concentration ranging between 0.6 and 6 at.%. At room temperature, a typical two-phase microstructure of crystalline (c-) precipitates embedded in amorphous (a-) nanoparticles is found in all studied samples. By combining information from EDXS, HRTEM and careful analysis of electron diffraction patterns, the crystal phase is identified as Ga16Rh3 or Ga21Rh4 and their derivatives (cf. Fig. 1a-d). *In situ* observation while heating the samples in the TEM was performed to elaborate the phase stability of the c-GaxRhy/a-GaRh nanoparticles, since the phase diagram of the Ga-Rh system is not safely established in the low Rh concentration range. Low-dose electron diffraction has been performed in order to minimize the beam effect as identified during *in situ* imaging experiments. Disappearing of sharp crystal rings is observed at elevated temperature, which is then followed by the fade-out of the second broad diffuse ring (cf. Fig. 1e), indicating a solid-liquid phase transformation. Higher Rh concentration show higher transformation temperature. These results shed light on the microscopic mechanisms underlying the high performance of Ga-Rh SCALMS in propane dehydrogenation.

References:

(1) Taccardi, N. et al. Nature Chemistry 9, (2017) p.862.

(2) M.W. and E.S. acknowledge financial support by DFG via GRK 1896 "In-situ Microscopy with Electrons, X-rays and Scanning Probes".

Fig. 1: Structure, composition and temperature-dependent phase properties of Ga-Rh nanoparticles. (a-d) Results from a sample with Rh = 2.7 at. % and (e) 0.9 at.%. (a) BF-TEM image of the nano-particles on SiO2 membrane. (b) EDXS composite map. (c) HRTEM image of a single nano-particle. (d) Zero-loss filtered diffraction pattern of pure amorphous Ga (left) and with Rh = 2.7 at. % (right half). Ga16Rh3 phase (ICSD No. 415871) is superimposed on the right half. (e) Few key frames of diffraction patterns taken during an in situ heating experiment from the samples.

Fig. 1

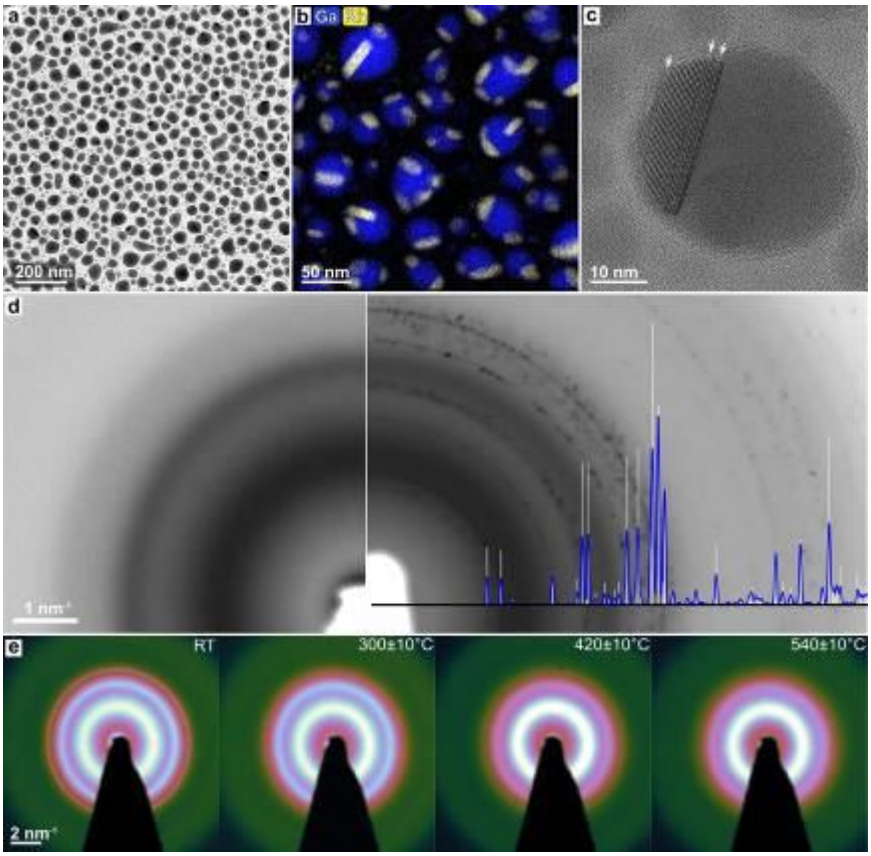

MS3.P004
Understanding Structure Changes during Cycling of MoS_2-based Mg Batteries by Pair Distribution Function Analysis

X. Mu[1], Z. Li[2], Z. Zhao-Karger[1,2], M. Fichtner[2], C. Kübel[1,2,3]

[1]Karlsruhe Institute of Technology, Institute of Nanotechnology, Eggenstein-Leopoldshafen, Germany
[2]Karlsruhe Institute of Technology (KIT), Helmholtz-Institute Ulm for Electrochemical Energy Storage (HIU), Ulm, Germany
[3]Karlsruhe Institute of Technology (KIT), Karlsruhe Nano Micro Facility (KNMF), Eggenstein-Leopoldshafen, Germany

Scanning/transmission electron microscopy (S/TEM) has been used as an important tool to characterize battery materials. However, the dis/charge processes often generate a large number of defects in the electrode materials strongly distorting their crystalline structure or even making them amorphous. This intrinsically limits application of atomically resolved imaging techniques and conventional diffraction. Furthermore, the signal of analytical methods such as EELS is obscured as the nanosized electrode particles are mostly surrounded by carbonaceous additives, which have to be used for enhancing electron conductivity of the electrode in realistic electrochemical environment (1).

The atomic pair distribution function (PDF) obtained from diffraction (2), measuring the interatomic distances and coordination, directly probes the atomic configuration, particularly for strongly distorted or disordered materials. In contrast to X-ray and neutron diffraction, electron diffraction in TEM provides highly flexible spatial resolution from micro- to tens of nanometer. The recently developed 4D STEM-PDF (3) approach offers PDF mapping with a nanometer spatial resolution and, at the same time, samples a statistically meaningful area representing the global sample properties. The power to answer structural questions of complex materials has been demonstrated by, e.g. analyzing phase transformation (2) and the structure of metallic nanoglasses (4).

In this talk, we demonstrate that electron PDF associated with multivariate statistical analysis (MSA) can overcome the above mentioned issues and provide detailed structural and bonding analysis for long-time cycled batteries. We investigated MoS_2-based Mg batteries, as the Mg^{2+} batteries are one of the most promising candidates for future battery technologies. Figure 1a, and d show the crystalline structure of the host material (MoS_2) is significantly destroyed during cycling because of strong interaction between Mg^{2+} and the host. It makes investigation by the conventional microscopy difficult. Interestingly, the PDF approach not only reveals a transition from a short- and medium-range order similar to 1H-MoS_2 to 2T-MoS_2 during cycling (Fig. 1g), but also detected the intercalation of solvated magnesium-ions ($[Mg(DME)x]^{2+}$) in the layered MoS_2 cathode (Fig. 1h) (5). This explains the fast kinetics of the intercalation mechanism. In addition, the spatially resolved 4DSTEM-PDF line scan in the charged sample (figure 1f, g) reveals a thin surface layer containing reduced Mo and the atomic arrangement differing from the H-type bulk. It explains the ambiguous correlation between the XPS) result and the electrochemistry.

Mu acknowledge DFG's support (MU 4276/1-1).

References:

(1) C Zhu et al., Science 358, 1400 (2017).

(2) X. Mu et al, J. Appl. Crystallogr. 46, 1105 (2013).

(3) X. Mu et al, Ultramicroscopy 168, 1, (2016).

(4) Y. Ivanisenko et al, Adv. Eng. Mat. 1, 1800404, (2018).

(5) Z. Li et al, Nat. Commun. 9, 5115 (2018).

Fig. 1: HRTEM (a) and STEM-HAADF image (b, c) of MoS_2 at 30th discharged (Mo^{2+}-in) state, (d) the FFT of highlighted area in (a). (e, f) are STEM-HAADF images of 30th charged (Mo^{2+}-out) state. (g) PDF analysis of the material, and the simulated PDFs of 2H- and 1T-MoS2. (h) MSA solution to the PDF curves, and the simulated PDF of a $[Mg(DME)3]^{2+}$cluster. (j) local PDFs at different depth from the surface of the 30th charged sample, being taken along the line highlighted in (f).

Fig. 1

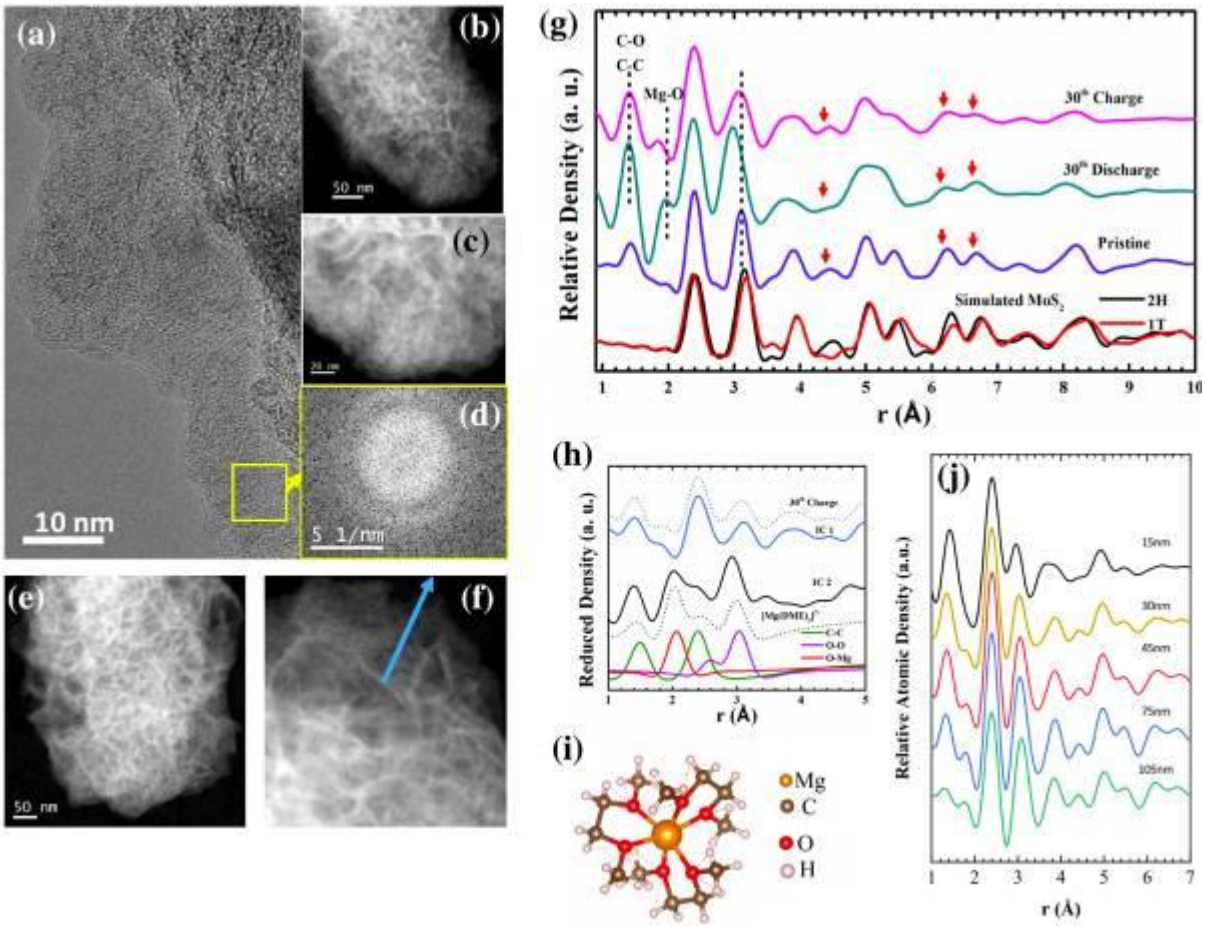
(a)
(b)
(c)
(d)
(e)
(f)
(g)
(h)
(i)
(j)
10 nm
50 nm
5 1/nm
C-O
C-C
Mg-O
30th Charge
30th Discharge
Pristine
Simulated MoS2
2H
1T
Relative Density (a. u.)
r (Å)
Reduced Density (a. u.)
Mg
C
O
H
Relative Atomic Density (a.u.)
15nm
30nm
45nm
75nm
105nm

MS3.P005
TEM Investigations on Low-Weight Battery Materials

U. Schürmann[1], K. Saleem[1], S. Hansen[1], H. Krüger[1], R. Adelung[1], L. Kienle[1]

[1]Christian-Albrechts-Universität Kiel, Institute for Materials Science, Kiel, Germany

Lithium-based batteries are widely used because of their high storage capacities and efficiencies in combination with low weight materials. Commercially available Li-ion batteries are limited in their energy density. With Li-Si-S batteries an increase in the energy density by a factor of two to three can be achieved. However, the morphology of the used Silicon as anode material is crucial to ensure structural stability in combination with the ability to store a high amount of Lithium. Additionally, CNTT (carbon nanotube tubes) material with Sulfur content is a promising candidate as cathode material.

Si anode materials with different high surface-to volume ratio morphologies - powdered and porous Si as well as Si microwires - are analyzed with TEM methods after electrochemical cycling to monitor the changes in the Solid Electrolyte Interface (SEI). The findings are compared with the results from electrochemical and Raman analysis. For this complex system the electrodes have to be compatible in a battery. Therefore, the distribution of Sulfur in CNTT material is investigated by means of Energy Filtered TEM (EFTEM).

HRTEM as well as High Angle Annular Dark Field (HAADF) Scanning TEM (STEM) was performed on Si samples in a FEI Tecnai F30 G² STwin equipped with an EDX detector (Si/Li, EDAX). EDX point measurements and elemental maps were performed in STEM mode. Electron diffraction patterns were recorded to get information about potentially present Li containing phases. Li-containing samples were ground inside a glove box and were transferred to the TEM in an Ar-filled bag. EFTEM imaging was performed at low temperatures using a cooling sample holder to avoid any sulfur sublimation inside the TEM.

EDX elemental maps in combination with HRTEM show the morphology of the SEI although the Li distribution cannot directly be observed by EDX measurements. The surface of the silicon structures shows thin amorphous layers containing elements of the formed SEI layer (S, O, F) with thicknesses in a range between 10 and 150 nm depending on the morphology and the number of charging cycles. Although the number of analyzed samples is low due to the elaborate measurements, a trend can be observed that the thickness of the SEI increases with the number of measured cycles (3, 5, 10).

With the given morphologies, the structural stability and the ability for SEI formation could be monitored. The thickness of the SEI increases with the amount of cycling numbers. The TEM investigation reflects the ability of specific charging in the different Si anode morphologies.

The authors want to thank the BMBF for funding (03XP0126 B).

Fig. 1: EDX elemental map of the SEI and corresponding TEM image of the amorphous/crystalline interface

Fig. 1

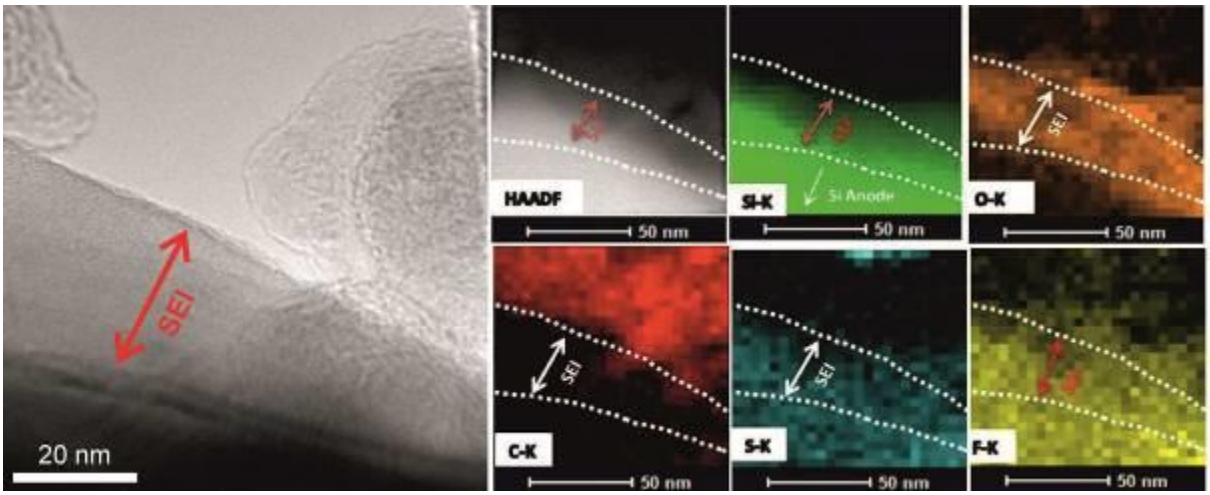

MS3.P006
Analysis of $Li_xMn_2O_4$ nanoparticles for oxygen-evolution-reaction (OER) catalysis with STEM-EELS

F. Schönewald[1], M. Baumung[1], V. Roddatis[1], M. Risch[1,2], C. Volkert[1]

[1]Georg-August Universität Göttingen, Institute for materials physics, Göttingen, Germany
[2]Helmholtz-Zentrum Berlin, Berlin, Germany

Controlling the oxygen evolution reaction (OER) is an important step in achieving a sustainable renewable energy future. At the moment, the process of generating molecular oxygen from water by chemical means is severely kinetically limited. $Li_xMn_2O_4$ is studied here as a model electrocatalyst to understand the role of valence state and covalency on the electron transfer reaction.

The goal of this study is to control the OER by manipulating the manganese valence via electrochemical de-/lithiation. Extensive characterization of the nanoparticles is performed before and after OER, including defect structures, surface faceting, composition and manganese valence for different lithiation states.

Cubic-spinel $Li_1Mn_2O_4$ nanoparticles (Sigma Aldrich) are electrochemically de-lithiated to reach compositions of $Li_xMn_2O_4$ where $0 \leq x \leq 1$. This results in a change in average manganese valence from 3.5 (x=1) to 4 (x=0) (1). The nanoparticles are then dispersed in THF and drop cast on lacey carbon TEM-grids. Polycrystalline electron diffraction patterns are taken at 300 kV with a Philips CM30 TEM to determine lattice constant changes due to de-lithiation. STEM-Dual-EELS spectral images (0-200 eV and 500-700 eV with 0.1 eV dispersion) are recorded from more than 10 particles at each lithiation state with spatial resolution of about 1 nm with a CS-corrected FEI Titan-ETEM at 300 kV. After zero-loss-peak correction and background subtraction, the manganese valence is calculated using two methods: the manganese L_3/L_2 intensity ratio and the oxygen K pre-peak to manganese L_3 peak distance.

The EEL spectra show significant differences between the bulk and surface regions of both pristine (x=1) and de-lithiated particles. A decreased Mn L_3/L_2 intensity ratio and changing Mn L_3 peak shape indicate a reduced Mn valence state in a 2 to 5 nm thick surface layer. At the same time, the oxygen K edge intensity decreases relative to the Mn L_3 and L_2 intensities and the oxygen pre-peak intensity decreases relative to the oxygen K edge. The O-K edge pre-peak has been attributed to transitions between 1s states and oxygen 2p bands hybridized with manganese 3d orbitals (2). Thus, the pre-peak intensity indicates weaker O-Mn covalency, giving rise to a reduced valence Mn surface state due to oxygen loss.

EEL spectra of pristine x=1 and electrochemically de-lithiated $Li_xMn_2O_4$ nanoparticles show no significant deviation of Mn valence in the bulk of different nanoparticles. The surface regions of the nanoparticles in both lithiation states show changes in both Mn L edges and the oxygen K edge, suggesting that the apparent Mn valence change is due to off-stoichiometry from oxygen loss. While there are no strong deviations detectable over different particles in the same lithiation state, it must be clarified how the reduced Mn surface state affects local structure and catalytic behavior.

References:

(1) Thackeray, MM, Manganese oxides for lithium batteries, Progress in solid state chemistry (1997)

(2) de Groot, F.M.F., Oxygen 1s x-ray-absorption edges of transition-metal oxides, Phys. Rev. B (1989)

Fig. 1: EEL spectra of pristine $Li_1Mn_2O_4$ particles from bulk and surface region.

Fig. 2: EEL spectra of delithiated $Li_xMn_2O_4$ particles from bulk and surface region.

Fig. 1

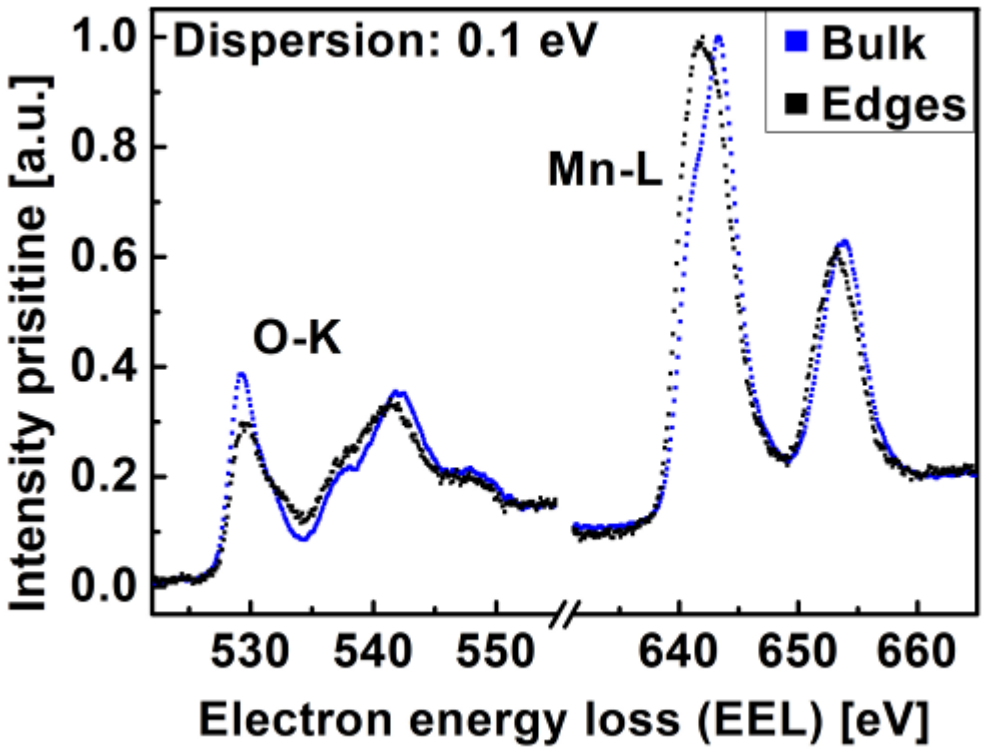
Dispersion: 0.1 eV
Bulk
Edges
Mn-L
O-K
Intensity pristine [a.u.]
1.0
0.8
0.6
0.4
0.2
0.0
530
540
550
640
650
660
Electron energy loss (EEL) [eV]

Fig. 2

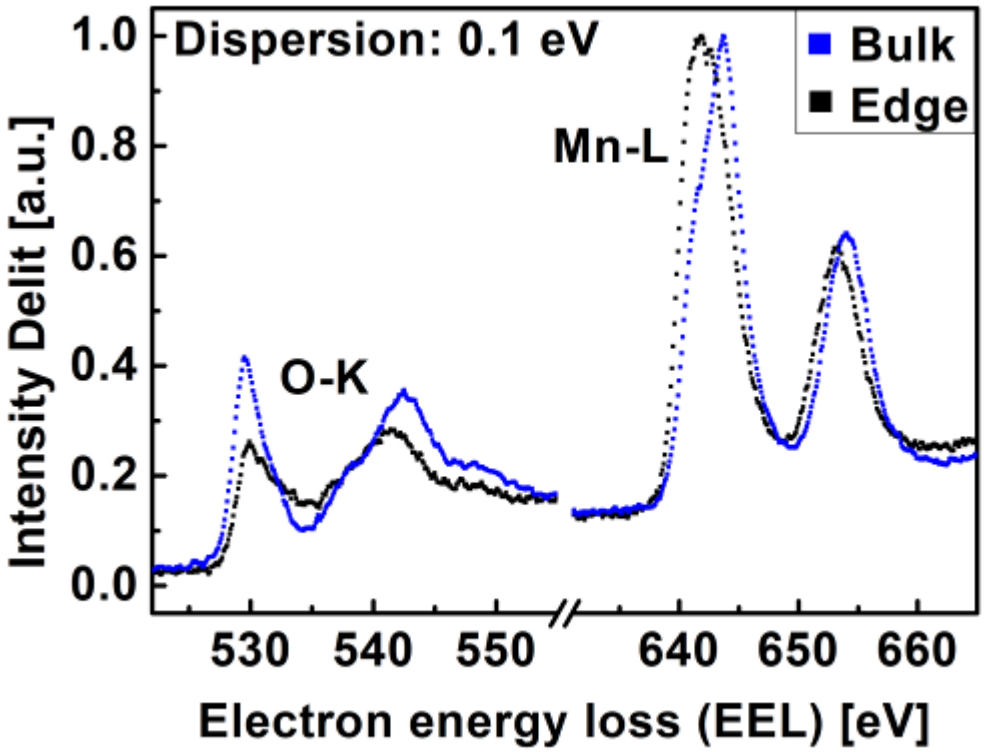
Dispersion: 0.1 eV
Bulk
Edge
Mn-L
O-K
Intensity Delit [a.u.]
1.0
0.8
0.6
0.4
0.2
0.0
530
540
550
640
650
660
Electron energy loss (EEL) [eV]

MS3.P007
Grain Boundaries in Ba(Zr,Ce,Y)O_3 Proton Conductors

W. Sigle[1], D. Zhou[1], Y. Huang[1], R. Merkle[1], P. A. van Aken[1], J. Maier[1]

[1]MPI for Solid State Research, Stuttgart, Germany

Proton-conducting ceramics play a key role in clean hydrogen-based electricity generation processes. Protonic ceramic fuel cells are promising due to reasons including lower operating temperature and absence of fuel dilution (allowing for high fuel utilization). We focus on the system of Ba(Ce,Zr,Y)O_3 electrolyte materials owing to its very high bulk proton conductivity and excellent chemical stability at temperatures of 400 ~ 700 ^oC (1). In the present investigation, two sintering methods are applied: (i) Solid-state reactive sintering (SSRS) employing NiO, which leads to the transient formation of a liquid phase and promotes grain growth (2). (ii) Spark-plasma sintering (SPS) which yields dense samples without presence of a liquid phase. Subsequent high-temperature annealing allows the acceptor dopants to accumulate or deplete close to the GB according to the GB core charge.

The main problem of this material system is the blocking character of GBs, which depends sensitively on the exact cation composition (the ratio of Ba to (Ce+Zr+Y)) as well as local concentration changes close to the GB. We studied the atomic-scale composition of the bulk and GBs by aberration-corrected analytical TEM techniques and correlate these with the ionic conductivities of bulk and GB regions. Energy-dispersive X-ray spectroscopy (EDXS) is used to quantify the GB composition. GBs showed decreased density for all elements. The relative concentrations increase for Y and Ni, and decrease for Zr and O (Fig.1). This confirms replacement of Zr by Y at the GB, which partially compensates the positive grain boundary core charge and decreases the blocking character. In some samples, GB excess of Ba was detected along with O deficiency indicating replacement of ABO_3 by BaO in the GB core. Using electron energy-loss spectroscopy (EELS), we detected a valence change of Ce towards Ce^{3+} close to the GB that also partially compensates the GB core charge. (3, 4)

References:

(1) K.D. Kreuer, Annu. Rev. Mater. Res. 33 (2003) 333.

(2) J. Tong, D. Clark, M. Hoban, R. O"Hayre, Solid State Ionics 181 (2010) 496.

(3) We acknowledge BMBF for funding (ProtoMem, No. 03SF0537C)

This project has received funding from the European Union"s Horizon 2020 research and innovation programme under grant agreement No. 823717 – ESTEEM3.

Fig. 1: (a) HAADF image of a SSRS-sintered Ni-doped $Ba_{1.015}Ce_{0.2}Zr_{0.664}Y_{0.136}O_{3-\delta}$ sample marking the analyzed grain boundary region by a red arrow; (b) EDXS line profiles of all the elements (excluding O).

Fig. 1

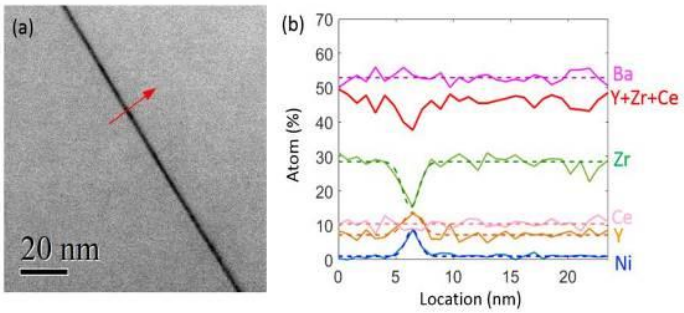

MS3.P008
In situ microscopic examination and electrochemical analysis of interaction of Light Harvesting Complex of Photosystem II with graphite layer of screen-printed electrode

M. Łazicka[1], A. Palińska-Saadi[2], B. Paterczyk[3], M. Maj-Żurawska[4], M. Garstka[1]

[1]Faculty of Biology University of Warsaw, Department of Metabolic Regulation, Warsaw, Poland
[2]Biological and Chemical Research Centre University of Warsaw, Bioanalytical Laboratory, Warsaw, Poland
[3]Faculty of Biology University of Warsaw, Laboratory of Electron and Confocal Microscopy, Warsaw, Poland
[4]Faculty of Chemistry University of Warsaw, Laboratory of Theoretical Basis of Analytical Chemistry, Warsaw, Poland

A screen-printed graphite electrode (GE) is made of a graphite paste comprising graphite powder and binder. The graphite paste is a heterogeneous material and contains dispersed spherical graphite particles linked by a binder and separated by large internal pores. Thanks to this, the graphite layer reveals high porosity, mechanical stability and enables the penetration of GE by small or large molecules. Furthermore, the GE layer is likely to have both polar and nonpolar properties.

The biohybrid systems that convert light energy into electrical energy are based on various preparations of isolated or recombinant chlorophyll-protein (CP) complexes. Light Harvesting Complex of Photosystem II (LHCII) is small (25 kDa) membrane protein and binds 22 molecules of chlorophyll and 4 molecules of xanthophyll. This complex absorbs light and transfers excitation towards the reaction centers. In biohybrid systems, LHCII seems to be less useful because it lacks special Chls pairs necessary for charge separation.

However, recently we have reported on the electrochemical properties of LHCII immobilized on GE and changes in its arrangement supported by the applied potential (1). Our results indicate that photoelectrochemical properties of the LHCII-GE system depends on the potential applied to electrode and the structural proximity of graphite and LHCII.

In this communication, we present results of studies on the *in situ* interaction of LHCII with graphite layer as well as electrochemical and fluorescence characterization of LHCII-GE system.

The structural arrangements of LHCII-GE were examined by scanning electron microscopy (SEM) and confocal laser scanning microscopy (CLSM). A three-dimensional view of LHCII fluorescence results was obtained from subsequent focal depths to form cross-sections of optical slices that were next combined into deconvoluted 3D images. We constructed a special holder for CLSM, which enables to perform simultaneous electrochemical and microscopic *in situ* experiments. Furthermore, next holder was used to investigate electrochemical and fluorescence behavior of LHCII in the presence of phenyl-p-benzoquinone by chronoamperometry in dark and light conditions.

Our *in situ* experiment indicates the potential-dependent migration of LHCII into the GE volumes [Fig. 1]. These processes convert the LHCII multilayer immobilized on GE into a permanent and stable graphite-LHCII three-dimensional structure. The location of LHCII inside porous graphite determined the chronoamperometric properties of LHCII-GE system.

Our study can help to construct biohybrid, photovoltaic systems based on carbon materials.

The project granted on the decision number DEC-2013/09/B/NZ1/01111 by the National Science Centre.

References:

(1) Piotrowska P, Łazicka M, Palińska-Saadi A, Paterczyk B, Kowalewska Ł, Grzyb J, Maj-Żurawska M, Garstka M (2019) Electrochemical characterization of LHCII on graphite electrodes –Potential-dependent photoactivation and arrangement of complexes. Bioelectrochemistry 127: 37-48.

Fig. 1: 3D images of Chl fluorescence from the same area of LHCII-GE before (A) and after 10 min. of photocurrent generation (B) at open circuit potential (OCP, -170 mV). As indicates the distribution of LHCII fluorescence on GE, before electrochemical treatment the complexes were localized over the graphite scraps (A). After applied potential, the flat layer of LHCII was changed into irregular surface (B)

Fig. 1

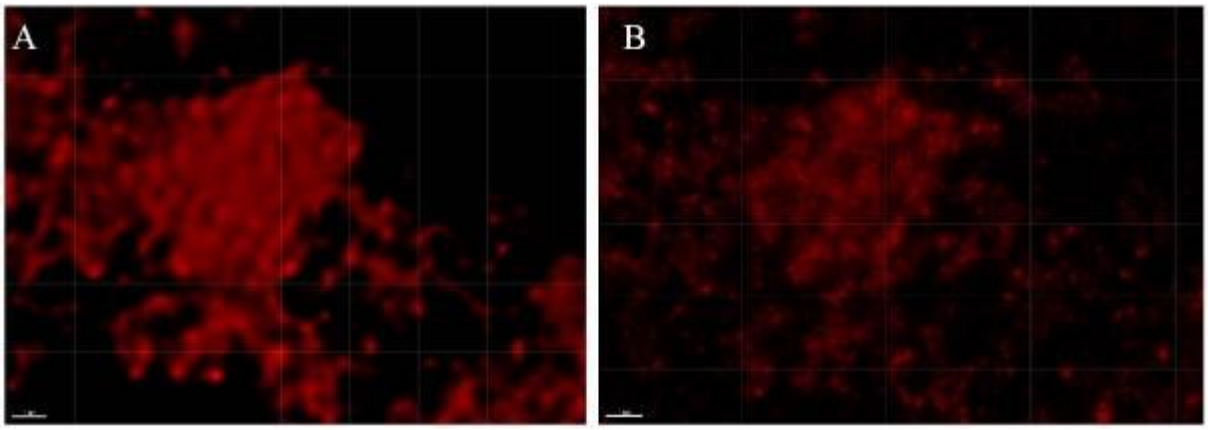

MS3.P009
TEM and XRD study of chemical segregation in sintered $NiCr_2S_4$

H. Großß[1], T. Dankwort[1], A. L. Hansen[2], D. Groeneveld[3], J. König[3,4], W. Bensch[5], L. Kienle[1]

[1]Kiel University, Institute of Materials Science, Kiel, Germany
[2]Karlsruhe Institute of Technology, Institute of Applied Materials, Karlsruhe, Germany
[3]University of Freiburg, Department of Microsystems Engineering, Freiburg, Germany
[4]Fraunhofer IPM, Thermal Energy Converters, Freiburg, Germany
[5]Kiel University, Institute of Inorganic Chemistry, Kiel, Germany

The efficiency of thermoelectric materials such as $NiCr_2S_4$ is governed by a high electrical conductivity and a low thermal conductivity. Both parameters can be engineered on the nanoscale, with complex structures being potentially beneficial for a thermoelectric's efficiency. Transmission Electron Microscopy (TEM) in conjunction with X-Ray Diffraction (XRD) were applied to investigate a segregation phenomenon in $NiCr_2S_4$.

Preliminary Scanning TEM (STEM) studies revealed a chemically segregated structure in sintered $NiCr_2S_4$, where Ni-rich and Cr-rich nanodomains were formed. Further, it was apparent that electron beam irradiation induced a phase transformation. XRD studies give insight into the phase constitution of the sample, while stoichiometry, domain constitution and coherence as well as structural stability can be examined via TEM methods.

Samples of $NiCr_2S_4$ were synthesized from the elements via high-temperature synthesis and sintered to pellets via spark-plasma sintering (SPS). TEM samples were cut from the bulk material, mechanically ground and subsequently polished in a Precision Ion Polishing System (PIPS) until electron transparency was reached. TEM studies and chemical analyses were performed in a FEI Tecnai F30 G² STwin equipped with an EDX detector (Si/Li, EDAX), further methods included High-Angle Annular Dark Field (HAADF) STEM and *in situ* cooling. Additional HRSTEM analyses were performed on a ThermoFisher Themis Z. XRD investigations were done on a PANalytical XPert Pro MPD diffractometer, temperature-dependent measurements were performed at beamline I15 at DLS, Didcot, UK.

XRD studies proved the material to be a mixture of multiple phases, including the stable Cr_3S_4-type, a metastable NiAs-type polymorph as well as traces of NiS_2; the latter could however be eliminated during sintering. (HR)STEM imaging revealed domains of ~ 5 nm in size, which could be proven to intergrow coherently in 3D. No strain or mismatch could be detected despite a difference of ~ 15 % in Ni or Cr content, respectively. A phase transformation from Cr_3S_4-type to NiAs-type was observed during prolonged electron beam irradiation, caused by the onset of Ni^{2+} ion mobility. *In situ* cooling experiments at 95 K could further show that the transformation still occurred, indicating a purely ballistically-induced interaction.

The chemical segregation in $NiCr_2S_4$ could be imaged and analysed in great detail. Despite a significant difference in composition, both Ni-rich and Cr-rich domains intergrew with complete 3D coherence. The beam-induced phase change from a Cr_3S_4-type structure to NiAs-type due to cation mobility could be proven to occur ballistically even at low temperatures.

The authors acknowledge funding from the DFG via the KI 1263/16-1 research grant and like to thank Arno Meingast of ThermoFisher Scientific for additional images.

Fig. 1: a) STEM micrographs of the chemically segregated structure with b) corresponding EDX elemental maps.

Fig. 1

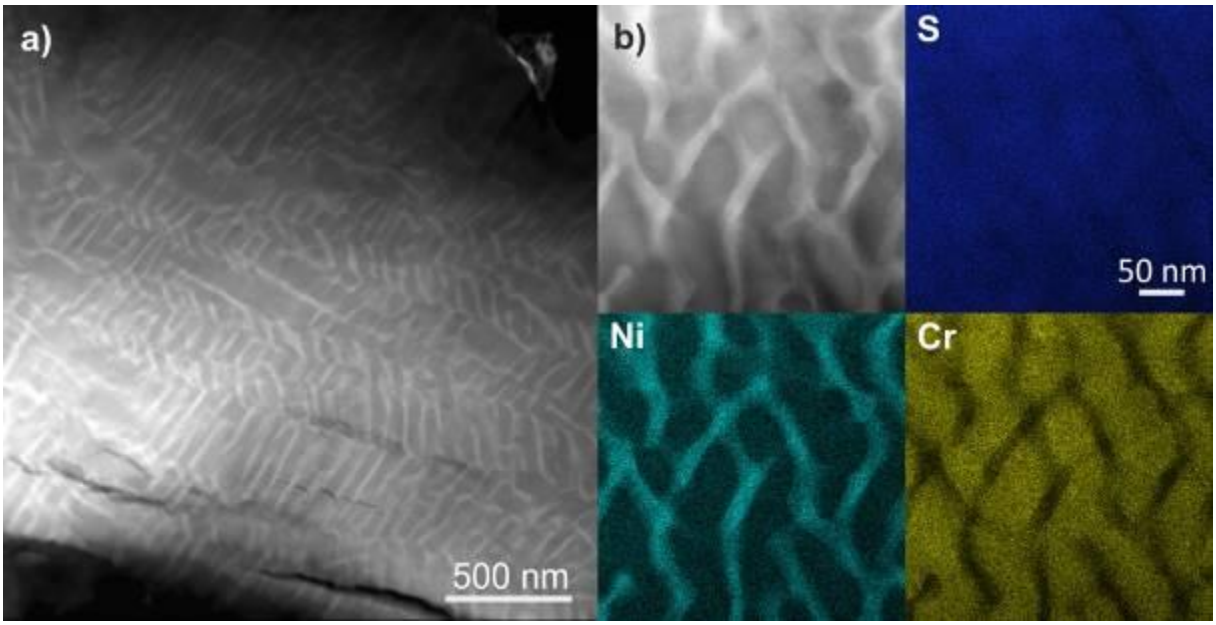

MS3.P010
STEM-EDXS tomography of a co-sintered solid oxide fuel cell anode

F. Jung[1], M. Meffert[1], P. Lupetin[2], D. Gerthsen[1]

[1]Karlsruhe Institute of Technology, Laboratory for Electron Microscopy, Karlsruhe, Germany
[2]Robert Bosch GmbH, Renningen, Germany

Solid oxide fuel cells (SOFCs) are expected to play a major role in future energy conversion systems. However, the commonly used cathode material $(La_{1-x}Sr_x)MnO_3$ contains manganese, which tends to be quite mobile and may diffuse through the cell during high-temperature sintering, potentially affecting cell performance. A design for an SOFC using thin functional layers on an inert substrate and a single co-sintering step was used to study the impact of Mn diffusion on the porous Ni/Y_2O_3-stabilized ZrO_2 (YSZ) anode. As a result of co-sintering, a MnO_x secondary phase (presumably MnO) with particle sizes down to 10 nm was observed in the anode. Depending on their location in the anode, these particles can reduce the triple phase boundary (TPB) length and impair anode performance. An investigation of the three-dimensional (3D) distribution of MnO_x in the anode was performed to estimate the impact of the secondary phase on the TPB length.

In this study, scanning transmission electron microscopy – energy-dispersive X-ray spectroscopy (STEM-EDXS) tomography was used to investigate the 3D distribution of MnO_x particles in a SOFC anode. STEM-EDXS yields better resolution than focused ion beam (FIB)-scanning electron microscopy (SEM) tomography, facilitates chemical contrast imaging even for thicker specimens and fulfils the projection requirement for tomography, making it the ideal choice for this study. Tomographic reconstruction was performed using the simultaneous iterative reconstruction technique algorithm in IMOD (1). 3D models were generated using the Avizo software (2). Specimen rods with diameters between 400 and 700 nm were prepared from a SOFC anode by FIB milling. All measurements were performed in a FEI Osiris 200 kV ChemiSTEM with high EDXS count rates and reduced detector shadowing due to its four-detector EDXS system. Tomography artefacts in the reconstructions were investigated to identify limiting factors for the tomogram resolution and quality.

Beam broadening due to the high specimen rod thickness is found to be the most limiting factor, but a high rod thickness was required to determine the positioning of MnOx particles in relation to Ni, YSZ and pores. MnO_x particles down to a size of 20 nm could be reconstructed and were found to be preferentially located inside or at the boundaries of Ni grains. Large particles were found to be located at TPBs, potentially impairing the anode performance. Fig. 1 shows a reconstruction with a typical distribution of MnOx particles (green) in the anode. MnO_x particles are located inside of Ni (red) and at the TPBs between Ni, YSZ (blue) and pores (transparent). The smallest reconstructed MnO_x particle in Fig. 1 has a size of 40 nm. This study demonstrates the possibilities and limits of STEM-EDXS tomography for 3D chemical imaging in materials science, because secondary phase particles down to a size of 20 nm could be successfully reconstructed even in comparatively thick specimens.

References:

(1) D. Mastronarde *et al.*, IMOD v4.9.8 (29.03.2018), University of Colorado.

(2) Avizo for FEI Systems – Materials Science v9.2.0 (31.07.2016), Thermo Fisher Scientific Inc.

We acknowledge funding by the German Federal Ministry for Economic Affairs and Energy (BMWi) as part of the KerSOLife 100 project.

Fig. 1

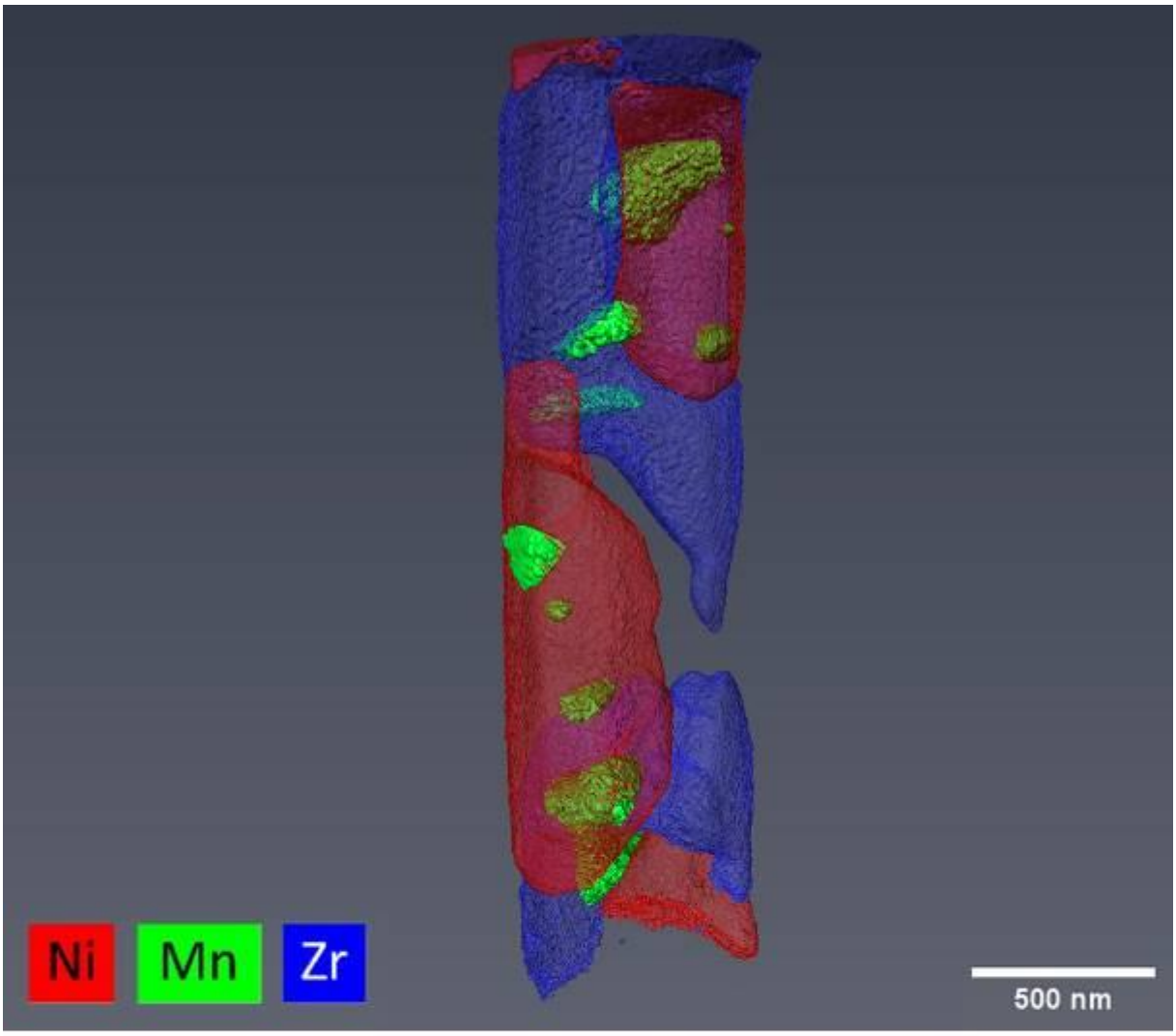

Fig. 1: STEM-EDXS tomography reconstruction of a SOFC anode rod specimen. The MnO_x secondary phase (green) particles are located inside of the Ni (red) and at the TPBs between Ni, YSZ (blue) and pores (transparent). MnO_x particles located inside Ni are generally smaller than those located at the border or outside of Ni grains. The smallest MnO_x particle in this reconstruction has a size of 40 nm.

MS3.P011
Enhancing Potassium-ion Battery Performance by Defect and Interlayer Engineering

Y. Li[1], Y. Xu[2], Y. Wu[2], Y. Lei[2], U. Kaiser[1]

[1]Ulm University, Electron Microscopy Group of Materials Science, Ulm, Germany
[2]Technische Universität Ilmenau, Institut für Physik & IMN MacroNano® (ZIK), Ilmenau, Germany

The greater abundance and accessibility of Na and K resources compared with Li resources have prompted researchers to investigate the feasibility of Na-ion and K-ion batteries (KIBs). Given the more negative redox potential of K^+ than Na^+, there could be no loss of cell capacity and energy density even though K^+ is bigger than Na^+, making KIBs very promising for large-scale stationary energy storage. However, the large size of K-ions may cause difficulties in potassium-ion diffusion in the batteries.

Two-dimensional transition metal dichalcogenides (2D TMDs) have gained worldwide attention in recent years and are being heavily studied in many research domains. TMDs possess a unique layered structure characterized by the weak van der Waals interaction between neighboring layers and strong in-plane covalent bonding within each layer. Such uniqueness allows the intercalation of guest species in the interlayer space without significant structural distortion. In this regard, 2D TMDs have been employed as electrode materials in KIBs very recently.

In this work, we propose a concept of defect and interlayer engineering to fully exploit the van der Waals gaps for K-ion storage. We chose MoS_2 as a demonstrator because it has received rapidly increasing attention as a KIB anode material, and controlled the ratio between the Mo and S precursors during synthesis. Our HRTEM observations at 80 kV show no defects in the layered MoS_2 with the stoichiometric ratio (Fig. 1a), while "cracks" were observed in the MoS_2 synthesized by reacting ammonium molybdate with excess thiourea (Fig. 1b). An interlayer spacing of 0.63 nm was observed in the defect-free MoS_2 (Fig. 1a), while 0.91 nm was observed in the defect-rich MoS_2 (Fig. 1b), demonstrating a substantial expansion of the interlayer spacing. The defect-rich MoS_2 exhibited a K-intercalation capacity that is 40% higher than that of the defect-free counterpart with pristine interlayer spacing. Fig. 2 shows the illustration of defect and interlayer engineering to enhance KIB performance. We attribute the enhancement to the increased K-ion diffusivity and surface charge storage, which is enabled by the expanded interlayer spacing and in-plane defects.

References:

(1) Yang Xu, Yueliang Li, Ute Kaiser, Yong Lei, et al., Nanoscale Horiz., 2019, 4, 202--207.

Fig. 1: HRTEM images of (a) defect-free and (b) defect-rich MoS_2. The "cracks" indicated by the arrows in (b) show the discontinuity of the side. Scale bars: 10 nm.

Fig. 2: Illustration of defect and interlayer engineering to enhance KIB performance.

Fig. 1

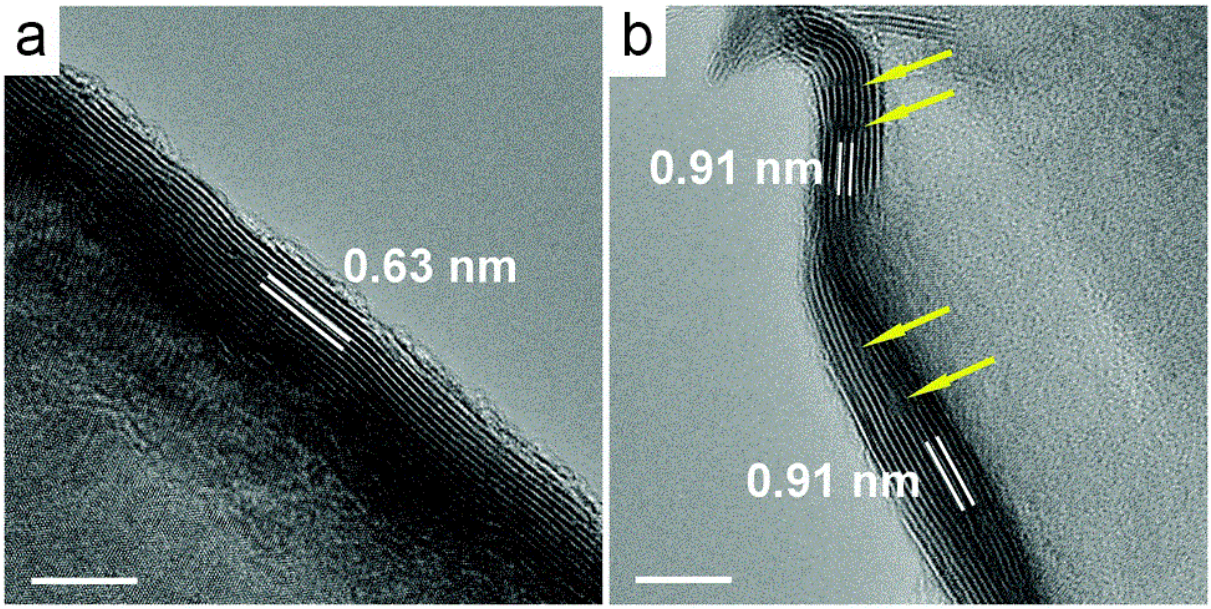

Fig. 2

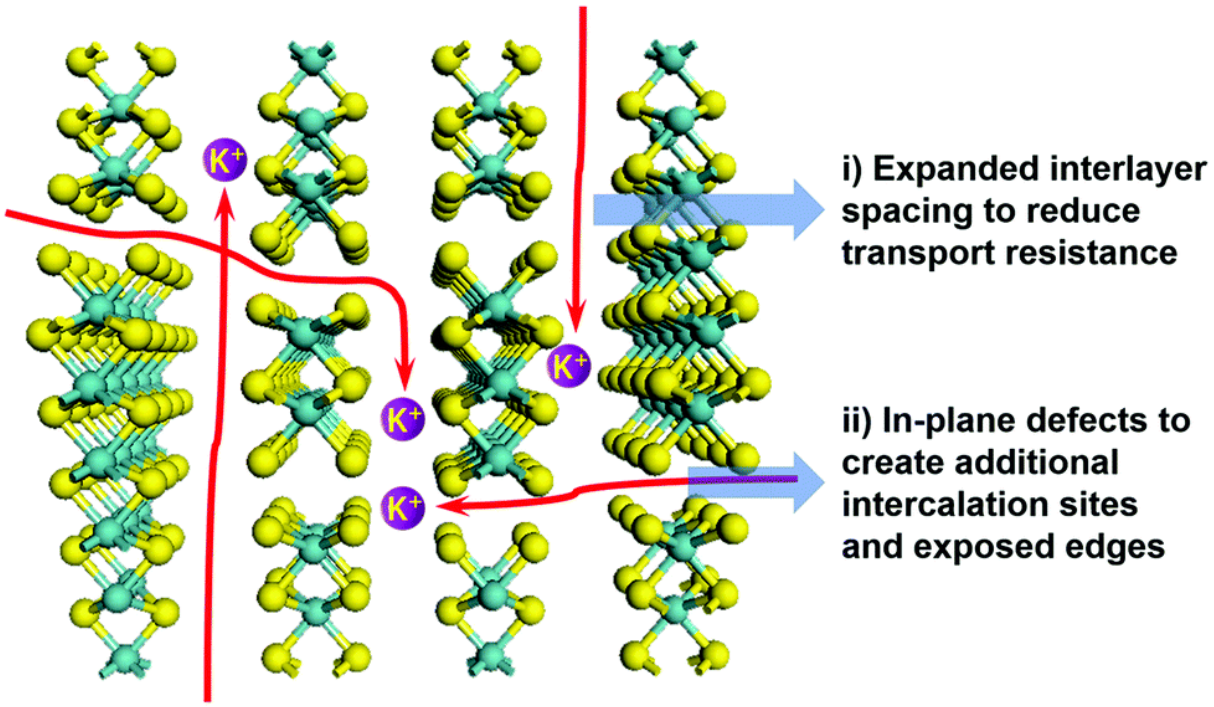
K+
K+
K+
i) Expanded interlayer spacing to reduce transport resistance
ii) In-plane defects to create additional intercalation sites and exposed edges

MS3.P012
Electron microscopy analysis of interfaces in all-solid-state batteries based on LLZO electrolytes

J. Schmieg[1], J. Szász[2], P. Braun[2], E. Ivers-Tiffée[2], P. Axmann[3], M. Wohlfahrt-Mehrens[3], D. Gerthsen[1]

[1]Karlsruhe Institute of Technology (KIT), Laboratory for Electron Microscopy (LEM), Karlsruhe, Germany
[2]Karlsruhe Institute of Technology (KIT), Institute for Applied Materials (IAM-WET), Karlsruhe, Germany
[3]Center for Solar Energy and Hydrogen Research ZSW, Electrochemical Energy Technologies Division, Ulm, Germany

All-solid-state lithium ion batteries are a new approach to overcome the issues in conventional lithium-ion batteries using liquid electrolytes. Non-flammable solid electrolytes may inhibit the formation of lithium dendrites, which results in improved safety for future energy storage systems. Garnet-type $Li_7La_3Zr_2O_{12}$ (LLZO) is a promising solid electrolyte material for this type of batteries due to its high Li+ conductivity and its chemical stability against metallic lithium (1). However, the performance of solid state batteries does not yet reach theoretical predictions. In particular, the high impedance and instability of interfaces between the garnet electrolytes and the active electrode material remain issues for their application in all-solid-state batteries.

For a detailed understanding of impedance contributions assessed by electrochemical impedance spectroscopy, microstructure features on different scales must be correlated with their influence on the charge transfer characteristics of solid/solid interfaces at the anode and cathode side of the battery. Limitations by electrochemically inactive secondary phases have to be overcome by surface treatment or protective interlayers between LLZO and electrodes that allow targeted optimization.

In this study, the solid electrolyte LLZO is combined with a lithium metal anode and a high voltage spinel cathode to create a model system for all-solid-state Li-ion batteries. Magnetron sputtering is applied to deposit metallic interlayers between LLZO and electrodes. Microstructure characterization by scanning electron microscopy (SEM) and (scanning) transmission electron microscopy combined with energy dispersive X-ray spectroscopy is used for imaging the properties of material interfaces and local chemical composition. However, preparation and handling of samples is hampered by degradation. Therefore, we use dry inert gas during handling and transfer to minimize sample exposure to ambient air. Moreover, LLZO quickly becomes amorphous when exposed to high-energy electron or ion beams. Electron-beam damage can be minimized for SEM imaging by selecting optimum electron energies (Figure 1).

The interface microstructures are compared for samples without and with protective interlayers between LLZO and cathode. For the LLZO/Li interface on the anode side, we study the microstructures of different LLZO surface modifications (polishing and metallic interlayers) aiming at low interfacial resistance. Results from electron microscopy are correlated with the electrochemical measurements, obtained by impedance spectroscopy.

Results are obtained within the US-German Cooperation on Energy Storage project (CatSE): "Interfaces and Interphases in Rechargeable Li Based Batteries: Cathode/Solid Electrolyte", sponsored by the Federal Ministry of Education and Research (BMBF).

References:

(1) S. Ramakumar et al., Progress in Materials Science, 88 (2017) 325-411

Fig. 1

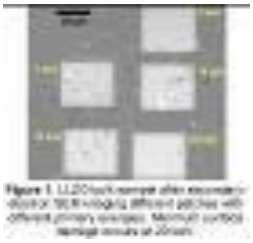

MS3.P013
Machine learning based 3D segmentation for battery materials

C. Rahe[1], T. Volkenandt[2], S. Freitag[2], S. T. Kelly[3], D. U. Sauer[4], J. Mayer[5], E. Figgemeier[1,4]

[1]FZ Jülich, IEK-12, Helmholtz Institut Münster, Helmholtz Institut Münster, Aachen, Germany
[2]Carl Zeiss Microscopy GmbH, Oberkochen, Germany
[3]Carl Zeiss X-ray Microscopy, Pleasanton, United States
[4]ISEA RWTH Aachen University, ISEA, Aachen, Germany
[5]RWTH Aachen, GFE, Aachen, Germany

Electromobility is becoming an important part of our urban transportation system. To further expand the impact of electric mobility, battery energy density, endurance and lifetime have to be improved. The analysis of the exact state-of-health (SoH) of a battery as well as the individual aging factors are still major challenges. In this work, results from 3D high-resolution x-ray microscopy (XRM) on battery samples in combination with machine learning based segmentation will be shown.

As XRM non-destructively provides an inside view of the electrode materials structure without any influence of sample preparation, the goal of this study was to image electrodes of different aging states for comparison and for visualization of structural changes. Advanced image segmentation using machine learning techniques should then enable estimation of the porosity and quantitative analysis of cover layers in-between particles.

For the high-resolution x-ray imaging, pouch cells (40 Ah) were opened, and single electrodes were extracted out of the complete cell. To avoid imaging artefacts the current collector was removed from the active material. The samples were imaged in 3D using a ZEISS Xradia 810 Ultra x-ray microscope, which uses monochromatic illumination and focussing x-ray optics to achieve a voxel resolution of down to 50 nm. Subsequently, image segmentation was carried out using the ZEISS ZEN Intellesis software module. Image segmentation is essential for quantitative evaluation and estimation of material properties. Here it was necessary to separate and distinguish pores, particles and potential cover layers. To eliminate any influence of the user on the segmentation this had to be done reproducibly and automatically. Intellesis makes use of machine learning to analyse features present in the image and perform the segmentation. After a short iterative process of manual labelling and training, a model is generated, capable of segmenting any number of similar datasets in the same way assuring consistent segmentation results. Due to the distinct allocation of voxels to the electrode materials a porosity calculation was performed.

3D XRM scans of pristine and aged electrodes (80% SoH) were segmented and used for further calculations. Out of the segmented images the porosity, as well as the area of accessible porosity, were derived. The porosity decreased about 6%. The reason for the change in porosity is the development of a cover layer. Herein, the extent of present cover layers was calculated and compared with respect to the electrode age. The formation of cover layers is an important change in the electrode structure for batteries. The growing layer may influence conductivity as well as inner resistance of the cell, thus enforcing changes in handling of the battery e.g. the charging rate.

In this contribution, we present internal high-resolution 3D x-ray scans of the electrode structure of battery electrodes. These images are independent of cutting edges, which is a main issue of comparable scanning electron microscopy (SEM) images. The quantitative estimation of material properties based on these datasets after segmentation using machine learning techniques allows to understand battery processes in further detail and to identify important material aging factors of batteries.

Fig.1: High-resolution XRM image of a battery anode and its segmentation result using machine learning

Fig. 1

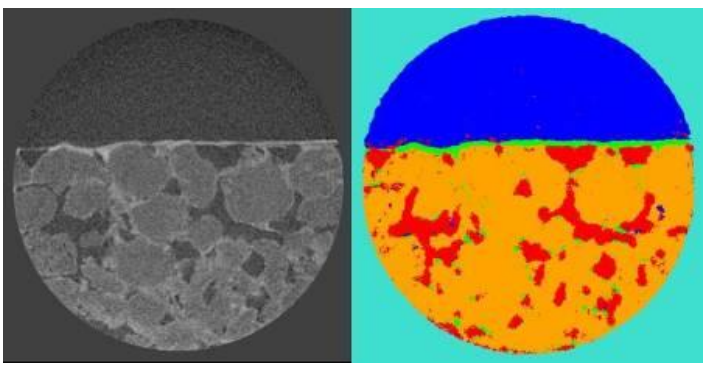

MS3.P014
A Quasi-in-situ Electrochemical Cell for Identical Location TEM

T. Götsch[1,2], S. Saddeler[3], G. Bendt[3], S. Schulz[3], A. Knop-Gericke[1,2], R. Schlögl[1,2], T. Lunkenbein[1]

[1]Fritz Haber Institute of the Max Planck Society, Department of Inorganic Chemistry, Berlin, Germany
[2]Max Planck Institute for Chemical Energy Conversion, Department of Heterogeneous Reactions, Mülheim an der Ruhr, Germany
[3]University of Duisburg-Essen, Faculty of Chemistry and Center for NanoIntegration (CENIDE), Essen, Germany

Owing to the current shift towards renewable energy sources, electrochemical processes become more and more important – for instance for storing excess power from wind or solar sources via electrolytic water splitting, or for utilizing carbon dioxide in the CO_2 reduction reaction.

In order to better understand the materials used in those reactions, it is necessary to investigate their dynamic changes during operation and deactivation at the nanoscale. However, while several commercially available cells for in situ TEM studies of liquid electrochemical systems exist, the reactions monitored therein are severely dominated by beam-induced effects that strongly alter the electrochemical response. (1) Hence, a quasi-in-situ approach, as recently developed for heterogeneous gas-phase reactions, (2) is required where the electrochemistry is separated from the microscopy. By using a conventional TEM grid loaded with the catalyst material as the working electrode, the electrochemistry can be studied without the influence of the electron beam and the same particles can be viewed as a function of the electrochemical treatments (identical location imaging). Such studies have previously been reported for Pt/C PEM fuel cell catalysts. (3,4)

Here, a miniaturized three-electrode cell which is constructed out of PEEK, suitable for static as well as flow measurements, is presented, enabling reproducible electrode geometries at a small scale. As the working electrode, a conventional TEM grid, loaded with the respective catalyst material, is used. The grid can easily be installed as well as removed under potential control and the cell can be operated in an inert environment, preserving the state of the catalyst during transfer. Furthermore, since 3 mm silicon nitride windows used for TEM are also compatible with operando XPS/XAS setups at the synchrotron (BESSY II), correlative synchrotron and TEM studies are possible.

The applicability of this cell is demonstrated with regularly shaped Co_3O_4 nanocubes that are used for the alkaline oxygen evolution reaction and that are imaged using a ThermoFisher Scientific Talos F200X as well as a double-corrected JEOL JEM-ARM200F for high resolution TEM and electron energy-loss spectroscopy.

References:

(1) Hodnik, N.; Dehm, G.; Mayrhofer, K. J. J., Importance and Challenges of Electrochemical in Situ Liquid Cell Electron Microscopy for Energy Conversion Research. *Acc. Chem. Res.* 2016, *49* (9), 2015-2022.

(2) Masliuk, L.; Swoboda, M.; Algara-Siller, G.; Schlögl, R.; Lunkenbein, T., A quasi in situ TEM grid reactor for decoupling catalytic gas phase reactions and analysis. *Ultramicroscopy* 2018**,** *195*, 121-128.

(3) Arán-Ais, R. M.; Yu, Y.; Hovden, R.; Solla-Gullón, J.; Herrero, E.; Feliu, J. M.; Abruña, H. D., Identical Location Transmission Electron Microscopy Imaging of Site-Selective Pt Nanocatalysts: Electrochemical Activation and Surface Disordering. *J. Am. Chem. Soc.* 2015**,** *137* (47), 14992-14998.

(4) Schlögl, K.; Mayrhofer, K. J. J.; Hanzlik, M.; Arenz, M., Identical-location TEM investigations of Pt/C electrocatalyst degradation at elevated temperatures. *J. Electroanal. Chem.* 2011**,** *662* (2), 355-360.

MS3.P015
SXES spectroscopy of Lithium Nickel Manganese Cobalt Oxide Battery cathode.

S. Matveev[1]

[1]JEOL (Germany) GmbH, Freising, Germany

Soft X-ray Emission Spectrometers (SXES) are analytical detectors for electron microscopes (SEM) and microprobes (EPMA) recently developed at Tohoku University (Japan) in collaboration with JEOL Ltd. SXES use diffraction gratings to project an array of X-ray wavelengths formed as a result of electron beam-sample interaction over the CCD detector, thus forming an X-ray spectrum. The spectrometers acquire soft X-ray spectra in the energy range from 50 to 2300 eV, allowing for chemical analysis of elements starting with Li. Advantage of the SXES lays in a very good energy resolution (from 0.3 eV Al-L, Fermi edge of metallic aluminium), which is significantly better than that of other x-ray analytical techniques (EDS, WDS), and thus allows for chemical state analysis. Acquired spectra can be re-processed after analysis, e.g. operators can change chemical elements or adjust spectral ROIs, which is expanding sample characterisation possibilities compared to quantitative WDS analysis. Very high signal sensitivity allows to achieve significantly better detection limits for soft x-rays compared to other SEM detectors (e.g. down to 20 ppm B).

SXES are used for Li analysis, detection of B, C, and N as well as their chemical states, chemical states of transition metals and other applications which number is constantly growing. Here we report new results widening the range of analytical tasks that can be solved with SXES technology.

Lithium Nickel Manganese Cobalt Oxide Battery cathode (NMC) surface and cross section were analysed using JEOL SXES-ER spectrometer and EDS installed on JEOL JSM-7200F FEG SEM. SXES mapping was performed at 5 kV, 50 nA with resolution 40 x 30 points, dwell time 30 sec per point, step size 1 µm. EDS element maps were acquired at 5kV, resolution 216x192 pixels and 5 min. acquisition time. Cross section cut was performed using JEOL ion cryo cross section polisher at 4kV, -120°C, and cutting duration 8h.

At low voltage analytical conditions suitable for high spatial resolution chemical mapping EDS provides information on distribution of C, O, F, and Ni. SXES elemental maps also show Mn and Co distribution in the sample. In addition, Ni and Co La, Lb peak shifts show that the elements are present in different chemical states (metal and oxide). Mapping tools were used to show distribution of Co and Ni in different chemical states across the specimen. Shoulder shift of C peak measured in the cathode binder was interpreted as indication of different bonding state of carbon, namely C-F and C-C.

SXES spectrometry allowed to determine distribution of C, O, F, Mn, Co, Ni, and Al in NMC cathode as a result of high-resolution low voltage (5kV) X-ray microanalysis. The spectra were used to identify chemical state of Ni and Co in the cathode material, as well as spatial distribution of oxide and metal phases. Careful examining of C peaks measured in the cathode binder suggests that C is present there in two bonding states C-C and C-F. Obtained results demonstrate that SXES spectroscopy allows for much more detailed characterisation of NMC cathodes compared to traditional analytical methods such as EDS and WDS.

MS3.P016
Evaluation of an in situ mapping analysis performance of precipitated metal lithium in sold electrolytes of Li-ion batteries by a SEM-EDS analyser utilizing Superconducting-Tunnel-Junction Array X-ray detector (SC-SEM)

M. Ukibe[1], G. Fujii[1], S. Shiki[1], M. Ohkubo[1]

[1]AIST, Nanoelectronics Research Institute, Tsukuba, Japan

Conditions of lithium (Li) in electrodes and an electrolyte of all solid Li-ion batteries, which have been developed as next generation batteries, have a big influence on its" capability, life time and safety. Thus, to improve those performance, it is very important to evaluate in situ an aging variation of the state of Li by the battery operation quantitively as well as qualitatively, which includes the spatial distribution of Li and other composition elements in there.

An EDS analyser combined with a SEM is suitable to obtain spatial and quantitative information on the elemental composition of a sample non-destructively. However, it is almost impossible to analyze the Li conditions in solid Li-ion batteries by the conventional SEM-EDS because Li-*Kα* line, of whose energy and emission yields are quite a low (54 eV) and a small (0.0003), respectively, can"t be resolved from the system noise and the other characteristics X-rays clearly.

In contrast, energy-dispersive X-ray detectors based on arrays of superconducting-tunnel-junctions (STJs) have simultaneously exhibited excellent energy resolution of <10 eV, relatively large detection area of >1 mm^2, high counting rate capability of >500 kcps, and high sensitivity for low energy X-rays (<1 keV).(1) We have been developing a SEM-EDS analyser utilizing an STJ array (SC-SEM) for analyses of light elements in advance functional materials with nanometer scale.(2)

We observed a characteristic X-ray of a metal Li to evaluate the performance of the in situ mapping analysis capability of metal Li with SC-SEM.

Fig. 1 shows a cross-sectional schematic illustration of the SC-SEM. The SC-SEM consisted of an FE-SEM (S-4500, HITACHI) and the STJ array detector. The STJ array was cooled to 0.31 K on a cold stage of a cryogen-free 3He cryostat. X-rays from the sample were detected by the STJ array via the polycapillary collimating X-ray lens for improving the collection efficiency and two X-ray windows. The metal Li was transferred by using a glove bag filled by Ar gas for preventing the oxidation of Li during the transfer. The X-ray spectra were obtained under the following conditions: acceleration voltage of 3 kV, probe current of 2 nA, measurement time of 3600 s.

As shown in Fig.2, clear characteristic X-ray peaks of C, N, O, F as well as Li were obtained. O-*Kα* and N-*Kα* originated from lithium oxide and nitride, respectively, formed during the sample transfer. C-*Kα* and F-*Kα* were emitted from contaminants generated during the sample preparation and the observation. A FWHM value for Li-*Kα* was about 8 eV. SC-SEM exhibited much higher sensitivity to Li-*Kα* than conventional SEM-EDS, because a clear Li-*Kα* peak couldn't be obtained by conventional SDDs. The throughput of the metal Li mapping by the present SC-SEM was evaluated based on the obtained spectrum. Metal Li mapping analyses of 10 µm square with a 500 nm resolution is estimated to be completed within 4 hours. In addition, when the present SEM is replaced by a Schottky FE-SEM, the required time for the same mapping analysis becomes less than 30 minutes.

The improved SC-SEM will become a strong candidate of the analytical instruments for the in situ analysis of the precipitated metal Li in sold electrolytes of all solid Li-ion batteries.

References:

(1) S. Friedrich, et. al., J. Low. Temp. Phys. 176 (2014) 553.

(2) G. Fujii, et. al., X-ray spec., 46 (2017) 325.

Fig. 1: Cross-sectional schematic illustration of the SC-SEM.

Fig. 2: Characteristic X-ray spectrum of metal Li sample.

Fig. 1

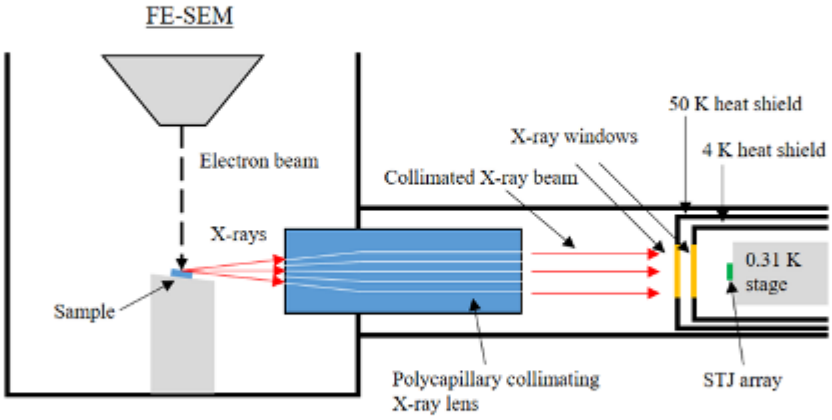
FE-SEM
Electron beam
X-rays
Sample
50 K heat shield
X-ray windows
4 K heat shield
Collimated X-ray beam
0.31 K
stage
Polycapillary collimating
X-ray lens
STJ array

Fig. 2

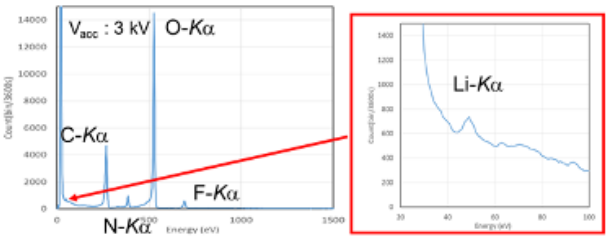
V_{acc} : 3 kV
O-Kα
C-Kα
F-Kα
N-Kα
Li-Kα

MS3.P018
Quantitative 3D Structure Studies of Supported Catalysts for Biomass Transformation

W. Wang[1,2], A. Villa[3], D. Wang[1,4], C. Kübel[1,4,5]

[1]Institute of Nanotechnology, Karlsruhe Institute of Technology, Eggenstein-Leopoldshafen, Germany
[2]Technical University of Darmstadt, Joint Research Laboratory Nanomaterials, Darmstadt, Germany
[3]Unioversity of Milan, Department of Chemistry, Milan, Italy
[4]Karlsruhe Institute of Technology, Karlsruhe Nano Micro Facility, Eggenstein-Leopoldshafen, Germany
[5]Karlsruhe Institute of Technology, Helmholtz-Institute Ulm for Electrochemical Energy Storage, Ulm, Germany

Supported metal nanoparticles play important roles in energy storage/conversion and catalysis for the sustainable production of fuels and chemicals (1). Porous materials such as different forms of carbon and zeolites are widely used as support to precisely control the nanoparticles inside the pores for the desired effect such as high dispersion, steric access of the reactant, enhanced stability, and so on. The locations of the nanoparticles have decisive influence on the catalyst performance (2). The structures of the nanocatalysts often show high complexity. Therefore electron tomography is an ideal technique to resolve the distribution of catalyst nanoparticles. Moreover, developing reconstruction and segmentation procedures to obtain the reliable structure features quantitatively is essential for the understanding of the mechanisms of the catalytic reactions.

In this work, quantitative 3D structural investigation was applied to three designed Pd catalysts with different distribution on carbon support in order to identify the most important structural aspects, which are responsible for the activity, selectivity and stability in liquid phase furfural hydrogenation.

Pd nanoparticles were loaded on ordered porous carbon support (CMK-3) by incipient wetness impregnation (PdIW/CMK-3), wet impregnation (PdIMP/CMK-3) and preformed colloidal nanoparticles with PVA protection agent (PdPVA/CMK-3), respectively. The three catalysts were tested in liquid phase furfural hydrogenation. HAADF-STEM tomography was used to characterize the 3D morphology before and after the catalytic reaction. Pd particles were distinguished according to their locations at outer surface of the support or inside pores based on reliable segmentation.

Pd nanoparticle size for all the catalysts are similar being around 2.5 nm measured from STEM images. Fig.1 shows a representative 3D view of PdIW/CMK-3 segmented data with surface particles marked by green and inside particles marked by red. Surface particle percentages of each Pd/CMK-3 catalyst are calculated from tomograms after segmentation and particle identification on several pieces of CMK-3 in different size and the results are shown in Fig.2. The proportion of Pd nanoparticles located on the support external surface was almost independent of the size of the carbon support for PdIW/CMK-3, while it was roughly proportional to the external surface fraction for PdIMP/CMK-3. PdPVA/CMK-3 showed particles exclusively at outer surface. Correlating quantitative analysis for the particle location with the catalyst selectivity, it was convincingly shown that Pd nanoparticles located inside pores promote the formation of 2-methyl furan, probably due to encapsulating effect favoring perpendicular orientation of furfural adsorbed on Pd and longer contact times. When Pd nanoparticles are on the external surface the yield of tetrahydrofurfuryl alcohol becomes much higher.

From the presented work, it has been shown that quantitative tomography was essential to understand the structural differences and correspondingly the modulated catalytic behaviors between the three designed catalysts.

References:

(1) Aricò A S, Bruce P, Scrosati B, et al. Nature materials, 2005, 4(5): 366-377.

(2) Friedrich H, Sietsma J R A, de Jongh P E, et al. Journal of the American Chemical Society, 2007, 129(33): 10249-10254.

Fig. 1

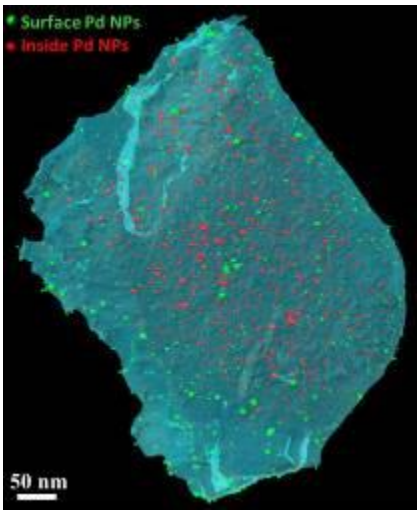
Surface Pd NPs
Inside Pd NPs
50 nm

Fig. 2

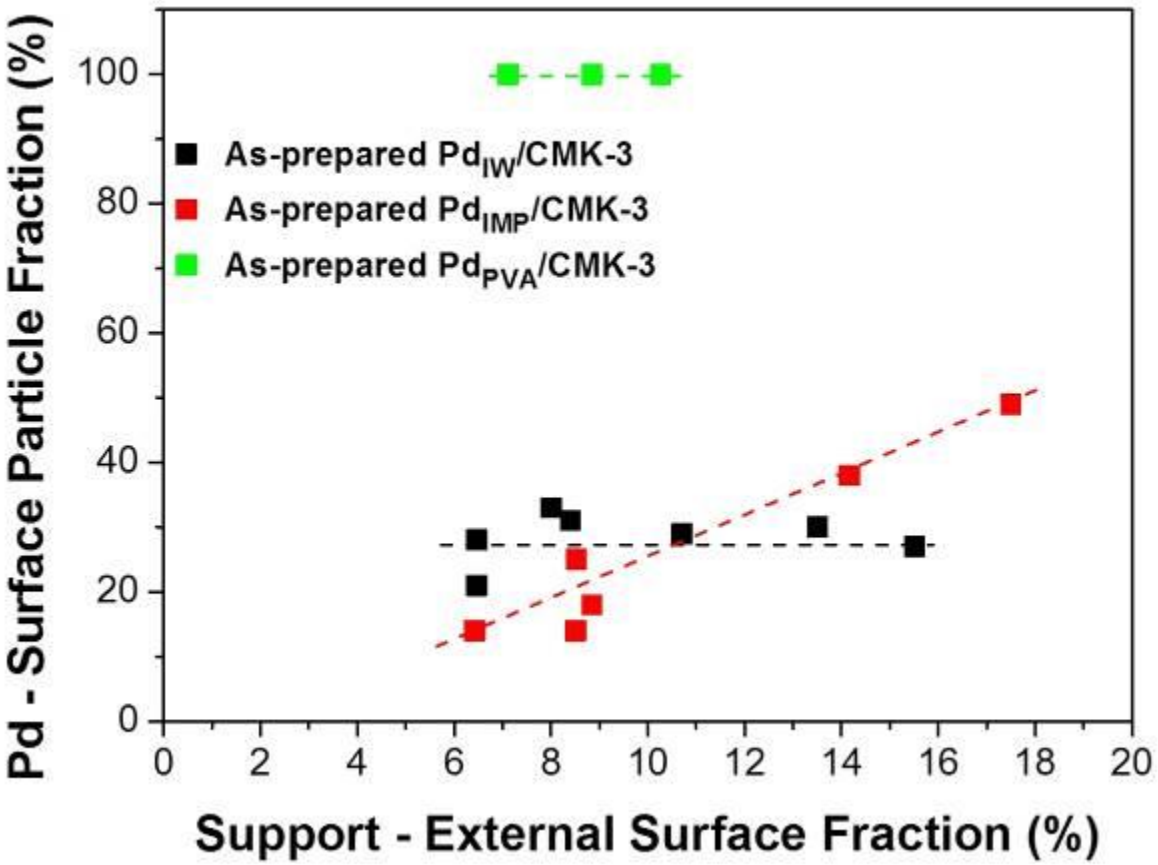
Pd - Surface Particle Fraction (%)
Support - External Surface Fraction (%)
As-prepared Pd$_{IW}$/CMK-3
As-prepared Pd$_{IMP}$/CMK-3
As-prepared Pd$_{PVA}$/CMK-3
0
20
40
60
80
100
0
2
4
6
8
10
12
14
16
18
20

MS3.P020
Investigation of the Surface Properties of HMX Particles by Scanning Probe Microscopy

E. Kosareva[1], N. Muravyev[1], I. Kuchurov[2], A. Pivkina[1]

[1]Semenov Institute of Chemical Physics, Laboratory of Enegetic Materials, Moscow, Russian Federation
[2]N.D. Zelinsky Institute of Organic Chemistry, Moscow, Russian Federation

HMX ($C_4H_8N_8O_8$, octogen) is widely used as a key component of high-energy compositions due to its high thermal stability, density, and energy content. A decrease in particle size up to a nanoscale is expected to lead to an increase in reactivity. The main problems limiting the practical use of fine powders are electrification of particles (which complicates the process of mixing and processing) and high sensitivity to mechanical stress.
A possible solvation to this problem is polymer coating of HMX particles. A method for the synthesis of nitramine/polymer composites in supercritical CO_2 is developed at the IOC RAS. Experiments to determine the mechanical sensitivity of the obtained composites, carried out at the ICP RAS, showed that sensitivity decreases even at low concentrations of the polymer. Moreover, for samples with highly dispersed HMX, a significant improvement in the flowability of the particles compared to the untreated powder was found. The purpose of this work was to find out which properties of the surface of the particles change due to modification, and also to find the connection between the change in these properties and the macroscopic characteristics of the powder, which is necessary for understanding and directional synthesis.

In this work, the topography, mechanical stiffness and surface potential distribution were studied using scanning probe microscopy for both HMX particles modified by various polymers (polymethylacrylate, ethylcellulose, polyurethane), and the original HMX sample without coating.
For composites with polymethylacrylate and ethylcellulose, it was found that the surface roughness increases with the precipitation of the polymer compared to untreated particles. At the same time, reduction in mechanical sensitivity is observed experimentally exactly for these composites. Apparently, "precipitating" the polymer under conditions of anti-dissolution by supercritical CO_2 leads to the localization of polymer globules on the surface, and not to the expected formation of a continuous polymer layer. In addition, it was shown that the introduction of the polymer reduces the charge localized on the particles, which prevents their adhesion due to electrostatic interaction and improves the flowability of the powder.

MS3.P021
High resolution STEM-EDS analysis of core-shell type ceria zirconia catalyst for automotive exhaust treatment

M. Ozawa[1], M. Hattori[1], M. Misaki[1], K. Higuchi[1], S. Arai[1]

[1]Nagoya University, IMaSS, Nagoya, Japan

By using HREM-STEM techniques, possible improvement using core-shell (cs) type ceria zirconia (CZ) support materials were investigated for designing low content platinum automotive catalysts. The STEM-EDS analysis revealed that the dispersed phase of CeO2 appeared to form a relatively thin layer or aggregates on the surface of ZrO2. Also, the present high-resolution analysis suggested that ZrO2 core phase was partially bare surround by the CeO2 islands on surface, having CeO2/ZrO2 interface. Pt-concentrated areas and agglomerate seemed to be stabilized on the areas that were Ce-rich shell on ZrO2 core particle. The reason of different dispersion is considered due to difference of the microstructure in CeO2 which has a role for anchoring Pt. The agglomeration of Pt will be inhibited due to the morphological feature of CeO2 NPs on ZrO2, which bring an important effect of csCZ support on reducing Pt.

MS3.P022
Characterization of Third Generation Photovoltaic Junctions on the Nanometer Scale by Scanning Transmission Electron Beam Induced Current

T. Meyer[1], P. Peretzki[1], B. Kressdorf[2], D. Ehrlich[1], C. Jooss[2], M. Seibt[1]

[1]University of Göttingen, IV. Physical Institute - Solids and Nanostructures, Göttingen, Germany
[2]University of Göttingen, Institute of Materials Physics, Göttingen, Germany

The efficiency of classical single-junction solar cells is limited by transmission of sub band gap photons and thermalization of hot charge carriers due to phonon scattering defining the well-known Shockley-Queisser limit (1). The aim of third generation photovoltaics is to include these energy fractions of the solar spectrum as contributions to the resulting electrical power, which has led to various approaches including organic materials, quantum dots, hybrid and perovskite materials. In this study, we focus on the latter by investigating a pn-heterojunction of inorganic transition metal oxide perovskites with strong electron phonon coupling, namely Pr1-xCaxMnO3 (PCMO) on Nb-doped SrTiO3 (STNO) and comparing it to a pn-homojunction of state-of-the-art monocrystalline silicon. Besides the interesting photovoltaic behaviour, the former system exhibits benchmark properties such as the excess charge carrier diffusion length on the nanometer scale which requires new approaches for characterization.

Electron beam induced current (EBIC) is a widely spread technique which has been employed over decades to investigate the interplay of drift and diffusion of excess charge carriers being very locally created by the incident electron beam and harvested as a current by a charge separating junction. Traditionally, EBIC is conducted in a scanning electron microscope (SEM) allowing for easy contacting and the examination of large sample areas. Nonetheless, despite the ability of modern SEMs to focus the electron beam to diameters below one nanometer, the spatial resolution of EBIC applied to bulk materials is ultimately limited by multiple scattering of the primary electrons inside the sample leading to a pear-shaped interaction volume. A classical approach to reduce the size of the latter and to improve the resolution is to lower the acceleration voltage of the electron beam. Though, since the lateral and depth extension of the interaction volume are of the same order of magnitude, this attempt leads to probing almost exclusively at the sample"s surface if nanometer resolution is necessary. Thus, resulting EBIC signals might be dominated by surface effects.

In this work, we follow the complementary approach of increasing the acceleration voltage and decreasing the thickness of the sample to electron transparency by employing a focused ion beam and transferring the experiment to the scanning transmission electron microscope (STEM) as it has been motivated in (2). The main advantage of scanning transmission EBIC (STEBIC) is the fact, that the high energy electron beam does not get spread significantly during the propagation of a few hundred nanometers, i.e. the sample is cut inside the very narrow top part of the pear-shaped interaction volume where its lateral expansion is much smaller than the sample thickness. In order to understand the sophisticated crosstalk between surface and bulk effects, a wedge-shaped geometry of the lamellas is used enabling continuous observation of the decreasing influence of the surfaces with increasing thickness. As a result, the thickness of electronically inactive surface layers as well as the surface recombination velocity and the bulk diffusion length of PCMO, STNO and silicon are quantified in good agreement with analytical and numerical models.

References:

(1) W. Shockley, H.J. Queisser, *J. Appl. Phys.* 32 (1961) 510

(2) P. Peretzki, B. Ifland, C. Jooss, M. Seibt, *Phys. Status Solidi RRL* 11 (2017) 1600358

MS3.P023
Electron Microscopy Study of Volume Expansion Behaviour of Aluminium-alloy Anode Material for Li-Ion Battery

F. Rohman[1], M. Meledina[1], M. R. Iskandar[1], J. Mayer[1], T. E. Weirich[1]

[1]Central Facility for Electron Microscopy - RWTH Aachen University, Aachen, Germany

Currently, the demand of high energy density Li-ion battery for future application, e.g. electric vehicles, has driven the improvement of anode material which offers higher specific capacity and excellent stability. Aluminium-alloy anode materials have been one of the most promising anode materials due to its higher specific capacity (993 mAh/g (for LiAl)) than conventional graphite (372 mAh/g). However, capacity fading related to high volume expansion is one of the serious problems which need to be understood and solved. Crack formation and pulverization of aluminium particles are the common issues leading to loss of electrical contact and poor cycling performance when used as anode for Li-ion batteries. Nevertheless, the exact mechanism of volume expansion of the aluminium particles in the practical application is still a matter of discussion. This prompted us to investigate the volume expansion behaviour of the aluminium particles in aluminium/graphite composite anodes after charge-discharge (cycles) using Scanning Electron Microscopy (SEM) and Transmission Electron Microscopy (TEM). Fresh aluminium anodes were used to determine the initial size of aluminium particles. The sample was not cycled and never in contact with the electrolyte. The other samples were cycled using 3:7 ethylene carbonate / ethylmethyl carbonate 1.2M LiPF6 with the addition of 10wt% monofluoro-ethylene carbonate as liquid electrolyte. All as-received samples (fresh and cycled) were prepared using cross-section an Ar-ion polisher for the SEM investigations. SEM-BSE images of first cycle samples show that the particle size of aluminium was not significantly changed and expanded. However, after ten cycles of charge-discharge some volume expansion of aluminium particles could be detected. Moreover, crack formation in the aluminium particle and the electrode was also present. Combination of SEM and energy dispersive X-ray (EDX) maps of the 10-cycled sample revealed that some of the elements i.e. phosphorous (P), fluorine (F) and oxygen (O) migrated into the expanded aluminium particles. Those elements could stem from the residue of organic electrolyte. Some of the aluminium-rich spots have been found surrounded by P, F and O elements as well. Detailed further investigations by means of selected-area electron diffraction (SAED) and bright-field (BF) TEM imaging techniques showed single aluminium particles that were pulverized and thus became smaller crystalline aluminium. Furthermore, the combination of STEM-HAADF image and EDX mapping showed that the pulverized aluminium particles were surrounded by P, F and O which penetrated to the interior of expanded aluminium particle. High-resolution TEM (HRTEM) image revealed the presence of nanoparticles which could be related to former lithium-aluminium particles.

From this finding, we conclude that the aluminium particle was expanded after lithiation-delithiation which lead to the crack formation and pulverization of the aluminium. As a consequence the liquid electrolyte which contains P, F and O migrates into the aluminium particle which increases the size of the particles.

Fig. 1

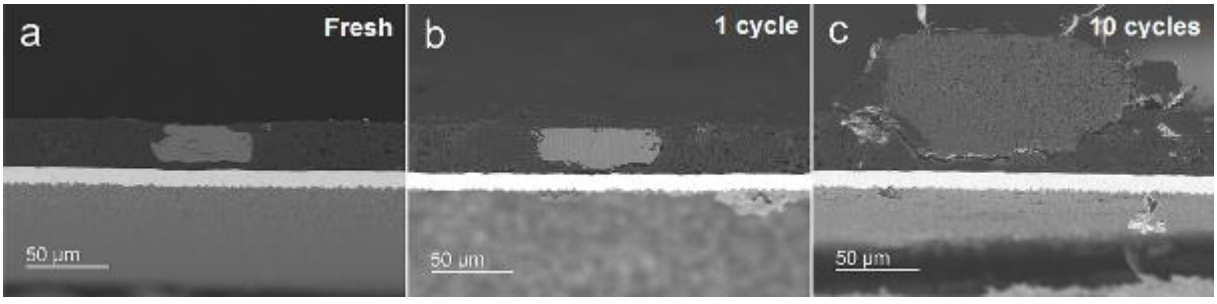

MS3.P024
TEM on $LiNi_{0.5}Mn_{1.5}O_4$ - Battery Materials

D. Geiger[1], M. K. Kinyanjui[1], P. Balasubramanian[2], P. Axmann[2], M. Wohlfahrt-Mehrens[2], D. Bresser[3], S. Passerini[3], U. Kaiser[1]

[1]Ulm University, Electron Microscopy Group of Materials Science, 89081 Ulm, Germany
[2]Center for Solar Energy and Hydrogen Research ZSW, 89081 Ulm, Germany
[3]Helmholtz Institute Ulm (HIU) , 89081 Ulm, Germany

Batteries offer nowadays more and more efficient storage of electric energy. The research activities in this area target to higher performance in terms of energy density, lifetime, safety and costs.

Investigations of new Li-ion battery materials for higher efficiency demand a detailed understanding of the morphology and crystallographic structure of the processed particles.

Aberration-corrected high-resolution transmission electron microscopy (AC-HRTEM) (1) is one of the most powerful methods contributing to clarification of the electrochemical processes at the atomic level. However, some challenges have to be mentioned: Most of the materials are in powder form, so that the crystal grains forming the particles are randomly oriented and overlapped with each other, they are often quite sensitive to the imaging electron beam and only relatively thin sample areas can be investigated. For our AC-HRTEM and EELS investigations we used the image Cs-corrected FEI Titan 80-300 kV with Gatan Image Filter (GIF), operated at 300 kV.as supported by the German Ministry for Education and Research (BMBF) in the frame of the joint research project "Li-EcoSa

In the frame of this work, $LiNi_{0.5}Mn_{1.5}O_4$ (LNMO), one of the newest high-voltage and high-capacity cathode materials for Li-ion batteries, was investigated, to identify the possible crystallographic structure corresponding e.g. to the space groups Fd-3m and $P4_332$ (2). A series of LMNO samples was annealed at different temperatures.

Two structures could be identified (Fig. 1) both in the high-resolution imaging mode and with selected area electron diffraction. EELS measurements in low loss area reveal valence changes of the manganese in the two structures (3).

The results confirm the successful application of transmission electron microscopy to battery materials investigations.

References:

(1) M. Haider et al., Ultramicroscopy75 (1998), p. 53.

(2) J.-H. Kim et al., Chem. Mater. 16 (2004), p. 906.

(3) M. K. Kinyanui et al., Phys. Rev. Materials 1 (2017), p. 074402.

This work wfe - Development of economical and safe lithium ion batteries".

Fig. 1: HRTEM image of a larger LNMO particle consisting of two grains taken with the FEI Titan 80-300 kV electron microscope at 300 kV. The FT of the two grain areas (red) are also included.

Fig. 1

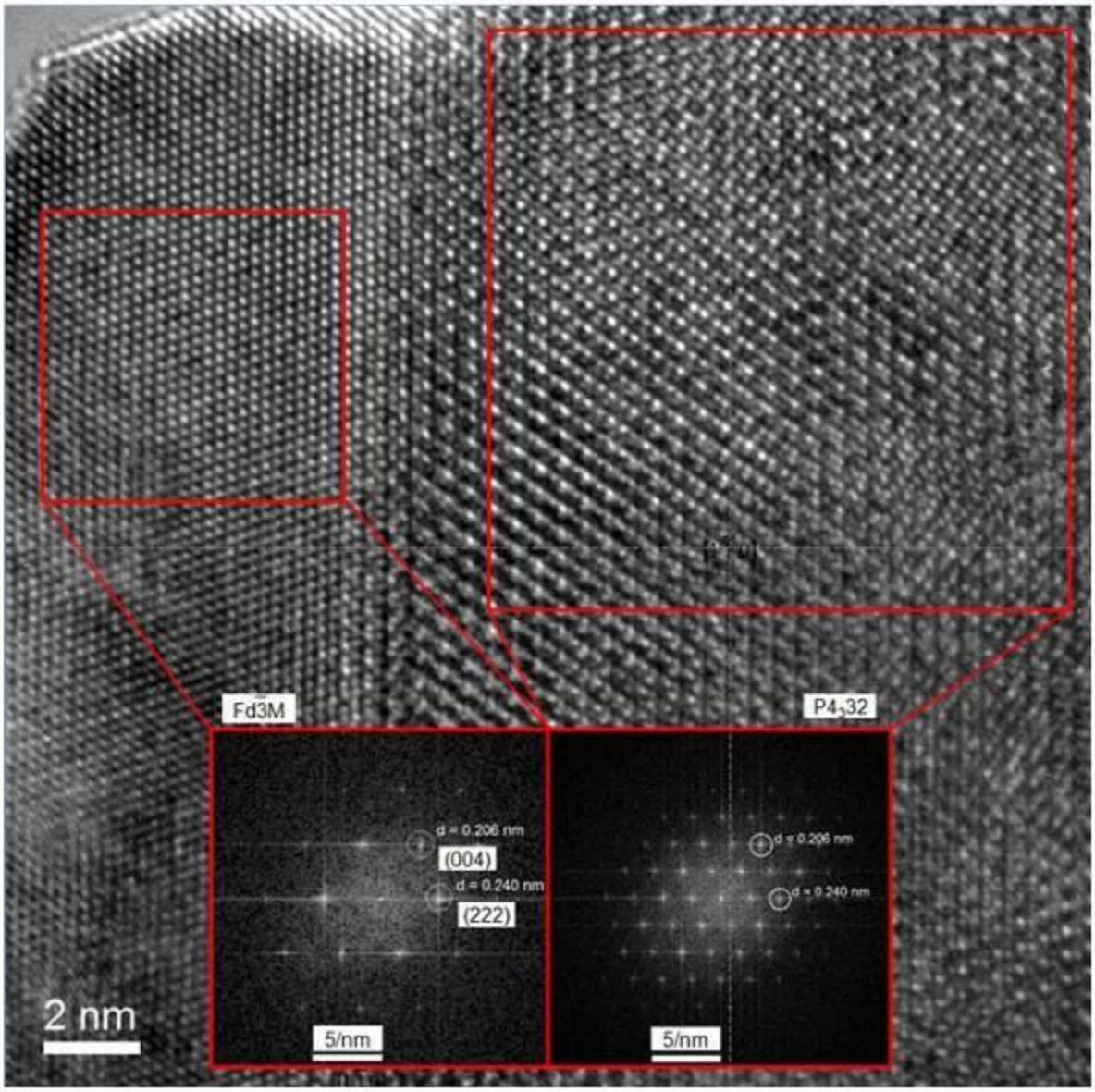
Fd3M
P4₃32
d = 0.206 nm
(004)
d = 0.240 nm
(222)
d = 0.206 nm
d = 0.240 nm
2 nm
5/nm
5/nm

MS3.P025
Post-treatment processes and their influence on the nanomorphology, crystallinity and efficiency of organic bulk heterojunction solar cells

C. Harreiß[1], S. Langner[2], M. Berlinghof[3], S. Rechberger[1], J. Will[1], T. Unruh[3], C. J. Brabec[2], E. Spiecker[1]

[1]Institute of Micro- and Nanostructure Research & Center for Nanoanalysis and Electron Microscopy (CENEM), Erlangen, Germany
[2]Institute of Materials for Electronics and Energy Technology (i-MEET), Erlangen, Germany
[3]Institute for Crystallography and Structural Physics, Erlangen, Germany

The power conversion efficiency (PCE) of solution-processed bulk heterojunction (BHJ) solar cells has seen a dramatic increase in the last decades due to the introduction of new donor and acceptor materials, as well as the development of new processing conditions (1). By mixing an electron donor with an electron acceptor a certain nanomorphology of the two phases is evolving depending on the composite materials and the post-processing conditions like, e.g., solvent vapor (SVA) or thermal annealing (TA) (Fig. 1). Since the nanoscale morphology of organic solar cells (OSC) determines the charge separation at the interfaces and the subsequent electron and hole transport to the respective electrode, it decisively influences the device performance. Therefore, understanding and controlling the nanostructure evolution is a necessity to further improve the PCE.

Electron energy-loss spectroscopy (EELS) and energy-filtered transmission electron microscopy (EFTEM) are powerful techniques for studying the nanomorphology of donor and acceptor phases since conventional TEM imaging techniques are mostly not sufficient to visualize and identify the small molecule and fullerene component. Due to their similar densities and complex crystallinity, conventional TEM delivers rather uniform contrast where no significant structures can be identified. In contrast, by using either ionization edge or plasmon loss electrons in EFTEM pronounced contrast can be generated enabling reliable discrimination of the two phases.

Here we report on a OSC system composed of a small molecule (DRCN5T) electron donor and a fullerene derivative ($PC_{71}BM$) as electron acceptor. We investigated the influence of three different solvent atmospheres ($CHCl_3$, THF, CS_2) on the nanomorphology, crystallinity and efficiency of our OSC system. We studied the nanomorpholgy evolution as a function of the solvent vapor atmosphere and the annealing time using EFTEM imaging techniques (Fig. 2). Thereby, we figured out that the choice of the solvent for SVA has a high impact on the evolving nanomorpholgy and the speed of phase separation and crystal growth. The crystallinity of the samples was investigated by energy-filtered electron diffraction (EF-ED) measurements where an energy selecting slit was positioned around the zero-loss peak in order to enhance the contrast of Bragg diffraction. Furthermore, we have shown that grazing-incidence wide-angle X-ray scattering (GIWAXS) can be used as a complementary technique and provides results in good agreement with EF-ED. The nanomorpholgy was then further correlated to the device performance. By that, an in-depth understanding of the relationship between post-processing, morphology, crystallinity and efficiency could be gained.

Currently we are performing *in situ* thermal annealing experiments in the TEM enabling the simultaneous observation of the nanoscale phase separation and the formation of an interpenetrating network of donor and acceptor phases as a function of the annealing time and temperature. This gives us new insights into the kinetics of BHJ film formation.

References:

(1) J. Min et al., J. Mater. Chem. A 5 (2017), p. 18101-18110.

Fig. 1: Scheme of the solution-processing of organic bulk heterojunction blends and their nanomorpholgy evolution due to post-processing treatments (DRCN5T: cyan; $PC_{71}BM$: red).

Fig. 2: EFTEM elemental maps of carbon for different solvent vapor atmospheres and various annealing times (WO: without post-treatment).

Fig. 1

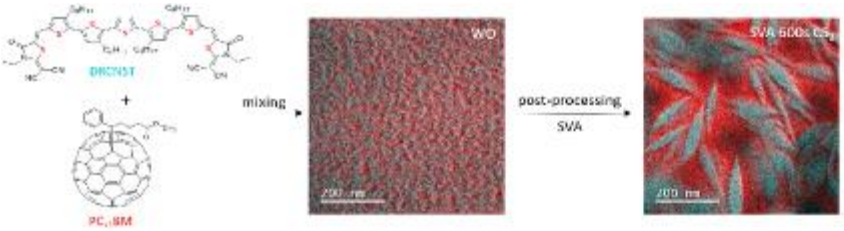
DRCN5T
PC71BM
mixing
WO
200 nm
post-processing
SVA
SVA 600s
200 nm

Fig. 2

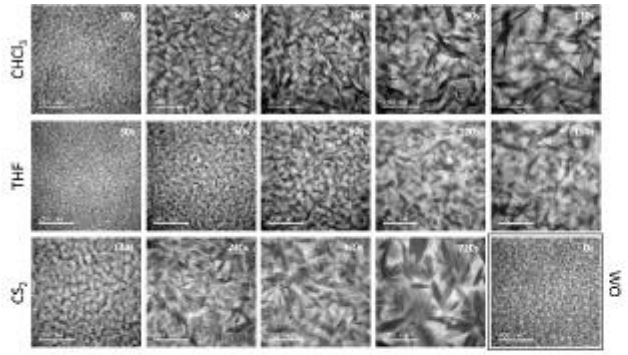
CHCl3
THF
CS2
WO

MS3.P026
STEM-EELS investigation of phase transformations in a ZnMn2O4 anode during long term cycling

G. Melinte[1], Z. Zhao[2], C. Kübel[1,3]

[1]Karlsruhe Institute of Technology (KIT), Institute of Nanotechnology (INT), Eggenstein-Leopoldshafen, Germany
[2]Karlsruhe Institute of Technology (KIT), Institute for Applied Materials (IAM), Eggenstein-Leopoldsh, Germany
[3]Karlsruhe Institute of Technology (KIT), Karlsruhe Nano Micro Facility (KNMF), Eggenstein-Leopoldsh, Germany

The recent shift towards green and more sustainable global energy polices has boosted research for new energy storage systems that can meet the growing demands for high energy and power density. The development of anode materials for LIBs with a specific capacity larger than conventional graphite electrodes is one important direction of research (1). Tetragonal spinel $ZnMn_2O_4$ has attracted particularly attention due to its high theoretical capacity (784 mAh g-1), low cost and environmental benignancy (2). Despite these advantages, the charging/discharging rates of $ZnMn_2O_4$ are relatively poor due to a large volume expansion and pulverization during cycling that are caused by repeated reconstructive phase transformations (3).

While studying the energy storage mechanism in nanosized $ZnMn_2O_4$, Z. Zhao et al.(3) had recently proposed a complete model for the phase transformations in the anode during cycling and correlated these phase changes with its cycling behavior. The *ex-situ* STEM-EELS analysis aims to offer a spatially resolved insight in the phase changes occurring in the anode during cycling. The morphological evolution study by STEM – HAADF will be completed by the EELS investigation of Mn oxidation state evolution during cycling.

Nanosized $ZnMn_2O_4$ was synthetized using a co-precipitation method described in Ref (3). For STEM measurements, all samples were prepared under an argon atmosphere inside a glovebox. The samples were transferred to the microscope using a Gatan TEM vacuum transfer holder. A Titan 80–300 operating at 300kV and equipped with a Tridiem Gatan image filter was used. The intensity ratio of L_3/L_2 white lines was used for determining the oxidation state of Mn. The L_3/L_2 ratio was extracted using the Double Atan Fitting (4) plug-in implemented in Digital Micrograph. All EELS spectra were re-calibrated using the π* transition of the carbon edge at 285eV.

The morphological transformations induced by the volume expansion during the first lithiation reactions are shown by STEM-HAADF imaging while the EELS analysis shows the reduction of Mn3+ to Mn2+ (Figss.1). However, after the first lithiation no metallic Mn nanoparticles could be clearly identified due to their cluster-like size embedded in an amorphous oxide framework. Similar, the first delithiation reactions do not lead to a separation of MnO and ZnO nanoparticles. The first ZnO individual nanoparticles separated from the framework are identified after 25 cycles. After 90 cycles, well-defined metallic Zn nanoparticles are decorating the amorphous framework and these nanoparticles do not reoxidize during the next delithiation reactions. The amount of metallic Zn nanoparticles seems to remain constant between the 90 and 150 cycles. STEM-EELS shows a complex variation of the oxidation state of Mn throughout the cycling, with significant amounts of litheated and delitheated products dragged unreacted in the next cycle.

STEM-EELS analysis has proven to be an important tool in deciphering the evolution of ZnMn2O4 anode during long term cycling. The results can be directly correlated with those offered by other investigation techniques and the energy storage mechanism of the ZnMn2O4 anode in LIBs.

References:

(1) Y. Deng et al., J. Mater. Chem., 2011, 21

(2) J. Zhao et al., J. Mater. Chem., 2012, 22

(3) Z. Zhao et al., J. Mater. Chem. A, 2018, 6

(4) H. Schmid, W. Mader, Micron, 2006, 37

Fig. 1

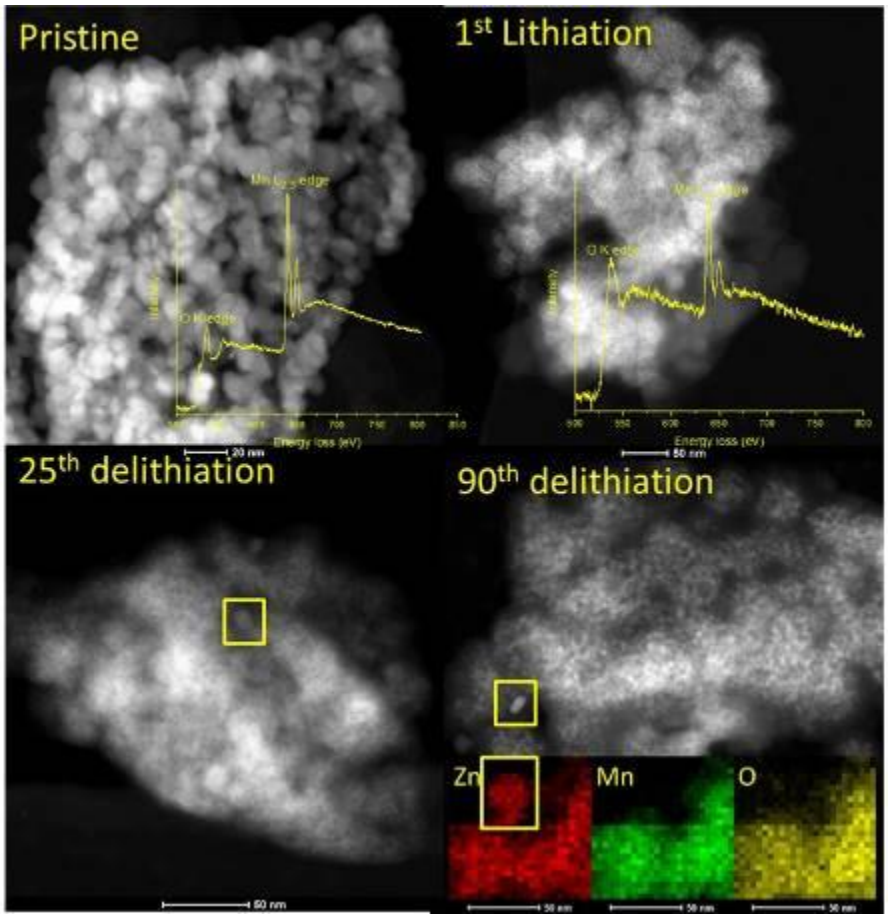
Pristine
1st Lithiation
25th delithiation
90th delithiation
Zn
Mn
O

MS3.P027
Direct observation of mild degradation in PtCu3 nanoparticles by high resolution identical location transmission electron microscopy

F. Ruiz-Zepeda[1], M. Gatalo[1], N. Hodnik[1], P. Jovanović[1], A. Pavlišič[1], M. Bele[1], G. Dražić[1], M. Gaberšček [1]

[1]National Institute of Chemistry, Ljubljana, Slovenia

In the field of energy conversion, particularly in fuel cells, performance indicators such as eficiency and stability depend crucially on several fundamental properties of the supported electrocatalysts. Pt-alloy based nanoparticles dispersed on high surface area carbon are the most commonly employed. Pt content and distribution in the nanoparticle, the structure, morphology and alloy composition, but also the conductivity and stability of the support, are among the most studied properties. Of especial interest is the in-situ formation of active sites after dealloying the as synthesized nanoparticles, an aspect which is commonly neglected in the literature. The mayority of as synthesized state of the art Pt-nanoalloys always exhibit morphological, structural and compositional changes when exposed to the severe environment of the fuel cell. Since the atomic arrangement at te surface governs mostly of the performance of the catalysts, it is of great importance to understand this phenomenon.

In the present work, we perform high resolution identical location scanning transmission electron microscopy (HR IL-STEM) to study how 20-30 nm PtCu3 nanoparticles evolve after being submitted to an activation protocol that causes mild degradation.

To track the morphological changes at the same location (1) during the activation protocol, we deposited as prepared PtCu3/C nanoparticles (2) on a gold finder TEM grid. Several spots were observed first at lower magnification on the TEM grid, and individual nanoparticles imaged at high resolution by STEM.

We have tracked morphological features at the atomic level by observing the same location before and after the activation protocol: reshaping, nanoparticles size reduction, pore formation and preferential anisotropic faceting in the following order {110}, {100} and then {111}. From these findings, we have constructed a physical model to simulate the dealloying process by Kinetic Monte Carlo modelling.

By using atomic resolution IL-STEM and studying PtCu3 nanoparticles before and after the activation protocol, we were able to perform image analysis and obtain precise information of the nanoparticle conditions at that stage. We estimated that nanoparticle size reduction can be from 16% to 26% and that facet dealloying is not uniform and happens preferentially on facets {110} and {100} before {111}.

References:

(1) Mayrhofer, K. J. J.; Meier, J. C.; Ashton, S. J.; Wiberg, G. K. H.; Kraus, F.; Hanzlik, M.; Arenz, M. Electrochem. Commun. 2008, 10, 1144-1147.

(2) Hodnik, N.; Jeyabharathi, C.; Meier, J. C.; Kostka, A.; Phani, K.L.; Rečnik, A.; Bele, M.; Hočevar, S.; Gaberšček, M.; Mayrhofer, K. J. J. Phys. Chem. Chem. Phys. 2014, 16, 13610-13615.

MS3.P028
Understanding intragranular nanopore evolution and phase transformation during electrochemical cycling in Ni-rich layered oxide cathode materials.

S. Ahmed[1], A. Pokle[1], S. Schweidler[2], A. Beyer[1], M. Bianchini[2], P. Hartmann[2], T. Brezesinski[2], J. Janek[2,3], K. Volz[1]

[1]Structure and Technology Research Laboratory, Department of Physics, University of Marburg, Marburg, Germany
[2]KIT/BASF Battery and Electrochemistry Laboratory (BELLA), Karlsruhe, Germany
[3]Justus-Liebig-Universität, Physikalisch-Chemisches Institut, Giessen, Germany

Nickel-rich layered oxides (e.g. NCM or NCA) are important commercial Cathode Active Materials (CAMs) for Lithium-ion Batteries (LIBs). Exhibiting high energy density, they are used in LIB cells for automotive applications. However, as trade-off for the high specific capacity of more than 200 mAh/g chemo-mechanical degradation during electrochemical cycling is observed. This has triggered a considerable amount of research within the battery community.

The requirement for higher energy densities within lithium ion batteries lead to the development of Ni-rich NCMs. Within this class we investigated a material with 85% Ni: Li1+x(Ni0.85Co0.10Mn0.05)1-xO2. Typically, NCMs are synthesized as secondary particles made from densely packed primary particles. The volume changes occurring during electrochemical cycling lead to strain within the primary particles due to charging/discharging. In previous investigations, surface reconstruction from a layered to a rock salt structure, formation of inter/intragranular cracks, and nanopores (or voids) have been reported. Among these, to the best of our knowledge, the presence of intragranular nanopores is not well characterized, and their presence in pristine samples is usually neglected (1). It has been suggested that nanopores are formed only during electrochemical cycling and can be reproduced by heating as well as chemically delithiating the material.

By employing Focused Ion Beam (FIB) and NanoMill sample preparation methods followed by aberration-corrected STEM (AC-STEM) analysis, we have studied the CAM. Replicating real battery conditions, the materials are cycled in single-layer pouch cells against graphite anode, and samples are collected after 200 and 500 cycles for characterization. In addition to observing phase transformation (leading to metal segregation) and inter/intragranular cracks, we have also investigated cation disordering within the nanopores at sub-angstrom resolution.

Using AC-STEM and Electron Energy Loss Spectroscopy (EELS), we confirm a rocksalt-like structure at nanopore boundaries. This rock salt structure also extends with electrochemical cycling with a change in the morphology. Interestingly, there are channels observed in the 200-cycled sample in between the nanopores. Nanopore boundaries provide a natural pathway to intragrain phase transformation, thereby increasing the intragrain rock salt fraction. Rocksalt regions are electrochemically inactive and increase the impedance of cathode materials

Intragranular nanopores are observed in a wide variety of layered oxide cathode materials, but so far it is not clear if and how they affect the performance of the materials. A detailed study on the effects of FIB preparation on the NCM material revealed that irrespective of cycling, nanopores are present in the primary particles. At the grain boundaries (GB), there is a formation of dense rock salt structure followed by spinel-like regions, which extend with electrochemical cycling, thus limiting the intergrain Li-ion transport. To the best of our knowledge, rock salt formation and extension at the GB has not been observed before in the inner primary particles of a secondary particle (which are not directly exposed to the electrolyte or free space).

References:

(1) P. Yan, et al., Nat Commun, vol. 8, Jan. 2017

MS4.001
High Resolution Insights into Structure and deformation Mechanisms of High-Mn Steels

M. Lipinska-Chwalek[1,2], C. H. Liebscher[3], M. Yao[3], M. Herbig[3], C. Scheu[3], J. Wittig[4], J. Mayer[1,2]

[1]Jülich Forschungszentrum GmbH, Ernst Ruska-Centrum für Mikroskopie und Spektroskopie mit Elektronen, Jülich, Germany
[2]RWTH Aachen University, Central Facility for Electron Microscopy, Aachen, Germany
[3]Max-Planck-Institut für Eisenforschung GmbH, Düsseldorf, Germany
[4]Vanderbilt University, Interdisciplinary Materials Science, Nashville, United States

Recently developed high-manganese steels (HMnS) evoke large research interest due to their superior combination of high strength and ductility. Since functional and structural properties are inseparably related to local structure of the material, understanding the processes controlling mechanical behaviour, requires thorough microstructure exploration down to the atomic level.

The main goal of our studies was to identify microscopic mechanism controlling the extraordinary mechanical properties of HMnS. The capabilities of high resolution (HR) scanning transmission electron microcopy (STEM) and atom probe tomography (APT) measurements in gaining insights into the underlying microstructural phenomena are presented.

The twinning induced plasticity (TWIP) deformation structure of Fe-16Mn-14Cr-0.3C-0.3N (wt.%) (1), after 20% tensile elongation at room temperature, was studied by a combination of HR STEM and convergent beam electron diffraction (CBED).

The lightweight, austenitic steel Fe-30Mn-8Al-1.2C (wt.%) was investigated in a k-carbide (Fe,Mn)3AlC precipitation-strengthened (2) state (aged at 600°C for 1, 4, 8 and 24 h), and after 5% tensile deformation, by STEM and correlative APT.

Structure characterisation was performed with the Cs probe-corrected STEM FEI Titan G2 80-200 and Titan Themis 60-300, operated at 200 kV and 300kV, respectively. High angle annular dark field (HAADF), bright field (BF) and annular bright field (ABF) detectors were used for imaging. TEM specimens were prepared as electropolished 3mm TEM discs or as lamellas cut with the focused ion beam (FIB). Corelative APT measurements were conducted with a local electrode probe 3000XHR on the needle-shaped samples extracted by FIB (investigated in STEM prior to APT).

TWIP behavior is attributed to the formation of mechanical twin boundaries (TBs) upon deformation. Fig. 1 shows TWIP deformation structure of the Fe-16Mn-14Cr-0.3C-0.3N steel. Though perfectly symmetrical appearance of deformation twins was observed in HR STEM images, a presence of significant misorientation at the TB interface was revealed by CBED (Fig.1 C). Due to accumulation of partial dislocations, a low-angle boundary is introduced at the mechanical TB, which destroys its perfect mirror symmetry. Non-perfect TBs are expected to act as much stronger obstacles to dislocation glide than the highly symmetrical ones, and therefore, to play a significant role for the work-hardening behavior of TWIP HMnS.

Microstructure of the lightweight Fe-30Mn-8Al-1.2C, after 600° ageing, consists of nm-sized k-carbides evenly distributed within the austenitic g-matrix, as shown in Fig.2. Insights into k-carbides growth kinematics, atomic structure, chemical ordering and the local strain state at the interfaces were obtained by HR HAADF measurements. g/k-interfaces remain fully coherent, but significant tetragonal straining of the g-matrix located in narrow channels, between closely arranged k-carbides, was detected (Fig.2.D-F). Corelative APT measurements resolved microchemistry and 3D distribution of k-carbides (3). Analyses performed for deformed material, identified dynamic slip band refinement, in {111}<110> fcc slip system, as the main strain-hardening mechanism of the alloy (2).

References:

(1) Mosecker L. et al., Mat. Sci. Eng. A 642 (2012)

(2) Yao M. et al., Acta Mat. 140 (2017)

(3) Liebscher C.H. et al., Phys. Rev. Mat. 2 (2018)

Fig. 1

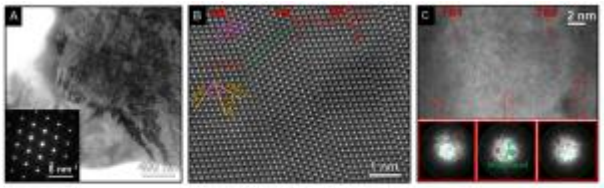

Fig. 1: TWIP deformation structure of Fe-16Mn-14Cr-0.3C-0.3N after 25% tensile elongation at room temperature, observed in an electropolished TEM sample. Images acquired with a crystallographic direction <110>$_{fcc}$ parallel to the electron beam direction in TEM. A) overview BF TEM and corresponding diffraction pattern, indicating presence of two sets of active deformation twinning systems, with (1-11) and (1-1-1) habit planes. B) HR HAADF STEM of mechanical TBs and stacking faults (SF). C) HAADF STEM of strongly misoriented mechanical TBs with corresponding CBEDs.

Fig. 2

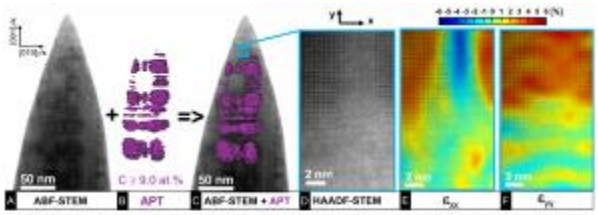

Fig. 2: (A) HRSTEM ABF image of an electron-transparent, needle-shaped APT specimen cut of 24h-aged Fe-30Mn-6Al-1.2C material with crystallographic orientation of <100>$_{fcc}$ direction parallel to the length axis of an APT specimen and electron beam direction in TEM. (B) Corresponding APT reconstruction, with κ-carbides morphology visualised by 9 at.% C iso-concentration surfaces. (C) Overlay of (B) on the top of (A) image. (D) STEM HAADF atomic resolution image of the local structure in position indicated in (C) with blue rectangle. (E,F) Local in-plane ε_{xx} and ε_{yy} strain maps extracted from the atomic column positions determined from the corresponding HAADF image shown in (D). ε_{xx} and ε_{yy} strain is defined as a difference between the local interatomic distance (in x and y direction, as indicated in D) and corresponding interatomic distance measured for the reference lattice of nondistorted fcc γ-matrix with a_γ = 0.369 nm. Images modified after [3].

MS4.002 invited
Electron Nanodiffraction of Metallic Glasses and Liquids

P. Voyles[1], D. Chatterjee[1], S. Muley[1], C. Cao[1], J. Ketkaew[2], J. Schroers[2], J. H. Perepezko[2]

[1]University of Wisconsin-Madison, Department of Materials Science and Engineering, Madison, United States
[2]Yale University, Department of Mechanical Engineering and Materials Science, New Haven, Germany

Glasses are complex, metastable materials which exist in a variety of thermodynamic states. Electron nanodiffraction probes these materials at the length scales that control their properties and processes. Temporal variations in nanodiffraction form the basis of electron correlation microscopy (ECM), a probe of nanoscale dynamics. Spatial variations in nanodiffraction form the basis of fluctuation electron microscopy (FEM), a probe of nanoscale structure. These techniques enable studies of the process by which a liquid becomes a glass on cooling and the structure of the resulting glass, respectively. We have used FEM to show that increased kinetic stability in Zr-Cu-Al metallic glasses is associated with increased icosahedral structural order. This observation is consistent with simulations that show that, compared to other structures, icosahedral arrangements of atoms are lower in energy and slower to rearrange. We have used ECM to probe atomic rearrangements in the supercooled liquid state of Pt57.5Cu14.7Ni5.3P22.5. ECM shows that the structural relaxation time, which measures the rate of atomic rearrangements, varies from place to place in the liquid at a length scale of 0.8-1.4 nm, depending on temperature. ECM also shows that in a ~1 nm thick layer near the surface of the liquid, the dynamics are an order of magnitude faster than in the bulk. A next-generation, ultrafast pixelated direct electron detection camera will enable combined studies of structure and dynamics using electron nanodiffraction.

MS4.003
Construction of structural models of amorphous materials from TEM images or diffraction patterns: the example of a metallic glass

C. T. Koch[1], K. Skudler[1], F. Peschel[1], T. S. Bechtel[1], T. C. Pekin[1], I. P. Ivanov[2], A. L. Greer[2]

[1]Humboldt-Universität zu Berlin, Institut für Physik & IRIS Adlershof, Berlin, Germany
[2]University of Cambridge, Department of Materials Science & Metallurgy, Cambridge, United Kingdom

Although amorphous materials have many technological applications (e.g. the gate oxide in transistors, inter-granular films in ceramics, or phase-change material [e.g. GeSbTe] for data storage), the techniques to study their atomic structure are rather limited. The standard reduced density function *G(r)* provides information about projected inter-atomic distances. Fluctuation electron microscopy (FEM) provides statistical information on higher-order correlations. We present characterization techniques that aim to recover three-dimensional local atomic environments from imaging and diffraction data obtained in the TEM, where the 3D information is recovered from the 2D data by applying physically reasonable constraints. No assumptions are made on the physical interaction of the atoms (e.g. the adoption of some inter-atomic potential model).

We have fitted atomic models to the phase of a complex electron wave function recovered from a focal series of TEM images (see Figs. 1 & 2) or to a series of nano-beam electron diffraction patterns. Refining the positions from a starting guess consisting of initially random coordinates is a high-dimensional optimization problem with low chances of finding the global optimum, or even a relatively close match between simulated and experimental data. We have therefore built the solution adding one atom at a time. One of the constraints being applied is the fact that the two-dimensional pair distribution function projected along any of the three axes of the model should be similar, minimizing the expression in Fig. 2, where E_{low} is a penalty for two atoms being closer than the sum of their Z-specific atomic radii.

Figure 1a shows three images taken from a focal series of a metallic glass consisting of layers with different composition ($Pd_{38}Zr_{62}$ and $Cu_{46}Zr_{54}$). Fig 1b shows amplitude and phase of the complex wave recovered from the focal series using the FRWR software (1,2). A small area of 1 nm x 1 nm has been extracted from a band-pass filtered version of the top left corner of this phase (see Fig. 2c) and an atomic model has been built, the band-pass-filtered projected potential of which is proportional to this phase map, minimizing χ^2 in the expression in Fig. 2 for different values of $weight_{2DPDF}$.

Figs. 2a and 2b show the phase simulated from the atomic models created without and with the 2D-PDF constraint being applied. Fig. 2d shows the partial pair distribution functions (pPDFs) of the model leading to the phase shown in Fig. 2b. Fig. 2e presents the 2D-PDFs of that very same model.

Results obtained from other experimental data (electron diffraction patterns, corellograms (3) and their variance, etc) and other constraints will be presented as well.

References:

(1) C.T. Koch, Ultramicroscopy 108 (2008) p. 141-150

(2) C.T. Koch, Micron 63 (2014) p. 69–75

(3) J.M. Gibson, M.M.J. Treacy, T. Sun, and N.J. Zaluzec, Phys. Rev. Lett. 105 (2010) 125504

Funding from the German Research Foundation (DFG)-funded core facility BerlinEM Network (grant no. KO2911/13-1) as well Projektnummer 182087777 – SFB951 is acknowledged

Fig. 1

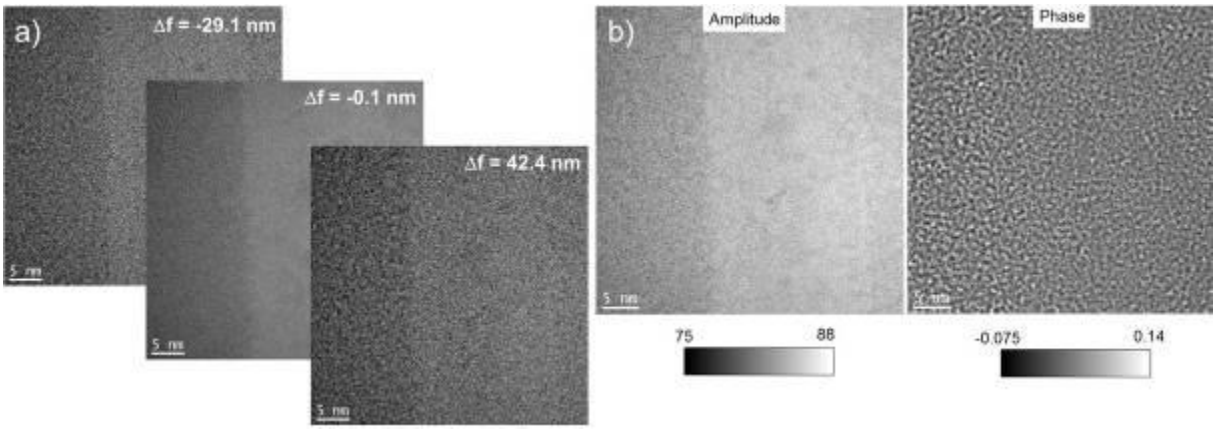
a)
Δf = -29.1 nm
Δf = -0.1 nm
Δf = 42.4 nm
5 nm
b)
Amplitude
Phase
75
88
-0.075
0.14

Fig. 2

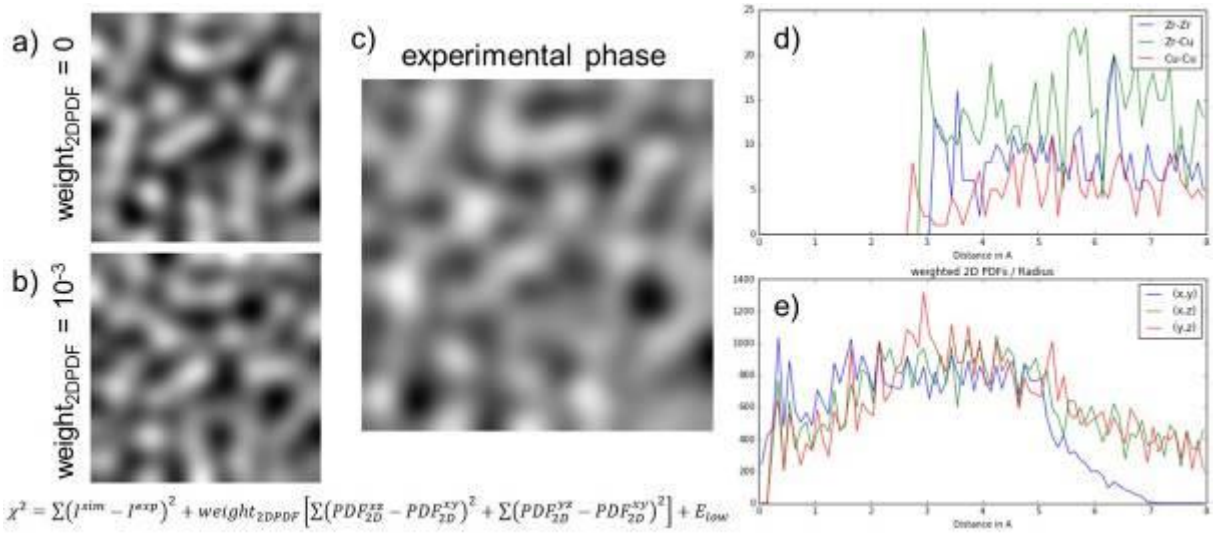
a)
weight2DPDF = 0
b)
weight2DPDF = 10-3
c)
experimental phase
d)
Zr-Zr
Zr-Cu
Cu-Cu
Distance in Å
weighted 2D PDFs / Radius
e)
(x,y)
(x,z)
(y,z)
Distance in Å
$\chi^2 = \Sigma(I^{sim} - I^{exp})^2 + weight_{2DPDF}\left[\Sigma(PDF_{2D}^{xz} - PDF_{2D}^{xy})^2 + \Sigma(PDF_{2D}^{yz} - PDF_{2D}^{xy})^2\right] + E_{low}$

MS4.004
Stereoscopy-based three-dimensional reconstruction of interfaces for experimentally informed simulations

L. Agudo Jácome[1], H. Lyu[2], G. Eggeler[3], E. Bitzek[2,4]

[1]Bundesanstalt für Materialforschung und -prüfung (BAM), 5. Materials Engineering, Berlin, Germany
[2]Friedrich-Alexander-Universität Erlangen-Nürnberg (FAU), Materials Science and Engineering, Institute I (MSE I)), Materials Science and Engineering, Institute I (MSE I), Erlangen, Germany
[3]Ruhr-Universität Bochum, Institut für Werkstoffe, Bochum, Germany
[4]Friedrich-Alexander-Universität Erlangen-Nürnberg (FAU), Erlangen, Germany

Interfaces critically determine many material properties. Precipitation-hardened alloys are an example where the interaction of dislocations with the interphase boundary (IPB) depends on the nature of the IPB. During high temperature creep (>1000 °C), Ni-base superalloy single crystals (SXs) develop dislocation networks on the once coherently cuboidal γ' precipitates ($L1_2$ ordered structure), which become raft-like structures together with the γ matrix (fcc solid solution). Diffusive and dislocation-mediated processes, and the IPB morphology influence each other during this microstructural evolution. A realistic representation of the evolved IPB morphology is thus important for any modeling attempt. Stereo-scanning transmission electron microscopy (STEM) offers an efficient way to reconstruct such interfaces.

In this contribution, it is showed that STEM stereoscopy can be used to extract three-dimensional (3D) landmarks to create realistic surface meshes for experimentally informed simulations. This is exemplified with γ/γ' IPBs in a crept Ni-base superalloy SX.

Creep loading is applied in tension along [110] at 1020 °C and 160 MPa on the Ni-base superalloy SX LEK 94, and stopped after 2% plastic deformation. TEM specimens are prepared electrolytically. STEM is performed at 200 kV in a field emission gun scope. Stereo-pairs are acquired at stereo-angles ≥ 15°. Fig. 1 exemplarily shows the steps (numbered blue arrows) taken for this proof of concept study. First, line segments in the IPB are reconstructed in Amira from stereo-pairs by connecting manually traced nodes such that their 3D positions match both projections in the stereo-pair (1). Second, the nodes act as 3D point clouds onto which a Delaunay triangulation is applied to construct the IPB as a surface mesh. The software Blender is used to create two closed surface meshes, one for the fcc γ and one for the $L1_2$ γ' phase. In a third step, these are filled with Ni, respectively Ni and Al atoms using nanoSCULPT (2) to model using molecular dynamics. In Fig. 1, the sample is scaled down by a factor of 10 as proof of concept.

The stereoscopic reconstruction of dislocation line directions is shown to have an angular uncertainty of up to 7°. The current manual tracking of dislocation lines in step 1 induces lines with only few points, which delivers rough surfaces in step 2. However, inclinations of up to 37° from (100) can be captured (Fig. 1, middle top). Further improvements of the interpolation of the surface between dislocation nodes could be achieved with energy minimizing algorithms, grain growth or phase field simulations with information on the orientation-dependent interface energy and misfit.

Following the outlined procedure, it is possible to reconstruct a 3D interfacial dislocation network via STEM stereoscopy and use it to interpolate the interface morphology, which can then be used in experimentally-informed simulations (3).

References:

(1) L.Agudo Jácome, K.Pöthkow, O.Paetsch, H.-C.Hege, Ultramicroscopy 195 (2018) 157-170

(2) A.Prakash, M.Hummel, S.Schmauder, E.Bitzek, MethodsX 3 (2016) 219-230

The Deutsche Forschungsgemeinschaft is acknowledged for funding of project AG 191/1-1 and of projects A1, A2 and C3 of the collaborative research centre SFB/Transregio 103.

Fig. 1: Steps (blue arrows) that define the procedure for (1) dislocation reconstruction, (2) interface extraction, and (3) molecular dynamics simulation.

Fig. 1

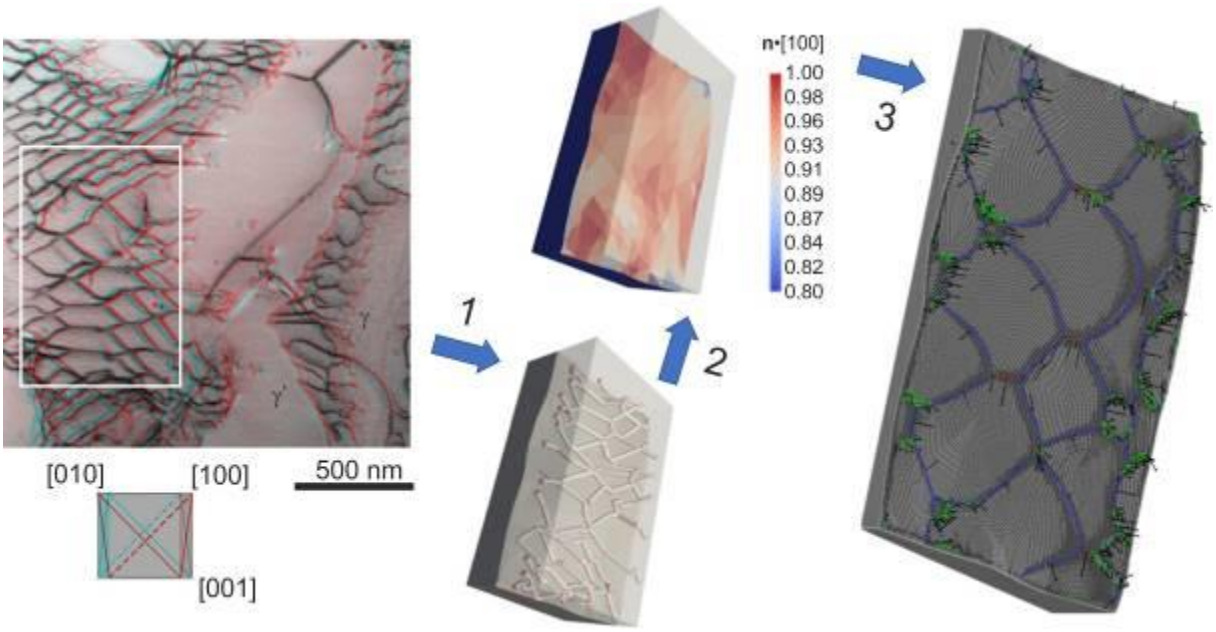
γ
γ'
[010]
[100]
500 nm
[001]
1
2
3
n·[100]
1.00
0.98
0.96
0.93
0.91
0.89
0.87
0.84
0.82
0.80

MS4.005
Deformation twinning in bcc iron - experimental validation of molecular dynamic simulations by means of EBSD, STEM and TEM

M. Ecke[1], O. Michael[1], S. Huetter[1], M. Wilke[1], M. Krueger[1,2], T. Halle[1]

[1]Otto von Guericke University Magdeburg, Metallic Materials, Magdeburg, Germany
[2]Forschungszentrum Juelich GmbH, Microstructure and Properties of Materials, Jülich, Germany

The mechanism of deformation twinning due to impact loading was investigated by experimental and numerical methods. In consideration of metal-physical properties like stacking fault energy, dislocation density, dislocation agility and grain boundary effects the formation of twins was studied. In order to address these effects, impact experiments at room temperature and at -196°C were carried out using pure iron, iron-aluminum and iron-chromium alloys showing different grain sizes (40 to 1000 µm) and pre-deformation states (0 to 50 % plastic strain). Aiming at the interpretation of the influence of the given parameters high resolution electron microscopic methods e.g. EBSD, TKD and STEM were executed after deformation of the samples. It was shown that major influences on the formation of twins are a decrease in temperature, stacking fault energy and dislocation density and an increase in grain size.

Using molecular dynamic simulations based on interatomic bonding energies a favored nucleation mechanism was identified. During impact loading a dislocation dissociation of a perfect ½ <111> dislocation was determined. Twin nucleation and twin growing occurred subsequently. Comparing the results to literature shows a good agreement to the Sleeswyk mechanisms (1) predicted in 1963. In STEM and TEM investigations, the results were proofed and validated.

References:

(1) A.W. Sleeswyk, Philos. Mag. 8 (1963) 1467–1486.

MS4.006
Evolution of microstructure under complex stress states during creep of single crystal Ni-base superalloy CMSX-4

N. Karpstein[1], M. Lenz[1], J. Cormier[2], E. Spiecker[1]

[1]Center for Nanoanalysis and Electron Microscopy (CENEM) and Institute of Micro- and Nanostructure Research (WW9), Friedrich-Alexander University Erlangen-Nuremberg, Department of Materials Science, Erlangen, Germany
[2]Institut Pprime, CNRS-ENSMA-Université de Poitiers, Département Physique et Mécanique des Matériaux, Poitiers, France

Nickel-base superalloys are used as high-temperature materials in gas turbines for industrial power plants and jet propulsion. The excellent high-temperature properties of these alloys rely on their γ/γ'' microstructure. Improvements in their high-temperature properties can be achieved if the deformation behavior and underlying mechanisms are thoroughly understood (1).

For practical applications of high-temperature materials, their behavior under complex loading scenarios is especially significant. In order to investigate the mechanical behavior and morphological evolution of the commercial Ni-base superalloy CMSX-4 under creep under both tension and compression, Caccuri et al. (2) produced monocrystalline specimens with a special V-shaped geometry (see Fig. 1a). During creep deformation, this geometry induces a complex stress state with regions of tensile and compressive stresses in the same specimen (Fig. 1b).

SEM analysis of the specimens after creep shows wide variations in the morphology of the γ/γ'' microstructure, which depends greatly on the sign of the stress. Directional coarsening occurs and changes direction from p- to n-type in the transitional region (Fig. 1c) (2).

For further TEM analysis of the microstructure and defects, multiple lamellae have been extracted from a creep specimen at different sites and in different orientations (Fig. 2a). This allows a thorough examination of defects present after creep (Fig. 2b-d) depending on the orientation and stress state. The investigated creep defects include channel dislocations, dislocation networks at the γ/γ'' interface as well as planar defects. Elemental segregation to the defects is investigated through EDX measurements and can help understand the mechanisms of defect formation, the dynamics of defects (3), and even their influence on the morphology such as aiding rafting and facilitating the dissolution of γ'' (4).

These investigations and especially the role of defects in microstructural degradation will support a more comprehensive knowledge of the mechanisms of plastic deformation at elevated temperatures. Understanding the mechanical properties of high-temperature superalloys, in turn, enables suggestions for improved alloy design for the next generation of superalloys.

The authors gratefully acknowledge financial support by the DFG via the collaborative research center SFB-TR 103. They further acknowledge Dr. S. Makineni from MPIE Düsseldorf for help with preliminary ECCI studies.

References:

(1) R. C. Reed, The Superalloys: Fundamentals and Applications, Cambridge University Press (2006).

(2) V. Caccuri et al., Materials & Design 131, pp. 487–497 (2017).

(3) D. Barba et al., Metallurgical and Materials Transactions 49A, pp. 4173–4185 (2018).

(4) P. Kontis et al., Scripta Materialia 145, pp. 76–80 (2018).

Fig. 1: (a) Schematic geometry of the V-shaped creep specimens and experimental parameters. (b) Region of interest in the creep specimen with varying stress state. (c) Transition between p- and n-rafting in the central part of the sample crept for 24 h.

Fig. 2: (a) Schematic representation of the lamellae extracted for TEM investigation from the region of interest (Fig. 1b) in the sample crept for 5 h. (b)-(d) Microstructure of regions exposed to different stress states observed via STEM, with the loading axis perpendicular to the image plane, showing channel dislocations and dislocation networks at γ/γ'' interfaces.

Fig. 1

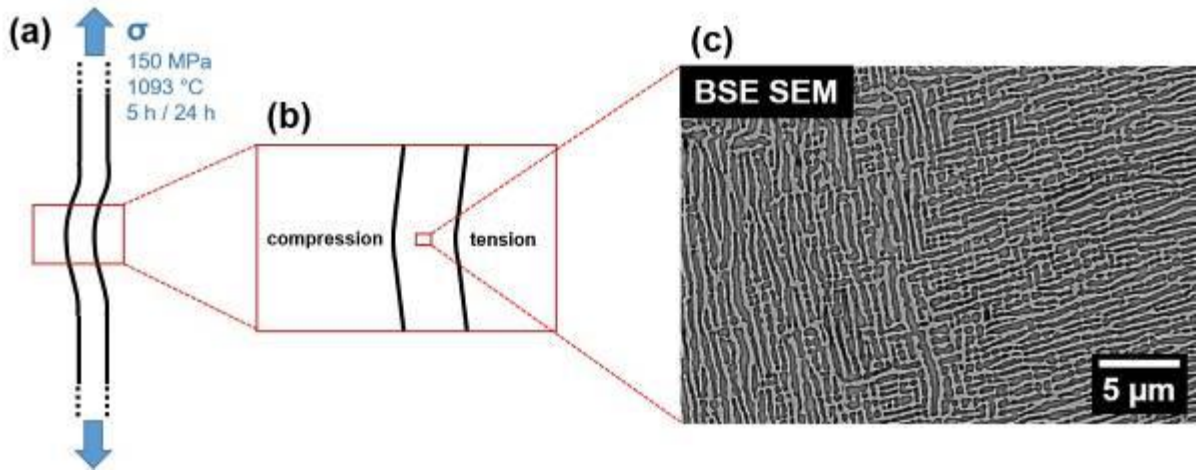
(a)
σ
150 MPa
1093 °C
5 h / 24 h
(b)
compression
tension
(c)
BSE SEM
5 µm

Fig. 2

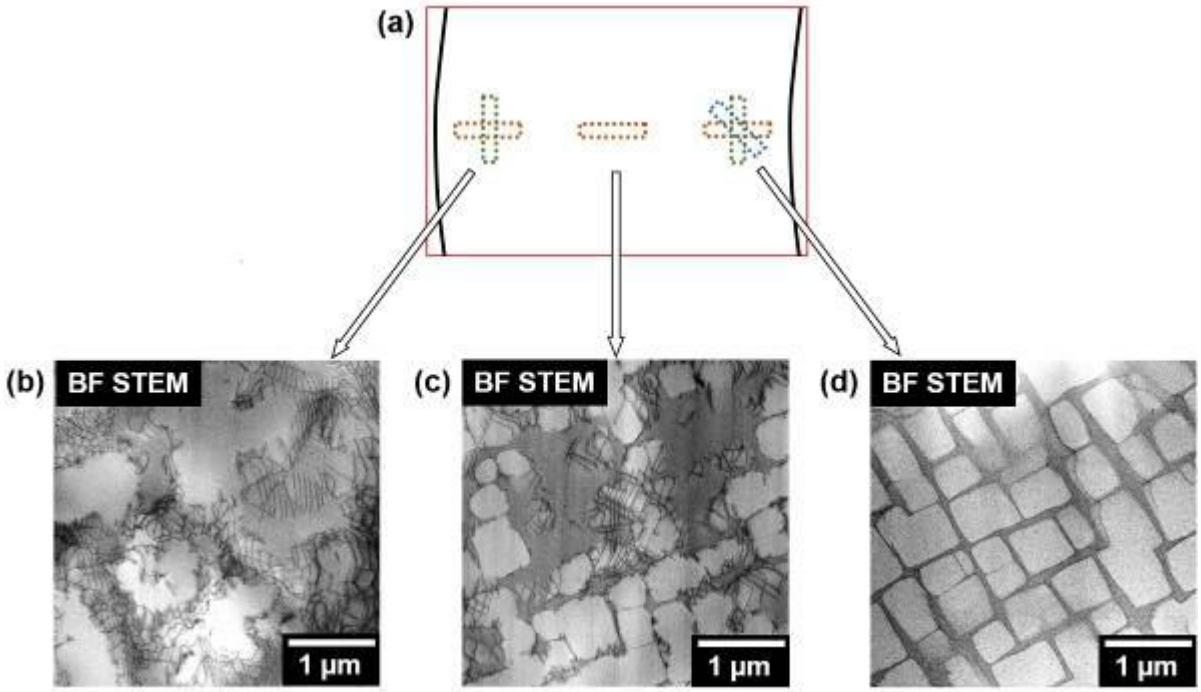
(a)
(b)
BF STEM
1 µm
(c)
BF STEM
1 µm
(d)
BF STEM
1 µm

MS4.LB.P01
Microstructural Characterization of High Mn Steels Using Conventional and High Resolution Transmission Electron Microscopy

J. Wittig[1], M. Lipińska-Chwałek[2,3], J. Mayer[2,3]

[1]Vanderbilt University, Materials Science, Nashville, United States
[2]Forschungszentrum, Enrst Ruska-Centre, Jülich, Germany
[3]RWTH University, GFE, Aachen, Germany

Understanding the relationship between the structure of high- Mn steels and their combination of high strength and ductility requires detailed microstructural characterization. For high-Mn steels with a fully austenitic microstructure that exhibit transformation and twinning-induced plasticity (TRIP-TWIP), conventional transmission electron microscopy (TEM) provides information necessary for the experimental determination of stacking fault energy (SFE) values. In addition, diffraction contrast is the preferred method for characterization of the planar defects produced by secondary deformation mechanisms. However, imaging at atomic resolution using aberration-corrected TEM and probe-corrected high resolution scanning TEM (HRSTEM) is critical for understanding the character of these planar defects and their interactions with dislocations.

A combination of diffraction contrast imaging and atomic resolution imaging provides a complete representation of the deformation mechanisms in high-Mn TRIP/TWIP steels in order to develop structure-property relationships that elucidates their mechanical behavior.

In this investigation, three Fe-Mn(22,25,28)-3Al-3Si (wt%) austenitic steels have been studied to understand the influence of Mn content on the SFE, deformation mechanisms, and work-hardening behavior. Electropolished 3 mm diameter disks from tensile samples deformed to 20% elongation were examined using a Philips CM20 at 200 keV and an FEI Titan operating at 300 keV.

Increasing the Mn content from 22 to 28 wt% Mn, increases the SFE from 14 to 39 mJ/m2, with a transition from TRIP to TWIP behavior (1). Conventional bright field (BF) – dark field (DF) diffraction contrast offers a quantitative method to characterize the type, spacing, and density of the planar defects for TRIP/TWIP steels (2). Figure 1 is an example where both epsilon martensite and mechanical twinning are present in a Fe – 25Mn3Al3Si (wt%) steel after 20% elongation in tension. Scanning electron microscopy methods such as EBSD with electron channelling contrast imaging (ECCI) offer complementary information. However, the EBSD-ECCI method cannot distinguish between TRIP and TWIP and lacks the spatial resolution to detect the smallest defects (< 10 nm). Imaging at atomic resolution using aberration-corrected TEM and probe-corrected high resolution scanning TEM (HRSTEM) is critical for understanding the character of these planar defects and their interactions with dislocations. Figure 2 shows HRSTEM images from a Fe-25Mn3Al3Si (wt%) steel after 20% deformation. The presence of both deformation twinning and epsilon martensite (ABAB stacking) is clearly observed.

The characterized spacing and density of these mechanical induced planar defects can be directly related to the strain-hardening behaviour of these alloys with smaller spacing between the defects increasing the strain hardening. Both the twin and martensite/austenite boundaries are obstacles for dislocation motion where partial dislocations can be trapped at the interface. Trapping occurs due to the spacing between boundaries and the repeated disruption of dislocation glide on subsequent planes.

References:

(1) Pierce, D.T.; Jiménez, J.A.; Bentley, J.; Raabe, D.; Oskay, C.; Wittig, J.E, Acta Mater. 68 (2014) 238-253.

(2) Benzing, J.T.; Poling, W.A.; Pierce, D.T.; Bentley, J.; Findley, K.O.; Raabe, D.; Wittig, J.E., Mater. Sci. Eng. A 711 (2018) 78-92.

Fig. 1

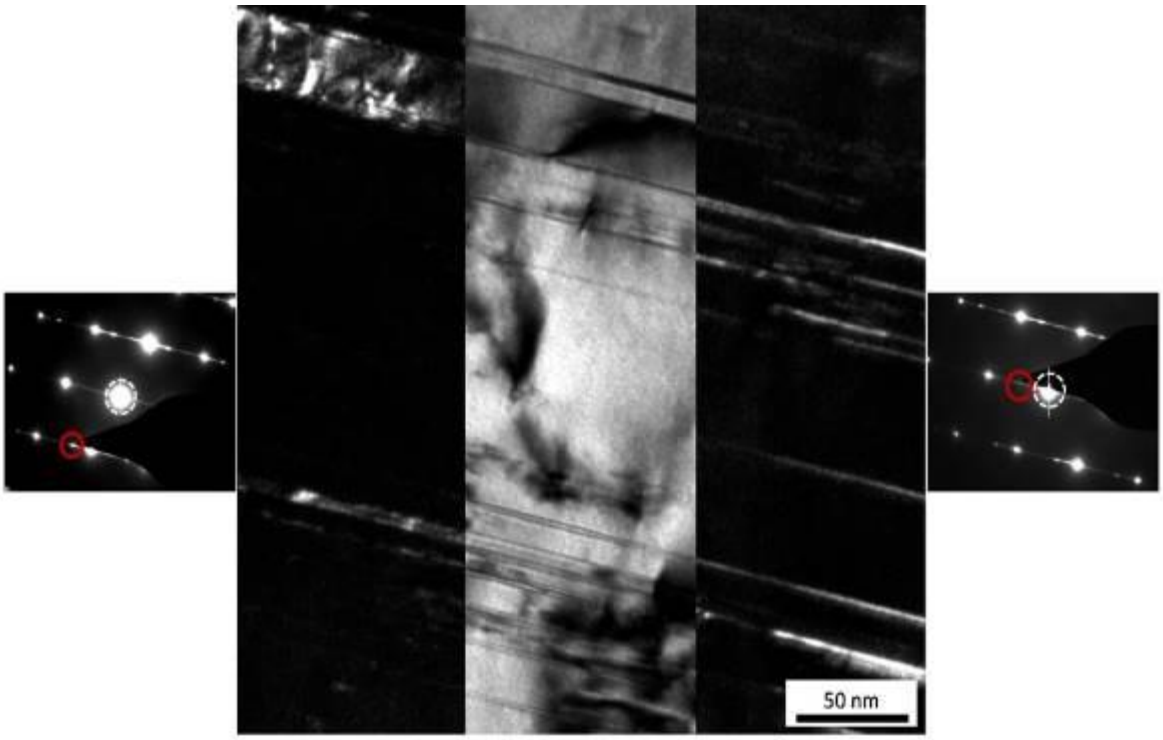

Figure 1: Bright field (BF) – dark field (DF) images and selected area electron diffraction patterns (SAED) of a Fe-25Mn3Al3Si (wt%) steel after 20% deformation. From the BF image in the centre, the DF image and SAED pattern (solid red circle) on the left reveals the mechanical twinning and the DF-SAED on the right, the epsilon martensite.

Fig. 2

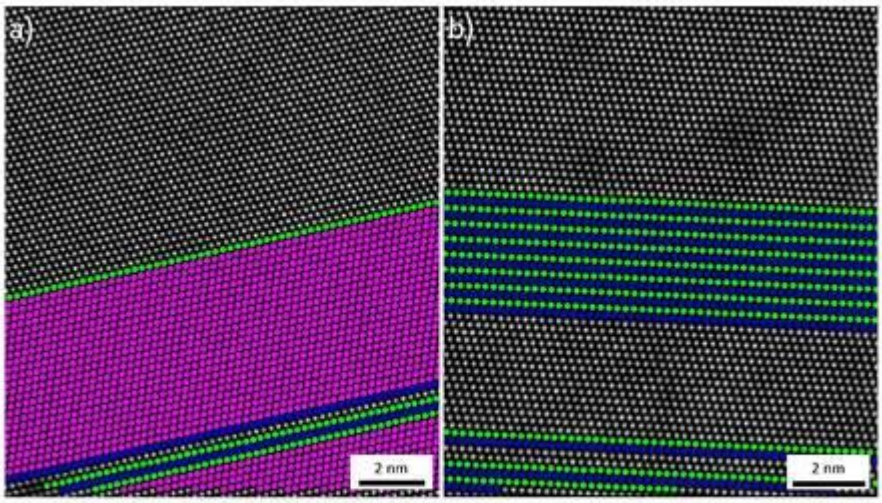

Figure 2 - (a) deformation twinning + ε martensite (b) strain-induced ε martensite. All hexagonal stacking sequences (ABAB) are highlighted with blue and green atom columns, while purple atom columns indicate a twin relationship with respect to the undeformed matrix.

MS4.LB.P02
Multi method electron crystallography for structural characterisation of novel phases in the Al-Cu-Ge-Mg system

M. R. Iskandar[1], A. Schwedt[1], J. Mayer[1], T. E. Weirich[1]

[1]RWTH Aachen University, GFE, Aachen, Germany

Within a recent study on the interface of TLP bonded aluminium sheets we identified a so far unreported hexagonal structure in the Al-Cu-Ge-Mg system by SEM-EBSD and SAED (1). For in detail structure analysis FIB lamellae normal and parallel to the c-axis have been prepared and were subsequently examined by SAED, HR-HAADF-STEM and EDX. Analysis of the SAED and HAADF-STEM data from the <001> direction confirmed the previously assumed hexagonal (trigonal) symmetry with an a-axis of about 0.4 nm. Evaluation of the corresponding HR-HAADF-STEM image by crystallographic image processing (2), shows that the symmetry of this projection is compatible with plane group p3 or p3m1, respectively. Analysis of the data from the <100> and <210> structure projections provide, however, a less unique picture and suggest structural variations along the sample. Thus evaluation of the data from the nominal same region indicates a unit cell with a c/a ratio of 5.81 for one projection and data for another orientation suggests a twice as long c-axis with a c/a ratio between 11.55 and 12.12. Nevertheless, both of these unit cells are based on an 21H stacking sequence of ideal packed layers of metal atoms (est. c/a = 17.86). As shown in the overlays in Fig. 2, both periodic unit cells can be obtained by a very slight incline to the direction of the ideal stacking (yellow arrows). Therefore an inclination of about 3° and 1.5° lead to the 7H and 14H respectively. It should be noted, that the here used nomenclature for the stacking sequence relates in all cases to the corresponding sequence in the underlying (ideal) 21H structure and does not describe the actual layering in the structures. In order to verify the derived partial structural models (heavy scattering atoms only) we combine information from atom column resolved STEM-EDX with dynamical EBSD pattern simulation (3) and compare these with the obtained experimental data.

References:

(1) Iskandar R. et al., Mat.-wiss. U. Werkstofftech. 2017, 48, 1257-1263, DOI 10.1002/mawe.201700155

(2) Zou XD., Hovmöller S., Oleynikov P. (eds.), Electron Crystallography: Electron Microscopy and Electron Diffraction, Oxford University Press 2011

(3) Program package "ESPRIT DynamicS" for HR-EBSD Pattern Simulation, Bruker Corporation

The authors thank the Deutsche Forschungsgemeinschaft (DFG) for financial support through the Collaborative Research Centre SFB 1120 (Precision Melt Engineering).

Fig. 1: (a): SAED pattern taken along the <001> direction of a novel phase in the Al-Cu-Ge-Mg system. The diffraction spots are linked by intensity streaks, which indicates some amount of disorder in the structure. (b): Lattice averaged HAADF-STEM image (p3 symmetry) along the <001> direction. The projection shows three types of atom columns with different scattering intensity in the structure. The indicated unit cell edges are about 0.4 nm long.

Fig. 2: Crystallographic image processing (2) of HAADF images taken along the <100> crystal direction. (a) Tilting the direction of the projection by about 3° off from ideal layer stacking (yellow arrow) leads to the structure with 7H stacking sequence. (b) Inclination by about 1.5° towards the direction of the ideal layer stacking results in the 14H structure. It should be noted that both structures contain also weak scattering atoms which is only barely resolved in these images. These atoms will be considered at a later stage for the development of the full structure model.

Fig. 1

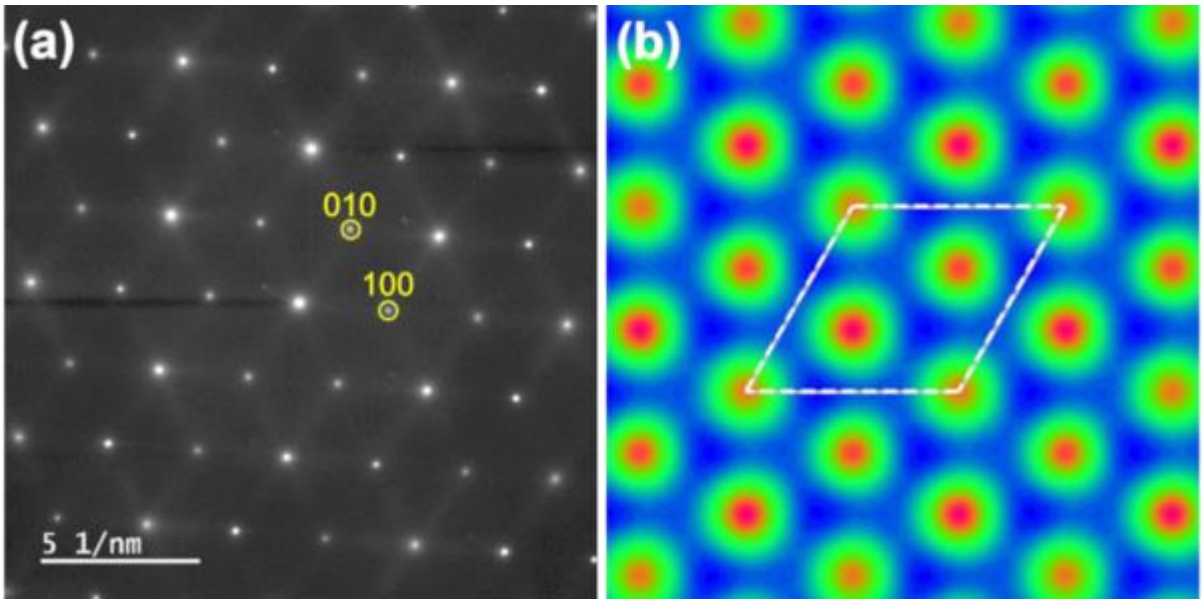

Fig. 2

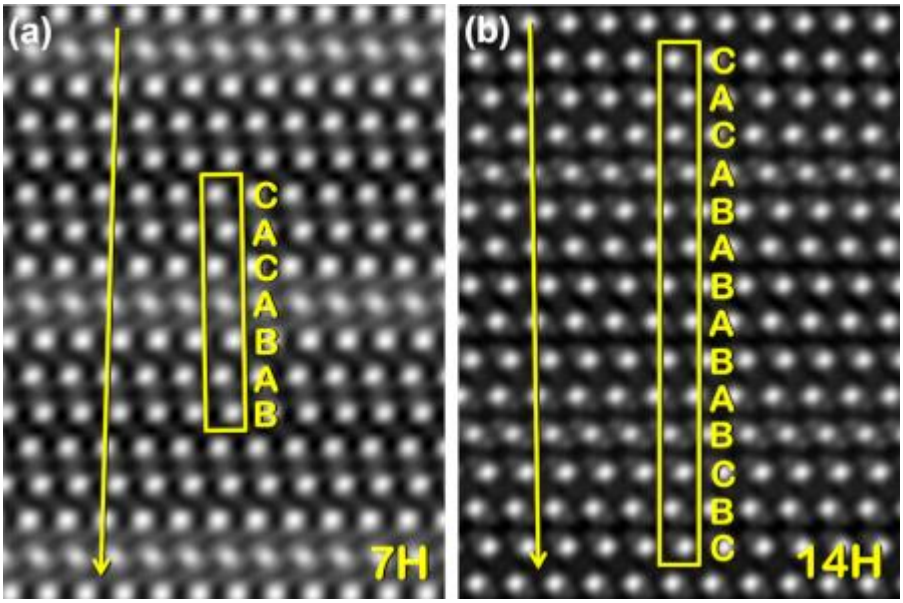

MS4.P001
In situ observation of dynamic reconfiguration of van der Waals interfaces in 2D-bonded Ge-Sb-Te phase-change memory alloys

A. Lotnyk[1], U. Ross[1], T. Dankwort[2], L. Kienle[2], B. Rauschenbach[1]

[1]Leibniz Institute of Surface Engineering (IOM), Leipzig, Germany
[2]Faculty of Engineering, University of Kiel, Kiel, Germany

Ge-Sb-Te phase-change alloys have attracted much attention due to their unique technologically important optoelectronic properties. The high importance of this class of alloys has been recently demonstrated by Intel, which introduced several commercial Optane memory products based on Ge-Sb-Te thin layers. While the conventional phase-change technology uses amorphous-to-crystalline phase transitions, the advanced memory technology is based on the phase changes within of crystalline van der Waals (vdW) bonded superlattices (SLs) (1). However, the switching mechanism in such SLs is still under debate. The proposed models are based on structural reconfigurations of interfaces between individual layers of SLs.

The present work aims to understand the switching mechanism in SLs. To achieve this, structural reconfiguration of vdW interfaces in emerging 2D-bonded Ge-Sb-Te phase-change memory alloys was studied by employing *in situ* atomic-resolution Cs-corrected scanning TEM (2).

Ge-Sb-Te thin films with layered structure were grown by PLD (2). *In situ* experiments were performed by using focused electron beam as a tool for *in situ* manipulation of atomic species in the crystal lattices.

Focused electron beam exposure of GeSb layer next to vdW gap within of a Ge-Sb-Te building block (Fig. 1a) resulted in the reconfiguration of (GeSb)Te bilayers with subsequent formation of a new vdW gap (Fig. 1). The adjacent building blocks reconfigured locally into 4-fold Te and 5-fold Te layered structures, resulting simultaneously in the formation of a (GeSb)Te bilayer defect. Depending on the beam dose, the newly formed vdW gap can either rearrange back to the initial state (Fig. 1) or move in later direction along the vdW interface (Figs. 2). Moreover, a model structure of the bilayer defect frequently reported in similar Ge-Sb-Te layered structures is also proposed (Fig. 2).

The present findings reveal the mechanism of structural reconfiguration of vdW interfaces in Ge-Sb-Te layered alloys (2). The results are relevant for an understanding of switching mechanism in chalcogenide based SLs since similar process of vdW gaps rearrangement has been recently proposed by theoretical calculations as the switching mechanism in SLs (3), supporting the idea of present work.

References:

(1) R.E. Simpson et al., Nat Nanotechnol 6 (2011) 501-505

(2) A. Lotnyk et al., Acta Mater 141 (2017) 92-96

(3) A.V. Kolobov et al., ACS Omega 2 (2017) 6223-6232

We thank Mrs. A. Mill for assistance in the FIB preparation and I. Hilmi for the growth of Ge-Sb-Te thin films.

Fig. 1: *In situ* imaging of reconfiguration of vdW interfaces in a Ge-Sb-Te layered structure under influence of focused electron beam irradiation. HAADF images of (a) initial state, (b) after reconfiguration of Te and GeSb planes and (c) recovery of initial state (a).

Fig. 2: HAADF images: (a) after reconfiguration of vdW interface (similar to Fig. 1b) and (b) motion of vdW gap into lateral direction. (c)-(d) Structure models of (a) viewed along various projections.

Fig. 1

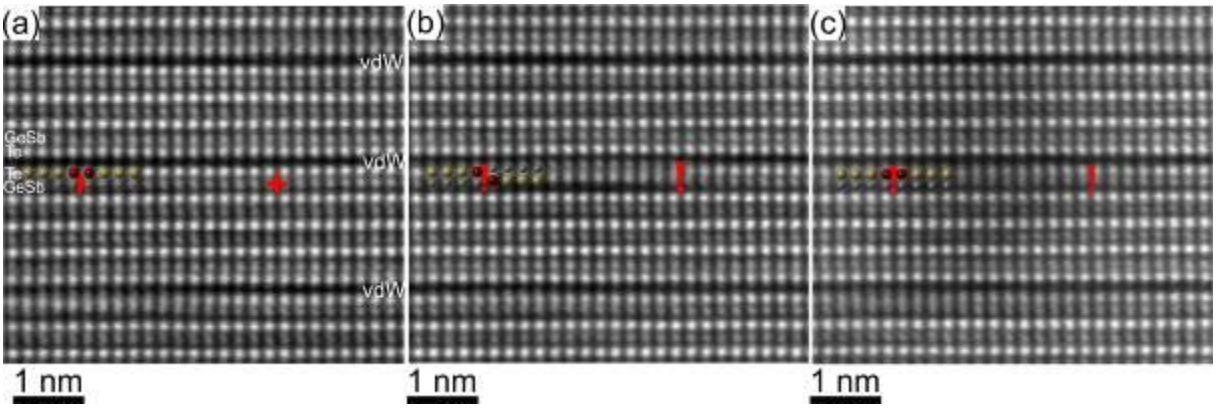
(a)
(b)
(c)
vdW
vdW
vdW
GeSb
Te
Te
GeSb
1 nm
1 nm
1 nm

Fig. 2

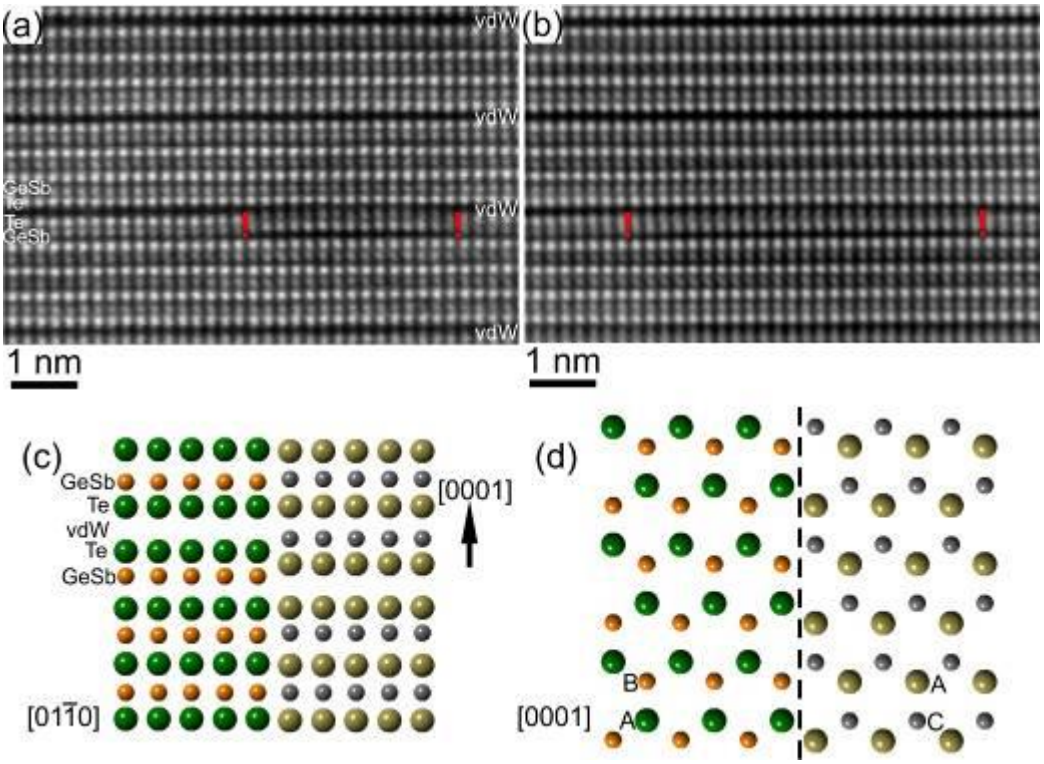
(a)
(b)
vdW
vdW
vdW
vdW
GeSb
Te
Te
GeSb
1 nm
1 nm
(c)
GeSb
Te
vdW
Te
GeSb
[0001]
[01$\bar{1}$0]
(d)
B
A
A
C
[0001]

MS4.P002
Evolution of nm sized, Nb-rich O-phase domains in α_2 lamellae of a γ-TiAl alloy

H. Gabrisch[1], T. Krekeler[2], M. W. Rackel[1], M. Ritter[2], F. Pyczak[1], A. Stark[1]

[1]Helmholtz-Zentrum Geesthacht, Metal Physics, Geesthacht, Germany
[2]Technische Universität Hamburg, Betriebseinheit Elektronenmikroskopie , Hamburg, Germany

Intermetallic gamma-based Titanium aluminides possess high specific strength at elevated temperatures, which qualifies them for structural applications in aircraft engines. For a good balance of mechanical properties the morphology of the main constituents γ (TiAl, tetragonal $L1_2$) and α_2 (Ti_3Al, hexagonal $D0_{19}$) is adjusted to a near lamellar microstructure, where the γ and α_2 phases are aligned parallel to their close packed lattice planes in lamellar (α_2 + γ) colonies. Regarding the chemical composition, Nb is often added for improved creep strength and oxidation resistance (1).

In Titanium-aluminides alloyed with Nb, a displacive transformation takes place within the α_2 phase at temperatures between 450°C and 670°C. The product is the orthorhombic O-phase (Ti_2AlNb, Cmcm) (2). HEXRD investigations of samples annealed for increasing lengths of time at 550°C show that the transformation is ongoing even after 4 weeks. On the other hand, above 700°C the orthorhombic phase re-transforms to the hexagonal α_2 phase that remains stable during cooling to room temperature under air-cooling rates (5-10 K/min). In this study the evolution of O-phase domains with increased annealing time is investigated.

The alloy Ti-42Al-8.5Nb (at.-%) was produced by powder metallurgy. It consists of lamellar (α_2+γ) colonies and is chemically homogeneous (3). Heat treatments were performed at 550°C for annealing times between 8 h and 672 h. TEM specimens were prepared of samples annealed for 8 h, 168 h and 672 h. TEM and HAADF STEM investigations were performed at the Helmholtz-Zentrum in Geesthacht with the Titan 80-300kV and the CM 200 operated at 300 kV and at 200kV, respectively. Atomic resolution HAADF STEM and EDX mapping were employed to characterize the size and elemental distribution within α_2/O-phase lamellae. The atomic resolution HAADF STEM images were obtained at the CNMS, at Oakridge National Laboratory using the Nion UltraSTEM 100 dedicated aberration-corrected STEM at 100 kV. Elemental EDX mapping was performed at the BEEM facility of the Technical University Hamburg using a SuperX detector system attached to an FEI-Talos F200XTEM operated at 200 kV with a probe current of 1 nA.

A comparison of atomically resolved HAADF-STEM images taken after 8 h and after 168 h of annealing shows that orthorhombic distortion is present in lattices of both samples. Additionally, Nb has concentrated in the distorted regions of the lattice after the longer annealing time, see **Fig.1**. After 672 h of annealing the Nb agglomeration has increased and the O-phase domains split into smaller regions. An illustration of the separation of larger O-phase regions into smaller one in given in **Fig. 2**.

These results indicate that the transformation from hexagonal α_2 to orthorhombic O-phase proceeds in at least two steps: the initial distortion of the lattice from hexagonal to orthorhombic without change in chemistry, followed by a segregation of Nb and Al/Ti towards orthorhombic and hexagonal regions of the lattice respectively.

References:

(1) F. Appel et al., Intermetallics 8, 1283 (2000).

(2) H. Gabrisch et al., Acta Materialia 135**,** 304 (2017).

(3) R. Gerling et al., Advanced Engineering Materials 6 1-2, 23(2004).

Fig. 1: Atomic resolution HAADF STEM images taken after 168 h of annealing.

Fig. 2: HAADF STEM images of specimens annealed at 550°C for 168 h (left) and 672 h (right).

Fig. 1

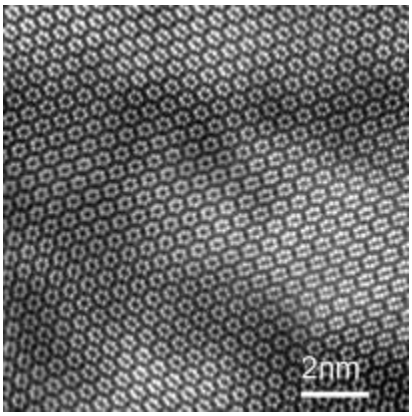

Fig. 2

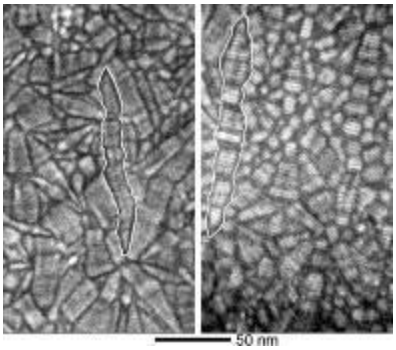

MS4.P003
Precipitation map for Al-Cu-Mg alloy (AA2024)

L. Briez[1,2], M. Sennour[2], V. Esin[2], A. Köster[2], J. Crépin[2], E. Gratiot[1]

[1]Dassault Aviation, Saint-Cloud, France
[2]MINES ParisTech - PSL University, Centre des Matériaux, Evry, France

The commercial 2024 aluminium alloy (AA2024) is one of the most used alloys in aircraft manufacturing for fuselage applications. The range of service temperature is usually considered to be between -55 and 85 °C for service lifetimes up to 20000 hours. AA2024 inherits its mechanical properties from the precipitation of hardening S-Al2CuMg phase obtained through an appropriate heat treatment. A number of different studies have been published so far on the ageing behaviour of AA2024. Particular attention was paid to the precipitation sequence and the evolution of mechanical properties as a function of ageing conditions (1-3). It is well known that the formation of stable S-Al2CuMg phase is preceded by the appearance of Cu-Mg co-clusters, Guinier-Preston-Bagaryatski (GPB) zones as well as different metastable S-phase precursors like S' and S'' (4). Despite the relatively small service temperature range (between -55 and 85 °C), the studies on ageing in AA2024 alloys are often limited to temperatures between 120 and 200 °C and to durations not exceeding 1000 hours. In the present work, differential scanning calorimetry (DSC) analysis and transmission electron microscopy (TEM) observations were combined to analyse the precipitation of Al-Cu-Mg alloy (AA2024) for a wide temperature range from 85 to 250 °C and ageing durations from 1 to 10000 hours. The obtained results are summarised in the precipitation map shown in Fig. 1. Depending on the ageing conditions, the AA2024 can contain the S-phase, GPB zones and co-clusters. These results were confirmed by high-resolution TEM (HRTEM) observations (Fig. 2). The formation of the equilibrium S-phase was observed, for the first time at 85 °C as of 1000 hours of ageing. It is believed that this is due to dislocation-assisted diffusion. Hardness values superposed with the precipitation map reveal that the maximum hardness for all studied temperatures is located at the frontier between S-phase + Guinier-Preston-Bagaryatski (GPB) zones and S-phase regions (Fig. 1).

References:

(1) N.D. Alexopoulos, Z. Velonaki, C.I. Stergiou and S.K. Kourkoulis, Mat. Sci. and Eng. A 700 (2017) p. 457.

(2) M. Prudhomme, F. Billy, J. Alexis, G. Benoit, F. Hamon, C. Larignon, G. Odemer, C. Blanc and G. Hnaff, Int. J. of Fat. 107 (2018) p. 60.

(3) F. Zhang, L.E. Levine, A.J. Allen, C.E. Campbell, A.A. Creuziger, N. Kazantseva and Ilavsky, Acta Mat. 111 (2016) p. 385.

(4) S.C. Wang and M.J. Starink, Int. Mat. Rev. 50 (2005) p. 193.

Fig. 1: Precipitation map for AA2024 initally in T3 state in the temperature range from 85 to 250 °C for ageing durations from 1 to 10000 hours: red squares: S-phase, blue circles: S-phase + GPB zones, orange stars: S-phase + GPB zones + co-clusters, open diamond: GPB zones, green triangles: GPB zones + co-clusters. The numbers represent the measured hardness values. (For interpretation of the references to colour in this figure legend, the reader is referred to the web version of this abstract).

Fig. 2: Observations using HRTEM for samples of AA2024 corresponding to different regions in Fig. 1: (a) initial T3 state (GPB zones + co-clusters), (b) 85 °C for 5000 hours (S-phase + GPB zones + co-clusters), (c) 120 °C for 5000 hours (S-phase + GPB zones) and (d) 200 °C for 100 hours (S-phase). The FFT patterns for the areas of observation are also given for the phase analysis.

Fig. 1

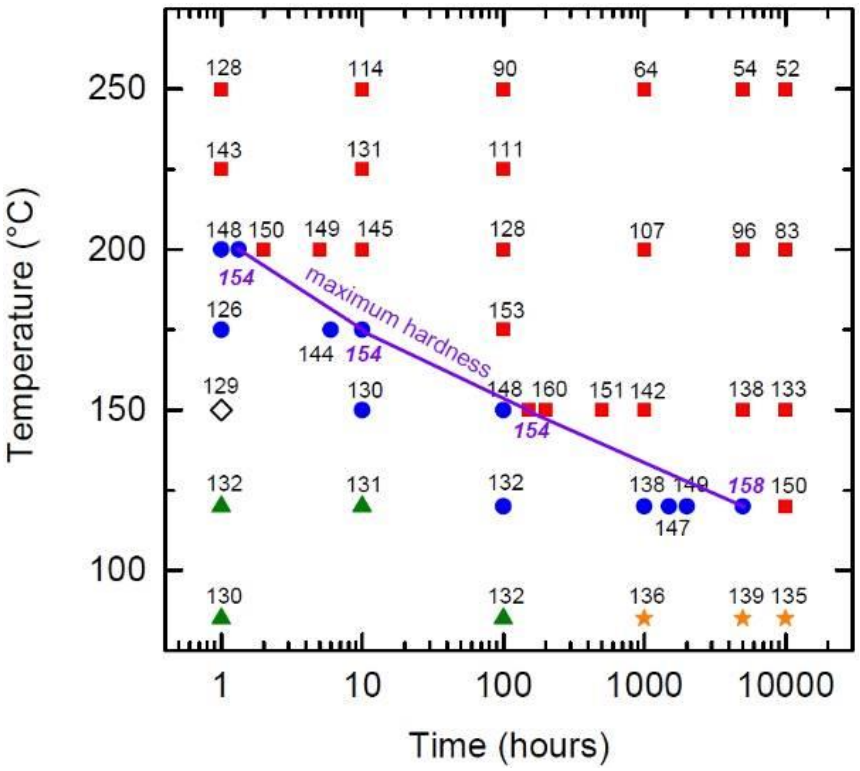
Temperature (°C)
Time (hours)
maximum hardness
250
200
150
100
1
10
100
1000
10000
128 114 90 64 54 52
143 131 111
148 150 149 145 128 107 96 83
154
126 153
144 154
129 130 148 160 151 142 138 133
154
132 131 132 138 149 158 150
147
130 132 136 139 135

Fig. 2

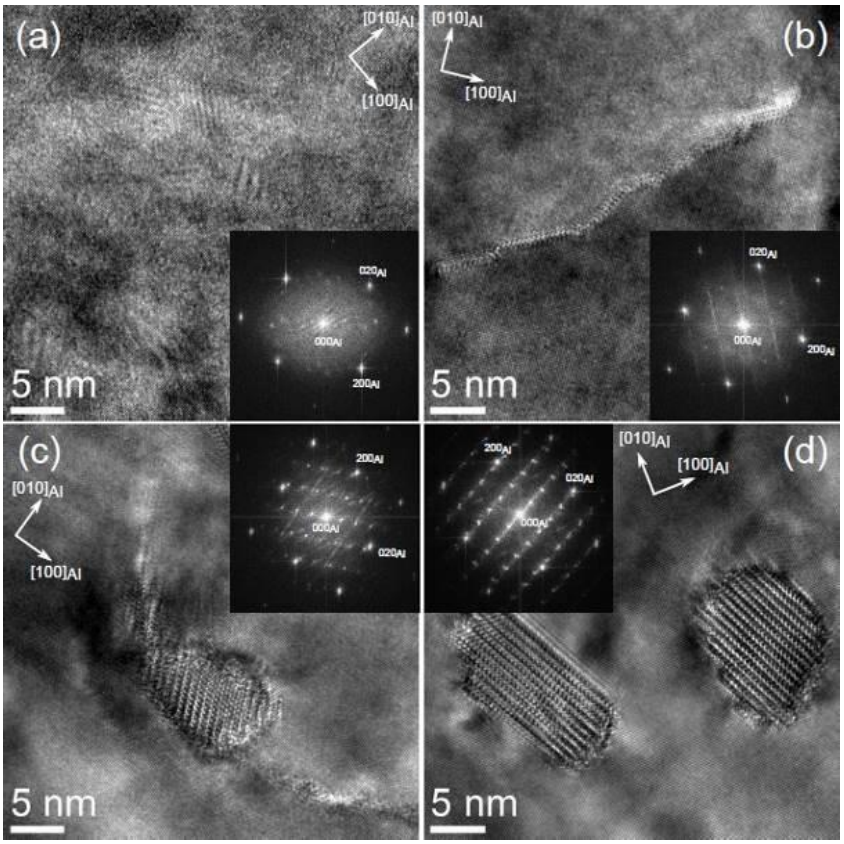
(a)
(b)
(c)
(d)
[010]Al
[100]Al
5 nm
020Al
000Al
200Al

MS4.P004
Crystal structure determination of microcrystalline compounds by the combination of TEM and microfocused synchrotron radiation

D. Günther[1], J. Wright[2], G. Vaughan[2], S. Wendl[3], L. Eisenburger[1,3], W. Schnick[3], O. Oeckler[1]

[1]Universität Leipzig, IMKM, Leipzig, Germany
[2]ESRF- The European Synchrotron, Grenoble, France
[3]LMU München, Chemie, München, Germany

Crystal structure determination of microcrystals has been a challenging task in crystallography for a long time. It can be tackled by powder diffraction or electron microscopy, but due to reflection overlap and dynamical diffraction, respectively, and many experimental limitations, it is still difficult to obtain precise structural parameters. Precession electron diffraction,(1) rotation electron diffraction,(2) and diffraction tomography (3) brought significant progress but have not reached the possibilities of X-ray crystallography. The advent of X-ray compound refractive lenses provides extremely brilliant synchrotron beams with diameters of several hundred nanometers (4). Yet, conventional crystal selection does not provide efficient access to single crystals of such small dimensions that could exploit the full potential of such beams. This can be done effectively by transmission electron microscopy, where EDX analyses easily detect the desired compositions and electron diffraction can confirm that the unit-cell metrics correspond to an unknown substance. The crystallites" positions on finder grids are documented so that the pre-characterized crystallites can be recovered relative to the grid at the synchrotron beamline using a telescope with large magnification. Precise centering is achieved by X-ray fluorescence scans while moving the TEM grid in different directions and by observing the intensity of diffraction patterns. Therefore the sample is scanned linearly while detecting fluorescence.

The efficiency of this method was first shown for $Pb_8Sb_8S_{15}Te_5$ (5). It has later been successfully applied to samples from very different classes of compounds, e.g. $AlP_6O_{3x}(NH_3)_{3-3x}$ and $La_3BaSi_5N_9O_2$.(6,7) As new examples, we present the crystal structures of $BaHP_6N_{11}$ and BaP_8N_{14}. Due to extreme conditions during their syntheses (4-6 GPa; 1000-1200 °C), only small crystals could be obtained. Data evaluation revealed new crystal structure types built up from vertex-sharing PN_4 tetrahedra, Crystal structure refinements demonstrate unprecedented precision and excellent data quality significantly better than in routine X-ray crystal structure analyses. For example, the refinement of BaHP6N11 yielded R1 = 0.0228 for 3926 reflections and 56 parameters up to a resolution of 0.6 Å.

We thank the Deutsche Forschungsgemeinschaft DFG (grants OE530/6-1 and SCHN 377/18-1) for funding and the ESRF, Grenoble, for granting beamtime in several projects.

References:

(1) P. A. Midgley, A. S. Eggemann, *IUCrJ* 2015, *2*, 126-136.

(2) D. Zhang, P. Oleynikov, S. Hovmöller, X. Zou, *Z. Kristallogr.* 2010, *225*, 94-102.

(3) U. Kolb, E. Mugnaioli, T. E. Gorelik, *Cryst. Res. Technol.* 2011, *46*, 542-554.

(4) G. B. M. Vaughan, J. P. Wright, A. Bytchkov, M. Rossat, H. Gleyzolle, I. Snigireva, A. Snigirev, *J Synchrotron Radiat* 2011, *18*, 125-133.

(5) F. Fahrnbauer, T. Rosenthal, T. Schmutzler, G. Wagner, G. B. M. Vaughan, J. P. Wright, O. Oeckler, *Angew. Chem. Int. Ed.* 2015, *54*, 10020-10023.

(6) L. Neudert, F. Heinke, T. Bräuniger, F. J. Pucher, G. B. Vaughan, O. Oeckler, W. Schnick, *Chem. Commun.* 2017, *53*, 2709-2712.

(7) D. Durach, L. Neudert, P. J. Schmidt, O. Oeckler, W. Schnick, *Chem. Mater.* 2015, *27*, 4832-4838.

MS4.P005
Dislocation movement in a 14%Cr ODS steel studied by in-situ TEM straining experiments

K. Vogel[1], F. Röder[2], C. Heintze[1]

[1]Helmholtz-Zentrum Dresden-Rossendorf, Institute of Resource Ecology, Dresden, Germany
[2]Technische Universität Dresden, Fakultät Physik, Dresden, Germany

In-situ TEM straining experiments are a powerful tool to observe deformation processes at the nanoscale. This is of great interest for oxide dispersion strengthened (ODS) alloys, where the strengthening is caused by pinning of dislocations at very small (<10nm) oxide particles. Here we will report on in-situ TEM straining experiments performed with a 14%Cr ODS steel in order to directly observe the movement of dislocations and to investigate their interaction with nanoscale oxide particles.

The 14%Cr ODS steel was prepared at Centro Sviluppo Materiali, Italy, using powder metallurgical techniques including mechanical alloying and hot extrusion (more details are given in reference (1). After heat treatment at 1050°C, mini tensile test specimens of 11.5mm x 2.5mm x 0.1mm were prepared by spark erosion, grinding and electrolytic jet polishing. The in-situ straining experiments were performed at room temperature in a FEI Talos F200X TEM using a Gatan single tilt straining holder. During straining, video sequences were acquired with a 16-megapixl CMOS camera (FEI Ceta 16M). In order to achieve a high time resolution and a sufficient field of view to follow the dislocation movement, we chose a short exposure time of 0.1 seconds and a medium magnification of 22.5 kx limiting the spatial resolution to a few nanometers (objective lens on). Additionally, the quality of the images is reduced due to large aberrations caused by the uncontrollable magnetic field emerging from the extensive volume of the magnetic specimen.

During straining, the movement of dislocations within a relatively large grain of about 1.5µm diameter was recorded. In the beginning of the experiment, a number of dislocation lines was visible, several of these dislocation segments started moving under straining. In some cases, it was possible to observe pinning of a dislocation at small particles, bowing of the dislocation line under the applied stress and finally unpinning of the dislocation (figures 1 and 2). These observations are in agreement with the results of in-situ TEM straining experiments by Malaplate (2) and Praud (3) performed with two different ODS steels of similar composition. The next steps of our work will include the determination of the Burgers vectors of the moving dislocations and the optimization of specimen preparation.

References:

(1) A. Das et al., Journal of Nuclear Materials 497 (2017) 60.

(2) J. Malaplate et al., Journal of Nuclear Materials 417 (2011) 205.

(3) M. Praud et al., Journal of Nuclear Materials 428 (2012) 90.

We thank Michaela Roßner and Mario Houska for preparation of the in-situ straining TEM specimens. The use of the HZDR Ion Beam Center TEM facilities and the support by its staff is gratefully acknowledged. In particular, we thank Dr. Rene Hübner, and we acknowledge the funding of TEM Talos by the German Federal Ministry of Education and Research (BMBF), Grant No. 03SF0451 in the framework of HEMCP.

Fig. 1: Dislocation movement during in-situ straining TEM of a 14%Cr ODS steel. Figures (a) to (f) are selected images from a video sequence showing the movement of two dislocations D1 and D2 initially pinned at small particles P1, P2 and P3.

Fig. 2: Pinning/unpinning of a moving dislocation. (a) Dislocation D is pinned at points 1, 2 and 3. (b) The dislocation is unpinned from point 2, but still pinned at points 1 and 3. (c) Difference of (a) and (b) showing in white the initial position and in black the final position of dislocation D.

Fig. 1

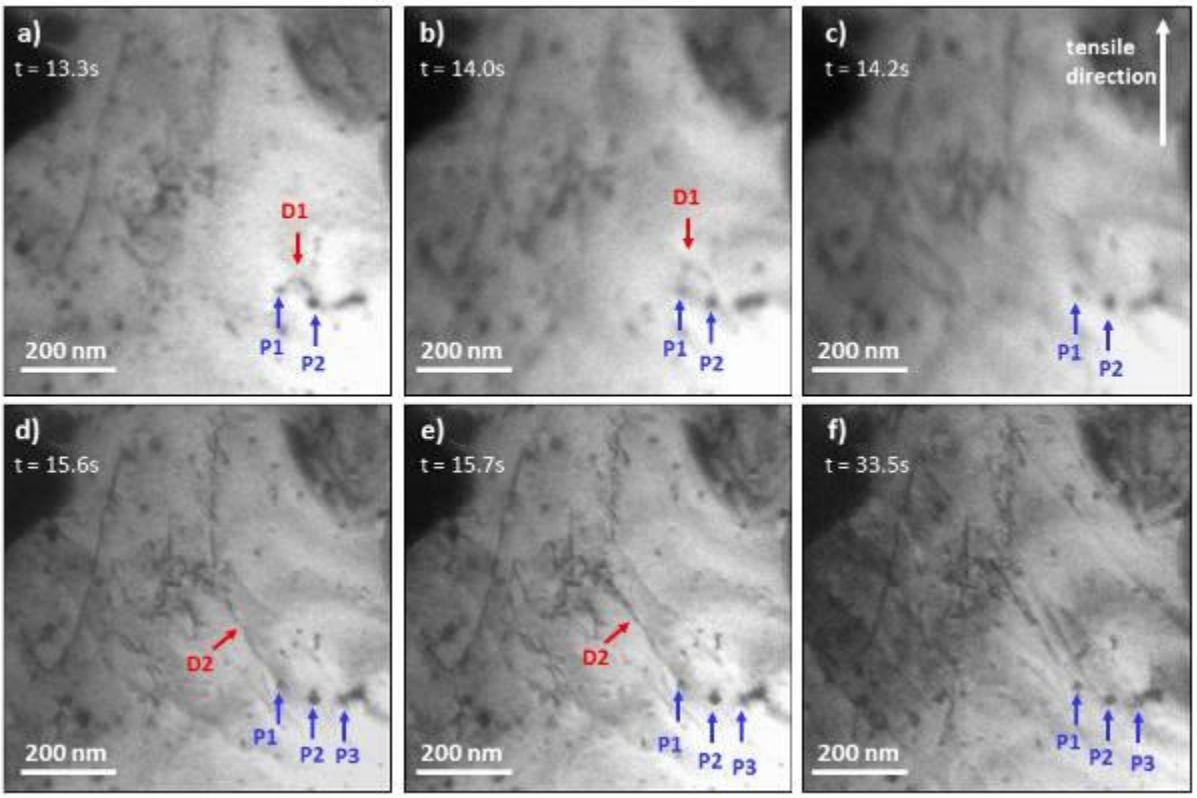
a)
t = 13.3s
D1
P1
P2
200 nm
b)
t = 14.0s
D1
P1
P2
200 nm
c)
t = 14.2s
tensile direction
P1
P2
200 nm
d)
t = 15.6s
D2
P1
P2
P3
200 nm
e)
t = 15.7s
D2
P1
P2
P3
200 nm
f)
t = 33.5s
P1
P2
P3
200 nm

Fig. 2

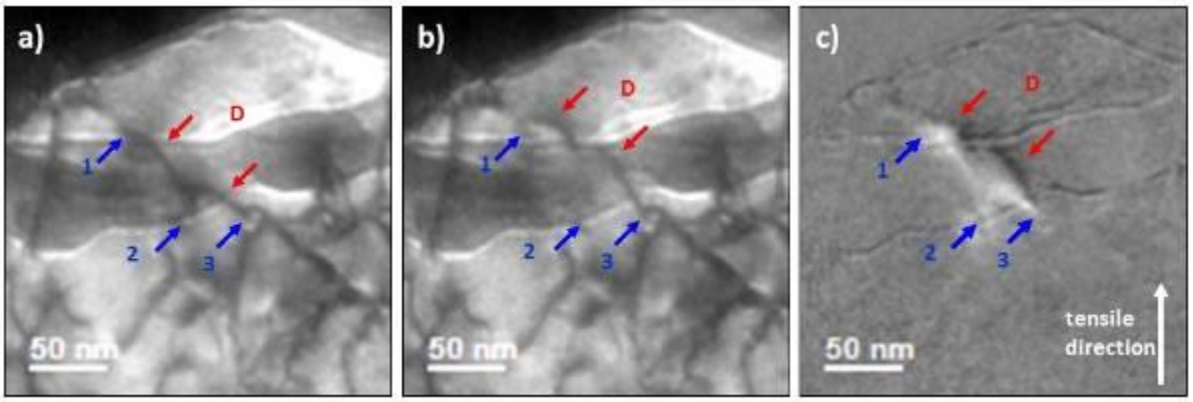
a)
D
1
2
3
50 nm
b)
D
1
2
3
50 nm
c)
D
1
2
3
50 nm
tensile direction

MS4.P006
Defects structures in UBe_{13} superconductor

I. Zelenina[1], P. Simon[1], A. Amon[1], M. Bobnar[1], M. Naumann[2], E. Svanidze[1], F. Arnold[1], H. Borrmann[1], U. Burkhardt[1], W. Schnelle[1], E. Hassinger[2], A. Leithe-Jasper[1], Y. Grin[1]

[1]Max Planck Institute for Chemical Physics of Solids, Dresden, Germany
[2]Technische Universität München, Physik Department, Garching, Germany

The influence of Al incorporation on the heavy fermion superconductor UBe13 was investigated to explain the sample dependence of physical properties (1). Clear evidence for incorporated Al in flux-grown UBe13 single crystals is presented by results from X-ray diffraction, NMR and X-ray spectroscopy. The increase of the lattice parameter and the concomitant change of the superconducting properties are caused by substitution of Be by 1 - 2 at. % Al. Furthermore, it was possible to locate the minute amounts of Al in the structure by atomic resolution transmission electron microscopy. Specific heat measurements reveal the strong influence of incorporated Al on the physical properties of UBe13. Upon long-term annealing, Al incorporated in single crystals can leave the structure, restoring properties of Al-free polycrystalline UBe13.

Figure 1. HR-TEM of a UBe13−xAlx single crystal in (a) as-grown condition: [110] zone, (b) after 38 d annealing: [100] zone, (c) after 76 d annealing: [100] zone. Al atoms are exemplarily highlighted by red circles, Be vacancies by green arrows. The idealized crystal structure is overlaid at the right hand side of the panels. Insets in (a,b) show simulation of Al substituting Be2. Inset in (c) shows simulation of a Be2 vacancy.

References:

(1) A. Amon, I. Zelenina, P. Simon, M. Bobnar, M. Naumann, E. Svanidze, F. Arnold, H. Borrmann, U. Burkhardt, W. Schnelle, E. Hassinger, A. Leithe-Jasper, Y. Grin, Tracking aluminum in UBe13 single crystals. *Sci. Rep.* 8, 10654 (2018)**.**

Fig. 1

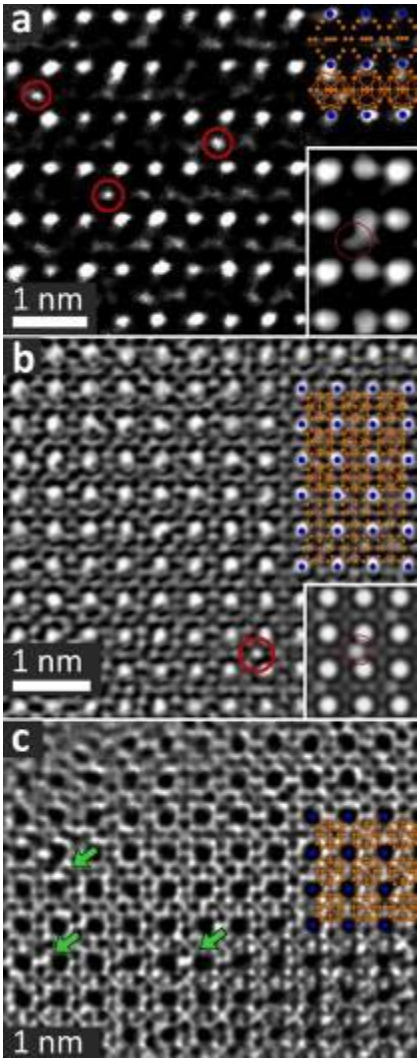

MS4.P007
Epitaxial recrystallization of 3D-bonded metastable Ge-Sb-Te based phase-change materials by single ns-laser pulse irradiation

M. Behrens[1], A. Lotnyk[1], J. W. Gerlach[1], B. Rauschenbach[1]

[1]Leibniz Institute of Surface Engineering (IOM), Leipzig, Germany

In today"s computer systems there is a big performance gap between memory technologies, such as Dynamic Random Access Memory and storage technologies, such as Solid-State Disks based on NAND Flash. This bottleneck becomes particularly evident in data-centric tasks like application of artificial intelligence or analyses of social networks. A promising contender bridging this access-time gap is the phase-change random access memory (PRAM) which recently developed to a mature technology with the entrance of Intel"s Optane chips to the market. However, there is still plenty of room for further development of PRAM. In particular, the employed phase-change material, which is reversibly switched between its crystalline and amorphous state by electrical or optical pulses is not yet fully understood. Therefore, besides the development of novel PRAM cell concepts and material compositions, fundamental investigations of basic structural transitions are of great importance.

The objective of this work is to employ epitaxially grown thin films of phase-change materials in optical switching experiments in order to gain access to the subtleties of structural transitions.

In this work, the chalcogenide compound Ge2Sb2Te5 (GST) is used as a prototypical phase-change material. By employing pulsed laser deposition, epitaxial GST thin films are prepared in the thermodynamically stable trigonal phase. This phase exhibits an intrinsic quasi 2D character indicated by Van-der-Waals bonded rocksalt-type building blocks resulting in a 2D-bonded layered structure (1). In order to provoke optical induced phase transitions, single ns-laser pulses were applied to the GST thin films. The structural changes were followed by high-angle annular dark field (HAADF) high-resolution scanning transmission electron microscopy measurements which were performed before and after ns-laser irradiation.

The results reveal a single ns-laser pulse induced partial transition of the initial 2D-bonded layered crystalline structure to the 3D-bonded crystalline structure of the metastable phase of GST via a transient molten phase (2). Remarkably, the recrystallized 3D-bonded structure obeys an equivalent orientation like the remaining 2D-bonded layered structure. Consequently, the ns-laser pulse irradiation induces an ultrafast epitaxial recrystallization process from the melt where an untransformed part of the thin film serves as a template for crystal growth.

In conclusion, the presented work offers useful insights into the mechanisms of solid-melt interface formation on ns-timescale. Moreover, the results suggest the use of epitaxial phase-change materials in order to increase memory writing times by bypassing the stochasticity of nucleation through ultra-fast crystal growth via stable 2D templates.

References:

(1) Acta Crystallogr. Sect. B-Struct. Sci., 2004, 60, 685-691.

(2) Nanoscale, 2018, 10, 22946-22953.

Fig. 1: *Left:* HAADF image of a GST thin film before ns-laser pulse irradiation, showing the Van-der-Waals bonded layered structure. *Right:* HAADF image of the thin film after ns-laser pulse irradiation, showing the interface between the initial 2D-bonded structure and the ns-laser pulse recrystallized 3D-bonded structure.

Fig. 1

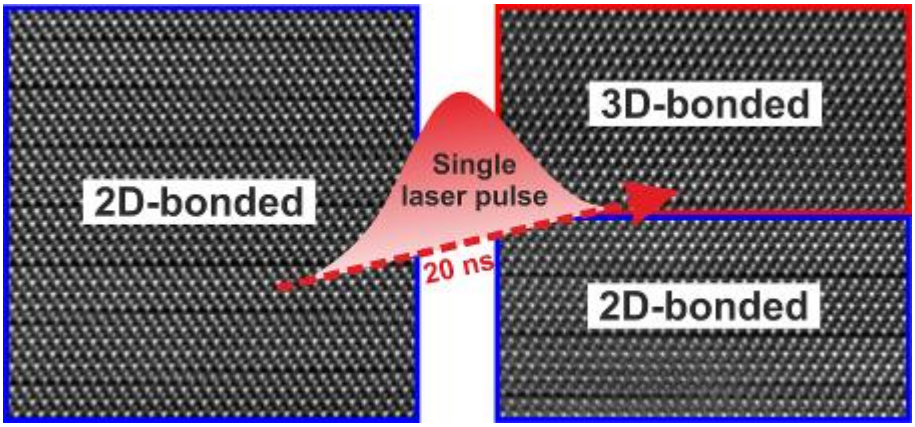

MS4.P008
Analytical STEM characterization of new 9% Cr reduced-activation ferritic-martensitic steels

M. Duerrschnabel[1], J. Hoffmann[1], M. Rieth[1]

[1]Karlsruhe Institute of Technology, Institute for Applied Materials, Eggenstein-Leopoldshafen, Germany

Highly stressed components of future fusion reactors demand for materials like reduced activation ferritic-martensitic (RAFM) steels that can withstand high neutron doses at elevated temperatures keeping their excellent mechanical properties e.g. hardness, creep resistance and strength. A key factor to ensure this is to optimize the composition and the distribution of nano-sized precipitates via optimization of the alloying process and the thermo-mechanical treatment (TMT).

Our objective was to determine size and spatial distribution as well as composition of different precipitates in these EUROFER-97 derived compounds. The microstructural results will be related with mechanical properties in structure-property relationships.

4 samples with slightly different elemental composition summarized in Table 1 were produced by OCAS NV, Belgium. The TMT was carried out similar to (1). TEM samples were prepared by electrochemical etching and analyzed in a Thermofisher Talos F200X scanning transmission electron microscope (STEM) equipped with a SuperX G2 energy-dispersive X-ray (EDX) detector and a Enfinium electron energy-loss (EEL) spectrometer. The grain size was determined by applying a threshold value in STEM-EDX mappings and measuring Feret"s diameter from the resulting binary images.

References:

(1) Hoffmann et al., JNME 16 (2018), pp. 88-94.

(2) Klimenkov et al., JPNUCENE, 57 (2012), pp. 8-13

Table 1: Chemical analysis of the alloys.

Fig. 1: STEM-EDX mappings of all 4 samples.

Fig. 2: Particle size distribution of carbide ($M_{23}C_6$) and nitride (MX) type precipitates. The data was determined from STEM-EDX mappings.

STEM-EDX analysis revealed that in the present sample batch only two types of precipitates seem to exist, namely $M_{23}C_6$ and MX. Furthermore, it was found that M=Cr,Fe,W in the carbide precipitates and that M=V,Ta,Ti in MX-type particles. X was found to be N in all 4 samples. Sample K473 was the only one with significant Ti precipitation acting as nucleation point for further nitride phases, i.e. (V,Ta)N. The $M_{23}C_6$ precipitates, which have a mean grain size of 100-300 nm are located at lath boundaries and are often decorated by smaller MX-type precipitates, which have a grain size that is by factor 2-3 lower. Isolated TaC precipitates or VN/TaC particle agglomerations as reported in former studies (2) were not observed. Moreover, we found that composition K473 yielded the smallest grain sizes and highest particle densities in both the $M_{23}C_6$ and the MX-type precipitates, whereas the largest grain sizes and lowest particle densities were observed in sample K468. The crystal structure of both type precipitates was checked by high-resolution phase contrast imaging and by analyzing the electron near edge fine structure (ELNES) of the C-K and the N-K edge, respectively. The experimental ELNES is in agreement with FeFF and WIEN2k simulations of VN and $Cr_{23}C_6$, respectively. In some cases, STEM-EDX revealed single MnS nanoimpurities.

This work has been carried out within the framework of the EUROfusion Consortium and has received funding from the Euratom research and training programme 2014-2018 under grant agreement No 633053. The views and opinions expressed herein do not necessarily reflect those of the European Commission. The authors thank the group of Dr. Bergfeldt for the chemical analysis and K. Kaleta for TEM sample preparation.

Table 1

	K465	K468	K473	K476
Element	at. %	at. %	at. %	at. %
Fe	bal.	bal.	bal.	bal.
Cr	9.844	9.984	10.030	10.190
C	0.468	0.380	0.380	0.373
Mn	0.436	0.017	--	0.016
V	0.202	0.207	0.230	0.231
Ti	0.000	0.000	0.033	--
N	0.175	0.103	0.061	0.104
W	0.327	0.348	0.352	0.455
Ta	0.031	0.030	0.033	0.031

Fig. 1

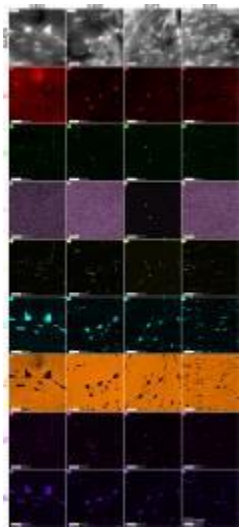

Fig. 2

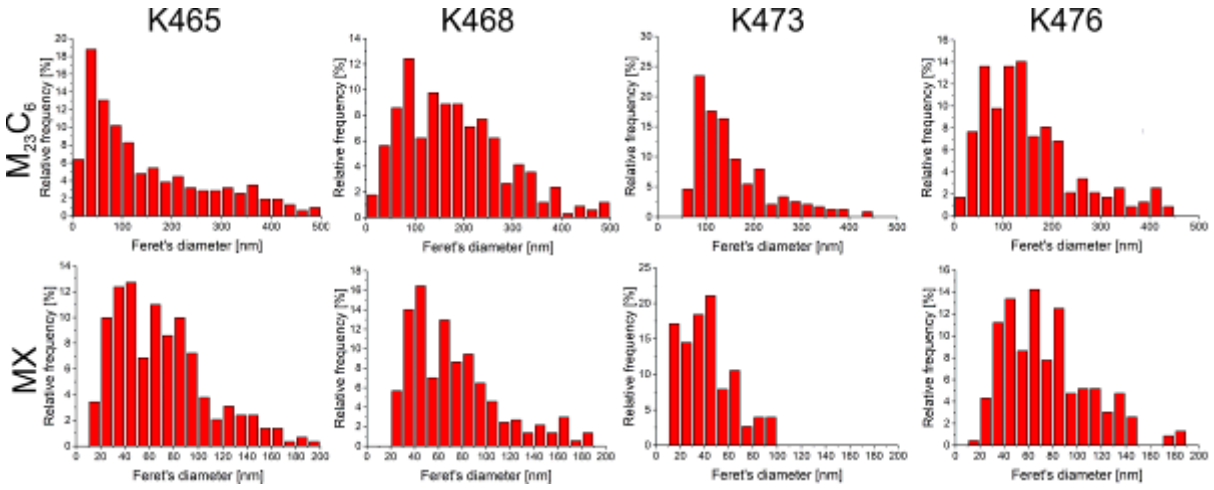

MS4.P009
Annealing behavior of cold rolled AKS-doped tungsten sheets studied by electron microscopy

M. Duerrschnabel[1], P. Lied[1], A. Hoffmann[2], J. Reiser[1]

[1]Karlsruhe Institute of Technology, Institute for Applied Materials, Eggenstein-Leopoldshafen, Germany
[2]Plansee SE, Reutte, Austria

W is the metal with the highest melting point of all metals and exhibits an outstanding performance in e.g. high-temperature strength, creep resistivity, and form stability. Possible high-temperature applications are e.g. in plasma facing components of future thermonuclear or solarthermal power plants, and chemical reaction vessels. Therefore, it is necessary to manufacture components on a larger scale like sheets, tubes etc. However, applications of technical pure W are limited by its recrystallization behavior. Doping by elements like Al, K and Si (AKS) improve e.g. the recrystallization behavior significantly. Intensive microstructural investigations on W lamp wires have already been carried out for decades, however, on technical relevant sheets such data is still missing.

Our objectives were:

- Determination of nanostructure and composition of single nanoinclusions (NI) in dependence on the annealing temperature
- Interaction of these NI with crystal defects like e.g. grain boundaries
- Possible effects of a high energy electron beam on the NI

The samples were manufactured by Plansee SE and the used parameters were similar to those used by Bonk et al. (1). After sintering and cold rolling, the final thickness of our analyzed sheets was 50 µm and about 60 ppm of K, 5 ppm of Si and 20 ppm of Al were contained in the samples. Afterwards samples were annealed in the range from 700°C-2400°C in H2 atmosphere.

TEM samples were prepared by electrochemical etching and analyzed in a Thermofisher Talos F200X scanning transmission electron microscope (STEM) equipped with a SuperX G2 energy-dispersive X-ray (EDX) detector.

In Figure 1 STEM-HAADF images were acquired in a sample annealed at 1400°C at different magnifications in order to reveal the grain structure and the NI size and distribution. Figure 2 shows STEM-EDX mappings at different annealing temperatures in order to determine the elemental distribution and composition of the NI at different annealing temperatures.

It was shown that in dependence of the annealing temperature the NI have a different form. Below 800°C they have an elongated form, which is typically 200-500 nm long and about 100 nm wide. At temperatures of 800°C a break-up via a Rayleigh-type process was observed that was completed at 1400°C. Then the NI had a circular form, but also faceted ones were observed. By STEM-EDX we determined that the NI consist of a Al-rich core and a K-rich shell up to temperatures of 1800°C. Beyond that temperature, most of the Al was removed from the inclusions. O was always present in the inclusions. Furthermore, we observed that an intense electron beam causes elemental redistribution within the inclusions. We found that Zener pinning of e.g. grain boundaries occurs at these inclusions, which hampers recrystallization and improves mechanical properties e.g. micro hardness.

References:

(1) Bonk et al. IJRMHM 60 (2016) pp. 92-98.

This work has been carried out within the framework of the EUROfusion Consortium and has received funding from the Euratom research and training programme 2014-2018 under grant agreement No 633053. The views and opinions expressed herein do not necessarily reflect those of the European Commission.

Fig. 1: STEM-HAADF images of a W sheet annealed at 1400°C on different length scales.

Fig. 2: STEM-EDX mapping of NI at different annealing temperatures.

Fig. 1

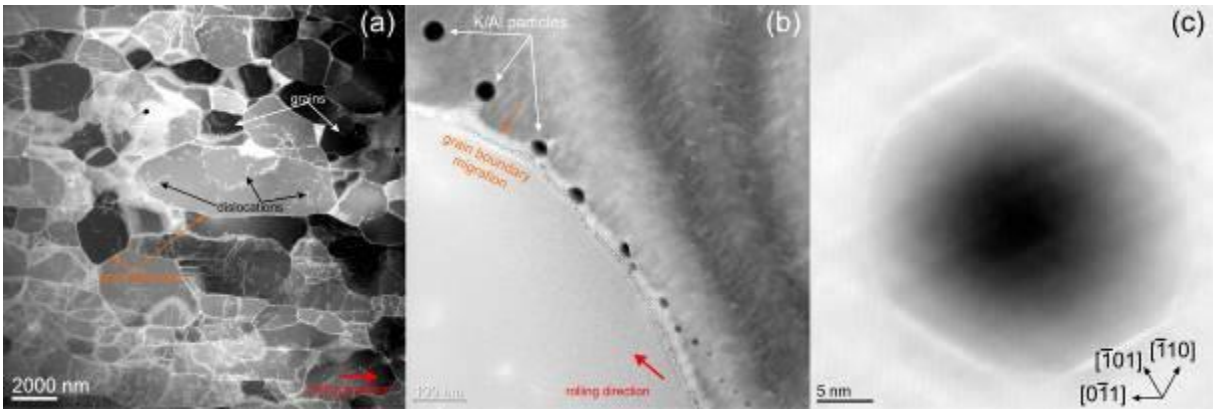
(a)
grains
dislocations
2000 nm
(b)
K/Al particles
grain boundary migration
rolling direction
(c)
5 nm
[$\bar{1}$01]
[$\bar{1}$10]
[0$\bar{1}$1]

Fig. 2

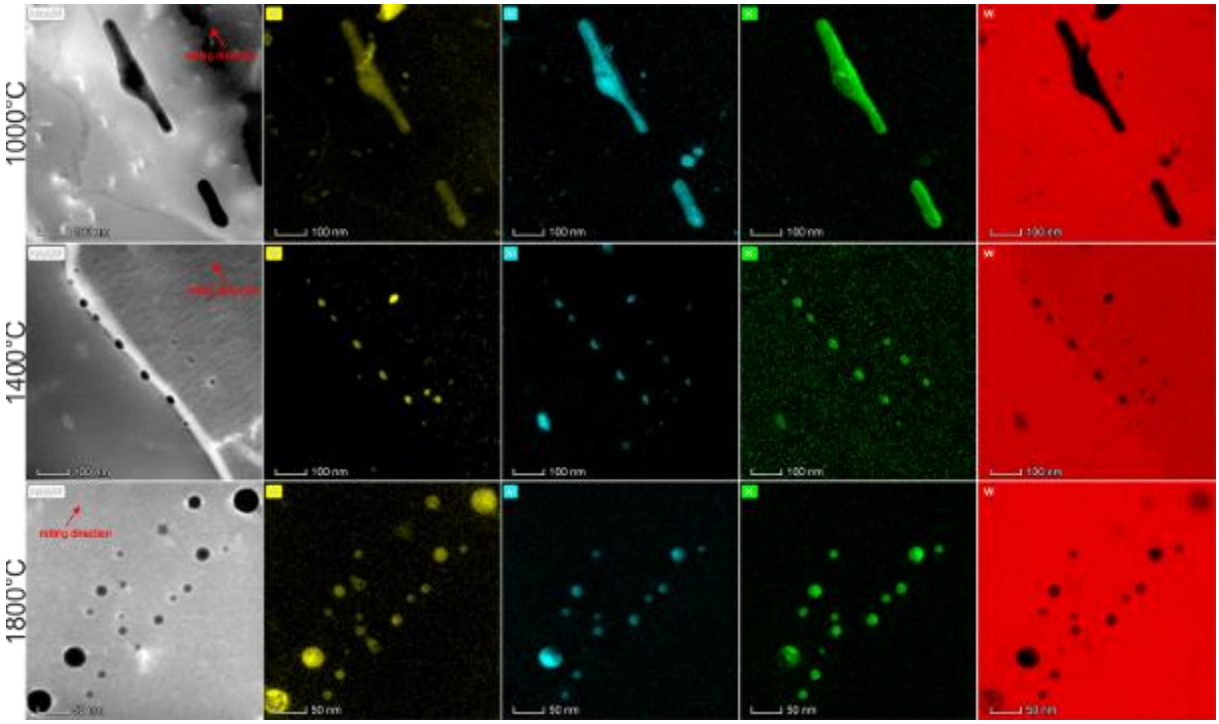
1000°C
1400°C
1800°C
rolling direction
100 nm
50 nm

MS4.P010
Microstructural evolution of the high entropy alloy CoCrFeMnNi during low cycle fatigue

D. Litvinov[1], J. Aktaa[1]

[1]Karlsruhe Institute of Technology, Eggenstein-Leopoldshafen, Germany

Microstructural characterization of the high entropy alloy CoCrFeMnNi before and after low cycle fatigue (LCF) at room temperature was carried out by transmission (TEM) and scanning (SEM) electron microscopy. For the determination of the actual composition, an energy-dispersive X-ray (EDX) spectroscopy was used. For the crystallographic investigations, conventional TEM with selected area diffraction was applied. The TEM samples after the LCF test were prepared by electrochemical thinning parallel to the loading direction.

The SEM overall view of the fracture surface observed after LCF is shown in Fig. 1. In macro view, semicircular lines that are perpendicular to the crack growth direction (dashed arrows) are observed. In macro view and in magnified image in insert we see that the lines are steps like facets (marked by solid arrows). The short lines (or facets) are more or less parallel. The distance between facets increases with the distance to the identified initiation site of the fatigue crack (bottom of SEM image). EDX maps from rectangle white area in insert reveals Cr-O round particles on the fracture surface. The quantitative SEM EDX analysis shows almost homogeneous distribution of the constituting elements (Co, Cr, Fe, Mn and Ni) over the long scale of the samples with a concentration of 20 ± 3 at % of each element.

Fig. 2 shows a comparison of TEM images of samples before and after LCF. As revealed by the diffraction pattern (not presented here), the investigated samples have face centered cubic structure (FCC). The sample before LCF (Fig. 2a) contains large grains with sizes up to 10 µm with very small dislocation (D) density. There are many grains without apparent dislocations. Some grains have dislocations with a density up to 10^{12} m^{-2}. The sample contains many small and long twins (TW). Moreover, many large grains have twin boundaries between themselves. The twin boundaries are arranged in {111} planes, what is typical for FCC structure. In comparison with Fig. 2a, in the sample after LCF (Fig. 2b) we observe much more dislocations with very high density as well as more twins inside many grains. The dislocations have a tendency to pile-up close to defect sites, e.g. grain boundaries. The twins are arranged in {111} planes. The damage during LCF probably initiates when a critical density of twins is achieved in the sample and propagates along twin boundaries. This might be explain why we observe the facets on the crack surface, as observed in Fig. 1, which are formed due to the high density of the additional twins. It is also noticeable, that the fatigue crack initiates in the region (bottom of Fig. 1) with extremely high twin density.

Fig. 1: SEM fracture surface image of specimen after LCF. In insert is magnified SEM image with EDX maps from rectangle white area. Dashed arrows show directions of the fracture. The steps on the surface are indicated by solid arrows.

Fig. 2: Bright-field TEM images of samples before (a) and after (b) LCF. By D indicated dislocations, TW - twins.

Fig. 1

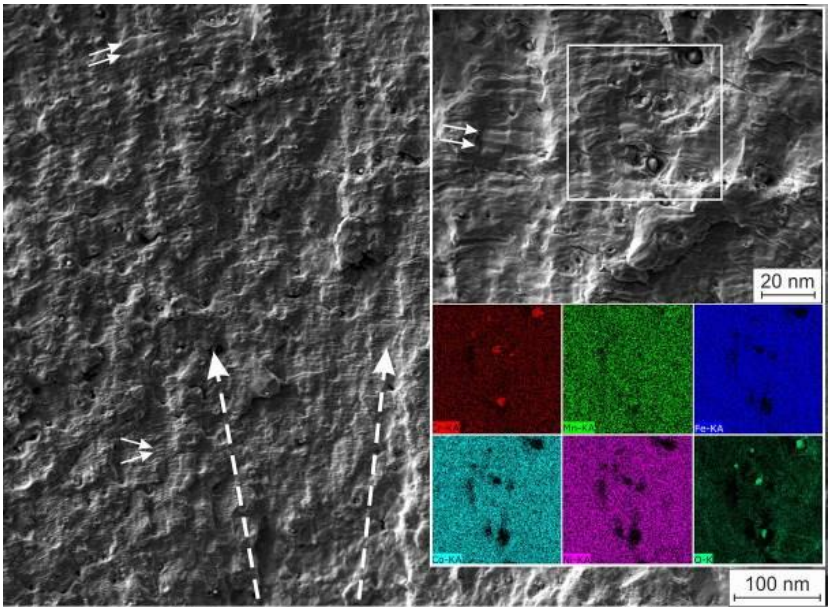

Fig. 2

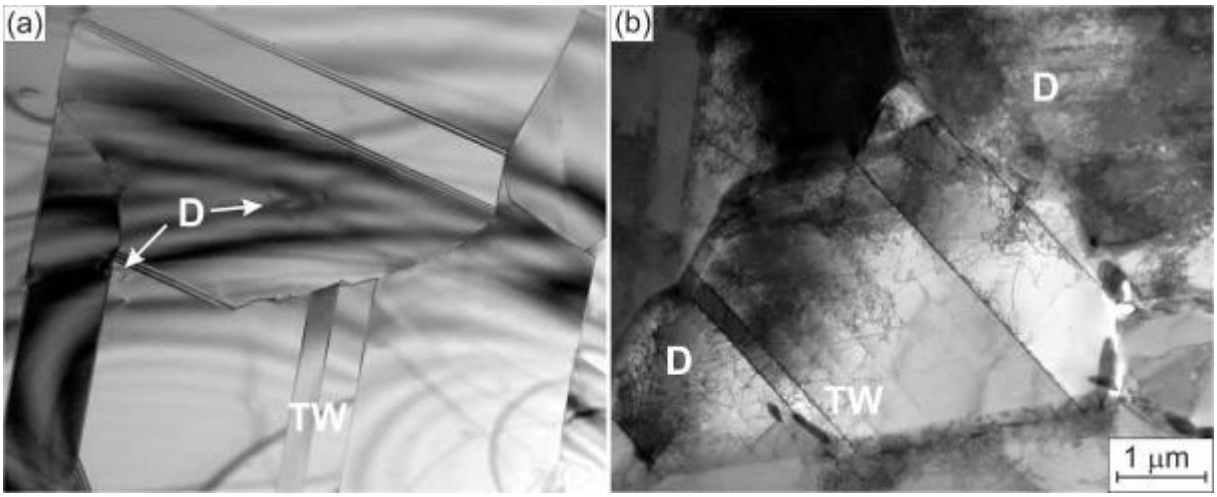

MS4.P011
Microstructures of Additive-Manufactured Metals Observed by Electron-Channelling Contrast Imaging

M. Godec[1], S. Zaefferer[2], Ļ Donik[1], E. Chernyshova[1,3]

[1]Institute of Metals and Technology, Ljubljana, Slovenia
[2]Max-Planc Institute for Iron Research, Duesseldorf, Germany
[3]National Institute of Chemistry, Ljubljana, Slovenia

In the past decade, additive manufacturing (AM) has become an increasingly established way of making not only prototypes, but also small-sized functional products. The advantages of different AM techniques are the high degree of design freedom and resource efficiency compared to conventional processes, thus enabling a tool-free manufacturing of highly complex components. Consequently, these technologies offer great opportunities to meet the increasing demand for an individual, resource-efficient production of complex parts.

The development of the metal microstructure of selective-laser-melted built parts can be significantly influenced by changing several process parameters, such as laser power, laser scanning speed, hatching strategy, powder size, and powder layer thickness. These parameters influence the shape and size of the laser-induced melt pool and also the localized heating and cooling, causing a thermal history of the deposition and influencing the microstructure development. On the other hand, through proper control of the deposition parameters direct microstructure manipulation is feasible. Depending on the AM process, parameters and material, the microstructures of the built parts are generally columnar in the building direction and declined towards the heat-transfer direction. Rapid melting and solidification cause the formation of a non-equilibrium solidification fine-grained microstructure with a large quantity of crystal defects in the AM built parts. Consequently, their mechanical properties are comparable to, if not even better than, those of products that are cast or forged, again greatly depending on the AM parameters. Rapid melting and subsequent solidification cause the formation of non-equilibrium environments in the melt-pool regions. This promotes the development of the fine microstructure and the appearance of a large number of dislocations.

By using electron-channelling contrast imaging (ECCI), which is an imaging technique in scanning electron microscopy based on electron channelling and applying a backscatter-electron detector, we were able to observe dislocations in additive-manufactured material. In the microstructures a lot of internal boundaries and a sub-grain structure were found, which form a kind of hierarchical structure. The cell structure is, in three dimensions, well-ordered nanotubes, the walls of which are dislocations. The results are shown on stainless steel, maraging steel, Inconel 718 and Inconel 625. The microstructures were correlated with the mechanical properties and some explanations were proposed to explain specific mechanical properties.

MS4.P012
Metallic sample preparation for advance investigation of crystallographic information with TEM and SEM

J Donik[1], M. Godec[1], S. Zaefferer[2], E. Chernyshova[3]

[1]Institute of Metals and Technology, Ljubljana, Slovenia
[2]Max-Planc Institute for Iron Research, Duesseldorf, Germany
[3]National Institute of Chemistry, Ljubljana, Slovenia

Transmission electron microscopy (TEM) is a very powerful tool for the investigation of the microstructure of materials, providing crystallographic information, small crystal irregularities and composition at the nanometer scale. Sample preparation is a very crucial procedure in TEM analysis and the methods involved in preparing the sample differs, depending on the nature of the material, the possibilities of your laboratory, the experience of the technicians and the results you would like to receive with TEM samples.

TEM samples for metallic materials are hard to prepare since the material should be transparent for electron beam and for metallic material that means from few nm up to few tens of nm. The classical TEM sample preparation for metallic materials involves preparation of thin slices, preparation of disks and thinning them to the transparency. This technique has advantages of greater area for TEM analyses, on the other hand, the disadvantage is that you cannot define the exact point of interest and assume that the sample is homogeneous and you will find the phenomenon everywhere in the material.

In the last decade when the Focused Ion Beam (FIB) is evolving rapidly, the SEM FIBs have high magnification with good resolution so the preparation of the TEM lamellas from exact spot, point of interest is possible and done on daily bases. The main disadvantages are long time for good preparation of the thin lamella, possible implantation of Ga ions on the lamella and last, observed the change of crystallography information. We have observed inducing of the circular dislocation loop that has not been observed by using electron-channelling contrast imaging (ECCI) on SEM. This technique is an imaging technique in scanning electron microscopy (SEM) based on electron channelling and applying a backscatter-electron detector. We were able to observe dislocations in additive-manufactured material and have not observe any circular dislocation loop. In the microstructures a lot of internal boundaries and a sub-grain structure were found, which form a kind of hierarchical structure but not the dislocation loop. This is why we assume that if the material is prone to circular dislocations, the preparation of the TEM lamellas should not be done with FIB or should be careful with interpretation of the results, especially for circular dislocation loops.

MS4.P013
Formation of an orthorhombic transition phase in a Ti-Al-3Mo alloy: *in situ* synchrotron diffraction and transmission electron microscopy studies

B. Rashkova[1], M. Musi[1], P. Erdely[1,2], A. Stark[3], P. Staron[3], N. Schell[3], H. Clemens[3,2], S. Mayer[2,3]

[1]Montanuniversität Leoben, Materials Science, Leoben, Austria
[2]Montanuniversität Leoben, Leoben, Austria
[3]Helmholtz-Zentrum Geesthacht, Institute of Materials Research, Geesthacht, Germany

Advanced intermetallic titanium aluminides are designed for high temperature application as lightweight materials which can withstand temperatures up to 750°C, while maintaining attractive structural and functional properties (1). Particularly, the so-called TNM alloy (Ti-43.5Al-4Nb-1Mo-0.1B, all in at.%) is already implemented as a structural material for turbine blades in the aerospace industry (2,3). At ambient temperatures these alloys consist of γ-TiAl ($L1_0$ structure), α_2-Ti3Al ($D0_{19}$) and βo-TiAl (B2). At certain temperatures, however, α_2 disorders to α-TiAl (A3 structure) and βo disorders to β-TiAl (A2). Only the γ-phase keeps its ordered state until dissolution (1). The addition of sufficient amount of Nb and/or Mo influences the existing phases and the formation of additional stable and metastable orthorhombic phases, such as O phase and B19 phase (4-10).

This work presents the evolution of the microstructure and formation of an orthorhombic phase in a Mo-containing γ-TiAl based alloy during reheating after quenching from the β single-phase field region.

The actual chemical composition of this model alloy is Ti-44.5Al-3.2Mo-0.1B (in at.%). The microstructure was studied by scanning electron microscopy (SEM) using a Zeiss EVO50 and transmission electron microscopy (TEM) using a Philips CM 12 microscope operating at 120kV and a Tecnai F20 operating at 200kV. *In situ* high-energy X-ray diffraction (HEXRD) measurements were performed at PETRA III at the Deutsches Elektronen Synchrotron (DESY), Germany.

In situ experiments showed that a metastable orthorhombic phase formed during annealing at 600°C and vanished at 720°C. This phase resulted in the formation of a modulated microstructure inside the α_2 phase as well as in the $\alpha_2^{"}$ martensite.

It is concluded that the orthorhombic phase acts as a transition phase between the α_2 and the γ phase (10).

References:

(1) H. Clemens, S. Mayer, Adv. Eng. Mater. 15 (2013) 191-215.

(2) H. Clemens, S. Mayer, Prakt. Metallogr. 52 (2015) 691-721.

(3) S. Mayer, P. Erdely, F.D. Fischer, D. Holec, M. Kastenhuber, T. Klein, H. Clemens, Advanced Engineering Materials 19/4 (2017) 1600735.

(4) E. Abe, T. Kumagai, M. Nakamura, Intermetallics 4 (1996) 327-333.

(5) D. Banarjee, Prog. Mater. Sci. 42 (1997) 135-158.

(6) T. Schmolzer, A. Stark, E. Schweighofer, T. Lippmann, S. Mayer, H. Clemens, Adv. Eng. Mater 14 (2012) 445-448.

(7) H. Gabrisch, U. Lorenz, F. Pyczak, M. rackel, A. Stark, Acta. Mater. 135 (2017) 304-313.

(8) F. Appel, J.D.H. Paul, M. Oehring, Mater. Sci. Eng. A 510-511 (2009) 342-349.

(9) L. Song, X.J. Xu, L. You, Y.F.Liang, J. Alloys Compd. 618 (2015) 305-310.

(10) M. Musi, P. Erdely, B. Rashkova, H. Clemens, A. Stark, P. Staron, N. Schell, S. Mayer, Materials Characterization 147 (2019) 398-405.

MS4.P014
Microstructural characterization of the influence of trace elements on early precipitation states in an Al-Cu alloy

U. Mühle[1], T. Schubert[2], F. Lotter[3], T. Staab[3], M. Elsayed[4], R. Krause-Rehberg[4], B. Kieback[1]

[1]TU Dresden, Inst. of Material Science, Dresden, Germany
[2]Fraunhofer Inst. for Manufact. Techn. and Adv. Mater, Dresden, Germany
[3]Technische Universität, Würzburg, Germany
[4]Martin-Luther-University, Halle, Germany

Aluminum and its alloys have a major importance for a broad variety of applications, e.g. as material for light weight construction. Especially the alloy system Al-Cu is the base for the whole family of commercial 2xxx alloys. Dependent on ageing temperature metastable and stable phases (Guinier-Preston I and II zones, Θ" and Θ) are forming by precipitation, leading to the strengthening. The most efficient increase in strength is achieved when Θ"-platelets with lateral dimensions of about 150 nm are formed (1).

The kinetics of precipitation is mainly determined by the diffusion of Cu-atoms in the Al-matrix and, thus, by the concentration of mobile vacancies. Additional alloying of elements with a high ability of vacancy binding like Sn or In influences this process (2). The hardness maximum is higher and will be reached faster (3). So, an Al-4wt.%Cu-alloy after solution anneal at 520°C and subsequent ageing at 150°C for 48 h shows a hardness HV0.5 of 105, but alloying additionally 0,044wt.% Sn or In increases this value to 135 HV0.5.

The optimum TEM-based method to evaluate the overall status of age hardening is electron diffraction for determine the phases of precipitates combined with imaging for size estimation. To characterize single precipitates STEM using the HAADF-detector is the better choice due to atomic resolution combined with different scattering contrast of the present elements (4).

The microstructural origin of the differences in strength are the finely distributed Θ"-particles in the material micro-alloyed with Sn, whereas these kind of precipitates are rare in the alloy without Sn (fig.1). Single precipitates are distinguished by the distance between two Cu-enriched lattice planes.

The binding of the trace elements to vacancies suppresses the precipitation of GPI and GPII-zones at lower temperatures. At about 150°C, the binding decreases so that vacancies are released and Θ"-precipitates start to form as most efficient particles for strengthening. Without this vacancy binding a major part of the Cu precipitates as GPII at lower temperatures and is not available for the process forming Θ".

In early stages of thermal treatment the trace element indium forms clusters, where every forth lattice plane of the Al-matrix is populated. At those clusters Θ"-particles start to grow, where every 2nd lattice plane is occupied by Cu (fig. 2). This mechanism promotes the formation of finely distributed precipitates and explains the faster increase of hardness.

References:

(1) Ostermann, F.; Anwendungstechnologie Aluminium; Springer-Verlag, 2014.

(2) Ringer, S.P., Hono, K; Mat. Char. 44 (2000): 101-131

(3) Lotter, F. et.al.; pss (a) 215 (2018); 1800375

(4) Tanaka, N.; Scanning Transmission Electron Microscopy of Nanomaterials; Imp. College Press London, 2015.

Fig. 1

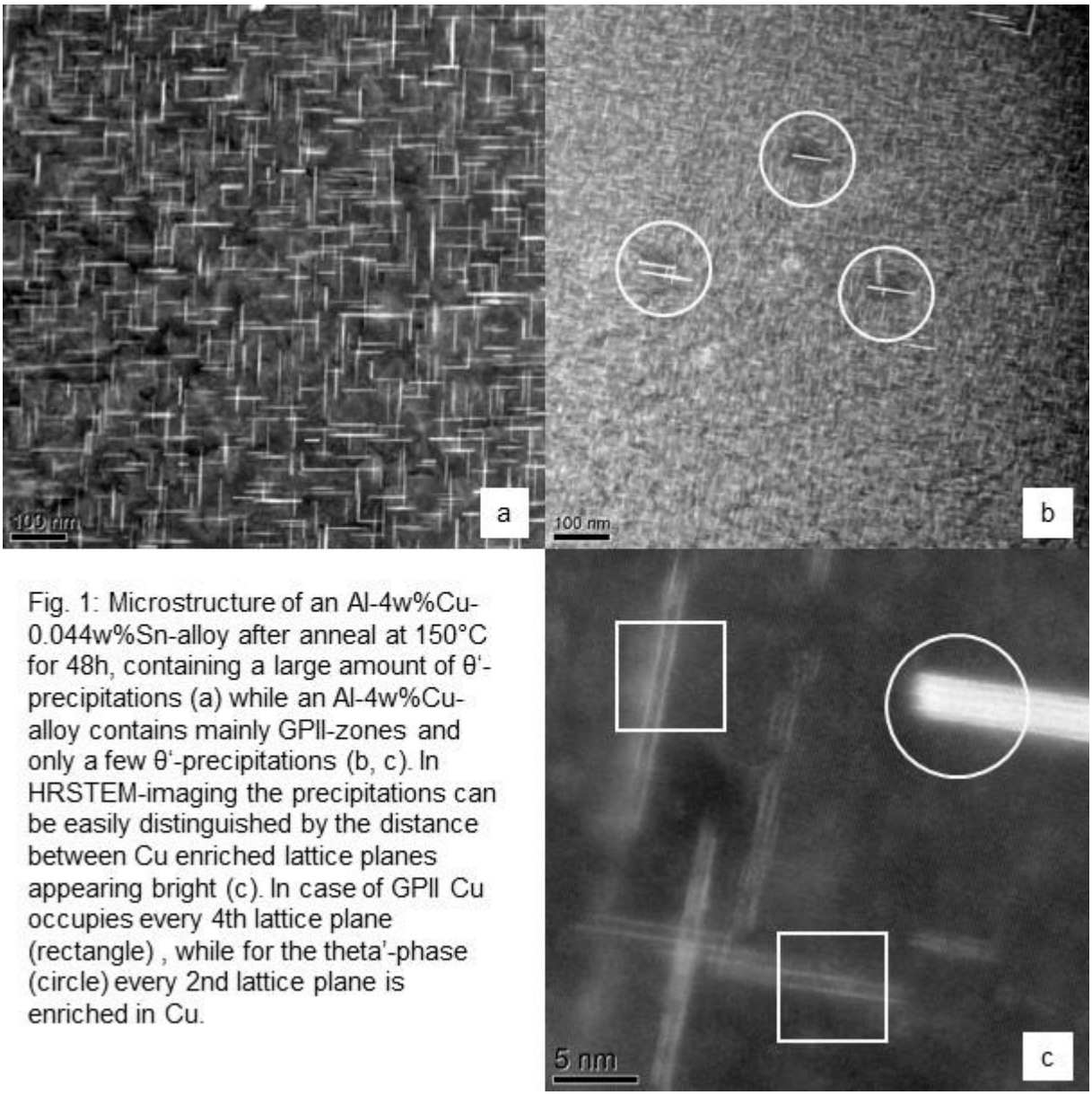

Fig. 1: Microstructure of an Al-4w%Cu-0.044w%Sn-alloy after anneal at 150°C for 48h, containing a large amount of θ'-precipitations (a) while an Al-4w%Cu-alloy contains mainly GPII-zones and only a few θ'-precipitations (b, c). In HRSTEM-imaging the precipitations can be easily distinguished by the distance between Cu enriched lattice planes appearing bright (c). In case of GPII Cu occupies every 4th lattice plane (rectangle) , while for the theta'-phase (circle) every 2nd lattice plane is enriched in Cu.

Fig. 2

Figure 2: Early state of precipitate in an Al-4w%Cu-0.044w%In alloy. Indium is enriched in a region of about 2nm in diameter, where In atoms occupy every 4th lattice plane of the Al-matrix (circle). The subsequent precipitation of θ'-plates (to the right to the indium) follows these location and builds up its structure by enriching Cu in the intermediate plane, too.

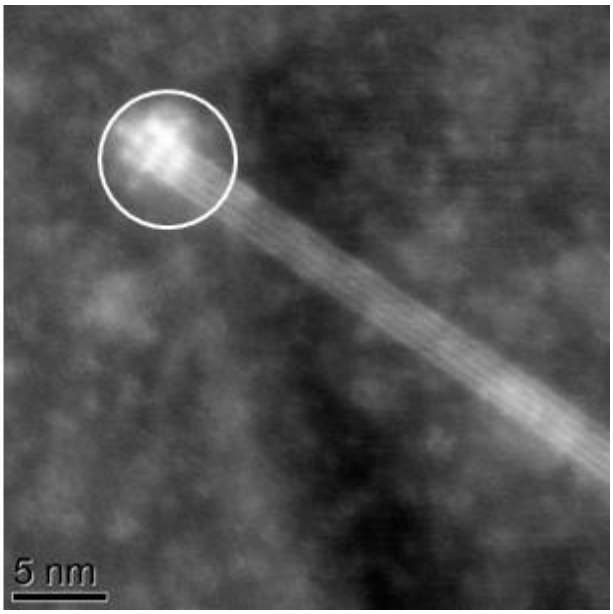

MS4.P015
SEM study of the precipitated carbides in a welded alloy of Inconel 600

L. Zamora Rangel[1]

[1]Instituto Nacional de Investigaciones Nucleares, Tecnologia de Materiales, Ocoyoacac, Mexico

The Inconel 600 alloy is used to make components in many systems of the nuclear industry. However, in welded joints this alloy, due to the effect of the high temperature generated by the welding process, is prone to generate intergranular stress corrosion cracking (IGSCC) due to the precipitation of second phases such as carbides type M6C and M23C6 at the grain boundaries, which results in the loss of corrosion resistance (1).

The objective of this study is to analyze by means of scanning electron microscopy (SEM), which is the effect on the variation of the composition in the areas adjacent to the formation of carbides in Inconel 600 alloy, after an welding process.

For this study a forged cylinder of inconel 600 of 15in diameter and 1.25in thickness was used and as counterpart a 304L stainless steel tube of equal diameter and thickness. The 82 and 182 inconel alloys were used as the filler material. The parameters for to apply the alloy 82 (root welding) were 120A, 12V and as argon protection gas. For the filling of the joint (filler weld) alloy 182 was used and the parameters were 75A and 23V. Once the joint was made, a sample was obtained from the inconel 600 zone including the fusion line and prepared for his analysis in the scanning electron microscopy (SEM), using a JEOL-6610 microscope equipped with an Oxford probe for dispersive energy analysis of X-rays (EDS). For microstructural analysis at higher magnifications were carried out to obtain the profile of compositions both for the carbide and for the areas adjacent to the same carbide.

Figure 1 shows the areas where the analyzes of composition EDS were performed and Table 1 shows the profile of compositions. Observing the EDS from 1 to 7 (see Table 1) it can be said that the carbide particle presents a composition with respect to the chromium content of 15% on average, but combined with carbon forms the carbide. While the EDS 8 and 9 have chromium contents of 9.44 and 7.16% respectively, which are in areas adjacent to the carbide and have a considerable chromium loss and leave this area prone to IGSCC. Likewise, the EDS 10 presents a chromium percentage of 16.50%, which is characteristic of the Inconel 600 alloy (2).Regarding niobium, which is an inhibitor of the formation of chromium carbides, the percentages obtained were not enough to avoid the loss of chromium in adjacent areas (1).

After the obtained results, it is observed that the high temperatures reached during the welding process, caused on the one hand the formation of carbides and on the other the decrease in the content of chromium in the areas adjacent to the carbide, which translates into loss resistance to IGSCC of the Inconel 600 alloy.

References:

(1) Lunding C. D. (1982) "Dissimilar Metal Welds-Transition Joints Literature Review". Welding Research Supplement, V.61 No.2 pp. 59-63.

(2) Zamora L., et al. 2015, "Dissimilar welds: in the system: SA533-E309-E308L-Alloy 82-Alloy 182- SB168", Microscopy Conference 2015, George-August-University Göttingen, September 6-11, 2015.

Fig. 1: SEM of the Inconel 600 Alloy (EDS).

Table 1: Chemical composition obtained by EDS in% by weight.

Fig. 1

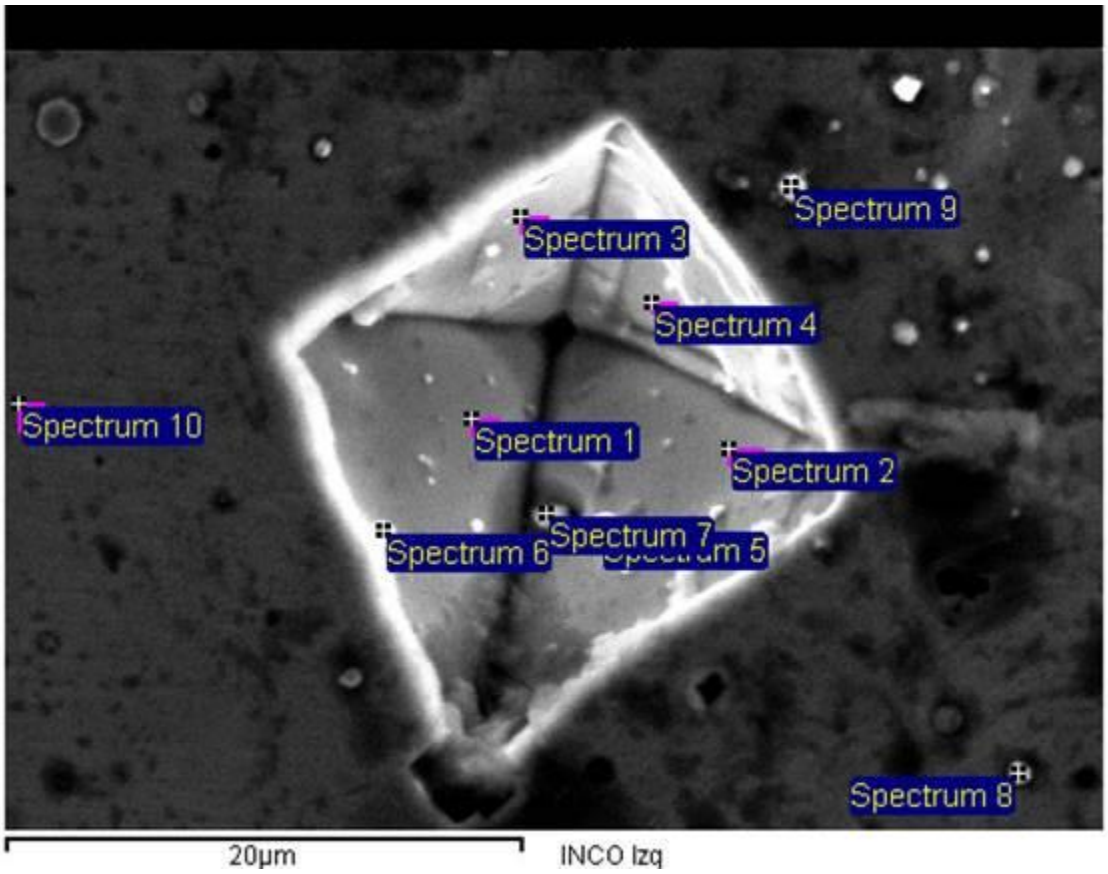

Fig. 2

Table 1. Chemical composition obtained by EDS in% by weight.

Spectrum	C	O	Cr	Mn	Fe	Ni	Nb
1	11.39	3.87	16.67	6.50	11.29	50.28	ND
2	7.46	ND	15.23	5.70	10.27	59.44	ND
3	7.66	ND	15.21	7.20	13.15	56.78	ND
4	ND	ND	16.80	5.63	12.52	65.04	ND
5	7.06	29.54	6.52	2.64	4.07	21.53	ND
6	7.45	5.46	13.93	6.22	9.68	44.39	ND
7	ND	4.43	14.03	8.34	10.34	45.51	4.73
8	7.34	12.16	9.44	2.58	6.29	32.07	3.21
9	8.38	24.03	7.16	3.41	5.24	25.54	3.36
10	ND	ND	16.50	5.27	11.41	66.11	ND

ND: Undetermined

MS4.P016
Electron Microscopy Characterization of Self-healing Aluminium Alloys

I. Paulin[1], Ļ Donik[1], M. Godec[1], S. Zaefferer[1]

[1]Institut of metals and technology, Ljubljana, Slovenia

Self-healing aluminium alloys are new generation of light metals with high strength, good corrosion resistant and well transformability. Adding a new property, possibility of self-healing process, to this excellent materials, the outstanding light metals are being developed.

Aluminium alloys are employed extensively for aircraft and automobile applications. In both cases the application is limited by slow fatigue damage evolution during service. If crack growth could be postponed the life span of components would be increased and the frequency of inspections reduced. An intriguing concept to achieve this is the incorporation of self-healing mechanisms into engineering materials. Self-healing of damage is an important concept in biological materials but is, so far, not common in engineering materials. Aluminium alloys, particularly, have been considered because they show, even at room temperature, high mobility of atomic species which allows dynamic precipitation in areas with high strain and/or damage.

In our study aluminium alloy of series AA 7xxx is being developed. Homogenized alloys will be solution-annealed and quenched to obtain supersaturated alloys. These will be submitted to different thermal treatments, including underaged, fully aged, and overaged conditions. In a second step a two-stage ageing treatment will be performed. The state of precipitation will be followed by hardness measurements and SEM or TEM observations of selected samples. Microstructures of selected samples from different stages of testing and ageing will be investigated with respect to their precipitation state and dislocation density using different electron microscopy techniques, mostly SEM with belonging analytics; EDX (electron x-ray diffraction), EBSD (electron backscattered diffraction), ECCI (electron channelling contrast imaging) and, for well-selected samples by atom probe tomography.

MS4.P017
In-situ TEM study of the crystallization of a gold-based metallic glass

I. P. Ivanov[1], C. Meylan[1], N. Panagiotopoulos[1], K. Georgarakis[2], A. L. Greer[1]

[1]University of Cambridge, Department of Materials Science & Metallurgy, Cambridge, United Kingdom
[2]Cranfield University, School of Aerospace, Transport and Manufacturing, Cranfield, United Kingdom

The report by Schroers et al. (1) of bulk glass-forming ability for the composition Au49Ag5.5Pd2.3Cu26.9Si16.3 (at.%) opened up a significant research field. Gold-based metallic glasses (MGs) are of interest for jewellery (2), providing scratch resistance combined with exceptional formability, and for many other potential applications (3). Crystallization in such systems is important for understanding the glass-forming ability, the stability of the glass once formed, and the prospects for generating useful (nano/micro) structures by partial or full transformation of the glass. Crystallization of Au-based MGs has been widely studied by differential scanning calorimetry (DSC), both conventional and ultrafast (i.e. "Flash-DSC", FDSC) (3). In FDSC, these compositions can be melted in-situ and then rapidly quenched back into the glassy state. The present work builds on these earlier studies by using in-situ transmission electron microscopy (TEM) to elucidate the sequence of phase transformations on heating a melt-spun ribbon of Au49Ag5.5Pd2.3Cu26.9Si16.3 MG.

A cross-sectional specimen with a final thickness of 50−100 nm was prepared by FIB milling using a Helios Nanolab FIB/SEM. The sample was transferred from the bulk specimen to a windowed point on a DENS chip. The FIB lift-out strategy was optimized to minimize milling damage and Ga contamination of the sample. Image acquisition and spectroscopic analysis were conducted using a FEI Tecnai Osiris with field-emission gun TEM/STEM operated at 200 keV, equipped with a Super-X windowless EDX detector. In-situ imaging at high temperatures up to 500°C was conducted using an in-situ heating holder from DENS Solutions. The resistance of the platinum coil in the heating chip is monitored in a four-point configuration, and the temperature is calculated with calibration constants provided by the manufacturer. Microstructural and chemical changes in the Au-based MG were studied at controlled film temperature under the TEM vacuum <10−6 Pa. The specimen was held for at least 2 min at each step at to reach equilibrium. At selected temperatures (related to our DSC data) chemical compositions have been analysed using an EDX detector. For the chosen temperatures a time-series of HAADF STEM images were recorded with the acquisition time of 1 sec. Because of the absence of thermal drift with current chip technology, data acquisition started immediately after each temperature increase.

These studies are integrated with FDSC studies, and they help to resolve the uncertainties left by earlier studies based on X-ray diffraction of samples after annealing (4). We conclude that, on heating, the first crystallization is polymorphic. Subsequently Au-rich and Cu-rich crystals are formed, with a Pd-Ag-Si phase at grain boundaries, and ultimately a network of nanosized silicides. Finally, we consider the implications for the development of engineering applications of gold-based bulk MGs.

References:

(1) J Schroers et al., *Appl. Phys. Lett.* 87 (2005) 061912.

(2) O Gross et al., *Mater. Des.* 140 (2018) 495–504.

(3) S Pogatscher et al., *Thermochim. Acta* 590 (2014) 84–90.

(4) G Fiore et al., *J. Non-Cryst. Solids* 356 (2010) 2218–2222.

Fig. 1: The HAADF images of the Au-based MG at different stages of in-situ TEM experiments. In inserts the corresponding SAED patterns are shown.

Fig. 1

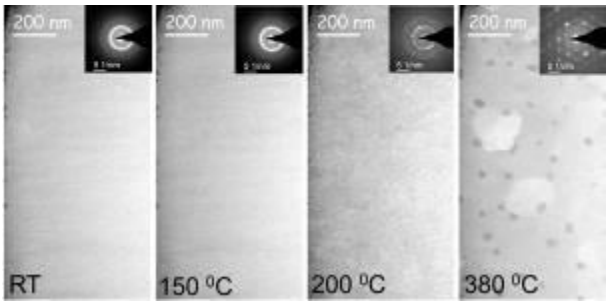

MS4.P018
Digital material representation of precipitation coarsening in alloy 2618A for the lifetime assessment of radial compressor wheels

C. Rockenhäuser[1], P. von Hartrott[2], M. Metzger[2], B. Skrotzki[1]

[1]Bundesanstalt für Materialforschung und -prüfung (BAM), Experimentelle und modellbasierte Werkstoffmechanik, Berlin, Germany
[2]Fraunhofer Institut für Werkstoffmechanik (IWM), Freiburg, Germany

The age-hardenable Al-Cu-Mg alloy 2618A is designed for long-term operation at elevated temperatures for automotive applications, especially for radial compressor wheels. The desired material properties (hardness, strength) are specifically adjusted by controlling the formation and coarsening of nanoscaled S-phase precipitates (Al2CuMg). It is well-known that due to the overaging of the precipitates the strength of the material declines during operation which influences component lifetime (1). This material degradation is mostly not included in lifetime models. However, these microstructural changes are not considered in current models for component lifetime prediction. The concept of digital material representation (DMR) implies that the relevant features of the microstructure can be included in aging models based on numerical simulations improving the resulting lifetime assessment (2).

The aim was to obtain quantitative data of the precipitate evolution in alloy 2618A to include it in a lifetime model for numerical component assessment. This required to systematically investigate the coarsening process by determining several aging parameters using transmission electron microscopy (TEM).

The precipitate radii distribution of the S-phase was determined for different aging conditions (190 °C up to 25000 h). Cross-section samples were investigated using dark-field TEM. The Al2CuMg precipitates form as rods along the <001>α direction of the α-Al matrix and were selectively imaged by suitable sample orientation.

The results were implemented into a lifetime prediction model.

Dark-field images of the precipitates show that the initial condition contains small and large precipitates (Fig 1a)), whereas after 1000 h of aging mainly large precipitates remain (Fig. 1 b)). Radii distributions were obtained from multiple images using a standard procedure which result in lognormal precipitate radii distributions for each aging state (Fig. 2a-c)). Obviously, the initially narrow distribution broadens during aging and the maximum moves to higher radii with increasing average precipitate radius (Fig. 2d)). After fast coarsening during the initial 1000 h of aging the coarsening process slows down. Further analysis of the average radii shows that the aging process from 1000 h onwards can be described by Ostwald ripening.

It was possible to describe the material aging as a function of time and temperature by considering the evolution of the radii distribution and the average radius of the precipitates. This allows to extend a time and temperature dependent deformation model for component lifetime prediction according to Chaboche, which describes the relevant phenomena of high temperature deformation and cyclic plasticity (4). It now considers material aging not only as a function of temperature, but also as a function of precipitate evolution.

References:

(1) M.J. Styles et al., Acta Mater 60 (2012) p6940.

(2) M. Pietrzyk et al., Computational Materials Engineering, 2015 Butterworth-Heinemann Elsevier.

(3) C. Rockenhäuser et al., Mat Sci Eng A-Struct 716 (2018) p78.

(4) P. von Hartrott et al., MTZ 10 (2018) p72.

Fig. 1: Dark-field images of precipitates oriented along the [001] zone axis of the matrix for a) the initial condition (T61), b) aged state.

Fig. 2: Lognormal distribution fits of the radii distributions for a) the initial state and aged states b-c). d) average precipitate radii over time.

Fig. 1

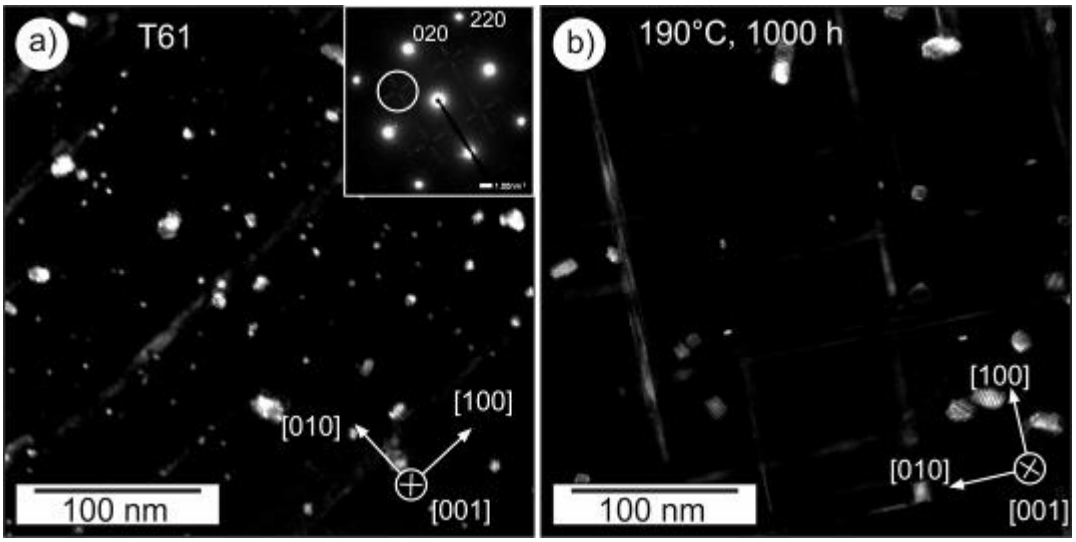
a)
T61
020
220
[010]
[100]
[001]
100 nm
b)
190°C, 1000 h
[100]
[010]
[001]
100 nm

Fig. 2

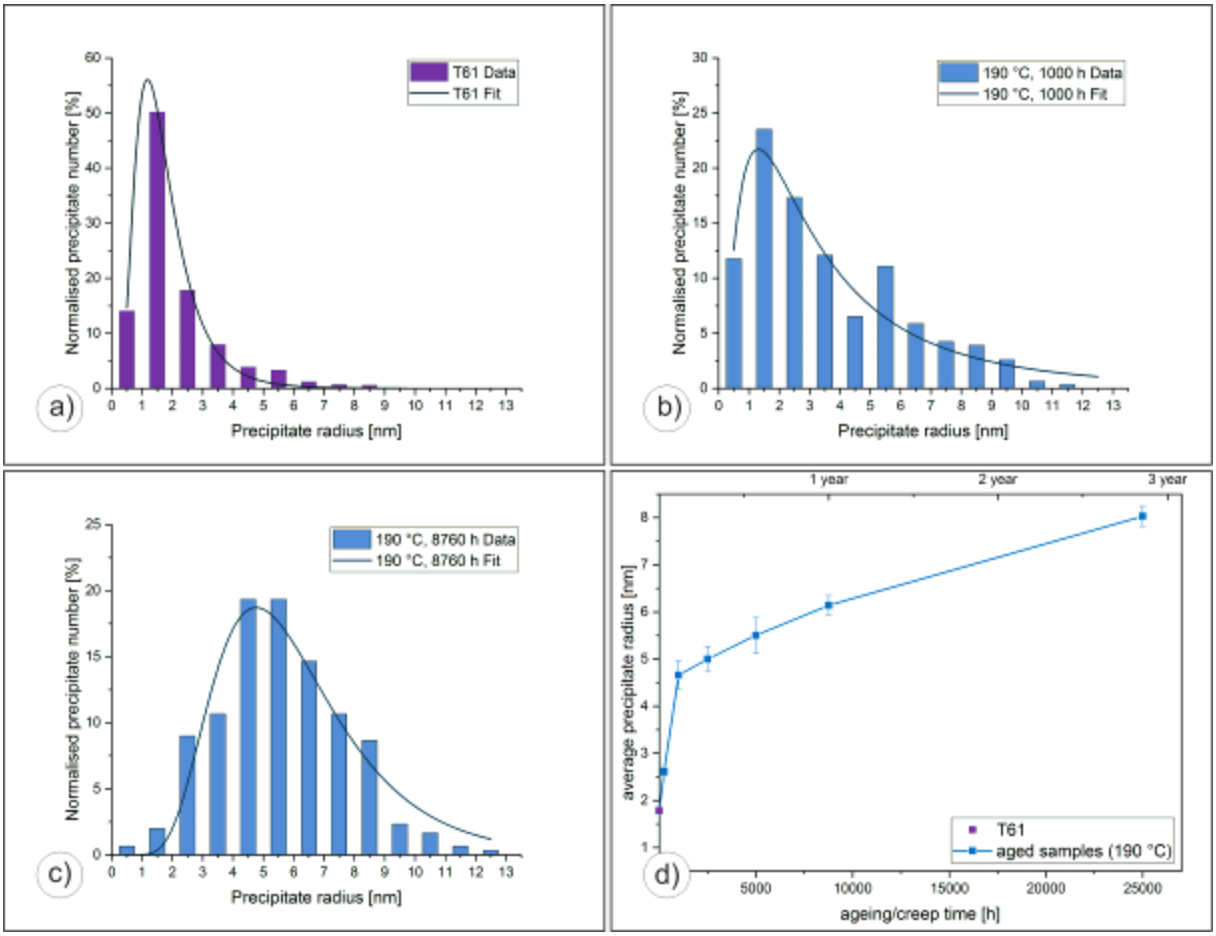
a)
T61 Data
T61 Fit
Normalised precipitate number [%]
Precipitate radius [nm]
b)
190 °C, 1000 h Data
190 °C, 1000 h Fit
Normalised precipitate number [%]
Precipitate radius [nm]
c)
190 °C, 8760 h Data
190 °C, 8760 h Fit
Normalised precipitate number [%]
Precipitate radius [nm]
d)
1 year
2 year
3 year
average precipitate radius [nm]
T61
aged samples (190 °C)
ageing/creep time [h]

MS4.P019
Phase analyses of surgical CoCrMo alloys in different conditions by SEM and EBSD

K. Harnisch[1], P. Rosemann[1], C. Klee[1], T. Baierl[1], T. Halle[1]

[1]Otto-von-Guericke-University Magdeburg, Institut für Werkstoff- und Fügetechnik, Magdeburg, Germany

Cobalt based alloys (e.g. CoCrMo) are widely used in the area of medical science as implant material. Cast or forged CoCrMo alloys are employed in artificial hip joints. Microstructure and volume fractions of the contained phases (ε – hcp and γ – fcc) are significantly determining the resulting properties of the implant components.

A frequently used implant alloy has been exposed to mechanical and thermal pre-treatments. Morphologies, area fractions and distribution of hcp and fcc phases have been evaluated using different microscopical methods after metallographic preparation. Typical problems with the visualization of microstructural characteristics of CoCrMo alloys using conventional optical and electron microscopy have been handled by using EBSD. In-situ tension testing within the SEM has been performed in order to analyze phase transformations during deformation. Results of microscopical investigations have been correlated with XRD and hardness measurements.

A differing morphology of the hcp phase has been observed depending on the method of pre-treatment. After a mechanical treatment (cold rolling) the hcp phase formed in a lamellar structure, whereas hcp grains formed after a heat treatment. Area fractions of hcp and fcc phases vary with type, duration and characteristics of the method of pre-treatment. An increasing fraction of hcp phase correlates with an increasing hardness. A suitable heat treatment enables systematic adjustments of the volume fractions of fcc and hcp phase (completely hcp, completely fcc, interstages).

Gained findings permit a target-oriented influence on the reachable structure and the resulting mechanical properties after different thermal and mechanical pre-treatments.

MS4.P020
Influence of prestraining on the aging response of an Al-Cu-Li alloy Influence of prestraining on the aging response of an Al-Cu-Li alloy

C. Rockenhäuser[1], B. Piesker[1], D. Heidl[1], B. Skrotzki[1]

[1]Bundesanstalt für Materialforschung und -prüfung (BAM), Experimentelle und modellbasierte Werkstoffmechanik, Berlin, Germany

Lightweight Al-Cu-Li alloys are materials of substantial interest for aerospace and automotive applications (1, 2). The addition of just 1 mass% lithium to aluminium leads to a significant increase in Young"s modulus and allows a considerable reduction of weight. The strength can be raised by the formation of T1 (Al2CuLi) and θ" (Al2Cu) precipitates during artificial aging. Earlier investigations of an Al-4 % Cu-1 % Li (mass %) alloy by transmission electron microscopy (TEM) were performed to investigate the alloy microstructure as a function of the heat treatment parameters and external load and compare the results to phase field simulations (3,4).

The aim of this work is to investigate additional parameters, namely disclocation density, on the microstructure of the alloy during hardening and ageing. These results will then be compared to phase field simulations of the hardening/ageing process.

The nominal chemical composition of the alloy is Al-4Cu-1Li-0.25Mn in mass % (Al-1.69Cu-3.87Li-0.12Mn in at. %). The high purity alloying elements were molten in a vacuum induction furnace and the alloy was subsequently poured into a water-cooled crucible. Afterwards the cast was homogenized at 515 °C for 24 h and water quenched. Extrusion of the homogenized material through a die-plate with a cross section of 15 mm × 70 mm was carried out at 420 °C followed by as solution heat treatment at 505 °C for 70 min and a water quench. The final step was stretching the extruded profile by about 2.9 % to straighten it. The resulting material was received as semi-finished block profiles with dimensions of 15 mm × 70 mm × 655-785 mm. This is designated "initial state" in the following.

To investigate the influence of the initial dislocation concentration on the hardening, some of the material was further strained to 4 % and 6 % and the three differently strained states were then heat treated at 180 °C up to 60 h. To reduce the dislocation concentration, several samples were resolutionized at 505 C for 70 min and following heat treatment up to 600 h.

The Brinell hardness HBW 2.5/62.5 was tested using an Emco Test M4C 035 hardness tester.

Fig. 1 shows the hardness of the alloy during ageing dependent on ageing time and strain. Increasing the strain from 3 % to 6 % increases the kinetics of the hardening process and maximum hardness. This is expected since the straining increases the dislocation density which in turn leads to a higher T1 and θ" precipitate density improving mechanical properties. Reducing the dislocation density leads to the opposite result which can be seen in Fig. 2 – the hardness of the resolutionised samples is substantially lower and the hardening process much slower.

Manipulating the initial dislocation density lead to the expected result regarding the hardening of the alloy. TEM investigations are pending for a planned quantitative comparison of dislocation density and precipitate parameters to phase field simulations.

References:

(1) A. Heinz et al., Mat Sci Eng A-Struct 280 (2000) p10.

(2) J. Hirsch, T. Al Samman, Acta Mater **61** (2013) p102.

(3) I. Häusler et al., Materials 10 (2017) p1.

(4) I. Häusler et al., Materials 12 (2019) p1.

Fig. 1: Hardness curves versus the ageing time for different initial strains (ageing temperature 180 °C).

Fig. 2: Hardness curves versus the ageing time for an initial strains of 6 % and resolutionised samples (ageing temperature 180 °C).

Fig. 1

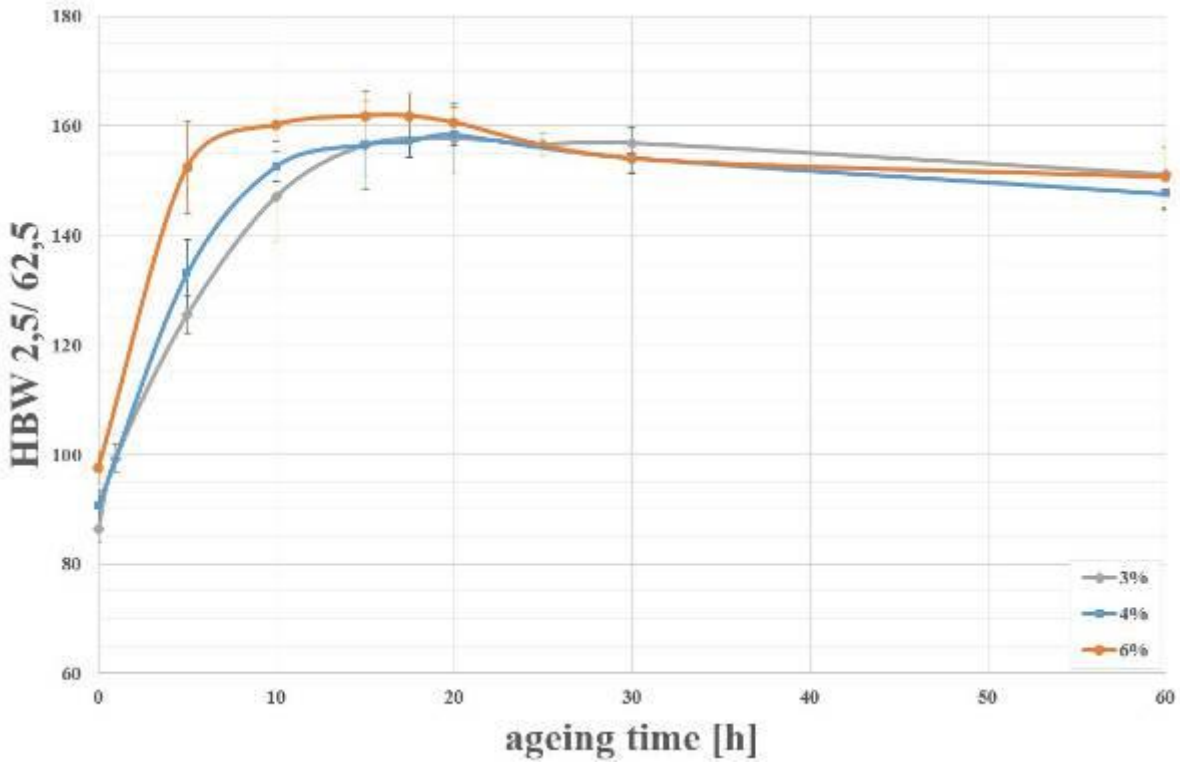

Fig. 2

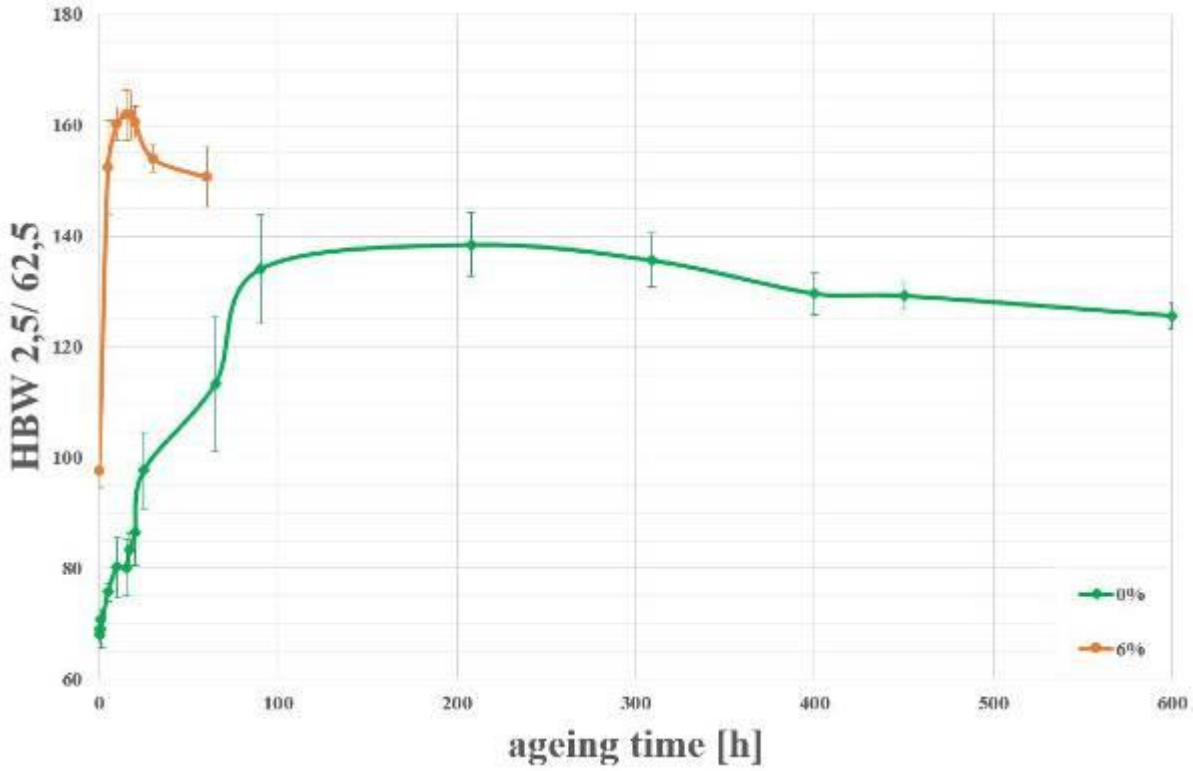

MS4.P021
Phase evolution and precipitation kinetics in a High Entropy Alloy system: an *in situ* heating study

L. S. Mantha[1], B. MacDonald[2], E. J. Lavernia[2], C. Kübel[1,3]

[1]Institute of Nanotechnology, KIT Campus Nord, Electron Microscopy and Spectroscopy Laboratory, Eggenstein-Leopoldshafen, Germany
[2]University of California, Department of Chemical Engineering and Materials Science, Irvine, California, United States
[3]Karlsruhe Nano Micro Facility, Karlsruhe Institute of Technology, Karlsruhe, Germany

High entropy alloys (HEAs) are an emerging class of materials with high potential in diverse applications. One approach to develop HEAs further and broaden their application range lies in deviating from equiatomic compositions and single phase microstructures to include classical strengthening approaches (1). Understanding the phase evolution, grain boundary and precipitation strengthening in these alloys are essential to optimize their mechanical properties.

To elucidate on the precipitation processes and stability of the secondary B2 phase formed during thermal annealing of a high-pressure torsion (HPT) deformed, non-equiatomic MnFeCoNiCu HEA system by *in situ* transmission electron microscopy (TEM).

The non-equiatomic HEA $Mn_{10}Fe_{27}Co_{26}Ni_{27}Cu_{10}$ was cast using electromagnetic levitation melting and homogenized at 1100 ºC for 12 hours. The alloy was mechanically deformed by HPT to achieve a nanocrystalline microstructure. X-Ray diffraction (XRD) and differential scanning calorimetry (DSC) were performed to characterize the phases and their stability. A detailed microstructural analysis of the different states was carried out both *ex-situ* and *in-situ* using scanning transmission electron microscopy (STEM), energy dispersive X-ray spectroscopy (STEM-EDX) and automated crystal orientation mapping (STEM-ACOM).

X-Ray diffraction of the HPT deformed sample and different annealed states indicates the formation of an increasing amount of B2 phase in the initial fcc solid solution matrix starting at around 425°C up to 885°C. *Ex-situ* EDX and ACOM analysis confirmed this evolution and showed that the B2 precipitates are 50 % Fe and 50% Co. *In situ* heating of the HPT deformed sample was used to follow the evolution of the B2 precipitates at different temperatures by ACOM phase and orientation mapping and STEM-EDX to understand their formation and evolution processes.

This study revealed decomposition of a non-equiatomic MnFeCoNiCu HEA to form Fe-Co rich B2 precipitates during heat treatment of the deformed sample and this decomposition was successfully investigated during *in-situ* annealing in TEM.

References:

(1) Z. Li and D. Raabe, "Strong and Ductile Non-equiatomic High-Entropy Alloys: Design, Processing, Microstructure, and Mechanical Properties," *JOM*, vol. 69, no. 11, pp. 2099–2106, Nov. 2017.

Fig. 1

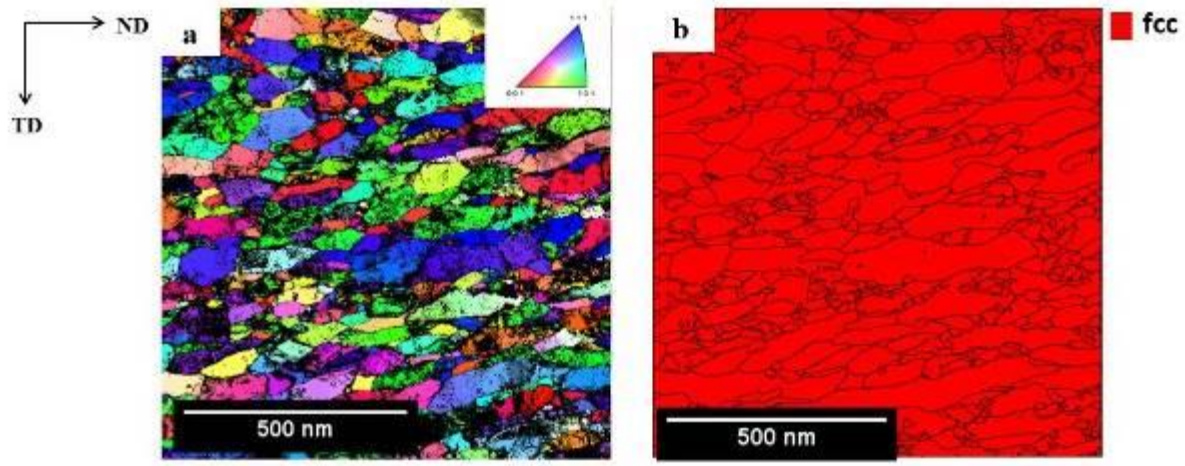

Figure 1 a) Orientation map of the deformed sample using HPT before heat treatment b) corresponding phase map indicating single phase microstructure.

Fig. 2

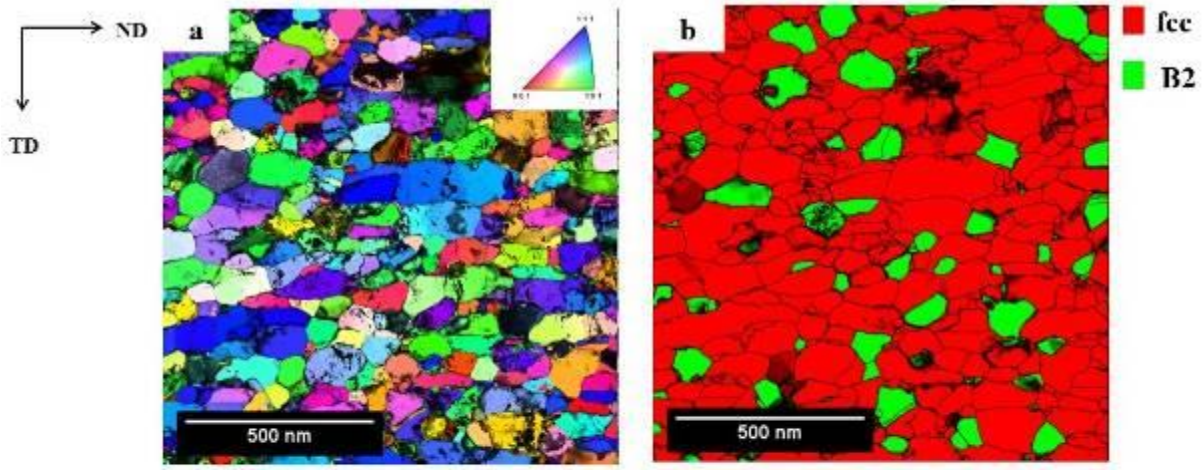

Figure 2 a) Orientation map of the deformed sample using HPT after heat treatment b) corresponding phase map indicating formation of second phase during heat treatment

MS4.P022
Variable-resolution fluctuation electron microscopy applied to shear bands of $Pd_{40}Ni_{40}P_{20}$

F. A.Davani[1], S. Hilke[1], H. Rösner[1], D. Geissler[2], A. Gebert[2], G. Wilde[1]

[1]Westfälische Wilhelms-Universität, Institute of Materials Physics, Münster, Germany
[2]Leibniz-Institute for Solid State and Materials Research Dresden (IFW Dresden), Institute for Complex Materials (IKM), Dresden, Germany

Bulk metallic glasses (BMGs) are of great interest due to their unique mechanical properties such as high strength and hardness. In this work, a $Pd_{40}Ni_{40}P_{20}$ bulk metallic glass (BMG) was produced by direct melting of palladium (purity 99.95 %) and Ni_2P ingots (purity 99.5 %) and casting into a copper mold using a melt spinner device under argon atmosphere. Plastic deformation of differently notched beams was imposed under 3-point bending conditions and in-situ monitored using optical microscopy. Plastic deformation at low and moderate temperatures is known to lead to shear localization and finally to the formation of shear bands in metallic glasses (1). We used focused ion beam (FIB) to prepare electron transparent lamellae out of the sheared regions following the shear steps on the surface of the deformed samples. Both undeformed and deformed states were compared using conventional transmission electron microscopy (cTEM) and high-angle annular dark-field (HAADF) scanning transmission electron microscopy (STEM). The combination of several quantitative electron scattering signals showed shear bands with alternating segments of decreased and increased density with respect to the surrounded matrix along the propagation direction (Fig. 1). Variable resolution fluctuation electron microscopy (VR-FEM) was performed by collecting nano-beam diffraction patterns (NBDPs) with different probe sizes from the shear band and its adjacent area (Fig. 2). The diffraction data was subsequently analyzed using the pair-persistence analysis (2). Changes in the medium range order (MRO) of undeformed and deformed states close to and far from shear bands have been observed. The results will be discussed with respect to the structural response of metallic glasses to shear.

References:

(1) Greer, A. L., Cheng, Y. Q., & Ma, E. (2013). Shear bands in metallic glasses. *Materials Science and Engineering: R: Reports*, *74*(4), 71-132.

(2) Gibson, J. M., Treacy, M. M. J., & Voyles, P. M. (2000). Atom pair persistence in disordered materials from fluctuation microscopy. *Ultramicroscopy*, *83*(3-4), 169-178.

Financial support by the Deutsche Forschungsgemeinschaft (DFG) under the grant number SPP1594 and PE 2290/2-1 are gratefully acknowledged as well as the funding of our TEM equipment by the DFG via the Major Research Instrumentation Programme under INST 211/719-1 FUGG.

Fig. 1: Top: HAADF-STEM image showing density variations in a shear band prepared from a notched 3-point bending test of $Pd_{40}Ni_{40}P_{20}$. The shear band was propagating from left to right displaying several contrast changes. Bottom: Relative density changes quantified along the propagating direction of the shear band with respect to the adjacent matrix.

Fig. 2: Normalized variance profiles of a notched 3-point bending test of $Pd_{40}Ni_{40}P_{20}$ calculated from 80 NBDPs of an (a) as cast sample and (b) deformed matrix. For each sample six different probe sizes were used to calculate the normalized variance profiles.

Fig. 1

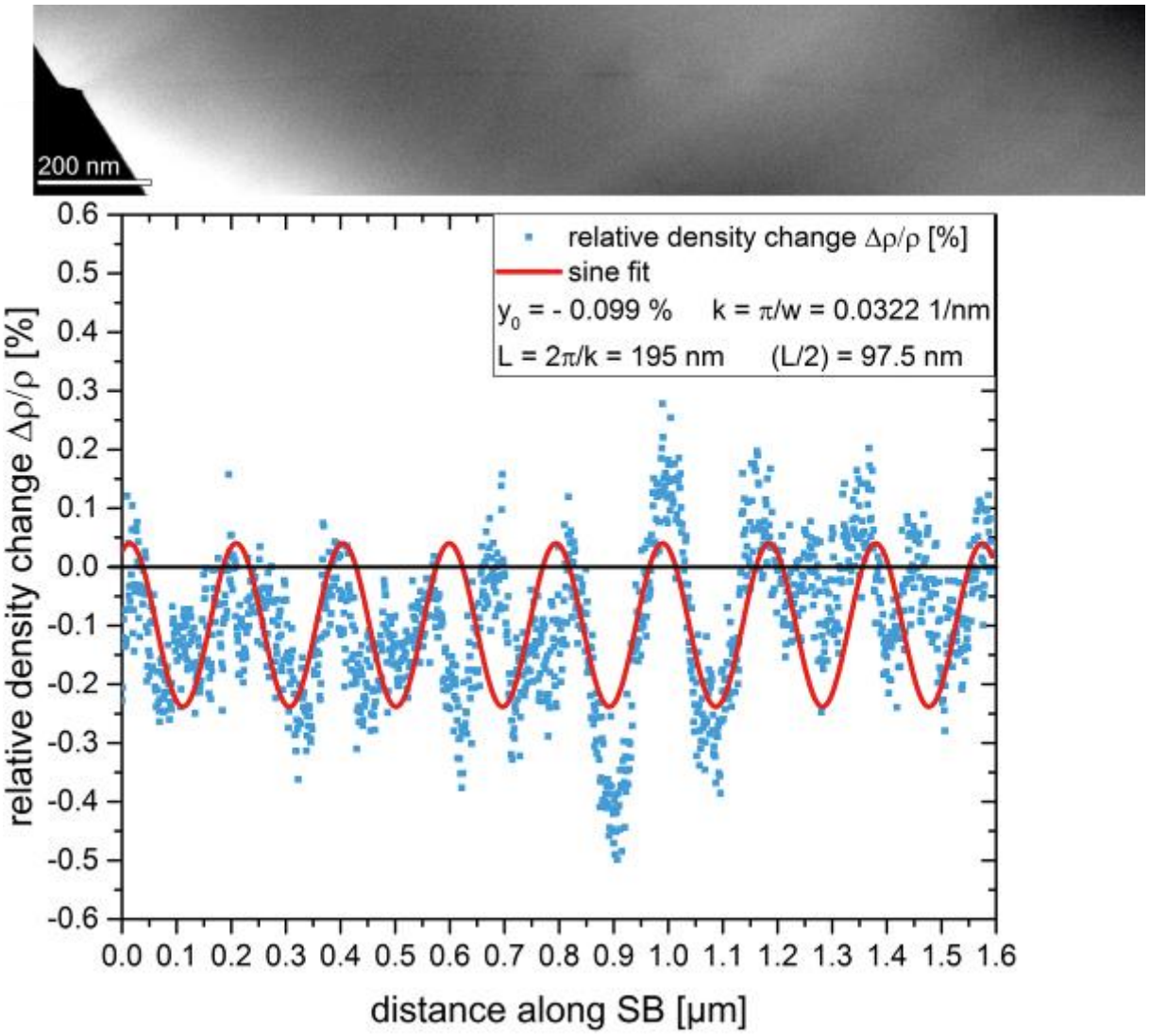
200 nm
relative density change Δρ/ρ [%]
sine fit
y0 = - 0.099 %
k = π/w = 0.0322 1/nm
L = 2π/k = 195 nm
(L/2) = 97.5 nm
relative density change Δρ/ρ [%]
distance along SB [µm]

Fig. 2

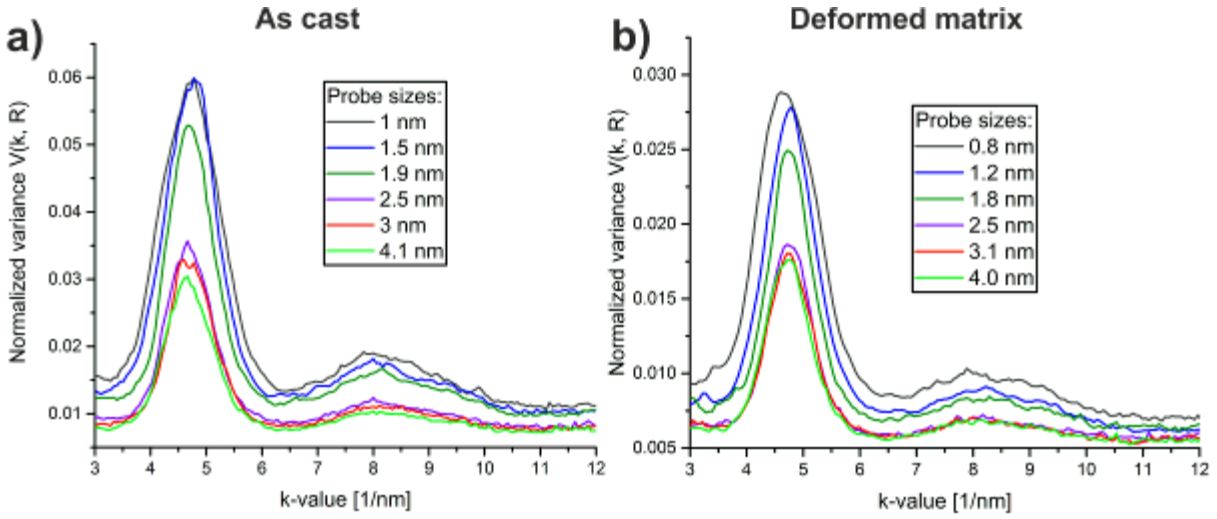
a)
As cast
Probe sizes:
1 nm
1.5 nm
1.9 nm
2.5 nm
3 nm
4.1 nm
Normalized variance V(k, R)
k-value [1/nm]
b)
Deformed matrix
Probe sizes:
0.8 nm
1.2 nm
1.8 nm
2.5 nm
3.1 nm
4.0 nm
Normalized variance V(k, R)
k-value [1/nm]

MS4.P023
Influence of fatigue on the dislocation and slip mechanisms of deep-drawing steel

V. Hoppe[1], S. Weiß[2], E. Ermilova[2], W. Dudzinski[3], A. Zak[4]

[1]Wroclaw University of Science and Technology, Centre for Advanced Manufacturing Technologies, Wroclaw, Poland
[2]BTU Cottbus–Senftenberg, Physical Metallurgy and Materials Technology, Cottbus, Germany
[3]Wroclaw University of Science and Technology, Faculty of Technology and Engineering, Wroclaw, Poland
[4]Wroclaw University of Science and Technology, Electron Microscopy Laboratory, Wroclaw, Poland

One of the most interesting phenomena occurring in metals with A2 crystallographic structure is slip asymmetry. The slip plane in a single crystal deformed by uniaxial compression differs from the slip plane during stretching while maintaining the same crystallographic orientation. Literature indicates that fatigue glide bands are different from glide bands caused by static loading. Fatigue glide bands are characterized by different width (1). Lüders' strain is the result of the formation of a micro-bulb and its movement along the length of the sample in form of a plastic wave. Plastic deformation causes accumulation of dislocations at grain boundaries as well as dislocation effects with misalignment of lattice planes and dislocation activation in additional slip bands.

The study focuses on the impact of low-cycle fatigue on the macroscopic appearance of the material due to the activation of different dislocation systems within unalloyed ferritic DC04 steel. Basic research on the material was published in Ref (2).

Tests were performed on flat samples of DC04 steel (1.0338) after low cycle fatigue (2). Macroscopic observations were compared with the results of scanning electron microscopy in combination with EBSD analysis. In addition transmission electron microscopy studies combined with SAED were carried out using a Hitachi H-800 TEM.

On the surface of the sample (fig. 1a) lines of plastic flow with a clear S-shaped crack are visible. Lüders lines are located in a slip plane oriented in the direction of maximum shear stresses (45° with respect to the direction of maximum normal stress). Crack initiation occurs within the glide bands in the ferrite grains. The inverse pole figure map (fig. 1b) shows large orientation variations inside the grains, indicating significant plastic deformation. Stress concentration becomes obvious from fig. 1c, corresponding with a significant number of subgrains, arranged in parallel families (fig. 1d). Stereographic projections obtained by means of TEM analysis (fig. 2) show that traces of glide planes {110} coincide with the directions of close-packed planes. Thus, slip systems are triggered in these directions in the network A2. Asymmetrical glide occurring in the network A2 is demonstrated in the TEM images with glide planes obtained by stereographic projection marked inside. Various cross slip dislocation systems were activated.

References:

(1) J. T. McGrath i W. J. Bratina, "Dislocation structures in fatigued iron-carbon alloys," *Philosophical Magazine Vol. 12, nr 120,* pp. 1293-1305, December 1965.

(2) Fedor Kazak and Sabine Weiß (2015). Comparability of structured and flat reference specimens made of thin sheet metal. Materials Testing: Vol. 57, No. 6, pp. 567-573.

Fig. 1: Macroscopic view (a) inverse pole figure map (b) kernel average misorientation map (c), grain boundary map (d)

Fig. 2: BF (a), DF (b) microstructures, corresponding SAED pattern (c) and stereographic projection (d) of slip defects

Examination of fatigue properties and impact of dislocation systems and slip systems on the macroscopic properties of fatigue unalloyed steels is reasonable. Stereographic projection enabled the planes, and determined the direction in which the slip took place in the area of ferrite grains It allowed to define directions in which the accumulation of dislocations in a material subjected to varying loads is observed.

Fig. 1

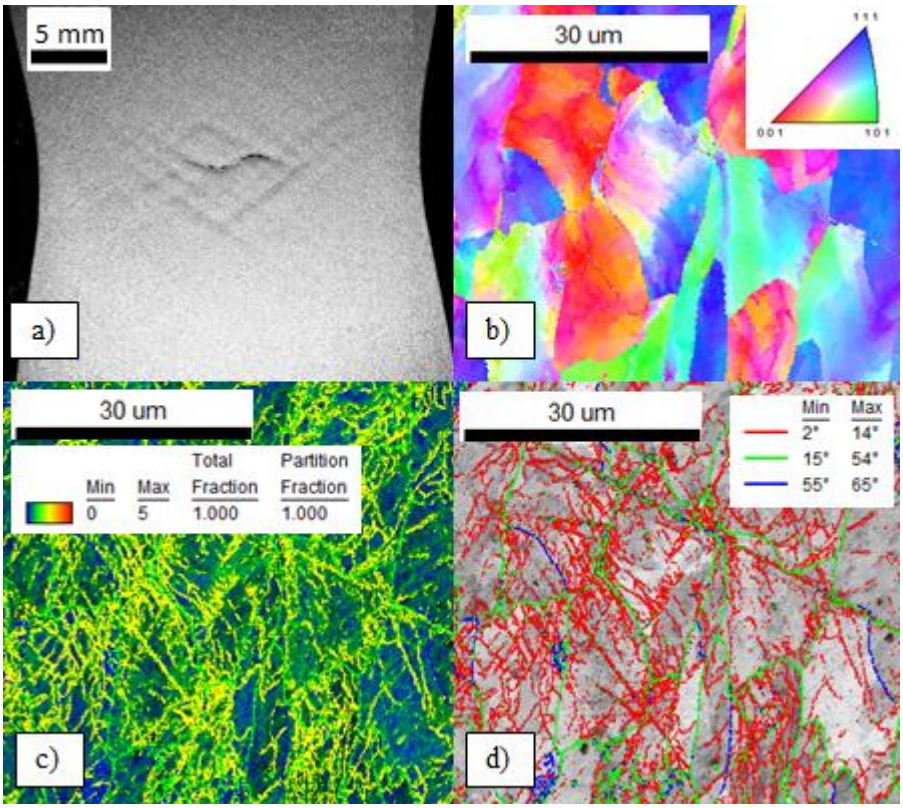
5 mm
a)
30 um
111
001
101
b)
30 um
Min Max Total Fraction Partition Fraction
0 5 1.000 1.000
c)
30 um
Min Max
2° 14°
15° 54°
55° 65°
d)

Fig. 2

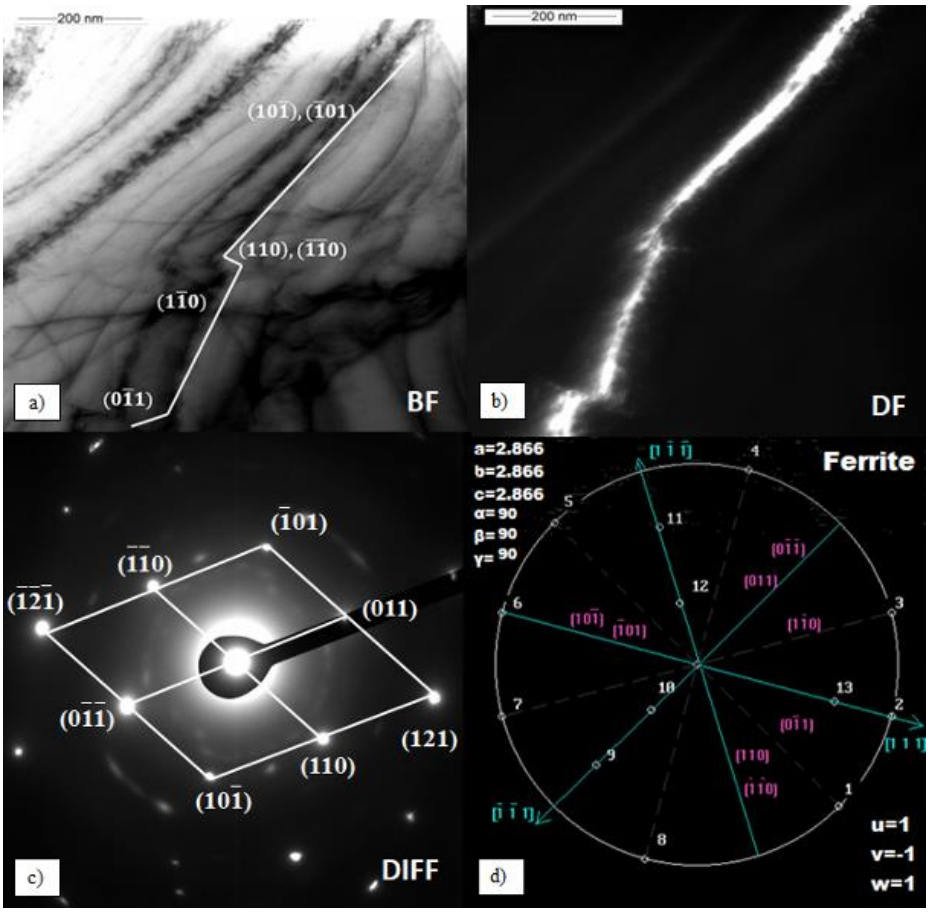
200 nm
(10$\bar{1}$), ($\bar{1}$01)
(110), ($\bar{1}\bar{1}$0)
(1$\bar{1}$0)
(0$\bar{1}$1)
a)
BF
200 nm
b)
DF
($\bar{1}$01)
($\bar{1}\bar{1}$0)
($\bar{1}\bar{2}\bar{1}$)
(011)
(0$\bar{1}\bar{1}$)
(121)
(110)
(10$\bar{1}$)
c)
DIFF
a=2.866
b=2.866
c=2.866
α=90
β=90
γ=90
Ferrite
u=1
v=-1
w=1
d)

MS4.P025
Cathodoluminescence analysis of AlO_2Sr_4/Al

N. Vaskovicova[1], N. Nakamura[2], K. Matsuda[2], S. Mikmekova[1], I. Müllerová[1]

[1]The Czech Academy of Sciences, Institute of Scientific Instruments, Brno, Czech Republic
[2]University of Toyama, Graduate School of Science and Engineering for Research, Toyama, Japan

Strontium aluminium nanophosphors are long afterglow luminescent materials at a green range of electromagnetic spectrum. To improve the luminescence properties, these phosphors are doped with Dy and Eu atoms. The phosphors are chemically and thermally stable with no radiation and tuneable emission wavelength from UV to red. The phosphor constituents can be incorporated into metals, alloys, gels, films, or fibers and these composite materials offer promising advantages for a wide range of applications (e.g. luminescent paints, display devices, sensors, light emitting diodes, emergency lighting, safety signage, bio-imaging, etc.) (1,2).

The aim of this study is to demonstrate a method for precisely identifying the AlO_2Sr_4: Eu, Dy phosphors in the Al matrix by investigating their cathodoluminescence (CL) spectra and images.

The material under investigation was AlO_2Sr_4: Eu, Dy phosphor in the Al matrix. SEM-CL system consists of a commercial SEM (Magellan 400L, Thermo Fisher Scientific) and the CL spectra were acquired using the MonoCL4 system (Gatan). The backscattered electron (BSE) images were collected by the Circular Backscatter Detector (CBS). The Energy-dispersive X-ray spectroscopy (EDS) analysis was carried out using the TEAM™ ENHANCED EDS System (EDAX). The CL spectra were collected at 5 keV acceleration voltage and the probe current was fixed at 1.6 nA. The setting of the photomultiplier tube (PMT) was: panchromatic mode (PAN) -450 V, monochromatic mode (MONO) -1100 V and for the spectra acquisition -1200 V.

Fig. 1 A shows SEM BSE image of the specimen obtained at 15 keV primary beam energy, together with the corresponding EDX map of elements distribution acquired at 10 keV (Fig. 1 B). The CL mapping in the PAN mode (Fig. 2 A) demonstrates the distribution of the AlO_2Sr_4: Eu, Dy phosphors inside the Al matrix and as visible, the effect of the different chemical composition is not obvious. Fig. 2 B shows the result of the merging of the MONO CL images captured on wavelengths 380 nm, 410 nm, 450 nm, 490 nm, 520 nm, 580 nm and 780 nm (the images were uniquely coloured for each particular wavelength as post-process in the Adobe Photoshop CS6 and merged into one). The CL spectra for particle 1 and 2 (marked in Fig. 2 A) are displayed in Fig. 2 C and D.

The SEM-CL analysis is a powerful tool for characterization of the AlO_2Sr_4: Eu, Dy phosphors distribution within the Al matrix. The CL analysis is more rapid, sensitive and effective than conventional methods, such as EDS.

References:

(1) Swart HC, et al. Physica B 407 (2012) 1664–1667.

(2) Sahu IP, et al. Res Chem Intermed (2016) 42:2791–2804.

Fig. 1: A) SEM BSE image of the specimen; B) EDS maps of elements distribution.

Fig. 2: A) CL mapping in PAN mode; B) CL mapping in MONO mode - image is merged from mono CL images; yellow coloured particles - two peaks, green coloured particles - one peak. C) CL spectrum of particle 1 (p1); D) CL spectrum of particle 2 (p2).

Fig. 1

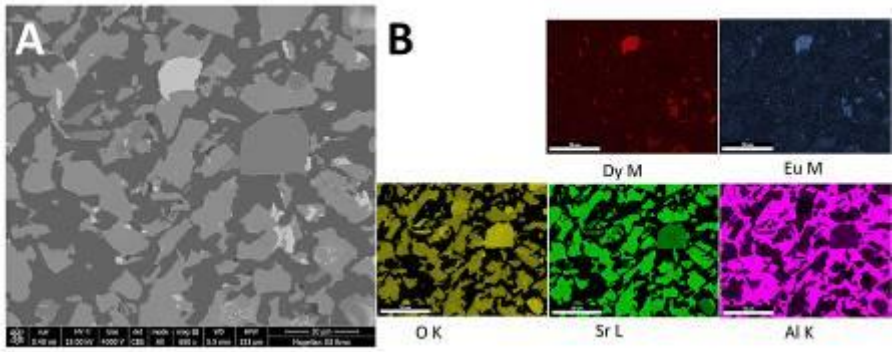

Fig. 2

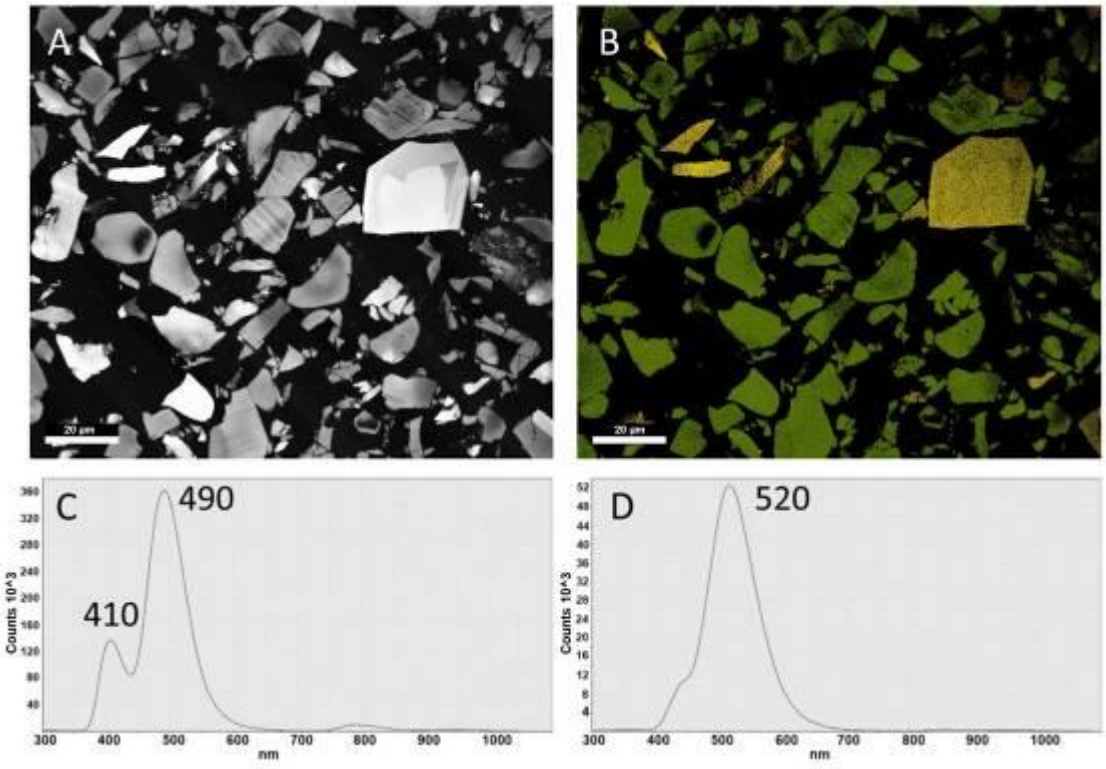

MS4.P026
Identification of the bainite morphology in medium-carbon, Si-rich steel after isothermal heat treatment

A. Krolicka[1,2], A. Zak[1], K. Radwanski[3]

[1]Wroclaw University of Science and Technology, Electron Microscopy Laboratory, Wroclaw, Poland
[2]Wroclaw University of Science and Technology, Faculty of Technology and Engineering, Wroclaw, Poland
[3]Institute for Ferrous Metallurgy, Gliwice, Poland

Of all the phases present in steels, bainite is the structure most complex and difficult to identify. The morphology of bainite depends mainly on the heat treatment parameters and the chemical composition. We can distinguish an upper, lower, granular and degenerate (lower or upper) bainite. Additionally, the silicon-rich steels exhibit a reduced amount of cementite (carbide-free bainite). Identification of the recieved morphology is possible only with the use of electron microscopy methods due to the necessity to determine the crystallographic orientation between the phases: ferrite, austenite, martensite and cementite.

The main aim of the research is identification of high silicon steel microstructure after isothermal heat treatment. In this research was put forward the thesis: conventional EBDS methods are insufficient to unequivocal identify the morphology of nanostructured bainite.

The research material was commercial 55Si7 steel with the chemical composition: 0.57%C, 0.69%Mn, 1.89%Si, 0.15%Cr and 0.19%Ni. The steel was austenitized at 900°C/30 min and then tempered at 325°C/72 h.

The microstructure identification was carried out using a high resolution SEM JOEL JSM 7200F with EBSD detector and using the conventional TEM HITACHI H-800.

On the basis of IPF Map (Fig. 1a) it was found that there are many close-packed plane (CP) ferrite groups in the area of preliminary austenite grain. The same parallel relationship of close-packed planes with austenite is compatible with K-S orientation. The Phased Distribution Map confirmed the presence of a small amount of retained austenite (Fig. 2b).

The presence of various bainite morphologies such as: upper bainite, degenerate upper bainite and carbide-free bainite was identified. The degenerated upper bainite was composed of ferrite, film austenite and coherent cementite precipitates (Fig. 2). The orientation of ferrite and austenite is consistent with the K-S orientation: <110> γ || <111> α. The orientation of ferrite and cementite is consistent with Isaichev relationship: <111> α || <010> θ

Due to the EBSD resolving possibility, the bainite morphology identification is easier available using TEM methods, in particular with the selected area electron diffraction pattern (SAED). Both research methods should be used together to investigations of multi-phase steels.

Despite the high concentration of silicon in the tested steel, the presence of coherent with ferrite plates cementite was identified. The carbides size did not allow their recognition by EBSD methods, but they were also possible for conventional SEM observations in the etched state.

In the tested steel both: lower, upper degenerate bainite and areas of carbide-free bainite (CFB) were found.

References:

(1) Takayama N, Miyamoto G, Furuhara T (2018), *Chemistry and three-dimensional morphology of martensite-austenite constituent in the bainite structure of low-carbon low-alloy steels*, Acta Materialia 145:154-164.

(2) Ohmori Y (2002), *Crystallographic aspects of bainite transformation in steels,* Scripta Materialia 47:201-206

Fig. 1: (a) IPF Map, visible different orientations of CP groups in grains (b) PD Map, visible small fraction of retained austenite

Fig. 2: (a) Bright field image of degenerate upper bainite (b) SAED with calculation (c) Dark field image from (1 1 3) reflection of filmy austenite

Fig. 1

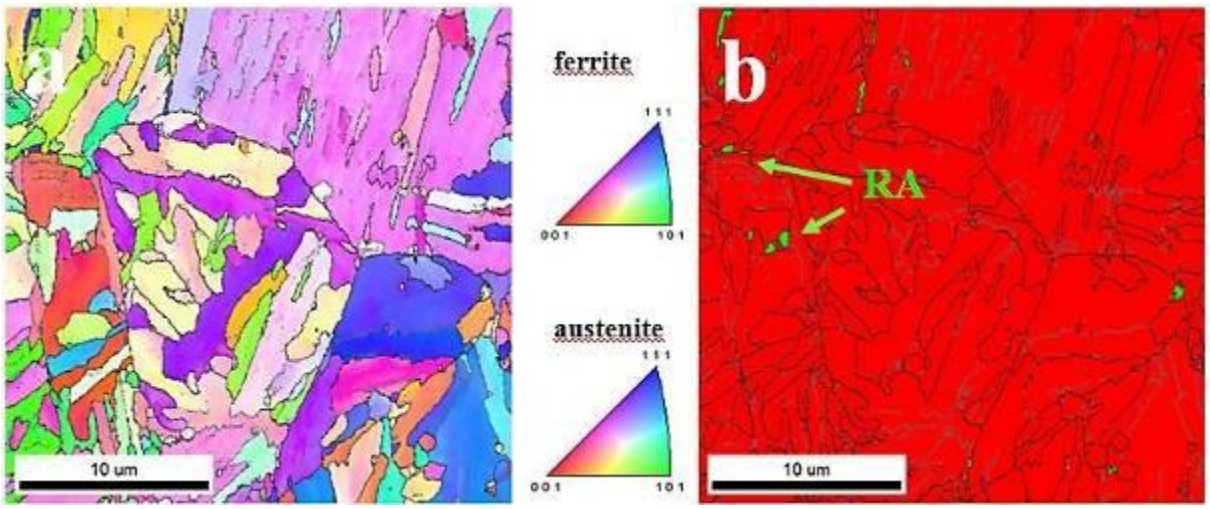
a
10 um
ferrite
austenite
b
RA
10 um

Fig. 2

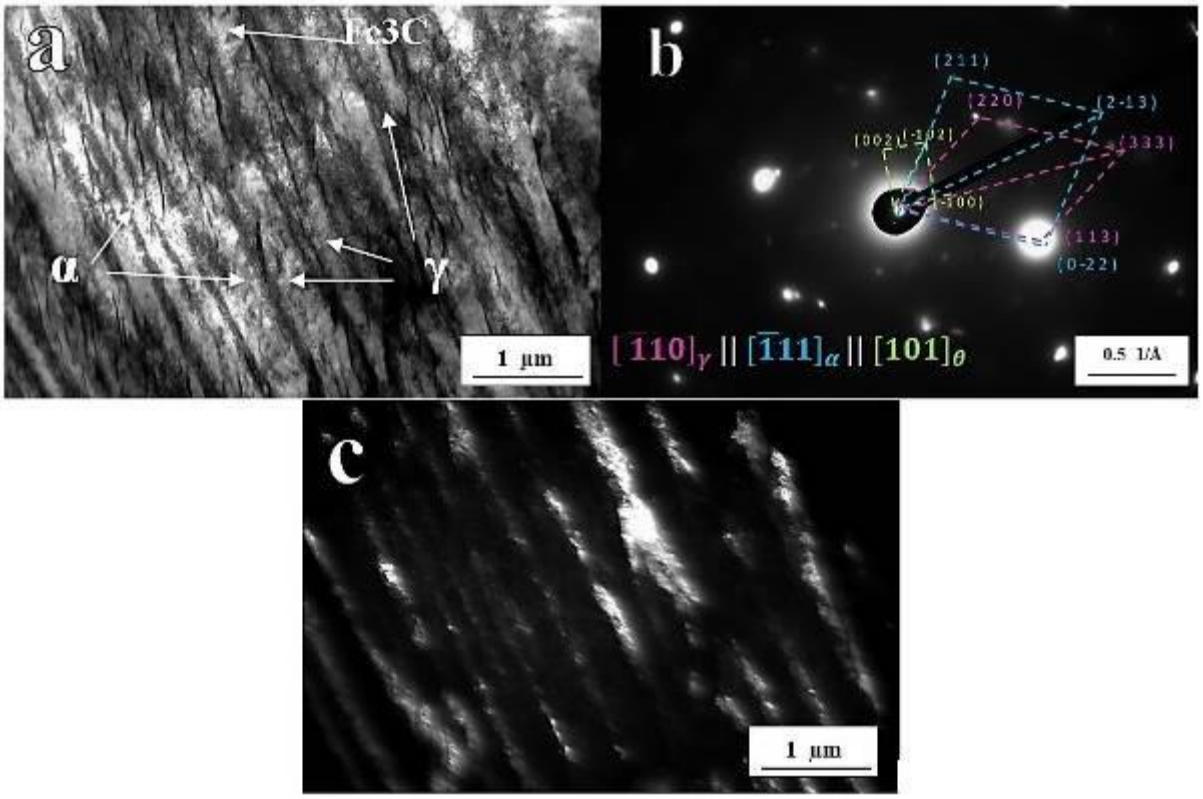
a
Fe3C
α
γ
1 μm
b
[110]γ || [111]α || [101]θ
0.5 1/Å
c
1 μm

MS4.P027
Microstructural evolution of EUROFER-ODS alloy under neutron irradiation

M. Klimenkov[1], U. Jäntsch[1], M. Rieth[1], A. Möslang[1]

[1]Karlsruhe Institute of Technology, Institute for Applied Materials - Applied Materials Physics (IAM-AWP), Karlsruhe, Germany

The neutron irradiated oxide dispersion strengthen (ODS) alloys show in a wide temperature range superior tensile and fatigue properties compared to the same type of steels without ODS particles. The detailed knowledge about radiation induced defects is of great importance for understanding the effect of ODS particles on radiation resistance and the relationship between irradiation modified microstructures and mechanical properties. Besides a detailed defect analysis, the present study also demonstrates that the formation of radiation induced defects depends not only on the irradiation temperature but also on the local distribution of ODS particles (i.e. size and local number density)

Two types of radiation induced defects – cavities and dislocation loops were observed and extensively characterized by TEM. Quantitative analysis of dislocation loops, that means determination of Burgers vector and nature, i.e. interstitial or vacancy loop, was performed by imaging of some selected grains with g-vectors of <011> and <002> types in orientation close to the [100] or [111] zone axes using visibility criteria (|g·b| values shown in Fig. 1) for each g vector near the mentioned zone axes.

Analytical investigations demonstrating the distribution of ODS particles in as-received material are shown in Fig. 2. The results demonstrate that Y_2O_3 ODS particles have a bimodal size distribution. This means that two areas with completely different spatial distribution and morphology of ODS particles exist. The "coarse area" is the region, where the size of ODS particles varied from 5 nm to 25 nm with a number density of $(2\pm0.5)*10^{20}m^{-3}$ (left side Fig. 2b). The "fine area" shows a very homogenous distribution of ODS particles with sizes less than 5 nm and number density of $(1.3\pm0.3)*10^{22}m^{-3}$ (right side Fig. 2b). TEM analysis show the significantly different formation of radiation induced defects with different distribution of ODS partickels for these areas.

Material irradiated at 350°C shows a complex structure of radiation induced defects which includes dislocation loops and voids located on ODS particles. In Fig. 3 two images are presented WBDF images with **g**(3**g**) with ***g***=[01-1] and **g**(3**g**) with ***g***=[020] vectors obtained at the orientation closely to the [100] zone axis. In part (e) the results of the Burgers vector analysis of dislocation loops in the circled area are shown. The different loops are imaged with different colors according to their Burgers vector; 8 loops of ½<111> type (yellow, green) and 9 loops of <100> type (red, blue) were detected. As it can be recognized in Fig. 3 inside the circle that 6 loops of <100> type (red) are ordered along crystallographic [100] direction. The Burgers vector of 5 loops in this area could not be unambiguously identified.

A second type of neutron radiation induced defects, namely voids were observed exclusively in "coarse area" on ODS particles. In Fig. 4 a bright field TEM image " with voids located on ODS particles is shown. The ODS particles were found to be in an amorphous state after irradiation at all temperatures.

Reviewing all experimental results, the conclusion can be drawn that ODS materials have a higher radiation resistance than equivalent alloys without ODS particles. Moreover, the ODS materials with nanoclusters and high number density show a higher radiation resistance (lower defects density) at all temperatures than materials with low number density of ODS particles.

Fig. 1

N bild	*b* / *g*	½[111]	½[$\bar{1}$11]	½[1$\bar{1}$1]	½[11$\bar{1}$]	[001]	[010]	[100]
1	[0$\bar{1}\bar{1}$]	**1**	**1**	**0**	**0**	**1**	**1**	0
2	[0$\bar{1}$1]	**0**	**0**	**1**	**1**	**1**	**1**	0
3	[020]	**1**	**1**	**1**	**1**	**0**	**2**	0
4	[002]	**1**	**1**	**1**	**1**	**2**	0	0

Table. 1 |b·g| values for all **g** vectors in orientations close to the [100] zone axis.

Fig. 2

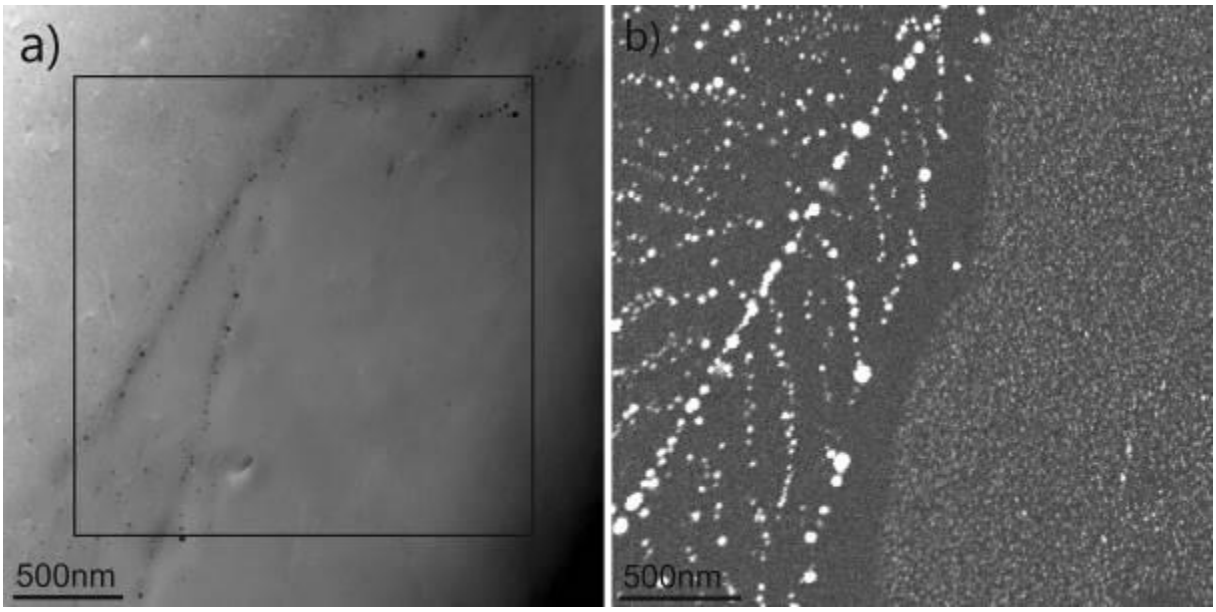
a)
500nm
b)
500nm

Fig. 3

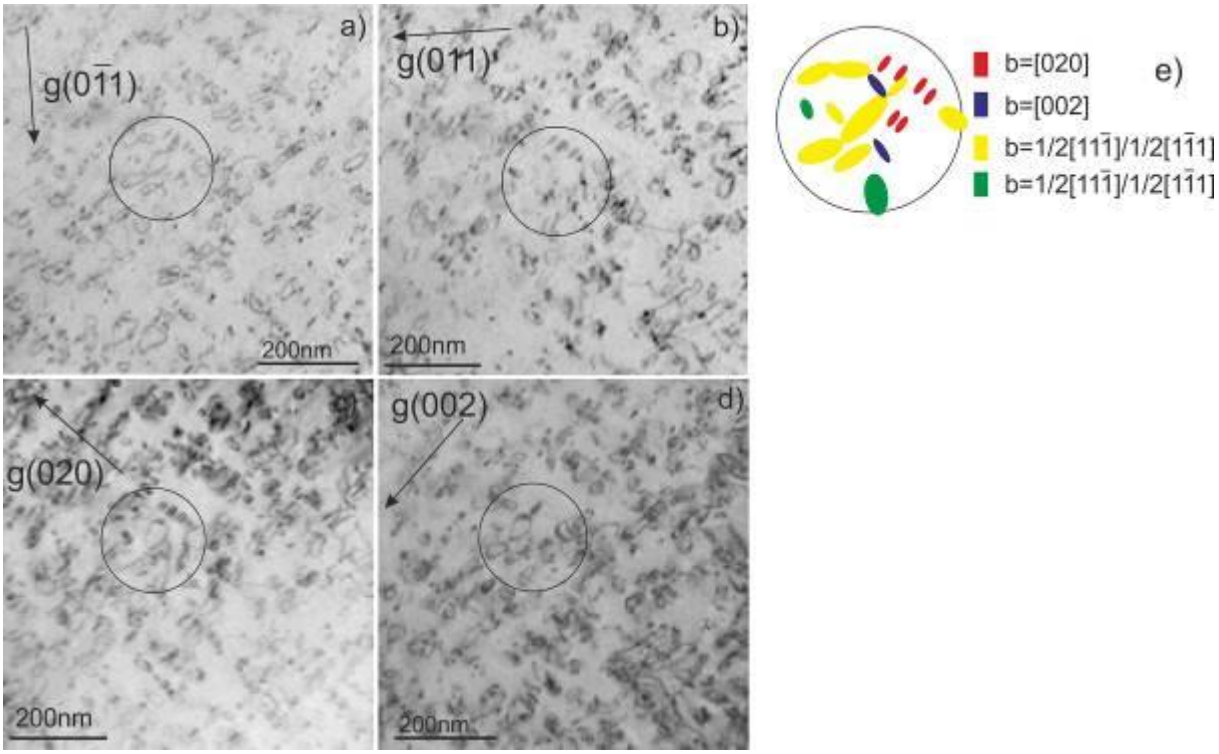
a)
g(0$\bar{1}$1)
200nm
b)
g(011)
200nm
g(020)
200nm
g(002)
d)
200nm
e)
b=[020]
b=[002]
b=1/2[11$\bar{1}$]/1/2[1$\bar{1}$1]
b=1/2[11$\bar{1}$]/1/2[1$\bar{1}$1]

Fig. 4

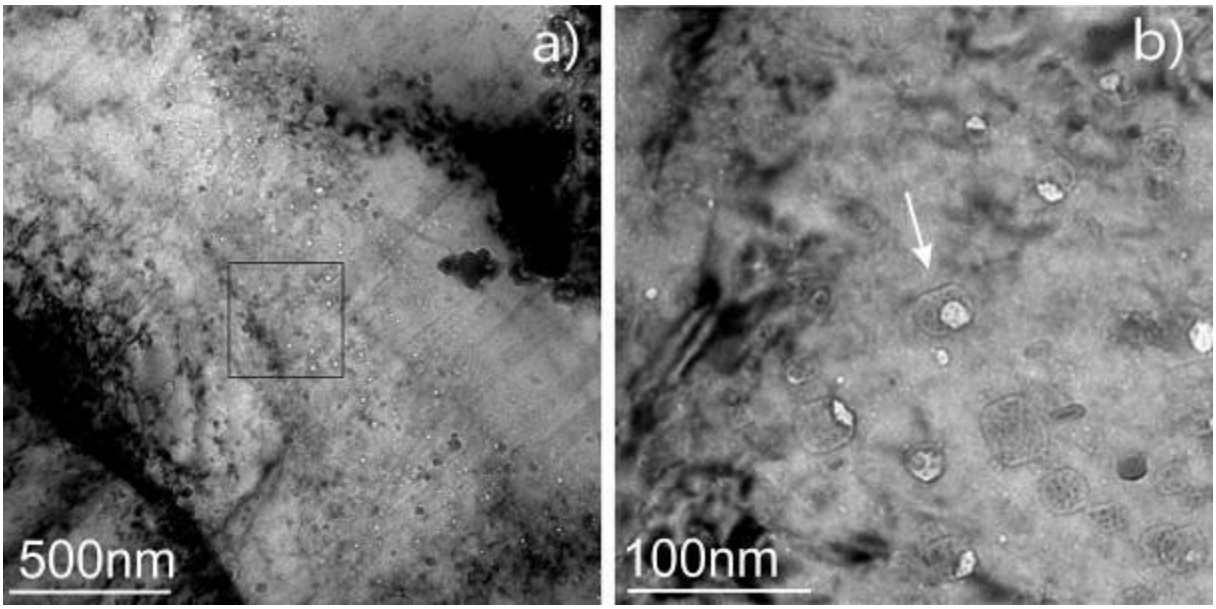

MS4.P028
In situ TEM micro-tensile testing of the deformation behavior of Ti-doped Fe-Co-Ni alloys

P. Loginov[1], D. Sidorenko[1], E. Levashov[1]

[1]NUST MISIS, Moscow, Russian Federation

Iron-based alloys, in particular Fe-Co-Ni, attract attention of researchers in the field of diamond containing metal matrix composites and tools. They can be described by high adhesion to diamond monocrystals and good combination of mechanical properties. Recent studies, focused on the development of Fe-Co-Ni alloys (1,2), demonstrate feasible techniques, that allow to produce material with ultrafine structure (average grain size 300 nm), bending strength 2000 MPa and hardness 110-115 HRB. Modification of Fe-Co-Ni alloys with small amounts of Ti (1-3 mass. %) leads to enhancement of strength up to 3000 MPa (3). However in this case the alloys don"t undergo major structural changes. In this study we made an attempt to answer a question: which mechanism is responsible for such a significant strength improvement.

The studies of structure, phase and chemical composition of Fe-Co-Ni and Fe-Co-Ni-Ti alloys were carried out using transmission electron microscope Jeol JEM 2100, equipped with Oxford EDS detector for elemental analysis. The behaviour of alloys at tensile stress was observed directly in the microscope. For this purpose we applied Hysitron PI 95 Picoindenter and Hysitron Push-to-Pull (PTP) devices, which are designed for testing of microscale samples with accumulation of quantitative load-displacement data. For these tests lamellas of hot pressed samples of Fe-Co-Ni and Fe-Co-Ni-Ti alloys were prepared by the focused ion beam (FIB) technique on a FEI Quanta 200 3D FIB instrument and mounted on PTP device. Tensile tests were carried out with constant displacement rate 1 nm/s.

The detailed investigation of Fe-Co-Ni-Ti alloy structure showed the presence of nanosized precipitates of intermetallic phase FeTi, located at grain boundaries of α-Fe grains. No other structural features were observed. The failure behavior at tensile tests Fe-Co-Ni-(Ti) lamellas was ductile. For both titanium modified and titanium free samples the crack formation was preceded by sliding of dislocations towards the thin area and dislocation pile-up at grain boundaries. The deformation of Fe-Co-Ni-Ti samples was accompanied with changes of the orientation of the grains, nearest to the crack. It was established, that the crack propagation mode was intragranular. The direct observation of «matrix-matrix» and «matrix-FeTi» interfaces showed its stability at tensile loads. It indicates, that grain boundary dislocation sliding is suppressed by FeTi precipitates, thus resulting in increasing of critical flow stress at plastic deformation.

The work was carried out with financial support from the Ministry of Education and Science of the Russian Federation in the framework of the Increase Competitiveness Program of NUST "MISiS" (No. К2-2018-013)

References:

(1) P. Loginov et al. Metals-Basel, 7 (2017), № 570.

(2) T. Furuta et al. J Mater Sci, 45 (2010), Pp. 4745–4753.

(3) P. Loginov et al. Int J Refract Met H, 79 (2019), Pp. 69-78.

MS5.001 invited
High-Resolution Imaging Using the Low-Voltage-Tunable SALVE Microscope to Study the Dynamic of Single-Atom Interactions

J. Biskupek[1], F. Börrnert[1], K. Cao[1], U. Kaiser[1]

[1]University of Ulm, Central Facility of Electron Microscopy, Ulm, Germany

Imaging single atoms in particular single light atoms and their interactions is at the heart of low-dimensional material"s characterization as their properties are often determined on the level of the single atoms. Thus, an instrument is requested, allowing extremely high resolution and contrast below the material"s knock-on damage threshold a specimen geometry that helps protecting the sample against damaging effects, resulting from incident electron – specimen electron interactions (1). Lowering the electron accelerating voltages to values of typically 80 kV drastically reduces knock-damage, but dedicated structures like fullerenes require investigations below 40 kV to image the materials in their pristine state.

Working at reduced voltages, however, decreases the obtainable resolution to about 0.2 nm at 80 kV when using standard 3rd order aberration correctors such as the hexapole-type correctors (2). The correction of 5th order geometric aberration correction together with chromatic aberration correction is necessary to archive atomic resolution at voltages at voltages even at 20 kV. The dedicated C_S/C_C SALVE (sub-Ångström low voltage electron microscopy) TEM (3) operates between 20 to 80 kV and still delivers sub-Å resolution at 40 kV.

We present examples of atomic imaging and local electron energy loss spectroscopy (EELS) obtained with the SALVE instrument using special specimen geometries. In the first two examples we use single-walled carbon nanotubes, which are filled in the first case with fullerenes containing small molecules as H_2O and HF (see Fig.1), and in the second with middle and late transition metal nanocatalysts (4) (see Fig. 2) and study their atomic scale dynamics. In a third example, we use two graphene sheets protecting the diffusion of Li-atoms. In particular we study the reversible and electrically controlled superdense ordering of lithium between two graphene sheets (5) (see Fig. 3).

References:

(1) R. F. Egerton et al. *Ultramicroscopy* 110 (2009) 991

(2) M. Haider et al. *Ultramicroscopy*, 75 (1998) 53

(3) M. Linck et al. *Phys. Rev. Let.* 117 (2016) 076101

(4) K. Cao et al. *Nature Communications* 9 (2018) 3382

(5) M. Kühne et al. *Nature* 564 (2018) 234

Fig. 1: – 30 kV C_C/C_S corrected HRTEM image of HF molecules inside C60 molecules embedded into carbon nanotubes. The line profile show the intensity and contrast of the single F-atoms inside the fullerene.

Fig. 2: 80 kV C/C_S corrected HRTEM image series of Re dimers in a carbon nanotube. The projected distance and configuration of the two Re atoms to each other change as function of time, respectively dose. Finally the Re dimers leaves the tube. (the number indicates the projected atomic distance)

Fig. 3: Imaging of lithium embedded in bi-layer of graphene. (a) 80 kV C_C/C_S corrected HRTEM raw image. (b) Fourier-filtered image with the graphene lattice removed. (c) magnified image showing the crystalline Li-lattice . (d) Gauss-filtered image of (c). (e) red and blue circles indicating single Li atoms and symmetric positions without Li atoms, respectively.

Fig. 1

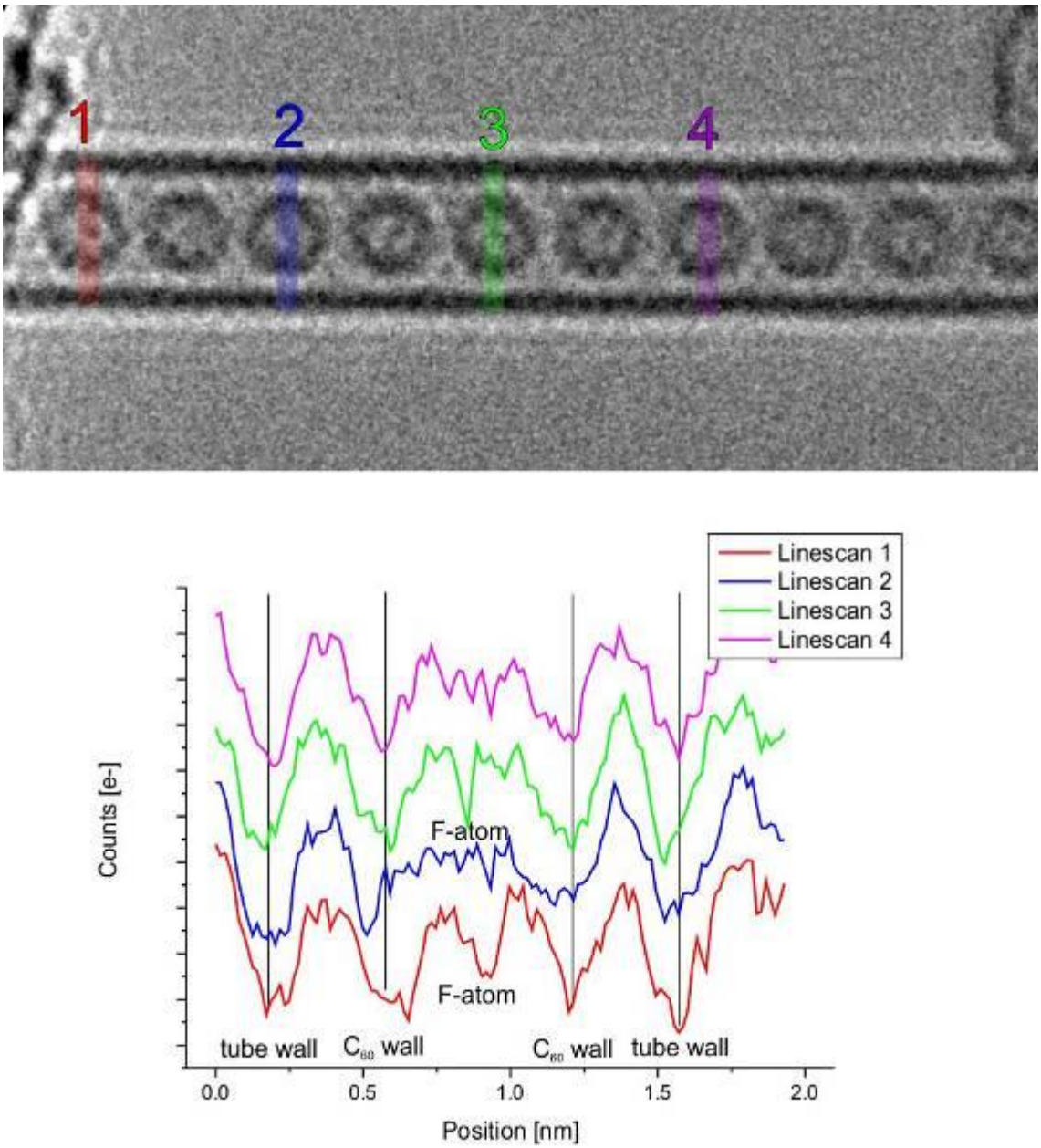
1
2
3
4
Linescan 1
Linescan 2
Linescan 3
Linescan 4
Counts [e-]
F-atom
F-atom
tube wall
C_{60} wall
C_{60} wall
tube wall
0.0
0.5
1.0
1.5
2.0
Position [nm]

Fig. 2

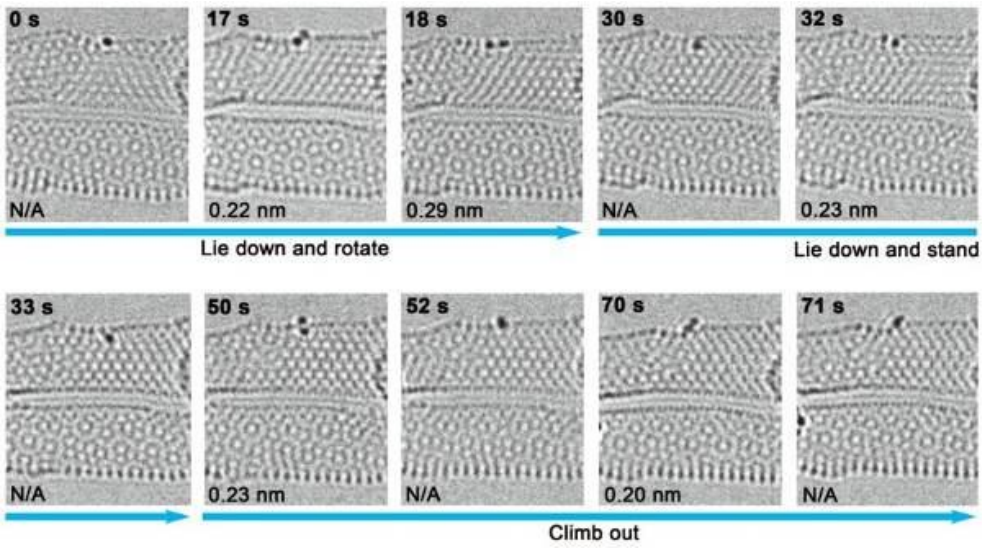
0 s
17 s
18 s
30 s
32 s
N/A
0.22 nm
0.29 nm
N/A
0.23 nm
Lie down and rotate
Lie down and stand
33 s
50 s
52 s
70 s
71 s
N/A
0.23 nm
N/A
0.20 nm
N/A
Climb out

Fig. 3

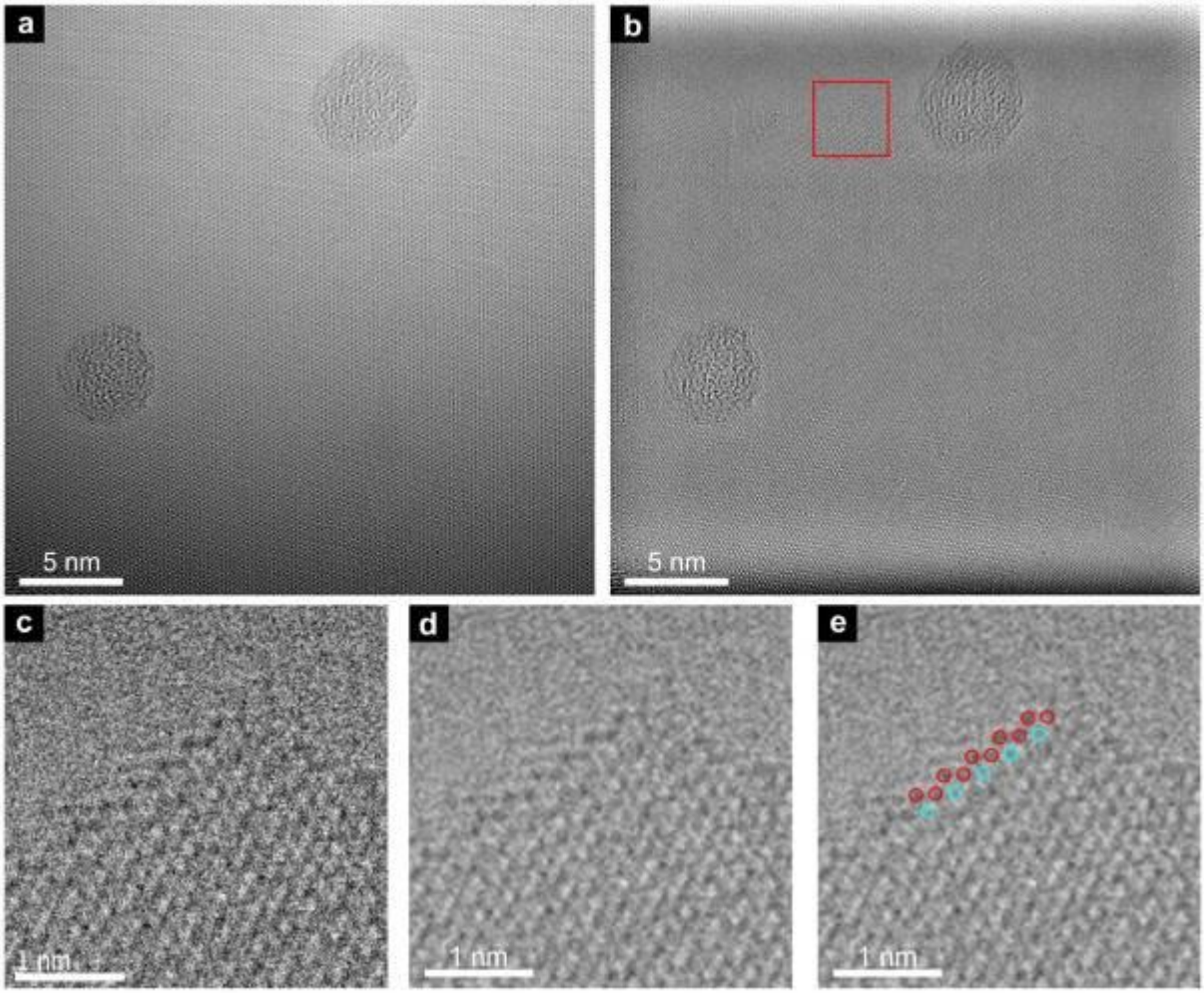

MS5.002
Investigation of dose reduction in TEM through compressed sensing

W. Van den Broek[1], B. W. Reed[2], A. Béché[3], J. Verbeeck[3], C. T. Koch[1]

[1]Humboldt-Universität zu Berlin, Institut für Physik & IRIS Adlershof, Berlin, Germany
[2]Integrated Dynamic Electron Solutions, Inc., Pleasanton, CA, United States
[3]Antwerp University, EMAT, Antwerp, Belgium

In the investigation of soft matter dose reduction is important as beam damage is often related to the total dose. Other damage mechanisms such as the temporal or spatial distribution of the dose are not considered here. Since compressed sensing (CS) (1) is capable of retrieving sparse signals from a low number of measurements it has often been considered for dose reduction in TEM.

Since a low number of measurements is not equivalent to a lower dose, it is examined here if a CS reconstruction can outperform a conventional Shannon scan that is recorded with the same electron budget and denoised with the same prior knowledge applied in the CS reconstruction. An important difference with much of CS literature is the use of positive, flux-preserving sensing matrices and the presence of Poisson noise.

In CS, the M measurements y are obtained by integrating the detector signal while the probe visits an arbitrary fraction p of the N pixels in the image x, where $p = 1/N$ yields the inpainting set-up. x is then retrieved by minimizing its total generalized variation, subject to the mean square residuals equaling the noise variance (2). Applying the same approach to a Shannon scan realizes denoising with the same prior knowledge.

In order to compare different settings, we calculate the detective quantum efficiency of the set-ups (DQE), yielding $(1-p)/(pN)$ and 1 for CS and Shannon scans respectively, in the absence of read-out noise (2). Next, it is illustrated that the DQE predicts the minimum of the mean squared error (MSE) of the reconstructions well, and can hence be used to predict optimal values for p and compare different set-ups.

A gold nanorod was recorded on a FEI Titan³ microscope operating in STEM mode at 300 kV. First, an image was raster scanned with a high intensity and after application of a 3 by 3 median filter, it served as ground truth to compute the MSE. Then an image was recorded with a 35 times lower dose and from it 9 inpainting recordings were extracted with M ranging from $0.1N$ to $0.9N$; from these recordings a reconstruction was computed. For comparison a denoising was calculated as well. In Figure 1 the recordings and selected reconstructions are presented, and it is shown that the MSE follows the predicted DQE of M/N well.

Since the DQE for CS is maximized for $p = 1/N$, an inpainting approach is the optimal CS set-up. Furthermore, for this value of p the DQE for CS is virtually equal to the DQE of a Shannon scan, leading to the conclusion that no improvement of reconstruction quality (measured through the MSE) is to be expected from CS, as was confirmed in the experiment. (3)

(1) J. Romberg, IEEE Signal Processing Magazine 25 (2008), p. 14.

(2) W. Van den Broek et al., IEEE Transactions on Computational Imaging, DOI:10.1109/TCI.2019.2894950

(3) Acknowledgements. WVdB: DFG project BR 5095/2-1. Hercules fund from the Flemish Government for the Qu-Ant-EM microscope. AB, JV: FWO project G093417N. CTK: DFG project CRC 951. Prof. L. Liz-Marzan for the TEM sample.

Fig. 1: *Left*: (*a*) Ground truth image. (*b*) Image at reduced dose. (*c*) Reconstruction from $M = 0.1N$, and (*d*) reconstruction from $M = N$ measurements. *Middle*: Profiles of the central vertical line. *Right*: Good match between DQE^{-1}s and MSEs.

Fig. 1

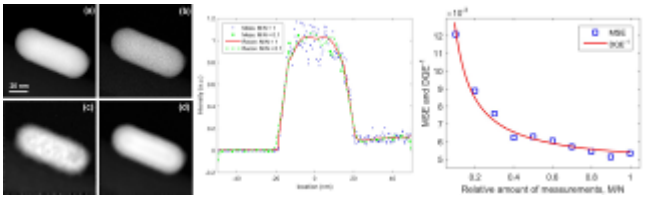

MS5.003
Prospects for atomic lattice imaging of organic crystals by Scanning Transmission Electron Microscopy

A. P. Brown[1], M. S'ari[1], R. Hooley[1], J. Cattle[1], M. Ilett[1], N. Hondow[1], R. Brydson[1]

[1]University of Leeds, School of Chemical and Process Engineering, Leeds, United Kingdom

The current generation of (scanning) transmission electron microscopes (S/TEMs) can readily provide atomic scale resolution to study the projected structure and chemistry of inorganic crystals and crystalline surfaces. Organic crystals however are so sensitive to electron irradiation that analysis by S/TEM generally requires limiting damage to the sample while extracting useful information (1). This leads to the concept of dose limited resolution for samples that are sensitive to such radiolysis damage and so informs how we might exploit improvements in detectors and techniques to obtain information at the highest possible spatial resolution.

Here, we will explore the use of an FEI Titan3 Themis G2 operated at 300 kV and equipped with a monochromator and integrated differential phase contrast to analyse materials sensitive to radiolysis damage. We will show that STEM offers potential benefits over TEM in the presence of hydrocarbon contamination for the detection of irradiation induced faults in the calcite lattice (2). And that for vitreous ice, cryo-preparations damage caused by the electron beam occurs at higher electron fluences in STEM compared to TEM due to diffusion limited damage by the radiolysis products generated in the ice (3). We will also explore enhancement of phase contrast in weakly scattering thin specimens such as zeolites and organic crystals by STEM iDPC and STEM scanning moire fringe imaging respectively (4).

We will demonstrate that these routes open up the possibility of crystal lattice resolution images of organic compounds used by the pharmaceutical industry and that this can provide important information on the effects of formulation processing on drug properties. Enabling for example, identification of sites of recrystallization in amorphous solid dispersions.

References:

(1) S'ari et al. Mol. Pharm. 2018, 15 (11), 5114-5123

(2) Hooley, Brown and Brydson, Micron 2019, 120, 25-34

(3) Ilett et al. Micron 2019, 120, 35-42

(4) S'ari et al. Micron 2019, 120, 1-9

MS5.004 invited
In situ Microscopy of graphene: mechanical cleaning, dislocation manipulation and single-molecule imaging

P. Schweizer[1], C. Dolle[1], P. Denninger[1], L. Vogl[1], D. Dasler[2], S. Gsänger[3], B. Meyer[3], F. Hauke[2], A. Hirsch[2], E. Spiecker[1]

[1]Institute of Micro-and Nanostructure Research, FAU Erlangen-Nuremberg, Materials Science, Erlangen, Germany
[2]Chair of Organic Chemistry II, FAU Erlangen-Nuremberg, Chemistry, Erlangen, Germany
[3]Computer Chemistry Center, FAU Erlangen-Nuremberg, Erlangen, Germany

Graphene is still one of the most studied materials with new and outstanding findings appearing almost every day. Recent findings include unusual superconductivity in twist bilayer graphene[1] and the possibility of direct manipulation of single impurity atoms in the graphene lattice[2]. Besides the fascinating intrinsic properties of graphene, the material is also a perfect test specimen for electron microscopy and materials science, promising new insights for both fields.

In this work an overview of our recent activities regarding *in situ* microscopy on graphene will be given. First, *in situ* mechanical cleaning will be discussed. The technique relies on fine tips that can be controlled using micromanipulators used in a broom-like fashion (see figure 1 a for a schematic representation). The tips effectively remove adsorbed contamination while leaving the graphene membrane intact entirely. Exemplary frames from an *in situ* cleaning experiment (performed in SEM) are shown in figure 1 c. Using two tips subsequently on each side of the membrane, contamination can be removed from both sides. Adapting the approach to TEM, atomic cleanliness achieved can be confirmed using HRTEM (d). The question of "how clean is clean" will be discussed on the example of surface-diffusion driven *in situ* synthesis of a turbostratic graphene layer in TEM.

While cleanliness improves the stability of graphene in TEM it also enables new experimental approaches entirely. While 1-dimensional line defects known as dislocations have long been studied in materials science, they have recently seen renewed interest due to the advent of 2D materials. With bilayer graphene being the thinnest material to host these extended defects it is the perfect playground to explore their fundamental behavior. Using micromanipulation and STEM in SEM individual dislocations are manipulated *in situ*[3]. The fundamental behavior of those line defects is confirmed and a new switching mechanism is demonstrated.

Finally, mechanical cleaning will be used to study individual molecules covalently attached to graphene. Graphene is functionalized with dodecyl moieties using an established wet-chemical approach. The Functionalization introduces sp^3 defects into the lattice which can be inferred from Raman spectroscopy. The direct observation however is hindered by residual contamination on the graphene sheets which is removed selectively by mechanical cleaning in TEM. After cleaning individual molecules attached to graphene are imaged using HRTEM. To understand the contrasts, complementary Molecular Dynamics simulations have been performed that served as input for dynamic HRTEM image simulations. Those simulations take the dynamic movement of an object during imaging in TEM into account and result in a very good fit between experiment and simulation. A dynamic movement and final desorption of the attached molecules could be induced with the electron beam.

References:

(1) Cao, Y. *et al. Nature* 556, 43 (2018).

(2) Tripathi, M. *et al. Nano Lett.* 18 (2018).

(3) Schweizer, P., Dolle, C. & Spiecker, E. *Sci. Adv.* 4 (2018).

Fig. 1: a) Artistic and schematic (b) representation of the cleaning process. c) Frames from an *in situ* cleaning Experiment of graphene achieving atomic cleanliness (d).

Fig. 2: a) Artistic representation and actual data (b) of dislocation manipulation performed on bilayer graphene. c) Dodecyl molecules covalently attached to graphene. d) HRTEM investigations of such moieties and their dynamical movement.

Fig. 1

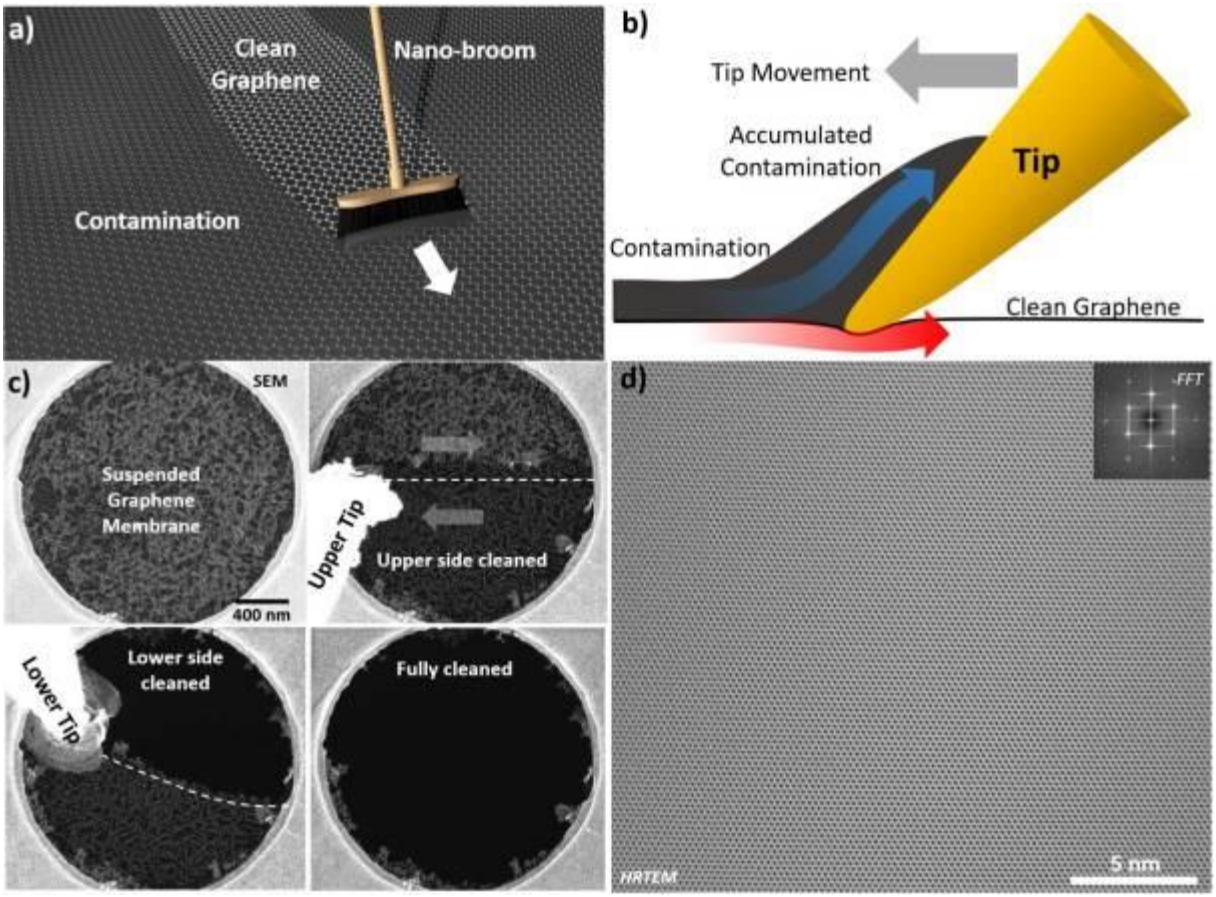
a)
Clean Graphene
Nano-broom
Contamination
b)
Tip Movement
Accumulated Contamination
Tip
Contamination
Clean Graphene
c)
SEM
Suspended Graphene Membrane
400 nm
Upper Tip
Upper side cleaned
Lower Tip
Lower side cleaned
Fully cleaned
d)
FFT
HRTEM
5 nm

Fig. 2

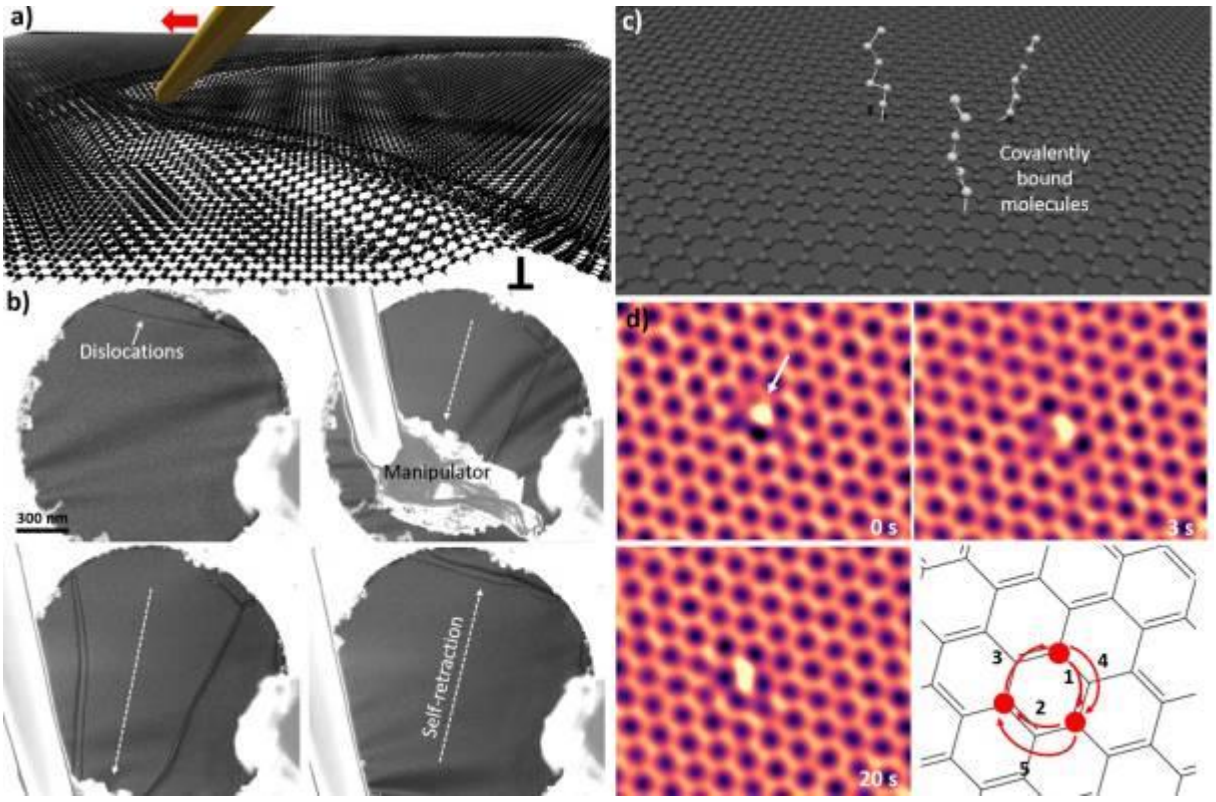
a)
b)
Dislocations
Manipulator
300 nm
Self-retraction
c)
Covalently bound molecules
d)
0 s
3 s
20 s
1
2
3
4
5

MS5.005
Exploring the color-coded properties of single-walled carbon nanotubes by advanced nano-area electron diffraction techniques

H. Jiang[1], Y. Liao[1], N. Wei[1], P. Laiho[1], Q. Zhang[1], E. Kauppinen[1]

[1]School of Science, Aalto University, Department of Physics, Espoo, Finland

It is well known that the controlled growth of single-walled carbon nanotubes (SWCNTs) with narrow chirality distributions is challenging but vital to their potential applications. We have recently1successfully achieved a direct synthesis of single-walled carbon nanotube thin films with various colors using a novel floating-catalyst-CVD process with ferrocene-based iron catalyst particles and CO as the carbon source. The color is tunable by adjusting the reactor conditions, i.e. the temperature and especially the addition of CO2. Based on electron diffraction analysis2of individual SWCNTs in our colorful SWCNT thin films, we have attributed the colors of the SWCNT thin films to their narrow diameter in certain ranges which give rise to absorption peaks in the visible region. It is demonstrated that the narrow (*n, m*) chirality distribution also accounts for the display of certain color of SWCNT thin films.

By optimizing the reaction conditions, we were able to obtain SWCNTs with narrow chirality distribution centered around the (11,9) tube, and more than 98% nanotubes having diameters in the range of 1.2-1.5nm. The center of the chirality distribution can further be downshifted to around (9,8) and (10,7) by just modulating the gas (CO2) flow rate and reaction temperature. Accordingly, the color of the SWCNT thin films can be tuned from grey, green, brown to grey.

Our findings have paved the way towards the controlled synthesis of SWCNTs with favorable structure. In particular, our color-coded SWCNT thin films may open new fields for novel applications of SWCNTs in optoelectronic devices.

References:

(1) Liao, Y.P., et. al, submitted to *JACS* (2018).

(2) Jiang, H. et. al, *Carbon,*45 (2007), 662.

MS5.006
4DSTEM Pair Distribution Function Mapping of Morphology and Structure of Amorphous Organic Material

X. Mu[1], A. Mazilkin[1], C. Sprau[2], A. Colsmann[2], C. Kübel[1,3,4]

[1]Karlsruhe Institute of Technology, Institute of Nanotechnology, Eggenstein-Leopoldshafen, Germany
[2]Karlsruhe Institute of Technology (KIT), Light Technology Institute (LTI), Karlsruhe, Germany
[3]Karlsruhe Institute of Technology (KIT), Helmholtz-Institute Ulm for Electrochemical Energy Storage (HIU), Ulm, Germany
[4]Karlsruhe Institute of Technology (KIT), Karlsruhe Nano Micro Facility (KNMF), Eggenstein-Leopoldshafen, Germany

Imaging organic materials at the nanoscale as well as analyzing their local atomic structure has been a long-time challenge as the weak scattering from carbon based matters as well as their amorphous structure and beam sensitive nature. Hereby, we propose a new low-dose approach for imaging the phase distribution and for analysing the local structure of amorphous or partially crystalline organic materials (1) based on scanning transmission electron diffraction (4DSTEM) pair distribution function analysis (PDF) (2).

We firstly show that PDF analysis of electron diffraction (3) can be used to characterize the short- and medium-range order in aperiodically packed organic molecules. As shown in figure 1, the structure evolution can be monitored, by which the beam induced modification of molecular packing and associated bond broken as well as the dose limit are understood. Moreover, we show that, as illustrated in figure 2, 4DSTEM-PDF does not only provide local structural information with a minimum spatial resolution to a nanometer, but can also be used to image the phase distribution of organic composites. The distinct and thickness independent contrast is generated by utilizing the structural difference between the different types of molecules and taking advantage of the dose efficiency due to use of the full scattering signal. Therefore, this approach is particularly interesting for imaging unstained organic or polymer composites without distinct valence states for electron energy loss spectroscopy. In addition, we will also demonstrate the 4DSTEM data can not only help us to optimise the conditions of convergence/scattering angle in conventional STEM-BF/DF to image phase distribution of organic molecules with reduced dose, but also provide but also provides phase contrast for ultralow dose imaging.

We explore the possibilities of this new approach using (6,6)-phenyl C61-butyric acid methyl ester (PCBM) and poly(3-hexylthiophene-2,5-diyl) (P3HT) as the archetypical and best-investigated semiconductor blend used in organic solar cells, compare our phase distribution with virtual dark-field analysis and validate our approach by electron energy loss spectroscopy (4).

References:

(1) X. Mu et al, Microscopy, (2019) accepted.

(2) X. Mu et al, Ultramicroscopy 168, 1–6 (2016).

(3) X. Mu et al, J. Appl. Crystallogr. 46, 1105–1116 (2013).

The authors thank Quantum Detector Ltd (UK) for sharing their Medipix3-S1 detector for the project. Xiaoke Mu acknowledges Deutsche Forschungsgemeinschaft"s (MU 4276/1-1) support for the development of STEM-PDF.

Fig. 1: Beam induced structural changes in the neat P3HT film measured at 300 keV acceleration voltage. (a) Azimuthally integrated diffraction profiles and (b) PDFs. The legend notes the dose. The top red and bottom green are PDFs of P3HT and PC61BM for comparison. The atomic model of the P3HT was contructed by MD simulation.

Fig. 2: (a) A typical (HR)TEM bright field image of the blend film. (b) Virtual STEM HAADF image. (c) Procedure for STEM-PDF analysis. (d) PDF maps of PCBM and (e) the P3HT phase at the same location as in b. (f) RGB color mix of d (green) and e (red). (g) A typical EFTEM map of the blend film. (h) PDFs of the P3HT-rich (red solid line) and PCBM-rich (green solid line) phases of the blend extracted from the STEM-PDF cube. PDFs of the neat P3HT (red dashed line) and PCBM (green dashed line) films obtained by using the SAED microscope setup. All scale bars are 100 nm.

Fig. 1

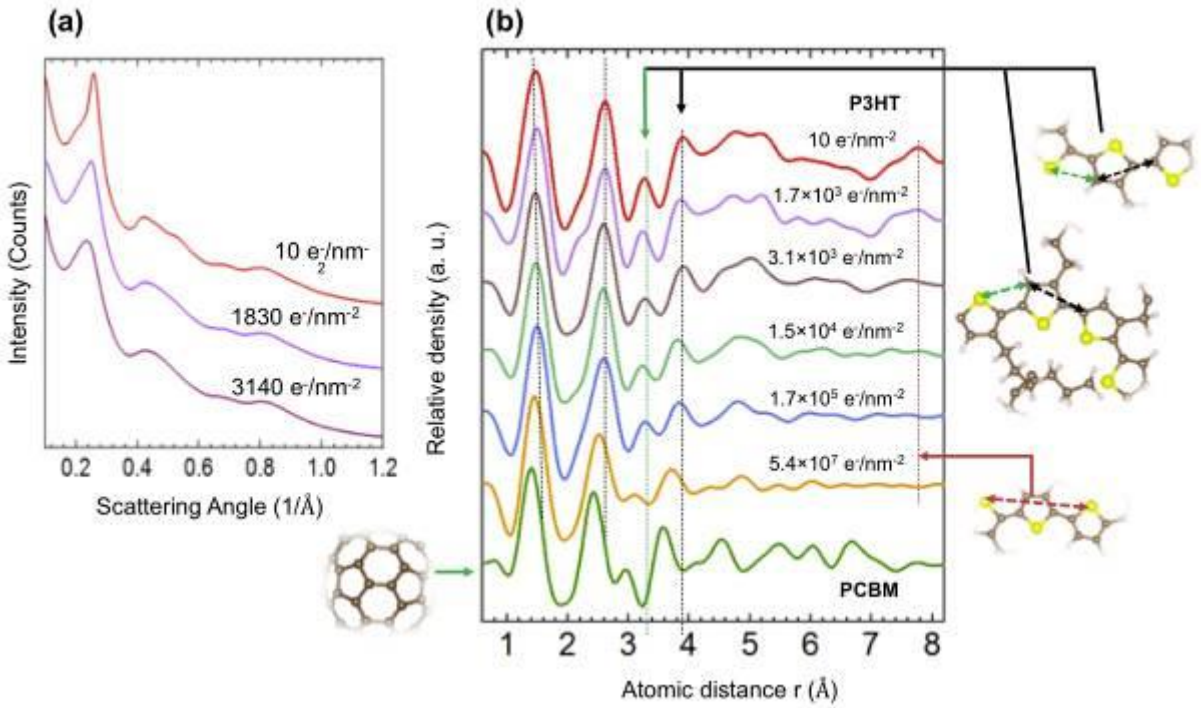
(a)
(b)
Intensity (Counts)
10 e⁻/nm⁻²
1830 e⁻/nm⁻²
3140 e⁻/nm⁻²
0.2 0.4 0.6 0.8 1.0 1.2
Scattering Angle (1/Å)
Relative density (a. u.)
P3HT
10 e⁻/nm⁻²
1.7×10³ e⁻/nm⁻²
3.1×10³ e⁻/nm⁻²
1.5×10⁴ e⁻/nm⁻²
1.7×10⁵ e⁻/nm⁻²
5.4×10⁷ e⁻/nm⁻²
PCBM
1 2 3 4 5 6 7 8
Atomic distance r (Å)

Fig. 2

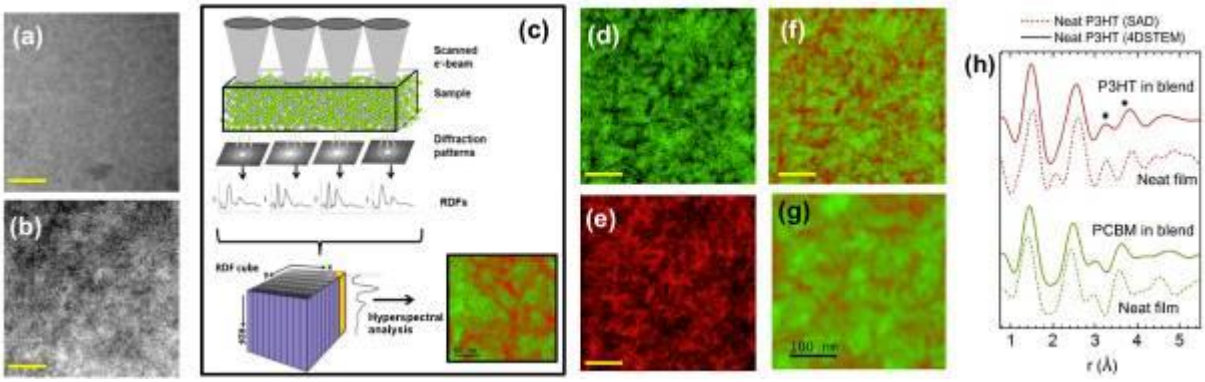
(a)
(b)
(c)
Scanned e⁻-beam
Sample
Diffraction patterns
RDFs
RDF cube
Hyperspectral analysis
(d)
(e)
(f)
(g)
100 nm
(h)
Neat P3HT (SAD)
Neat P3HT (4DSTEM)
P3HT in blend
Neat film
PCBM in blend
Neat film
1 2 3 4 5
r (Å)

MS5.P001
Towards functionalised cyanine dyes with novel structural and photo physical properties

B. Schade[1], A. K. Singh[2], V. Wycisk[3], H. von Berlepsch[1], R. Haag[2], C. Böttcher[1]

[1]Freie Universität Berlin, Forschungszentrum für Elektronenmikroskopie und Gerätezentrum BioSupraMol, Berlin, Germany
[2]Freie Universität Berlin, Institut für Chemie und Biochemie - Organische Chemie, Berlin, Germany
[3]Oxford University, Department of Chemistry - Chemistry Research Laboratory, Oxford, United Kingdom

Cyanines constitute a fascinating group of organic dyes. In aqueous solution, planarity and dispersive forces of their chromophores drive the self-assembly into diverse nanostructures with considerably different photophysical properties. Basically, two types of aggregates can be distinguished by their shift in absorption, H-aggregates and J-aggregates. The latter are of special interest because their enhanced fluorescence serves the development of photosensitizers, functional materials, and biomedical applications. In 1995 Dähne *et al.* created cyanine dyes with pronounced amphiphilic character introducing long hydrocarbon chains at the hydrophobic rim of the TDBC chromophore.[1] Since then, spectroscopic and electron microscopic investigations had promoted our knowledge on the influence of molecular arrangements on supramolecular and photophysical properties of these aggregates.[2-4] Physical and molecular models were applied to understand the unique characteristics.

Of special interest are tube-like J-aggregates. They mimic light-harvesting antenna of green sulphur bacteria, while their charge mobility is attractive for optoelectronic applications.[5] In a current project we attempt to outmatch intermolecular interactions of the chromophores to produce novel supramolecular assemblies with new properties and determine their correlation with the molecular structures. One task aims at replacing the ionic head groups with uncharged polyhydroxy groups along with the introduction of well-defined chirality. Other emphasis is placed on the introduction of super hydrophobic fluorocarbons.

Next to the development of synthetic strategies, we elucidated the self-assembled structures using electron cryo-microscopy (cryo-TEM) as well as electron cryo-tomography (cryo-ET) and complemented the results with absorption and fluorescence spectroscopy techniques. We also employed statistical image analysis and phase plate enhanced close to focus TEM where indicated.

Absorption spectra indicate various J-aggregation of stereoisomers and mixtures in water. Cryo-TEM discloses the formation of single tubes for achiral compounds and planar sheets for enantiomers. A delicate influence of the intrinsic head group chirality on the aggregation behaviour is found that was not observed before.[6]

Moreover, the introduction of fluorocarbons drives self-assembly towards various novel supramolecular structures. The most striking is a branched tube with Y-junctions. The three-dimensional shape of this absolutely new ultrastructure was unequivocally elucidated by cryo-ET.[6]

Our results proof that chirality of head groups may be one clue to a structural differentiation of the molecular assemblies and highlight the key role of the stereochemistry in the tube formation process. The introduction of fluorocarbons does not only modify the molecular aggregation behaviour, but also introduces completely new supramolecular features, which may lead to materials with interesting properties.

References:

(1) De Rossi, U. et al., *J prakt Chem* 1995, *337*, 203.

(2) von Berlepsch, H. et al., *J Phys Chem B* 2000, *104*, 5255.

(3) Didraga et al., *J Phys Chem B* 2004, *108*, 14976.

(4) von Berlepsch, H. et al., in *J-Aggregates, Vol. 2* (Ed.: Kobayashi), 2012, 119.

(5) Bricks, J. L. et al., *Meth Appl Fluores* 2017, *6*, 012001.

(6) Schade, B. et al. *manuscript in preparation* 2019.

Fig. 1

new aminopropanediol cyanine dyes

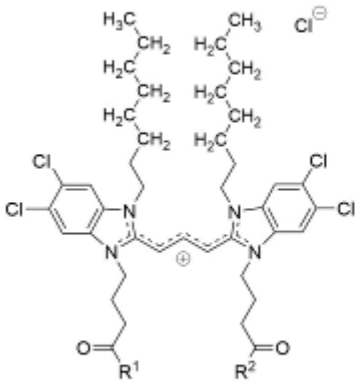

well-known parent dye C8O3

$R^1 = R^2 =$ OH

R-enantiomer $R^1 = R^2 =$

S-enantiomer $R^1 = R^2 =$

mesomer $R^1 \neq R^2 =$

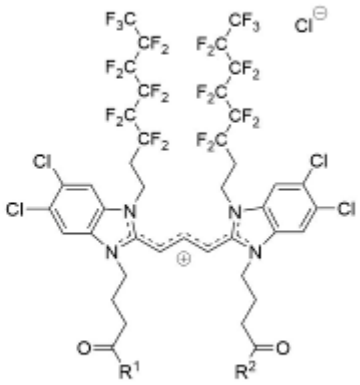

MS5.P002
First evidence of octacalcium phosphate@osteocalcin nanocomplex as skeletal bone component directing collagen triple–helix nanofibril mineralization

P. Simon[1], D. Grüner[2], H. Worch[3], W. Pompe[3], H. Lichte[4], T. El Khassawna[5], C. Heiss[5,6], S. Wenisch[6,7], R. Kniep[1]

[1]Max-Planck-Institut für Chemische Physik fester Stoffe, Chemische Metallkunde, Dresden, Germany
[2]Forschungszentrum Jülich, Institut für Energie- und Klimaforschung, Jülich, Germany
[3]Technical University of Dresden, Institute of Materials Science, Dresden, Germany
[4]Technical University of Dresden, Institute of Structure Physics, Dresden, Germany
[5]Justus-Liebig University of Giessen, Institute for Experimental Trauma Surgery, Giessen, Germany
[6]University Hospital of Giessen-Marburg, Giessen, Department of Trauma, Hand and Reconstructive Surgery, Giessen, Germany
[7]Justus-Liebig University of Giessen, Giessen, Department of Veterinary Anatomy, Giessen, Germany

TEM investigations reveal bone ultrastructure formation of human and rat trabeculae at atomic resolution (1). The collagen triple–helices and microfibrils are mineralized by hydroxyapatite (HAP) forming a chemical organic-inorganic composite. In Fig. 1a mineralized bundles of collagen fibrils are shown where individual triple–helices can clearly be distinguished. In the further zoomed area even the individual alpha–chains wound around each other become visible (Fig. 1b). The model of a triple–helix is added to demonstrate the ideal case. The width of 1.5 nm of the fibrils corresponds to the expected value of a triple-helical molecule. Individual alpha–chains within the triple–helix are visualized and the typical helical winding periodicities of 0.86, 2.86 and 8.6 nm along the collagen fibril could be resolved, see Figs. 2a,b. Further analysis of the TEM micrographs reveals that the non–collagenous protein (NCP) osteocalcin (OC) is present at/on the calcified collagen together with octacalcium phosphate (OCP). In overview TEM images, the soluble non–collagenous protein osteocalcin is visible as white globular structures of about 2 nm in diameter along the collagen fibrils. The molecular weight of osteocalcin is ~5.5 kDa containing 46–50 amino acids, which in comparison is significantly smaller than other non–collagenous protein such as osteopontin (glycoprotein) with a molecular weight of 44 kDa (33 kDa nascent). Therefore, it can act as favored mediator molecule for the nucleation and growth of HAP as well as OCP in the intrafibrillar space of collagen fibrils (2). Mostly, osteocalcin appear as single spherical specimen as well as pearl necklace strings attached to the collagen fibrils. It interacts with the calcium sites on the (100) dominated HAP platelets where the binding sites of the globular osteocalcin of 5.45 and 9.5 Å could be visualised (Figs. 3a,b). Osteocalcin limits HAP expansion by the epitaxial relation (100)HAP ≙ (100)OCP and by reduction of pH. Furthermore, the interaction of OC with the (100) planes of HAP and OCP is supported by the fact that the OH groups of HAP can easily react with the protons of the more acidic medium to H2O, and by the presence of layers of water molecules, a structure which is characteristic for OCP (Fig. 3c).

We propose the following possible crystallization scenario at the atomic scale deduced from the high-resolution images. First, likely the individual triple–helices within thinner fibrils are mineralized along the *c*–axis. Supposable, this scenario starts with binding of Ca2+ and (PO4)3- ions to the charged functional groups along the fibril. By further diffusion of ions small HAP plates are formed. When these first seeds meet each other ripening takes place giving rise to massive crystallization (Figs. 4a-d) with platy habit (100) and the *c*–axis direction in parallel orientation to the fibril extension. Subsequently, attachment of highly acidic osteocalcin on the composite surface (collagen fibril and HAP nanoplatelets) takes place, lowering the pH < 6.5 (Fig. 4e) accompanied by epitaxial growth of (100) HAP / (100) OCP) of octacalcium phosphate (OCP, blue) on HAP (red) (Fig. 4f).

References:

(1) P. Simon, D. Grüner, H. Worch, W. Pompe, H. Lichte, T. El Khassawna, C. Heiss, S. Wenisch, R. Kniep. First Evidence of Octacalcium Phosphate@Osteocalcin Nanocomplex as Skeletal Bone Component Directing Collagen Nanofibril Mineralization. Sci. Rep. 8**,** 13696 (2018).

Fig. 1

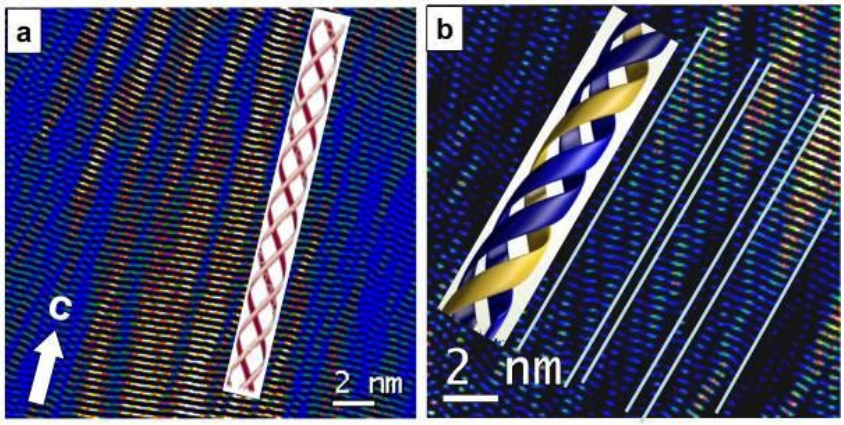

Fig. 2

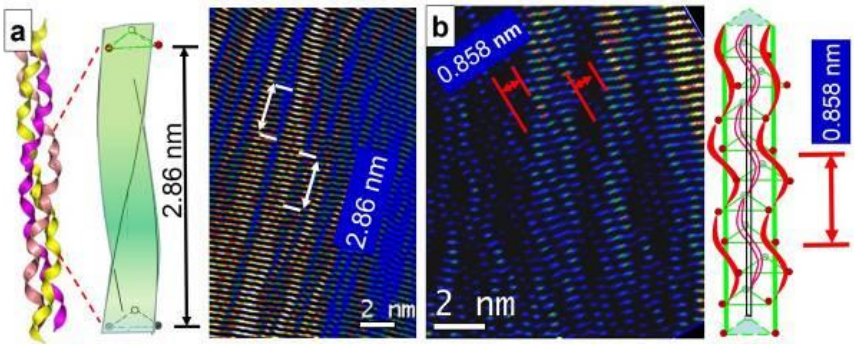

Fig. 3

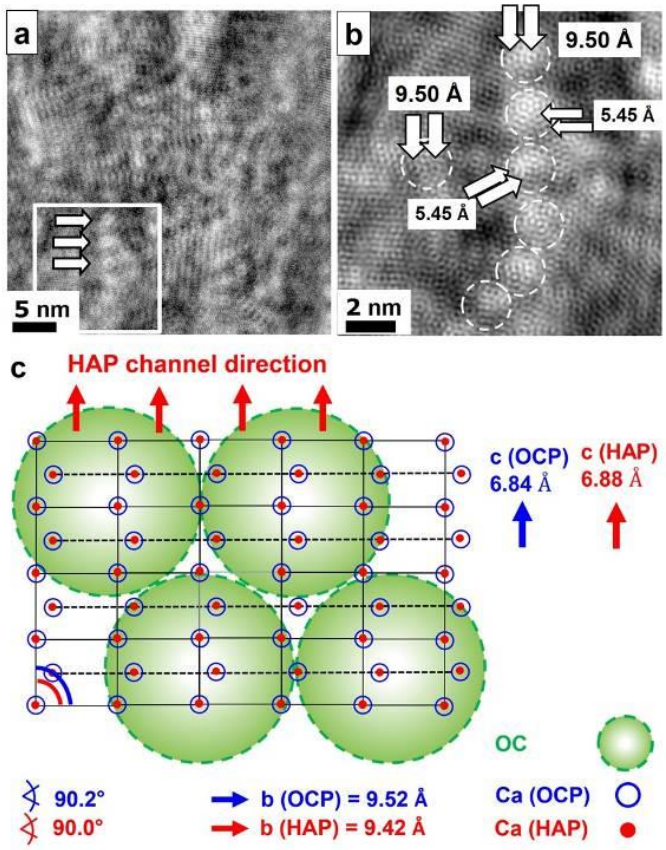

Fig. 4

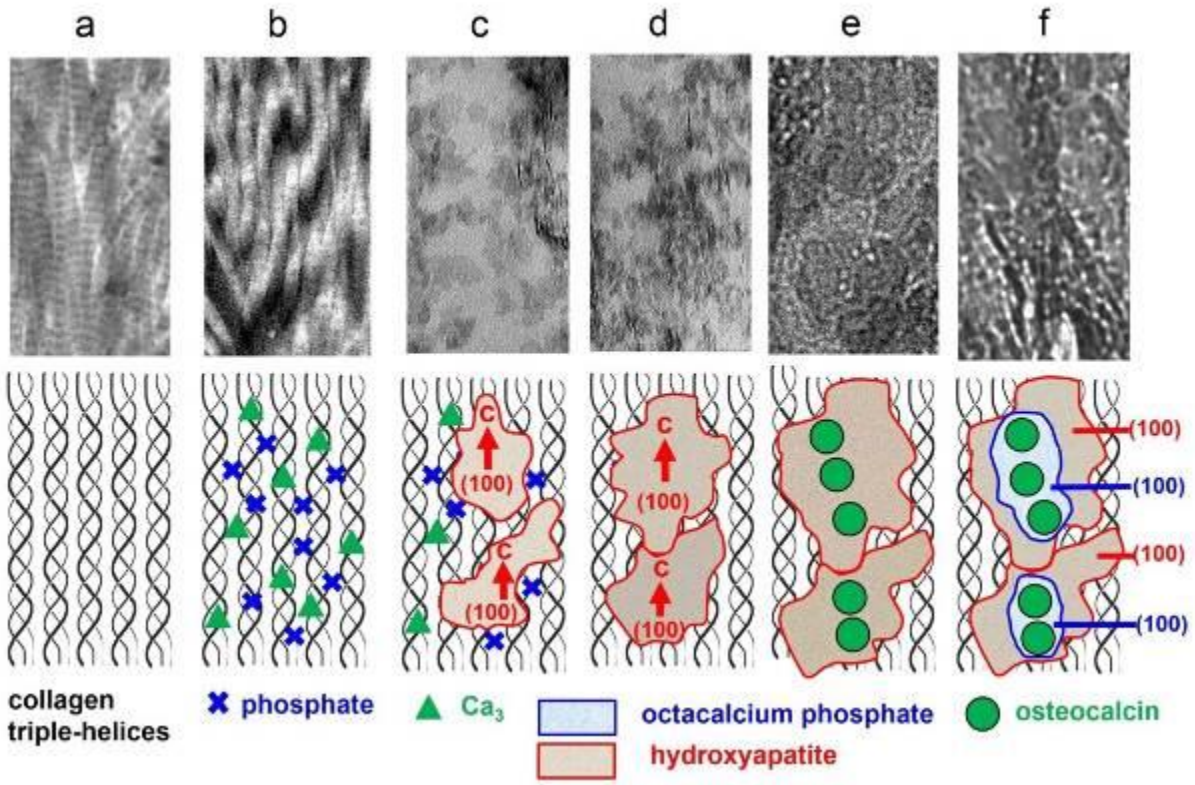
a
b
c
d
e
f
C
(100)
C
(100)
C
(100)
C
(100)
(100)
(100)
(100)
(100)
collagen
triple-helices
phosphate
Ca3
octacalcium phosphate
hydroxyapatite
osteocalcin

MS5.P003
Correlating crystallinity and material phase distributions in organic photovoltaics containing non-fullerene acceptors

W. Köntges[1], P. Perkhun[2], R. R. Schröder[1,3], R. Alkarsifi[2], O. Margeat[2], C. Videlot-Ackermann[2], J. Ackermann[2], M. Pfannmöller[1]

[1]Centre for Advanced Materials (CAM), Heidelberg University , Heidelberg, Germany
[2]Aix-Marseille Univ, CNRS, CINaM, Marseille, France
[3]Cryo Electron Microscopy, BioQuant, Heidelberg University Hospital, Heidelberg, Germany

Over the last years efficiency and stability of organic solar cells (OSCs) increased considerably due to the development of new acceptor materials, particularly non-fullerene acceptors (NFAs) (1). OSCs typically consist of polymer and small molecule materials acting as electron donor and acceptor. The optoelectronic properties depend crucially on the morphology of the active layer. Three morphological parameters seem to have the most impact: (i) the crystallinity of the different materials, (ii) the domain sizes and material phase distribution and (iii) the composition and extent of the donor-acceptor interface.

To deduce mechanisms for optimized charge separation we correlate these three parameters of NFA blends using transmission electron microscopy (TEM) at unprecedented detail. We show that it is essential to derive information from high-resolution, phase contrast of crystallites and from spectroscopic imaging for assigning material phases of different compositions.

We investigated a 30 nm thin photoactive layer of a PBDB-T:ITIC blend. For microscopy we used an aberration corrected TEM (ZEISS Libra 200 at 200 kV) equipped with a monochromator and corrected Omega filter.

Fig. 1 shows what appears to be one crystallite recorded by conventional TEM. As seen in Fig. 2a, only minor spectral differences for discriminating PBDB-T and ITIC signals are found in the optical excitation spectra. However, spectral differences are observed for π and σ plasmon excitations, yielding energy-filtered images with inverse material contrast (Fig. 2b). Applying machine learning (2) to a series of inelastic images we determine material distribution maps to visualize the domain compositions.

Overlaying the phase contrast and the material distribution map in Fig. 2c shows a direct interface of connected PBDB-T and ITIC crystallites instead of a uniform crystallite of one material. This finding is confirmed by a precise measurement of the lamellar spacings from selected parts of the conventional TEM image (Fig. 2d).

As shown, correlating phase-contrast and analytical TEM imaging opens up new possibilities to visualize so far unexpected structural details of OSC blends. At present we focus on NFA-based morphologies, relating optimized function to the occurrence of the newly described donor-acceptor crystal contacts.

References:

(1) Cheng, Y. et.al., Nat. Rev. Mater. 3, 18003 (2018).

(2) Pfannmöller, M. et.al., Nano Letters 11, 3099-3107 (2011).

(3) Acknowledgements: FunTECH-3D, MWK, 33-753-30-20/3/3, sds@hd, Marie Skłodowska-Curie grant agreement No713750, ANR, A*MIDEX (n° ANR- 11-IDEX-0001-02)

Fig. 1: TEM image of a 30 nm thin PBDB-T:ITIC blend and its power spectrum (inset). Scale bar represents 5 nm.

Fig. 2: Electron energy loss spectra of pure, 30 nm thin PBDB-T and ITIC layers. The green and red boxes within the spectrum mark the acquisition regions of the inelastic images in (**b**). **b**: Inverse contrast appears related to the spectral differences of both materials. **c:** Overlay of the TEM image (Fig. 1) and the material distribution map determined from a series of inelastic images, including those in (**b**). **d:** Analysis of the crystallinity of crystalline subareas (marked green and red) assigned from map in (**c**). The inset power spectra of the two areas selected indicate different crystal periodicity for the corresponding materials. Scale bars represent 5 nm.

Fig. 1

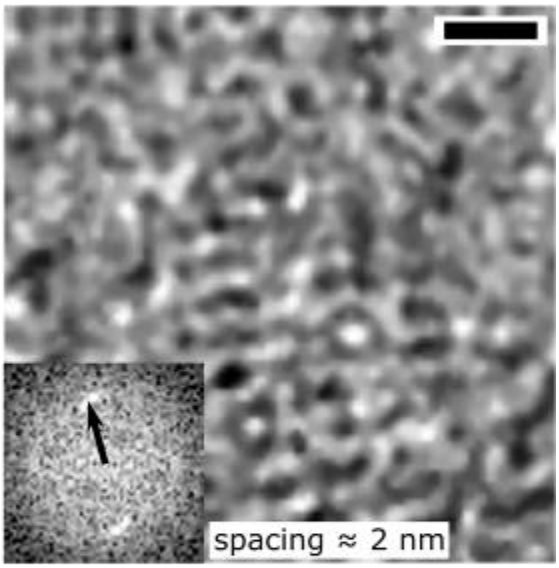
spacing ≈ 2 nm

Fig. 2

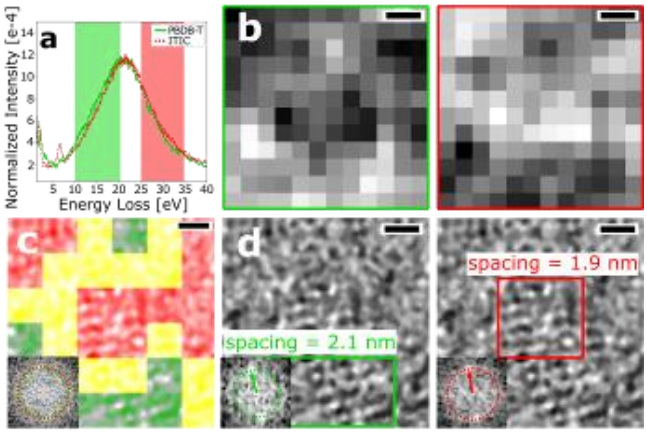
a
P6DB-T
ITIC
Normalized Intensity [e-4]
Energy Loss [eV]
b
c
d
spacing = 2.1 nm
spacing = 1.9 nm

MS5.P004
GIGADALTON PEPTIDE ASSEMBLY STRUCTURES

R. Fernandes[1], N. Ernst[2], H. von Berlepsch[3], D. J. Mikolajczak[1], N. Hosogi[4], M. Weber[2], B. Koksch[1], C. Böttcher[3]

[1]Freie Universität Berlin, Institut für Chemie und Biochemie, Berlin, Germany
[2]Zuse Institut Berlin, Mathematics for Life and Materials Sciences, Berlin, Germany
[3]Freie Universität Berlin, Forschungszentrum für Elektronenmikroskopie und Gerätezentrum BioSupraMol, Institut für Chemie und Biochemie, Berlin, Germany
[4]JEOL, Ltd. Nakagami, Tokyo, Japan

Straight forward synthetic access, high diversity in sequence and structure as well as a high degree of biocompatibility make peptides attractive components for biomaterials research. Studying the self-assembly of rationally designed peptides is a well-established method helping to understand fundamental aspects of protein folding phenomena.

A synthetic peptide (STAP1) was rationally designed with a primary sequence of three key features to promote a multi-lateral assembly process: Leucine (L) was incorporated into suitable positions to trigger assembly due to the hydrophobic interactions, lysine (K) and glutamic acid (E) were placed in a complementary and alternating manner to selectively introduce intra- and inter-helical electrostatic interactions. Cy5 was attached to the N-terminus of the peptide sequence as optical sensor.

Conformation and stability of STAP1 assemblies was monitored by circular dichroism (CD) spectroscopy. The spatial arrangement of Cy5 was provided by linear dichroism (LD) and fluorescence microscopy. Detailed structural characterisation was provided by electron cryo-microscopy (cryo-TEM) and electron cryo-tomography (cryo-ET) in combination with image analysis techniques. MD simulations were employed to support molecular models.

We report on the self-assembly of the peptide STAP1 that folds into two structurally defined but morphologically different Gigadalton assemblies (Figure 1). Adoption of the two different ultrastructures of STAP1 can be directed by pH adjustment. Interestingly, Gigadalton structure formation requires the Cy5 building block attached to the N-terminus of the peptide sequence. In case Cy5 is missing or substituted by other building blocks, other types of aggregates, mostly amyloid fibers, are observed. Cryo-TEM and electron cryo-tomography (cryo-ET) data analysis revealed the precise three-dimensional ultrastructures of both Gigadalton assemblies and eventually allowed an understanding of the packing principles by complementary MD simulations. (1)

Gigadalton peptide assemblies have been detected earlier. (2) Although similarities in the overall structure with the STAP1 at pH 7 are obvious (Figure 1a), the molecular organisation turns out to be fundamentally different. Moreover, to the best of our knowledge, the possibility to switch between different Gigadalton peptide ultrastructures, has not been reported yet. Thus, the here reported results offer the expansion of our knowledge about the principles that nature uses to construct and organize biologically relevant matter.

References:

(1) Fernandes, R.; Ernst, N.; Berlepsch, H.v.; Mikolajczak, D.J.; Hosogi, N.; Weber, M.; Böttcher, C.; Koksch, B. *in preparation*.

(2) Sharp, T. H.; Bruning, M.; Mantell, J.; Sessions, R.B.; Thomson, A.R.; Zaccai, N.R.; Brady, R.L.; Verkade, P.; Woolfson, D.N. *Proc. Natl. Acad. Sci.* 2012**,** 109, 13266–13271.

Fig. 1: Cryo-TEM images of Gigadalton assembly preparations formed by a 28 amino acid peptide (STAP1) at different pH. (top) Solid layered rod with regular striations of 4.4 nm along and perpendicular to the long-axis at ph 7.4 (bottom) Membranous assemblies with regular hexagonal pattern at pH 3.4.

Fig. 1

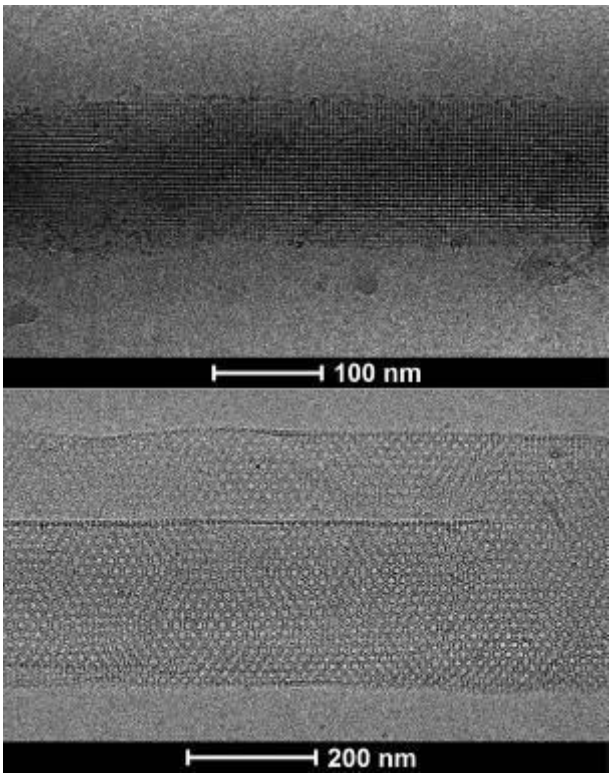

MS5.P005
Application of heavy metal staining to detect micro- and nanoplastics in aqueous environment

A. C. Swertz[1], N. Pfänder[2], E. Schmidt[1]

[1]University of Wuppertal, Institute of Particle Technology, Wuppertal, Germany
[2]Max-Planck-Institut für Chemische Energiekonversion, Mülheim an der Ruhr, Germany

Plastic litter is a severe problem and has gained more attention in recent times. (1) The term "microplastics" is often used in this context referring to plastic particles with a diameter < 5 mm. (2) These particles are not only widespread in marine environments but can also be detected in inland water and soils. Environmental impacts, like UV radiation, cause degradation of the plastic to smaller particle sizes in the nanometer range. (3) These "nanoplastics" are difficult to detect because of their small particle size and the resultant low contrast in electron microscopy.

Especially in (S)TEM the contrast of polymeric nanoparticles decreases with smaller particle size. To overcome this issue heavy metal staining is applied prior to microscopical analysis. This technique is well known for enhancing contrast of biological samples (4) but rarely used in material science. By choosing a specific staining agent a selective staining of polymers with different chemical compositions (e. g. functional groups) is possible.

In this study commercial polymer powders and polymeric nanospheres (e. g. PS, PE, PVC) were used to optimise the heavy metal staining technique. As stains aqueous solutions of common staining reagents as $KMnO_4$ or OsO_4 were used. STEM images and EDX mappings were acquired using a C_S-corrected Hitachi HD-2700 dedicated STEM equipped with two EDAX Octane T Ultra W SDD detectors. SEM images were obtained using an FEI Quanta 450 FEG Environmental Scanning Electron Microscope.

The addition of heavy metals to the structure of the polymers can be observed by an increased contrast especially in HAADF images as shown in figure 1. Here polystyrene spheres with a diameter of 200 nm were treated with an aqueous solution of KMnO4overnight. The EDX mapping of the spheres clearly shows the distribution of manganese at the surface of the spheres and therefore the desired effect of negative staining.

Negative staining with heavy metals as used for biological samples could be successfully transferred to sample preparation of polymeric micro- and nanoparticles. The enhanced contrast allows an easier (S)TEM analysis of polymers with a small particle size. The aim of this study is to apply the presented sample preparation strategy to nanoplastics extracted from contaminated water samples from inland water bodies.

References**:**

(1) Derraik, J. G., Mar. Pollut. Bull., 44(9), 842–852 (2002).

(2) Arthur, C., Baker, J. and Bamford, H., National Oceanic and Atmospheric Administration Technical Memorandum NOS-OR&R-30, p. 49 (2008).

(3) Mattsson, K., Hansson, L.-A. and Cedervall, T., Environ. Sci.: Processes Impacts, 17, 1712-1721 (2015).

(4) Watson, M. L., J. Biophysic. And Biochem. Cytol, 4(4), 475 ff. (1958).

Fig. 1: Example of stained polymer particles: HAADF-STEM image of stained PS spheres and corresponding EDX elemental maps of C (brown) and Mn (magenta). The higher density after staining with $KMnO_4$ is clearly visible through an increased contrast of the polymeric spheres.

Fig. 1

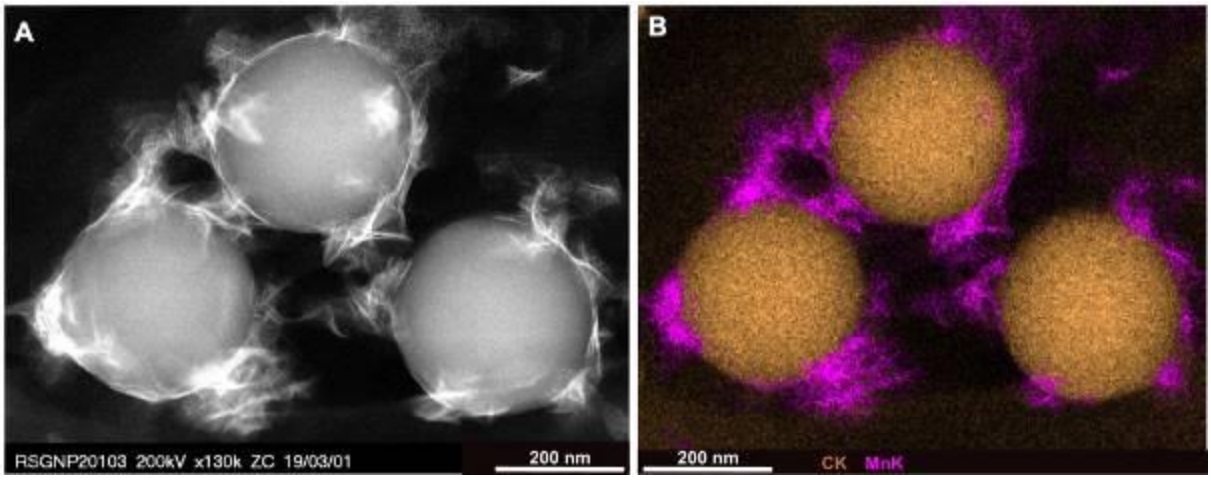

MS5.P006
Nanocrystalline graphene at high temperatures: a time resoled HRTEM study

C. N. Shyam Kumar[1,2], M. Konrad[1], V. S. K. Chakravadhanula[1], S. Dehm[1], D. Wang[1], W. Wenzel[1], R. Krupke[1,2], C. Kübel[1,2,3]

[1]Karlsruhe Institute of Technology, Institute of Nanotechnology , Eggenstein-Leopoldshafen, Germany
[2]Technical University Darmstadt, Department of Materials and Earth Sciences, Darmstadt, Germany
[3]Karlsruhe Institute of Technology, Karlsruhe Nano Micro Facility, Karlsruhe, Germany

Graphitization of polymers to produce graphenoid (graphene like) materials is a well-established process(1). Recently, graphitization at small length scales has gained importance because of the developments in carbon micro electro mechanical systems and nano electro mechanical systems (C-MEMS and NEMS)(2). A proper understanding of the graphitization process is important to tailor the structure and properties of these materials for different applications.

We employ *in situ* transmission electron microscopy to understand the catalyst free thermal formation of free-standing nanocrystalline graphene (ncg) films from a thin polymer precursor film. Following the graphitization using *in situ* TEM techniques provided new insights into the chemical and structural evolution during the pyrolysis process. During the high temperature pyrolysis of polymer thin films, nanocrystalline graphene with a high defect density, active edges and various nanostructures are formed. This catalyst free transformation forms mobile and stationary (pinned) carbon nanostructures structures with varying size and shape (3). Studying these structures at high temperatures provided insights in to the mechanisms responsible for the growth of graphitic layers at high temperatures. Using time resolved *in situ* transmission electron microscopy, we show that the reactivity of defects and unsaturated edges plays an integral role for the structural dynamics. In addition to the migration and merging of the graphitic subunits (figure 1), strong structural and size fluctuations of individual graphitic subunits at high temperatures were observed. Graphene nano flakes are highly unstable and tend to loose atoms or groups of atoms to adjacent larger domains indicating an Ostwald-like ripening in these 2D materials (figure 2) as an additional growth mechanism. Beam off heating experiments were carried out to understand the effect of electron beam on the observed processes. All the processes observed during continuous imaging (beam on) were also observed during the beam off experiments. This confirms that the observed dynamics are inherent temperature driven and the electron beam is only providing additional activation energy, thereby increasing the reaction kinetics. Molecular dynamic simulations were carried out to estimate the activation energy for the different processes and indicated a critical role of defects in the substrate for the observed dynamics.

This study revealed several temperature-driven mechanisms for atom rearrangements contributing to the growth of the graphitic domains, partially involving catalyzing unsaturated sites. This shows that the high temperature behavior and stability of nanocrystalline graphene is fundamentally different from coarse-grained graphene because of the high defect density in ncg.

References:

(1) L. Zhang et al., Catalyst-free growth of nanographene films on various substrates, *Nano Res.* 4 (2011) 315–321.

(2) S. Jiang et al., Scalable fabrication of carbon-based MEMS/NEMS and their applications: A review, *J. Micromechanics Microengineering* 25 (2015) 113001.

(3) C. N. Shyam Kumar et al., Understanding the graphitization and growth of free-standing nanocrystalline graphene using in situ transmission electron microscopy, *Nanoscale* 9 (2017) 12835–12842.

Fig. 1: Lateral (white arrows) and vertical merging (red arrows) of graphene flakes.

Fig. 2: a) Simultaneous shrinking of a small flake (white arrow) and growth of an adjacent large one (black arrow).

Fig. 1

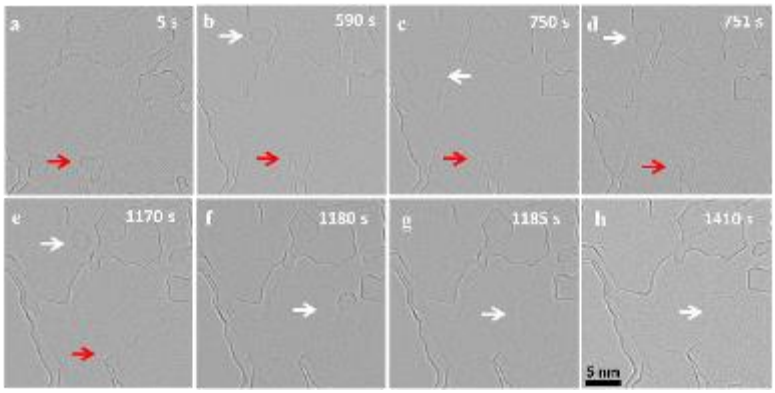
a
5 s
b
590 s
c
750 s
d
751 s
e
1170 s
f
1180 s
g
1185 s
h
1410 s
5 nm

Fig. 2

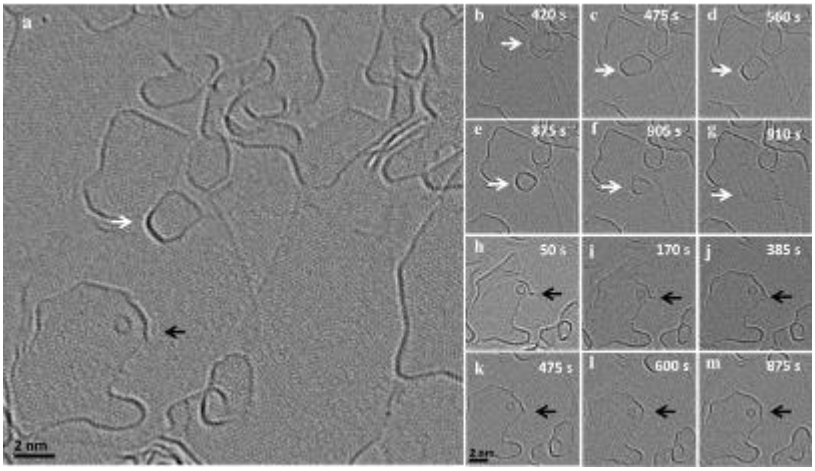
a
2 nm
b
420 s
c
475 s
d
560 s
e
875 s
f
905 s
g
910 s
h
50 s
i
170 s
j
385 s
k
475 s
l
600 s
m
875 s

MS5.P007
TEM and EELS Study of sp3 Bonded Tetrahedral Amorphous Carbon

S. Rubanov[1], P. Olivero[2,3], A. Battiato[3], F. Picollo[2,3], A. Suvorova[4]

[1]University of Melbourne, Bio21 Institute, Melbourne, Australia
[2]University of Torino, Physics Department, Torino, Italy
[3]National Institute of Nuclear Physics (INFN), Section of Torino, Torino, Italy
[4]University of Western Australia, Perth, Australia

The amorphous diamond-like carbon with high sp3 fraction (up to 88%) has outstanding mechanical properties. Recently, purely sp3 tetrahedral amorphous carbon was obtained from glassy carbon using high pressure (50 GPa) laser annealing (1800 oK) (1). We report TEM and EELS studies of purely amorphous diamond fabricated by a new method using a combination of FIB milling, ion implantation and thermal annealing.

A number of trenches (10 μm x 1.5 μm x 0.2 μm) were initially fabricated using FIB milling into the surface of synthetic single crystal diamond. Following 1 MeV He+ ion implantation with fluence 2.5×1017 ions/cm2 a continuous implanted layer has been formed at depth 1.8 μm with channels of disordered carbons below the trenches at the depth ~ 3 μm. The annealing was conducted in vacuum at 950 oC for 2 hours.

TEM images and diffraction pattern revealed the amorphous structure of the continuous implanted layer and the channels. The carbon K-edge in EELS spectra shows the prominent peak at 285 eV (π* peak) indicating the presence of sp2 bonded carbon in the implanted layer and in the channels after ion implantation. Thus, despite the suppression of swelling in disordered channels and large internal strain there is transition of some sp3 to sp2 bonds. TEM study of implanted diamond after thermal annealing showed that continuous implanted layer became graphitic without changes in structure of channels that remained amorphous. EELS study of carbon K-edge revealed the absence of peak at 285 eV in the channels. The disappearance of π* peak indicates the complete conversion of sp2 bonds back to sp3 bonds and the formation of 100 % sp3 bonded tetrahedral amorphous carbon or pure amorphous diamond. Plasmon energy in low loss spectra is a function of valence electron density and in amorphous channel was measured to be 25-27 eV in continuous implanted layer and 31 eV in channels. Plasmon energy in channels after annealing was measured to be 32.6 eV which corresponds to the density of 3.27 g/cm3. This density is lower than diamond (3.52 g/cm3) but is consistent with a random distribution of sp3 sites (2). The transition of some sp3 to sp2 bonds during ion implantation results in density reduction with corresponding swelling and volume extension in direction normal to the diamond surface in continuous layer. In channels the situation is different: small implantation volume and rigid properties of diamond lattice allowed to supress swelling. While the temperature during annealing was significantly lower than reported in (6) the high internal pressure in channels could result in similar conditions for reverse transition of sp2 bonds to sp3 bonds. The density reduction through volume extension in implanted channels could happen in TEM lamellas during sample preparation using FIB milling.

References:

(1) Z. Zeng et al., Nat. Comm. (2017) DOI: 10.1038/s41467-017-00395-w.

(2) A.C. Ferrari et al., Phys. Rev. B 62 (2000) 11089.

MS5.P008
STEM observation of antibacterial effect of silver-decorated polymeric nanoparticles

C. Takahashi[1]

[1]National Institute of Advanced Industrial Science and Technology, Magnetic Powder Metallurgy Research Center, Nagoya, Japan

Bacteria are well known to adhere to solid surfaces by forming biofilms. It is difficult to remove from the substrate using antibacterial drugs, once the biofilm is formed. As a result, biofilm infections have become a serious problem. Recently, some researchers have revealed that organic-metal hybrid materials have antibacterial efficacy against bacteria. Particularly, silver nanoparticles are often used as catalysis for preparation of composite materials. In the present study, we successfully prepared silver-decorated poly (DL-lactide-co-glycolide) (PLGA) nanoparticles and silver-decorated Soluplus® (Sol) polymeric micelles to treat biofilm infection disease. To understand their antibacterial effect to the bacterial cells under the biofilm, structure of prepared silver-decorated polymeric nanoparticles and interaction behavior between silver-decorated polymeric nanoparticles and the biofilms were visualized using scanning transmission electron microscopy (STEM).

The bacterial strain used in this study was *Staphylococcus epidermidis* (ATCC14990T). The biofilm was grown in a 24-well plate. Polymeric nanoparticles using PLGA and Sol were prepared by the emulsion solvent diffusion method in aqueous medium. The AgNO3 and NaBH4 were used for the silver decoration of polymeric nanoparticles. The electron microscopes used in the present study were JEOL JEM-2100F equipped with EM-31160 cooling holder and JEOL JEM-1400 Plus. The ionic liquid: 1-butyl-3-methylimidazolium tetrafluoroborate was used for sample pretreatment of STEM observation. The ultrathin section method was used for TEM observation. Antibacterial assays were also performed using the LIVE/DEAD BacLight bacterial viability kit and colony counting.

We successfully revealed the antibacterial activity of silver-decorated polymeric nanoparticles against *S. epidermidis* bacterial cells by STEM observation. This result would be useful for understanding not only the precise structure of prepared silver-decorated polymeric nanoparticles, but also their interaction behavior between silver nanoparticles and the bacterial cells under the biofilm and detoxification mechanism of the bacteria. The results of antibacterial assay supported the electron microscopy studies. This study showed that silver-decorated PLGA and silver-decorated Sol can be used as compatibility nanocarriers for drug delivery system with high antibacterial activity. This information can contribute to the design of suitable nanocarriers for treatment of biofilm infections.

This study was partially supported by JSPS KAKENHI Grant Numbers JP15K18849, JP 17KK0178, and JP18K18388. A part of this work was conducted in Nagoya Institute of Technology, supported by Nanotechnology Platform Program of the Ministry of Education, Culture, Sports, Science and Technology (MEXT), Japan.

MS5.P010
Polyamide – Insights into its process-induced Morphologies

R. Boldt[1], Y. Spoerer[1], M. Auf der Landwehr[1], I. Kuehnert[1]

[1]Leibniz Institute of Polymer Research Dresden e.V., processing, Dresden, Germany

Optical and mechanical properties of processed polyamides are affected by the morphology, which in turn is influenced by the thermal and rheological process conditions. For instance, during injection molding or foil extrusion high temperature differences between the polymer melt and mold or ambient temperature, respectively, occur. Both, occurring temperature differences and cooling rates have a strong effect on the morphology.

The aim of this study are investigations of process-induced morphology of polyamide using optical light microscopy (OLM), electron microscopy (EM), X-Ray and differential scanning calorimetry (DSC). X-Ray and DSC were used for the evaluation of crystallinity as well as for the calculation of lamellae thicknesses and crystallite sizes. The obtained results were compared with those of EM analysis. OLM was carried out for visualization of size and distribution of spherulites using polarization contrast. For detailed study of morphology scanning electron microscopy (SEM) was performed in correlation with OLM. Furthermore, transmission electron microscopy (TEM) was applied to ultrathin slices stained with RuO4 in terms of characterization of crystalline structures in nm-range.

It could be observed that depending on the cooling conditions, different structures and morphologies occur within the processed material (Figure 1). The number of spherulites and the size of crystalline structures in regions with high cooling rates differ from those in regions with slow cooling rates.

Fig. 1

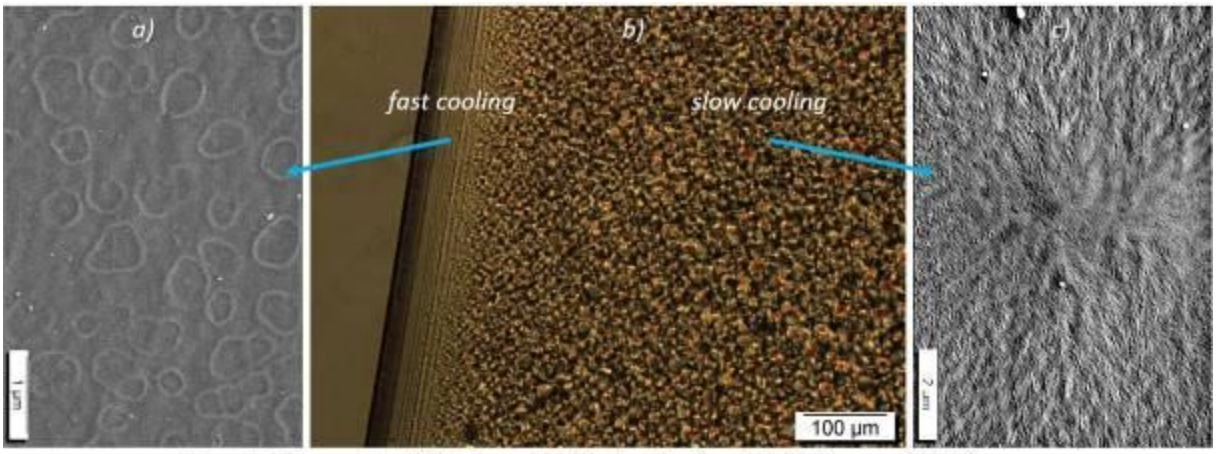

Figure 1. Micrographs of injection molded Polyamide a) and c) SEM images, b) OLM image

MS5.P011
Imaging of switchable MOFs by low-dose TEM technique

V. Bon[1], Y. Han[2], S. Kaskel[1]

[1]Technische Universität Dresden, Inorganic Chemistry I, Dresden, Germany
[2]King Abdullah University of Science and Technology, Thuwal, Saudi Arabia

Metal-Organic Frameworks (MOFs), a class of highly porous materials, constructed from metal ions or clusters and multi-topic organic ligands using modular building principle. (1) MOFs attracted considerable interest due to their outstanding characteristics like high specific surface areas and pore volumes in conjunction with crystallinity. Apart from the broad application field ranging from gas storage, separation, catalysis, sensing to fabrication of electronic devices, (2) several dozens of MOFs feature stimuli-responsive reversible structural switching from porous to non porous or less porous state. Usually guest molecules, external pressure, temperature and even electromagnetic irradiation could be used as triggers, initiating phase transition. (3) Beside the fundamental interest to the switching itself, flexible MOFs are discussed for applications ranging from separation, sensing and adsorptive gas storage. Reversible structural transformations in response to external stimuli like temperature, electromagnetic irradiation and adsorption of guest molecules are unique behaviors observed in flexible MOFs. These transformations can have great impact on the nature and physical properties of the framework mainly on its porosity and adsorption behavior.

Ni2(ndc)2(dabco) (ndc – 2,6-naphtalenedicarboxylate, dabco - 1,4-diazabicyclo[2.2.2]octane), further denoted as DUT-8(Ni), belongs to the pillared layer MOFs and shows a "gate pressure" type switching with largest amplitude between the "close pore" and "open pore" phases, known for gas adsorption induced transitions yet.4 Recently we observed a strong crystallite size dependency of switching for DUT-8(Ni), namely pronounced switching for crystallites larger than 1 µm and rather rigid behavior for smaller particles (Figure 1). (4, 5)

References:

(1) M. Eddaoudi, D. B. Moler, H. Li, B. Chen, T. M. Reineke, M. O"Keeffe, O. M. Yaghi *Acc. Chem. Res.*, 2001, 34**,** 319-330.

(2) S. Kitagawa, R. Kitaura, S.-i. Noro *Angew. Chem. Int. Ed.* 2004, 43, 2334 – 2375.

(3) A. Schneemann, V. Bon, I. Schwedler, I. Senkovska, S. Kaskel, R. A. Fischer *Chem. Soc. Rev.*, 2014, 43, 6062-6096.

(4) N. Kavoosi et al., *Dalton Trans.*, 2017, 46**,** 4685–4695.

(5) H. Miura et al., *Dalton Trans.*, 2017, 46, 14002–14011.

Fig. 1: Crystallite size dependent switching behavior in DUT-8(Ni).

The most outstanding and challenging task, which is still not addressed by the community is the investigations of the switching kinetics and its cooperativity. A rapid development of low-energy, cryo TEM and in situ techniques could be considered as an opportunity to investigate the time scale of the stimuli responsive structural switching in MOFs. In the following we used low-dose technique for high-resolution imaging of both open and closed-pore phases of DUT-8(Ni) which well correlates with crystal structures of the corresponding phases (Figure 2).

Fig. 2: TEM images for DUT-8(Ni) op (left) and DUT-8(Ni) cp (right).

Fig. 1

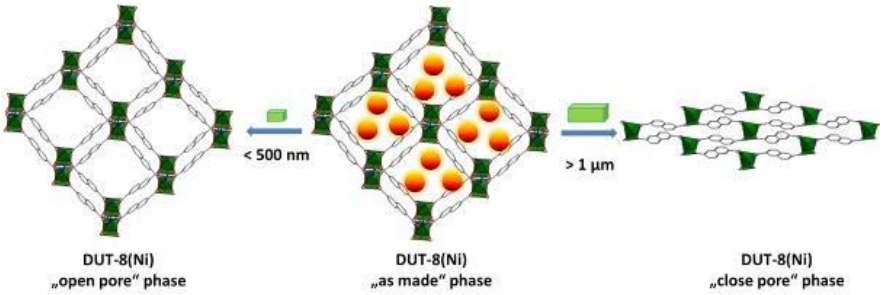
< 500 nm
> 1 µm
DUT-8(Ni)
„open pore“ phase
DUT-8(Ni)
„as made“ phase
DUT-8(Ni)
„close pore“ phase

Fig. 2

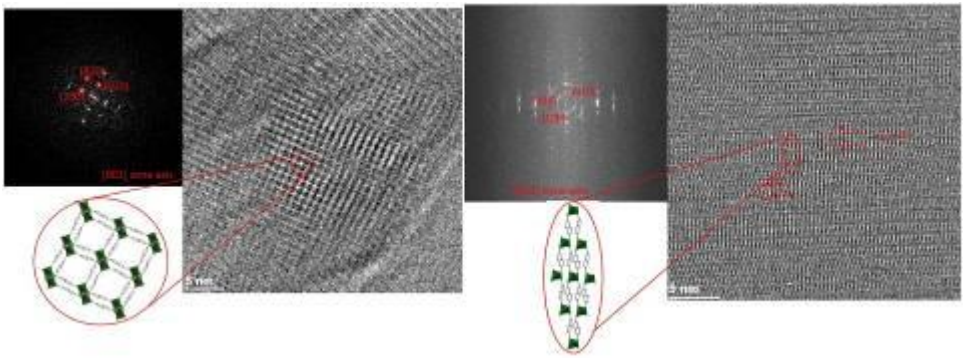

MS5.P012
Thermal modification of polystyrene nanosphere lithography masks analysed by SEM and in-situ TEM

T. Riedl[1,2], J. K. N. Lindner[1,2]

[1]Paderborn University, Physics, Paderborn, Germany
[2]Center for Optoelectronics and Photonics Paderborn (CeOPP), Paderborn, Germany

Nanosphere lithography enables the cost-effective creation of regular nanopatterns on solid surfaces. In this technique, hexagonally close packed mono- or double-layers of spherical colloidal particles serve as lithographic masks for use in material deposition and etching processes. By utilising the mask openings for the structure definition, arrays of semiconductor quantum dots and nanorods for optoelectronics and of tailored metal nanoparticles for plasmonic devices (1) have been realized. Thermal annealing leading to a shrinkage of the mask openings (2) provides an additional possibility of adjusting the size and shape of the resulting structures (1).

Since the size and size homogeneity of nanoparticles strongly affect their application-relevant properties, the present study aims at determining and understanding the evolution of the size distribution of monolayer polymer mask openings in the course of thermal treatment. Moreover, the mechanisms effectuating the shape change of the initially spherical colloidal particles in the mask and therefore of the mask openings are elucidated.

Monolayers of submicron polystyrene spheres have been prepared by convective self-assembly on Si substrates. Subsequent thermal annealing was performed in air at temperatures of 100-110°C. Then, the samples were imaged in a Raith field-emission SEM, generating the input for statistical correlative size analyses of the polystyrene particles, sintering necks and openings. The latter task was accomplished by means of a self-written program employing customized image recognition coupled with intensity profiling and thresholding. In addition, in-situ thermal annealing experiments were carried out in a Jeol JEM-ARM200F TEM. Morphological changes of the polystyrene particles were tracked by EFTEM thickness mapping.

SEM image analysis demonstrates that while the average opening size decreases with increasing annealing duration, the spread of opening diameters increases. Remarkably, the broadening occurs only for large openings (Fig. 1) indicating that the annealing induces the formation of new sintering necks between spheres that were initially separated by small gaps. Furthermore, in-situ TEM annealing experiments reveal two dominant mechanisms leading to polystyrene particle shape changes (Fig. 2). In the initial stage of annealing the opening size is reduced by a capillary-driven quasi-elastic enlargement of the sphere-sphere contact areas. In a later stage the spheres flatten by viscous flow.

Defects in nanosphere lithography masks strongly influence the evolution of opening size distribution during thermal annealing. Morphological changes of the masks are effectuated by time and temperature dependent quasi-elastic and viscous deformations of the polymer particles.

References:

(1) C. Brodehl et al.: Materials Today: Proc. 4 (2017) S44

(2) T. Riedl et al.: MRS Symp. E-Proc. 1663 (2014) mrsf13-1663-ww03-75

Fig. 1: (a,b) SEM images, (c) evaluated size coefficient of variation (CV) for different mask opening subsets and annealing durations at 105°C of 0.37 µm polystyrene sphere monolayers.

Fig. 2: (a) EFTEM thickness map, (b) sphere and mask opening diameters of a 0.22 µm polystyrene sphere triple evaluated at four selected times during an in-situ TEM ramp-up annealing experiment.

Fig. 1

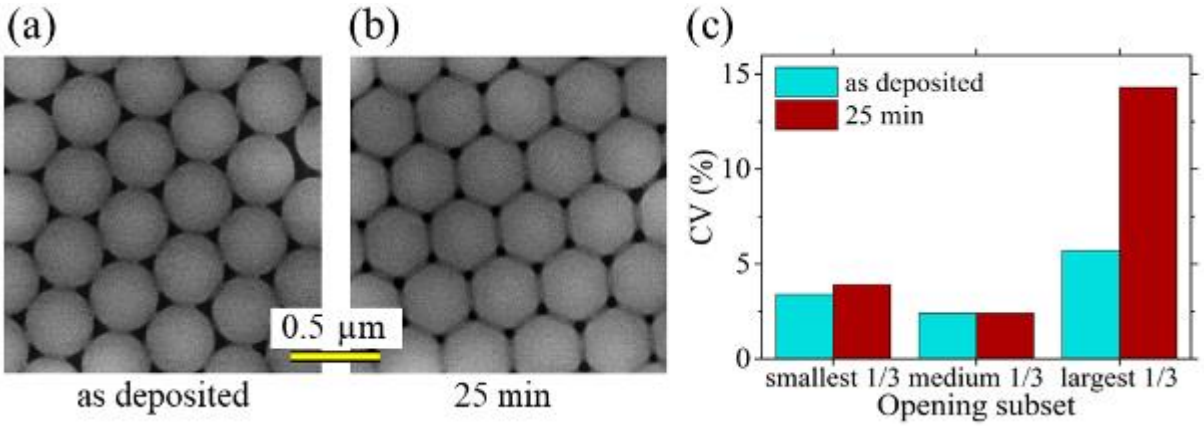
(a)
(b)
(c)
0.5 µm
as deposited
25 min
as deposited
25 min
CV (%)
15
10
5
0
smallest 1/3
medium 1/3
largest 1/3
Opening subset

Fig. 2

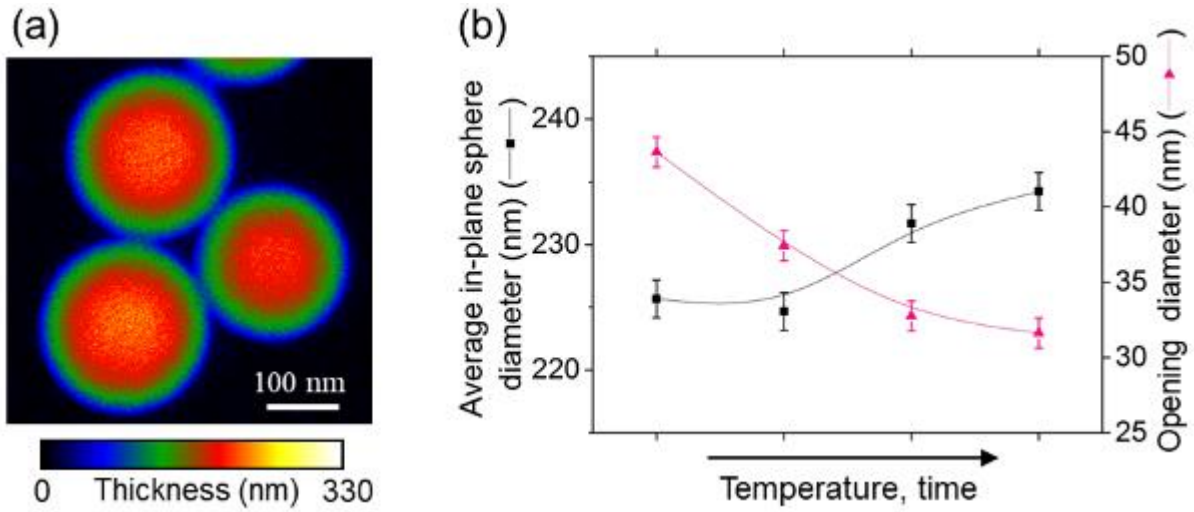
(a)
100 nm
0
Thickness (nm)
330
(b)
Average in-plane sphere diameter (nm)
240
230
220
Opening diameter (nm)
50
45
40
35
30
25
Temperature, time

MS5.P013
Characterization of Laser Beam Modified Carbon Fibres

K. Engelkemeier[1,2], K. Duschik[1,2], J. Bürger[3,1,4], K. P. Hoyer[1,2], N. Buitkamp[1,5], W. Bremser[1,5], M. Schaper[1,2], J. K. N. Lindner[3,1,4]

[1]Institute of Light Weight Design with Hybrid Systems (ILH), Paderborn, Germany
[2]Paderborn University, Faculty of Mechanical Engineering, Paderborn, Germany
[3]Paderborn University, Department of Physics, Paderborn, Germany
[4]Center for Optoelectronics and Photonics Paderborn (CeOPP), Paderborn, Germany
[5]Paderborn University, Department of Chemistry, Paderborn, Germany

Carbon fibres allow for the strengthening of materials with respect to tensile forces and therefore play an important role in the fabrication of light weight materials, leading to reduced masses of tools and machines and thus to reduced amounts of energy required for their motion. Carbon fibres have the advantage of a particularly high specific strength. The transfer of loads in fibre reinforced materials from the matrix into the fibre is usually governed by the morphology and chemistry of their interfaces. Carbon fibres are chemically inert and thus difficult to modify at their surface.

Laser beam treatment offers the opportunity of non-equilibrium processing of surfaces and tailoring properties via laser beam parameters, such as wavelength, pulse intensity, pulse duration and repetition rate. In this study the morphological and structural changes of commercial carbon fibres are investigated as a function of laser processing parameters.

Uncoated genuine carbon fibres of 6-8 µm diameter fabricated from acryl nitrile are used as starting material. Individual fibres carried on a glass substrate are irradiated in air with the focused beam of a yttrium vanadate fibre laser at a wavelength of 1064 nm and 25 W output power using pulses of 4 ns length and repetition rates of 10-50 kHz. Fibres are analyzed using a Renishaw Raman spectrometer and a Zeiss Ultra Plus FE-SEM. Individual fibres were prepared for cross-section TEM investigations with a Zeiss Neon 40 FIB and analyzed with a probe Cs-corrected JEOL JEM-ARM200F equipped with a GIF Quantum ER energy filter for EELS and EFTEM.

Depending on laser power and repetition rate, different carbon nanostructures – some of them with fractal architecture – are formed in the laser plasma and deposited on the fibre surfaces. Among them, carbon onions are found agglomerating on the fibres, where the onion size and agglomeration behavior can be tailored by laser parameters. An increase of the Raman sp^3 to sp^2 ratio with increasing pulse repetition rate is measured and correlated to the EELS signal and carbon morphology observed in TEM.

By combining Raman and EEL spectroscopy, SEM and TEM the materials modification on the surface of carbon fibres is analyzed. The increasing fraction of sp^3 bonds with laser pulse frequency is correlated to the occurance of carbon onions at the fibre surface.

Fig. 1: FE-SEM image of a laser modified carbon fibre (a) and respective nanostructure at higher magnification (b).

Fig. 2: TEM image of a laser modified carbon fibre (a) and respective carbon onions (b). Background corrected core-loss EEL spectra of (c) a FIB thinned part of the fibre and (d) carbon onions recorded in dual-EELS mode.

Fig. 1

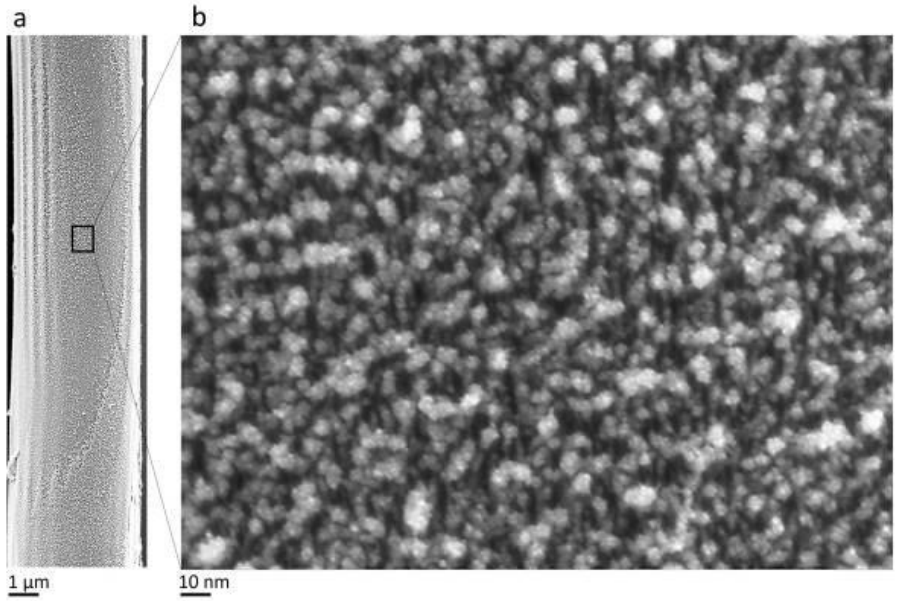
a
b
1 µm
10 nm

Fig. 2

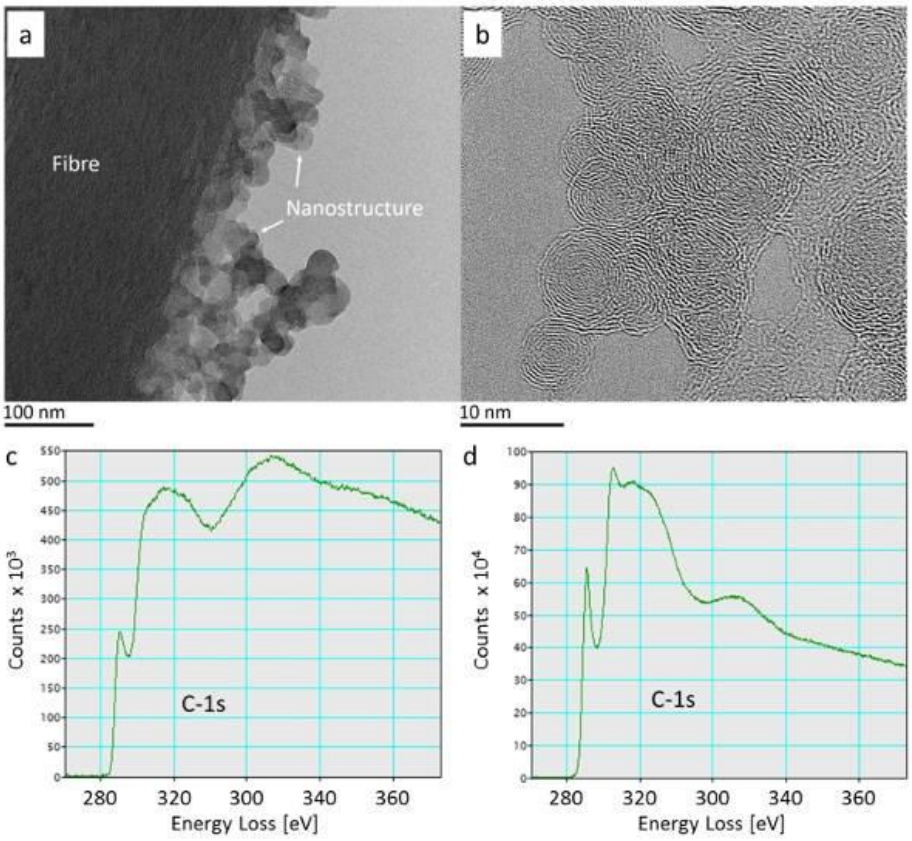
a
Fibre
Nanostructure
100 nm
b
10 nm
c
Counts x 10³
C-1s
Energy Loss [eV]
d
Counts x 10⁴
C-1s
Energy Loss [eV]

MS5.P014
Insights into protein and polymer self-assembly by Cryo-TEM

Z. Kochovski[1], G. Yang[2], W. Zhang[3], G. Chen[2], J. Yuan[3], Y. Lu[1]

[1]Helmholtz-Zentrum Berlin (HZB), Soft Matter and Functional Materials, Berlin, Germany
[2]Fudan University, Department of Macromolecular Science, Shanghai, China
[3]Stockholm University, Department of Materials and Environmental Chemistry, Stockholm, Sweden

Self-assembly processes in principle mimic complex systems formation in nature. Self-assembly of proteins plays a key role in most biological processes and has attracted considerable scientific interest in recent years due to various potential applications in diagnostics, biosensing, signaling or the design of biocompatible and biodegradable materials. The design and construction of artificial protein nanostructures through strategies for self-assembly offers a unique way of understanding the basic principles for the creation of diverse functional materials with advanced properties. Furthermore, polymer self-assembly has also become a topic of increasing interest in recent years for similar reasons. While transmission electron microscopy (TEM) has established itself as the standard technique of choice for the structural and morphological analysis of self-assembled nanostructures in solution, often the sample preparation involves drying and staining steps which in many cases can affect the structure and morphology of the sample. In the case of cryogenic TEM (cryo-TEM), samples are preserved in frozen hydrated state, closest to their native one, though vitrification and studied in the TEM at cryogenic temperatures. Using Cryo-TEM, Cryo Electron Tomography (Cryo-ET) and single-particle cryo-electron microscopy (Cryo-EM) we have elucidated a number of self-assembled protein and polymer structures such as nanowires and two dimensional sheets (1), nanotubes (2) and Poly(Ionic Liquid) Nanoparticles (3).

References:

(1) G. Yang, HM. Ding, Z. Kochovski et.al., Angew .Chem. Int.Ed. 2017, 56 ,10691 –10695

(2) G. Yang, X. Zhang, Z. Kochovski et.al., J. Am. Chem. Soc., 2016, 138 (6), pp 1932–1937

(3) W. Zhang, Z. Kochovski et.al., ACS Nano, 2016, 10 (8), pp 7731–7737

MS5.P016
Voltage-dependent quantitative analysis of electron-dose-limited resolution for imaging two-dimensional organic crystals

B. Liang[1], H. Qi[1,2], H. Sahabudeen[2], X. Feng[2], U. Kaiser[1]

[1]University Ulm, Central facility for Electron Microscopy, Group of Electron Microscopy of Materials Science, Ulm, Germany
[2]Dresden University of Technology, Department of Chemistry and Food Chemistry & Center of Advancing Electronics Dresden, Dresden, Germany

Two-dimensional polymers (2DP) in which the organic building units were connected by lateral covalent bounds, forming into a layer-like polymer membrane, are promising candidates for organic electronics and next-generation energy storage. In recent study, the large size two-dimensional (2D) polyimine polymer with high crystallinity was successfully synthesized [1, 2]. However, due to electron irradiation damage, high resolution (HR) TEM imaging of 2DPs remains challenging, posing a strong limitation on the structural elucidation of these organic 2D materials. One common way of circumventing irradiation damage is to apply low-dose method. To that end, it is necessary to unravel the correlation between total electron dose and achievable specimen resolution for specific specimens. Here, by using 2D polyimine, we determined the tolerance dose for each specimen resolution under different acceleration voltages (300, 150, 80, 40 kV).

Since the diffraction spots are secondary electron sources forming the HRTEM image, to investigate the relationship between total electron dose and achievable specimen resolution, we performed dose-series analysis in electron diffraction mode. Figure 1a shows the selected area electron diffraction (SAED) patterns acquired under 300 kV after a total dose of 4.8, 48 and 168 $e^{-}\cdot Å^{-2}$, respectively. With accumulating electron dose, the higher order reflections gradually vanish, representing the degradation of specimen resolution. For quantitative analysis, we plotted the intensity of Friedel pairs against the accumulated electron dose (Fig. 1b) and determined the tolerance dose for each specimen resolution (Fig. 1c). Our method offers quick and straightforward determination of dose-related specimen resolution under different voltages. These results lay the foundation for the HRTEM imaging of beam sensitive organic crystals, such as, 2D polymers, metal-organic frameworks, and covalent-organic frameworks.

Fig. 1. a) SAED patterns at 300 kV with accumulated dose of 4.8, 48 and 168 $e^{-}\cdot Å^{-2}$ respectively, the visible highest order reflections are marked. The intensity of the higher order reflections from 7 0 0 to 13 0 0, are extracted from line profile and plotted against the accumulated dose in b). For each order, the intensity first decays, then reaches a plateau. The accumulated dose where the plateau begins indicates the tolerance dose. Graph c) shows the correlation of electron tolerance dose with resolution limit at 300 kV.

References:

(1) Sahabudeen, H. et al. Wafer-sized multifunctional polyimine-based two-dimensional conjugated polymers with high mechanical stiffness. Nat. Commun. ***7,*** 1–8 (2016).

(2) Dong, R. et al. Interface-Assisted Synthesis of 2D Materials: Trend and Challenges. Chem. Rev. *118,* 6189–6325 (2018).

Fig. 1

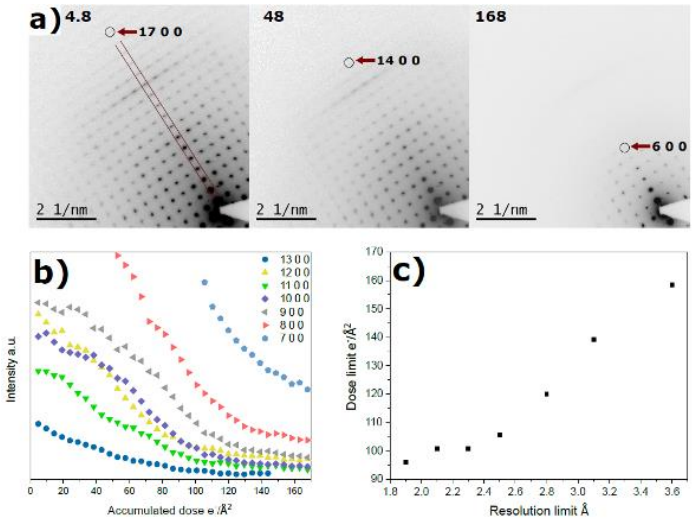

MS5.P017
Eletcron microscopy as a tool to characterize polymer membranes

C. Abetz[1], A. L. Höhme[1], E. Schneider[1]

[1]Helmholtz-Zentrum Geesthacht, Institute of Polymer Research, Geesthacht, Germany

Membrane technology plays an increasingly important role to address societal grand challenges such as the climate change or clean water. Among different membrane materials, polymers are having a pig potential as they are cheap, easy to process and they are mechanically robust. Disadvantages may be their lower thermal stability and chemical robustness for certain applications. When developing and fabricating membranes for these different applications, i.e. membranes for separation of carbon dioxide from gas mixtures, or membranes for the separation of particles, viruses and bacteria from polluted water, their morphology is of biggest relevance. As membranes are typically asymmetrically composed films with a thickness in the range of approx. 0.01 to 100 microns, scanning and transmission electron microscopy are very strong tools to investigate their surface and cross section.

Different electron microscopic techniques are applied to determine the thickness of selective layers of integral asymmetric membranes and also thin film composite membranes by taking advantage of either morphological differences or elemental contrast of different components in the selective top layer of the membranes and the structure underneath.

The polymer membranes discussed in this contribution are prepared from commercially available multiblock copolymers (PolyActive) as dense thin film composite (TFC) membranes for gas separation and from tailor made polystyrene-block-poly(4-vinylpyridine) diblock copolymers as isoporous integral asymmetric membranes for ultra-filtration.

A TEM Tecnai G2 F20 (Thermo Fisher Scientific) and a SEM Merlin (Zeiss) were used for morphological investigations. Samples for TEM analysis were prepared by cryo ultramicrotomy. Cross sections for SEM were either obtained by manual cryo fracturing using liquid nitrogen or by argon ion milling using a PECS II (Gatan). Samples for TEM were stained with iodine or osmium tetroxide. Samples for SEM were coated with platinum or carbon.

Characterisation of TFC membranes: the selective multiblock copolymer layer was prepared with different thickness on top of a porous support membrane covered by a thin polydimethylsiloxane (PDMS) membrane. With Ar ion milling a defect free cross section could be prepared of these very soft membranes. Due to the strong elemental contrast between PDMS and the multiblock copolymer, the thickness of the top layer could be determined and related to other properties, such as permeance for different gases and thermal transitions.

Characterisation of isoporous integral asymmetric membranes: the postfunctionalisation of the pore forming block with an alkyl iodide leads to a strong contrast and can be used for visualisation of the different components of the diblock copolymer in the membrane structure using back scattered electrons. Bulk morphology of this block copolymer revealed a well ordered microphase structure, as visualized by TEM.

SEM and TEM are powerful techniques to characterize polymer membranes and are indispensable to obtain structure properties relationships in highly complex thin film systems, such as polymer membranes.

MS5.P018
Biological objects investigated by TEM techniques

I. Ennen[1], B. Kaltschmidt[1], A. Hütten[1]

[1]Bielefeld University, Department of Physics, Bielefeld, Germany

Supported by the establishment of transmission electron microscopes (TEM) specialized for cryo-microscopy and the improvement of preparation techniques, which e.g. makes staining procedures not mandatory necessary, TEM analysis techniques come into focus in biological research. A challenge in imaging biological specimen is the fast beam damage process which strongly limits the electron dose under investigation. Nevertheless, numerous studies have utilized Cryo-microscopy for the discovery of e.g. membrane proteins or RNA polymerase transcription (e.g. see (1,2)) and even an observation of conformational changes of proteins come into reach.

Recognizing this highly interesting tasks in the field of biology, we have started to analyze biological objects utilizing our TEM (JEOL JEM 2200FS). Here we concentrate on two main questions: First, can we observe differences in the lamellarity of liposomes under the influence of terpenoids? And second: Can we visualize the structure of polysomes and control the success of nanoparticle labelling?

Furthermore, in this work different preparation techniques of the same biological entity were compared regarding to contrast and visibility of microstructural features.

Different samples have been investigated including e.g. liposomes, polysomes and collagen fibres. Liposomes are nanoscale spherical vesicles, which were prepared by extrusion of phosphatidyl choline from soy bean. The influence of terpenoids on the lamellar structure of liposomes were studied by a Cryo-TEM approach, whereas a staining procedure with uranyl acetate has been used to check the success of nanoparticle labelling of polysomes. Polysomes are supramolecular structures that catalyze the last step of protein synthesis where the genetic code is decoded and have been isolated from Arabidopsis thaliana by sucrose gradient centrifugation. Such nanocomplexes consist of a transcript, several ribosomes and nascent peptide chains (3).

An influence of terpenoids like thymol, menthol or campher on the lamellar structure of liposomes have been clearly observed in Cryo-TEM images. We found the highest amount of unilamellar vesicles in liposomes treated with thymol, which might be the reason for a higher antibacterial activity observed in further experiments.

Polysomes prepared with and without a nanoparticle labelling, have been investigated in a dried and stained condition. We found that each component of these nanocomplexes can serve as a labelling target and, therefore, can be used to isolate the whole complex by using magnetic nanoparticles functionalized with different biological probes: complementary nucleotide sequences can be used to address the transcript while antibodies can label the ribosome or the nascent protein.

We have shown a microstructural analysis of different biomolecules like liposomes and polysomes. It has been shown that a conventional TEM is a powerful tool for answering biological questions.

References:

(1) C. Bernecky, F. Herzog, W. Baumeister, J.M. Politzko, P. Cramer, Nature 529 (7587) 551

(2) S. Asano, B. D. Engel, W. Baumeister, J. Mol. Bio. 428, 332-343

(3) M. Wegener, I. Ennen, V. Walhorn, D. Anselmetti, A. Hütten and K.-J. Dietz, submitted to Nanomaterials (2019).

MS5.P019
Applying AFM-IR, EELS and EDX to study metal-polymer interphase region

P. Formanek[1,2], C. Heintze[2], M. Malanin[1], K. J. Eichhorn[1], S. Morsch[3], Y. Liu[3]

[1]Leibniz-Institut für Polymerforschung, Dresden, Germany
[2]Helmholtz-Zentrum Dresden-Rossendorf, Institute of Resource Ecology, Dresden, Germany
[3]The University of Manchester, School of Materials, Manchester, United Kingdom

Epoxy resins are widely used industrial materials, with applications including the matrix component of corrosion-protection paints. The long-term performance (e.g. the adhesion and delamination of coatings) is assumed to depend on the existence and properties of the interphase - chemically and physically distinct polymeric region adjacent to interface with inorganic (e.g. metallic) substrates. However, the mere existence of such interphase region is frequently disputed. Little is known about the formation mechanism and extent of such interphase regions.

Our goal is to prove or disprove the existence of interphase in diglycidyl ether of bisphenol-A (DGEBA) cross-linked with triethylenetetraamine (TETA) on gold or iron substrates.

(a) Thickness-dependent epoxy-group excess in cured films on steel and on gold was determined by ATR-FTIR spectroscopy. (Fig. 1a)

(b) Curing reaction was monitored by FTIR in-situ for ~100 µm films coated onto on Au and Fe. (Fig. 1b)

(c) The possibility of iron complex formation at the interphase was explored using EFTEM, EELS (Fig. 2a), STEM-EELS and STEM-EDX (Fig. 2b) of cross-section of cellulose acetate/40 nm Fe/epoxy sandwich in a similar way as in (1).

(d) Possible chemical gradients and gradients of local thermal properties in the above mentioned sandwich were examined with AFM-IR and nanothermal analysis. (Fig. 3)

(a) No difference was found between steel and gold substrate, thus amine consumption via organometallic complexation is negated. The epoxy-group excess was reduced by covering the films with parafilm during the cure. Therefore amine loss from the top surface of films is the reason for the epoxy-group excess.

(b) No difference was found between Au and Fe substrate, eliminating catalytic effects as reason for epoxy-group excess.

(c) No Fe was found within few tens of nm from the Fe layer.

(d) No epoxy-group concentration gradient and no gradient of thermal properties could be detected.

The combination of EDX, EFTEM, EELS and AFM-IR demonstrate the non-existence of micron scale interphase in TETA-crosslinked DGEBA coatings on iron. No evidence was found for extensive organometallic formation by amine complexation. Epoxy-group excess in thin films develops as a result of amine consumption at the air-polymer interface. The residual epoxy measured in thin films does not correspond to a chemical gradient associated with an interphase structure. AFM-IR analysis was, for the first time, applied to acquire uniquely high resolution infrared spectra and maps of polymer/metal interphase regions.

The HZDR Ion Beam Center"s TEM facilities and its staff support are gratefully acknowledged, particularly the funding of TEM Talos by the German Federal Ministry of Education and Research (BMBF), Grant No. 03SF0451 in the framework of HECMP. Dr. S. Morsch is grateful to the Leibniz-Institut für Polymerforschung Dresden e.V., and to AkzoNobel, for materials and financial support.

References:

(1) Meiser et al, Int. J. Adhes. Adhes. 2010, 30, 170–177.

Fig. 1: Relative epoxy-group excess as a function of (a) film thickness and (b) curing time.

Fig. 2: (a) TEM image, EELS spectra and (b) STEM-EDX maps of the epoxy/Fe/acetate sandwich.

Fig. 3: (a) AFM-IR images of the acetate/Fe/epoxy sandwich: height; IR amplitudes at 916 cm^{-1} and 1508 cm^{-1}; ratio map. (b) Epoxy thermal transitions as a function of the distance from the Fe film.

Fig. 1

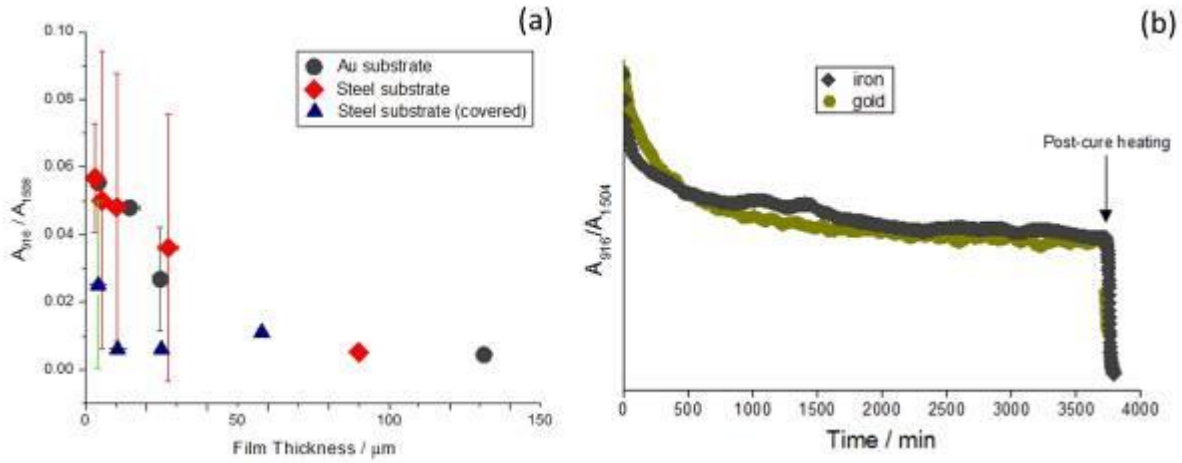

Fig. 2

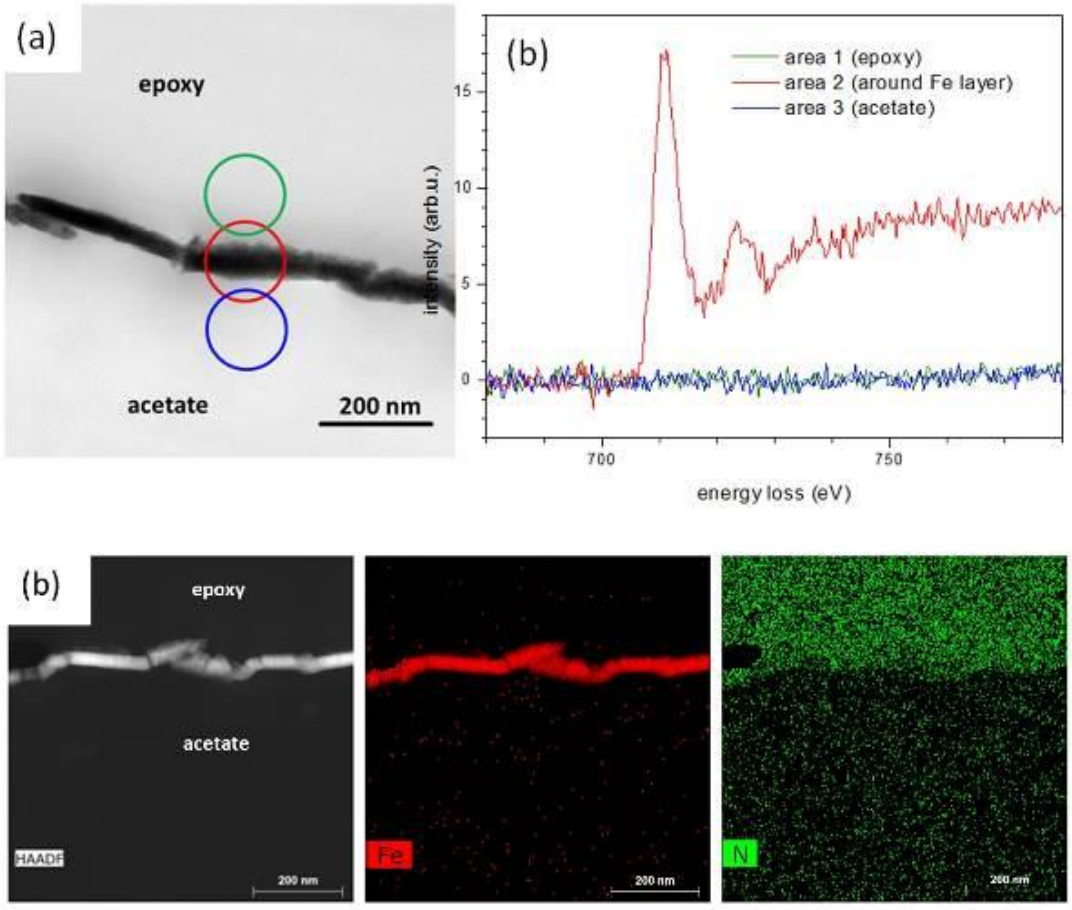

Fig. 3

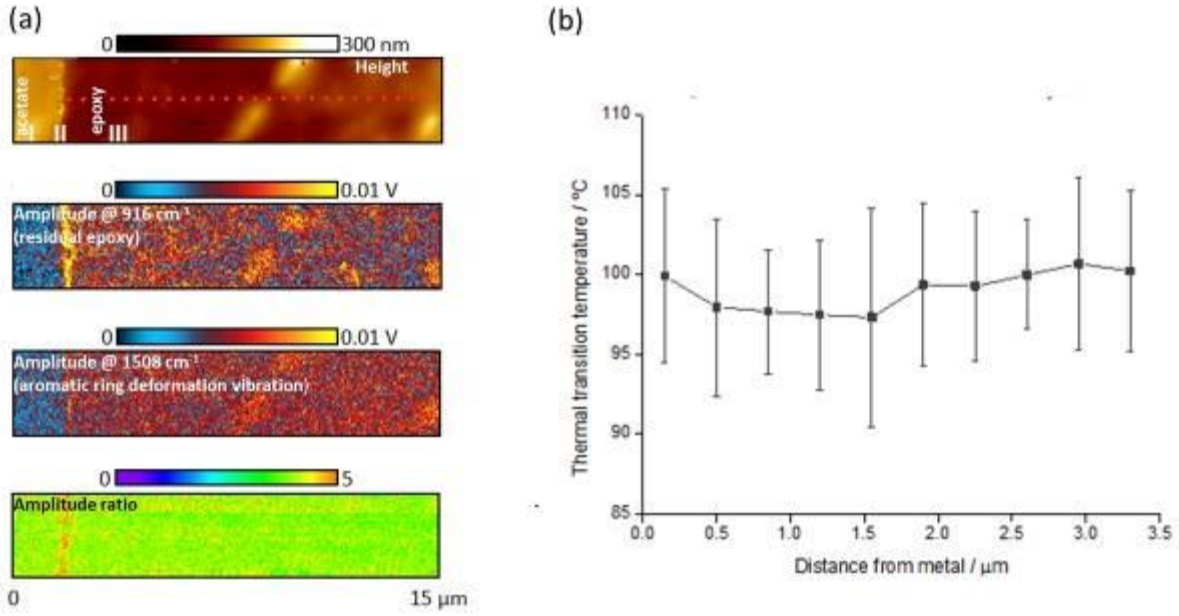
(a)
0
300 nm
Height
acetate
epoxy
I
II
III
0
0.01 V
Amplitude @ 916 cm⁻¹
(residual epoxy)
0
0.01 V
Amplitude @ 1508 cm⁻¹
(aromatic ring deformation vibration)
0
5
Amplitude ratio
0
15 µm
(b)
Thermal transition temperature / °C
110
105
100
95
90
85
0.0
0.5
1.0
1.5
2.0
2.5
3.0
3.5
Distance from metal / µm

MS5.P020
Pair distribution function analysis of organic polymer thin films and particles

C. Rohner[1], R. Schlögl[1,2], T. Lunkenbein[1]

[1]Fritz-Haber-Institut der Max-Planck-Gesellschaft, Inorganic Chemistry, Berlin, Germany
[2]MPI for Chemical Energy Conversion, Mühlheim a.d. Ruhr, Germany

Organic polymers are one of the most important material classes due to their low production cost, light weight and wide range of application. Unfortunately, as plastics are ubiquitous in our daily life, a large amount of waste material ends up as pollution in the environment. Especially in the water compartment, degradation products in the form of micro- and nanoplastic particles are considered a possible threat to microorganisms and by extension to a larger part of the trophic chain.(1) Transmission electron microscopy (TEM) can help to structurally identify small size fractions of plastics. However, for reliable results, beam induced effects on the materials have to be carefully evaluated, and subsequently minimized.

The aim of the study is to identify and distinguish organic polymers by pair distribution function (PDF) analysis of electron diffraction (ED) measurements in the TEM. Time resolved ED allows for the examination of the beam damage within the semicrystalline polymers.

The two most common polymers, polyethylene (PE) and polypropylene (PE), differ only by one methyl group in the repeating monomeric unit. In advantage over other microscopic techniques, TEM can identify this difference with spatial resolution. In particular, PDF analysis of ED data is an emerging technique for the characterization of amorphous or semicrystalline organic materials.(2) In brief, the PDF G(r) gives the probability density of finding a neighbor atom at a certain distance from a chosen atom. This can directly be related to the number of atoms in a coordination sphere around an atom. Thus, structural information can be gained, if the data was suitably acquired and processed.(3)

PDF analyses of a number of "fresh" or artificially aged model samples of PE and PP show the position of the first two peaks at 1.4 Å and 2.5 Å (Figure 1.). These peaks correspond to the conformation-independent distances between one C atom and its first and second neighbor, respectively, in the C chain. For higher distances, the shape of the functions shows a strong variation among the measured samples. This indicates differences in the material structure and crystallinity. Time resolved diffraction measurements at 80 kV and 200 kV show the disappearance of diffraction spots after about 8-10 s of exposure. The loss in crystallinity is evident in the PDFs by damped oscillations of the function around 0 (Figure2).

PDF analysis of ED data allows for the identification of the chemical structure of amorphous and semicrystalline materials locally in thin films or in submicrometer size particles.

Acknowledgement

We thank Ulrike Braun and Korinna Altmann of the Bundesanstalt für Materialforschung und –prüfung, Berlin for the provision of the samples.

References:

(1) O. S. Alimi, J. F. Budarz, L. M. Hernandez, and N. Tufenkji, Environ. Sci. Technol. 52, 1704-1724.

(2) T. E. Gorelik, M. U. Schmidt, U. Kolb and S. J. L. Billinge, *Microsc. Microanal.*, 2014, 21, 459–471.

(3) E. Takeshi and S. J. L. Billinge, *The Method of Total Scattering and Atomic Pair Distribution Function Analysis*, 2012, vol. 16.

Fig. 1: Reduced PDFs G(r) of PE and PP.

Fig. 2: Reduced PDFs G(r) measured immediately after exposure to the beam and after prolonged exposure. Beam-induced amorphisation is evident in the marked regions by a damped oscillation of G(r) closer to zero.

Fig. 1

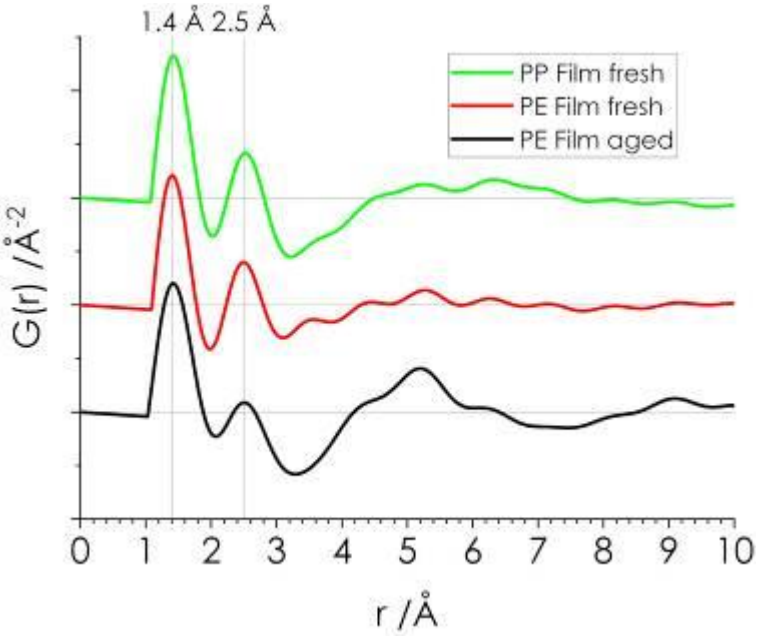
1.4 Å 2.5 Å
PP Film fresh
PE Film fresh
PE Film aged
G(r) /Å-2
0 1 2 3 4 5 6 7 8 9 10
r /Å

Fig. 2

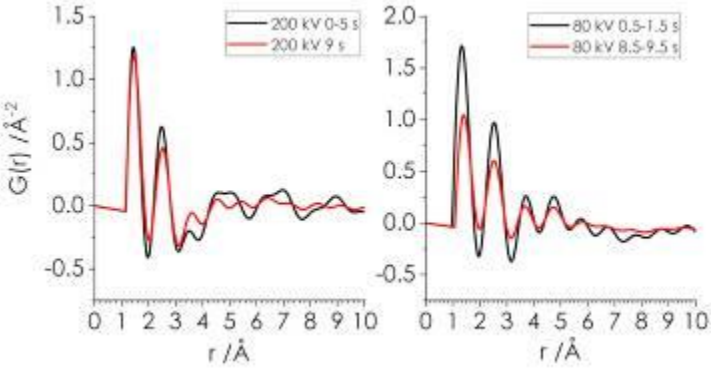
200 kV 0-5 s
200 kV 9 s
80 kV 0.5-1.5 s
80 kV 8.5-9.5 s
G(r) /Å-2
r /Å
r /Å

MS6.001 invited
Revealing secrets of nature – crystal structure solution on disordered nanoparticles by automated electron diffraction tomography (ADT)

U. Kolb[1]

[1]Uni Mainz, Institut für Anorganische Chemie und Analytische Chemie, Mainz, Germany

Transmission electron microscopes (TEMs) always comprised the major tool for structural characterization of nanocrystalline particles and improved in recent decades significantly due to vast technological developments in imaging, spectroscopy as well as diffraction. Automated electron diffraction tomography (ADT), published in 2007, was the first electron diffraction technique utilizing tomographic electron diffraction data for ab initio structure analysis on a single nano crystal providing access to hitherto unsolvable crystal structures (1). Since then, the electron diffraction tomography (EDT) community has grown rapidly and several methods were developed differing from ADT mainly in terms of data acquisition strategy and equipment used. One major issue the tracking of the crystal necessary to correct for sample movement due to mechanical tilt of the stage. In ADT TEM or STEM images are acquired after a selectable number of tilt steps and cross correlation is used to determine the needed electron beam shift. Alternatively, a crystal tracking file can be produced in a prior crystal tilt and applied during s second tilt movement for solemn diffraction data acquisition (Fast-ADT). For data processing and analysis the program packages ADT3D and eADT were used. The below reported samples consist mainly of crystals of a few tens of nanometers in size. For electron dose reduction, contrast enhancement and accurate beam positioning µ-STEM imaging using nano electron diffraction (NED) (down to 20nm semi-parallel illumination) was applied.

ADT has been applied in the last decade to a large variety of application fields, sometimes constituting only of crystals with a few tens of nanometers size. One example, is the CaCO3, one of the most abundant materials in the world. Produced over millions of years mainly from sediments of skeletal remains of marine organisms (chalk, limestone) it is plays a major role in nature (bio-mineralisation, global carbon cycle) as well as industry (e.g. cement). Using ADT it was possible to solve the hitherto unknown crystal structure of the third polymorph of pure CaCO3 (vaterite) (2) as well as to identify and characterize a fully unknown new hydrated crystal phase, monohydrocalcite (CaCO3·1H2O) (3).

References:

(1) Towards automated diffraction tomography. Part I - Data Acquisition, U. Kolb, T. Gorelik, C. Kübel, M.T. Otten, D. Hubert, Ultramicroscopy, 107, 507-513 (2007)

(2) Ab Initio Structure Determination of Vaterite by Automated Electron Diffraction, E. Mugnaioli, I. Andrusenko, T. Schüler, N. Loges, R. Dinnebier, M. Panthöfer, W. Tremel and U. Kolb*, Angewandte Chem.Int. Ed., 51(28) 7041-7045 (2012), Angewandte Chem., 124(28) 7148-7152 (2012).

(3) A New Hydrated Crystalline Calcium Carbonate Phase: Calcium Carbonate Hemihydrate, Zhaoyong Zou, Wouter J.E.M. Habraken, Galina Matveeva, Anders C. S. Jensen, Luca Bertinetti, Matthew A. Hood, Chang-yu Sun, Pupa U.P.A. Gilbert, Iryna Polishchuk, Boaz Pokroy, Julia Mahamid, Yael Politi, Steve Weiner, Peter Werner, Sebastian Bette, Robert Dinnebier, Ute Kolb, Emil Zolotoyabko, and Peter Fratzl, Science, 363, 396-400 (2019).

MS6.002
Revealing the 3D structure of graphene defects and electron-beam induced out-of-plane dynamics

C. Hofer[1,2], V. Skákalová[2], C. Kramberger[3], M. Monzam[2], C. Mangler[2], A. Mittelberger[2], T. Susi[2], J. Kotakoski[2], J. C. Meyer[1,2]

[1]University of Tübingen, Institute of Applied Physics, Tübingen, Germany
[2]University of Vienna, Vienna, Austria
[3]Vienna University of Technology, Vienna, Austria

Identifying the three-dimensional (3D) position of every atom is the ultimate goal of structural characterization. Electron tomography has emerged as powerful technique to determine three-dimensional structures down to atomic resolution. However, it requires that the atomic structure does not change under the high cumulative dose arising from a large number of projections. Here,we obtain the 3D atomic structure of graphene grain boundaries from only two projections. We obtain the 3D structure iteratively in an optimization process where simulated images are compared to the experimental data, and both the atomic positions as well as the imaging parameters are subject to optimization. We first demonstrate that this method works using an embedded defect in graphene that allows direct comparison to the computationally calculated three-dimensional structure. We then apply this method to reveal new insights into the three-dimensional structure of defects in graphene, in particular grain boundaries (1) and Silicon dopants (2). Our approach also allows to visualize interesting electron beam induced dynamics, which would not be observable when the sample is not tilted. Our resulting atomic models reveals limited resolution in out-of-plane direction, due to the limited signal to noise ratio of the individual images. To lower the requirement of the data, we use a hybrid approach where both, the match between simulated and experimental images as well as the calculated energy of the structure is optimized. As a result, we obtain a structure where the atomic network and larger-scale deformations are in excellent agreement with the two experimental images, while at the same time the local atomic bonding (variations below the experimental precision) is given by the computational potential.

References:

(1) Hofer et. al, 2D Materials , Volume 5, Number 4 (2018)

(2) Hofer et. al, Appl. Phys. Lett. 114, 053102 (2019)

Fig. 1

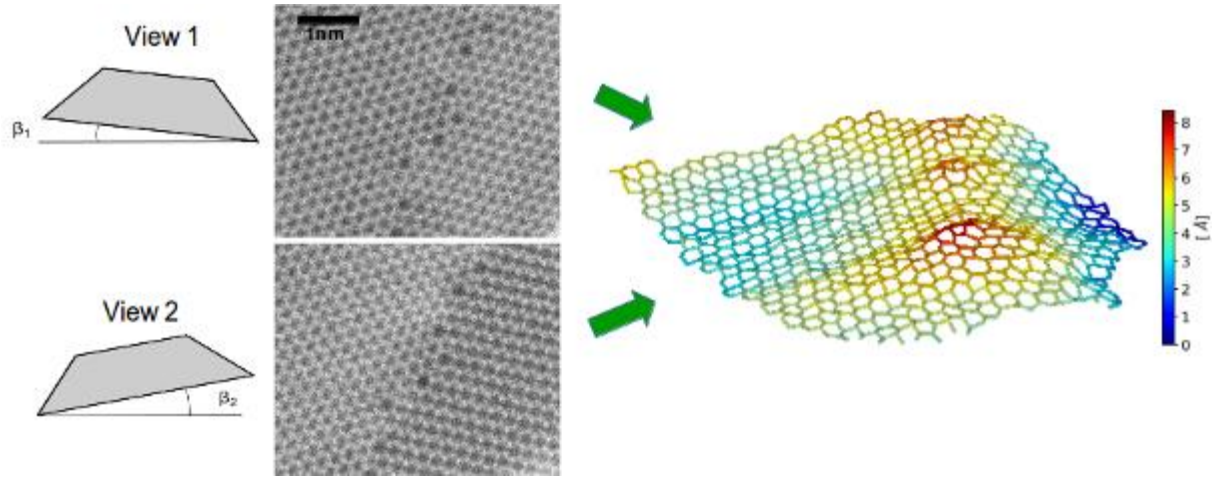

MS6.003
Electron-Beam-Stimulated Structure Evolution of Single-layer $MoTe_2$: From Point to Extended Defects

T. Lehnert[1], M. Ghorbani-Asl[2], J. Köster[1], Z. Lee[1], A. Krasheninnikov[2,3], U. Kaiser[1]

[1]Ulm University, Electron Microscopy Group of Materials Science, Ulm, Germany
[2]Helmholtz-Zentrum Dresden-Rossendorf, Institute of Ion Beam Physics and Materials Research, Dresden, Germany
[3]Aalto University, Department of Applied Physics, Aalto, Finland

Aberration-corrected high-resolution transmission electron microscopy (TEM) experiments combined with first-principle calculations are performed to investigate defect-induced structural transformations and properties. The data was acquired at 40 kV with the Cc/Cs-corrected SALVE (Sub-Angström Low-Voltage Electron microscopy) instrument, to benefit from increased resolution and contrast (1,2).

Here, we report about the electron-beam-induced atom-by-atom evolution of single Te vacancies and Te column divacancies in a single-layer $MoTe_2$. Ballistic damage due to the electron beam interaction should be excluded at 40 kV because of the high mass of Te and Mo (3). Very likely, chemical etching is responsible for the appearance of the first vacancies. Further damage production may then be caused by localized beam-induced electronic excitations on the vacancies.

We show that the observed defects evolve into different types of tetravacancies (cf. fig. 1 (a)) and trefoil-like defect structures as well as line defects in zigzag direction (4). Just single vacancy lines were found as shown in fig. 1 (b), which originate from the agglomeration of single vacancies. First-principles calculations were carried out to determine the electronic properties (cf. fig. 1(c)) and the driving force for the reported defect evolutions.

Furthermore, we show that the evolution of the defects can result in Te-deficient inversion domains with 4|4P and 4|4E mirror twin boundaries and even in strain-induced, local phase transformations from the 2H to the 1T" phase.

Our results point out that various nano-scale defects such as metallic islands of the T"-phase, vacancy lines and mirror twin boundaries embedded into a semiconducting material, pave the way to add new functionalities into single-layer $MoTe_2$.

References:

(1) M. Linck et al., Phys. Rev. Lett. 2016, 117, 076101

(2) Z. Lee et al., Ultramicroscopy 2012, 112(1), 39-46

(3) H.-P. Komsa et al., Phys. Rev. Lett. 108 (2012) 196102

(4) T. Lehnert et al., 2019, submitted

Fig. 1: 40 kV Cc/Cs-corrected high-resolution SALVE images of different defect structures in MoTe2. (a) shows a tetravacancy which is magnified and superimposed with the DFT-based structure simulation. In (b), a HRTEM image of a single Te vacancy line with four missing Te atoms is shown which is located between the red triangles in the right panel. Furthermore, spin-polarized density of states (DOS) for pristine MoTe2 and a single Te vacancy line are calculated (c). Along the vacancy line, states appear which can be interpreted as band gap reduction. The dotted lines depict the band edges of the pristine system.

Fig. 1

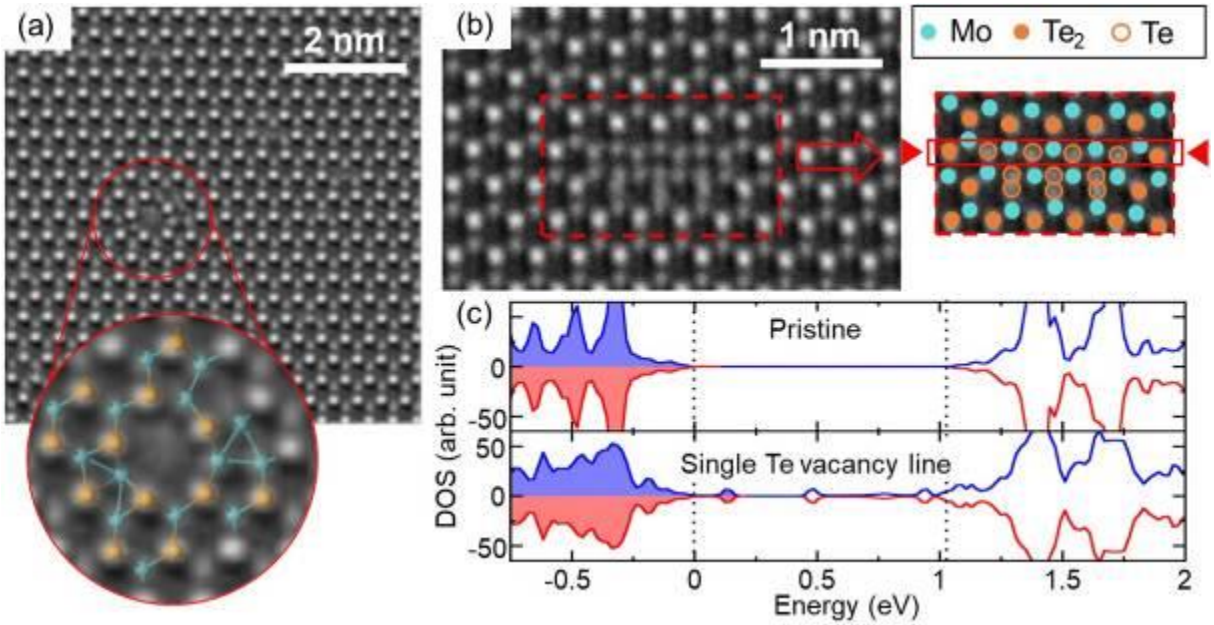
(a)
2 nm
(b)
1 nm
Mo
Te2
Te
(c)
Pristine
Single Te vacancy line
DOS (arb. unit)
50
0
-50
-0.5
0
0.5
1
1.5
2
Energy (eV)

MS6.004
Measurements of strain in 3D strained dealloyed nanoporous gold

C. Mahr[1,2], K. Müller-Caspary[3], T. Grieb[1,2], M. Simson[4], R. Ritz[4], M. Schowalter[1,2], F. F. Krause[1,2], A. Lackmann[2,5], A. Wittstock[2,5], H. Soltau[4], A. Rosenauer[1,2]

[1]University of Bremen, Institute of Solid State Physics, Bremen, Germany
[2]University of Bremen, MAPEX Center for Materials and Processes, Bremen, Germany
[3]Forschungszentrum Jülich, Jülich, Germany
[4]PNDetector GmbH, München, Germany
[5]University of Bremen, Institute of Applied and Physical Chemistry, Bremen, Germany

Application of electric potentials in an electrolyte or exposure to gases or liquids causes reversible macroscopic length changes of porous materials such as dealloyed nanoporous gold (npAu). Thus, these materials are interesting candidates for applications as actuators and sensors. Macroscopic length changes are linked to microscopic changes of crystal lattice parameters. Furthermore, the microscopic strain state of the sample has also an influence on the catalytic activity of npAu (1,2). Hence, for the characterisation and improvement of npAu as a functional material measurement of local crystal lattice strain is clearly required. Most transmission electron microscopy based methods for the measurement of strain obtain their results from two-dimensional measurements on three-dimensionally strained samples. The results are interpreted as the average strain state along the electron beam direction (3,4). In this contribution, we show by evaluation of simulations that this assumption can be valid for measurements of strain from high-resolution scanning transmission electron microscopy (STEM) images (5) (Fig. 1a) and that it is valid with constraints also for measurements of strain using nano-beam electron diffraction (NBED) (6) (Fig. 1b).

Fig.1: Comparison between in electron-beam direction averaged strain of a simulated test structure and strain measured from simulated STEM-images (a) or series of NBED patterns (b).

From continuum theory and atomistic simulation it is expected that cylindrically shaped parts of npAu ligaments show compressive lattice strain along the ligament axis and tensile strain in radial direction (7). We confirm this expectation by a measurement of the tetragonal distortion (i.e. the ratio of lattice plane distances in two linearly independent crystallographic directions) using NBED (Fig. 2a). Furthermore, we examine to what extent the measurement of tetragonal distortions is influenced by distortions of the diffraction patterns (8). Such distortions can be caused by lens aberrations as well as by the detectors used for the acquisition of the diffraction patterns. Finally, we demonstrate a method to correct this effect. Density functional theory predicts predominantly inward crystal lattice relaxation for the majority of flat Au surfaces (9). Our atomically resolved measurements of strain variations confirm this prediction for curved npAu surfaces (Fig.2b).

Fig. 2: Measurements of strain in nanoporous gold. (a) Tetragonal distortion of npAu in a region including a partially cylindrically shaped ligament. (b) High-resolution crystal lattice strain variations at the surface of an npAu ligament.

To obtain information on the 3D strain distribution tomography based methods are required. We investigate the method proposed by Goris et al (10) to retrieve three-dimensional information on strain by evaluation of multislice tomography simulations calculated for 3D strained structures.

References:

(1) Mavrikakis et al., Catal. Lett**.** 64 (2000), p.101.

(2) Deng et al., J. Catal. 309 (2014), p.351.

(3) Mahr et al., Mater. Res. Lett. 6 (2018), p.84.

(4) Johnstone et al., Microsc. Microanal. 23 (2017), p.1710.

(5) Bierwolf et al., Ultramicroscopy 49 (1993), p.273.

(6) Müller et al., Microsc. Microanal. 18 (2012), p.995.

(7) Weissmüller et al., Acta Mater. 58 (2010), p.1.

(8) Mahr et al., Ultramicroscopy 196 (2019), p.74.

(9) Guan et al., Solid State Commun. 149 (2009), p.1561.

(10) Goris et al., Nano Lett. 15 (2015), p.6996.

Fig. 1

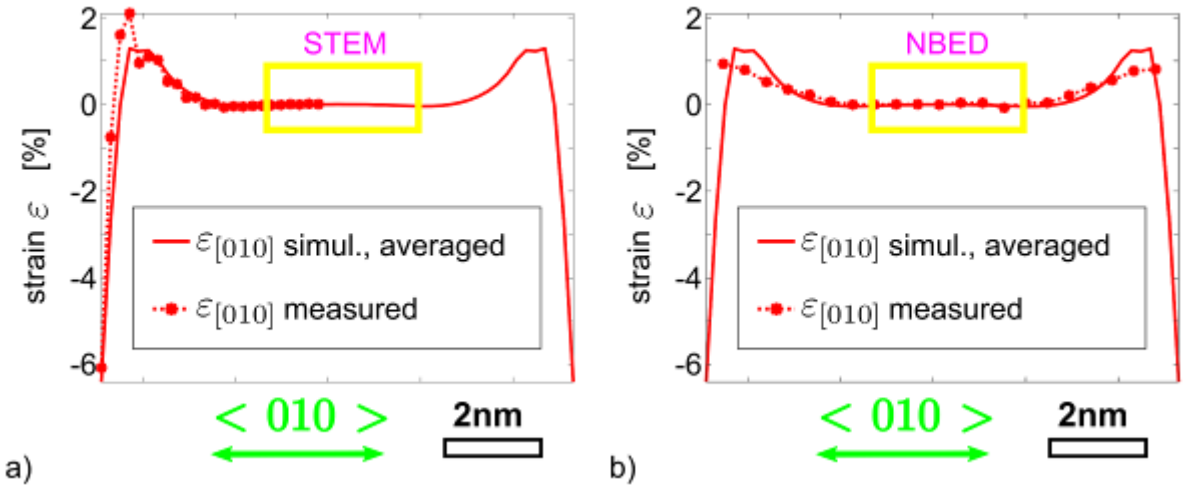

Fig. 2

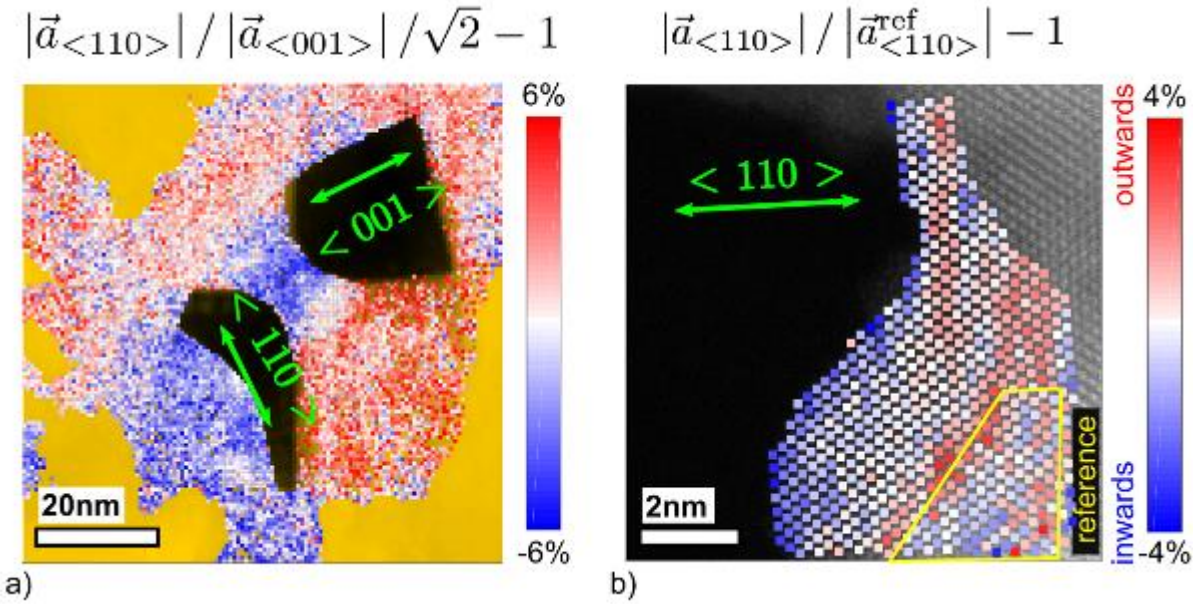

MS6.005
Memory effect for the creation of nanoporous ultrastructures

M. Kamp[1], A. Tymoczko[2], U. Schürmann[1], J. Jakobi[2], C. Rehbock[2], S. Barcikowski[2], L. Kienle[1]

[1]University, Institute for Material science, Kiel, Germany
[2]University, Technical Chemistry and Center for Nanointegration, Duisburg-Essen, Germany

The synthesis of nanoporous and hollow Au structures and the tailoring of their morphology expand the possible application in catalysis and sensing. The open and nanoporous structure offers an increased density of active surface sites and a curved surface with significant lattice strain. Chemical dealloying of alloys results in porous structures and represents a selective etching process in which the less noble element of an alloy is removed. The application of this process to educt materials, such as alloy and complex phase segregated nanoparticles, may yield novel nanoporous structures with versatile applications.

The aim of the research is the investigation of the novel template Au-Fe alloy system for the synthesis of nanoporous Au by dealloying. Educts with complex ultrastructures, like alloy and phase segregated nanoparticles are used to tailor the porosity. Further, the conversion process and the respective stability will be examined in more detail by looking at different ultrastructures and compositions.

The one-step synthesis of Au-Fe nanoparticles by pulsed laser ablation in liquids (LAL) generates core shell, solid solution, yolk shell and multicore nanoparticles from bulk Au-Fe alloy targets as a function of the target composition and solution. The Investigation of its ultrastructure is performed by SEM and (scanning) TEM applying versatile methods, like high resolution phase and Z-contrast imaging, accompanied by nanoprobe EDX elemental mapping (Tecnai F30 STWIN G with 300 kV). Nanoparticles are synthesized by LAL with an 8 ns Nd:YAG laser (RofinSinar Technologies, Plymouth).

The dealloying of Au-Fe Nanoparticles results in nanoporous Au and versatile kind of hollow NPs. Furthermore, a novel formation mechanism for the stabilization of ultrathin Au shells is depicted. Within this process, a direct correlation of the ultrastructure to the educt morphology is observed. Despite the etching, the morphology of the non-porous educts is conserved for the porous nanoparticulate products indicating a memory effect. This novel process includes oxidation of Fe and the Kirkendall effect, which seem to stabilize hollow nanoporous structures. The starting points for the dealloying experiments are the unique metastable Au-Fe alloy NPs with complex ultrastructures, which are only available by LAL. Due to this variety of template educt nanoparticles, nanoporous Au particles, hollow nanoporous Au shells, and yolk-shell-like Au nanoparticles encapsulated in ultrathin Au shells are synthesized.

The memory effect of dealloying, that is present in the novel Au-Fe alloy system, allows the synthesis of versatile nanoporous and hollow structures by an easy process. These structures are stabilized by a unique formation mechanism that is based on dealloying in combination with the Kirkendall effect. The combination of this process and the diverse ultrastructures of educt materials that can be produced by LAL can produce a wide variety of nanoporous structures for versatile applications.

Funding by the German Research Foundation (Projects KI1263/15-1) is acknowledged.

References:

(1) Kamp, M. *et al.* Temperature-Dependent Ultrastructure Transformation of Au–Fe Nanoparticles Investigated by in Situ Scanning Transmission Electron Microscopy. *Cryst. Growth Des* 18**,** 5434–5440 (2018).

(2) Tymoczko, A. *et al.* How the crystal structure and phase segregation of Au–Fe alloy nanoparticles are ruled by the molar fraction and size. *Nanoscale* 10, 16434–16437 (2018).

MS6.006
Correlative tomography and electrochemical tests on single Pt/Ru catalyst networks

T. Gänsler[1], K. Hengge[1], C. Scheu[1]

[1]Max-Planck-Institut für Eisenforschung GmbH, Nanoanalytics and Interfaces, Düsseldorf, Germany

Energy materials are widely investigated due to the demand of new energy production and storage systems. While needed at a global scale, their fundamental working principles have to be understood at the nanoscale. Electron micrographs are suitable, but usually do not provide three-dimensional (3D) information. In this work, we focus on 3D reconstructions of networks of precious metal nanoparticles (NPs) of a fuel cell catalyst in order to correlate degradation mechanisms and electrochemically driven processes.

Pt/Ru metal catalyst particles as used in commercial fuel cells are tracked over their accelerated lifetime in cyclic voltammetry (CV) studies. A scratch sample of the catalyst supported by a transmission electron microscopy (TEM) grid is used as the electrode in an electrochemical cell (1) where the applied voltage is cycled in the range of [0–1.0] V_{RHE} thousands of times, followed by scanning TEM (STEM) analysis. We present the tomographic reconstructions of Pt/Ru NPs before and after cycling, tracking them using identical location STEM. Energy-dispersive X-ray spectroscopy (EDS) mapping provides information about their chemical composition. STEM measurements were carried out on a C_S-corrected Titan Themis 60-300 equipped with a Bruker Super X-EDX detector. Dissolution of small particles and coalescence are already clearly visible by eye in early stages as seen in Figure 1. High-angle annular dark-field (HAADF) STEM tilt series were then three-dimensionally reconstructed by using a sequence of simultaneous iterative reconstruction techniques (SIRT) and discrete algebraic reconstruction techniques (DART). Quantification shows a constant decrease in accessible surface area, but with an initial increase in volume which later declines (2) The findings are attributed to differing degradation effects at various stages of the catalyst"s lifetime, namely dissolution, agglomeration, coalescence and Ostwald ripening. (2) Complementary EDS measurements show a decreasing Ru/Pt ratio, revealing a faster dissolution rate of Ru.

Despite the plentiful challenges in identical location tomography like damaging of the sample grid and loss of specimen (Figure 2), by careful selection of support material and operation procedures during the experiments we achieved a full overview from initial to end-of-life state of a fuel cell catalyst. Tomographic data could be linked to electrochemical as well as chemical composition data and degradation mechanisms could be identified. We will extend the studies towards nanostructured materials where the location of catalytic NPs play crucial roles in efficiencies.

References:

(1) J.C. Meier et al., Energy Environ Sci 5 (2012), 9319.

(2) K. Hengge et al., Int J Hydrogen Energy 42 (2017), 25359.

We acknowledge Enrico Pizzutilo for electrochemical measurements as well as the financial support by the German Federal Ministry for Economy and Energy within the program ZIM-KOOP (KF2001502ZG4).

Fig. 1: *(top)* STEM HAADF micrographs showing Pt/Ru catalyst NP networks in initial state, after 5000, 15000 and 25000 cycles in the potential range of (0–1.0) V_{RHE} (data taken from (1)) and their corresponding reconstructed 3D volumes *(bottom)*.

Fig. 2: STEM HAADF overview of a TEM grid (dark) with Pt/Ru catalyst NPs on carbon (bright). The comparison of the initial state (left) with the grid after the experiments (right) shows that despite severe damaging still intact regions remain.

Fig. 1

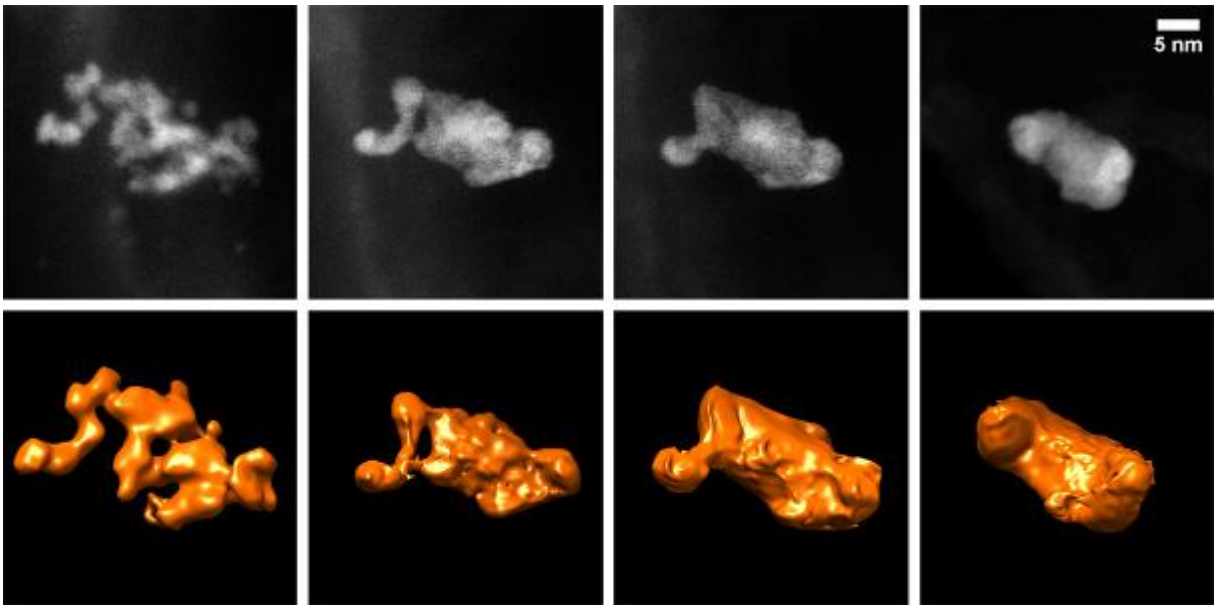

Fig. 2

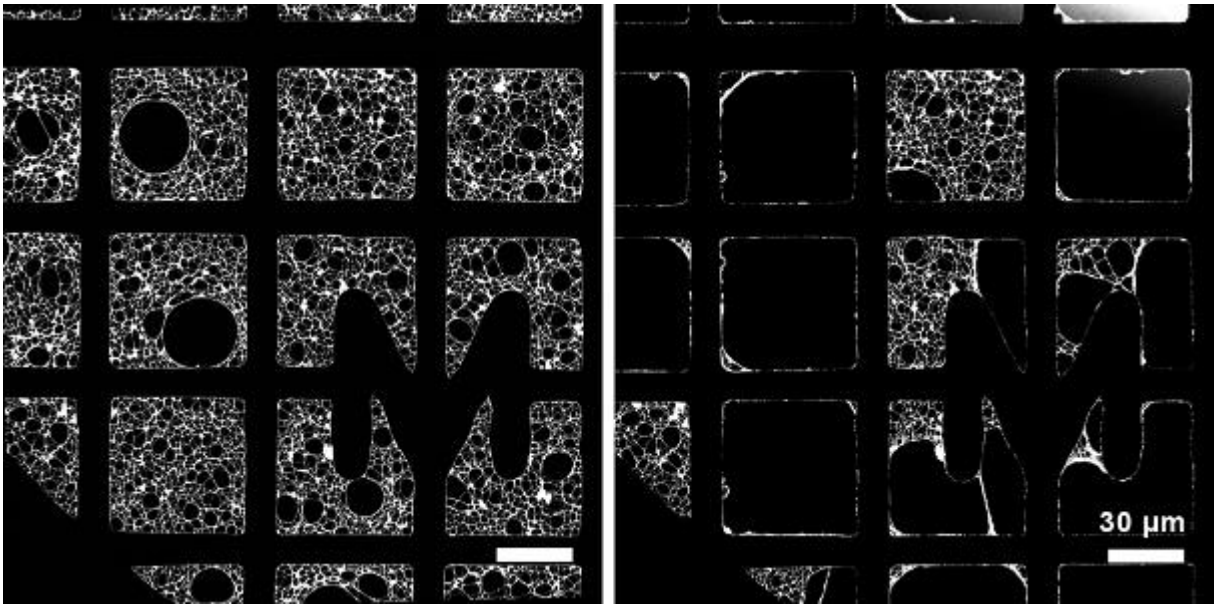

MS6.007
Scale-bridging 3D characterization of micro-/macroporous MFI-type zeolite crystals combining nano X-ray tomography and 360° electron tomography

D. Drobek[1], B. Apeleo Zubiri[1], T. Weißenberger[2], J. Wirth[1], S. Englisch[1], W. Schwieger[2], E. Spiecker[1]

[1]FAU-Erlangen-Nürnberg, Institute of Micro- and Nanostructure Research, Erlangen, Germany
[2]FAU-Erlangen-Nürnberg, Chair of Chemical Reaction Engineering, Erlangen, Germany

The combination of lab-based high-resolution X-ray microscopy tomography (Nano-CT) with 360° electron tomography (ET) enables three-dimensional (3D) imaging of complex material structures across multiple length scales without missing-wedge artifacts. This kind of scale-bridging 3D analysis is necessary to obtain realistic and reliable structure and morphology information about nanoparticulate materials exhibiting a hierarchical pore system.

Here, we study microporous MFI-type zeolite crystals with sizes of about 3 µm featuring a well-interconnected intracrystalline macroporous network (1), which are promising for the application in heterogeneous catalysis. The crystal and pore dimensions approach the resolution limits of both ET at its low end, typically allowing for the investigation of sample sizes up to (3 µm)³ with spatial resolutions down to (1 nm)³, and Nano-CT at its high end, which reaches spatial resolutions down to (50 nm)³ of sample sizes up to (64 µm)³.

The macroporous zeolite crystals are synthesized via a steam-assisted-crystallization (SAC) process, where mesoporous silica sphere (MSP) primary particles serve as a macropore template and are inversely transformed into the MFI-type zeolite framework. The microporous structure with its high specific surface and interconnected hierarchical pore system delivers an ideal subject to demonstrate the benefit of combining 360° ET and Nano-CT to unveil and understand the morphological changes at different stages of the crystallization process (Figs 1, 2).

A Zeiss Xradia 810 Ultra in phase contrast mode is used for Nano-CT and a FEI Titan Themis 300 at 300 kV in high-angle annular dark field (HAADF) scanning transmission electron microscopy (STEM) mode is applied for 360° ET experiments. To obtain optimized imaging conditions, individually selected zeolite particles or particle agglomerates are prepared on the plateau of tips utilizing our recently developed stamping transfer technique (2) in a dual-beam FEI Helios NanoLab 660.

The higher resolution of the 360° ET reconstructions exposes the internal sample morphology like internal pores, pore connections or the evolution stage of the converting MSPs during a certain transition state (Figs 1d, 2d). Moreover, Nano-CT allows the 3D reconstruction of particle agglomerates to deliver statistically relevant data and to unravel the interparticle pore space (Fig. 2e). Combining both techniques enables the scale-bridging 3D characterization of the micro-/macroporous zeolite crystals throughout the complete SAC process.

We gratefully acknowledge the German Research Foundation (DFG) for funding through the priority program SPP 1570, the research training group GRK1896, the project SP648/8 and the DFG EXC 315.

References:

(1) A.G. Machoke et al., Adv. Mater. 27 (6) 1066-1070, 2015.

(2) T. Przybilla et al., Small Methods 2, 1700276, 2018.

Fig. 1: (a) Scanning electron microscope (SEM) image of completely crystallized macroporous zeolite particles. (b) SEM image of zeolite particles. (c) HAADF STEM image of the 360° ET tilt series. (d) Surface rendering of the 3D reconstruction.

Fig. 2: (a) SEM image of macroporous zeolite particles in a transient state. (b) HAADF STEM image of the 360° ET tilt series. (c) Nano-CT image of the tilt series in phase contrast mode. (d) Slice through the 3D reconstruction. (e) Volume rendering of the CT reconstructions.

Fig. 1

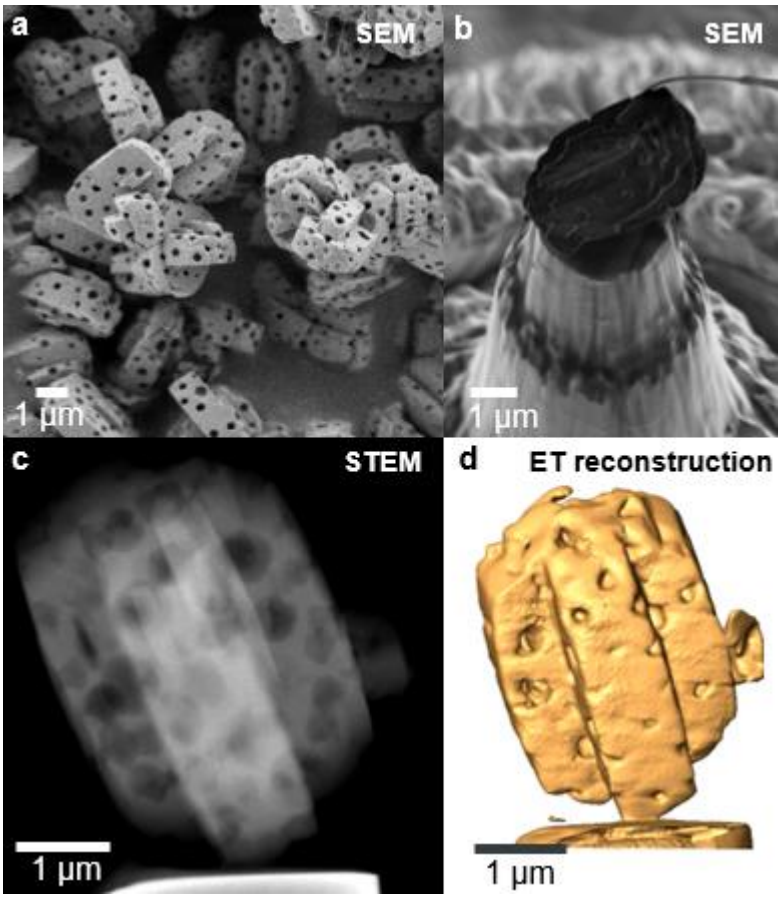
a
SEM
1 µm
b
SEM
1 µm
c
STEM
1 µm
d
ET reconstruction
1 µm

Fig. 2

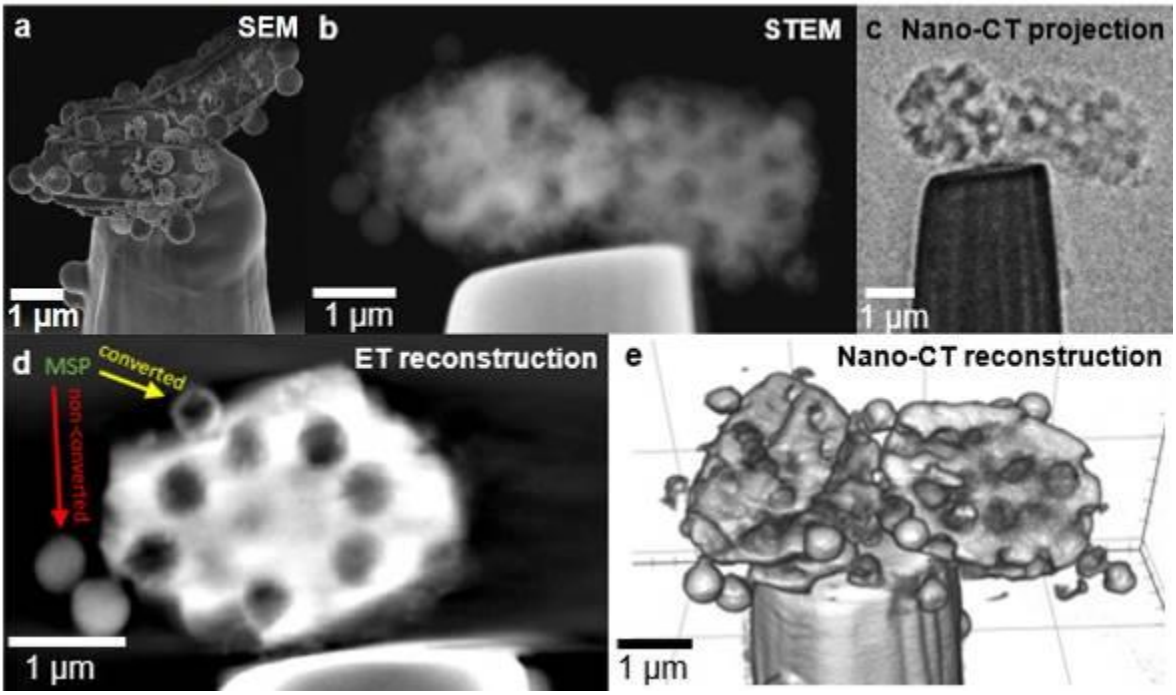
a
SEM
1 µm
b
STEM
1 µm
c
Nano-CT projection
1 µm
d
MSP
converted
non-converted
ET reconstruction
1 µm
e
Nano-CT reconstruction
1 µm

MS6.LB.P01
Study of the ion intercalation between the MXene membranes for the water membrane application

M. Helal[1,2], K. Mahmoud[1]

[1]Qatar Foundation - Hamad Bin Khalifa University, Qatar Environment and Energy Research Institution (QEERI), Doha, Qatar
[2]Qatar Foundation - Hamad Bin Khalifa University, Qatar Environment and Energy Research Institution (QEERI), Doha, Qatar

MXenes showed great promise as gas separation and water purification membranes. It was proposed that MXene can reject ions by both charge and size sieving mechanisms(1, 2). Generally, it is expected that the interlayer spacing between the MXene nanosheets acts as a trap for the ions and the negatively charged surface of MXene allows for spontaneous intercalation of cations from aqueous salts. However, detailed ion sieving mechanism through the layered MXene sheets hasn"t been fully explored. We aim to have a clear and thorough understanding of the water/ions intercalation between the MXene layers by using advanced spectroscopic characterization techniques. Ions with different charges and hydration radios are expected to have different interaction pattern with MXene. Here we use to study the entrapment of various cations. In this work, we use in situ XRD-DSC system and in situ environmental SEM to investigate the effect of dehydration and temperature variation on the interlayer spacing of MXene membrane. XRD and SEM have revealed different intercalation patterns with ions and insignificant changes to the interlayer spacing of MXene with water, as compared with graphene oxide membrane where a pronounced swilling/contraction was observed with increasing/decreasing humidity. Hence, this study not only allows to understand the ion sieving mechanism of MXene, but also will help to understand and perhaps to help improve the stability of MXene membranes stability in aqueous media applications.

References:

(1) Lu, Ming, Wenjuan Han, Haojie Li, Wen Shi, Jiaheng Wang, Bingsen Zhang, Yan Zhou, Haibo Li, Wei Zhang, and Weitao Zheng. 2019. "Tent-Pitching-Inspired High-Valence Period 3-Cation Pre-Intercalation Excels for Anode of 2D Titanium Carbide (MXene) with High Li Storage Capacity." Energy Storage Materials 16: 163–68. https://doi.org/10.1016/j.ensm.2018.04.029

(2) Zhu, Xiaolei, Bingchuan Liu, Huijie Hou, Zhenying Huang, Kemal Mohammed Zeinu, Long Huang, Xiqing Yuan, Dabin Guo, Jingping Hu, and Jiakuan Yang. 2017. "Alkaline Intercalation of Ti3C2MXene for Simultaneous Electrochemical Detection of Cd(II), Pb(II), Cu(II) and Hg(II)." Electrochimica Acta 248: 46–57. https://doi.org/10.1016/j.electacta.2017.07.084.

MS6.LB.P02
Correlation between densification and ferromagnetic resonance of Rare-Earth substituted magnetic oxides

A. Manzoor[1,2]

[1]GCUF, Pakistan, Physics, Faisalabad, Germany
[2]TU Berlin, Berlin, Germany

In the present study, we report the dopant- and size-dependent variations in high-frequency magnetic and electrical transport properties of Ho-substituted Li-Mn polycrystalline ferrites. Thermal stability and phase identification were confirmed by thermal gravimetric analysis and X-ray diffraction experiments. The overall average crystallite size decreased from 29.6 to 17.5 nm, whereas the bulk density increased from 3.47 to 4.29 g/cm3 with increasing Ho content. Ferromagnetic resonance (FMR) measurements at the X-band revealed significant shifts in FMR linewidths and resonance positions as a function of composition. Both, FMR linewidth and porosity, were found to decrease with the systematic addition of Ho from 2538 to 2359 Oe and from 26 to 15.4 %, respectively. The substitution of Ho3+ for Fe3+ reduced the net magnetization of the spinel lattice from 53 to 41 emu/g. Electrical measurements revealed that the resistivity is higher in samples with smaller grains possessing a greater number of thin insulating grain boundaries. The activation energy ΔE required for hopping increases from 0.09 to 0.16 eV with Ho addition, which may be well explained by the increase in resistivity. The substitution of Ho3+ for Fe3+ causes a decrease in Curie temperature Tc due to the damping of A-B exchange interactions.

MS6.LB.P03
Nano- tubes, "rails", flakes synthesized by gas transport reactions for Ti-Se system

V. Kolosov[1], A. Titov[1], A. A. Yushkov[1]

[1]Ural Federal University, Ekaterinburg, Russian Federation

Transition metal chalcogenides and TiSe2, are of growing interest, in particular based on charge density waves (1) and 2D applications. Ti-Se nanoobjects studied were obtained in the process of TiSe2 single crystals syntheses by gas-transport reactions with an excess of selenium as a carrier gas medium (2). The transport occurred at the cold end of the ampoule at 600 C, with the hot end kept at 800 C. TEM samples are from the fine powder at the hot end of the ampoule (left after extraction of the larger single TiSe2 crystals), transferred to the grid for TEM studies from the surface of distilled water. TEM was performed at 200 kV using bright and dark field imaging, SAED and nanodiffraction, EDX and HREM supported by some 80 kV studies.

The TEM reveals mixture of various nanoobjects besides TiSe2 microcrystals and nanoflakes. The most interesting and novel are linearly elongated nanorod-like objects, ~ 20 - 50 nm wide and 100 nm - 1 micron in length, demonstrating crystalline diffraction and some internal structure. TEM identifies 2 types of linear nano-objects, resembling multi-layered nanotubes and "nanorails" with stair-step profiles (steps parallel to the nanorod axis), Fig 1. Initially, nano-objects tend to have straight edges. Fig. 1 a, d, e, f - h. According to preliminary data from EDX, Ti prevails in their composition (up to ~ 80-90%). Agglomerates of nanorods exhibit primarily diffraction rings, Fig. 1b, whereas for individual nano rods/rails diffraction spots and arcs appear, Fig. 1c. The regular change of transparency along some objects indicates the layered crystal character with different number of atom layers better visualized at 80kV. SEM detects nanorods of high aspect ratio with similar stair-step morphology also at μm scales, Fig. 1j. Separate thin crystalline nanoflakes of the initial material were also studied, Fig. 2. HREM images show their perfect single crystalline structure, Fig. 2 d. Under the action of TEM electron beam the flakes acquire labyrinthine structure and finally (in ~ 10 min) were amorphized, Fig. 2a, b.

The authors of TEM study of TiSe2 (3) propose that nanotubes should have a stoichiometric composition, facilitating the twisting of TiSe2 layers. Our studies show that the presence of intercalate (super stoichiometric Ti) leads to a wide variety of nano-objects for Ti-Se system including nano- tubes, rails.

References:

(1). F.J. Di Salvo, J.V. Waszczak., Phys. Rev. B, V. 17, p. 3801-3807 (1978)

(2). A.N. Titov, A.I. Merentsov et al., J. Alloys Comp., V. 737, p. 829-835 (2018)

(3). Jun Chen, Zhan-Lyang Tao et al., Adv. Mater., V. 15, p. 1379-1382 (2003)

Support of project 3.6121.2017/8.9 (RF Ministry of Sci. & High Educ.) and Agreement No 02.A03.21.0006 (Act 211 RF Government) are acknowledged.

Fig. 1: a - TEM of nanorods/tubes agglomeration; b – corresponding SAED; c - SAED from a separate nanotube; d - nanotube with holes in the wall; e - nanotube fragment; f, g, h – TEM of nanorails with different steps in thickness along the axis; j – SEM of similar high-aspect ratio microrod.

Fig. 2: a - TEM of the crystalline nanoflake with SAED (inset) before e-beam exposure to the e-beam; b – the same one after exposure for 10 min.; c – TEM of other nanoflake; d - HREM of it.

Fig. 1

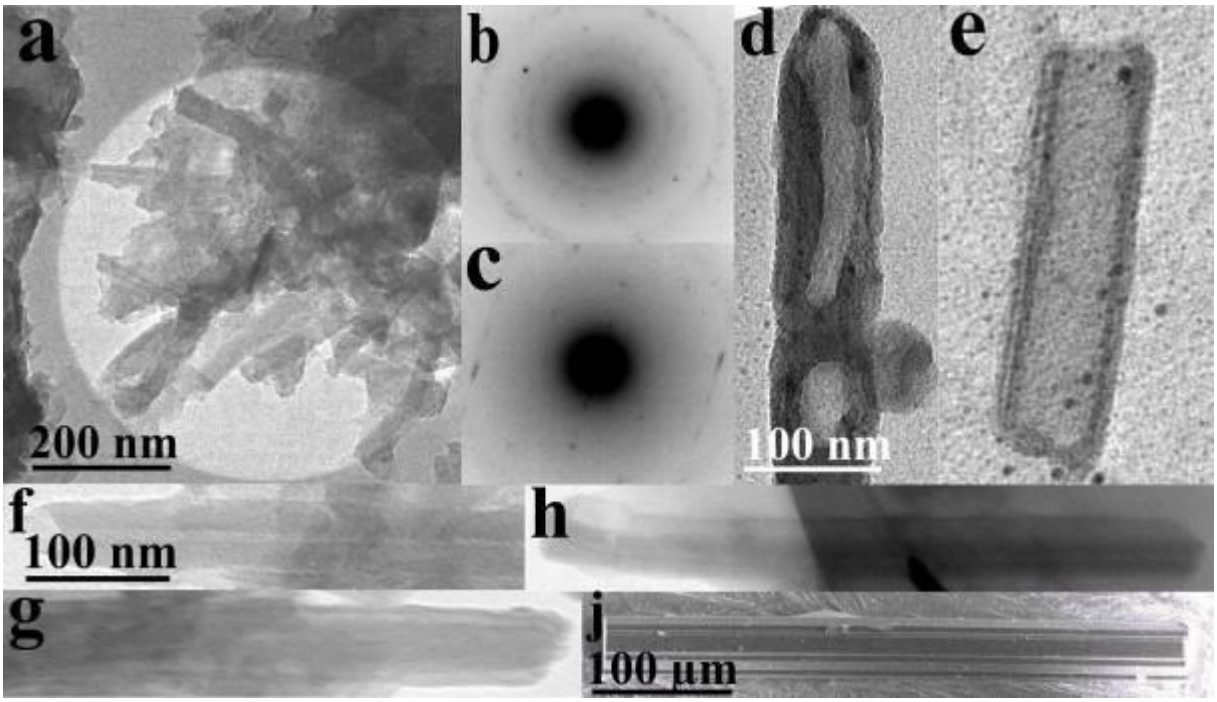

Fig. 2

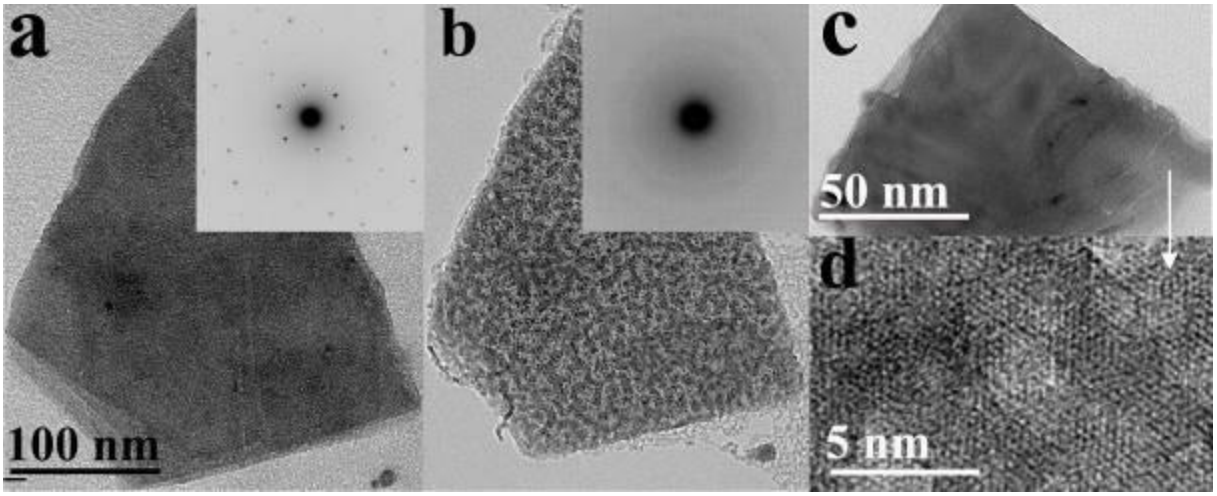

MS6.P001
Scattering angle distributions of thin carbon foils - Comparison of TSEM measurement and simulation

W. Häßler-Grohne[1], E. Buhr[2], T. Klein[1], D. Hüser[1]

[1]Physikalisch-Technische Bundesanstalt, 5 Precision Engineering, Braunschweig, Germany
[2]Physikalisch-Technische Bundesanstalt, 4.2 Imaging and Wave Optics, Braunschweig, Germany

A quantitative characterization of the three dimensional size and shape of objects at the nanoscale is both challenging and rewarding.

Electron microscopy delivers projected two dimensional images of nanostructures. From this, the geometry of nanostructures, such as carbon particles and aggregates, is to be estimated by solving an inverse problem. Therefore, simulations of the electron scattering process are employed to deduce quantitative information about the third dimension from measurements of nanostructures.

We have performed electron transmission measurements on carbon foils using an SEM in transmission mode (TSEM). Angular distributions may be obtained by means of a bright field and several dark field rings of a transmission detector. This involves procedures to calibrate the signal of detector elements with respect to each other. The obtained angular distributions are compared to the results of Monte Carlo simulations of electron scattering. These simulations employ Salvat-Jablonsky elastic scattering models and inelastic energy loss function models derived from dielectric function theory.

MS6.P002
Nanoparticle size measurement by TEM; How many particle should be counted?

K. Yamamoto[1], E. Grulke[2]

[1]National Institute of Advanced Industrial Science and Technology (AIST), National Metrology Institute of Japan (NMIJ), Tsukuba, Japan
[2]University of Kentucky, Chemical & Materials Engineering, Lexington, United States

Nanomaterials have recently been used in many industrial fields. The Organization for Economic Co-operation and Development (OECD) has decided to make a regulation of nanomaterials. The European Union (EU) announced their definition of nanomaterial in 2012. According to the EU definition, nanomaterial means a natural, incidental or manufactured material containing particles, in an unbound state or as an aggregate or as agglomerate and where, for 50 % or more of the particles in the number size distribution, one or more external dimensions is in the size range 1 nm - 100 nm. They also announced that the particle size of the primary particles in agglomerates or aggregates should be considered. Transmission electron microscope (TEM) is a most useful technique that can provide precise information on the size and shape of the primary nanoparticles. Standardization in the field of nanotechnologies is examined Technical Committee (TC) 229 of International Organization for Standardization (ISO). Recently, international standard of particle size distribution measurement of nanoparticles by using TEM is developed in ISO/TC229 (1). In this study, size and size distribution of nanoparticles by TEM were evaluated statistically.

Polystyrene latex （PSL） nanoparticle dispersion was used as a model material of mono-dispersed case, and titanium dioxide (TiO2) were used as model materials of aggregated cases. TiO2 powder was dispersed by ultrasonication in an aqueous solution of sodium hexametaphosphate (NaPO3)6. The carbon membrane surface of a TEM microgrid was made hydrophilic by plasma-treatment. The test material dispersion of 12μL was collected using a micropipette, and dripped onto the microgrid with support membrane, then the microgrid was dried. Acceleration voltage of TEM was 200kV. Images of PSL and TiO2 particles were taken at a resolution of 0.1964nm/pixel and 0.1529nm /pixel, respectively. Particle size of each nanoparticle was obtained by using Image-J software. Primary particle of aggregate was distinguished by tracing manually.

Typical TEM image of TiO2 is shown in Figure 1(a). TiO2 particles are aggregated. Small particles with size of 1 nm attaching on a surface of TiO2 particles are chemical dispersant. Primary particles of aggregate are detected by tracing manually. An equivalent circle diameter (ECD) is obtained from projection area of each particle. Dependence of mean value of ECD and standard deviation on a counted particle number are shown in Figure 1 (b) and (c), respectively. Mean diameter shows the varied value below a counted number of 500, and shows a constant value of 25.2 nm at a counted number more than 600. Standard deviation is also converging to the value of 6.7 nm at a counted number more than 600. Mean standard error, which is shown in Figure 1 (d), decreases rapidly with increasing counted particle number of 400, and that decreases slightly with counted particle number of more than 500 particles. Therefore, counting more than 500 particles is needed for the sufficient accuracy of size distribution. We summarize that counting particle at least 500 is required for the reliable particle size measurements statistically.

References:

(1) ISO IS 21363

Fig. 1: Typical TEM images of TiO2 particles (a), and counted particle number dependence of mean diameter (b), standard deviation (c), and mean standard error (d), respectively.

Fig. 1

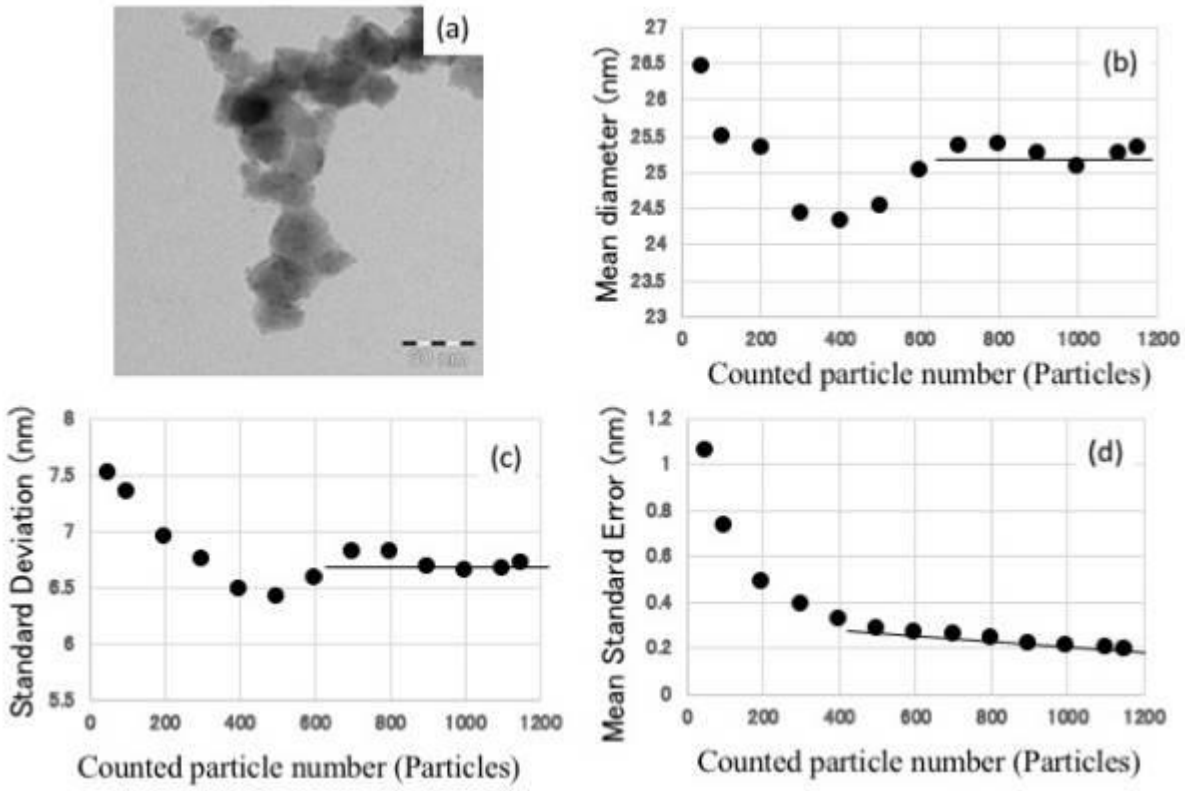
(a)
(b)
Mean diameter (nm)
27
26.5
26
25.5
25
24.5
24
23.5
23
0
200
400
600
800
1000
1200
Counted particle number (Particles)
(c)
Standard Deviation (nm)
8
7.5
7
6.5
6
5.5
0
200
400
600
800
1000
1200
Counted particle number (Particles)
(d)
Mean Standard Error (nm)
1.2
1
0.8
0.6
0.4
0.2
0
0
200
400
600
800
1000
1200
Counted particle number (Particles)

MS6.P003
HAADF-STEM Study of Local Lattice Strain in Gold Nanorods

K. Aso[1], J. Maebe[1,2], T. Yamamoto[1], S. Matsumura[1,3]

[1]Kyushu University, Applied Quantum Physics and Nuclear Engineering, Fukuoka, Japan
[2]Ghent University, Solid State Science, Ghent, Belgium
[3]Kyushu University, The Ultramicroscope Research Center, Fukuoka, Japan

Metal nanoparticles have attracted many research interests and are applied to various functional materials, such as optical devices, catalysts and so on. It is well known that lattice strain in nanoparticles affects the functional properties through local variation in the electron state. It is quite important to understand basic mechanisms to cause the local strain in nanoparticles. The present study was aimed to analyse systematically the local lattice strains in gold nanorods as a function of the aspect ratio by HAADF-STEM atomic resolution observations.

Our specimens were three single-crystalline Au nanoparticles which were the almost same in width as ~9.0 nm but were different in length, or in the aspect ratio (AR) such as 1.0, 2.1 and 3.6. The long axis was along to (001). Atomic resolution HAADF-STEM observations of the gold nanorods oriented to (-110) were carried out using a JEM-ARM200CF at an acceleration voltage of 120 kV (1). The coordinates of atom columns were determined as the peak positions of 2D Gaussian functions fitted to the image intensity profiles. The inter-columnar distances $d_{1/2,1/2,0}$ and d_{001} measured from the coordinates were distributed around the mean values of $\langle d_{1/2,1/2,0} \rangle$ and $\langle d_{001} \rangle$ with the standard deviations less than 4 pm. Besides, molecular dynamics (MD) simulations were conducted for the corresponding shapes using LAMMPS with an Embed Atom Method (EAM) potential for Au (2,3).

It was found that the ratio of lattice constants $c/a(=\langle d_{001} \rangle / \sqrt{2} \langle d_{1/2,1/2,0} \rangle)$ decreases from one to 0.98 with the increase of AR from one. It indicates the crystal lattice is distorted to be tetragonal in the rod form. The MD simulations also showed the tetragonal deformation of crystal lattice corresponding well to the experimental results. It is concluded that the tetragonality comes from the anisotropic shape of the rod-like nanoparticles. Local displacements of atom columns were measured as deviations from the averaged periodic lattice points, and then the local strains $e_{xx}(x,y)$ and $e_{yy}(x,y)$ were evaluated. Here, x and y directions are parallel to (001) of the long axis and the perpendicular (110), respectively. The surface lattice contraction was recognized around the surfaces in the three nanoparticles. It is explained in terms of surface tension due to less number of coordinating atoms at the surface (4). Moreover, it was found that positive $e_{xx}(x,y)$ about ~0.7 %, or dilatation strain along x direction, occurs localized in the tip parts in the nanorods. The MD simulations were also confirmed to reproduce well the localized dilatation strain along the long axis in the rod shape.

References:

(1) K. Aso, *et al.*, *Microscopy*, 65(2016), 391.

(2) S. Plimpton, J*ournal of Computational Physics,* 117(1995), 1.

(3) G. P. Purja Pun, *to be published* (The potential is on the web"Interatomic Potentials Repository")

(4) W. J. Huang, *et al.*, Nature Materials, 7(2008), 308.

MS6.P004
Nanopatterned carbon formed by graphitic foam

P. Simon[1], X. J. Feng[1], M. Bobnar[1], P. Höhn[1], U. Schwarz[1], W. Carrillo-Cabrera[1], M. Baitinger[1], Y. Grin[1]

[1]Max-Planck-Institut für Chemische Physik fester Stoffe, Chemische Metallkunde, Dresden, Germany

We present the synthesis route to carbon with hierarchical morphology on the nanoscale. The structures are generated using crystalline orthorhombic lithium carbide (Li_2C_2) as precursor with nanolamellar organization. Careful treatment by SnI_4 oxidizes carbon at the fairly low temperature of 80 °C to the elemental state and keeps intact the initial crystallite shape, the internal lamellar texture of particles, and the lamellae stacking. The reaction product is amorphous but displays in the microstructure parallel band-like arrangements with diameters in the range of 200 nm up to 1 µm (Fig. 1a) forming a nanopatterned carbon plate. The thickness of the plate of about 20 nm was assessed by the edge. These bands exhibit internal fine structure made up by thin strips of about 60 nm width running inclined with respect to the long axis of the band. The stripes of neighboring columns sometimes meet and give rise to arrow-like arrangements in the microstructure with a tilt angle of 37° (Fig. 1b). Another enlarged region of interest shows bands of 200−500 nm in size with nanopatterning. The fine lines inside the bands are tilted with respect to the long axis of the bands and give the impression of a helical winding or herringbone arrangement of twins running through the bands (Fig. 1c). High-resolution image of carbon obtained by oxidation of Li_2C_2 reveals a network of differently sized pores with sizes in the range 2−6 Å. In certain regions (para)crystal-like ordering observed, see Fourier-filtered image Fig. 1d.

This is an alternative preparation method of nanostructured carbon from an inorganic precursor by a chemical redox route without applying physical methods such as ion implantation, printing, or ablation. The polymerization reaction of the triple bond of acetylide anions gives rise to a network of carbon sp^2 species with statistically sized and distributed pores with diameters resembling to zeolite structures. The pores show partially paracrystal-like ordering and may indicate the possible formation of carbon species derived from graphitic foams. Fig. 2a displays a model of the smallest possible 1 × 1 variant (2), whereas Fig. 2b represents a graphitic foam with 3 × 3 phenyl groups as a building block. Clathrate II, another possible sp^3 carbon allotrope shows similar d-spacings from the (110) zone as observed (Fig. 3a) (3).

Fig. 1

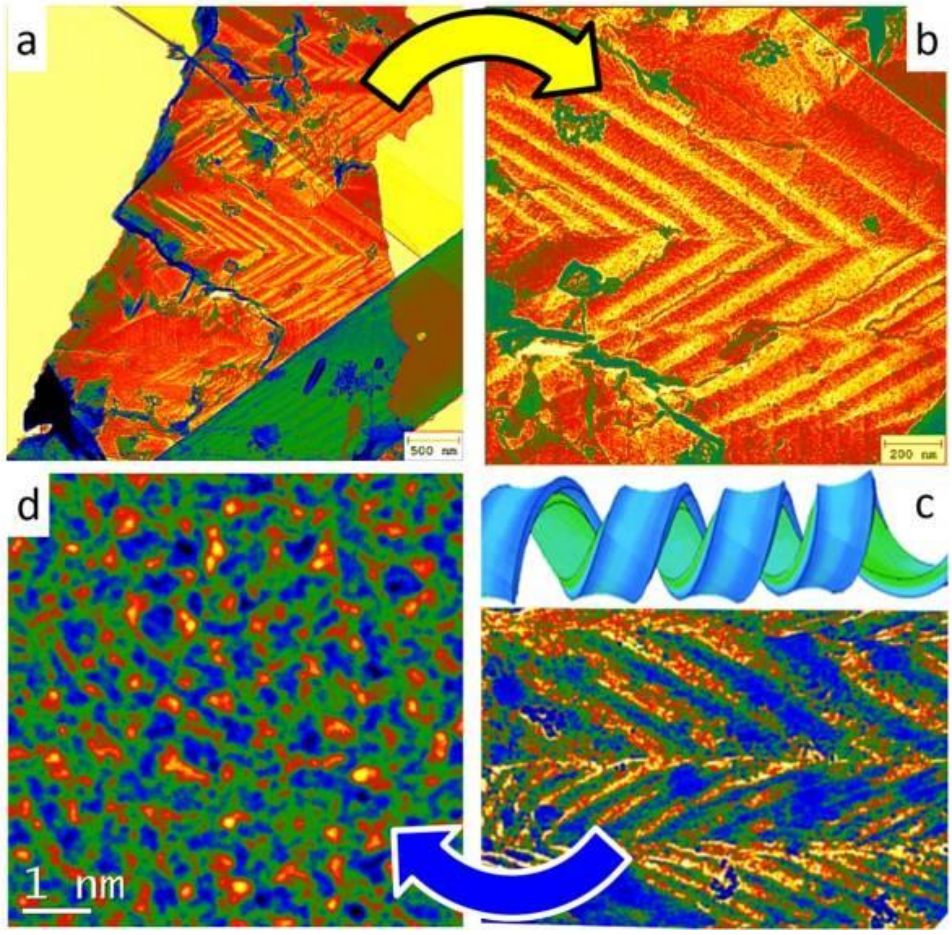

Fig. 2

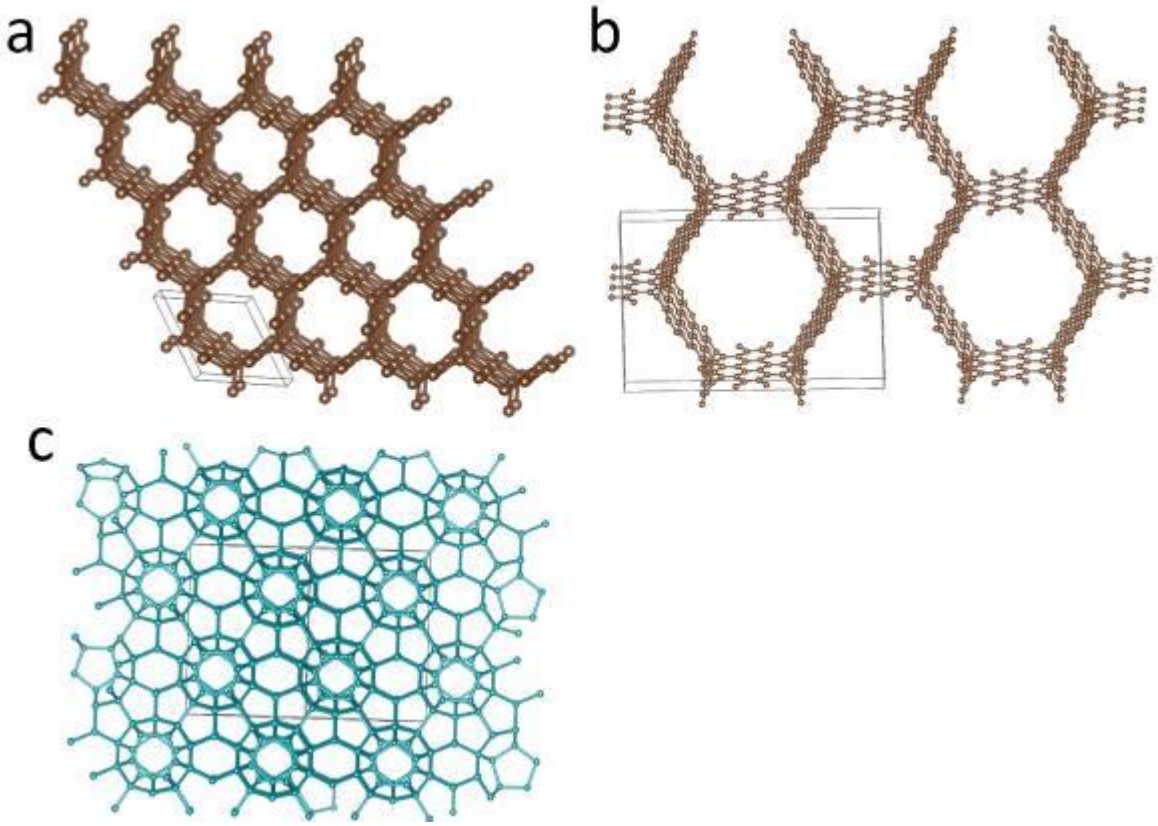

MS6.P005
Monolithic Hierarchical Large-Pore Mesoporous Silica for Immobilization of Enzyme Conjugates

D. Poppitz[1], G. Mhanna[1], R. Gläser[1]

[1]Universität Leipzig, Institute of Chemical Technology, Leipzig, Germany

Mesoporous silica materials enable a wide range of applications due to their remarkable properties such as high specific surface area, ordered pore structure and various morphologies. Furthermore, large-pore mesoporous silica (LPMS) materials are a prominent candidate for the immobilization of enzymes due to their eminent biocompatibility, chemical inertness and modifiable surface. In most of the biological systems, more than one enzyme is used to realize metabolic pathways. To adopt this, hierarchical pore systems can be applied to establish new opportunities for multi-step enzyme catalyzed reactions.

The synthesis of monolithic LPMS materials can be achieved by pseudomorphical transformation to create a hierarchical pore network. Thus, the possibility of controlling the volume ratio of the different pore systems is a goal for realizing consecutive reactions. To control this process, there is a special focus on high-resolution transmission electron microscopy where the hierachical pore networks are imaged.

Hyydrothermal synthesis and partial pseudomorphic transformation result in silica with two interconnected mesoporous system of MCM-41 and a highly ordered mesoporous silica (HMS). Therefore, the extent of the partial pseudomorphic transformation was controlled by varying the ratio of the structure-directing agents. The materials were characterized by nitrogen sorption at 77K (ASAP 2010, micrometrics), X-ray powder diffraction, scanning electron microscopy (Leo Gemini 1530, Zeiss), pulsed field gradient (PFG) NMR spectroscopy and transmission electron microscopy (JEM-2100Plus, Jeol) comprising ADF and BF detectors, a 4K CMOS based camera (F416, TVIPS) and an EDS system for elemental analysis (Octance, EDAX).

The focal point of the present study is on high-resolution imaging of the hierarchical pore structures in the created LPMS materials. The textural properties of the materials were characterized by nitrogen sorption isotherms. Thereby, the progress of the partial transformation was followed and an increase in the specific pore volume of MCM-41 was detected, whereas the pore volume of the LPMS decreases. By means of PFG NMR, the connectivity of the pore systems was investigated using n-hexane as diffusant. The resulting poly-exponential curves indicate the presence of more than one diffusion coefficient. By means of TEM, the presence of the pore network was clearly shown. For analyzing of the partial pseudomorphic transformation, intermediates as well as the parent and fully converted LPMS was investigated. Different sizes and arrangement of domains of the two mesoporous silica next to each other provide insight into the formation of the hierarchical pore system. Furthermore, the domain boundaries are studied in detail to characterize the connectivity of the different pore structures and to predict the accessibility for external guests.

For the realization of consecutive reactions over multi-enzyme conjugates, hierarchical LPMS materials were synthesized by pseudomorphic transformation. These materials were investigated concerning their textural properties and interconnectivity of the pore system. Moreover, high-resolution imaging of the LPMS gives an idea of the pore network evolution showing different extents of the transformation process.

MS6.P006
4D-STEM Characterization of Materials in a Transmission-SEM

B. Haas[1], J. Müller[1], C. T. Koch[1]

[1]Humboldt-Universität zu Berlin, Department of Physics & IRIS Adlershof, Berlin, Germany

Here, we demonstrate mapping of strain, electric fields, crystal orientation and structural phase in a range of materials by means of 4D-STEM in a modified transmission-SEM. Details about the development of the system containing a pixelated electron detector and 6-axis piezo stage are reported by J.M. in the instrumentation session of this meeting.

Mapping in a modified SEM is not only significantly more cost efficient in comparison to STEM in a TEM/STEM, it also has unique benefits like ultra-low voltage and very large fields of view. These features are exploited in the following to map large areas – bridging the gap from the nano to the macro scale – and to investigate certain systems completely nondestructively.

In Fig. 1 (a) a virtual dark field image from a 4D-STEM map of a WS2 layer on top of a holey carbon film obtained with a 15 keV electron beam is shown along with some individual diffraction patterns from characteristic regions. The diffraction of a mono layer and double layer are distinctly different and allow the mapping of mono layer regions. Even through the amorphous support layer the diffraction is strong enough to see the structure of the (mono) layer on top. This was used to obtain a continuous large area 4D-STEM map of graphene, from which an orientation map depicting the grain distribution of the (mono) layer was calculated and is shown in (b).

However, it is also possible to characterize rather conventional materials as shown in Fig. 2 with the example of an GaN/AlN/ Al2O3 layer system in cross-section preparation. In (a) an overview secondary electron image is shown alongside two 30 kV diffraction patterns from GaN and Al2O3. A 4D-STEM map of the marked area was obtained and yields a virtual dark field image as well as maps of the lattice variation that reveal the state of relaxation of GaN and AlN, as depicted in (b).

In this contribution we will also show results of other materials including piezoelectric fields in nanowires and maps of phase segregation in CsPbBr3, underlining the versatility of the transmission-SEM setup.

The authors thank Xiaomin Xu and Norbert Koch from Humboldt-Universität zu Berlin for WS2 samples and Gerardo Algara-Siller from Fritz-Haber-Institute for graphene samples. Jonas Lähnemann from Paul-Drude-Institut and Sebastian Lehmann from Lund University is thanked for nanowire samples. The authors thank Anna Mogilatenko from Ferdinand-Braun-Institut for the GaN/AlN sample and Hannah Funk from Helmholtz-Zentrum Berlin for collaboration on the CsPbBr3. B.H. and C.T.K. acknowledge the German Research Foundation (DFG)-funded core facility BerlinEM Network (grant no. KO2911/13-1) and project no. 182087777 – SFB951.

Fig. 1: (a) Virtual dark field image from 4D-STEM data set showing a WS2 film on a holey C film obtained at 15 kV. Individual diffraction patterns for mono and double layer WS2 are strong and distinctly different. A pattern of a monolayer on top of the amorphous carbon shows still clear diffraction spots. (b) An (in-plane) orientation map of a graphene monolayer reveals the grain distribution over almost 80x80 µm2.

Fig. 2: (a) Secondary electron image of a thinned GaN/AlN/Al2O3 sample with an indication of the mapped area depicted in (b) and two representative 30 kV diffraction patterns from GaN and Al2O3 regions. (b) Virtual dark field image and maps of the lattice variation in growth direction and perpendicular to it revealing almost fully relaxed layers.

Fig. 1

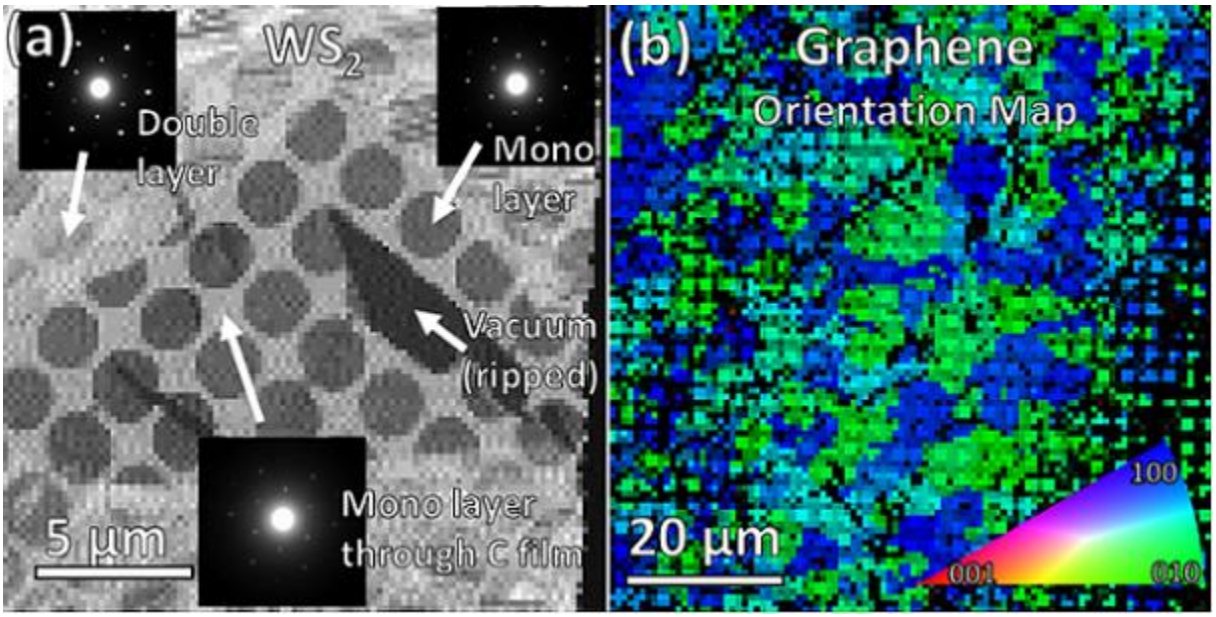
(a)
WS_2
Double layer
Mono layer
Vacuum (ripped)
Mono layer through C film
5 µm
(b)
Graphene
Orientation Map
20 µm
100
001
010

Fig. 2

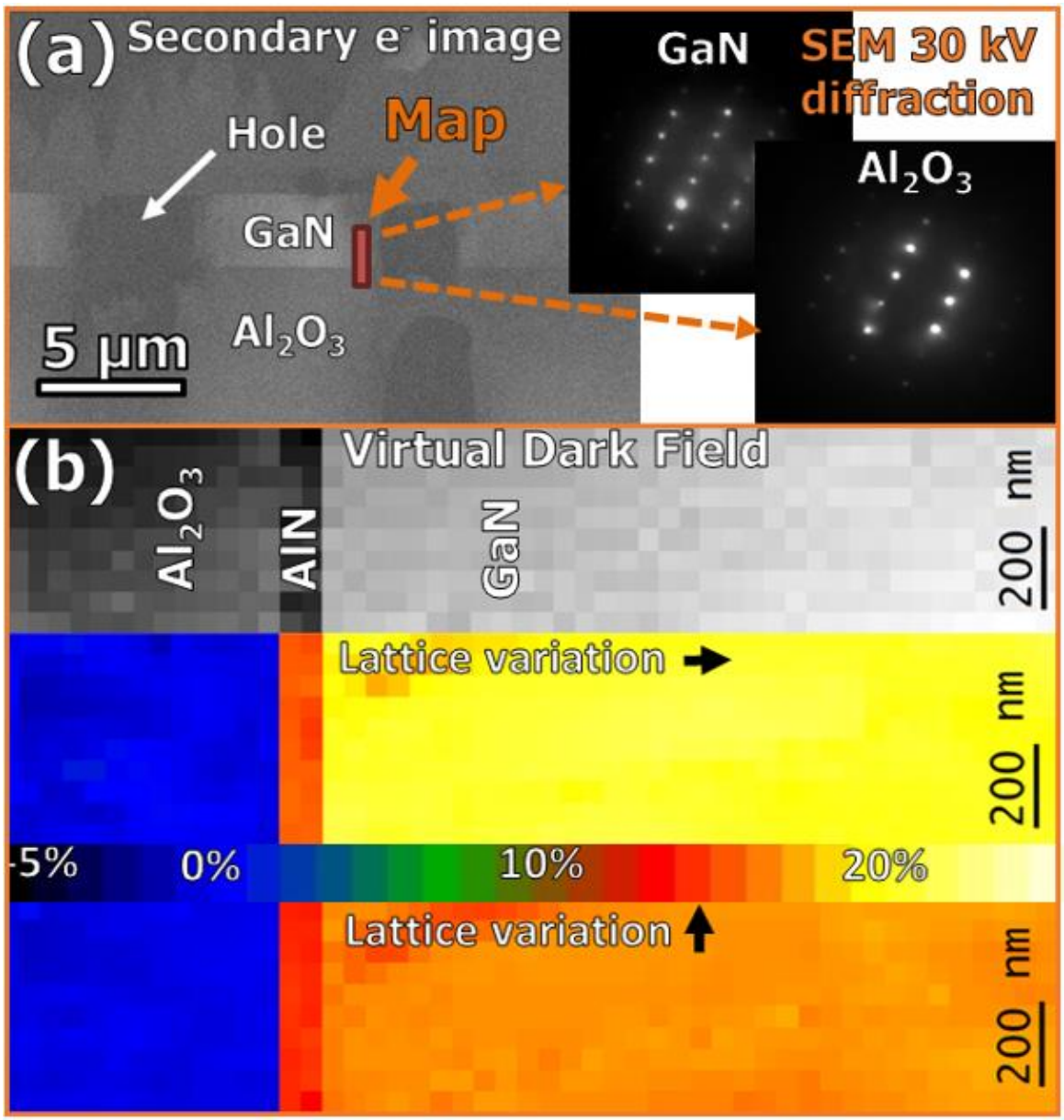
(a)
Secondary e⁻ image
Hole
Map
GaN
Al_2O_3
5 µm
GaN
SEM 30 kV diffraction
Al_2O_3
(b)
Al_2O_3
AlN
GaN
Virtual Dark Field
200 nm
Lattice variation
200 nm
-5%
0%
10%
20%
Lattice variation
200 nm

MS6.P007
Study of tattoo inks with SEM-EDS

M. Sysoltseva[1], R. Winterhalter[1], H. Fromme[1]

[1]Bavarian Health and Food Safety Autority, Department of Chemical Safety and Toxicology, Munich, Germany

Many people worldwide have body tattoos and in the recent time tattooing became even more popular and the number of people with tattoos has considerably increased. During tattooing the tattoo inks are inserted into the dermis. Recent studies have found that part of the tattoo ink migrate in the human body via the lymphatic system. The extent of migration increases with decreasing particle size and is miost important for nanosized pigments. The tattoo inks consist of organic or inorganic pigments and various additives such as water and glycerol. Carbon black is commonly used as black tattoo pigment, while titanium dioxide (TiO_2) is used as white pigment. As colour pigments organic polyaromatic compounds, phthalocyanins and azo compounds are applied in tattoo inks.

In this study five tattoo inks were studied. The tattoo inks were in colour black, pink, purple, blue and green. The inks were studied by means of scanning electron microscopy (SEM) and energy dispersive X-ray spectroscopy (EDS) in order to determine the particle size and their chemical composition. For SEM analysis the tattoo inks were diluted with distilled water 1:1000. For SEM analysis the dispersion of tattoo inks were applied on the Ni-TEM grids and allowed to dry. The use of Ni-grids allows measuring of Cu-containing particles of tattoo inks.

It was found that pigments of black tattoo inks composed of carbon nanoparticles. The size of primary particles was between 30 and 40 nm. The size of formed aggregates was up to 500 nm (Fig.1). The colour tattoo inks were composed of two pigments: first pigment was titanium dioxide and second was an organic pigment (Fig.2). TiO_2 particles were present as agglomerates consisting of primary particles with diameters larger than 100 nm. The organic pigment, for example of the green ink Pigment Green 36 (1,3,8,16,18,24-Hexabromo-2,4,9,10,11,15,17,22,23,25-decachloro-29H,31H-phthalocyoaninato(2-)-N29,N30,N31,N32]copper) could be further characterized by the presence of copper and chlorine in the EDS-spectra. The size of the organic pigment particles ranged between 40 and 400 nm.

In conclusion, all studied tattoo inks contained particles in the nanometre range.

Fig. 1: SEM image of carbon nanoparticles founded in black tattoo ink.

Fig. 2: Titanium dioxide and green pigment particles of green ink

Fig. 1

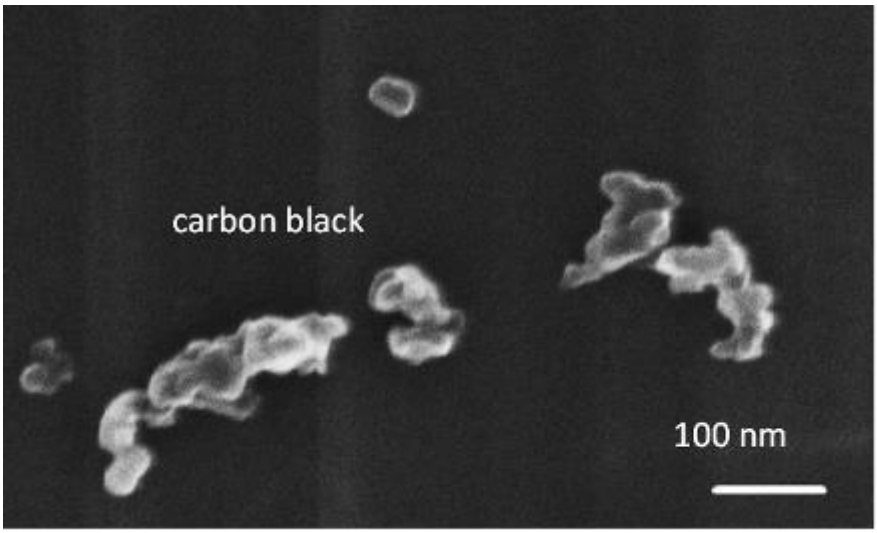

Fig. 2

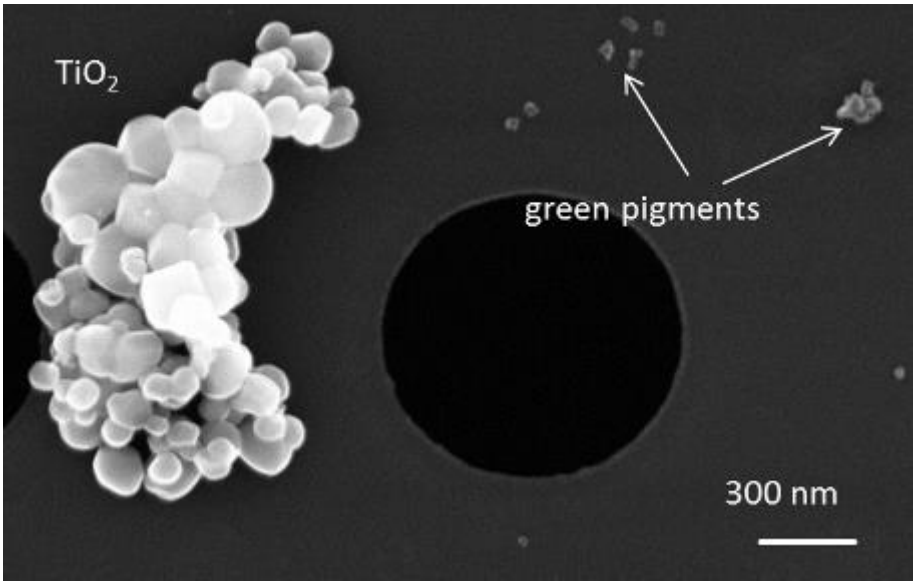

MS6.P008
Synthesis and Analysis of Highly Reactive Sm Nanoparticles

O. Wenzel[1], D. Bartenbach[2], R. Popescu[1], C. Feldmann[2], D. Gerthsen[1]

[1]Karlsruhe Institute of Technology (KIT), Laboratory for Electron Microscopy (LEM), Karlsruhe, Germany
[2]Karlsruhe Institute of Technology (KIT), Institute for Inorganic Chemistry (AOC), Karlsruhe, Germany

The element samarium, as most rare earth elements, is valuable due to its scarcity and its use in a wide range of high-tech applications. As all lanthanides, it is a highly reactive metal, which upon exposure to oxygen reacts immediately to Sm_2O_3 with its favored 3+ oxidation state. These properties relate to the bulk crystalline material. As nanoparticles (NPs), Sm is even more reactive given the increased surface-to-volume ratio. Furthermore, amorphous NPs could have different properties compared to crystalline NPs due to their disordered structure. Up to now, there are next to no studies of crystalline NPs and even less of amorphous NPs of elemental Sm. This lack of data stems primarily from the high reactivity of the Sm^0 with oxygen, which hinders analysis of the material. Therefore, we synthesized amorphous Sm^0 NPs and used electron microscopic techniques to analyze the material properties. Synthesis and sample preparation took place under argon atmosphere with a Schlenk line and in a glove box. A transfer TEM holder protects the volatile material from oxidation.

The amorphous Sm^0 NPs are precipitated under supersaturation conditions. High-resolution and scanning transmission electron microscopy in the high-angle annular dark-field mode (HRTEM, HAADF-STEM) and energy dispersive X-ray spectroscopy (EDXS) were used to determine structure, morphology and chemical composition. Electron energy loss spectroscopy (EELS) with the aid of reference materials was used to determine the oxidation state of the material.

STEM-HAADF images in Fig. 1(a-b) show that the material consists of NP agglomerates with sizes in a narrow range between 1.9-2.5 nm and a median size of 2.1 nm. More details are visible in the HRTEM image Fig. 2(a). The majority of NPs is amorphous as demonstrated in the Fourier-transform (FT) in Fig. 2(c). The first ring in the FT pattern is located at a reciprocal distance of 1/3.09 $Å^{-1}$ and corresponds to the (001) lattice distance of crystalline Sm^0. Some particles, such as the NP marked with a red square, have a hexagonal P63/mmc crystal structure (ICSD 652632) according to FT analysis (cf. Fig. 2(b)), which is expected for Sm. EELS analysis of the amorphous NPs shows that the Sm $M_{4,5}$ edge shares similarities of the near edge structure with the Sm^0 bulk reference material. Further, the O-K edge with the lack of fine-structural features gives very little evidence of oxide compounds. The oxygen concentration is low in the regions of the agglomerated NPs compared to the background of the lacey film und underlines that oxidation was prevented.

This study shows that Sm^0 was successfully synthesized as small amorphous NPs with a narrow size distribution. Notably, the compositional and structure analysis with HRTEM and EELS, as well as EDXS, shows that the sample was effectively protected from any contact with air, which was one of the major hurdles of this study.

Fig. 1

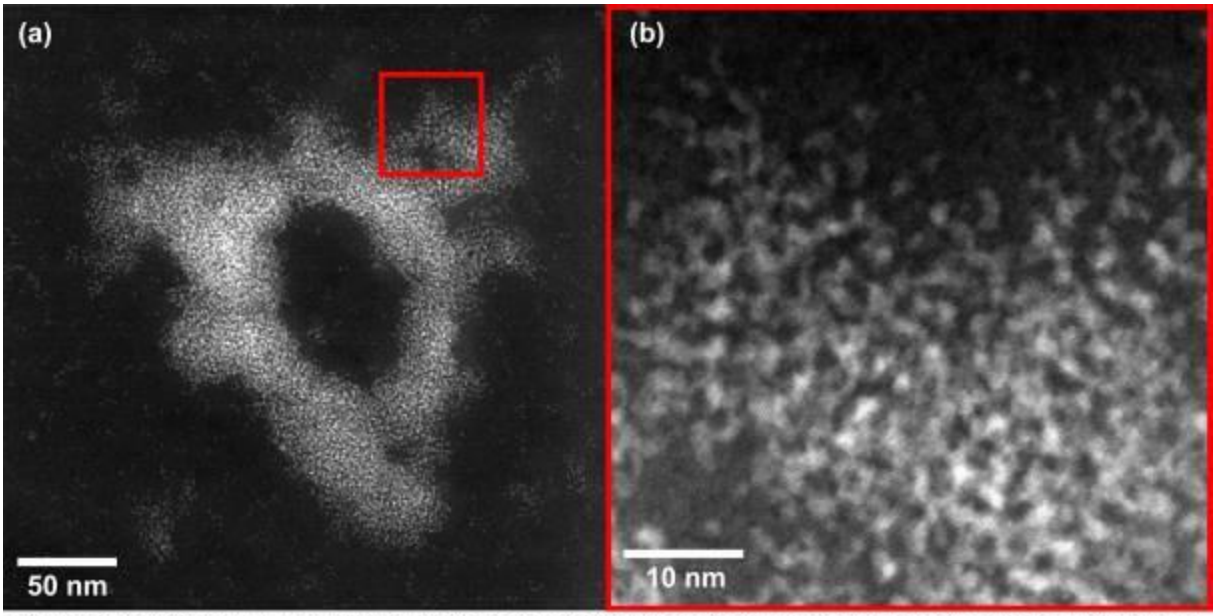

Figure 1 (a) Overview HAADF-STEM image and **(b)** magnified image of the region in the red square.

Fig. 2

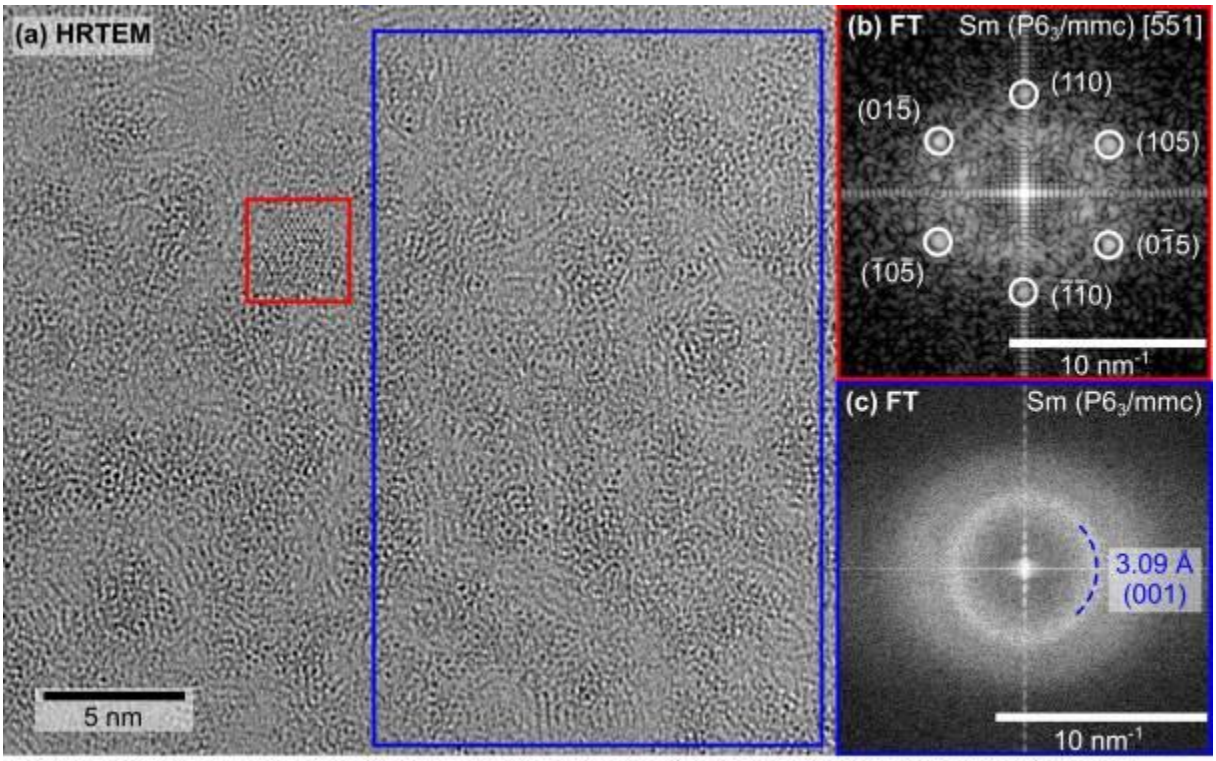

Figure 2 (a) HRTEM image with **(b)** FT of crystallite marked in **(a)** with red square and **(c)** FT of amorphous particles.

MS6.P009
Correlation between photophysical and structural properties of the core/shell structure of indium phosphide-based quantum dots

K. Mader[1], I. Häusler[1], K. D. Wegner[2], U. Resch-Genger[2], M. Lehmann[1]

[1]Technische Universität Berlin, Institut für Optik und Atomare Physik, Berlin, Germany
[2]Federal Institute for Materials Research and Testing (BAM), Division Biophotonics, Berlin, Germany

The unique optoelectronic properties of semiconductor nanocrystals also known as quantum dots (QDs) made them to a well-established class of nanomaterials with a wide application range. Although the most popular element for the synthesis of QDs is Cadmium, the strict EU regulations concerning their use of Cd-containing materials in electrical and opto-electronic devices limits the commercial use. This has drawn the interest to alternative Cd-free materials with reduced toxicity but comparable photophysical properties. The most promising candidates are indium phosphide-based (InP) QDs. InP QDs with a bulk band gap of 1.35 eV and an exciton Bohr radius of about 10 nm allow tuning the photoluminescence (PL) emission from the visible to the near-infrared. A prerequisite for high PL quantum yields (QYs) and enhanced photostability, is the passivation of the InP QD core with a shell of a large band gap semiconductor. Although ZnS is the most popular shell material, the large lattice mismatch of 7.7% between zinc blende InP and ZnS is challenging for the realization of a thick shell and thus high-quality optical properties. ZnSe has a lower lattice mismatch with the InP core (3.3%) and was already used successfully as a lattice adapter between the InP core and a ZnS outer shell.

In this contribution, we report on the influence of different thicknesses of the intermediate ZnSe shell on the structural and photophysical properties of InP/ZnSe/ZnS core/shell/shell systems. The synthesis of the InP core was performed using an established method based on indium halides and tris(diethylamino)phosphine as phosphorous precursor. The shells were grown layer by layer using zinc carboxylates and either selenium or sulfur in order to prepare the ZnSe or ZnS shell, respectively. Then, the QDs were characterized regarding their photophysical properties using absorbance, stationary, and time-resolved PL measurements. Their structural properties were analyzed using TEM. Their element distribution maps were generated and evaluated using EDX and EFTEM. The gained data was used to correlate the photophysical and the structural properties.

The successful preparation of a set of InP/ZnSe/ZnS multishell systems with varied ZnSe shell thickness was confirmed by absorption and TEM measurements (Fig 1). The strong absorption increase below 450 nm is assigned to the changes in ZnSe thickness. The increasing QD size obtained from TEM confirms this assumption. Ensemble and single-particle PL measurements further reveal improved photophysical properties with increasing ZnSe shell thickness. Particularly important for the study was the characterization with HRTEM, EDX and EFTEM techniques to decipher the position of the InP core within the QD and how shape, lattice parameter, and overall size that all influence the optical properties of these QDs.

In summary, our study shows that the correlation between structural and photophysical properties provides unique insights in core/shell heterostructures. The interplay between structural and photophysical analysis provides the rational basis to improve and fine-tune nanomaterial syntheses and contributes e.g. to a better understanding of the shell growth mechanism. This will pave the way for the development of core/shell heterostructures with increased chemical and photostability.

Fig. 1: Absorption spectra (**a**) and TEM measurements incl. size analysis (**b**) of InP/ZnSe/ZnS with different thicknesses of ZnSe intermediate shell

Fig. 1

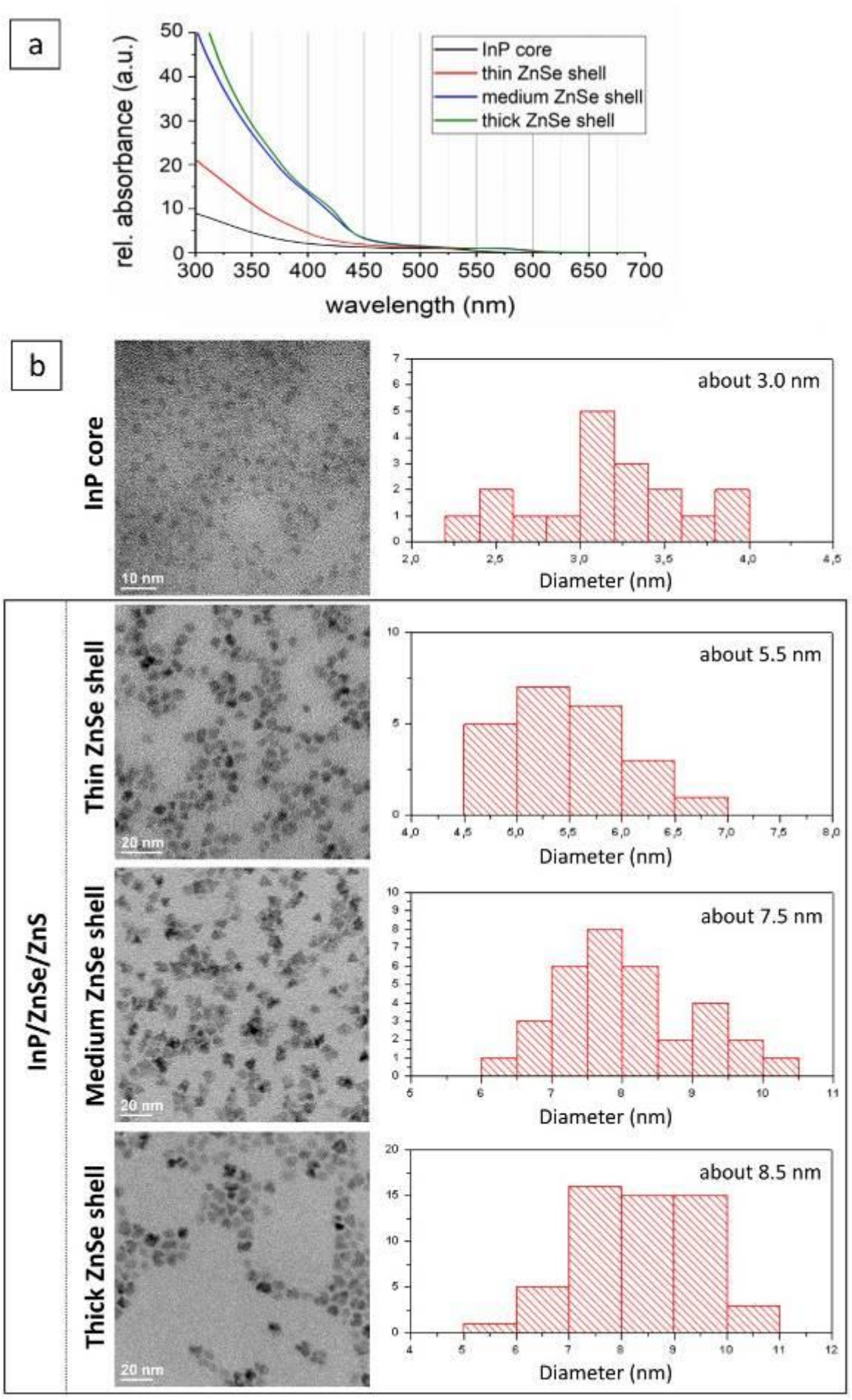
a
rel. absorbance (a.u.)
wavelength (nm)
InP core
thin ZnSe shell
medium ZnSe shell
thick ZnSe shell
b
InP core
10 nm
about 3.0 nm
Diameter (nm)
InP/ZnSe/ZnS
Thin ZnSe shell
20 nm
about 5.5 nm
Diameter (nm)
Medium ZnSe shell
20 nm
about 7.5 nm
Diameter (nm)
Thick ZnSe shell
20 nm
about 8.5 nm
Diameter (nm)

MS6.P010
Structure and chemical composition of triple-shell upconverting nanocrystals by TEM

R. Popescu[1], D. Hudry[2], B. S. Richards[2], D. Gerthsen[1]

[1] Karlsruher Instituts für Technologie (KIT), Laboratorium für Elektronenmikroskopie (LEM), Karlsruhe, Germany
[2] Karlsruhe Institute of Technology (KIT), Institute of Microstructure Technology (IMT), Karlsruhe, Germany

Increasing the variety of emission spectra from lanthanide-doped upconverting nanocrystals (UCNCs) is of major technological interest in the field of photonic markers. Over the past decade, significant progress was made in color-tuning by using multi-shell structures. In this context, detailed investigations on the chemical organization and crystal structure of such architectures are necessary to better understand the structure–property relationships. Indeed, the energy migration pathways that control the optical properties of multi-shell UCNCs depend on the chemical and structural order.

In this work, triple-shell (CS3) UCNCs are investigated (cf. schemes in Fig. 1 g-i). The same singly-doped NaGdF4:Er core NCs are used as starting seeds for the growth of all $CS3_x$ (x=I, II, or III) UCNCs by the controlled hot injection method (1). All synthesis parameters are kept constant except for the relative Yb content of the first inner shell that was increased from $CS3_I$ to $CS3_{III}$. Samples for transmission electron microscopy (TEM) are prepared by drop-casting a diluted colloidal suspension of UCNCs onto an amorphous carbon film. Structural and chemical analyses of as-prepared UCNCs are carried out with a FEI Titan^3 80-300 and a FEI Osiris ChemiSTEM by high-resolution (HR) TEM and high-angle annular dark-field scanning TEM (HAADF-STEM) combined with energy-dispersive X-ray spectroscopy (EDXS). The local chemical composition of the triple-shell NCs was reconstructed from EDXS spectra by using an iterative algorithm (2).

HAADF-STEM images (Fig. 1 a-c) show the formation of quasi-spherical NCs. All $CS3_x$ NCs are larger than the starting seeds (mean diameter of 4.9±1.5 nm) with mean diameters of 12.4±4.2 nm ($CS3_I$), 14.8±2.1 nm ($CS3_{II}$) and 18.9±5.1 nm ($CS3_{III}$). HRTEM supports the formation of single domain UCNCs with a hexagonal structure (P-6, 174). Despite the formation of diffuse interfaces, the core and shells of $CS3_x$ NCs can be defined based on their EDXS concentration profiles (Fig. 1 d-f) and the following considerations. Firstly, the core is defined as the region that mainly contains Gd and Er, like the initial seeds, and has a similar size (C in Fig. 1 g-i). Interestingly, the degree of Yb intermixing within the core increases from $CS3_I$ to $CS3_{III}$. Not only Yb diffuses more deeply into the core region but its local concentration increases too. Secondly, the first inner shell (1-st IS) contains Yb with increasing local concentration from $CS3_I$ to $CS3_{III}$, but also Gd from the 2-nd IS (Tm does not seem to diffuse) and Gd/Er from C (1-st IS in Fig. 1 g-i). Thirdly, the 2-nd IS comprises the whole region containing Tm (2-nd IS in Fig. 1 g-i). We also observe an increasing Yb concentration for $CS3_I$ to $CS3_{III}$ and a slight thickness increase from 2 nm to 3 nm. Finally, the outer shell (OS) with a thickness of ~1 nm for all CS3 NCs only contains Y (OS in Fig. 1 g-i). The emission spectra can be well correlated with the lanthanide distribution in the shells. Whereas the Er (red) emission is the most intense for $CS3_I$, this trend reverses for $CS3_{II}$ and $CS3_{III}$, where the Tm (blue) emission dominates.

In conclusion, we demonstrate the close relation between the structure and emission spectra of core/triple-shell UCNCs, which provides an efficient tool for color tuning in sub-20 nm UCNC photonic markers.

References:

(1) D. Hudry et al., J Mater Chem C, 7, 1164 (2019)

(2) D. Hudry et al., Adv. Mater 2019, in press, adma201900623

Fig. 1

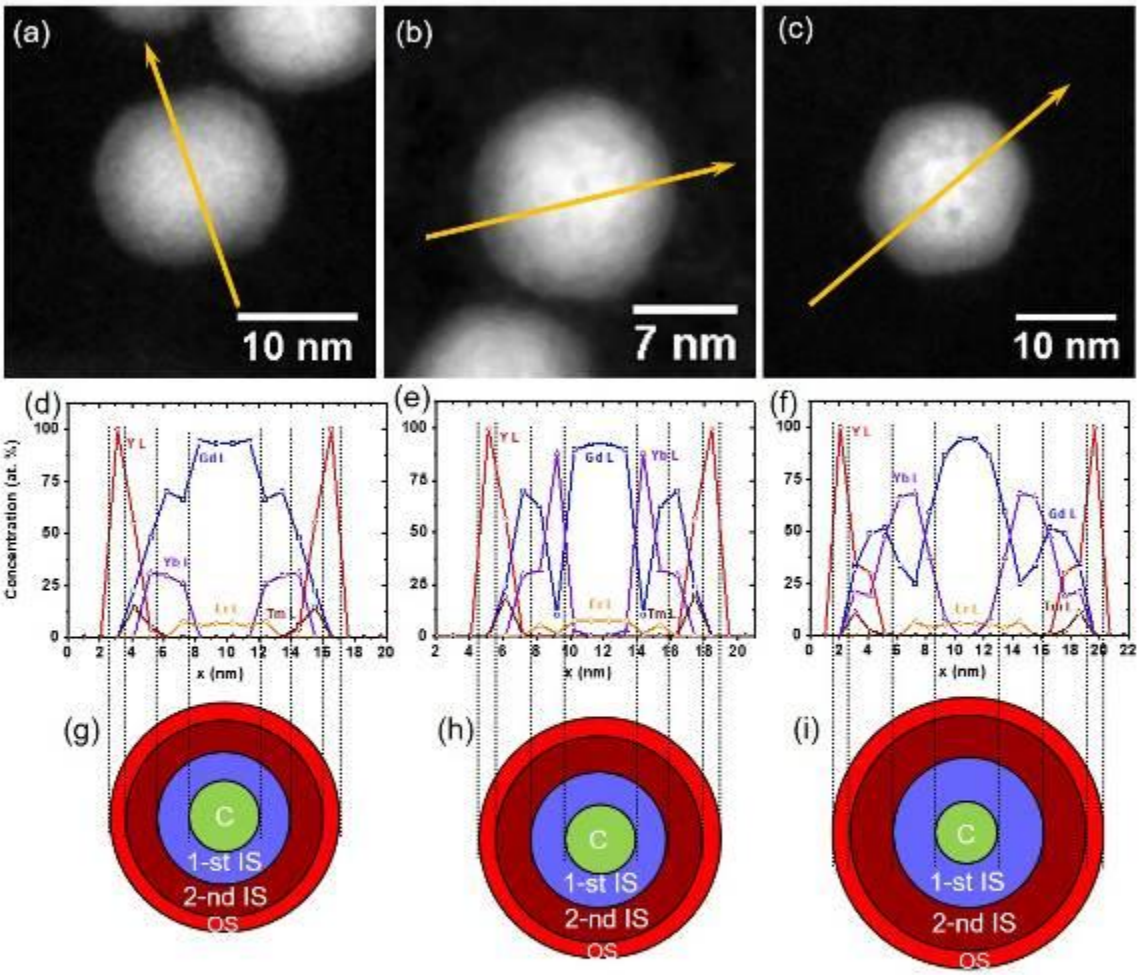

Figure 1. *HAADF-STEM images with yellow arrows indicating the energy dispersive X-ray spectroscopy (EDXS) scan directions of individual (a) $CS3_i$, (b) $CS3_{ii}$ and (c) $CS3_{iii}$ UCNCs. Corresponding structure-independent concentration profiles of individual (d) $CS3_i$, (e) $CS3_{ii}$ and (f) $CS3_{iii}$ UCNCs. Schematic representation showing the experimentally determined chemical compositions of various regions of (g) $CS3_i$, (h) $CS3_{ii}$ (i) and $CS3_{iii}$ UCNCs. Here, C: core; 1-st IS: 1-st inner shell; 2-nd IS: 2-nd inner shell; OS: outer shell.*

MS6.P012
Development of a method for measuring the flexural rigidity of nanofibres

R. Fortini[1], H. Sturm[1], D. Kehren[2], A. Meyer-Plath[2]

[1]Bundesanstalt für Materialforschung und -prüfung, Nanotribology and Nanostructuring of Surfaces, Berlin, Germany
[2]Bundesanstalt für Arbeitsschutz und Arbeitsmedizin, Berlin, Germany

Toxicological studies have shown that some types of carbon nanotubes may provoke asbestos-like effects including chronic inflammation and lung cancer. Inhaled carbon nanotubes may reach the deep lung tissue. Alveolar macrophages are responsible to remove such foreign objects from the alveoli in a process called phagocytosis. If a macrophage fails to uptake a nanotube completely, cell lesions may give rise to inflammation. It is currently assumed that short, flexible and long as well as granularly agglomerated (tangled) nanofibres are clearable by macrophages, whereas biodurable long and rigid nanotubes may persist in lung tissue. The flexural rigidity of nanofibres is therefore believed to be an important material property that governs fibre toxicity and needs to be investigated. The present work aims at determining the rigidity of nanofibres by detecting their resonance frequencies using a Dynamic Scanning Electron Microscope (DySEM) setup. By depositing and fixing a nanofibre to an oscillating support, it can be excited to vibrations and treated as a cantilevered beam. This way, its elastic modulus can be determined via Euler-Bernoulli"s beam theory. Multi-walled carbon nanotubes (MWCNTs) were deposited on high frequency piezoelectric quartz crystals mounted on a scanning electron microscope (SEM) holder. When introduced into the SEM chamber and connected to a frequency-sweeping waveform generator, the quartz crystal actuates the deposited fibre. A lock-in amplified processes the secondary electron detector signal resulting from the electron beam modulated by the vibrating nanofibre. Whenever a fibre resonance is detected, the SEM image of the fibre is stored to identify the fibre oscillation mode. The found resonance frequencies and modes allow determining the elastic modulus accordingly. Since the frequency spacing of resonances is predicted by Euler-Bernoulli, the mode number can be identified and elastic modulus values be averaged. A significant number of individual MWCNTs were classified according to their level of rigidity. The applicability and reliability of the method will be discussed.

Fig. 1: DySEM image of a MWCNT 7.4 µm long with no frequency input (left), in the fundamental mode at 750 KHz (center) and in the first harmonics at 4.750 MHz (right).

Fig. 1

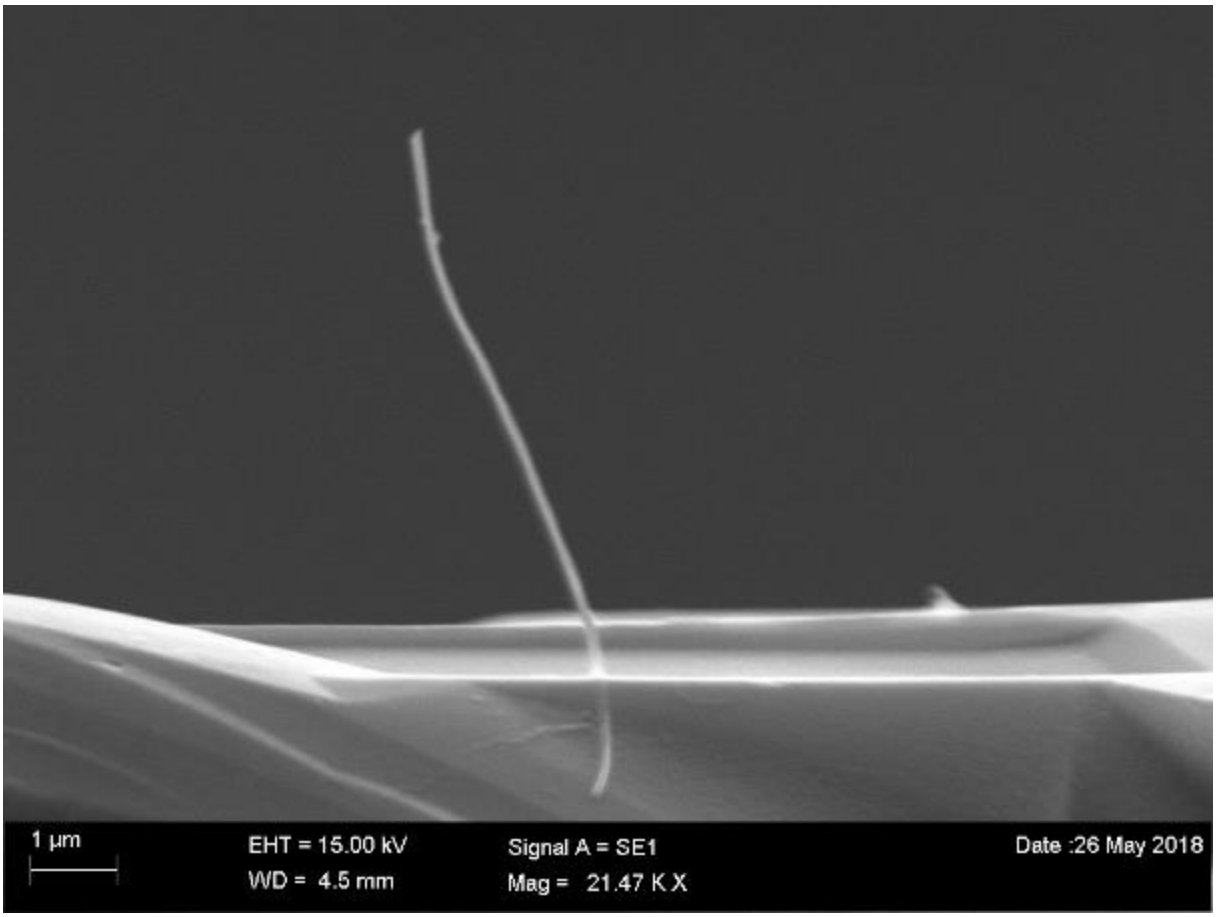

Fig. 2

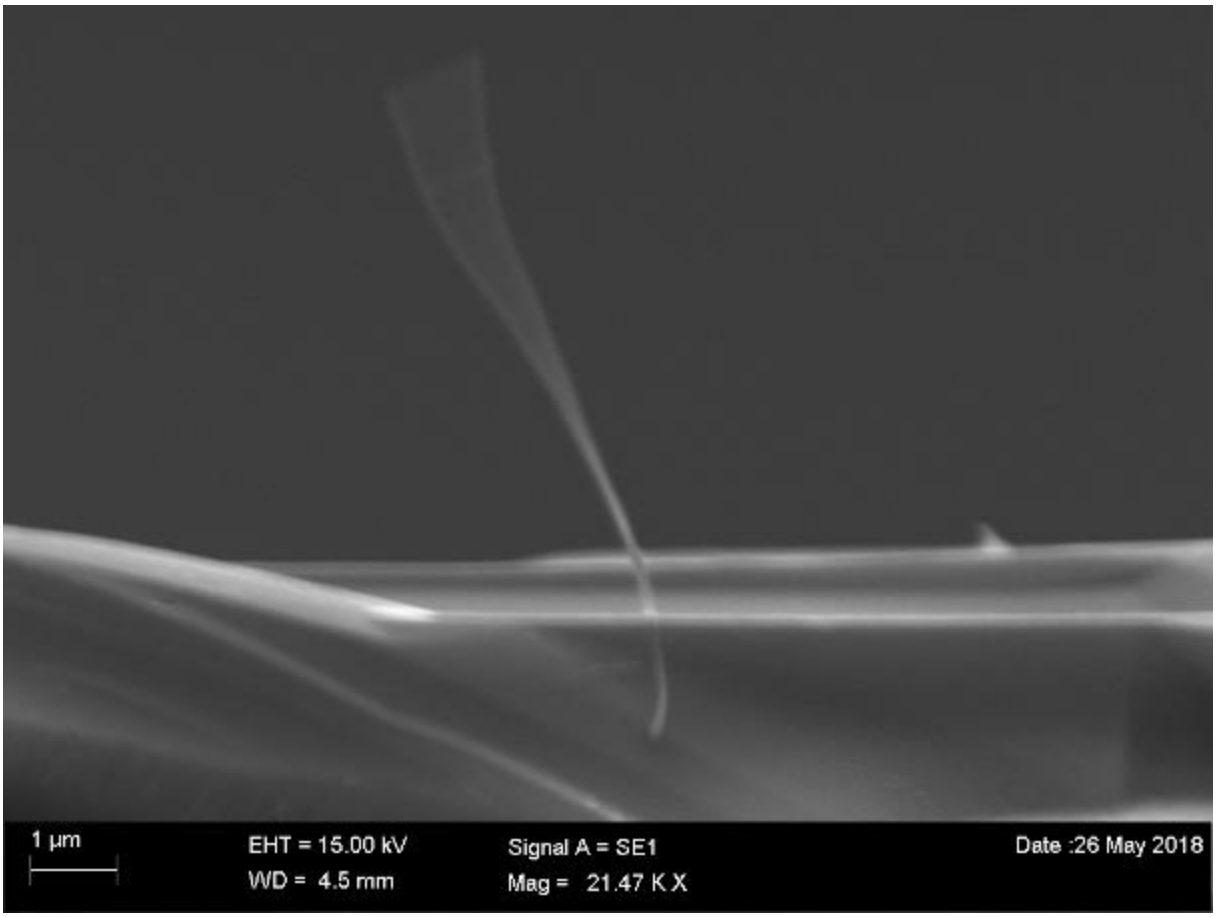
1 µm
EHT = 15.00 kV
WD = 4.5 mm
Signal A = SE1
Mag = 21.47 K X
Date :26 May 2018

Fig. 3

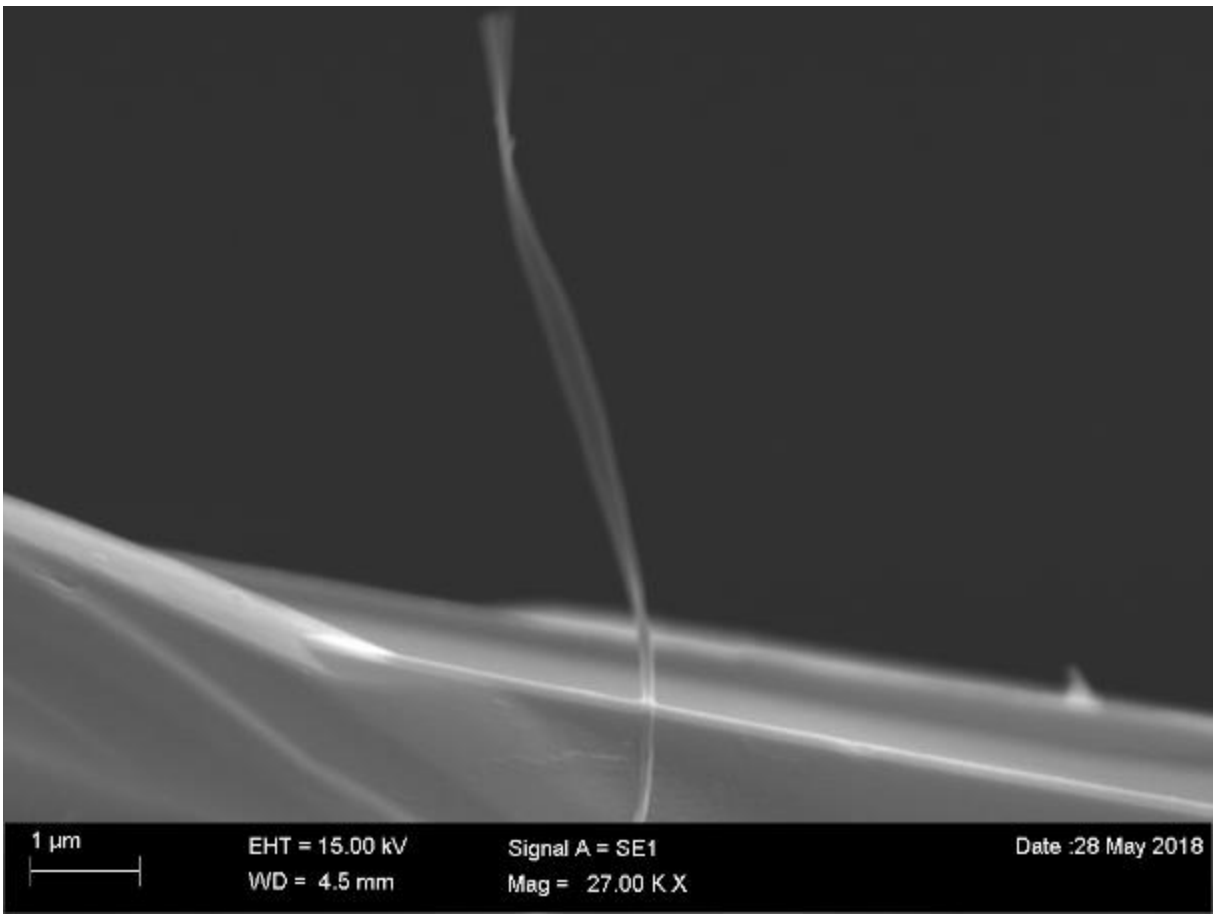
1 µm
EHT = 15.00 kV
WD = 4.5 mm
Signal A = SE1
Mag = 27.00 K X
Date :28 May 2018

MS6.P013
Towards automated manipulation of substitutional heteroatoms in graphene using electron irradiation

A. Postl[1,2], J. Madsen[2], M. Tripathi[2], K. Mustonen[2], A. Chirita[2], A. Markevich[2], J. Kotakoski[2], T. Susi[2]

[1]University of Vienna, VDS Physics, Boltzmanngasse 5, Vienna, Austria
[2]University of Vienna, Faculty of Physics, Boltzmanngasse 5, Vienna, Austria

Scanning transmission electron microscopy (STEM) has emerged as a new tool for the direct assembly of nanostructures due to the ability to alter the position of single atoms with the help of its Ångström-sized focused electron beam. In contrast to scanning probe microscopies, due to the greater interaction energy scale, any configurations assembled in STEM will remain stable at room temperature.
Rearrangements in the atomic structure can be induced if the kinetic energy that can be transferred to a single atom by an energetic probe electron is comparable to the strength of covalent bonds in the material (1). Recent experiments have demonstrated excellent atomically precise control over Si heteroatoms in the graphene (2) and single-walled carbon nanotube (3) lattices. Other potential manipulation targets include B and N (4), and P and Al (5), although currently these appear to be more challenging.
To open the full range of future possibilities for this method, the reliable preparation of clean samples (6), rapid image recognition (7), and the development of software for automated microscope control are required. Enabling automated manipulation requires accurate knowledge of the positions of the atoms in real time. We take advantage of recent advances in deep learning to build a robust method for detecting the position and species of individual atoms in noisy images (7). Our implementation of the method provides readily interpretable feedback in real time from which the human operator, or eventually our autonomous control program, can adjust the microscope in response. In addition, accurate measurement of our STEM instrumental characteristics including scan distortions and probe shape will help evaluate the precision of detected atom positions as well as offer more precise dose estimates for the further development of atomistic models of the dynamics (8).
We will present the latest steps on our way to the atomically precise fabrication of two-dimensional nanostructures from multiple substitutional heteroatoms, including a "probe inspector" module for the Nion Swift software that uses measured aberrations, image contrast and quantitative image simulations (9) to accurately determine the size and intensity distribution of the electron probe.

References:

(1) Susi, T., et al., Physical Review Letters 113.11 (2014): 115501.

(2) Tripathi, M., et al., Nano Letters 18.8 (2018): 5319-5323.

(3) Mustonen, K., et al., arXiv: 1902.03972 (2019).

(4) Susi, T., et al., 2D Materials 4.4 (2017): 042004.

(5) Cong, S., et al., Science Advances, accepted; arXiv:1803.01369 (2019).

(6) Tripathi, M., et al., Physica Status Solidi RRL 11.8 (2017): 1700124.

(7) Madsen, J., et al., Advanced Theory and Simulations 1.8 (2018): 1800037.

(8) Chirita, A., et al., arXiv:1811.04011 (2018).

(9) Susi, T., et al., Ultramicroscopy 197 (2019): 16-22.

Funding by the European Research Council (ERC) Grant No. 756277-ATMEN and the Vienna Doctoral School in Physics is gratefully acknowledged.

MS6.P014
Topography and strain at freely suspended WSe_2-monolayers

J. Sickel[1,2], M. Asbach[1,2], R. Schneider[1], R. Bratschitsch[1], H. Kohl[1,2]

[1]Universität Münster, Physikalisches Institut, Muenster, Germany
[2]Universität Münster, Interdisziplinäres Centrum für Elektronenmikroskopie und Mikroanalyse (ICEM), Muenster, Germany

Freely suspended 2D materials such as graphene (1) and MoS_2 (2) exhibit ripples, as has been demonstrated by selected area diffraction (SAED). If tensile strain is applied to the monolayer, a preferred orientation of these ripples along the pulling direction and a change in corrugation occurs (3). Indeed both topography and strain affect the mechanical properties of 2D materials but they also influence optical properties, such as single photon emission (4).

In this work, we investigate the topography and strain of freely suspended WSe_2 monolayers. The WSe_2 monolayers were mechanically exfoliated and transferred onto a silicon nitride grid using a polydimethylsiloxane (PDMS) pad as support. The fabrication induces considerable strain in the monolayer and sometimes even leads to folds. Additionally adhesive residuals also impact the stability and strain distribution. Geometrical phase analysis (GPA) of high-resolution images at folds indicates a strain distribution which is influenced by the polymer residuals. Due to the need of atomic resolution for this type of analysis, the investigated area is less than 250nm × 250nm.

With the help of tilted SAED images we confirmed the ripple structure of the WSe_2 monolayer. It is even possible to pin down different regions around a fold with different orientations of the ripple structure. The spatial precision of this technique is limited by the spherical aberration of the objective lens and the size of the SAED aperture. In regions near folds the spots of the tilted diffraction pattern tend to become elongated. This elongated shape is related to a corrugation of the ripples which are aligned towards the fold. This preferred orientation of the ripples is less prominent at larger distances to the fold. This is an indication of a strain field gradually decaying with increasing distance from the fold.

In conclusion, a combination of HRTEM and tilted SAED pattern permits to characterize the strain and topography of freely suspended monolayers on the atomic scale up to the micrometer range. It also allows to investigate the influence of local changes of the topography which accrue close to folds.

References:

(1) Meyer, J. C., et al. "The structure of suspended graphene sheets" *Nature* 446, 60-63 (2007).

(2) Brivio, J., et al. "Ripples and layers in ultrathin MoS_2 membranes" *Nano Letters* 11, 5148-5153 (2011).

(3) Ludacka, U., et al. "In situ control of graphene ripples and strain in the electron microscope" *npj 2D Materials and Applications* 2, 25 (2018).

(4) Kern, J., et al. "Nanoscale positioning of single-photon emitters in atomically thin WSe_2" *Advanced Materials* 28, 7101-7105 (2016).

MS6.P015
Advances in Polymer-based TEM Specimen Preparation for Two-Dimensional Materials

J. Köster[1], B. Liang[1], U. Kaiser[1]

[1]Electron Microscopy Group of Materials Science, Ulm University, Ulm, Germany

Two-dimensional (2D) materials and their heterostructures are interesting, because they offer a wide field of new applications (1) based on their exciting physical and chemical properties, for instance magnetic behaviour (2), electric conductivity (3), and charge density waves occurrence (4).

Aberration-corrected transmission electron microscopy (TEM) offers the possibility for analysing freestanding single layers on the scale of the single atom. Thus, it is intuitively understandable that TEM sample preparation is an extremely crucial part for defining the achievable resolution in the image. A commonly used sample preparation method for freestanding 2D materials is the scotch tape method, a wet-etching method with potassium hydroxide (KOH) solution (5). For oxidation sensitive materials, such as Transition Metal Phosphorus Trisulfide (TMPT) and the semimetal transition metal dichalcogenides (TMDs), we found that the method causes a crucial degradation in the thin layers, presumably caused by oxidation.

Therefore, we present a preparation method excluding the wet-chemical etching with KOH, found to be the main factor for oxidation enhancement. On the example of $MnPS_3$ and $FePS_3$ thin layers, we were able to demonstrate a gentle way to enhance the quality of the 2D -TEM samples. Polymer coating (PMMA and PVA) of Si/SiO2 substrates enabled the avoidance of KOH, (see fig. 1). SEM and TEM experiments were performed to demonstrate the improvement in sample quality.

To conclude, thin layers of $FePS_3$, $MnPS_3$, $TiSe_2$, MoS_2, graphene, TaS_2, and TaS_3 were successfully prepared by the polymer assisted methods. Spinning PVA and PMMA on Si/SiO_2 substrates and transferring the material flakes to TEM grids. The crystallinity of the oxygen sensitive materials was better preserved in comparison to the former applied KOH method.

References:

(1) Sun, Zhipei, Amos Martinez, and Feng Wang. "Optical modulators with 2D layered materials." *Nature Photonics*4 (2016): 227.

(2) Wildes, A. R., et al. "Static and dynamic critical properties of the quasi-two-dimensional antiferromagnet MnPS 3." *Physical Review B*9 (2006): 094422.

(3) Worsley, Marcus A., et al. "Synthesis of graphene aerogel with high electrical conductivity." *Journal of the American Chemical Society*40 (2010): 14067-14069.

(4) Neto, AH Castro. "Charge density wave, superconductivity, and anomalous metallic behavior in 2D transition metal dichalcogenides." *Physical review letters*19 (2001): 4382.

(5) Meyer, Jannik C., et al. "Hydrocarbon lithography on graphene membranes." *Applied Physics Letters*12 (2008): 123110.

Fig. 1: The basic preparation steps for the polymer assisted preparation method. In a), scotch tape with material flakes on top are pressed on the polymer coated Si/SiO_2 wafer. After removing the tape, material flakes are deposited on the polymer layer, the TEM grid was brought into contact with the material flakes by using isopropyl alcohol. After dissolving the polyvinyl alcohol (PVA) or poly (methyl/methacrylate) PMMA layer with water or anisole/acetone, respectively, the grid with material flakes is remaining (c).

Fig. 1

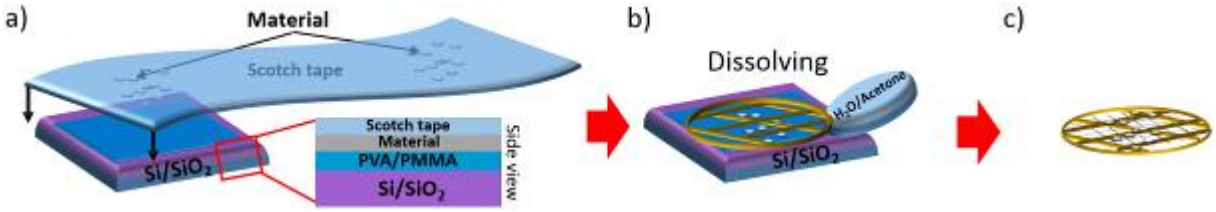
a)
Material
Scotch tape
Si/SiO2
Scotch tape
Material
PVA/PMMA
Si/SiO2
Side view
b)
Dissolving
H2O/Acetone
Si/SiO2
c)

MS6.P016
Defect formation and evolution in single-layer WSe2 – life of atoms under 80kV electron irradiation

R. Leiter[1], Y. Li[1], U. Kaiser[1]

[1]Universität Ulm, AG Materialwissenschaftliche Elektronenmikroskopie, Ulm, Germany

Transition metal dichalcogenides (TMDs), such as MoS2 and WSe2, have received increasing attention in recent years. This is due to the fact that they possess a layered structure and can be exfoliated down to monolayers. These 2D crystals have distinct mechanical, electrical and magnetic properties and are suitable for a whole range of electronic and optoelectronic applications.(1) Lattice defects in these 2D monolayers can magnificently alter these properties, attracting more and more research interests.(2) Understanding how to introduce certain defects in a controlled manner will be crucial for future applications.

In this work, we investigate the formation and evolution of lattice defects in single-layer tungsten diselenide (WSe_2) under 80kV electron irradiation at the atomic scale.

To this end, we use the novel Cc- and Cs-corrected SALVE (Sub Ångström Low Voltage Electron microscope) instrument operated at electron acceleration voltage of 80 kV. The instrument is corrected for axial geometric aberrations up to the fifth order, off-axial geometric aberrations up to the third order and chromatic aberrations in the first order and reaches a resolution of 0.76 Å in a large field of view in a single-exposure image, necessary to capture many defect formation processes.(3) We use the QSTEM software package to perform image simulation aimed at a quantitative match with the experimental HRTEM images.

Our results show the whole life of WSe_2 single layers under electron irradiation. The defect formation starts with point defects, as selenium atoms are ejected from the lattice. These single and double vacancies are shown to be highly mobile and can add up to more complex structures like trefoil defects whose formation is observed to be more complex than previously suggested from theoretical calculations.(4) With increasing electron dose, line defects begin to form and eventually extended two-dimensional defects form. These larger defects appear in the form of inversion domains, which are limited by several types of mirror twin boundaries (MTBs), previously reported to possess interesting electrical and magnetic properties.[4] In addition, we have observed MTBs that were previously unreported for tungsten diselenide as well as a completely new type of boundary, not reported in any TMD so far. Towards the end, holes begin to form in the film. We also show that tungsten atoms remain in the lattice until a very late stage, when the local selenium concentration is reduced to about 50%.

In conclusion, we have shown the formation and evolution of different types of defects at the atomic scale over the whole lifespan of the WSe_2 single layer, showing different stages after defined electron dose. This may help in future to tailor heterostructure devices composed of defined defect-controlled TMD monolayers with specific properties.

References:

(1) Radisavljevic, B. et al. *Nat. Nanotechnol.* (2011).

(2) Komsa, H.-P. & Krasheninnikov, A. V.. *Adv. Electron. Mater.* **3,** 1600468 (2017).

(3) Linck, M. et al. *Phys. Rev. Lett.* (2016).

(4) Lin, Y. C. et al. *Nat. Commun.* **6,** 1–6 (2015).

Fig. 1: Aberration-corrected HRTEM image of a WSe_2 single layer showing a variety of beam induced defect structures at atomic resolution. Trefoil defect (a), a line defect (b) and a small inversion domain (c) are highlighted.

Fig. 1

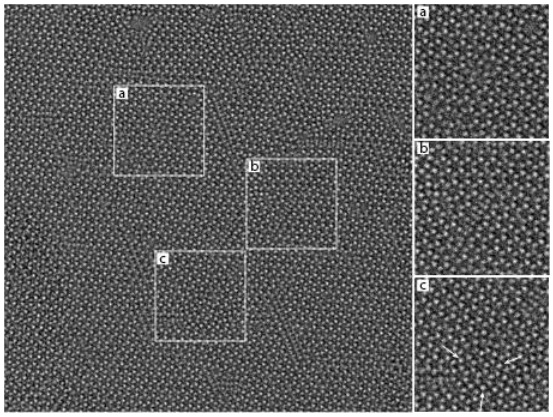

MS6.P017

Correlative *in situ* microscopy of highly directional nanowires grown from MoS2 flakes – structure and functional properties

L. Vogl[1], P. Schweizer[1], M. Wu[1], E. Spiecker[1]

[1]Friedrich-Alexander University Erlangen-Nuremberg, Institue of Micro-and Nanostructure Research, Erlangen, Germany

Molybdenum based nanowires are very promising for many technical applications, ranging from energy storage to micromechanics. However, the controlled synthesis of metal oxide nanowires remains challenging. In this work we present a novel approach to synthesize molybdenum dioxide (MoO2) nanowires directly from Molybdenum Disulfide (MoS2) *in situ*, using microscopy as a direct feedback-mechanism enabling parameter optimization as well as the analysis of growth kinetics and the functional properties. The interlink between structural aspects and the outstanding functional properties make MoO2 Nanowires a promising building block for future Nanodevices.

The Nanowire Synthesis is carried out in an *in situ* Light Microscopy heating chamber under controlled oxygen atmosphere (see figure 1a). This allows us to directly measure the growth rate using digital image correlation and to see the characteristic growth angle of 60 ° between two wires, reflecting the 6-fold symmetry of the MoS2 flake (inset figure 1a). Figure 1b shows growth rates of nanowires grown at different temperatures and classification of different growth regimes. In the temperature range between 650 °C and 710 °C the growth rate shows an exponential dependence on the temperature with an activation energy of 596 kJ/mol, according to the Arrhenius equation.

Correlative Electron Microscopy and Spectroscopy is used to characterize the crystal structure and growth direction as well as to analyze the chemical composition of the wires. Figure 1c shows a BF-STEM overview of a processed MoS2 flake with several nanowires growing out of the side and figure 1d shows a correlative SEM image of a processed flake. The nanowire thickness ranges from 50-250 nm with a length of up to several tens of micrometers. The cross-section of a nanowire shows the crystal structure of MoO2 in high resolution as shown in figure 1e. To confirm the result, EELS measurements and Diffraction Analysis are performed.

In Addition to the analysis of the growth behavior of the nanowires, the functional properties are elucidated. To determine the electrical properties *in situ* four probe measurement in an SEM are performed on the micro-scale (see figure 2a and b). With the estimated wire length and cross-section the resistivity was determined, which puts the wires right into the spectrum of metallic conductors. Additionally, intergrowing Nanowires are measured. Remarkably, there is almost no difference in the resistivity between the single wire and the wire junction. This indicates that wire intergrowth produces interfaces with high structural quality. Next to the electrical properties, field emission experiments have been performed *in situ* in a TEM using a STM Holder and Differential Phase Contrast imaging (see Figure 2c and d), to determine the local field strength at the MoO2 nanowire tip.

To test the mechanical properties *in situ* bending tests are done to evaluate the mechanical properties of the nanowires (see Figure 2e and f). The Young`s modulus of the wire is calculated to 383 GPa from the Force-Displacement Curves. This result was verified by *in situ* resonance measurements (see figure 2g and h) with a calculation of Young`s Modulus according to the simple beam theory.

Besides the outstanding electrical and mechanical properties, nanostructured MoO2 is also a promising candidate for next generation Ion Batteries. Currently, *in situ* TEM studies on the potassium intercalation process are done.

Fig. 1

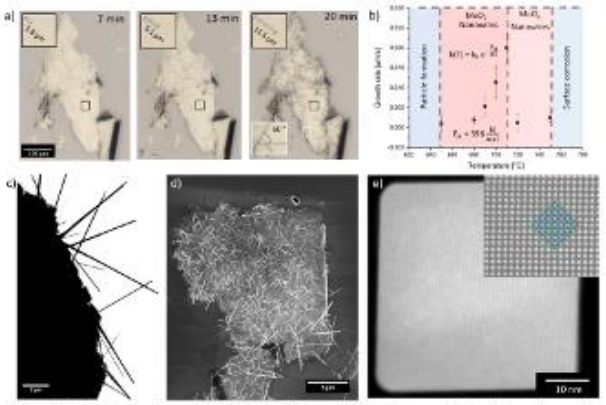

Figure 1: a) Evaluation of nanowire growth based on in situ Light Microscopy b) Growth rates of nanowires grown at different temperatures and classification of different growth regimes c) BF-STEM overview of a processed MoS_2 flake d) Correlative SEM image e) STEM image of a nanowire showing the crystal structure of MoO_2 in high resolution (inset).

Fig. 2

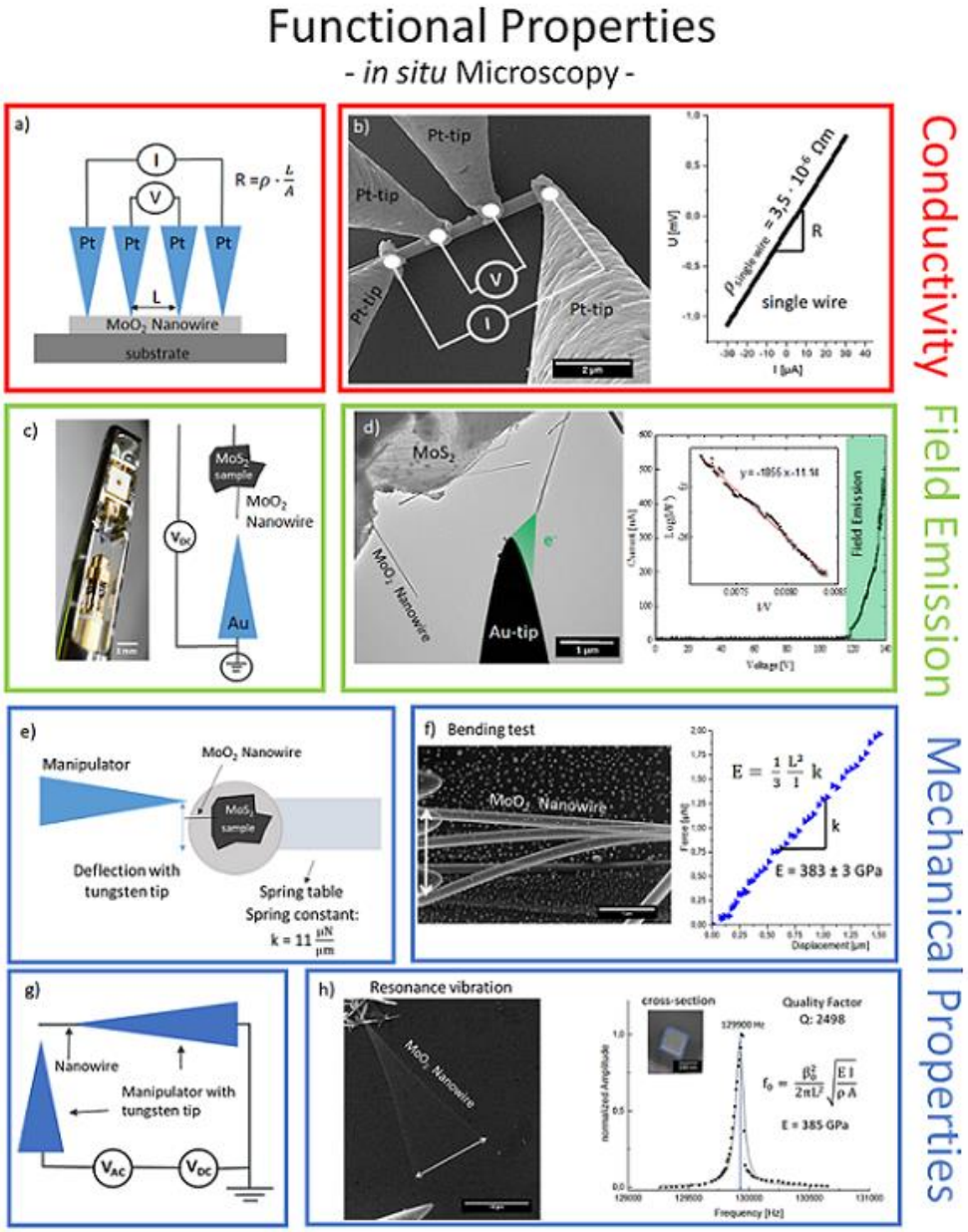

Figure 2: Functional properties of the Nanowires. a) Schematic of the four probe measurement i b) Measured I-V curve in SEM c) Schematic for field emission experiment d) Measured I-V curve in TEM e) Schematic for bending tests f) Measured Force-Displacement Curve in SEM g) Schematic for resonance measurements f) Resonance curve of a Nanowire

MS6.P018
Nanohybrid materials and thin films for battery applications

A. Frank[1], M. Dias[2], S. Peglow[2], W. Bodnar[2], A. Kruth[2], C. Scheu[1,3]

[1]Max-Planck-Institut für Eisenforschung GmbH, Nanoanalytics and Interfaces, Düsseldorf, Germany
[2]Leibniz Institute for Plasma Science and Technology e.V.(INP), Greifswald, Germany
[3]RWTH Aachen University, Materials Analytics, Aachen, Germany

Boosted not only by the threatening greenhouse effect but also scarcity of the commonly used fossil fuels and, at the same time, increasing energy demands of our society the research on energy and energy related (nano)materials is intensified. One main research interest is to develop energy storage concepts which have a high overall performance to meet our energy needs. This is for example possible by already widely used lithium ion batteries. However, new materials are sought-after which can withstand many cycles and the often harsh electrolytes. One way to achieve such materials is the hybridization of carbonaceous structures with metal oxides.

In this work, we present different plasma-based synthesis concepts to achieve a thorough combination of different carbon nanostructures with various metal oxides. Well suited approaches are synthesis concepts which are, for example, plasma-enhanced deposition processes as they allow to reduce deposition temperatures by at the same time reaching comparable characteristics, or even direct synthesis methods like plasma-in-liquid processes. However, to control these processes a deep understanding of the plasma properties in relation to the quality of the deposited material is crucial. For observing material characteristics like crystallinity, oxidation state, chemical composition and other, (scanning) transmission electron microscopy ((S)TEM) is a very powerful tool, especially when imaging is combined with electron diffraction, energy-dispersive X-ray (EDX) spectroscopy and/or electron energy-loss spectroscopy (EELS). The here presented results have been achieved by using two Titan Themis 300 – one C_S probe-corrected and one C_S image-corrected – both equipped with a Super X-EDX detector system from Bruker and the probe-corrected one additionally with an Gatan Quantum ERS image filter for EELS measurements.

To link plasma properties and material properties, we first deposited vanadium oxide (VO_x), a very interesting material for use in lithium ion batteries but also solar cells, on silicon substrates by a plasma ion assisted deposition (PIAD) process. It could be shown that variations in the deposition parameters can clearly be linked to prominent features in the as-deposited VO_x films (Figure 1).

Furthermore, first results of a plasma-in-liquid (PIL) process are very promising for preparing carbon metal-oxide hybrid materials in one single step. By simply using isopropanol as carbon precursor and igniting the plasma inside the solvent nanostructured, layered carbon structures can be achieved (Figure 2a and b). Additionally, nanometer sized nanoparticles could be observed which are most likely related to the electrode assembly (Figure 2c). Combining this with organometallic precursor solutions opens up pathways to wide variations of nanohybridic materials with excellent contact in-between.

Fig. 1: Comparison between bright field TEM image (left) and the gas flow of the plasma source (right). Fluctuations in the gas flow directly correlate to the crystallinity in the VO_x film.

Fig. 2: Bright field TEM images of carbonaceous structures and nanoparticles synthesized by the plasma-in-liquid method using isopropanol as carbon precursor. (a) Overview image of the observed structures, (b) high resolution image of a layered carbon structure, and (c) high resolution image of one exemplary nanoparticle.

Fig. 1

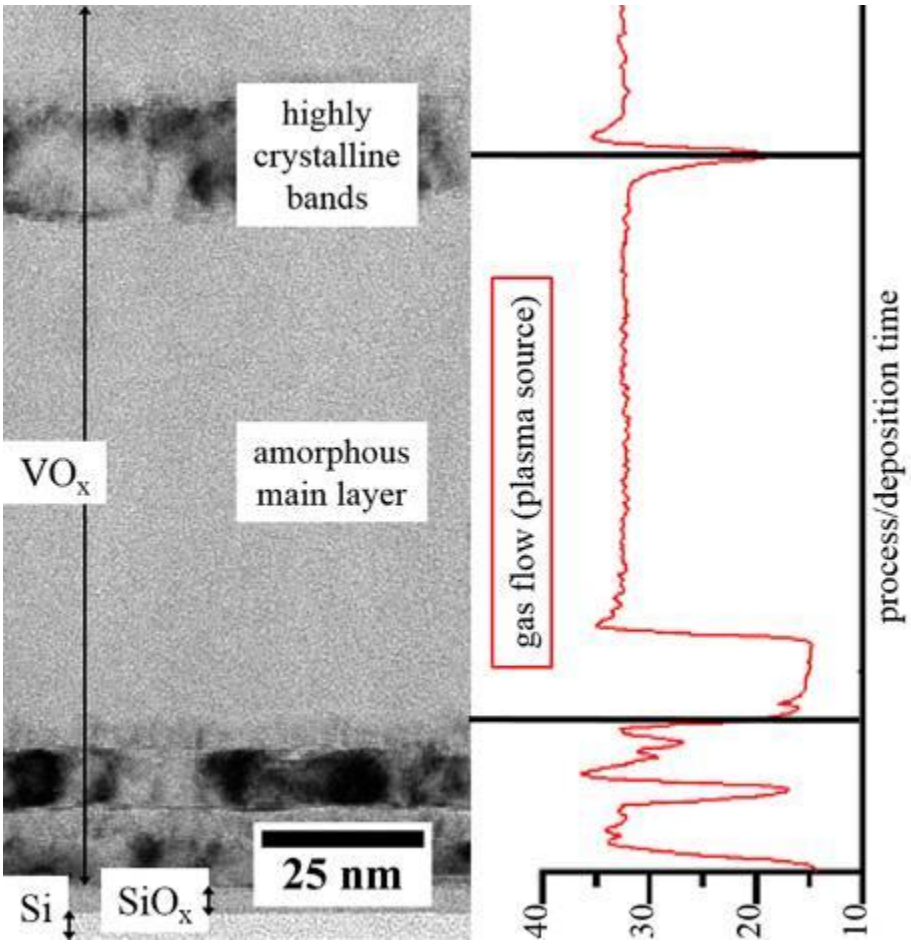
highly crystalline bands
amorphous main layer
VOx
25 nm
Si
SiOx
gas flow (plasma source)
process/deposition time
40
30
20
10

Fig. 2

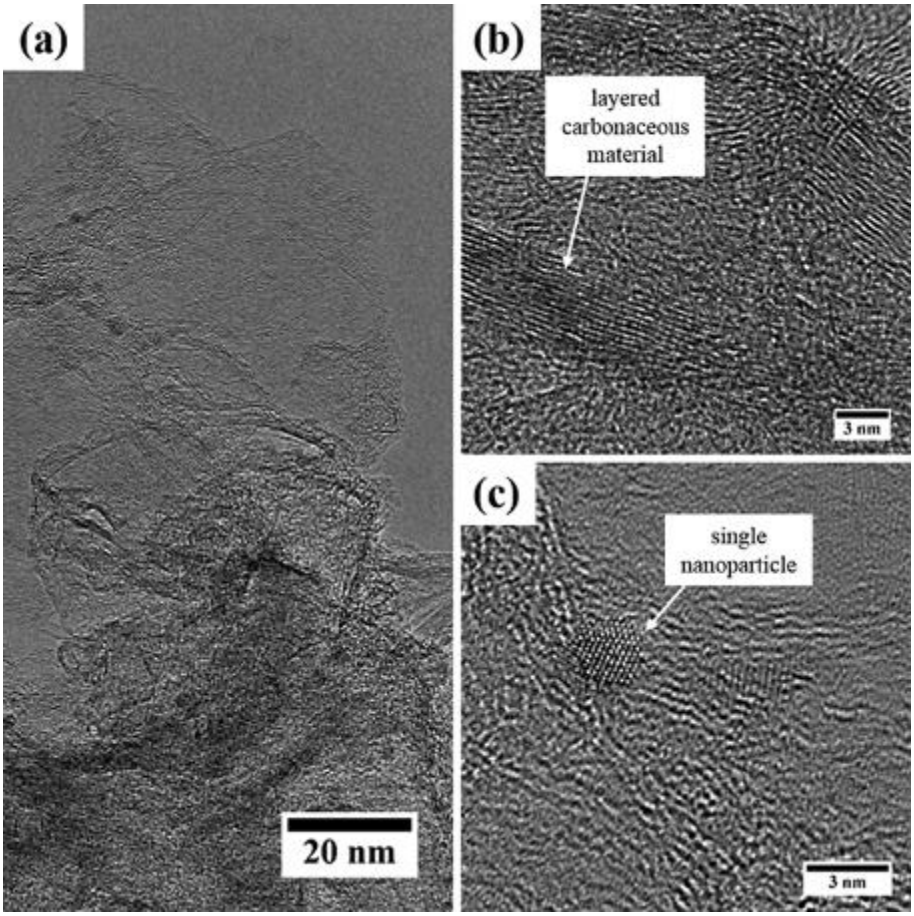
(a)
20 nm
(b)
layered carbonaceous material
3 nm
(c)
single nanoparticle
3 nm

MS6.P019
Propagating Wedge Polaritons Interacting With Patterned Defect Structures in Bi_2Se_3 Nanoplatelets

R. Lingstädt[1], N. Talebi[1], M. Hentschel[2], S. Mashhadi Sheikholharam[1], M. Burghard[1], H. Giessen[2], P. A. van Aken[1]

[1]Max Planck Institute, Solid State Research, Stuttgart, Germany
[2]University, 4th Physics Institute, Stuttgart, Germany

Dielectric properties describe the interaction of materials with electromagnetic radiation. For highly anisotropic permittivity tensors, where one or two principle components become negative, a hyperbolic dispersion results, giving rise to unique material properties that enable intriguing nanophotonic applications, such as sub-wavelength focusing or tailoring light emission and absorption. Besides the realization of hyperbolic media through artificially created metamaterials, these properties also occur in natural materials within various energy ranges.(1,2) One example is the topological insulator Bi_2Se_3, a van der Waals material consisting of stacked quintuple layers, which shows hyperbolicity in the technologically relevant near-infrared to visible wavelength range.(3) Wedge polaritons can be excited by fast electrons and were shown to propagate along particle wedges, rendering them a promising candidate for wave-guiding applications. These hybrid modes result from the coupling of polaritons that propagate along the upper and lower wedge of the particle.(4)

In this study, we have investigated the behavior of wedge polaritons in Bi_2Se_3 nanoplatelets by analytical transmission electron microscopy techniques in combination with finite-difference time-domain simulations. In particular, electron energy-loss spectroscopy has been used to analyze Fabry-Pérot-like resonances emerging in wedge-polariton propagation along particle edges. Regarding possible applications, the influence of bent contours of the guiding edge and local defects is of fundamental interest. For that purpose, we have patterned particle edges with open and closed nanocavities by focused-ion-beam milling. Our experimental findings, supported by numerical simulations, reveal coupling of localized polaritons to the propagating wedge modes and in general signify an extraordinary capability to cope with present defects, which is favorable for future applications such as optoelectronic circuitry devices.(5)

References:

(1) D. N. Basov, M. M. Fogler, F. J. García de Abajo. Polaritons in van der Waals materials. *Science* 354, 6309 (2016).

(2) T. Low, A. Chaves, J. D. Caldwell, A. Kumar, N. X. Fang, P. Avouris, T. F. Heinz, F. Guinea, L. Martin-Moreno, F. Koppens. Polaritons in layered two-dimensional materials. *Nature Materials* 16, 182–194 (2017).

(3) M. Esslinger, R. Vogelgesang, N. Talebi, W. Khunsin, P. Gehring, S. de Zuani, B. Gompf, K. Kern. Tetradymites as natural hyperbolic materials for the near-infrared to visible. *ACS Photonics* 1**,** 1285–1289 (2014).

(4) N. Talebi, C. Ozsoy-Keskinbora, H. M. Benia, K. Kern, C. T. Koch, P. A. van Aken. Wedge Dyakonov waves and Dyakonov plasmons in topological insulator Bi_2Se_3 probed by electron beams. *ACS Nano* 10, 6988–6994 (2016).

This project has received funding from the European Union"s Horizon 2020 research and innovation programme under grant agreement No. 823717 – ESTEEM3.

MS6.P020
Tailoring the crystallinity of multinary alloy nanoparticles

A. Garzon Manjon[1], B. Völker[2], H. Meyer[3], M. Meischein[3], A. Ludwig[3], C. Scheu[1]

[1]Max-Planck-Institut für Eisenforschung GmbH, Düsseldorf, Germany
[2]RWTH Aachen Univerity, Aachen, Germany
[3]Ruhr-Universität Bochum, Bochum, Germany

Recently it has been shown that multinary nanoparticles (MNPs) are promising candidates for energy applications. Their thorough characterization is important to reach further progress in this field. Direct current sputtering (DCS) and high-power impulse magnetron sputtering (HiPIMS) from five elemental targets (Cr-Mn-Fe-Co-Ni) were used to synthesize MNPs within ionic liquids. The ionic liquid can act as an electronic as well as a steric stabilizer preventing particle growth and particle aggregation. Thus, leading to the formation of extremely small nanoparticles with a strong effect on the structure of the latter.

In our work we are investigating MNPs by various microscopy techniques, such as Cs-corrected high-resolution (scanning) TEM (HR(S)TEM), energy-dispersive X-ray spectroscopy (EDS) and we are studying their growth using *in situ* experiments.

With these techniques, information on size, shape, crystallinity, and chemical composition of the MNPs is obtained. Furthermore, we characterize the mobility of the elements, which can lead to alloying, phase separation, phase transition, among other process during the *in situ* experiments.

The fabricated MNPs appear amorphous after the DCS synthesis. In order to obtain crystallized MNPs three different routes were studied (1). One possibility is *in situ* transmission electron microscopy (TEM): after DCS, illumination with a 300 keV electron beam generates structural changes of the MNPs. Up to 40 min exposure time, the MNPs remain in the amorphous state. Above 40 min, the illumination of the MNPs leads to a structural transformation to a crystalline state. A second strategy is *ex situ* crystallization. MNPs were annealed at 100°C for up to 15 h. After this annealing treatment, crystalline MNPs were obtained A third method is applying HiPIMS. MNPs are already in the crystallized state after HIPIMS synthesis, since the sputtered species are more energetic. Therefore, crystalline particles can be generated at lower temperatures. In order to understand their excellent catalytic behaviour, which is comparable to Pt in the oxygen reduction reaction (2) new characterization strategies have to be developed. Thus, our aim is to study the crystallization mechanism of MNPs at the sub-nanometer scale using *in situ* heating experiments and IL TEM to achieve a thorough understanding of the active sides involved in the catalytic process.

In conclusion, we have shown that the crystalline state of MNPS can be tailored by the synthesis conditions. Electron beam bombardment, as well as *in situ* and *ex situ* annealing lead to crystalline MNPs.

Figure: Illustration and experimental results using Cs corrected high-resolution TEM images of MNPs after their *in situ* and *ex* situ crystallization or synthesis via HiPIMS. We thank Creative Studio Lena Heel for the scheme (2).

References:

(1) Garzón-Manjón, A., Meyer, H., Grochla, D., Löffler, T., Schumann, W., Ludwig, W., Scheu, C. Controlling the amorphous and crystalline state of multinary alloy nanoparticles in an ionic liquid. Nanomaterials. 8 (11), 903 (2018)

(2) Löffler, T., Meyer, H., Savan, A., Wilde, P., Garzón-Manjón, A., Chen, Y.T., Ventosa, E., Scheu, C., Ludwig, A., Schuhmann, W. Discovery of a multinary nobel metal free oxygen reduction catalyst. Adv. Energy. Mater. 8 (4), 1802269 (2018).

This work was funded by German Science Foundation (DFG) via the project SCHE 634/21-1 and LU1175/23-1 as well as the BMBF project NEMEZU.

Fig. 1

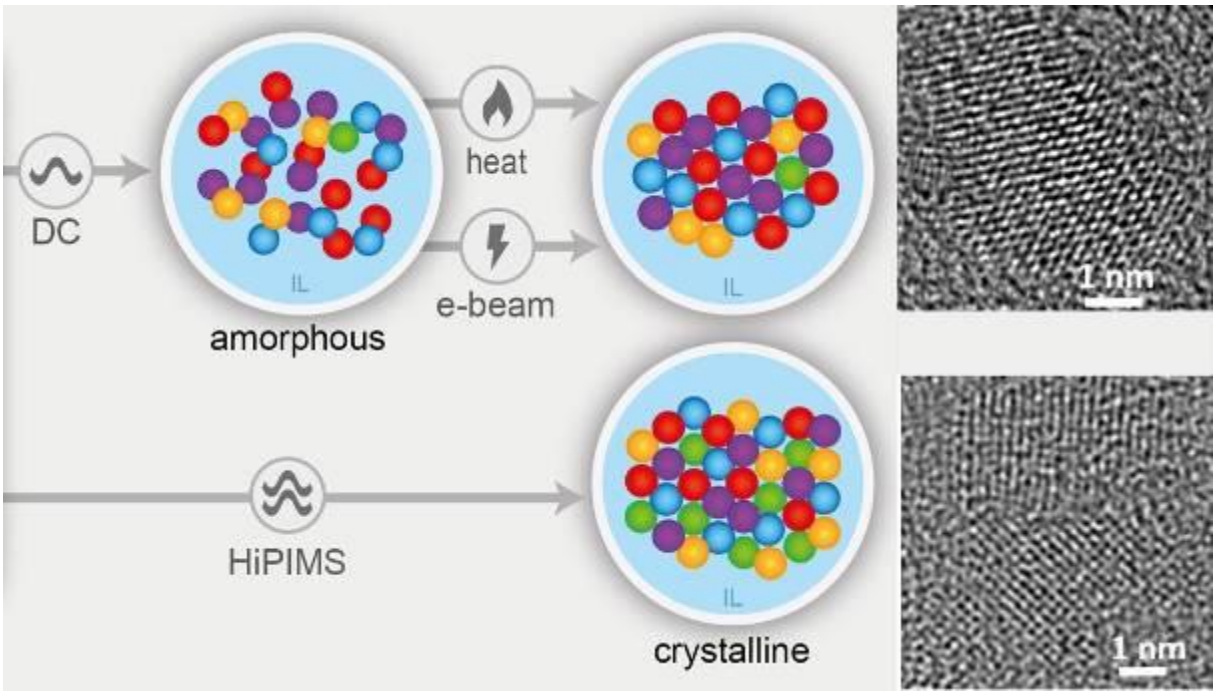

MS6.P021
Inducing structural disorder and topological defects in charge density waves through electron-beam irradiation

M. K. Kinyanjui[1], T. Lehnert[1], J. Köster[1], U. Kaiser[1]

[1]University of Ulm, Ulm, Germany

Charge density waves (CDW) are periodic modulations of charge density observed in many low dimensional metals including quasi two-dimensional 1T-TaS_2 and 1T-$TaSe_2$. The CDW state is also characterized by a periodic lattice distortion (PLD) which is the modulation of atomic positions. A sliding CDW under an electric field is predicted to have transport properties similar to a superconducting state. However this is often not observed since the sliding CDW is often trapped by crystalline defects. It is therefore important to understand how the CDW/PLD structure is affected by lattice defects (1)-(2).

Here we present the results of a HRTEM investigation where in-situ defect generation capabilities of the electron beam in the transmission electron microscope (TEM) have been used to create lattice defects in 1T-TaS_2 and 1T-$TaSe_2$ thin layers. At the same time we also analyze the effects of these defects on the CDW/PLD structure (3).

Few-layers thick 1T-TaS_2 and 1T-$TaSe_2$ samples were obtained through mechanical exfoliation from bulk. HRTEM imaging was performed on a FEI Titan 80-300 TEM equipped with an objective lens spherical aberration corrector and operated at 80 kV. To investigate the effects of electron-beam generated defects on the CDW/PLD, successive HRTEM images were obtained from the same sample region over time and at a constant electron dose rate in the order of 10^6 e^-/nm^2.

Figure 1 (a) shows a HRTEM image from CDW distorted 1T-TaS_2 obtained at 100 K. Figures 1(b) and (c) show the respective CDW/PLD structures obtained using Fourier analysis of the HRTEM before and after prolonged electron beam exposure respectively. The increase in CDW disorder is observed after prolonged electron beam exposure as can be seen by comparing CDW structures in Figs 1(b) and (c) respectively. In addition to increased disorder topological defects in form of CDW dislocations and disclinations can also be observed. In the Voronoi analysis of the CDW/PLD is shown in Fig.1 (d) two types of topological defects can be identified, CDW/PLD disclinations which are represented by single non-six-sided polygons (4, 5, 7, 8) and CDW/PLD dislocations which consist of pairs of 7/5 disclinations . The atomic scale derivation of the 2D CDW/PLD strain tensor (Figs. 1(e), (f)) also shows the presence of topological defects in form of CDW/PLD dislocations (marked by a dotted circle). A single CDW dislocation core is shown in Fig 1(g) (3).

In conclusion we have investigated the effects of electron beam induced damage on the charge density wave structure in 1T-$TaSe_2$/1T-TaS_2 We observe the development of topological dislocation-like defects and loss of long range order in the PLD structure with exposure to the electron beam.

References:

(1) J. Wilson, F. D. Salvo, and S. Mahajan, Adv. Phys. 24, 117 (1975).

(2) P. Monceau, Adv. Phys. 61, 325 (2012).

(3) M. K. Kinyanjui, T. Bjorkman, T. Lehnert, J. Koster, A. Krasheninnikov, U. Kaiser , Phys. Rev. B 99, 024101(2019)

Fig. 1: (a) HRTEM image of CDW distorted 1T-TaSe2 (b) CDW/PLD structure from the Fourier analysis of the HRTEM image (c) CDW//PLD structure after prolonged electron beam exposure (d) A Voronoi diagram with CDW/PLD maxima in 1(a). Calculated atomic scale CDW/PLD strain map for (e) ε_{xx} (f) ε_{yy} (g) A single CDW dislocation core

Fig. 1

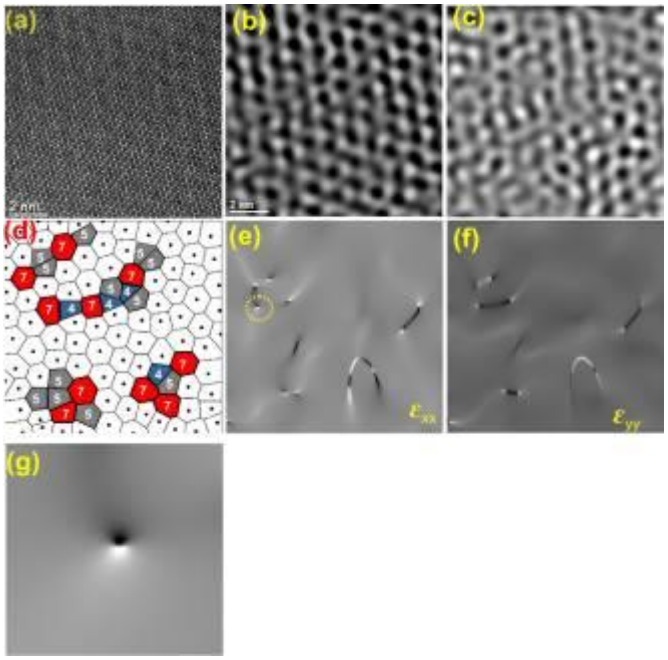

MS6.P022
Multimodal Characterization of Nanoparticles by Correlation of Scanning Electron and Atomic Force Microscopy

M. Kesting[1], T. Ogbazghi[1], C. Thomas[1]

[1]Hamm-Lippstadt University of Applied Science, Lippstadt 1, Hamm, Germany

Nanoparticles (NP) have unique properties due to their enlarged surface to volume ratio allowing a wide range of applications. However, there are several concerns regarding toxicity for organisms and the environment (1). A relevant example is the food additive TiO2 (labelled as E171) which consists up to one-third of NP due to manufacturing processes (2). In this context studies refer to possible relations of TiO2 NP with genotoxicity and other health impacts on rats and mice (2-4). NP have sizes of approximately 1 nm to 100 nm in at least one dimension and must be declared (in the EU) in food and care products (5). To characterize such NP an investigation method is requisite, which provides 3D-information as well as the elemental composition of NP extracted from food and food additives.

In this contribution, a multimodal method is developed and applied using 2D-information and element analysis provided by a Scanning Electron Microscope (SEM) with Energy Dispersive X-ray Spectroscopy (EDS) in addition to 3D-information from an Atomic Force Microscope (AFM). The two independent microscope systems are correlated as it is already established for Correlative Light and Electron Microscopy (CLEM), e.g. by Zeiss" Shuttle & Find, for material as well as life science applications (6-9).

To investigate NP contained in food and care products, different samples are dissolved in water and ultrafiltrated. The extracted colloidal suspension is ultrasonicated and dried. For characterization, the samples are investigated by SEM to find and identify NP as it is quite fast and provides high resolution. Subsequently, the same particles are relocated and characterized in the AFM to achieve 3D-information and material specific details like surface potential or elasticity.

An application of this method shows NP in commercially available chocolate coated peanuts. In figure 1 the particles are investigated by SEM. This characterization shows lateral shapes of the particles which are suitable for separation of NP and statistical analyses. Additionally, the particles can be identified as TiO2 NP by EDS. Precise relocation enables investigation of the same region in an AFM as shown in figure 2. This image shows 3D-information in height-depending colour shades.

The evolved multimodal characterization method has shown to be applicable and beneficial. Correlation of SEM and AFM allows analysing elemental compositions of NP as well as their 3D metrology. Furthermore, material specific investigations like Kelvin Probe Force Microscopy or Force Spectroscopy can be applied.

References:

(1) Böhmert, et al., Bundesgesundheitsbl 60, 722, 2017

(2) Simkó, et al., NanoTrust Dossier 034, 2012

(3) Trouiller, et al., Cancer Res 69(22), 8784-9, 2009

(4) Bettini, et al., Sci. Rep. 7, 40373, 2017

(5) Greßler, et al. NanoTrust Dossier 039, 2013

(6) Elli, et al., Optik & Photonik 1, 32, 2012

(7) Meyer, et al., J. Vis. Exp. (112), e53870, 2016.

(8) Ogbazghi, et al., Materials Today: Proceedings 4, 237, 2017

(9) Kharkwal, et al., J Virol 90:7257-7267, 2016

Fig. 1: SEM image of TiO2 particles extracted from choclate coated peanuts.

Fig. 2: Topografic analysis of TiO2 particles relocated in AFM.

Fig. 1

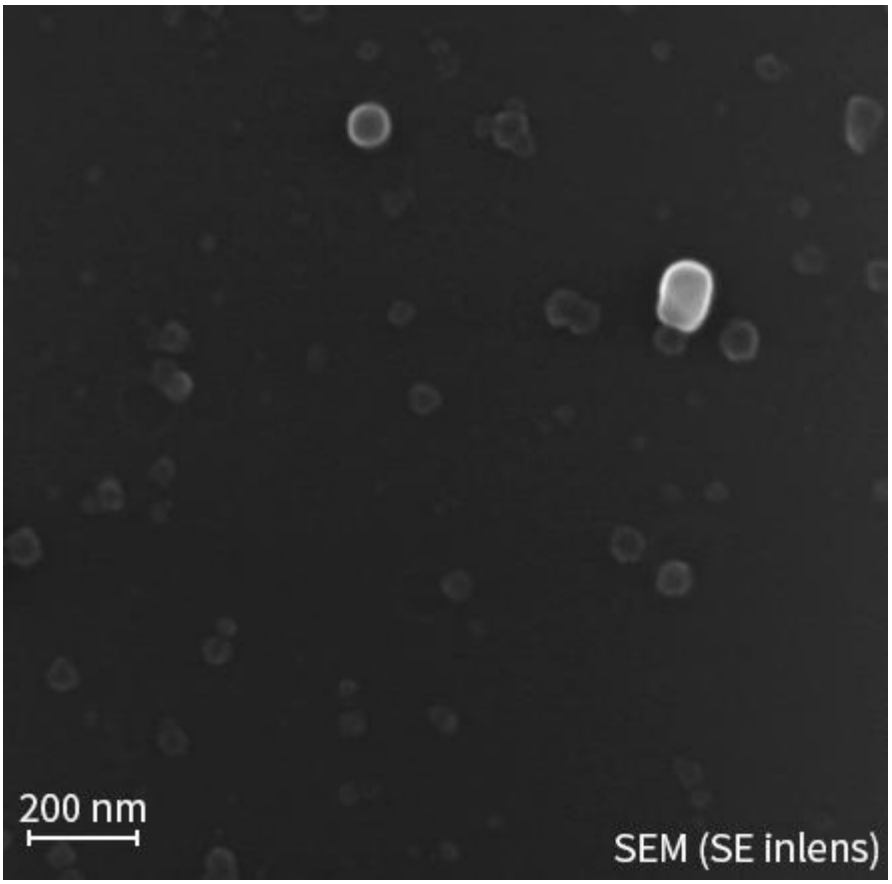

Fig. 2

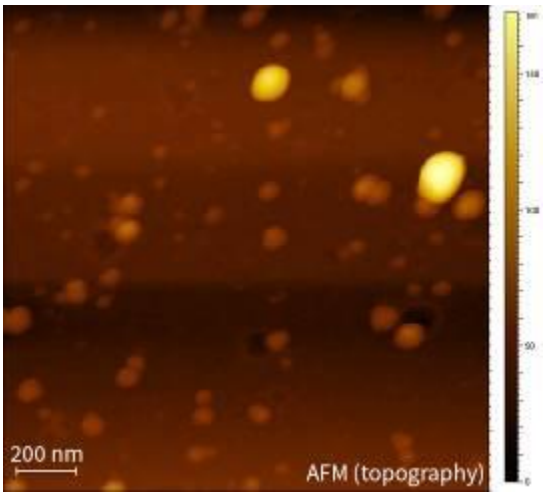

MS6.P023
TEM investigations of growth defects in wurtzite and sphalerite ZnS nanowires

I. Plesco[1], V. Duppel[2], I. Tiginyanu[1], L. Kienle[3]

[1]Technical University of Moldova, National Center for Materials Study and Testing, Chisinau, Moldova
[2]Max Planck Institute for Solid State Research, Stuttgart, Germany
[3]Institute for Materials Science, University of Kiel, Kiel, Germany

Semiconductor nanowires (NWs) are widely required for assembly of electronic and photonic devices. In particular, direct wide band gap ZnS NWs can serve as building blocks for sensor, LED and laser applications, quantum computing or UV-energy conversion. For their integration into devices low or controllable level of defects represents a crucial factor. Here we report on Au catalyzed growth of ZnS NWs via Hydride Vapor Phase Epitaxial (HVPE) process and their crystallographic analysis and defect evaluation by TEM techniques.

ZnS NWs of two different morphologies and crystal structures obtained in the same process and sample are analyzed with TEM techniques. The type of crystal structure and the nature of defects are revealed by combined SAED and HRTEM study. Chemical composition and stoichiometry are investigated by means of STEM-EDX.

ZnS NWs were synthesized in HVPE process, using CdS powder precursor on a ZnO substrate covered with Au nanoparticles in H2 atmosphere. The ZnO substrate contains tetrapodal crystals. Due to the reduction of ZnO in H2 at high temperature, a ZnS shell is formed on the surface of ZnO tetrapods which serves as a source for ZnS NW formation.

HRTEM and SAED were performed on ZnS NWs in an FEI Tecnai F30 G² STwin 300 kV/FEG equipped with an EDX detector (Si/Li, EDAX) and a Philips CM30 300 kV/LaB6.

The chemical composition of the samples studied by STEM-EDX measurements confirmed the ZnS content. Studied NWs exhibit both wurtzite and sphalerite structures, in some cases NWs with planar intergrowth of both phases can be found. ZnS NWs with straight edges and diameters of 40-50 nm showing the pure wurtzite crystal structure grow along (001). NWs which have jagged edges and their diameters within the range of 70 and 170 nm exhibit sphalerite crystal structure with growth direction along (2-10). It is notable, that wurtzite NWs don"t have observable defects, while sphalerite NWs show twinning.in parallel, perpendicular and 30º orientations to the growth direction.

The possibility to synthesize high quality wurtzite and sphalerite NWs was demonstrated, as well as the synthesis of high quality wurtzite ZnS NWs in a HVPE process. In sphalerite NWs, planar (111) defects are oriented along, perpendicularly and with 30º to growth direction.

IP acknowledges material support of DAAD Research Grant (57381333, no. 91696787). IP and IT acknowledge the support from the European Commission under the Grant #810652 "NanoMedTwin".

Fig. 1: a) HRTEM micrograph of a pure wurtzite NW grown in *c* direction without observable lattice defects, the inset shows the Fast Fourier Transform; b) HRTEM micrograph of a wide sphalerite NW with numerous twinning defects oriented parallel and perpendicular to growth direction, insets show simulated micrographs for (011) zone axis and a Fourier-filtered image of the marked regions with different twin orientations; c) an overview TEM image of a); d) an SEM image of the sample showing arrangement of NWs on the substrate on micro-scale; e) an overview TEM image of b).

Fig. 1

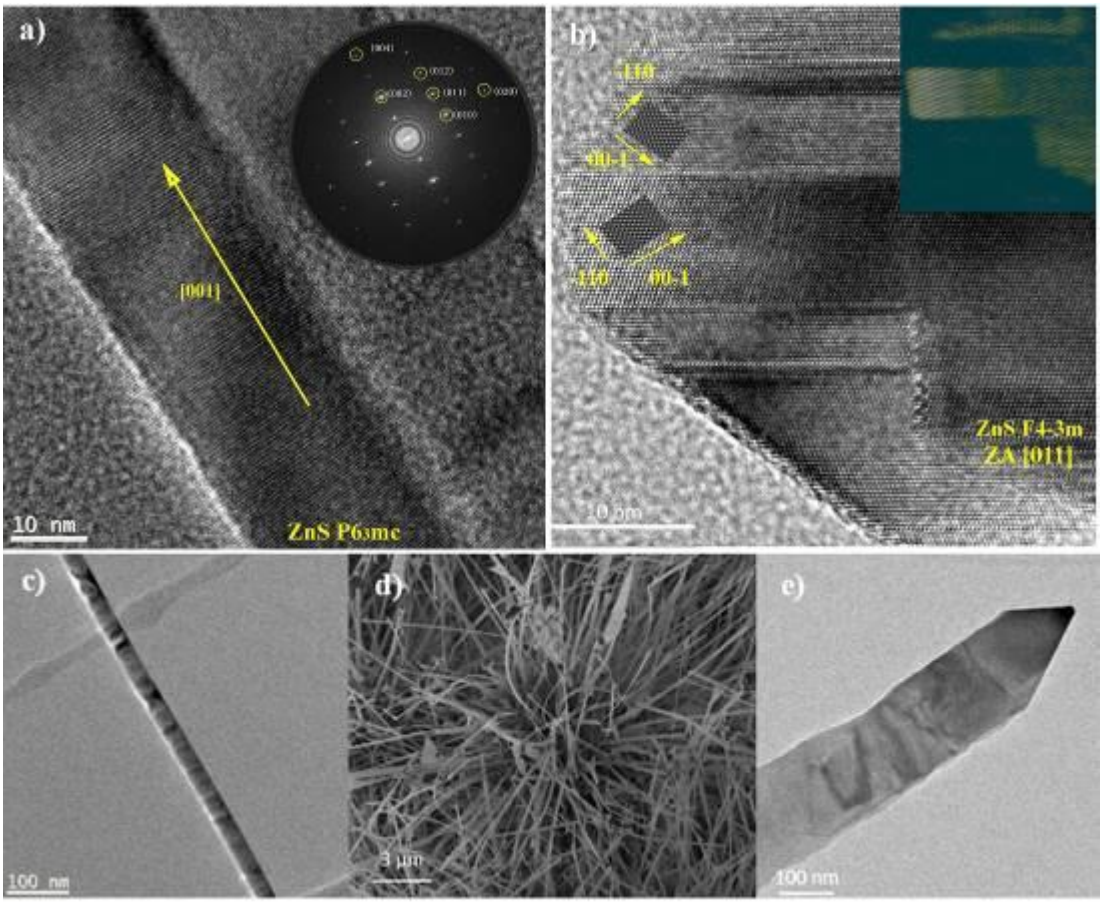
a)
[001]
10 nm
ZnS P63mc
b)
-110
00-1
110
00-1
ZnS F-43m
ZA [011]
10 nm
c)
100 nm
d)
3 μm
e)
100 nm

MS6.P024
Influence of synthesis temperature on microstructure and optoelectronic properties of CdSe quantum dots

S. Neumann[1], C. Menter[2], A. Mahmoud[2], D. Segets[3], D. Rafaja[1]

[1]Institute of Materials Science , TU Bergakademie Freiberg, Freiberg, Germany
[2]Institute of Particle Technology and Interdisciplinary Center for Functional Particle Systems, FAU Erlangen, Erlangen, Germany
[3]Process Technology for Electrochemical Functional Materials and Center for Nanointegration Duisburg-Essen (CENIDE), University Duisburg-Essen, Duisburg, Germany

CdSe quantum dots (QDs) have gained widespread interest during the past decades due to their tunable optoelectronic properties that enables their application, for instance in solar cells and light emitting diodes. Hot injection is a widely used technique for the preparation of QDs, however, the lack of knowledge on the role of manifold process parameters complicates the establishment of design rules for scalable processes.

The aim of this work is to study the influence of the synthesis temperature on the microstructural and the optoelectronic properties of CdSe QDs synthesized by hot injection.

The CdSe QDs under study were synthesized via hot injection in an automatic platform. After the as-prepared Cd oleate precursor was heated to 225, 235 and 250°C, respectively, the cold precursor consisting of trioctylphospine selenide (TOP-Se) dissolved in octadecene was injected therein to form CdSe QDs. Absorbance and emission spectra were analyzed in a micro titer plate (MTP) reader. The microstructure of the CdSe QDs was investigated by means of high-angle annular dark-field scanning transmission electron microscopy (HAADF-STEM), selected area electron diffraction (SAED), X-ray diffraction (XRD) and high-resolution transmission electron microscopy (HRTEM) in combination with fast Fourier transforms (FFTs) of the HRTEM micrographs in order to analyze the phase composition of the CdSe QDs and the microstructure defects.

Particle size distributions that were derived from the optical absorbance measurements as described in (1) and complemented by statistical analysis of several HAADF-STEM images were almost identical for all samples. The absorption and emission spectra of different samples showed no remarkable differences in the measured wavelength range. XRD as well as SAED revealed a zinc blende crystal structure (space group *F*-43*m*) of the QDs regardless of the synthesis temperature. The cubic crystal structure of the QDs was confirmed by FFT/HRTEM. Still, HRTEM disclosed the presence of stacking faults and twins on the cubic lattice planes {111} within the QDs. The presence of such planar defects was corroborated by XRD, where a different shift of XRD lines with different diffraction indices hkl was observed, as typical for planar defects located on the (111) planes of cubic CdSe (2). Both kinds of planar defects produce a change in the stacking sequence of the cubic crystal structure resulting in clusters within the cubic crystallites that resembles the stacking sequence of wurtzitic CdSe (space group $P6_3mc$). The amount of planar defects decreased with increasing synthesis temperature.

In summary, the synthesis temperature during the hot injection preparation of CdSe QDs does not have a substantial influence on the size and the optoelectronic properties of the QDs within the investigated temperature range. The crystallization of the QDs in the zinc blende crystal structure containing planar defects on the (111) lattice planes was observed to be an intrinsic phenomenon of the CdSe QDs synthesized by the method applied here.

References:

(1) D. Segets, J. Gradl, R.K. Taylor, V. Vassilev, W. Peukert: Analysis of optical absorbance spectra for the determination of ZnO nanoparticle size distribution, solubility, and surface energy, ACS Nano 3 (2009), pp. 1703-1710.

(2) B.E. Warren: X-ray Diffraction, Newburyport, Dover publications (1990).

MS6.P025
Spectroscopic properties of monolayer, few-layer, and bulk FePS3 - experiments and simulations.

A. Storm[1], J. Köster[1], M. K. Kinyanjui[1], M. J. Mohn[1], U. Kaiser[1]

[1]Universität Ulm, Materialwissenschaftliche Elektronenmikroskopie, Ulm, Germany

Transition metal phosphorus trichalcogenides (TMPTS) are two-dimensional layered structures which exhibit interesting properties as bandgaps in the 1.3 eV-3.5 eV range as well as 2D magnetic ordering (1). This makes them ideal candidates for optoelectronic and spintronic device applications (2). $FePS_3$ is an interesting TMPT characterized by a "zigzag" antiferromagnetic (AFM) ordering and a bandgap of 2.18 eV in the monolayer (ML) case (2-3). While electronic properties of bulk $FePS_3$ have been systematically studied, those of MLs $FePS_3$ are still largely unexplored.

Here we present low-loss electron energy loss spectroscopy (VEELS) results on a freestanding ML $FePS_3$. The experimental results are supported by density functional theory (DFT) calculations. Our results provide insight into the changes in the electronic properties of $FePS_3$ from the extended to the isolated layer case as a result of lowering the dimensionality.

ML $FePS_3$ used in the experiments were prepared from bulk through mechanical exfoliation. VEELS spectra were acquired at 80 kV using a GIF attached to a Titan 80-300. The energy resolution was determined to be 0.6 eV. Ab initio calculations of the electronic structure and EELS spectra were used to interpret the EELS experimental spectra. Ground state DFT calculation were done in the local density approximation (LDA), and with the inclusion of a one sided hubbard model (LDA+U) to treat correlation effects caused by the localized Fe-3d electrons. In addition, time-dependent density functional theory (TDDFT) in the random phase approximation (RPA) is used to calculate the low-loss EELS with the GPAW code (4). AFM ordered supercells were used in the calculations for both ML and bulk structures.

Fig. 1(a) displays a TEM image of a ML FePS3. The EELS spectra for a ML and few layers thick $FePS_3$ are shown in Fig. 1(b) and c). Eventually, the spectra in both cases are dominated by a plasmon peak. A shift and broadening of this peak is observed from the few-layer (21 eV) to the ML (15 eV) case, see Fig.1 b) and c) respectively. These findings are in good agreement with the results observed for other TMPTS (5), where similar shifts and broadening were observed. In addition, we illuminate several changes in the EELS spectra due to damage caused by the incident electron beam and due to contamination accumulation of this sensitive material in the few-layer case, especially in comparison with our ab initio calculations. Moreover, the importance of inclusion of correlation effects due to the Fe-3d electrons in the theoretical calculations is emphasized.

As a result from our theoretical and experimental study we can conclude that the shift and broadening of the plasmonic peak can be used to differentiate between ML, few-layer, and bulk $FePS_3$ structures.

References:

(1) A. Hashemi et al. (2017). J. Phys. Chem. C 121, 27207

(2) X. Zhang et al. (2016). Adv. Sci. 3, 1600062

(3) Z. Cheng et al. (2018). Adv. Mater. 30, 1707433

(4) M. Walter et al. (2008). J. Chem. Phys. 128, 244101

(5) M.K. Kinyanjui et al. (2018). Phys. Rev. B 98, 035417

Fig. 1: (a) 80kV BF-TEM image of $FePS_3$ with different layer thicknesses: the blue rectangle marks the few-layer region, the red rectangle the monolayer $FePS_3$ region, where the EELS spectra in (b) and (c) were taken from: (b) EELS spectra of few-layer $FePS_3$, (c) EELS spectra of monolayer $FePS_3$. The dotted lines (b) and (c) mark the position of the main plasmon peak.

Fig. 1

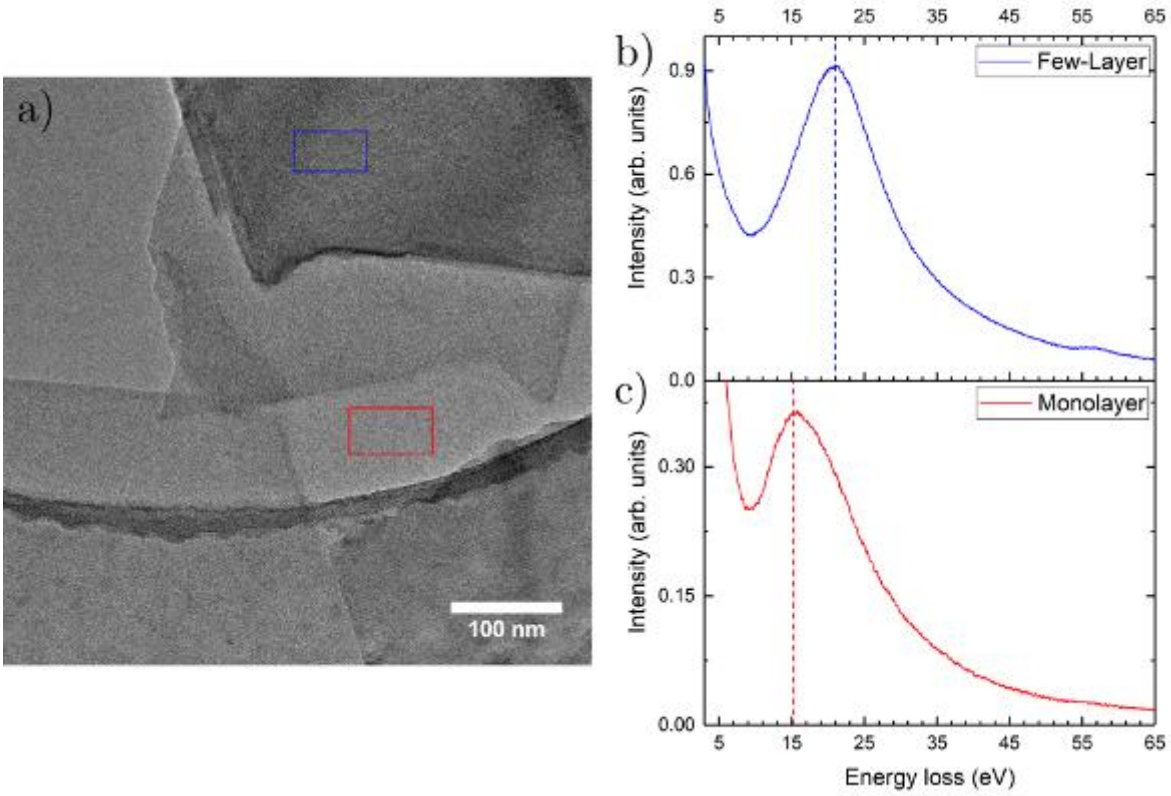
a)
100 nm
b)
Few-Layer
Intensity (arb. units)
0.0
0.3
0.6
0.9
c)
Monolayer
Intensity (arb. units)
0.00
0.15
0.30
5
15
25
35
45
55
65
Energy loss (eV)

MS6.P026
In-situ measurement of contact angles on single multifunctional, porous polymer microparticles *utilizing* ESEM

Y. Pieper[1], K. Kratz[1], M. Heuchel[1], A. Lendlein[1]

[1]Institute of Biomaterial Science/Helmholtz-Zentrum Geesthacht, Micro and Nanotechnology, Teltow, Germany

Particulate absorber materials intended for the detoxification of blood have to fulfill numerous different functions. Such absorbers should be mechanically stable with a size around 250 µm to provide low backpressure, have to be sterilizable, blood cell- and hemocompatible and need a hydrophilic, protein repellant outer surface, while the core should be hydrophobic, have a high surface area and should be capable to adsorb hydrophobic uremic toxins from the blood of renal failure patients. Here we present poly(ethylene gycol) (PEG) modified porous polyetherimide (PEI) absorber microparticles matching the above mentioned multiple demands (1-4).

In the current study SEM investigations were conducted to examine the particle size and surface morphology (pore size), while ESEM experiments were applied to explore the change in water wettability of PEI microparticles before and after chemical modification with PEG.

Multifunctional PEI microparticles were prepared by a spraying/coagulation process according to the method previously described in Ref. (1, 2). The hydrophilic surface modification (enabling the protein repellence function) was realized by post treatment of the PEI microparticles with an aqueous solution of 4 wt% amino terminated poly(ethylene gycol) (*M*n ~ 3000 g×mol-1) at 90 °C for 30 minutes.

In-situ microwettability investigations were conducted with ESEM (FEI Quanta FEG 250) equipped with a cooling stage and a gaseous secondary electron detector at 2±1 °C. Dewetting was achieved by slowly decreasing the pressure below 705 Pa, while for wetting the pressure was slowly increased to 800 Pa.

The contact angles were determined either from the condensed droplet on the particle surface or from the water meniscus condensed between two polymer particles.

SEM investigations revealed the fabrication of spherical particles with a diameter with a diameter of 226±14 µm, while a similar nanoporous surface morphology with pore sizes ranging from 100 to 300 nm was observed for both non-modified and PEG-modified PEI microparticles (Fig. 1a). The ESEM investigations confirmed the hydrophobic nature of the pure PEI microparticle surface, which is documented by the condensation of a discrete water microdroplet on the particle and an advancing water contact angle of *q*adv = 100±6° (Fig. 1b). In contrast, for PEI-PEG microparticles a wetting film between the particles was observed, corresponding to an *q*adv of 68±5, which can be classified as hydrophilic (Fig. 1c).

The changes in microwetting behavior of highly porous PEI microparticles before and after hydrophilic modification could be qualitatively and quantitatively followed utilizing in-situ ESEM experiments.

References:

(1) S. Basu et al., *Polymers for Advanced Technologies* 2015, *26*, 1447.

(2) M. Heuchel et al., *Polymers for Advanced Technologies* 2017, 28, 1269.

(3) S. D. Tetali et al., *Clinical Hemorheology and Microcirculation* 2015, 61, 657.

(4) S. Braune et al., *Clinical Hemorheology and Microcirculation* 2016, 64, 345.

Fig. 1: SEM image of nanoporous PEI microparticle surface (a) and ESEM images showing the water microwetting of PEI (b) and PEI-PEG microparticles (c).

Fig. 1

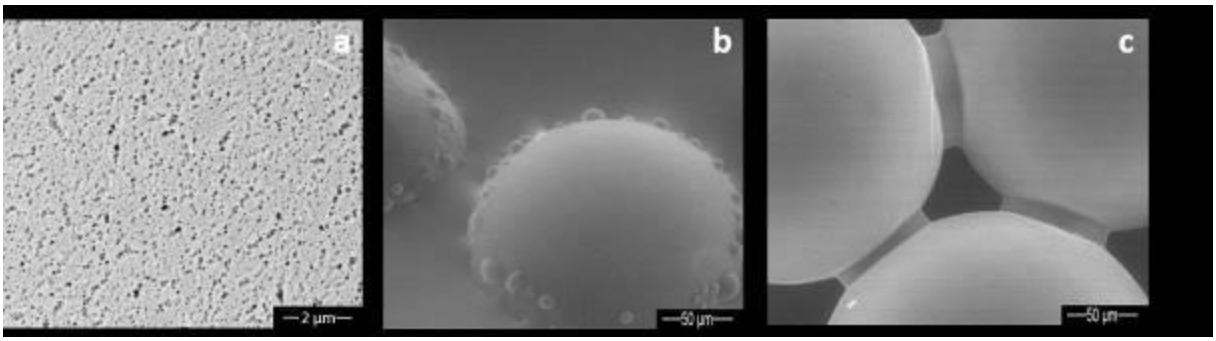

MS6.P027
HRTEM of Alkali-Halide Clusters Deposited on Graphene using Electrospray Ion-Beam Deposition

N. Vats[1], Y. Wang[1], S. Sen[1], S. Siliyazgi[1], H. Ochner[1], S. Abb[1], W. Sigle[1], S. Rauschenbach[1,2], M. Burghard[1], K. Kern[1], E. Besley[3], P. A. van Aken[1]

[1]Max Planck Institute for Solid State Research, Stuttgart, Germany
[2]Oxford University, Oxford, United Kingdom
[3]University of Nottingham, Department of Physical and Theoretical Chemistry, Nottingham, United Kingdom

Atomic clusters are an important class of structures, as they lie in between discrete atoms/molecules and solid material systems. Furthermore, clusters provide a link to the transitions between the gaseous and condensed states of matter. It is, therefore, important to understand how structure, stability and electronic properties of atomic clusters change with their size. Among the different types of cluster systems, alkali-halide clusters have been studied comprehensively using mass spectrometry (1). However, detailed atomic-scale characterization of alkali-halide clusters has not been performed.

In this work, we have used aberration-corrected high-resolution transmission electron microscopy and electron energy-loss spectroscopy (EELS) for atomic-scale structural and chemical analysis of cesium-iodide clusters $(CsI)_nCs^+$ deposited by electrospray ion-beam deposition (2,3) on free-standing graphene.

Small cesium-iodide clusters consisting of 4, 6, and 7 atoms are exclusively observed on single-layer graphene (Fig. 1a) while on bi-layer graphene only two-dimensional monolayer and bi-layer cesium-iodide crystals (Fig. 1b) are observed. These results show that the phase evolution of the adsorbate sensitively depends on the nature of the underlying substrate. This knowledge can be useful in the synthesis and atomic-scale characterization of other long/short-range two-dimensional alkali halide superlattices on graphene (4).

References:

(1) Campana, J. E. and Barlak, T. M. and Colton, R. J. and DeCorpo, J. J. and Wyatt, J. R. and Dunlap, B. I.Physical Review Letters, 1981. 47(15):p.1046-1049.

(2) Rauschenbach, S., Stadler, F. L., Lunedei, E., Malinowski, N., Koltsov, S., Costantini, G. and Kern, K.Small, 2006. 2(4): p. 540-547.

(3) N Vats, S Rauschenbach, W Sigle, S Sen, S Abb, A Portz, M Dürr, M Burghard, PA van Aken, K Kern. Nanoscale, 2018. 10(10): p. 4952-4961.

(4) This project has received funding from the European Union"s Horizon 2020 research and innovation programme under grant agreement No. 823717 – ESTEEM3.

Fig. 1: Atomic-scale imaging of cesium iodide cluster on graphene. (a) HRTEM image of six atoms and four atoms cesium-iodide clusters on single-layer graphene, marked by yellow and red arrows, respectively. (b) Annular dark-field (ADF) image of two-dimensional single-layer cesium-iodide crystal on bi-layer graphene.

Fig. 1

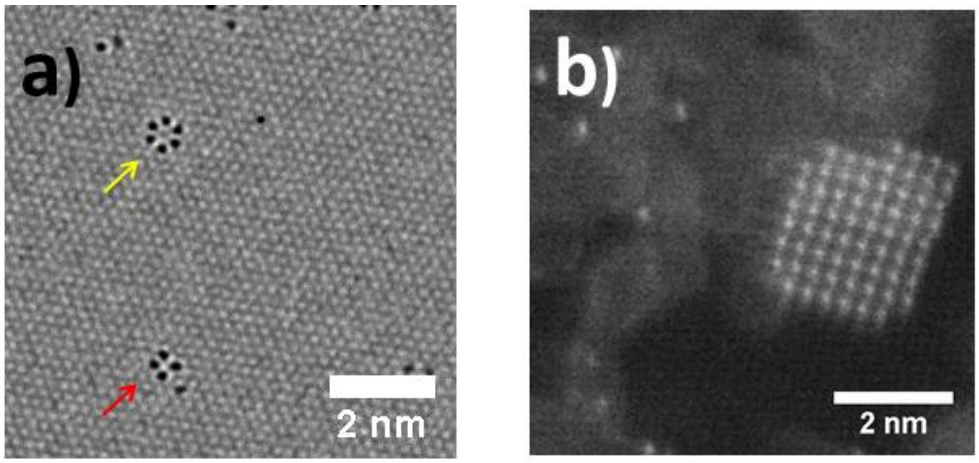

MS6.P028
Characterization of Gold rich Nanostructures on AIII-BV Semiconductor Surfaces by Electron Microscopy and Machine Learning Techniques

B. R. Jany[1], A. Janas[1], W. Piskorz[2], K. Szajna[1], A. Kryshtal[3], G. Cempura[3], P. Indyka[2], A. Kruk[3], A. Czyrska-Filemonowicz[3], F. Krok[1]

[1]Marian Smoluchowski Institute of Physics Jagiellonian University, Department of Solid State Physics, Krakow, Poland
[2]Jagiellonian University, Faculty of Chemistry, Krakow, Poland
[3]AGH University of Science and Technology, International Centre of Electron Microscopy for Materials Science, Krakow, Poland

The AIII-BV semiconductors has been considered for decades as a promising material to substitute silicone for electronic devices manufacturing. One of the important aspects are gold-semiconductor interactions at nano and atomic level, which may result in the formation of Schottky or Ohmic contact. Gold is also widely used to catalyze the growth of standing AIII-BV nanorods.

We investigated the formation of defined Au nanostructures on different AIII-BV semiconductor surfaces (InSb, InP, InAs, GaSb, GaP, GaAs) at atomic and nano level via controlled thermally induced self-assembly processes in Ultrahigh Vacuum Conditions.

For the characterization, we first performed the SEM morphology studies together with SEM EDX Spectrum Image (SI) measurements of formed structures using SEM Quanta 3D FEG (1). Next, atomically resolved HAADF STEM measurements were performed on FIB-prepared sample cross-sections with FEI (S)TEM Titan3 G2 60-300 to reveal the details of atomic structure of the nanostructure morphology.

The collected SEM EDX SI data allowed us to quantify the chemical composition of the formed nanostructures after Blind Source Separation processing Fig. 1. This successful separation of SEM EDX spectra of nanostructures from other signals overcomes the spatial resolution limitations of SEM EDX (quantitative chemical analysis of nanostructures of the size ~50 nm) (1).

The atomic structure of nanostructures and their interface was investigated by atomically resolved HAADF STEM. This allowed us to characterize the Au-rich phase at the nanostructure and to derive the epitaxial orientation relationship between the nanostructure and the AIII-BV substrate. We observed that the interface type changes systematically with the AIII-BV semiconductor binding energy. We also found that the Au content in the nanostructure depends on the AIII-BV semiconductor binding energy. We observe that the Au diffusion into the bulk semiconductor happens only for InSb, which results in the formation of the gold-enriched subsurface region. We employed the Machine Learning HAADF Image quantification to quantify the observed Au diffusion process at the atomic level in InSb (2). The results of the performed image quantification show that the amount of Au diffusion is different for indium and antimony atomic columns Fig. 2. This diffusion effect was confirmed and further studied in detail by the Density Functional Theory calculation with the inclusion of the temperature via vibrational analysis (2).

Our systematic studies at the atomic level allowed us to suggest the mechanism and the process-driven main chemical reaction running on the sample surface of AIII-BV semiconductor.

References:

(1) B.R. Jany, A. Janas, F. Krok, Nano Letters, Vol. 17, Issue 11, 6507-7170 (2017)

(2) B.R. Jany, A. Janas, W. Piskorz, K. Szajna, O. Kryshtal, G. Cempura, P. Indyka, A. Kruk, A. Czyrska-Filemonowicz, F. Krok Chemically driven growth of Au rich nanostructures on AIII-BV semiconductor surfaces (2019) arXiv:1811.02488

Fig. 1: SEM EDX data at the nanoscale in the form of Spectrum Image from metallic nanowires (size ~50nm) together with results of Blind Source Separation which allows chemical quantification overcoming spatial limitations of SEM EDX (1).

Fig. 2: Machine Learning HAADF STEM image quantification of Au diffusion area formed in the Au/InSb nanowires system a). The Au concentration was determined separately for Sb and In atomic sublattice b)-c) (2).

Fig. 1

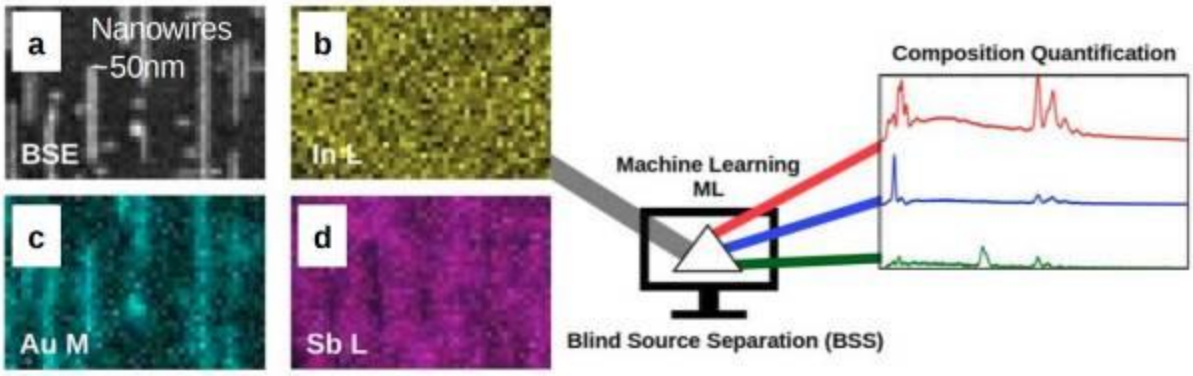
a
Nanowires
~50nm
BSE
b
In L
c
Au M
d
Sb L
Machine Learning
ML
Blind Source Separation (BSS)
Composition Quantification

Fig. 2

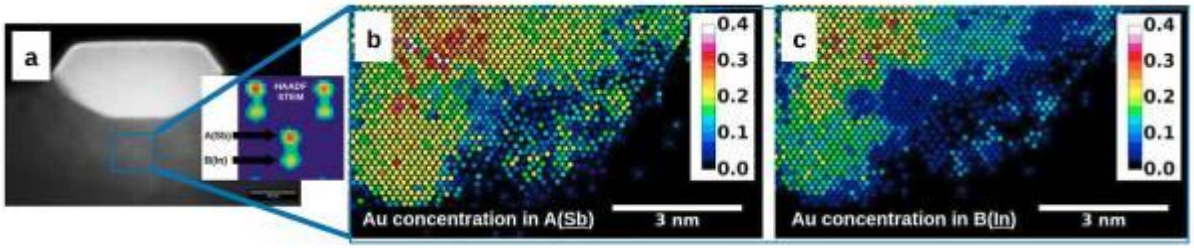
a
b
0.4
0.3
0.2
0.1
0.0
Au concentration in A(Sb)
3 nm
c
0.4
0.3
0.2
0.1
0.0
Au concentration in B(In)
3 nm

MS6.P029
Void Dynamics in Nanoscale Diffusion Couples of Au and Pd During Bimetallic Interdiffusion

S. W. Chee[1], Z. M. Wong[2], Z. Baraissov[1], S. F. Tan[1], T. L. Tan[3], U. Mirsaidov[1]

[1]National University of Singapore, Center for BioImaging Sciences, Singapore, Singapore
[2]National University of Singapore, Department of Chemistry, Singapore, Singapore
[3]Institute of High Performance Computing, Singapore, Singapore

Bimetallic nanoparticles (NPs) are promising materials for applications in catalysis, plasmonics and biomedical research. There is significant interest in synthesizing NPs with more complex morphologies and then modifying them with heat treatments to tailor their properties. In particular, hollow NPs can be created by exploiting the Kirkendall effect (KE). KE is a classic phenomenon in bulk metallurgy that is associated with the interdiffusion of two metals and void formation. It was found that monometallic NPs can transform into hollow nanostructures during oxidation due to KE. However, it is unclear if bimetallic NPs also become hollow during heating due to KE. One reason is the lack of direct studies that unambiguously correlate void formation with bimetallic interdiffusion.

Here, we study the interdiffusion of Au and Pd in core-shell nanoparticles. Pd is known to diffuse faster in Au compared to Au diffusing into Pd and so, NPs with Pd cores should form hollow core NPs because of KE.

We synthesized two types of core-shell NPs; Pd-core/Au-shell and Au-core/Pd-shell, and deliberately used cuboidal cores to make it easier to interpret the interdiffusion (Figure 1(a)). Morphological evolution of these NPs was followed during heating with both in situ transmission electron microscopy (TEM) and time-lapse scanning transmission electron microscopy (STEM) with energy dispersive x-ray spectroscopy (EDX) mapping.

The STEM-EDX maps from different temperatures show that the diffusion of Pd was indeed faster than Au. However, void formation occurred at the bimetallic interface for both NP types. Surprisingly, these voids then migrated towards the surface. See Figure 1(b) for an example of this behavior in a Au-core/Pd-shell NP. This unexpected behaviour cannot be explained by conventional theory about KE.

To address this discrepancy, we performed density functional theory calculations (Figure 2) for the vacancy formation energies at the bimetallic interface. Our calculations suggest that the higher formation energy of vacancies in Pd compared to Au can lead to a reversal of the expected vacancy flux towards Pd. Instead, vacancies diffused towards Au.

Our results show that KE in bimetallic NPs may not be as straightforward as commonly assumed. Although the bimetallic interface shifted in the direction expected for KE with Pd diffusing faster than Au, the hollowing behavior predicted in theory was not observed. More significantly, these *in situ* TEM studies provided novel observations of void migration in bimetallic NPs.

Fig. 1: (a) Schematics of the two Au-Pd nanoscale diffusion couples. (b) An image sequence showing the morphology of a Au-core/Pd-shell NP as it was heated from 200 °C to 600 °C. Two of the voids that formed are highlighted as 1 and 2. Between 430 °C and 575 °C, void 1 migrated from the bimetallic interface to the surface. Void 2 changed positions intermittently between 575 °C and 600 °C, and after 60 s at 600 °C.

Fig. 2: Change in vacancy formation energy as a vacancy in Pd diffuses across the bimetallic interface into Au. Two geometries were modelled to account for the strain introduced by lattice mismatch between Au and Pd. A Pd vacancy diffusing into Au also means that a Au atom crosses the bimetallic interface. In (c) and (d), the orange and cyan points compare the cases where the Au atom stays at the interface or continues to diffuse into Pd (denoted by *).

Fig. 1

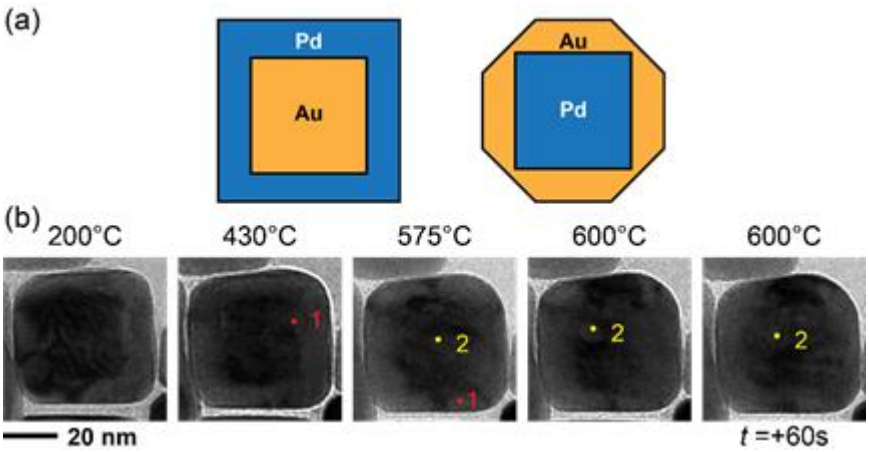
(a)
Pd
Au
Au
Pd
(b)
200°C
430°C
575°C
600°C
600°C
1
2
1
2
2
20 nm
t =+60s

Fig. 2

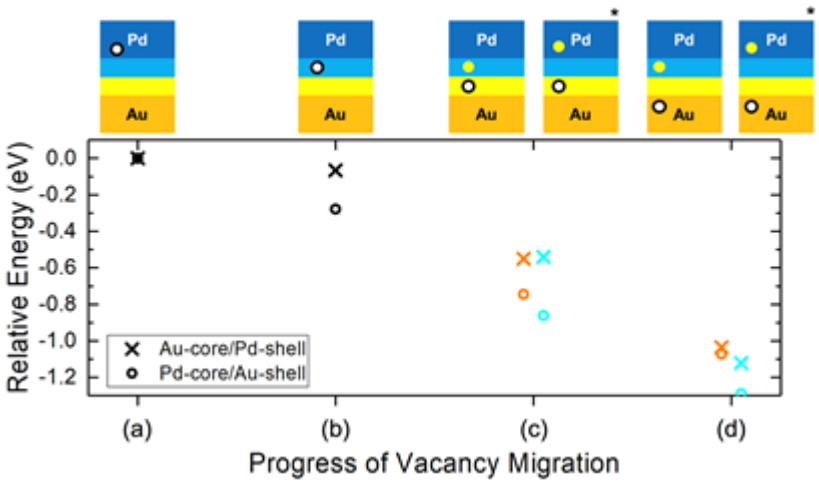
Pd
Au
Relative Energy (eV)
0.0
-0.2
-0.4
-0.6
-0.8
-1.0
-1.2
Au-core/Pd-shell
Pd-core/Au-shell
(a)
(b)
(c)
(d)
Progress of Vacancy Migration

MS6.P030
Insights in pore-interconnected hollow (Sn,Ti)O_2 nanoparticle networks for lithium-ion battery anodes

J. Lim[1], J. H. Um[2], K. Hengge[1], W. S. Yoon[2], J. K. Lee[3], Y. E. Sung[3], C. Scheu[1]

[1]Max-Planck-Institut für Eisenforschung GmbH, Düsseldorf, Germany
[2]Sungkyunkwan University, Suwon, South Korea
[3]Seoul National University, Seoul, South Korea

Nanostructured TiO_2 is a promising anode material in Li ion batteries (LIB) because of its relatively high working voltage (~1.7 V vs. Li/Li^+) and very small volume changes (~4%) upon (de)intercalation of Li ions. TiO_2 has a rapid discharge/charge behavior, long cycle life, and high safety. However, the lower theoretical capacity of TiO_2 than commercial graphite (Li_1TiO_2, 335 mAh g^{-1}) demands the use of an additional high capacity material. One possible candidate is SnO_2 which is also a promising anode material due to its high theoretical capacity of 783 mAh g^{-1}. The Li storage mechanism of SnO_2 is the conversion ($SnO_2 + 4Li^+ + 4e^- \rightarrow Sn + 2Li_2O$) and the following alloying/de-alloying reaction ($Sn + xLi^+ + xe^- \leftrightarrow Li_xSn$, $0 < x \leq 4.4$). The large amount of Li per Sn induces a large volume change (~300%) which results in a pulverization of active material. Because this the material is disconnected from the electrical contact, the capacity is decreasing. Considering the similar cationic size of Ti^{4+} (0.68 Å) and Sn^{4+} (0.71 Å), and common crystal structure formation of TiO_2 and SnO_2 into rutile phase, a (Sn,Ti)O_2 solid-solution nanocomposite can be obtained. This nanocomposite is expected to have a high Li storage ability and long cycle stability because of two times higher capacity of SnO_2 than TiO_2 and the much smaller volume variation ~4% of TiO_2, compared to the ~300% of SnO_2.

In this work, we characterized in depth (Sn, Ti)O_2 nanoparticle networks which are used as anode material in LIB. The (Sn,Ti)O_2 nanoparticle networks were synthesized via a soft template method applying polyacrylic acid (PAA) aggregates as a core (1). PAA@(Sn,Ti)O_2 core@shell nanoparticles were obtained by hydrolysis and condensation reaction of Sn^{4+} and Ti^{4+} precursor in the presence of PAA aggregates. After removing the PAA core by a simple washing step, hollow (Sn,Ti)O_2 nanoparticle networks are expected to form. To confirm the homogeneous mixing of Sn^{4+} and Ti^{4+}, energy disperse X-ray spectroscopy was used. The hollow morphology and the crystalline structure was analyzed by (scanning) transmission electron microscopy and electron diffraction pattern. Especially, it was crucial to apply 3D electron tomography to understand the nature and connectivity of pores, which could improve the reaction kinetics between the anode material and electrolyte. The 3D electron tomography reconstruction revealed that the pores are interconnected and confirmed that the (Sn,Ti)O_2 nanoparticles are hollow. In terms of the LIB performance, the enhanced lithium storage ability of the hollow (Sn,Ti)O_2 nanoparticles, the consistent alloying/de-alloying reactions of Sn through the Sn-O-Ti bonding structure were monitored with long cycle life. The detailed synthesis and characterization, especially 3D electron tomography of the hollow (Sn,Ti)O_2 nanoparticles will be discussed.

References:

(1) J. H. Um*, J. Lim*, K. Hengge, C. Scheu, W.-S. Yoon, J.-K. Lee, Y.-E. Sung, *Composites Part B: Engineering* 2019**,** *166*, 613-620. (*equally contributing authors)

J. Lim acknowledges financial support from the Alexander von Humboldt Foundation, Germany.

Fig. 1: (a) Scanning transmission electron microscopy image, (b) 3D reconstructed volume, and (c) and (d) cross-sectioned volume of hollow (Sn, Ti)O_2 nanoparticle. Modified images from (1)

Fig. 1

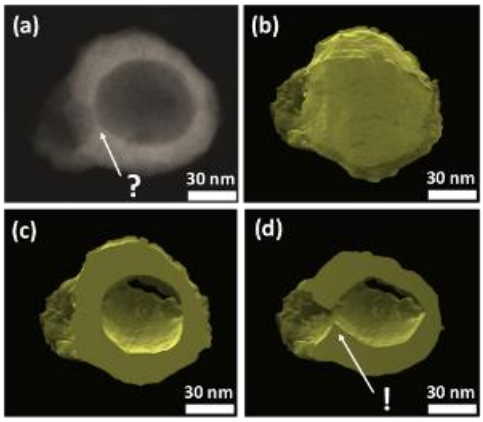

MS6.P031
Electron microscopy investigations of Lanthanide-doped oxides

R. Changizi[1], S. Zhang[1], T. Schwarz[1], C. Scheu[1]

[1]The Max-Planck-Institut für Eisenforschung GmbH, Nanoanalytics and Interfaces, Duesseldorf, Germany

Doping lanthanides into semiconductors holds great potential in many light emitting devices (1). Presence of very sharp luminescent lines in their transition spectra has made lanthanides fascinating to work with. Due to the selection rules, lanthanides have to be doped in a semiconductor host in order to be able to emit light. To have a better understanding of the luminescent properties of these elements, various hosts have been used since the early discovery of the 4f elements to present (2).

This research focuses on the study of Praseodymium (Pr) doped into KCa2Nb3O10as the semiconductor host considering two nominal different Pr concentration. Our goal is to correlate the acquired emission spectrum of each particle with its chemical composition and corresponding crystal structure. In this regard, scanning electron microscopy (SEM) is used to investigate the morphology of the particles, transmission electron microscopy (TEM) is performed to understand the crystal structure and the emission spectra are acquired using a cathodoluminescence (CL) detector attached to a SEM. Energy dispersive X-ray spectroscopy (EDX) is used to analyze the composition. All measurements have been done at identical location by using finder grids.

Most of the particles are micrometer sized and have a facetted morphology. EDX measurements reveal different chemical compositions such as changes in Pr to Nb ratio. CL spectra for individual host and Pr doped particles are successfully acquired. Differences in chemical composition lead to different transition peaks. The transition peaks are labeled based on comparison with literature where Pr was doped into four different host including LnCl3, LaAlGe2O7, K2LaCl5and heavy metal borate glass systems. Moreover, the CL spectra show a different bandgap for our host particles compared to literature values which indicates the presence of defects. This was also confirmed in TEM where e.g. grain boundaries were found within the individual particles. A correlation between the chemical composition of each particle and its spectrum was achieved and the presence of defects in our particles has been proved.

References:

(1) Di Bartolo, B. and Forte, O. (2006). Advances in Spectroscopy for Lasers and Sensing.Dordrecht: Springer, pp.403-432.

(2) Hehlen, M., Brik, M. and Krämer, K. (2013). 50th anniversary of the Judd-Ofelt theory: An experimentalist"s view of the formalism and its application. Journal of Luminescence, 136, pp.221-239.

The authors would like to thank Christian Ziegler and Bettina Lotsch for providing the samples.

Fig. 1

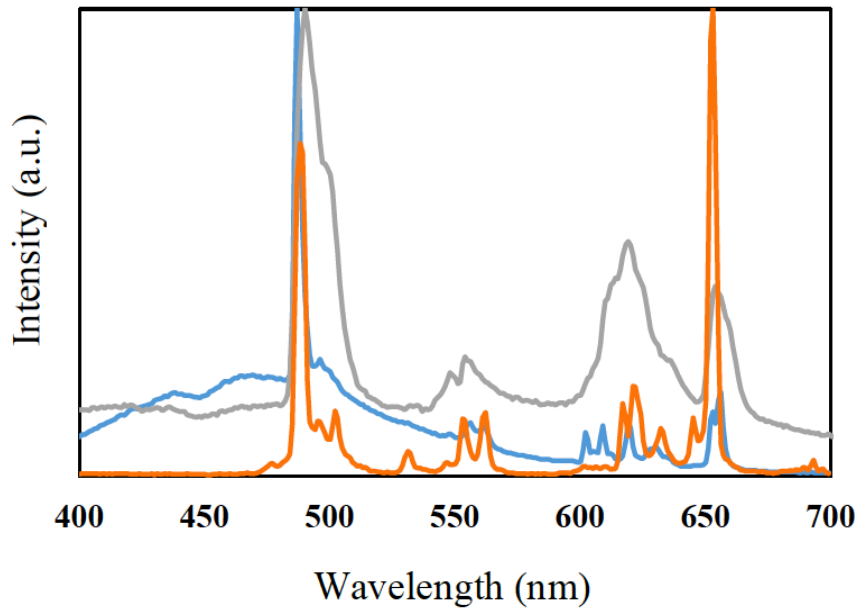

Figure 1: Different emission spectra observed for Pr doped particles having different chemical compositions.

Fig. 2

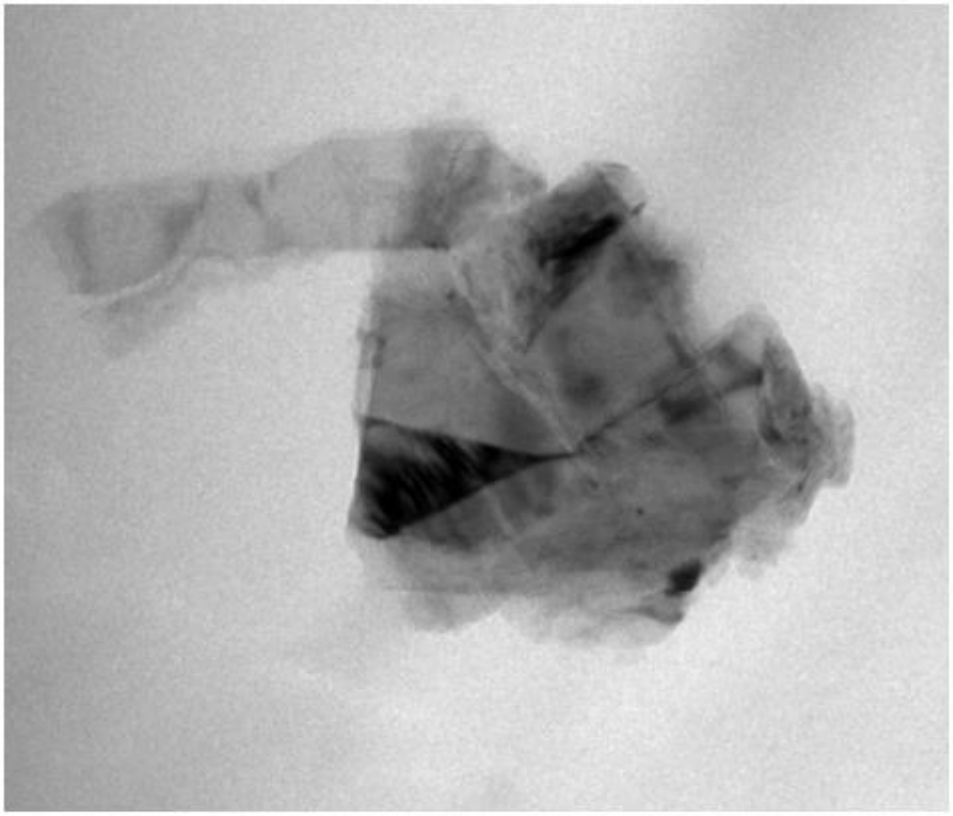

Figure 2: TEM image of a micrometer sized particle showing several planar defects.

MS6.P032
The microscopic structure of ballistic graphene nanoribbons

M. Gruschwitz[1], H. Schletter[1], I. Alexandrou[2], R. Egoavil[2], C. Tegenkamp[1]

[1]TU Chemnitz, Chemnitz, Germany
[2]Thermo Fisher Scientific, Eindhoven, Netherlands

Epitaxial graphene nanoribbons on SiC were shown to host ballistic transport channels, even under ambient conditions (1). Thereby, the transport along these 40 nm wide ribbons, which are grown via self-assembly on sidewalls of SiC (0001) mesa structures, depends crucially on atomistic details of the structure (2). Here we present high resolution STEM investigations done on such ribbons.

The focus in research lays on epitaxial graphene on structured 6H-SiC. A complete understanding of this mesoscopic system requires investigations of the structure at atomic scale as well as the interactions between the atoms. If the relation between the structure and the outstanding electronic properties is known, a controlled influence on the properties of the mesa structure by tuning the structural properties is possible. This is a big leap towards large scale application in nanoelectronics.

Structural and electronic properties of sidewall nanoribbons compared to epitaxial graphene on SiC (0001) are investigated by STEM. The cross section sample preparation was achieved using a dual beam FIB. A double CS corrected ThemisZ STEM from ThermoFisher that was operated at 80 keV provided insights in the atomic structure. The system also allowed spectroscopic analysis by EDX and EELS at atomic resolution with a narrow beam energy dispersion amounting to 0.2 eV.

For ribbons along the (1-100)-direction STM reveals zig-zag edge nanoribbons. (2) Thereby, the lower edge merges into the SiC (0001) terrace giving rise to hybridization and formation of an edge state. This growth mode is confirmed by STEM investigations. Cross sectional STEM reveals freestanding graphene separated from the facet by more than three times the distance of graphene on SiC (0001). Moreover, the EDX and EELS capabilities of the HRTEM were used to characterize the surface near areas in detail. Unlike other groups (3) we conducted depth resolved EELS analysis. Upon growth of graphene by desorption of silicon by high temperature annealing, the topmost three SiC bilayers reveal an increasing silicon deficiency towards the interface. This depth dependent concentration confirms XPS measurements applied at these systems. (4, 5) However, a rise of sp2-hybridization has already been observed at a depth of one 6H-SiC unit cell. Compared to the facets, it turns out that these residual imperfections in SiC are more frequent at (11-2n) terraces. Combined with a weakened bonding of surface atoms at the sidewall a premature decomposition at the facet is observed, resulting in selectively growing graphene nanoribbons. The absence of a buffer layer at the facet was confirmed by EELS measurements.

The freestanding graphene nanoribbons could be confirmed by STEM micrographs. We found a gradient decomposition of the substrate due to sample production. The weakened bonding of sidewall atoms allow a premature decomposition at the facet resulting in selective growth.

References:

(1) J. Aprojanz et al., Nat. Comm. 9, 4426.

(2) A.A Zakharov et al., arXiv:1809.10001.

(3) G. Nicotra et al., ACS Nano 2013, 7, 4, 3045-3052.

(4) J.D. Emery et al. Phys. Rev. Lett. 111, 215501.

(5) M. Conrad et al., Phys. Rev. B 96, 195304.

MS6.P033
TEM-based analysis of the crystal structure of a Ge-rich layer sandwiched between spintronic Fe_3Si

H. Kirmse[1], B. Jenichen[2], E. Willinger[3], X. Huang[3], B. Haas[1], C. T. Koch[1]

[1]Humboldt University of Berlin, Physik AG SEM, Berlin, Germany
[2]Paul Drude Institute Berlin, Berlin, Germany
[3]Fritz Haber Institute Berlin, Berlin, Germany

The magnetic properties of Fe_3Si make it an excellent candidate for spintronic applications (1). For a switchable device, two layers of Fe_3Si have to be separated by a thin semiconducting interlayer. Ge was chosen for this interlayer having a thickness of 3 nm only. Parallel alignment of the magnetization of the two adjacent Fe_3Si layers passes current through the device while antiparallel alignment blocks. The device performance drastically depends on the structure-related physical properties of the semiconductor interlayer.

This work aims at both, crystal structure and composition analysis of the semiconductor interlayer by transmission electron microscopy (TEM)-based techniques. In particular, nano-beam diffraction (NBD), high-angle annular dark-field atomic-resolution scanning TEM (HAADF ARSTEM) imaging and energy dispersive X-ray spectroscopy (EDXS) were applied for full crystallographic phase analysis.

Sharp interfaces between the different layers were ensured by solid phase epitaxy (2) which is a two-step approach consisting of a layer deposition at 150 °C and recrystallization at 300 °C. From bulk crystals the Fm3m space group is expected for Fe_3Si and Fd3m for Ge (3). For structure analysis along two different directions laying in-plane to the interfaces viz. [100] and [110] two samples were prepared conventionally including mechanical pre-thinning and final Ar^+ ion milling. Both, NBD and EDXS were performed at a TEM/STEM JEOL 2200FS. HAADF ARSTEM imaging was performed at a probe Cs-corrected JEOL ARM200. Both instruments were operated at an accelerating voltage of 200 kV.

The detected crystallographic phase of Fe_3Si perfectly corresponds to both, the expected crystal structure and the chemical composition. In contrast to that, superstructure reflections along (001) are observed for the nominal Ge layer. This implies ordering along [001]. Moreover, EDXS revealed a composition ratio of about 6:3:1 for Ge:Fe:Si. Both results point to an unexpected crystallographic phase of the semiconductor interlayer (4). For gaining real space information, HAADF ARSTEM imaging was performed along the [100] and [110] directions (see Fig. 1, center and right image, correspondingly). Bright spots correspond to atomic columns. The brightness is proportional to the mean atomic number of the individual atomic column. Both projections consistently reveal ordering along [001]. Brighter spots are assigned to Ge and weaker spots to Fe columns. Filled interlayers exhibit a larger distance along (001) of z = 0.52 compared to z = 0.48 for the empty layers.

The semiconductor interlayer is composed of tetragonal (P4mm) layered $FeGe_2$ (see Fig. 1 left) (4). The deviation of the position of the atomic columns from the expected positions at 0.00 and 0.50 for Ge and 0.75 for Fe is most likely due to the relaxation of strain introduced by the ordering.

References:

(1) K. Hamaya et al., Appl. Phys. 113 (2013) 183713.

(2) S. Gaucher et al., Appl. Phys. Lett. 110 (2017) 102103.

(3) B. Jenichen et al., Phys. Stat. Sol. A 206 (2009) 1740.

(4) B. Jenichen et al., Phys. Rev. Materials 2 (2018) 051402.

Fig. 1: Unit cell of FeGe2 (left) and HAADF ARSTEM images of the structure along (100) (center) and [110] (right).

Fig. 1

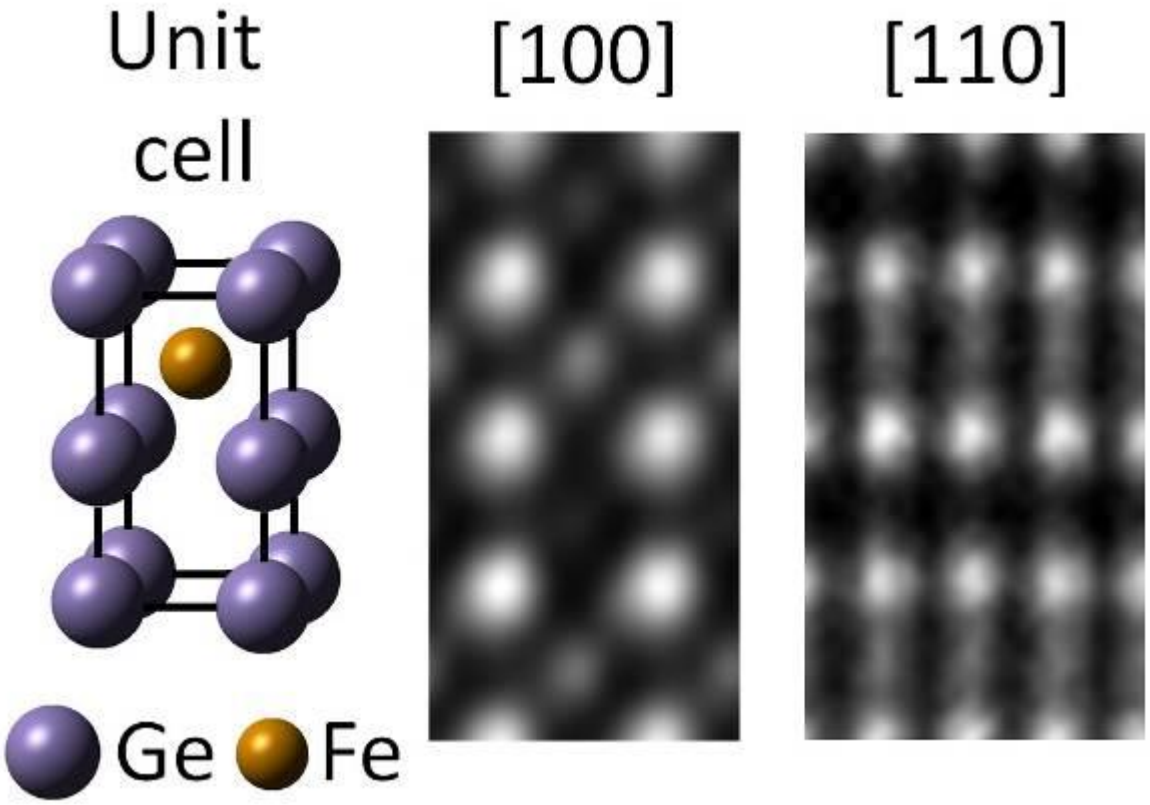

MS6.P034
DYNAMICS OF DIRHENIUM MOLECULE WITH MULTIPLE BONDS

K. Cao[1], S. T. Skowron[2], J. Biskupek[1], C. T. Stoppiello[2], C. Leist[1], E. Besley[2], A. N. Khlobystov[2], U. Kaiser[1]

[1]Ulm University, Ulm, Germany
[2]University of Nottingham, School of Chemistry, Nottingham, United Kingdom

The multiple bonds between metal atoms relate to the most basic chemical nature of the relevant molecules containing metal-metal core and their reactions (1). The discovery of the Re–Re quadruple bond in $[Re_2X_8]^{2-}$ in 1964 opened the door to the new world of multiple metallic bond chemistry (2, 3). The characteristics, including bond length, bond order, energetics and spectroscopic signatures, of these compounds are conventionally analyzed by the nuclear magnetic resonance (NMR), infrared spectroscopy (IR), X-ray diffraction (XRD) *etc.* applying bulk crystals or solution as specimens (4-6). The existence of unligated M-M cores, which are actually the metallic homonuclear diatomic molecules with multiple bonds, have been theoretically predicted and experimentally detected in the rare gas matrices (7, 8).

However, the preparation and analysis of an isolated individual metallic homonuclear diatomic molecule containing multiple bonds have not been realized. Understanding the multiple bonds in metallic diatomic molecule is important for studying the compounds with metal-metal core and related relations.

By applying the C_C/C_S-corrected SALVE (Sub-Ångström Low-Voltage Electron microscopy) instrument, we directly observed with atomic resolution the dirhenium molecules containing multiple bonds confined in a single walled carbon nanotube (SWNT). The Re_2@SWNT sample is prepared by inserting $Re_2(CO)_{10}$ molecules into end-opened SWNT as precursor followed by washing. The dirhenium molecules are formed by cleaving $Re_2(CO)_{10}$ using the incident electron beam in TEM with an electron acceleration energy of 80keV.

Utilizing the electron beam both as stimulus and probe, the dynamics and the bond order changing of dirhenium molecule are monitored (Figure 1). Direct imaging of the Re-Re bond breaking process reveals a high amplitude vibrational stretch of Re-Re, once the bond order decreases below 1, preceding the bond dissociation.

In this study, we generated Re_2 molecules where the Re-Re bond is unsupported by ligands. Imaging at atomic-scale revealed the dynamics of Re_2 adsorbed on a graphic lattice. It allowed direct measurement of Re-Re bond lengths for individual molecules that changes in discrete steps correlating with bond order from 1 to 4, depending on the orientation of the Re_2 molecule with respect to the carbon lattice.

References:

(1) F. A. Cotton, *et.al,* Multiple bonds between metal atoms (book), *Springer Science and Business Media,* (2005).

(2) F. A. Cotton, *et.al, Science,* 145, 1305-1307 (1964).

(3) F. A. Cotton, *Inorg. Chem.,* 4, 334 – 336 (1964).

(4) T. Nguyen, *et.al, Science*, 310, 844-847 (2005).

(5) F. R. Wagner, *et.al, Nat. Chem.,* 1**,** 529-536 (2009).

(6) K. A. Kreisel, *et.al, J. Am. Chem. Soc.*, 129, 14162-14163 (2007).

(7) L. Gagliardi, *et.al, Nature,* 433, 848-851 (2005).

(8) Z. Hu, *et.al, J. Chem. Phys.* 95, 2206-2209 (1991).

Fig. 1: A 80kV HRTEM time-series showing dirhenium molecule movements under electron beam irradiation acquired with the SALVE instruction.

Fig. 1

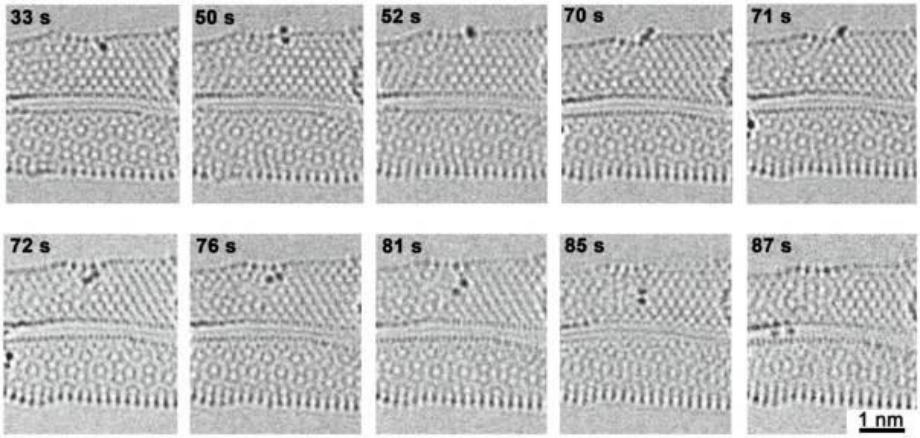

MS6.P036
Imaging Zeolite A

G. Algara-Siller[1], C. Pratsch[1], D. Ivanov[1], R. Schlögl[1,2], T. Lunkenbein[1]

[1]Fritz-Haber-Institute der Max-Planck-Gesellschaft, Inorganic Chemistry, Berlin, Germany
[2]MPI für Chemische Energiekonversion, Heterogeneous Reactions, Mülheim a.d.R., Germany

Nanoporous materials such as zeolites have had a great impact in industrial processes due to their wide range of framework arrangements and to the flexibility to adjust their properties depending on the extra-framework atoms, type of cages and channel sizes. These extra framework atoms are an important constituent for the catalytical activity. Although the framework of zeolites has been described extensible by diffraction methods, the localization of the extra-framework atoms has been experimentally challenging because these atoms are delocalized within the structure. Zeolites are, in general, beam sensitive materials. The radiation damage in zeolites can be correlated to 3 parameters: water content, types of extra-framework atoms, and the Si to Al ratio (the smallest achievable ratio being one and the lower this ratio the more sensitive). Therefore, electron microscopy works have taken great efforts in sample preparation (dealumination, drying or ion exchange) and advanced characterisation techniques to be able to atomically resolve the structure and to describe the average position of the extra-framework atoms in the structure (1).

In this work we aim to obtain the optimum instrument settings and digital processing algorithms to atomically resolve the framework and the extra-framework atoms from a highly sensitive material such as Zeolite A. At the same time, deriving possible morphological and phase changes within the crystal structure.

The zeolite A used in this study has a Si to Al ratio of 1, Na and/or K as extra-framework cations and a high water content. The TEM characterisation was performed in an aberration-corrected JEOL ARM 200F and FEI Titan 80-300 operated, both, at 200 kV under low dose rate imaging conditions (<1000 e/nm^{2}s). Recorded sets of images were, firstly, drift corrected using FFT cross-correlation. The resulted drift-corrected set was afterwards processed by template matching with hierarchical clustering and then averaged.

In the resulting atomically resolved image, the extra-framework atom positions are visible as well as the main aluminosilicate framework. The results presented were achieved by finely tuning the sample preparation i.e. big cubic zeolite A crystals of approx. 15 um lateral dimensions, characterising the dose rate limitations (max dose 1000 e/nm^{2}s), and optimizing case by case (e.g. size and number of the templates),the image post-processing algorithms.

This work presents, thus, a methodology towards electron microscopy characterisation of radiation sensitive materials, exemplified here, by the atomic structural description of zeolite A (LTA framework).

References:

(1) K. Yoshida et al. Scientific Reports. Vol 3 (2013).

MS6.P037
In-situ TEM measurements of temperature-dependent reshaping of gold bypiramids and nanotriangles

A. Zak[1], P. Obstarczyk[2], N. Tarnowicz[2], R. Deska[2], K. Matczyszyn[2], J. Olesiak-Banska[2], L. Szczepanski[1]

[1]Wroclaw University of Science and Technology, Electron Microscopy Laboratory, Wroclaw, Poland
[2]Wroclaw University of Science and Technology, Advanced Materials Engineering and Modelling Group, Wroclaw, Poland

Nanostructures such as gold nanoparticles (GNPs), exhibiting unique plasmonic and physicochemical properties, have found their applications in various advanced fields. The growing interest in such structures is associated with the need for a better understating of their nature, including their thermal stability, e.g. post-synthetic reshaping of GNPs via thermal route (using femtosecond laser) has been previously reported (1). TEM imaging allows for a clear description of the particle morphology since the extinction spectra do not always give unequivocal results. Our TEM with temperature control technique also enables to describe thermal or photothermal stability of synthesized nanoparticles (2).

The aim of the study was to examine the impact of temperature treatment on the shape and plasmonic properties of gold nanobipyramids and nanotriangles.

Gold bipyramid nanoparticles were synthesized by a modified method of Weizzman et al. through seed-mediated growth (3). The obtained products were then purified by silver overgrowth, flocculation, and silver etching. Gold nanotriangles were synthesized via previously reported biological approach (4), using mint extract (*Mentha piperita*) as a bioreducing, capping and stabilizing agent. The in-situ heating experiment was performed on a modified Hitachi heating stage, using a Hitachi H-800 TEM. The sample was freshly pipetted with 2µl of aqueous solution on a carbon on copper grid and air-dried.

Since plasmonic properties of gold nanoparticles are dependent on the nanostructure shape and size, the extinction spectra of thermally degraded bipyramids and triangles tend to brad and blue-shift. During the in-situ heating of triangles, the particles were shape-stable up to 695 K. Then, in a very narrow temperature range, rapid degradation and spheroidization occurred. Polygonal structures exhibited slightly lower stability than triangular structures (Fig. 1). Further heating to temperature of 900 K did not cause any significant changes in morphology. Micrometric triangular structures (not shown in the picture) were stable over the entire temperature range. In situ heating of the bipyramid structures did not cause any structural changes up to 500 K. Above this temperature it was possible to observe the rounding of one or both ends of the nanoparticles, without significantly marked one or two-sided nature of this process (Fig. 2). This enabled to partially achieve asymmetrical structures not described in the literature previously.

References:

(1) M. Gordel, J. Olesiak-Banska, K. Matczyszyn, C. Nogues, M. Buckleb, M. Samoc, Post-synthesis reshaping of gold nanorods using a femtosecond laser, Phys. Chem. Chem. Phys., 2014 (16), 71.

(2) M. Klekotko, J. Olesiak-Banska, K. Matczyszyn, Photothermal stability of biologically and chemically synthesized gold nanoprisms, J Nanopart Res, 2017 (19), 327.

(3) J.-H. Lee, K. Gibson, G. Chen, Y. Weizmann, Bipyramid-templated synthesis of monodisperse anisotropic gold nanocrystals, Nat Commun, 2015 (6), 7571.

(4) M. Klekotko, K. Matczyszyn, J. Siednienko, J. Olesiak-Bańska, K. Pawlik, M. Samoć, Bio-mediated synthesis, characterization and cytotoxicity of gold nanoparticles, Phys. Chem. Chem. Phys. 2015 (17), 43.

Fig. 1: Nanotriangles shape evolution during heating experiment.

Fig. 2: Nanobypiramids shape evolution during heating experiment.

We acknowledge funding from First Team "NONA - nonlinear optics, nanoparticles and amyloids".

Fig. 1

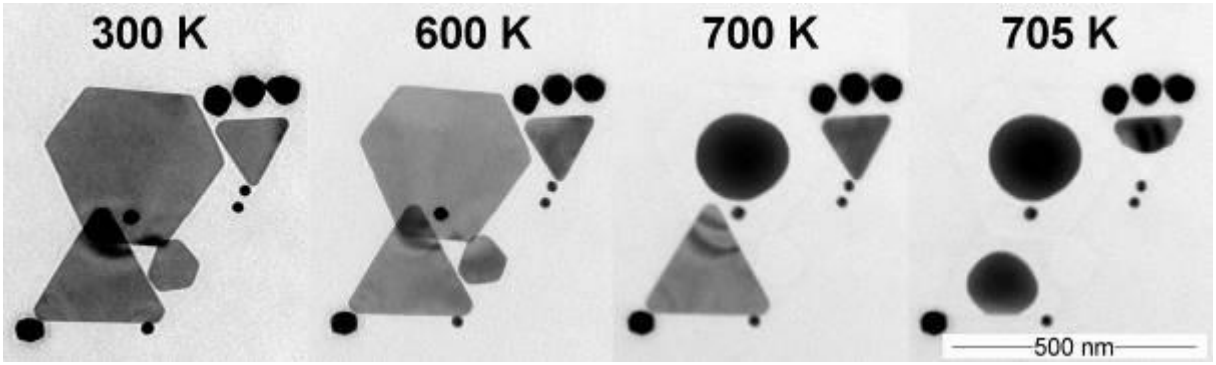

Fig. 2

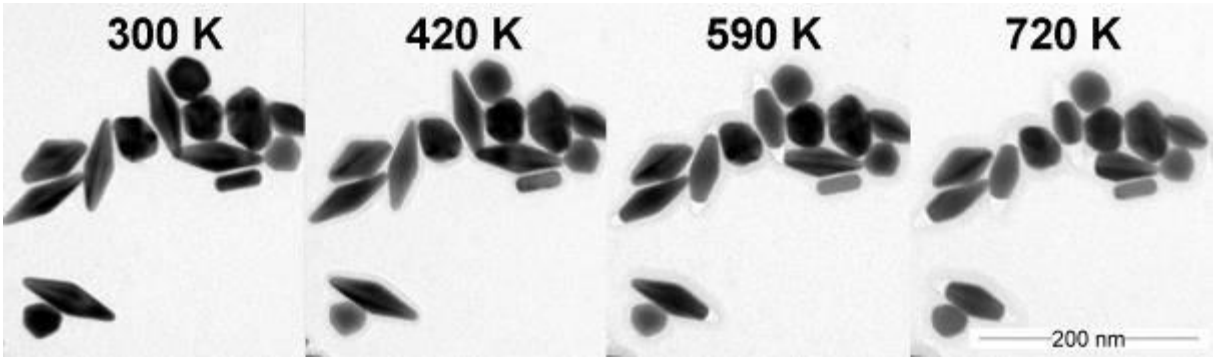

MS6.P038
Plasmonic properties of silver amalgam nanoparticles studied by analytical transmission electron microscopy

M. Horák[1], F. Ligmajer[1,2], T. Šikola[1], M. Fojta[2,3], A. Daňhel[2]

[1]CEITEC, Brno University of Technology, Brno, Czech Republic
[2]Institute of Biophysics, Czech Academy of Sciences, Brno, Czech Republic
[3]CEITEC, Masaryk University, Brno, Czech Republic

Silver amalgam is one of the most suitable solid electrode materials in electroanalysis of various reducible organic and inorganic compounds. These include heavy metals, agrochemicals, colorants, drugs, environmental pollutants, or biologically important compounds such as DNA, proteins and their constituents, and vitamins. The main advantage of silver amalgam within this context is its wide cathodic potential window, high mechanical stability, adequate sensitivity, and advantageous strong interaction with biopolymers (e.g. DNA and proteins).

Nanostructuring the amalgam promises improved electrochemical performance and brings along the prospect of plasmonic activity. However, currently there is a lack of knowledge about the optical properties of nanostructured or even bulk silver amalgam which prevents its using in spectroelectrochemical and photochemical studies. We present a study of optical properties of silver amalgam and demonstrate the plasmonic nature of its nanoparticles.

To understand the nature of plasmonic modes in silver amalgam particles, we focused on studying single nanoparticles by analytical transmission electron microscopy including EDS for material analysis and EELS for measuring the plasmon resonances. Silver amalgam nanoparticles were prepared by controlled electrodeposition on a conductive indium tin oxide (ITO) support from a mixed solution of silver and mercury ions (1). In order to prepare the samples for EELS, silver amalgam nanoparticles were washed off the ITO into demineralized water in an ultrasonic bath and the resulting solution was dropped and dried on a standard silicon nitride membrane for TEM.

A typical rod-shaped nanoparticle is shown in Fig. 1. The chemical composition of this amalgam nanoparticle measured by EDS is homogeneous and in weight percent corresponds to 55% of Ag 45% of Hg. The rod-shaped silver amalgam nanoparticle exhibits three different resonant modes which were also complemented by the numerical simulations using boundary element method (BEM): the longitudinal dipole at 1.77 eV, the transversal dipole mode at 2.8 eV, and the quadrupole mode at 3.2 eV. By changing the size of the nanoparticle, plasmon resonances can be tuned from ultraviolet to mid-infrared region.

Our results establish silver amalgam nanoparticles as promising candidates for applications within photochemistry and spectroelectrochemistry, where the synergy between their plasmonic and electrochemical qualities can be fully utilized (2).

References:

(1) A. Daňhel, F. Ligmajer, T. Šikola, A. Walcarius, M. Fojta, Electrodeposition of Silver Amalgam Particles on ITO - Towards Novel Electrode Material, J. Electroanal. Chem. 82 (2018) 53-59.

(2) Supported by Czech Science Foundation (17-23634Y), ERDF under the SYMBIT project (CZ.02.1.01/0.0/0.0/15_003/0000477), MEYS CR under the projects CEITEC Nano RI (LM2015041, 2016-2019) and CEITEC 2020 (LQ1601), and Brno University of Technology (CEITEC VUT-J-19-5945).

Fig. 1: Silver amalgam rod-shape nanoparticle: (a) STEM HAADF micrograph and chemical composition mapped by EDS, (b) ZLP and background subtracted EEL spectra integrated over the orange squares in (c) complemented by numerical simulation, (c) STEM ADF micrograph and measured EEL maps at the energy of peaks in (b), (d) simulation model of the rod followed by calculated EEL maps and calculated surface charge distribution at the energy of peaks in (b).

Fig. 1

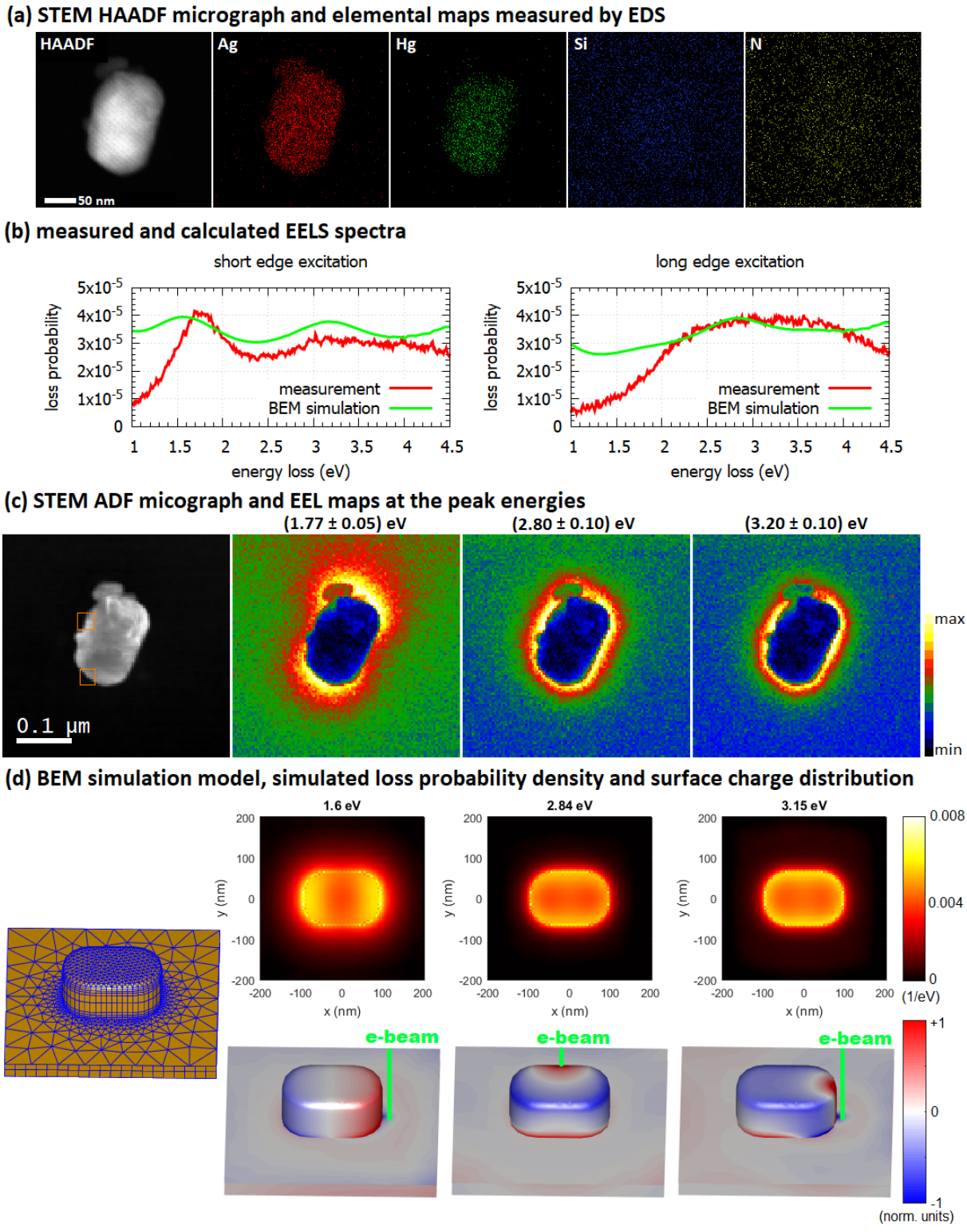
(a) STEM HAADF micrograph and elemental maps measured by EDS
HAADF
Ag
Hg
Si
N
50 nm
(b) measured and calculated EELS spectra
short edge excitation
long edge excitation
loss probability
energy loss (eV)
measurement
BEM simulation
(c) STEM ADF micograph and EEL maps at the peak energies
(1.77 ± 0.05) eV
(2.80 ± 0.10) eV
(3.20 ± 0.10) eV
0.1 µm
max
min
(d) BEM simulation model, simulated loss probability density and surface charge distribution
1.6 eV
2.84 eV
3.15 eV
y (nm)
x (nm)
(1/eV)
e-beam
(norm. units)

MS7.001 invited
ATOMIC-SCALE ASPECTS OF TWINNING IN MINERALS

A. Rečnik[1], V. Jordan[1], S. Tominc[1], N. Stanković[2], S. Drev[1], L. Jin[3], M. Komelj[1], V. Ribić[4], G. Dražić[5], V. Šrot[6], H. J. Kleebe[7], M. Pósfai[8], N. Daneu[1]

[1]Jožef Stefan Institute, Nanostructured Materials, Ljubljana, Slovenia
[2]Vinča Institute of Nuclear Sciences, Belgrade, Serbia
[3]Ernst-Ruska Centre for electron microscopy, Jülich, Germany
[4]Institute for Multidisciplinary Research, Belgrade, Serbia
[5]National Institute of Chemistry, Ljubljana, Slovenia
[6]Max Planck Institute for Solid State Research, Stuttgart, Germany
[7]Institut für Angewandte Geowissenschaften, Darmstadt, Germany
[8]University of Pannonia, Veszprém, Hungary

Twinning and related phenomena have always been an exciting topic for crystallographers. In their most strict sense, twins are produced by well defined symmetry operations that bring the two crystal domains into special crystallographic setting. However, quite often, we find twins that show chemical, as well as crystallographic disorder. Depending on their formation mechanism, we differentiate (i) deformation, (ii) transformation, (iii) growth, (iv) topotaxial and (v) attachment twins. The highest degree of lattice order can be seen in deformation twins, where slight lattice displacements due to mechanical strain cause the formation of twinned domain texture. The twin boundaries are devoid of any dopants. Examples of this type of twins are calcite, feldspars, quartz, etc. Transformation twins are characteristic for structures that are inherently polytypic with cubic to hexagonal stacking modulations. Due to alternating stacking the appearance of such twins is lamellar. Examples of transformation twins are: diamond-lonsdaleite, sphalerite-wurtzite, rock salt-troilite, etc. While dopants do not directly stabilize the twin boundaries, they can shift the transition temperature considerably. The third type of twins starts to cause controversy. They can not be described by simple crystallographic operations as their interface chemistry is changed. While the twin operation alone does not normally involve any change in chemistry, growth twins are known to accommodate elements that are normally not present in the parent structure. Based on the analogy with modular polytypes some researchers suggested that the local chemistry of growth twins must encompass these impurity elements in same structural manner as in the polysomatic phases (1). Confirmation of this hypothesis was not possible until the development of modern electron microscopy that enabled a direct insight into the structure of twin boundaries at the atomic scale. It has been shown that impurity elements stabilize the twin boundary that dictates the growth of such crystal as long as the dopant is available for their formation. Their further growth is characterized by reentrant angles. Fine examples of growth twins are sphalerite (2), spinel (3) and pyrite (4); sometimes the 'twins' are not really twins, such as bixbyite (5). The perfection of twin operation is further disrupted when twins form as a result of topotaxial replacement reactions. Here not only that the interface can be a layer of another phase, but also the relation between the twin domains is no more crystallographic. Good examples are twins of rutile (6), cassiterite or chrysoberyl. The highest disorder (crystallographic as well as chemical) can be seen on twins that are result of oriented attachment. An example is self-assembly of rutile (7). Once attached they can grow and adopt near-twin orientation. They are a result of orientation-specific macromolecular van der Waals interactions that are not yet fully understood. In this lecture examples of all twin types will be presented and discussed.

References:

(1) Takeuchi: Tropochemical cell-twinning. Tokyo (1997)

(2) Šrot et al.: Am. Mineralogist 88(2003)1809

(3) Daneu et al.: Phys. Chem. Minerals 34(2007)233

(4) Rečnik et al. Min. Mag. 80(2016)937

(5) Kleebe et al. Cryst. Res. Technol. 43(2008)1143

(6) Daneu et al. 99(2014)612

(7) Jordan et al. Sci. Reports 6(2016)24216

Fig. 1

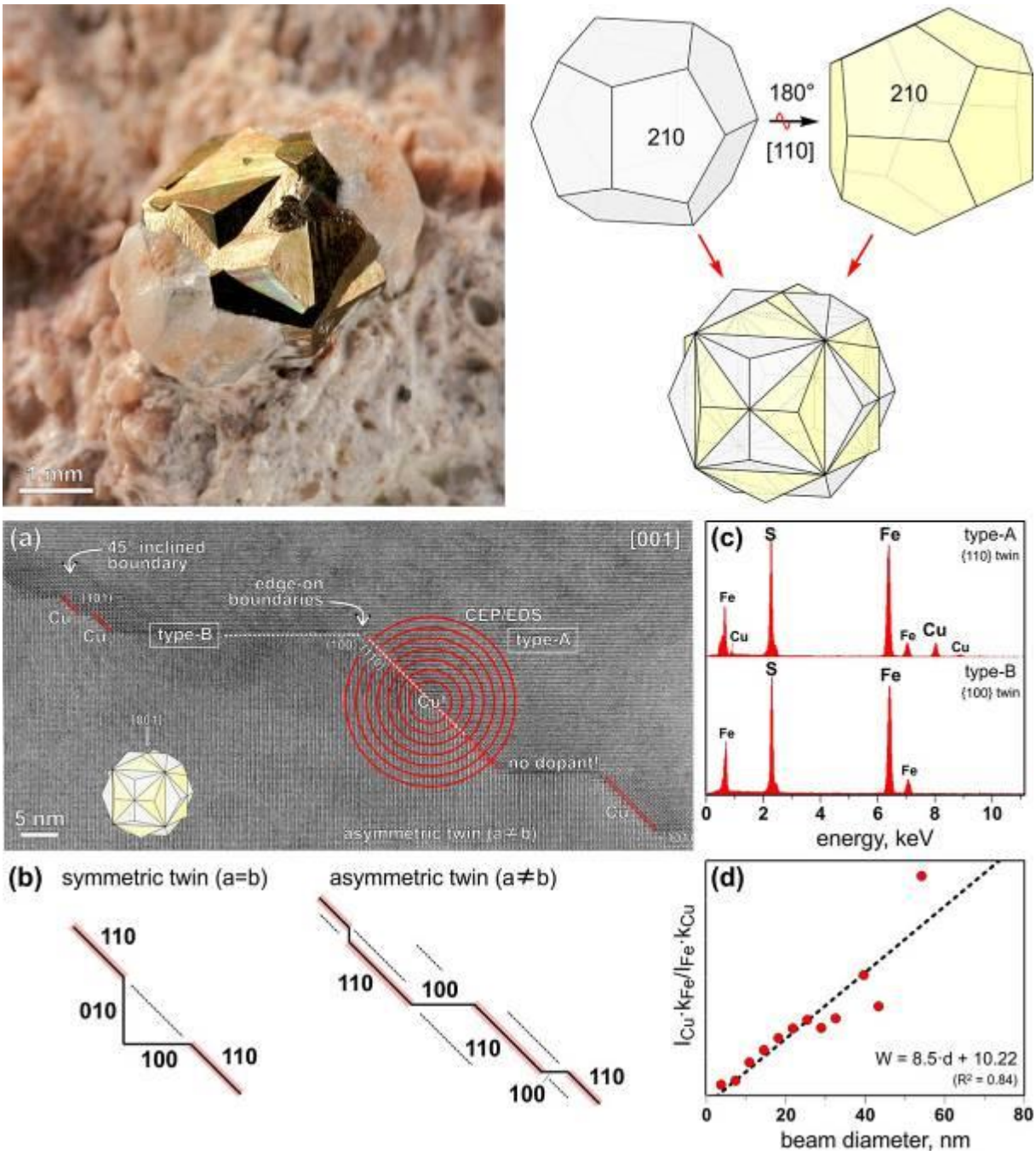
1 mm
210
180°
[110]
210
(a)
45° inclined boundary
edge-on boundaries
CEP/EDS
type-B
type-A
[001]
Cu
no dopant!
5 nm
asymmetric twin (a≠b)
(c)
type-A
{110} twin
type-B
{100} twin
S
Fe
Cu
energy, keV
(b)
symmetric twin (a=b)
asymmetric twin (a≠b)
110
010
100
(d)
W = 8.5·d + 10.22
(R² = 0.84)
beam diameter, nm

MS7.002
$Cd_xNb_6(O,F)_{16}$ – an almost perfectly ordered structure

F. Krumeich[1], M. Wörle[1]

[1]ETH Zürich, Department of Chemistry and Applied Biosciences, Zürich, Switzerland

The so-called pentagonal column (PC) is an important structural element in many transition metal oxides. The center of a PC is a pentagonal bipyramid MX_7 (M = Nb, Ta; X = O, F) which is attached to five octahedra MX_6 via edge-sharing (1). All polyhedra are located in this plane and connected by corner-sharing in the perpendicular direction forming the PCs. Such PCs frequently occur in structures related to the tetragonal tungsten bronzes, e.g. in $Nb_8W_9O_{47}$ (2). $LiNb_6O_{15}F$ consists of PCs only. In this structure type, two PCs build up a framework $Nb_{12}(O,F)_{32}$ with Li ions being incorporated into square channels (3). Several isostructural several niobium and tantalum oxides with different cations embedded inside the square channels exist as well. For the characterization of such bronze-type oxides, HRTEM has been a well-established and favored method since the 1970ies, mostly using Scherzer conditions with the cation positions appearing dark (4). In comparison, HAADF-STEM imaging is an excellent alternative with the advantage that the image contrast is directly interpretable due to incoherent scattering resulting in Z-contrast. Here we report on new insights into the cadmium compound $Cd_xNb_6(O,F)_{16}$ (5) obtained by single crystal X-ray diffraction and electron microscopy investigations.

The re-determination of the $Cd_xNb_6(O,F)_{16}$ structure revealed a shift of the Nb positions out of the mirror plane along the short *b* axis (space group *Pmma*). The composition was refined to $Cd_{0.25}Nb_6O_{14.5}F_{1.5}$. The ratio Cd:Nb was confirmed by EDXS measurements on ca. 30 crystals. SEM images show the frequent intergrowth of crystallites on the micrometer scale. In contrast, high-resolution HAADF-STEM images reveal the presence of a perfect order in wide areas. A single defect was discovered yet, namely a grain boundary which connects two perfectly ordered domains (Figure 1a). Remarkably, the structures in the adjacent areas are tilted by 4 degree in respect of each other (Figure 1b). Partly, the domains are coherently connected in a way observed here for the first time. Note that additional defects are present at irregular intervals. (6)

References:

(1) M. Lundberg, M. Sundberg, A. Magnéli, J. Solid State Chem. 1982, 44, 32-40.

(2) A. W. Sleight, Acta Chem. Scand. 1966, 20 1102-1112.

(3) M. Lundberg, Acta Chem. Scand. 1965, 19, 2274-2284.

(4) S. Iijima, J.G. Allpress, Acta Crystallogr. A 1974, 30, 22-29.

(5) F. Krumeich, R. Gruehn, Z. anorg. allg. Chem. 1990, 580, 95-102.

(6) Electron microscopy was performed at the Scientific Center for Optical and Electron Microscopy (ScopeM) of ETH Zurich.

Fig. 1: (a) HAADF-STEM image of $Cd_xNb_6(O,F)_{16}$ along (010).) Lines mark direction of the *a* axis on both sides of the grain boundary. (b) Magnified section of (a) with the arrangement of the pentagonal columns (PC) marked by pentagons. PCs in defects are marked yellow. Lines indicate the *c*-axis in the two domains with the 4° tilt. Two unit cells are framed. Microscope: double corrected JEM-ARM300F ("Grand ARM", JEOL) operated at 300 kV.

Fig. 1

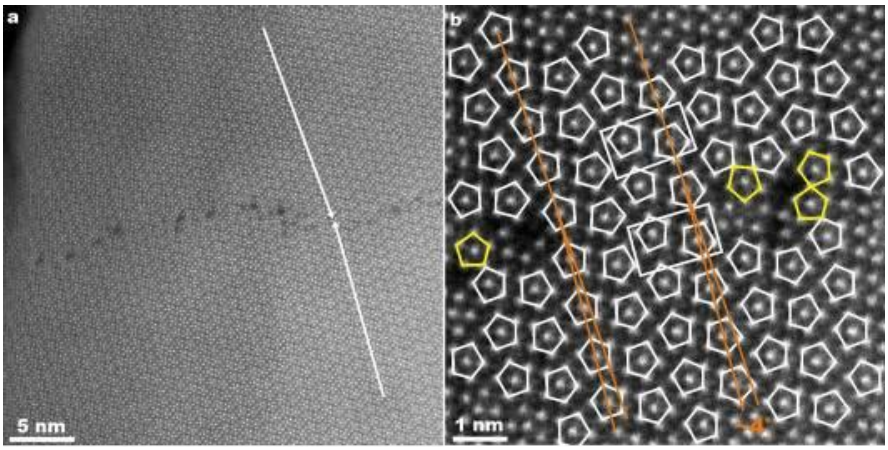

MS7.003
Transmission electron microscopy investigations of fatigue-induced changes in the cement binder structure of ultra-high performance concrete

G. Schaan[1,2], S. Rybczynski[2], M. Ritter[1], F. Schmidt-Döhl[2]

[1]Hamburg University of Technology, Electron Microscopy Unit, Hamburg, Germany
[2]Hamburg University of Technology, Institute of Materials, Physics and Chemistry of Buildings, Hamburg, Germany

This contribution presents early experimental results on the fatigue behavior of ultra-high performance concrete (UHPC). UHPC is a specialized form of concrete distinguished from ordinary concrete by its high robustness of 150 to 200 N/mm^2 and a low w/c ratio of less than 0.25. Instead of coarse sand or gravel, it contains fine-grained aggregate components such as quartz and silica fume as well as fine-grained cement.

UHPC is widely used in structures such as bridges, high-rise buildings and offshore wind turbines. While a large number of reports have been published on the structure, composition and properties of UHPC, (1,2) little is known about its behavior in the case of fatigue-induced failure. Specifically, subtle changes in the microstructure of the cement binder matrix that might lead to the formation of cracks and, ultimately, failure have not been investigated in great detail so far.

In our work, UHPC cylinders (height 180 mm, diameter 60 mm) are subjected to uniaxial cyclic loading with an upper and lower stress limit of 80% and 5% of the material strength, respectively. Cyclic loading is stopped at specific points on the life curve of the sample, which is then prepared for electron microscopy investigations.

As components used in UHPC have a broad size distribution, ranging from several tens of microns down to the nanometer scale, we use a variety of SEM, FIB and TEM techniques to characterize the material.

To assess the integrity of the sample structure, we collect statistically robust information on the size, shape and distribution of the constituent components by using automated large-area SEM. However, no apparent changes in the structure of the binder matrix can be observed on the micrometer scale. Thus, we utilize TEM on lamellae prepared by FIB techniques with a thickness of ca. 100 to 200 nm to trace changes in the structure to their origins on a nanometer level.

Figures 1 and 2 contrast scanning TEM high-angle annular dark-field (HAADF) images from a pristine sample and one that failed due to fatigue, respectively. Whereas the binder matrix largely exhibits a distinct, finely fibrous morphology typical for C-S-H phases (3) in the pristine sample, it appears solidified afterwards, with numerous needle-shaped precipitates or cavities having formed.

The origin of these objects and the cause of the noticeable change in appearance of the matrix is the subject of ongoing research and might be a crucial factor in the fatigue behavior of UHPC.

References:

(1) Z. Rong, W. Sun, Y. Zhang, Int. J. Impact Eng., Vol. 37 (2010), 515–520.

(2) T. Oertel, U. Helbig, F. Hutter, H. Kletti, G. Sextl, Cem. Concr. Res., Vol. 58(2014), 121–130.

(3) I. G. Richardson, G. W. Groves, J. Mater. Sci., Vol. 28 (1993),265–277.

Fig. 1: STEM-HAADF images of a pristine UHPC sample. The binder matrix appears finely fibrous.

Fig. 2: STEM-HAADF images of a UHPC sample that failed due to fatigue. The binder matrix appears solidified, with numerous needle-shaped precipitates or cavities.

This research is funded and supported by the Deutsche Forschungsgemeinschaft (DFG; German Research Foundation), grants RI 1516/2-1, DO 2026/2-1 and SCHM 1473/29-1: SPP 2020 "Cyclic Deterioration of Ultra-High Performance Concrete in an Experimental-Virtual Lab".

Fig. 1

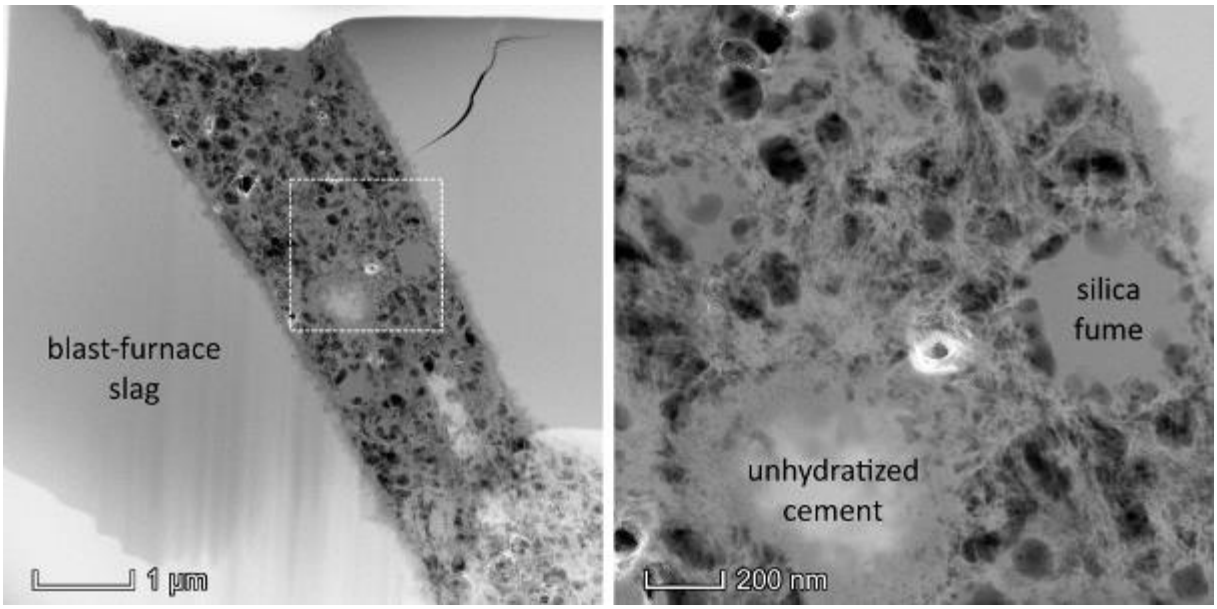
blast-furnace
slag
1 µm
silica
fume
unhydratized
cement
200 nm

Fig. 2

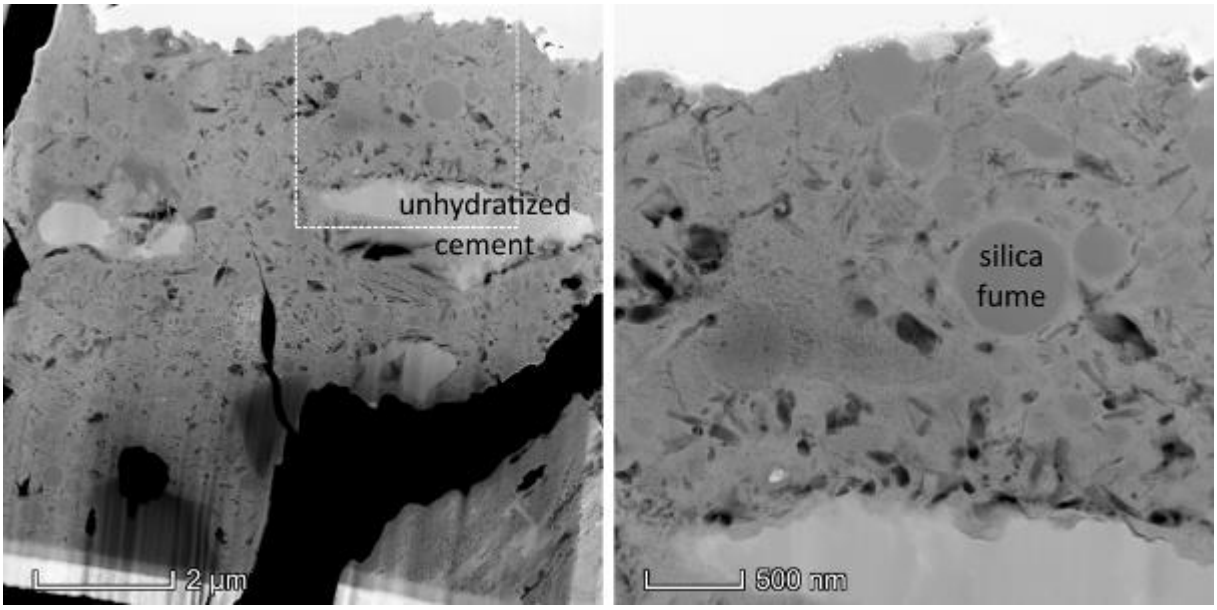
unhydratized
cement
2 µm
silica
fume
500 nm

MS7.004 invited
Olivine grain boundary plane distributions in static and dynamic equilibrium

K. Marquardt[1,2], L. Hansen[3], F. Ferreira[2], U. Faul[4]

[1]Imperial College London, Center for Advanced Structural Ceramics, London, United Kingdom
[2]Universtity of Bayreuth, Bayerisches Geoinstitut, Bayreuth, Germany
[3]University of Oxford, Oxford, United Kingdom
[4]MIT, Cambridge, United States

The character and plane distribution of interfaces in ceramics, mineral aggregates and rocks influences macroscopic properties. Olivine is the dominant phase of the upper mantle. The strength of olivine single crystals differs significantly compared to that of polycrystalline olivine aggregates during plastic deformation. Until recently, neither the anisotropic frequency distribution nor its dependence on chemical composition has been studied for rock forming minerals. The lack of knowledge is even more severe when it comes to the distribution of interfaces that evolve in response to continuous deformation.

To investigate the effect of grain boundaries in olivine plastic deformation we performed a series of experiments in diffusion creep and dislocation assisted grain boundary sliding (disGBS). We aim at linking microstructures, especially interfacial distributions to properties with the ultimate goal to model resulting bulk rock properties and interpret geophysical observables, such as seismic properties, electrical conductivity, viscosity or permeability.

We characterized interfaces in different aggregates of olivine. The different aggregates where synthesized with varying chemical compositions ranging from Mg_2SiO_4 forsterite to $Mg_{1.8}Fe_{0.2}SiO_4$ and $Mg_{1.0}Fe_{1.0}SiO_4$ olivine and different additions of incompatible elements that are known to segregate to the interfaces. We analysed the grain boundary character and plane distribution (GBCD and GBPD) in doped aggregates is diffusion creep and in the disGBS regime using a torsion deformation setup.

The samples where characterized using electron backscatter diffraction (EBSD) and transmission electron microscopy (TEM). To obtain the area distribution of the geometrically varying interfaces, we used EBSD data from over $4x10^4$ grains, corresponding to more than 6000 mm grain boundary length per sample. Subsequently, we used a stereological approach to determine the (GBCD), defined as the relative areas of grain boundaries of different types distinguished by their five degrees of freedom.

In the diffusion creep experiments, we studied the effect of segregation, while deformation in torsion (disGBS) gives insight into the interaction of dislocations with grain boundaries during plastic deformation.

We found that (i) all undeformed starting materials show a preference for low index planes which is in agreement with observations on other materials (e.g. MgO, TiO_2, $SrTiO_3$, $MgAl_2O_4$). (ii) The GBPD varies systematically between pure samples and samples with added incompatible elements. (iii) Olivine aggregates with incompatible elements segregated to the interfaces are systematically weaker than pure aggregates. (iv) The interaction of dislocations of the dominant slip system control the grain boundary plane distribution during disGBS. A characteristic GBPD for the deformation mechanism forms as a result of coupling of inter and intragranular deformation mechanisms.

The combination of statistical and local information allows to gain a physical understanding of the role of grain boundaries during plastic deformation in experiments mimicking deformation in the Earth upper mantle.

MS7.005
Behavior of secondary phase inside Mo-substituted lanthanum tungstate for H_2 separation

K. Ran[1,2], W. Deibert[3], H. Du[1,2], D. Park[1,2], M. Ivanova[3], W. Meulenberg[3,4], J. Mayer[1,2]

[1]RWTH Aachen University, Central Facility for Electron Microscopy (GFE), Aachen, Germany
[2]Forschungszentrum Jülich GmbH, Ernst Ruska-Centre for Microscopy and Spectroscopy with Electrons ER-C, Jülich, Germany
[3]Forschungszentrum Jülich GmbH, Institute of Energy and Climate Research IEK-1, Jülich, Germany
[4]University of Twente, Faculty of Science and Technology, Enschede, Netherlands

For an ideal H_2 separation membrane, considerable mixed electronic-protonic conduction at high temperatures in H_2-containing atmospheres and reasonable stability under atmospheres containing CO_2, H_2O and H_2S, are among the top prerequisites. A novel class of ceramics, lanthanum tungstate with a general formula $La_{28-x}W_{4+x}O_{54+\delta}v_{2-\delta}$ (LWO), showing the potential to fulfill the required conductivity and stability in relevant environments, has therefore received increasing research attention.(1,2) However, below 700 °C, the lack of electronic conductivity hinders its application for H_2 permeation. Various strategies have been proposed to improve the mixed conductivity, including dual-phase composite membranes, Mo/Re substitution,(3) asymmetric membrane system and so on. After all the aforementioned attempts, phase purity of the membranes is usually questionable, as any defective doping or impure starting materials could lead to unfavorable secondary phases (SP).

Our work focuses on the SP inside LWO membrane, which was prepared by a high temperature solid state reaction. The LWO membrane has a nominal La/W ratio of 5.4 (in atomic percent), while nominally 20 at.% W was substituted by Mo (LWO-Mo_{20}). Individual SP grains were located and identified, employing various transmission electron microscopy techniques. Surprisingly, part of the SP grains was incorporated into single LWO-Mo_{20} grains through smart orientations, where massive structural defects in both the host and the SP grain, even along their interfaces, are efficiently avoided. Slight elemental disorder is limited within a few atomic layers. In contrast, the LWO-Mo_{20} grains share barely common feature with neighboring SP grains, and behave more vulnerable under electron beam irradiation. Origin of the SP was tracked back to the impure precursors.

Our results could be further linked with the separation performance of the membrane and potential optimizations of the membrane syntheses.

We acknowledge support from the Bundesministerium für Bildung und Forschung (BMBF) under the Grant ProtOMem (FK 03SF0537A and 03SF0537B)

References:

(1) J. Seeger *et al*., Inorg. Chem. 52, 10375-10386 (2013).

(2) A. Fantin *et al*., J. Appl. Crystallorgr. 49, 1544-1560 (2016).

(3) M. Amsif *et al*., Chem. Mater. 24, 3868-3877 (2012).

Figure (a) HAADF image and EDX mapping from the secondary phase, which was identified as $La_{2/3}(Mg_{1/2}W_{1/2})O_3$ (LMWO), with W sites partially occupied by Mo, Fe and Al. (b) SP located inside a single LWO-Mo_{20} grain. (c) HAADF image showing the interface between SP and LWO-Mo_{20}, indicating no structural defects to any degree of significance.

Fig. 1

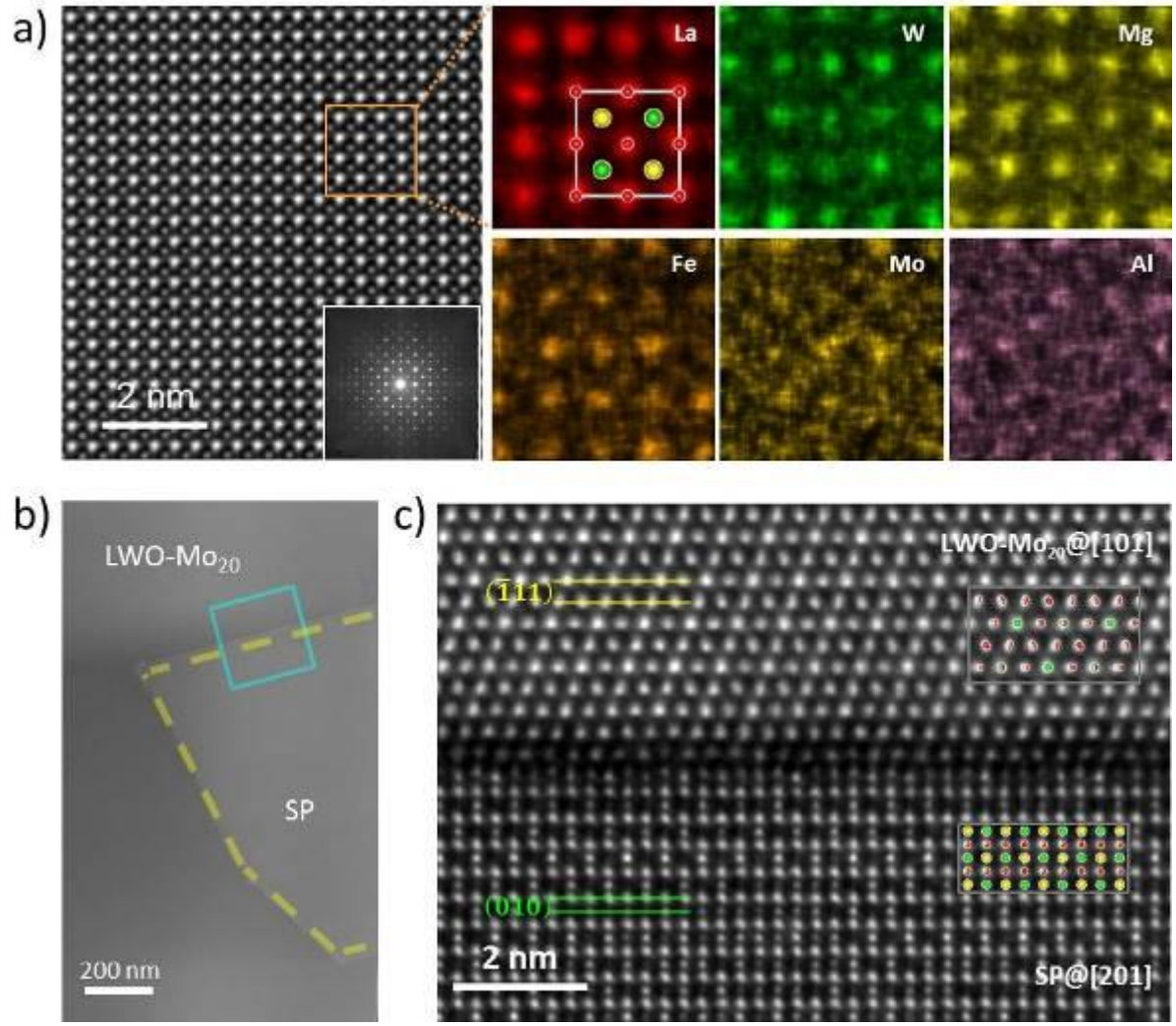
a)
La
W
Mg
Fe
Mo
Al
2 nm
b)
LWO-Mo20
SP
200 nm
c)
LWO-Mo20@[101]
(1̄11)
(010)
2 nm
SP@[201]

MS7.006
Strain-Driven Metal-to-Insulator Transition in a Geometrically Frustrated Spinel Oxide LiV_2O_4

Y. M. Wu[1], U. Niemann[1], Y. Wang[1], T. J. Pennycook[1], M. Kim[1], H. Takagi[1], P. A. van Aken[1]

[1]Max Planck Institute for Solid State Research, Stuttgart, Germany

The coupling of local atomic configurations and electronic degrees of freedom plays a fundamental role in understanding metal-insulator transitions and the formation of orbital and charge ordering (1). This competing interaction between phases becomes more pronounced in systems, whose lattice structures are geometrically frustrated due to fluctuations in the charge, spin and orbital channels. In particular, the pyrochlore lattice in the spinel structure possesses strong frustration, which provides a fertile playground for studying these many-body quantum states (2). Among them, the mixed-valence spinel LiV_2O_4 is of special interest since its unusually strong electron-lattice coupling gives rise to the presence of competing phases between the metallic heavy-fermion state and the insulating charge-ordered state (3,4). Such phase instability is often associated with changes in atomic positions, such as octahedral distortions and the transition metal-oxygen bond lengths, which can be externally controlled by pressure and epitaxial strain. However, the microscopic mechanism driving such competition remains undetermined.

Here, we report atomic-resolution scanning transmission electron microscopy imaging and spectroscopy investigation of LiV_2O_4 thin films on $SrTiO_3$ and MgO (001) substrates (Fig. 1(a)). Due to the different lattice spacing of the substrates, two competing behaviors of the thin films are found on the two substrates, the metallic charge-disordered phase on the $SrTiO_3$ substrate and the insulating charge-ordered phase on the MgO substrate. Figure 1(b) and (c) show the distortions of edge-sharing VO_6 octahedra caused by the geometrical frustration, which could be closely linked with the phase instability in LiV_2O_4. Analogous to a spin-glass state, the charge fluctuations can freeze into an insulating "charge-glass"-like state, when epitaxial strain is applied and relieves the frustration. Therefore, the microscopic investigation of the atomic arrangements in these two cases will help to understand the charge-order correlations with structure and electronic states. Aside from the case of LiV_2O_4, these investigations will provide insights into the electronic phase transitions in other frustrated spinel and related systems (5).

References:

(1) E. J. W. Verwey, Nature 144, 327–328 (1939).

(2) P. W. Anderson, Phys. Rev. 102, 1008 (1956).

(3) K. Takeda *et al.*, Physica B 359–361, 1312-1314 (2005).

(4) L. Pinsard-Gaudart *et al.*, Phys. Rev. B 76, 045119 (2007).

This project has received funding from the European Union's Horizon 2020 research and innovation programme under grant agreement No. 823717 – ESTEEM3.

Fig. 1: Scanning transmission electron microscopy measurements of the spinel oxide LiV_2O_4. (a) Low-magnification high-angle annular dark-field (HAADF) images of the LiV_2O_4 thin films grown on the $SrTiO_3$ and MgO(001) substrates. (b) Crystal structure of LiV_2O_4, showing the trigonal distortions of the VO_6 octahedra along [110] projection. (c) The HAADF and annular bright-field (ABF) images of zoom-in views of atomic structure showing the distorted VO_6 octahedra.

Fig. 1

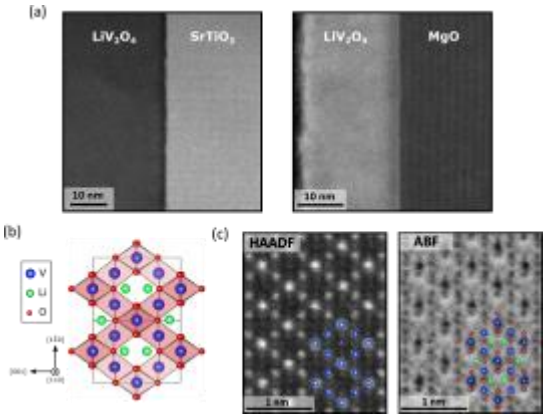
(a)
LiV_2O_4
$SrTiO_3$
10 nm
LiV_2O_4
MgO
10 nm
(b)
V
Li
O
(c)
HAADF
1 nm
ABF
1 nm

MS7.LB.P01
Cobalt doped ZnO nanopowders synthesized by MW-HTS and their XRD, SEM and Optical Properties

M. Caglar[1], S. Aksoy[2], Y. Caglar[1], K. Gorgun[3]

[1]Eskisehir Technical University, Physics, Eskisehir, Turkey
[2]Sinop University, Physics, Sinop, Turkey
[3]Eskisehir Osmangazi University, Chemistry, Eskisehir, Turkey

Nanostructured materials are very popular due to their interesting properties that distinguish nanostructured materials from bulk materials. The properties of the materials at nano-scale level are completely different from the macroscopic scale, and as they approach the nanoscale, many special and useful events and new features emerge. Zinc oxide (ZnO) is a versatile and important material that is noticeable because of its permeability in the visible region, it"s being a direct band-pass material (3.2-3.4 eV), its non-toxic nature and its abundance in nature (1). The hydrothermal method has a long deposition time and high temperatures are required for production. The microwave-assisted hydrothermal method (MW-HT) has superior properties compared to the conventional hydrothermal method in terms of both short deposition time and lower temperatures (2).

The aim of this work is to invetigate the effect of Co dopant on the morphological, structural and optical properties of ZnO nanopowders by MW-HTS in detail.

Cobalt (Co) doped ZnO nanopowders were synthesized via microwave assisted hydrothermal synthesis (MW-HTS) using zinc acetate dihydrate, cobalt II acetate and sodium hydroxide. 0.149 M of Zn(CH3COO)2.2H2O, and 4.60 M NaOH, aqueous solutions were prepared with deionized water on the magnetic stirring at 30oC. After stirring the zinc acetate aqueous solution for 5 min, the NaOH aqueous solution was slowly added until a milky solution formed. Cobalt II acetate added to the solution in appropriate amounts of additives. These solution were irradiated using a temperature-controlled microwave synthesis system (CEM Discover Microwave unit, 300W) at 95oC at different times 10min. After microwave processing, the solution of the mixture was cooled to room temperature naturally. The resulting white precipitates were collected by filtration and washed with deionized water and ethanol for several minutes. The final products were dried in an oven at 60oC for 24 h. The synthesized ZnO nanopowders were further calcined in air at 500oC for 1 h.

The effect of Co dopant on the structural and morphological properties of ZnO nanopowders was investigated. To investigate the crystalline structure and the orientation of the doped ZnO nanopowders, XRD patterns were used (Fig. 1). As can be seen from Figure 1, there are five diffraction peaks for the Co doped ZnO nanopowders which is identified as having the hexagonal wurtzite structure. The lattice parameters values of these nanopowders were determined. Surface morphology and elemental analysis of the Co doped ZnO nanopowders were studied using a ZEISS SUPRA 50VP model scanning electron microscope (SEM) and BRUKER AXS energy dispersive X-ray spectroscopy (EDX), respectively (Fig 2 and Fig 3). The surface morphology of ZnO nanoparticles is influenced by the Co dopant. The optical band values of Co doped ZnO nanopowders were found via reflectance measurements using kubelka-munk function.

This work was supported by Eskisehir Technical University Commission of Scientific Research Projects under Grant No. 1706F385

References:

(1) Wang, J. Du, Q. Zhen, R. Zhang, X. Wang, X. Du, Talanta. 191 (2019) 193–201.

(2) Caglar, K. Gorgun, and S. Aksoy, *Spectrochim. Acta - Part A Mol. Biomol. Spectrosc.*, 138 (2015) 617–622.

Fig. 1

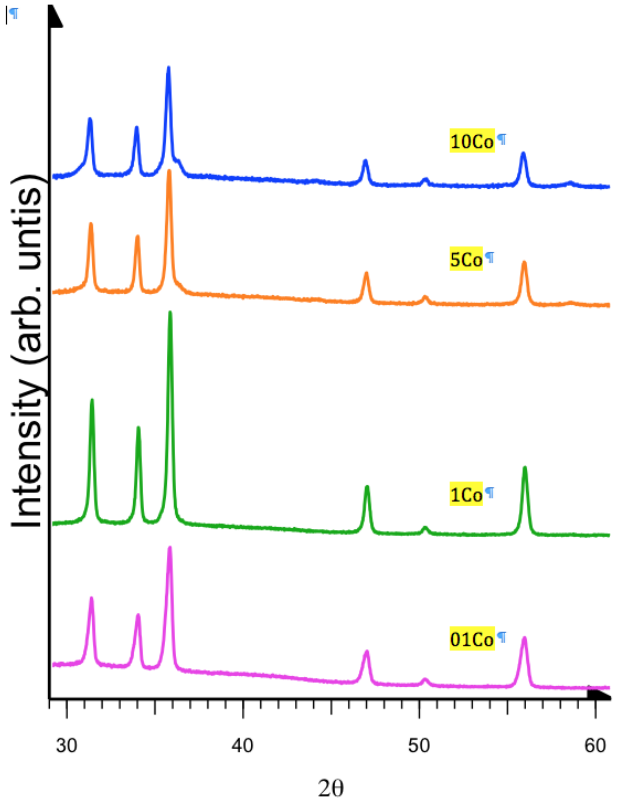
Intensity (arb. untis)
10Co
5Co
1Co
01Co
30
40
50
60
2θ

Fig. 2

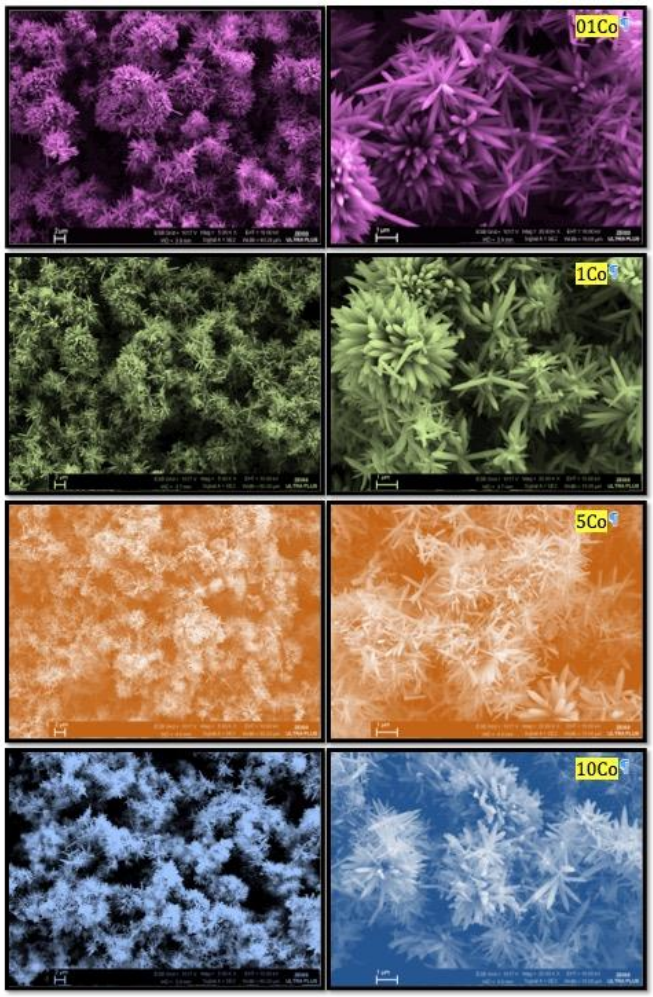
01Co
1Co
5Co
10Co

Fig. 3

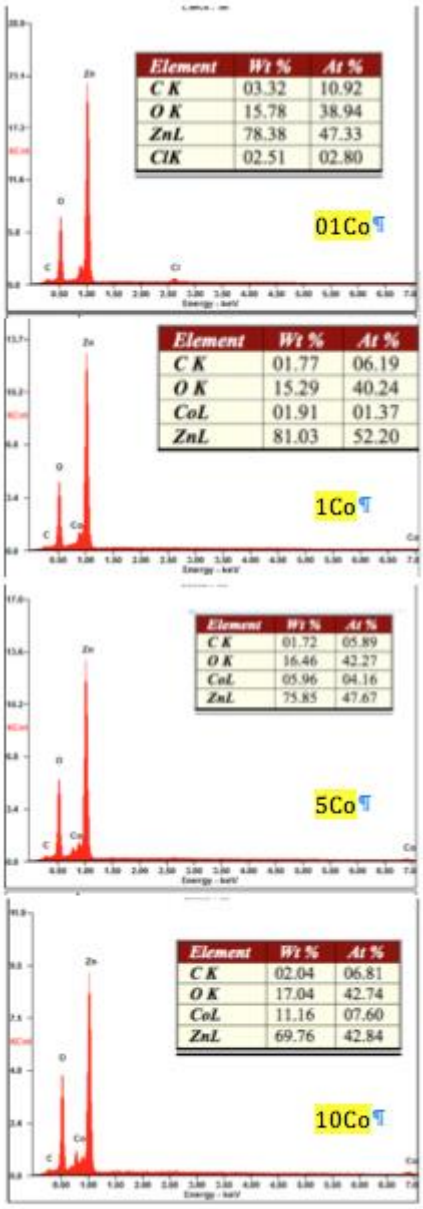
Element Wt % At %
C K 03.32 10.92
O K 15.78 38.94
ZnL 78.38 47.33
ClK 02.51 02.80
01Co
Element Wt % At %
C K 01.77 06.19
O K 15.29 40.24
CoL 01.91 01.37
ZnL 81.03 52.20
1Co
Element Wt % At %
C K 01.72 05.89
O K 16.46 42.27
CoL 05.96 04.16
ZnL 75.85 47.67
5Co
Element Wt % At %
C K 02.04 06.81
O K 17.04 42.74
CoL 11.16 07.60
ZnL 69.76 42.84
10Co

MS7.LB.P02
EFFECT OF DIFFERENT ELEMENT MORPHOLOGY ON THE PHOTOVOLTAIC PARAMETERS OF ZnO BASED DSSC

Y. Caglar[1], K. Gorgun[2], S. Aksoy[3], M. Caglar[1]

[1]Eskisehir Technical University, Physics, Eskisehir, Turkey
[2]Eskisehir Osmangazi University, Chemistry, Eskisehir, Turkey
[3]Sinop University, Physics, Sinop, Turkey

DSSCs are important devices. Because they are expected to respond to many environmental and energy problems. DSSCs have many advantages compare to other photovoltaic devices, such as a superior performance in conditions of low intensity, low angle of incidence and high temperature. Since Zinc oxide (ZnO) has better electrical properties, its use in DSSCs is considered to be the best alternative to TiO2. ZnO has a large excitation binding energy (60 eV), is available at low-cost, and is stable against photo- corrosion. Techniques such as thermal decomposition techniques, hydrothermal, sol-gel method, spraying, microwave assisted hydrothermal are used to obtain ZnO nanopowder. The hydrothermal method is a method based on high pressure crystallization from high temperature aqueous solutions. Many factors affect the performance of DSSC, such as the morphology and thickness of the electrode and the type of dye.

The effect of different element such as In, Mg, Ni on the performance of ZnO-DSSCs has been investigated. Firstly, In, Mg, Ni doped ZnO films were obtained by doctor blade method using this nanopowders synthesized by MW-HTS method and then it was successfully applied as photoanode for the fabrication of DSSCs.

In, Mg, Ni doped ZnO nanopowders were produced by hydrothermal synthesis method. Zinc nitrate hexahydrate and Sodium hydroxide were used as initail materials for the ZnO nanopowders. Indium acetate, Magnesium acetate and Nickel acetate added to the solution in appropriate amounts of additives. These solution were irradiated using a temperature-controlled microwave synthesis system. After microwave processing, the solution of the mixture was cooled to room temperature naturally. The white precipitates were collected by filtration and washed with deionized water and ethanol for several minutes. The final products were dried in an oven at 60oC for 24 h. The synthesized ZnO nanopowders were further calcined in air at 500oC for 1 h. The doped ZnO films have been fabricated by doctor blade method. Then the film was calcined at 400°C for 1 h. After the film cooled down to room temperature, it was immersed into the dye solution consisting N719 for 2 h at room temperature. Finally, the dye loaded ZnO films were assembled with the prepared Pt counter electrodes to form a sandwich-type DSSCs using a sealing plastic. The structure of ZnO nanopowders and films was examined using field emission scanning electron microscopy and X-ray diffraction were used to analyze the phase. The current–voltage (*I*–*V*) characteristics of the DSSCs were recorded by a solar cell measurement system.

The effect of In, Mg, Ni dopant on the structural and morphological properties of ZnO nanopowders was investigated using XRD and SEM, respectively. XRD results showed that the nanopowders have hexagonal wurtzite structure. The lattice parameters were calculated. SEM images showed that all the samples were formed in nanorod structure and the average diameter of the rods changed with the variety of dopant (Fig 1). The current–voltage characterization of fabricated DSSCs was performed by AM 1.5 simulated sunlight at 100 mW/cm2. Isc, Voc, n% and FF of ZnO-DSSCs were determined (Fig 2). The best performance was obtained for In:ZnO-DSSC.

This work was supported by Eskisehir Technical University Commission of Scientific Research Project under Grant No. 1706F385.

Fig. 1

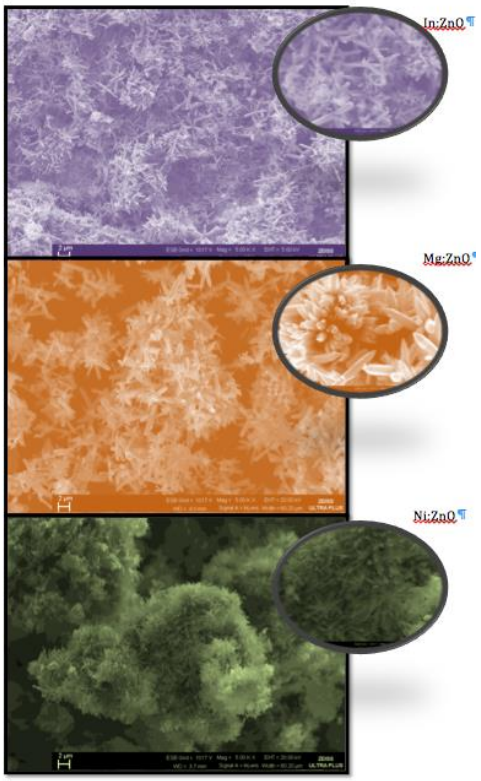
In:ZnO
Mg:ZnO
Ni:ZnO

Fig. 2

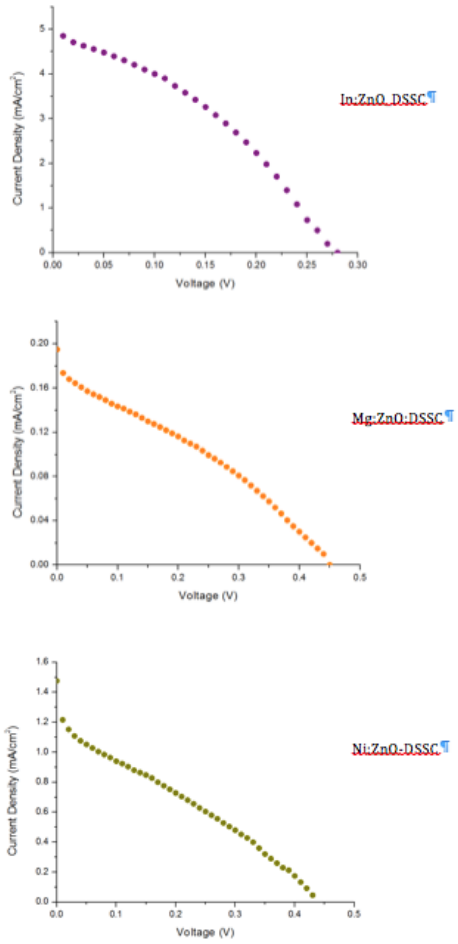
In:ZnO DSSC
Mg:ZnO:DSSC
Ni:ZnO:DSSC
Current Density (mA/cm²)
Voltage (V)

MS7.LB.P03
Analytical TEM Methods for Neolithic Materials

K. Saleem[1], U. Schurmann[1], W. Höfgen[2], J. Kneisel[2], C. Horn[3], F. Jürgens[2], J. Müller[2], C. von Carnap-Bornheim[4], L. Kienle[1]

[1]Institute for Material Science, Christian-Albrechts-Universität, Kiel, Germany
[2]Institute of Prehistoric and Protohistoric Archaeology, Kiel, Germany
[3]Department of Historical Studies, University of Gothenburg, Sweden, Gothenburg, Sweden
[4]Schleswig-Holstein State Museum, Schloss Gottorf, Schleswig, Germany

All over the world artefacts were brought to the surface by archaeologic excavations. Often these artefacts, particularly their microstructure and composition, raise questions of inter- and transdisciplinary relevance which cannot be answered by conventional routine analyses. This work shows examples how analytical techniques from the material science like electron microscopy methods as well as spectroscopic techniques can help to clarify the origin and the manufacturing process of these findings.

The range of investigated samples vary from weapons like axes to rocks probably used as anvil to colorful minerals used by human beings. For instance, the microstructure and chemical composition of Neolithic axes were examined with Scanning (SEM) and Transmission Electron Microscopy (TEM) and Energy-Dispersive X-Ray Spectroscopy (EDX). Additionally, the mineralogic context of sample compositions, e.g., give an indication which purpose artefacts served, e.g. gold and silver traces or hematite remains as surface contamination of purely silica based rocks.

Mineral samples were scratched from the surfaces of the rocks, ground and dispersed on TEM grids. Samples from valuable artefacts can be prepared by Focused Ion Beam milling in a FEI Helios Dual Beam system without leaving visible destruction. Electron diffraction, HRTEM as well as High Angle Annular Dark Field (HAADF) Scanning TEM (STEM) was performed in a FEI Tecnai F30 G² STwin equipped with an EDX detector (Si/Li, EDAX). EDX point measurements and elemental maps were performed in STEM mode.

The Neolithic copper axes were examined by SEM-EDX to study the chemical composition at the surface. FIB lamellae were extracted from one axe to get insights in the structure and composition beneath the surface. Silver as trace component was found not only on the surface but also inside the bulk of the copper axe. This is a hint that the silver is not a part of a decoration layer but already a compound of the primary material before processing. Nano nuggets of gold, copper and nickel were found in samples of a rock which was supposed to be used as an anvil for goldwork. Comparative measurements at the backside of the rock prove the absence of these elements and hint towards its use as tool for metal work. The study of the structure of red pigments by electron diffraction verifies the presence of hematite on a stone where it is not intended to be in conjunction with the accompanying minerals and therefore support the assumption of human involvement.

Analytical techniques of the materials science are valuable tools to reveal new insights into the production, origin, and use of historic artefacts and are therefore powerful tools in inter- and transdisciplinary studies.

The authors would like to thank the Cluster of Excellence "ROOTS - Social, Environmental, and Cultural Connectivity in Cast Societies" for financial support.

Fig.1: a) Excerpt from a FIB lamella extracted from a Neolithic copper axe. The inset shows an EDX elemental map of a region with silver inclusions. b) Au nugget in an agglomeration of silicate grains removed from the surface of an anvil rock.

Fig. 1

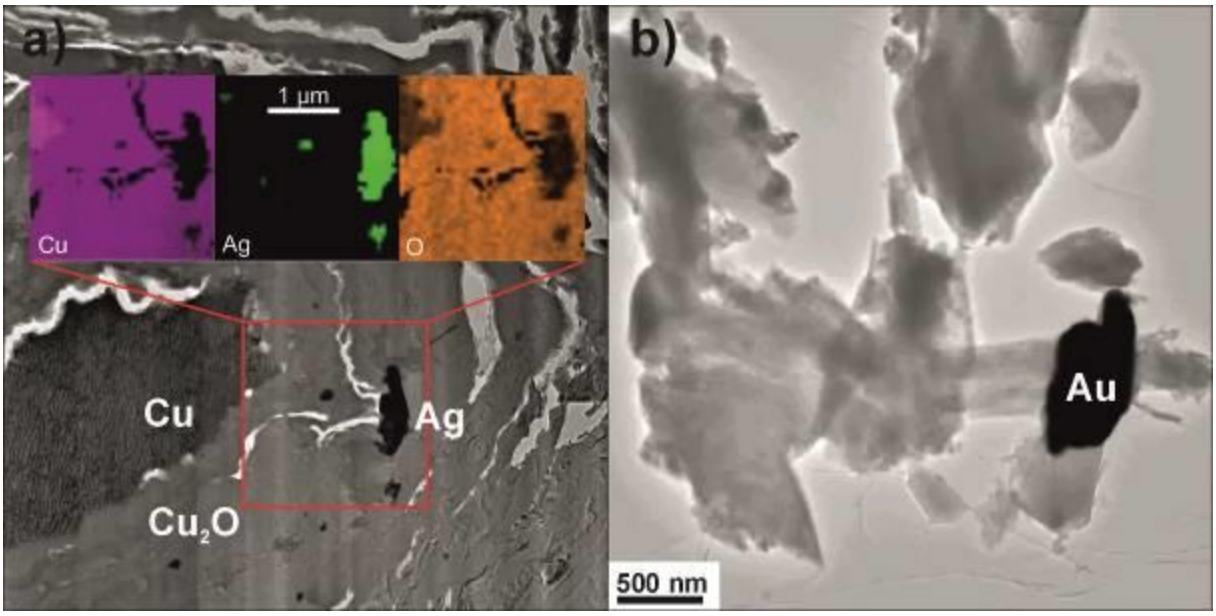

MS7.P001
STEM EDS/EELS for Deep-Mantle Rock Assemblages Analyses Assisted by Machine Learning

H. Chen[1], F. Nabiei[1], J. Badro[1], D. T. L. Alexander[1], C. Hébert[1]

[1]École Polytechnique Fédérale de Lausanne, Lausanne, Switzerland

Scanning transmission electron microscopy (STEM) is a powerful technique employed in the study of minerals and rocks. In addition to providing high-resolution images, STEM generates a variety of additional signals that are often employed for analyzing geological samples. The two most prominent techniques among them are energy-dispersive X-ray spectroscopy (EDS) and electron energy-loss spectrometry (EELS). EDS is a simple technique for chemical analysis. EELS is a more challenging technique but is capable of not only measuring elemental composition, but also giving information about chemical bonding and oxidation state, etc. These two methods are both applicable for the quantitative chemical analysis of mineral phases which do not overlap across the thickness of the TEM sample. In the scenario where phases instead overlap in the projected volume, 2D EDS/EELS is insufficient to obtain accurately the composition of every single phase. Although this problem can be tackled using electron tomography, the minerals may experience severe sample degradation under the extensive beam exposure. In this paper, we instead look to address this problem via use of data processing algorithms.

EDS/EELS information bridged by data processing algorithms are applied to quantify mineral assemblages in lower mantle

The starting material is a synthetic pyrolite glass doped with Nd, Sm, Hf, Lu, and U (0.3 wt.% for each). Four samples were made by compressing the pyrolite to the pressure range of 46 GPa to 88 GPa in diamond anvil cell (DAC). The samples were molten by double-sided laser heating and then slowly cooled down below the solidus temperature before quenching. Thin sections for STEM analysis were made by focused ion beam (FIB) lift-out technique from the recovered samples after decompression. EDS maps were obtained on a FEI Tecnai Osiris equipped with 4 SDD EDS detectors. Data processing was done using Hyperspy (1), an open source Python package for multi-dimensional data analysis.

Fig. 1 shows the overlapping of three mineral phases, ferropericlase, bridgmanite and Ca perovskite in sample. Principal component analysis (PCA) was applied as a pre-processing step for EDS data, and then non-negative matrix factorization (NMF) was implemented on the PCA denoised data to perform a decomposition. As shown in Fig. 2, the segmented phase compositions are similar to the composition of bridgmanite, ferropericlase (with metallic iron mixed in), and Ca perovskite, respectively (2). Although the algorithm failed to separate metallic iron from the ferropericlase. We are currently evaluating the ability of EELS to fulfill this differentiation by measuring the distribution of electronic states of iron, in order to achieve a more accurate phase segmentation and to characterize elemental partitioning dependence on pressure.

References:

(1) F de la Pena et al., Microsc. Microanal, 23 (2017), p. 214–215.

(2) K Hirose et al, Science, 358 (2017), p. 734–738.

Fig. 1: HAADF image and EDS maps of the 46 GPa sample consisting of bridgmanite, ferropericlase, Ca perovskite minerals and metallic iron particles.

Fig. 2: (a) PCA scree plot of STEM EDS data, (b)-(d) representive component loadings and (e)-(g) component factors of NMF decomposition. Insets give the corresponding quantified composition for each component.

Fig. 1

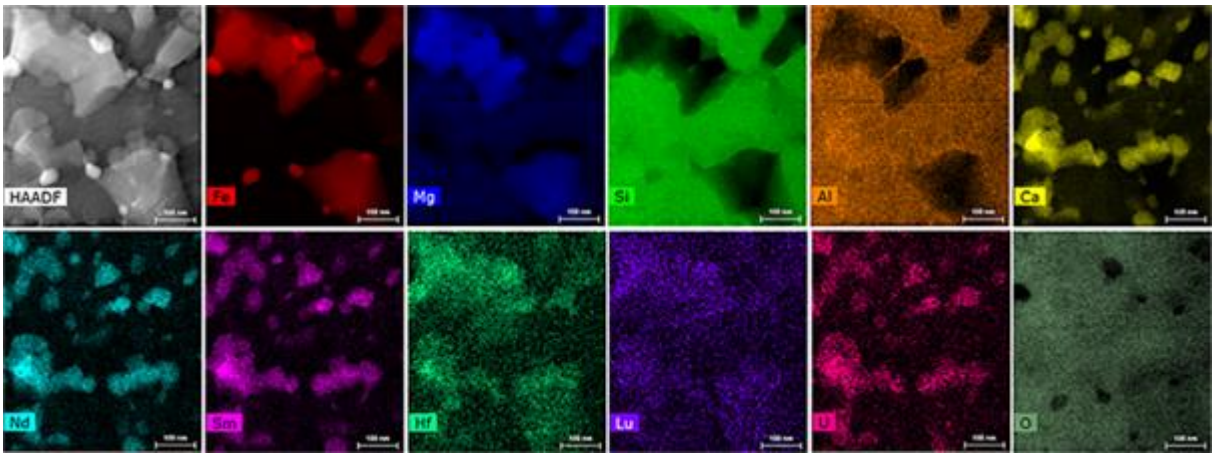
HAADF
Fe
Mg
Si
Al
Ca
Nd
Sm
Hf
Lu
U
O

Fig. 2

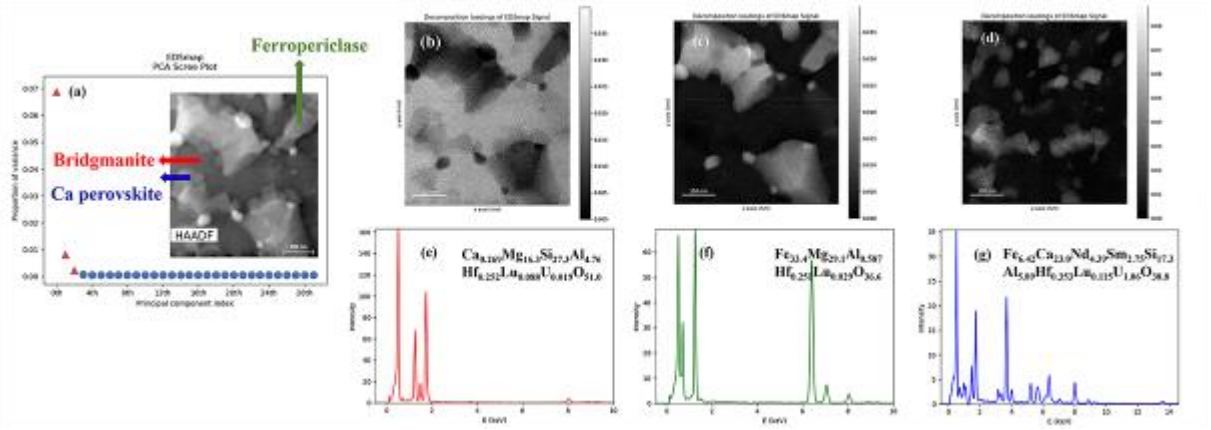
Ferropericlase
Bridgmanite
Ca perovskite
HAADF
(a)
(b)
(c)
(d)
(e)
(f)
(g)

MS7.P002
In-situ electron microscopy investigations of reduction of Co_3O_4 nanocrystals

X. Chen[1], B. van den Bosch[1], M. A. van Huis[1]

[1]Utrecth University, Soft condensed matter group, Utrecht, Netherlands

Co_3O_4 nanocrystals are promising materials in several applications, including catalysis, Li-ion batteries, and gas sensors. The investigation of the reduction processes and mechanisms is significant to controlling the properties in application (1-2). In this work, the reduction process of Co_3O_4 nanocrystals are investigated during in-situ heating in electron microscope. The Co_3O_4 nanocrystals were heated in vacuum from room temperature to 800 ºC. The phase transition to CoO was detected at 400 ºC by selected area electron diffraction (SAED) (shown in fig.1 b). And with temperature lifting, the contours of the particle become uneven (shown in fig.1 a).

References:

(1) N.A. Mayer, et al, *Thermochimica Acta* 625 (2017) 109-118.

(2) L. Garces, et al, *J. Phys. Chem C* 119 (2015) 5484−5490.

Fig. 1

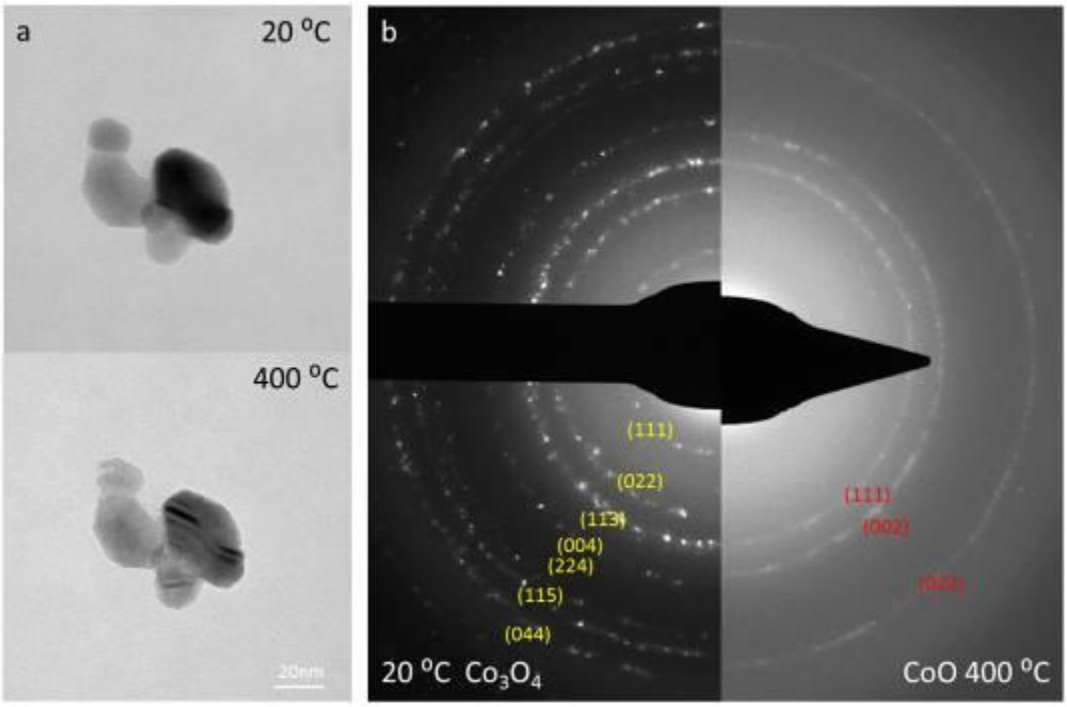

MS7.P003
Oxidation mechanisms of MoSi2–HfB2–MoB ceramics: a microstructural investigation

A. Potanin[1], P. Loginov[1], S. Vorotilo[1], Y. Pogozhev[1], N. Shvyndina[1], E. Levashov[1]

[1]Nust Misis, Moscow, Russian Federation

Transition metals silicide-based composites are advance as high-temperature oxidation and corrosion-resistant structural materials and coatings. They can withstand the mechanical loads at temperatures up to 1700–2000 °C in aggressive environments. Among these materials, MoSi2-based composites attract special interest. In particular, they are applied as the heating elements in high-temperature industrial furnaces and exhaust systems of internal combustion engines.

In this work, influence of the composition and microstructure of the ceramics MoSi2–HfB2–MoB on mechanisms of oxidation and formation of protective oxide layers in furnace static conditions at 1200 °C and 1650 °C as well as in plasma torch dynamic conditions at 2000 °C was investigated.

The studies of microstructure were carried out using transmission electron microscope Jeol JEM 2100, equipped with Oxford EDS detector for elemental analysis. The lamella was made from the investigated specimens by the focused ion beam (FIB) technique on a FEI Quanta 200 3D FIB instrument

At 1200 °C, oxidation of single-level structure (SLS) and two-level structure (TLS) ceramics produced two-layered oxide films. In the case of SLS ceramic, SiO2-based oxide film was comprised of top 9–12 μm wide Hf-doped amorphous silica layer and bottom 3–5 μm crystalline α-SiO2 layer. In the case of TLS ceramic, top layer consisted of crystalline α-SiO2, whereas the bottom layer was formed by HfSiO4 grains with preferential (200) orientation. Precipitation of nanoscale HfSiO4 grains in the SiO2 matrix occurs at 1650 °C during static oxidation for the SLS ceramics and at 2000 °C during dynamic oxidation for the TLS ceramics. During the static oxidation at 1200 and 1650 °C, the TLS ceramic demonstrated the highest weight gain due to preferential oxidation of fine HfB2 grains and formation of 5–8 μm wide crystalline HfSiO4 sublayer. However, in the case of dynamic oxidation under the plasma torch, this sublayer provided sufficient protection against plasma flow and defined the best performance of TLS ceramic under the plasma torch test.

This work was carried out with financial support from the Russian Science Foundation in the framework of project No. 19-19-00117.

IM1.001 invited
Magnetic Cc/Cs-corrector compensating for the chromatic aberration and the spherical aberration of electron lenses

H. Rose[1], A. Nejati[2], H. Mueller[2]

[1]Ulm University, Electron Microscopy Group of Materials Science, Ulm, Germany
[2]CEOS GmbH, Heidelberg, Germany

Aberration correction in electron microscopy has provided atomic resolution for beam energies ranging from 20keV to 1.2MeV (1, 2). Chromatic aberration becomes negligibly small at high voltages for conventional electron sources whereas it is the dominant aberration at low voltages, necessitating the correction of both spherical and chromatic aberration. Nevertheless, for new applications using pulsed beams with energy spreads in the order of 100eV chromatic aberration will become the limiting factor even at energies of several MeV (3). Present Cc/Cs correctors with straight optic axis employ mixed electric and magnetic quadrupoles for eliminating the chromatic aberration and octopoles compensating for the spherical aberration. Unfortunately, the application of mixed electric and magnetic quadrupoles for Cc correction becomes infeasible for voltages above about 300kV. To enable feasible chromatic-aberration correction at higher voltages purely magnetic multipole systems offer a possibility. Although the chromatic aberration of magnetic system with straight optic axis is unavoidable (4), this restriction is not valid for magnetic systems with curved optic axis. Here, we propose a feasible doubly symmetric magnetic multipole system with curved optic axis compensating for the primary chromatic and spherical aberration of electron lenses at voltages up to several MV without introducing second-order aberrations and dispersion.

References:

(1) M. Linck et al., Phys. Rev. Lett. 117 (2016) 076101

(2) T. Akashi et al., Appl. Phys. Lett. 106 (2015) 074101

(3) W. Wan, F. R. Chen, Y. Zhu, Ultramicroscopy 194 (2018) 143

(4) H. Rose, Optik 26 (1967) 280

IM1.002
Development of a dedicated TEM sample holder for Electron Holographic Vector Field Tomography

S. Sturm[1], D. Wolf[1], A. Lubk[1], B. Büchner[1]

[1]Leibniz-Institut für Festkörper- und Werkstoffforschung Dresden e. V., Dresden, Germany

Transmission Electron Microscopy (TEM) only provides 2D projections of a specimen. Electron tomography (ET) strives to overcome this loss of information by reconstructing a 3D object (tomogram) out of a series of projections at different specimen tilt angles, ideally comprising a range of 180°. The combination of electron holography (EH) and tomography (1), furthermore, allows not only reconstruction of the electrostatic potential, but also of magnetic field components (2) in 3D, provided a full tilt series of 360° (3) is recorded. In order to reconstruct all three components of the magnetic vector field (i.e. Vector Field Tomography (VFT)), three full 360° tilt series with independent tilt axes are ideally needed (Fig. 1).
In order to overcome the limitation of state of the art tomographic specimen holders, a dedicated holder for tomography of VFT has been developed. Standard holders usually are limited in tilt range, eventually causing a loss of information in the tomogram. Furthermore, none of the available sample holders allows recording of the third independent tilt series, needed for a direct tomographic reconstruction of the third vector field component.
In order to achieve the necessary tilt geometries, a TEM holder with dedicated holder head has been developed for VFT, enabling the recording of three full 360° tilt series of fully independent tilt axes (see Fig. 2). To this end, the holder has its own two built-in rotation axes: one main axis, parallel to the goniometer tilt axis, that can be adjusted with a precision of 0.1° for recording of each tilt series and a second axis 55° to the main axis, directly at the tip of the holder, enabling selecting each independent object axes (x,y,z) on the main tilt axis. The holder-head has been designed to hold needle-shaped tips, on which the nanometer sized objects can be mounted.
We report of first successful field tests of a dedicated TEM sample holder with an unique rotation mechanism for Electron Holographic Vector Field Tomography.

References:

(1) D Wolf et al. Ultramicroscopy, 110(5) (2010), pp 390-399

(2) P Simon et al. Nano Lett., 16 (1), (2016), pp 114–120

(3) D. Wolf, et al., Chem. Mater., Chemistry of Materials, (2015), 27, pp 6771-6778

This project has received funding from the European Research Council (ERC) under the European Union’s Horizon 2020 research and innovation programme (grant agreement No 715620)

Fig. 1: Principle of EH VFT with three tilt axes. 1. The object, consisting of electrostatic potential V and magnetic field B, is probed by the electron wave. 2. The object wave is brought to interference with an empty reference wave by means of a biprism, resulting in the so called hologram. 3. The projected phase of the object wave is retrieved numerically. 4. a, b, c) Three different tilt series are recorded, by tilting the object 360° around each of the three independent tilt axes x, y, z. 5.&6. a, b, c) The electrostatic & magnetic parts of the phase are separated for all three tilt series 7.&8. a, b, c) V & all three components of B are tomographically reconstructed. 9. The complete object (V and B) is recomposed from its individual components.

Fig. 2: CAD Model of the VFT sample holder.

Fig. 1

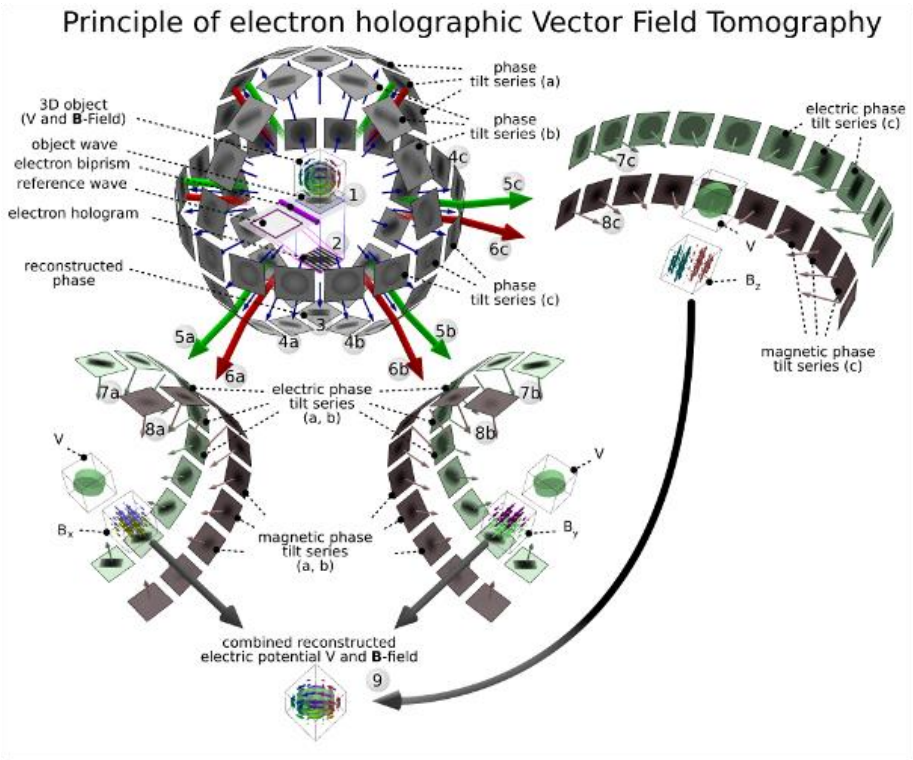
Principle of electron holographic Vector Field Tomography
3D object
(V and B-Field)
object wave
electron biprism
reference wave
electron hologram
reconstructed
phase
phase
tilt series (a)
phase
tilt series (b)
phase
tilt series (c)
electric phase
tilt series (c)
magnetic phase
tilt series (c)
electric phase
tilt series
(a, b)
magnetic phase
tilt series
(a, b)
combined reconstructed
electric potential V and B-field
1
2
3
4a
4b
4c
5a
5b
5c
6a
6b
6c
7a
7b
7c
8a
8b
8c
9
V
B_x
B_y
B_z

Fig. 2

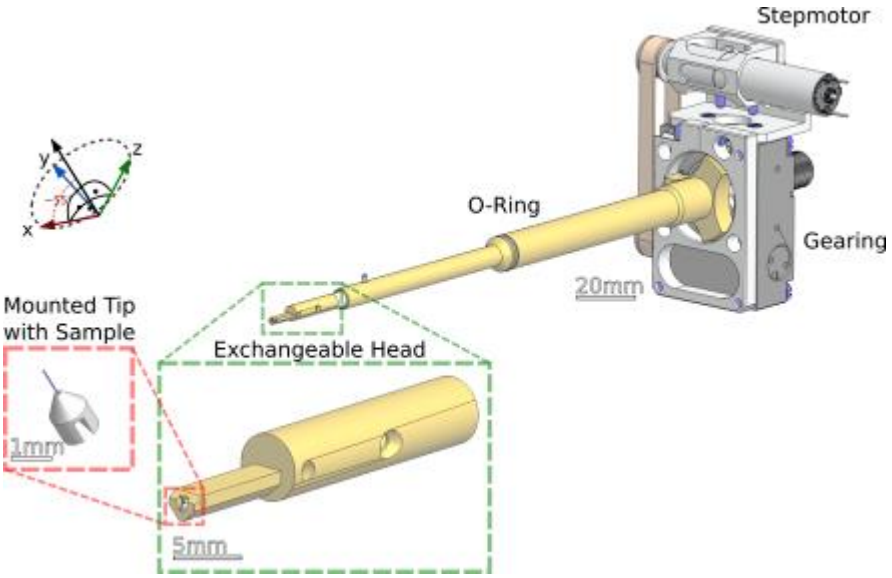
Stepmotor
O-Ring
Gearing
20mm
Mounted Tip
with Sample
Exchangeable Head
1mm
5mm
x
y
z

IM1.003
Software tools for automated Transmission Electron Microscopy

M. Schorb[1], I. Haberbosch[2,3], W. Hagen[4,5], Y. Schwab[1,3], D. Mastronarde[6]

[1]EMBL, Electron Microscopy Core Facility, Heidelberg, Germany
[2]University Hospital, Department of Hematology, Oncology and Rheumatology, Heidelberg, Germany
[3]EMBL, Cell Biology and Biophysics Unit, Heidelberg, Germany
[4]EMBL, Structural and Computational Biology Unit, Heidelberg, Germany
[5]EMBL, Cryo-Electron Microscopy Service Platform, Heidelberg, Germany
[6]University of Colorado, Dept. of Molecular, Cellular & Developmental Biology, Boulder, United States

In the recent years, electron microscopy for structural and cellular biology has witnessed an increasing demand for high-throughput data collection. Here we present a combination of software tools that enable automated acquisition guided by image analysis for a wide variety of Transmission Electron Microscopy acquisition schemes. *SerialEM* offers control of the microscope and its imaging detectors in a very flexible manner. While its core is made available as open source, it can communicate with microscope and camera hardware of various manufacturers using a plugin scheme. Features for automation are the Navigator which is the key element for imaging multiple regions of a specimen with pre-defined acquisition parameters in an automated manner and the built-in scripting functionality, allowing users to create and perform highly customized acquisition routines. *Py-EM* is an open source Python module that integrates common image analysis applications and provides SerialEM with the necessary coordinate and image information for automated acquisition. Automatically identifying features of interest using specimen-specific image analysis pipelines consequently enables feedback microscopy.

As example applications using the presented software, we demonstrate dose-reduction in single particle cryo-EM experiments, fully automated acquisition of every single cell in a plastic section and automated targeting of selected features on serial sections for 3D volume imaging even across multiple grids.

Fig. 1

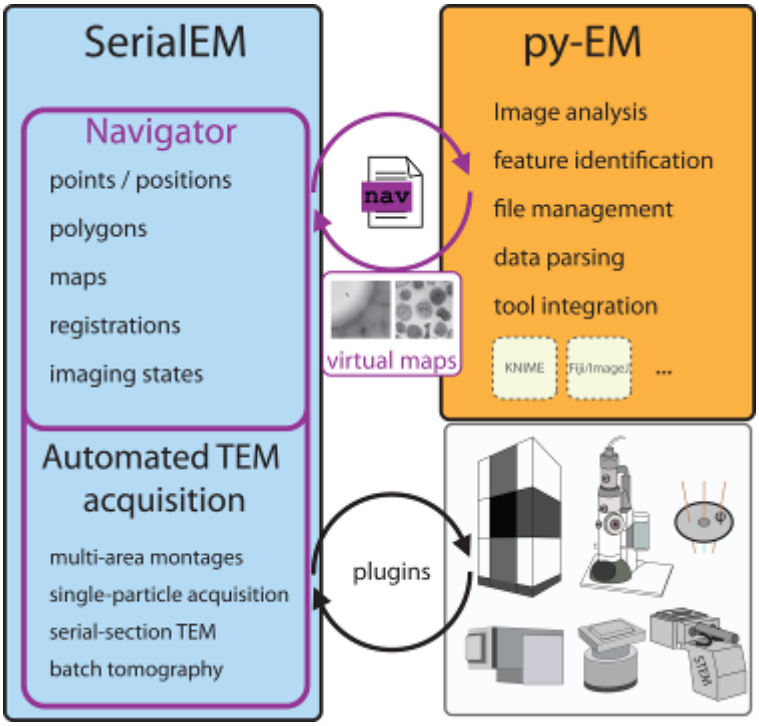

IM1.004 invited
Advances in Ultra-High Energy Resolution EELS

O. Krivanek[1,2], G. Corbin[1], N. Dellby[1], M. Hoffman[1], N. Johnson[1], C. Meyer[1], A. Mittelberger[1], T. Lovejoy[1]

[1]Nion Co., R&D, Kirkland, United States
[2]Arizona State University, Physics, Tempe, Arizona, United States

Ultra-high energy resolution electron energy loss spectroscopy (EELS) in the electron microscope continues to advance rapidly. Since the first demonstrations that vibrational EELS can be performed in an electron microscope in 2014 (1, 2), the energy resolution has improved about 3x, and completely new application areas have opened up. This abstract summarizes recent progress.

The improvement in energy resolution is illustrated in Fig. 1: ~5 meV resolution at 30 keV can now be achieved with suitable instrumentation. This allows many new types of experiments, such as isotopic imaging, done by identifying energy shifts due to isotopic substitution, e.g. of 13C for 12C in an amino acid (L-alanine) (3). Spectra of radiation-sensitive samples such as L-alanine are typically acquired with the electron beam in the vacuum outside the sample (aloof geometry). This decreases the attainable spatial resolution to about ~30 nm, but it largely avoids radiation damage (4).

Much better spatial resolution can be reached when the beam is on the sample and the scattering angles accepted into the spectrometer are large, thus allowing highly localized "impact" scattering to contribute to spectra and vibrational maps. This has led to nm-level spatial resolution in vibrational mapping of BN (5), and more recently to 2 Å-level spatial resolution in BN (6) and in Si (7).

Fundamental advances have also been made in understanding the momentum dispersion of phonons excited by fast electrons. The variation of vibrational losses (w) as a function of the scattering angle and hence momentum transfer q has been investigated along high symmetry directions in the Brillouin zone (BZ) (8). This demonstrated that when q > 0, acoustic phonons can be excited in addition to optical phonons. However, the phonon signal at large q is weak, and serial acquisition of complete w-q diagrams can take tens of minutes to hours (8).

In Fig. 2 we explore parallel acquisition of w-q diagrams, using a 0.125 x 2 mm slot aperture located in the spectrometer entrance plane, and rotating the diffraction pattern by adjusting the microscope"s projector lenses so that selected high-symmetry directions in the BZ are sampled by the slot. The shown w-q diagrams were recorded along the G-M-G" and G-K-M-K"-G" directions in hexagonal BN in 5 minutes each.

References:

(1) O.L. Krivanek et al., Nature 514 (2014) 209

(2) T. Miata et al., Microscopy 63 (2014) 377

(3) J. Hachtel et al., Science 363 (2019) 525–528

(4) P. Rez et al., Nature Comms 7 (2016) 10945, doi: 10.1038/ncomms10945

(5) C. Dwyer et al., Phys. Rev. Lett 117 (2016) 256101

(6) F.S. Hage et al., Phys. Rev. Lett 122 (2019) 016103

(7) K. Venkatraman et al., arXiv:1812.08895 (2018)

(8) F.S. Hage et al., Sci. Adv. 2018;4:eaar7495 1-5

Fig. 1: Vibrational spectra of guanine. EELS1 and FTIR spectra are from 2016 (4), EELS2 is from 2019 and shows 5.9 meV energy resolution. Nion HERMES with Iris spectrometer, 30 keV.

Fig. 2: w-q experimental diagrams obtained from hexagonal BN in parallel acquisitions spanning G-M-G"-M" (left) and G-K-M"-K"-G" (right) directions in the Brillouin zone. 30 kV, 15 pA beam current.

Fig. 1

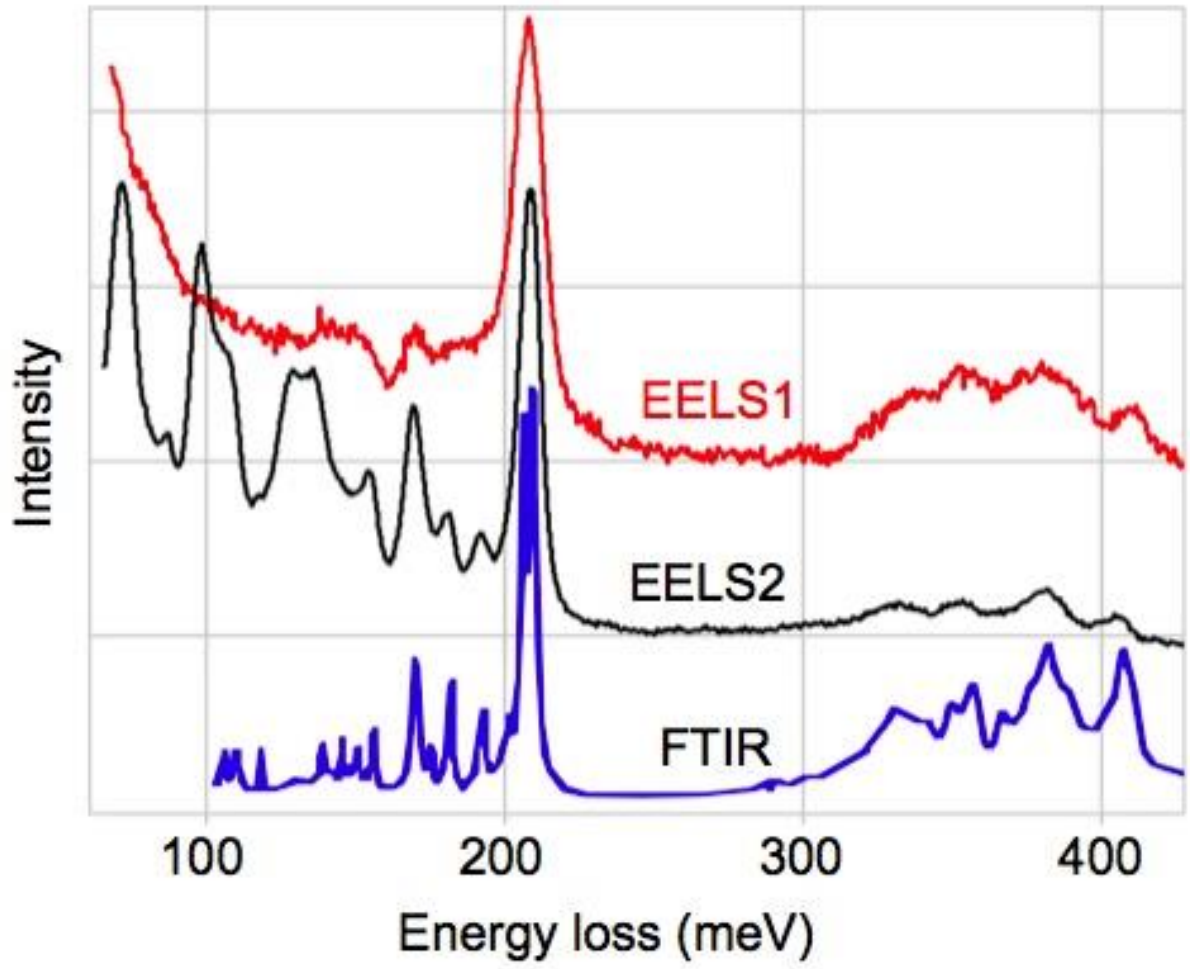
Intensity
EELS1
EELS2
FTIR
100
200
300
400
Energy loss (meV)

Fig. 2

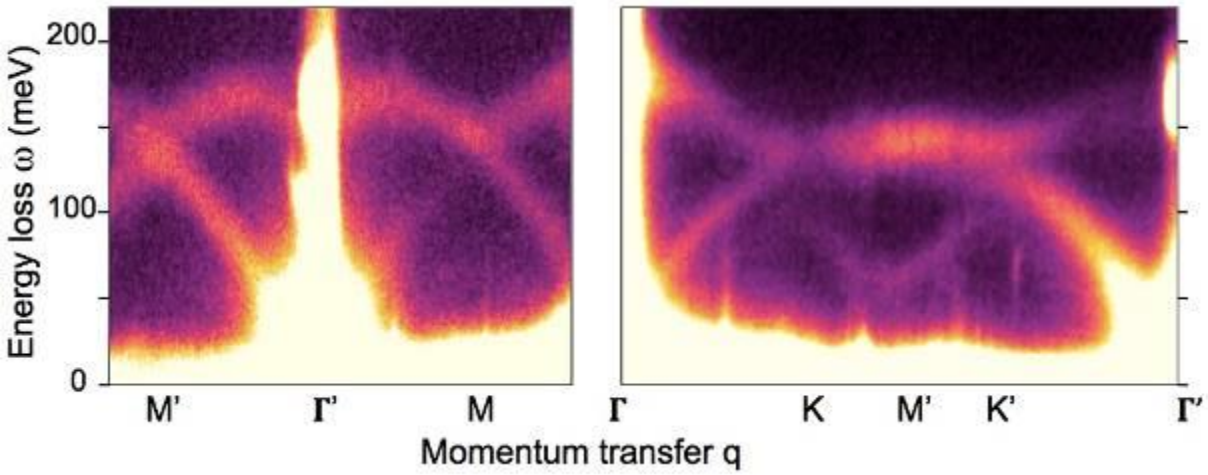
Energy loss ω (meV)
200
100
0
M'
Γ'
M
Γ
K
M'
K'
Γ'
Momentum transfer q

IM1.005
A posteriori Synchronization of Scanning Transmission Electron Microscopy Signals with Kilopixel per Second Acquisition Rates for Multimodal Experiments

T. Meyer[1], S. Lopatin[2], M. Seibt[1], V. Roddatis[3]

[1]University of Göttingen, IV. Physical Institute - Solids and Nanostructures, Göttingen, Germany
[2]King Abdullah University of Science and Technology (KAUST), Core Labs, Thuwal, Saudi Arabia
[3]University of Göttingen, Institute of Materials Physics, Göttingen, Germany

During the last decades, the variety of attachable detectors and collectable signals in the scanning transmission electron microscope (STEM) has grown tremendously. In addition, e.g. due to the development of direct detectors, possible acquisition speeds of classical STEM signals like electron energy-loss spectra (EELS and diffraction patterns (DP) were raised to the kilopixel per second regime at very high detection efficiencies. Besides the opportunities offered by these achievements, they demand for an accurate synchronization of the beam movement of the scanning process and all desired detectors enabling for multimodal experiments. The latter becomes particularly difficult if detectors of various manufacturers are involved and commercial solutions are often not available.

In this work, we present a modified scanning pattern allowing for a posteriori data reconstruction of arbitrarily many signals which are recorded independently, i.e. there is no synchronization during the acquisition. The key of the modified pattern is to move the beam before and after each scanning line to a predefined marker position. Subsequently, the signal of the marker position is localized in the continuously read-out signals and used in order to reconstruct the scanning positions.

The method is proven to be applicable to kilopixel per second scanning speeds on the atomic scale. Furthermore, its versatility is demonstrated by correlating STEM, EELS, and energy-dispersive X-ray (EDX) data, which is taken using a digital multimeter and two independent computers. Obviously, since there is no live synchronization during the acquisition process, the proposed method might cause a spatial blur of the signal. Nevertheless, in addition to standard STEM distortions (1), this blur is quantified to be only roughly half the pixel spacing in the horizontal scanning direction whereas the vertical resolution remains. Hence, samples with translational symmetry in one dimension, e.g. lattice planes of an epitaxial thin film, can be analysed without any restrictions in terms of spatial resolution.

Moreover and in addition to its high versatility, the method"s acquisition process is demonstrated to be 12% faster than a commercial hardware-synchronized solution since there are no waiting periods to maintain synchronicity during the scanning. This speed gain can be particularly advantageous when high detection efficiencies respectively short acquisition times are needed, e.g. in the case of very beam sensitive materials. On top of this, the scanning pattern can potentially be modified in a more sophisticated way to match other experiment"s requirements as it has been done in a sparse sampling approach in (2).

References:

(1) S. Ning, T. Fujita, A. Nie, Z. Wang, X. Xu, J. Chen, M. Chen, S. Yao, T.-Y. Zhang, *Ultramicroscopy* 184 (2018) 274-283.

(2) L. Kovarik, A. Stevens, A. Liyu, N. D. Browning, *Applied Physics Letters* 109 (16) (2016) 164102.

IM1.006
Pushing the Analytical Capabilities of Silicon Drift Detectors for EDX Imaging of Low-Z Materials down to Lithium

A. Niculae[1], T. Barros[1], A. Liebel[1], H. Soltau[1], L. Strüder[2,3]

[1]PNDetector GmbH, Munich, Germany
[2]University of Siegen, Physics, Siegen, Germany
[3]PNSensor GmbH, Munich, Germany

Recent developments in the field of new materials and composites have been pushing for more powerful instrumentation in electron microscopy. Energy Dispersive X-ray spectroscopy (EDX) is one of the commonly used techniques for determining the elemental composition of the EM samples. As a pioneer in the development and manufacturing of Silicon Drift Detectors for EDX Microanalysis, we have been continuously working on pushing the performance values of the SDDs towards the physical limits (1).

With the grown interest for renewable energies, the research activities on Li-ion batteries have gained more and more significance also in the field of electron microscopy (2). Extending the energy detection limits of the SDDs for light elements down to Lithium (54 eV) has become one of our major development objectives in the last years.

When it comes to detect very low energy X-rays like e.g. in the range 50 to 100 eV, the EDX detector has to fulfill some conditions. First of all, a windowless detector is mandatory; any external window in the front of the sensor would substantially absorb low energy X-rays. Secondly the electronic noise contribution of the detector must be reduced to very low levels. Fig.1a shows the calculated energy resolution (FWHM) of a detector as a function of the incoming photon energy. Whereas at higher photon energies the so-called Fano (statistical) noise is the dominant component, for very low energies the detector electronic noise becomes the dominant contribution to the energy resolution. In order to be able to detect 54 eV X-rays, a noise level well below 30 eV in FWHM is necessary. The third ingredient is a loss-free detector entrance window (i.e. the very thin passive layer on the SDD sensor), its quality being described by the incomplete charge collection (ICC) as a function of the penetration depth. Our elaborated window technology insures ICC values of 95% at Si - dead layer interface, while increasing to 100% in 200 nm depth.

Owing the integration of the first FET on detector chip level, the total input capacitance of the detector can be reduced to as low as 50 fF for the sensor type SDD^{GL}. Combined with very low leakage current technology an electronic noise level below 20 eV FWHM is being achieved for such sensors. Fig. 1b shows the EDX spectrum from a Carbon sample measured with a SDD^{GL} sensor in a windowless configuration. Fig.2 shows EDX spectra of low energy X-rays measured with a 10 mm^2 SDD^{GL} sensor. The Al-L peak at 68 eV is well separated from the noise peak (20 eV FWHM), as is the Li-K peak @ 54 eV in Fig. 2b.

The analytical capability of the SDDs in detecting Li-K X-rays demonstrates that EDX spectroscopy and mapping on Lithium containing samples is feasible with such detectors.

References:

(1) Niculae A. et al., Microscopy and Microanalysis, Volume 19, Issue S2, 2013, pp. 1270-1271

(2) Muto S., Tatsumi K., Microscopy, 2017, pp. 39–49

Fig. 1: (a) Energy resolution of the detector as a function of incoming photon energy for different values of the detector intrinsic noise (given as FWHM); (b) EDX spectrum of a carbon sample measured with a detector having a noise level of 19 eV in FWHM.

Fig. 2: EDX spectra measured in an SEM from (a) Al sample showing the Al-L line at 68eV and (b) pure Lithium sample showing the Li-K at 54 eV peak which can be clearly distinguished from the noise.

Fig. 1

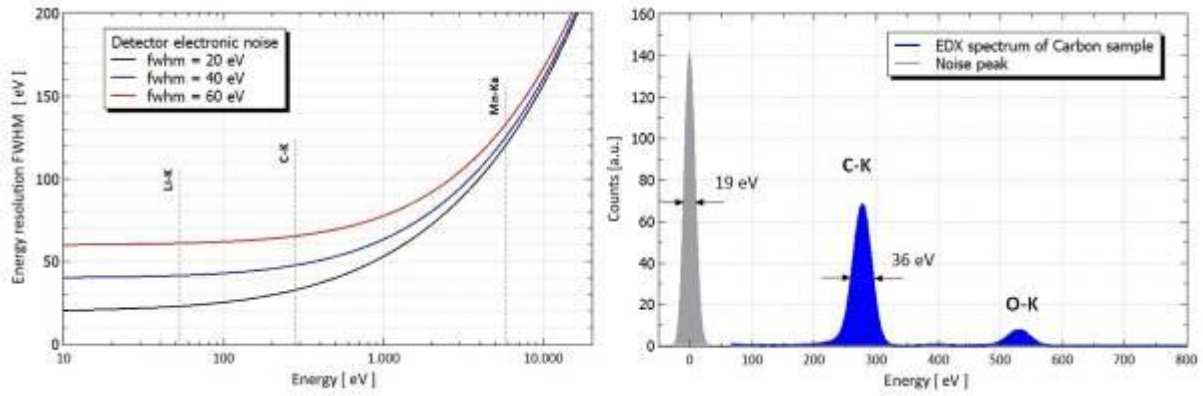
Detector electronic noise
fwhm = 20 eV
fwhm = 40 eV
fwhm = 60 eV
Energy resolution FWHM [eV]
Energy [eV]
Li-K
C-K
Mn-Ka
EDX spectrum of Carbon sample
Noise peak
Counts [a.u.]
19 eV
36 eV
C-K
O-K

Fig. 2

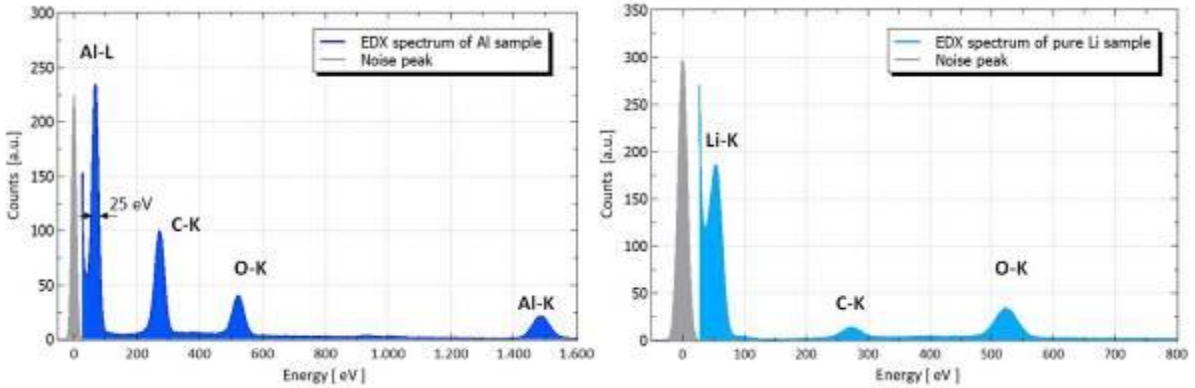
EDX spectrum of Al sample
Noise peak
Counts [a.u.]
Energy [eV]
Al-L
25 eV
C-K
O-K
Al-K
EDX spectrum of pure Li sample
Noise peak
Li-K
C-K
O-K

IM1.007
STEM Ptychography Using Binary 4D Datasets

C. M. O'Leary[1], E. Liberti[1,2], S. M. Collins[3], D. N. Johnstone[3], M. Rothmann[1], J. Hou[3], C. S. Allen[1,2], J. S. Kim[1,2], T. D. Bennett[3], P. A. Midgley[3], A. I. Kirkland[1,2], P. D. Nellist[1]

[1]University of Oxford, Department of Materials, Oxford, United Kingdom
[2]Diamond Light Source, electron Physical Sciences Imaging Centre (ePSIC), Didcot, United Kingdom
[3]University of Cambridge, Department of Materials Science and Metallurgy, Cambridge, United Kingdom

Fast pixelated detectors (FPDs) in scanning transmission electron microscopy (STEM) have enabled the acquisition of a convergent beam electron diffraction (CBED) pattern with high signal-to-noise ratio at each probe position in a raster scan (1-2). Such detectors have provided a wealth of possibilities for nanoscale characterization, particularly in the field of electron ptychography. Many FPDs possess a large *dynamic range* – this is essential for acquiring simultaneous high-angle annular dark-field (HAADF) and focused-probe ptychography data while avoiding saturation of the bright-field disk (3).

The super-resolution and low-dose capabilities of electron ptychography using FPDs have seen many recent developments (4), but relatively slow readout speeds are ultimately a severe limitation (i.e. 10^{-3} s per frame vs 10^{-5} s for ADF imaging). It is possible, however, to increase the frame rates in certain electron counting detectors by decreasing the usable dynamic range. This significantly reduces both the cumulative dose for a given beam current, and scan distortions. In this contribution, we explore the capabilities of binary (1-bit) ptychography in STEM as a low-dose phase-reconstruction technique using a standard monolayer of MoS_2 as a test sample.

Figure 1(a) shows an example CBED pattern from one of 512x512 probe positions recorded for a MoS_2 monolayer. The data was recorded using a Medipix3 detector on a JEOL ARM300CF (HT = 80kV, α = 31 mrad, dose ≈ 10,000 e $Å^{-2}$). The counter depth of the Medipix3 was set to 2x1-bit (10kHz) instead of conventional 12-bit (1kHz) and 6-bit (2kHz) modes. Figure 1(b) shows the phase of the Fourier transform of the acquired 4D STEM data for one specific spatial frequency (28 mrad). This demonstrates that, even for low-dose CBED patterns with isolated electrons, the phase of the diffracted beams is still strongly expressed in the data. Figure 2 shows the phase reconstruction obtained from the acquired 4D data set using single side-band ptychography (5-6). Following reconstruction, the MoS_2 monolayer structure is visible.

The application of SSB ptychography and other ptychographic techniques on binary CBEDs will be compared and discussed. Finally, the application of low-dose binary ptychography to metal-organic frameworks (UiO-66) and other beam-sensitive materials will be presented.

References:

(1) H. Ryll *et al*, Proceedings of Microscopy & Microanalysis (2014) p. 1122–1123.

(2) D. McGrouther *et al*, Proceedings of Microscopy & Microanalysis (2015) p. 1595-1596.

(3) H. Yang *et al*, Nature Communications 7 (2016), p. 12532.

(4) Y. Jiang *et al*, Nature 559 (2018), p. 343-349.

(5) J. M. Rodenburg, B. C. McCallum and P. D. Nellist, Ultramicroscopy 48 (1993), p. 304-314.

(6) T. J. Pennycook *et al*, Ultramicroscopy 151 (2015), p. 160–167.

(7) The financial support of JEOL (UK) Ltd. and the EPSRC is gratefully acknowledged.

Fig. 1: (a) Example of a binary convergent beam electron diffraction (CBED) pattern acquired for monolayer MoS_2. (b) Phase of Fourier transform ("trotter") of the acquired 4D data set for a specific spatial frequency (28 mrad). The trotter has been masked to show only regions of constructive interference. Color bar: phase (radians).

Fig. 2: Ptychographic phase reconstruction of a monolayer of MoS_2 using the single side-band method. Scale bar: 1nm. Color bar: phase (radians).

Fig. 1

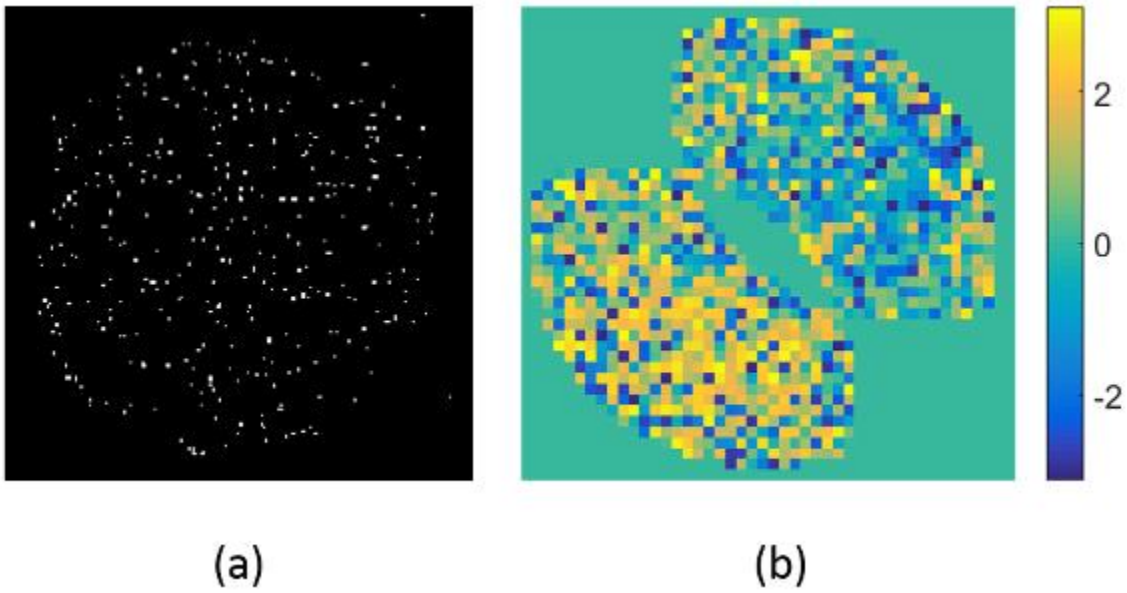

Fig. 2

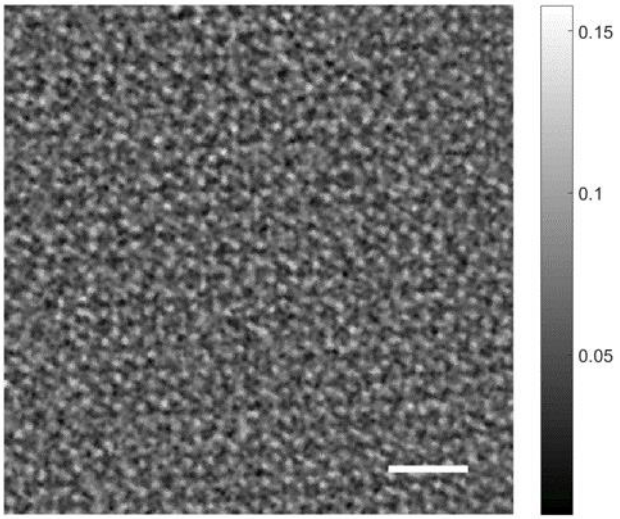

IM1.008
In-situ Secondary Ion Mass Spectrometry Analysis in a Transmission Electron Microscope: Instrument development and optimization of analytical conditions

M. Mousley[1], S. Eswara[1], T. Wirtz[1]

[1]Luxembourg Institute of Science and Technology, Materials Research and Technology, Belvaux, Luxembourg

Transmission Electron Microscopy (TEM) is a well-established technique for high-resolution imaging. However, analysis of light elements (Z < 6) and trace concentrations using typical analytical techniques in a TEM such as Energy-Dispersive X-Ray Spectroscopy (EDX) or Electron Energy-Loss Spectroscopy (EELS) is challenging or even impossible. For the advancement of science and technology in a broad range of research fields, the ability to map low-Z elements and trace concentrations at high-resolution is an increasingly important characterization need. In this context, Secondary Ion Mass Spectrometry (SIMS) imaging offers the possibility to image all elements including isotopes along with the high-sensitivity needed for the analysis of trace elements. However, the main limitations of the SIMS technique are that quantification (MM1) of chemical composition is not straight-forward because of matrix effect (1) and the lateral resolution is fundamentally limited to ~ 10 nm set by the ion-solid interaction volume. By comparing the strengths and weaknesses of TEM and SIMS techniques, it can be seen that they are complementary. In order to have the benefits of TEM and SIMS in a single instrument, we modified the octagon of a FEI Tecnai F20 TEM such that a Ga+ FIB and a SIMS can be integrated around the TWIN objective lens pole-pieces of the TEM (2), (3). A compact magnetic-sector mass spectrometer was designed and developed in-house. A special TEM holder capable of high-voltage (± 5 kV) sample bias was developed to enhance the secondary ion collection efficiency. Proof-of-concept of the in-situ TEM-SIMS technique was demonstrated using isotopically labelled Li compounds (2). The instrumentation and the analytical methodology are currently being optimized to enhance the collection and ionization efficiencies in order to improve the SIMS useful yield.

In this presentation, we will discuss recent developments in the instrumentation and the optimization of analytical methodology for correlative microscopy combining TEM and SIMS. Examples taken from the analysis of cycled cathode materials from Li-ion batteries and dopants in crystalline Si solar cells will be presented. Furthermore, algorithms for correlating multimodal (TEM and SIMS) images from the same ROI with mismatch in pixel-sizes will be explored (4).

References:

(1) A. Benninghoven, F. G. Rüdenauer, and H. W. Werner, *Secondary ion mass spectrometry: basic concepts, instrumental aspects, applications, and trends*. New York: J. Wiley, 1987.

(2) L. Yedra, S. Eswara, D. Dowsett, and T. Wirtz, "In-situ Isotopic Analysis at Nanoscale using Parallel Ion Electron Spectrometry: A Powerful New Paradigm for Correlative Microscopy," *Sci. Rep.*, vol. 6, no. 1, p. 28705, Jun. 2016.

(3) S. Eswara *et al.*, "Correlative Microscopy Combining Transmission Electron Microscopy and Secondary Ion Mass Spectrometry: A General Review on the State-of-the-Art, Recent Developments and Prospects," *Appl. Phys. Rev.*, vol. Accepted, 2019.

(4) F. Vollnhals *et al.*, "Correlative Microscopy Combining Secondary Ion Mass Spectrometry and Electron Microscopy: Comparison of Intensity–Hue–Saturation and Laplacian Pyramid Methods for Image Fusion," *Anal. Chem.*, vol. 89, no. 20, pp. 10702–10710, Oct. 2017.

Fig. 1: In-situ SIMS images (H- and D-) overlaid on a corresponding TEM image from a sample containing a physical mixture KD2PO4 and KH2PO4 powders.

Fig. 1

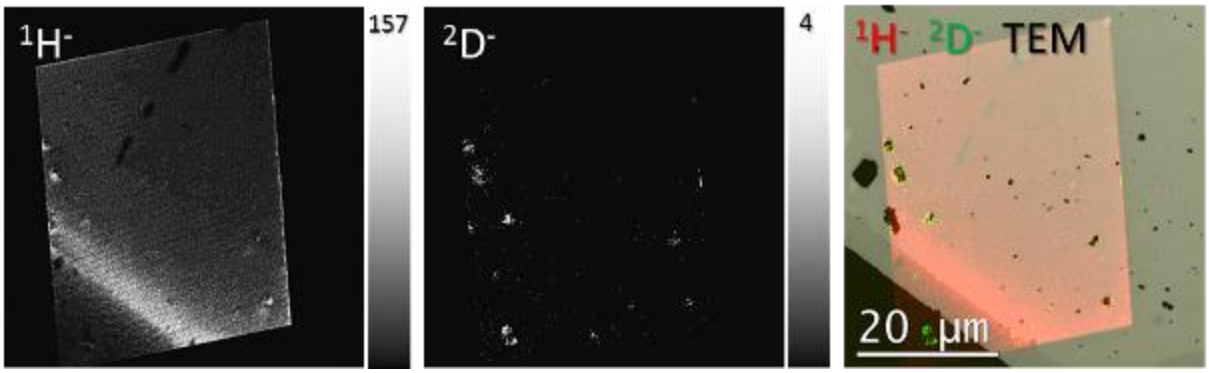

IM1.LB.P01
Model-Based EELS Quantification and ELNES Phase Mapping Using Experimentally Measured Cross-Sections

B. Schaffer[1], L. Spillane[2], P. Thomas[2]

[1]Gatan GmbH, Munich, Germany
[2]Gatan Inc., Pleasanton, United States

Electron-energy-loss spectroscopy (EELS) can reveal a wealth of information about the sample under investigation with high sensitivity and high spatial resolution. However, extracting this information in an optimal manner is often non-trivial for a variety of reasons. In recent years, model-based quantification has both simplified and improved the accuracy of the quantification process in EELS (e.g. (1, 2)). It could be shown that using a combination of a power-law decaying background along with theoretically computed cross-sections as first-order approximation of the expected edge shape gives a reasonably robust way of performing compositional quantification, automatically separating out contributions of overlapping edge shapes in many commonly encountered situations. Provided a suitable EELS low-loss spectrum is available, plural scattering effects can also be incorporated into such an analysis to further improve the quantification. While this approach can greatly improve the reproducibility and accuracy of quantification and allows for very fast map computations in the spectrum-imaging application, some groups of tightly overlapping edges can still not be sufficiently separated automatically. This inability is caused by the theoretical cross-sections not correctly reproducing the electron loss near-edge fine-structure (ELNES) features that are present in experimentally measured spectra.

The improved quantification scheme presented here utilizes experimentally measured cross-sections to improve the situation. The cross-section shape is readily derived from background-subtracted spectra, ideally corrected for plural scattering effects, to create an edge "standard". This edge standard can often (and ideally) be obtained directly from the spectrum-image data to be analyzed itself. Scaling of the standard is then either achieved by normalization with theoretically computed cross-sections, or it can be derived from the *a-priori* knowledge of the sample composition and thickness.

This new approach combines the advantages of the multiple linear least-square (MLLS) fitting of static reference spectra with the model-based quantification scheme. MLLS fitting of pre-measured standards has been shown previously to yield superior quantification compared to conventional background subtraction (3). It can also achieve clean separation of edges for complex overlapping scenarios and incorporates plural scattering correction at the same time, yielding more accurate maps for specimens with thickness variations across the data (Fig.1). This is achieved in a simple, unified workflow. Furthermore, by allowing multiple concurrent experimental cross-section references to be specified for each individual core-loss edge, ELNES finger-printing can be incorporated into the same quantification routine (Fig. 2). This allows the separation of elements of different chemical states to be performed routinely, with plural scattering correction applied, as part of the regular elemental mapping process. This approach will be described, along with practical examples of common application use cases.

References:

(1) J. Verbeeck et al, Ultramicroscopy 106 (2006) 11

(2) P.J. Thomas et al., Microsc. Microanal. 18 (Suppl 2), 2012, p968.

(3) K. Riegler et al, Ultramicroscopy 110 (2010) 8

Fig. 1: Comparison of elemental intensity maps and quantified area-spectrum.

Fig. 2: ELNES finger-printing by providing multiple concurring experimental cross-sections during quantification.

Fig. 1

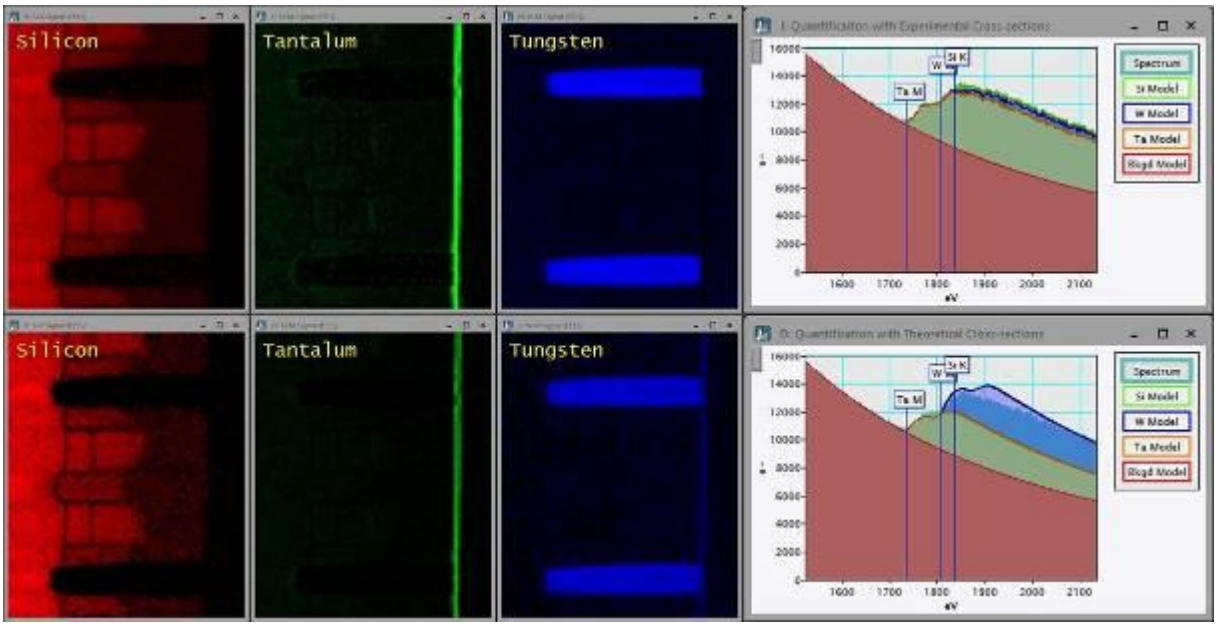
Silicon
Tantalum
Tungsten
Spectrum
Si Model
W Model
Ta Model
Bkgd Model
eV

Fig. 2

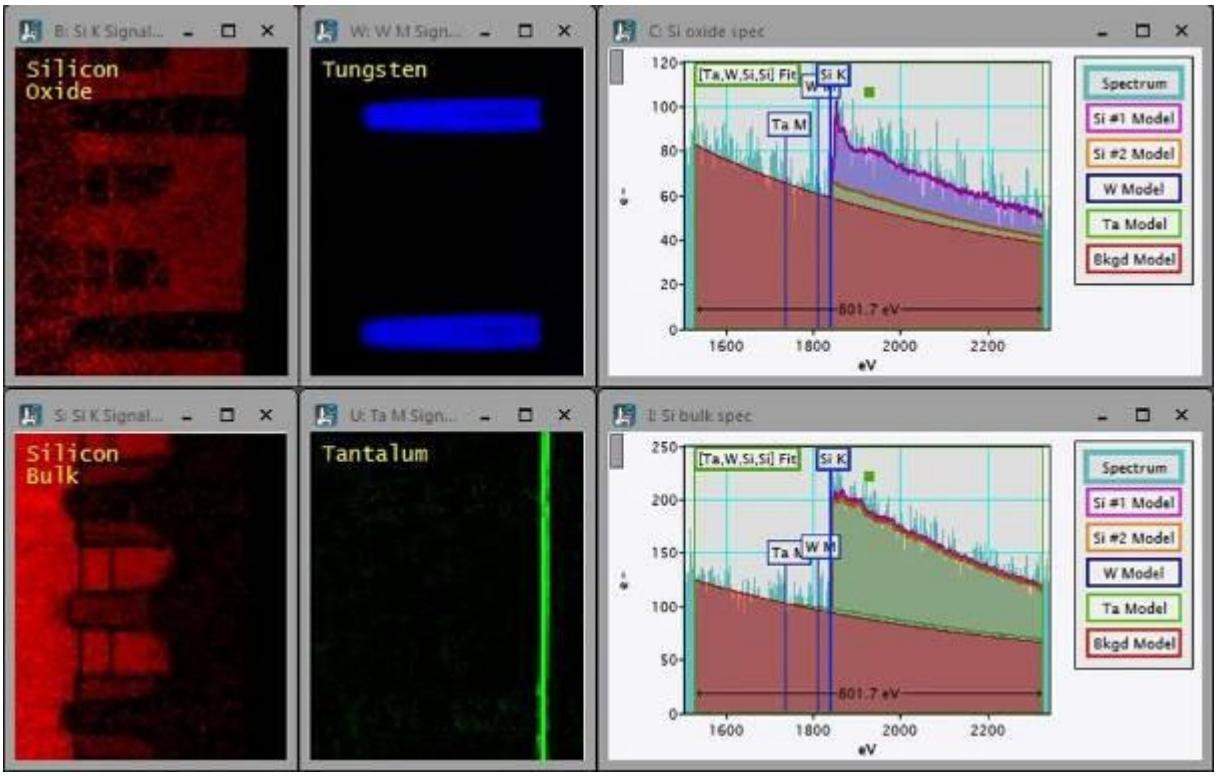
Silicon Oxide
Tungsten
Silicon Bulk
Tantalum
[Ta,W,Si,Si] Fit
Si K
Ta M
801.7 eV
Spectrum
Si #1 Model
Si #2 Model
W Model
Ta Model
Bkgd Model
eV

IM1.P001
Interference Experiment with Optically Zero Propagation Distance between Double-Slit and Observation Plane

K. Harada[1,2], T. Kodama[3], T. Akashi[4,5], Y. Takahashi[4], K. Shimada[1], Y. Ono[1], D. Shindo[1,6], H. Shinada[4], S. Mori[2]

[1]RIKEN, CEMS, Hatoyama, Japan
[2]Osaka Prefecture University, Materials Science, Sakai, Japan
[3]Meijo University, Science & Technology, Nagoya, Japan
[4]Hitachi Ltd, Research and Development, Hatoyama, Japan
[5]Kyushu University, Applied Quantum Physics, Fukuoka, Japan
[6]Tohoku University, IMRAM, Sendai, Japan

Yang"s double-slit experiments show interferences owing to the long propagation distance from a double-slit to the observation plane. We performed a double-slit interference experiment under a short propagation distance, i.e., under the "pre-Fraunhofer condition" (1). In the experiment, however, because of the existence of a propagation distance, two waves passed through the right and left slits always overlapped and controlling the waves was difficult. To overcome this difficulty, we devised an optical system for imaging the double-slit on the observation plane under the infocus condition. This experimental condition can be considered as an optically zero propagation distance from the double-slit to the observation plane.

Two electron biprisms were installed in the optical system to superimpose the two waves and to control the interference. In addition, we used a V-shaped double slit (V-DS) of Cu foil made with a focused ion beam instrument to observe in a single image the interference features before, during, and after overlapping of electron waves from the left and right slits.

An example of the interference pattern of the V-DS is shown in Fig. 1. The images of the right and left slits are overlapped and observed as an X-shaped form. The interference fringes appeared at the overlapped region of two electron waves, while uniform single electron distributions are obtained in the pre- and post-interference regions. This result indicates that interference occurred only when no information was obtained on which slit the electrons passed through.

References:

(1) K. Harada *et al.*, Scientific Reports, **8** (2018) 1008.

(2) This work was supported by JSPS KAKENHI, Grant Number (B) 18H03475.

Fig. 1: *Interference patterns on the V-shaped double-slit through the application of voltages to the biprisms.*

Fig. 1

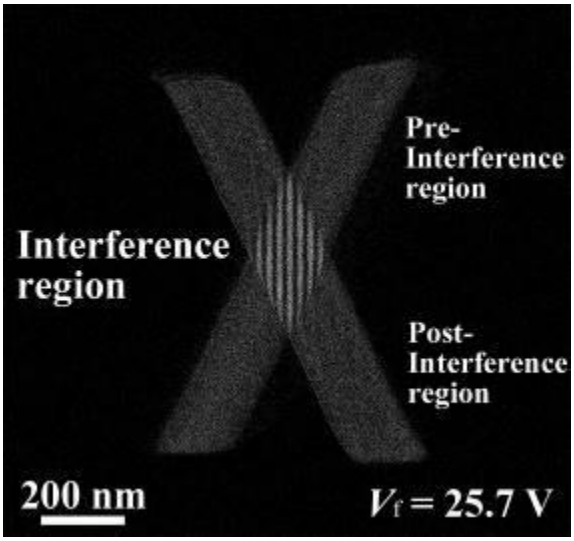

IM1.P002
The estimation of charge densities from differential phase contrast in the TEM

S. Schulze[1], I. Alexandrou[2], C. Tegenkamp[1]

[1]TU Chemnitz, Physics, Chemnitz, Germany
[2]Thermo Fisher Scientific, Eindhoven, Netherlands

As early as 40 years ago the use of a four quadrant detector geometry was proposed to get Differential phase contrast (DPC) in the scanning electron microscope.

Recent developments in conjunction with aberration corrected Scanning Transmission Electron Microscopes (STEM) demonstrated the ability to achieve atomic resolution DPC images.

Since the shift in the centre of intensity of the diffraction disc is proportional to the force on the beam electrons, one can directly use it to image the local field distribution in the specimen plane.

Due to the difficulty however to display and interpret vector fields attempts have been made to display the one dimensional potential that causes the fields rather than the originally recorded field. The potential can be calculated by integrating the measured electric field yielding integrated Differential Phase Contrast (iDPC). Regardless of the used mathematical technique to integrate the measured field noise makes the low frequency behaviour of the potential distribution quite inconsistent. In addition, any image processing based on the integration of image data leads to broadening of image structures i.e. a lack of clarity.

That"s why we decided here to go the opposite way and differentiate the measured field distribution to derive the charge density distribution generating the electrical field according to $\rho(\mathbf{r})=\varepsilon_0(\boldsymbol{\nabla}\cdot\mathbf{E}(\mathbf{r}))$.

As positively and negatively charged areas balance in a neutral sample, changes of sign are a basic property of such charge density distributions. This can be illustratively visualized with colour images showing such as positive charge densities in blue and negative charge densities in yellow colors.

To study epitaxial grown graphene layer structures on SiC substrates cross section samples for (S)TEM analysis have been prepared by a Thermo Scientific Scios 2 Dual Beam. The samples were then DPC-imaged in a Thermo Scientific double c_s corrected Themis Z (S)TEM operated at a primary electron energy of 80 keV to prevent knock-on damage in the graphene.

Charge density distributions derived from DPC image components show densely packed planes of Atoms in blue separated by bonding electron charges in yellow (Fig. 1). Line scans perpendicular to particular crystallographic planes in HR images can be averaged to receive charge densities in and between the densely packed planes of atoms. In Silicon Carbide for example, there are 24 bonding electrons per square nanometer between the densely packed (111) planes with equal numbers of Si- and C-Atoms. So for neutrality the atomic planes are charged with the same amount of positive in plane charge.

As compared with these known face densities in the SiC substrate we observe much higher amounts of face charge on and between the graphene layers overgrown to the SiC surface amounting to about 60 … 70 electrons per square nanometer (Fig. 2).

We demonstrate that charge density distributions are capable of delivering high quality quantitative evaluable atomically resolved images from differential phase contrast component images.

Fig.1: Display of the High Resolution Differential Phase Contrast in terms of charge densities: Positive charge densities are displayed in blue and negative densities in yellow.

Fig. 2: Charge density distribution along the the red stripe in Fig. 1. The intensity is averaged in horizontal direction to improve statistics.

Fig. 1

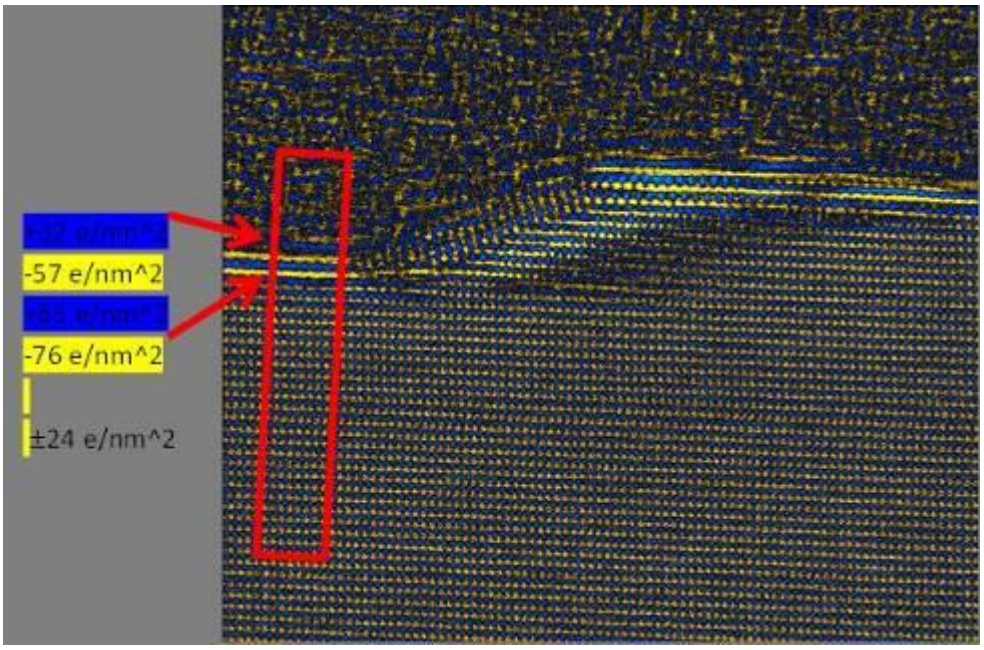

Fig. 2

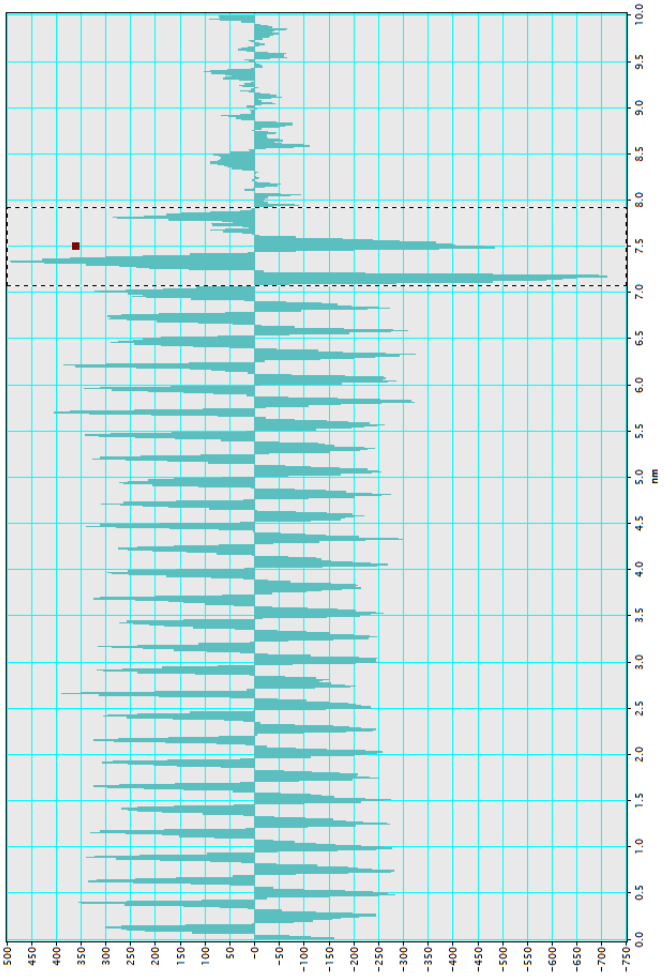

IM1.P003
Regularized optimization for ptychography - A gradient based ptychographic reconstruction algorithm

M. Schloz[1], T. C. Pekin[1], W. Van den Broek[1], C. T. Koch[1]

[1]Humboldt Universität zu Berlin, Institut für Physik & IRIS Adlershof, Berlin, Germany

Ptychography is a coherent imaging technique that recovers the phase shift of the scattering radiation within the probed object from a series of diffraction patterns, each of which is obtained by illuminating the sample with a spatially limited probe. For each measurement, the probe is shifted such that a sufficient overlap of the illuminated areas guarantees information redundancy which is required for a robust computational reconstruction of the phase. Because of its advantage of not being limited by optical aberrations and due to ever-improving computing power and detector technology, ptychography has found numerous applications.

Here we introduce regularized optimization for ptychography (ROP) which is a derivative-based phase retrieval algorithm that uses a conjugate gradient method. ROP is an extension to the inversion of dynamical electron scattering (IDES) that has been demonstrated to successfully reconstruct from simulated high resolution transmission electron microscope images and diffraction data (1,2). Its framework is based on a multislice approach (3) that splits the reconstruction into a series of axial slices to account for multiple scattering in the specimen. ROP retrieves the electrostatic potential, the electron probe and the probe positions, allows to freely choose the error metric and can incorporate a regularization to the solution.

In Figure 1. the results from simulated diffraction patterns are shown. The sample is a (001) oriented Si-wedge, increasing in thickness from 0 to 15 nm. CBED patterns were simulated with the multislice algorithm FDES (4), the acceleration voltage was 60 kV, the semi-convergence angle of the probe was 20 mrad, the probe was defocused by 3.7 nm, the scan step was 0.066 nm, and the slice thickness was 0.1 nm. For the reconstruction the thickness was assumed known, the initial defocus was set to 7.7 nm, the beam positions were given a random displacement away from the true values of 0.036 nm on average, and incorporation of the multislice formalism ensured a sufficiently accurate treatment of the multiple scattering with a slice thickness of 1 nm and all slices constraint to be equal. The object potential is reconstructed faithfully and the probe and probe positions are retrieved as well. (5)

References:

(1) W. Van den Broek and C.T. Koch, Phys. Rev. Lett. 109 (2012) p. 245502.

(2) W. Van den Broek and C.T. Koch, Phys. Rev. B 87 (2013) p. 184108

(3) P. Goodman and A. F. Moodie, Acta Cryst. A30 (1974) p. 280

(4) W. Van den Broek, X. Jiang and C.T. Koch, Ultramicroscopy 158 (2015) p. 89

(5) M.S., T.C.P. and W.V.d.B. acknowledge financial support from the DFG Grant No. BR 5095/2-1

Fig. 1: From left to right: a typical CBED pattern (logarithmic grayscale); reconstructed potential; profiles of initial, optimized and true probe; initial, optimized and true probe positions from the area in the second image, average deviation from true positions after optimization: 0.0036 nm.

Fig. 1

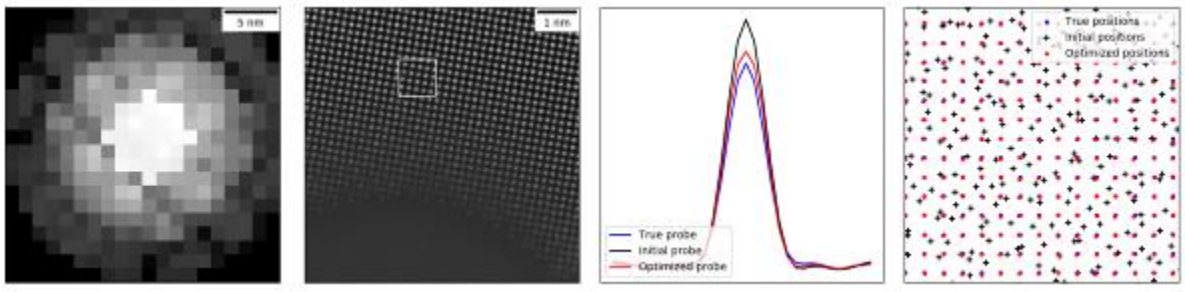

IM1.P004
MONOCHROMATIZING WITHOUT FILTERING: PROPOSAL FOR A MICROWAVE BASED LOW LOSS MONOCHROMATOR FOR S(T)EM

R. Janzen[1]

[1]Roland Janzen Consulting, Zwingenberg, Germany

Commonly used monochromators are energy filters. The majority of the particles with undesired energies is removed. Thus the output current diminishes with increasing degree of monochromatization. Monochromators in the original meaning of the word that would affect the energy of the particles by an energy selective acceleration can only be realized by use of dynamic fields.

Dynamic field applications without exception involve a condition between the phase of the dynamic field and the entrance point of time of the particle into the field. If this condition is fulfilled, the dynamic field application works exactly. Unfortunately the width of the time interval where the condition is fulfilled is mathematically zero. Thus up to now dynamic field applications in charged particle optics limit themselves to a small time interval around the periodically recurring point of optimum phase where the condition is fulfilled to a good approximation. For that purpose bunches are formed around the optimum phase point. Unfortunately bunch forming suffers from Liouville"s theorem: The product of the bunch length and the energy spread within it is a constant.

In this work a concept is presented that circumvents this dilemma. A circularly polarized standing wave deflects the charged particle beam to a rotating orbital feeding the particles into a propagating wave that rotates within a toroidal wave guide (see figure 1). The circular deflection supplies a time coding. The entrance point of time of any particle is locked to its azimuthal position. Provided that the deflecting field and the rotating propagating wave (denoted by working field in the following) are synchronized correctly the optimum phase condition is fulfilled exactly and constantly. Time uncertainty vanishes within the limits of technical & practical implementing of the concept. The working field may be cascaded. It can be used for a large variety of applications such as monochromatizing, spread inversion (and not covered by this talk: time focusing, accelerating, pulse forming, spread amplification, and aberration correction). In the end the spiral orbital may be focused to an inverse circular deflector that undoes the action of the first circular deflector and thus leads the particles back to the original axis (see figure 2.).

A monochromator based on circular deflection was demonstrated to work by computer simulation assuming theoretically ideal TE10 mode microwaves as dynamic fields. The energy spread vanishes within the limits of technical & practical implementing of the concept without any loss of current. The working field acts like a cool thermodynamic reservoir absorbing heat from the electrons.

In this talk I focus on some details of circular deflection. Furthermore a simplified type of the circular deflection based monochromator for probe forming applications is proposed. In this special case it is possible to economize on the undoing circular deflector by combining the crossing (of the deflected axis with the original axis) with an image of the electron source.

Fig. 1: Five snapshots of an animated schematic drawing illustrating the principle of a typical circular deflection application.

Fig. 2: Schematic drawing (cross sectional view) of a simplified monochromator design based on circular deflection. Note that in difference to figure 1 the electrons are assumed to move from left to right.

Fig. 1

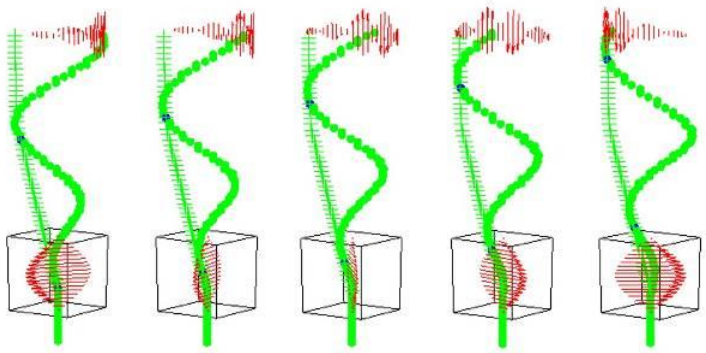

Fig. 2

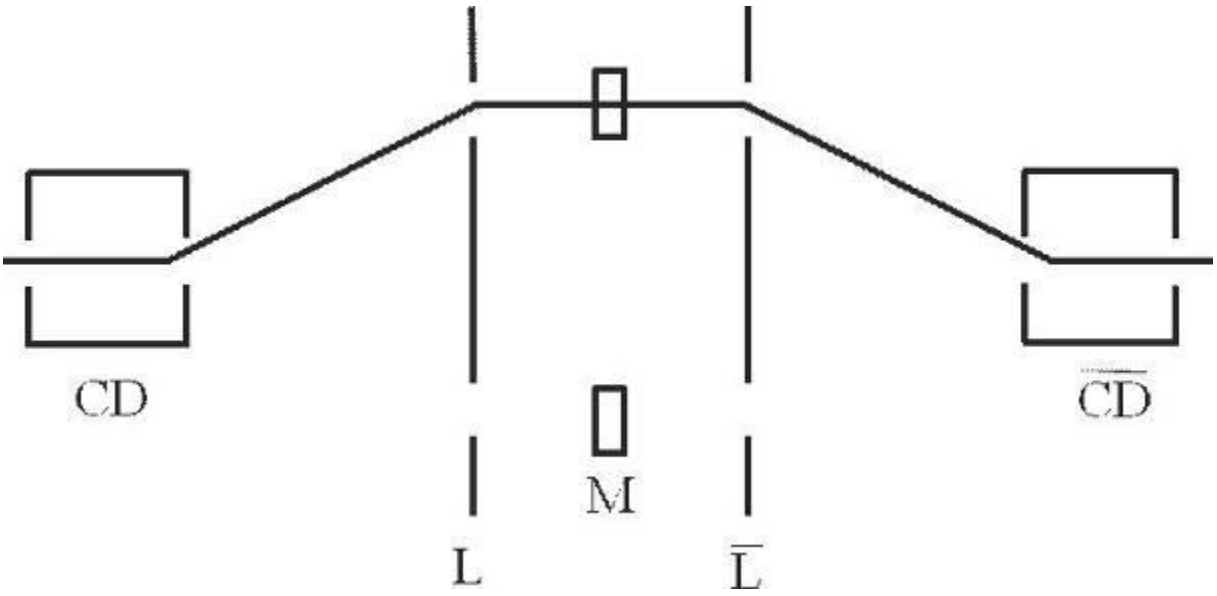

IM1.P005
Fast multimodal STEM imaging of complementary information accessible via a new segmented STEM sensor, a scintillator based camera and XEDS detector

D. Stroppa[1], S. Thomassen[1], C. Maunders[1], Y. Rikers[1], E. Kok[1], B. Freitag[1]

[1]Thermo Fisher Scientific, Eindhoven, Netherlands

STEM acquisition allows to simultaneously record multimodal information on structure, properties and composition of materials at the same time. The geometry, sensitivity and speed of the multimodal sensors like conventional ring or disk detectors, cameras for 4D STEM recording and XEDS, EELS detectors need optimization to allow for high quality simultaneous recording.

In this contribution we present a new segmented STEM sensor array for bright field (BF, ABF,(i)DPC) and dark field (ADF,HAADF) imaging. The geometry is optimized for multimodal simultaneous acquisition of HAADF, 4D STEM or EELS and XEDS signals. The capabilities of a new software in multimodal acquisition is demonstrated.

We benchmark the new sensor array by recording different STEM imaging signals at the same time on Talos and Themis class of instruments in various applications. The capability of newly developed software to record multimodal signal efficiently is demonstrated using and XEDS detector (DualX, SuperX), 4D STEM conventional scintillator based camera (Ceta) and HAADF STEM detector. The configuration of the used hardware is shown in the schematics in figure 1.

In figure 2 a simultaneously recorded HAADF, XEDS and 4D STEM data on SrTiO3 at 300kV is presented. The maximum speed of Ceta recording of 4D STEM data is 300fps for a 512x512 pixel and even ~600fps at 256x256 pixel sampling can be achieved. Multiple examples in 4D STEM in combination with XEDS are demonstrating the capability of the new solution. The optimum set-up in camera length, probe current and convergence angle for high quality multimodal results is examined systematically and discussed.

We show the benefits of a new STEM sensor array, demonstrate the capabilities of a Ceta camera in 4D STEM application and enable new simultaneous multimodal recording capabilities on the Themis and Talos platform. The new capabilities allow for a more efficient, faster and higher quality acquisition of compositional and structural information in STEM mode.

Fig. 1: Schematics of the multi detector configuration indicating the position and type of the different sensors used

Fig. 2: Multimodal acquisition of HAADF, 4D STEM and XEDS data on SrTiO3 at 300kV. The HAADF signal (upper left), diffraction pattern (upper right), XEDS (lower left) are recorded with a 10ms exposure time per pixel. An intensity profile across the diffraction pattern is shown in the lower right figure.

Fig. 1

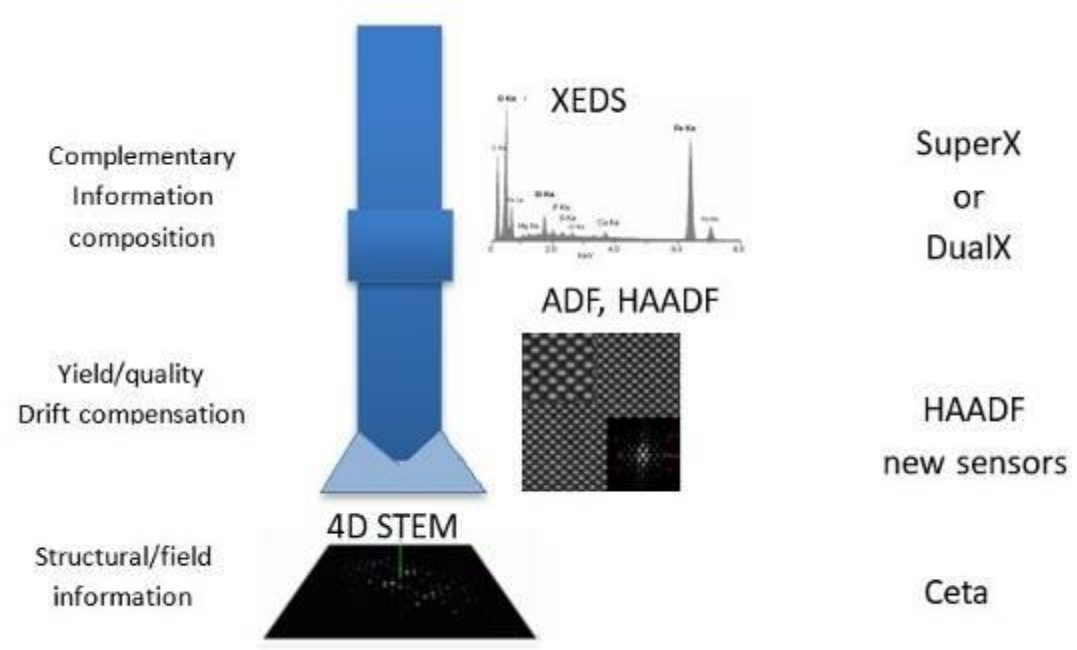
Complementary
Information
composition
XEDS
SuperX
or
DualX
ADF, HAADF
Yield/quality
Drift compensation
HAADF
new sensors
4D STEM
Structural/field
information
Ceta

Fig. 2

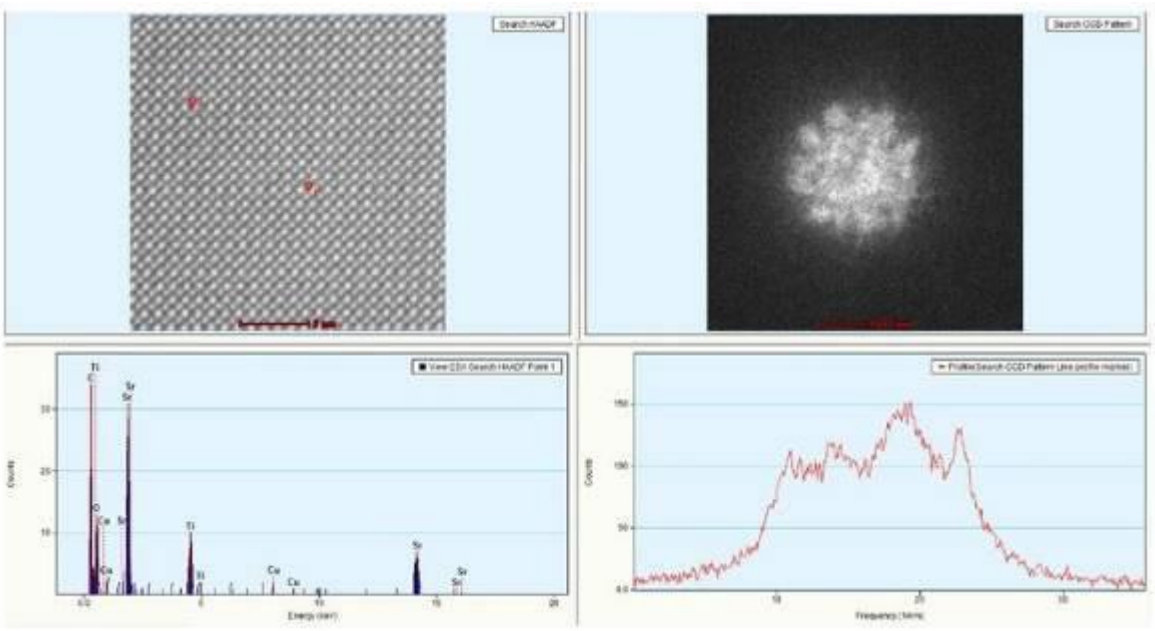

IM1.P006
Automated acquisition of large areas at high resolution with SEM/TEM/STEM and EDS correlative imaging

D. Stroppa[1], A. Yalcin[1], H. Sekiguchi[1], E. Emrah Yücelen[1], D. Kočár[1], D. Lichau[1], R. Kelley[1], A. Bright[1], B. Freitag[1], Y. Rikers[1]

[1]Thermo Fisher Scientific, Eindhoven, Netherlands

The need for large area correlative imaging at high resolution has increased over the recent years, for retrieving statistically meaningful data in nanoparticles and catalysis samples, and also to analyze large lamellae prepared with a (Plasma) Focused Ion Beam (P/FIB), e.g. from aerospace and aviation components. Automation is key to be successful in acquiring and analyzing large data sets to come to statistically meaningful data or to bring highly local (atomic) resolution results into context or macroscopic parameters.

In this contribution, we present the Thermo Scientific MapsTM software that automatically acquires multiple images or EDS maps on a sample by means of shifting the compustage, changing magnification and subsequently focusing, aligning and stitching all the images to create one large final image.

Maps acquisition, which can take any time between a minute and days, is done unattended, and typically the long runs are done overnight, for the most efficient use of the microscope time and shortest time-to-data. Additionally, powered by the Thermo Scientific AvizoTM Software, processing is possible for automated on-the-fly processing and statistics.

Multiscale data is required to navigate efficiently on the material to find relevant areas. The capability to navigate across platforms provides an efficient way to screen large specimen volumes and mark relevant areas for deeper analysis.

One signal is not providing a complete picture of the sample. Therefore Maps has the capability to acquire multiple signals and allows to acquire automatically STEM/TEM/SEM and EDS data and allows to pick multiple areas from which only one particular signal or a higher resolution image has to be acquired. In figure 1, is the analysis of 30-micron superficial layer of shot-peened, aerospace grade Aluminum alloy (A7075-T651). The very large 30x70 µm lamella was prepared using a Thermo Scientific Helios G4 PFIB. The STEM imaging and EDS analysis was done on a Thermo Scientific TalosTM F200X G2 S/TEM enabled by VeloxTM Software. The shot-peening greatly improves the fatigue life of aerospace and aviation components by introducing compressive residual stress into the materials surface. Image correlation between large (micro)cracks and dislocations as well as chemical analysis are essential to understand the materials properties.

Modern material science require multimodal, statistical meaningful data to capture the essence of the properties on multiple length scales and modalities across platforms. Maps automates navigation across multiple length scales to characterize large volumes fast and reproducible, and provides pinpoint analysis on relevant areas with context.

Fig. 1: Analysis of a 30-micron superficial layer of shot-peened, aerospace grade Aluminum alloy (A7075-T651)); Large area STEM and EDS at high resolution;

1. a) 3x5 tiles stitched LM-STEM
2. b) 7x11 tiles stitched STEM Maps + EDS Maps with total area of 17.6x11.3 µm with a few nm resolution. Individual tiles can be setup to contain even more tiles to increase the resolution
3. c) Digital zooms of b)

Fig. 1

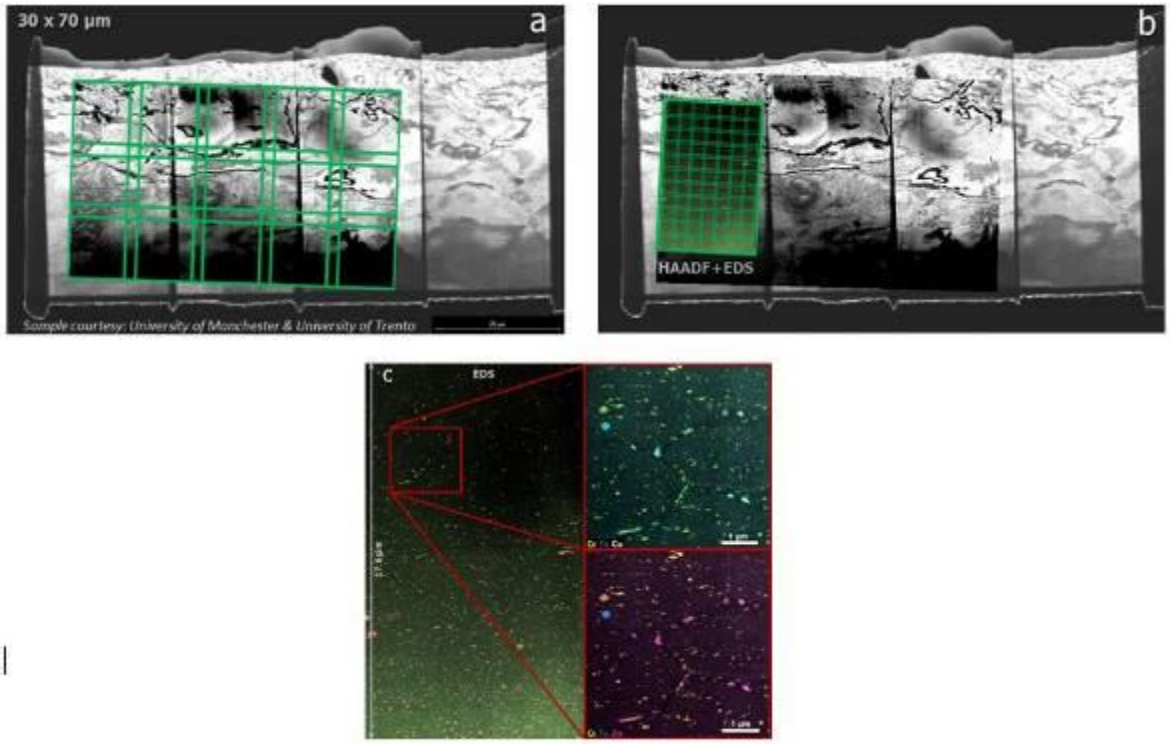
30 x 70 µm
a
Sample courtesy: University of Manchester & University of Trento
b
HAADF+EDS
c
EDS

IM1.P007
Universal Pressure Scanning Electron Microscopy (UPSEM) - Improvements in Environmental Scanning Electron Microscopy

J. Rattenberger[1], H. Fitzek[1], T. Achtsnit[1], H. Schroettner[1,2], F. Hofer[1,2]

[1]Graz Centre for Electron Microscopy - ZFE, Graz, Austria
[2]Graz University of Technology, Institute of Electron Microscopy and Nanoanalysis - FELMI, Graz, Austria

With an Environmental Scanning Electron Microscope (ESEM) electrically insulating, biological and even liquid samples as well as wetting experiments can be performed (1). The imaging gas inside the sample chamber suppresses negative charging and prevents outgassing of the sample. The negative side effect is the poor image quality at high chamber pressures. As a result, experiments must be done at lowest possible pressure, high electron energies, long dwell times and large electron beam currents.

However, state of the art microscopes are working far away from physical limits. The key to high image quality at high pressures is to reduce primary beam scattering as far as possible while maintaining ideal operation conditions for the secondary electron detector (2, 3).

In the Thermo Fisher Scientific (FEI) Quanta series ESEMs the gaseous environment in the sample chamber is separated by two Pressure Limiting Apertures (PLA) and a differential pumping system from the high vacuum inside the electron column. Nevertheless, a lot of gas streams through the PLA upwards and a significant amount of electrons are lost for imaging before the beam is entering the sample chamber. The most straightforward way to improve image quality is to decrease the PLA diameter, which unfortunately also reduces the maximum available field of view. In this work, a new pressure limiting aperture holder is presented which improves the high pressure performance of the microscope even at the same field of view.

Usually the secondary electron detector in ESEMs is a flat positively biased electrode positioned sideways or directly at the end of the pole piece. Secondary electrons are attracted and accelerated towards the detector and on their way collision ionization amplifies the signal. With increasing pressure the amplification efficiency decreases because electrons do not gain enough energy between collisions to ionize the gas. However, nearby a needle detector with very small tip radius (R < 10 µm) the electric field is strong enough for amplification and by positioning the needle on the sample table it operates at ideal conditions regardless of pressure and working distance. A by-product of this design is that the conventional position of the backscatter electron detector (BSE) at the end of the column is no longer blocked by the SE detector. In figure 1 the new design can be seen in comparison the design of the Quanta series microscopes.

With this optimized high pressure design the limits of conventional ESEM technology can be crossed (see figure 2). Imaging at higher chamber pressures up to one atmosphere (see figure 3), investigations of living organisms (see figure 4) and much more is possible.

References:

(1) Danilatos, G.D, Advances in Electronics and Electron Physics Vol. 71, 109-250, 1988

(2) Fitzek H., Schroettner H., Wagner J., Hofer F., Rattenberger J., Journal of Microscopy, DOI: 10.1111/jmi.12347

(3) J. Rattenberger, H. Fitzek, H. Schroettner, Imaging & Microscopy, Vol 20, 38-40. 2018

Fig. 1: Comparison of the different designs (left: Quanta Series, right: FELMI-ZFE) (ED: environmental distance, WD: working distance, SGT: stagnation gas thickness)

Fig. 2: Overall performance comparison (5kV, 1500 Pa H2O, 30 µs dwell time, 0.4 nA)

Fig. 3: Copper wire imaged at atmospheric pressure (30 µm PLA diamter, 30 kV)

Fig. 4: Rehydration of a water bear (tardigrade) inside the UPSEM (800 Pa H2O; 5 keV)

Fig. 1

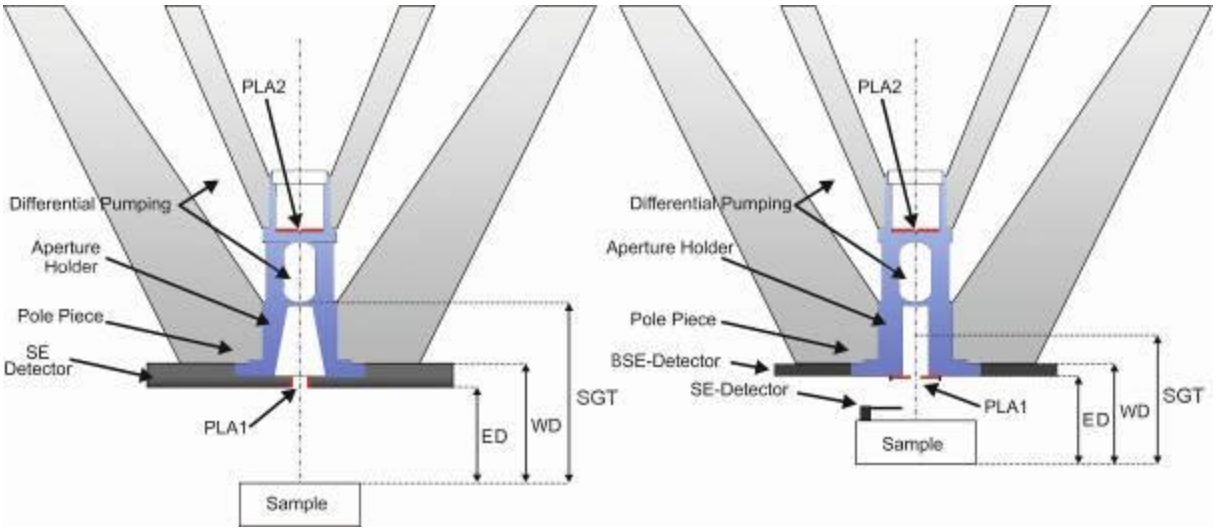
PLA2
Differential Pumping
Aperture Holder
Pole Piece
SE Detector
PLA1
ED
WD
SGT
Sample
PLA2
Differential Pumping
Aperture Holder
Pole Piece
BSE-Detector
SE-Detector
PLA1
ED
WD
SGT
Sample

Fig. 2

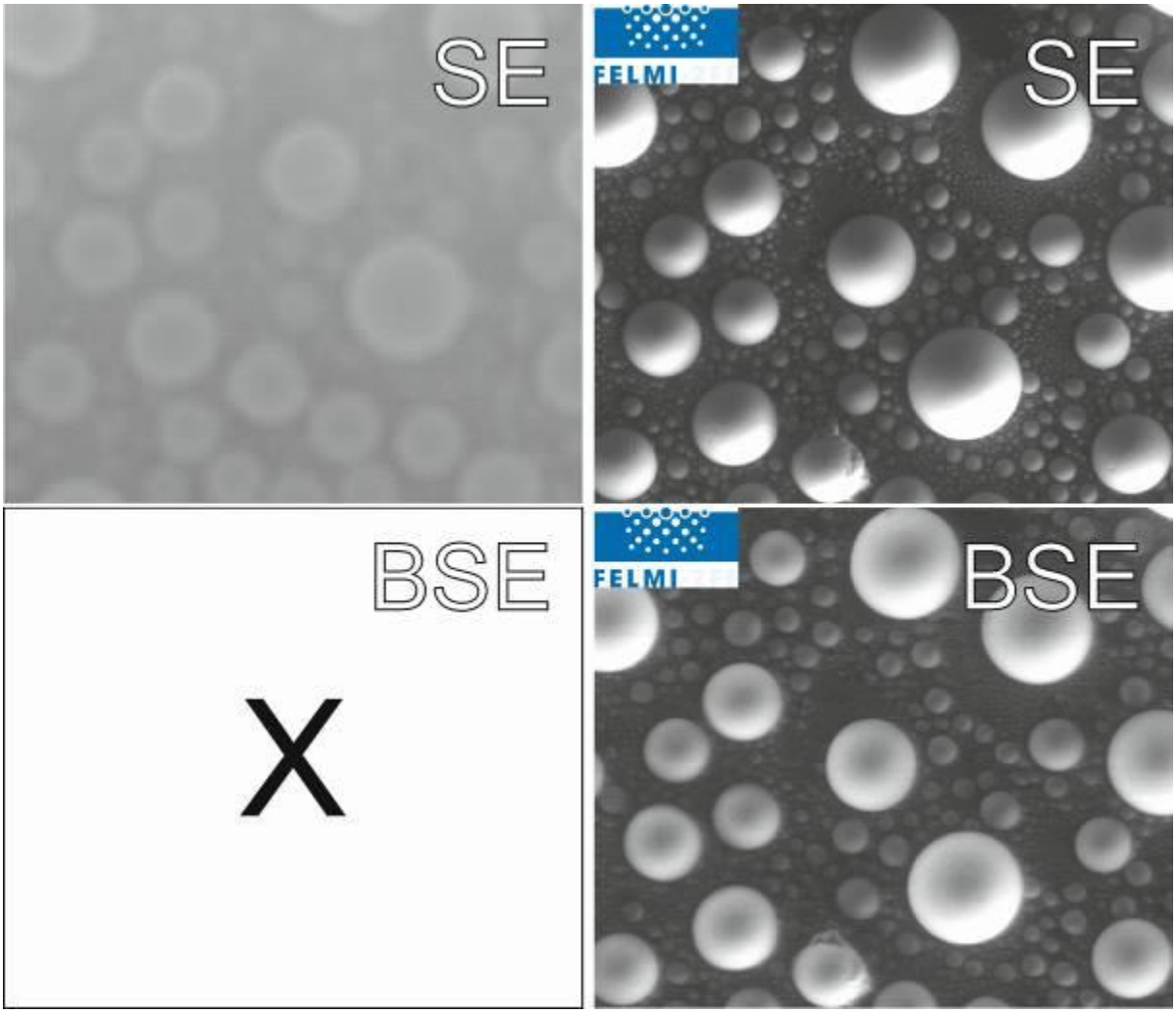
SE
FELMI
SE
BSE
X
FELMI
BSE

Fig. 3


HV
30.0 kV
Det
LFD
WD
3.3 mm
Spot
6.0
HFW
15.20 µm
Mag
10000x
Pressure
1ATM
5.0µm

Fig. 4

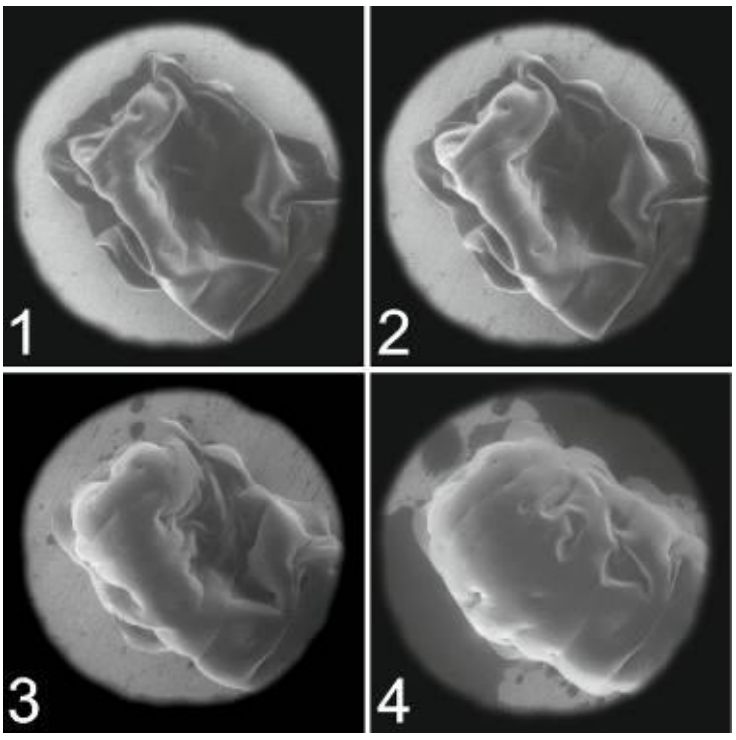
1
2
3
4

IM1.P008
ChemiTEM – an easy to use TEM with optimised workflows for chemistry and material synthesis applications

W. Hetaba[1,2], R. Imlau[3], M. G. Willinger[2], S. Kujawa[3], R. Schlögl[1,2], T. Lunkenbein[2]

[1]Max-Planck-Institute for Chemical Energy Conversion, Heterogeneous Reactions, Mülheim an der Ruhr, Germany
[2]Fritz Haber Institute of the Max Planck Society, Department of Inorganic Chemistry, Berlin, Germany
[3]Thermo Fisher Scientific, Eindhoven, Netherlands

Analytical transmission electron microscopy (TEM) has become an important and widely implemented part of the workflow in a modern catalysis research institute. TEM is a key technique for the investigation of local elemental composition, surfaces, core-shell structures and atomic interfaces, all crucial to the functionality of the system. However, usually TEM specialists perform the necessary tasks for a thorough study of the materials of interest. The research efficiency will be tremendously improved by enabling chemical engineers and research scientists in chemical laboratories to perform standardised investigations such as material screening or qualitative compositional analysis. The ChemiTEM project as a collaboration between the Fritz Haber Institute (FHI) and Thermo Fisher Scientific aims to generate standard procedures and workflows optimised for non-expert TEM users for applications in material synthesis and chemistry. The hardware used in this project is a Thermo Scientific Talos F200X analytical TEM, equipped with a SuperX energy dispersive X-ray spectroscopy (EDS) system comprising of four silicon drift detectors.

In the first step of the ChemiTEM project, typical questions relevant to chemists were collected and statistically analysed by investigating 40 samples of the FHI and its collaboration partners. The results are shown in figure 1, together with an overview of the applied TEM techniques and the most common faced challenges during investigation. In the second step, the aforementioned examinations were used to develop workflows guiding the user through every decision necessary for a successful TEM investigation, including sample preparation, investigation and data analysis. An overview of one branch of the experimental workflow''s structure is shown in figure 2. In the third step of the ChemiTEM project, the workflow is implemented into a tablet app enabling non-expert TEM users to perform even applications they have no experience with so far by guiding them through the whole decision process. This includes optimisation strategies and quality control. 20 users have already been successfully trained within the ChemiTEM project and are using the developed tools on a regular basis. Additionally we are working on a separate workflow for data analysis.

The ChemiTEM project will deliver a knowledge base of standard procedures and workflows necessary for TEM investigations in chemical laboratories. Additionally, the requirements a TEM has to fulfil in order to serve as standardised lab equipment for time efficient screening and judgement of synthesis success are defined. The developments in the reported ChemiTEM project, together with additional automation, both in hardware and software, will extend the TEM user base and make this important analytical instrument a standard tool in chemistry laboratories.

Fig. 1

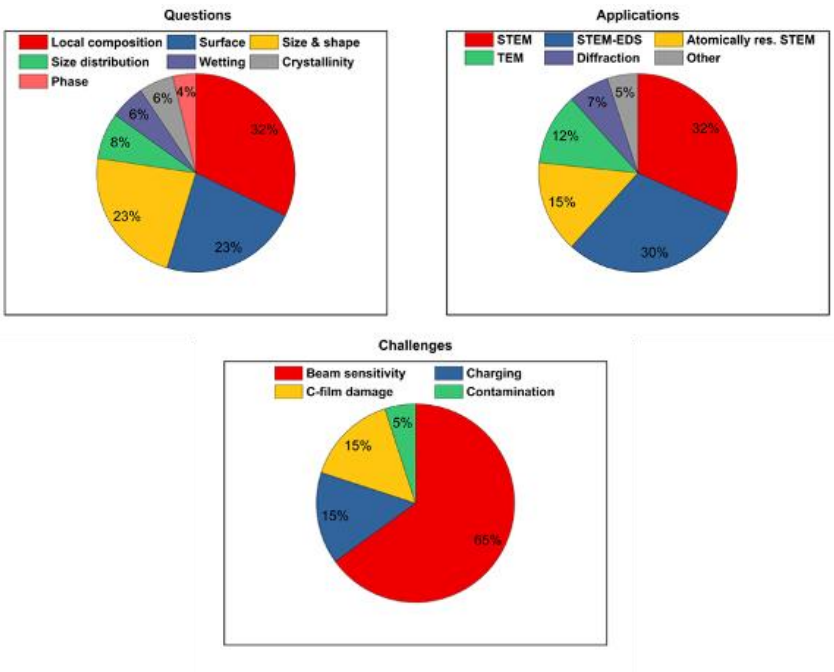

Fig. 2

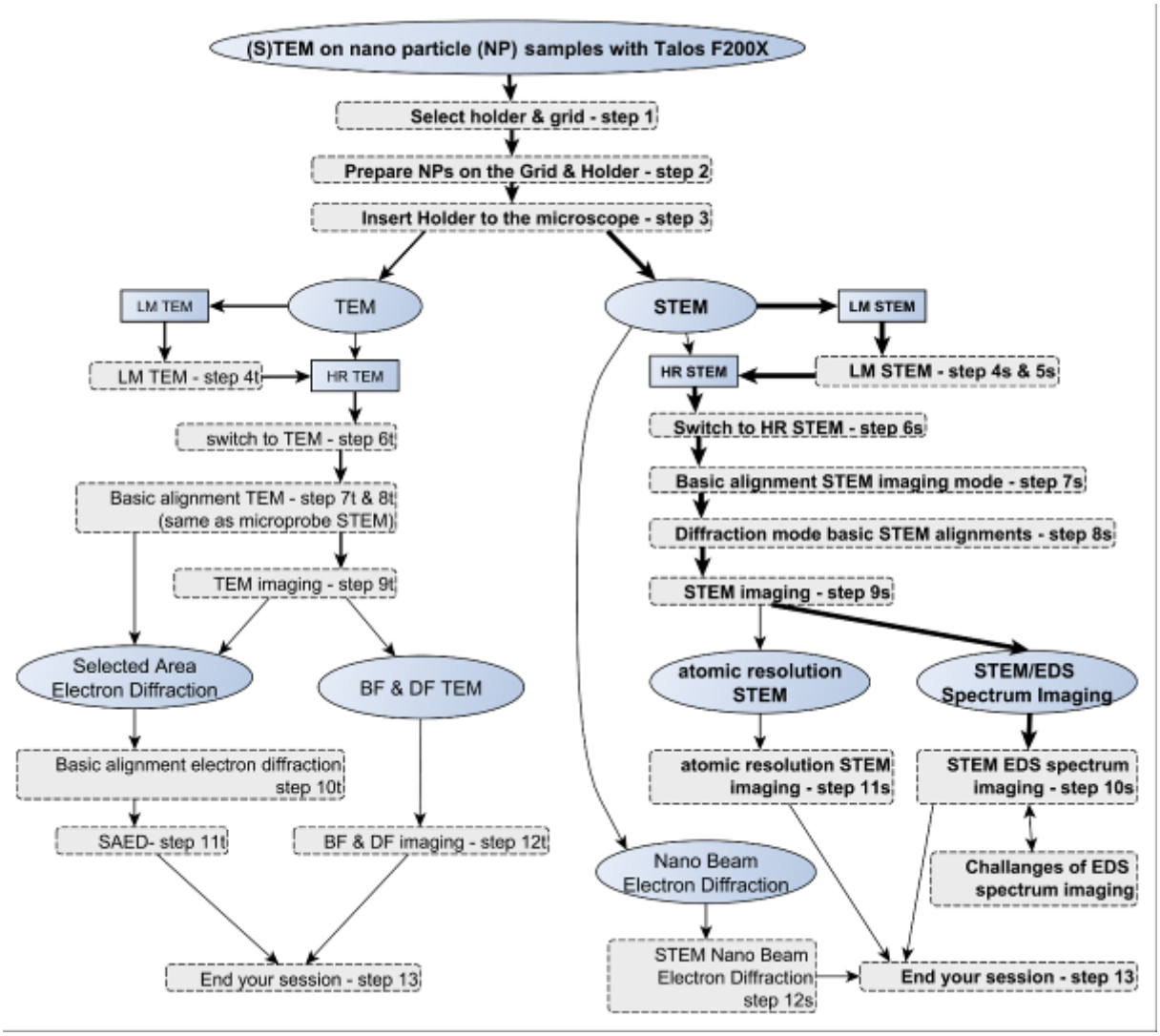
(S)TEM on nano particle (NP) samples with Talos F200X
Select holder & grid - step 1
Prepare NPs on the Grid & Holder - step 2
Insert Holder to the microscope - step 3
TEM
LM TEM
LM TEM - step 4t
HR TEM
switch to TEM - step 6t
Basic alignment TEM - step 7t & 8t (same as microprobe STEM)
TEM imaging - step 9t
Selected Area Electron Diffraction
BF & DF TEM
Basic alignment electron diffraction step 10t
SAED- step 11t
BF & DF imaging - step 12t
End your session - step 13
STEM
LM STEM
HR STEM
LM STEM - step 4s & 5s
Switch to HR STEM - step 6s
Basic alignment STEM imaging mode - step 7s
Diffraction mode basic STEM alignments - step 8s
STEM imaging - step 9s
atomic resolution STEM
STEM/EDS Spectrum Imaging
atomic resolution STEM imaging - step 11s
STEM EDS spectrum imaging - step 10s
Challanges of EDS spectrum imaging
Nano Beam Electron Diffraction
STEM Nano Beam Electron Diffraction step 12s
End your session - step 13

IM1.P010
Bayesian Analysis of Electron Spectroscopic SEM Images

J. Eisele[1], B. Schindler[2,3], D. Preikszas[2], D. Fischer[3], R. R. Schröder[4]

[1]University of Heidelberg, Centre for Advanced Materials, Heidelberg, Germany
[2]Carl Zeiss Microscopy, Oberkochen, Germany
[3]Carl Zeiss SMT, Oberkochen, Germany
[4]University Hospital of Heidelberg, Cryo Electron Microscopy, Heidelberg, Germany

The new SEM prototype "Delta" (1) manufactured by Zeiss is chromatically and spherically corrected, offering up to 0.7nm lateral resolution at 100eV primary electron energy. The Delta includes a SE&BSE spectrometer based on retarding potentials. All this opens up new analytic possibilities, cf. (2).

In a first step we want to determine locally highly resolved electron spectra and material properties, such as work function (cf. (3)), by inverting the microscope response including the complex retarding potential. In a second step we test if this information can be used to determine the composition of a simulated materials mix. The inference procedure should not loose information, be based on physics and errors resulting from physically inherent signal noise should be estimated correctly.

In theory, this information can be obtained by Bayesian inference as long as the applied statistical model is perfect and the inference exact. We use approximate Bayesian inference (4) combined with physically motivated forward modeling of the measurement process.

The applied model manages to infer the expected steep slope of the SE peak (fig. 1b,c,d), while measured data appears to show a completely different spectral shape. This broadening of the spectra can be explained by the low energy resolution of the current detector design, however, the inference process increases the effective energy resolution significantly. In spite of that, the model does not yet reproduce the long SE tail. Future inference of local work function and Fermi energy will not only critically depend on better device characterization but also on the theory for SE generation applied (such as 5, 6): E.g. an inferred SE spectrum FWHM of 5 eV corresponds to Fermi energy of 4.6 eV vs 4.0 eV for models (5) vs (6). When decomposing a simulated material mixture, it is clear that errors are estimated depending on the physical noise (fig. 2).

Bayesian Inference inherently deals with noise, provides error estimates and it will push information gain to its theoretical limits if the model used is good. Therefore it is especially suited for low dose, high resolution imaging and spectroscopy of the novel DELTA SEM.

References:

(1) M Steigerwald et al, FCMN (2009)

(2) R R Schröder et al, J Kammerer et al, D Ryklin et al, W-S Zhang et al, MC2019

(3) J Cazaux, J Ultramic 110, 242 (2010)

(4) B Carpenter et al, J Stat Softw, 76 (2017)

(5) M S Chung et al, J Appl Phys 45, 707 (1974)

(6) M S Chung, J Appl Phys 46, 465 (1975)

(7) We thank BMBF for funding (FKZ: 13GW0044) and sds@hd/MWK/DFG (grant INST 35/1314-1 FUGG) for storage

Fig. 1: Inverting the microscope response for Aluminium by Bayesian inference (black: measured data, orange: median of inferred properties; cumulative (a) vs differentiated signals (b)); comparison with theoretical spectra (derived from models (5) blue (c) or (6) red (d)), both parametrized with a Fermi level of 5.63 eV and a work function of 4.16 eV (3). A 6 eV shift of the Fermi level compared to the published value (3) had to be introduced.

Fig. 2: Simulated deduction of material composition by Bayesian inference assuming linear mixture of SE spectra; left: reference spectra (colors: pure compounds; dotted: mixture of 30% comp. 1, 10% comp. 2 and 60% comp. 3); right: inferred compositions (5%, 25%, 50%, 75%, 95% quantiles of posterior distributions). Note: perfect material decomposition is gained at higher dose.

Fig. 1

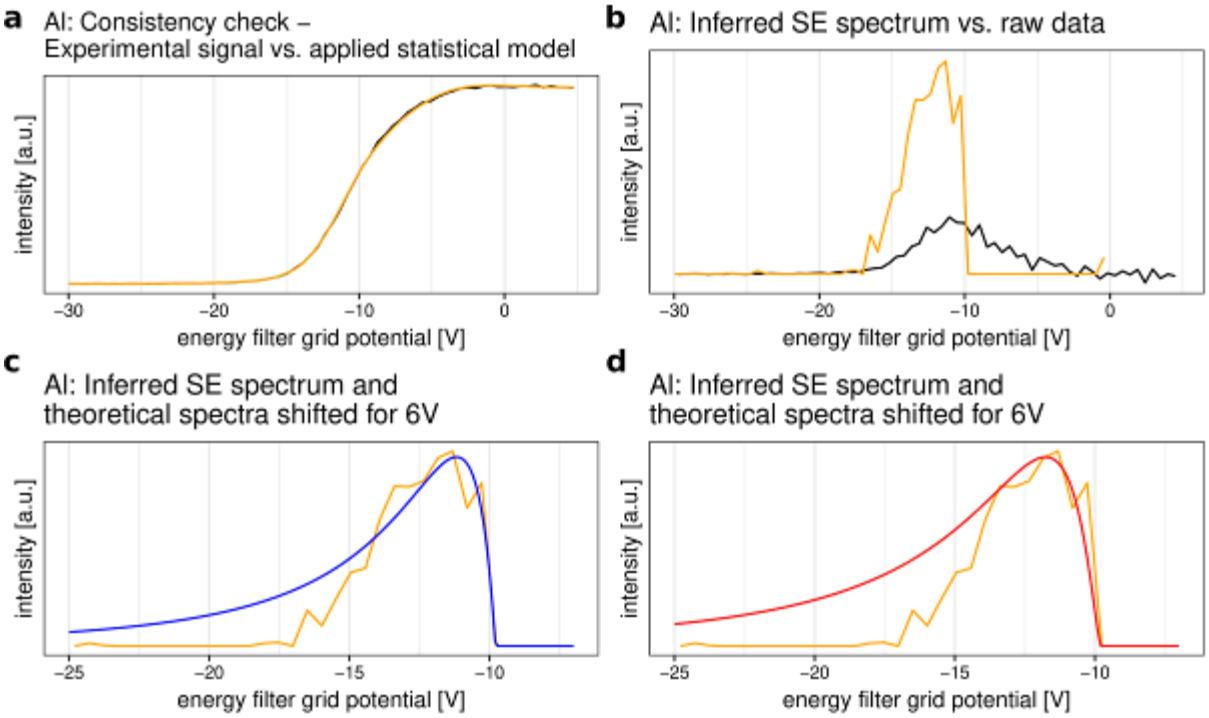
a
AI: Consistency check –
Experimental signal vs. applied statistical model
intensity [a.u.]
−30
−20
−10
0
energy filter grid potential [V]
b
AI: Inferred SE spectrum vs. raw data
intensity [a.u.]
−30
−20
−10
0
energy filter grid potential [V]
c
AI: Inferred SE spectrum and
theoretical spectra shifted for 6V
intensity [a.u.]
−25
−20
−15
−10
energy filter grid potential [V]
d
AI: Inferred SE spectrum and
theoretical spectra shifted for 6V
intensity [a.u.]
−25
−20
−15
−10
energy filter grid potential [V]

Fig. 2

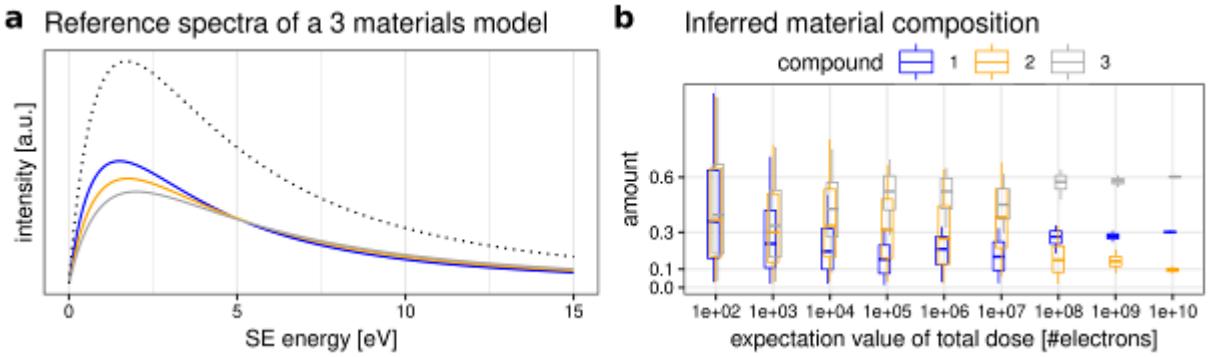
a
Reference spectra of a 3 materials model
intensity [a.u.]
0
5
10
15
SE energy [eV]
b
Inferred material composition
compound
1
2
3
amount
0.6
0.3
0.1
0.0
1e+02
1e+03
1e+04
1e+05
1e+06
1e+07
1e+08
1e+09
1e+10
expectation value of total dose [#electrons]

IM1.P011
Application of The Correlative Probe and Electron Microscopy (CPEM™) in Advanced Sample Surface Analysis

J. Neuman[1], Z. Novacek[1], M. Pavera[1], V. Novotná[1]

[1]Nenovision s.r.o., Brno, Czech Republic

Combination of various techniques into one simultaneous measurement is advantageous in many scientific areas. Atomic force microscopy (AFM) and scanning electron microscopy (SEM) are widely used techniques for imaging the nanoworld in fields of material sciences, nanotechnology, semiconductors or life sciences. Correlative probe and electron microscopy CPEM™ is a unique technique combining both AFM and SEM. Advantages of this approach are demonstrated on a sample of graphene layer formed on the surface of SiC prepared by thermal decomposition of the material.

The goal of this article is to show the benefits of the CPEM™ technique in sample surface analysis. Both AFM and SEM provide different information about the specimen. Combination of multiple signals can answer a number of questions regarding the quality and properties of the sample. CPEM™ provides information which cannot be obtained by independent AFM and SEM measurements.

AFM LiteScope™ by NenoVision was used for correlative microscopy. It is compact AFM carefully designed for direct integration into various SEM"s. This microscope is equipped with CPEM™ technology. Using this method neither the electron beam nor the AFM probe tip is scanning. The movement is done by the piezo scanner with the sample while the AFM tip and the electron beam have a constant shift of known value. CPEM™ can accommodate several signals from different detectors (SE, BSE) or related techniques like FIB, EBIC or local spectroscopy. All signals are collected simultaneously at the same conditions including pixel size, coordinate and scanning system and environment. Each signal is represented by a unique colour mask and brings new information for further sample analysis.

One of the major benefits of CPEM™ is presented on graphene layer analysis. Graphene was prepared by thermal decomposition of SiC. During the sample etching at 1400 – 1600°C the silicon atoms evaporate from the surface and the remaining carbon atoms form into a graphene layer. The advantage of the graphene on SiC is that it is prepared directly on the non-conductive substrate so additional transport for further use is not necessary.

Using CPEM™ images of graphene layers on SiC were obtained. The analysis showed that graphene layers start to grow from the edges of the SiC substrate and then continue to grow on the surface of the terraces. Presumably, it is due to the larger area leading to higher evaporation of silicon atoms. After some time, multiple layers start to grow from the edges. It is necessary to optimize the temperature and time of etching to get a single layer of graphene. Thanks to this method number of graphene layers can be detected.

Based on the SEM image (Fig. 1a) itself it is uncertain if there are steps or if it is only material contrast which can be seen in the image. The AFM image (Fig. 1b) brings information about the topography and clarifies the results together with the correlated 3D CPEM™ view (Fig. 1c).

Fig. 1: CPEMTM correlative imaging. a) AFM image, b) SEM image, c) 3D CPEM view.

The AFM-in-SEM LiteScope™ with CPEM™ technique allowed fast and more precise analysis of graphene layer grown on SiC. It was confirmed that the graphene layers always grow from the edges. Because the graphene growth is not uniform across the sample it would be impossible to get this result using AFM and SEM separately.

Fig. 1

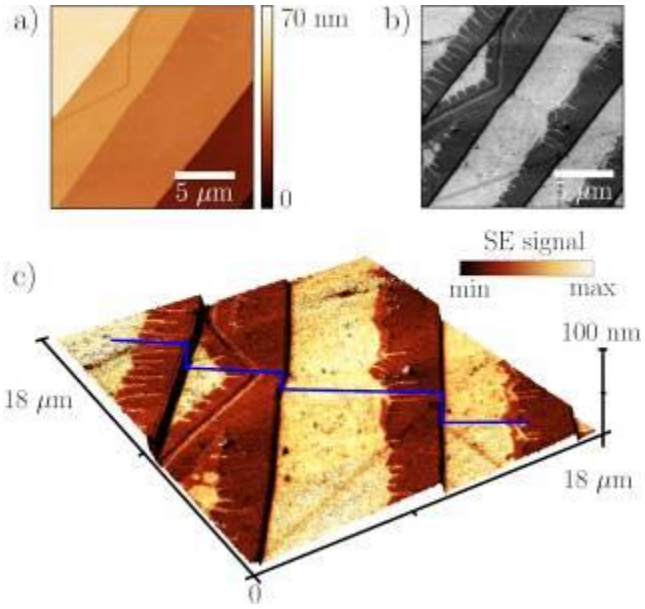

IM1.P012
Towards an efficient lamella navigation setup for high throughput imaging of semiconductor devices with automated (S)TEM using PCA image analysis

G. T. Martinez[1], D. Batuk[1], E. Grieten[1]

[1]imec, Leuven, Belgium

The development of devices in semiconductor industry has reached a level in which high throughput characterization is a requisite in order to keep up with the technology demands. The use of automated (S)TEM workflows enables the delivery of information in a timely manner and with the required accuracy and precision. It has become a choice for research and development, failure analysis or device fabrication process control (1) due to its capability to characterize a high number of samples in a short period of time (2). This technique relies on standardized sample preparation and inspection recipes to acquire the images in an automated fashion (3). In this work, we focus on the challenges when developing recipes for automated inspection.

The navigation of automated (S)TEM recipes often fail due to lamella and process variation. To create a more robust imaging recipe we are evaluating the use of PCA image analysis in order to improve the performance of the navigation.

In order to acquire images, the automated routine extracts information about the sample based on image analysis. The navigation setup finds the lamella and drives to the device line to acquire the desired images. We used a selection of images obtained with a probe corrected FEI Metrios microscope. These images show the overview of the sample. An in-house Matlab routine aligned and performed PCA decomposition of the stack of images in order to identify the different image features. Then, the component that showed the features of interest most clearly is then used to improve the success rate of edge finder and pattern match routines built in the Metrios Recipe Editor software.

Fig1 shows the average image of 20 samples and its corresponding PCA images up to the 19th component. These images correspond to an edge of an array of fins. By using a PCA decomposition, we can observe that each component carries distinct information about the sample. Components from 1 to 3 show features clearly identifiable to the edge of the array while the other components are more affected by lamella bending contours and carbon grid support. When running the acquisition recipe, we can then decompose the image in specific components that show more clearly the structure of interest and use this to improve the navigation to this region of interest. We study the use of this approach for different types of inspections and characterization of several devices in order to evaluate the feasibility and benefits to improve automated (S)TEM and increase the throughput of the technique.

Automated (S)TEM for the characterization device development is the route to achieve high throughput information with the required accuracy and precision. We use PCA image analysis in order to improve the robustness of edge finder and pattern match routines. PCA offers the possibility to retrieve the image features of interest for different devices improving the performance of (S)TEM automation.

References:

(1) Y. Jiang, et al., Nature, 559, 343-349, (2018).

(2) M. Strauss, et al., Proc. SPIE 8324, (2012)

(3) O. Ugurlu, et al., 2017 FCMN conf. proc. 48, (2017)

Fig. 1: Average image and PCA images up to 19th component of a stack of images of lamellae containing an edge of an array of fins.

Fig. 1

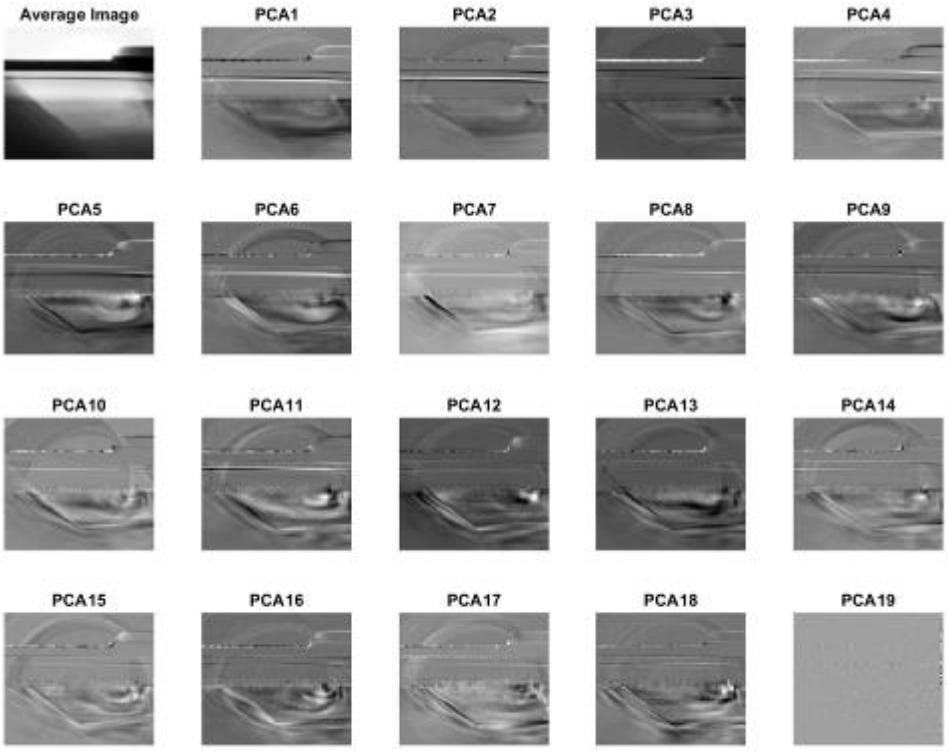
Average Image
PCA1
PCA2
PCA3
PCA4
PCA5
PCA6
PCA7
PCA8
PCA9
PCA10
PCA11
PCA12
PCA13
PCA14
PCA15
PCA16
PCA17
PCA18
PCA19

IM1.P013
Helios 5 – state-of-the-art DualBeam with fully automated TEM sample preparation

A. Prokhodtseva[1]

[1]Thermo Fisher Scientific, Eindhoven, Netherlands

Increasing needs for extreme high SEM resolution, the most fast and reliable fabrication of ultra-thin S/TEM samples, direct-write patterning of materials for nanoprototyping have been constantly driving innovations in the Focused Ion Beam and SEM technology. Over the last decade Thermo Fisher Scientific has introduced several generations of DualBeam™ instruments, every time pushing the boundaries of the technology and delivering state of the art solutions. In its turn, advanced technology should be reliable, accessible and easy to learn and use for operators with all levels of expertise, thus answering the demand for the fastest time to high quality results.

Helios 5 is the newest generation of the Helios DualBeam technology that combines both best SEM and FIB performance together with unprecedented ease of use and automation. It features the innovative Elstar electron column with high-current UC+ technology for extreme high-resolution (XHR) imaging and the highest materials contrast. Tomahawk HT™ or Phoenix™ ion column allow the fastest, easiest, and most precise high quality sample preparation. Alignments of SEM and FIB columns are done entirely automatically, making sure that at all times system is ready for however complex tasks. With Helios 5 we have introduced FLASH – a new image optimization feature that combines focus, stigmation and lens align tuning all at once in a single function. New concept of "System Presets" allows operator to setup and store beam, detector, patterning parameters creating manual workflows for common use cases or very specific applications with many different processes and/or beam conditions. These presets are stored for future use or as an instructional tool for novice users.

Finally, Helios 5 can be configured with AutoTEM 5 - the first application software that brings full automation to all steps of the lamella in-situ lift-out process. While allowing the completely autonomous operation, AutoTEM 5 possesses unique flexibility and is suitable for the large variety of material science samples, resulting in the most efficient, high throughput S/TEM sample preparation.

IM1.P015
Automatic quantification of parasite cell infection from confocal microscopy images

M. Ramos[1], L. López[2], A. Solari[1], C. Robello[2], F. Lecumberry[3,1]

[1]Institut Pasteur de Montevideo, Signal Processing Lab, Montevideo, Uruguay
[2]Institut Pasteur de Montevideo, Host-Pathogen Interactions Lab, Montevideo, Uruguay
[3]Universidad de la República, Signal Processing Deparment, School of Engineering, Montevideo, Uruguay

Image processing methods allow to create powerful procedures for extracting quantitative information of events in images. This allows to automatize and systematize the detection, segmentation, and quantification of features in an objective manner, drastically reducing user interaction and manual inspection. This work presents a complete procedure to quantify the Infection Index of cells in a sample from a stack of confocal microscopy images.

THP 1 cells were infected with Trypanosoma cruzi (Dm28c, strain). THP 1 nucleus were stained with DAPI and parasites were stained with an antibody that recognized the a cytosolic enzyme. An alexa fluor 546 conjugated α-IgG was used as secondary. Images were acquired in a Zeiss LSM 800, with a 20x/0.8 Plan Apochromat objective and a 512x512 image size.

The proposed procedure is depicted in Fig 1. Stacks contain two fluorescent channels with pixels' intensities proportional to the presence of parasites and nuclei. The procedure was completely developed as a plugin for Fiji (1) and is in process of being release for public use.

Z-projection of maximum intensity is performed, assuming there is no overlap between parasites. Median filtering reduces noise while maintain edge information. ROIs are defined by binary masks obtained by automatic pixel intensity clustering, followed by binary mathematical morphology operations to fill holes and close edges (see Fig. 2b-c). Obtained ROIs are filtered using shape descriptors such as area, circularity and roundness; range of valid parameters are user defined given sample and acquisition settings. Segmentation of nuclei (cyan) and parasite (yellow) are shown in Fig. 2d.

In order to associate each detected parasite with a nucleus several steps are considered. First, since no information related with the cells' cytoplasm or membrane is provided, a Voronoi diagram divides the whole image into regions based on the distance to nuclei's edges (green curves in Fig. 2e). Second, a parasite is discarded if it is far than a certain threshold from its closest nucleus. Third, parasites are grouped in order to be associated them to a nucleus, two parasites are considered to be part of the same group if they are closer than a certain threshold. A group of parasites is associated with the closest nucleus by its centroid, and the nucleus is labeled as infected. Finally, if the area Ap of a ROI in the parasite channel in greater than a certain threshold then this ROI is considered to have N=floor(Ap/Am) different parasites, where Am is the mean parasite area.

The Infection Index is calculated as (#infected cells)(#parasites)/(#cells). This process is repeated for all the stack and the statistics are reported to the user.

The proposed method automatize and systematize objective identification of parasites and nuclei and calculates the Infection Index. Increasing the number of processed stacks improves the statistics and reduces the effect of errors in parasite association where no cell membrane information is present.

References:

(1) Schindelin, J, et al. "Fiji: an open-source platform for biological-image analysis." Nature methods 9.7 (2012): 676.

Fig. 1: Block diagram of procedure.

Fig. 2: (a) Representative input image, parasites (green) and nuclei (blue) channels merged. (b-c) Channels segmentations. (d) Merged information from (b-c) into (a). (e) Voronoi diagram (green) defines nucleus' neighborhood.

Fig. 1

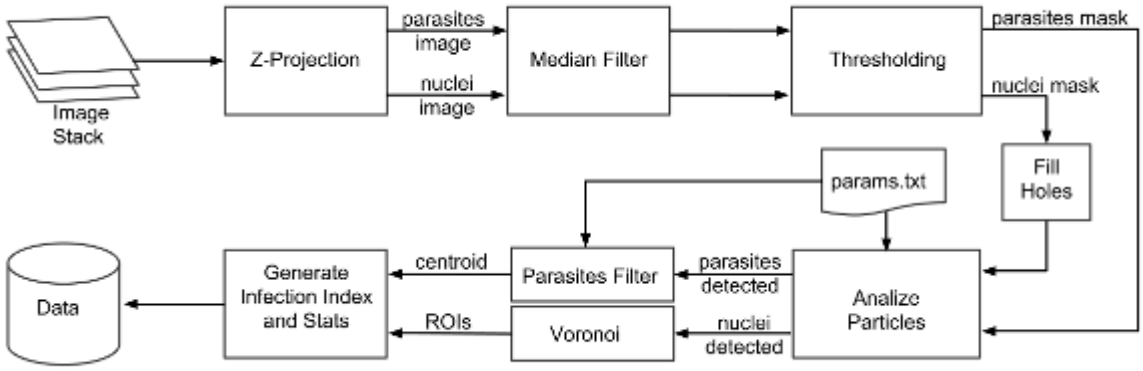
Image Stack
Z-Projection
parasites image
nuclei image
Median Filter
Thresholding
parasites mask
nuclei mask
Fill Holes
params.txt
Analize Particles
parasites detected
nuclei detected
Parasites Filter
Voronoi
centroid
ROIs
Generate Infection Index and Stats
Data

Fig. 2

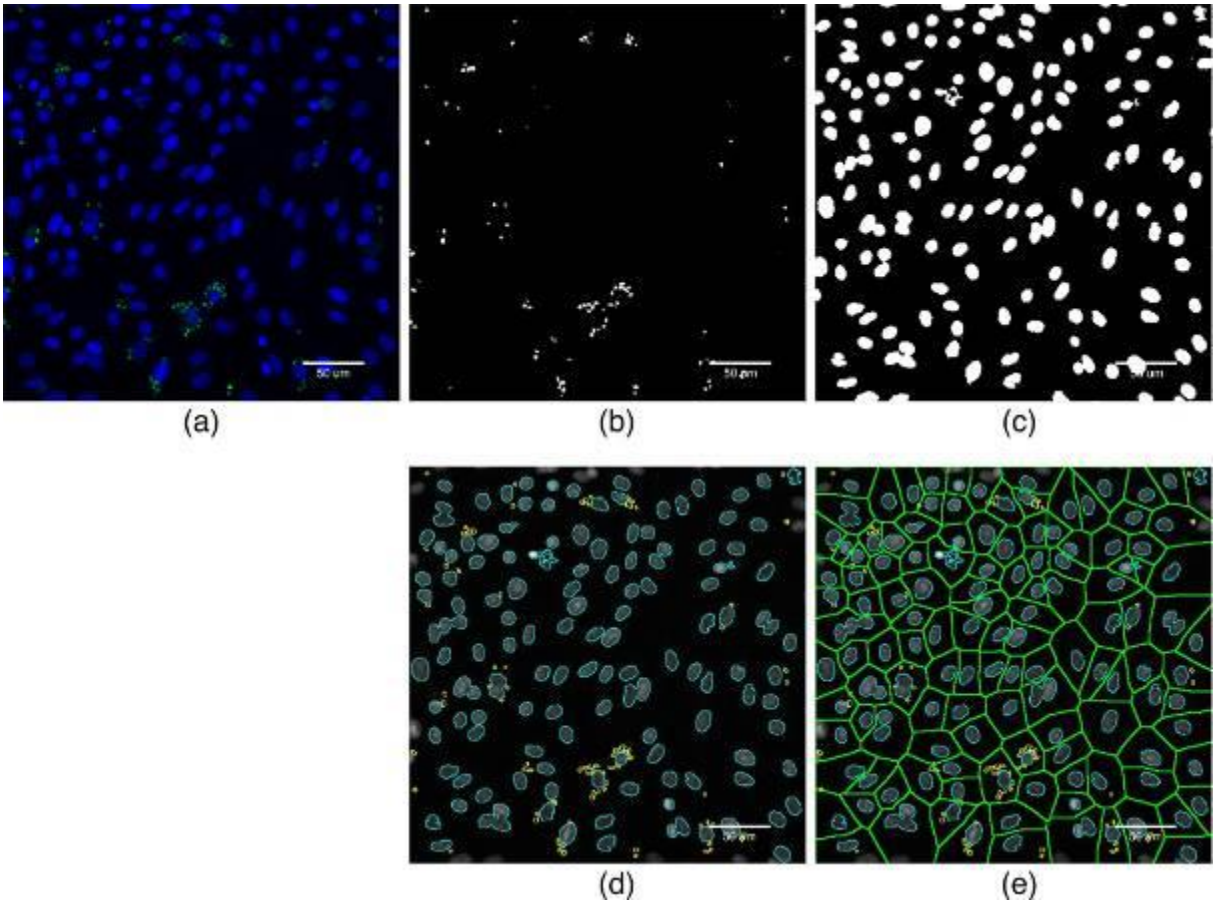
(a)
(b)
(c)
(d)
(e)

IM1.P016
Customized STEM electronics in daily routine: comparison, experiences and applications

S. Selve[1], H. Romanus[2], D. Berger[1], U. Grauel[3], W. Joachimi[3], G. Moldovan[3], C. Sichting[3]

[1]Technische Universität Berlin, Center for Electron Microscopy (ZELMI), Berlin, Germany
[2]Technische Universität Ilmenau, Zentrum für Mikro- und Nanotechnologien (ZMN), Ilmenau, Germany
[3]point electronic GmbH, Halle, Germany

STEM is a well-established technique whenever diffraction, thickness and material contrasts need to be distinguished or when it is required to reduce beam damages on sensitive materials. Equipped with a High Angle Annular Dark Field (HAADF) detector STEM allows to suppress diffraction effects in the images and to locate regions of different atomic numbers (Fig. 1A). This enables the characterization of nanoparticles on rough or porous supports and thus fulfills many requirements specific to catalytic applications.

These benefits for the characterization of catalysts have led to the upgrade of our 200 kV LaB6 TECNAI TEM to STEM. Upgrading microscopes from previous generations with original hardware is quite expensive, which makes a customized solution very attractive. In collaboration with specialized suppliers for custom electron microscope electronics, an up-to-date scan unit is installed to the already existing scan coils of the TEM. The present electronics allow pixel dwell times down to 200 ns/pixel and an image resolution of up to 16k x 16k pixels. A BF/ADF/HAADF sensor on a retractable slider is also installed in a custom detector housing, especially designed to attach to the existing CCD-camera mechanics (Fig. 1B). An adapted alignment procedure was developed on the basis of the microscope's proprietary *direct alignments*, containing i.a. eucentric focus, pivot points, beam shift, rotation center and diffraction alignment. Further magnification/image settings were calibrated along to the TEM mode. To expand the possibilities for elemental mapping, parts of the EDX-System were upgraded to deliver a common interface with the scan control. Using the Genesis EDX software package, a drift correction allows for long-term EDX mappings or linescans and a wide range of data post-processing options (Fig. 1C).

In this paper, we present comparative measurements of this custom system and a standard 200 kV LaB6 TECNAI equipped with original STEM in terms of resolution and contrast sensitivity (Fig. 1D/E). So far we achieve a similar resolution as the tested factory STEM. We get feedback about handling and stability on selected applications, based on daily use experiences and show further potential for optimization of this system, e.g. accessing all 13 (instead of 4) segments/channels of the STEM detector allows to act as a kind of "virtual Dark Field aperture" for observing textures on crystalline materials. Further optimizations using a smaller Wehnelt aperture or a different cathode geometry to increase the resolution are subject of current investigations.

Fig. 1: A) Fe-NPs on N-doped Carbon: In comparison STEM-HAADF is less sensitive to thickness contrasts, delivering a clear particle distribution on a mesoporous support material. B) CAD drawing of the customized detector housing. C) Enhanced EDX functionality: Elemental distribution of Fe catalysts and Silica residuals on N-doped Carbon support material for fuel cell application. D) Custom STEM images of SiC particles in polycrystalline Mg and E) comparative images from a factory STEM.

We kindly acknowledge the German Ministry for Economic Affairs and Energy (BMWi) via the project "innoKA" (number 03ET6096B) and the German Research Foundation (DFG) via the Cluster of excellence "UNICAT" for financial support of the TEM, Dr. Tomas Vikström from EDAX/AMETEK for the technical support and Dr. Alireza Ghasemi from the workgroup of Prof. Fleck (TU Berlin) for the scientific support.

Fig. 1

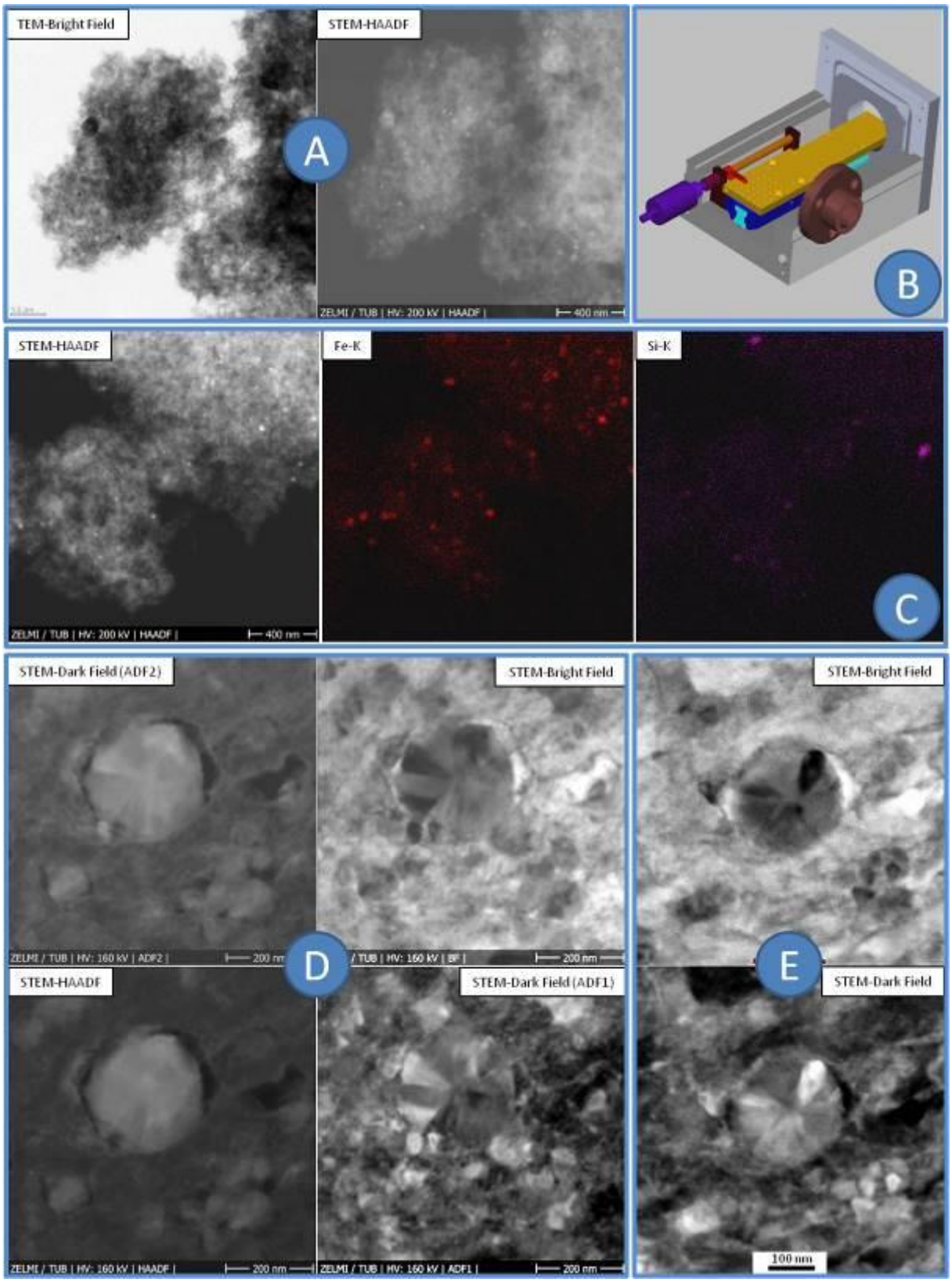
TEM-Bright Field
STEM-HAADF
A
B
STEM-HAADF
Fe-K
Si-K
C
STEM-Dark Field (ADF2)
STEM-Bright Field
STEM-Bright Field
D
E
STEM-HAADF
STEM-Dark Field (ADF1)
STEM-Dark Field
100 nm

IM1.P017
Post acquisition processing as a solution to the SNR problem for dose sensitive samples.

C. Pratsch[1], G. Algara-Siller[1], S. Tragl[1], L. Masliuk[1], T. Lunkenbein[1], R. Schlögl[1,2]

[1]Fritz-Haber-Institut der Max-Planck-Gesellschaft , Department of Inorganic Chemistry, Berlin, Germany
[2]Max Planck Institute for Chemical Energy Conversion, Department of Heterogeneous Reactions, Mülheim an der Ruhr, Germany

Modern electron microscopes are powerful enough to resolve single atoms or individual atomic columns. However, the acquisition of images with a sufficient signal to noise ratio is often problematic since high electron doses will damage fragile structures.

In life science, this problem is even more pronounced than in material science. Nowadays, the invention of single particle averaging and subtomogram averaging allows to circumvent the problem for proteins. (1) Both post acquisition processes use the redundancy of information in several physical copies of the same object. We present examples for numerical post acquisition processing that transfer this idea of redundancy of information to increase the signal to noise ratio and reveal previously hidden features to heterogeneous catalysts.

The presented approach for the numerical post acquisition processing uses the redundancy of information in repeated structures to improve the image quality. In addition, the algorithm can be used to detect the presence and variations of local lattices as well as defects in crystalline samples.

The benefit of this post processing algorithm is exemplified on STEM and TEM images of zeolites.

The presented algorithm combines pattern matching (2) and k-mean clustering to analyse the experimental data. The image is classified into small repeated basic components via iterative application of a normalized cross correlation based pattern matching algorithm. Afterwards, each class is separately refined by k-mean clustering. The generated centroids are then plotted into a new image and the intersections are smoothed by using weighting function based on a partition of unity. Three cases of application are considered. Firstly, the algorithm can be applied to increase the visibility of repeated structures in a single image. Secondly, the algorithm can be applied to a series of low dose images of the same object. Finally, it can be applied to suppress noise in images that include several parallel detection channels. Due to the averaging over similar structures in the images, changes in the unit cell that occur only once or extremely rarely will be suppressed in the post processed image. This effect can be used to identify defects. These locations will show a strong change if the original data is superimposed with the post processed image.

Fig.1. shows a comparison between the raw data and the post processed data for a STEM image acquired with an ADF and BF detector. In the post processed images, the structure of the zeolite is better visible. As an additional application, the classification leads to a segmentation of the images.

Numerical post acquisition processing can increase the signal to noise ratio and show previously hidden features if the sample was recorded either with multiple detectors or the sample itself consists of repeated features.

References:

(1) Joachim Frank, Three-Dimensional Electron Microscopy of Macromolecular Assemblies, Oxford University Press, 2006

(2) J. P. Lewis, "Fast Normalized Cross-Correlation", Industrial Light and Magic, (1995)

(3) JH, Ward. "Hierarchical grouping to optimize an objective function." Journal of the American Statistical Association. 58(301): pp. 236–44. (1963)

Fig. 1: left column: Raw annular dark field (ADF) and bright field (BF) images of a TS-1 zeolite. Right column: In the post processed images the structure of the zeolite is no longer blurred by the low signal to noise ratio.

Fig. 1

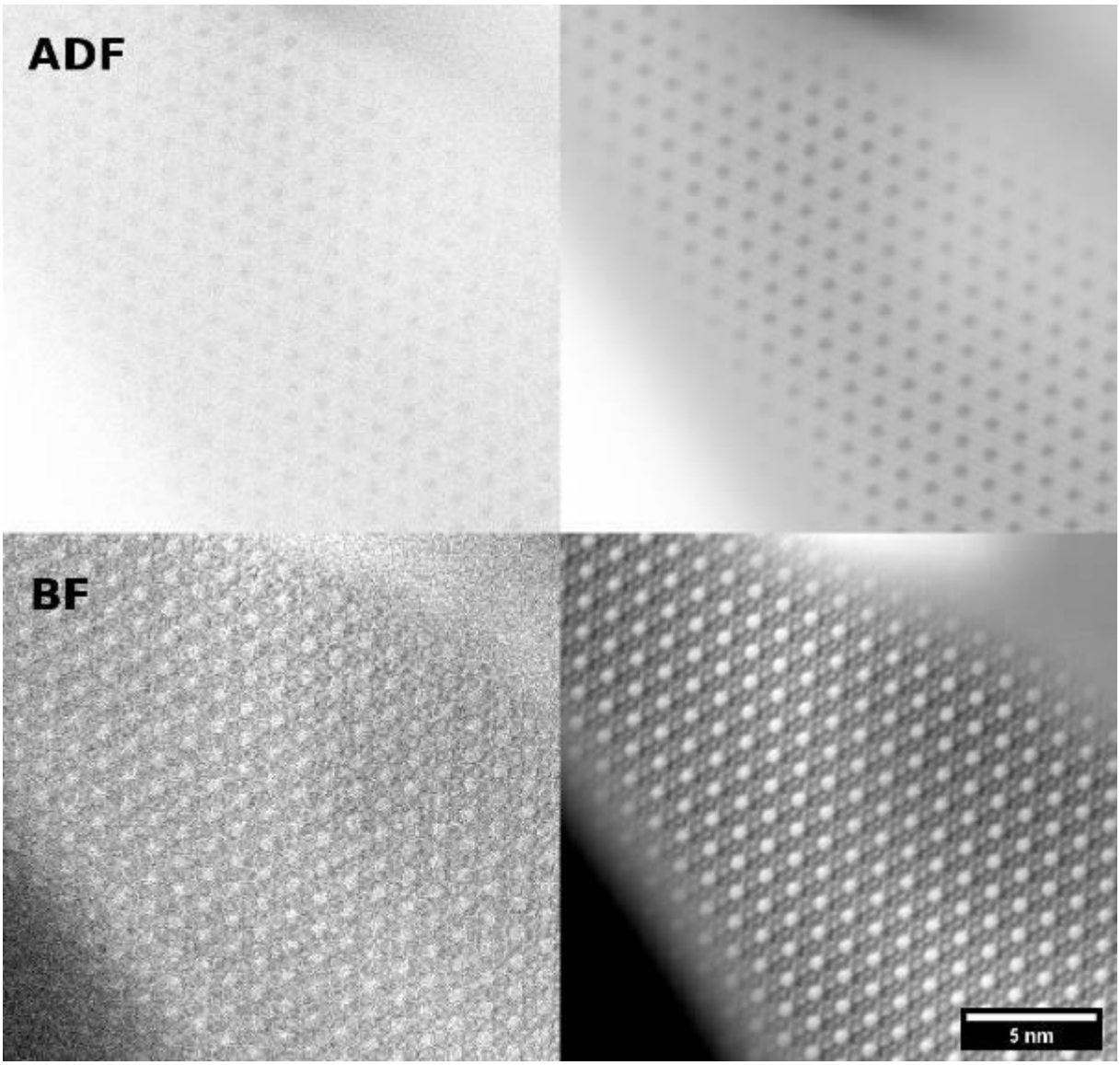

IM1.P018
The combination of electron microscopy, Raman microscopy and energy dispersive X-ray spectroscopy – new methodic possibilities for materials science

A. Zankel[1,2], H. Fitzek[2], C. Mayrhofer[2], M. Nachtnebel[2], R. Schmidt[1,2], H. Schroettner[1,2]

[1]Graz, University of Technology, Institute of Electron Microscopy and Nanoanalysis, Graz, Austria
[2]Graz Centre for Electron Microscopy, Graz, Austria

Recently the system RISE (Raman Imaging and Scanning Electron microscopy) was developed, which combines a scanning electron microscope (SEM) with a Raman microscope (1). At our institute RISE is complemented with energy dispersive X-ray spectroscopy (EDXS) for versatile correlative microscopy.

It is the aim of this work to present first results of this new configuration and to point out synergies, potential pitfalls during both sample preparation and measurements and to show best practices rules.

The SEM Zeiss Sigma 300 VP is equipped with an inlens detector, an Everhart-Thornley-detector (SE2) and an angle selective backscattered electron (BSE) detector (HDAsB, Fig. 1). In the variable pressure (VP) mode the dedicated C2D detector measures secondary electrons (SE) using nitrogen as imaging gas. The VP mode enables the investigation of electrically nonconductive samples without coating, which is mandatory for further Raman investigations. A confocal Raman microscope from WITec and the EDXS silicon drift detectors X-Max 80 by Oxford (England) are attached to the SEM. Materials for Raman mapping have to smooth which is realized by microtomy or polishing.

Several types of specimens were investigated like metal-oxides, mineralogic specimens, inclusions in metals, polymers, organic-inorganic compounds and diverse particles. As an example Fig. 2 shows the cross section of an embedded experimental electrode for a Li-battery. The upper left image is an overlay of a Raman map on an SEM image which was measured in the VP mode using the C2D detector. Beside this correlative result the Raman spectra of the different phases are highlighted with the appropriate colors. The image below is an EDXS map within the same region of interest providing additional elemental information. All the different phases are listed in Fig. 2. Alternatively to the VP mode, the low voltage mode is an option to avoid coating and keeping potential beam damage low for e.g. the investigation of polymers (2).

All the methods require specific expertise regarding sample preparation, instrument operation and interpretation. Aspects like influence of the electron beam on the surface before Raman measurement have to be assessed and appropriate handling has to be developed. Several parameters like beam energy, frame time and pixel resolution may influence the quality of sequential investigation. All these aspects were assessed during the first investigations, methodic skills were acquired and, as a result, methodic recommendations are deduced.

References:

(1) J. Jiruse et al., Integrating focused ion beam–scanning electron microscope with confocal Raman microscope into a single instrument, J. Vac. Sci. Technol. B 32(6), 2014

(2) R. Schmidt et al., The combination of electron microscopy, Raman microscopy and energy dispersive X-ray spectroscopy for the investigation of polymeric materials, Macromol. Symp., Issue "Polymertec 2018", submitted Dec. 2018

Fig. 1: Pole piece of the SEM with several detectors, described in the text.

Fig. 2: Upper image: Raman map within the correlated SEM image (width = 100 µm) beside the Raman spectra with corresponding colors. Lower image: EDXS map within the SEM image beside the listing of the detected phases. (See text for details.)

Fig. 1

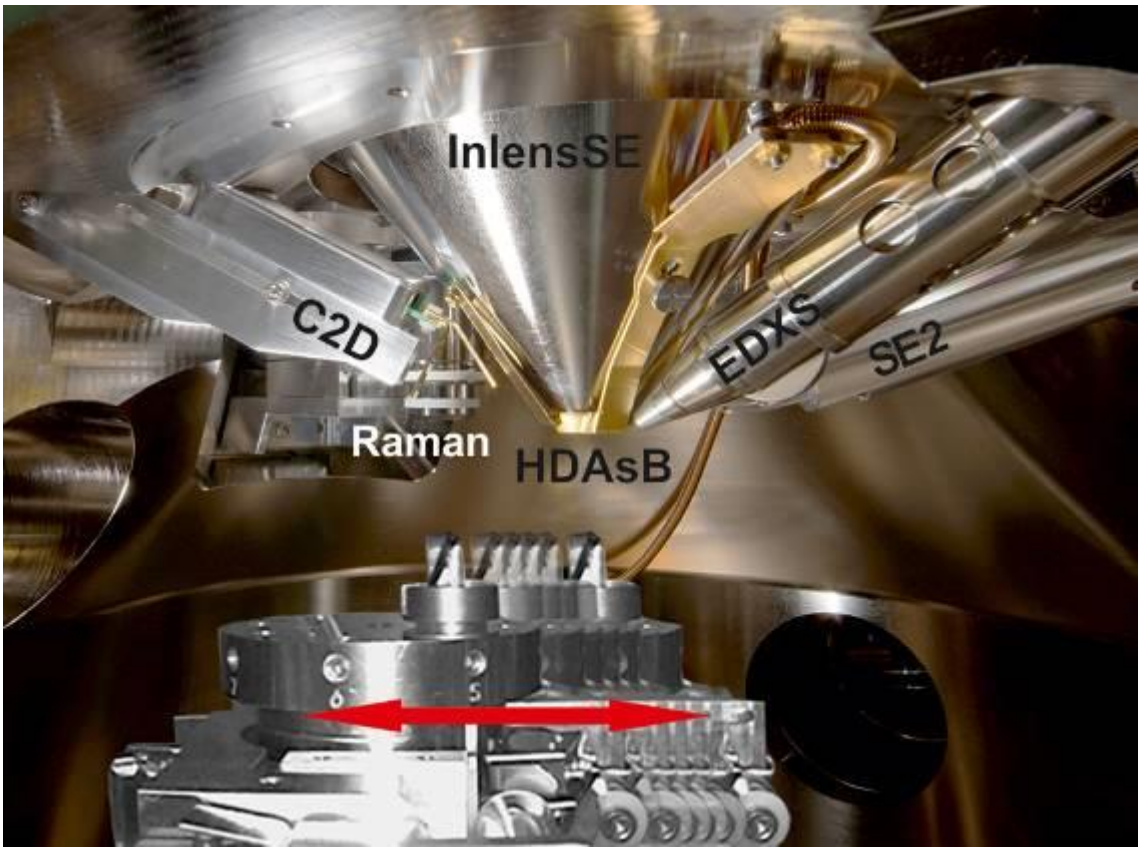
InlensSE
C2D
EDXS
SE2
Raman
HDAsB

Fig. 2

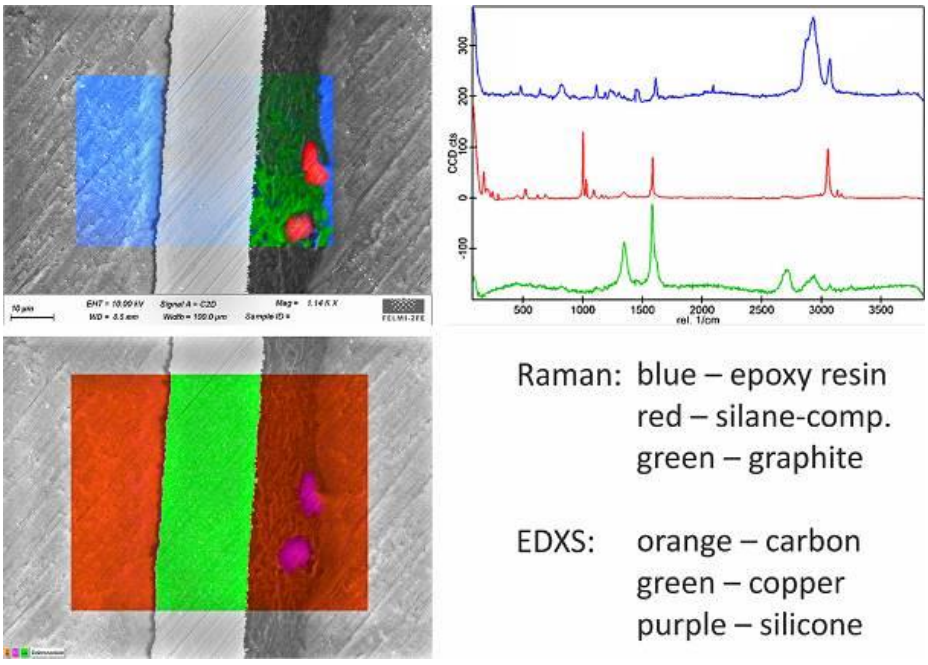
CCD cts
rel. 1/cm
Raman: blue – epoxy resin
red – silane-comp.
green – graphite
EDXS: orange – carbon
green – copper
purple – silicone

IM1.P019
Electron Counting Mode with Fiber-Optically Coupled Camera System

R. Ghadimi[1], D. Tietz[1], M. Oster[1], A. Wisnet[1], H. Tietz[1]

[1]TVIPS GmbH, Gauting, Germany

Former scintillator-based CMOS camera systems with a classical 3 transistor pixel design already proved their usefulness several years ago (1). Recent improvements in signal clarity for low dose applications with direct detecting camera systems can be mainly attributed to the use of drift correction and counting mode acquisition (2). For certain applications, as low voltage microscopy (3) and imaging conditions with very high beam current densities, even last-generation fiber-optically coupled camera systems provide the most favourable imaging properties (4).

We report on the advances of our latest CMOS camera system with a large field of view of 63.5 x 63.5 mm² structured in 4k x 4k pixels, which are implemented in a state-of-the-art 4 Transistor Pixel Design with a Floating Diffusion node for on-chip Correlated Double Sampling (CDS) and an additional buried capacitance for on-demand extension of the intrinsic dynamic range.

For drift correction and counting mode acquisition, the essential requirements are a high frame rate and of course single electron sensitivity. To achieve both features at the same time, on-chip CDS is mandatory. On-chip CDS results in superior signal-to-noise ratio (S/N) due to the excellent time correlation of reset and image signal and is also beneficial for reading out the sensor rapidly. We could achieve full sensor readout with 48 frames per second (fps) and 380 fps for subareas, all at true 16 bit digitization. The sensitivity is sufficient to detect single electron events (SEE) for acceleration voltages from 20kV to 400kV (cf. Figure 1). Since the electron sensitive surface is directly exposed to the vacuum and the primary electrons do not need to pass through insensitive passivation and metal layers, fiber-optically coupled systems offer an advantage in terms of signal clarity and detector longevity over direct detecting cameras for low-voltage applications. This extends the applicability of the system to the field of low energy electron microscopy or even low voltage SEMs for highly sensitive pixelated EBSD or STEM detectors.

Compared to direct detectors, fiber-optically coupled camera systems can offer a much larger intrinsic full well capacity, resulting in a better capability of faithfully recording large intensity differences in a single acquisition (integration or linear mode) with only one readout and hence minimized readout noise. The large field of view, high sensitivity and intrinsic high dynamic range therefore render the system an ideal detector for high-resolution diffraction experiments like MicroED. Advanced diffraction experiments like precessed 4D-STEM are enabled by the possibility of modulating the beam and reading out the camera synchronously (cf. Figure 2).

References:

(1) M Stumpf et al, Microsc. Microanal. 16 Suppl 2 (2010), p. 856.

(2) McMullan et al, in “Methods in Enzymology Vol. 579”, p. 1-17. (3) C Kealhofer et al, Ultramicroscopy 159 (2015), p. 19-25.

(4) JA Rodriguez and T Gonen in “Methods in Enzymology Vol. 579” p. 369-392.

Fig. 1: Histogram of the integrated intensities around SEEs at 80kV (A). The inset shows several detected SEEs. Reconstructed image of a graphite specimen probed by 19 million electrons at an acceleration voltage of 120kV (B).

Fig. 2: Precessed CBED patterns from a mapping experiment. (A) shows the average diffraction pattern for all 10000 scan positions with the contrast scaled such that the high angle intensities are visible. (B) shows the diffraction pattern of a single scan position. (C) shows the dynamic of the line scan data from the region depicted in (B). Scale bars are 10 mrad.

Fig. 1

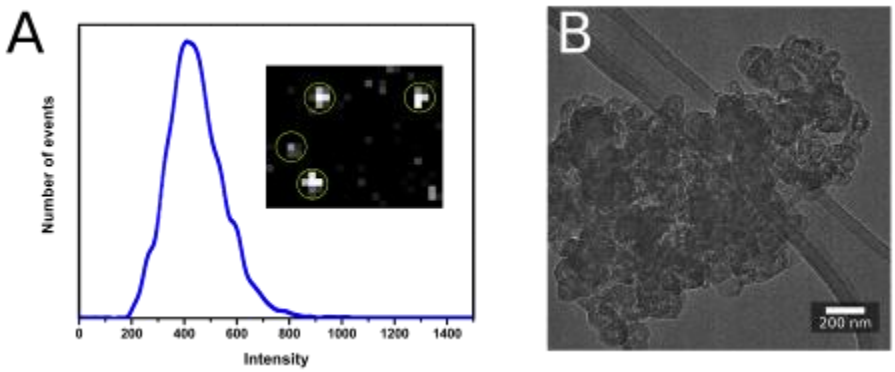
A
Number of events
0
200
400
600
800
1000
1200
1400
Intensity
B
200 nm

Fig. 2

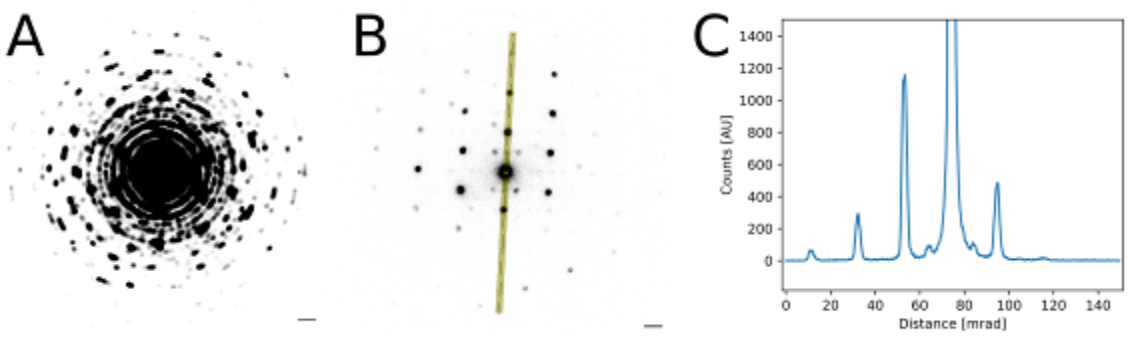
A
B
C
Counts [AU]
0
200
400
600
800
1000
1200
1400
0
20
40
60
80
100
120
140
Distance [mrad]

IM1.P020
Energy-filtered STEM – an experimental study using a fast, pixelated detector

S. S. Firoozabadi[1], P. Kükelhan[1], A. Beyer[1], J. O. Oelerich[1], K. Volz[1]

[1]Philipps-Universität Marburg, Physics, Marburg, Germany

Scanning transmission electron microscopy (STEM) is widely applied in nanostructures" characterization. The combination of high angle annular dark field (HAADF) images and simulations, considering only elastic scattering, allowed quantitative evaluation on an atomic scale (1). To this aim, multi-slice simulations based on frozen lattice approximation were applied to compute the convergent beam electron diffraction (CBED) for every probe position and consequently the HAADF images (2). Besides, incorporation of plasmon scattering improved the matching of simulated and experimental results for amorphous Si (3). Hence, taking into account plasmon scattering can improve the quantitative evaluation of HAADF-STEM images.

Here, we study the influence of inelastic scattering on experimental CBED patterns. A first comparison to corresponding image simulations taking into account plasmon scattering will also be performed. As an example single-crystalline silicon in different crystal orientations is used. The CBED pattern at every probe position is investigated for unfiltered, zero-loss filtered, and plasmon-loss filtered conditions. This was done using an in-column energy filter, which is positioned above a fast, pixelated detector. Besides, the energy-filtered high resolution STEM images were recorded using a HAADF detector installed below the energy filter.

Silicon electron transparent samples were prepared in [110] and [010] directions by ion milling using focused ion beam (JEOL JIB-4601F, JEOL Ltd.) and low voltage ion polishing using a NanoMill® (Model 1040, E. A. Fischione Instruments). The combination of a double aberration-corrected JEOL JEM2200FS operating at 200keV (JEOL Ltd.) and an in-column, omega energy filter along with pre- and post-filter annular dark field (ADF) detectors allowed atomic resolution energy filtered imaging (4). Additionally, a pixelated detector (pnCCD (S)TEM Camera, PNDetector) made it possible to record the CBED or the energy loss spectrum for every probe position. Taking into account inelastic scattering, a modified version of the STEMsalabim software package was applied to simulate the CBED and STEM image intensities for an energy loss range of 0 to 30eV (2, 3).

CBED patterns as well as position-averaged CBED (PACBED) patterns were recorded for different orientations of the Si specimen applying no energy filtering, zero-loss filtering and filtering at energetic positions were the plasmon peak arises. There are distinct differences in the angular dependence of the scattering/diffraction dependent on the energy range of electrons used. This will be discussed in the presentation. Moreover, energy-filtered HAADF images retrieved from the ADF detector below the energy filter and integrated from the CBEDs recorded with the fast, pixelated detector will be presented. The initial results will be compared to image simulations.

In this work, unfiltered, plasmon-loss as well as zero-loss filtered STEM diffraction patterns and the corresponding HAADF images were investigated with the example of single crystalline silicon using a fast, pixelated detector. The impact of energy-filtering on diffraction as well as imaging will be presented.

References:

(1) LeBeau, J. M., Ultramicroscopy 108(2008)1653–1658.

(2) Oelerich, J. O., Ultramicroscopy 177(2017)91–96.

(3) Mkhoyan, K. A., Physical Review Letters 100, 025503(2008).

(4) Hutchison, J. L., Ultramicroscopy 103(2005)7–15.

IM1.P021
Absolute radiometric calibration of the twin micro-spectroscope apparatus over a broad VIS/NIR spectral range using a nanoparticle thin-film luminescent etalon

J. Valenta[1]

[1]Charles University, Department of Chemical Physics and Optics, Prague, Czech Republic

Common fluorescence/luminescence measurements, including microscopic or micro-spectroscopic detection, are performed with a relative intensity scale, due to technical difficulties. However, the absolute calibration should enable to get much more insight into the processes taking place in a luminescing material. Here we describe our imaging-micro-spectroscopy set-up with two parallel detection channels for visible and near-infrared regions. This apparatus is calibrated first relatively using a radiation standard and then absolutely using special thin-layers of luminescing Si nanocrystals with the luminescence quantum yield determined in a separate apparatus. This luminescence etalon is easy to be applied and possess long-term stability. The capabilities of our calibrated micro-spectroscope are demonstrated by studies of several model materials, e.g. solar cell electroluminescence.

IM1.P022
Retrieving SEM sample positions under limited relocation accuracy using digital image processing

J. Schumann[1], D. Bäger[1], N. Dziurowitz[1], C. Thim[1], A. Meyer-Plath[1]

[1]Bundesanstalt für Arbeitsschutz und Arbeitsmedizin, Gruppe 4.5 "Partikelförmige Gefahrstoffe, Innovative Materialien", Berlin, Germany

For many applications in SEM, it is of high relevance to retrieve selected regions-of-interest (ROI) in previously acquired images, e.g., for analyses that require different microscopes or working distances (WD). Repeated measurement of a ROI to study changes from intermittent processing steps motivate high accuracy retrieval. SEM stage accuracy is limited by motorization and position control hardware and generally exceeds a few microns (1). We have developed a software-based approach that aligns SEM images with high accuracy. It is beneficial especially for repeated automated specimen mapping. Its usefulness is demonstrated for studying the progress of a dry-etching process and of the motility of nanofibres.

Our software controls stage movement and image acquisition. It combines mechanical and numerical alignment procedures to optimize ROI retrieval. It starts from a previously stored ROI location and image data and then moves the stage to the specified location to acquire a second image. A matching algorithm, using Förstner- or histogram-based feature recognition, then searches for characteristic features in both images and calculates an affine image alignment transformation. If, due to inaccurate stage relocation, only insufficient numbers of features are recognized, image alignment may fail or not reach desired accuracy. In this case, a lower resolution image is acquired to obtain surrounding specimen features. For successful alignment, image stitching or iterative stage re-adjustment to maximize region overlap are possible. Retrieved ROIs allow additional analyses for multi-channel specimen information, e.g., EDS at large WD combined with high resolution SEM at short WD. Our retrieval procedure was studied for progress monitoring of dry-etching processes and nanofibre motility by acquiring image stacks and differences.

The accuracy of numerical image alignment depended on the presence of a sufficiently large number of well-localized features. The pores of track-etched membranes were well-suited. Resulting alignment quality is shown in Fig.1. It reveals tiniest movements of the nanofibres during successive analyses and excellent alignment of the filter pores. For pore edge-derived image features used by our histogram-based alignment approach for these filter specimen, accuracies well below two pixels were achieved. Fig. 2 compares a mixture of nanofibers and soot prior and after a dry-etching step and reveals a selective removal of soot.

Our approach enables retrieving relevant specimen regions in consecutive SEM analyses and allows acquiring additional analysis data, high-resolution image stitching and identification of specimen modifications caused by intermittent processes. The stage control, image acquisition and alignment software can overcome hardware-related relocation limitations to well below two pixels.

References:

(1) Moré et al.: Relocation of defined sample positions with an automated stage navigation tool for SEM. Proceedings of the MC2017 Lausanne, S.481-483.

Fig. 1: Difference image of two track-etch membrane filter images with nanofibres that were aligned numerically.

Fig. 2: Initial (left) and retrieved (middle) SEM image of a mixture of nanofibres and soot before (left) and after (middle) dry-etching in oxygen plasma. Also shown (right) is a difference image of the two aligned images. The pore diameter of the membrane is about 250 nm.

Fig. 1

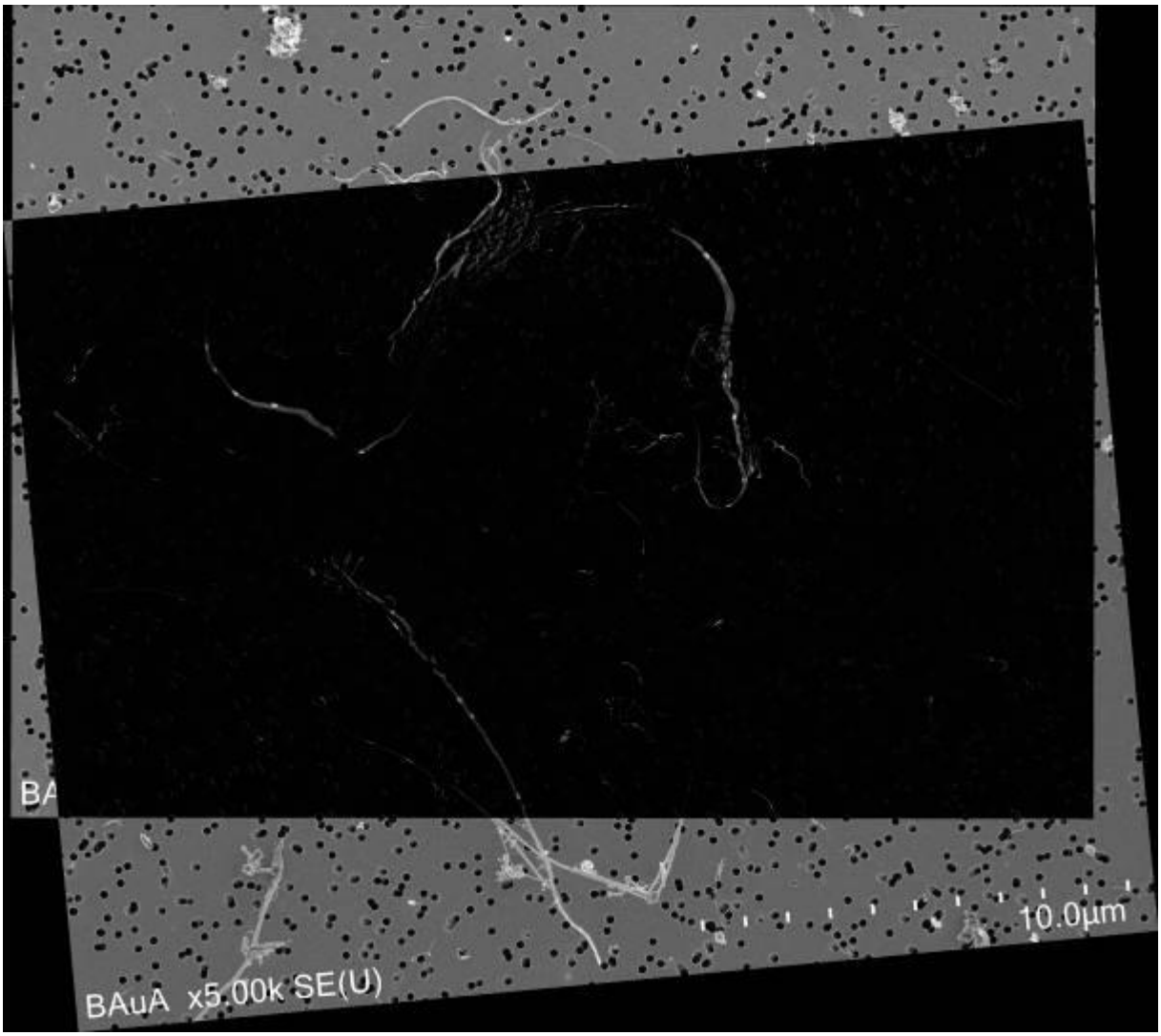

Fig. 2

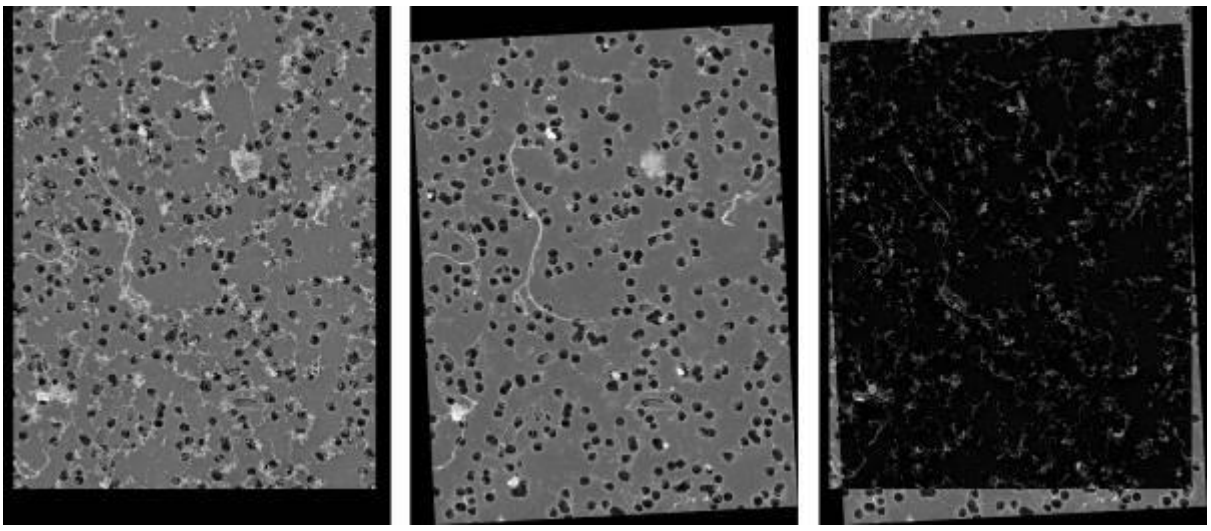

IM2.001 invited
Phase imaging beyond the diffraction limit with electron ptychography

D. Muller[1]

[1]Cornell University, Applied and Engineering Physics, Ithaca, United States

The past three decades have seen the rapid development and maturation of aberration-corrected electron lenses. With the recent advances in detector technology and reconstruction algorithms, the resolution limits are now dominated by counting noise through the maximum allowable dose, either by radiation damage to the sample, or by recording times. Ptychographic phase retrieval algorithms offer an approach to using all of the scattered electrons – potentially enhancing both the resolution and dose-efficiency. Here we show how in-focus ptychography enables imaging at more than double the diffraction limit of the lens, and how out-of-focus ptychography improves the dose efficiency compared to all traditional imaging modes. Benchmarked against the widely-used annular dark-field STEM mode, ptychography simultaneously provides a four times faster acquisition, at double the information limit and with double the precision.

Image resolution is dominated by the energy (or wavelength) of the electron beam and the quality of the lens. Two-dimensional materials are imaged with low beam energies to avoid damaging the samples, limiting spatial resolution to ~1 Å. By combining our new design of electron microscope pixel array detector (EMPAD) (1) which has the dynamic range to record the complete distribution of transmitted electrons at every beam position, and a ptychographic phase retrieval algorithm (2) to process the data, we have been able to increase the spatial resolution well beyond the traditional lens limitations reaching a 0.39 Å resolution for MoS2, at 80 keV, the same dose and imaging conditions where conventional imaging modes reach only 0.98 Å (3). The improved resolution, dose efficiency and robustness to environmental noise enabled by ptychography make it easy to identify defects such as sulfur monovacancies, as well as subtle structural arrangements and tilts on the sulfur sublattice that are undetectable by conventional imaging modes. For twisted bilayers we are able to resolve the shear distortions and interactions between the layers (Figure 1). (3)

In-focus ptychography, like conventional STEM, is not well suited to imaging large areas at high spatial resolution – as the resolution is increased, the number of samples required grows quadratically in dwell time or dose. Operating out-of-focus decouples the resolution and real-space sampling requirements (4), provided the detector has sufficient dynamic range and pixels. With improved probe diversity, we have been able to image 120 nm fields of view with 0.69 Å resolution at 80 keV producing 6000x6000 pixel images, showing a roughly factor of two advantage in precision for ptychography over ADF at the same dose.

Ptychography also provides benefits for imaging magnetic fields, where the field-free conditions at the sample limit the performance of traditional lenses. As magnetic deflections due to the Lorentz force are extremely small, the measurement precision is dominated by the maximum recorded current. The high dynamic range and dose rates supported by the EMPAD have enabled us to reach precisions better than 0.1 µrad of beam deflection. This allows high-quality plan-view imaging of magnetic domain structures in magnetic films only 3-5 atomic layers thick. With these advances we are able to image the internal structures of both magnetic and ferroelectric skyrmions, including their singular points that are critical for accurately describing the topological properties of these field textures.

References:

(1) MW Tate, *et al*, Microscopy and Microanalysis 22 (2016), p. 237.

(2) A Maiden, *et al*, Ultramicroscopy 109 (2009), p. 1256.

(3) Y. Jiang *et al*, Nature 559, (2018), p343.

(4) C. S. Allen, *et al*,. Microscopy and Microanalysis, 24**(**S1**)**, (2018) p. 186–187.

Fig. 1: Real space resolution demonstration of full-field, in-focus ptychography using a twisted bilayer MoS2. (a) Synthesized ADF image; (b) Phase image from ptychographic reconstruction of same data set.

Fig. 1

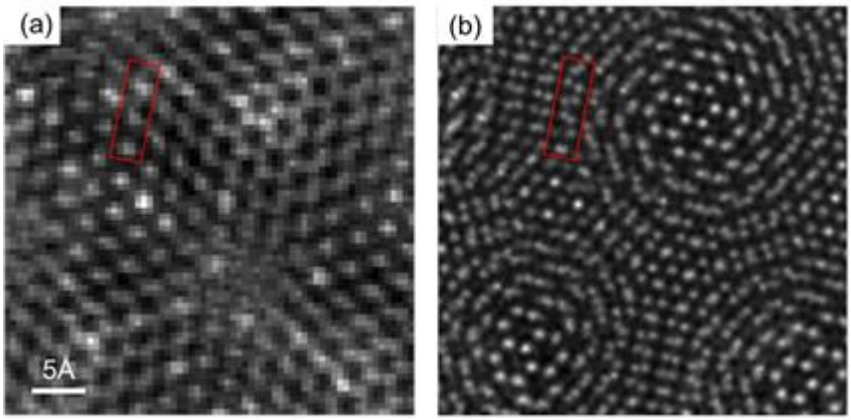

IM2.002 invited
Developments for operando electrical measurements in off-axis electron holography

C. Gatel[1], R. Serra[1], A. Masseboeuf[1], L. Chapuis[1], J. Dupuy[1], B. Warot-Fonrose[1], M.J. Hÿtch[1]

[1]CEMES (CNRS) Toulouse, Toulouse (Cedex 4), Germany

Electron holography (EH) is an established technique for measuring electric and magnetic fields at the nanoscale. The accurate measurement of the electric contribution to the phase shift coming from only an excess of charge or ferroelectric domains is difficult to achieve because additional effects interfere and have to be taken into account in the analysis. However, quantitatively mapping the electric field or the charge distribution at the nanoscale on nanostructures by EH under external stimuli combined to complementary structural and chemical TEM investigations would potentially open new possibilities of studying fundamental physical phenomena at the nanometer scale and mastering the physical processes. But the difficulty lies in applying the technique on working devices. Samples must be sufficiently thin for electron transparency but also electrically contacted. We have then developed methods of sample preparation combining FIB, FEBID, chip-based electrical connections and dedicated sample holders for observing working electrical devices (1,2).

Nevertheless, the studies of weak contributions to the phase shift coming from low charge densities or small magnetic volumes need to improve the signal-to-noise ratio limited by exposure times of a few seconds. Even using a very stable microscope dedicated to interferometric experiments, it is very rare to record holograms for more than 10 s due to remaining instabilities, mainly the fringe and sample drift. I will briefly present our method for acquiring holograms with an unlimited time and a smart acquisition without recording series of holograms. We will see that the solution has been found in the fast processing of images allowing to measure instabilities and their correction in real time (3).

These approaches have been used for studying nanocapacitors composed of Si or Ti electrodes separated by SiO2 or Si3N4 insulating layers by quantitative *in situ* electron holography. The electric phase was mapped across the device at nanometre spatial resolution for different applied biases. Dynamic automation to correct drift during the *in situ* experiments allows the collection of high quality data (3). The internal and external fields are modelled by finite element method and compared with the experimental results. The influence of surface amorphous layers and beam-induced charging will also be discussed.

References:

(1) L. de Knoop, F. Houdellier, C. Gatel, A. Masseboeuf, M. Monthioux, and M.J. Hÿtch, Micron 63, 2–8 (2014).

(2) J. F. Einsle, C. Gatel, A. Masseboeuf, R. Cours, M. A. Bashir, M. Gubbins, R. M. Bowman, and E. Snoeck, Nano Research 8, 1241 (2015).

(3) C. Gatel, J. Dupuy, F. Houdellier, M.J. Hÿtch, Appl. Phys. Lett. 113, 133102 (2018).

The research leading to these results has received founding from the European Union Horizon 2020 research and innovation program under grant agreement No. 823717 – ESTEEM3. This work has been carried out in the framework of the French national project IODA (ANR-17-CE24-0047) and of the MIMETIS project (No. ANR-10-EQPX-38-01) supported by the French National Research Agency under the "Investissement d'Avenir" program.

IM2.003
Small-Angle Electron Diffraction and its application to Magnetic Materials

H. Nakajima[1], A. Kotani[1], K. Harada[1,2], Y. Ishii[1], S. Mori[1]

[1]Osaka Prefecture University, Department of Materials Science, Naka-ku, Sakai, Osaka, Japan
[2]RIKEN, Hatoyama, Saitama, Japan

Small-angle electron diffraction (SmAED) experiments in a transmission electron microscope (TEM) have some advantages that a real-space image and electron diffraction with high angular resolution can be obtained (1). Here we report an electron-optical system with an objective mini-lens to realize SmAED with high-angle resolution of ~10-6 rad in the conventional TEM without any special equipment. The schematic electron-optical systems for SmAED mode and Foucault imaging mode are shown in Fig. 1. In this electron-optical system, we are able to switch between SmAED mode and Foucault imaging mode, keeping the crossover position on the SA aperture plane (2,3). Furthermore, this electron optical system make it possible to carry out Foucault imaging and SmAED experiments in external magnetic fields without changing the illumination system (2).

We applied this electron-optical system to observation of magnetic textures in magnetic materials such as La1-*x*Sr*x*MnO3 and Ba ferrites (4,5,6). Figure 2 shows a Foucault image exhibiting the 180° magnetic domains in La1-*x*Sr*x*MnO3 for x=0.30. The SmAED pattern with a camera length of 150 m is shown in the inset of Fig. 2(a). The 000 spot in the SmAED pattern was split by the magnetic deflection due to the 180° magnetic domains with magnetic moments antiparallel between two neighboring domains. Thus, we investigated changes of magnetic domain structures by applying external magnetic field perpendicular to thin film. It was found that a reconstruction of magnetic domains took place when a magnetic field of 50 mT was applied parallel to the optical axe, as shown in Fig. 2(b).

References:

(1) R. H. Wade, *Phys. Status Solid*, 19, 847 (1967), R. H. Wade and J. Silcox, *Phys. Status Solid*, 19, 57 (1967).

(2) H. Nakajima *et al*., *Microscopy* 65, 473 (2016)

(3) H. Nakajima *et al*., Surface and Interface Analysis, 48(11), 1166-1168 (2016)

(4) H. Nakajima *et al*., *Phys. Rev. B* 94, 22442 (2016).

(5) A. Kotani *et al.*, *Phys. Rev. B* 94, 024407 (2016)

(6) A. Kotani *et al*., *Phys. Rev. B*, submitted.

Fig. 1

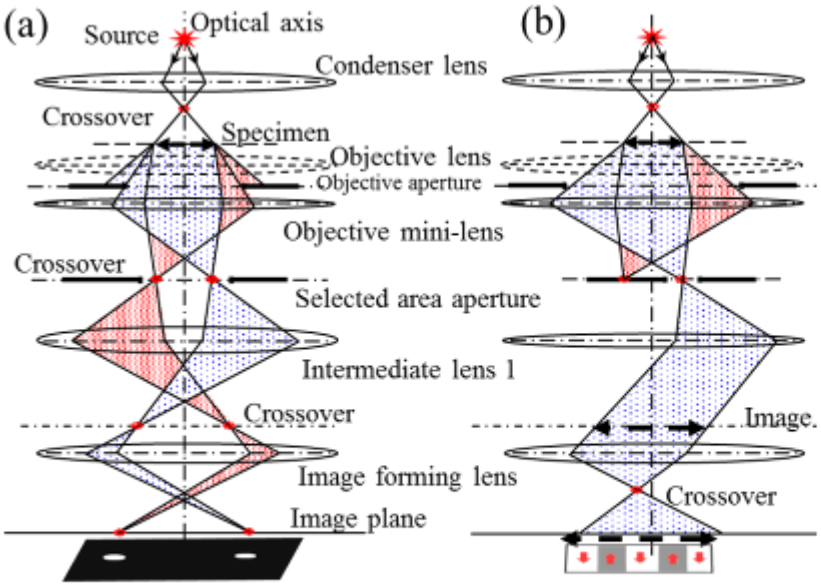

FIG. 1. *Schematic illustration of electron optical systems of (a) SmAED mode and (b) Foucault imaging mode.*

Fig. 2

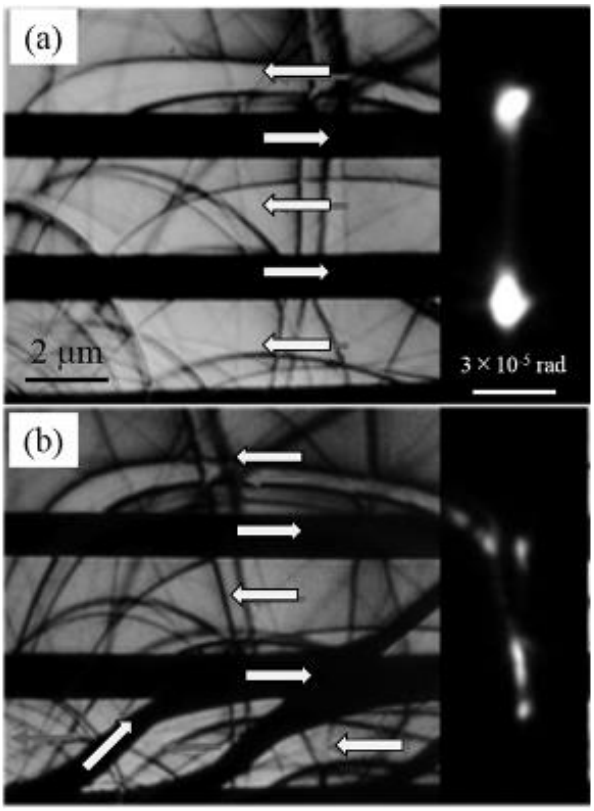

FIG. 2. Foucault images (a) without a magnetic field and (b) with a applied magnetic fierld of 50 mT. (Insets) SmAED patterns.

IM2.004
Holography in Scanning Transmission Electron Microscopy

T. Harvey[1,2], F. Yasin[2], J. Chess[2], C. Ophus[3], B. McMorran[2]

[1]Georg-August-Universität Göttingen, IV. Physicalisches Institut, Göttingen, Germany
[2]University of Oregon, Department of Physics, Eugene, OR, United States
[3]Lawrence Berkeley National Laboratory, Molecular Foundary, Berkeley, CA, United States

Off-axis electron holography has for many years been the premier technique for retrieving the phase of electrons. However, the resolution of off-axis electron holography is fundamentally limited because interference fringes are recorded in real space; standard reconstruction of the phase has a resolution on the order of the fringe spacing (1).

A similar technique is possible in scanning transmission electron microscopy (STEM). In this case, a biprism or diffraction grating produces a focused reference and imaging beam; holograms are recorded in diffraction space as the beams are scanned. Resolution is limited only by the size of the focused beams at the specimen. Early approaches to STEM holography (2,3) worked around the slow speed of pixelated detectors at the time by using physical masks placed atop a monolithic detector to map fringe shifts onto intensity variations. As this method was technically challenging, the technique never found widespread use. Today, with fast detectors that allow rapid recording of a diffraction pattern at each position in STEM, and with nanofabricated diffraction gratings (4) that can produce identical probe beams, STEM holography is an excellent technique for producing highly interpretable phase contrast. We show that phase retrieval is straightforward and intuitive and present several proof-of-principle demonstrations (5-8).

We employ a nanofabricated diffraction grating with a 150 nm pitch and 50 um diameter as the probe-forming aperture in the TEAM I instrument at the National Center for Electron Microscopy. With a 4 mrad convergence semi-angle, this grating produces beams separated by 120 nm at the specimen. We scan the beams across a specimen and record one diffraction pattern per probe position¸ as shown in Fig. 1. Shifts of the fringes in diffraction correspond to phase shifts at each probe position. As a first demonstration of the technique, we imaged gold on an amorphous carbon substrate.

The phase contrast provided by STEM holography provides high contrast on low-atomic-number materials; indeed, in Fig. 2(a), the phase image, we can clearly see a spot of contamination in the upper left that is barely distinguishable in the simultaneously ADF image, Fig. 2(b).

STEM holography offers highly interpretable contrast on both high- and low-atomic-number materials. In addition, unlike any other phase contrast STEM technique, because of the vacuum reference for phase measurement, STEM holography can quantitatively measure electric and magnetic fields. Because resolution is limited only by the probe size and dose, atomic resolution is achievable (6). STEM holography is highly versatile and may become a workhorse tool for efficient, interpretable imaging in the electron microscope.

References:

(1) H. Lichte, Advances in Optical and Electron Microscopy 12, 25 (1991).

(2) T. Leuthner et al., phys. stat. solidi (a) 116, 113 (1989).

(3) Y. Takahashi et al., Japanese J. of Appl. Phys. 33, L1352 (1994).

(4) T.R. Harvey et al., New J. Phys. 16, 093039 (2014).

(5) F.S. Yasin et al., J. Phys. D: Appl. Phys. 51, 205104 (2018).

(6) F.S. Yasin et al., Nano Lett. 18, 7118 (2018).

(7) F.S. Yasin et al., Appl. Phys. Lett. 213, 233102 (2018).

(8) T.R. Harvey et al., Phys. Rev. Appl. 10, 061001 (2018).

Fig. 1

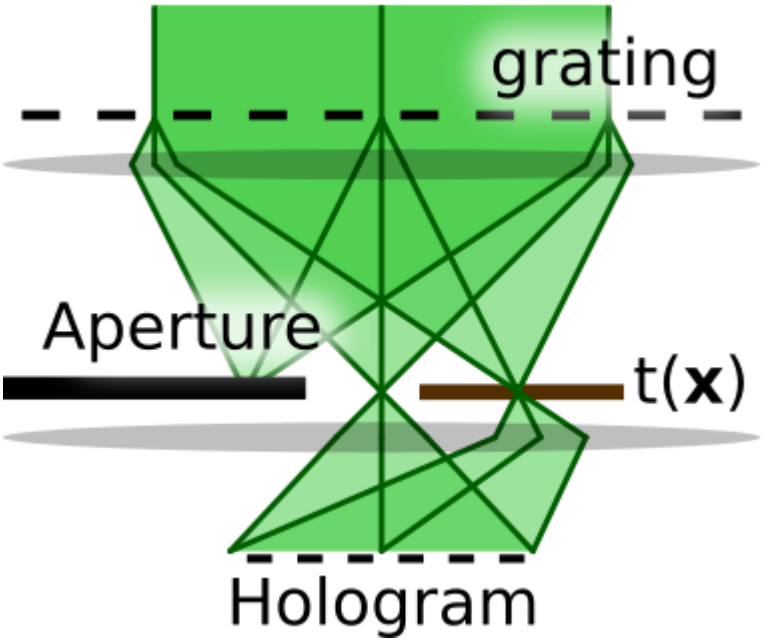

Fig. 2

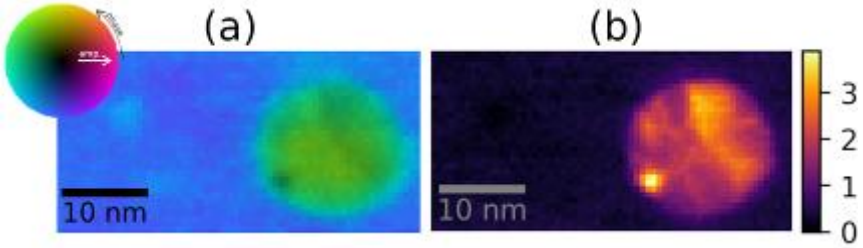

IM2.005
Applications of Nanosecond Electron Holography by Interference Gating

T. Wagner[1], D. Berger[2], T. Niermann[1], M. Lehmann[1]

[1]Technische Universität Berlin, Institut für Optik und Atomare Physik, Berlin, Germany
[2]Technische Universität Berlin, Zentraleinrichtung Elektronenmikroskopie (ZELMI), Berlin, Germany

If the high spatial resolution of transmission electron microscopes (TEM) is combined with a temporal resolution in the nanosecond range, an unbeatable tool for dynamic imaging is created. Unfortunately, such high time resolutions in TEM are difficult to realize. The most common way is via stroboscopic illumination through a laser-pulsed electron emitter (1,2).

The interference gating (iGate) is a novel alternative method for robust time-resolved electron holographic (EH) measurements (3). The basic idea is the direct control of the phase relation between object wave and reference wave, while the specimen is permanently illuminated. By using a biprism in the condenser aperture plane as a fast electric phase shifter, the interference pattern can be disturbed on nanosecond time scales. A synchronized destruction of the interference pattern for a defined period of time during exposure produces a time-resolved hologram. The holographic reconstruction itself acts as the temporal filter that only retains the information of the undisturbed interferogram outside this period. Hence, the readout time of the detector does not affect the time resolution at all.

There are many possible applications for EH with nanosecond time resolution. Due to its access to phase information of the electron wave, thus to the projected potential distribution in and around an object, this method is almost predestined for the dynamic investigation of electrical or magnetic nano-devices in operation.

As a first application (and the basis for all following applications) the transient response of the biasing holder system is measured by investigating the dynamic behavior of the electric field between two electrodes on the MEMS chip. Fig. 1 shows the principle acquisition scheme and evaluation of the time resolved phase gradient between the electrodes.

Knowing the dynamic behavior of the setup, this scheme can be used to investigate the dynamics of a specimen like the FIB prepared diode in Fig.2. The potential jump of the reverse biased (300 mV) p-n junction is clearly visible in the reconstructed phase of the conventional hologram. By applying a square wave signal to the diode, iGate is used to record the temporal development of this potential jump.

While the transition to more complex semiconductor devices (e.g. transistors) is a challenge in terms of preparation, our current results show the benefits of this method in this field. The interference gating paves the way towards a closer look on fast dynamic processes with high temporal and spatial resolution.

References:

(1) O. Bostanjoglo et al., Ultramicroscopy 81, 141 (2000).

(2) A. Feist et al., Ultramicroscopy 176 (2017) 63.

(3) T. Niermann et al., Ultramicroscopy 182 (2017) 54-61.

Fig. 1: Voltage plot: 1 MHz sine-signal U_c applied to capacitor (red line) and the gating signal U_g applied to the electrical deflector for the gate position at 250 ns (5 periods are plotted on top of each other). Reconstructed time-resolved phases (100 ns time resolution) for different gate positions (250 ns, 300 ns, 350 ns and 750 ns) with an exemplary phase profile illustrating the gradient.

Fig. 2: SEM image of a p-n diode prepared as a TEM lamella connected to the electrodes, reconstructed phase of the reverse biased diode (300 mV) and a phase profile showing the potential drop of the p-n junction.

Fig. 1

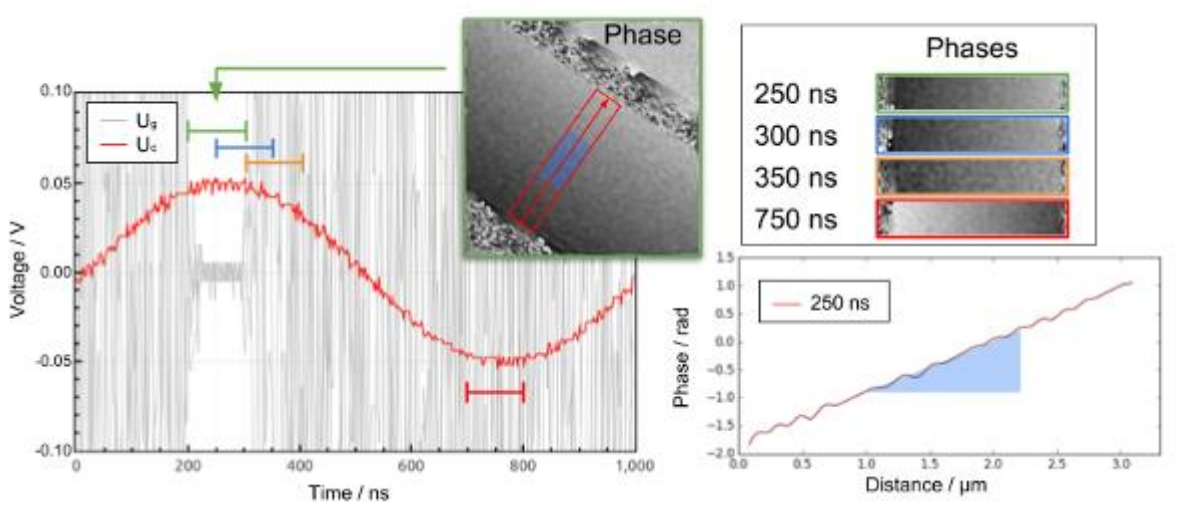
Phase
Phases
250 ns
300 ns
350 ns
750 ns
Voltage / V
Time / ns
Phase / rad
Distance / µm
250 ns

Fig. 2

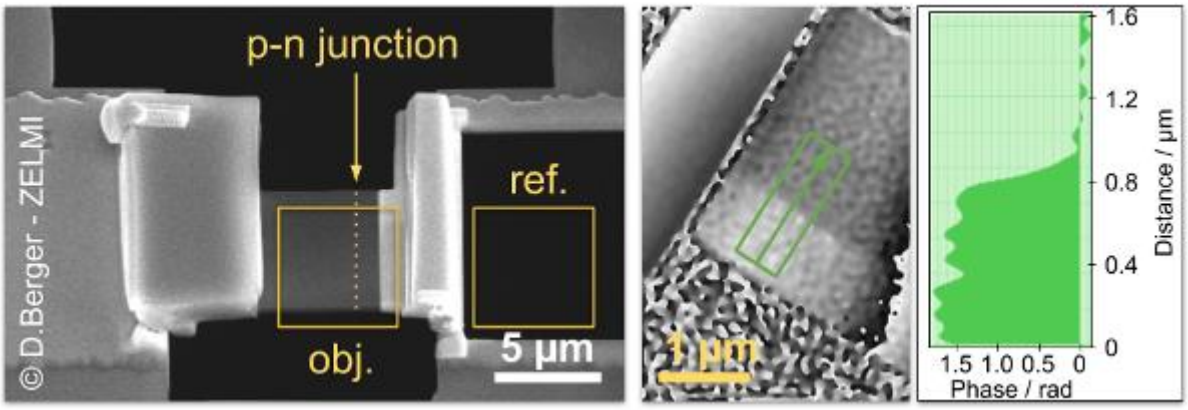
p-n junction
ref.
obj.
5 µm
© D.Berger - ZELMI
1 µm
Distance / µm
Phase / rad

IM2.006
Mode converters realize unitary operators on a two-state quantum system

S. Löffler[1], P. Schattschneider[1,2]

[1]TU Wien, USTEM, Vienna, Austria
[2]TU Wien, Institute of Solid State Physics, Vienna, Austria

Electron vortex beams and the closely related pi-beams have been attracting increasing interest in the community. Their applications have long expanded from measuring energy-loss magnetic chiral dichroism (EMCD) to include the mapping of plasmons, sample chirality, and much more. Here, we present a new aspect of pi-like beams, namely that they can be used to model a quantum-mechanical two-state system including the possibility to realize all unitary operators on this system.

As a basis of the two-state system, we use Hermite-Gaussian (HG) beams of first order which have pi-like symmetry. They are closely related to vortex beams, which have the topology of Laguerre-Gaussian (LG) beams, with $LG_{0,1} \propto HG_{1,0} + i\, HG_{0,1}$. Here, $HG_{1,0}$ corresponds to a pi-like beam aligned in x-direction, while $HG_{0,1}$ corresponds to a y-aligned one. Thus, HG beams can be converted to LG beams and vice versa by means of a $\pi/2$ phase shift which can be realized, e.g., by means of a so-called "mode converter" comprised of two carefully tuned quadrupoles (see fig. 1) (1,2). Similar to vortex beams, the set of all HG beams forms a basis of L^2, the Hilbert space of square-integrable functions. Likewise, two HG beams of first order form a basis of a two-state quantum-mechanical system. One can assign $|0\rangle := HG_{1,0}$ and $|1\rangle := HG_{1,0}$.

However, mode converters can do much more than simply convert HG to LG beams. In fact, they can be used to produce an arbitrary phase shift between the $HG_{1,0}$ and $HG_{0,1}$ components by altering the alignment procedure. This is especially interesting because apart from an irrelevant global phase shift, all unitary operators on two-state systems can be written as a relative phase shift between the two basis states, followed by a rotation of the basis and, subsequently, another relative phase shift (see fig. 2). An effective rotation of the HG basis states can be achieved simply by changing the excitations of the quadrupoles in a mode converter. Thus, two consecutive mode converters can be used to model all possible unitary operators on the two-state system described here.

Having the possibility to realize a quantum-mechanical system with all unitary and hermitian operators (the latter corresponding to measurements) opens up new possibilities for quantum-physical experiments, with the full arsenal of TEM techniques at the experimenter"s disposal. Together with the fact that inelastic scattering leads to entanglement (3,4), it is even conceivable to use electrons as a model system for a quantum computer.

References:

(1) Schattschneider, Stöger-Pollach, Verbeeck, PRL 109 (2012) 084801

(2) Kramberger, Löffler, et al., Ultramicroscopy, submitted

(3) Schattschneider & Löffler, Ultramicroscopy 190 (2018) 39

(4) Schattschneider, Löffler et al., J El Spec Rel Phen (2019), in print

(5) P.S. acknowledges financial support by the Austrian Science Fund (FWF) under grant nr. P29687-N36.

Fig. 1: Principle of the symmetric mode converter using two quadrupoles (cylinder lenses) to convert a HG beam (left) to a LG beam (right) (2). The phase is color-coded as indicated in the inset color-wheel.

Fig. 2: Bloch sphere illustrating how all states on the sphere can be reached by combinations of rotations and mode converters. The phase is color-coded as in fig. 1.

Fig. 1

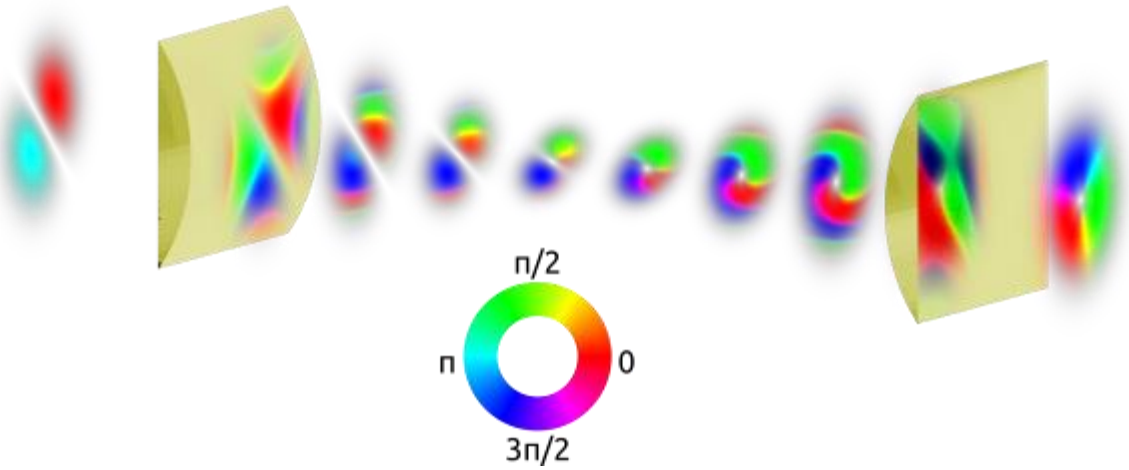
π/2
π
0
3π/2

Fig. 2

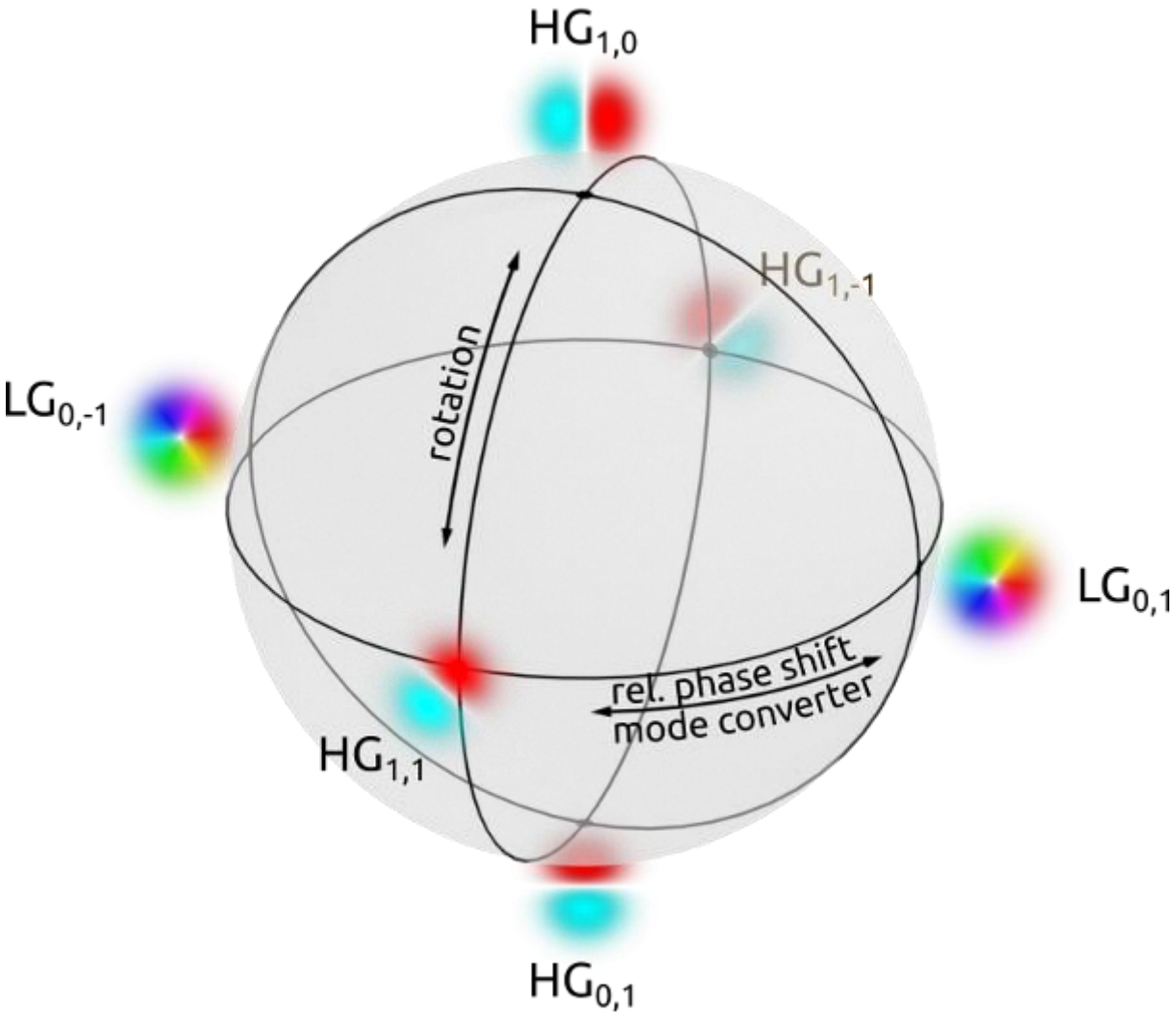
HG1,0
HG1,-1
LG0,-1
rotation
LG0,1
rel. phase shift
mode converter
HG1,1
HG0,1

IM2.LB.P01
Orbital angular momentum spectrum measured by forked gratings and its relation to angular Fourier transform

K. Saitoh[1], L. Wei[1,2], M. Uchida[1,3]

[1]Nagoya University, Institute of Materials and Systems for Sustainability, Nagoya, Japan
[2]Dalian Polytechnic University, School of Information Science and Engineering, Dalian, China
[3]Saitama Institute of Technology, Advanced Science Research Laboratory, Saitama, Japan

Electron beams carrying orbital angular momentum (OAM) (1) have been attracting a great attention and applied to many studies, such as chirality determination of molecules (2), interaction with magnetic materials (3) and magnetic field measurement (4). Electron OAMs in the propagating waves are considered as an important physical parameter for next-generation phase sensing microscopy.

OAM of electron beams can be measured by several techniques using different kinds of amplitude and phase masks such as forked grating, pinholes, polygonal slit, a spatial-light-modulator type device, etc. The present study discusses what we can measure from the diffraction intensities using the forked grating method and its relation to OAM spectrum, the components of the cylindrical harmonics in the wave, which are given by the angular Fourier transform. We discuss the spatial resolution, dispersion of OAM spectrum, influence of misalignment and aberration, from simulations.

Figure 1 shows a phase map of a two-dimensional (2D) test object function, whose absolute amplitude is constant across the whole 2D space. The test object function has ten phase singularities at positions denoted as 1 to 10 in Fig. 1. Figures 2a-i show a series of the maps showing the distribution of the cylindrical harmonics, $\exp\{im\varphi\}$ (m= 0, ±1, ±2, ...), in the test object function. Figure 2j shows absolute squares of the angular Fourier coefficients as a function of harmonic order m, or OAM spectra, at positions of the phase singularities of 1 to 10. The spectra clearly show the OAM located at the phase singularities.

Figures 3a-e show plots of diffraction intensities of a forked grating with a topological charge of 1 as a function of diffraction order, when the topological charges of the incident beam are 3 (a), 1 (b), 0 (c), -1 (d) and -3 (e), respectively. The diffraction intensities are sampled at the centers of diffracted beams. The relation between the OAM spectra obtained by the two techniques is discussed.

References:

(1) M. Uchida and A. Tonomura, *Nature* 464, 737 (2010).

(2) A. Asenjo-Garcia, et al., Phys. Rev. Lett., 113, 066102 (2014).

(3) J. Verbeeck, H. Tian & P. Schattschneider, *Nature* 467, 301 (2010).

(4) V. Grillo et al., Nature Commun.8, 15536 (2017).

Fig. 1

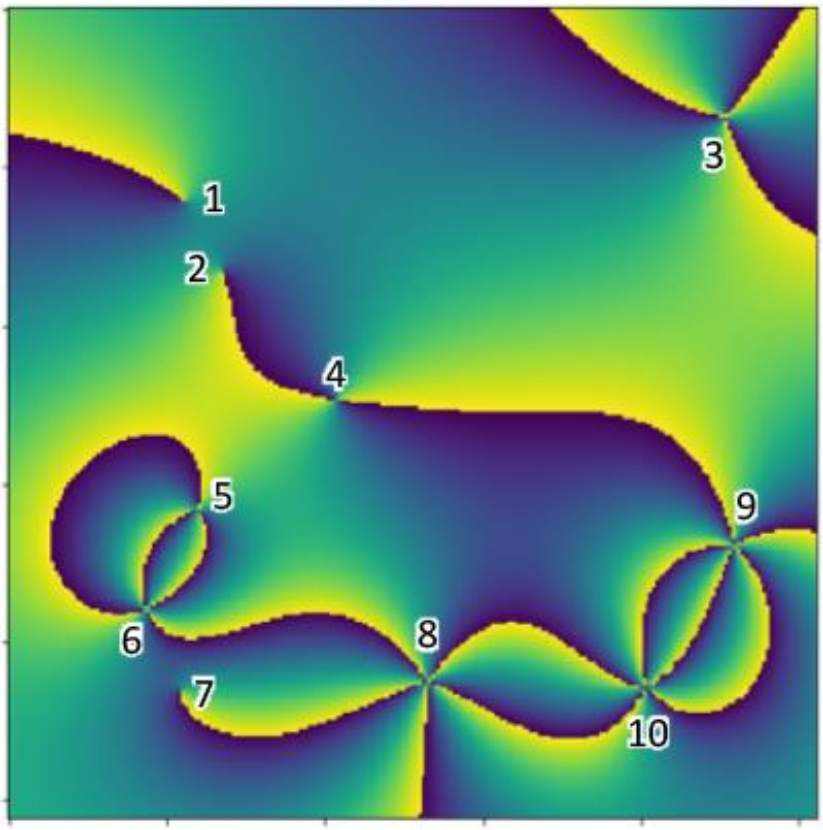

Fig. 2

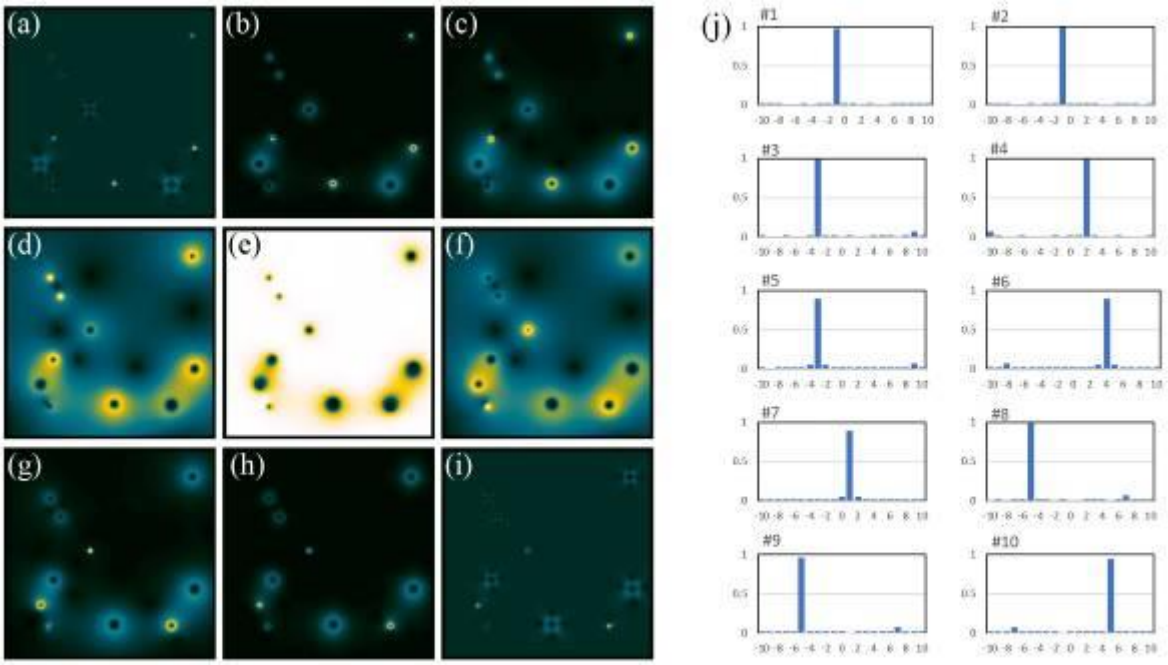

Fig. 3

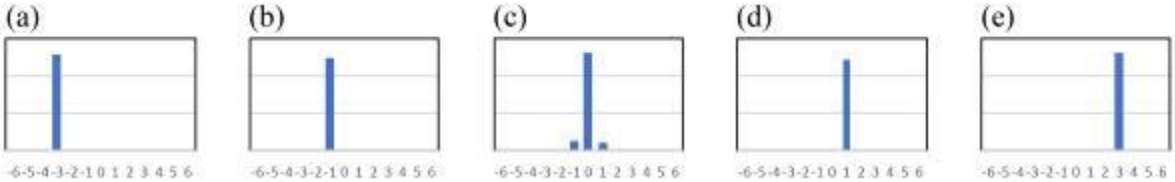

IM2.LB.P02
Imaging single proteins with Low Energy Electron Holography

H. Ochner[1], S. Szilagyi[1], J. Gault[2], S. Abb[1], S. Rauschenbach[1,2], K. Kern[1,3]

[1]Max-Planck-Institut für Festkörperforschung, Stuttgart, Germany
[2]University of Oxford, Chemistry Research Laboratory, Department of Chemistry, Oxford, United Kingdom
[3]École Polytechnique Fédérale de Lausanne, Lausanne, Switzerland

Low Energy Electron Holography (LEEH) (1) is a lens-free in-line imaging method in which the sample is radiated by coherent low energy electrons (50-200eV) (2) to form holograms that in principle contain full 3D information of the object. Recently, Low Energy Electron Holography has been shown to be able to image proteins at the single molecule level (without averaging), while avoiding radiation damage (3).

Thus, this technique can serve as a complementary method for protein structure determination, especially for types of proteins that are hard to access using other methods such as Cryo-EM or X-ray crystallography.

In this poster, we present the workflow and current state of the instrumentation of our LEEH setup along with latest results on single antibodies in which we could demonstrate submolecular resolution and extract 3D information regarding the adsorption geometry of the proteins.

References:

(1) Phy. Rev. Lett, 65, 1204-1206 (1990).

(2) Phys. Scr., 38, 260 (1988).

(3) PNAS 114, 1474-1479 (2017).

IM2.LB.P03
Influence of the experimental setup on inline electron holography reconstructions

M. R. S. Huang[1], A. Eljarrat[1], C. T. Koch[1]

[1]Humboldt-Universität zu Berlin, Institut für Physik, Berlin, Germany

To optimize the reliability of electron wave functions obtained by inline electron holography, the influence of various experimental settings was studied systematically. Focal series were acquired in a JEOL JEM2200FS microscope equipped with an in-column Omega energy filter. A simple but robust test sample with uniformly sputtered Au nanoparticles of an average size of 5-10 nm was prepared on a Cu grid with holey carbon films (inset in Figure 1(a)). To reconstruct as large as possible a bandwidth of spatial frequencies, quadratic defocus sampling was strategically employed. The full-resolution wave reconstruction (FRWR) approach (1-2) based on a flux-preserving approximation to image formation was used to extract phase and amplitude of the electron wave function from the experimental dataset. Fourier ring correlation (FRC) profiles as well as azimuthally averaged power spectra (AAPS) were also calculated to facilitate a quantitative comparison.

Figure 1(a) illustrates the nonlinear defocus sampling scheme. Considerable variation in the average intensity between the recorded slices has been noticed, which is caused by a change in magnification and electron beam convergence as a result of adjusting the objective lens current during the through-focus acquisition. Comparison of the recovered phases from the pre-normalized and un-normalized focal series (Figure 1(b)) reveals the presence of artifacts of very low spatial frequencies (0.03-0.05 nm-1) primarily in the periphery of the image, corresponding to the boundary between the padding (3) and the experimental area (more visible in their difference image). Such false phase arises because the intensity variation is not properly applied within the padded region. The influence of using an objective aperture (OA) and energy-selection slit (ES) was also investigated. Because the images were not sampled finer than the lattice spacing corresponding to all the diffracted beams, without the OA, the bright diffraction contrast that moves across the images with changing the defocus produces phase images that appear rather blurred and uneven, as shown in Figure 2(a). The reason for this effect is that at the sampling being employed for these images, spatial frequencies corresponding to the strong diffracted beams cannot be faithfully represented. Figure 2(b) exhibits a systematic drop in the phase correlation with decreasing exposure time, in particular at high spatial frequencies. This deterioration normally accompanied by poor alignment of the image stack indicates that the recovery of the relatively weak high-frequency signals is more strongly affected by noise than the low-frequency regime.

References:

(1) C.T. Koch, Ultramicroscopy 108, 141-150 (2008)

(2) C.T. Koch, Micron 63, 69-75 (2014)

(3) C. Ophus and T. Ewalds, Ultramicroscopy 113, 88-95 (2012)

Fig. 1

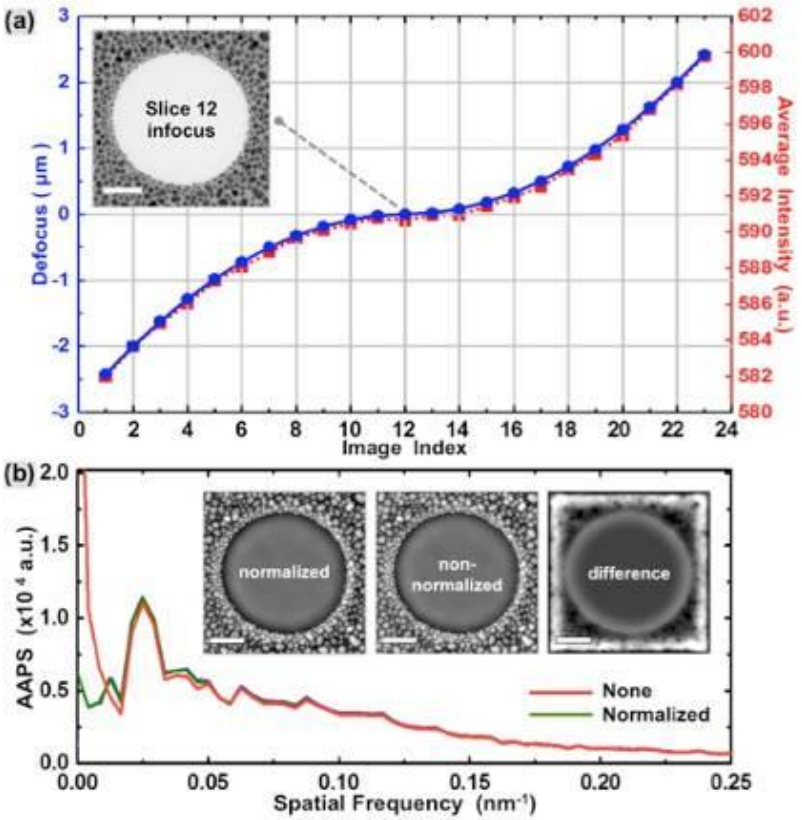

Figure 1. **(a)** Profiles of the quadratic defocus sampling (blue) and the average intensity (red). The inset shows the central frame of the focal series. **(b)** AAPS of the reconstructed phases with (green) and without (red) intensity pre-normalization. The difference image is also shown. Scale bar: 50 nm.

Fig. 2

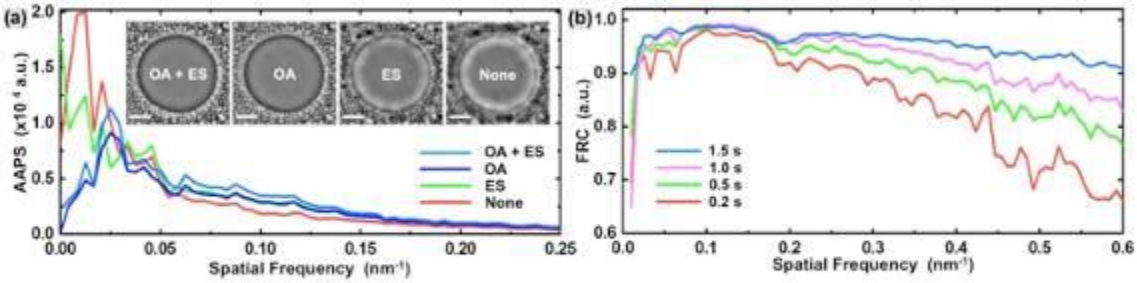

Figure 2. **(a)** AAPS of the retrieved phases (inset) using an OA and/or ES. Scale bar: 50 nm. **(b)** Plot of the FRC calculated from the focal series with varying exposure time using the result of 2.0 s as the reference.

IM2.LB.P05
Creation and detection of electron vortex beams in a scanning electron microscope

T. Řiháček[1], F. Mika[1], M. Horák[2], T. Schachinger[3,4], M. Matějka[1], S. Krátký[1], I. Müllerová[1]

[1]Institute of Scientific Instruments of the Czech Academy of Sciences, Brno, Czech Republic
[2]Central European Institute of Technology, Brno University of Technology, Brno, Austria
[3]Institute of Solid State Physics, TU Wien, Wien, Austria
[4]University Service Centre for Transmission Electron Microscopy, TU Wien, Wien, Austria

Although knowledge on electron vortex beams (EVB) has significantly developed since their first experimental observation (1), all experiments and applications have been considered almost solely in the (scanning) transmission electron microscope ((S)TEM). Our aim is to apply this tool in the scanning electron microscope (SEM).

Determining the probe structure in SEM is rather challenging task since there is no conventional tool for visualizing the spot. Scanning over a sample, which consists of an appropriate contrasting pattern, and collecting secondary electrons (SE) (2, 3) can be used. Since the contrasting structure effectively serves as a detector, we further refer it as a detection structure (DS). To reach better resolution of the beam structure, dimensions of DS must be significantly reduced. However, the measured signal decreases with diminishing surface area of DS. For small DS size and low current, this method does not provide a sufficiently strong signal.

Our solution consists of introducing a small aperture hole as DS and detecting transmitted electrons in the STEM mode instead of SE. This setup significantly increases both the contrast between the DS and the surroundings, and a portion of detected electrons.

For creation of EVB we used the holographic reconstruction method (HRM) (1). Although more efficient methods are available, HRM produces a well-defined and highly pure vortex beam, which is advantageous for treating the spot shape in SEM. The experiment was adapted for the SEM FEI Magellan 400L, see the scheme in Figure 1. A fork-type amplitude diffraction grating (40 nm Si3N4 + 30 nm Pt) is placed in the optical column above the objective lens. For the presented results we used the topological charge and the primary electron energy of 5 keV. The primary beam is tilted in such a way that the desired vortex spot propagates along the optical axis. Other diffraction orders are removed by a modified probe-forming electron aperture (referred as a separation aperture). A defocused vortex probe is then scanned over a DS formed by a set of small aperture holes in silicon nitride membrane coated with gold (diameters 100 – 165 nm, see Figure 2a) placed in the sample plane. The transmitted signal is then detected using a bright field of a standard segmented STEM detector.

The measurement of the vortex probe without separation aperture is shown in Figure 2b, c. For clarity, we present only positive diffraction orders. Although the probe current in the first diffraction order is only about 3.3 pA, we can see a clear image of the vortex spot. We can also observe a clear second diffraction order due to the duty cycle of the grating being different from 50%.

We thus created a vortex beam with the primary energy of 5 keV in SEM. Moreover, we observed the shape of the defocused vortex spot and measured the intensity distribution. The results show that this method is capable to visualize the current distribution even for low current density.

References:

(1) Verbeeck, J. et al., Nature 467 (2010) 301.

(2) McMorran, B. et al, Ultramicroscopy 106 (2006) 356.

(3) Řiháček, T. et al. Proceedings of the 16th International Seminar (2018) 66.

(4) We thank B. Seďa and L. Novák from Thermo Fisher Scientific for help with instrumentation.

The work is supported by TA CR, project No TN01000008.

Fig. 1: Scheme of the experimental setup.

Fig. 2: a) Detection structure in STEM (left) and SE (right); b) defocused vortex probe; c) rescaled detail of b).

Fig. 1

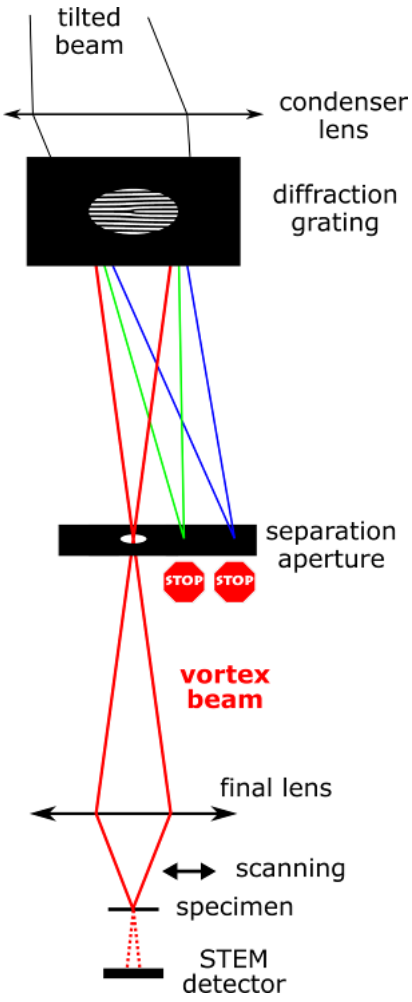
tilted
beam
condenser
lens
diffraction
grating
separation
aperture
STOP
STOP
vortex
beam
final lens
scanning
specimen
STEM
detector

Fig. 2

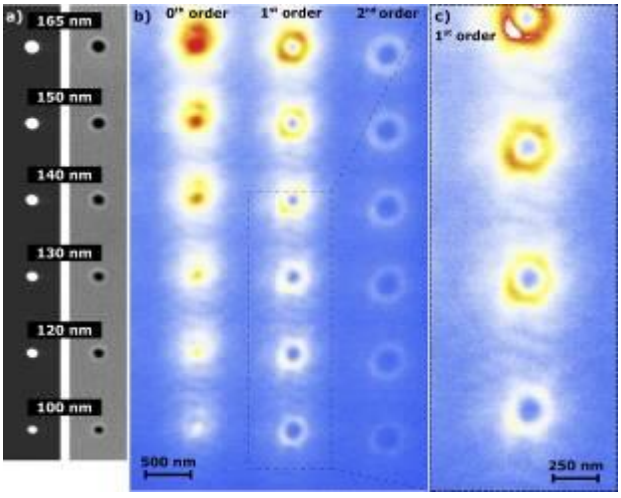
a)
165 nm
150 nm
140 nm
130 nm
120 nm
100 nm
b)
0th order
1st order
2nd order
500 nm
c)
1st order
250 nm

IM2.P001
Magnetic textures in a hexaferrite thin film and their response to magnetic fields revealed by phase microscopy

A. Kotani[1], K. Harada[1,2], M. Malac[3,4], S. Mori[1]

[1]Osaka Prefecture University, Department of Materials Science, Naka-ku, Sakai, Osaka, Japan
[2]RIKEN, Saiatama, Japan
[3]Nanotechnology Research Centre, National Research Council, Edmonton, Canada
[4]University of Alberta, Department of Physics, Edmonton, Canada

Phase microscopy (PM), especially with a hole-free phase plate (HFPP) (1) in a transmission electron microscope (TEM) has a potential advantage that the highly magnified images can be obtained *in-focus,* thus not suffering from Fresnel fringes caused by defocusing. Unlike in electron holography, PM observation does not require a reference wave to extract the local magnetization (2). In this report, we demonstrate that PM with an HFPP can be applied to observe the nanoscale magnetic textures, such as stripe-shaped magnetic domains and magnetic bubbles, in a uniaxial ferromagnet Sc-substituted *M*-type hexaferrite, $BaFe_{10.35}Sc_{1.6}Mg_{0.05}O_{19}$ (BFSMO).

PM observations revealed semi-quantitative magnetization distributions of stripe-shaped magnetic domains, magnetic bubbles, and their responses to applied external magnetic fields. In the zero magnetic field, the magnetization in the domain walls between the adjacent stripe-shaped magnetic domains is oriented parallel to the in-plane direction. On the other hand, the magnetization in both stripe-shaped magnetic domains and magnetic bubble domains is oriented perpendicular to the thin film (parallel to the easy axis). As the strength of the magnetic field applied is increasing, the width of the stripe-shaped magnetic domains is decreased and simultaneously the diameter of the magnetic bubbles is reduced due to the Zeeman effect.

In addition, it was revealed that the magnetization distribution in the magnetic textures of the remnant state depends strongly on the specimen thickness in the PM observation. Figure 1 shows that a large number of magnetic bubbles were formed with the formation ofstripe-shaped magnetic domains in the remnant state. The out-of-plane component in the stripe-shaped domains gradually appeared as the film thickness increased, as shown in the magnetization maps I and II. It is found that magnetic bubbles tends to be formed in the thicker regions. In the magnetization map of the region III, the magnetization distribution of magnetic bubbles with the CW or CCW spin rotation in the magnetic domain wall can be seen clearly, and those magnetic bubbles are formed locally in a triangular lattice. The black and white balls in Fig. 1 correspond to the magnetic bubbles with CW and CCW rotation of the magnetization, respectively. It can be seen in Fig. 1 that those magnetic bubbles exists on the equal proportion and the magnetization helicities are oriented in the random way. Therefore, these results suggested that the energies in the magnetic bubbles with the CW or CCW helicities are equivalent in the remnant state.

References:

(1) M. Malac *et al*., *Ultramicroscopy* 118, 77 (2012).

(2) A. Kotani *et al*., *AIP Adv.,* 8, 055216 (2018).

Fig. 1

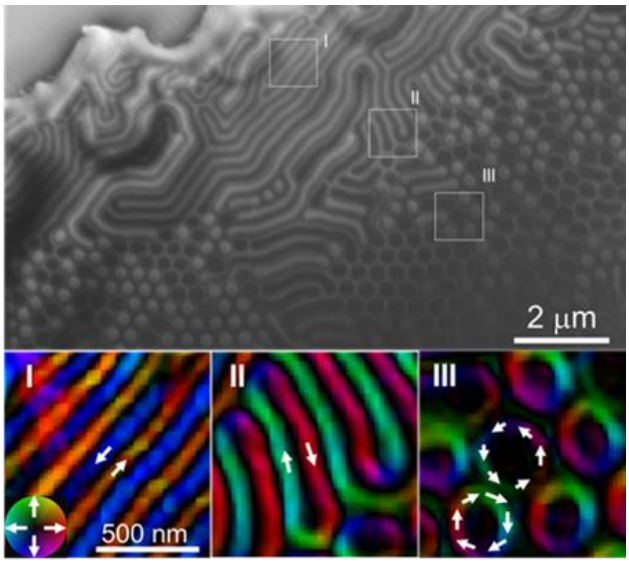

IM2.P002
Hollow-Cone Foucault Imaging for Magnetic Structure Observations

K. Harada[1,2], A. Kawaguchi[2], A. Kotani[2], Y. Fujibayashi[2], K. Shimada[1], S. Mori[2]

[1]RIKEN, CEMS, Hatoyama, Japan
[2]Osaka Prefecture University, Materials Science, Sakai, Japan

Lorentz microscopy is considered as an effective and practical method for observing magnetization structures. Both Fresnel and Foucault imaging modes, however, have the following disadvantages: in the Fresnel imaging mode no additional contrast can be generated on the domains because of just defocusing for images and in the Foucault imaging mode only the filtered out information can be obtained from selected domains. To overcome these difficulties, hollow-cone Foucault (HCF) imaging was developed (1), where an incident electron beam on the specimen was tilted with respect to the optical axis and was circulated in all azimuths around the optical axis. Both magnetic domains and domain walls were simultaneously visualized with sufficient contrasts under the infocus condition.

Figures 1(a) and (b) show the bright-field and dark-field HCF images for different inclination angle conditions. Figure 1(a) is a bright-field HCF image, where domain walls are observed as white lines and several domains have slight dark contrast. On the other hand, Fig. 1(b) shows a dark-field HCF image, where the contrast is reversed from that of the bright-field HCF image.

In addition, schlieren imaging mode, obtained under the specific inclination angle of the illumination beam between the bright-field and dark-field modes, can qualitatively show magnetic field leaking from the specimen over a wide range and to a far distance.

The developed HCF imaging method has advantages of both Fresnel and Foucault imaging modes; therefore, the HCF imaging method can be called the third Lorentz microscopy. We hope the HCF imaging will be widely used for analyzing electromagnetic properties in materials in the future.

References:

(1) K. Harada *et al.*, Appl. Phys. Exp., **12** (2019), https://doi.org/10.7567/1882-0786/ab0523.

(2) Authors would like to thank Dr. Y. A. Ono of RIKEN for his valuable discussion, Prof. H. Numakura at Osaka Prefecture University for providing us the Fe0.88Ga0.12 alloy, and Mr. K. Uchihashi of Osaka Prefecture University for his technical support.

This work was supported by KAKENHI, Grant Number (B) 18H03475.

Fig. 1: (a) Bright-field HCF image, (b) dark-field HCF image, (c) schematic drawing of magnetic domain structure.

Fig. 1

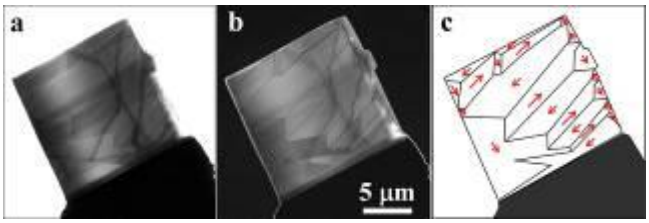

IM2.P003
Three-Dimensional Electrostatic Field at an Electron Nano-Emitter Determined by Differential Phase Contrast in Scanning Transmission Electron Microscopy

M. Wu[1], A. Tafel[2], P. Hommelhoff[2], E. Spiecker[1]

[1]University of Erlangen-Nürnberg, Materials Science, Erlangen, Germany
[2]University of Erlangen-Nürnberg, Department of Physics, Erlangen, Germany

Revealing and quantifying the three-dimensional (3D) electrostatic field of field emission nano-emitters is key to answer the fundamental question of how the field interacts with the sharp tips, which has not yet been adequately addressed despite its long history. Here, we determine the 3D electrostatic field in situ at an electron nano-emitter. Differential phase contrast in scanning transmission electron microscopy has been applied to image nanoscale electrostatic fields of a sharp tungsten electron emitter with an apex radius of about 20 nm under field emission condition. Assuming axial symmetry of the nano-emitter, we derived a method based on the inverse Abel transform to quantitatively reconstruct an axial slice of the 3D electrostatic field from a single projection measurement. The highest field strength of 2.92 V/nm is measured at the nano-emitter apex under condition of a bias voltage of 140 V with respect to the grounded counter electrode located about 650 nm from the apex, resulting in an emission current of more than 2 uA. The experimental results are compared with simulations based on a finite element numerical Maxwell equation solver. Quantitative agreement between experiment and simulation has been achieved.

References:

(1) M. Wu, A. Tafel, P. Hommelhoff and E. Spiecker, Applied Physics Letters 114 (2019) 013101.

M.W. and E.S. acknowledge financial support by DFG via research training group GRK 1896 "In-situ Microscopy with Electrons, X-rays and Scanning Probes" and usage of instrumentation acquired within the DFG Cluster of Excellence EXC 315 "Engineering of Advanced Materials". A.T. and P.H. acknowledge funding by the ERC grant "Near Field Atto."

Fig. 1: Schematic illustration of the experimental setup. The DPC signal, as a projection measurement of electron beam deflection while it pass through the electrostatic field, is calculated and quantified from the four images as obtained by the quadrant detector segments. Assuming a cylindrical symmetry of the nano-emitter, the 3D electrostatic field is reconstructed based on inverse Abel transformation. The results show excellent agreement to simulation.

Fig. 1

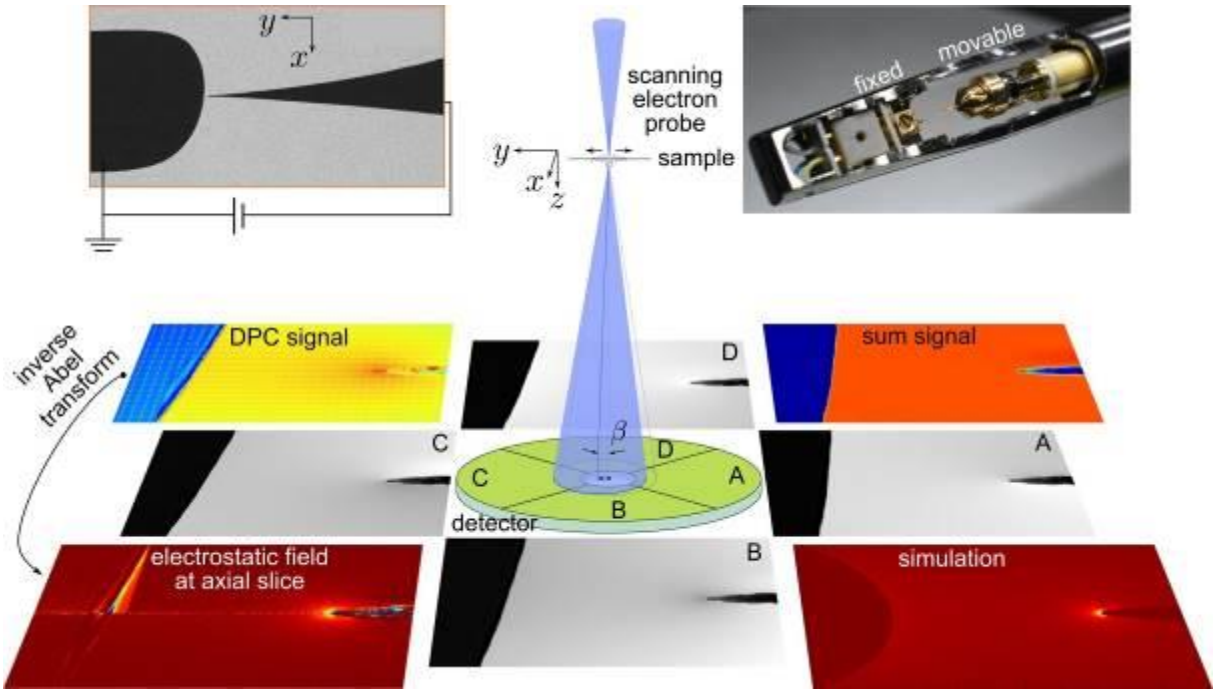

IM2.P004
Influence of shape imperfections on the magnetic states of permalloy nanodisks studied using off-axis electron holography

T. Weßels[1], S. Finizio[2], P. Diehle[1], J. Caron[1], A. Kovács[1], V. Migunov[1,3], S. Gliga[4], J. Raabe[2], R. Dunin-Borkowski[1]

[1]Forschungszentrum Jülich, Ernst Ruska-Centre for Microscopy and Spectroscopy with Electrons and Peter Grünberg Institute 5, Jülich, Germany
[2]Paul Scherrer Institute, Swiss Light Source, Villigen, Switzerland
[3]RWTH Aachen University, Central Facility for Electron Microscopy (GFE), Aachen, Germany
[4]University of Glasgow, SUPA, School of Physics and Astronomy, Glasgow, United Kingdom

Magnetic nanostructures are of interest from a fundamental perspective and for applications that include data storage, medical imaging and drug delivery. As new applications require nanostructures that have ever smaller dimensions, the characterisation of their structural, chemical and magnetic properties becomes increasingly challenging. Here, the intrinsic magnetisation of lithographically patterned, circular permalloy elements is determined quantitatively using off-axis electron holography (EH) and a model-based iterative reconstruction algorithm.

Permalloy disks with thicknesses of between 50 and 200 nm and diameters of up to 1.5 µm (Figure 1a) were fabricated on silicon nitride membranes using electron beam lithography, thermal evaporation of permalloy and lift-off. Transmission electron microscopy (TEM) was used to study the structures, compositions and magnetic fields of the disks quantitatively with high spatial resolution. For magnetic characterisation, the samples were studied in magnetic-field-free conditions in Lorentz mode in an aberration corrected FEI Titan TEM operated at 300 kV. Both the Fresnel mode of Lorentz TEM and off-axis EH were used to study the magnetic states of the permalloy disks. The latter technique is used to measure the magnetic contribution to the electron optical phase shift, which is sensitive to the projected in-plane component of the magnetic flux density within and around the sample and is separated from the electrostatic contribution to the recorded phase shift by turning the sample over inside the TEM using a dedicated holder and recording holograms of the same region of interest. Each pair of phase images was aligned and half of the difference between them was evaluated, in order to obtain the magnetic contribution to the phase shift (Figure 1b). The projected in-plane magnetisation was then reconstructed from the magnetic phase images by using a model-based iterative algorithm.

Both the magnetic phase images and the reconstructed magnetisation distributions reveal the presence of magnetic vortex states in permalloy elements that have a diameter of 1250 nm and a nominal thickness of 50 nm (Figures 1b, c). The vortex core is estimated to have a diameter of 15 nm. On the assumption that the nominal specimen thickness is correct, the average magnitude of the in-plane magnetisation is inferred to be 0.8 T, which is smaller than the value of 1 T expected for permalloy. This difference is expected to result from the fact that the true magnetic thickness of the disk is smaller than its nominal value, in part because of slight oxidation.

Cross sections of the disks were also prepared using focused ion beam milling, revealing that they had slightly distorted bowl-like shapes, instead of being flat. The curvature of the disks was found to increase with their thickness. The three-dimensional nature of the magnetic structure and its relationship to the disk shapes will be discussed.

Fig. 1

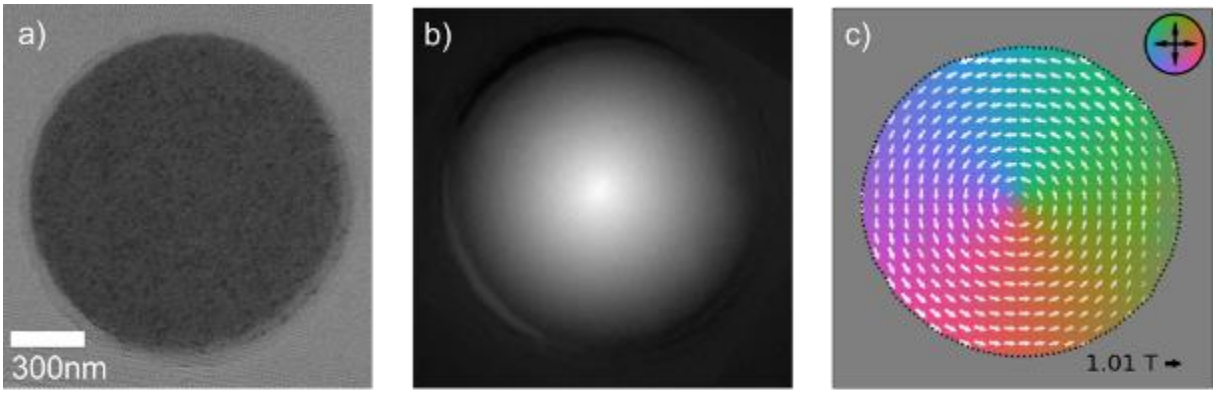

Figure 1. (a) Off-axis electron hologram of a permalloy disk of diameter 1250 nm and thickness 50 nm. (b) Magnetic contribution to the phase shift. (c) Reconstructed projected in-plane magnetisation showing a vortex state. The length of each arrow corresponds to the magnitude of the magnetisation.

IM2.P005
The effect of dynamical scattering in ferroelectrics on the measurements of internal electric fields by momentum-resolved STEM

A. Strauch[1,2], A. Rosenauer[3], A. Sokolov[4], E. Tsymbal[4], K. Müller-Caspary[1]

[1]Forschungszentrum Jülich, Ernst Ruska Centre, Jülich, Germany
[2]RWTH Aachen University, Aachen, Germany
[3]University of Bremen, IFP, Bremen, Germany
[4]University of Nebraska-Lincoln, Lincoln, NE, United States

Ferroelectric tunnel junctions (FTJs) are one focus of next-generation memories, in which the polarisation represents a logical bit. With these non-volatile memories, higher memory densities by significantly less energy consumption are possible. Recently, it was observed that devices with $BaTiO_3$ tunnel junctions cannot be reversibly polarised if the thickness of the ferroelectric layer becomes lower than approximately 3nm (1).

To investigate these geometries that are relevant for applications, a STEM method would be desirable to map the ferroelectric domain structure in ferroelectric nanofilms. This method should exploit the recently accessible four-dimensional data sets from momentum-resolved STEM. (2)

In this contribution, we address the impact of systematic errors arising from dynamical scattering, tetragonality, violated inversion symmetry, and redistributions of electrons due to chemical bonding in a simulation study accompanied by experiments in the materials $BaTiO_3$, $PbTiO_3$ and $PbZr_xTi_{1-x}O_3$.

First the effects of dynamical scattering in these materials are simulated with the software STEMsim. In a centrosymmetric unit cell, the unit-cell average of the in-plane momentum of the electrons is zero due to symmetry arguments also in thicker specimen in the presence of dynamical scattering. However, the displacement of the atoms, that is the reason for the ferroelectricity, breaks inversion symmetry. This leads to a non-zero unit-cell average of the in-plane momentum of the electrons, even without the presence of internal fields, resulting in a systematic error δ of the unit-cell averaged electric field depending on the detailed experimental conditions. (3)

We investigate the effect of the displacement of the atoms, the sample thickness, the acceleration voltage, the convergence angle, the zone axis and the sample tilt on δ. The parameters used for STEMsim is shown in Table 1. The dependence of δ on the specimen thickness for different accelerating voltages with a convergence angle of 25mrad are shown in Fig. 1. δ has strong fluctuation with thickness, but tends to lower values for thicker specimen. On average, higher acceleration voltages leads to lower δ. In Fig. 2, similar behaviours for different convergence angles at 300kV are shown. Obviously a larger convergence angle leads to a lower systematic error δ.

In general, a high acceleration voltage and a large convergence angle should be used. The ferroelectric polarisation of $BaTiO_3$ is in the order of 30µC/cm2 that corresponds to a huge electric field. Even in the presence of screening, fields in order of 10 MV/cm can be expected. So, δ is much smaller than the fields that should be measured. It should be noted that surface charges can lead to accumulation of free charges at the boundaries inducing a depolarising field that reduces the internal electric field, which we discuss in addition.

Next, structure factors due to the ionicity of the atoms are used. These are calculated using the density functional theory (DFT) with the software WIEN2k. Finally, surface effects will be discussed.

References:

(1) Garcia et al., Nature Comm. 5, 4289 (2014)

(2) K. Müller et al., Nature Commun. 5, 5653 (2014)

(3) K. Müller-Caspary et al., Ultramicroscopy 178 (2017)

Funding from the Initiative and Network Fund of the Helmholtz Association under contract VH-NG-1317 is gratefully acknowledged

Table 1

STEM sampling	30x30 pix
Sample size	17x17 unit cells
C_s	1 pm
Detector	0-50 mrad

Fig. 1

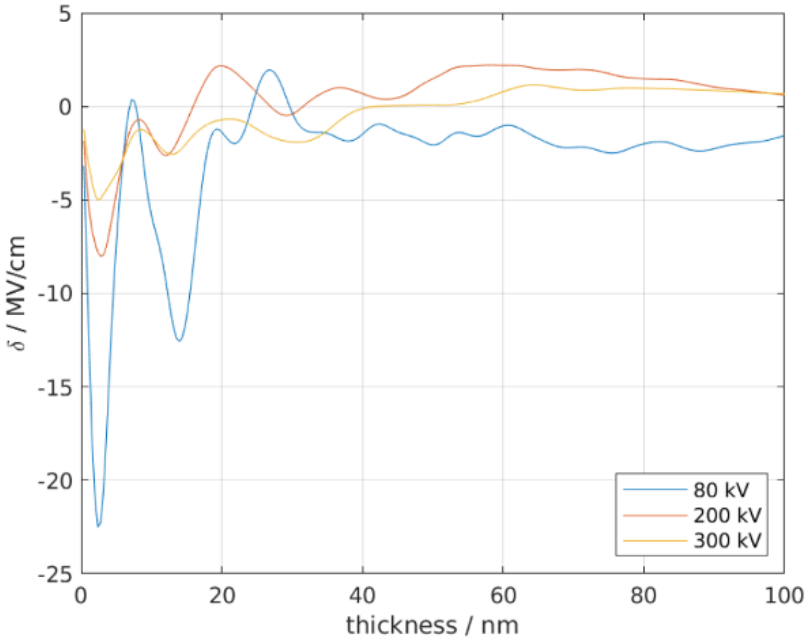

Figure 1. Dependence of the systematic error δ on sample thickness for different accelerating voltages using a convergence angle of 25mrad. Simulation assuming isolated atoms.

Fig. 2

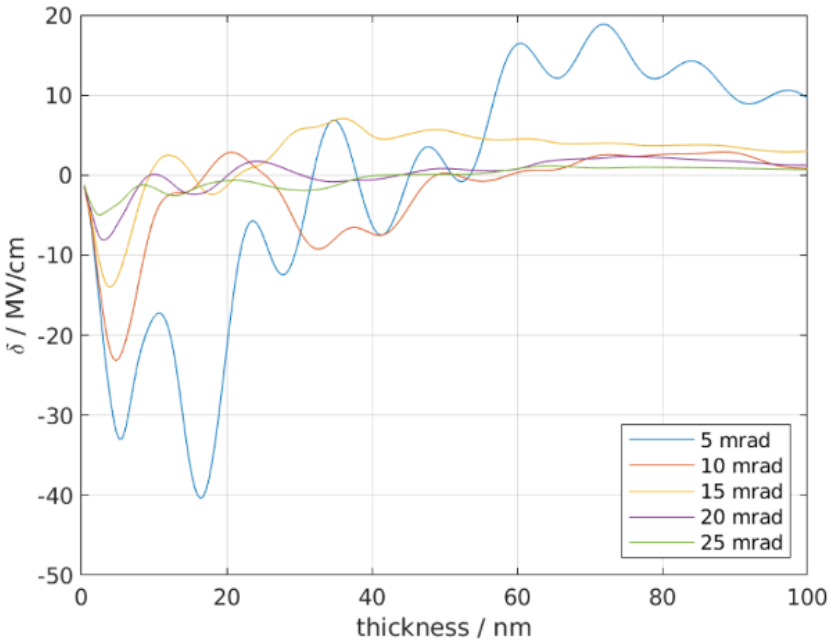

Figure 2. Dependence of the systematic error δ on sample thickness for different convergence angles. Simulation assuming isolated atoms and 300keV electrons.

IM2.P006
Quantitative comparison of momentum-resolved STEM and off-axis electron holography at atomic resolution

F. Winkler[1], J. Barthel[1], R. Dunin-Borkowski[1], K. Müller-Caspary[1]

[1]Forschungszentrum Jülich GmbH, Ernst Ruska-Centre, Jülich, Germany

Off-axis electron holography (OAEH) is an established technique that can be used to record an electron wavefunction in a transmission electron microscope (TEM) with high spatial resolution. For a very thin specimen, the phase of the wavefunction can be related directly to the electrostatic potential of the specimen (1). However, OAEH puts high demand on the stability of microscope and specimen in order to achieve high spatial and signal resolution. Another promising technique, which is referred to as momentum-resolved scanning TEM (MR-STEM), is increasingly used to measure electrostatic fields in materials at atomic resolution. The latter technique involves recording diffraction patterns at each scan position and relating the first moment of the intensity distribution to the projected electrostatic field, according to Ehrenfest"s theorem (2). Both techniques are sensitive to electrostatic potentials or fields respectively and offer prospects for the quantitative measurement of fundamental material properties with atomic spatial resolution. The aim of the present work is to investigate experimental conditions of the two techniques producing similar or even equivalent results. This may enable us to benefit from particular advantages offered by a technique in aspects such as better dose efficiency, reduced irradiation damage, relaxed experimental limitations, or lower requirements for instrumental quality and stability. We present a case study for a thin $SrTiO_3$ crystal, where the signal can be related directly to the electrostatic potential or field. The different illumination setups that are required for the two techniques, i.e. parallel illumination in OAEH and convergent illumination for MR-STEM, are found to lead to different responses of the recorded signal to dynamical diffraction. We study, under which conditions, a quantitative measurement of these quantities is achievable with the two techniques and how experimental parameters, such as defocus, can be optimized for a straightforward interpretation of the recorded signal (c.f. Fig. 1). We further show that thermal diffuse scattering (TDS) is negligible even for thicker specimens. Finally, we discuss practical aspects of the applicability of each technique.

Fig.1: Reconstructed electrostatic potentials (divided by specimen thickness) obtained from MR-STEM and OAEH simulations for $SrTiO_3$. Each of the first 3 columns corresponds to a different specimen thickness. The defocus is labelled in the top right corner of each image. The signal is observed to change significantly with specimen thickness for each setup. The scale bar is 0.1 nm. The right hand column shows reference electrostatic potential distributions calculated from neutral atomic scattering factors for both approaches, including the influence of Debye-Waller factors and probe-forming (imaging) apertures.

References:

(1) S. Borghardt et al., *Physical Review Letters* 118 (8), 086101

(2) K. Müller et al., *Nature communications* 5, 5653

Fig. 1

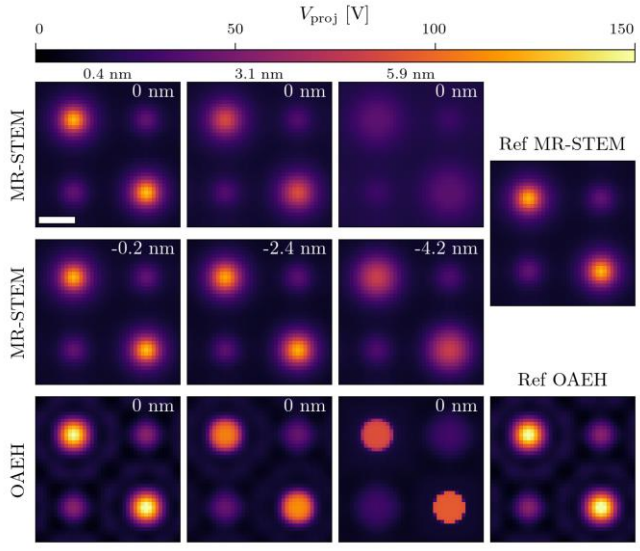

IM2.P007
Theoretical and experimental classification of the detection precision of a PSD based non-pixelated COM detector for differential phase contrast microscopy

F. Schwarzhuber[1], S. Pöllath[1], P. Melzl[1], J. Zweck[1]

[1]University of Regensburg, Institute for Experimental and Applied Physics, Regensburg, Germany

The development of probe-corrected STEM allows the measurement of picometre scale potential variations using differential phase contrast microscopy (atomic DPC) (1-4). In contrast to conventional DPC (cDPC), the potential gradient across the electron probe is no longer constant, resulting in a diffractive redistribution of intensity in the diffraction disk. Müller-Caspary showed that the intensity weighted centre of the diffraction disk, called centre of mass (COM) can be related to the average lateral momentum the electron ensemble gains by interacting with the specimen and therefore to strength and direction of the deflecting fields (3).

We use a duo-lateral-position sensitive diode (PSD), which combines fast detection speed and comparably low pricing of semiconducting diodes with the ability of pixelated cameras to track the absolute position of the diffraction disk"s COM. Additional advantages of a PSD are that, in contrast to cDPC, the measurement yields absolute COM positions, facilitating calibration massively. With our setup, we are able to measure beam deflections with an accuracy of ~0.5 µrad (5) at an acquisition speed of 5-10 µs per pixel.

To evaluate the performance of the PSD we present an analytical description and simulations on the achievable precision, taking into account the current density on the detector, the diffraction disk radius and beam broadening in the detector material (Fig. 1). Further we derived an analytical model describing the dependence of the standard deviation of the COM detection on the diffraction disk radius R, primary beam intensity and beam broadening in the detector material. We will verify our theoretical work with experimental results where we determined the measurement error (standard deviation) in dependence on the beam intensity and diffraction disk radius. Based on this work we derive criteria for microscope settings enabling optimal conditions (best detection sensitivity) for DPC measurements with the new detector.

We also discuss the precision of the COM detection with pixelated detectors. We performed simulations on the positional error that occurs when measuring the COM with an array of pixels of a certain size. Fig. 2 shows the dependence of the COM detection error on the pixel size for a diffraction disk with R=1 mm. For pixel sizes larger than ~0.18*R oscillations of the standard deviation occur and the error starts to deviate from the constant PSD error. Below this value the error matches the one of the PSD (deviations below 1%). With these results we are able to determine the minimal number of pixels needed to obtain a comparable precision as with the PSD setup for a certain disk size.

References:

(1) K. Müller et al, Nat. Com., 10.1038/ncomms6653, 2014

(2) N. Shibata et al, Nature Physics, 10.1038/nphys2337, 2012

(3) K. Müller-Caspary et al, Ultramicroscopy, 10.1016/j.ultramic.2016.05.004, 2016

(4) I. MacLaren et al, Ultramicroscopy, 10.1016/j.ultramic.2015.03.016, 2015

(5) F. Schwarzhuber and P. Melzl et al, Ultramicroscopy, 10.1016/j.ultramic.2018.05.003 ,2018

Fig. 1: Theoretical description of the minimal measureable beam displacement (**a**) and standard deviation STD (**b/c**) in dependence on electron count and diffraction disk radius.

Fig. 2: Dependence of the positional error of the COM on the pixel-size of the detector (simulations with R=1 mm).

Fig. 1

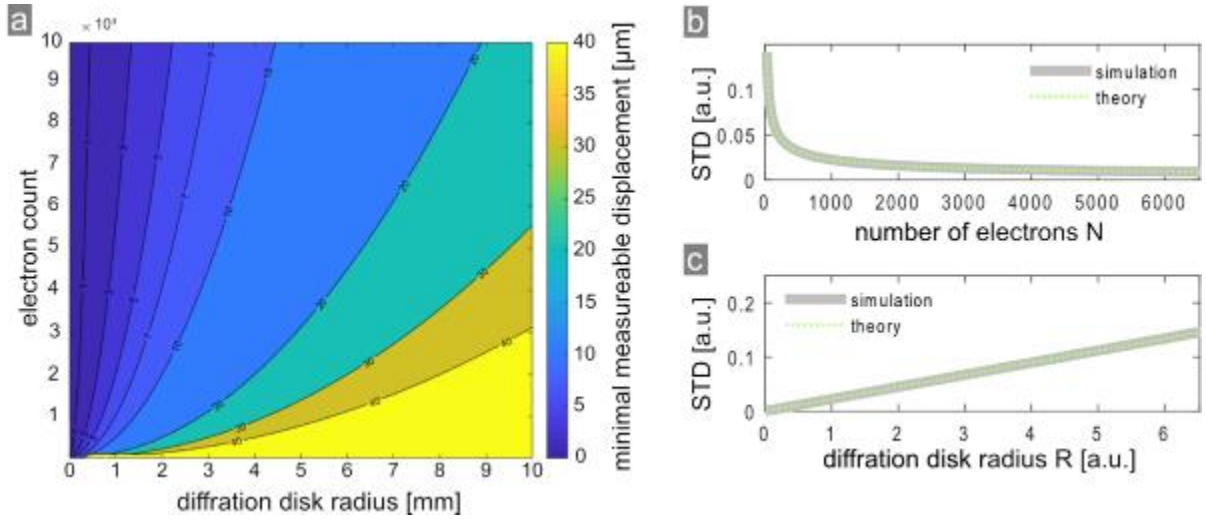
a
b
c
electron count
diffration disk radius [mm]
minimal measureable displacement [µm]
STD [a.u.]
number of electrons N
simulation
theory
diffration disk radius R [a.u.]

Fig. 2

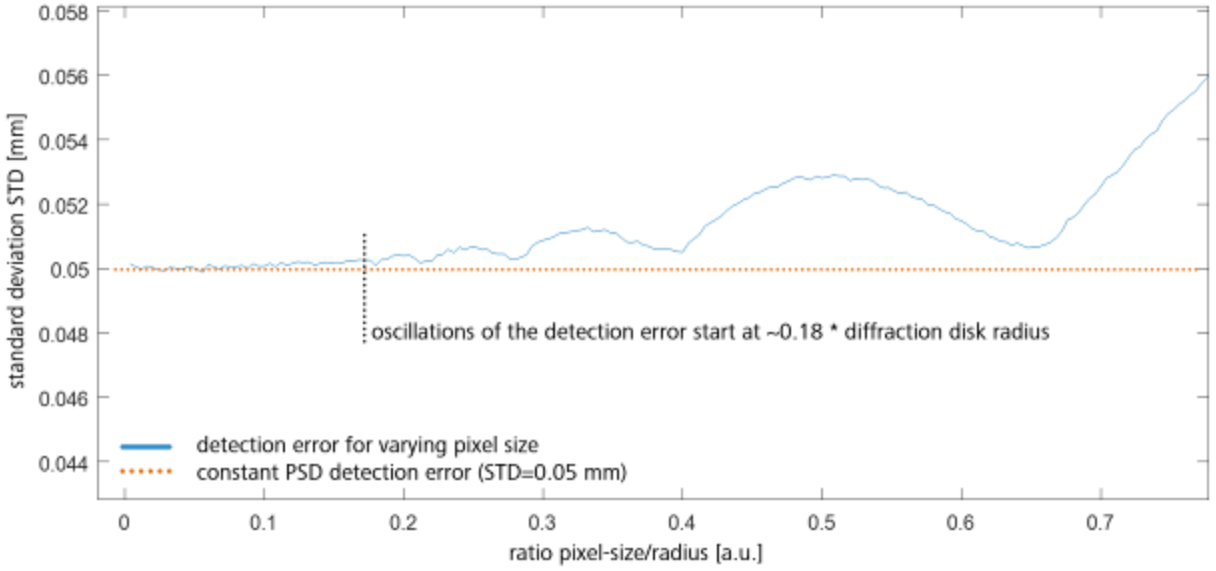
standard deviation STD [mm]
oscillations of the detection error start at ~0.18 * diffraction disk radius
detection error for varying pixel size
constant PSD detection error (STD=0.05 mm)
ratio pixel-size/radius [a.u.]

IM2.P008
Reconstruction of the magnetisation in a hard magnetic needle using model-based electron holographic tomography

P. Diehle[1,2], J. Caron[2], A. Kovács[2], J. Ungermann[3], K. Žagar Soderžnik[4], M. Charilaou[5], R. Dunin-Borkowski[2]

[1]Fraunhofer-Institut für Mikrostruktur von Werkstoffen und Systemen IMWS, Werkstoffe und Bauelemente der Elektronik, Halle, Germany
[2]Forschungszentrum Jülich, Ernst Ruska-Centre for Microscopy and Spectroscopy with Electrons, Jülich, Germany
[3]Forschungszentrum Jülich, Institute for Energy and Climate Research, Jülich, Germany
[4]Jožef Stefan Institute, Department for Nanostructured Materials, Ljubljana, Slovenia
[5]University of Louisiana at Lafayette, Department of Physics, Lafayette, LA, United States

The development of an experimental technique that allows the three-dimensional (3D) magnetic state of a nanoscale object to be measured quantitatively is of great importance for fundamental and applied research in magnetism. Off-axis electron holography is a powerful technique that allows the phase shift of an electron wave that has passed through a specimen in the transmission electron microscope (TEM) to be recorded. The phase shift is, in turn sensitive to the in-plane component of the magnetic induction within and around the specimen projected in the electron beam direction. A combination of electron holography and conventional tomographic reconstruction has previously been applied to recover the 3D magnetic induction within and around materials (1, 2). Here, we use model-based iterative reconstruction (MBIR) to retrieve the 3D magnetization in a Nd-Fe-B needle from a tilt series of magnetic phase images recorded using electron holography (3).

A Nd-Fe-B needle was prepared using focused ion beam milling (Fig. 1a) and is examined in a dedicated 360° tomography holder. A 360° tilt series of off-axis electron holograms was recorded with a tilt increment of 5°. Linear geometric distortions originating from the projection system of the TEM were removed from each reconstructed phase image. In order to separate the magnetic and electrostatic (mean inner potential) contribution, each phase image was subtracted from a corresponding phase image recorded with the sample turned over to obtain a 180° tilt series of magnetic phase images and a corresponding 180° tilt series of mean inner potential phase images. The latter images were used to reconstruct the 3D morphology of the needle (Fig. 1b) using a conventional tomographic algorithm. This 3D shape was used as a mask to define the outer boundary of the magnetic moments that were recovered using the MBIR algorithm. A 3D magnetic buffer zone was also used to take account of contributions to the magnetic phase images from magnetic objects outside the field of view. The final reconstructed 3D magnetisation distribution (Fig. 2) comprises four magnetic domains, which are oriented in opposite directions orthogonal to the needle axis. These experimental findings are compared with micromagnetic simulations and a good agreement between experiment and theory is found.

References:

(1) A. Lubk, D. Wolf, P. Simon, C. Wang, S. Sturm and C. Felser. Appl. Phys. Lett., 2014, 105, 173110.

(2) D. Wolf, L. A. Rodriguez, A. Béché, E. Javon, L. Serrano, C. Magen, C. Gatel, A. Lubk, H. Lichte, S. Bals, G. Van Tendeloo, A. Fernández-Pacheco, J. M. De Teresa and E. Snoeck. Chem. Mat., 2015, 27, 6771-6778.

(3) M. Soderžnik, M. Korent, K. Žagar Soderžnik, M. Katter, K. Üstüner and S. Kobe. Acta Mater., 2016, 115, 278-284.

Fig. 1: a) Bright-field TEM image and b) reconstructed 3D morphology of the Nd-Fe-B needle-shaped specimen.

Fig. 2: Reconstructed 3D magnetisation distribution in the Nd-Fe-B needle-shaped specimen obtained by applying the MBIR algorithm to a dataset recorded using off-axis electron holographic tomography.

Fig. 1

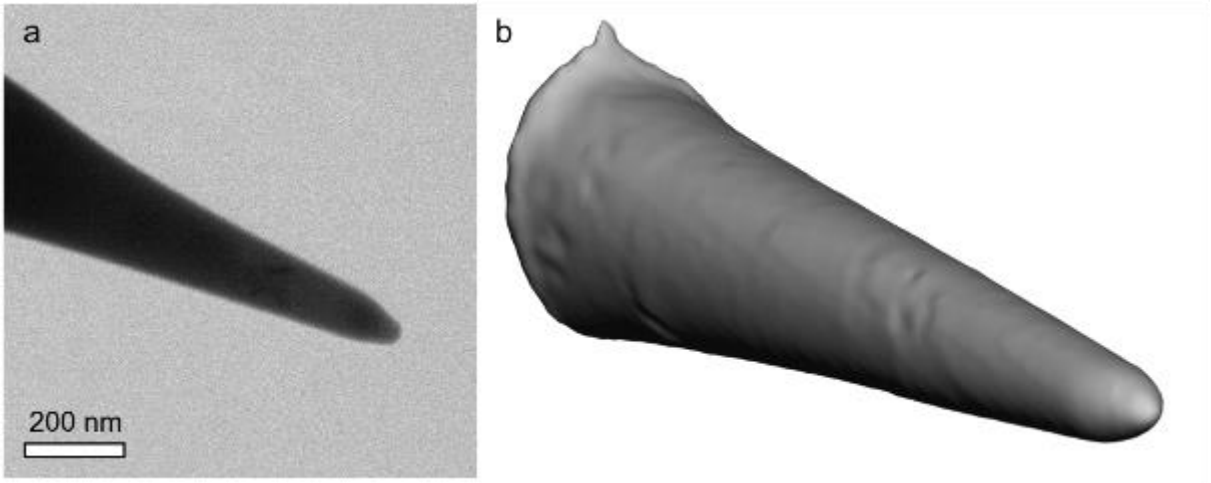

Fig. 2

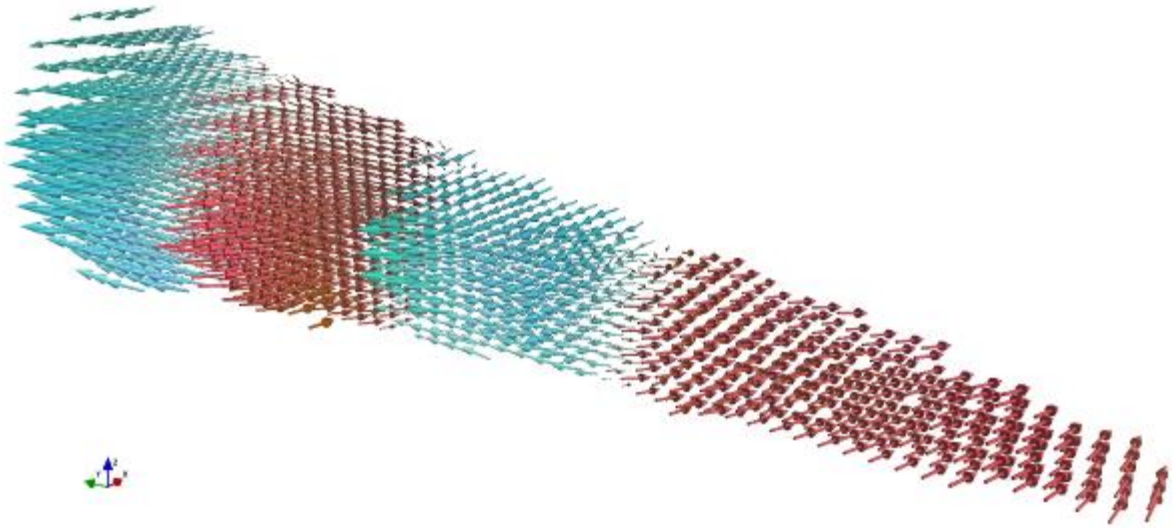

IM2.P010
Reducing the Influence of Electric Stray Fields on the Reference Wave in Biasing Electron Holography

R. Kraft[1], T. Wagner[1], E. Geer[1], D. Berger[2], I. Häusler[1], M. Lehmann[1]

[1]Technische Universität Berlin, Institut für Optik und Atomare Physik, Berlin, Germany
[2]Technische Universität Berlin, Zentraleinrichtung Elektronenmikroskopie (ZELMI), Berlin, Germany

Off-axis electron holography enables the measurement of the phase shift of an electron wave propagating through or nearby a specimen and hence enables the investigation of pure phase objects such as electric potentials (1). The reconstructed phase of the measured image wave results hereby from phase differences between object wave and reference wave. As a consequence, the measured phase does not give any direct information about the specimen itself, if the phase of the reference wave is unknown. Since TEM specimens need to be flat, an electrode geometry for biasing these specimens will always have a bad aspect ratio and, therefore, produce inhomogeneous electrical stray fields around the specimen. These stray fields may influence the reference wave (2,3). Therefore, a measurement depends strongly on the position of the biprism and the reference area, which reflects on reproducibility and stability of a measurement.

The investigated sample is a focused ion beam (FIB) prepared MEMS heating chip (DENSsolutions wildfire), on which the conducting path is separated to form the electrodes of a coplanar capacitor (Figure 1 left). For further investigations and comparison, additional finite element simulations are made (Figure 1 right) with ONELAB (4).

In order to reduce the influence of stray fields on the reference wave while remaining in an area close to the specimen, a reference window is cut into one electrode of the capacitor. Consequently, a closed loop on a conducting surface at a constant electric potential is created resulting in an nearly undisturbed area for the reference wave.

The feasibility of the reference window is tested by measuring the slopes of the projected potential distribution between the electrodes of the capacitor (object area) while the reference region is selected from different locations (reference area) in front of the electrodes and inside the reference window (Figure 2 left). The plotted slopes (Fig. 2 right) are normalized to the simulated slope in the object area. The simulation shows clearly that the reference wave taken from the window is flatter than in front of the capacitor, and the slope values are closer to the real slope in the capacitor. The measured values show the same behaviour. The difference between simulation and measured values can mainly be explained by the nitrite layer on the MEMS chip, which was not simulated. chip, which was not simulated.

In conclusion, it is shown that a window in an electrode provides better conditions for the reference wave. In addition to more accurate measurements, such a geometry also has advantages in terms of reproducibility and stability.

References:

(1) A.C. Twitchett et al., Physical Review Letters 88 (2002) 238-302.

(2) P. A. Midgley et al., Proceedings EUREM11 Volume 1, (1996) 416-417.

(3) T. Wagner et al., Proceedings EMC 2016, 729-730.

(4) C. Geuzaine et al., International Journal for Numerical Methods in Engineering 79, (2009) 1309-1331.

Fig. 1: SEM overview and FEM simulation (color displays the equipotential surfaces in the cross section through the electrodes and in 3-dimensional space).

Fig. 2: Projection of the simulated potential with the different reference areas and plot of the normalized phase slopes of the image wave (measured and simulated) in dependency of the distance between object wave and reference wave.

Fig. 1

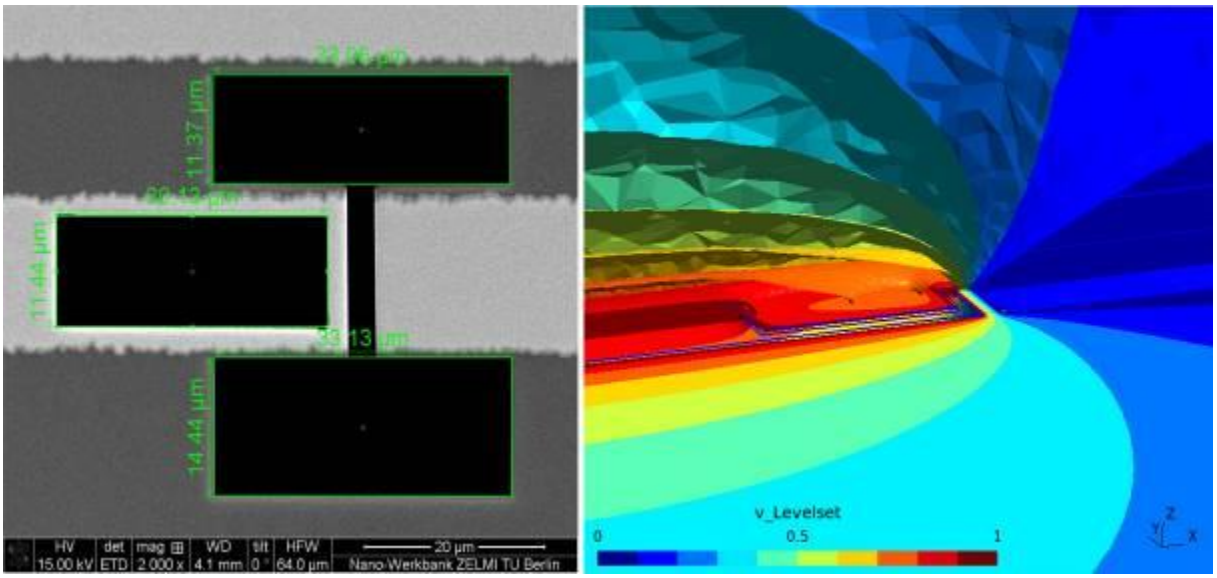
11.44 µm
33.13 µm
14.44 µm
HV 15.00 kV
det ETD
mag 2 000 x
WD 4.1 mm
tilt 0 °
HFW 64.0 µm
20 µm
Nano-Werkbank ZELMI TU Berlin
v_Levelset
0
0.5
1

Fig. 2

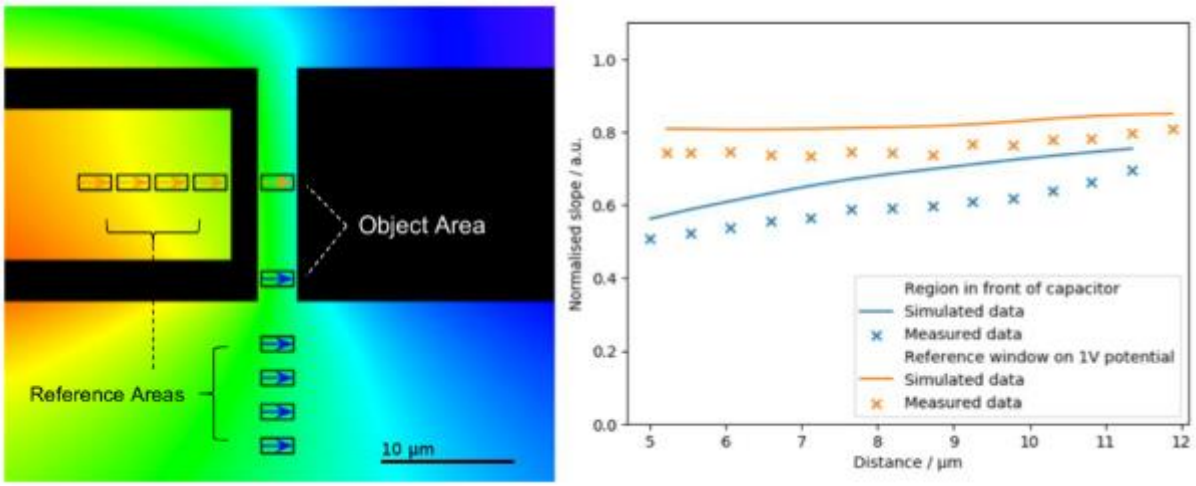
Object Area
Reference Areas
10 µm
Normalised slope / a.u.
Distance / µm
Region in front of capacitor
Simulated data
Measured data
Reference window on 1V potential
Simulated data
Measured data

IM2.P011
Direct Correction of Residual Symmetric Aberrations in Electron Holograms of Weak Phase Objects

F. Kern[1], M. Linck[2], D. Wolf[1], T. Niermann[3], H. Arora[4], N. Alem[5], A. Erbe[4], S. Gemming[4], A. Lubk[1]

[1]Leibniz Institute for Solid State and Materials Research Dresden , Institute for Solid State Research, Dresden, Germany
[2]CEOS GmbH, Heidelberg, Germany
[3]Technische Universität Berlin, Institut für Optik und Atomare Physik, Berlin, Germany
[4]Helmholtz-Zentrum Dresden Rossendorf, Dresden, Germany
[5]The Pennsylvania State University, Department of Materials Science and Engineering, University Park, United States

Thin TEM specimen are regarded as weak phase objects (WPOs), if the amplitude variation of the electron wave by the specimen can be neglected and the phase modulation is very small. Large classes of topical materials can be described in this approximation, such as most 2D materials, organic semiconductor materials or biological specimen. Due to the lack of amplitude (and hence intensity) contrast, conventional TEM (CTEM) investigations on WPOs are commonly performed under a certain defocus, which transfers part of the phase information to the recorded intensity. This intermixing contrast transfer from amplitude to phase and vice versa is commonly described by the phase contrast transfer function (PCTF), while the non-mixing contrast transfer for amplitude and phase is referred to as amplitude contrast transfer function (ACTF). Due to the transfer gap in the PCTF, the CTEM contrast transfer at low spatial frequencies is degraded in defocused images of WPOs (Fig. 1). By employing electron holography, however, both amplitude and phase of the electron wave can be reconstructed without a transfer gap. Having the whole wave information also enables the *a-posteriori* correction of geometric aberrations as it was already proposed in D. Gabor"s seminal paper from 1948 (1). The realization of his idea, however, remains challenging in the absence of additional knowledge about the sample, due to the lack of a criterion for a successful aberration correction.

Here we present a novel method for the *a-posteriori* correction of symmetric geometric aberrations in electron holograms, which analytically exploits the constant amplitude in images of WPOs and does not need any further knowledge about the object. The correction of residual aberrations results in a constant contrast transfer over a large band that only decreases at higher spatial frequencies due to incoherent aberrations (Fig. 1).

This technique is demonstrated on electron holograms of multilayered boron nitride (h-BN), acquired at the Cc-corrected TEAM 1 microscope (2), where it is facilitating quantitative atomic-resolution imaging (Fig. 2). These aberrations are partially set deliberately (e.g., defocus) to select a proper region of interest on the sample as they lead to transfer of phase information to the amplitude (Fig. 2a) but also to a damping of higher spatial frequencies in the reconstructed phase (Fig. 2b).

The corrected phase (Fig. 2d) exhibits atomic resolution in the multi-layered parts while preserving large range phase modulations stemming from the different projected potentials of different numbers of h-BN monolayers. The corrected amplitude (Fig. 2c) shows almost no amplitude variations proofing the validity of our approach.

The ease of use of the proposed methods facilitates a flexible application to a wide range of WPOs including dose sensitive ones, benefitting from the "dose-free" aberration correction.

References:

(1) D. Gabor, Nature 161 (1948), p. 777-778

(2) M. Linck et al., Microscopy and Microanalysis 19, p. 1222-1223.

Fig. 1: PCTF and ACTF as well as temporal and spatial envelope for typical high-resolution microscope parameters.

Fig. 2: Reconstructed phase (a) and amplitude (b) of h-BN multilayers. The amplitude contrast can be explained as transferred phase information in the weak phase object approximation. Amplitude (c) and phase (d) corrected with the presented method.

Fig. 1

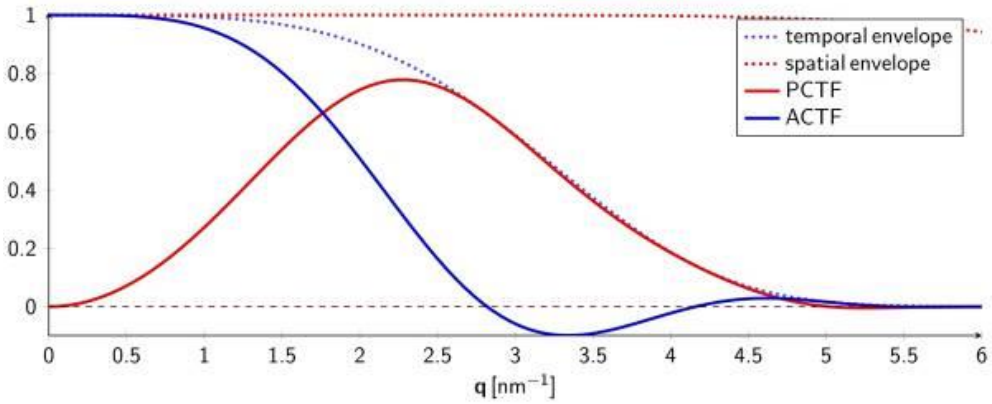
temporal envelope
spatial envelope
PCTF
ACTF
1
0.8
0.6
0.4
0.2
0
0
0.5
1
1.5
2
2.5
3
3.5
4
4.5
5
5.5
6
q [nm^{-1}]

Fig. 2

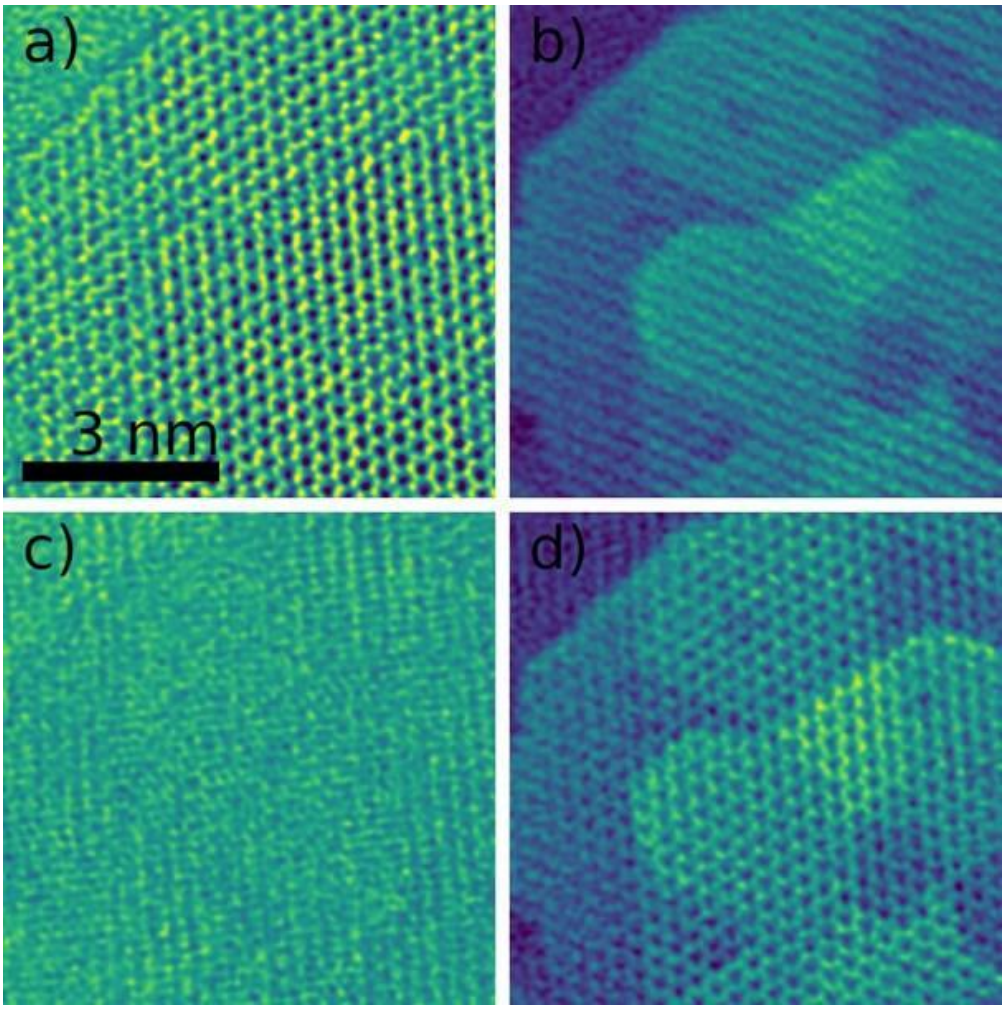
a)
3 nm
b)
c)
d)

IM2.P012
Electrostatic potential mapping of p-n junctions in homo- and hetero-structured nanowires by off-axis electron holography

E. M. Fiordaliso[1], N. Anttu[2], D. Lindgren[2,3], J. Svensson[2,3,4], M. Beleggia[1]

[1]DTU Nanolab, Lyngby, Denmark
[2]Aalto University, Department of Electronics and Nanoengineering, Aalto, Finland
[3]SolVoltaics AB, Lund, Sweden
[4]Lund University, Department of Nano Electronics, Lund, Sweden

Semiconductor nanowires (NWs) are key elements of nano-scaled electronic, optoelectronic and photovoltaic devices. Crucial to their fabrication is the ability to achieve desired dopant concentrations and distributions, and to control the electric fields at the homo/heterojunctions within complex NW structures. Doping can be assessed by various techniques (1) and off-axis electron holography (EH) in a TEM is one of the most powerful ones (2,3). EH allows to measure the spatially-resolved phase shift ort h electron wave crossing a specimen, caused by the electrostatic potential generated by active dopants. It provides the means to localize p-n junctions, measure built-in potentials and depletion layer widths, and to retrieve information on the doping distribution. We use EH to map the electrostatic potential across axial p-n junctions in GaAs/AlGaAs and InAs-GaSb nanowires, which are used for solar cell and transistor applications, respectively.

Figure 1 shows an illustration ort h GaAs/AlGaAs NW (a), the potential map extracted from the holographic phase image (b) and the potential profile measured along the NW (c). The p- and n-type doped regions ort h NW are seen as areas of darker (p-type) and brighter contrast (n-type). A potential difference of ~1V is measured across the junction, over a depletion region of ~300 nm. These results correlate well with complementary techniques such as CL, EBIC, and IV characterization.

Figure 2 (a) shows an illustration ort h InAs-GaSb NW heterostructure with a p-i-n junction. The potential map and the profile measured along the NW are shown in Figure 2 (b) and (c), respectively. An apparent potential difference of ~1.2V is measured across the junction, over a depletion region of ~60 nm. A maximum is measured at the n-side ort h interface, in the i-GaSb segment. This is possibly due to a strong diffraction contrast at the interface, since it is also visible in the amplitude image. The actual built-in potential can be estimated at around 0.8V by taking into account the difference between the mean inner potentials (~0.4 V) ort h two materials. This value correlates nicely with the expected band offset.

The NW junctions highlights several interesting aspects ort h performance of EH in semiconductor NWs. First, the junction is on top of a conducting mambrane, but otherwise floating. No current can flow across the device, which is in open-circuit conditions. In this scenario, the expected built-in potential could be affected by the finite capacitance ort h NW. Second, the passivation shell makes the NW surface equipotential. Finally, the thickness profile ort h NW creates further complications in converting the phase image into potential map, especially for two sides of a junction made of different materials. These uncertainties can be assessed through modelling. A simple electrostatic model is being developed ort he purpose of assisting the interpretation of experimental results and will be presented at the conference.

References:

(1) Wallentin, J. et al. *J. Mater. Res.* 26 (2011), 2142.

(2) Tonomura A. *Springer, Berlin, Heidelberg* 70 (1999).

(3) Dastjerdi, M. H. T., et.al. *Nano letters* 17(10) (2017), 5875.

Fig. 1: (a) Illustration of a GaAs/AlGaAs NW with an axial p-n junction. (b) Potential map and (c) corresponding potential profile along the NW.

Fig. 2: (a) Illustration of a InAs-GaSb NW with an axial p-i-n junction. (b) Potential map and (c) corresponding potential profile along the NW.

Fig. 1

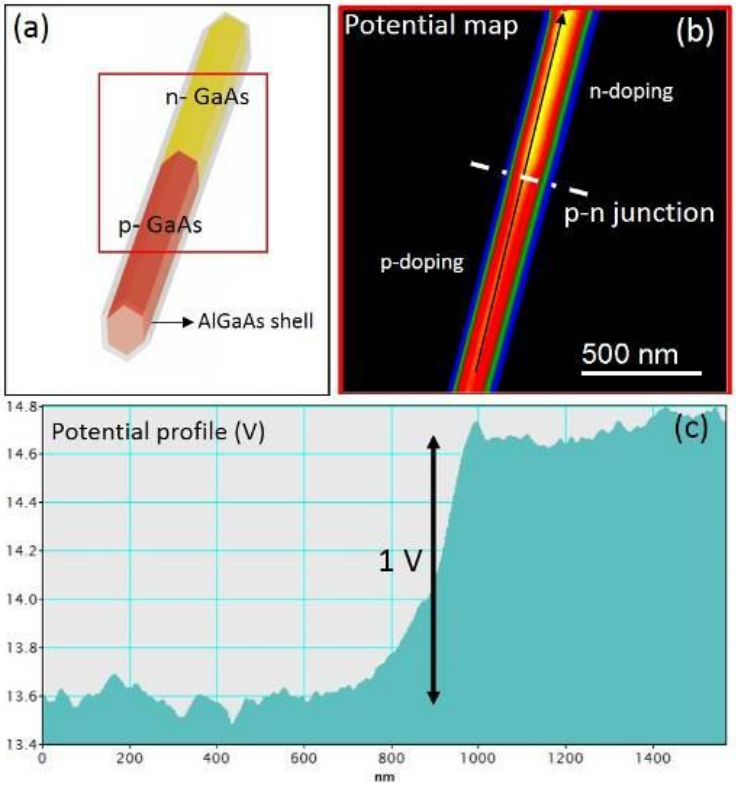
(a)
n- GaAs
p- GaAs
AlGaAs shell
Potential map
(b)
n-doping
p-n junction
p-doping
500 nm
Potential profile (V)
(c)
1 V
14.8
14.6
14.4
14.2
14.0
13.8
13.6
13.4
0
200
400
600
800
1000
1200
1400
nm

Fig. 2

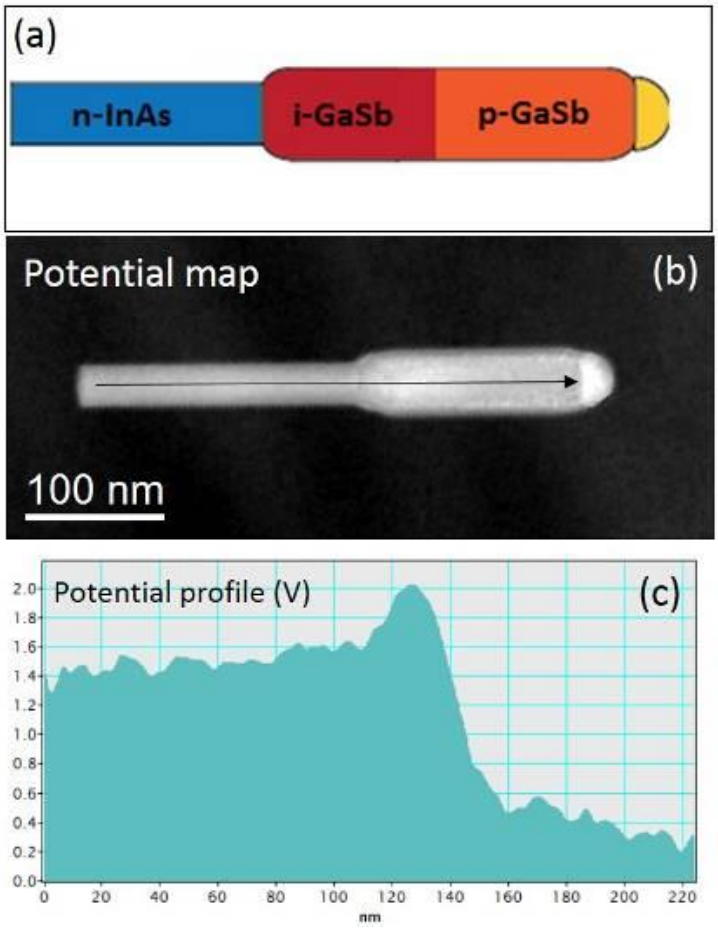
(a)
n-InAs
i-GaSb
p-GaSb
Potential map
(b)
100 nm
Potential profile (V)
(c)
2.0
1.8
1.6
1.4
1.2
1.0
0.8
0.6
0.4
0.2
0.0
0
20
40
60
80
100
120
140
160
180
200
220
nm

IM2.P013
The role of spatial coherence for the creation of and imaging with atom size electron vortex beams

D. Pohl[1,2], S. Löffler[3], S. Schneider[2], P. Tiemeijer[4], S. Lazar[4], K. Nielsch[2], B. Rellinghaus[1]

[1]TU Dresden (DCN), Dresden, Germany
[2]IFW Dresden, Dresden, Germany
[3]TU Wien, University Service Centre for Transmission Electron Microscopy, Wien, Austria
[4]Thermo Fisher Scientific, Eindhoven, Netherlands

Recently discovered electron vortex beams, which carry quantized orbital angular momenta (OAM) L, promise to reveal magnetic signals (1). Since electron beams can be easily focused down to sub-nanometer diameters, this novel technique promises the possibility to quantitatively determine local magnetic properties with unrivalled lateral resolution. To generate the spiralling wave front of an electron vortex beam with an azimuthally growing phase shift of up to 2π and a phase singularity in its axial centre, specially designed apertures are needed (2).

In order to produce single electron vortex beams, we recently developed a method which allows to generate user-defined OAM beams (3). Although today, atom size electron vortex beams can be readily generated and atomically resolved HRSTEM and EELS data can be acquired with OAM-selected EVBs, the application as a probe for local measurements of the electron energy loss magnetic chiral dichroism (EMCD) suffers from a poor S/N ratio.

The monochromator provides the flexibility to tune the degree of coherence on the vortex aperture by allowing to continuously vary the gun lens (GL) excitation. In this work we have investigated the influence of the gun lens excitation on the coherence of the electron vortex beam. As a measure of this coherence, the central intensity dip of the imaged probe is determined (see fig1) (5). Images of the vortex probe have been acquired utilizing two types of electron guns: (i) a standard Shottky FEG (SFEG) and (ii) a so-called high-brightness gun (XFEG). Normalized rotationally averaged profiles of the images are used to analyse the dependency of the EVB quality on the coherence (gun lens excitation).

Both electron guns show an improvement of the spatial coherence with increasing gun lens excitation, measured by the central intensity dip in the |L| = 1 ħ EVB. For the XFEG operated at 200kV, a central intensity dip of LDip/Imax = 0.3 can be reached. The improved coherence is found to result in an enhanced visibility of the donut-like intensity distribution in the intensity of the atomic columns. Adding additional phase shifts to the electron probe, e.g. by 2-fold astigmatism results in a splitting of the ring intensity into two side-lobes, which is directly visible in the HR-STEM image (see fig. 2).

EVBs generated from fully coherent primary beams may be the missing piece to the puzzle of substantially improving quantitative magnetic signals as obtained from individual atomic columns. Additionally, using aberrations to modify the EVB might be useful for advanced orbital or plasmon mapping.

References:

(1) J. Verbeeck et al., Nature 467 (2010), p. 301-304

(2) J. Verbeeck et al., Ultramicroscopy 113 (2012), p. 83-87

(3) D. Pohl et al., Sci. Rep. 7 (2017) 934.

(4) P. Schattschneider et al., Ultramicroscopy 111 (2011), p. 1461-1468

(5) P. Schattschneider et al., Ultramicroscopy 115 (2012), p. 21-25

Fig. 1: Images of the EVB for different gun lens excitations using a XFEG @ 200kV. Insets show normalized and rotationally averaged intensity profiles.

Fig. 2: HR-STEM image of $BaFe_{11}TiO_{19}$ [100] using EVB with L=+1 ħ with and without 2-fold astigmatism. The donut-like intensity distribution of individual atomic columns is seen from dips in the intensity profile. The effect becomes even more evident from the occurrence of a splitting into two separate arcs upon introducing some two-fold astigmatism.

Fig. 1

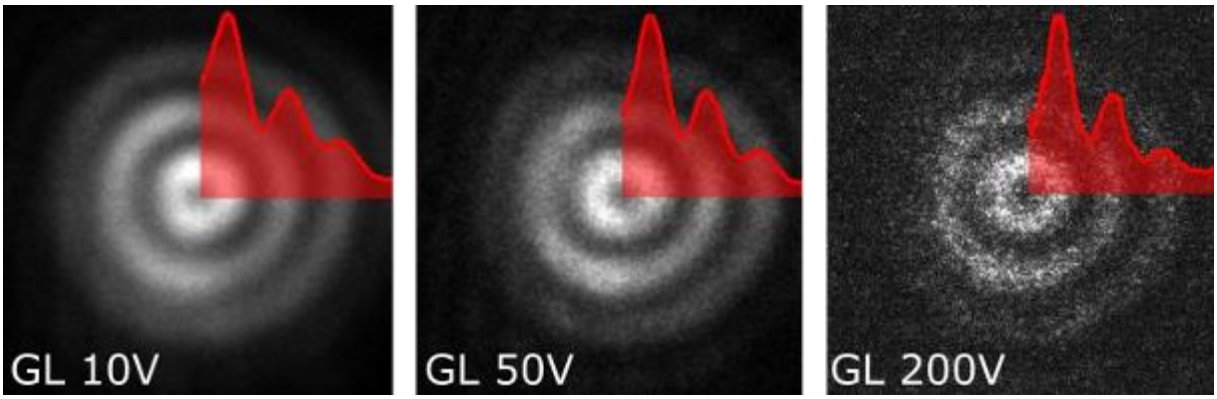

Fig. 2

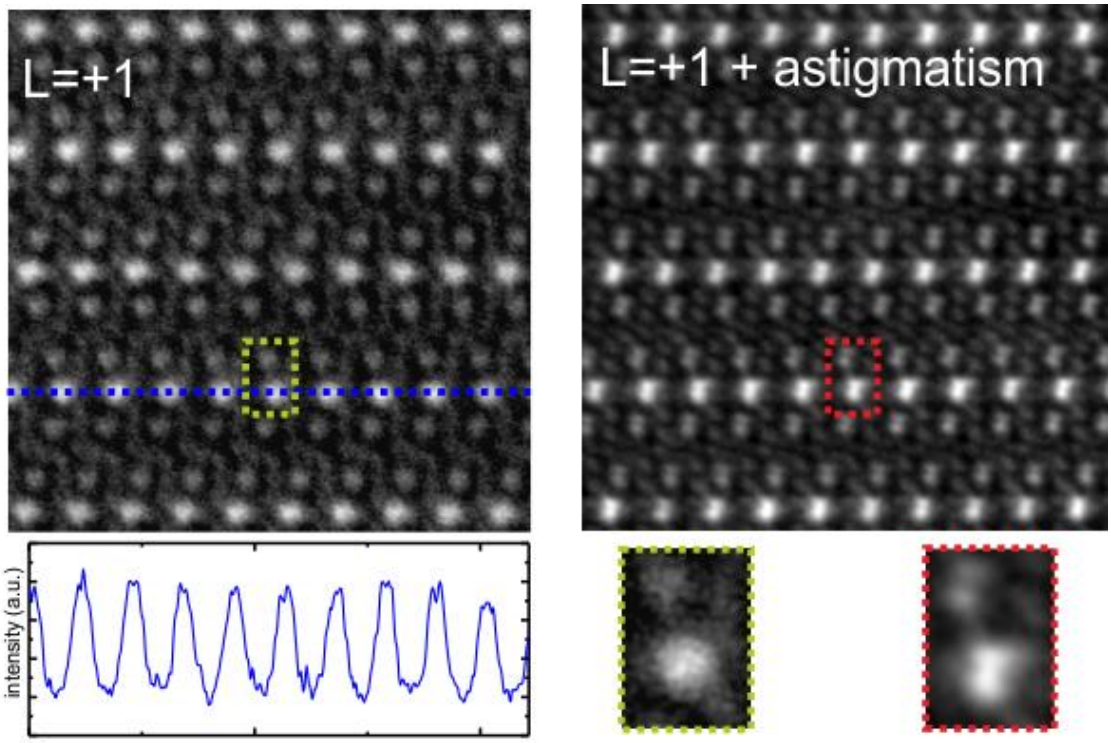

IM2.P014
Diagnostic assessment of model-based iterative reconstruction of magnetisation distributions from electron-optical phase images recorded using off-axis electron holography

J. Caron[1], P. Diehle[1], J. Ungermann[2], A. Kovács[1], M. Riese[2], R. Dunin-Borkowski[1]

[1]Forschungszentrum Jülich GmbH, Ernst Ruska-Centre for Microscopy and Spectroscopy with Electrons, Jülich, Germany
[2]Forschungszentrum Jülich GmbH, IEK-7, Jülich, Germany

Nanoscale magnetic materials play an important role in modern technology, *e.g.*, in data storage and catalysis. However, characterization of the magnetisation distribution in a sample with nm spatial resolution is a difficult task. The transmission electron microscopy technique of off-axis electron holography enables the recording of the phase shift of an electron wave that has passed through an electron-transparent sample. This phase shift encodes information about electromagnetic potentials within and around the sample (1).

For the reconstruction of magnetisation distributions from electron-optical phase images recorded using off-axis electron holography, either in projection or in three dimensions, we have developed an iterative model-based inversion algorithm and applied it successfully to the characterization of different magnetic structures (2, 3). This algorithm makes use of *a priori* information about the sample, *e.g.*, the positions of magnetised regions, while minimising exchange energy by means of Tikhonov regularisation of first order. The strength of the regularisation is controlled by a parameter λ, which is chosen before reconstruction.

For a full analysis, diagnostic measures can be introduced to assess the quality of the retrieved magnetisation and the influence of a variety of reconstruction parameters.

In particular, an L-curve analysis (4) can be used as a heuristic method to find the optimal regularisation strength to achieve an optimal trade-off between compliance with the experimental measurements (which always contain recording noise and can be affected by artefacts) and with the specified *a priori* information.

The influence of the chosen regularisation strength on the reconstructed magnetisation distribution can then be assessed by means of optimal estimation linear diagnostics (5) which provide a "gain matrix" that describes the propagation of phase noise to the reconstructed magnetisation, as well as an "averaging kernel", which provides a measure of the resolution of the reconstruction.

Approaches that can be used to tackle other challenges, including the presence of magnetised regions outside of the field of view, phase ramps, phase offsets and errors in the determination of the edges of the magnetised regions will be discussed.

References:

(1) Y. Aharonov and D. Bohm, Physical Review, vol. 115, no. 3, pp. 485–491, 1959.

(2) D. Song, Z.-A. Li, J. Caron, A. Kovács, H. Tian, C. Jin, H. Du, M. Tian, J. Li, J. Zhu, and R. E. Dunin-Borkowski, Physical Review Letters, vol. 120, no. 16, p. 167204, 2018.

(3) Z.-A. Li, F. Zheng, A. H. Tavabi, J. Caron, C. Jin, H. Du, A. Kovács, M. Tian, M. Farle and R. E. Dunin-Borkowski, Nano Letters, vol. 17, no. 3, pp. 1395–1401, 2017.

(4) P. C. Hansen, SIAM Review, vol. 34, no. 4, pp. 561–580, 1992.

(5) C. D. Rodgers, ser. Series on Atmospheric, Oceanic and Planetary Physics. Singapore and River Edge: World Scientific, vol. 2, 2000.

Fig. 1

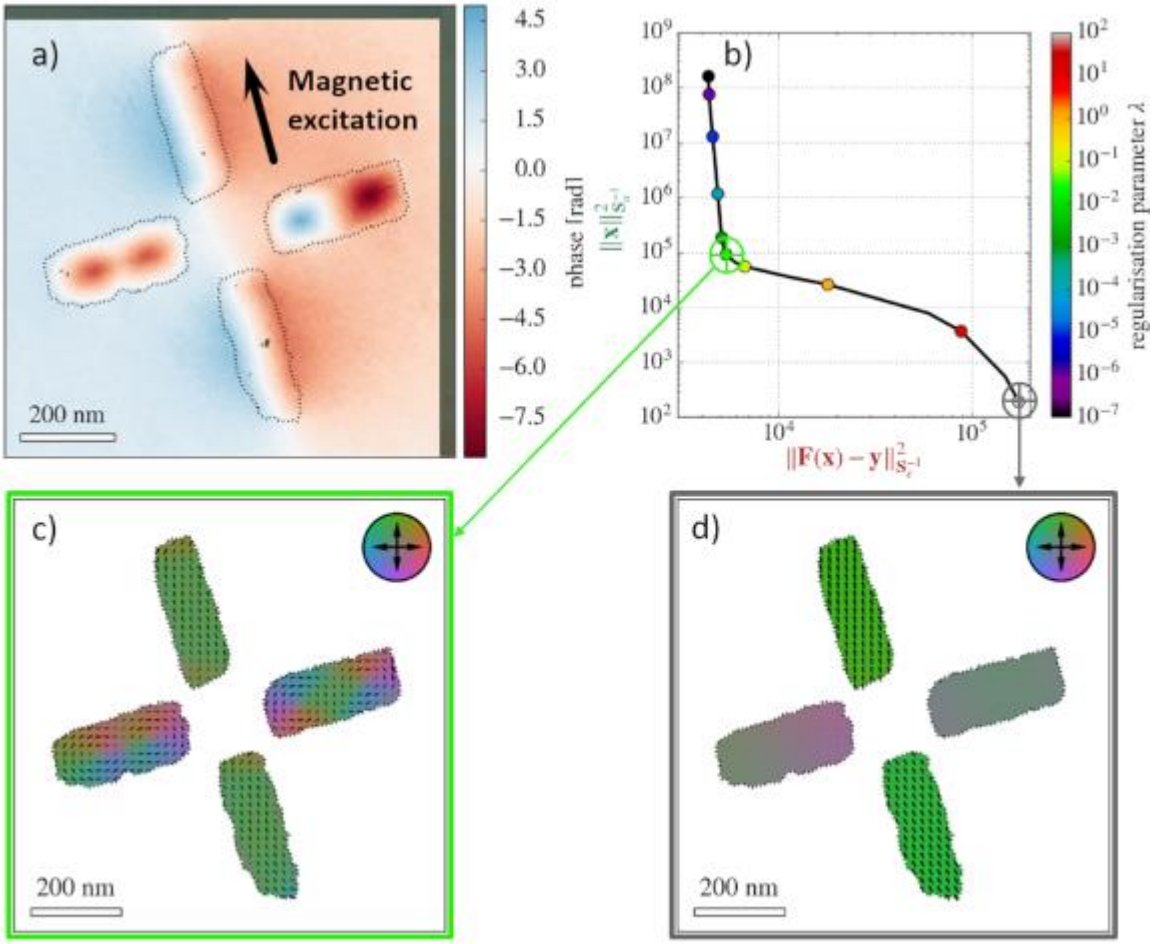

Figure 1: a) Magnetic phase image of a lithographic Co pattern. **b)** L-curve plot analysing the trade-off between compliance with measurements (abscissa) and *a priori* information (ordinate). **c)** Reconstruction for an optimal regularisation parameter. **d)** Reconstruction for overtuned regularisation, with features smoothed away.

IM2.P016
Model-based magnetization retrieval from holographic phase images

F. Röder[1], K. Vogel[2], D. Wolf[3], O. Hellwig[4,5], S. H. Wee[5], S. Wicht[6], B. Rellinghaus[6,7]

[1]Fakultät Physik / Technische Universität Dresden, Dresden, Germany
[2]Institute for Resource Ecology / Helmhotz-Zentrum Dresden-Rossendorf, Dresden, Germany
[3]Institute for Solid State Research / IFW Dresden, Dresden, Germany
[4]Institut für Physik / Technische Universität Chemnitz, AG Magnetische Funktionsmaterialien, Chemnitz, Germany
[5]HGST / a Western Digital Company, San Jose, United States
[6]Institute for Metallic Materials / IFW Dresden, Dresden, Germany
[7]Dresden Center for Nanoanalysis (DCN) / Technische Universität Dresden, Dresden, Germany

The phase shift of the electron wave as reconstructed by Electron Holography is a well established measure for quantitative mapping of nano-scale electric and magnetic fields (1). However, its direct interpretation in terms of solid state properties is often difficult and requires special assumptions.

In this work, we concentrate on magnetic nanostructures, which can possess different magnetization configurations due to individual degrees of freedom and coupling mechanisms among their constituents (2,3). A direct measurement of these individual magnetization states is not possible in general, because the phase shift is proportional to the projected magnetic flux density of magnetic objects, which includes both the magnetization and the stray fields. We show that a prevailing presence of stray fields prohibits a direct interpretation of the phase in terms of magnetization modulus and direction.

We therefore present a model-based approach for retrieving the magnetization by considering the projected shape of the nanostructure and assuming a homogeneous magnetization therein (4). This bears on a decomposition of an arbitrary magnetic nanostructure into independent components of individual magnetization (Fig.2). For each component, the phase shift due to magnetization and fringing fields is then computed as a function of geometry, thickness distribution and its magnetization vector. Considering the analytic solution for the phase shift of a homogeneously magnetized cuboid (Fig.3), we adopt the geometry of each component by parting the respective thickness distributions into a set of equally magnetized cuboids with suitable dimensions. The sum of the phase shifts of all cuboids returns a magnetization model for a certain nanostructure component as a function of two free parameters: the modulus and the direction of the magnetization vector. Thus, each component can be treated as a magnetically homogeneous entity with varying magnetization vector. The sum over the phase images of all components yields a calculated phase image as a function of the magnetization vectors of all independent components. This allows to directly fit these vectors to the experimental phase image by determining the least square root. We apply this method to FePt nano-islands epitaxially grown on a $SrTiO_3$ substrate. The result of this approach indicates an inclination of the magnetization direction of these islands relative to the structural easy magnetic (001) axis. By means of this real-world example, we discuss prospects and limits of the approach.

References:

(1) H. Lichte et al., Rep. Prog. Phys. 71 (2008) 016102.

(2) R. E. Dunin-Borkowski, et al., Mic. Res. Tech. 64 (2004) 390402.

(3) M. Varón, et al., Sci. Rep. 3 (2013) 1234.

(4) F. Röder, et al., Ultramic. 176 (2017) 177.

Fig.1: a) Electron holographic set-up. b) Hologram of FePt nano-islands epitaxially grown on $SrTiO_3$. c) Fourier transformation and low-pass filtering of the upper sideband. d) Reconstructed amplitude. e) Reconstructed phase.

Fig. 2: Scheme of the decomposition of a magnetic nanostructure into individual components of equal magnetization modulus (M_i) and direction (α_i). Each component c is further parted into a set of n_c cuboids.

Fig. 3: Analytic solution of the phase shift for homogeneously magnetized cuboids of different shapes and with the identical magnetization vector (m_0M=1T, thickness 25nm). The isoline spacing is 0.05rad.

Fig. 1

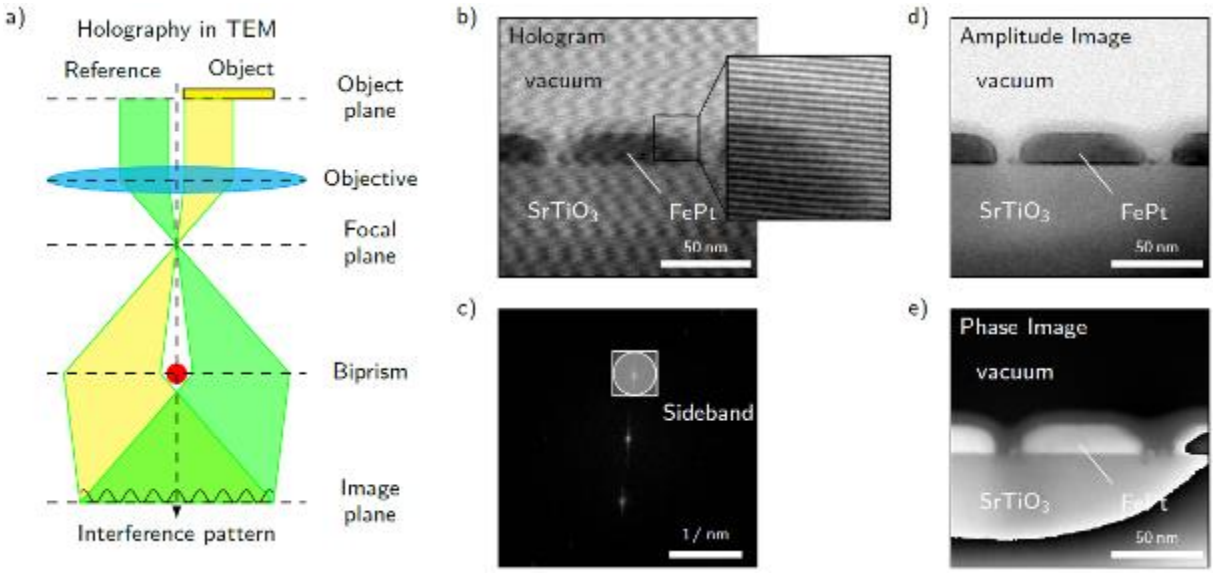

Fig. 2

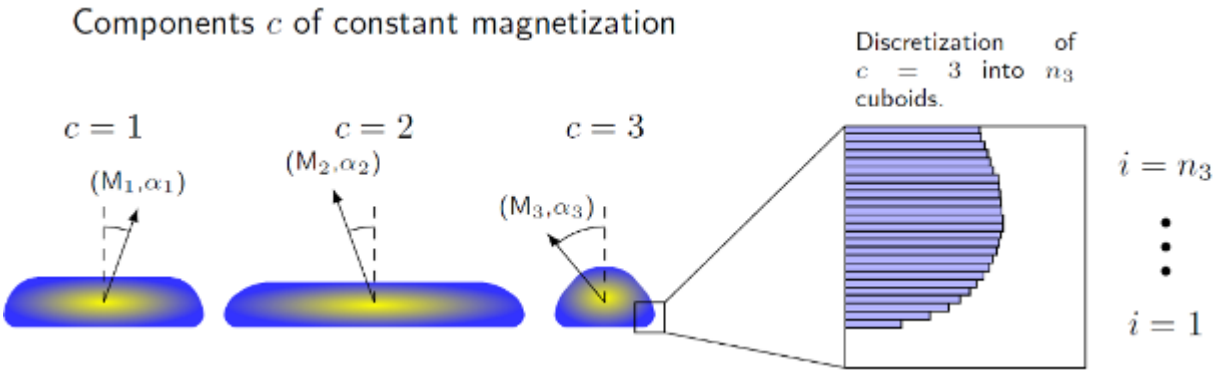

Fig. 3

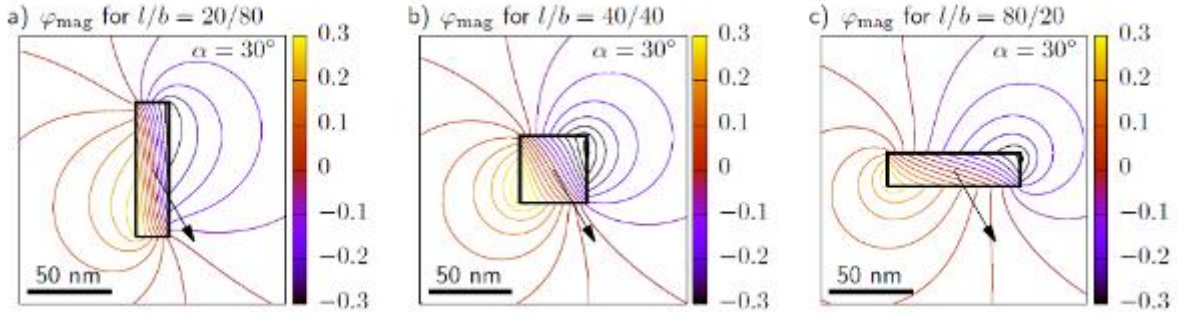

IM2.P017
Gradual Zernike phase plates for phase contrast imaging with reduced fringing artifacts in transmission electron microscopy

M. Obermair[1], S. Hettler[2], D. Gerthsen[1]

[1]Karlsruhe Institute of Technology, Laboratory for Electron Microscopy, Karlsruhe, Germany
[2]Universidad de Zaragoza, Instituto de Nanociencia de Aragón, Zaragoza, Spain

Organic objects show weak contrast in transmission electron microscopy (TEM) images. Physical phase plates enable the generation of phase contrast without the need of a strong defocus by inducing a relative phase shift between scattered and unscattered electrons in the back focal plane (BFP) of the objective lens. The Zernike phase plate (ZPP) (1) exploits the mean inner potential of a thin amorphous carbon (aC) film to shift the phase of the scattered electrons, while the unscattered electrons propagate through a structured hole and remain unaffected. The optimal relative phase shift of π/2 is tuned by the thickness of the film. However, rapid aging of the aC film and fringing artifacts induced by the abrupt onset of the phase shift at the edge of the ZPP hole limit the application possibilities. While aging is reduced by heating (2) or the use of alternative materials (3), the fringing may be computationally corrected only to a limited degree (4). Preliminary simulations showed, that the intensity of the fringing artifacts around the object in a ZPP TEM image can be significantly reduced by replacing the abrupt thickness onset at the edge of the ZPP hole with a smooth thickness gradient. The thickness gradient results in a smooth phase shifting profile. Within this work, gradual ZPPs were fabricated to investigate their impact on the formation of fringing artifacts in phase-plate TEM images.

A 24 nm aC film was deposited by physical vapor deposition using a freshly cleaved mica sheet as a substrate. The aC film was floated off the mica substrate on a distilled water surface and placed on a gold grid. Standard and gradual ZPP holes were prepared in the different meshes of the grid using a focused ion beam. The dimensions of the ZPP holes are 750 nm and 1 µm respectively. The gradual ZPPs have a concentric thickness gradient around the holes in the range from 750 nm to 1 µm and 1 µm to 3 µm respectively. The ZPP were implemented in the objective lens BFP of a Philips CM200 FEG/ST and heated to 150°C. As a test sample, bundles of carbon nanotubes (CNTs) are dispersed on a holey aC film, so that free-standing CNTs can be investigated in vacuum regions.

Fig. 1a shows the application of a standard ZPP (1 µm) without thickness gradient to the CNTs sample. The image shows intense equidistant fringes around the bundles of CNTs. The periodicity of ~ 8 nm is consistent with the cut-on frequency of 0.12 nm^{-1} that corresponds to the 1 µm ZPP hole. Fig. 1b shows an image of the same sample region acquired with a gradual ZPP (1 µm / 3 µm). The intensity of the fringes around the object is significantly reduced.

Fringing artifacts caused by the sharp edge of a ZPP hole can be considered as a large obstacle to image interpretability of phase contrast images. Using a gradual ZPP with a thoroughly considered hole diameter and thickness gradient can relieve this problem and fringing artifacts are substantially reduced (5).

References:

(1) R Danev, K Nagayama, Ultramicroscopy 88 (2001), 243-252.

(2) R Danev *et al*, Ultramicroscopy 109 (2009), 312-325.

(3) M Dries *et al*, Ultramicroscopy 189 (2018), 39-45.

(4) R Danev, K Nagayama, Ultramicroscopy 111 (2011) 1305–1315.

Funding by Deutsche Forschungsgemeinschaft (DFG) is acknowledged.

Fig. 1

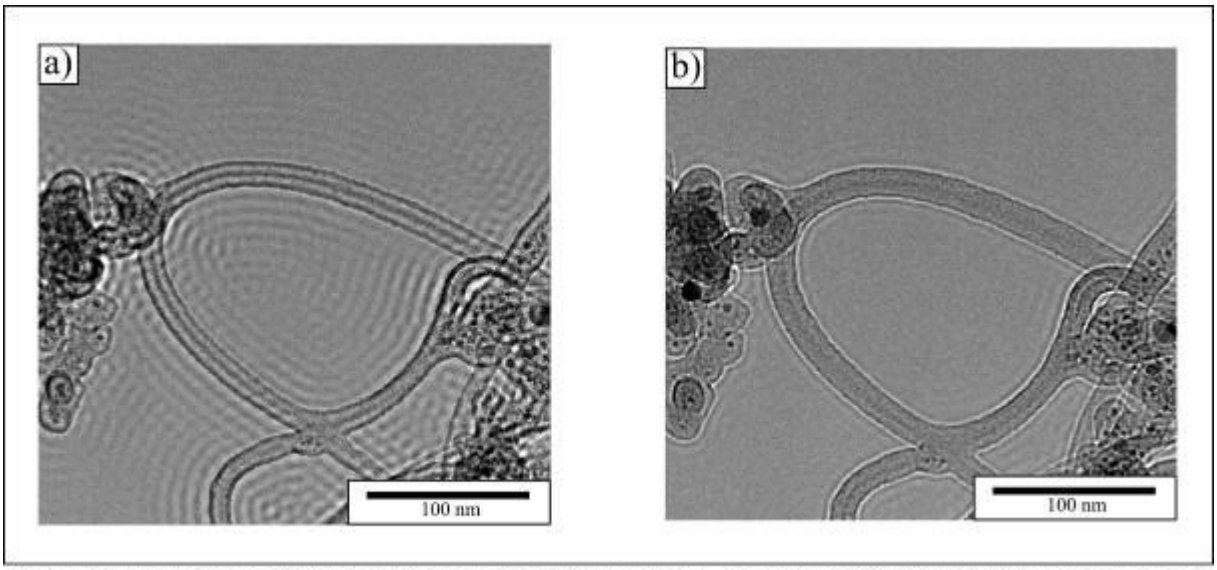

Fig. 1: Close to focus ZPP TEM images of a CNTs sample acquired with (a) a ZPP (1 μm hole) and (b) a gradual ZPP (1 μm) with a thickness gradient in the range of 1 μm / 3 μm.

IM2.P018
Cryo-transmission electron microscopy with Zach phase plates in experiment and simulation

M. Obermair[1], S. Hettler[2], C. Hsieh[3], M. Dries[1], M. Marko[3], D. Gerthsen[1]

[1]Karlsruhe Institute of Technology, Laboratory for Electron Microscopy, Karlsruhe, Germany
[2]Universidad de Zaragoza, Instituto de Nanociencia de Aragón, Zaragoza, Spain
[3]New York State Department of Health, Wadsworth Center, Albany NY, United States

Phase plates (PPs) are promising devices to enhance the weak contrast of life-science objects in transmission electron microscopy (TEM). PPs are implemented in the back focal plane (BFP) of the objective lens and induce a relative phase shift between the scattered and unscattered electrons, thus strongly enhancing phase contrast. Among numerous PP concepts (1), the electrostatic Zach PP (2,3) consists of a single rod carrying an isolated and shielded open gold electrode. The formation of a strongly localized electrostatic potential at the tip of the electrode is used to impose a tunable voltage-dependent phase shift on the unscattered electrons. However, undesirable artifacts caused by the phase shifting profile of the inhomogeneous electrostatic potential and the blocking of electrons by the rod exacerbate the interpretability of Zach PP TEM images. Within this work, image simulations are used to substantiate the understanding of artifact formation in experimental Zach PP TEM images.

A Zach PP is implemented in the magnified BFP of a JEOL JEM 3200FSC/PP. Ice embedded T4 bacteriophages (T4s) are used as a test sample. For the image simulations, a simplified wave function of a T4 as a pure phase object is modelled. Fig. 1a shows the modelled wave function of two perpendicular oriented T4s with a maximal phase shift of 0.25 π compared to a noisy background with a phase shift of 0.04 π that represents amorphous ice. The phase shifting profile of the Zach PP (Fig. 1b) is determined by simulating and integrating the electrostatic potential of the open electrode with finite element method.

Experimental and simulated Zach PP TEM images of a T4 are compared in Fig. 2. Fig. 2a shows a close to focus Zach PP TEM image of a T4 with a phase shift of 0 π. The contrast of the experimental T4 image is darker compared to the simulated T4 image in Fig. 2c which could be attributed to amplitude contrast of the T4 not considered in the simulation. Applying a voltage of -2 V delivers an optimal phase shift of -0.5 π (Fig. 2b) and strongly enhances the contrast of the T4. The observed contrast in experimental and simulated image (Fig. 2d) are in qualitative agreement. The contrast of the T4 is dependent on its orientation to the PP rod resulting from the inhomogeneous potential and the obstruction of electrons from the rod. Remaining differences between experiment and simulation may be linked to, e.g., additional phase shift stemming from charging of the rod.

Image artefacts in experimental Zach PP images of T4s agree qualitatively with simulated images of a reasonable modelled wave function of T4s. Arbitrary phase shifting profiles can be configured to simulate various PP types and extend the understanding of artifacts in PP TEM. (4)

References:

(1) R M Glaeser, Rev. Sci. Instrum. 84 (2013), 111101.

(2) S Hettler *et al*, Microsc Microanal 18 (2012), 1010-1015.

(3) N Frindt *et al*, Microsc Microanal 20 (2014), 175-183.

Funding by Deutsche Forschungsgemeinschaft (DFG) is acknowledged.

Fig. 1

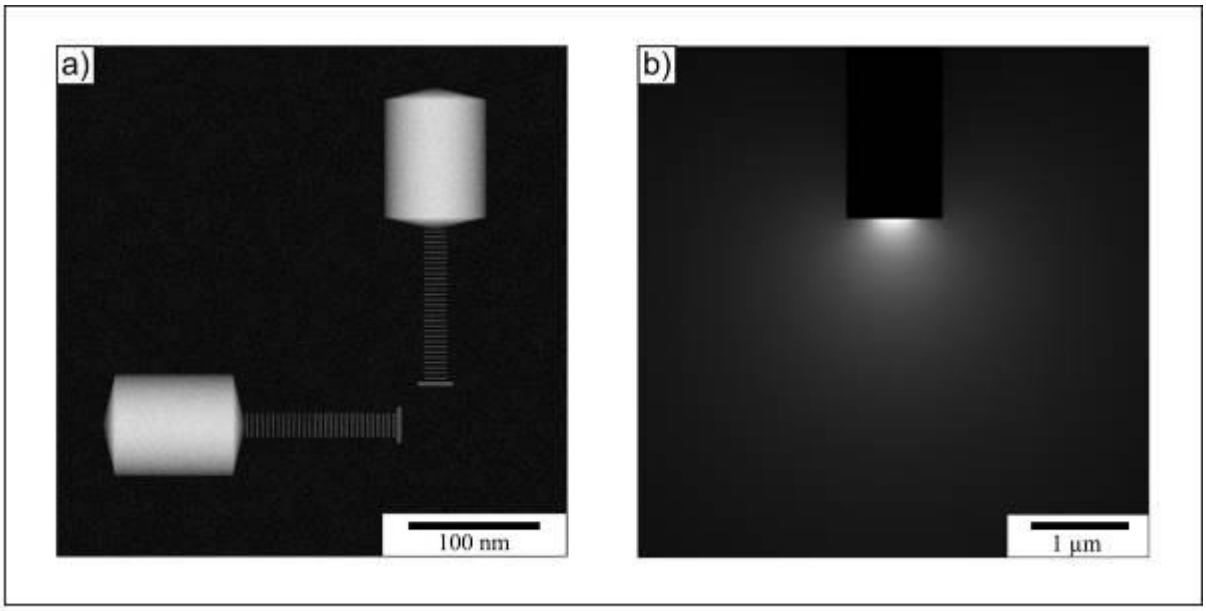

Fig. 1: (a) Wave function of two perpendicularly oriented T4s with a maximal phase shift of 0.25 π (white) and a noisy background with a maximal phase shift of 0.04 π (black). (b) Inhomogeneous phase shifting potential of the Zach PP.

Fig. 2

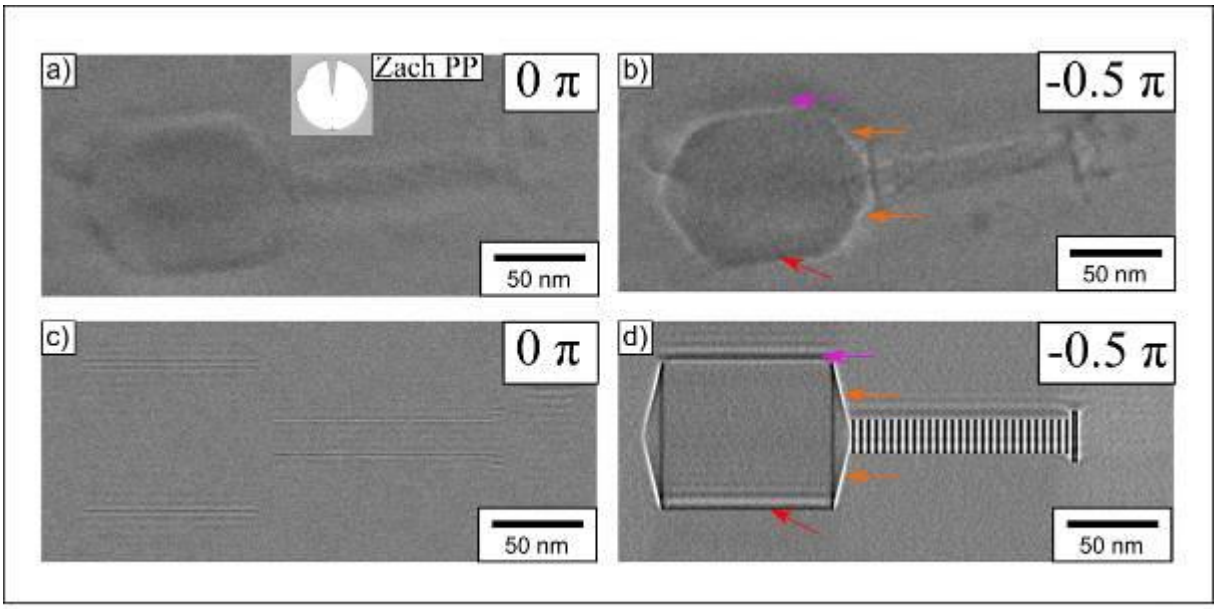

Fig. 2: Zach PP TEM images in experiment and simulation. Experimental images of a T4 with a phase shift of (a) 0 π and (b) -0.5 π. Simulated images of a T4 with a phase shift of (c) 0 π and (d) -0.5 π.

IM2.P019
TEM Imaging with Hollow-Cone Bright-Field Illumination at Low Voltages

Z. Lee[1], Y. Li[1], J. Biskupek[1], H. Rose[1], U. Kaiser[1]

[1]University of Ulm, Electron Microscopy Group of Materials Science, Ulm, Germany

Hollow-cone bright-field (HC-BF) illumination applied in transmission electron microscopy (TEM) is a phase-imaging method conjugate to the scanning transmission electron microscopy (STEM) by using a ring detector (1). Compared with parallel illumination applied in TEM, HC-BF illumination can improve the point resolution about 30%. However, in order to employ this method, some requirements need to be fulfilled. Firstly, it is necessary to eliminate or largely suppress the chromatic aberration of the microscope, in order to improve the information limit of the microscope. Secondly, the phase plate needs to be engineered in such a way that the average phase shift between the scattered wave and the tilted incident wave is the optimum (π/2 for weak phase objects).

With the help of Cc/Cs-correction within the SALVE instrument, the resolution of sub-Angstrom has been achieved for HRTEM at 40kV (2-4). By using the HC-BF illumination instead of parallel illumination, sub-Angstrom resolution will be reachable at 30kV. Figure 1 shows HRTEM images simulated for 2H-SiC imaged by using parallel illumination and HC-BF illumination in a Cc/Cs-corrected SALVE at 30kV. As shown in the contrast transfer function (CTF) plots in Figure 1, the point resolution is around 1.03Å (0.97Å^{-1}) for parallel illumination and 0.75Å (1.34Å^{-1}) for HC-BF illumination. The S-C bond is 0.93Å in [100] projection. In this case, the Si-C bond is only able to be resolved with a HC-BF illumination.

HC-BF TEM experiments are performed with the Cc/Cs-corrected SALVE instrument aimed at determination of the experimental conditions for demonstrating the predicted resolution increase.

References:

(1) H. Rose, Ultramicroscopy 2 (1977) 251-267.

(2) U. Kaiser et al., Ultramicroscopy 111 (2011) 1239.

(3) M. Linck et al., Phys. Rev. Lett., 117 (2016) 076101.

(4) F. Börrnert and U. Kaiser Physical Review A 98 (2)(2018) 023861-1–10.

Fig. 1: Simulated 30kV Cc/Cs-corrected TEM images of SiC-2H (left) for parallel illumination (middle) and hollow-cone bright-field illumination (right). The corresponding CTF plot is displayed beneath each image. Hollow-cone illumination results in an improved transfer of the low and high spatial frequencies. The simulations are performed by assuming C5=2mm, a residual focus spread of 5Å and an image spread of 25pm. Scale-bar: 0.2nm.

Fig. 1

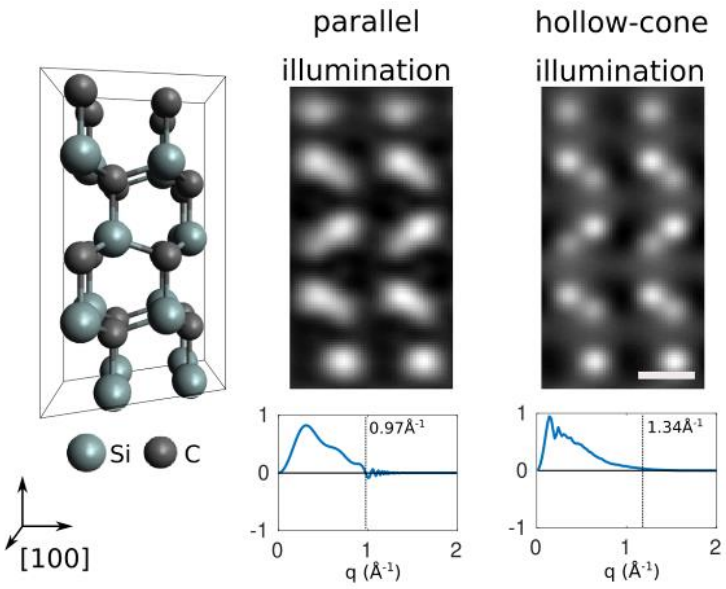

IM2.P020
Towards Tomographic Reconstruction of 3D Electrostatic Potential Distribution Measured by Electron Holography

E. Geer[1], T. Wagner[1], R. Kraft[1], D. Berger[2], I. Häusler[1], M. Lehmann[1]

[1]Technische Universität Berlin, Institut für Optik und Atomare Physik, Berlin, Germany
[2]Technische Universität Berlin, Zentraleinrichtung Elektronenmikroskopie (ZELMI), Berlin, Germany

In contrast to most conventional transmission electron microscopy (TEM) methods, off-axis electron holography (EH) enables the measurement of the phase shift of the electron wave that has passed through a object. This phase shift can provide information about local changes in the magnetic induction (1) or the electrostatic potential (2) inside and outside the object.

However, in EH only the projected potential can be measured directly. Previous works (3,4) showed that through a series of different projection directions (e.g. specimen tilt), 3D information of the specimen can be obtained. Fig. 1 illustrates the measurement process and the subsequent phase reconstruction of such a series schematically. In (4) the electric potential of a focused ion beam (FIB) prepared flat capacitor is investigated. To reduce the influence of beam-induced specimen charging, a special normalisation process for the measurements is required utilizing phase measurements of the short-circuited capacitor.

To brake the symmetry of the electric potential, we present a new geometry with a third electrode inside a coplanar capacitor (Fig. 2). The structure is milled via FIB in the conducting path of a MEMS based heating chip (DENSsolutions wildfire) creating three electrodes on two separated electric potentials. The rectangular hole in one of the electrodes serves as reference area reducing the influence of the stray field on the reference wave.

Analogous to the measurement, a series of projections through the scalar electrostatic potential simulated by the three-dimensional finite-element-method (FEM) is made for multiple angles. The numerical simulations were made with Onelab (5). Additionally, post processing electrostatic stray-fields into the area of the reference wave are taken into account. The gradients of the reconstructed and simulated phases are compared, exemplary shown in Fig. 2. The good visual agreement shows that this method is well suited for measuring three-dimensional electrical potential distributions of more complicated geometries.

The next step is to check to what extent the data sets generated by the series (measured and simulated) can be used with tomographic reconstruction algorithms. A promising method seems to be the holographic back-projection shown in (3). However, the large missing wedge, caused by the biasing holder, will significantly complicate a tomographic reconstruction of the measured data.

References:

(1) M. Beleggia et al., Ultramicroscopy 110 (2010) 425−432.

(2) A.C. Twitchett et al., Physical Review Letters 88 (2002) 238-302.

(3) D. Wolf et al., Ultramicroscopy 110 (2010) 390−399.

(4) T. Wagner, Proceedings IMC19 (2018) 500.

(5) C. Geuzaine et al., International Journal for Numerical Methods in Engineering 79, (2009) 1309-1331.

Fig. 1: Schematic overview of the EH measurement process, the 3D FEM simulation including post processing and their comparison.

Fig. 2: SEM image of the specimen and exemplary visualization of the reconstructed phase of measured electron hologram and the corresponding post processed FEM simulation.

Fig. 1

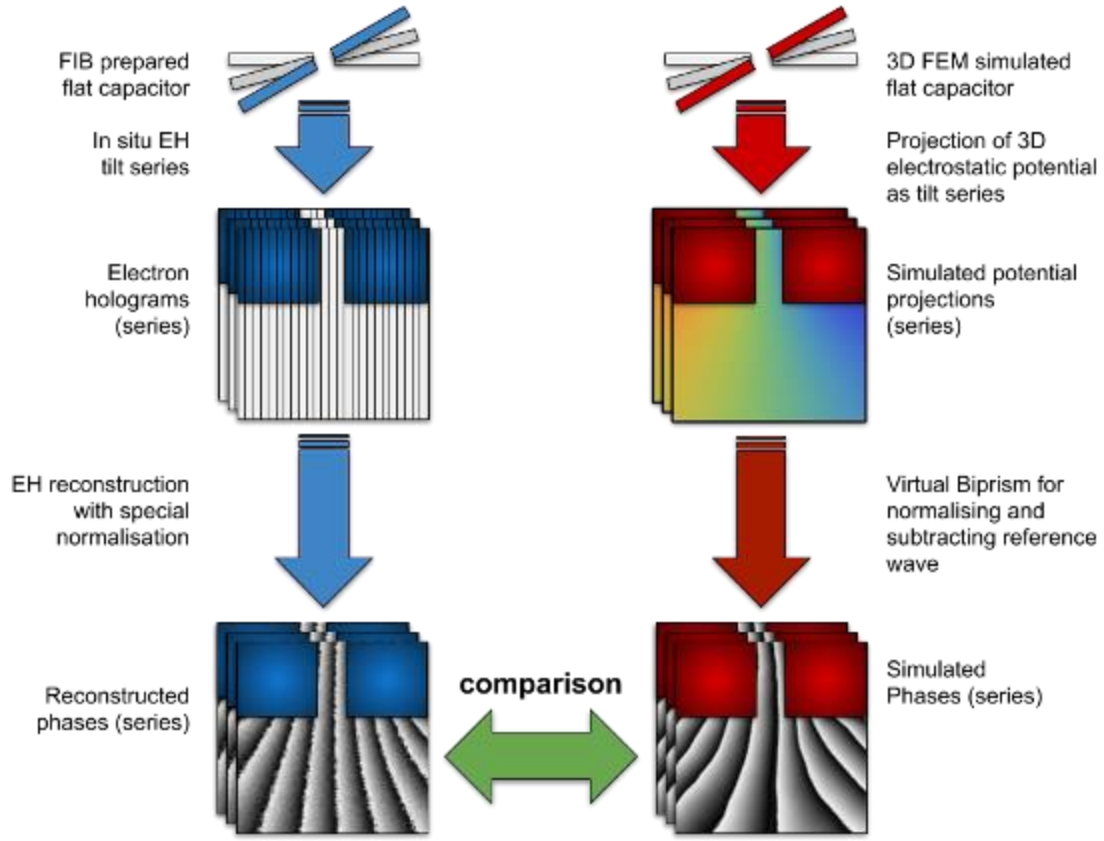
FIB prepared flat capacitor
In situ EH tilt series
Electron holograms (series)
EH reconstruction with special normalisation
Reconstructed phases (series)
comparison
3D FEM simulated flat capacitor
Projection of 3D electrostatic potential as tilt series
Simulated potential projections (series)
Virtual Biprism for normalising and subtracting reference wave
Simulated Phases (series)

Fig. 2

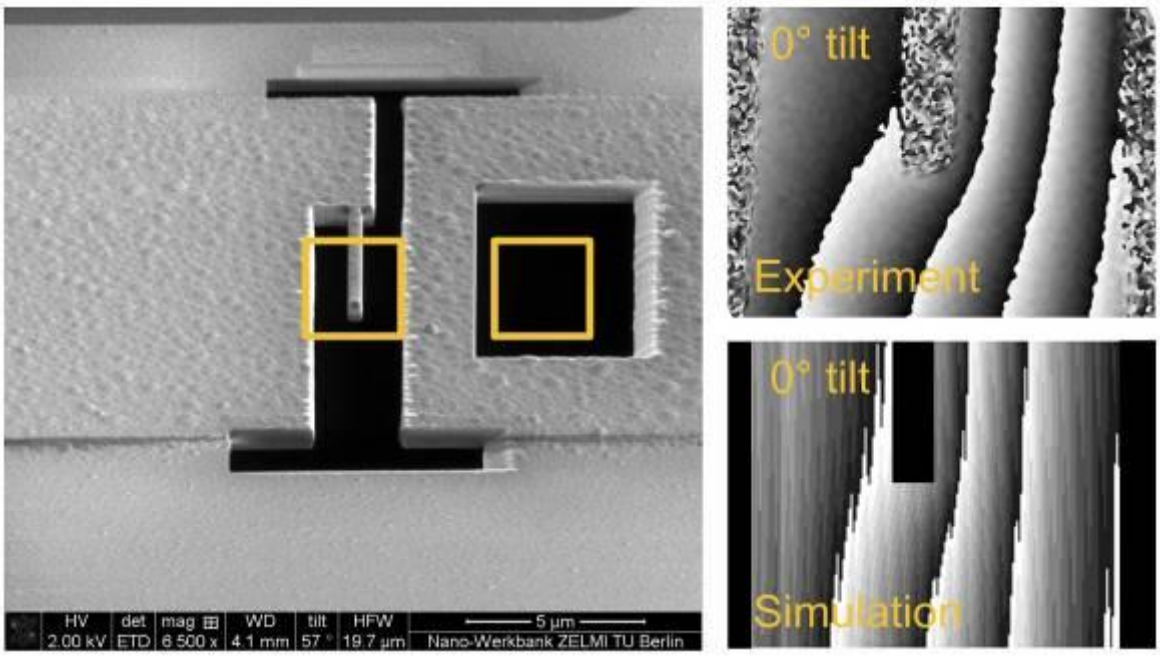
HV
2.00 kV
det
ETD
mag
6 500 x
WD
4.1 mm
tilt
57 °
HFW
19.7 µm
5 µm
Nano-Werkbank ZELMI TU Berlin
0° tilt
Experiment
0° tilt
Simulation

IM2.P021
Development of a Multi Layered Electric Phase Shifter for Electron Holography

T. Wagner[1], D. Berger[2], J. Simke[2], E. Geer[1], C. M. Günther[2], M. Lehmann[1]

[1]Technische Universität Berlin, Institut für Optik und Atomare Physik, Berlin, Germany
[2]Technische Universität Berlin, Zentraleinrichtung Elektronenmikroskopie (ZELMI), Berlin, Germany

The advantage of having access to amplitude and phase information of an object exit wave makes off-axis electron holography (EH) a powerful tool for analyzing potential distributions down to the atomic level. The ability to selectively manipulate the phase of the incident electron wave by a selective phase shifter also opens up new possibilities and microscopic methods, such as the direct interferometric measurement of the coherence length of an electron wave packet (1, 2) suggested by Möllenstedt, programmable phase plates (3) or time-resolved electron holography (4).

In principle, such a phase shifter is realized by passing one of two coherent electron beams through an electrostatic potential surrounded by a grounded electrode to shield stray fields while the other beam propagates undisturbed in vacuum. In reality, this poses several challenges: On the one hand, the production of multiple insulated conductive layers in a very small space is not trivial. On the other hand, for an electron holographic measurement of such a phase shift, contributions from external disturbances (e.g. magnetic field variation or electrical charging) cannot simply be separated. Here we present the multi-stage development process of such a phase shifter, which eliminates these problems.

With focused ion beam (FIB) milling, a four-hole structure was created (Fig. 1) allowing relative measurement by simultaneously overlapping two holes on the same and two holes on different electric potentials. The resulting two partial holograms contain phase information of shifted and unshifted electron waves in one image. Since external disturbances affect both partial holograms likewise, the unshifted partial hologram provides a reference hologram for compensation. Finite element simulations (FEM) of the structure were performed with ONELAB (5) for further verification (Fig.2).

In order to increase the phase shift, a 5 µm high block of aluminium (milled out of flattened foil via FIB) was placed on the partially stripped conductor path of a MEMS heating chip (DENSsolutions Wildfire). For electrical isolation of the upper side of the block, an approx. 200 nm thick Formvar film was placed in the middle of the chip (Fig. 2). An approx. 100 nm thick layer of gold on top and bottom serves as shielding. In a final step, the structural properties were milled, the multi layered phase shifter is shown in Fig. 1 (right).

First experiments showed a good agreement with the simulation and the benefits of this four-hole geometry. However, leakage currents turned out to have an impact but will be reduced in future process step optimization.

References:

(1) G. Möllenstedt et al., Proceedings 7th European Congress on EM (1980).

(2) H. Schmidt, Dissertation - Universität Tübingen (1985).

(3) J. Verbeeck et al., Ultramicroscopy 190 (2018) 58-65.

(4) T. Niermann et al., Ultramicroscopy 182 (2017) 54-61.

(5) C. Geuzaine et al., International Journal for Numerical Methods in Engineering 79, (2009) 1309-1331.

Fig. 1: Single layer four-hole structure as phase shifter (left) allowing relative EH measurement, its scheme (middle) and multi layered phase shifter (right).

Fig. 2: Top view of the MEMS chip with isolating Formvar, schematic cross-section of the layer structure and visualisation of the surface mesh from the FEM simulation.

Fig. 1

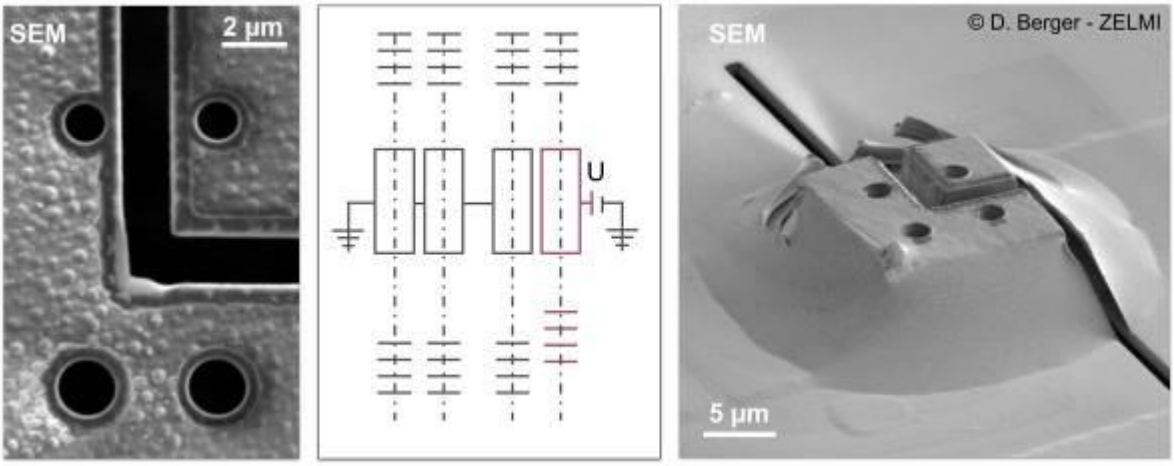
SEM
2 µm
U
SEM
© D. Berger - ZELMI
5 µm

Fig. 2

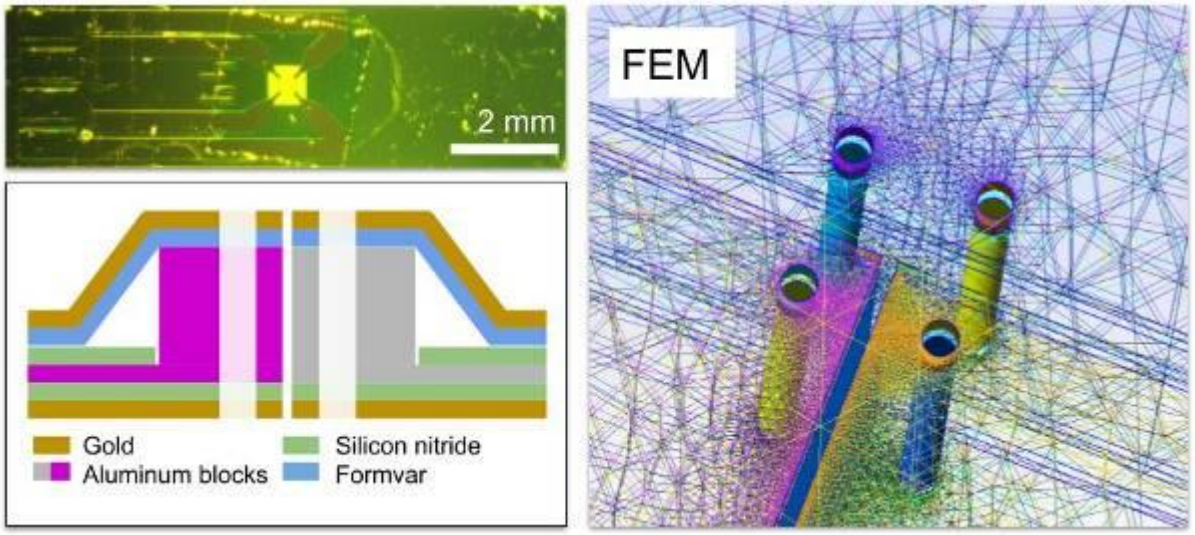
2 mm
Gold
Aluminum blocks
Silicon nitride
Formvar
FEM

IM2.P022
Quantitative characterization of the magnetic properties of manganite thin films using off-axis electron holography

Q. Lan[1,2], C. Wang[3], J. Caron[1], T. Denneulin[1], L. Jin[1], A. Kovács[1], X. Y. Zhong[2], R. Dunin-Borkowski[2]

[1]Forschungszentrum Jülich, Ernst Ruska-Centre for Microscopy and Spectroscopy with Electrons and Peter Grünberg Institute, Jülich, Germany
[2]Tsinghua University , National Center for Electron Microscopy in Beijing, School of Materials Science and Engineering, Beijing, China
[3]Max Planck Institute of Microstructure Physics, Halle, Germany

Detailed local characterization of the magnetic properties of epitaxial perovskite magnetic oxide films is essential for providing a fundamental understanding of structure-magnetism correlations for their applications in spintronic devices. Epitaxial $La_{0.67}Sr_{0.33}MnO_3$ (LSMO) thin films are of great interest as they exhibit colossal magnetoresistance, high spin polarization and a relatively high Curie temperature TC of 370 K. They also provide a highly attractive model system for applications in magnetoelectric devices, for example as bottom electrodes in thin film devices and active magnetic layers in magnetoresistive tunnel junctions. In tunnel junctions, the tunneling rate depends on the relative orientations of the magnetic spins on both sides of the barrier (1). Off-axis electron holography (EH) and Lorentz transmission electron microscopy (TEM) are powerful techniques for characterising magnetic field distributions in materials with high spatial resolution (2). However, the quantitative study of magnetization distributions in LSMO films using off-axis EH is challenging.

Here, we use off-axis EH to measure the magnetic field distribution in an epitaxial 200-nm-thick LSMO film deposited on a Nb-doped $SrTiO_3$ (NSTO) substrate. A cross-sectional specimen was prepared using a dual-beam focused Ga ion beam system (ThermoFisher Helios 440). Surface damage on the lamella was reduced by using low-energy Ar ion milling with an ion energy of below 1 keV (Fischione Nanomill). TEM measurements were performed both at room temperature and at cryogenic temperature using a liquid-nitrogen-cooled TEM specimen holder (Gatan 636) in an aberration-corrected transmission electron microscope operated in Lorentz mode (ThermoFisher Titan 60-300). Off-axis electron holograms were recorded using a direct electron detection camera (Gatan K2 IS). The magnetic contribution to the total recorded phase shift was separated from the mean inner potential contribution by tilting and magnetizing the specimen using the conventional objective lens of the microscope. The projected in-plane magnetisation distribution was calculated from the magnetic contribution to the phase by using a model-based iterative reconstruction algorithm.

Our results suggest that the LSMO film consists of a ferromagnetic layer with a T^C of 339 K adjacent to the NSTO substrate and a paramagnetic layer with a T_C of 279 K above the ferromagnetic layer, as shown in Figure 1. The in-plane magnetisation in the ferromagnetic layer was estimated to be approximately 536 emu/cc. This value is two times larger than the value of 258 emu/cc measured using Superconducting Quantum Interference Device (SQUID) magnetometry, which measures the average magnetization in the entire LSMO film. Our measurements reveal new information about magnetic interactions between different phases in LSMO films and can be used provide an improved understanding of device performance.

References:

(1) Majumdar, S. & Dijken, S. Pulsed laser deposition of La1−xSrxMnO3: thin-film properties and spintronic applications J. Phys. D: Appl. Phys. 47 (2014) 034010

(2) Kovács, A. & Dunin-Borkowski, R. Magnetic imaging of nanostructures using off-axis electron holography, vol. 27 (2018) 59-154 (ed E. Brück, Elsevier)

Fig: 1: In-plane magnetic phase images (a-c) and corresponding magnetic induction maps (d-f) of a LSMO film on a NSTO substrate at 290 K, 240 K, 93 K, respectively.

Fig. 1

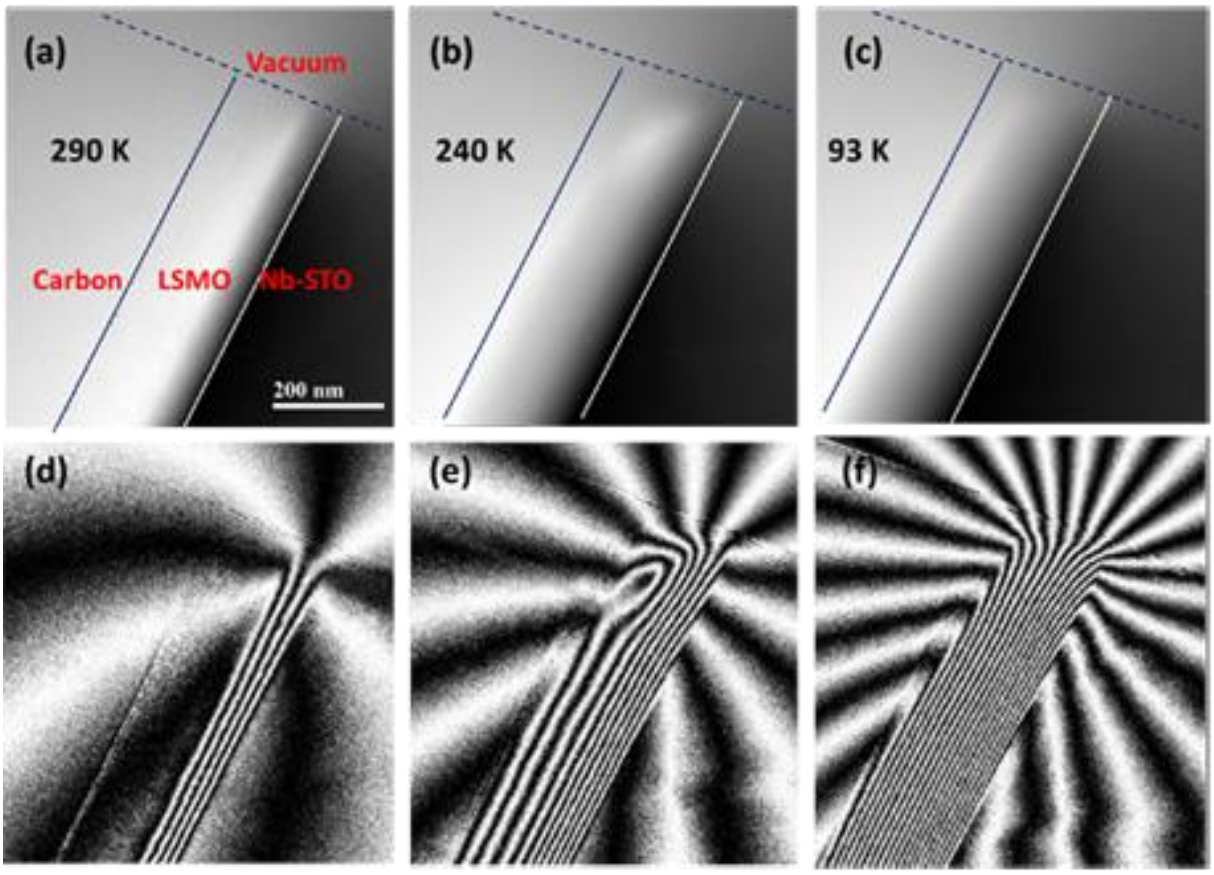

IM2.P023
Influence of lens aberrations, specimen tilt and thickness on differential phase contrast images of crystalline specimens

J. Bürger[1,2], T. Riedl[1,2], J. K. N. Lindner[1,2]

[1]Paderborn University, Department of Physics, Paderborn, Germany
[2]Center for Optoelectronics and Photonics Paderborn (CeOPP), Paderborn, Germany

Differential phase contrast (DPC) in scanning transmission electron microscopy (STEM) enables the measurement of material properties that previously could not be accessed with comparably high spatial resolution and information content. By detecting the specimen-induced electron beam deflection with a segmented detector, electric and magnetic field components can be quantified. State-of-the-art Cs-correctors allow to obtain DPC-STEM images with a resolution smaller than typical atomic distances. Nevertheless, even a corrected electron probe exhibits residual aberrations which render the reliable quantification of electric and magnetic fields more tricky.

The main objective of the present study consists in determining which features in DPC images originate from specimen structure or residual aberrations, specimen thickness or tilt. To that end, comparisons of experimental with simulated DPC images are required in order to understand the individual and combined effects of these parameters on DPC images.

STEM-DPC image simulations for monocrystalline $SrTiO_3$ and Si are carried out with the multi-slice algorithm based program *Dr. Probe* (1). DPC measurements of a Si specimen oriented in [110] zone axis are performed by using a probe Cs-corrected JEOL JEM-ARM200F microscope having a maximum resolution of 70 pm. The microscope is equipped with an eight-fold segmented annular detector for DPC. For an appropriate comparison of simulations with the DPC measurements microscope parameters such as the size of detector segments are determined. For quantification of electric fields EFTEM thickness measurements are used. Atomic column positions are obtained from STEM-HAADF images.

We show that multi-slice simulations on the example of $SrTiO_3$ reveal the influence of residual lens aberrations, specimen tilt and thickness on DPC images. Increased lens aberration in particular defocus and specimen thickness reduce the DPC signal strength, leading to an erroneous quantification of electric fields. In addition, the shapes of DPC image features alter in a characteristic manner when varying lens aberrations, specimen tilt and thickness. While higher order aberrations are quite stable, low order aberrations like defocus and two-fold astigmatism have to be corrected frequently. DPC measurements for a specimen thickness above 35 nm show an inverted electric field distribution (Fig. 1). Analogous multi-slice simulations indicate a similiar behaviour (Fig. 2).

Comparisons between STEM-DPC simulations and measurements provide new insights on how the DPC signal is affected by specimen thickness, specimen tilt and residual lens aberrations.

References:

(1) J. Barthel, *Dr. Probe: A software for high-resolution STEM image simulation*, Ultramicroscopy 193 (2018) 1-11.

Fig. 1: (a) Multi-slice simulation of a 1.63 nm thick Si crystal in [110] orientation without any aberration. (b) DPC measurement of a 35 nm thick Si specimen in [110] direction shows inverted electric field distributions. Atomic column positions are indicated with white dots.

Fig. 2: (a) STEM-HAADF multi-slice simulation with usual lens aberrations of a 35 nm thick Si crystal in [110] orientation. Simultaneously generated DPC signal (b) is more prone to present aberrations (in particular coma and three-fold astigmatism) and shows inverted electric field distributions. Atomic column positions are indicated with white dots.

Fig. 1

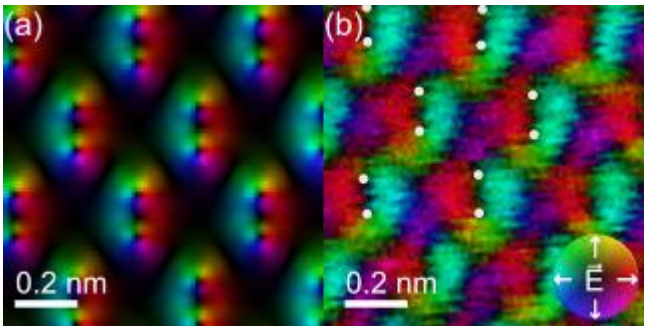

Fig. 2

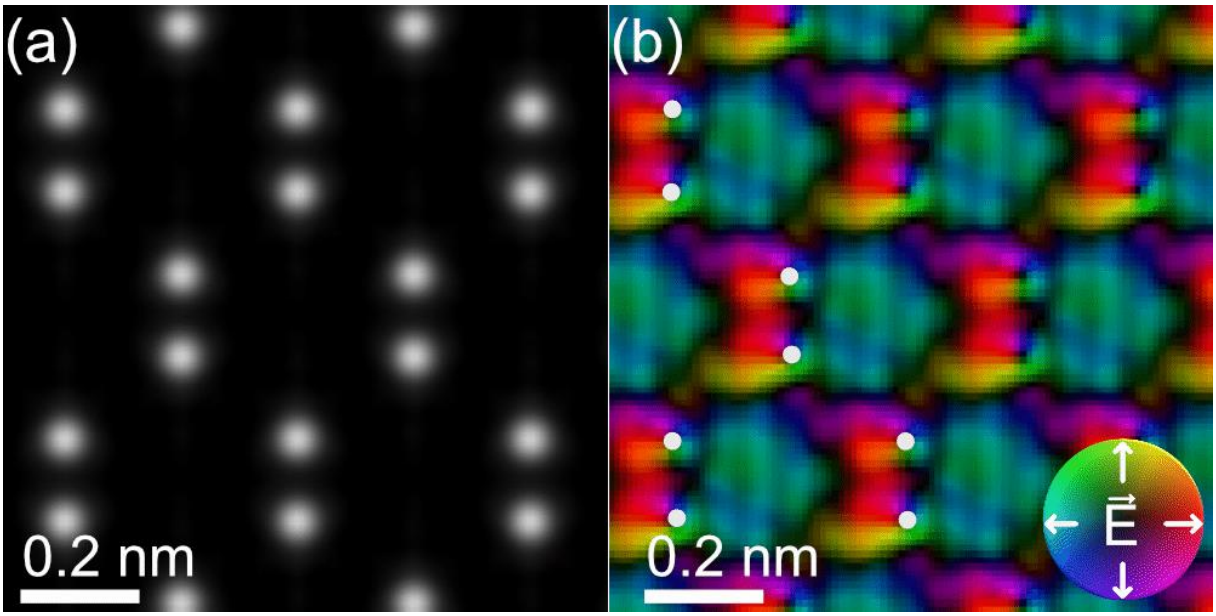

IM3.002
Fast chemical reactions in oxide nanocrystals studied by ultrafast electron microscopy

F. Banhart[1], A. Khammari[1], S. K. Sinha[1], M. Picher[1], F. Roulland[1], N. Viart[1], T. Lagrange[2]

[1]University of Strasbourg, IPCMS, Strasbourg, France
[2]EPFL, LUMES, Lausanne, Switzerland

Ultrafast or dynamic TEM using ultrashort electron pulses has shown a high potential for investigating short timescales in nanosystems. A pump-probe approach is used to study reversible or irreversible transformations of the object in the stroboscopic (1) or single-shot (2) mode. Due the irreversible nature of most fast chemical reactions, they are challenging to study and require the single-shot approach with its inherent difficulties. Our recent achievements in single-shot ultrafast TEM (2) now allow us to carry out imaging, electron diffraction and EELS with single nanosecond electron pulses.

Here we present the first comprehensive ultrafast TEM study of a fast irreversible reaction in nanometer-sized particles. Of interest is the kinetics of the reaction which has hitherto been difficult to analyze due to the exceedingly fast reaction rates that occur in the nanoscale materials. Thus, the studies must be carried out with both high spatial and high temporal resolution. We study the fast kinetics of the solid-state reduction of nickel oxide nanocrystals on a carbon film. The reaction speed is determined and evidence for a temporary liquid transition state is given.

20 nm thick NiO layers with crystal sizes around 5 nm were produced by pulsed laser deposition on amorphous carbon films. TEM experiments were carried out in the single-shot approach (2). An IR laser pulse with 7 ns duration first initiated the reduction of the NiO crystals which is probed using a single electron pulse also with a 7 ns duration that follows after the IR pulse with adjustable delay. The experiment was repeated on different specimen areas for different pump-probe delays, allowing the time-resolved reconstitution of the reaction.

Figures 1a and 1b show conventional TEM images of NiO before (a) and Ni after (b) reduction with a laser pulse. Ripening caused the growth of larger Ni crystals. Figure 1c shows single-shot images at different delays after laser excitation. While the NiO crystals cannot be resolved, the appearance of the larger Ni crystals starts at 1.5 µs and reaches the final state after 3 µs. Figure 2a shows the temporal evolution of the chemical composition measured by EELS. The O-K edge vanishes between 1 and 5 µs after the excitation. The evolution of the diffraction (fig. 2b) shows that the NiO reflections disappear at the same timescale as the O-K edge in EELS. However, the Ni reflections appear with a much longer delay from nanoparticles which continue to evolve even after 100 µs which indicates that the reduced Ni is in a liquid state before crystallization.

Hence, by single-shot TEM, reaction speeds at the nano- to microsecond and the detection of short-living transient states during solid-state reactions becomes feasible.

Funding by the Agence Nationale de Recherche (ANR-11-EQPX-0041) and by the University of Strasbourg Institute of Advanced Studies is gratefully acknowledged.

References:

(1) K. Bücker, M. Picher, O. Crégut, T. LaGrange, B. W. Reed, S. T. Park, D. J. Masiel, F. Banhart, *Ultramicroscopy* 171, 8 (2016).

(2) M. Picher, K. Bücker, T. LaGrange, F. Banhart, *Ultramicroscopy* 188, 41 (2018).

Fig. 1: Transformation of NiO (a) to Ni (b) imaged by a static electron beam. (c): Single-shot images after different delays.

Fig. 2: (a): EELS with single electron pulses after different delays. t = 0 corresponds to NiO and t = ¥ to Ni. (b): Profile through diffraction patterns taken with single electron pulses.

Fig. 1

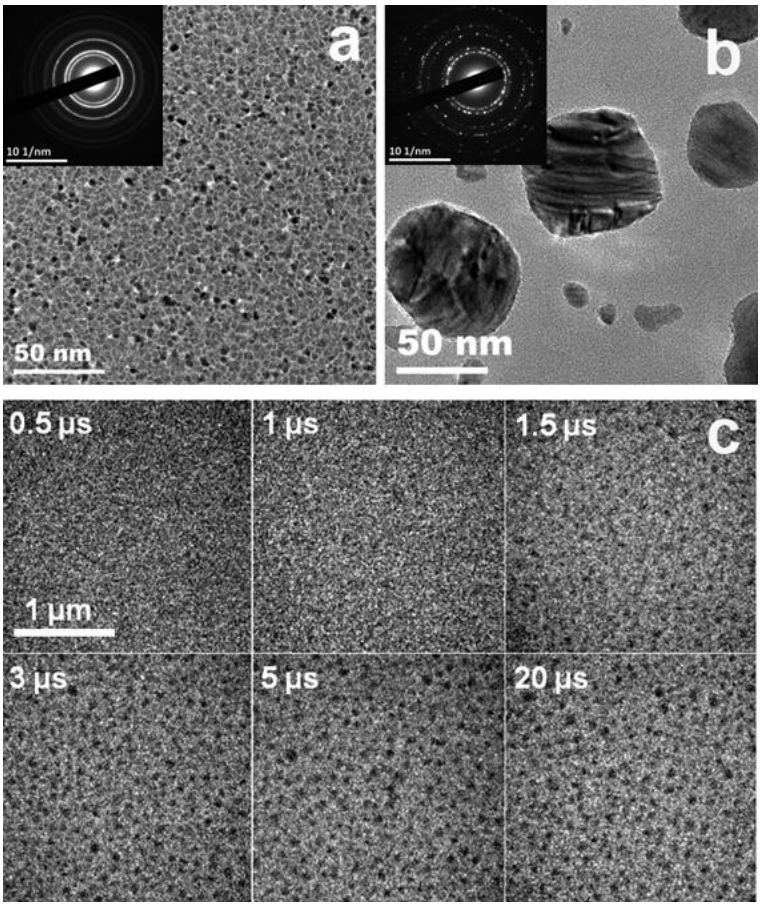
a
10 1/nm
50 nm
b
10 1/nm
50 nm
c
0.5 µs
1 µs
1.5 µs
1 µm
3 µs
5 µs
20 µs

Fig. 2

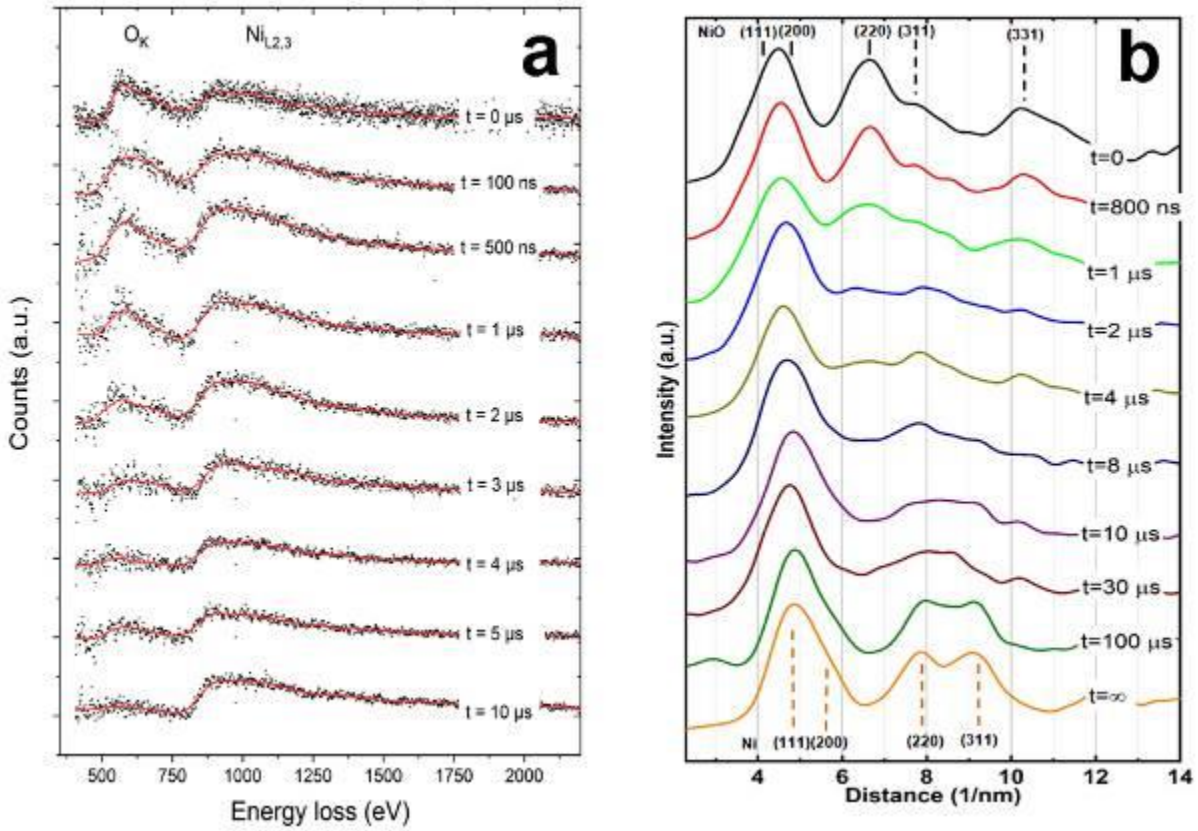
a
O_K
Ni_L2,3
t = 0 µs
t = 100 ns
t = 500 ns
t = 1 µs
t = 2 µs
t = 3 µs
t = 4 µs
t = 5 µs
t = 10 µs
Counts (a.u.)
500
750
1000
1250
1500
1750
2000
Energy loss (eV)
b
NiO
(111)(200)
(220)
(311)
(331)
t=0
t=800 ns
t=1 µs
t=2 µs
t=4 µs
t=8 µs
t=10 µs
t=30 µs
t=100 µs
t=∞
Ni
(111)(200)
(220)
(311)
Intensity (a.u.)
4
6
8
10
12
14
Distance (1/nm)

IM3.003
Watching Nanodroplets Jump

P. Olshin[1], J. Voss[1], M. Drabbels[1], U. Lorenz[1]

[1]EPFL, Lausanne, Switzerland

The manipulation of liquids at nanoscale dimensions is a central goal of the emergent nanofluidics field. Naturally, such efforts extend to nanodroplets, ubiquitous objects whose controlled generation and manipulation is crucial to a number of technologically important endeavors, such as jet printing with droplets of ever smaller dimensions.

Here, we employ time-resolved electron microscopy to elucidate a process that generates monodisperse nanodroplets in free space and accelerates them to high velocities. We flash-melt a thin metal nanostructure with a laser pulse to directly observe how the nascent nanodroplet contracts into a sphere and jumps off its substrate. The ensemble averaged trajectories reveal dewetting velocities of up to 80 m/s, with the droplet jumping in under 10 ns. At the same time, we observe significant variations in the trajectories of individual droplets, which points to nanoscale heterogeneity of friction at the liquid-solid interface.

Our experimental approach opens up new avenues for studying the fast morphological dynamics of nanodroplets through direct observation. Moreover, it provides an opportunity to study the nanoscale dynamics of the contact line and investigate liquid friction on its inherent length scale.

IM3.004
Multi-scale Operando Electron Microscopy for the Investigation of CO Oxidation over Pt catalysts

T. Lunkenbein[1], M. Plodinec[1], L. Sandoval-Diaz[1], R. Schlögl[1,2]

[1]Fritz-Haber-Institut der Max-Planck-Gesellschaft, Inorganic Chemistry, Berlin, Germany
[2]Max Planck Institute for Chemical Energy Conversion, Department of Heterogeneous Reaction, Mülheim an der Ruhr, Germany

Recent developments of more robust MEMS devices give rise to new opportunities for operando electron microscopy (EM) studies of heterogeneous catalysts.(1) These MEMS-based nanoreactors allow the characterization of catalysts" active state under relevant conditions, at pressures up to 15 bar and temperatures up to 1000 °C.(2,3) The first visualization of time-resolved reactions inside a MEMS-based nanoreactor system with simultaneous acquisition of the reaction conversion by mass spectrometry (MS) has been reported by Vendelbo *et al.*(4)

Environmental scanning electron microscope ESEM and *in situ* TEM can be used as complementary methods in terms of obtainable resolution, to gain information on local and global dynamics, as well as applicable pressure ranges.(5) As such, this setup can provide new insights into the fundamental understanding of how heteregenous catalysts work in reaction conditions, providing information about surface and subsurface interactions in different gas environments.

Here, we use home-built gas-feeding setups that have been prevously installed at FHI (5,6) and slightly modified recently. Each setup is equipped with a MS to conduct real-time *operando* experiments inside the chamber of an ESEM and TEM using commercially available gas-flow TEM holders. To test the capabilities of the *operando* TEM and ESEM setups, we used CO oxidation over Pt catalysts as a model reaction. Using these two techniques we were able to correlate structural and morphological changes of Pt catalysts with activity at different spatial resolution from sub-nm to several mm, at pressures from 0.01 to 1000 mbar and at temperatures between 25-1000 °C (Figure 1).

The obtained results suggest that CO oxidation does not only involve the Pt surface, but that the reactivity is also influenced by an interplay of surface, subsurface and bulk ordering. The direct correlation of structural changes with the catalytic conversion over several length scales generates new insights into the activation and deactivation mechanisms of catalysts that will allow us to better understand structure-reactivity relationships.

In summary, the combination of *operando* TEM and ESEM can deliver new insights into the fundamental understanding of how heteregenous catalysts work.

Dr. Marc G. Willinger, Dr. Ramzi Farra, and Dr. Zhu-Jun Wang are acknowledged for the installation of the gas feeding setups during their stay at FHI.

Figure 1. a) Operando TEM setup. b) Atomic resolution TEM image of a Pt nanoparticle (CO:O2=1:5; 700 mbar; 200 °C). c) MS data during ramping from RT to 500 °C (CO:O2=1:5; 700 mbar; 20 µl/min; 1 °C/min). ESEM image of a Pt foil d) before and e) during CO oxidation. f) Corresponding MS data during CO oxidation in the ESEM (CO:O2=1:5; 0.52 mbar; 440 °C and 550 °C).

References:

(1) J. F. Creemer *et al.*, Proc. IEEE Conf. MEMS, Sorrento, Italy, (2009), p. 76.

(2) J. F. Creemer *et al.*, Proceeding of MEMS 2011 (2011), p. 1103.

(3) G. M. Bremmer *et al.*, Faraday Discuss., 197 (2017), p. 337.

(4) S.B. Vendelbo *et al.*, Nature Materials, 13 (2014), p. 884.

(5) R. Farra *et al.*, Microsc. Microanal. 22 (2016), p. 736.

(6) Z.-J. Wang., PhD Thesis: "In-situ scanning electron microscopy studies on the dynamics of metal-catalyzed CVD growth of graphene", TU Berlin (2017) http://dx.doi.org/10.14279/depositonce-7391, (2017).

Fig. 1

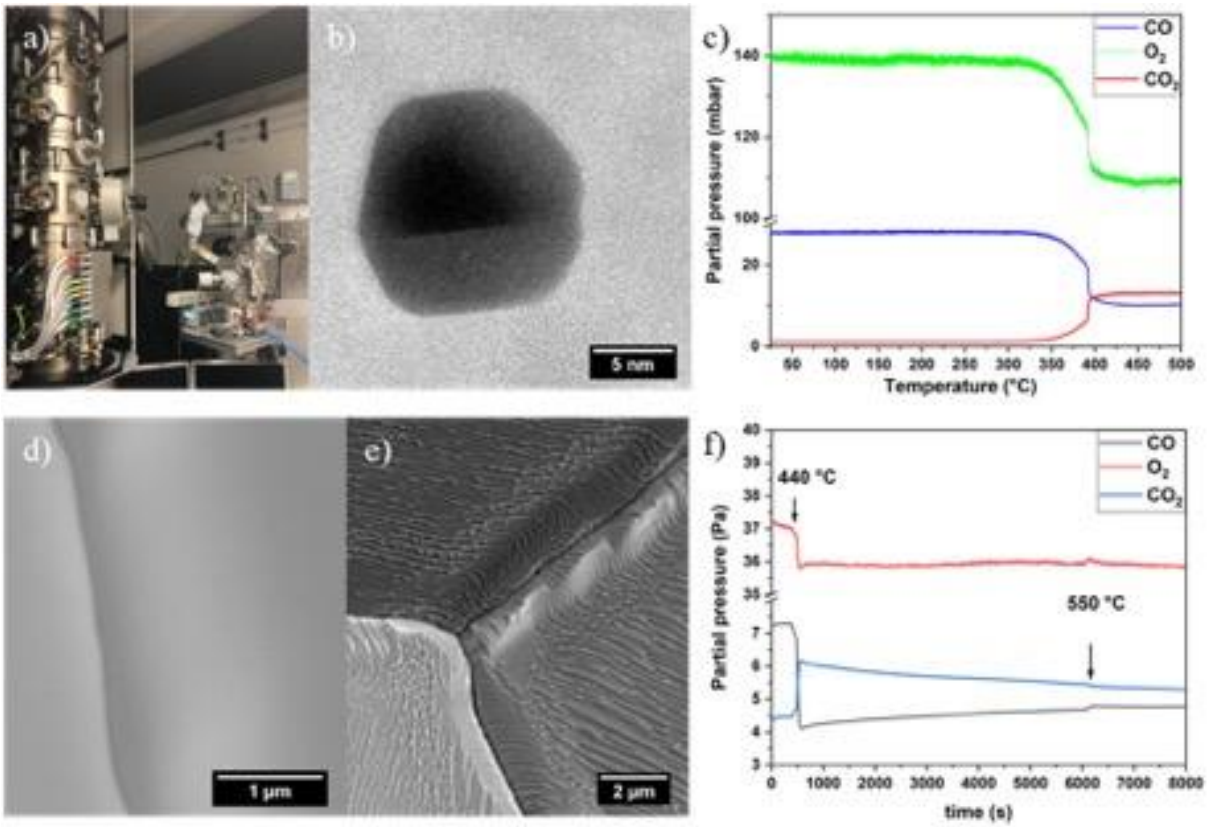
a)
b)
5 nm
c)
CO
O_2
CO_2
Partial pressure (mbar)
Temperature (°C)
d)
1 µm
e)
2 µm
f)
440 °C
550 °C
Partial pressure (Pa)
time (s)

IM3.005
In-Situ Electron Microscopy Observations of Structural Transformations in Two-Dimensional CoSe2

D. Gavhane[1], M. A. van Huis[1]

[1]Debye Institute for Nanomaterials Science, Utrecht University, Physics, Utrecht, Netherlands

Alteration of materials properties via phase transitions without adding any external atoms is of high scientific and technological value. Imaging these transitions in real time provides insight into synthesis routes and property tuning. We have used in-situ Transmission Electron Microscopy (TEM) to follow the structural transformations in 2D-CoSe2.

The primary objective of this study is to observe structural transformations in CoSe2 at the atomic scale and in real time by heating in-situ in the TEM.

Samples of bulk CoSe2 were first synthesized via a hydrothermal route after which the CoSe2 was exfoliated using a probe sonicator, to obtain few-layer-thick nanosheets. The in-situ TEM study was performed on FEI Titan microscope with aberration correction for imaging. CoSe2 samples for in-situ heating experiments were prepared by drop casting it directly onto MEMS chips with SiN membranes, which were mounted on a DENS solutions heating holder. The temperature was increased from room temperature to 1100 oC in steps of 20 oC. A Direct Electron camera was used to record movies and images for observing dynamical structural transformations.

As-prepared orthorhombic-CoSe2 (o-CoSe2) samples were first heated from room temperature to 500 oC. At this temperature, the sample remains stable not showing any significant structural changes. Upon heating to 600 oC, it transforms into an intermediate phase with the slightly changed structure. At around 720 oC it goes through a transition phase where atoms in the material are observed to rearrange continuously, without forming a well-defined stable structure. Further incrementing the temperature results in the cubic-CoSe2 (c-CoSe2) structure via atomic relaxations. The cubic structure was found to stabilize at a temperature of 760 oC without showing further changes in time. Another two highly unstable transition phases were observed each at temperature 780 oC and around 800 oC. The unstable nature of both of these intermediate phases could be the result both rearrangement of atoms and removal of Se atoms, which leads to the stable hexagonal-CoSe structure in the temperature range of 800-900 oC. The compositional change accompanying the transformation from c-CoSe2 to CoSe was confirmed by EDS measurements. In previous studies, it has been reported that in transition metal dichalcogenides, the chalcogen atoms tend to be removed due to an electron beam and thermal effects. Further increment in the temperature above 900 oC results in breaking of h-CoSe layers to form islands of tetragonal-CoSe (t-CoSe). The trend of structural transition in CoSe2 is shown in Figure 1. Figure 2 depicts the HR-TEM images of o and c- CoSe2, h, and t- CoSe respectively along with FFT and schematic of their unit cells.

The transition process starts with the rearrangement of atoms followed by relaxation processes. A number of intermediate and transition phases were observed and characterized during heating. Repeating the experiments under the same conditions confirms that o-CoSe2 always transforms into basal-plane oriented h-CoSe. Our results provide microscopic insights into the transformation process of 2D-CoSe2 and can be used to tune the properties of these intriguing 2D materials by modifying their structure for various applications.

Fig. 1

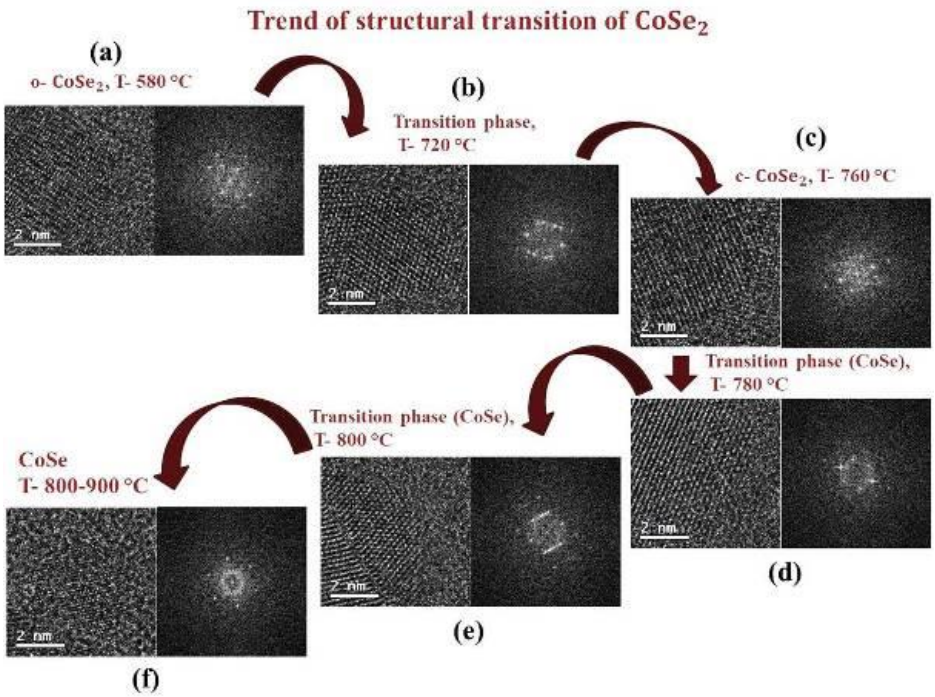

Figure1: HR-TEM images recorded during structural transition of $CoSe_2$ with FFT for, (a) o-$CoSe_2$, (b) transition phase between o and c- $CoSe_2$, (c) c- $CoSe_2$, (d) and (e) intermediate and transition phases between c- $CoSe_2$ and h- CoSe and (f) h-CoSe.

Fig. 2

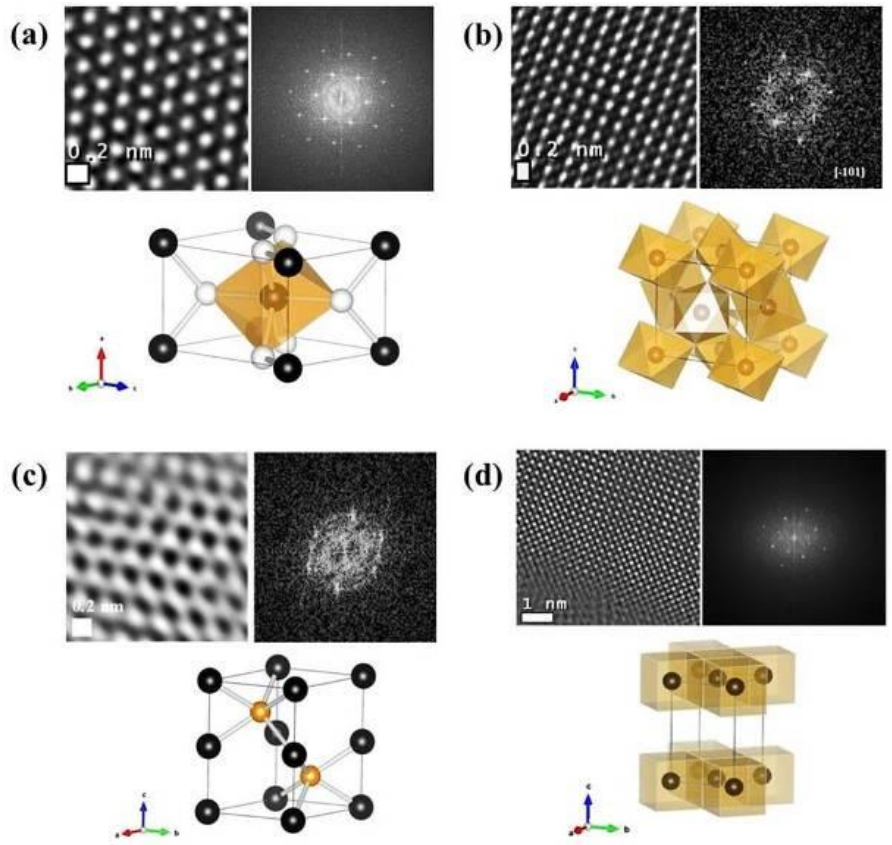

Figure 2: HR-TEM and FFT images (filtered) with schematic of unit cell for (a) o-$CoSe_2$, (b) c- $CoSe_2$, (c) h- CoSe and t- CoSe respectively.

IM3.006
In situ Observation of Gold Nanoparticle Growth in Thin Ionic Liquid Layers

D. Keller[1], T. R. Henninen[1], R. Erni[1]

[1]Empa, Swiss Federal Laboratories for Materials Science and Technology, Electron Microscopy Center, Duebendorf, Switzerland

Dynamic processes in liquids, such as the nucleation and growth of nanoparticles (NPs), are most commonly studied in situ by means of liquid-cell transmission electron microscopy (LC-TEM). However, the achievable resolution is often a limiting factor in LC-TEM. Therefore, alternative approaches that enable window-free observations of thinner liquid films at higher resolution are explored. Ionic liquids (ILs) provide a complementary and simple tool for in situ studies in liquid media at high resolution (1,2,3) Due to their low vapor pressure, ILs can be studied in the TEM as free-standing, thin liquid layers without any encapsulation. Their large versatility further allows for designing systems with specific properties that can trigger processes in situ.

In this work we use two different ILs to study the formation of gold NPs in thin liquid layers. The growth process is induced by heat and irradiation and observed at high spatial resolution (1).

The gold precursor, sodium tetrachloroaurate ($NaAuCl_4$), and the IL, either 1-butyl-3-methylimidazolium chloride ([BMIm][Cl]) or tetrabutylammonium chloride ($[Bu_4N][Cl]$), are dissolved in ethanol and transferred to an E-chip compatible with the Fusion 500 heating holder from Protochips. Heating (100-200°C) and electron irradiation trigger the particle growth in situ. The experiments are performed on a FEI Titan Themis at 300 kV in scanning (S)TEM mode. A sketch of the experimental setup is shown in Fig. 1.

After initiating the growth of gold NPs, two different phases are distinguished: small, spherical particles are formed first, followed by an anisotropic growth phase that generates larger, well-defined, faceted particles. During the initial, isotropic growth phase, different mechanisms are active in parallel, i.e. growth by monomer attachment, by particle coalescence and growth by Ostwald ripening. Fig. 2 illustrates a time series of several gold particles during the first growth phase. An example of particle coalescence is shown by the particles colored in red, and the particles colored in yellow represent an Ostwald ripening event. Under longer irradiation times at elevated temperatures, we observe a shift from the initial isotropic growth towards anisotropic NP growth, typically resulting in tetrahedral, octahedral and decahedral particles.

Based on different examples of gold NP formation in ILs, our work highlights the potential of IL systems for in situ TEM studies as a complementary technique to LC-TEM. The results provide insights into the early growth procedure of the gold NPs. Our work in ILs reveals details on the growth mechanisms, deepens the understanding about the behavior of different ILs under electron beam irradiation and provides essential information to improve the control over the system and the mechanism that triggers the particle growth.

References:

(1) D. Keller et al., *Micron* 117, 16-21 (2019).

(2) T. Uematsu et al., *J Am Chem Soc* 136, 13789–13797 (2014).

(3) Y. Kimura et al., *J Am Chem Soc* 136, 1762–1765 (2014).

This project has received funding from the European Research Council (ERC) under EU's Horizon 2020 research and innovation program (Grant Agreement No. 681312).

Fig.1: Experimental setup.

Fig. 2: Gold NP growth in IL captured after 0, 19, 32, 35, 145, 190, 195 and 105 s of electron irradiation and at 100°C. The particles highlighted in red show an example of particle coalescence and the particles highlighted in yellow are involved in an Ostwald ripening event.

Fig. 1

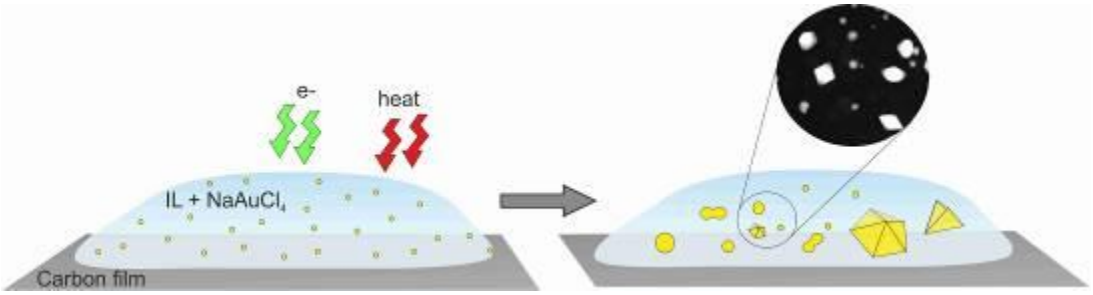
e-
heat
IL + NaAuCl4
Carbon film

Fig. 2

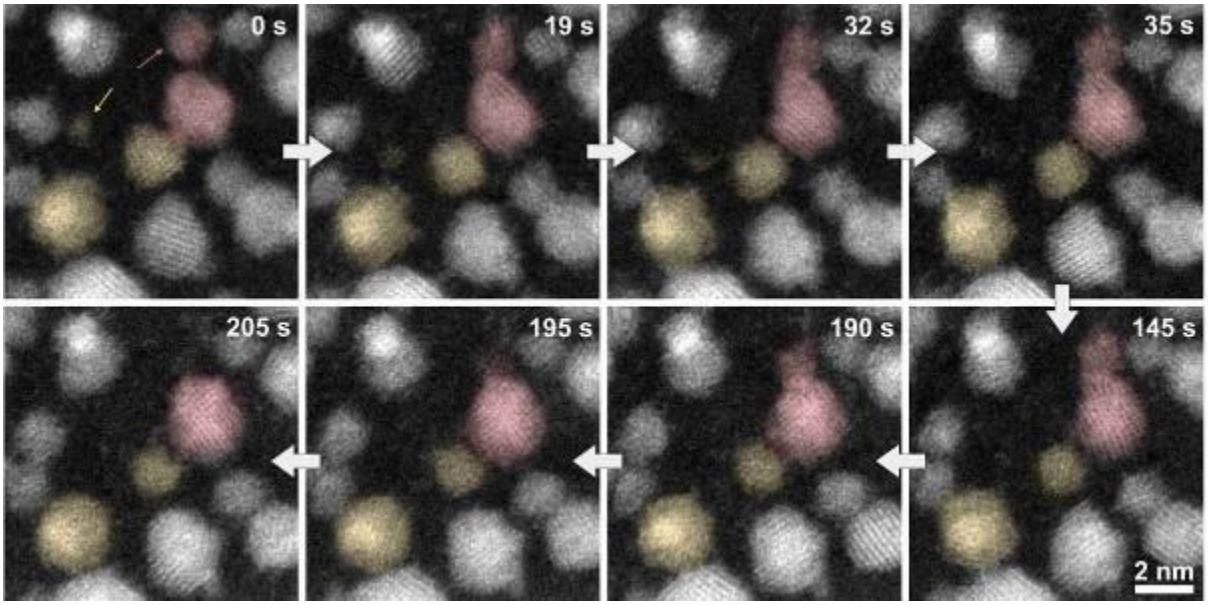
0 s
19 s
32 s
35 s
205 s
195 s
190 s
145 s
2 nm

IM3.007
In-situ TEM observation of phase transformations in inorganic cesium-lead-halide perovskites using multivariate analysis

H. Funk[1], A. Eljarrat[2], O. Shargaieva[1], E. Unger[1], D. Abou-Ras[1], C. T. Koch[2]

[1]Helmholtz-Zentrum Berlin für Materialien und Energie, Berlin, Germany
[2]Humboldt-Universität zu Berlin, Berlin, Germany

With power conversion efficiencies surpassing 22% in 2018, hybrid organic-inorganic lead-halide perovskites solar cells attract ever more interest in the photovoltaics community (1). Photo-induced phase separation was reported for a range of mixed-halide perovskites, which limits the available band-gap energies for photovoltaic applications (2,3). An enhanced understanding of the phase-separation mechanism is essential to rationalize limitations and to design stable perovskite semiconductors. Up to now, phase separations have been detected by means of X-ray diffraction (XRD), photoluminescence, and cathodoluminescence experiments (4,5).

During electron microscope experiments, the electron beam may cause changes in halide perovskites (5, 6). In the present work, we report electron-beam-induced phase transformations. Inorganic $CsPb(Br_xI_{1-x})_3$ thin films were deposited by spin-coating, and the phase transformation investigated in-situ using transmission electron microscopy. The acquired time series were evaluated by means of multivariate analysis (principal/independent component analysis, PCA/ICA) to classify the structural change over time, as depicted in Figure 1. By this approach, it was possible to monitor directly the phase separation of $CsPb(Br_{0.5}I_{0.5})_3$ thin films into $CsPbI_3$ and probably $PbBr_2$ domains on the nanoscale.

References:

(1) Brenner, T. *et. al. Nat. Rev. Mater.* 2016, 1, 15007

(2) E. T. Hoke et al., Chem. Sci.,2015, 6, 613

(3) E. L. Unger et al. *J. Mater. Chem. A*,2017, 5, 11401

(4) Barker et. al*, ACS Energy Lett.* 2017, 2, 1416−1424

(5) W. Li, et al., *Adv. Energy Mater.* 2017, 7, 1700946

(6) Z. Dang et al., *ACS Nano* 2017, 11, 2124−2132

Fig: 1: a) $CsPb(Br_xI_{1-x})_3$ after 3 min of electron-beam irradiation. b) The algorithm "scans" the TEM image, generating a fast Fourier transform (FFT) for each patch. c) Multivariate analysis using PCA/ICA. Exemplary abundance map (left) and corresponding electron diffractogram (right). Each pixel in the abundance map represents a patch, and its intensity depends on how well the local FFT is in accordance with the diffractogram.

Fig. 1

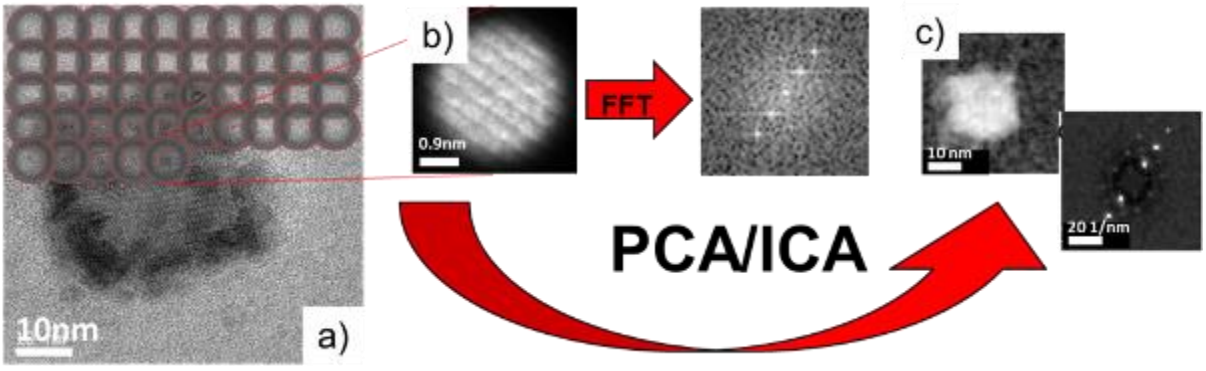

IM3.008
Electron Beam Induced Dynamics in Experiment and Simulation

F. Hofer[1], D. Knez[2], G. Kothleitner[1], G. Haberfehlner[1]

[1]Graz University of Technology, Institut for Electron Microscopy and Nanoanalysis, Graz, Austria
[2]Graz Centre for Electron Microscopy, Graz, Austria

Further advances in nanotechnology require the ability to develop smaller structures and devices down to the atomic level which also rely on quantum effects. Here, scanning transmission electron microscopy could play a pivotal role, on the one hand because of its extremely high resolution but also because of the intense interaction of the electrons with the specimen.

Although these processes may even lead to specimen damage, they give rise to some interesting phenomena which can be also harnessed for materials modification and fabrication at the atomic level. For instance, the electron beam induced fabrication of atomic-scale structures in silicon (1) or the creation of hollow and toroidal NiO clusters were reported (2).

The fact that atoms move during the observation in a STEM is generally known, but how this motion is driven by the temperature of the specimen or by the energy transfer from the fast electrons is not always clear (3). Therefore, we have to develop a fundamental understanding of the motion of single atoms and adatom clusters on different substrates, e.g. on carbon or silicon. To study the effect of the electron beam on adatom motion we recorded a time-resolved STEM HAADF image series of Pt atoms on the surface of a thin silicon crystal. Using a novel image processing approach the dynamics of the silicon substrate is separated from that of the adatoms and automated particle tracking enables the detailed analysis of the diffusive motion of the Pt adatoms on the silicon surface (4).

To elucidate the dynamics of single metallic clusters we combined experimental and computational methods. On the one hand, we performed time-resolved STEM HAADF experiments, which allow observing the dynamics of clusters under the controlled influence of the electron beam. To evaluate image series consisting of several hundred images we use automatic image processing techniques. On the other hand, we developed a computational framework to simulate elastic electron damage processes in solids and to obtain deeper insights into the observed dynamics. Our approach is based on the combination of molecular dynamics and Monte Carlo techniques (5). Figure 1 shows a STEM HAADF image series for a Janus type Ag-Au cluster on an amorphous carbon support. The two cluster phases show highly different behaviour under electron irradiation, due to differences in atomic mass and binding energies between Ag and Au. While the Au cluster mostly retains its size during the experiment, the Ag cluster exhibits significant mass loss due to surface sputtering which is confirmed by the computational approach.

References:

(1) B. M. Hudak et al., Microsc. Microanal. 24, Suppl. 1 (2018) 158-159.

(2) D. Knez et al., Ultramicroscopy 176 (2017) 105-111.

(3) D. Van Dyck et al., Micron 68 (2014) 158-163.

(4) T. Furnival et al., Appl. Phys. Lett. 113 (2018) 183104-1-5.

(5) D. Knez et al., Ultramicroscopy 192 (2018) 69-79.

Fig: 1: (a) Experimental STEM HAADF image series of an Ag-Au cluster showing the effect of selective Ag sputtering, dependent on the applied dose in number of electrons; (b, c) simulation of beam induced dynamics in carbon supported clusters initially comprised of either 350 Au or Ag atoms, demonstrating significant surface sputtering of Ag atoms at 300 keV electron energy.

Fig. 1

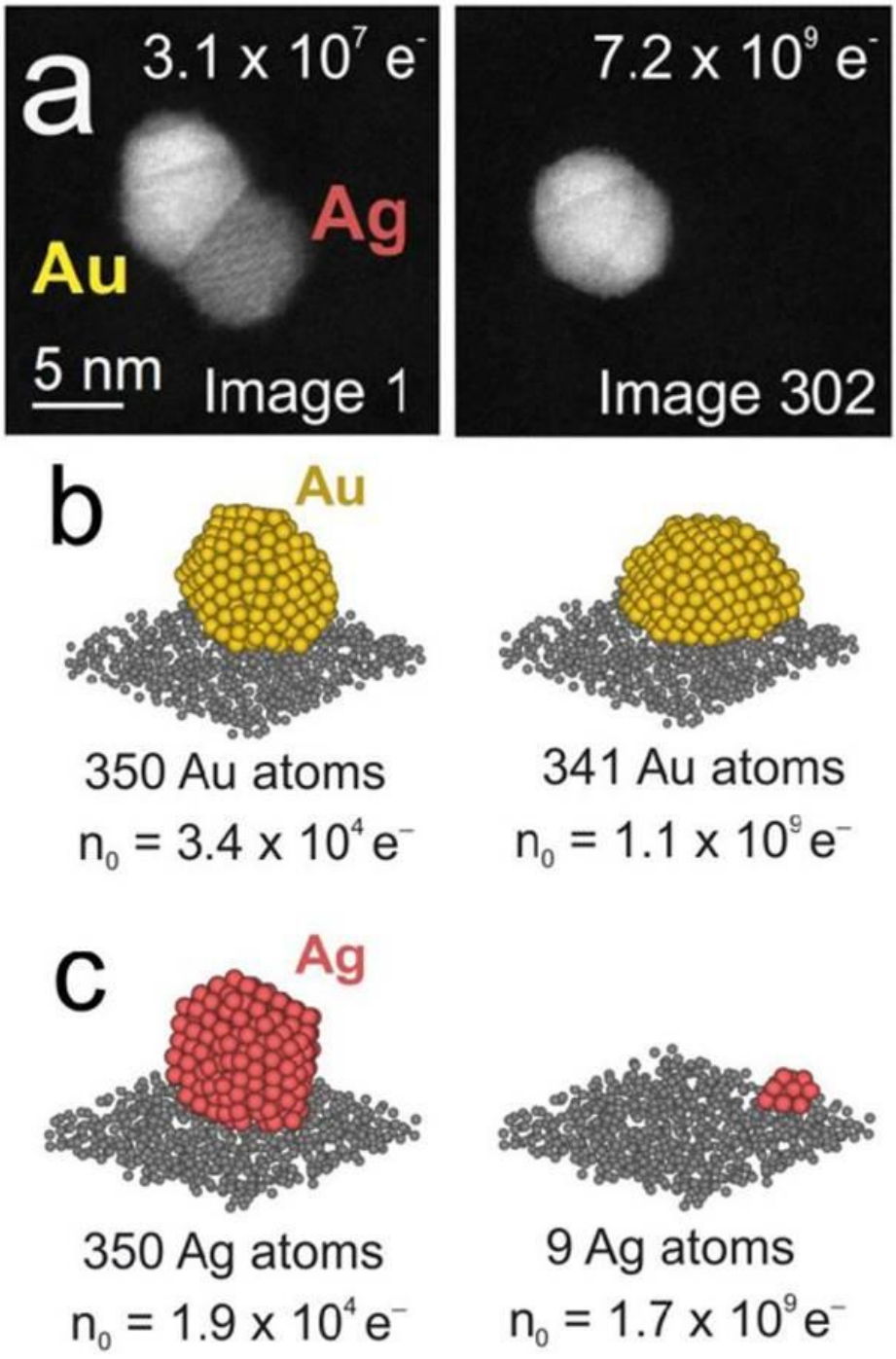
a
3.1 x 10^7 e^-
Ag
Au
5 nm
Image 1
7.2 x 10^9 e^-
Image 302
b
Au
350 Au atoms
n0 = 3.4 x 10^4 e^-
341 Au atoms
n0 = 1.1 x 10^9 e^-
c
Ag
350 Ag atoms
n0 = 1.9 x 10^4 e^-
9 Ag atoms
n0 = 1.7 x 10^9 e^-

IM3.009
Four Dimensional Scanning Transmission Electron Microscopy during the *in situ* Annealing of a CuZrAl Bulk Metallic Glass

T. C. Pekin[1,2,3], C. Gammer[4], C. Ophus[3], R. Ritchie[2,5], A. Minor[2,3]

[1]Humboldt Universtiaet zu Berlin, Physik, Berlin, Germany
[2]University of California, Berkeley, Materials Science and Engineering, Berkeley, United States
[3]Lawrence Berkeley National Laboratory, National Center for Electron Microscopy, Molecular Foundry, Berkeley, United States
[4]Erich Schmid Institute of Materials Science, Leoben, Austria
[5]Lawrence Berkeley National Laboratory, Materials Science Division, Berkeley, United States

Four dimensional scanning transmission electron microscopy (4D-STEM) is a powerful, diffraction-based imaging technique in which many diffraction patterns are acquired sequentially at high speed, for later analysis (1-5). The speed of data acquisition has in turn made *in situ* 4D-STEM possible, allowing for materials to be analyzed as they are dynamically perturbed (4,6).

Recent developments in 4D-STEM analysis have been made in adapting this technique to amorphous materials (6,7), moving beyond fluctuation electron microscopy, which is the traditional technique for amorphous specimens [8,9]. Particularly, the addition of a spatial component to the structural characterization of amorphous materials has allowed for the mapping of structural inhomogeneities that exist in bulk metallic glasses (7,10). Here, we extend 4D-STEM to *in situ* annealing of a bulk metallic glass (BMG) to analyze the relationship between amorphous and crystalline phases during the crystalline phase"s growth in a Cu46Zr46Al8 BMG.

Fig. 1 shows one frame from the *in situ* 4D-STEM time series. While the sample was annealed at 400 C for over two hours on a Protochips heating holder, this virtual bright field image shows the crystallite"s size, from a region that originally had no crystallinity. From the same dataset, the virtual selected area diffraction patterns show the various crystalline orientations present, and their relationship to each other.

Fig. 2 shows subsequent *ex situ* energy dispersive x-ray spectroscopy (EDS) to provide chemical information of these phases. This research shows how 4D-STEM can be used to simultaneously study crystalline and amorphous phases *in situ*, to understand more fully the dynamic processes that govern phase nucleation and growth in amorphous materials (11).

References:

(1) V. B. Ozdol *et al*, Applied Physics Letters 106 (2015), p. 253107.

(2) D. Carvalho *et al*, Scientific Reports 6 (2016), p. 28459.

(3) E. Rauch and M. Véron, Materials Characterization 98 (2014), p. 1-9.

(4) T. C. Pekin *et al*, Scripta Materialia 146 (2018), p. 87-90.

(5) K. Muller *et al,* Applied Physics Letters 101 (2012), p. 212110.

(6) C. Gammer *et al*, Applied Physics Letters 112 (2018), p. 171905.

(7) A. C. Y. Liu *et al*, Physical Review Letters 110 (2013), p. 205505

(8) P. M. Voyles, J. M. Gibson and M. M. J. Treacy, Journal of Electron Microscopy 49 (2000), p. 259-266.

(9) P. M. Voyles and D. Muller, Ultramicroscopy 93 (2002), p. 147-159.

(10) S. Im *et al*, Ultramicroscopy 195 (2018), p. 189-93.

(11) The authors acknowledge support from the Director, Office of Science, Office of Basic Energy Sciences, Materials Sciences and Engineering Division, of the U.S. Department of Energy under Contract No. DE-AC02-05-CH11231 within the Mechanical Behavior of Materials program. Work at the Molecular Foundry was supported by the Office of Science, Office of Basic Energy Sciences, of the U.S. Department of Energy under Contract No. DE-AC02-05CH11231. T.C.P. acknowledges funding from the DFG project BR 5095/2-1 ("Compressed sensing in ptychography and transmission electron microscopy").

Fig. 1: a) Virtual bright field image from the aperture shown in b), with color coded virtual selected area apertures. b,c,e,f) Virtual selected area diffraction patterns. d) Virtual dark field image from e).

Fig. 2: HAADF and EDS maps of crystalline and amorphous region from Fig. 1. Note the chemical segregation between the central Zr and O-rich region, and the Al-rich outer crystalline region.

Fig. 1

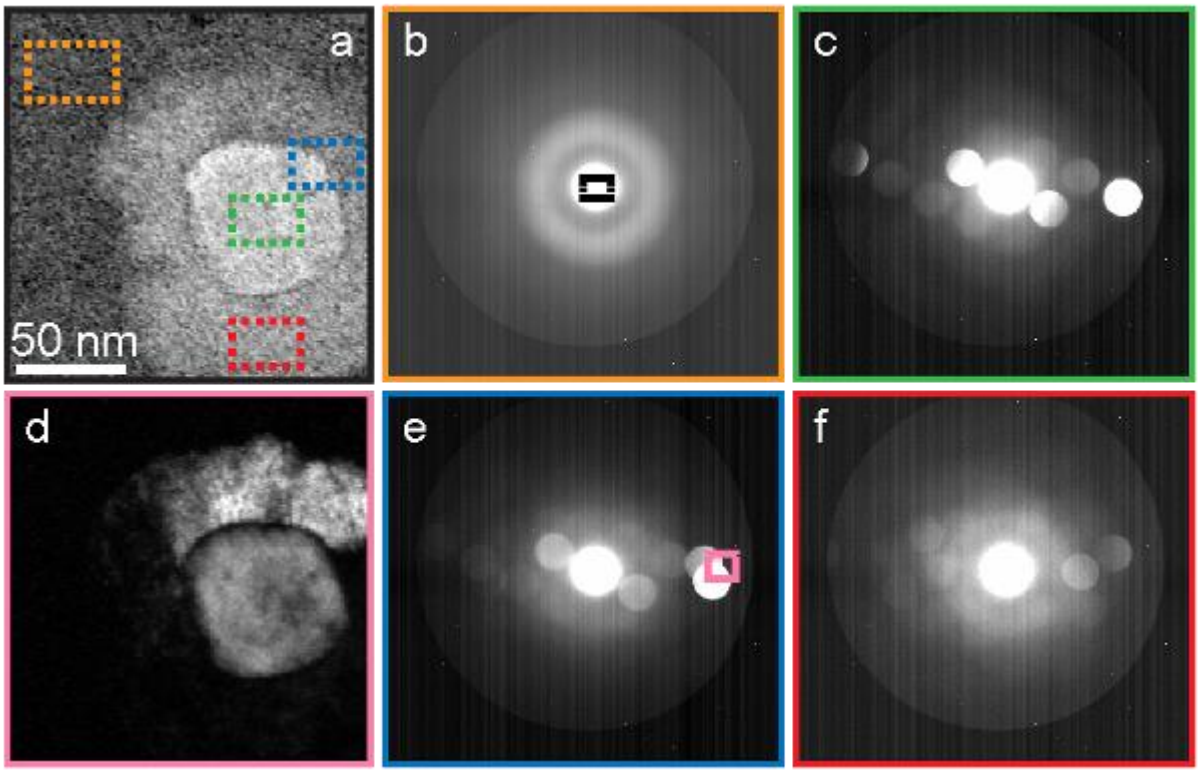

Fig. 2

IM3.LB.P01
In-Situ Electrochemical/Liquid S/TEM Studies of Electrolyte Interphase (SEI) Formation on Glassy Carbon Electrode

W. Dachraoui[1], S. Kranz[1], T. Kranz[1], B. Roling[1], K. Volz[1]

[1]Philipps-Universität Marburg, Department of Physics, Marburg, Germany

During the first charging of lithium-ion battery (LIB), a solid electrolyte interphase is formed on carbon anodes. This interphase layer is very important for the operation of the LIB, where is known as a passivating layer, which avoid further decompositions of the electrolyte by blocking the transport of electrons and solvent molecules, while maintaining the Li^+ conductivity (1). The SEIs are very fragile and reactive, thus, to study their true morphology, structure and composition the use of in situ techniques is highly desirable (2).

In-this study, we have conducted in situ liquid scanning transmission electron microscopy (S/TEM) to investigate in real time the kinetic, morphology and the structure evolution of the SEI during its formation on a glassy carbon (GC) electrode.

In-situ S/TEM experiments were performed using an aberration corrected JEOL JEM-2200FS. The microscope was operated at 200KV in both TEM and STEM modes. The electron beam have been optimized to avoid any effect on our measurements. The TEM holder used is a Protochips poseidon 510 owing both microfluidic flow system and an electrochemical measurement system with three electrodes. The microbattery is loaded by encapsulating the liquid between two silicon Echips; the top one contain a printed electrodes and the bottom one with spacer (500nm). Both Echips have a window with Si3N4 membranes. The electrolyte is flown with very slow rate using the microfluidic system. Cyclic voltammetry (CV) experiments were conducted using an ultra-low current Gamry potentiostat.

After a careful loading of the cell (figure1.a) the liquid electrolyte (LiPF6/EMC/EC/DMC) was injected inside the cell, then cyclic Voltammetry measurements were performed with a scan rate of 100mV/s. The growth of SEI layers on GC electrode during discharge was followed using TEM and high-angle annular dark-field STEM (HAADF-STEM) imaging. A typical HAADF-STEM image of the interface between the electrolyte and the GC electrode is shown in figure 1.b. The formed SEI layer after one cycle can be clearly seen. This layer is composed with two different contrast; an inner layer with a brighter contrast of around 30 nm and an outer layer with less brighter contrast of around 320nm, which is in accordance with the result discussed by T. Kranz et al (1). The contrast is related to the density and thickness of the layers, the inner layer is denser than the outer layer.

In-situ liquid S/TEM is a powerful technique to understand the mechanism involved in the interface formation between a liquid electrolyte and a glassy carbon electrode. The morphology and growth of the SEI layer can be observed in real time during the negative scan and shows the formation of two different layers (inner and outer).

References:

(1) Sebastian Kranz, *et al*. Journal of Power Sources (2019).

(2) Lukas Lutz, *et al*. NanoLetters (2018).

Fig. 1: (a) A schematic presentation showing a cross-sectional illustration of the in situ electrochemical TEM cell with the different electrodes. (b) HAADF-STEM image showing the SEI layers with the corresponding a cyclovoltammogram.

Fig. 1

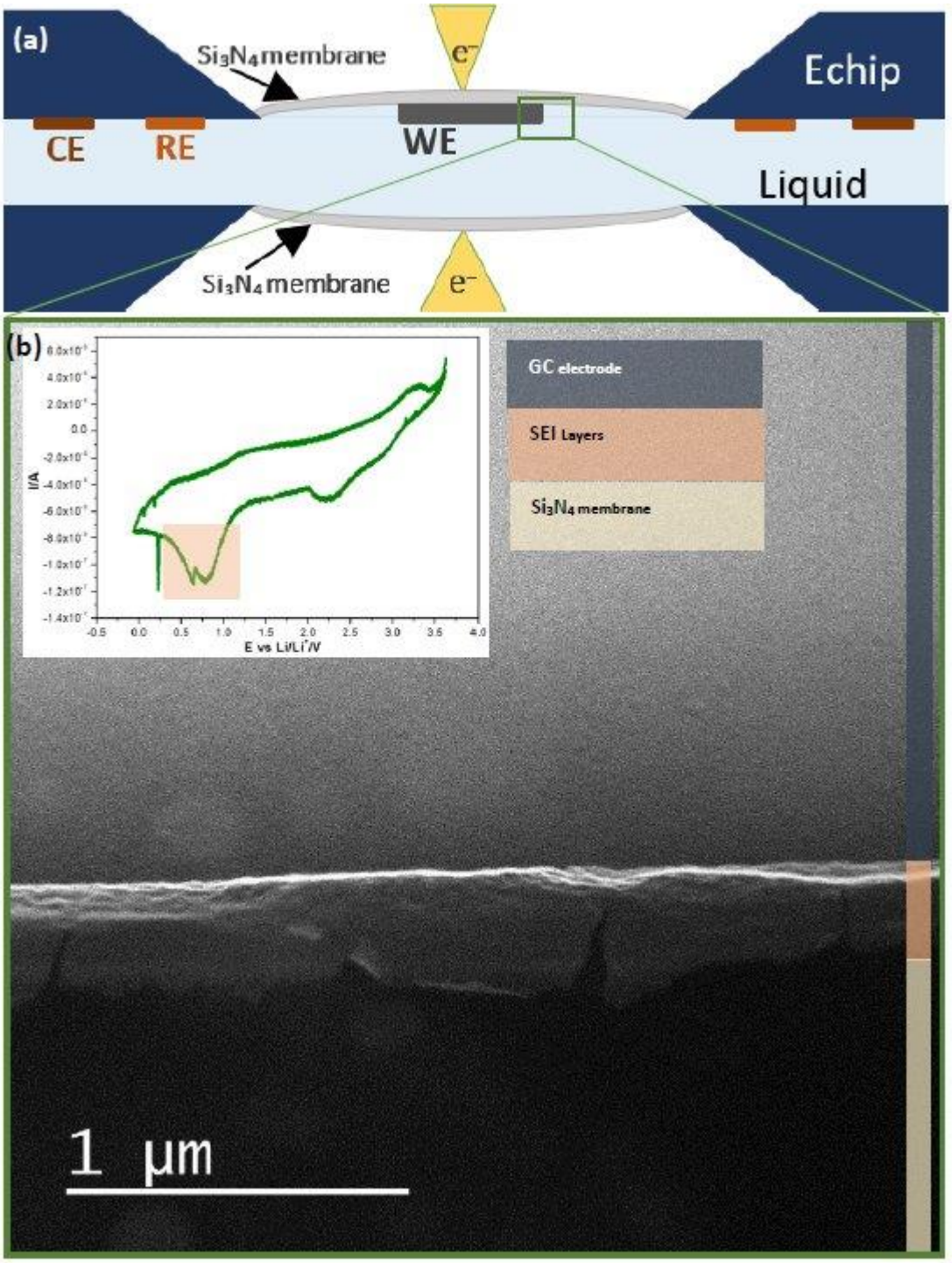
(a)
Si3N4 membrane
e⁻
Echip
CE
RE
WE
Liquid
Si3N4 membrane
e⁻
(b)
I/A
E vs Li/Li+/V
GC electrode
SEI Layers
Si3N4 membrane
1 µm

IM3.LB.P02
In-situ TEM VLS Growth Investigations of GaP Nanowires

M. Widemann[1], D. Krug[1], A. Beyer[1], K. Volz[1]

[1]Philipps-University Marburg, Department of Physics and Materials Science Center, Marburg, Germany

Nanowires (NW), especially those consisting of III/V semiconductor materials, are used for many technical applications, like photonic devices as for example LEDs, photo detectors, lasers and solar cells. A widely used fabrication process of these materials is metal organic vapor phase epitaxy (MOVPE), which is capable for layer growth as well as for nanowire formation. However, structural investigations of the samples are usually carried out post growth. *In-situ* studies of the growth process promise an improvement of the performance of the fabricated materials. But it comes along with several challenges, like the realization of the growth conditions inside a TEM or the incongruent evaporation of the group V compound at elevated temperatures. *In-situ* (scanning) transmission electron microscopy ((S)TEM) allows to investigate dynamic processes, which occur during the growth of III/V semiconductor materials. Gas environmental cells and heating holders enable to supply gases while heating the sample, so that conditions comparable to those during the MOVPE process can be realized.

To this end, a commercially available Protochips *in-situ* system has been modified. In order to allow the usage of toxic and pyrophoric gases, like the precursor gases used in MOVPE growth, a gas mixing system, an appropriate gas monitoring system as well as a gas scrubbing system have been added. A double C_S-corrected JEOL JEM 2200FS operating at 200 kV was used for the TEM observations. Samples were prepared by depositing Au nanoparticles (NP) from a suspension droplet onto a micro electro mechanical system (MEMS) chip. Growth takes place through vapor liquid solid (VLS) growth catalyzed by the Au NP. Precursors used for GaP growth are tertiarybutylphosphine (TBP) and trimethylgallium (TMGa) at partial pressures between 10^{-1} and 10^{-4} hPa and a V/III ratio of around 10. Additionally, N_2 is used as carrier gas at pressures of several hundred hPa. The temperatures at which the growth takes place are in the range of 400°C to 500°C.

Our results show straight growing NW, which change their growth direction after random distances, producing kinking angles. Statistics of these angles show a predominance of 70° angles which are related to twin boundaries in the GaP NW. The growth rate of the NW can be controlled by the partial pressures of the precursor gases and the temperature. Furthermore, our results show that the growth rate is proportional to the surface ratios of the catalyst droplet and the growth plane. That means, that the contact angle of the droplet determines the growth rate.

We demonstrated the safe handling of toxic and pyrophoric gases with an extension of a commercial *in-situ* system, allowing the investigation of dynamic processes during III/V semiconductor growth. Atomic resolved images showing the defects causing the kinking of the NW are still to come and are not easily produced due to single tilt capabilities of the gas cell holder.

IM3.LB.P03
Investigating electrostatic conditions in an environmental TEM

U. Roß[1], V. Roddatis[1], J. Lindner[1], C. Jooss[1]

[1]Georg-August Universität Göttingen, Material Physics, Göttingen, Germany

The in-situ investigation of materials and physical processes is among the fastest growing fields in electron microscopy. The conditions under which such observations are possible are, amongst other factors, limited by the mechanics of signal generation. With the introduction of gases into the vicinity of the thin sample, it has become desirable to investigate in-situ surface electrochemistry (1). However, the electrostatic field distribution around such an experimental setup, as well as the influence of the external potential and ionizing incident electron beam on relevant gases and sample materials is, thus far, not fully explored. The aim of the work presented here is thus to gain insight into the electrostatic environment around a microscopic two-electrode setup at varying gas pressures.

A two-electrode experimental setup was realized inside a 300kV FEI Titan ETEM G2 by mounting ion-milled specimens in a Nanofactory STM holder. A cylindrical tungsten tip was created by electrochemical etching and subsequent focused ion beam shaping, and mounted in the piezo-controlled side of the STM holder to serve as a moveable counter-electrode (Fig. 1a). The instrument was operated in scanning (microprobe) mode at H2O pressures between 10-6 and 0.4 mbar in order to record the electrostatic beam deflection of the STEM transmitted disc on the bottom-mounted CCD camera (4DSTEM) (2). Results are evaluated in analogy to a rigid-shift DPC image (3).

A COMSOL finite elements simulation of the expected field distribution along the tip axis of an isolated two-electrode geometry is shown in Figure 1b. Depending on ionisable gas concentration and tip-sample separation, the potential distribution is expected to vary between a linear gradient and a flat outer potential with a large drop across a surface charge double-layer. The calibration curve for a static beam position DPC measurement inside a 200nm electrode gap in vacuum can be seen in Figure 2a. Electric field steps are resolved with 1V/200nm or better, however the importance of instrument stability is also highlighted by the constant linear drift. Position-dependent measurements are thus only compared against 0V reference curves. Furthermore, the reference-corrected DPC profiles across the electrode gap (Fig. 2b) do not show a drastic dependence on beam position, due to the extended stray field around a microscopic tip. Most notably, the identifiable trend in the DPC deflection runs counter to the modelled behaviour, since the peak deflection is largest at highest pressure, indicating significant beam ionization effects. The behaviour of the electrostatic beam deflection inside an ETEM thus differs from the naïve model picture, and significant adjustments need to be made in order to relate in-situ experiments to ex-situ electrochemistry.

Funding by the Deutsche Forschungsgemeinschaft (DFG) via the CRC 1073, project C02 and Z02, is gratefully acknowledged.

References:

(1) L. Mitra *et. al.*: Ultramicroscopy 170 (2016) 86-95

(2) C. Ophus: Microsc. Microanal. 25, 3 (2019) 563-582

(3) L. Clark *et. al.*: Phys. Rev. A 97 (2018) 043843

Fig. 1: (a) STEM image of two-electrode tip-sample geometry, (b) calculated potential distribution across electrode gap for variable ion concentrations at 0.125V/300nm.

Fig. 2: (a) DPC measurement at static beam position in vacuum, (b) DPC line profiles along the electrode gap, at 20V applied potential, as marked by red arrow in Figure 1.

Fig. 1

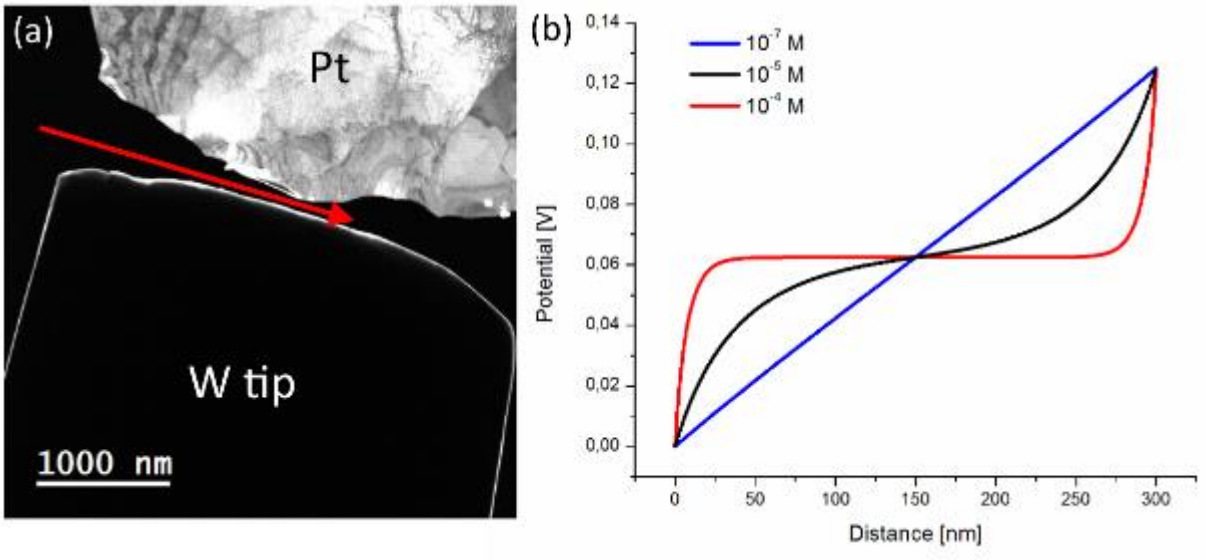
(a)
Pt
W tip
1000 nm
(b)
10-7 M
10-5 M
10-4 M
Potential [V]
Distance [nm]

Fig. 2

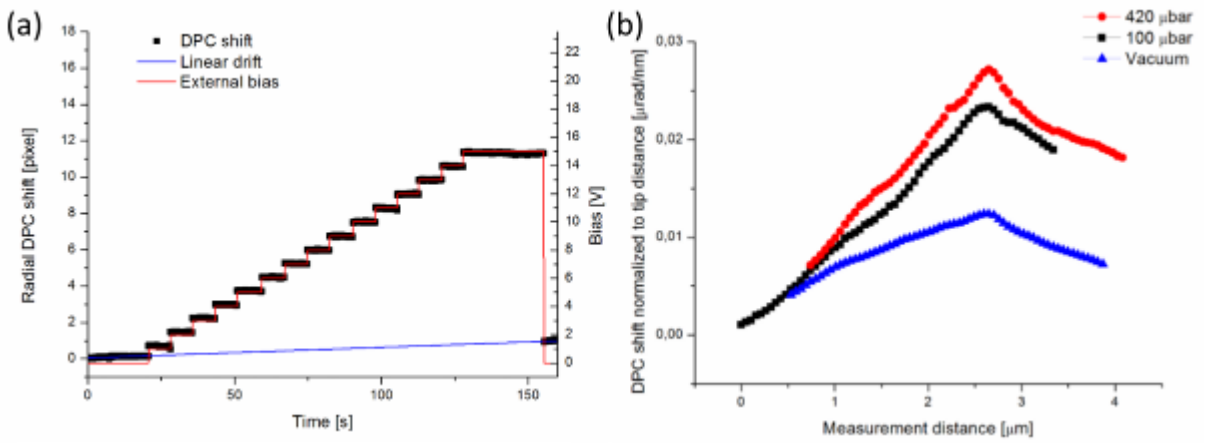
(a)
DPC shift
Linear drift
External bias
Radial DPC shift [pixel]
Bias [V]
Time [s]
(b)
420 µbar
100 µbar
Vacuum
DPC shift normalized to tip distance [µrad/nm]
Measurement distance [µm]

IM3.P001
In-Situ Observation of the Reversible Electrochemical Deposition of Fe in a Transmission Electron Microscope

U. Wolff[1], B. Ambrozic[2], K. Zuzek Rozman[2], K. Leistner[1], K. Nielsch[1], S. Sturm[2]

[1]IFW Dresden, Dresden, Germany
[2]Jozef Stefan Institute, Nanostructured Materials, Ljubljana, Slovenia

Recently, materials science benefits largely from in-situ transmission electron microscopy (TEM) for the investigation of atomistic reaction mechanisms at interfaces. With these novel approaches, the mechanism of dynamical processes can be revealed, reaction kinetics can be quantified, and even electrochemical processes can be studied in-situ in the microscope (1). So far, only the in-situ electrodeposition of noble metals such as Pt and Cu are investigated (2). We are interested in the electrodeposition of Fe, which has regained increasing attention because of the unique catalytic, electronic, and magnetic properties of Fe nanostructures. Tailored shapes of Fe nanoparticles and self-termination phenomena in ultrathin films are currently discussed with regard to the role of hydrogen evolution that accompanies Fe electrodeposition (3).

The detailed atomistic processes involved are still under debate. Therefore, we investigate the initial stages of Fe electrodeposition by in-situ TEM. A glassy carbon electrode has been used as a working electrode and Pt as reference and counter electrode in a liquid TEM cell. The experiments were performed on a JEM-2100 (JEOL Ltd., Tokyo, Japan) microscope. A Poseidon 510 TEM holder (Protochips Inc., Raleigh, NC, USA) was used with a Gamry Reference 600 potentiostat (Gamry Instruments, Warminster, PA, USA) for conducting the electrochemical experiments. The liquid cell consists of two chips with 50 nm thin amorphous SiNx windows, where the smaller one has a spacer height of 50 nm, thus controlling the total thickness of the liquid layer between the two windows. The upper, larger chip contains the glassy carbon working electrode, the Pt reference and the Pt counter electrode. A Fe sulphate aqueous solution at a pH = 2 was used as electrolyte.

Applying a potential of -1.1 V vs. Pt stimulates the electrodeposition of amorphous islands of Fe preferably at the edges of the glassy carbon working electrode, which subsequently crystallize to Fe and FeOx/Fe(OH)x, respectively. The nucleation of the crystal growth occurs instantaneously upon reaching a critical potential. Switching the potential to -0.8 V vs. Pt leads to the dissolution of the previously formed species. The deposition-dissolution process is repeatable for many cycles (Fig. 1). Radial integration of the electron diffraction patterns reveals the presence of crystalline g-Fe (fcc), which was confirmed by fitting the experimental selected area diffraction pattern (SAED, Fig. 2). In order to minimize artifacts such as the beam-induced radiolysis of water or secondary radical chemistry, the electron beam was blocked during the electrodeposition.

We have successfully shown for the first time the in-situ Fe deposition-dissolution process in a liquid TEM cell and affirmed that the Fe particles grow through electrochemical deposition rather than by virtue of the electron beam. The nucleation, morphology, and composition of the deposited Fe particles are discussed (4).

References:

(1) BL Mehdi *et al*, Nano Letters 15 (2015), p. 2168

(2) GZ Zhu *et al*, J. Phys. Chem. C 118 (2014), p. 22111

(3) K Leistner *et al*, Nanoscale 9 (2017), p. 5315

(4) Dr. B Rellinghaus is thanked for many fruitful discussions to this work.

Fig. 1: Series of TEM images showing the reversible deposition and dissolution of Fe particles

Fig. 2: Experimental and fitted SAED pattern revealing the existence of crystalline g-Fe

Fig. 1

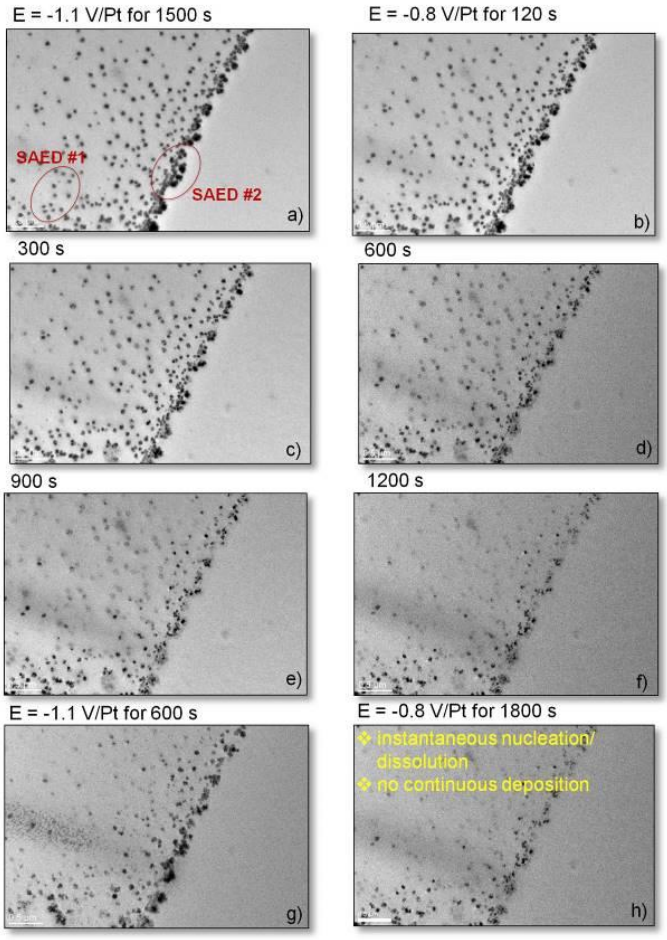

Fig. 2

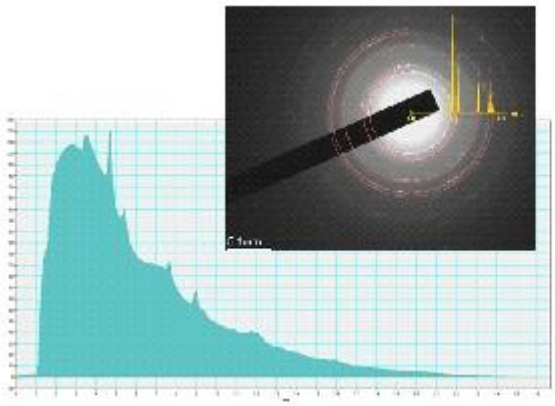

exp. data SAED	γ-Fe (44862)
nm^{-1}	nm^{-1}
4.66	4.75
5.37	5.48
7.62	7.75
8.96	9.09
11.8	11.95
14.06	14.0
16.2	16.05

IM3.P002
In-situ annealing of TiAl multilayers in TEM

M. Seifert[1], E. Lattner[1], S. Menzel[1], S. Oswald[1], T. Gemming[1]

[1]Leibniz Insitute for Solid State and Materials Research, Dresden, Germany

The TiAl alloy is a well-known and widely used material for a broad range of applications e.g. in the field of aerospace, power plant turbines or automotive due to its outstanding mechanical properties and a good corrosion and oxidation resistance. Besides these applications where TiAl is used as a bulk material or thick film, thin TiAl films in the range of a few 100 nm became interesting as electrodes for high temperature surface acoustic wave (SAW) devices (1).

One way to realize the TiAl phase in thin films is to deposit Ti-Al multilayers which are annealed to induce the interdiffusion and phase formation. The aim of this work is to follow these diffusion processes in-situ in the transmission electron microscope and to compare the results with the films which were annealed ex-situ.

Ti-Al multilayers starting with Ti were deposited by magnetron sputtering with an individual thickness of 20 nm and a total thickness of 200 nm on thermally oxidized Si substrates (denoted as $(Ti_{20nm}Al_{20nm})_5$). A 20 nm thick SiO_2 cover layer was used as oxidation barrier. The samples were annealed in an oven at temperatures up to 800 °C for 10 h under high vacuum. The phase formation was verified at room temperature by X-ray diffraction. The local morphology and chemical composition was investigated by TEM together with EDX.

A TEM lamella of such a sample in the as-deposited state was prepared by the focussed ion beam technique and annealed in-situ in the TEM up to 750 °C. The interdiffusion was followed by imaging and measuring of EDX line profiles.

Pole figure measurements revealed a strong formation of the gamma-TiAl phase after annealing at 600 °C under high vacuum. TEM images of the sample show a layered structure of the film consisting of a Ti and Si rich layer at the top of the substrate with a small content of Al_2O_3, followed by TiAl (Fig. 1(a)). It seems that the initial interfaces between an Al and Ti (Al at the bottom followed by Ti) layer disappear during the annealing while the interfaces between Ti and Al remain.

Annealing at 800 °C under high vacuum leads to a complete oxidation of the Al. On top of the substrate there is a thin layer of Al_2O_3, followed by a layer consisting of Ti, Si and O. In the central region of the films there are mainly Al_2O_3 grains. The upper region of the film is a mixture of Al_2O_3 and Ti-Si-O grains (Fig. 1(b)).

The in-situ TEM experiments show a partly interdiffusion of the Ti and Al layers at 200 °C. With increasing temperature the interfaces between the layers become more and more blurred (Fig. 2(a) and (b)). Heating up to 600 °C leads to an almost complete interdiffusion between the layers (Fig. 2(c)).

The gamma-TiAl phase was successfully generated by annealing of Ti-Al multilayers. The films are stable up to 600 °C under HV. Al is oxidized completely during annealing at 800 °C. In-situ annealing of a Ti-Al multilayer TEM lamella allows to follow up the diffusion processes.

References:

(1) E. Lattner, M. Seifert et al. J. Vac. Sci. Technol. A 35(6) (2017) 061603.

Financial support by BMBF IPT 03IPT610Y is gratefully acknowledged.

Fig. 1: CTEM images of a $(Ti_{20nm}Al_{20nm})_5$ film on SiO_2/Si after ex-situ annealing under HV for 10 h at (a) 600 °C and (b) 800 °C.

Fig. 2: STEM images of a $(Ti_{20nm}Al_{20nm})_5$ film on SiO_2/Si (a) in the as-prepared state and after in-situ annealing in the TEM at (b) 400 °C and (c) 600 °C.

Fig. 1

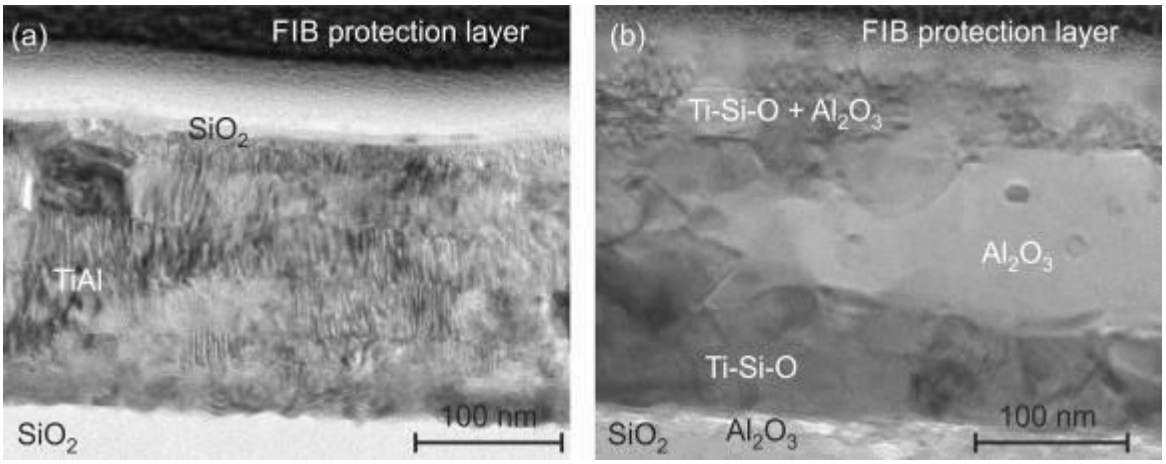
(a)
FIB protection layer
SiO_2
TiAl
SiO_2
100 nm
(b)
FIB protection layer
Ti-Si-O + Al_2O_3
Al_2O_3
Ti-Si-O
SiO_2
Al_2O_3
100 nm

Fig. 2

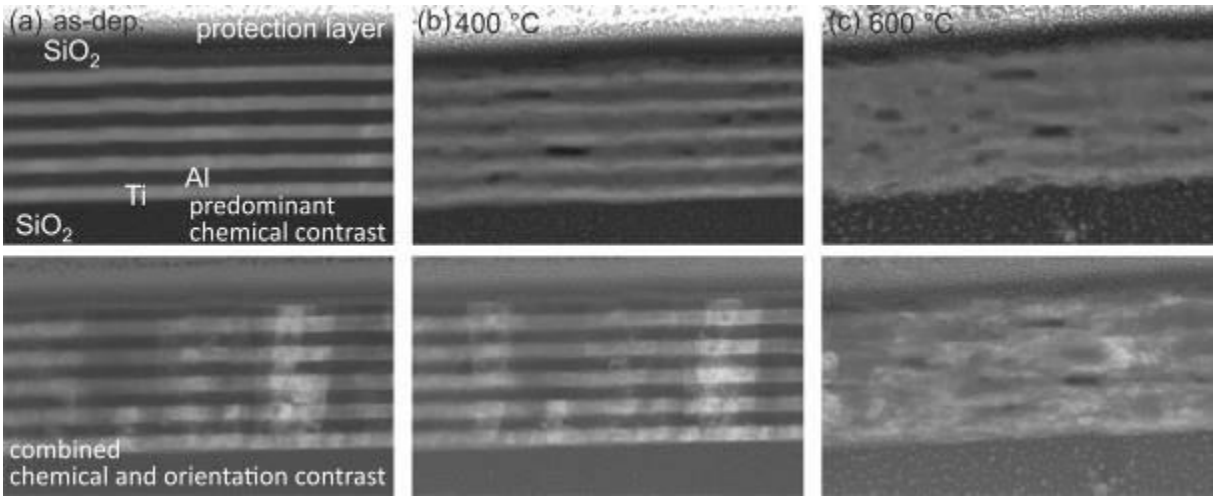
(a) as-dep.
protection layer
SiO_2
Ti
Al
predominant
chemical contrast
SiO_2
(b) 400 °C
(c) 600 °C
combined
chemical and orientation contrast

IM3.P003
Low-dose LC-STEM characterization of the chemical composition of rod-like silica colloids

S. Sadighikia[1], A. Grau-Carbonell [1], T. A. J. Welling [1], F. Hagemans [1], A. Imhof [1], M. A. van Huis [1], A. van Blaaderen [1]

[1]Soft Condensed Matter, Debye Institute for Nanomaterials Science, Utrecht University, Utrecht, Netherlands

The widespread application of anisotropic colloidal particles in the self-assembly of new materials is driven, amongst others, by the ability of such systems to also form colloidal liquid crystal phases. A recently developed model system of (fluorescent) silica rods in our group is a powerful model system to study the self-assembly of such systems in real space (1,2). Although the synthesis of these rod-shaped particles has been studied extensively, there are few studies on their chemical composition. Rod-shaped silica colloids prepared by ammonia-catalyzed hydrolysis and condensation of tetraethyl orthosilicate in water droplets containing polyvinylpyrrolidone cross-linked by citrate ions in pentanol were found to have an inhomogeneous chemical structure along the length of particle (3). Liquid Cell (Scanning) Transmission Electron Microscopy (LC-(S)TEM) is a promising technique to study the chemical composition of these rod-shaped silica particles. However, the presence of high energy electrons may change the conditions of *in-situ* experiments compared to *ex-situ* experiments.

The main objective of this work is to determine the conditions for which the *in situ* chemical etching reaction agrees with what we observe in *ex situ* experiments and to minimize the effect of the electron beam, as well as analyzing the chemical structure of these particles.

Silica rods were synthesized as described by Kuijk et al (1). *In situ* STEM images and movies were acquired using a 200 kV FEI Tecnai 20F TEM. A Hummingbird Scientific Liquid flow holder was used for the liquid cell experiments performed. Freshly prepared NaOH solutions were flowed into the cell for each *in situ* experiment.

The internal chemical structure of silica colloidal particles can be studied by observing their etching behavior in basic conditions. Therefore, we used the LC-(S)TEM technique to study this chemical process at the single particle level in real time. In this work we determined the conditions for which the *in-situ* chemical reaction agreed with what we observed in *ex-situ* experiments, and thus the conditions for which the effects of the electron beam are minimized. The observed inhomogeneities in the chemical structure are the result of the way the rod grows out of a water droplet that is continuously attached to the flat end of the bullet-shaped particles (1,3). Thus, the etching of silica takes place with a varying rate along the length of the particle (Fig. 1). We found that by tuning the pH of the solution in which the particles are dispersed by flowing NaOH basic solutions in the cell, and by using low-dose imaging conditions (~1 e nm^{-2} s^{-1}), one can control the silica etching behaviour during LC-(S)TEM observations.

We expect that using similar low-dose imaging conditions and optimized flow-rates of solutions as found in this work, will allow for investigations of chemical reactions with colloids using the LC-(S)TEM technique with negligible effects of the electron beam and thus as a powerful new technique to also probe varieties at the single particle level.

References:

(1) Kuijk, A., van Blaaderen A. & Imhof, A.. J. Am. Chem. Soc., 133(8)**,** 2346–2349 (2011)

(2) Kuijk, A., Imhof, A., Verkuijlen, M.H.W., Besseling, T.H., van Eck, E.R.H. & van Blaaderen, A.*. Part. Part. Syst. Charact.* 31, 706–713 (2014).

(3) Hagemans, F., van der Wee, E. B., van Blaaderen, A. & Imhof, A.. *Langmuir,* 32**,** 3970–3976 (2016).

Fig. 1

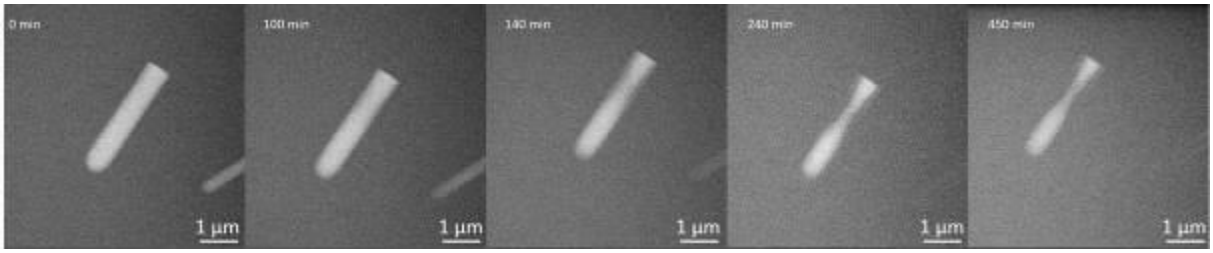

IM3.P004
Single-shot and stroboscopic imaging, diffraction and electron energy-loss spectroscopy in an ultrafast TEM

M. Picher[1], A. Khammari[1], S. K. Sinha[1], T. Lagrange[2], F. Banhart[1]

[1]CNRS IPCMS, DSI, STRASBOURG, France
[2]EPFL, Interdisciplinary Center for Electron Microscopy, Lausanne, Switzerland

In the past decade, transmission electron microscopy has begun to focus on *in-situ* experiments to investigate the fast dynamics of a variety of processes. Prior the inception of Ultrafast microscope technologies, the temporal resolution of such studies has not gone beyond the ms range because of limited acquisition frequencies of the detectors and the small signal/noise ratio at short exposure times. However many processes at the nanoscale occur at much shorter timescales, ranging down to the femtosecond domain.

Higher temporal resolution can now be obtained by using short electron pulses in a pump-probe approach. After excitation by a short laser pulse (pump), the sample is probed with an electron packet having a synchronized, adjustable time delay with respect to the excitation pulse. Repeating the same experiment at different delays allows us to study time-resolved progression of the excitation dynamics in the sample. Two operating modes are possible: (1) the **single shot mode**, where one unique high-intensity pulse with a sufficient number of electrons probes the sample. In this configuration, irreversible transformations can be studied; (2) **the stroboscopic mode**, where a train of pulses is used to build integrated data of the sample dynamics but it is limited to reversible phenomena.

In this contribution, we present the setup and characteristics of an Ultrafast Transmission Electron Microscope (UTEM) where stroboscopic as well as single-shot modes are realized in one instrument (1, 2). In the single-shot approach, up to 109 electrons are compressed into one pulse, leading to electron-electron interaction that results in significant energy broadening and a loss in electron beam coherence. Nevertheless, temporal, spatial and energy resolutions of 7 ns, 20 nm and 30 eV can be achieved (2). In the stroboscopic mode, the pulses contain fewer electrons (< 105) and repulsion effects are less important, allowing resolutions of 2 ps, 0.2 nm and 1 eV, respectively (1).

Due to energy broadening effects, meaningful EELS analysis within the single-shot approach has been thought to be unfeasible. Here, we show that by energy filtering in a modified photoelectron gun under emission conditions for minimizing the energy spread and maximizing the electron collection provides appropriate conditions for EELS in single shot mode (2). Figure 1 shows an **EEL spectrum taken with a single electron pulse of 7 ns duration** from a nickel oxide film. This allows the quantitative analysis of nanomaterials with nanosecond resolution during chemical reactions (fig.2).

As an example for an application, we show the **first comprehensive single-shot studies of fast irreversible chemical reactions in nanometer particles**. The fast high-temperature kinetics of solid-state reactions in nanocrystals is investigated by combined imaging, diffraction and EELS. Reaction rate constants in the microsecond regime are determined with nanosecond precision, and the temporary presence of a short-lived transition state is evidenced.

Funding by the Agence Nationale de Recherche (ANR-11-EQPX-0041) and by the University of Strasbourg Institute of Advanced Studies is gratefully acknowledged.

References:

(1) K. Bücker, *et al.* Ultramicroscopy, 171, 8 (2016)

(2) M. Picher, *et al.* Ultramicroscopy, 188, 41 (2018)

Fig. 1: EELS taken with a single 7 ns electron pulse from a NiO layer on an amorphous carbon film.

Fig. 2: Temporal evolution of the EELS Oxygen over Nickel signal ratio.

Fig. 1

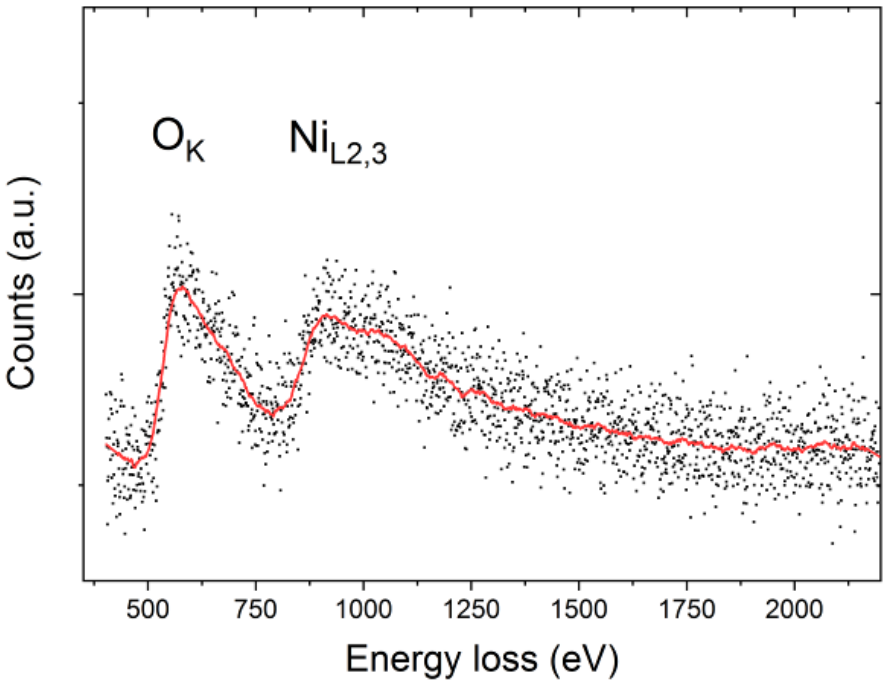
O_K
Ni_L2,3
Counts (a.u.)
500
750
1000
1250
1500
1750
2000
Energy loss (eV)

Fig. 2

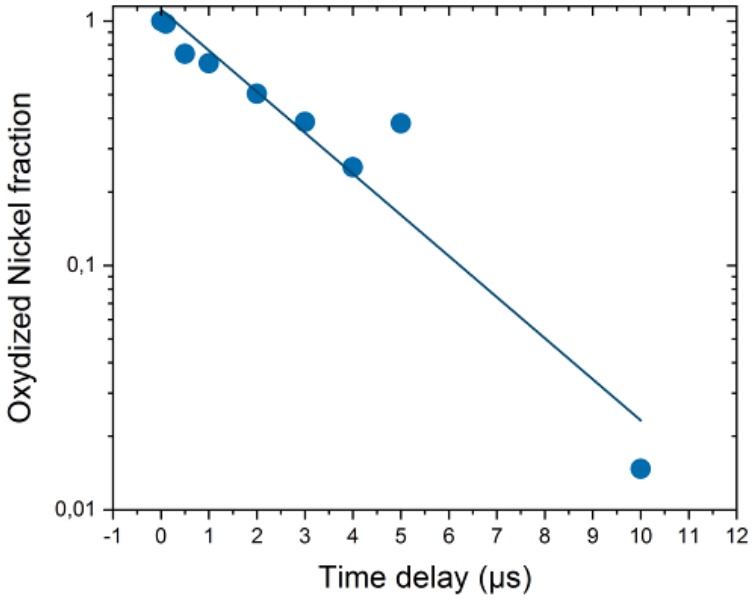
Oxydized Nickel fraction
1
0,1
0,01
-1
0
1
2
3
4
5
6
7
8
9
10
11
12
Time delay (µs)

IM3.P005
EDX measurements in state-of-the-art low vacuum SEM

C. Fahrenson[1], D. Berger[1]

[1]Technische Universität Berlin, Zentraleinrichtung für Elektronenmikroskopie, Berlin, Germany

EDX is a standardised method to determine the qualitative and quantitative element distribution in SEM. For many solid materials like metals, these measurements are performed in high vacuum. But for many specimens, that are non-conductive, beam sensitive or hydrated, the examination in high vacuum requires extensive specimen preparation steps. Polymers, ceramics and building materials are well-known examples of this kind of specimens that need to be coated with a thick layer of gold or carbon to be suitable for high vacuum SEM. This coating has a strong influence on the EDX-analysis, especially if the specimen it selves contains Au and C or if the X-rays are strongly absorbed in the coating. Alternatively, these specimens can be examined in low vacuum condition. The residual gas molecules help to remove charging and heating of the specimen. Thereby even EDX-measurements at high electron energies and high currents of polymers and building materials are feasible.

For this reason, the low vaccum SEM has been remarkable improved in the last years by adding an additional aperture (beam sleeve, see fig. 1) below the objective lens that separates the chambers low vacuum from the high vacuum of the electron column. This aperture being close to the specimens surface allows for high resolution imaging as well because the electron path in low vacuum is as short as possible. At the same time, the Inlens detectors still are usable and the lowest magnification is not over-restricted. Nevertheless, the pressure orifice and its mounting might shadow the EDX-detector and force the use of larger working distance (WD).

The aim of this contribution is to analyse the geometric conditions, restrictions and benefits of EDX-measurements in low vacuum SEM partly in comparison to high vacuum conditions. We used a GeminiSEM G500 by ZEISS equipped with a Bruker Quantax X-Flash 6|60 EDX-system at pressures up to 500 Pa. The obtained results are valid for low vacuum SEM and EDX-systems of other manufacturers accordingly.

The shadowing of the EDX-detector by the holder of the beam sleeve reduces the solid detection angle. Therefore, it is essential to find the appropriate position of the EDX detector during installation and an appropriate WD during operation. Figure 2 shows the method to determine the shadow-free specimen position by a WD-scan.

In the next step it is necessary to check the accurateness of the element quantification. On one hand, we successfully proofed that the EDX quantification result is not changed during the WD-scan since the WD is (automatically) integrated into the quantification routine. On the other hand, we compared the EDX-performance in different vacuum conditions. Figure 2 shows for comparison a WD-scan without beam sleeve in high vacuum mode as well. Figure 3 reveals the insignificant differences of the EDX-spectra in low vacuum (500Pa) and fine vacuum condition (30Pa). Although the intensity of the EDX-signal is reduced at low vacuum it is proofed that the EDX-spectra are similar and that the EDX-quantification is stable. Finally, we examined the negligible influence of the X-ray fluorescence of the increased number of nitrogen molecules in low vacuum on the EDX-quantification of nitrogen-containing specimens.

Fig. 1: LowVacuum-SEM with additional aperture

Fig. 2: Shadowing of the EDX-Detector by the beam sleeve in dependence of WD, Specimen: brass @ 20 kV

Fig. 3: Comparison of EDX-spectra with different vacuum

Fig. 1

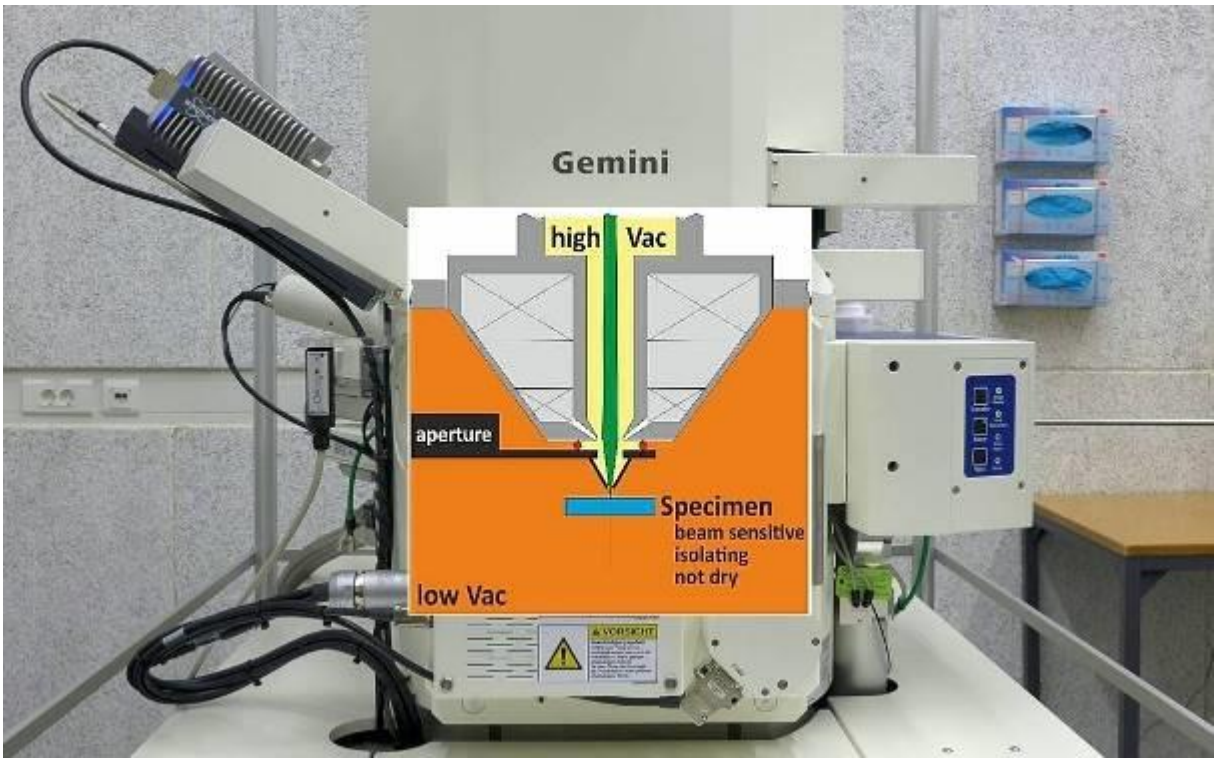
Gemini
high Vac
aperture
Specimen
beam sensitive
isolating
not dry
low Vac

Fig. 2

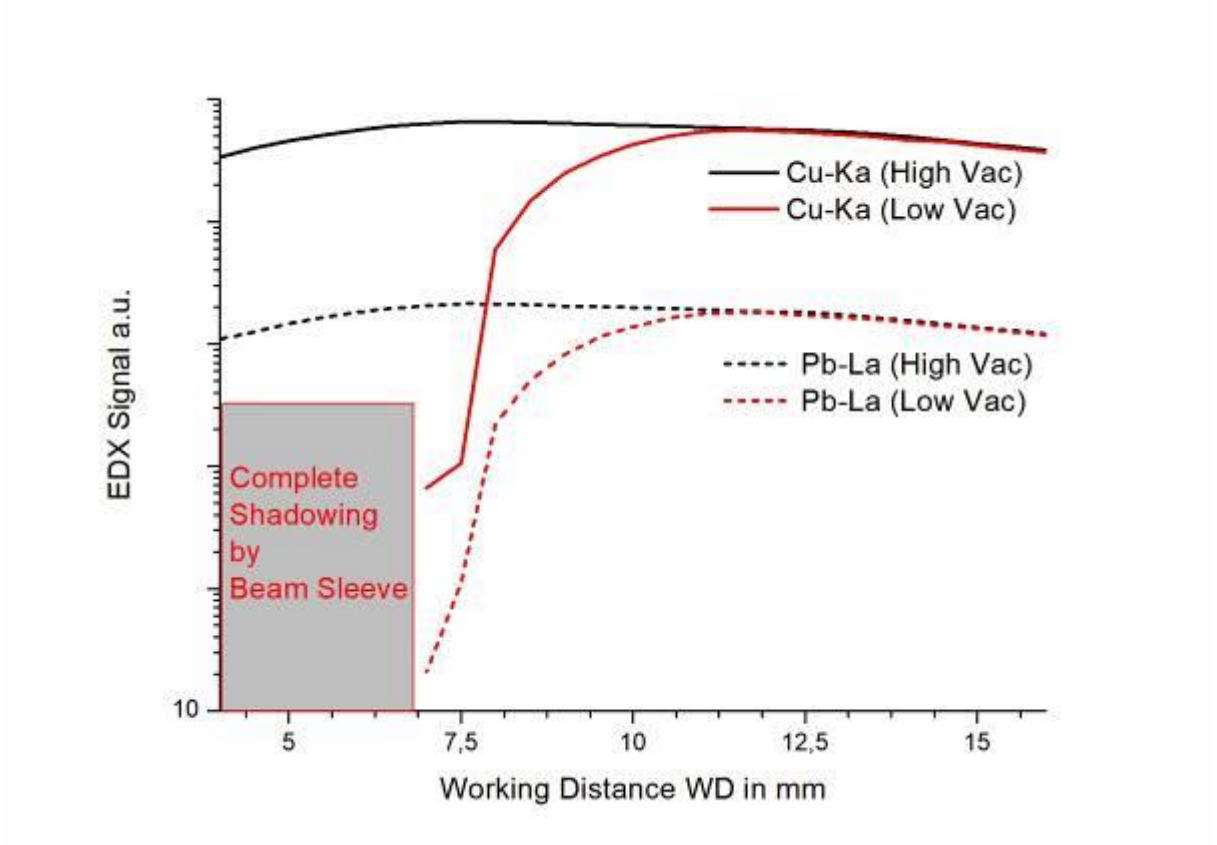
Cu-Ka (High Vac)
Cu-Ka (Low Vac)
Pb-La (High Vac)
Pb-La (Low Vac)
Complete
Shadowing
by
Beam Sleeve
EDX Signal a.u.
10
5
7,5
10
12,5
15
Working Distance WD in mm

Fig. 3

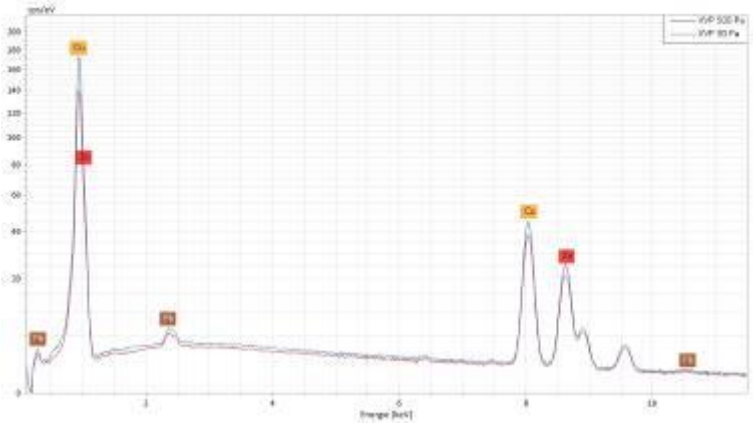

IM3.P006
Correlative In-Situ Analysis on the Nanoscale by combination of AFM and SEM

C. H. Schwalb[1], P. Frank[1], S. Hummel[1], J. Sattelkov[2], R. Winkler[2], G. Fantner[3], H. Plank[2]

[1]GETec Microscopy GmbH, Vienna, Austria
[2]University Graz, Institute for Electron Microscopy and Nanoanalysis, Graz, Austria
[3]EPFL, Laboratory for Bio- and Nano-Instrumentation, Lausanne, Switzerland

The combination of different analytical methods into one instrument is of great importance for the simultaneous acquisition of complementary information. Especially the in-situ combination of scanning electron microscopy (SEM) and atomic force microscopy (AFM) enables completely new insights in the micro and nano world. In this work, we present a novel AFM – the AFSEM - that can be easily integrated into the high-vacuum environment of almost any scanning electron microscope (SEM) or other host system (e.g. dual beam microscopes). It allows direct in-situ combination of these complementary techniques due to the simultaneous operation of SEM and AFM inside the vacuum chamber. (1,2) Therefore, SEM imaging, chemical information by EDX, real 3D topography, phase information, mechanical, electrical, and magnetic properties by AFM can be combined in an easy and interactive way. Furthermore, due to the open design it can be combined with additional add-ons, e.g., tensile stages, nano-indentors (2) or nano-manipulators (Figure 1a).

We will present a variety of case studies to highlight the advantages of correlative in-situ analysis for different materials. We show results for *in-situ* electrical characterization of nanostructures by combining SEM and conductive AFM measurements for dose-dependent conductivity measurements of nanogranular Pt(C) structures after focused electron beam induced processing (Figure 1b). In addition, we will demonstrate the analysis of bone tissue and show how the SEM allows to quickly identify the area of interest, in this case the lacunae on the surface of the bone structure (Figure 2a). The AFM then provides the real 3D topography inside the lacunae (Figure 2b) and enables the detailed analysis of the collagen fibers within the lacunae area (Figure 2c+d). Finally, we show results for monolayer growth characterization of 2D materials, failure mechanic analysis by in-situ tensile stress measurements of metal wires or polymer structures.

Based on the broad variety of applications regarding the characterization of different materials and devices we anticipate the AFSEM to be one of the driving characterization tools for correlative SEM/AFM analysis in the future.

References:

(1) D. Yablon, P. Werten, M. Winhold and C.H. Schwalb, Microscopy and Analysis 31(2) 14-18 (2017)

(2) J. Kreith, T. Strunz, E.J. Fantner, G.E. Fantner and M.J. Cordill, Rev. Sci. Instr. 88 053704 (2017)

Fig. 1

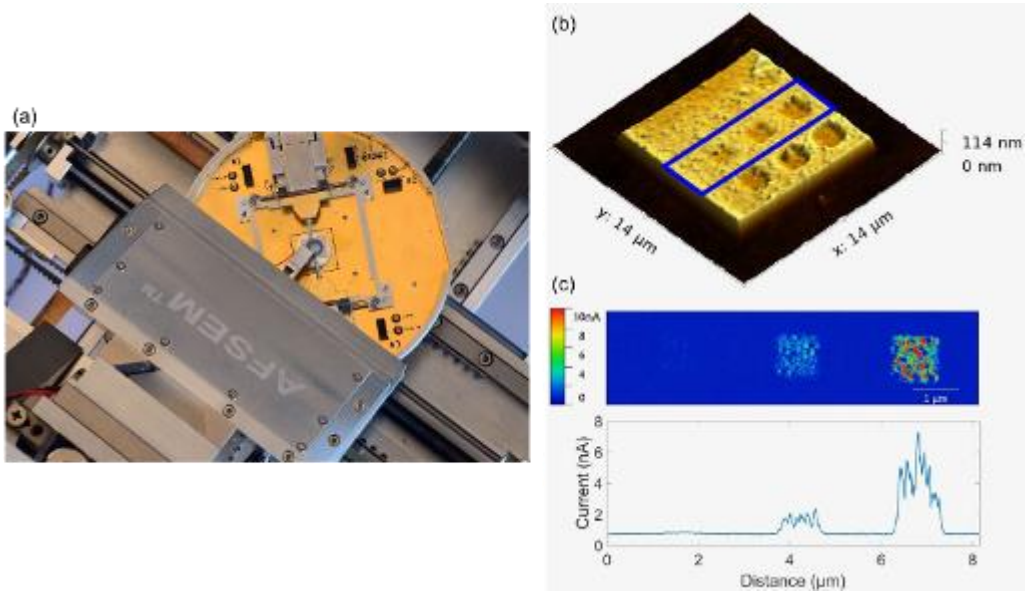
(a)
(b)
114 nm
0 nm
y: 14 µm
x: 14 µm
(c)
Current (nA)
Distance (µm)

Fig. 2

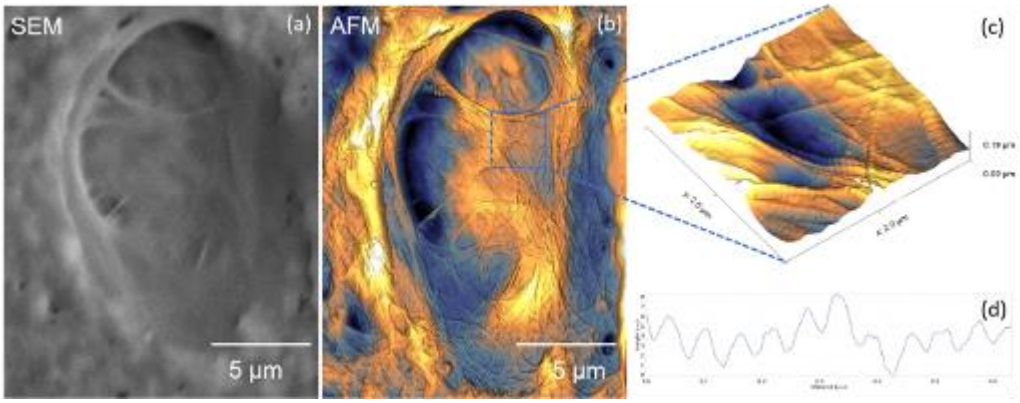
SEM
(a)
5 µm
AFM
(b)
5 µm
(c)
(d)

IM3.P007
Real-space Imaging of Phase Transitions Using Ultrafast Transmission Electron Microscopy

T. Domröse[1], T. Danz[1], C. Ropers[1]

[1]Georg-August-Universität Göttingen, 4th Physical Institute, Göttingen, Germany

Ultrafast Transmission Electron Microscopy (UTEM) provides insights into ultrafast dynamics within a laser-pump/electron-probe scheme. It enables nanoscale imaging of structural, electronic and magnetic dynamics in heterogeneous materials in both real and reciprocal space, and with femtosecond temporal resolution (1). Here, we present an ultrafast and spatially resolved investigation of charge density wave (CDW) dynamics in the transition metal dichalcogenide tantalum disulphide (1T-TaS_2).

Employing dark-field microscopy, spatially resolved order parameter mapping of structural phase transitions is conducted within a stroboscopic laser-pump/electron-probe scheme. The phase transition induced by laser excitation is followed with femtosecond temporal and nanometer spatial resolution. The laser fluence dependence of the transition process and subsequent relaxation channels are investigated.

Due to strong electron-phonon coupling and the quasi two-dimensionality of the crystalline structure consisting of trilayers, several transition metal dichalcogenides (TMCDs) such as 1T-TaS_2 favor periodic modulation of the electron density, i.e., the formation of charge density waves (2). A periodic lattice distortion (PLD) coupled to the CDW introduces a crystalline superlattice, apparent in diffraction patterns via corresponding satellite spots coordinated around the Bragg spots of the undistorted crystal lattice. For example, 1T-TaS_2 undergoes several phase transitions linked to CDW formation, with PLD dynamics accessible by UTEM down to the femtosecond time-scale. The Göttingen UTEM thereby provides a spatial resolution down to the sub-nanometer regime with down to 200 fs temporal resolution by triggering photoemission of probing electron pulses from a Schottky emitter (3). Thin films of 1T-TaS_2 in a sample design ensuring sufficient thermal coupling to a heat sink allow for spatially resolved mapping of transient lattice distortions associated with the NC phase over a range of excitation fluences.

Real-space images of the phase transition process reveal structural evolution over different time scales after laser excitation. Following a global suppression of the NCCDW amplitude within a few hundreds of femtoseconds, parts of the sample experience an NC CDW recovery on the picosecond time scale. The remainder of the sample is subject to formation of domains of the incommensurate (IC), high-temperature type, which subsequently grow over the course of a few hundreds of picoseconds. Relaxation of the system to the initial state takes place after a few nanoseconds.

In conclusion, we present the first real-space femtosecond imaging of a phase transition in UTEM. In the future, we expect the method to provide further insights into spatiotemporal, ultrafast dynamics on the nanoscale.

References:

(1) A.H. Zewail, Science 328, pp. 187-193 (2010)

(2) Rossnagel, K., Journal of Physics: Condensed Matter 23(21), 213001 (2011)

(3) A. Feist et al., Ultramicroscopy 176, 63 (2017)

IM3.P008
Large Chamber-SEM in-situ investigation of bending-induced mechanisms

A. Dunlap[1], A. Aretz[1], A. Schwedt[1]

[1]RWTH Aachen, Central Facility for Electron Microscopy, Aachen, Germany

Formability of metals reaches its limits mainly due to the mechanisms of damage, strain hardening and residual stresses. When designing a process route to produce metal parts, the damage is often not considered, only failure. The focus of a transregional collaborative research center (TRR 188), including groups of RWTH Aachen University and TU Dortmund University, is to investigate specifically the damage evolution in forming processes.

To increase the control of the metal forming process, a better understanding of the influencing physical mechanisms during deformation is necessary. It will lead to an enhanced process design with optimal parameters, regarding damage. This understanding is achieved by performing in-situ bending tests.

The material used for this study is a 16MnCrS5 ferritic-pearlitic steel, typically used in cold forming with high concentration of manganese sulfides, since ductile damage is most likely to nucleate at inclusions. A large chamber scanning electron microscope (LC-SEM) allows an easy implementation of various in-situ devices. To investigate the physical mechanisms of 16MnCrS5, an in-situ bending device is used. Bending samples are cut out of rods and the surface under tensile loading is prepared for SEM observation. The sample is notched to introduce an area with increased stress, which is observed. The bending is performed intermittently under static and cyclic load. Images are recorded after every step and DIC is used to gain information on surface strains. Afterwards ex-situ electron backscatter diffraction (EBSD) is performed on selected samples to obtain information on strain hardening and dislocation density.

In situ observation of the surface, bent under static tensile loading reveals the gradual formation of shear bands, the flow of material and nucleation of damage in form of voids at MnS inclusions (Figure 1). DIC shows a relatively low surface tension in the direct vicinity of voids. Due to the good formability of the material cracks or failure do not occur. EBSD measurements ranging from tensile to compressive loading along a bent and cross-sectioned sample reveal the neutral axis with a low dislocation density. Voids are more likely to appear on the side under tensile loading. Cyclic loading shows no flow of material, but a small decohesion of MnS from the matrix material, most likely to lead to ductile damage creation.

Figure 1: DIC analysis of a 16MnCrS5 bending sample. After a static displacement of 5 mm, shear bands and the formation of von Mises strain is observable. The surface strain in the vicinity of a nucleating void remains low (as marked by the red circle).

Fig. 1

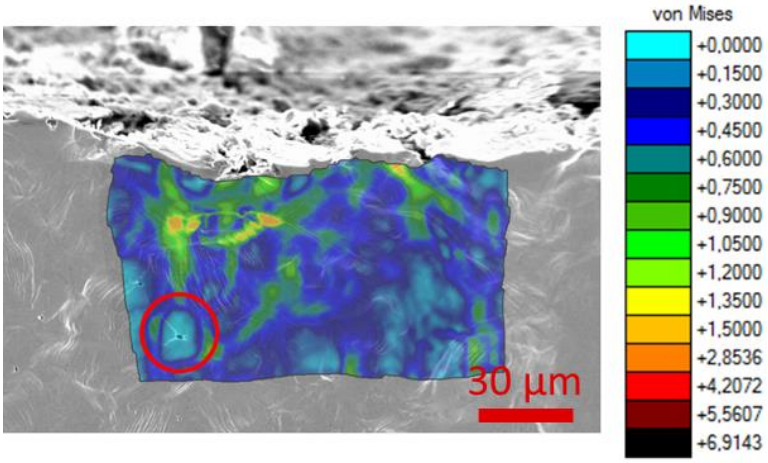

IM3.P009
Quasi in situ STEM investigation of structural changes in orthorhombic $(Mo,V)O_x$

L. Masliuk[1], A. Trunschke[1], R. Schlögl[1,2], T. Lunkenbein[1]

[1]Fritz-Haber-Institut der Max-Planck-Gesellschaft , Inorganic Chemistry , Berlin, Germany
[2]MPI für Chemische Energiekonversion, Mülheim a.d.R., Germany

Owing to their complexity in composition and structure relevant heterogeneous catalysts are difficult to analyze. Moreover, the performance of a catalyst is determined by the delicate interplay of bulk and surface, atoms mobility as well as defects chemistry. Tailoring of heterogeneous catalysts, therefore, requires unprecedented atomistic knowledge of the applied functional materials. Scanning transmission electron microscopy (STEM) can deliver local and visual descriptions of the composition, geometry and electronic structure of the catalyst in the bulk and at the surface with atomic resolution. To track the structural response of a catalytic system to the applied conditions different *quasi in situ* and *in situ* TEM approaches have been developed.(1-3) However, the interpretative depth of the obtained micrographs might be limited by drawbacks regarding the reaction pressure, electron-gas and electron-matter interaction, conversion detection and/or limitations in resolution.

In order to obtain relevant information about the working structure a catalyst has to be exposed to catalytic relevant conditions (gas composition, pressure, temperature), which also includes the detection of conversion, and identical locations have to be compared.

To fulfill these prerequisites we have developed a *quasi in situ* TEM grid reactor that combines relevant, homogeneous and well-controlled conditions for all catalyst particles at ambient pressure with high resolution imaging of identical particles.(3) Furthermore, the catalytic conversion can be detected by using an ultra-sensitive proton-transfer reaction mass spectrometer (PTR-MS). We have examined the structural response of an XRD phase-pure, but defective orthorhombic $(Mo,V)O_x$ (4), which is an active and selective material for the oxidative dehydrogenation of ethane (ODE), to different atmospheres via both *quasi in situ* and *is situ* TEM.

In all cases we have observed nanoscale structural rearrangements in defect-rich areas, such as surface and intergrowth, with ultimate resolution. Differences in the structural responses can be correlated to the environment and, in case of *in-situ* heating imaging, to pressure-gap related effects.

The observed structural dynamics of the catalyst can be further linked to stability and performance. As a consequence catalytic performance and lifetime may be enhanced.

Figure 1: a) STEM image of a pristine orthorhombic $(Mo,V)O_x$ particle oriented along [001]; (b) schematic view of the TEM grid reactor; (c) STEM image of the identical location after heat treatment in nitrogen atmosphere.

References:

(1) Creemer, J. F.; Helveg, S.; Kooyman, P. J.; Molenbroek, A. M.; Zandbergen, H. W.; Sarro, P. M. Journal of *Microelectromechanical Systems*, 19, 254-264 (2010).

(2) Janbroers, S.; Louwen, J. N.; Zandbergen, H. W.; Kooyman, P. J. *Journal of Catalysis*, 26, 235-242 (2009).

(3) Masliuk, L.; Swoboda, M.; Algara-Siller, G.; Schlögl, R.; Lunkenbein, T. *Ultramicroscopy*, 195, 121-128 (2018).

(4) Masliuk, L.; Heggen, M.; Noack, J.; Girgsdies, F.; Trunschke, A.; Hermann, K. E.; Willinger, M. G.; Schlögl, R.; Lunkenbein, T. *The Journal of Physical Chemistry C*, 121, 24093-24103 (2017).

Fig. 1

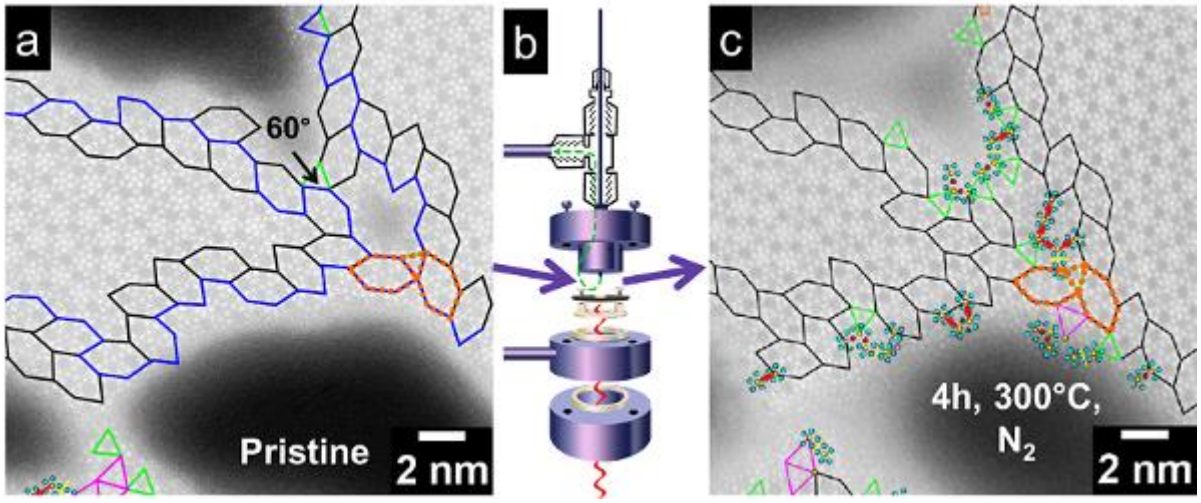

IM3.P010
Evaluation of sample damage by electron beam in atomic resolution elemental analysis

I. Ohnishi[1]

[1]JEOL Ltd., EM Business Unit, Tokyo, Japan

Recent progress of aberration corrected scanning transmission electron microscope (STEM) allows us to conduct atomic resolution elemental mapping with energy dispersive X-ray spectroscopy (EDS) and/or electron energy loss spectroscopy. In the mapping, a sample receives more damage than that in imaging due to its larger probe current. However, detail of the damage at atomic resolution level has been still poorly understood. In this paper, we investigated the rate of sample damage for a Si_3N_4 crystal at atomic resolution using a technique of time-resolved EDS mapping, in order to estimate threshold of conditions and reduce sample damage.

In our experiments, we used an aberration corrected 300 kV S/TEM (JEM-ARM300F) equipped with a cold field emission electron gun and two windowless silicon drift detectors, whose sensor areas are 158 mm^2 and total solid angle of X-ray collection is 2.21 sr (1). Sample lamella of Si_3N_4 poly-crystal was prepared by Ar^+ ion milling (ION SLICER^{TM}). The thin area of a grain oriented to [0001] was used for analyses in this study. The thickness was measured to be approximately 50 nm by Zeta-factor method (2). To estimate the rate of sample damage, we measured a decay of N and Si X-ray (Kα) gross intensities, using the time-resolved X-ray mapping software (3) at 200 and 300 kV with probe currents of ~30 and ~100 pA. The scanning areas, map sizes, and dwell times were 4 x 4 nm^2, 256 x 256 pixels, and 10 μs/pixel, for the mapping.

Fig. 1 shows decay profiles and decay rates of N and Si Kα gross intensities of the sample with ~29 pA at 200 kV. The decay rate of N is slightly faster than that of Si, and this tendency is similar among all the experimental conditions. Figures 2 and 3 show the decay profiles of sum of N and Si X-ray on different accelerating voltages and probe currents. The decay rates, total doses at the final scans and annular dark field (ADF) images at the first and final scans for the profiles are also shown in Figures 2 & 3. The decay rate of 200 kV is slower than that of 300 kV under the same probe current (Fig. 2). The ADF images indicate that the image after mapping at 300 kV shows darker than that at 200 kV (Fig. 2). And the decay rates under the same acceleration voltages are almost similar between smaller and larger probe current (Fig. 3). The ADF image with smaller probe current in Fig. 3 shows less damaged than that with larger current even under the same total dose.

The results suggest that lower accelerating voltage and smaller probe current are effective for reduction of the damage of Si_3N_4, and obtaining a good atomic resolution elemental map, as showing the results with 29 pA at 200 kV in Fig. 4.

References:

(1) I. Ohnishi *et al.*, e-J. Surf. Sci. Nanotech. 16 (2018), 286-288.

(2) M. Watanabe *et al.*, Ultramicroscopy 65 (1996), 187-198.

(3) I. Ohnishi *et al.*, Microsc. Microanal. 18 (S2) (2012), 1052-1053.

Fig. 1: Decay profiles and decay rates of N and Si Kα gross intensity with 29 pA at 200kV for Si_3N_4 (0001).

Fig. 2: Decay profiles and decay rates of the sum of N and Si Kα gross intensity with 85 pA at 200 kV and 95 pA at 300 kV for Si_3N_4 (0001).

Fig. 3: Decay profiles and decay rates of the sum of N and Si Kα gross intensity with 85 and 29 pA at 200 kV for Si_3N_4 (0001).

Fig. 4: Atomic resolution STEM image and elemental maps for Si_3N_4 (0001) with 29 pA at 200 kV. (a) STEM ADF image, (b) N Kα, (c) Si Kα, and (d) overlay of N and Si maps. Maps were processed by Wiener filter.

Fig. 1

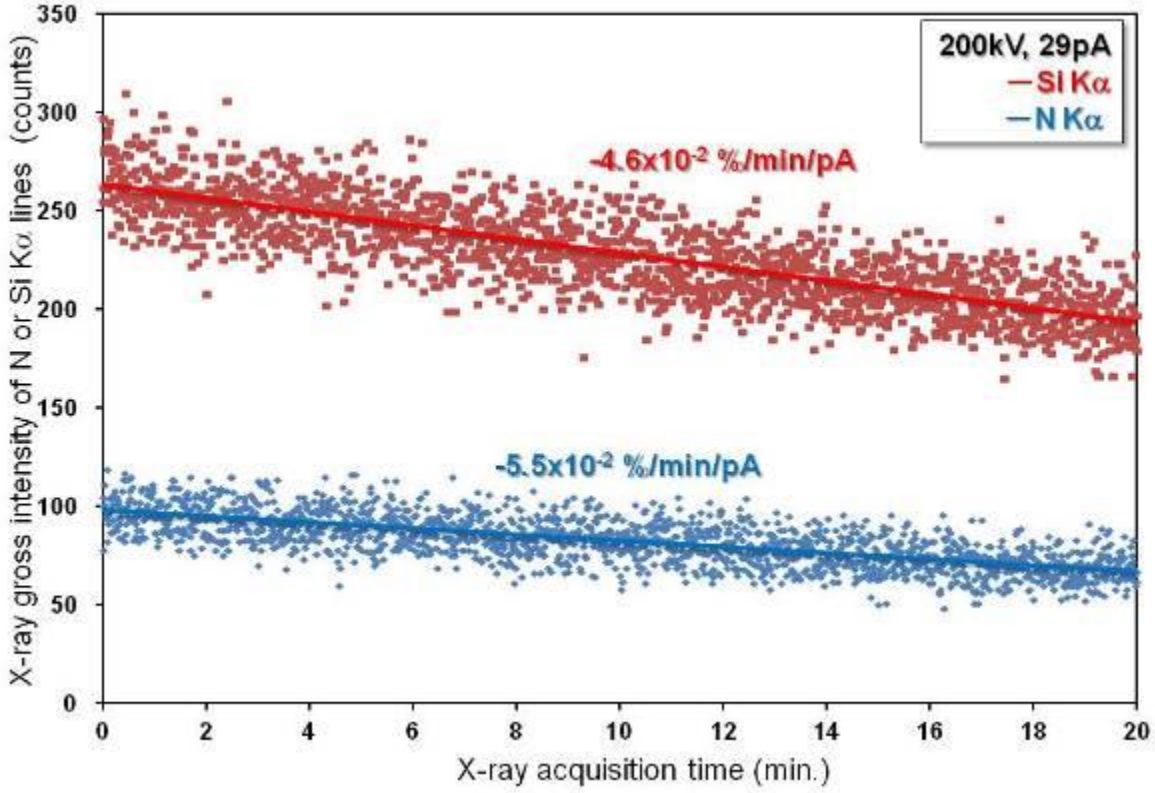
200kV, 29pA
Si Kα
N Kα
-4.6x10-2 %/min/pA
-5.5x10-2 %/min/pA
X-ray gross intensity of N or Si Kα lines (counts)
X-ray acquisition time (min.)
0
50
100
150
200
250
300
350
0
2
4
6
8
10
12
14
16
18
20

Fig. 2

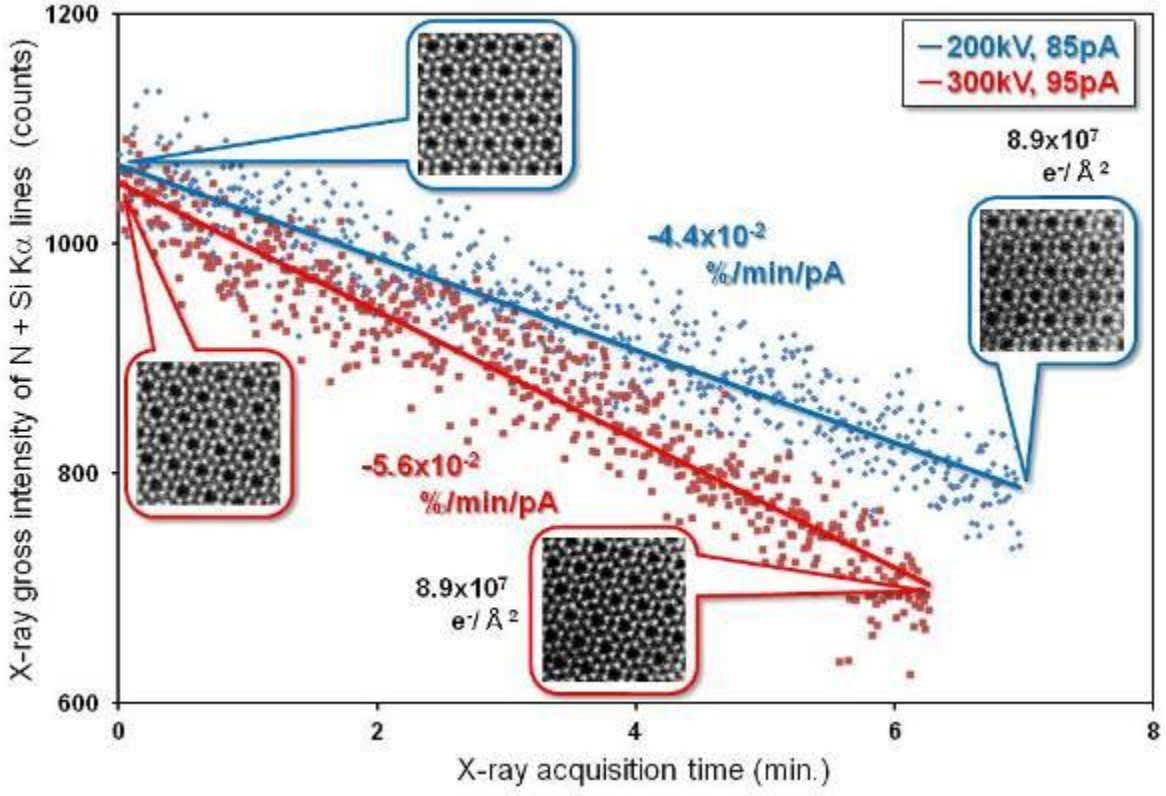
200kV, 85pA
300kV, 95pA
8.9x10⁷ e⁻/Å²
-4.4x10-2 %/min/pA
-5.6x10-2 %/min/pA
8.9x10⁷ e⁻/Å²
X-ray gross intensity of N + Si Kα lines (counts)
X-ray acquisition time (min.)
600
800
1000
1200
0
2
4
6
8

Fig. 3

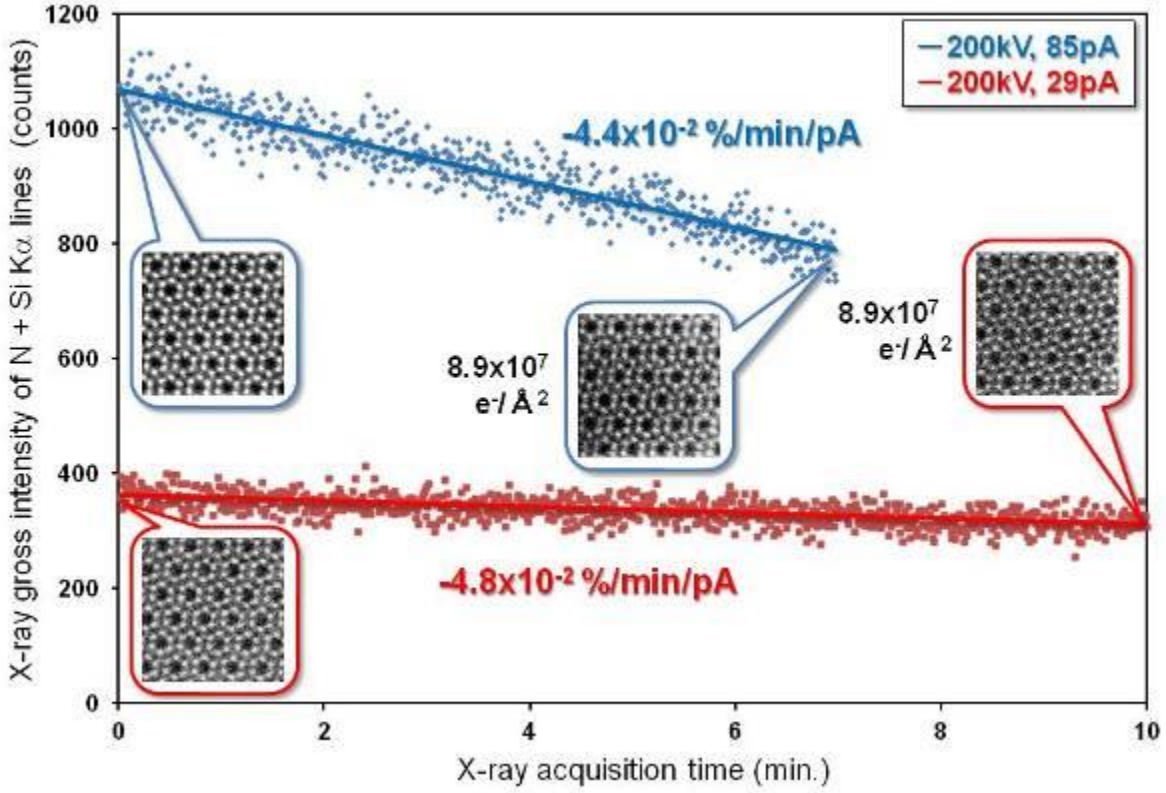
200kV, 85pA
200kV, 29pA
-4.4x10-2 %/min/pA
8.9x10^7 e-/Å2
8.9x10^7 e-/Å2
-4.8x10-2 %/min/pA
X-ray gross intensity of N + Si Kα lines (counts)
X-ray acquisition time (min.)
0
200
400
600
800
1000
1200
0
2
4
6
8
10

Fig. 4

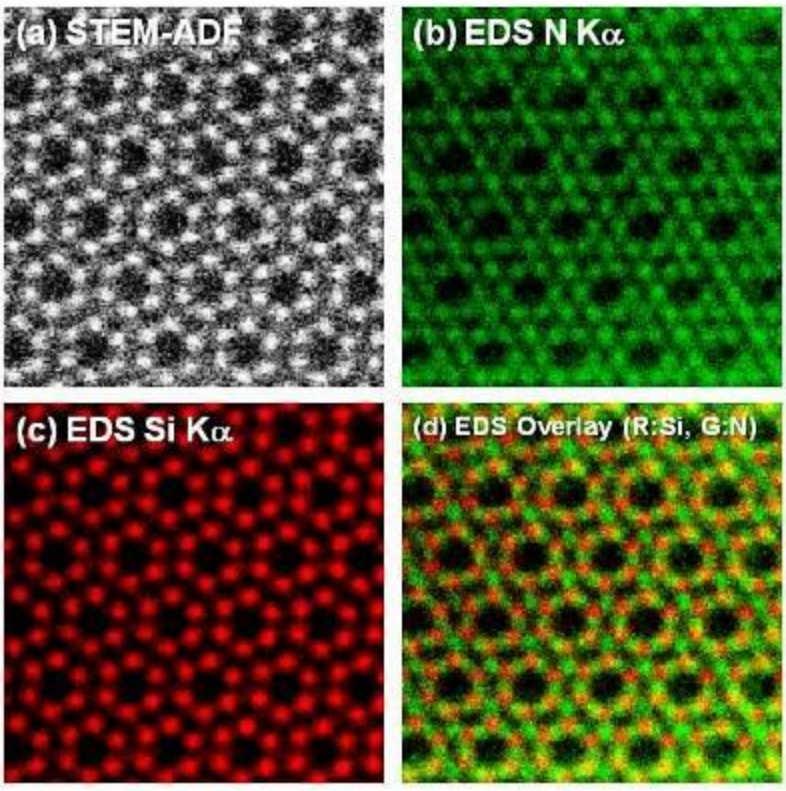
(a) STEM-ADF
(b) EDS N Kα
(c) EDS Si Kα
(d) EDS Overlay (R:Si, G:N)

IM3.P011
Atomic-resolution study on the thermal stability of nanocrystalline materials by *in-situlex-situ* experiments

Z. Zhang[1]

[1]Erich Schmid Institute of Materials Science, Austrian Academy of Sciences, Leoben, Austria

Nanostructured materials show extremely high strength compared to coarse-grain bulk materials, and have received unprecedented attention in material research also due to its potential applications in industry. Severe plastic deformation is an emerging and quite efficient route to generate nanocrystalline materials out of normally immiscible systems. However, the main issue on nanostructured materials is its thermal stability (1). Here, the thermal stability of nanocrystalline materials prepared by high pressure torsion (HPT) is explored using spherical aberration-corrected transmission electron microscopy (TEM).

The objective is to reveal the thermal stability of nanocrystalline materials at the atomic scale by *in-situ/ex-situ* experiments.

Cu-based alloys, i.e. Cu-Cr (2), Cu-Fe (3) and Cu-Ag, were deformed by HPT at room temperature. Normally immiscible Cu-Fe alloy system was mechanically alloyed directly from blended powders and vacuum arc-melted bulk respectively which contain different levels of content of oxygen impurity using HPT. Cu-Ag raw materials were commercially produced (GoodFellow, UK). A JEOL 2100F equipped with an image-side CS-corrector was used. Both conventional heating holder (Gatan) and new generation heating holder (Dens solutions) were applied. *Ex-situ* heating experiments were performed in an oven filled with Ar atmosphere.

The evolution of the structural and chemical composition in nanostructured materials with temperature was tracked in *real-time*. i) It showed that the nanostructured materials are not only subjected to a structural change but also to chemical composition fluctuations upon annealing. The destabilization process in the nanostructured materials can initiate at quite a low temperature while the grain sizes remain unaltered. ii) *Real-time* chemical composition determination shows the element concentration varying with annealing temperature. This allows further analyzing the dynamic behavior in nanocrystalline materials in details, i.e. deducing the instantaneous diffusion coefficients and excess vacancy concentration generated by severely plastic deformation, and observing the interface sharpening phenomenon. The experiment also exhibits an approach to directly evaluate the excess vacancy concentration in nanocrystalline materials via measuring the elemental profiles.

Moreover, iii) the thermal stability of nanocrystalline materials changes with the impurity level (i.e. oxygen) in nanostructured materials. One example, such as Cu-Fe deformed using powders precursors which contain a different content of oxygen, is given, demonstrating a total different behavior upon annealing. Nanometer scale oxides surprisingly form firstly, and then followed by a decomposition of supersaturated solid solution upon heating (3). As for Cu-Ag, it displays a dissimilar behavior as compared to Cu-Cr and Cu-Fe during *in-situ* heating.

The thermal stability studies show that the destabilization of nanocrystalline materials may occur at quite a low temperature without obvious structural change. The thermal stability is affected by materials chemistry and impurity level.

References:

(1) R.Z. Valiev *et al.,* Mater. Res. Lett., 4(2016) 1–21.

(2) Z.L. Zhang *et al.,* Acta Materialia 138 (2017) 42-51.

(3) J. Guo *et al.,* Nature communications, 9 (2018)946.

IM3.P012
Dry reforming of methane on Ni catalyst studied by ESEM

L. Sandoval-Diaz[1], M. Plodinec[1], R. Schlögl[1], T. Lunkenbein[1]

[1]Fritz Haber Institut der Max Planck Gesellschaft, Anorganische Chemie, Berlin, Germany

The structure of heterogeneous catalysts dynamically adapts to the chemical potential under working conditions (1). Thus, it becomes locally different compared to its pristine analogue and in some cases the new structure is only stable under specific conditions of pressure, gas composition, and temperature. A major goal in research related to heterogeneous catalysis is to characterize such working structures with the aim to understand their properties such as oxidation states, adsorbed species, dynamical evolution, and activation/deactivation mechanisms. Such knowledge can potentially lead to accurate structure-activity correlations and simplify catalyst tailoring. We used a modified ESEM adapted to the study of heterogeneous catalysis. Unlike conventional SEM that operates under (U)HV conditions, the specimen chamber in an ESEM is continuously pumped through a series of small apertures located at the column. This allows building up chamber pressures as high as 2000 Pa by continuous gas feeding, while keeping the electron gun in UHV (2).

The objective of the present study is to characterize the working structure and the surface dynamics of a Ni catalyst during the dry reforming of methane (DRM), a reaction that transforms greenhouse CO2 and CH4 into syngas (3).

A commercial ESEM (FEG Quanta 200) was equipped with a customized laser (808 nm) heating stage and a home-built gas feeding station provided with MFCs (4). A continuous catalytic reactor made of quartz (12 cm x 6 mm ID) with 2 windows was used for keeping the sample under reproducible gas flow conditions. The exit of the reactor was connected to a mass spectrometer (Pfeiffer Prisma QMS 200) for gas composition measurement (fig. 1).

Our in-situ results show that Ni oxidizes during DRM at 770 °C. At early stages of DRM the surface undergoes reconstruction and faceting, and then the oxide grows in well-defined orientations on top of the nickel substrate. Formed oxides are rapidly consumed with the increase of the temperature to 890 °C, with an increase in the catalytic conversion. Cycling of the reaction temperature between 770 °C and 890 °C showed reversibility between oxidized low-activity state and reduced high-activity state, suggesting that the working structure more likely links to the reduced surface.

The authors acknowledge the contribution of Dr. M. G. Willinger and Dr. Z.-J. Wang for the construction of the gas feeding station and laser heating stage during their stay at FHI.

References:

(1) K. F. Kalz et al., ChemCatChem, 9, 17-29 (2016).

(2) G. J. Millar et al., J. Catal., 169, 143-156, (1997)

(3) K. Yuan et al., ACS Catal., 6, 4330-4339, (2016)

(4) Z.-J. Wang., PhD Thesis: " In-situ scanning electron microscopy studies on the dynamics of metal-catalyzed CVD growth of graphene", TUB, https://depositonce.tu-berlin.de//handle/11303/8240 10.14279/depositonce-7391, (2017)

Fig. 1: A. Block diagram of ESEM. The PLA system keeps the UHV at the electron gun while the chamber is continually fed with gas. B, C. FEG Quanta 200 with customized gas feeding station. D. Home-built continuous-flow reactor with 2 circular windows placed between the gas inlet and outlet. E. Metal sample placed in-between the windows for imaging and heating purposes. F. Ni oxidizes at 770 °C during DRM, but the surface is mostly metallic at 890 °C. Catalytic conversion correlates with the morphological changes induced by temperature variation, suggesting that reduced Ni is the active form of the DRM.

Fig. 1

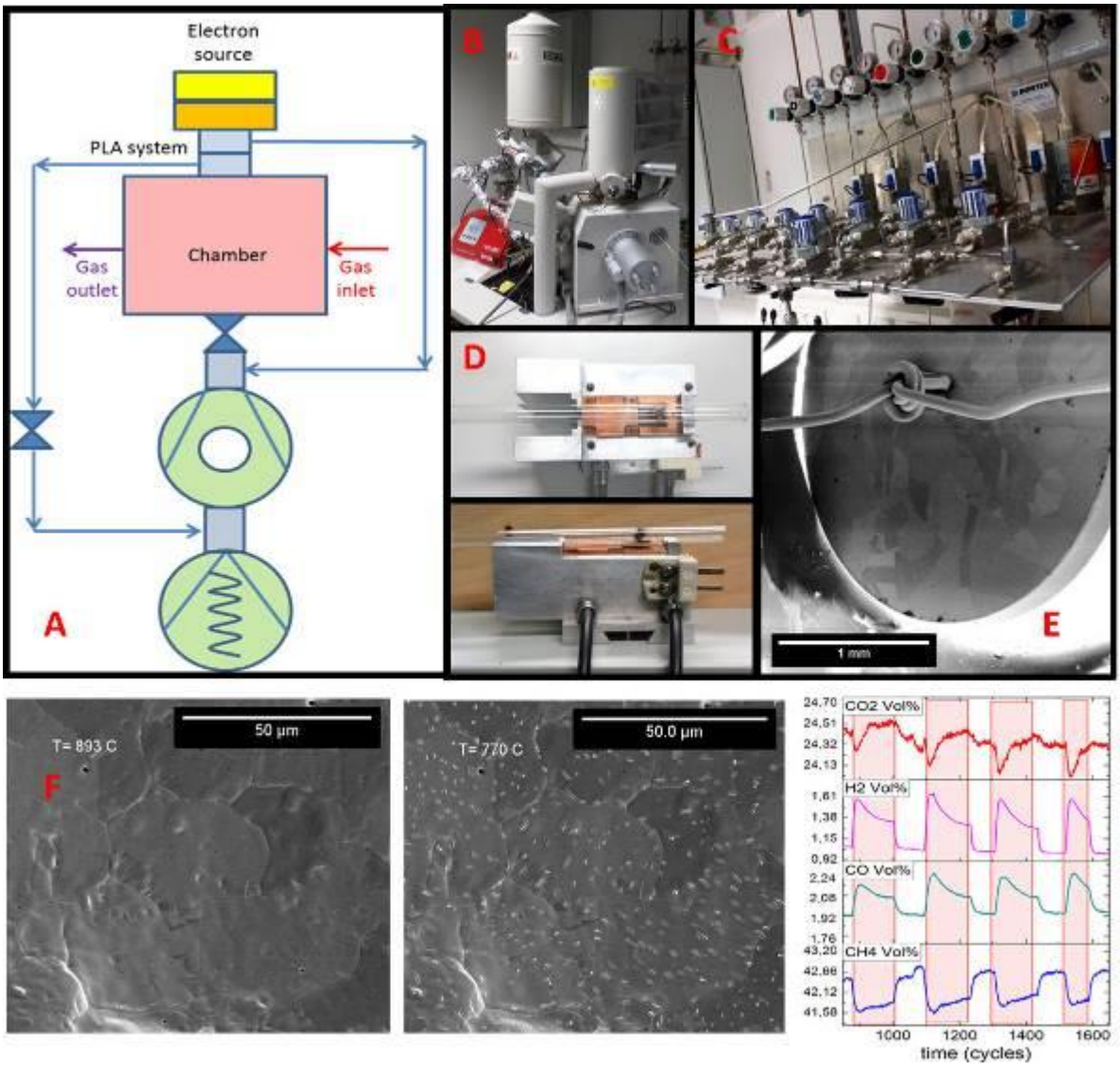
Electron source
PLA system
Chamber
Gas outlet
Gas inlet
A
B
C
D
E
1 mm
F
T= 893 C
50 µm
T= 770 C
50.0 µm
CO2 Vol%
H2 Vol%
CO Vol%
CH4 Vol%
time (cycles)

IM3.P013
In-situ mapping of relaxation and local dynamics in amorphous nanorods

K. Spangenberg[1], S. Hilke[1], M. Peterlechner[1], G. Wilde[1]

[1]WWU Münster, Institute of Materials Physics, Münster, Germany

Metallic glasses (MGs) are promising candidates for engineering materials due to their outstanding mechanical strength and elasticity. For a systematic production of MGs, a basic understanding of the structure as well as the dynamics is inevitable. MGs lack long-range order, however, consist of structural motives, often denoted as medium-range order (MRO). The MRO can be measured by fluctuation electron microscopy (FEM) (1) i.e. the evaluation of intensity fluctuations in diffraction or dark-field images. It has been shown experimentally that the dynamics of MGs are related to their mechanical properties, and are therefore of great interest to study on a local scale.

Spatial maps of atomic dynamics can be recorded by electron correlation microscopy (ECM) (2). However, it must be pointed out the ECM was yet only applied to the undercooled liquid. The focus of the present study is to measure atomic dynamics of nanorods using ECM and FEM at temperatures below the glass transition. The goal is to observe the non-equilibrium dynamics, extending previous ECM works. Sample preparation routes are presented and the possibilities of in-situ sample analysis, which enables an observation of the microstructure and reactions at the atomic level during e.g. heat treatment, are analyzed.

Nanorods of FeNiP were electrochemically synthesized, as reported earlier (3). Self-organized alumina templates were used for electrochemical deposition of Fe40Ni40P20 (at. %). The samples were analyzed using a Titan Themis 60-300, including a Ceta camera to record series of dark-field images.

An energy dispersive X-ray (EDX) map of a nanorod is shown in Figure 1. The structure frequently shows a layered structure, with Ni-rich and Fe-rich areas. A dataset of 2000 dark-field images over a period of 2000 seconds was used to obtain their correlation as a function of time. The time correlation was fitted using a stretched-exponential function, to plot the correlation-decay time (t) as shown in Figure 2. Ni-rich layers show shorter times, in line with faster dynamics. Longer times are detected in Fe-rich layers and at the surfaces.

Based on the results it is evident that the decay times are correlated with the respective structure. Since the measurement is accomplished at room temperature, it is concluded that intrinsic heterogeneous dynamics can be measured without heating.

References:

(1) Voyles, Gibson, Treacy, J. Electron Microsc. (Tokyo). 49 (2000) 259–66.

(2) L. He, P. Zhang, M.F. Besser, M.J. Kramer, P.M. Voyles, Microsc. Microanal. 21 (2015) 1026–33.

(3) N. Winkler, M. Peterlechner, G. Wilde, J. Mater. Chem. C 3 (2015) 7543–7551.

Financial support by the Graduate School of Molecules and Interfaces (Department of Physics and Chemistry, WWU Münster), the Deutsche Forschungsgemeinschaft (DFG) under the grant number PE 2290/2-1 and the Major Research Instrumentation Programme under INST 211/719-1 FUGG is gratefully acknowledged.

Fig. 1: EDX maps of an electrodeposited FeNiP nanorod. A layered structure on a 20 nm scale is detectable.

Fig. 2: The characteristic times (t) of the correlation decay in a dark-field image series acquired at room temperature. A beam current of 7 nA was used at a spatial resolution of about 1 nm. Fe-rich layers and the surface are less dynamic. The color code shows the time in seconds.

Fig. 1

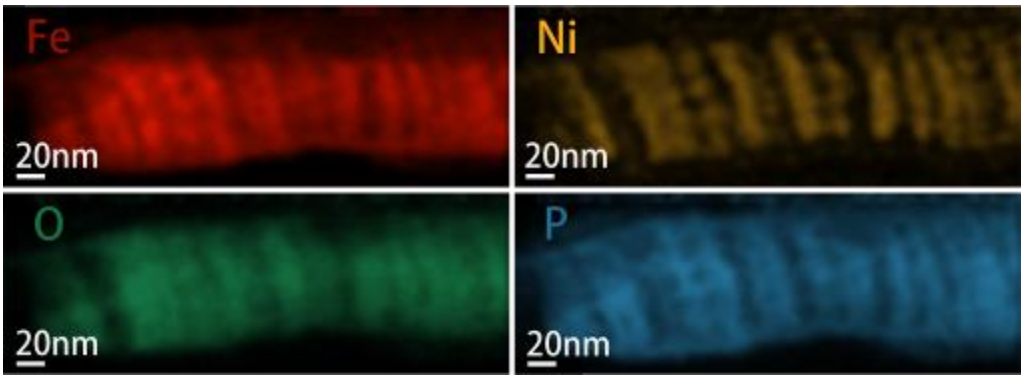

Fig. 2

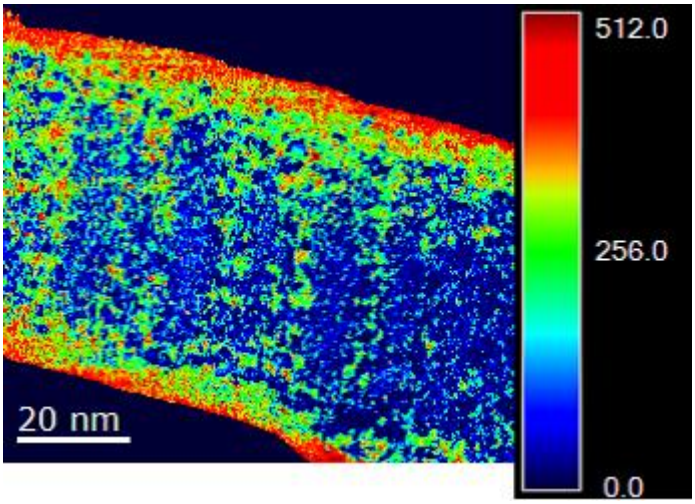

IM3.P014
Activation of iron oxide precursors for ammonia synthesis studied by high pressure *quasi in situ* TEM

K. Dembélé[1], J. Folke[2], H. Ruland[2], L. Masliuk[1], M. Swoboda[1], R. Schlögl[1,2], T. Lunkenbein[1]

[1]Fritz-Haber Institute of Max Planck Society, Department of Inorganic Chemistry, Berlin, Germany
[2]Max Planck Institute for Chemical Energy Conversion, Department of Heterogeneous Reactions, Mülheim, Germany

Quasi in situ transmission electron microscopy (TEM) allows to study local changes of the same area of a sample before and after the treatment which can be done at relevant conditions (high pressure and temperature).(1) Thereby, the sample is treated in a special TEM grid reactor outside the TEM. In addition, the transfer to the TEM is achieved without exposing the sample to ambient air. Thus, it is a powerfull approach to investigate local morhological and/or microstructural changes that occur during the reduction and operation of the catalysts.

The control of the reduction conditions (H_2/N2 ratio and flowrate, temperature and heating rate) of iron oxide precursors is an important step for optimizing the active catalyst for the ammonia synthesis process.(2,3) The aim of this work is to study the changes that occur on non-stoichiometric commercially available iron oxides (wüstite) samples during their reduction into metallic iron at relevant conditions.

We have designed a high pressure *quasi in situ* TEM grid reactor that enables us to investigate commercial wüstite samples (Sigma-Aldrich) under relevant reduction condition (pressures above 1 bar, 500 °C). Identical location imaging was performed using a double corrected Jeol ARM 200F electron microscope that was operated at 200 kV.

Our preliminary results show the wüstite ($Fe_{1-x}O$) particle before reaction at different magnifications (Fig. 1a,b). In addition, electron diffraction (Fig. 1c) shows a polycristalline structure, which is characteristic for a wüstite sample. After the reduction treatment (10 bar, 500 °C), identical location imaging reveals morpholological changes of the wüstite sample (Fig. 1d, e). Electron diffraction analysis (Fig. 1f) suggest the partial disproportionation of wüstite into magnetite and metallic iron.

We have shown the ability of high pressure *quasi in situ* TEM to investigate local changes of the morphology and the structure of the catalysts at relevant activation conditions. Prosepectively, this approach can be extended to investigate changes during ammonia synthesis at elevated pressures and to study pressure dependencies during the reductive activation.

References:

(1) L. Masliuk, M. Swoboda, G. Algara-Siller, R. Schlögl, T. Lunkenbein, *Ultramicroscopy* 2018, *195*, 121–128.

(2) J. R. Jennings, Ed., *Catalytic Ammonia Synthesis: Fundamentals and Practice*, Springer US, 1991.

(3) H. Liu, W. Han, *Catalysis Today* 2017, *297*, 276–291.

Fig. 1: (a) Identical location TEM investigation and electron diffraction of a commercial wüstite sample before (a, b and c) and after (d, e and f) exposure to a total flow of 15 mL/min of a H_2/Ar =3:1 mixture at 10 bar and 500 °C.

Fig. 1

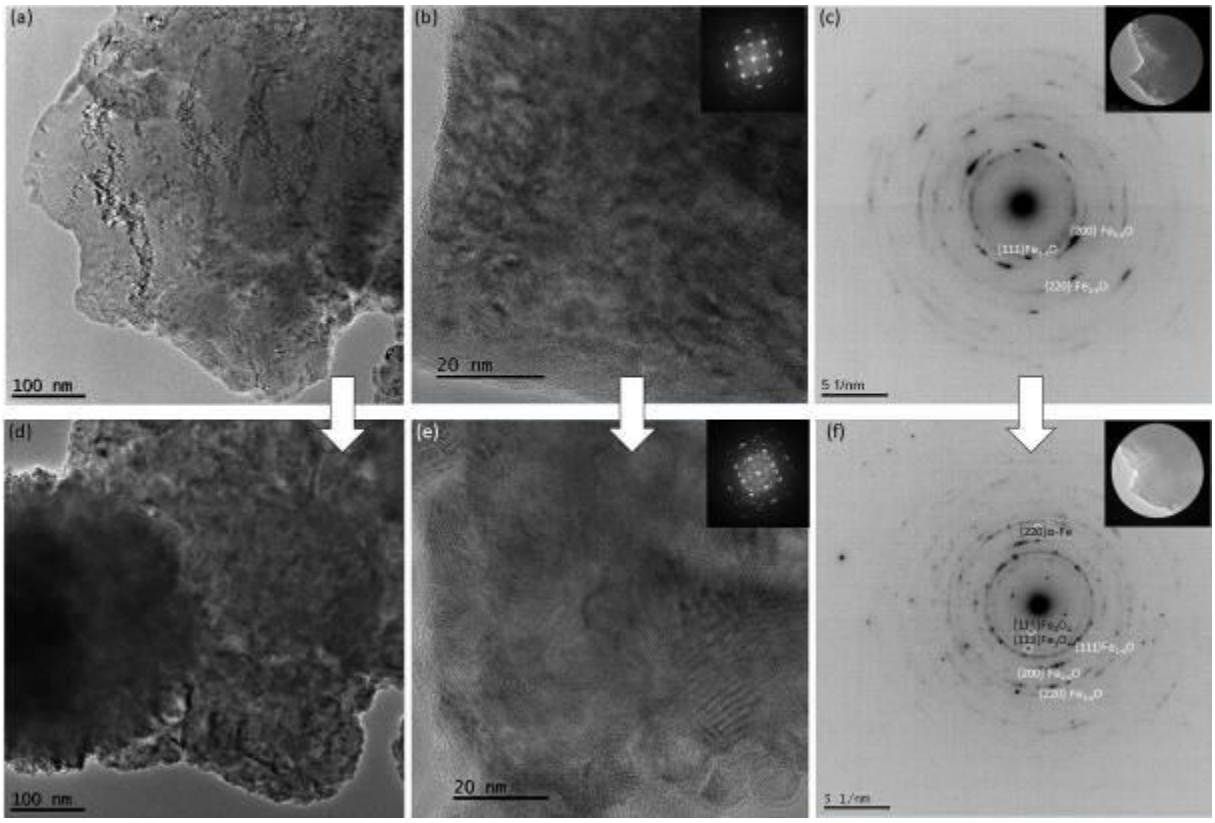

IM3.P015
LIQUID-PHASE ELECTRON MICROSCOPY of WEAKLY SCATTERING OBJECTS in THIN LIQUID LAYERS

S. Keskin[1], N. de Jonge[1,2]

[1]Leibniz Institute for New Materials, Saarbrücken, Germany
[2]Saarland University, Department of Physics, Saarbrücken, Germany

Liquid-phase electron microscopy (LPEM) provides unique information about the structure and function of matter. Liquid cells assembled from silicon microchips with silicon nitride (SiN) membrane windows (typically 50 nm in thickness) are used to confine a small volume of liquid in specialized sample holders for transmission electron microscopy (TEM). This design offers advantages such as in-situ liquid flow or electrochemical biasing during an experiment (1). Considering that the electron scattering properties of an object strongly depends on its Z, observing weakly scattering objects such as proteins in water is challenging in such liquid cells (2).

As an alternative, graphene liquid cells have been used to image nanoparticles encapsulated in a small volume of liquid (3). Atomic resolution is readily obtained for high-Z materials due to the negligible substrate background from graphene. We have used this approach to encapsulate microtubule proteins and image them with phase-contrast TEM (Figure 1). The protofilaments were visible as parallel lines with 5 nm spacing (Figure 1b), that are observed in the corresponding fast Fourier transform (FFT) image at a spatial frequency of f = 1/5 nm^{-1} (Figure 1b inset). We acquired successive images from the same sample region to determine the tolerance of the sample to cumulative electron dose and examined radiation damage using 5-nm spatial features (protofilament structure). The results were compared with cryo-electron microscopy (cryoEM) of microtubules at the same imaging conditions. We found that the graphene-encapsulated microtubules exhibited one order of magnitude higher radiation tolerance than cryo-frozen microtubules (4).

Although a graphene liquid cell provides a better resolution than its SiN-based counterpart, it doesn't possess important utilities such as in-situ liquid flow, and it is typically difficult to control the liquid thickness. Therefore, we also examined the options to improve the spatial resolution obtained with a SiN-based liquid cell. One reason for having poor image quality in particular from weakly scattering objects with such liquid cells is a large liquid thickness caused by excessive bulging of the SiN membranes towards the vacuum of the microscope. We used a pressure controller setup to reduce the internal pressure of the liquid cell, and thus reduce the liquid thickness. Our results show that the liquid thickness can be reduced with this system down to a level in which phase contrast images on low-Z materials can be obtained.

Figure 1**.** TEM of graphene-encapsulated microtubules. a) Schematic of graphene liquid cell. b) TEM image of a microtubule with an electron dose of 10 $e^-/Å^2$. Its FFT image is shown inset. c) Intensity of the 0.2 nm^{-1} spatial frequency in the FFT image (different experiment) as a function of cumulative dose. Dashed line represents the noise level and dotted line the maximal dose (D_{max}=720 $e^-/Å^2$), where the signal intensity goes below the noise level. Adapted with permission from Nanoletters 18 (12) 7435–7440. Copyright (2018) American Chemical Society.

References:

(1) N. de Jonge and F. M. Ross, Nature Nanotechnology, 6 (2011).

(2) N. de Jonge, Ultramicroscopy, 187, (2018).

(3) Yuk et al., Science, 336, 6077 (2012).

(4) S. Keskin, N. de Jonge, Nanoletters, 18, 12 (2018).

We thank the Deutsche Forschungsgemeinschaft: SFB1027 (C7), M. Koch and P. Kunnas for experimental help, and E. Arzt for his support through INM.

Fig. 1

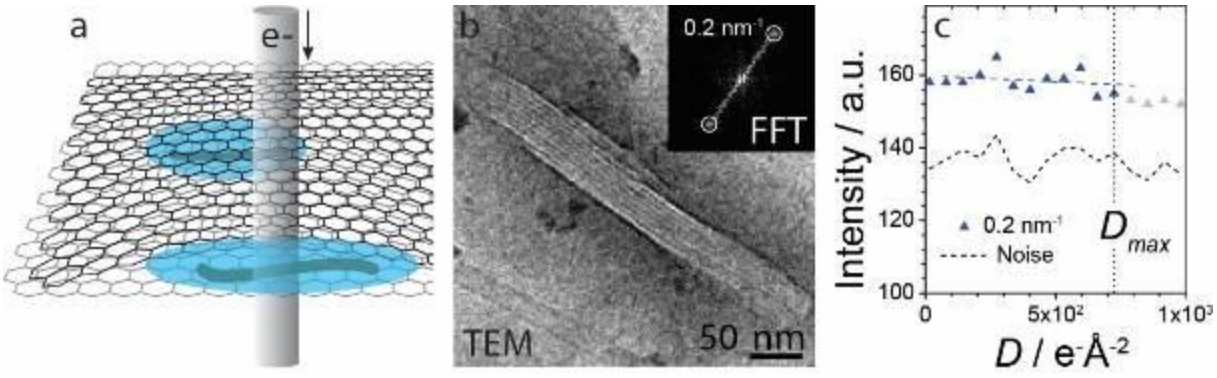
a
e-
b
0.2 nm-1
FFT
TEM
50 nm
c
Intensity / a.u.
160
140
120
100
0
5x10²
1x10³
0.2 nm-1
Noise
D max
D / e-Å-2

IM3.P016
In-situ SEM imaging of reduction and oxidation in a µReactor device

L. Novák[1], K. Bukvišová[2], M. Kolíbal[2,3], T. Vystavěl[1], E. J. Vesseur[4]

[1]Thermo Fisher Scientific, Brno, Czech Republic
[2]Brno University of Technology, Institute of Physical Engineering, Brno, Czech Republic
[3]CEITEC BUT, Brno University of Technology, Brno, Czech Republic
[4]Thermo Fisher Scientific, Eindhoven, Netherlands

The in-situ study of reduction and oxidation processes in the SEM typically suffers from issues with stability, temperature limitations, or process cleanliness. In this paper we present a means to overcome these issues with a novel µReactor device. We present two examples of heat and gas mediated processes monitored in-situ in a FIB-SEM system.

We demonstrate the system cleanliness proven by absence of undesired oxidation of the µReactor by experiments on nickel and copper. A movie accessible from (1) shows modification of a Ni sample, which starts with surface cleaning at 600°C in the presence of pure hydrogen. The following oxidation-reduction cycles were driven by changes of the gas flowing to reactor from hydrogen to air and back to hydrogen at a temperature of 800°C. Fast reduction of the Ni surface at 800°C in 200 Pa of pure hydrogen is shown in three ensuing images of Fig. 1, which were taken within 30 seconds. The cleaning of a copper sample by pure hydrogen is demonstrated in movie (2).

The local overpressure inside the µReactor is combined with high vacuum operation of the FIB-SEM system, which provides possibility for better image resolution compared to Environmental SEM. Image sequence in Fig. 2 and movie (3) show tungsten-oxide nanowires formation from a WS2 nanotube in water vapor environment at 550°C (5). This oxidation starts by the formation of tungsten trioxide nanoparticles which are subsequently reduced to substochiometric oxide nanowires. The mechanism is inherent to 2D WS2 oxidation irrespective of its initial morphology (nanotubes (3) or flakes (4)).

The µReactor device, which can in principle be combined with any FIB-SEM system, assures sample heating up to 1200°C using a MEMS heating plate (6). The pressure limiting aperture separating the reactor space from the SEM chamber (Fig. 3) enables to reach pressures up to 1 kPa within the reactor, while the pressure in the SEM chamber stays below 1E-2 Pa in the standard high vacuum operation mode of the FIB-SEM system. A retractable lid allows to open the reactor during FIB assisted sample preparation (7). Low inlet flow rates enable the usage of reactive gases, which cannot be used in environmental SEM mode because of safety or functional reasons.

In conclusion, the µReactor allows for improved temperature and gas environment control, enables extended chemistry possibilities and novel sample preparation methods formerly not available for investigations of reactions *in situ*.

References:

(1) https://youtu.be/9QbYjdZl5LE

(2) https://youtu.be/61OQEzzt2mU

(3) https://youtu.be/Jh2o5wQeQys

(4) https://youtu.be/UB6_T66__3w

(5) Kolíbal et al. Formation of Tungsten Oxide Nanowires by Electron-Beam-Enhanced Oxidation of WS2 Nanotubes and Platelets, submitted.

(6) Mele et al. A MEMS-based heating holder for the direct imaging of simultaneous *in-situ* heating and biasing experiments in scanning/transmission electron microscopes (2016). *Microscopy Research and Technique*, doi: 10.1002/jemt.22623.

(7) Novák et al. (2016). MEMS-based Heating Element for in-situ Dynamical Experiments on FIB/SEM Systems. *Microscopy and Microanalysis, 22*(S3), 184-185. doi:10.1017/S143192761600177X.

The authors acknowledge funding from Technology Agency of the Czech Republic, TE01020118.

Fig. 1: Reduction of nickel at 800°C in hydrogen atmosphere. Scale bar: 10 µm

Fig. 2: WS2 nanotubes oxidizing in water atmosphere. Scale bar: 100 nm

Fig. 3: µReactor device

Fig. 1

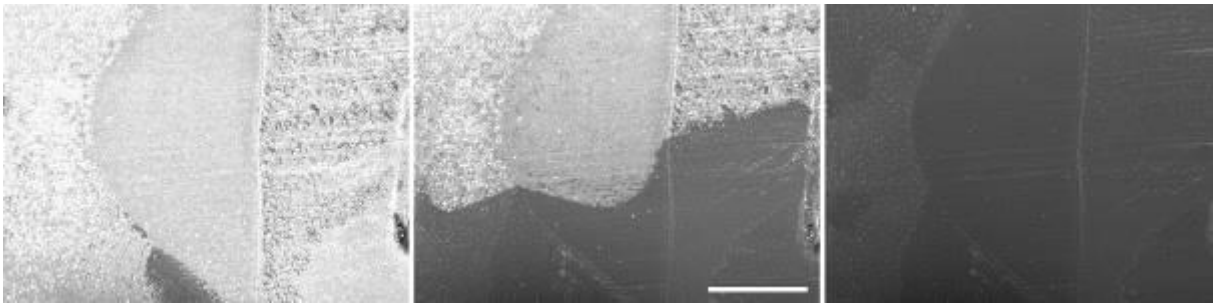

Fig. 2

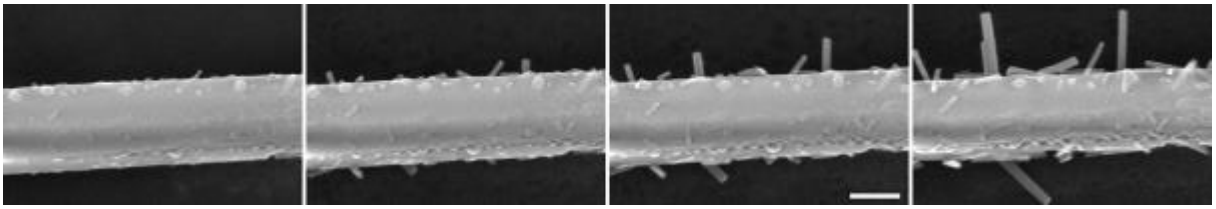

Fig. 3

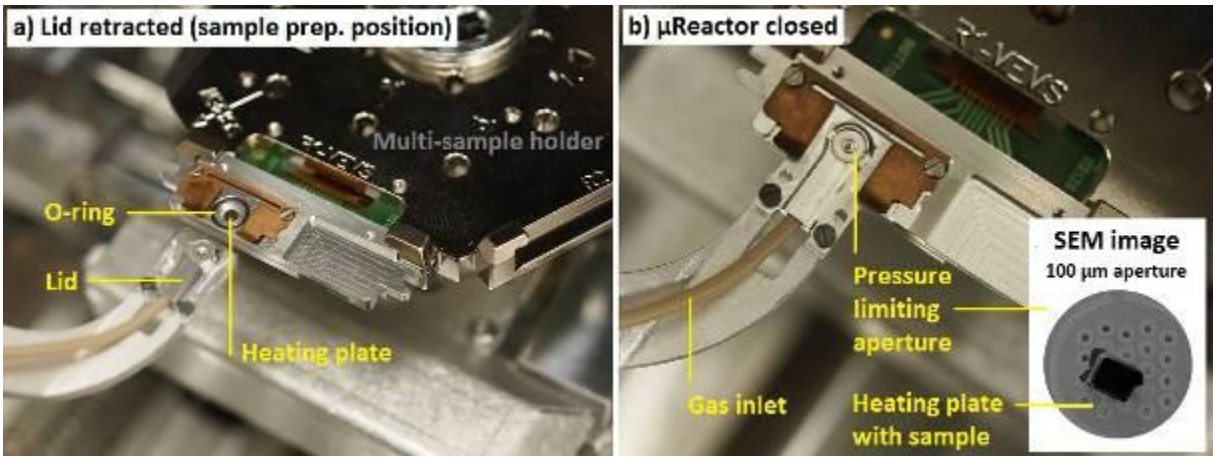

IM3.P017
A novel method for direct adhesion measurement at diamond/metal binder interface

D. Sidorenko[1], P. Loginov[1], A. Bondarev[1], A. Orekhov[2], E. Levashov[1]

[1]National University of Science and Technology "MISIS", Scientific Educational Center of Self-Propagating High-Temperature Synthesis, Moscow, Russian Federation
[2]NRC «Kurchatov Institute», Moscow, Russian Federation

Diamond cutting tools are widely used for cutting, drilling, and grinding of hard-to-machine materials, such as natural stone, reinforced concrete, cemented carbides, ceramics and so on. Diamond tool is a composite material consisting of diamond grains and a binder, typically metal.

Binder is intended to retain diamond grains until their complete wear, ensuring self-sharpening of the tool. Up to now, no methods for direct measurement of diamond-binder adhesion were published. We offered a novel method of direct adhesion measurement in transmission electron microscope.

In situ experiments were carried out using a Jeol JEM 2100 transmission electron microscope equipped with a special Hysitron PI 95 Picoindenter holder for mechanical tests. A 2.5 µm dogbone-shaped sample was cut from the diamond-metal (Fe-Ni-Mo) binder interface using a Versa 3D two-beam microscope (FEI, USA). A push-to-pull loading scheme was implemented for mechanical tests.

As a result of experiments using the diamond-metal binder system as an example, it was shown that the proposed method makes it possible to directly determine the adhesive strength in cases when other methods are not suitable.

IM3.P018
A GHz Phase Shifter for Time-Resolved Electron Holography by Interference Gating

A. Zein Al-Din[1], T. Wagner[2], G. Ronniger[1], L. Kasper[1], M. Lehmann[2]

[1]Technische Universität Berlin, Institut für Hochfrequenz- und Halbleiter-Systemtechnologien, Berlin, Germany
[2]Technische Universität Berlin, Institut für Optik und Atomare Physik, Berlin, Germany

Dynamic measurements in a Transmission Electron Microscope (TEM) require a suitable shutter or gating mechanism, which is unfortunately difficult to realize. The most popular approach for such a shutter is the stroboscopic illumination utilizing a laser driven field emitter (1, 2). A simple, yet promising alternative for such a temporal gating is the interference gating (iGate) (3). An electron biprism in the condenser aperture plane (Fig. 2) acting as an electric phase shifter is used to produce time-resolved holograms. The time resolution depends mostly on its bandwidth limitation. Here the high frequency (RF) capabilities of such a phase shifter is tested via electron holography (EH) and the circuit for generating phase sequences in the GHz range, pushing the time resolution towards picoseconds, is presented.

The requirement on this circuit is to switch between two states. One state can be described as a noise signal, while the other state consists of a 0 V DC signal. The duration of the second state determines the shortest possible averaging time, which limits the achievable time resolution. The signals applied to the phase shifter must be synchronized to the signal used to excite the actual sample. This determines the total length of the periodic switching pattern and the duration of the first state. Currently, we want to achieve durations as short as 9 ns and 1 ns for the first and second state respectively with 100 ps transients between them. This RF signal is fed via a coaxial cable to the deflector of the TEM. Fig. 1 shows the functional structure of this principle.

The RF signals sent to the phase shifter will experience strong reflections at the condenser biprism, as no termination is present there. This reflected power must be absorbed to avoid multiple reflections and interference. This is achieved by suitable impedance matching at the circuit output. The output reflection factor S22 (Fig. 1 red) used to quantify this matching should be as small as possible and below -20 dB for reasonable performance. Additionally, the combined insertion loss S21 (Fig. 1 blue) of switch and impedance matching should be only a few dB.

The RF-capabilities of the phase shifter are tested by applying a sine-signal with an amplitude A to the condenser biprism. The fringe contrast of a recorded hologram then shows a 0-th Bessel function dependency on the amplitude of the sinusoidal phase shifting, where a phase shift of 2.4048 radians produces the first zero crossing of the contrast.

For 10 MHz an amplitude of A = 0.502 Vpp produces the first zero crossing. The voltage of the first zero crossing is determined by a fit of the Bessel function to the measured data. For 2.4 GHz, just a drop of the deflection efficiency to roughly a quarter is observed (mostly due to capacitive dampening and reflections in the cabling), which proves the feasibility even at such high repetition rates.

References:

(1) O. Bostanjoglo et al.: Ultramicroscopy 81 (2000) 141.

(2) A. Feist et al.: Ultramicroscopy 176 (2017) 63.

(3) T. Niermann et al.: Ultramicroscopy 182 (2017) 54-61.

Fig. 1: Schematic functional structure of the phase sequence generation and diagram of the simulated scattering parameters S21 and S22.

Fig. 2: Schematic EH setup with the electric deflector and normalized fringe contrast in dependence of the amplitude A at frequencies of 10 MHz and 2.4 GHz of the sine-signal applied to phase shifter.

Fig. 1

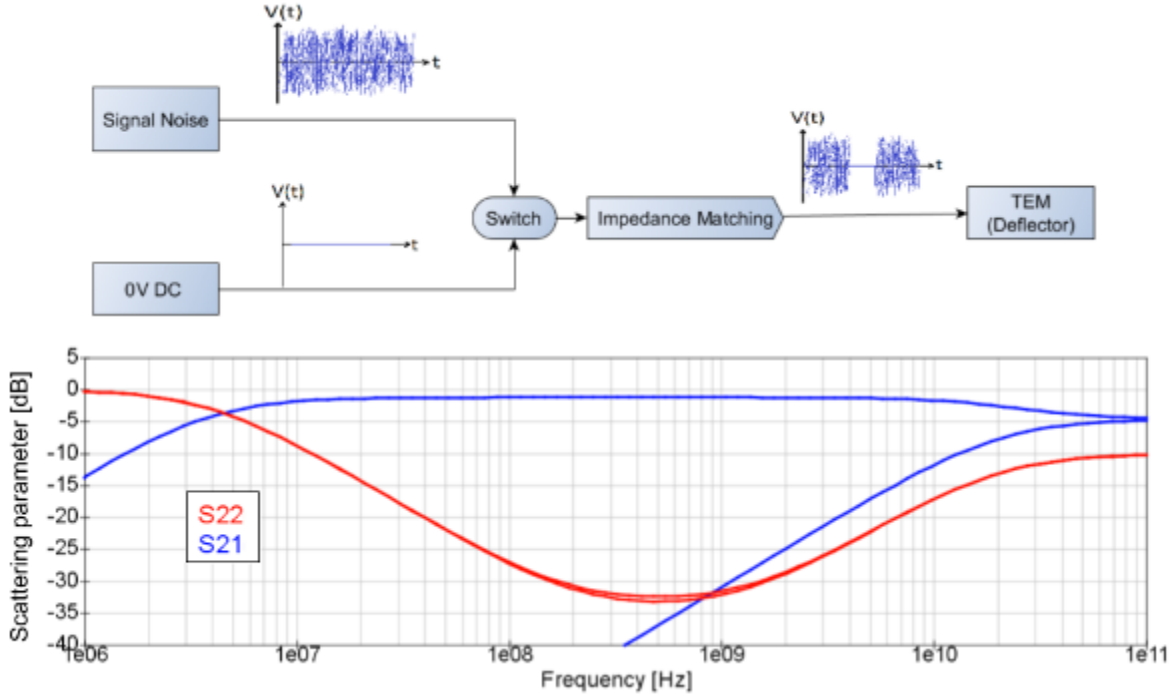
V(t)
t
Signal Noise
V(t)
t
0V DC
Switch
Impedance Matching
V(t)
t
TEM
(Deflector)
Scattering parameter [dB]
5
0
-5
-10
-15
-20
-25
-30
-35
-40
S22
S21
1e06
1e07
1e08
1e09
1e10
1e11
Frequency [Hz]

Fig. 2

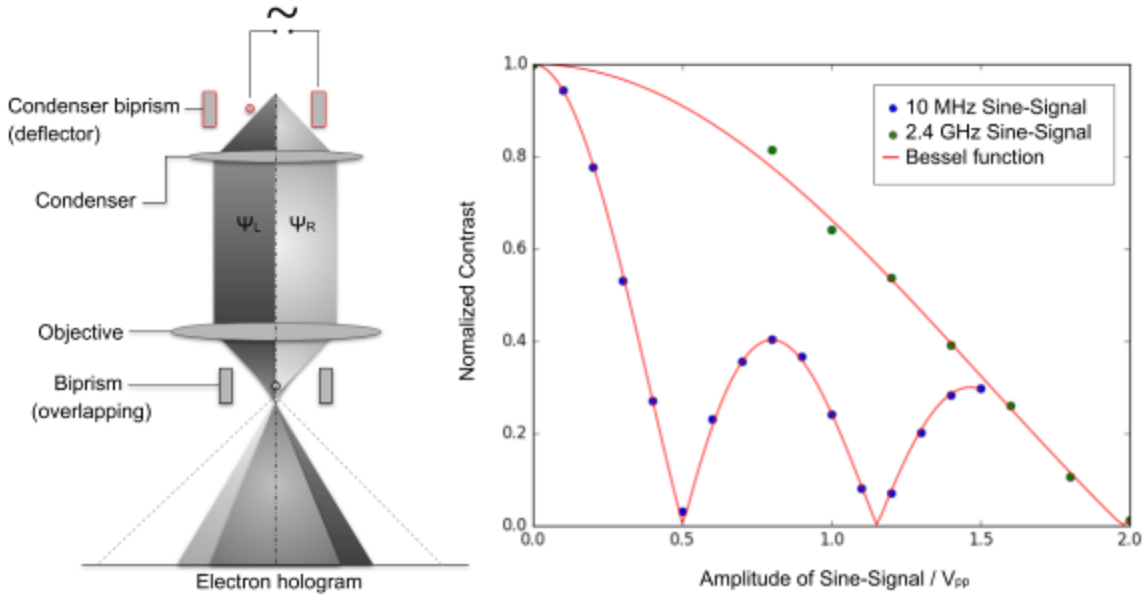
2
Condenser biprism
(deflector)
Condenser
Ψ_L
Ψ_R
Objective
Biprism
(overlapping)
Electron hologram
Nomalized Contrast
1.0
0.8
0.6
0.4
0.2
0.0
10 MHz Sine-Signal
2.4 GHz Sine-Signal
Bessel function
0.0
0.5
1.0
1.5
2.0
Amplitude of Sine-Signal / V_{pp}

IM3.P019
Environmental SEM combined with outlet gas analysis: example of NiO reduction

S. Poitel[1,2], L. Sandoval-Diaz[3], T. Lunkenbein[3], J. Van Herle[2], C. Hébert[1]

[1]Ecole Polytechnique Federale de Lausanne (EPFL), Laboratoire de spectroscopie et de microscopie électronique (LSME), Lausanne, Switzerland
[2]Ecole Polytechnique Federale de Lausanne (EPFL), Group of Energy Material (GEM), Lausanne, Switzerland
[3]Fritz Haber Institute of the Max Planck Society, Inorganic Chemistry, Berlin, Germany

Environmental SEM is of great interest to study in-situ reactions happening on the surface of various materials by giving insight on surface microstructure changes while exposing a sample to various gases up to 1000°C. Understanding of reactions could be enhanced by online monitoring of the reaction products. In this work, a mass spectrometer (MS) was connected to the outlet of the chamber of a modified FEI Quanta 200 ESEM while observing in-situ reactions. Obtaining simultaneous information from sample observation and gas analysis simplifies the correlations and saves time. As example we studied the reduction of nickel oxide as used in a solid oxide fuel cell (SOFC) anode.

These anodes are made from nickel oxide (NiO) powder and yttrium stabilized zirconia (YSZ) powder sintered together to create a slightly porous composite material. During first use, nickel oxide is reduced by hydrogen or methane (CH4) leading to an electronic conductive nickel network and larger pores in the anode. By combining ESEM and mass Spectrometry (MS) it is possible to see how NiO reduction takes place (fig.1) and simultaneously follow the extent of the reaction which occurs within a short period of time. Using methane as reducing agent (which produces CO2 upon NiO reduction), the MS data (fig. 2) indeed show the reaction of the whole sample to be fast.

Fig. 1: SEM images of Ni-YSZ anode surface during in-situ reduction: (a) at the beginning of reduction, (b) after 1 minute exposed to hydrogen at 800°C, (c) after 2 minutes exposed to hydrogen at 800°C. Circles highlight the pores development and nickel grain shrinkage.

Fig. 2: Online-MS during in-situ reduction of a NiO-YSZ SOFC anode. The increase of carbon dioxide and decrease of methane can be clearly seen (arrow) when the sample is reduced.

Fig. 1

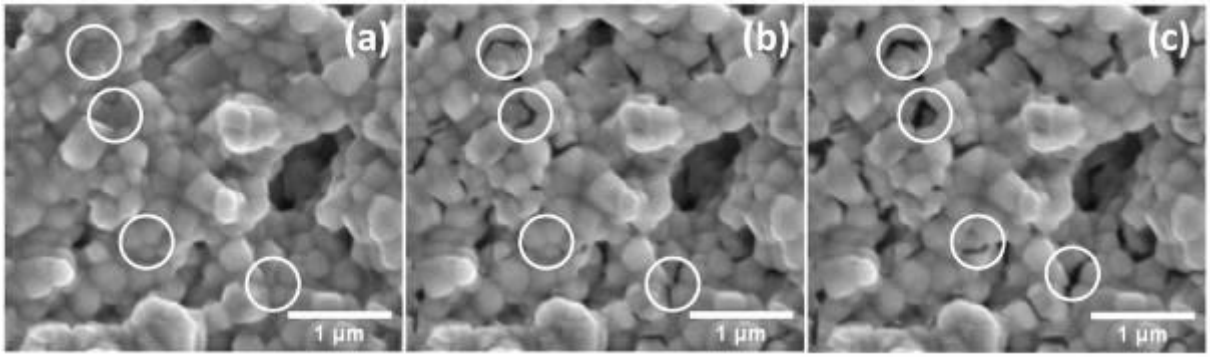

Fig. 2

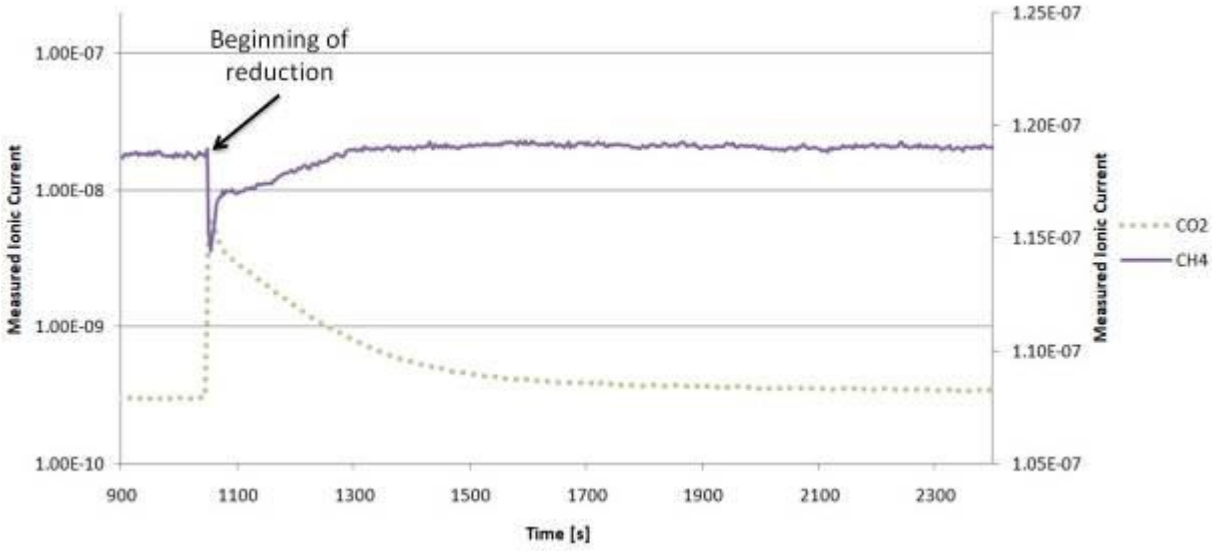
Beginning of reduction
1.00E-07
1.00E-08
1.00E-09
1.00E-10
Measured Ionic Current
1.25E-07
1.20E-07
1.15E-07
1.10E-07
1.05E-07
Measured Ionic Current
CO2
CH4
900
1100
1300
1500
1700
1900
2100
2300
Time [s]

IM3.P020
In situ TEM annealing as a method for observations of nanocrystallization of FeMoCuB and FeCoSiBMoP metallic glasses

A. Zak[1], A. Laszcz[2], M. Hasiak[2]

[1]Wroclaw University of Science and Technology, Electron Microscopy Laboratory, Wroclaw, Poland
[2]Wroclaw University of Science and Technology, Departament of Mechanics, Material Science and Engineering, Wroclaw, Poland

Nowadays, when energy saving becomes a significant global issue, the demand for more energy efficient electrical devices increase considerably. As a result, Fe-based amorphous and nanocrystalline alloys start to play an important role as most promising energy efficient materials due to their exceptional soft magnetic properties, such as high permeability, low coercivity and low core losses (1). These unique properties of the metallic glasses stem from their partially crystallized nanostructure in which α-Fe nanograins are evenly embedded in the amorphous matrix (2). In this case in situ TEM annealing is a valuable observation method providing useful information about crystallization process, including nucleation and grain growth, morphology of different grains or grain size distribution. Following that fact, the aim of this study was to observe and compare the nanocrystallization processes in two types of amorphous Fe-based materials: FeMoCuB and FeCoSiBMoP.

The investigated FeMoCuB and FeCoSiBMoP alloys where prepared from high purity elements under protective argon atmosphere in a form of thin (~20 μm thick) ribbons using melt spinning method. The samples for TEM observations were prepared by the way of electropolishing and ion polishing. Observations was taken on Hitachi H-800 TEM equipped with modified Hitachi heating stage.

The direct observation at room temperature (Fig. 1ab, fig. 2ab) confirmed that both studied materials were fully amorphous in the as-prepared state. The subsequent annealing inside the TEM column led to the appearance of the first stages of crystallization. At about 660 K for the FeMoCuB and 600 K for the FeCoSiBMoP the first spherical, single nanometer in size grains precipitated evenly in the investigated samples (fig. 1d). The following heat treatment induced the grains growth, which started to nucleate into bigger grains. The SEAD pattern taken at this stage of crystallization confirmed that observed crystallites were α-Fe nanograins (fig. 2c). Further increase of annealing time and temperature contributes to the second stage of crystallization, where mainly detrimental Fe2B precipitated from the amorphous matrix (fig. 1ef). It is worth noticing that in case of the FeCoSiBMoP alloy second stage of crystallization was more complicated than in the FeMoCuB alloy, as some other phases were observed on SAED patters (fig. 2e).

In situ observations of nanocrystallization process in the amorphous FeMoCuB and FeCoSiBMoP alloys were possible due to the annealing procedure performed directly in the TEM column. The adopted observation method allowed to follow the whole crystallization process of the investigated materials from the first appearance of α-Fe nanograins up to the fully crystallized nanostructures. Moreover, presented research put emphasis on the differences between crystallization behavior of two types (FeMoCuB and FeCoSiBMoP) of amorphous/nanocrystalline materials.

References:

(1) H.R. Lashgari, et al., Composition dependence of the microstructure and soft magnetic properties of Fe-based amorphous/nanocrystalline alloys: A review study, J Non Cryst Solids.: Vol. 391, pp. 61-82 (2014).

(2) Y. Yoshizawa, et al., New Fe-based soft magnetic alloys composed of ultrafine grain structure, J Appl Phys.: Vol. 64, No. 10, pp. 6044-6046 (1988).

Fig. 1: FeMoCuB metallic glass SAED and microstructure evolution

Fig. 2: FeCoSiBMoP metallic glass SAED and microstructure evolution

Fig. 1

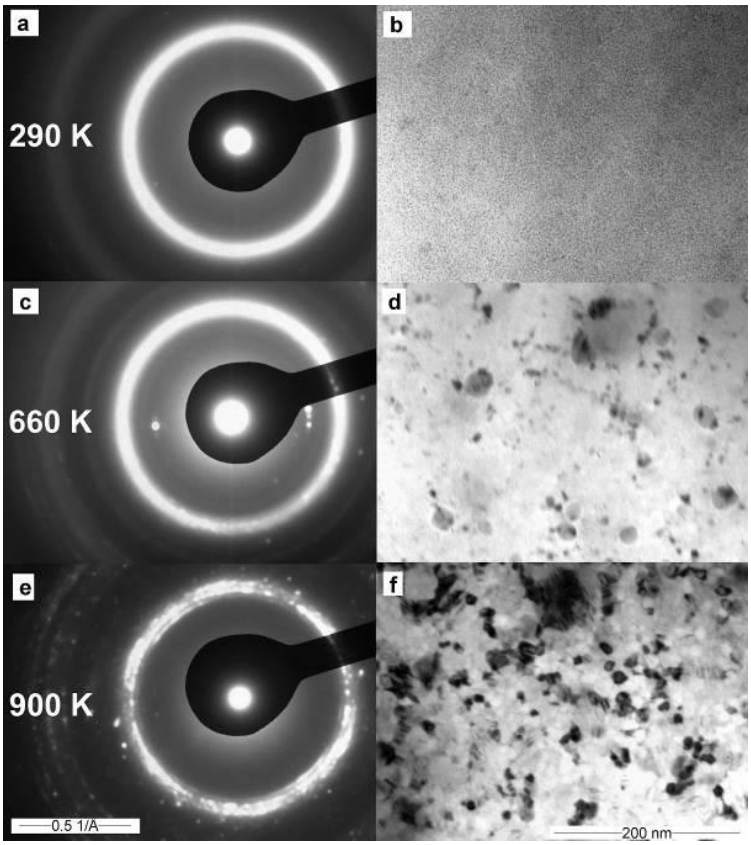
a
290 K
b
c
660 K
d
e
900 K
f
0.5 1/A
200 nm

Fig. 2

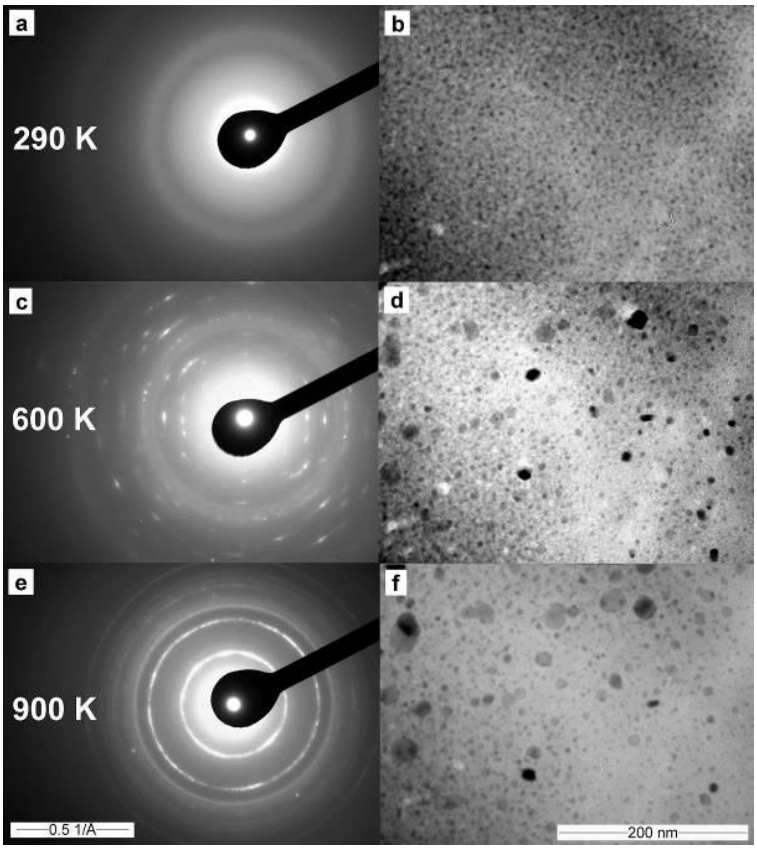
a
290 K
b
c
600 K
d
e
900 K
f
0.5 1/A
200 nm

IM3.P021
Watching ZSM-5 zeolites hollowing with liquid phase electron microscopy

H. Wu[1], T. Li[2], H. Friedrich[1], J. A. Van Bokhoven[2], N. A. J. Sommerdijk[1], J. P. Patterson[1]

[1]Eindhoven University of Technology, Eindhoven, Netherlands
[2]ETH Zürich, Zürich, Switzerland

Zeolites are generally crystalline porous aluminosilicates with inherent micropores of molecular dimensions. The micropores provide remarkable size and shape selectivity, but impose limitations on molecular transport. (1) To address this problem, mesopores have been widely introduced in zeolites to allow faster guest molecule transfer from and to active sites. (2)

To fabricate mesoporous zeolites, alkali-based desilication is an efficient approach. Nevertheless, so far, the dynamics of the desilication process has not been fully understood. (3) To this end, Liquid Phase Electron Microscopy (LPEM) offers an opportunity to monitor the pore formation with a unique combination of high temporal and spatial resolution. (4) However, studying the chemical reaction dynamics of such highly beam-sensitive materials in liquid is still extremely challenging because of the complicated beam-sample/liquid interactions in such confined space.

To image the zeolite hollowing process with good contrast and high temporal resolution with negligible beam effects

ZSM-5 zeolite nanoparticles (ca. 400 nm) were used to investigate the desilication process.

LPEM experiments were carried out on an FEI Tecnai 20 (type Sphera) TEM microscope operated with a 200 keV LaB6 filament and a 4K × 4K Zeta CCD camera, by using a DENSsolutions liquid cell holder (Ocean). The liquid cell was prepared with the assistance of the ultra-low volume dispenser (SciTEM, sciNION, Germany).

Here we discuss our recent efforts in probing the zeolite hollowing process by LPEM. We show an ultra-low volume dispenser assisted liquid cell preparation method. (5) Figure 1(a and c) shows an overview of the dry liquid cell window with a few zeolite nanoparticles before flowing the base solution in. We discuss strategies we applied to minimize the beam effects, including developing the low dose electron imaging protocol. We present how data processing enables us to extract quantitative information from the results obtained by 5 e-.nm2-.s- liquid phase imaging. We also discuss different ways to validate the LPEM observations, for example cryo-TEM (6). For the first time, we show that LPEM can track single zeolite particle hollowing process at nanoscale. Figure 2(d-f) shows the zeolites gradually hollow after 20 h, and the shape of the zeolites stay the same.

We successfully implemented quantitative visualization of ZSM-5 hollowing process on an individual particle level by LPEM. We anticipate a promising future for the use of LPEM to study the chemical reaction dynamics of beam-sensitive materials in solution.

References:

(1) Y Tao et al., Chem Rev 106 (2006), p. 896.

(2) V Valtchev et al., Chem Soc Rev 42 (2013), p. 263.

(3) T Li & H Wu et al., Journal of Materials Chemistry A 7 (2019), p. 1442.

(4) FM Ross, Science 350 (2015), p.

(5) JP Patterson et al., Microscopy and Microanalysis, (2016), p. 1.

(6) A Ianiro & H Wu et al., Nature chemistry 1 (2019).

Fig. 1: Low dose LPEM imaging of the leaching process. a. Low magnification (LM) TEM image of the liquid cell before flowing NaOH solution. b. LM LPEM image shows the cell is filled with liquid; c. Zoom-in TEM image of the area highlighted by the black dash square in (a); d-e. LPEM images show zeolite nanoparticles gradually become hollow over time: 0 h (d), 5 h (e) and 20 h (f). Electron dose: 5 e-.nm2-.s-.

Fig. 1

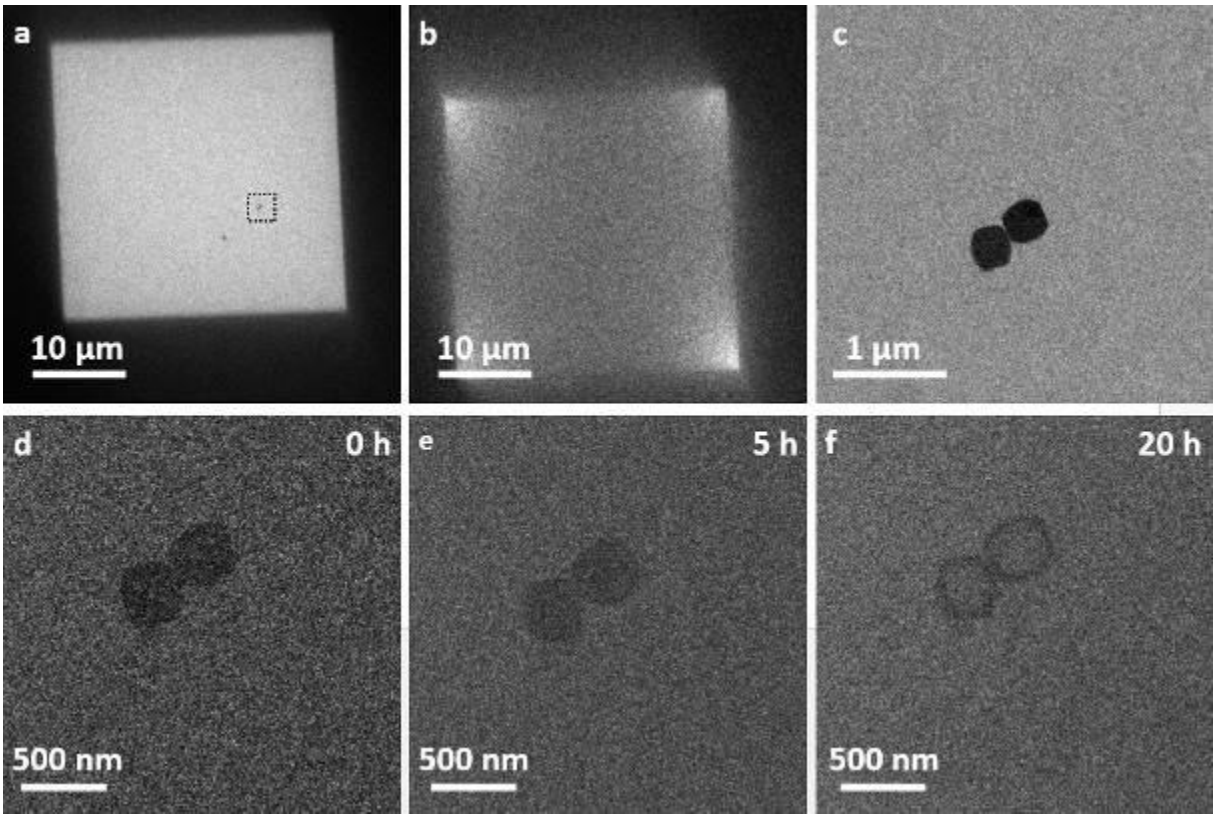

IM3.P022
In situ TEM transformation of Copper precipitates in a martensitic steel during high-temperature ageing

L. Szczepanski[1], A. Zak[1]

[1]Wroclaw University of Science and Technology, Electron Microscopy Laboratory, Wroclaw, Poland

It is known that Cu leads to strength increase in steels containing more than 0.7 mass-% by precipitation hardening of nanosized Cu-precipitates when quenched from the austenite region and tempered around 673-923 K (1). Due to the low solubility of Cu in ferrite, nanometer-sized Cu-rich precipitates form within the material matrix following the sequence: bcc-Cu->9R/2H->3R->ε-Cu (1,2). Compared to ferritic steels, the effect of strength increase is less prominent in the case of martensitic steels where the hardness increase during Cu precipitation counteracts material softening during tempering (3). However, it was shown that Cu precipitation within the martensite leads to an increase in both the static and the cyclic strain hardening exponent during loading (4). The metallurgical reasons for this effect are still unknown.

In order to better understand the effect of Cu precipitates on strengthening during straining, in-situ and ex-situ TEM analysis was conducted during and after ageing of an experimental Cr-Ni-Mo martensitic steel alloyed with 1-1.5 mass-% Cu. As reference samples, as-quenched samples (with no precipitations) and tempered samples (723 K for 3h and 6h) were used. This approach was to first recognize the shape and phase of Cu nanoparticles, and then describe their precipitating process during the in-situ experiment.

Samples for TEM observations were prepared using mechanical thinning down to a thickness of 100 µm, followed by electrolytic polishing and then ion polishing. The samples were observed using a Hitachi H-800 TEM operated at an accelerating voltage of 150 kV. The microscope was equipped with a modified Hitachi holder with the possibility of heating up to 923 K. The heating rate was approximately 10 K/min.

The performed analysis confirmed the presence of nanometer-sized coherent and semi-coherent Cu precipitates distributed within the martensitic matrix, appearing above 750K. The TEM observations suggest that a shear-based transformation of coherent bcc to semi-coherent 9R/2H structures occurs after as well as after straining (fig. 1.).

The coherent and semi-coherent Copper-rich precipitates could be detected by means of SEAD. The characteristic "cross satellite spots" diffraction pattern (fig. 1) was invisible to the as-quenched sample, but appeared in the furnace tempered sample as well as during the in-situ tempering of quenched sample.

References:

(1) Deschamps, A.; Militzer, M.; Poole, W. J.: Precipitation Kinetics and Strengthening of a Fe-0.8wt%Cu Alloy. In ISIJ International, 2001, 41; pp. 196–205.

(2) Goodman, S. R.; Brenner, S. S.; Low, J. R.: An FIM-atom probe study of the precipitation of copper from Iron-1.4 at. pct copper. Part I: Field-ion microscopy. In Metallurgical Transactions, 1973, 4; pp. 2363–2369

(3) Maruyama, N. et al.: Precipitation and phase transformation of copper particles in low alloy ferritic and martensitic steels. In Materials transactions, JIM, 1999, 40; pp. 268–277.

(4) Margarita D. Bambach, Wolfgang Bleck, Hendrik S. Kramer, Marcus Klein, Dietmar Eifler, Tilmann Beck, Holger Surm, Hans-Werner Zoch, Franz Hoffmann, and Aurel Radulescu, "Tailoring the Hardening Behavior of 18CrNiMo7-6 via Cu Alloying", steel research international, 2016, 87, Nr. 5, S. 550-561.

Fig. 1: SAED and microstructure evolution during in situ observations

The authors wish to express their thanks for the research support and the materials to Margarita Doncheva Bambach.

Fig. 1

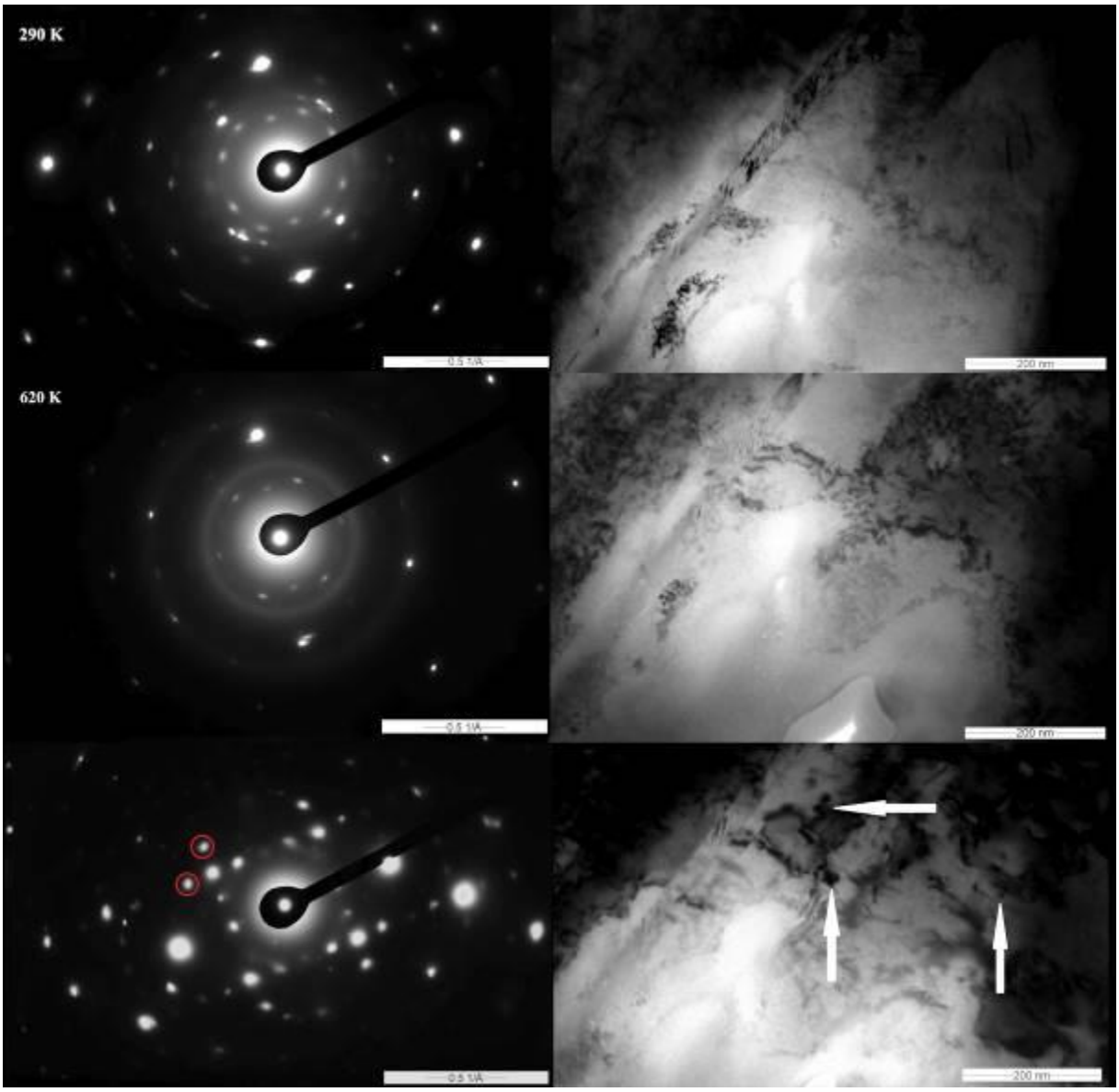

IM3.P023
In-situ TEM heating using a MEMS-based holder: study of refractory W-HfO_2 metamaterials.

S. S. Rout[1], T. Krekeler[1], M. Störmer[2], M. Ritter[1]

[1]Hamburg University of Technology, Electron Microscopy Unit, Hamburg, Germany
[2]Helmholtz-Zentrum Geesthacht Center for Materials and Coastal Research, Institute of Materials Research, Geesthacht, Germany

Micro-electro-mechanical system (MEMS)-based heating holders provide high temperature stability and reproducibility during in-situ annealing experiments in a transmission electron microscope (TEM). They have been recently used to successfully study nano-particles, thin films, and extraterrestrial materials (1-5). Here we report the use of a MEMS-based heating holder to study refractory W-HfO_2 metamaterials.

Recently, it was demonstrated that the W-HfO_2 multilayer metamaterial can be used as a wavelength-selective thermal emitter to increase the efficiency of thermophotovoltaic (6). The optical properties of the refractory W-HfO_2 multilayer were stable after annealing them until 1000°C, but at 1100°C there is a change in the absorptivity after annealing for 3 hours. SEM study of the multilayers did not show any structural degradation after the high temperature annealing but at 1100°C oxygen diffuses from the HfO_2 nanolayer and oxidizes the W nanolayer. Our objective it to anneal monolayers of W and HfO_2, and multilayers of W-HfO_2-W in-situ in the TEM to better understand the structural and chemical degradations until 1100°C.

Single layers of W (20 nm thickness) and HfO_2 (100nm thickness) were deposited directly on MEMS chips from ThermoFischer scientific and a multilayer system of HfO_2-W-HfO_2 (100nm-20nm-100nm thickness) was deposited on a silicon substrate. All these thin-films were deposited by magnetron sputtering of the constituent materials. The MEMS chips were attached to a NanoEX-i/v heating & biasing holder and the in-situ study was carried out in a FEI Talos F200X TEM operating at 200 keV.

The polycrystalline 20 nm W film did not show any changes until 900°C (Fig. 1). After 1000°C the W crystals reoriented themselves and the film showed signs of recrystallization. This was exhibited by the formation of triple junction grain boundary between the W grains and formation of voids along the grain boundaries (Fig. 2). After continued annealing at 1000°C and 1100°C, nanoparticles (< 10 nm) of W started forming on the W thin-film. One grain of HfO_2 within the HfO_2 thin-film was studied and it showed no changes until 800°C. But after annealing above 800°C the grain started to reorient and the whole thin-film also recrystallized above 1000°C.

Significant changes in the absorption spectrum of W-HfO_2 multilayer thin-film was observed after annealing it at 1100°C but no structural degradation was observed in the SEM images (6). Our in-situ annealing experiments shows that W and the HfO_2 thin-films recrystallized above 1000°C and this could explain the change in the absorptivity of the W-HfO_2 multilayer seen by (6). To further understand the degradation of the W-HfO_2 multilayer metamaterials we will anneal the HfO2-W-HfO2 thin-film up to 1100°C.

References:

(1) M. Chi et al. (2015). *Nat Commun* 6, 8925.

(2) M. A. Asoro et al. (2013). *ACS Nano* 7, 7844-7852.

(3) J. Y. Howe et al. (2014). *Nanoscale Res Lett* 9, 614.

(4) F. Niekiel et al. (2016). *Acta Mater* 115, 230-241.

(5) M. S. Thompson et al. (2016). *Meteorit Planet Sci* 52, 413-427.

(6) P. N. Dyachenko et al. (2016). *Nat Commun* 7, 11809.

Fig. 1: Bright field (BF) TEM image of the 20 nm W thin film annealed up to 100°C. Also shown is the polycrystalline diffraction pattern from the region.

Fig. 2: BF-TEM image of the 20 nm W thin film annealed up to 1100°C and the polycrystalline diffraction pattern from the region.

Fig. 1

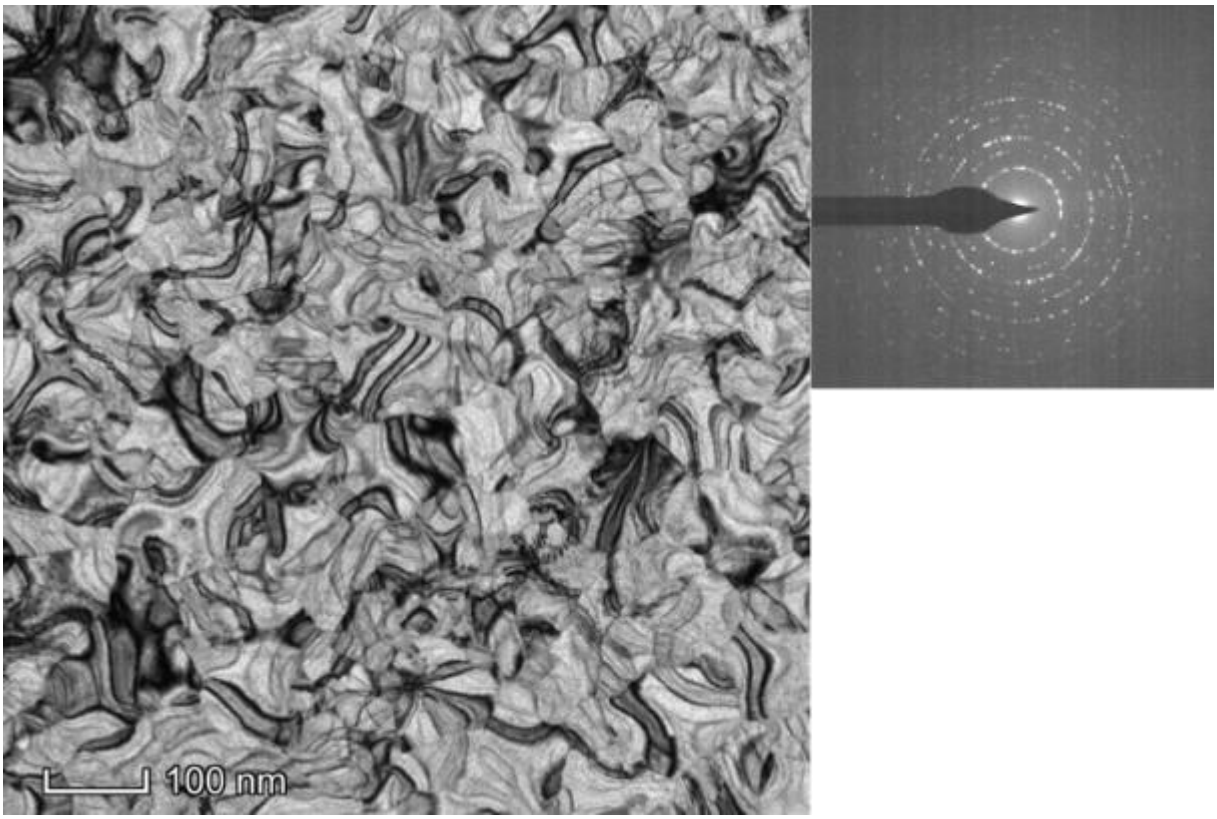

Fig. 2

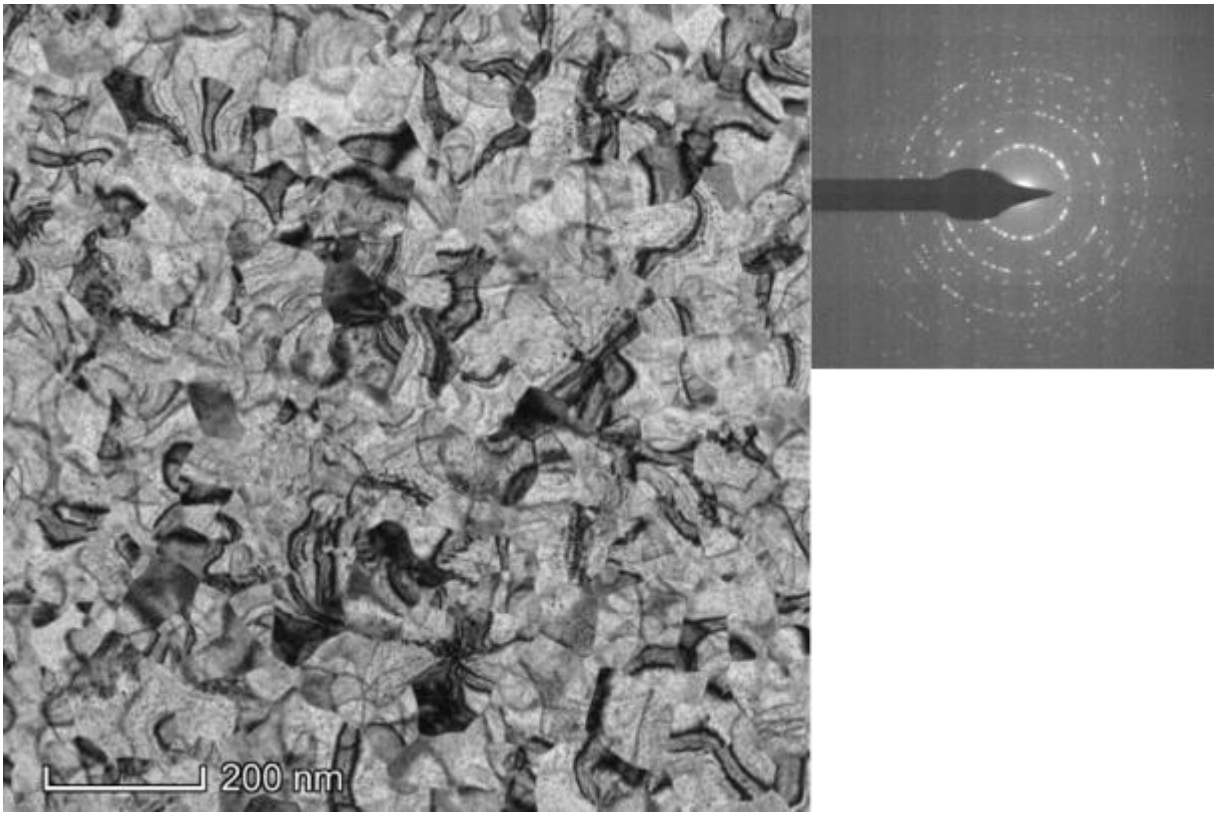

IM3.P024
Lithiation of microreference electrode for reproducible cycling of lithium ion battery systems in liquid TEM

J. Hou[1], V. Tileli[1]

[1]École polytechnique fédérale de Lausanne, Institute of Materials, Lausanne, Switzerland

Recently developed liquid cell transmission electron microscopy (LCTEM) allows *in situ* observation of electroactive material evolution at atomic resolution while monitoring its electrochemical performance (1). Few studies on electrode material analysis in liquid cells hold a stable reference which is a critical element for reproducible battery tests where normally a three-electrode configuration is utilized with lithium as the reference (2). Herein, the focus is placed on stabilizing the reference electrode in the micro-cell system in order to have a more reliable and reproducible platform for lithium ion battery cycling using LCTEM.

Benchtop (in an Ar filled glovebox) and *in situ* (sealed) lithiation has been carried out on gold electrodes on electrochemical chips as presented in Fig. 1a (Hummingbird Scientific, Lacey, WA, USA). Au was selected for its alloying properties with lithium. Two patterned electrodes were connected (Fig. 1b) for lithium electroplating utilizing both chronopotentiometry (CP) and cyclic voltammetry (CV) using BioLogic SP-300 potentiostat (Bio-Logic). Metallic lithium, LP57 (1M $LiPF_6$ in EC:EMC 3:7, BASF) and $LiFePO_4$ (LFP) nanoparticles were used as the lithium source.

Successful electroplating of lithium on the targeted Au electrodes using three different lithium sources has been observed from electrochemical measurements where the potential of the lithiated electrode reduced to around 0.1 V vs. Li/Li^+ by application of constant current (Fig. 1c). However, LFP was primarily considered for reference stabilizing for *in situ* studies of battery systems in the TEM, as gold lithiation from LFP delithiation can not only stabilize the reference for measuring cathode performance individually, but also provide $Li_{1-x}FePO_4$ as areliable anode for battery cycling. Therefore, post mortem analysis focused on the electrodeposition using LFP. Products have been confirmed as LiF and Li_xAu by high resolution TEM (Fig. 2a), elemental mapping using EDX and EELS (Fig. 2b&c). To confirm the stability of the prepared reference, three-electrode CV measurements between the LFP (working electrode), a gold counter electrode, and lithiated gold as the reference were performed. Reproducible CV over cycles indicate the reliability of using lithiated gold as reference for LIB cycling in the liquid cell.

Ultimately, *in situ* gold lithiation by delithiating $LiFePO_4$ with constant current is the optimal choice for stabilizing reference for *in situ* microscale lithium ion battery cycling.

References:

(1) Ross, F. M. Opportunities and challenges in liquid cell electron microscopy. *Science,* 350, (2015).

(2) Zeng, Z., et al., In situ TEM study of the Li-Au reaction in an electrochemical liquid cell. *Faraday Discuss.* 176, 95–107 (2014).

Fig. 1: (a) Schematic of top electrochemical microchip patterned with three electrodes. (b) Graphic representation of two electrodes connection for anode lithiation using chronopotentiometry. (c) Potential evolution of lithiated gold vs. Li/Li^+ during lithiation. The overlaid SEM micrographs indicate the morphology of the initial gold electrode and the lithiated one using $LiFePO_4$ particles as Li source.

Fig. 2: (a) HRTEM of the lithiated gold electrode and the corresponding FFT indicating the alloying after electrodeposition. (b) EDX chemical analysis on the bare and lithiated gold electrode showing F signal. (c) EELS spectrum of lithiated gold and inset indicating the Li K edge fingerprint.

Fig. 1

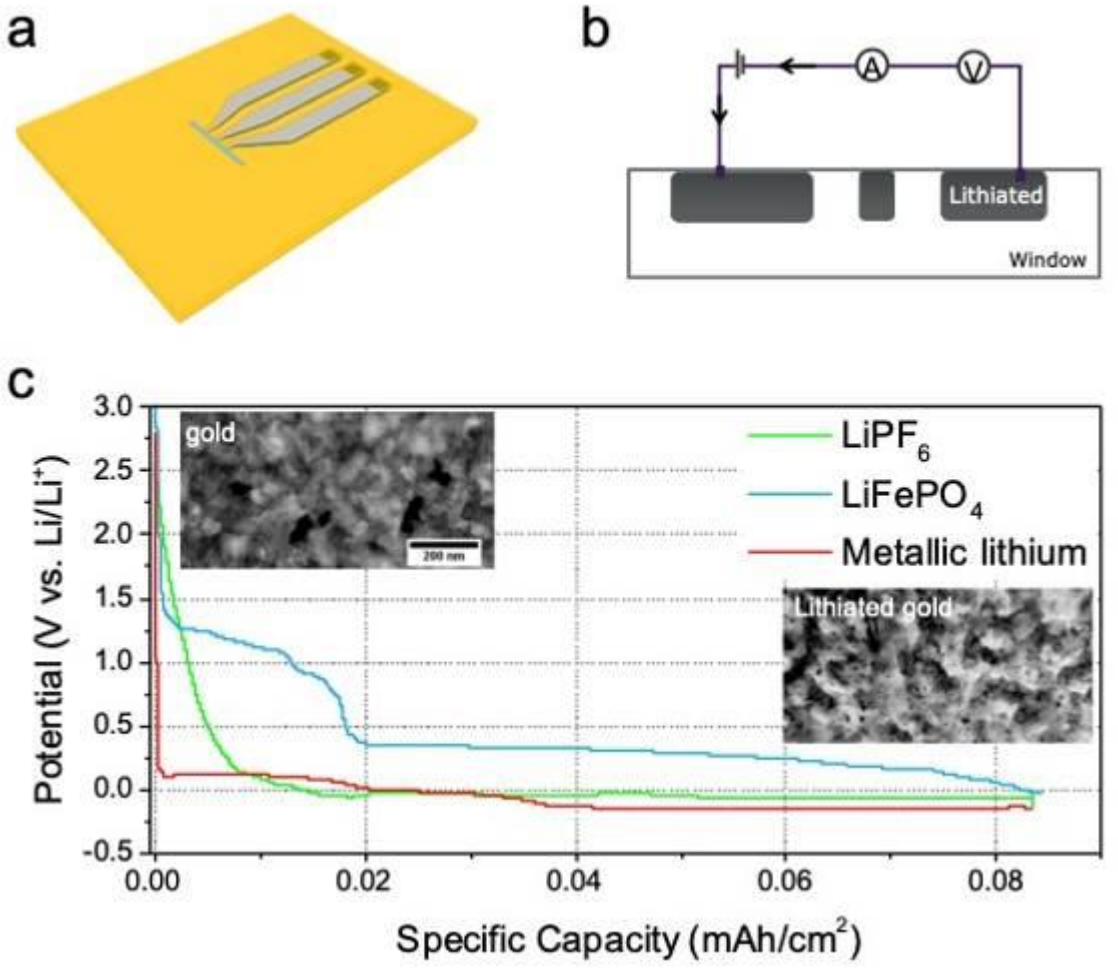
a
b
A
V
Lithiated
Window
c
gold
200 nm
LiPF6
LiFePO4
Metallic lithium
Lithiated gold
Potential (V vs. Li/Li+)
Specific Capacity (mAh/cm2)
3.0
2.5
2.0
1.5
1.0
0.5
0.0
-0.5
0.00
0.02
0.04
0.06
0.08

Fig. 2

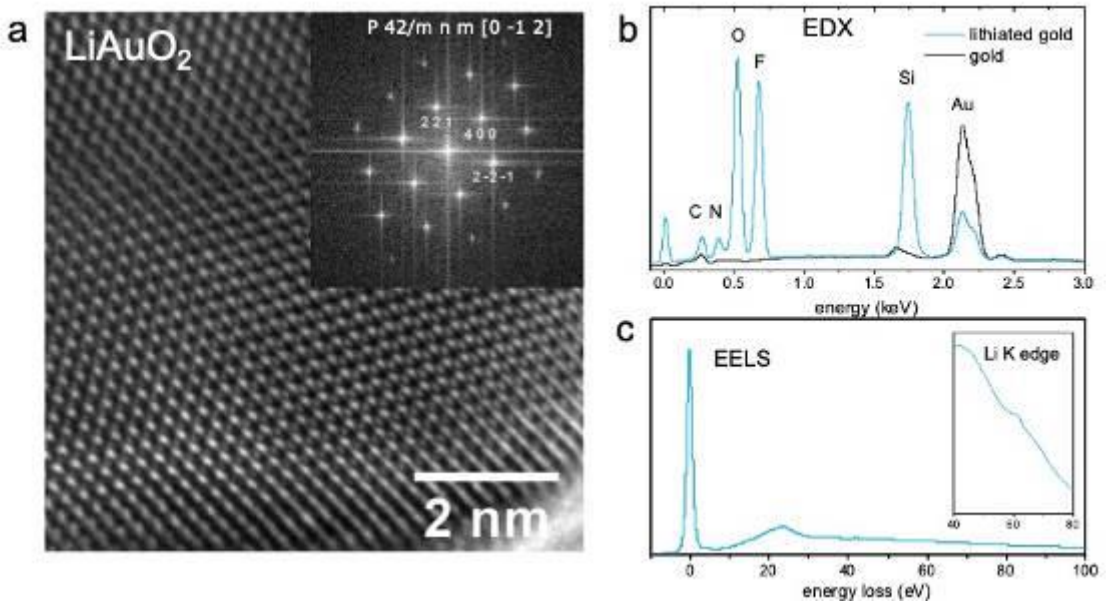
a
LiAuO2
P 42/m n m [0 -1 2]
2 2 1
4 0 0
2 -2 -1
2 nm
b
EDX
lithiated gold
gold
O
F
Si
Au
C N
0.0
0.5
1.0
1.5
2.0
2.5
3.0
energy (keV)
c
EELS
Li K edge
0
20
40
60
80
100
energy loss (eV)

IM3.P025
Revealing the texture evolution during coarsening of Pt thin films *via in situ* segmented hollow cone dark field TEM

C. Wiktor[1,2], M. Wu[1], E. Spiecker[1]

[1]Lehrstuhl für Mikro- und Nanostrukturforschung & Center for Nanoanalysis and Electron Microscopy (CENEM), Universität Erlangen-Nürnberg, Werkstoffwissenschaften, Erlangen, Germany
[2]now at Institut für Mikro- und Nanoanalytik, Universität Siegen, Maschinenbau, Siegen, Germany

Controlled dewetting and grain coarsening of metal thin films promise tailored crystalline nanoparticles and arrays for application in plasmonic devices, catalysts etc., but can also be a failure mechanism in electric coatings and contacts. (1,2) Both are commonly accompanied by the formation of preferred crystallographic textures. This process is highly complex and to utilize it, a thorough understanding of the underlying mechanisms is needed.

Time resolved microscopic studies on the orientation of individual grains are ideally suited to achieve this goal. In commonly applied orientation mapping techniques orientation information is derived from diffraction patterns acquired at each point of a scanning field in SEM (3) or STEM (4) or on a spatially resolved reconstruction of diffraction space based on conical dark field TEM scans. (5) Both require acquisition times of minutes to hours, too slow to reveal texture/coarsening dynamics which require time resolution in seconds or even faster. We developed a method to reveal the dynamic texture evolution in real space at a time resolution of a few seconds via segmented hollow cone dark-field TEM (HCDFTEM).

To reduce acquisition time to a few seconds per orientation map, a limited conical dark field scan of a single set of significant lattice reflections is scanned. In our dewetting and coarsening *in situ* studies of FCC metal thin films we found the development of a major (111) and a minor (100) texture. (6) The (220) reflections of FCC metals are sufficient to distinguish the two by re-occurring strong Bragg contrast within a set of DFTEM images recorded over a full precession cycle under an angle of $2\theta_{220}$. The acquisition time for a single DFTEM image was set to an integer fraction of the precession cycle time, i.e. segments of the hollow cone conventional HCDFTEM would be based on (see. Fig. 1b).

To verify the reliability we tested it on Pt nanoparticles prepared by dewetting and compared the derived orientation (see. Fig. 1c) to electron diffraction patterns of individual Pt particles. We used the technique to perform an *in situ* study on heat-induced grain coarsening and texture formation in a Pt thin film at unprecedented time resolution of a few seconds (see Fig. 2 for individual frames taken from the acquired series of orientation maps). The technique is applicable to virtually all FCC metals and potentially also other crystalline materials.

References:

(1) C. V. Thompson, *Annu. Rev. Mater. Sci.* 30, 159-190 (2000).

(2) F.Leroy, *Surf. Sci. Rep.* 71, 391-409 (2016).

(3) D. J. Dingley, *IOP Conf. Ser.: Mater. Sci. Eng.* 375**,** 012003 (2018).

(4) S. A. Jang, *APL Mater.* 3, 126103 (2015).

(5) G. Wu, *Ultramicroscopy* 109, 1317-1325 (2009).

(6) F. Niekiel, *Acta Mater.* 115, 230-241 (2016).

Fig. 1: a) BFTEM image of Pt NPs prepared by dewetting. b) Center: Conventional HCDFTEM image of a single NP highlighted in a). Around the central HCDFTEM: Diffraction pattern of Pt particle. Dashed circles denote range probed by HCDFTEM. Rainbow-colored segments illustrate size of cone segment for a segmented HCDFTEM image. Outer images: Segmented HCDFTEM images recorded over a full precession of the electron beam. c) Orientation map. Red, green and blue represent reoccurring reflections in the (220) ring of Pt at 60°, 90° and 180° respectively.

Fig. 2: a-g) Chosen orientation maps recorded during the heat-induced grain coarsening of a Pt thin film. The heating profile of the experiment is shown in h).

Fig. 1

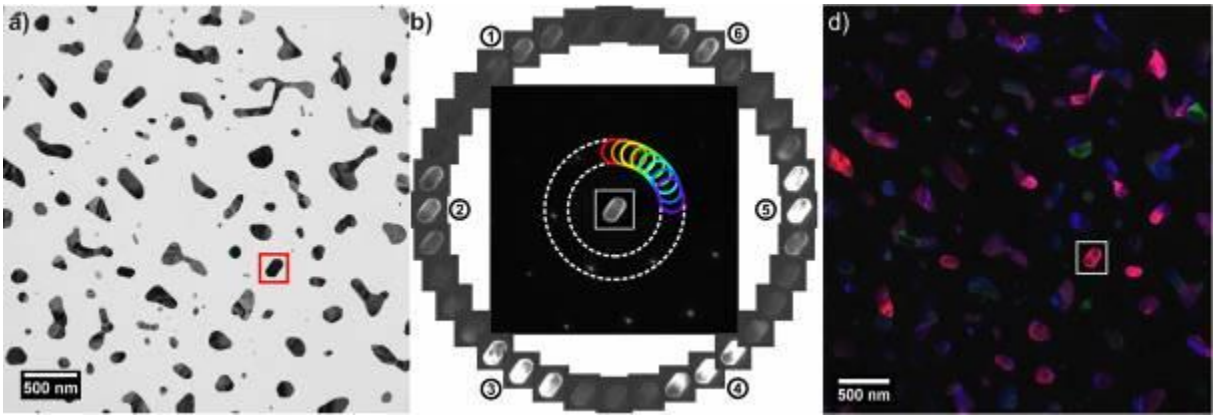

Fig. 2

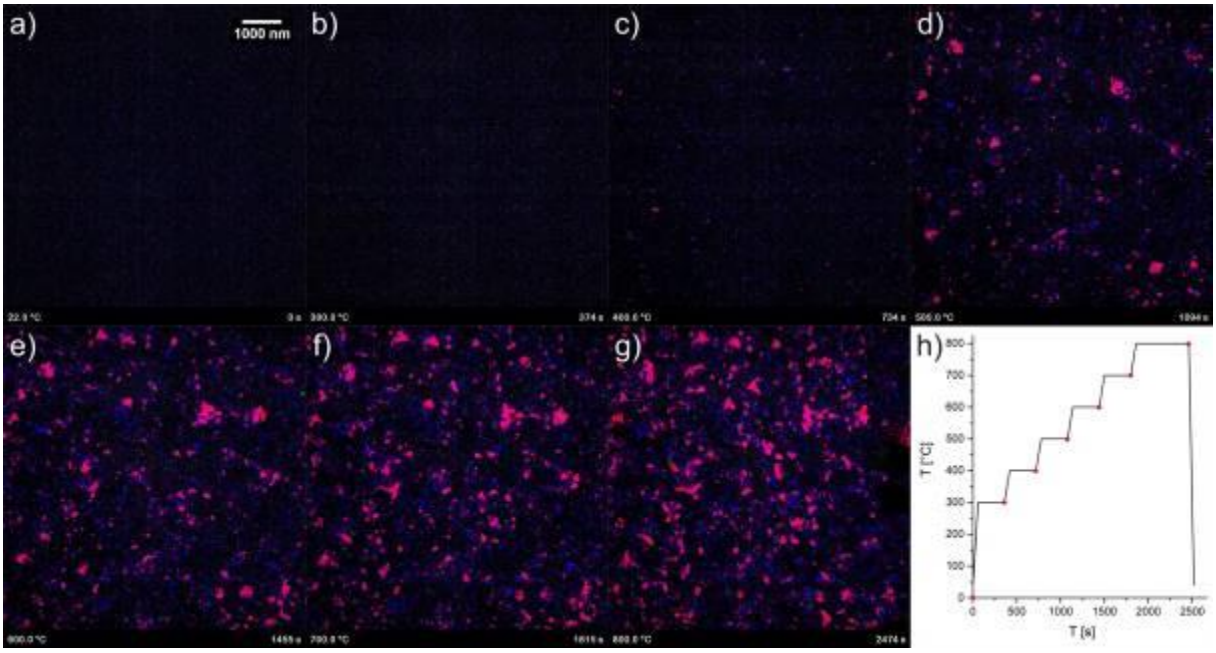

IM4.001 invited
Electron crystallography of nanosized crystals.

A. Stewart[1], G. Mangan[1]

[1]University of Limerick, Physics, Limerick, Ireland

The last decade has seen the introduction of electron diffraction tomography (EDT) to the repertoire of techniques applied in the transmission electron microscope (TEM) research. Traditionally it was assumed orientated zone diffraction patterns, and corresponding images were required to solve sub-micron sized crystals, in 2009 it was demonstrated that randomly orientated crystals whereas many reflections as possible are collected leads to reliable structure solution for small molecules. EDT is primarily used to determine the average crystal structure and of an unknown compound. The technique has developed quickly over the last decade with four different flavours (1,2,3,4) of electron diffraction tomography emerging to serve different experimental conditions and microscope setups. These methods have been applied to almost every type of sub-micron/nano-crystal from metals to metal organic framework through to proteins, making this technique versatile and applicable to hard and soft matter and even at the interfaces between the two.

We will present structure solutions from a wide range of materials using the newest of the four EDT methods, which is known as MicroED. MicroED is the experimental setup closest to mimicking the X-ray crystallography experiment within the TEM, where the crystal undergoes a continuous rotation while a detector with a fast readout speed is used to minimise the loss of data during readout dead time. These experiments are exceedingly efficient, taking only a few minutes to collect an entire three-dimensional data set once the crystal is aligned.

Among the materials analysed are pharmaceutical crystals grown in a magnetic field, where the fields are used to control the nucleation and polymorphism of the crystal form. Understanding the polymorphism (5) and its influence on the nanocrystal formation is a critical step in the drug design and manufacturing process, each new polymorph is a potential new patent, and showing polymorph stability is essential for obtaining approval to bring a drug to market.

We will compare and contrast the different EDT techniques and where their strengths and best-suited applications lie. Along with a discussion of how best to optimise the experimental setup to obtain the best signal to noise ratio for EDT and MicroED data collection.

References:

(1) E. Mugnaioli, T. Gorelik, U. Kolb Ultramicroscopy (2009) Volume 109, 758-765

(2) Zhang, D.L., Hovmöller, S., Oleynikov, P. and Zou,X.D., Z. Kristallogr. 225 (2010) 94-102.

(3) Jan Pieter Abrahams, Dilyana Georgieva, Linhua Jiang, and Igor Nederlof, Uniting Electron Crystallography and Powder Diffraction, (2011) edited by Ute Kolb, Kenneth Shankland, Louisa Meshi, Anatoly Avilov, William I.F David, 389-998.

(4) Dan Shi, Brent L Nannenga, Matthew G Iadanza, Tamir Gonen, eLife, (2013) 2:e01345

(5) Aurora J. Cruz-Cabeza, Susan M. Reutzel-Edens, and Joel Bernstein, Chem. Soc. Rev., 2015,44, 8619-8635

IM4.003
Extending Geometric Phase Analysis (GPA)

M. Hytch[1], N. Cherkashin[1], A. Ishizuka[2], K. Ishizuka[2]

[1]CEMES-CNRS, Toulouse, France
[2]HREM Research Inc, Tokyo, Japan

Geometric phase analysis (GPA) of HR(S)TEM images has become a standard technique for strain mapping over the years (1). Whilst successful, the approach is not without limitations. Elastic strains should be determined relative to the relaxed crystal structure, which is not necessarily the same as the reference used for the analysis (see Figure 1). Elastic strains can even have opposite signs to strains measured with respect to a region of substrate. Furthermore, GPA requires the reference region to be within the image to be analysed. Such internal references may not be present or may not have common, or closely related, reciprocal lattice vectors.

Here, we present a theoretical extension of GPA that in large part overcomes these problems. It allows the study of strain in nanocrystals, where no reference region is generally present, in epitaxial heterostructures, where the materials can be very different from the substrate, and across grain boundaries, where no common lattice planes in general exist. The new theory has the added advantage of correcting global optical distortions. It is little known, for example, that a global shear applied to an image will cause errors to conventional strain analysis. Large in-plane rotations across grain boundaries and domain walls will also be accommodated by the new procedure.

We apply the method to some representative examples and highlight the implications for other strain mapping techniques based on images or diffraction.

References:

(1) M.J. Hÿtch, E. Snoeck and R. Kilaas, Ultramicroscopy 74, 131–146 (1998).

Fig. 1: Illustration of the reference problem: elastic strains are measured with respect to the relaxed (unstrained) crystal whereas GPA measures the image deformation with respect to an internal reference, often the substrate (as here). The new theory addresses this and other problems.

Fig. 1

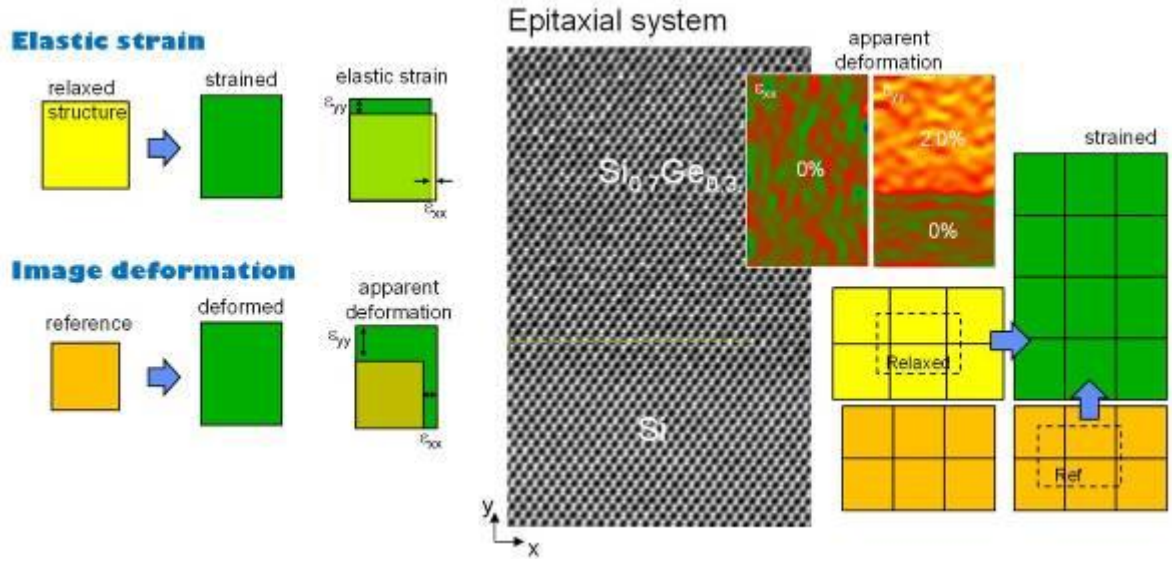

IM4.004
Atom column detection from STEM images using the maximum a posteriori probability rule

J. Fatermans[1,2], A. J. den Dekker[2], C. M. O'Leary[3], P. D. Nellist[3], S. Van Aert[1]

[1]University of Antwerp, EMAT, Antwerp, Belgium
[2]University of Antwerp, imec-Vision Lab, Antwerp, Belgium
[3]University of Oxford, Department of Materials, Oxford, United Kingdom

Recently, the maximum a posteriori (MAP) probability rule has been proposed as an objective method to detect atom columns and even single atoms from high-resolution high-angle annular dark field (HAADF) scanning transmission electron microscopy (STEM) images (1,2). The method quantifies how more likely an obtained atomic structure is as compared to other structures. The MAP probability rule has been shown to be especially useful for the analysis of the structure of beam-sensitive nanomaterials, typically resulting into images of low signal-to-noise ratio (SNR) and contrast-to-noise ratio (CNR). Visual inspection of such images is unreliable and might lead to biased results. As an example, the MAP probability rule has been applied to an experimental STEM image of graphene (1) which is shown in Figure 1.

The relation of atom detectability with common quality measures, such as SNR and CNR, has been investigated. From this analysis, it follows that the detectability strongly depends on the contrast in an image. Therefore, CNR relates better to atom detectability than SNR. The relation between CNR and detection rate, though, depends on the atom type, incoming electron dose and in particular pixel size. For this reason, the integrated CNR (ICNR) has been proposed where the total intensity of electrons scattered by a column is taken into account. The ICNR is a more robust measure for atom detectability than CNR (2), which is illustrated in Figure 2(a)-(c).

In addition, the performance of the MAP probability rule in detecting atoms has been compared with other model-order selection criteria (2). The performances are shown in Figure 2(d)-(f) for three different ICNR values. A positive value of the detection error refers to the detection of too many atoms, whereas a negative value refers to the detection of too few atoms. From Figure 2(d), it can be seen that the MAP probability rule outperforms the other criteria for an ICNR value of less than 3.0. For increasing ICNR values, the performances of the different criteria tend to become more equal, as shown in Figure 2(e) and (f).

To conclude, the MAP probability rule can be used as a tool to evaluate the relation between image quality measures and atom detectability. This has resulted into the introduction of the ICNR as a new image quality measure that better correlates with atom detectability than conventional measures. Furthermore, it has been shown that the performance of the MAP probability rule is superior to that of other model-order selection criteria, allowing for more accurate atom detection.

References:

(1) J. Fatermans et al., Phys. Rev. Lett. 121, 056101 (2018).

(2) J. Fatermans et al., Ultramicroscopy, https://doi.org/10.1016/j.ultramic.2019.02.003 (2019).

Fig. 1: (a) Synthetic ADF image of graphene obtained from an experimental 4D STEM data set. (b) MAP probability rule evaluated for (a). (c) Most probable parametric model of (a) as indicated by the maximum in (b).

Fig. 2: Observed detection rate of an individual atom by the MAP probability rule as a function of ICNR from simulated HAADF STEM images for (a) varying atom type, (b) varying incoming electron dose, and (c) varying pixel size. Average frequency of various selected orders for different model-selection criteria for detecting the number of atoms from simulated HAADF STEM images for an ICNR value of (d) 3.0, (e) 4.0, and (f) 5.0. The insets show simulated images disturbed by Poisson noise with the noise-free images as references.

Fig. 1

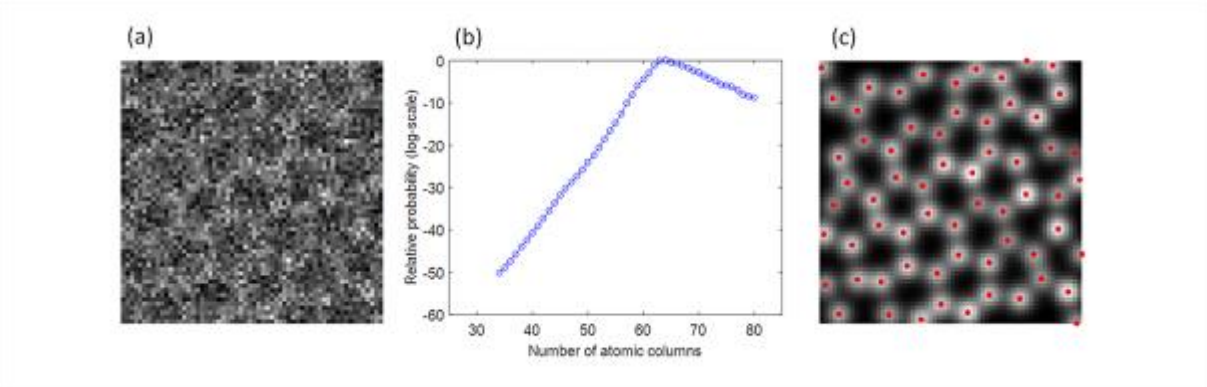
(a)
(b)
(c)
Relative probability (log-scale)
Number of atomic columns

Fig. 2

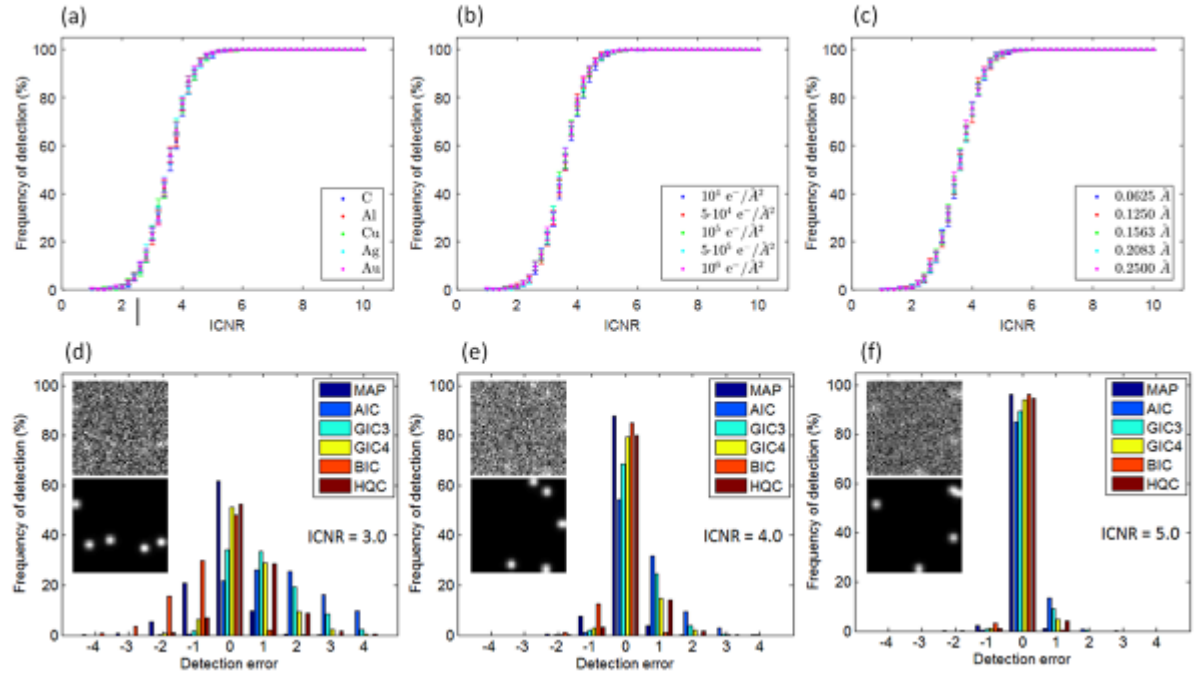
(a)
(b)
(c)
(d)
(e)
(f)
Frequency of detection (%)
ICNR
C
Al
Cu
Ag
Au
MAP
AIC
GIC3
GIC4
BIC
HQC
ICNR = 3.0
ICNR = 4.0
ICNR = 5.0
Detection error

IM4.005
Momentum-resolved STEM as a tool to study angle-dependent electron scattering in nanostructures

H. L. Robert[1,2], A. Rosenauer[3], N. Ravishankar[4], D. Van Dyck[5], K. Müller-Caspary[1]

[1]Forschungszentrum Jülich, Ernst Ruska-Centre for Microscopy and Spectroscopy with Electrons, Jülich, Germany
[2]RWTH Aachen, Physics, Aachen, Germany
[3]IFP Universität Bremen, Bremen, Germany
[4]Indian Institute of Science, Materials Research Centre, Bangalore, India
[5]University of Antwerp, Electron Microscopy for Materials Science, Antwerp, Belgium

In the field of STEM, the momentum-resolved imaging mode denotes the use of a fast camera to record a complete diffraction pattern at each raster position of the convergent electron beam. Through the recording of such four-dimensional data stacks, and the development of specific algorithms for their treatment, it becomes possible to directly correlate features in reciprocal and real space. This new generation of techniques opens the way to novel quantitative measurement methods of physical quantities, at the (sub-)atomic scale, by exploring the detailed distribution of the scattered intensity.

The theory of electron scattering, as it was developed for simulation and interpretation of (S)TEM images, is mainly based on elastic interactions between the incoming beam and atoms. Frozen phonon approaches also allow to account for vibrational modes of the lattice. In recent studies, a mismatch was found between angle-dependent intensity curves (azimuthally-integrated diffraction patterns) from state-of-the-art simulations and experiments for low-angle scattering in semiconductors (1). This calls for a need to introduce an improved theoretical framework, in which more contributions to the angular distribution of scattered electrons are taken in account. An emphasis is put on inelastic interactions such as e.g. plasmon excitations, which, from preliminary studies, are believed to have a more important role at low scattering angles.

In the framework of this project, the disagreement between theoretical and experimental approaches is characterized for different materials and thicknesses (2). Additional approaches for the extraction of physical quantities, e.g. vertical positions of atomic columns' centers of mass, with support from theory, are also investigated. As a first platform for the studies, an interest is taken in cylindrical metal samples, e.g. Au nanowires and nanorods, and semiconductor or metal bulk crystals, e.g. wedge-shaped [110]-oriented Pt for the mapping of continuous thickness-gradient areas.

The quantitative understanding of angle-dependent scattering, altogether with experimental results from state-of-the-art instrumentation (a resolution of 50 pm can be achieved), is to provide the basis for a precise composition mapping of materials with high potential for Bio/Nanotechnologies and Material Science. In particular, the project focuses on ultrathin (1 to 2 nm in diameter) Au nanowires, alloyed with Pt, Pd or Cu, for their possible applications as catalysts, bio/electrochemical sensors and nanoelectronic interconnects.

References:

(1) Müller-Caspary, K. *et al.*; Materials characterization by angle-resolved scanning transmission electron microscopy; *Scientific Reports* **6**, 37146 (2016)

(2) Funding from the Initiative and Network Fund of the Helmholtz Association under contract VH-NG-1317 is gratefully acknowledged.

Figures: (a) Images of an ultrathin Au nanowire reconstructed using different angular ranges. (b) Angle-dependent scattered intensity for different thicknesses and compositions in ultrathin nanowires. The division by S indicates a normalization with regards to solid angle.

Fig. 1

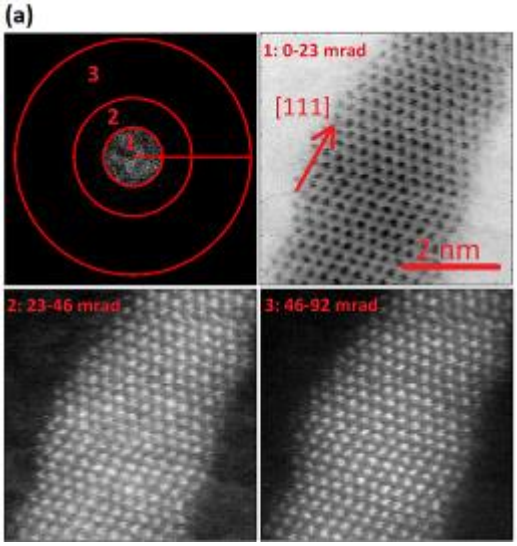
(a)
3
2
1
1: 0-23 mrad
[111]
2 nm
2: 23-46 mrad
3: 46-92 mrad

Fig. 2

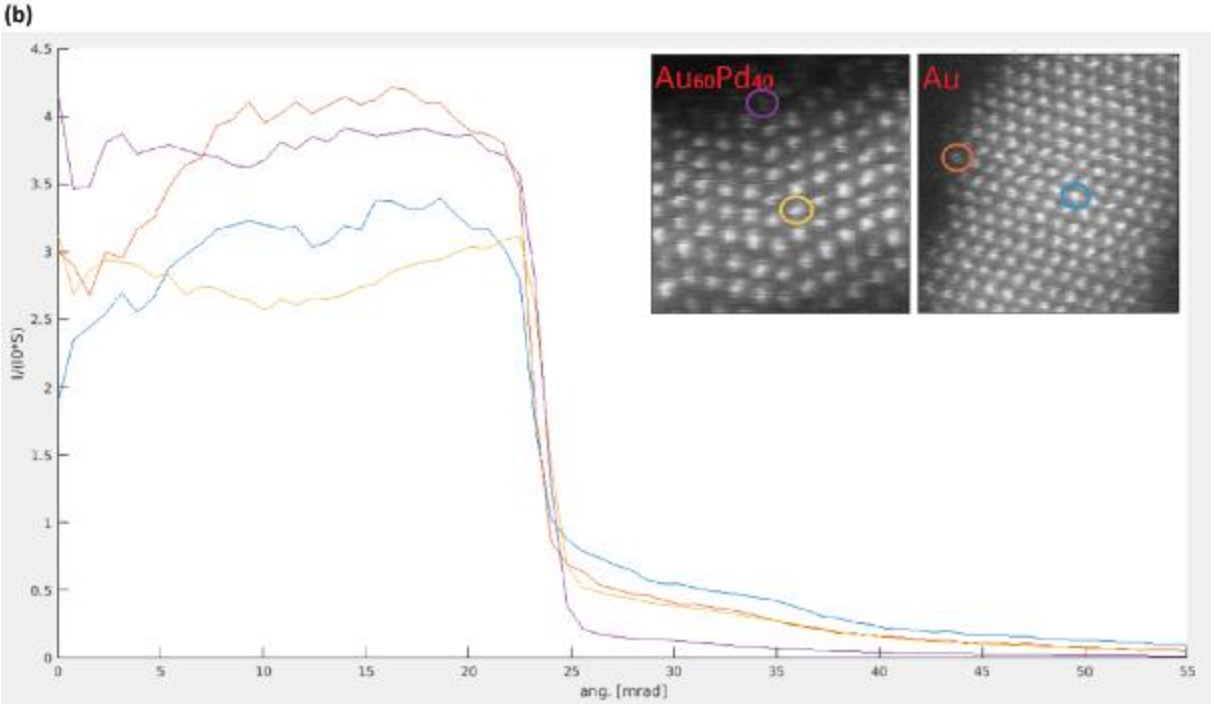
(b)
Au60Pd40
Au
I/I(0*S)
ang. [mrad]
0
0.5
1
1.5
2
2.5
3
3.5
4
4.5
0
5
10
15
20
25
30
35
40
45
50
55

IM4.006
Diffraction mapping of amorphous structures: Sensitivity to structure and dynamics

M. Peterlechner[1], S. Hilke[1], K. Spangenberg[1], G. Wilde[1]

[1]Institute of Materials Physics, University of Muenster, Faculty of Physics, Muenster, Germany

Metallic glasses (MGs) are well studied amorphous model systems, showing relations of dynamics with properties. It is thus important to measure dynamics and structure the same time, to correlate it. In MGs, typically topological order on a scale of 0.5 to 3 nm is present, often denoted as medium range order (MRO). MRO can be detected by fluctuation electron microscopy (FEM) (1). To measure dynamics, recently electron correlation microscopy (ECM) was introduced (2), shown to measure dynamics in the undercooled melt. To extend the temperature limitation, the present work focuses the FEM/ECM sensitivity at room temperature.

The detectability of local rearrangements is analysed using simulated structures (molecular dynamics – MD) and experimental data. Image simulations for transmission electron microscopy (TEM) is made by STEMcl (3). Different MD time steps, missing atoms and detector collection-angles are used.

Structures from MD simulations of Si (4) are used. The STEMcl image simulations where performed using typically 150 detector segments, and FEM data were deduced according to (4).

A MD box of amorphous Si was used to simulate FEM data, shown in Figure 1. Different MD time steps are simulated, and the corresponding FEM data show subtle changes over a broad range of k-values. Additionally, a FEM signal of a well relaxed structure is simulated as shown in Figure 2. The FEM signal changes more clearly on a longer time scale.

The results show, that the amount of the FEM signal change depends on the k-value. Since the simulated FEM data of the individual time steps shows subtle changes, it is concluded that even thermal vibrations can theoretically be detected by FEM, however, on experimentally not accessible time scales. ECM is more sensitive to track longer time scale dynamics and is expected to reflect basically the FEM signal time evolution, at a particular k-value.

References:

(1) M.M.J. Treacy, J.M. Gibson, L. Fan, D.J. Paterson, I. McNulty, Reports Prog. Phys. 68 (2005) 2899–2944.

(2) L. He, P. Zhang, M.F. Besser, M.J. Kramer, P.M. Voyles, Microsc. Microanal. 21 (2015) 1026–33.

(3) M. Radek, J.-G. Tenberge, S. Hilke, G. Wilde, M. Peterlechner, Ultramicroscopy 188 (2018) 24–30.

(4) S. Hilke, J. Kirschbaum, V. Hieronymus-Schmidt, M. Radek, H. Bracht, G. Wilde, M. Peterlechner, Ultramicroscopy (2019).

Financial support by the Deutsche Forschungsgemeinschaft (DFG) under the grant number PE 2290/2-1 is gratefully acknowledged as well as the funding of our TEM equipment from the Deutsche Forschungsgemeinschaft via the Major Research Instrumentation Programme under INST 211/719-1 FUGG.

Fig. 1: Comparison of simulated FEM data of a MD box of amorphous silicon. Three different time steps are shown, with 1 ns per step. Local atomistic jumps lead to a subtle scatter of the FEM data.

Fig. 2: Simulated FEM data of an MD box of amorphous silicon as-quenched and relaxed (1 us). Small but detectable changes occur. Measuring the differential as a function of time, like in ECM measurements, is expected to be most sensitive at k-values where the normalized variance changes as well.

Fig. 1

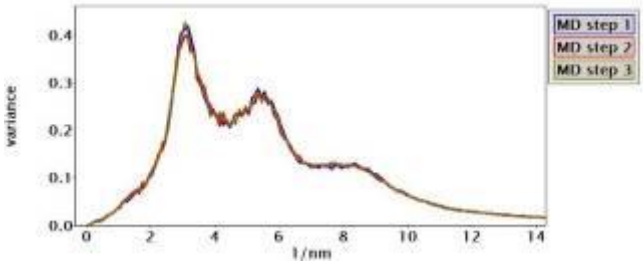
MD step 1
MD step 2
MD step 3
variance
0.0
0.1
0.2
0.3
0.4
0
2
4
6
8
10
12
14
1/nm

Fig. 2

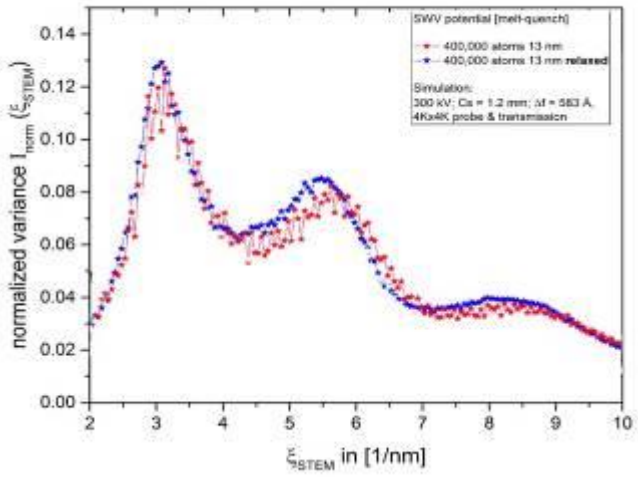
SWV potential [melt-quench]
400,000 atoms 13 nm
400,000 atoms 13 nm relaxed
Simulation:
300 kV; Cs = 1.2 mm; Δf = 583 Å
4Kx4K probe & transmission
normalized variance I_{norm} (ξ_{STEM})
0.00
0.02
0.04
0.06
0.08
0.10
0.12
0.14
2
3
4
5
6
7
8
9
10
ξ_{STEM} in [1/nm]

IM4.LB.P01
Investigation of morphology and composition of quaternary InAs/InAlGaAs and ternary InAs/InP quantum dots emitting in the low loss telecom wavelength range

M. Schowalter[1], C. Carmesin[1], M. Lorke[1], T. Grieb[2], K. Müller-Caspary[3], S. Banyoudeh[4], V. Sichkovskyi[4], M. Yacob[4], J. P. Reithmaier[4], M. Benyoucef[4], A. Rosenauer[2], F. Jahnke[1]

[1]Universität Bremen, Institut für Theoretische Physik, Bremen, Germany
[2]Universität Bremen, Institut für Festkörperphysik, Bremen, Germany
[3]Forschungszentrum Jülich, Ernst-Ruska-Centrum, Jülich, Germany
[4]Universität Kassel, Institut für Nanostrukturtechnik, Kassel, Germany

InAs/InAlGaAs/InP and InAs/InP are promising material systems for the realization of advanced laser diodes such as single photon emitters and tunnel injection lasers with an emission wavelength in the low-loss telecom band (1-3). For achieving a deeper understanding of the emission properties of such devices the comparison of experimentally measured photoluminescence properties with atomistic tight-binding simulations based on structure models including the composition distribution in the dots and their morphology is required (4). For the composition determination of the ternary InAs/InP the method published in (5) was adopted, whereas for the quanternary InAs/InAlGaAs material system strain and Voronoi intensity were determined and assigned to each atomic position. The specimen thickness was measured in the InAlGaAs barriers by a comparison of the normalized experimental intensities with a dataset of simulated intensities for different specimen thicknesses, In and Al concentrations and was then interpolated within the quantum dot region. The composition in the barriers was measured using energy dispersive x-ray spectroscopy being in good agreement with the nominal composition. Using the known specimen thickness, In and Al concentrations of each atomic position was found by minimizing the deviation between experimental and theoretical pairs of strain and Voronoi intensity in a least square sense.

References:

(1) L. Brusberg, C. Herbst, M. Neitz, H. Schröder and K. D. Lang, 2014 The European Conference on Optical Commuication (ECOC), pp. 1-3, ISSN 1550-381X.

(2) M. Benyoucef, M. Yacob, J.P. Reithmaier, J. Kettler and P. Michler, Appl. Phys. Lett. 103 (2013) 162101.

(3) M. Yacob, J. P. Reithmaier and M. Benyoucef, Appl. Phys. Lett. 104 (2014) 022113.

(4) C. Carmesin, M. Schowalter, M. Lorke, D. Mourad, T. Grieb, K. Müller-Caspary, M. Yacob, J.P. Reithmaier, M. Benyoucef, A. Rosenauer and F. Jahnke, Phys. Rev. B 96 (2017) 235309.

(5) A. Rosenauer et al., Ultramicroscopy 109 (2009) 1171.

IM4.LB.P02
Model-Based Geometry Reconstruction Of Quantum Dots From TEM

A. Maltsi[1], T. Koprucki[1], T. Niermann[2], T. Streckenbach[1], K. Tabelow[1], J. Polzehl[1]

[1]Weierstrass Institute, Berlin, Germany
[2]Technische Universität, Institut für Optik und Atomare Physik, Berlin, Germany

The growth of semiconductor quantum dots (QDs) with desired electronic properties would highly benefit from the assessment of QD geometry, distribution and strain profile in a feedback loop between epitaxial growth and analysis of their properties. To assist the optimization of QDs imaging, transmission electron microscopy (TEM) can be used. However, a direct 3D geometry reconstruction from TEM of bulk-like samples, by solving the tomography problem is not feasible due to its limited resolution (0.5-1 nm), the highly nonlinear behaviour of the dynamic electron scattering and strong stochastic influences due to uncertainties in the experiment, e.g. excitation conditions.

We present a novel concept for 3D model-based geometry reconstruction (MBGR) of QDs from TEM images. This will include (a) an appropriate model for the QD configuration in real space including a categorization of QD shapes (e.g., pyramidal or lense-shaped) and continuous parameters (e.g., size, height), (b) a database of simulated TEM images covering a large number of possible QD configurations and image acquisition parameters (e.g. bright field/dark field, sample tilt), as well as (c) a statistical procedure for the estimation of QD properties and classification of QD types based on acquired TEM image data.

For the In(Ga)As QDs under consideration, the lattice-misfit between In(Ga)As and GaAs (surrounding matrix) induces mechanical stresses in the nanostructure. The dynamic electron scattering in semiconductor nanostructures, is influenced by spatial variations in the chemical composition and by local deformations of the lattice due to elastic strain. In order to create a virtual TEM both, the strain field and the electron scattering process, have to be described. For the elastic relaxation of the misfit-induced strain we employ continuum mechanics and the concept of Eshelby's inclusion. For the numerical simulation of the TEM images we employ an elasticity solver to obtain the strain profile, which enters a solver for the Darwin-Howie-Whelan equations, describing the propagation of the electron wave through the sample.

The ultimate goal of our approach is the reconstruction of the geometry of QDs from measured TEM images. We will start analysing the properties of simulated TEM images that are generated by the methods described above. The database contains series of TEM images for QDs with various shapes, sizes and indium concentrations as well as excitation conditions of the electron beam. By variation of the excitation conditions the sensitivity of the imaging can be tuned, e.g., to different components of the strain. This database is a key element of our concept for MBGR and can be used for a) determination of the class or type of QD based on machine learning techniques and b) establishing a statistical procedure for the estimation of geometric properties such as size, height or depth. We will present results on the database of simulated TEM images and our current state of understanding of inference methods for geometric properties of the quantum dots.

Fig. 1

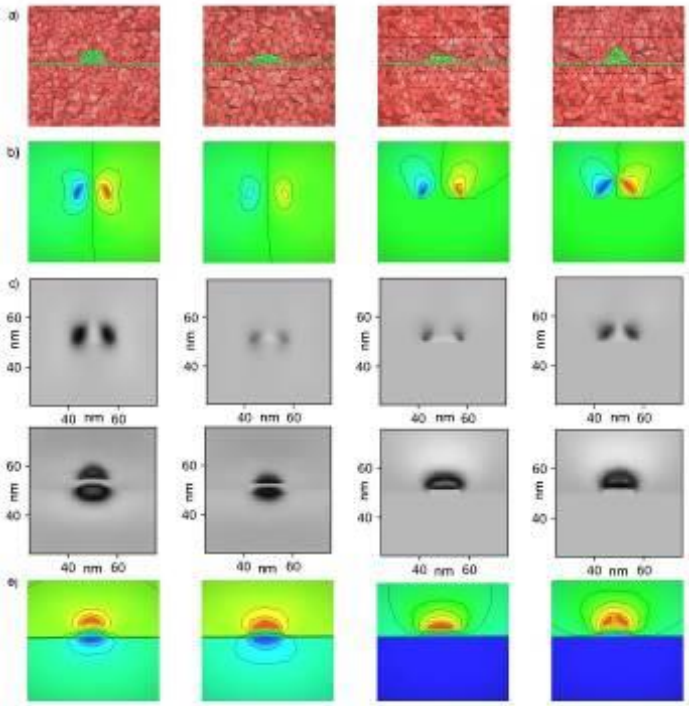

Figure 1: InGaAs quantum dots (indium content 80%) embedded in a GaAs matrix with different shapes: lens-shaped QDs with circular base (two left columns) and pyramidal QDs (two right columns) with different vertical aspect ratios, respectively. FEM simulation of the elastic relaxation of the misfit induced strain: (a) geometry and FEM mesh (b) u_y component and (e) u_z component of the displacement field along a yz-cross-section through the center of the QDs. Simulated TEM images for two different excitations: (c) dark field for $\langle 040 \rangle$ reflection for excitation under (040) strong beam conditions and (d) dark field for (004) reflection for excitation under (004) strong beam conditions. Due to the excitation conditions, the image contrast (c) is sensitive to the [010]-component of the displacement field corresponding to u_y in (b) and the image contrast (d) is sensitive to the [001]-component of the displacement field corresponding to u_z in (e). In all cases a coffee-bean like contrast can be observed.

IM4.LB.P03
Correction for linear drift in middle- and high-resolution STEM images

P. Potapov[1], A. Lubk[1]

[1]Leibniz Institute for Solid State and Materials Research Dresden, Dresden, Germany

Acquisition of STEM images typically requires an order of magnitude longer time than shooting fixed-beam TEM images. Since different instabilities (for instance, drift of the sample) always exist in the system, this might distort noticeably the resulted image. It is not exceptional to observe the slightly elliptic shape of the actually round particles or to see the monoclinic distortion of the assumable rectangular lattice cell. These distortions can be however corrected a posteriori. Objectives

Since the STEM distortions depend on the scanning direction, the issue can be relaxed by taking two STEM images of the same area with the different (best mutually perpendicular) scanning directions (1-3). Analyzing such images allows to deduce the magnitude and direction of the drift in the course of acquisition and remove it by image processing.

In the present work, we assume a linear drift in the course of both acquisitions. Then, in the case of middle range magnifications, the cross correlation between the original and 90°-rotated images allows to deduce the direction and magnitude of the drift and remove it from both the images by warping (Fig.1).

In case of atomic-resolution images, the cross-correlation strategy mostly does not work as the lattice might be essentially same everywhere. Alternatively, the drift can be estimated from the distortion of the lattice geometry. In Fig.2, left, the quadratic unit cell of SrTiO3 is slightly vertically elongated in the original image while compressed in the 90°-rotated image not mentioning the monoclinic distortion. These distortions can be quantified from the comparative analysis of the FFT transforms of both images and finally removed by image warping (Fig.2, right).

STEM distortions related to a linear drift can be deduced from the cross-correlation of two images (middle magnification range) or the analysis of FFT (high resolution range) and successfully removed. The DigitalMicrograph plugin for that can be free downloaded at www.temdm.com.

References:

(1) L. Jones et al. Microscopy and Microanalysis 19 (2013) 1050.

(2) X. Sang et al. Ultramicroscopy 138 (2014) 28.

(3) C. Ophus et al. Ultramicroscopy162 (2016) 1.

Fig. 1: Correction of middle resolution images.

Fig. 2: Correction of high resolution images.

Fig. 1

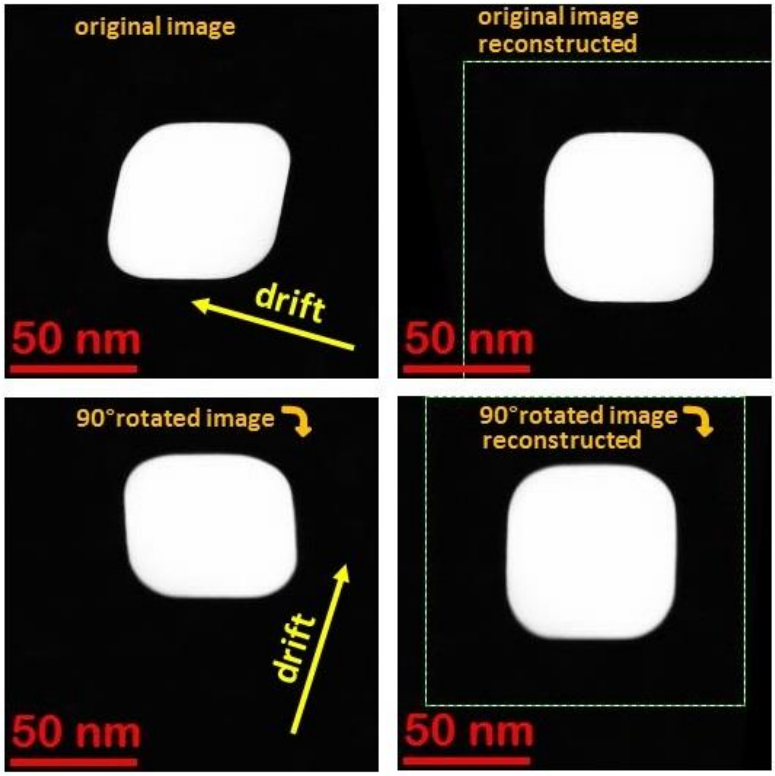
original image
drift
50 nm
original image
reconstructed
50 nm
90°rotated image
drift
50 nm
90°rotated image
reconstructed
50 nm

Fig. 2

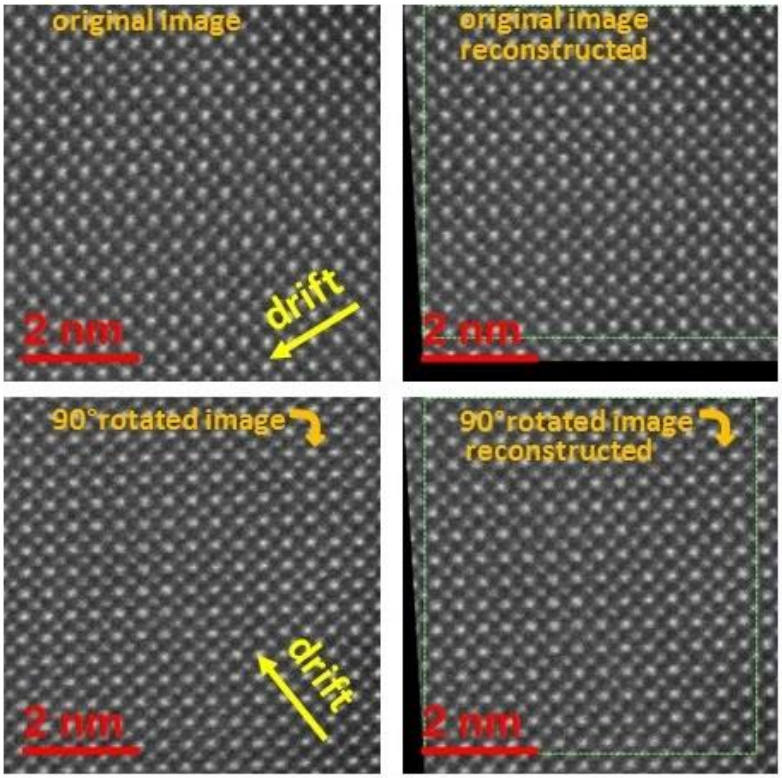
original image
drift
2 nm
original image
reconstructed
2 nm
90°rotated image
drift
2 nm
90°rotated image
reconstructed
2 nm

IM4.P001
Optimization of imaging conditions for composition determination of ternary III-V semiconductors by ADF-STEM

P. Kükelhan[1], A. Beyer[1], K. Volz[1]

[1]Philipps University Marburg, Materials Science Centre and Faculty of Physics, Marburg, Germany

III-V semiconductors are technologically relevant for a large variety of applications. To improve device performance, structural characterization provides an important contribution alongside theory and growth. Quantitative scanning transmission electron microscopy (STEM) is an established method for analysis of nanostructures, in particular composition determination. Absolute composition determination can be achieved by comparing experimental STEM results to complementary image simulations (1). Local composition determination up to single-atom accuracy is possible with annular dark field (ADF) STEM in certain cases (2).

Here, we are looking to optimize the imaging conditions for composition determination in different material systems. This includes the optimization of imaging parameters like the convergence angle and in particular the detector range. The angular dependence of the scattered intensity is explored in detail. Especially, the influence of different material systems is investigated. This is carried out by a simulation study and comparison to experimental results.

Image simulations are performed with the software package STEMsalabim (3) which is based on the multi-slice algorithm. Simulations are carried out for varying compositions of ternary III-V semiconductors.

Experimental sample preparation is based on focused ion beam milling (JEOL JIB4601F) and low voltage ion polishing (Fischione NanoMill™). ADF-STEM images and convergent beam diffraction patterns are acquired with an aberration-corrected JEOL JEM 2200FS and a pixelated detector (PNDetector pnCCD).

Optimization of imaging conditions with respect to the accuracy in composition determination is possible. The optimal parameters are depending on the material system. In particular, the detector range for image acquisition should be taken care of. Experimental demonstration is based on the results of a simulation study.

ADF-STEM is a powerful method for local composition determination of III-V semiconductors. Optimizing the imaging conditions for every material system even enhances its potential for highly accurate local composition determination.

References:

(1) Rosenauer et al., Ultramicroscopy 111 (2011), pp. 1316-1327

(2) Duschek et al., Ultramicroscopy (2019)

(3) Oelerich et al., Ultramicroscopy 177 (2017), pp. 91-96

IM4.P002
Fast and automated diffraction tomography: a universal acquisition module

S. Plana Ruiz[1,2], Y. Krysiak[3,4], J. Portillo[5,6], S. Estradé[2], U. Kolb[1,3]

[1]Technische Universität Darmstadt, Institut für Angewandte Geowissenschaften, Darmstadt, Germany
[2]Universitat de Barcelona, Enginyeria Electrònica i Biomèdica, Barcelona, Spain
[3]Johannes Guttenberg-Universität Mainz, Institut für Chemie und Analytische Chemie, Mainz, Germany
[4]Czech Academy of Sciences, Prague, Germany
[5]Universitat de Barcelona, Centres científics i tecnològics, Barcelona, Spain
[6]Nanomegas, Brussels, Belgium

Electron diffraction tomography (EDT) has reached a point where it has become a routine technique for single-crystal diffraction studies at the nanometer scale. The usual methods to obtain accurate structure determinations deal with x-rays. The problem with x-rays is that they cannot sample diffraction information from an isolated nanocrystalline domain. Although this could not be a problem for single-phase powders or "big-enough" crystals, it becomes a challenge when crystallographic analyses have to be performed on multiple-phase powders, nanocrystals embedded in different phase matrices or crystals with some kind of disorder. At this point, EDT can be a valuable method to overcome the challenges outlined above by enabling the reconstruction of the intensity-weighted reciprocal lattice from a single nanocrystal. However, the routine acquisition of such datasets has been confined to few labs due to the lack of automatization and universal application.

In this context, a new acquisition module was developed in Digital Micrograph scripting as well as in Matlab environment to provide a versatile platform for EDT acquisition, so called Fast-ADT (Fast Automated Diffraction Tomography). The program is based on two tilt scans of the goniometric stage between the desired tilt range; the first one to monitor the crystal displacement with respect to the tilt angle in order to generate a crystal tracking file, and the second one to acquire the diffraction tomography according to the crystal positions of the tracking file. This procedure allows reliable diffraction acquisitions down to 20 nm crystals provided that the stage has been aligned for tomography experiments and the used holder is kept in good condition. The program allows to choose between TEM or STEM modes of the microscope as well as the diffraction pattern acquisition approach, i.e. sequential or continuous, in an attempt to create an acquisition module as general as possible to fit the experimental requirements of different samples. A few examples are shown using such module in order to demonstrate how the module is suitable for structure solution, refinement using the dynamical scattering theory and analysis of disorder features. In other words, it covers from the average phase of a crystal to its finest crystallographic details. In this way, the authors intend to provide an all-in-one platform to provide a useful tool for materials characterization to the scientific community.

IM4.P003
Fluctuation electron microscopy of amorphous materials: simulation meets experiments

S. Hilke[1], H. Rösner[1], G. Wilde[1], M. Peterlechner[1]

[1]Westfälische Wilhelms-Universität Münster, Institut für Materialphysik, Münster, Germany

The method of fluctuation electron microscopy (FEM) is a powerful tool, which is highly sensitive to medium range order (MRO). In the following, MRO denotes coherently scattering domains on a length scale beyond 0.5 nm, or in other words, (pair-pair-) correlations of structural units like (frustrated) icosahedra and other sub-structures. Thus, it is a method of choice to study amorphous materials as for instance metallic glasses (MGs) or amorphous Si. In the present work, different molecular dynamics (MD) boxes of various materials with different compositions and treatments were generated, FEM simulations performed and analysed regarding their MRO. Using large MD boxes, it is feasible to analyse sub-structural units with respect to the MRO, and to gain knowledge on the sensitivity. The hollow cone "variable coherence" mode of FEM was emulated in the simulation using a recently in-house developed multislice algorithm (STEMcl) (1) and analysis approach (2). The simulated results were subsequently compared with experimental data of Pd-based (see Fig. 1) and Zr-based (see Fig. 2) metallic glasses. Using variable resolution FEM (VR-FEM) we have recently shown that the MRO in Vit105 ($Zr_{52.5}Cu_{17.9}Ni_{14.6}Al_{10}Ti_5$) was changed after deformation, in line with a structure containing significant icosahedral- and crystal-like MRO (3). It is shown that heterogeneity of sub-structural units at the MRO scale is measurable in both MD (4) and experiment. Sub-structural components like icosahedral-like MRO were found in both systems (Pd- and Zr-based alloys). However, more importantly, in addition to crystal- and icosahedral-like MRO clusters, tetragonal clusters were also found in PdNiP resembling the sub-structural units of as-cast NiP MGs (5). This was not observed for the Zr-based materials. It is concluded that the covalent bonding of phosphorous caused the heterogeneity to increase in terms of more possible cluster types and thus increasing the ductility of such materials. This suggests that the ductility of MGs is strongly connected to topological order (MRO sizes, volume fractions and structures) and might be tailored accordingly.

References:

(1) Radek, M., Tenberge, J. G., Hilke, S., Wilde, G., & Peterlechner, M. *Ultramicroscopy* 188 24-30 (2018).

(2) Hilke, S., Kirschbaum, J., Hieronymus-Schmidt, V., Radek, M., Bracht, H., Wilde, G., & Peterlechner, M. *Ultramicroscopy* (2019) in press.

(3) Hilke, S., Rösner, H., Geissler, D., Gebert, A., Peterlechner, M., & Wilde, G. *Acta Materialia* Available at SSRN 3289660 (2018) under review.

(4) Hilke, S., Lagogianni, A., Hassani, M. R., Varnik, F., Wilde, G., & Peterlechner, M. unpublished manuscript.

(5) Zhan, X., Zhang, P., Voyles, P. M., Liu, X., Akolkar, R., & Ernst, F. *Acta Materialia* 122 400-411 (2017).

Financial support by the Deutsche Forschungsgemeinschaft (DFG) under the grant number PE 2290/2-1 and Projektnummer 325408982 are gratefully acknowledged as well as the funding of our TEM equipment by the DFG via the Major Research Instrumentation Programme under INST 211/719-1 FUGG. We want to thank the Groups of Prof. F. Varnik and Prof. K. Albe for providing MD boxes.

Fig. 1: Comparison of normalized variance profiles: simulation via (2) using $Ni_{80}P_{20}$ MD boxes (asterisk) and experimental data of $Ni_{80}P_{20}$ (5) and $Pd_{40}Ni_{40}P_{20}$ (lines).

Fig. 2: Comparison of normalized variance profiles: simulation via (2) of Zr-based MD boxes (asterisk) and experimental data of Vit105 (lines).

Fig. 1

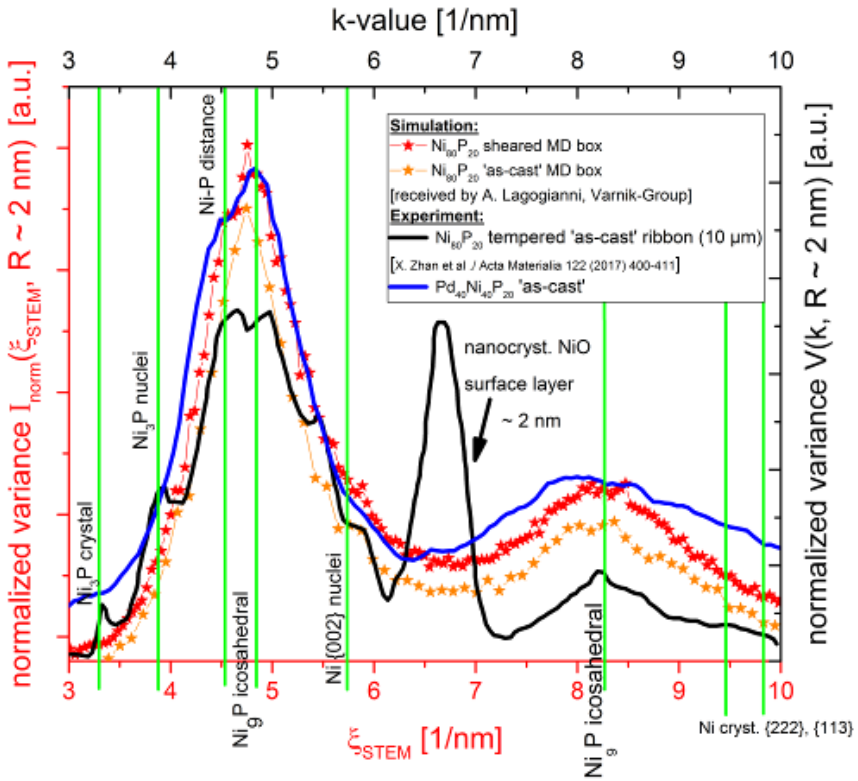
k-value [1/nm]
normalized variance $I_{norm}(\xi_{STEM}, R \sim 2$ nm) [a.u.]
normalized variance V(k, R ~ 2 nm) [a.u.]
ξ_{STEM} [1/nm]
Simulation:
$Ni_{80}P_{20}$ sheared MD box
$Ni_{80}P_{20}$ 'as-cast' MD box
[received by A. Lagogianni, Varnik-Group]
Experiment:
$Ni_{80}P_{20}$ tempered 'as-cast' ribbon (10 µm)
[X. Zhan et al. / Acta Materialia 122 (2017) 400-411]
$Pd_{40}Ni_{40}P_{20}$ 'as-cast'
Ni-P distance
Ni_3P nuclei
Ni_3P crystal
Ni_gP icosahedral
Ni {002} nuclei
nanocryst. NiO
surface layer
~ 2 nm
Ni_gP icosahedral
Ni cryst. {222}, {113}

Fig. 2

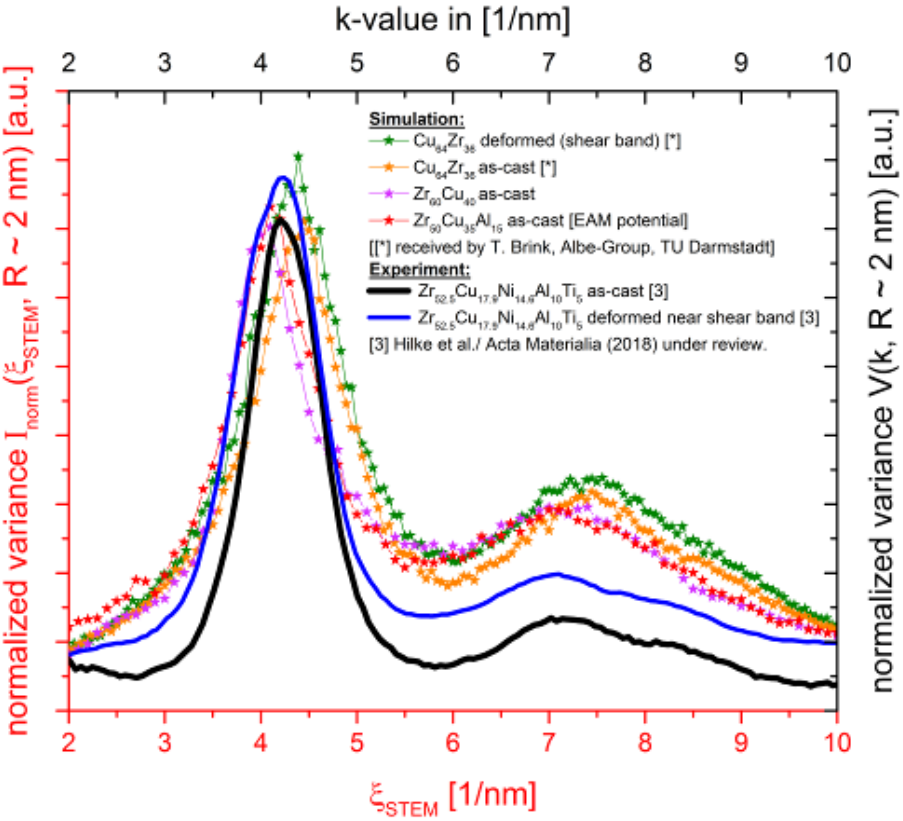
k-value in [1/nm]
normalized variance $I_{norm}(\xi_{STEM}, R \sim 2$ nm) [a.u.]
normalized variance V(k, R ~ 2 nm) [a.u.]
ξ_{STEM} [1/nm]
Simulation:
$Cu_{64}Zr_{36}$ deformed (shear band) [*]
$Cu_{64}Zr_{36}$ as-cast [*]
$Zr_{60}Cu_{40}$ as-cast
$Zr_{60}Cu_{35}Al_{15}$ as-cast [EAM potential]
[[*] received by T. Brink, Albe-Group, TU Darmstadt]
Experiment:
$Zr_{52.5}Cu_{17.9}Ni_{14.6}Al_{10}Ti_5$ as-cast [3]
$Zr_{52.5}Cu_{17.9}Ni_{14.6}Al_{10}Ti_5$ deformed near shear band [3]
[3] Hilke et al./ Acta Materialia (2018) under review.

IM4.P004
Reduction of Systematic and Excessive Noise in Charge-Coupled Device Measurements

T. Heil[1]

[1]Max Planck Institute of Colloids and Interfaces, Colloid Chemistry, Potsdam, Germany

When dealing with low-signal measurements, usually neglected noise can become an important factor in the signal-to-noise ratio. With TEM CCD measurements, random noise can be successfully flattened via multi-frame acquisition. However, systematic noise cannot be countered this way and intense random noise, like x-ray spikes, might not be reduced sufficiently.

Removing the sources for systematic noise and eliminating the influence of x-ray events are therefore a suitable way to improve the quality of low-signal measurements. One such removable source is excessive noise in the reference images, which are automatically applied to correct flaws of the CCD chip. For example, x-ray spikes in the dark-reference image can become an issue in drift-corrected multi-frame images (figure 1a) or in measurements integrated over a larger number of pixels, like EELS spectra (figure 1b). The later can become especially problematic for the energy-offset correction method, otherwise a suitable way to counter the systematic noise (1,2), since the intensity of the normally easily spotted negative spike will be distributed over the whole range of the applied energy offset.

The benefit of a high-quality dark-reference image has been acknowledged before (3,4), but so far only simple multi-frame approaches have been reported. However, having access to a stack of images offers the possibility to apply routines to separate intense outlier noise like x-ray spikes from wanted features like hot pixels and to remove their influence on the merged image altogether, instead of only diminishing it by simple merging (5). This approach is not limited to dark-reference images, but can be used for any suitable multi-frame data set.

References:

(1) M. Bosman, V.J. Keast Ultramicroscopy 108 (2008) 837–846.

(2) Y. Wang, M.R.S. Huang, U. Salzberger, K. Hahn, W. Sigle, P.A. van Aken Ultramicroscopy 184 (2018) 98–105.

(3) V.D.-H. Hou Microscopy and Microanalysis 15 (2009) 226–227.

(4) L. Jones, A. Varambhia, D. Kepaptsoglou, Q. Ramasse, R. Freer, F. Azough, S. Lozano-Perez, R. Beanland, P. Nellist EMC 2016: Proceedings (2016) 809.

(5) T. Heil, G.J. Tatlock Microscopy 67 (2018) 123–132.

Fig 1: a) Artefacts in a drift-corrected multi-frame EFTEM image caused by x-ray noise in the dark-reference image. The artefacts can easily be recognised as similar shaped clusters of darker pixels. b) EELS spectrum with artefacts caused by x-ray noise in the dark-reference image (dark pointers) and during the signal acquisition (bright pointers).

Fig. 1

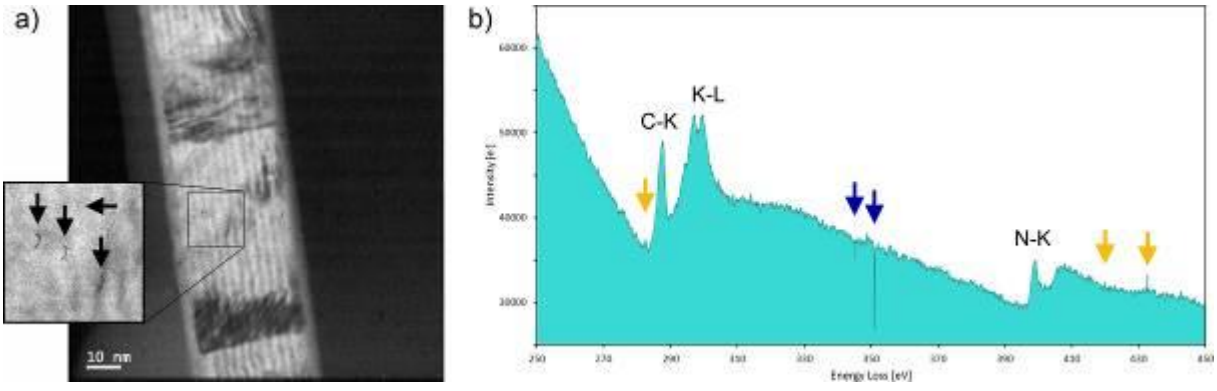

IM4.P005
Accurate determination of low-order crystal structure factors using large-angle rocking CBED patterns

D. Morikawa[1], K. Tsuda[2]

[1]Tohoku University, Institute of Multidisciplinary Research for Advanced Materials, Sendai, Miyagi, Japan
[2]Tohoku University, Frontier Research Institute for Interdisciplinary Sciences, Sendai, Miyagi, Japan

A structure analysis method using convergent-beam electron diffraction (CBED), which was developed by Tsuda and co-workers (1), enables us to directly observe an orbital-ordered state (2) (cf. Fig. 1(b)). The disk size of the conventional CBED pattern is limited by the Bragg angle of the nearest reflection. This also restricts the sensitivity to the parameters to be determined.

Our target is the development of a technique for accurate determination of low-order crystal factors using large-angle rocking CBED patterns. Recently, the techniques to obtain large-angle rocking patterns without disk-overlapping from nm-scale specimen area were reported (3,4). In this study, we focus on the analysis of orbital ordered state.

We chose a spinel oxide $FeCr_2O_4$ as an example for an analysis of orbital ordered state. $FeCr_2O_4$ undergoes a structural phase transformation at 135K from a cubic spinel structure to a tetragonal structure. Figure 1(a) shows a schematic crystal structure and a ferro-type orbital ordering of 3d electrons of Fe atoms expected at tetragonal phase. An ideal orbital ordered state was calculated by using orbital scattering factors (5). Large-angle rocking CBED patterns were simulated using the software MBFIT (1), which is based on Bloch wave calculation.

Figure 2(a) shows an intensity difference of large-angle rocking CBED pattern between the orbital ordered state and non-ordered state. Only 000 disk with (100) incidence for large rocking angle is shown here. A solid circle indicates an angle for conventional CBED pattern. The area with the angle between 3.5 to 14.5 mrad shows significant difference, which indicates these area has higher sensitivity for the orbital ordered state. Figure 2(c) shows a Bloch state which has high excitation amplitude at the cross point in Fig. 2(a). The Bloch wave has relatively high existing possibility at Fe sites. Figure 3 shows Goodness-of-fit (GOF) values for different rocking angle. The simulated pattern with an ideal orbital ordered state is used for the pseudo experimental data. The case of high rocking angle shows rapid decreasing of GOF, which means high sensitivity for the perturbation of crystal structure factor.

Large angle rocking CBED patterns have higher sensitivity for a determination of low-order crystal structure factors on orbital ordered state.

References:

(1) K. Tsuda and M. Tanaka, Acta Cryst., A55, 939 (1999).

(2) K. Tsuda, D. Morikawa et al., Phys. Rev. B 81, 180102(R) (2010).

(3) C. T. Koch, Ultramicroscopy, 111, 828 (2011).

(4) R. Beanland et al., Acta Cryst., A69, 427 (2013).

(5) R. J. Weiss and A. J. Freeman, J. Phys. Chem. Solids, 10, 147 (1959).

Fig. 1: (a) Crystal structure of spinel oxide $FeCr_2O_4$ at orbital ordered phase. (b) The part of the result of CBED analysis at Fe site. Anisotropic distribution of electrostatic potential was directly observed. (2)

Fig. 2: (a) Intensity difference of 000 disk with [100] incidence for orbital ordered state and non-ordered state. Solid circle shows the disk size of conventional CBED pattern. The rocking state between 4.5 to 13.5 mrad shows significant difference. (b) Schematic picture of $FeCr_2O_4$. (c) The Bloch wave excitation seeing from (b) condition, which has high existence possibility at the tilting condition indicated in (a) as a cross.

Fig. 3: Goodness-of-fit (GOF) for different rocking angles. GOF shows rapid decreasing for larger rocking angle.

Fig. 1

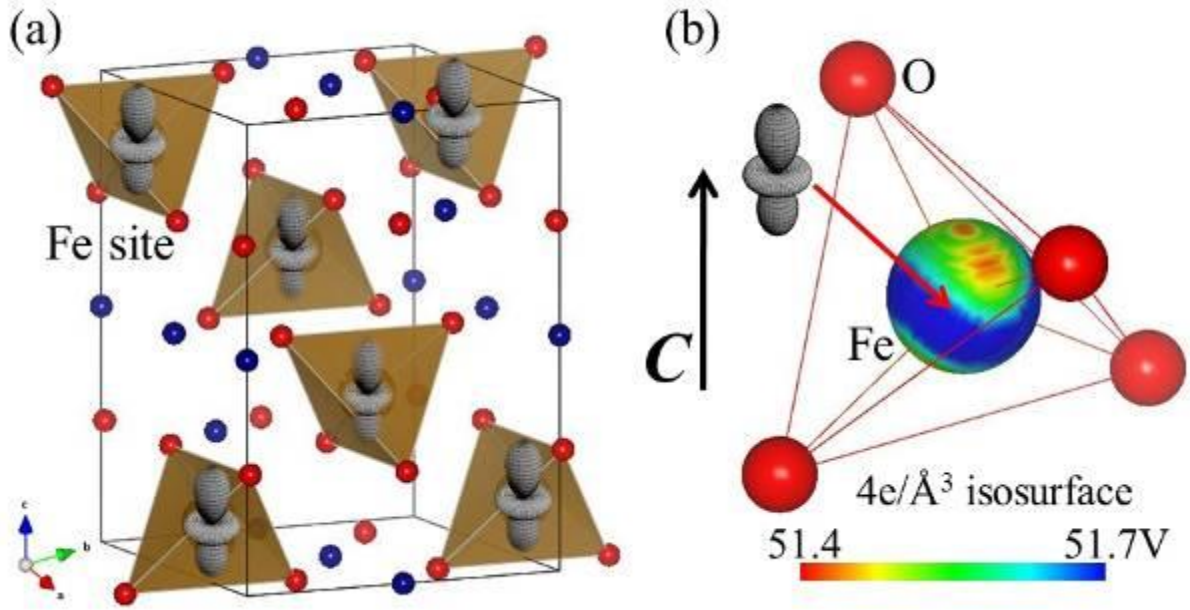
(a)
Fe site
(b)
O
C
Fe
4e/Å3 isosurface
51.4
51.7V

Fig. 2

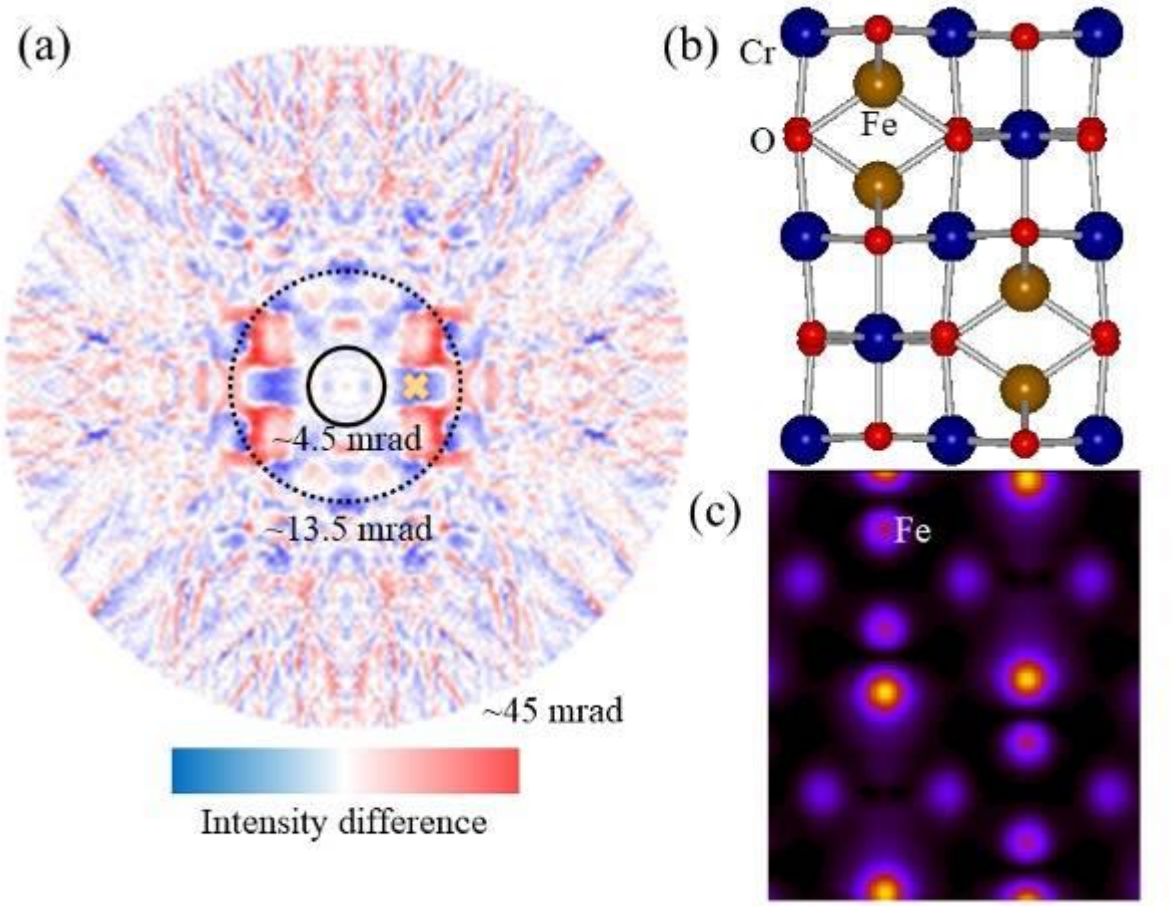
(a)
~4.5 mrad
~13.5 mrad
~45 mrad
Intensity difference
(b)
Cr
O
Fe
(c)
Fe

Fig. 3

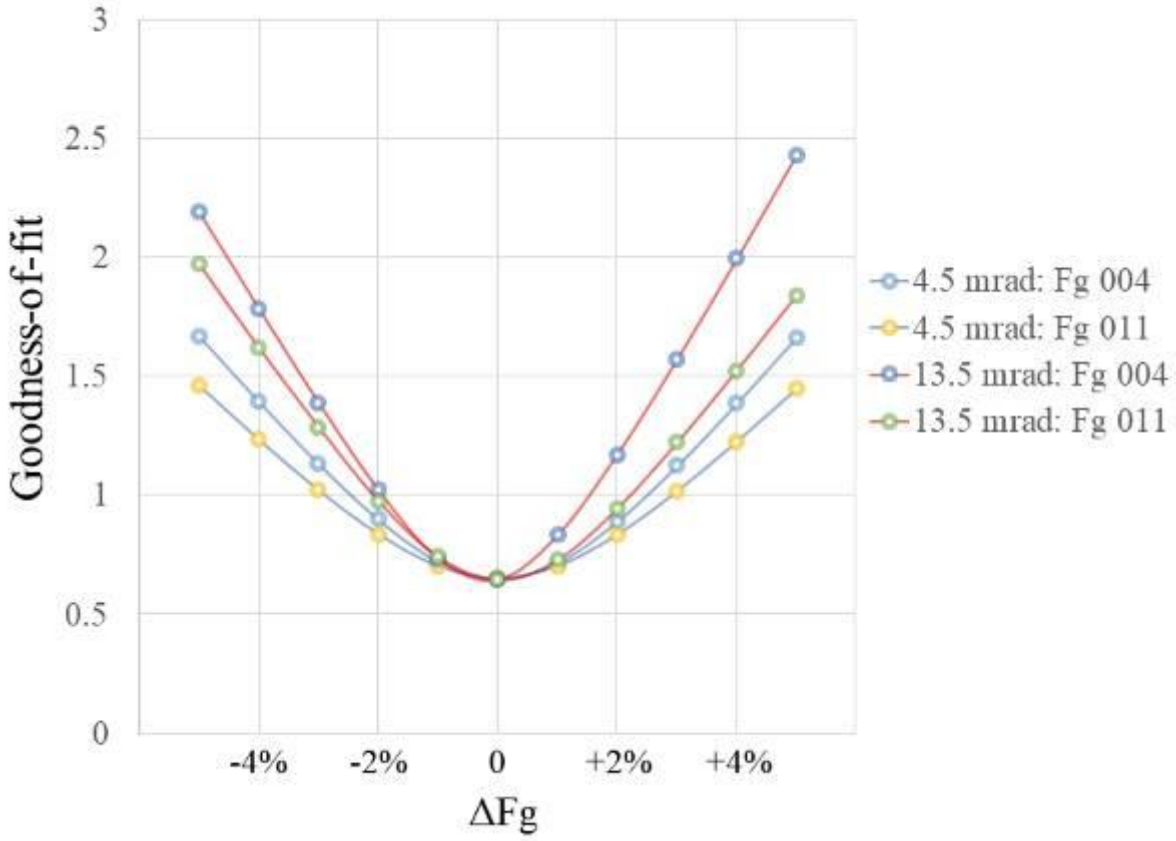
Goodness-of-fit
3
2.5
2
1.5
1
0.5
0
-4%
-2%
0
+2%
+4%
ΔFg
4.5 mrad: Fg 004
4.5 mrad: Fg 011
13.5 mrad: Fg 004
13.5 mrad: Fg 011

IM4.P006
Fundamental aspects of phonon scattering

T. Niermann[1]

[1]Technische Universität Berlin, Institut für Optik und Atomare Physik, Berlin, Germany

Electrons scattered into high angles are often used for imaging using high angle annular dark field (HAADF) detectors. These HAADF-images normally allow a straight-forward qualitative interpretation, since the observed contrast is strongly depends on the atomic number.

However, the full nature of these signals is more complicated, since several physically distinct effects intermingle: phonon scattering (generation and annihilation of phonons), thermal effects (the object is not in a pure quantum mechanical state for non-vanishing temperatures), and multiple elastic and inelastic scattering. We investigate theoretically how these effects contribute to the scattering.

To quantitatively evaluate HAADF-images commonly Frozen-lattice calculations are applied, where the results of scattering simulations for fixed atom positions are incoherently averaged over the atom position probability density (see e.g. (1)). This can be done with (Phonon model) or without (Einstein model) statistical correlations between atom positions. When all electrons regardless of energy-loss contribute to the diffraction pattern, the Frozen-lattice method is correct for single scattering, i.e. within the 1st order Born approximation, due to the completeness of phonon states and the locality of the coulomb interaction. In literature this is mostly discussed in context of absorption factors due to thermal diffuse scattering (2)

However, the question arises, whether these simulations are even correct for multiple scattering, since obviously here the results are averaged over atom positions, while correctly they must be averaged over initial phonon-states, and partial coherence effects between atom positions (even for one and the same atom) remains. A rigorous proof is given based on quantum-mechanical scattering theory (S matrix theory), which reveals that for multiple scattering (independent whether elastic or inelastic) the frozen lattice method is a valid approximation for relevant energies and specimen thicknesses. It should be noted that the assumption of an Einstein model is not needed.

The theoretical investigations are accompanied by calculations of a model system consisting of a single vibrating atom. Scattering calculations of this model system are sufficient numerical feasible to avoid further approximations of the underlying physics and even allow testing some commonly applied approximations. The obtained scattering cross-sections can be used to calculate elastic/inelastic images, diffraction patterns or EELS-spectra.

Differential scattering cross sections (averaged over the azimuth) are shown in Fig. 1 for 200 keV electrons as scattered by a single gold atom vibrating within a harmonic potential. For scattering angles larger than 100 mrad, the inelastic cross-section due to phonon-scattering is larger than elastic scattering by several magnitudes. Here it can be concluded, that the prevailing HAADF-signal for this angular range is caused by phonon scattering, while thermal effects only have a diminishing influence on the cross-section.

References:

(1) R. F. Loane, P. Xu, J. Silcox; Acta Cryst. A 47, 267 (1991)

(2) M. J. Whelan; Journal of Applied Physics 36, 2103 (1965)

(3) C. R. Hall, P. B. Hirsch; Proc. Roy. Soc. A 286, 158 (1965)

Fig. 1

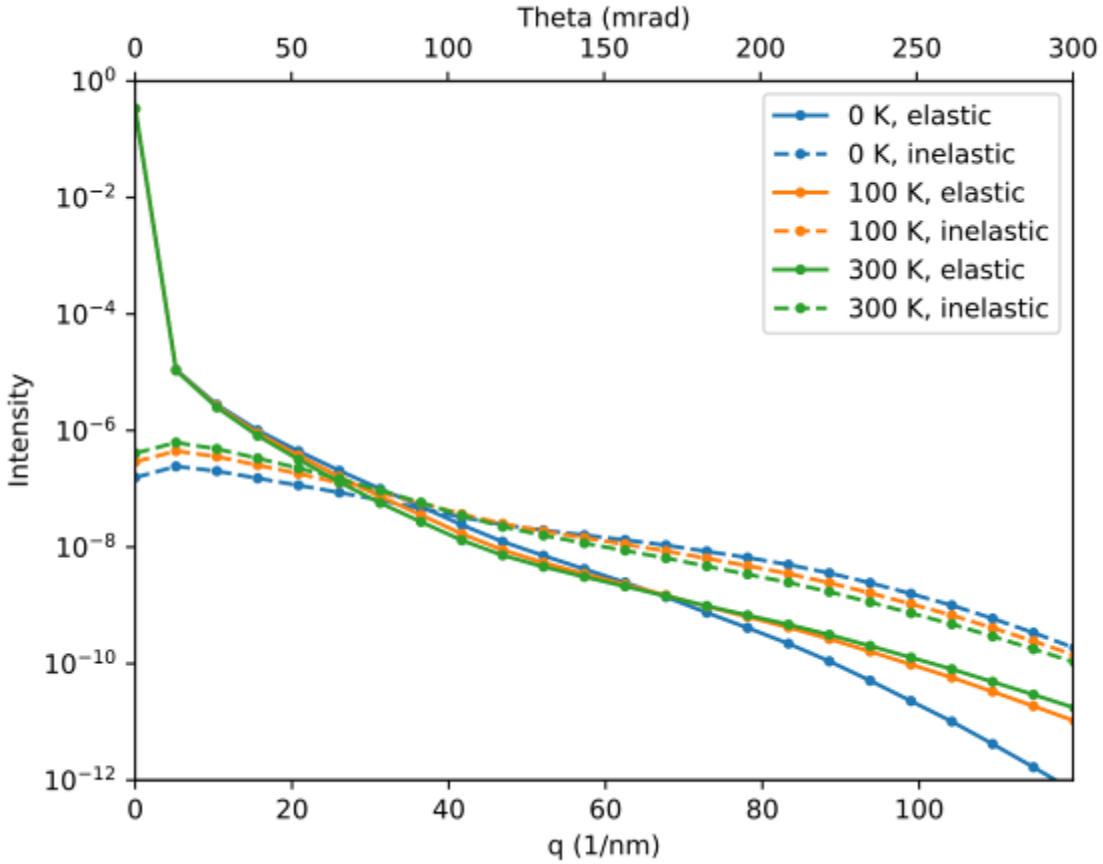
Theta (mrad)
0
50
100
150
200
250
300
10^{0}
10^{-2}
10^{-4}
10^{-6}
10^{-8}
10^{-10}
10^{-12}
Intensity
0
20
40
60
80
100
q (1/nm)
0 K, elastic
0 K, inelastic
100 K, elastic
100 K, inelastic
300 K, elastic
300 K, inelastic

IM4.P007
Dynamical electron scattering at inhomogeneous strain fields

L. Meißner[1], T. Niermann[1], D. Berger[2], M. Lehmann[1]

[1]Technische Universität Berlin, Institut für Optik und Atomare Physik, Berlin, Germany
[2]Technische Universität Berlin, Zentraleinrichtung für Elektronenmikroskopie, Berlin, Germany

Semiconducting devices like quantum dots and MOSFETs have often a three dimensional inhomogeneous strain field which influences the optical and electrical properties. By means of dark-field electron holography, the phase can be measured over different spatial scales of strain fields. The phase is proportional to the displacement field when the displacement field is homogeneous in electron beam direction. However, having additionally a changing displacement field in electron beam direction a more complex behaviour is recognisable.

In calculations we approximated the quantum dots by spherical precipitates and added the displacement field of the precipitates (Figure 1). The spherical precipitates have all the same geometry and only differ in their depth within the structure. To visualize the influence of the dynamical scattering on the phase we performed calculations based on the numerical propagation of the Darwin-Howie-Whelan equation (1). Figure 2 shows the phases for the (400)-beam. A sign change of the phase along the (400)-beam for different depths of the spherical precipitates is visible. Changing also the thickness of the structure a change in the values of the phases around the spherical precipitates is recognisable. This shows that the phase depends also on the thickness of the structure and the depth of the inhomogeneous displacement field.

We also investigate the influence of the dynamical scattering on three dimensional displacement fields experimentally. Therefore our specimen has a displacement field varying in electron beam direction. For the correct interpretation of the phase concerning such three dimensional strain fields, the dynamical scattering has to be considered.

The investigated structure contains a pseudomorphically grown InGaAs layer surrounded by a GaAs matrix. A lamella with an inclined layer structure was prepared by utilizing the focused ion beam (2). The InGaAs layer encloses an angle of 45° with the lamella surface. An inclined layer structure has the advantage of correlating the position of the associated displacement field in depth of the lamella with their lateral position.

Figure 3 shows the reconstructed phase profiles of the measured (0-22) dark-field electron holograms for the inclined layer structure. The phase profiles are produced by averaging the phase along the inclined layer structure where the geometry of the specimen is the same. The phase profiles are shown for different beam tilts and different lamella thicknesses. The beam tilt describes the distance to the two beam excitation in the diffraction pattern. The measurements are compared to calculated phase profiles by using the Darwin-Howie-Whelan equation and the same geometry parameter and excitation conditions like in the experiment. The measured and the calculated phases have an impressive agreement within the projected InGaAs layer concerning the increasing and decreasing gradient of the phases including the position of 2π-jumps and the transition to an oscillating behaviour at certain beam tilts.

The complex phase behaviour of inhomogeneous strain fields can also be used for investigating the three dimensional structure of the specimen.

References:

(1) M. de Graef, "Introduction to Conventional Transmission Electron Microscopy", Cambridge University Press, Cambridge, (2003)

(2) D. Berger, S. Selve, U.U.R. Hömpler, L. Meißner, MC 2017 Proceedings, p. 479.

Fig. 1

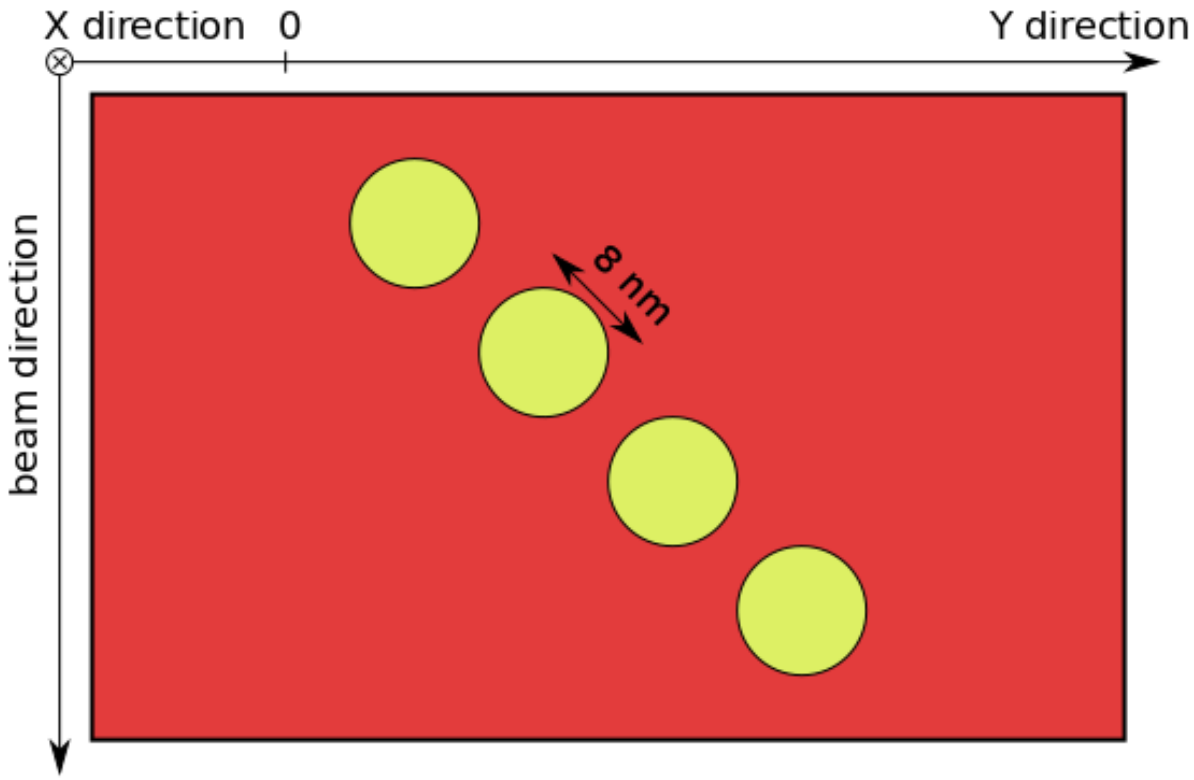
X direction
0
Y direction
beam direction
8 nm

Fig. 2

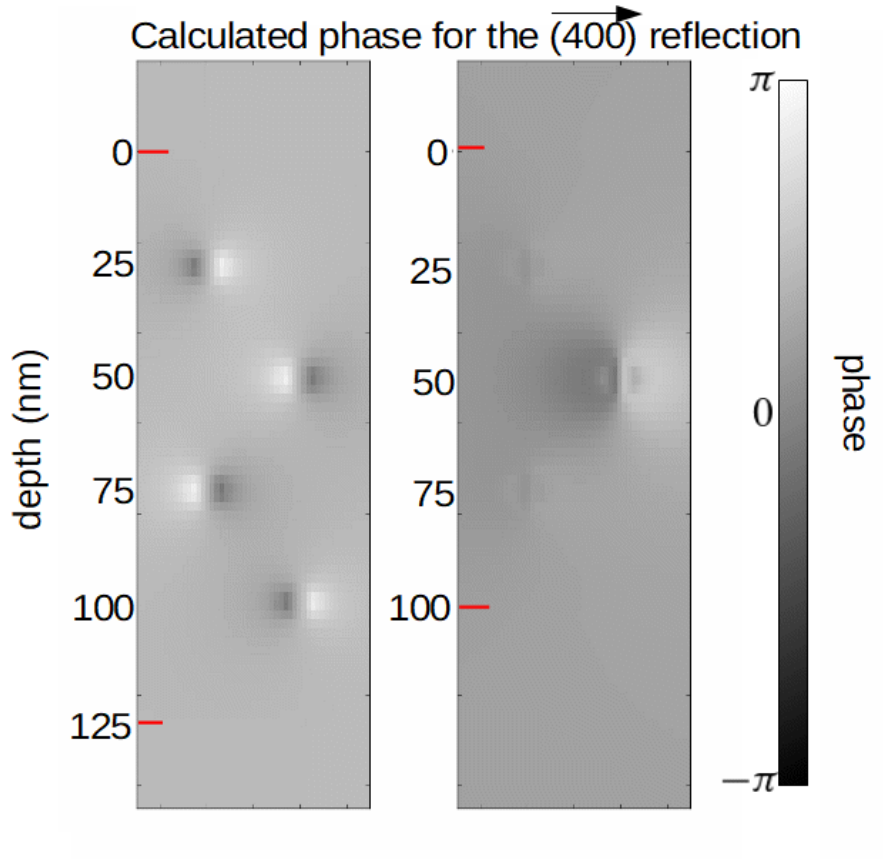
Calculated phase for the (400) reflection
depth (nm)
0
25
50
75
100
125
0
25
50
75
100
π
0
−π
phase

Fig. 3

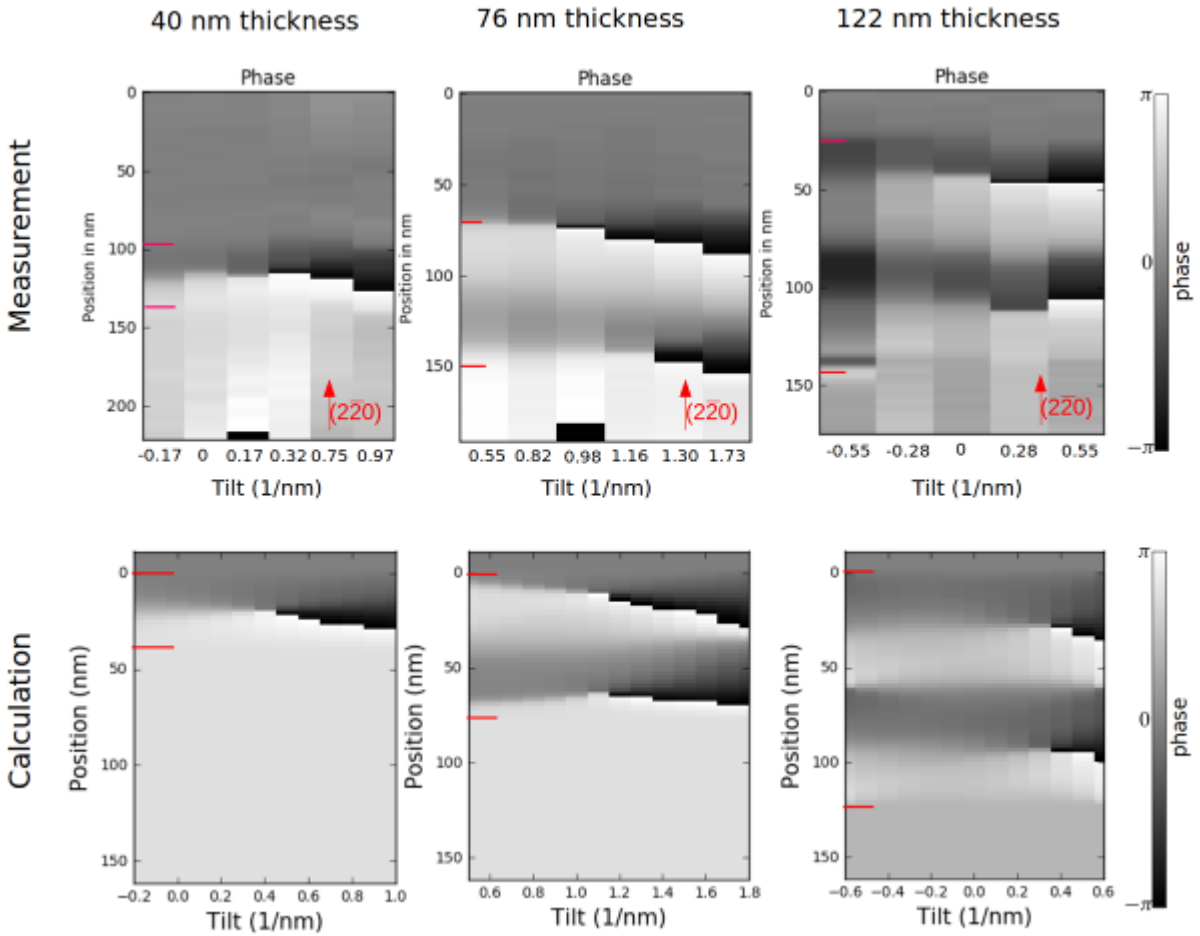
40 nm thickness
76 nm thickness
122 nm thickness
Measurement
Calculation
Phase
Position in nm
Position (nm)
Tilt (1/nm)
(2$\bar{2}$0)
phase
π
0
−π

IM4.P008
Dynamics of electron propagation inside perovskite and Ruddlesden-Popper oxides

Y. Wang[1], W. Sigle[1], P. A. van Aken[1]

[1]Max Planck Institute for Solid State Research, Stuttgart Center for Electron Microscopy, Stuttgart, Germany

Perovskite and Ruddlesden-Popper (RP) oxides have shown very attractive and versatile magnetic, electrical, and structural functionalities, which are beneficial for many energy and electronic devise. The RP phase comprise consecutive perovskite building blocks alternating with additional rock-salt layers along *c*-axis (1), which leads to a reduction of the lattice symmetry. The functionalities of these oxides are critically depending on the distortion of their crystal lattice. Atomistic understanding of these distortions and elucidation of their influence on the final properties requires imaging and measuring the atomic positions for both cations and oxygen (2, 3). Annular bright-field (ABF) imaging enables to image light elements (4), which makes the ABF technique especially interesting for the investigation of perovskite oxides. In the ABF image, the contrast of light atomic columns are basically related to the forward elastic scattering, whereas the contrast of heavy atomic columns are contributed from both thermal diffuse scattering and elastic scattering components (5). Past studies suggest (4, 6) that the images of atomic columns can be displaced from their real column positions, which calls into question the robustness and interpretability of STEM images over crystal atomic configuration and sample thickness.

In this contribution, using SrTiO3 (STO) and LaSrAlO4 (LSAO) as model systems, we combine experiments and simulations to investigate the propagation of a STEM electron probe through crystal environments with high and lower symmetry and their impact on resultant atomic positions in ABF images, respectively. Observing STO along the [010] direction, the pure-O atomic column (marked by a square in Fig.1) in STO is surrounded by atomic columns in a 2-fold symmetry. Consequently, the electron probe symmetrical propagates along the (010) direction. In the case of LSAO, the O atomic column marked by a square is also in a 2-fold symmetry enviroment, however the O atomic column marked by a circle shows lower symmetry, more specifically the O atomic column sits between Al/O and La/Sr atomic columns along [100], and between La/Sr atomic columns along [001]. The intensity of the electron probe is symmetrically distributed in [100] direction. In contrast in [001] direction, the de-channeled electrons distribution is no longer symmetric along the electron propagation direction. The electron intensity oscillates at the Al/O and La/Sr column positions through the thickness. We will further discuss the impact of these differences on the resultant atomic column position in ABF images and the comparison to experimental results. These results highlight that caution in needed in quantifying the atomic displacement from ABF images at interfaces or grain boundaries, where crystal symmetry and thickness changes.

References:

(1) A F Wells, Structural Inorganic Chemistry. Oxford: Clarendon. (1984), p.602.

(2) Y Wang *et al*., ACS Appl. Mater. Interface 8 (2016), p. 6763.

(3) Y Wang *et al*., Ultramicroscopy 168 (2016), p.46.

(4) S D Findlay *et al*., Appl. Phys.Lett. 95 (2009), p.191913.

(5) S D Findlay *et al*., Ultramicroscopy 110 (2010), p. 903.

(6) R Hovden *et al*., Phys. Rev. B 86 (2012), p. 195415.

Fig. 1: a) Atomic structure model of STO. (b) Realspace images of the electron-probe amplitude on the pure O atomic column after passing through 15 nm of STO. (c) 2D beam-intensity-depth profiles of a simulated STEM electron probe on O atomic column.

Fig. 2: (a) Atomic structure model of LSAO. (b) Realspace images of electron-probe amplitude on the O atomic column (marked by circle) after passing through 15 nm of LSAO. (c) and (d) 2D beam intensity depth profiles of a simulated STEM electron probe propagating on the apical-O atomic column along [100] and [001] directions, respectively.

Fig. 1

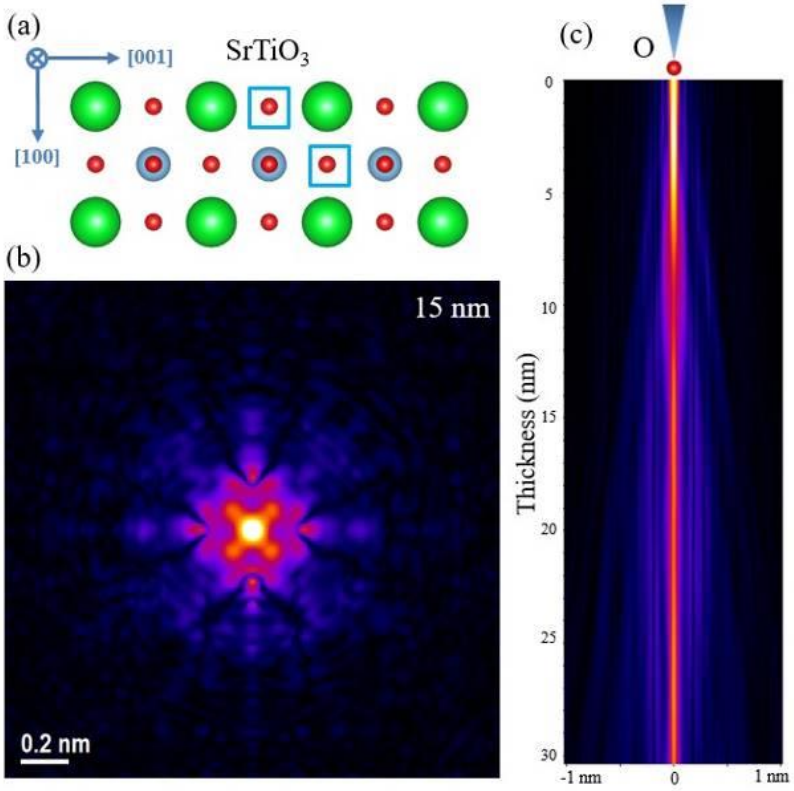
(a)
[001]
[100]
$SrTiO_3$
(b)
15 nm
0.2 nm
(c)
O
Thickness (nm)
0
5
10
15
20
25
30
-1 nm
0
1 nm

Fig. 2

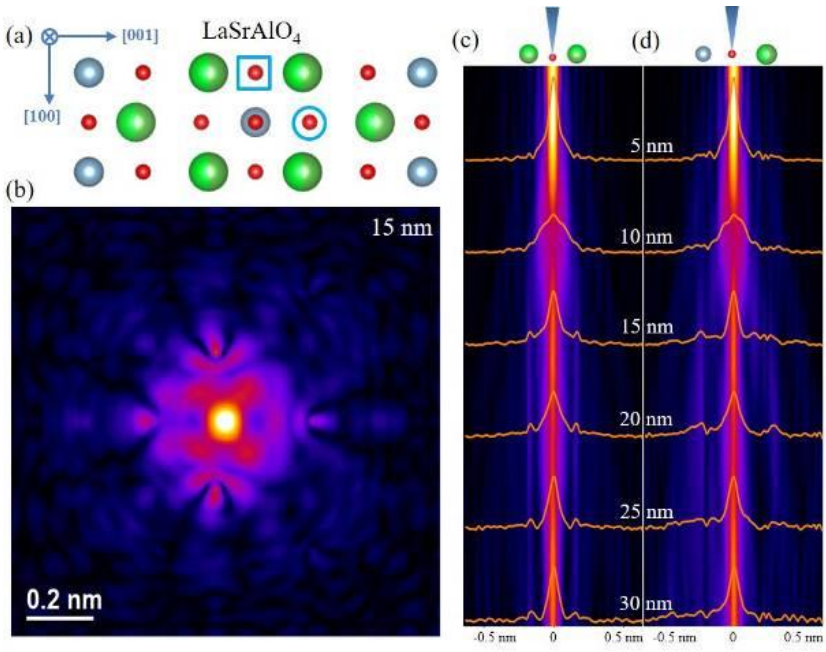
(a)
[001]
[100]
$LaSrAlO_4$
(b)
15 nm
0.2 nm
(c)
(d)
5 nm
10 nm
15 nm
20 nm
25 nm
30 nm
-0.5 nm
0
0.5 nm
-0.5 nm
0
0.5 nm

IM4.P009
How to improve STEM XEDS spectrum-images with Principal Component Analysis?

P. Potapov[1], A. Lubk[1]

[1]Leibniz Institute for Solid State and Materials Research Dresden, Dresden, Germany

STEM XEDS (X-ray Energy-Dispersive Spectroscopy) spectrum-images can be drastically denoised by application of the Principal Component Analysis (PCA). However, there is a number of hidden obstacles hampering the treatment and leading to dubious results.

A typical issue is following: PCA is able to remove the superimposed noise only if the latter is homogeneous in any given fragment of a dataset. In fact, XEDS spectra are corrupted by Poisson noise, which does not satisfy this condition. The issue can be relaxed by equalization of the noise across the datasets through the so-called weighting pre-treatment (1).

The efficiency of the weighting pre-treatment was numerous times proved for EELS data. Unexpectedly, this procedure can fail completely in the case of XEDS spectrum-images. This paper uncovers the reasons for this failure and shows the possible solutions resulting in the artefact-free denoised data.

We consider a representative experimental STEM XEDS spectrum-image with Si, O, N, Ti, Hf, Ta, Al signals and a typical applied dose. In parallel, we generate a twin synthetic object that mimics the real one in its essential features. An advantage of the synthetic data is the possibility to compare the noisy data with the noise-free reference, which allows to quantify the effect of the pre-treatment on PCA denoising and highlight the potentially induced problems. Materials & methods

The experimental spectrum-image was recorded in the Titan G2 microscope operating at 300 kV and equipped with ChemiSTEM. The simulated spectrum-images of the synthetic object were generated using the program DTSA-II (NIST).

The weighting procedure involves the normalization of data on the square root of their average spectrum (or average image). A peculiarity of typical STEM XEDS data is their high sparsity, which causes the significant deviation of an average spectrum from the true reference. As a consequence, the normalization to the small unprecise values induces the instability and the weighting procedure fails. The issue is magnified with decreasing the applied dose, i.e. with increasing sparsity.

The most evident way to solve the sparsity issue is to smooth datasets prior the PCA treatment. For instance, a 2D Gaussian kernel filtering fills very efficiently the empty data elements while deteriorates only slightly the spatial resolution. The accuracy of the resulted average spectrum and average image is regained, which recovers the correctness of the weighting procedure and improves dramatically the overall efficiency of PCA denoising.

References:

(1) M.R. Keenan and P.G. Kotula, Surf.Interface Anal., 36 (2004), 203.

Fig. 1 shows the effect of pre-treatment on the quality of the PCA decomposition for the first 10 principal components. In an ideal case, every component coincides with its true reference (a). In reality (b-d), the components are retrieved only approximately that looks like a redistribution of the projection of each component to the others. Apparently, the only filtering+weighting treatment variant delivers the satisfactory proximity between the observed and true components.

STEM XEDS spectrum-images acquired with modern STEM instrumentation and typical acquisition settings can be noticeably denoised by application of PCA. However, two pre-treatments are ultimately needed for the successful PCA: smoothing raw data and their weighting.

Fig. 1

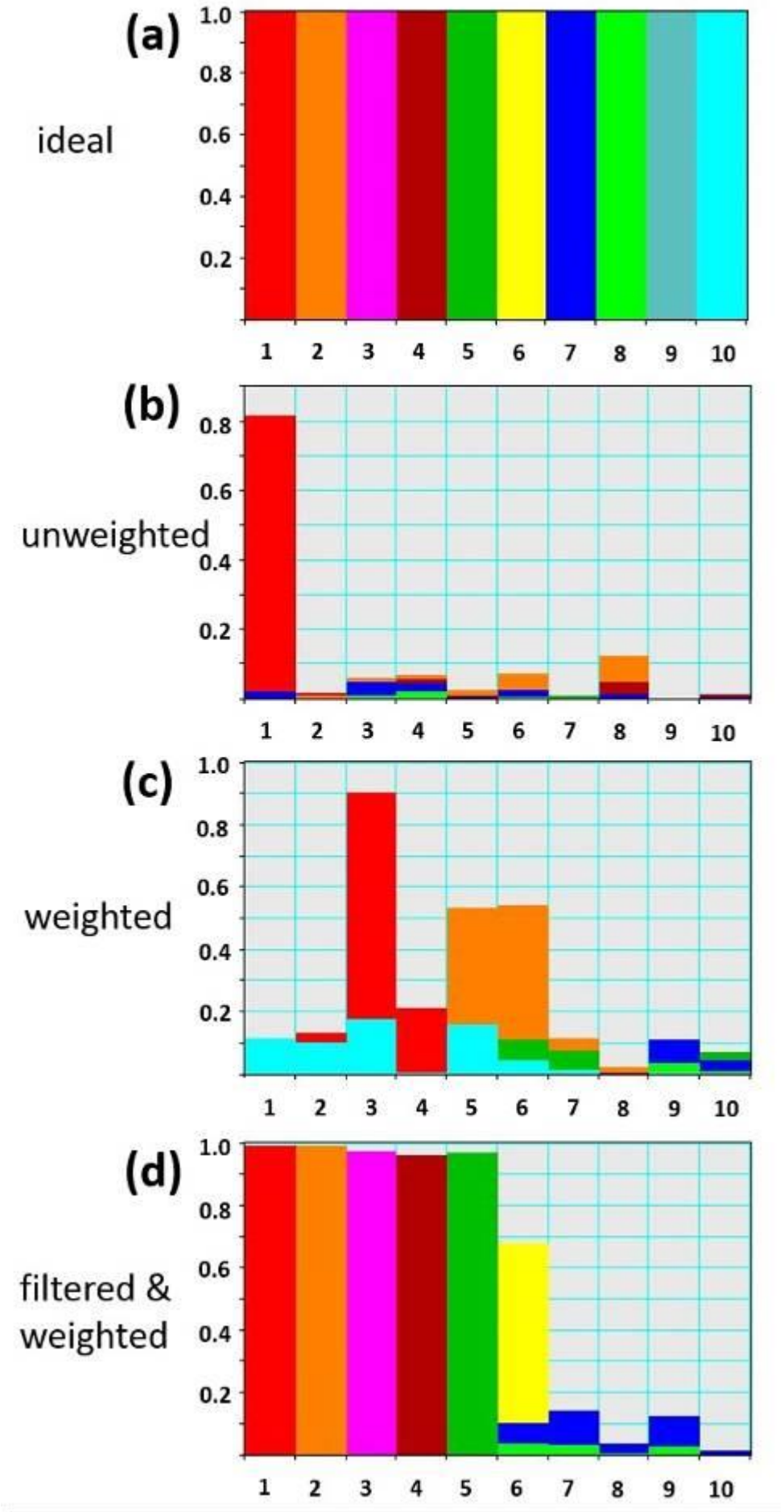
(a)
ideal
1.0
0.8
0.6
0.4
0.2
1 2 3 4 5 6 7 8 9 10
(b)
unweighted
0.8
0.6
0.4
0.2
1 2 3 4 5 6 7 8 9 10
(c)
weighted
1.0
0.8
0.6
0.4
0.2
1 2 3 4 5 6 7 8 9 10
(d)
filtered &
weighted
1.0
0.8
0.6
0.4
0.2
1 2 3 4 5 6 7 8 9 10

IM4.P010
Blind denoising STEM images with deep convolutional neural network

F. Wang[1], T. R. Henninen[1], R. Erni[1]

[1]Swiss Federal Laboratories for Materials Science and Technology, Electron Microscopy Center, Duebendorf, Switzerland

Modern scanning transmission electron microscopy (STEM) can provide images with sub-ångström resolution (1). Despite of the instrumental improvements that enabled this progress, a major limitation in nowadays high-resolution imaging concerns the beam sensitivity of specimens. One approach to avoid radiation damage is to reduce the electron dose to minimize scattering events that cause radiation damage, which however also reduces the events that are necessary to form an image. Lowering the electron dose thus results in noisy images with a poor signal-to-noise ratio (SNR) less of even less than 0 dB. Such noisy data complicate the extraction of relevant specimen information (2).

We developed a denoising algorithm based on a deep convolutional neural network (CNN) to address this problem. In our approach, the input images are pre-processed by a single-layered CNN composed of four conventional low-pass-filters (LPFs). Then, these output images are assembled to map a clean image with a deep CNN. When passing the noisy images to this program, nearly all the background intensities are diminished, even if the inputs are recorded under different configurations with unknown noise types and of unknown levels. As is demonstrated in Fig. 1, even if the beam current, the exposure time or the image resolution differ from one to another, our algorithm can still make robust predictions. Accelerated with a commercially available graphics processing unit (GPU) such as a Nvidia GTX 1080 Ti, this neural network can even make real-time prediction (more than 440 frames per second (fps) for images of resolution 128x128 acquired at 150 fps), reducing valuable time for post-processing data when comparing with conventional denoising methods (see, e.g. (3)), as is shown in Fig. 2.

Our approach enables to reduce the necessary electron dose to acquire images which contain relevant structural information, i.e. the algorithm allows for increasing the tolerable noise level in high-resolution micrographs which is of particular interest to enhance acquisition speeds in electron microscopy imaging and to investigate beam sensitive materials which are prone to radiation damage.

References:

(1) R. Erni, M. D. Rossell, C. Kisielowski & U. Dahmen. Atomic Resolution Imaging with a sub-50 pm Electron Probe, *Physical Review Letters* 102 (2009) 096101.

(2) Henninen, T. R. et al. Dynamics and crystallinity of sub-nm platinum clusters at elevated temperatures. submitted (2019).

(3) K. Dabov. et al. Image denoising by sparse 3D transform-domain collaborative filtering, IEEE Trans. Image Process., vol. 16, no. 8, pp. 2080-2095, (2007).

This project has received funding from the European Research Council (ERC) under EU"s Horizon 2020 research and innovation program (Grant Agreement No. 681312).

Fig. 1: Original and denoised STEM images acquired under different experimental setups and at different magnifications.

Fig. 2: Performance benchmark with conventional BM3D method.

Fig. 1

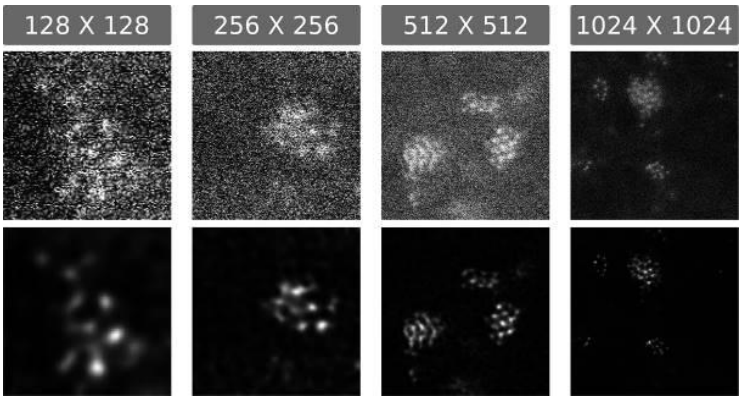
128 X 128
256 X 256
512 X 512
1024 X 1024

Fig. 2

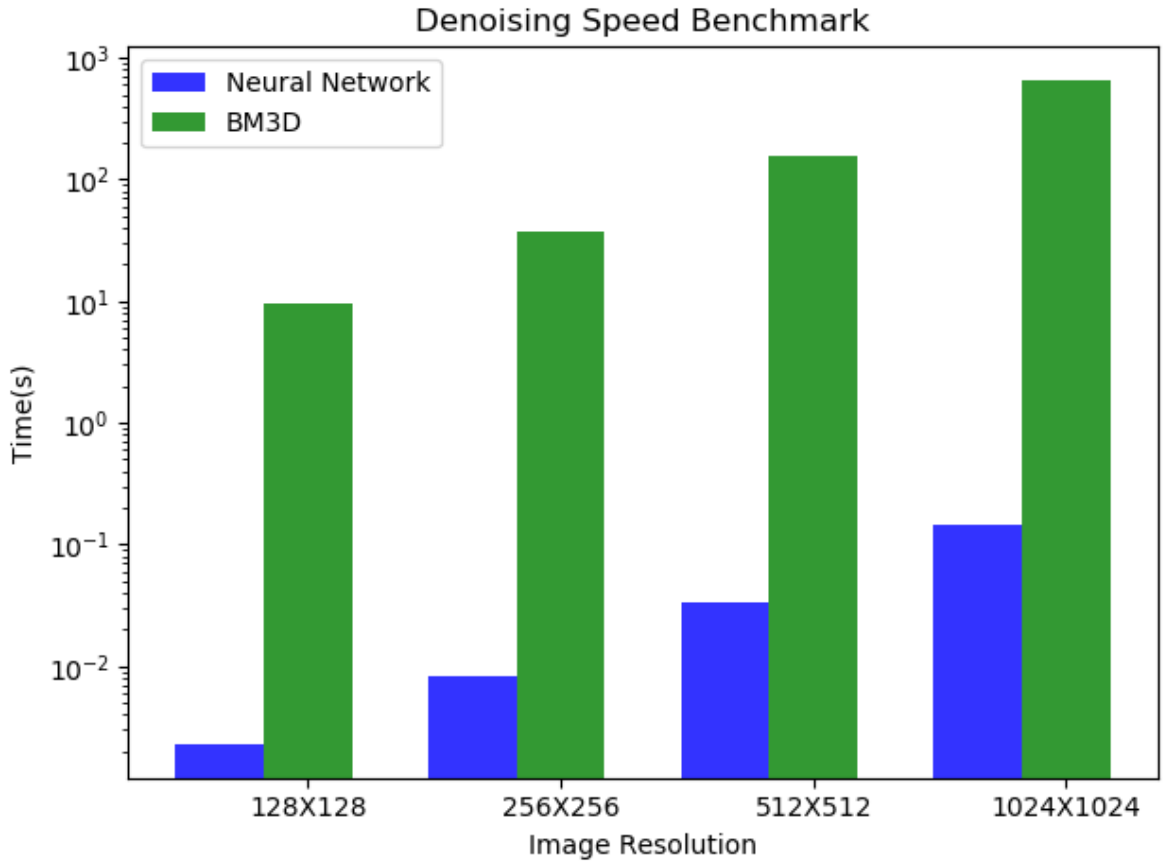
Denoising Speed Benchmark
Neural Network
BM3D
Time(s)
10^{3}
10^{2}
10^{1}
10^{0}
10^{-1}
10^{-2}
128X128
256X256
512X512
1024X1024
Image Resolution

IM4.P011
Measuring single electrons – advantages for quantitative analysis

M. Huth[1], H. Ryll[2], R. Ritz[1], C. O´Leary[3], I. Griffiths[3], P. D. Nellist[3], R. Sagawa[4], Y. Kondo[4], H. Soltau[1]

[1]PNDetector GmbH, Munich, Germany
[2]PNSensor GmbH, Munich, Germany
[3]University of Oxford, Department of Materials, Oxford, United Kingdom
[4]JEOL Ltd., Tokyo, Japan

In today´s electron microscopy research, samples get increasingly challenging by having a complex structure or higher thickness. A deep understanding requires the comparison of experimental results to simulations, which is only possible if the measured intensities are accurate, especially in situations where the statistics is weak. Recent experiments which indicate that only few electrons passing through the sample already carry enough information to deduce sensitive information like electric or magnetic field distributions underline the need for a precise intensity measurement.

In such context, the capability of measuring single electrons is the ultimate goal and various pixelated direct detectors claim to achieve this. However, the readout schemes of detectors available differ dramatically in how the energy of the primary electron, which is deposited in the bulk silicon, is converted to intensity signal which is finally stored in the data.

Figure 1. a) Measured tracks of a single 80keV electron. b) Top view of several simulated tracks of 80 keV electrons all entering at the same point. c) Intensity line profile along one detector channel crossing signal from three primary electrons. Red dotted line represents a possible threshold position and is shown for visualizing discussed topics about thresholding.

In this work we present unprocessed true single electron data from the pnCCD (S)TEM camera (1), together with electron track simulations in silicon (Fig. 1a, 1b). Combining the real analogue detector response to electron impingement and sophisticated event analysis achieves a high accuracy in finding the true number of electrons per diffraction pattern. Here even the effect that some of the primary electrons hitting the detector only leave a fraction of their full energy in the detector (backscattered electrons) can be accounted for.

A discussion is presented by evaluating the effects of preprocessing the detector response by applying thresholds to true analogue data (Fig. 1c) and simulated counting detector data.

Figure 2. a) Software "PNOnline" for data acquisition and controlling the 4D Canvas camera. b) Picture of the 4D Canvas Detector, which is the JEOL integrated version of the pnCCD (S)TEM camera.

References:

(1) Ryll, H., et al, Journal of Instrumentation 11 (2016)

Fig. 1

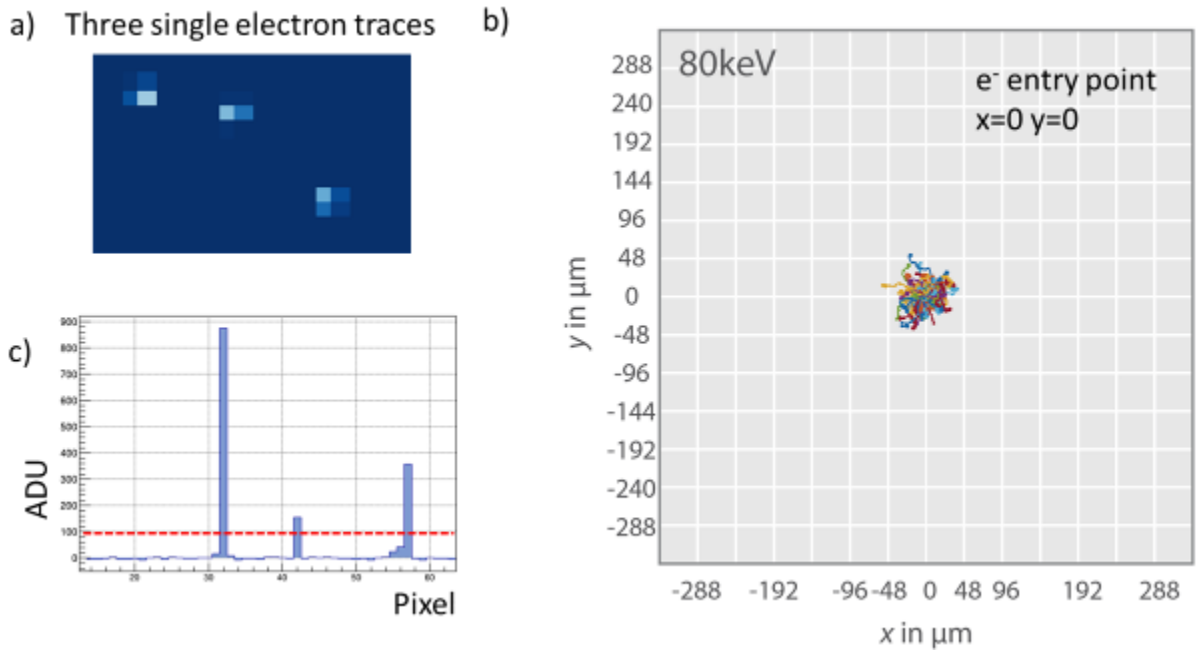
a) Three single electron traces
b)
80keV
e- entry point
x=0 y=0
288
240
192
144
96
48
0
-48
-96
-144
-192
-240
-288
y in µm
-288 -192 -96 -48 0 48 96 192 288
x in µm
c)
ADU
Pixel

Fig. 2

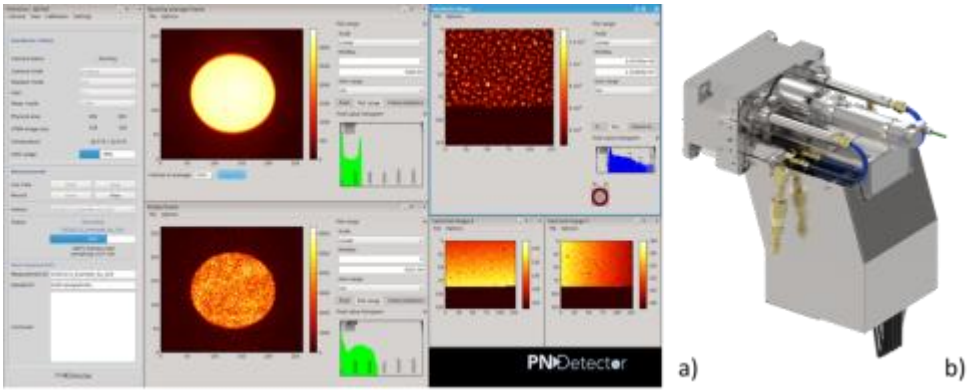
PNDetector
a)
b)

IM4.P012
A simplified approach for measuring sample thickness and mis-tilt from position-averaged convergent-beam electron diffraction patterns

M. Cattaneo[1], J. Barthel[1], K. Müller-Caspary[1], K. MacArthur[1], R. Dunin-Borkowski[1]

[1]Ernst Ruska-Centre for Microscopy and Spectroscopy with Electrons, Forschungszentrum Jülich GmbH, Aachen, Germany

In recent years, high-resolution scanning transmission electron microscopy (STEM) has been applied successfully to the analysis of the atomic structure of solid materials. Many approaches have been proposed for extracting quantitative information about local atomic structure from STEM images, including the matching of image simulations to experimental images on an absolute scale (1). It is highly desirable to determine as many unknown experimental parameters as possible from independent measurements in order to improve comparisons. Sample thickness and mis-tilt from a chosen crystallographic orientation are examples of parameters that are often difficult to measure experimentally. The analysis of position-averaged convergent beam electron diffraction (PACBED) patterns has been shown to provide accurate measurements of sample thickness and mis-tilt, with reduced requirements for a priori knowledge about other experimental parameters (2). However, it is still challenging to match the details of simulated and experimental PACBED patterns accurately and robustly. In the present work, we investigate possibilities for extracting quantitative sample information from PACBED patterns with reduced demands on prior knowledge. We focus on the determination of sample thickness and mis-tilt from integrated intensities rather than pattern recognition. For example, the integrated bright-field and low angle dark-field intensity is found to decrease monotonically with sample thickness (Fig. 1). This measure can be calibrated with respect to the intensity of the incident probe by recording reference patterns without the sample present (but under otherwise identical conditions) and used to determine the sample thickness with a precision of few nanometres. The evaluation is insensitive to small sample mis-tilt. For larger sample tilt angles, an estimate of the mis-tilt can be determined from the cross-overs of Kikuchi lines, which are visible in patterns recorded from thicker samples (e.g., Fig. 2). Our approach is particularly applicable to momentum-resolved STEM data, from which the sample thickness and mis-tilt can be obtained with unit cell resolution. Although sample thickness has previously been measured from averaged intensities recorded using a high-angle annular dark-field detector (3), quantification then requires careful prior calibration of the detector sensitivity to scale the experimental image intensity as a fraction of the incident probe intensity.

References:

(1) J.M. LeBeau et al., Phys. Rev. Lett. 100 (2008) 206101.

(2) J.A. Pollock et. al., Ultramic. 181 (2017) 86-96.

(3) A. Rosenauer et al., Ultramic. 109 (2009) 1171-1182.

Fig. 1: Integrated intensity of simulated PACBED patterns of SrTiO3 in the [001] zone axis orientation plotted as a function of sample thickness for 200 keV electrons. The integration area is a disk centred on the zero beam with a radius of 44 mrad, which corresponds to twice the semi-convergence angle of the incident probe. The intensity is plotted as a fraction of the incident probe current. The horizontal blue line marks the intensity value obtained from the experimental PACBED pattern shown in Fig. 2, for which the estimated sample thickness is 39 nm.

Fig. 2: Experimental (left) and simulated (right) PACBED patterns of SrTiO3 in the [001] zone axis orientation. The experimental pattern was recorded using a probe CS-corrected FEI Titan instrument operated at an accelerating voltage of 200 kV. The white circle marks the circular integration area used to measure the intensity value marked in Fig. 1.

Fig. 1

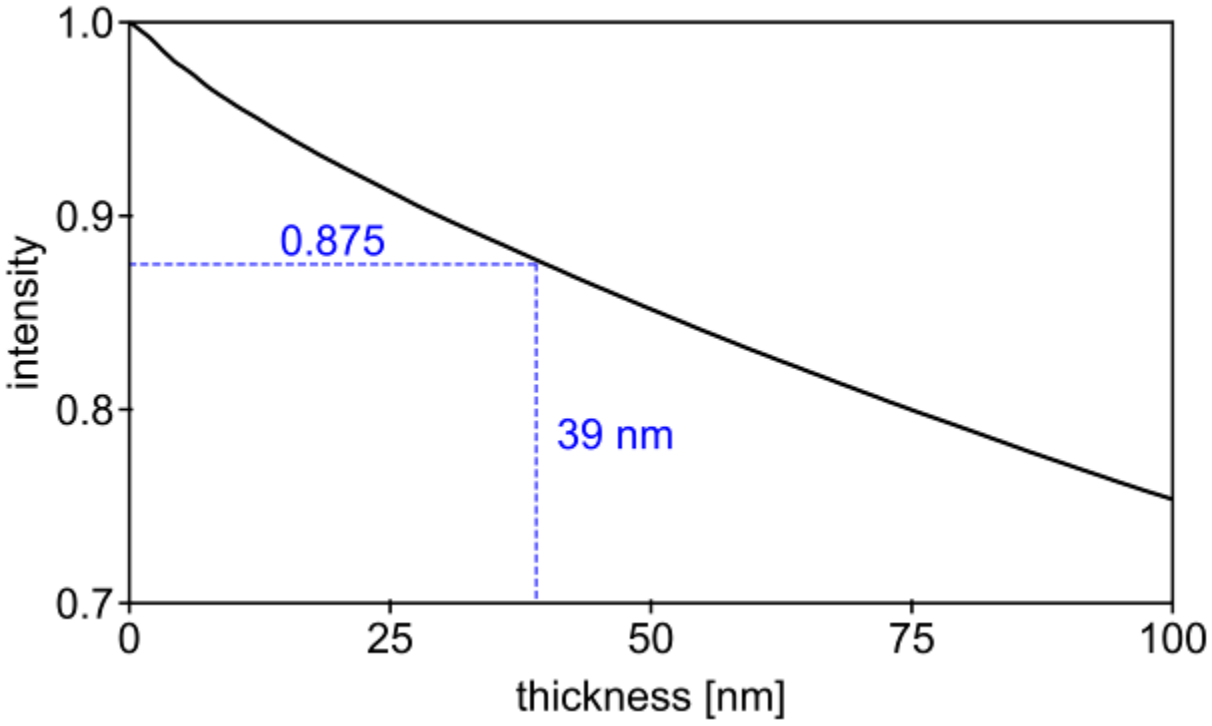
1.0
0.9
0.8
0.7
intensity
0.875
39 nm
0
25
50
75
100
thickness [nm]

Fig. 2

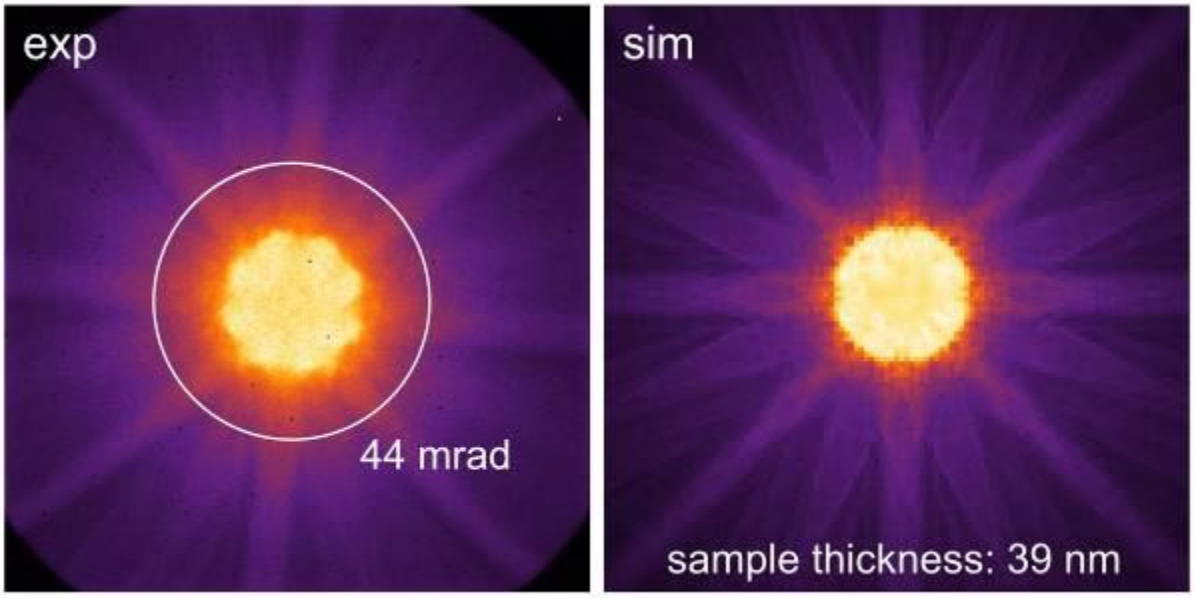
exp
44 mrad
sim
sample thickness: 39 nm

IM4.P013
Long-range internal stresses close to deep trenches in Silicon devices by cross-correlation EBSD

E. Hieckmann[1], M. Fugmann[1], S. Kaiser[1], P. Chekhonin[2], J. Gambino[3], U. Mühle[4]

[1]TU Dresden, Faculty of Physics, Institute of Applied Physics, Dresden, Germany
[2]Helmholtz-Zentrum Dresden-Rossendorf, Dresden, Germany
[3]ON Semiconductors, Gresham, United States
[4]Fraunhofer Inst. for Ceramic Techn. and Systems, Dresden, Germany

Deep trenches in Silicon, used for electric isolation in high-voltage/high-frequency devices are manufactured in a process flow that includes etching, oxide deposition, polysilicon filling and annealing (1). In consequence, thermo-mechanical stresses are generated and can cause dislocations and slip in the vicinity of the deep trenches. The aim of this study is to determine quantitatively the strain and stress fields around a deep trench by cross-correlation electron backscatter diffraction (ccEBSD) (2) for a fully processed Si wafer.

The measurements were carried out on a cross section of the wafer in a scanning electron microscope ZeissUltra55, equipped with field emission gun, EBSD Nordlys detector and Channel 5 software. Figure 1 (a) shows the trench imaged by secondary electrons, with the coordinate system of the stress tensor and the crystallographic orientation. The diffraction patterns were taken along lines parallel to the *x*-axis which was the tilt axis of the sample in the EBSD set up. The patterns (Figure 1 (b)) were acquired at about 2000 measuring positions with a step size of 10nm in *x*-direction for several distances *y* from the original wafer surface. The calculations of all the components of the elastic strain tensor (precision 10-4) and of the stress tensor were performed for each measuring point with respect to a reference pattern taken at an unstrained crystal region according to the cross-correlation approach for the Fourier transform of the diffraction patterns described in (3).

The acceleration voltage of the electron beam determines the size of the scattering volume in bulk samples and therefore the size of the region where the ccEBSD method provides a mean stress for. To check this effect at deep trenches with stress gradients the investigations were performed at 20 kV as well as at 10 kV. The von Mises stress σ_{vM} as a general stress indicator is shown in Figure 2 along scan lines at several depths *y* for both voltages. At the deep trench, in the middle of the diagrams, no evaluable diffraction patterns can be measured. Obviously, the stressed region is restricted to the direct vicinity of the deep trench but the calculated stress values and their local distribution depend on the acceleration voltage. This observation will be discussed as suggested above but taking into account also parameters of the numeric evaluation procedure.

References:

(1) J.P. Gambino, Y. Watanabe, Y. Kanuma, B. Greenwood, D. Price, A. Suwhanov, S. Hose, O. Whear, *Int. Symp.on Physical & Failure Analysis of Integrated Circuits (IPFA)*, 2016, 321-325

(2) A.J. Wilkinson, G. Meaden, D.J. Dingley, *Ultramicroscopy.* 106 (4-5), 2006, 307-313

(3) E. Hieckmann, M. Nacke, M. Allardt, Y. Bodrov, P. Chekhonin, W. Skrotzki, J. Weber, *J. Vis. Exp.* 111, e53872, 2016, 1-14

Fig. 1: (a) Deep trench with *x-y-z* coordinate system, crystal orientation of the wafer and position of the EBSD scan line at *y* = 15 µm. (b) EBSD diffraction pattern measured on the first measuring position on the left hand side of the scan line.

Fig. 2: von Mises stress σ_{vM} along the scan lines across the deep trench at several depths *y* measured at an acceleration voltage of (a) 20 kV and (b) 10 kV.

Fig. 1

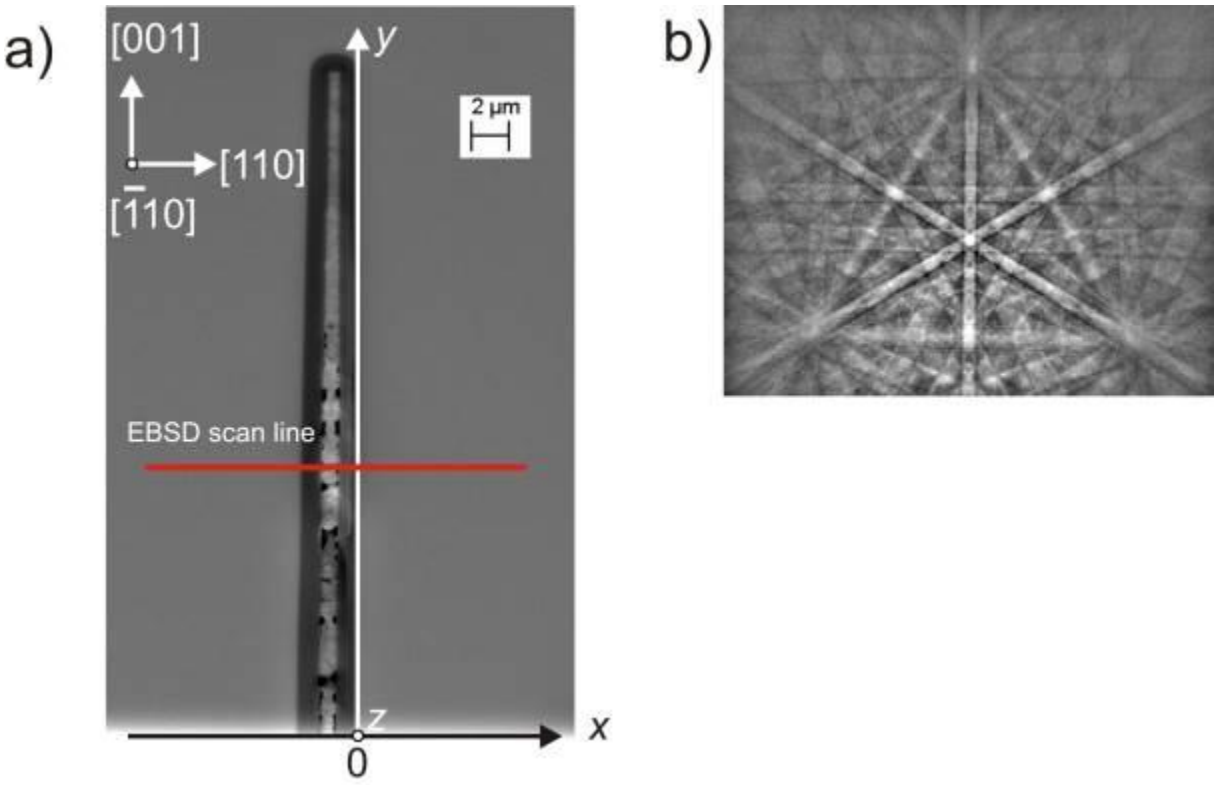
a)
[001]
y
[110]
[$\bar{1}$10]
2 µm
EBSD scan line
z
x
0
b)

Fig. 2

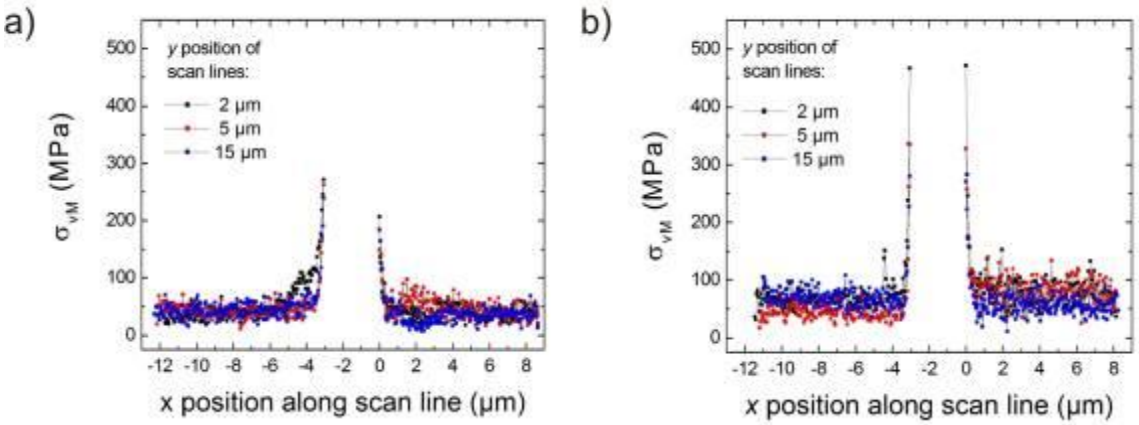
a)
y position of scan lines:
2 µm
5 µm
15 µm
σvM (MPa)
x position along scan line (µm)
b)
y position of scan lines:
2 µm
5 µm
15 µm
σvM (MPa)
x position along scan line (µm)

IM4.P014
Measurement of absorbed current for quantitative evaluation of scattered electrons in a scanning electron microscope

K. Morimoto[1], Y. Ito[1], M. Kotera[1]

[1]Osaka Institute of Technology, Major in Electrical, Electronic and Mechanical Engineering, Osaka, Japan

Electron beam (EB) has been used for various nanotechnologies such as observation and microfabrication of a specimen. Electrons are so light that they easily scatter in a specimen around the irradiation point of the EB, and some of them are emitted from the surface. Fogging electrons (FGEs) are produced by multiple re-backscattering events between the specimen surface and the objective lens plate, and they distribute laterally in cm order. If the specimen is an insulator, FGEs may cause a global charging phenomenon throughout the specimen chamber.

In order to quantify the contribution of FGEs in a scanning electron microscope (SEM), we measure the absorbed current at some electrodes set in the specimen chamber. One of them was attached to the specimen stage, and the other was attached to the bottom of the objective lens.

Fig. 1 shows the experiment setup. The specimen is the patterned Cu printed circuit board with a central isolated Cu disk. There is also an isolated electrode in the large Cu surface to measure incident EB current. In the measurement of secondary electron (SE) and slow FGE at the large Cu surface, the influence of the collection electric field from the SE detector attached to the SEM is so large that it cannot be ignored in the present experiment. Therefore, we set a shutter to prevent the electric field leaks toward the specimen, while EB is irradiated the specimen and FGE current is measuring. The electrode attached to the bottom of the objective lens plate is made of aluminum. The EB current is 1 nA and the working distance is 20 mm.

As it is illustrated in Fig. 1, FGE current at the bottom of the objective lens is that flows toward the ground, and FGE current at the specimen is that flows toward the floated potential given by the specimen bias voltage.

Fig. 2 shows the results of the FGE current of the electrode on the specimen. First, in the case of applying a positive bias to the specimen will be described. When the acceleration voltage is 0.8 and 2.0 kV, the maximum value of the current shows with the low applied bias and the measured current tends to decrease with the increase of the bias. When the acceleration voltage is 5.0 and 30 kV, the change in the current amount is gentle. Next, in the case of applying a negative bias, the FGE current is almost zero, if the bias is less than -10V, and in this condition FGEs can hardly exist on the surface.

It was found that the FGE current tends to be different depending on the EB acceleration voltage. At the low acceleration voltage, the FGE current shows its peak at about 10 V of the bias voltage. This is because low energy electrons show a trajectory of a parabola such as a fountain because of the application of the positive bias voltage, and if the bias is too large, the size of the fountain shrinks and emitted slow electrons cannot reach the outside of the central electrode, and FGE current decreases rapidly with the applied bias voltage.

References:

(1) Y. Ito, et al, "Simulation of fogging electron trajectories in a scanning electron microscope", SPIE Photomask Technology + EUV Lithography 2018; Proc. SPIE 108100B.

Fig. 1: Schematic diagram of absorption electron current measurement.

Fig. 2: FGE current at the specimen.

This work was supported by KAKENHI (C) 16K063234

Fig. 1

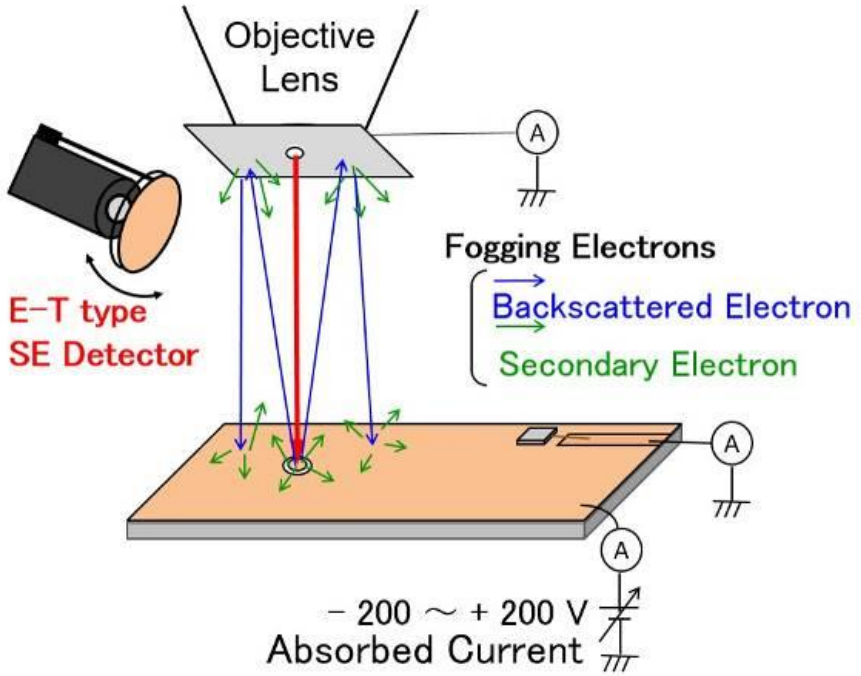
Objective
Lens
A
Fogging Electrons
Backscattered Electron
Secondary Electron
E-T type
SE Detector
A
A
− 200 ～ + 200 V
Absorbed Current

Fig. 2

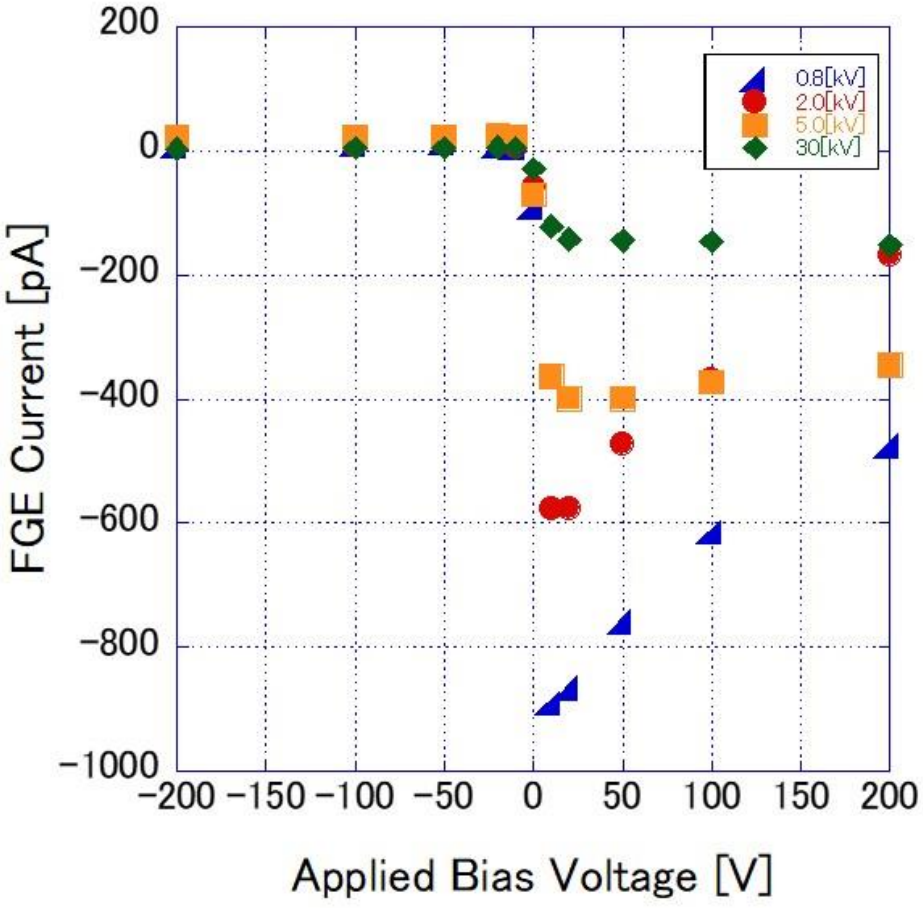
0.8[kV]
2.0[kV]
5.0[kV]
30[kV]
FGE Current [pA]
200
0
−200
−400
−600
−800
−1000
−200 −150 −100 −50 0 50 100 150 200
Applied Bias Voltage [V]

IM4.P015
Simulation of multiply scattered electron trajectories in scanning electron microscope specimen chamber

Y. Ito[1], K. Morimoto[1], M. Kotera[1]

[1]Osaka Institute of Technology, Major in Electrical, Electronic and Mechanical Engineering, Osaka, Japan

Electron beam (EB) can be focused in nanometer scale, and it is an essential tool in nanotechnology, such as processing and observation. It is found recently that in a vacuum specimen chamber of scanning electron microscope (SEM), fogging electrons (FGEs) are generated by multiple backscattering events of electrons between the specimen surface and the pole piece of objective lens plate, and they give a large influence on the spatial resolution. FGEs spread up to more than 10 mm from the beam irradiation point. They may be responsible for a global charging phenomenon on a specimen, if it is made of insulators.

In this study, the structure in the SEM specimen chamber is simplified and three dimensional electron trajectories are traced in the specimen and in the objective lens electrode by a Monte Carlo simulation, and the trajectories are also traced in the vacuum, where an electric field is present. On the other hand, experiments with the same boundary condition around the specimen are carried out to obtain FGE current by EB exposure. If the simulation results agree with the experimental results, the effectiveness of the simulation is proved and other quantities obtained by the simulation may be valid.

Electron scattering events in the material are simulated by the Monte Carlo method. Since both backscattered electron (BSE) and secondary electron (SE) yields are adjusted to each experimental data, the number of FGEs we obtain here should be reasonable. The volume of the three dimensional space of the SEM specimen chamber assumed here is 100 mm x 100 mm x 100 mm.

Fig. 1 shows an illustration of the measurement system of the FGE current. EB is irradiated the grounded and isolated central electrode. Emitted BSEs and SEs produced at the central electrode hit the electrode set on the bottom of the objective lens. Some of electrons in the electrode may come back as FGEs to irradiate the specimen stage.

Fig. 2 shows a comparison between the experimental and the present simulation results for Cu and Cu_2O electrodes. If we assume the electrode is made of Cu, the FGE current is larger than experimental data for both EB acceleration voltages of 0.8 and 2.0 kV. On the other hand, if we assume that the electrode is made of Cu_2O, the FGE current is closer than the case mentioned above for both acceleration voltages of 0.8 and 2.0 kV. In the experiment, we used a commercially available Cu print circuit board (Cu-PCB) as the electrode, and the Cu surface is more likely to be oxidized.

We developed a simulation to take into account electron trajectories in a specimen, in the objective lens plate and the vacuum between them. Based on the fair agreement in the comparison with the simulated results and the experimental results, the absorbed FGE current is explained by the fact that the surface of the Cu is oxidized to be Cu_2O. The present simulation can be expected to quantify how much FGE is spatially distributed, and based on the knowledge obtained by the simulation, conditions to avoid global charging phenomena in the case the specimen is made of insulators.

References:

(1) M. Kotera, A. Osada, M. Otani, Y. Ohara, Journal of Vacuum Science and Technology, B 29 (6) 06F316-1-06F316-6 (2011).

Fig. 1: Pattern diagram of the measurement of the FGE current.

Fig. 2: FGE current at the specimen.

This work was supported by KAKENHI (C) 16K063234

Fig. 1

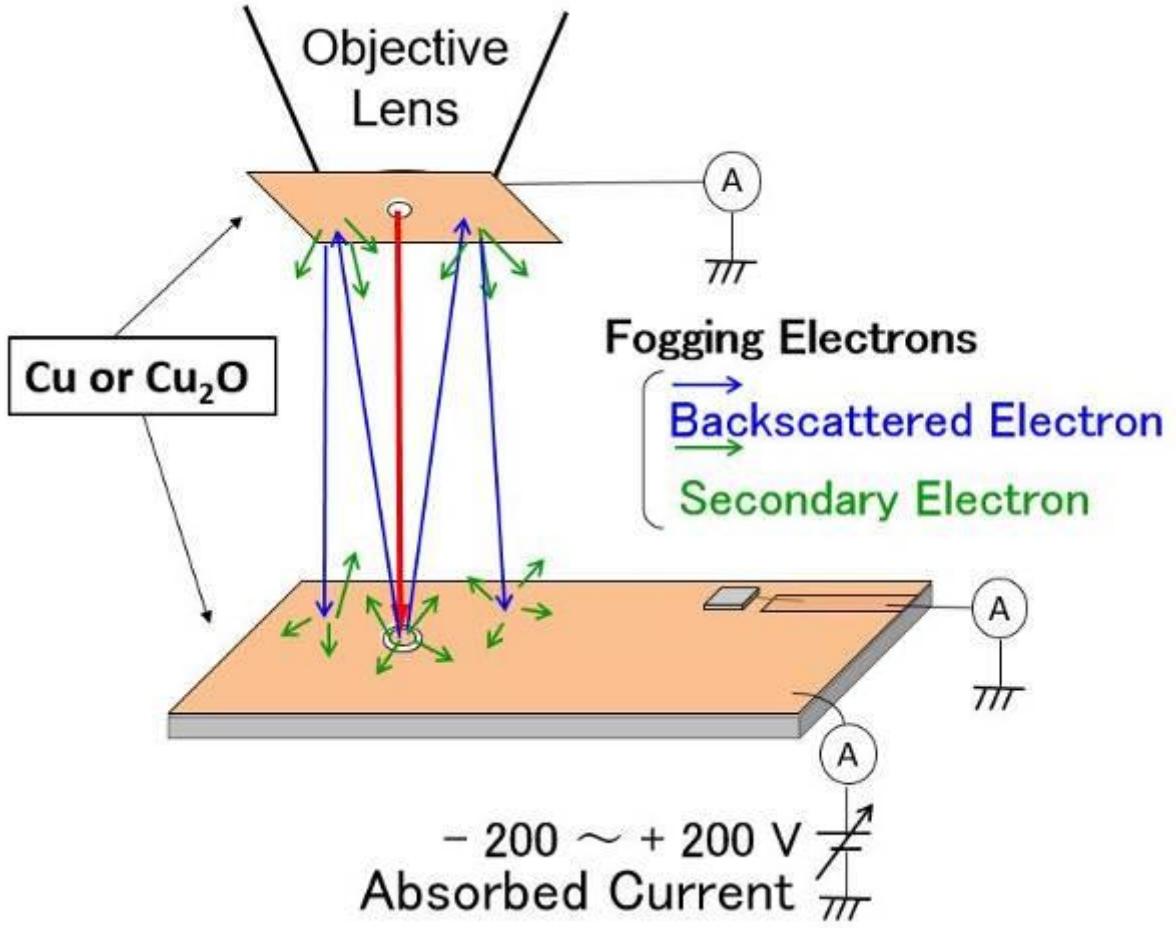
Objective Lens
A
Cu or Cu_2O
Fogging Electrons
Backscattered Electron
Secondary Electron
A
A
− 200 ～ + 200 V
Absorbed Current

Fig. 2

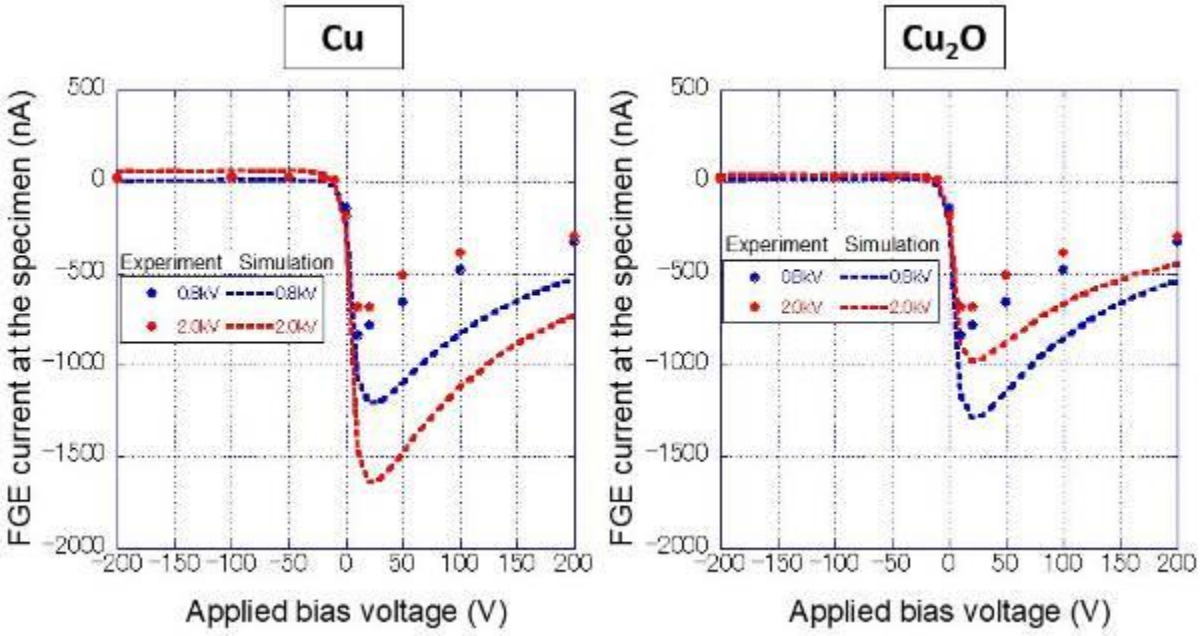
Cu
Cu_2O
FGE current at the specimen (nA)
Applied bias voltage (V)
Experiment Simulation
0.8kV 0.8kV
2.0kV 2.0kV
500
0
−500
−1000
−1500
−2000
−200 −150 −100 −50 0 50 100 150 200

IM4.P016
Serial protein crystallography in a STEM

R. Bücker[1], P. Hogan-Lamarre[1,2], P. Mehrabi[1], E. C. Schulz[1], M. de Kock[1], P. Pelz[1], G. H. Kassier[1], R. J. D. Miller[1,2]

[1]Max Planck Institute for the Structure and Dynamics of Matter, Hamburg, Germany
[2]University of Toronto, Departments of Chemistry and Physics, Toronto, Germany

X-ray-based serial crystallography has become a highly successful approach for observing structure and dynamics of radiation-sensitive macromolecules. By computationally merging a crystallographic data set from single-shot data of thousands of crystals, cumulative radiation damage inherent to conventional rotation acquisition is avoided. This, in turn, allows to use crystals down to sub-micron sizes, making a large class of radiation-sensitive systems such as proteins and nanoporous materials amenable to crystallographic structure determination. In this low-dose, small-crystal regime, electron radiation, as compared to X-rays, provides the significant advantage of a more favorable ratio of elastic scattering to damaging energy deposition by three orders of magnitude. Indeed, it has been shown that protein structures can be solved from single to few well-formed nanocrystals using rotation crystallography with electrons.

Combining the virtues of both serial and electron approaches promises to further extend limits in terms of low crystal size and high radiation sensitivity, while allowing for a high degree of automation and ease of use. We conceived and implemented a highly automated scheme for serial electron crystallography employing a nanobeam in a scanning transmission electron microscope (STEM).

We serially address and diffract from nanocrystals by synchronized beam motion and data acquisition using a Medipix-based direct diffraction detector at up to kilohertz rates. Automatic mapping of crystal positions in low-dose STEM imaging obliterates the need for complex sample delivery schemes, while arbitrary scan patterns are used to maximize throughput and provide full automation. Dose fractioning through movie-mode acquisition is applied when exposing each crystal, allowing to determine the optimal exposure dose *a posteriori*.

Using our automated workflow, we solved structures of proof-of-principle systems at competitive resolutions. Results on proteins and nanoporous compounds are presented, along with a thorough discussion of the data acquisition and analysis pipeline. We will also give an outlook on single-particle coherent imaging of amorphous objects following the approach of low-dose ptychography, as recently implemented in our setup. Simulations promise a dose-efficiency increase of two orders of magnitude with respect to standard techniques; we also present first experimental results.

Our successful implementation of serial crystallography using only slightly modified standard hardware, software, and sample preparation methods, paves the way for routine high-throughput, automated acquisition of high-resolution diffraction data from extremely small and radiation-sensitive crystalline, and potentially amorphous, specimens. This new method is applicable to a wide class of systems from structural biology, as well as material science and organic chemistry.

Figure 1: STEM and diffraction data from protein nanocrystals. Left panel: STEM mapping image showing crystals placed randomly on a vitrified grid. Red dots indicate the automatically found crystal centroid positions. Colored circles identify those crystals the diffraction patterns of which are shown. Right panel: typical diffraction patterns, taken from the four crystals labeled in the STEM image, with corresponding colors.

Fig. 1

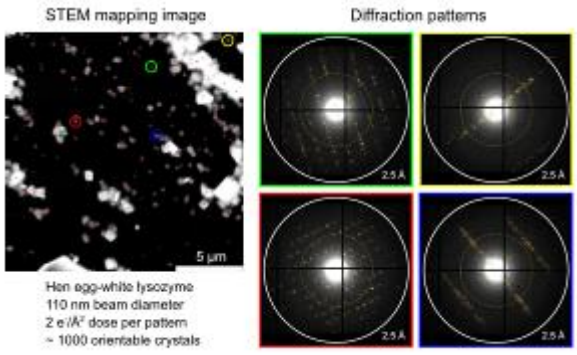

IM4.P017
HRSTEM of $LaMnO_3/SrMnO_3$ Superlattices: Quantitative Analysis of HAADF and iDPC Images

V. Roddatis[1], U. Roß[1], S. Lopatin[2], J. P. Bange[3], M. Keunecke[3], V. Moshnyaga[3]

[1]Georg-August-Universität Göttingen, Institut für Materialphysik, Göttingen, Germany
[2]King Abdullah University of Science and Technology, Core Labs, Thuwal, Saudi Arabia
[3]Georg-August-Universität Göttingen, Erstes Physikalisches Institut, Göttingen, Germany

Superlattices (SLs) of $LaMnO_3$ (LMO) and $SrMnO_3$ (SMO) have long been attracting scientific interest due to the observation of interfacial magnetism (1). Rapidly developing TEM methods have facilitated the discovery of new atomic structure features in these systems, correlating them with physical properties (2, 3). In particular, reconstructions of the oxygen sublattice near the interface regions have been reported in several studies of LMO/SMO SLs (4, 5). Here and after we distinguish between SMO/LMO and LMO/SMO interfaces, for example in the LMO/SMO notation the SMO layer is closer to the substrate. Recently, it was shown that only the SMO/LMO interface exhibits high temperature interfacial ferromagnetism (6). In this study we shed light onto structural peculiarities of LMO/SMO SLs using HRSTEM HAADF and iDPC (integrated Differential Phase Contrast) imaging.

The $(LMO)_m/(SMO)_n$ SLs with bilayer thickness, $\Lambda=(m+n)=6\div20$ unit cell were grown on $SrTiO_3(100)$ substrates by means of a metalorganic aerosol deposition technique. TEM specimens were prepared by lift-out technique using a FEI Nova NanoLab 600 dual beam instrument, and studied in a Thermo Fisher Themis Z microscope.

HAADF and iDPC images of 6/6 and 12/6 SLs are shown in Figure 1. Both LMO and SMO materials can be easily distinguished in the HAADF images by the layer thickness and Z-contrast. Careful analysis of the HAADF and iDPC signals reveals periodic modulations of the Mn-O bond length and bond angles in LMO which in addition depend on the layer thicknesses. The Mn-O bond length in SMO increases with decreasing layer thickness. For the m/n ~ 1, the La/Sr sublattice in both layers form a common framework. Meanwhile, the Mn-O bond angle in LMO decreases as the layer thickness is reduced, while it remains constant for SMO of equal thickness. The factor, which controls the Mn-O sublattice structure, appears to be the layer thickness, while the La/Sr lattice distortion is determined by the relative layer thickness ratio (m/n). Thus, the distortion of LMO and SMO lattices due to strain results in a peculiar Mn-O network, which is probably responsible for changes in electronic structure and associated magnetic properties.

References:

(1) B. Mercey, et al, Mater. Chem., (1999) 9, 233–242.

(2) B. Schaffer, et al, Microsc Microanal., (2008) 14 (Suppl 2).

(3) I. Lazić, et al, Ultramicroscopy, (2016) 160 265–280

(4) A. Y. Borisevich, et al, PRL (2010) 105 087204.

(5) G. Sanchez-Santolino, et al Microsc. Microanal., (2014) 20, 825–831.

(6) M. Keunecke, et al, Advanced Functional Materials, (2019) 1808270.

Authors thank Ricardo Egoavil and Ivan Lazić (Thermo Fisher Scientific), Volker Radisch[1], for collection of data, and DFG (SFB 1073, TP B04 and Z02) for financial support.

Fig. 1: (a,d) HRSTEM HAADF, (b,e) iDPC images, and (c, f) maps of Mn/O bonds for 6/6 and 12/6 SLs, respectively.

Fig. 1

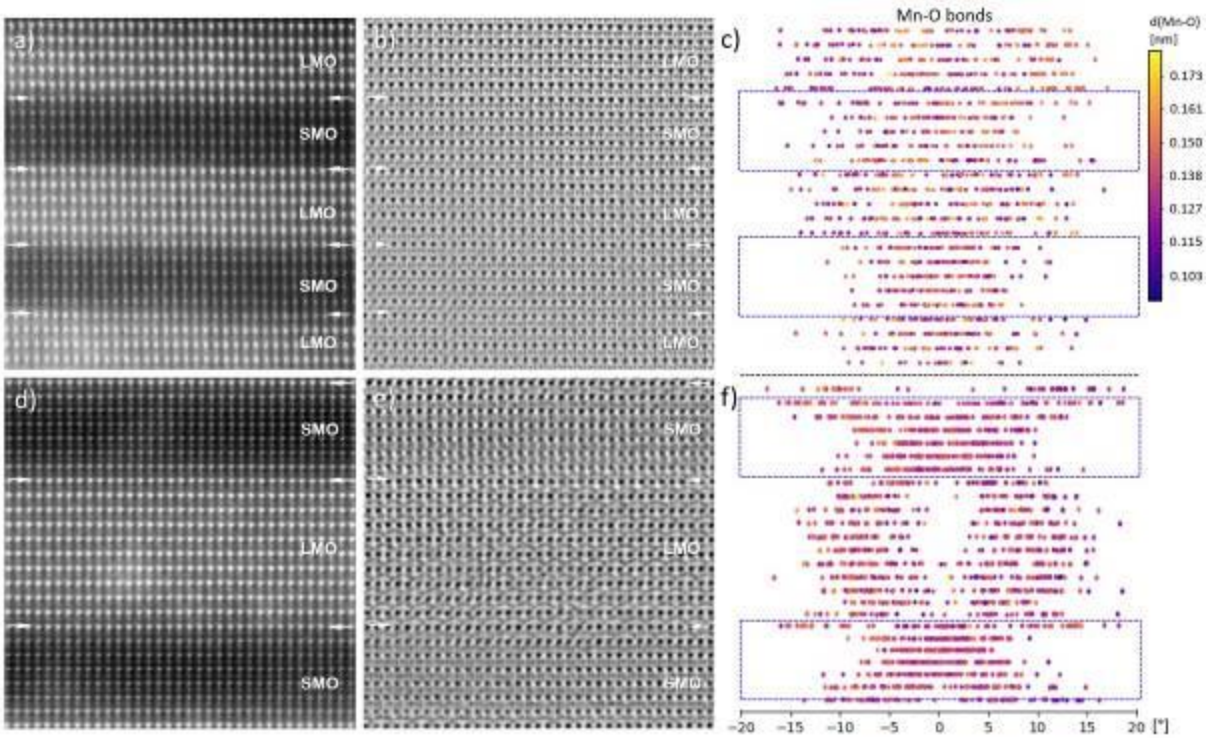
a)
LMO
SMO
LMO
SMO
LMO
b)
LMO
SMO
LMO
SMO
LMO
c)
Mn-O bonds
d(Mn-O) [nm]
0.173
0.161
0.150
0.138
0.127
0.115
0.103
d)
SMO
LMO
SMO
e)
SMO
LMO
SMO
f)
−20 −15 −10 −5 0 5 10 15 20 [°]

IM4.P018
A Comparative Investigation between Transmission Kikuchi Diffraction (TKD) and Precession Electron Diffraction (PED)

G. Sneddon[1], X. Zhou[1], G. Thompson[1], J. Cairney[1]

[1]University of Alabama, Metallurgical & Materials Engineering, Tuscaloosa, Alabama, United States

Transmission Kikuchi Diffraction (TKD) in the SEM and Precession Electron Diffraction (PED) in the TEM are methods used to achieve higher spatial resolution for grain misorientation and grain size mapping as well as grain texture quantification. Using a polycrystalline Cu foil, a comparison of these techniques to these types of grain characteristic measurements has been undertaken.

In the nanocrystalline Cu sample, the TKD analysis indexed more grains with a higher confidence than PED. The origin of the difference is explain by how the diffraction patterns are captured. In TKD, the diffraction events are derived from within a few to ten nanometers of the exiting surface. In this case, the diffraction is then limited (typically) from a single grain even if other scattering events occurred by grains that may be above the exiting grain. In PED, the diffraction events are through the entirety of the foil, thus the collected patterns can be a convolution of more than one grain's diffraction pattern if such grains overlap where the beam penetrates. Nonetheless, when the grains did not overlap, PED's spatial resolution for mapping the smallest grains was more evident as compared to TKD. Though both methods could index twin structures in the Cu foil, PED appears to be more sensitive to identifying twin structures that were not captured by TKD. Interestingly, in PED when twins were close to a {001} zone axis of a grain, the twin but was observed but was resolved by TKD.

A comparison of the pattern collection as a function of foil thickness was also undertaken. TKD was able to index diffraction patterns in foils up to ~ 350 nm in thickness whereas PED pattern recognition was limited to ~ 140 nm in a same Cu foil. Though the TKD scans were done at 20 keV and the PED at 200 keV, suggesting a peculiar contradiction in that higher keV would enable deeper electron penetration, the difference in pattern detection as a function of foil thickness is explained in the origins of the diffraction events themselves. TKD patterns originate from inelastic scattered electrons that satisfy the Bragg condition. If these electrons are able to escape the foil to yield a sufficient detected intensity, they will provide a TDK pattern. In contrast, PED patterns originate from pseudo-kinematical scattered electrons. If these electrons undergo multiple scattering events with continual penetration into the volume of the material, their ability to satisfy the Bragg condition is lost and no pattern is detected.

In summary, both TKD and PED provide complementary means of quantifying nanoscale grain characteristics. Rather than being competitive techniques, each method has particular strengths and weaknesses dependent on the sample type, foil thickness, and spatial resolution needed.

Figure 1: **(a)** TKD and PED map of nanocrystalline Cu. The circled regions identify where PED revealed a higher spatial detection of twins whereas the boxed region is a TKD identified twin absent in the PED scan. **(b)** A profile of collected Cu grains from the same region between TKD and PED as a function of foil thickness (measured by EELS). Note the further detection of the patterns for TKD.

Fig. 1

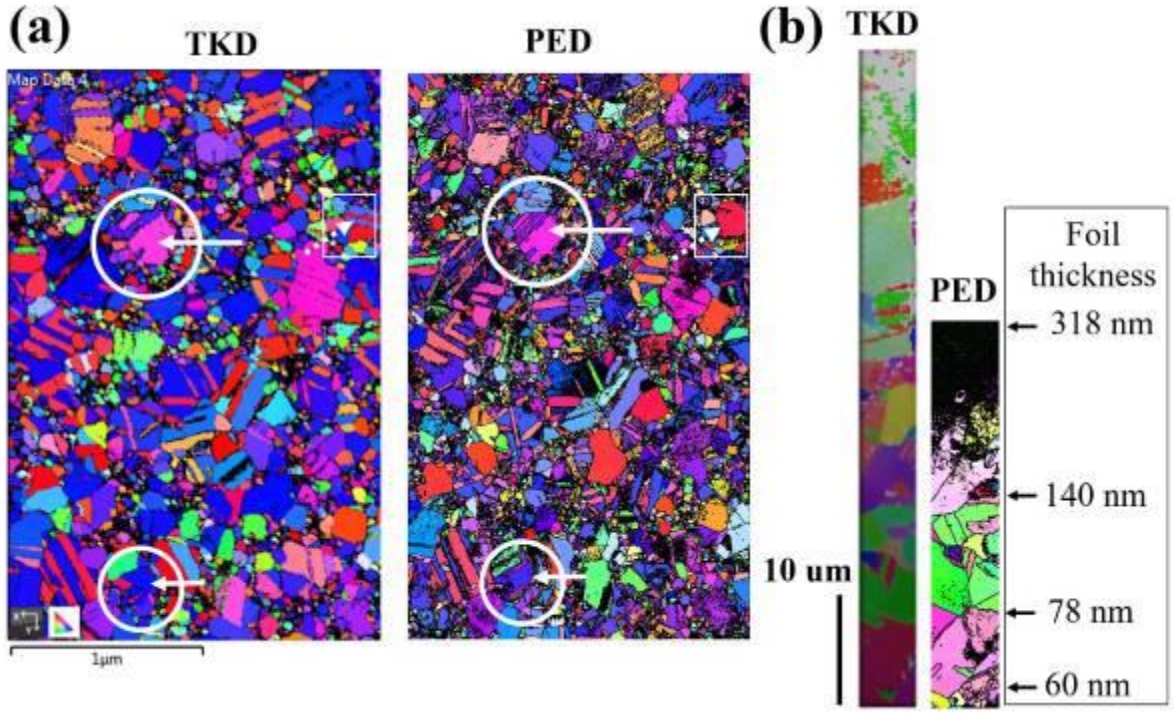
(a)
TKD
PED
1μm
(b)
TKD
PED
Foil thickness
318 nm
140 nm
78 nm
60 nm
10 um

IM4.P019
Stability and dynamics of sub-nm Pt clusters on a carbon surface and in ionic liquid

T. R. Henninen[1], D. Keller[1], F. Wang[1], R. Erni[1]

[1]Empa, Swiss Federal Laboratories for Materials Science and Technology, Electron Microscopy Center, Dübendorf, Switzerland

The formation of solid matter as modelled by classical nucleation theory, assumes the solid forms a spherical nucleus. However, initially at sub-nm scale, non-spherical atomic clusters form with structures deviating from bulk. Thus, understanding the dynamics in this regime requires considering individual atoms. Knowledge of this initial cluster formation enables improved control of nanomaterial fabrication and potentially creating new materials.

In our work, we study the metastable structures of the smallest possible nucleates; sub-nm clusters down to a few atoms in size. Aberration-corrected scanning transmission electron microscopy (STEM) has sufficient resolution to directly image these. By optimizing the microscope for high-framerate dynamic imaging, along with neural network denoising, from the quantitative STEM contrast we can identify the crystalline structures and atomic dynamics of these clusters.(1)

Following the demonstration of atomic resolution imaging in ionic liquid, (2) we further study atomic-scale nucleation phenomena in an environment closer to realistic nucleation, by sputtering Pt into suspended thin films of the vacuum compatible ionic liquid 1-Butyl-3-methylimidazolium chloride. Such thin films (~10-50 nm) were reproducibly deposited onto Protochips heating E-chips, freely suspended in the holes of the chip's carbon film. (3) This was possible by making thin films of ionic liquid highly diluted in ethanol, formed in a hoop (akin to a soap bubble wand), that is soft enough to directly touch the dilute liquid film onto the fragile electron-transparent window of the chip. After drying the ethanol, only a very thin film of ionic liquid remains.

On a carbon surface, sub-nm Pt clusters are unstable, forming molten 2D sheets, analogue to a droplet wetting the surface. Upon heating above 300°C, the clusters start forming crystalline structures, mainly classified into 4 categories (fig. 1a-d). The most stable and frequent clusters are in the range of 12-15 atoms, centred around the magic-number symmetrical structures of the 14-atom fcc cube, 13-atom fcc cuboctahedron, 13-atom hcp triangular orthobicupola and the 13-atom icosahedron, with stability decreasing in order fcc cuboids, fcc cuboctahedrals, hcp, icosahedrals (fig. 1e). Meanwhile, in ionic liquid, clusters are stable down to 10-15 atoms in size, and can be induced by heating to nucleate and coalesce from concentrated atomic dispersions (fig. 2). Altogether, we demonstrate identifying the structures and dynamics of the smallest clusters created in the initial step of solid phase nucleation.

References:

(1) Henninen, et al. Dynamics and crystallinity of sub-nm platinum clusters at elevated temperatures. Under review. 2019

(2) Miyata, et al. Real-space analysis of diffusion behavior and activation energy of individual monatomic ions in a liquid. 2017

(3) Keller, Henninen, Erni. Formation of gold nanoparticles in a free-standing ionic liquid triggered by heat and electron irradiation. 2019

This project has received funding from the European Research Council (ERC) under EU"s Horizon 2020 research and innovation program (Grant Agreement No. 681312).

Fig. 1: **a** Pt_{13} fcc cuboid. **b** Pt_{13} fcc cuboctahedron. **c** Pt_{15} hcp. **d** Pt_{16} icosahedron. **e** Stability of the 4 types of structure in a-d.

Fig. 2: 3 clusters of ~15 atoms, where the two top clusters coalesce into a larger cluster, while the bottom cluster gradually disintegrates. **a** At 0 seconds. **b** 4 seconds. **c** 35 seconds.

Fig. 1

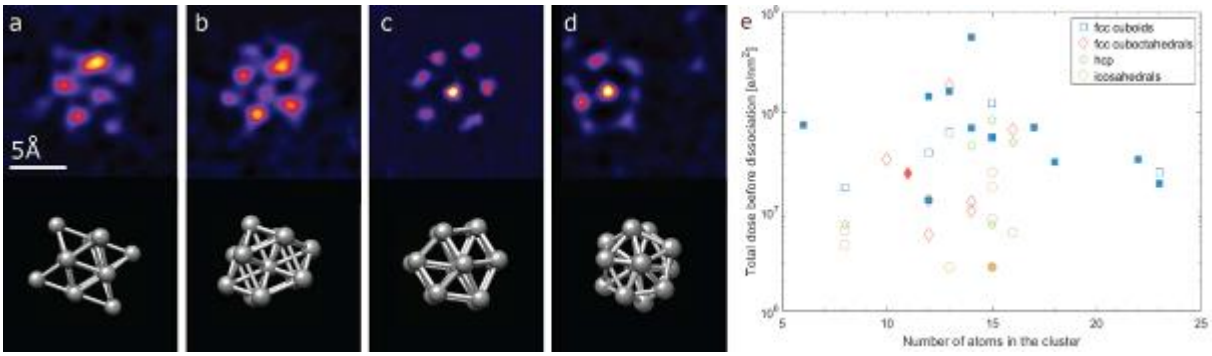
a
b
c
d
5Å
e
fcc cuboids
fcc cuboctahedrals
hcp
icosahedrals
Total dose before dissociation [e/nm²]
Number of atoms in the cluster

Fig. 2

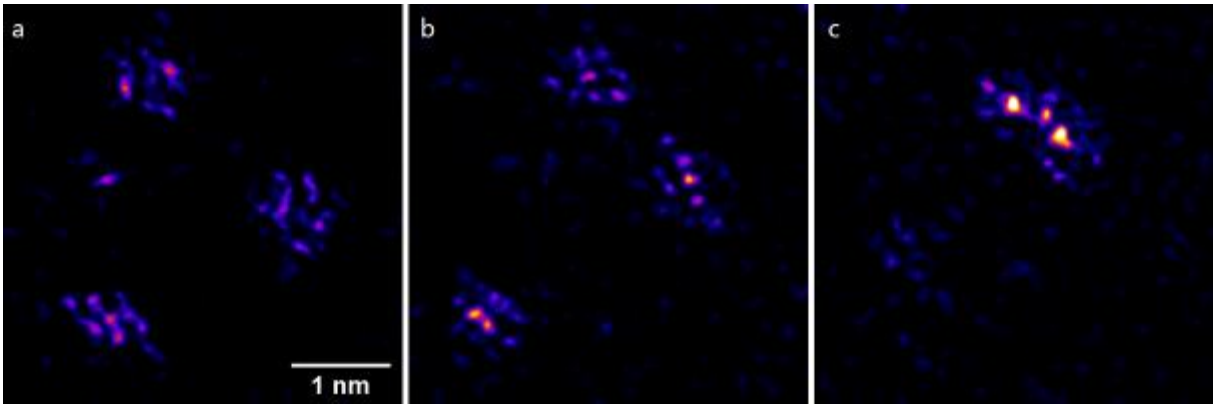
a
b
c
1 nm

IM4.P020
Quantitative structural optimization in multiple dimensions against transmission electron diffraction data

R. S. Pennington[1], T. Ober[1], J. M. Zuo[2], Y. T. Shao[2], C. T. Koch[1]

[1]Humboldt-Universitaet zu Berlin, Institut fuer Physik, AG SEM , Berlin, Germany
[2]University of Illinois at Urbana-Champaign, Department of Materials Science and Engineering and Fredrick Seitz Materials Research Laboratory, Urbana, IL, United States

Transmission electron diffraction can probe material structures at the nano- and sub-nanometer scales. TEM diffraction data's high sensitivity to structural characteristics makes it ideal for quantitative analysis. (1) In particular, convergent-beam electron diffraction (CBED) and related techniques that encompass multiple incident beam tilts provide a wealth of structural information without tilting the specimen. Furthermore, this structural sensitivity includes structural changes along the beam direction - the PRIMES algorithm retrieves variations along the beam direction from a single CBED pattern. (2-4) However, applying these advanced algorithms to experimental data requires solving several challenges. In this work, we focus on the challenges of processing and interpreting experimental data within PRIMES.

This work has three objectives: a robust comparator that can provide goodness-of-fit measurements against experimental data, then ensuring that any pre-processing of experimental data doesn't inhibit structural characterization, and finally being able to verify simulated structural models' accuracy and establish the operational zone for our advanced algorithms.

We apply computational methods to experimental data. Our experimental data are 200kV CBED patterns of BaTiO3. We use density functional theory (DFT) to calculate realistic electronic structure, necessary for modeling beam-specimen interactions. (5) We also use GPU co-processorsfor matrix exponentials on calculated structure-factor matrices, enabling multiple orders of magnitude faster diffraction-data computation compared to conventional approaches. (6) Finally, our other main tool is PRIMES - Parameter Retrieval and Inversion from Multiple Electron Scattering. (2-4) PRIMES iteratively analyzes stacked-Bloch-wave simulations using methods developed within neural-network theory to provide quantitative parameter determination for crystalline specimens. Within PRIMES, we developed a linear-regression-based algorithm for comparing simulated and experimental data. Additionally, we incorporated filter kernel processing into the PRIMES toolbox.

We have found that linear-regression-based algorithms for coordinating experimental target-data with simulated candidate-data work well, and provide a verifiable goodness-of-fit measurement against experimental data. Figure 1 shows disc fit quality with thickness on the vertical axis, g on the horizontal, and disc fit as the intensity. Kernel-based filter processing is promising and kernel construction is a key avenue for future work.

PRIMES-based comparisons with experimental data can be quantitatively verified, and method refinement holds promise for future research.

References:

(1) J. M. Zuo, M. Kim, M. O'Keeffe, and J. C. H. Spence, Nature 401, 49 (1999).

(2) R. S. Pennington, C. Coll, S. Estradé, F. Peiró, and C. T. Koch, Phys. Rev. B 97, 024112 (2018).

(3) R. S. Pennington and C. T. Koch, Ultramicroscopy 155, 42 (2015).

(4) R. S. Pennington, W. Van den Broek, and C. T. Koch, Phys. Rev. B 89, 205409 (2014).

(5) J. Enkovaara, et al., J. Phys.: Cond. Mat 22, 253202 (2010).

(6) R. S. Pennington, F. Wang, and C. T. Koch, Ultramicroscopy 141, 32 (2014).

RSP thanks DFG project PE2500/1-1 (PolaRIS-3D) for funding. JMZ and YTS were supported by U.S. DoE, Office of Basic Energy Sciences under contract DEFG02-01ER45923.

Fig. 1

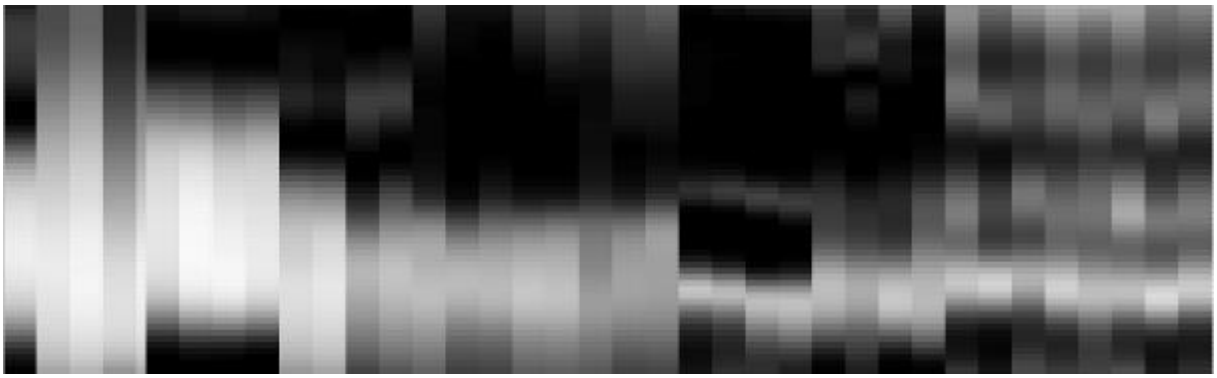

IM4.P021
High frequency electromagnetic fields induced ultrastructural changes on secretory granules of pancreatic beta cells in rats: unbiased stereological analysis

S. Paraš[1], N. Vojinović[1], R. Gajanin[1], J. Paspalj[1]

[1]University of Banja Luka, Cell Biology, Banja Luka, Bosnia And Herzegovina

Cavalier's principle of stereological measurements can be applied to the analysis of the ultrastructural structure of cells. The results of these measurements are safer and more accurate, because they are empirical and impartial. The beta cell secretory granules are generally of the correct circular shape on electron micrographs and are good for the application of the Cavalier analysis. Changes occurring on the secretory granules of rat beta cells after staying in high frequency electromagnetic fields (HF EMF) are difficult to detect without stereological, unbiased principles. The display of changes caused by secretion granules of beta cells shows the effect of these fields on the pancreas as a whole in rats.

To examine the applicability of Cavalier's principle for the quantitative proof of effects high-frequency electromagnetic fields on ultrastructure of secretory granules in pancreatic beta cells.

Ten Albino Wistar rats age 2 months were used as an in vivo animal model for the effects of staying in HF EMF. The characteristics of HF EMF were: 1.9 GHz frequency, 0.24 A/m intensity, electric field strength of 4.79 V/m and specific absorption rate value of 2.0 W/m2. Exposure time was 7 hours per day, 5 days per week, over the course of sixty days. Ten other Albino Wistar rats of the same age did not stay in these fields and were a control group. Sixty days after exposure, pancreatic beta cells of all twenty rats were analyzed on a Transmission Electron Microscopy Zeiss EM902. Analysis was measured following the stereological parameters of the number, diameter, volume density, surface density and numerical density of secretory granules. Stereological unbiased measurements of beta cells in both experimental groups were taken using Cavalieri"s principle 16.0 point-counting MBF software system (MBF Bioscience, Williston, VT, USA), Application Suite 3.0.0., with P2 spacing grid. Statistical analysis was performed using parametric (ANOVA and t-test) and nonparametric tests (Kruskal-Wallis and Mann-Whitney U-test) depending on data distribution.

High frequency electromagnetic fields led to a change in stereological parameters in secretory granules on pancreatic beta cells in rats. HF EMF increases the number and numerical density of secretory granules in beta cells. HF EMF reduces diameters, volumetric density and surface density secretory granules in beta cells. The results indicate that the secretory granules of beta-cell pancreatic cells are changed in rats exhibited in these fields relative to the control group. Changing the structure and the number of secretory granules has changed the functioning of pancreatic beta cells.

This study was performed as a contribution to the evidence of the effect of HF EMF on pancreatic beta cells in rats. Although these EMFs induced several changes in the pancreatic beta cell structure, they were not relevant and represent a normal and reversible response of rat's pancreas to the presence of HF EMFs in their environment. Stereology analyses of beta cells reactions further confirmed that these electromagnetic fields possess therapeutic potential.

Secretory granules in beta cell of the pancreas with Cavalier grid, magnification 18500x

Fig. 1

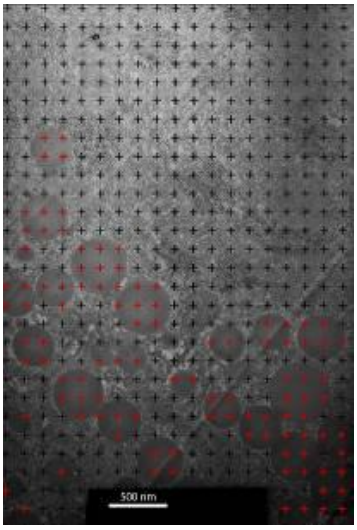

IM4.P022
Quantitative data through automated imaging and analysis with MiniTEM™ as decision support in the development of viral vector-based therapies

G. Kylberg[1], V. Carvalho[2], K. Lidayová[1], M. Pihlström[1], M. Ryner[1], I. M. Sintorn[1]

[1]Vironova AB, Research and Development, Stockholm, Sweden
[2]Vironova AB, Electron Microscopy Services, Stockholm, Sweden

Viral vector-based therapies are on the rise in the biopharma industry. These therapies include gene therapy, vaccines, and oncolytic virotherapy. During the development of these viral vectors, it is critical to have access to accurate analytical data. This holds for both early and late-stage process development. Reducing risk and having access to the right information allows quick decision making which directly translates into savings of time and money for the manufacturers of the viral vectors.

Two important aspects to consider at different process stages during the manufacturing process of viral vectors are the purity and integrity of the virus particles. Purity is important to keep track of since host cell debris and manufacturing impurities are linked to side effects when administered into the patient. Particle integrity is also an essential quality metric since a too high concentration of excess viral vectors with no therapeutic effect can push the patient immune system to produce anti-drug antibodies which will cause low efficacy.

Different purification steps can display varying success of removing impurities and can, at the same time, stress the primary particles to such an extent that their integrity deteriorate. Hence, measuring the integrity of the virus particles as well as the purity of the sample within the size range of these particles is of utmost importance to be able to understand the process. It can be very difficult or even impossible, to characterize the sample regarding these properties using other analytical techniques than TEM.

A few single TEM images of a sample from a process step in virus vector production can give an indication regarding purity and particle integrity but the data is far from enough to serve as a robust measurement of these properties. To be able to compare different samples in a quantitative manner enough images must be acquired of the TEM grid so that a representative dataset is obtained. The resulting images, that could be several hundred per grid, must be analyzed in a reproducible way to detect intact and non-intact primary particles to assess sample integrity as well as measuring the amount of debris for assessing sample purity.

The MiniTEM™ system offers automated imaging and the possibility to set up image analysis workflows that measure particle integrity and sample purity. The combination of reproducible imaging and image analysis makes MiniTEM™ able to provide quantitative analytical data that can be used for example to compare different purification strategies. In this way, the system can provide decision support in several steps of the development of viral vector-based therapies.

In addition to solving the analytical need in this application area, the MiniTEM™ system is an easy to use general purpose low voltage TEM operating at 25 keV. It is designed to be placed in an ordinary lab next to your workbench. The system does not impose any special requirements on the facilities since it runs without cooling water, is robust to vibrations, and takes its power from an ordinary wall outlet.

Fig. 1: Comparing sample purity between two samples with MiniTEM.

Fig. 2: The MiniTEM system in operation.

Fig. 1

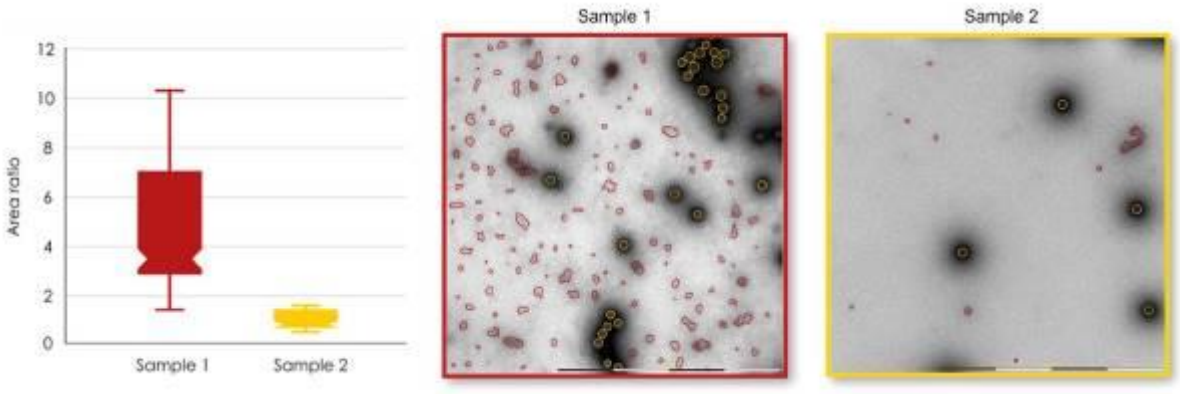

Fig. 2

IM4.P023
Using Molecular Dynamics for Frozen Phonon Multislice Simulations of Thermal Diffuse Scattering

F. F. Krause[1], D. Bredemeier[1], M. Schowalter[1], T. Mehrtens[1], T. Grieb[1], A. Rosenauer[1]

[1]Universität Bremen, Institut für Festkörperphysik, Bremen, Germany

For simulation of images and diffraction patterns in transmission electron microscopy, the accurate inclusion of thermal diffuse scattering by phonons, i.e. lattice vibration excitations, is important. In the frozen phonon multislice algorithm, this is possible, if thermal displacements according to the realistic, quantum mechanical distribution can be accurately generated. For pure crystals, quantum mechanical calculations based on DFT yield those displacements, but for alloys, one is usually restricted to the Einstein approximation, where correlations between atoms are neglected.

In this contribution, the use of molecular dynamics simulations as an alternative method for displacement calculation is demonstrated and investigated. Employing an empirical Stillinger-Weber type potential, classical motion is used as an approximation for the quantum mechanical dynamics: The simulated supercell is heated up to the desired temperature using a Nose-Hoover thermostat and after equilibrium is reached, snapshots of the atom positions are acquired. Thereby, correlations as well as possible static atomic displacements are inherently included.

An appropriate potential is devised for AlGaN by fitting to force constant matrices determined from DFT for the pure materials of AlN and GaN and to elastic constants. It becomes apparent that an inclusion of second-nearest neighbour terms is vital for this. Comparison shows that the constructed empiric potential is capable of reproducing phonon dispersions and displacement expectations from DFT references.

The validity for alloys is successfully demonstrated by comparison to DFT calculations in special quasi-random structures of AlGaN with various aluminum concentrations. These structures are periodic lattices with medium sized unit cells, for which neighbour composition correlations are minimized, thereby realising the best approximation to a random alloy that is possible for a given periodicity (hence quasi-random) while still allowing for DFT calculations exploiting the periodicity. In further studies, optimal parameters for the molecular dynamics simulation were found.

Subsequently, molecular dynamics with the optimised potential were used in multislice simulations of both conventional and scanning TEM images. For pure AlN and GaN, the resulting images are in very good agreement with DFT based calculations, while a slight yet significant error of the Einstein approximation results can be seen, which can be attributed to the neglect of correlations in the latter. For mixed crystals, where DFT is not possible, molecular dynamics constitutes a unique tool to avoid this inaccuracy. The presented Stillinger-Weber type potential hence proves to be a useful tool for accurate TEM simulations of AlGaN alloys. For other wurtzite materials, more sophisticated empirical potentials have to be used. Reasons and solutions for this are discussed for InGaN.

IM4.P024
Reference Based Atom Counting: Inclusion of Column Crosstalk in Precise Specimen Thickness Determination from Voronoi Averaged STEM Intensities

F. F. Krause[1], M. Schowalter[1], C. Mahr[1], T. Grieb[1], T. Mehrtens[1], A. Rosenauer[1]

[1]Universität Bremen, Institut für Festkörperphysik, Bremen, Germany

For the investigation and characterisation of nanoscopic structures, scanning transmission electron microscopy has proven to be a very important tool. With its capability of atomic resolution, it can give very precise and accurate projections of such structures. However, in many cases, the full geometry has to be determined. For this, it is of high value to know the height of each projected atomic column with the highest possible precision, ideally with single-atom precision. Methods, which have this capability, are referred to as "atom counting" and have been of high interest in the past years.

To this end, two types of methods have been developed: Statistical approaches and techniques that are based on the comparison of measured STEM images to simulations. Former can constitute a challenge in their computational demands due to a necessary model fit in a high-dimensional parameter space. However, these fits inherently include possible crosstalk between neighbouring atomic columns. Latter, on the other hand, are relatively simple to apply, because they only require a lookup in the simulation references. The crosstalk that can occur due to scattering or channelling effects of heavy columns is usually neglected.

This contribution will present a method to determine the crosstalk between columns from simulations and subsequently take this crosstalk into account in the evaluation of measured experimental images in an evaluation based on the average STEM intensity in each column"s Voronoi cell in the image. For this purpose, frozen phonon multislice simulations of supercells with roughened surface are created, which as a result consist of columns of different height. These simulated images are evaluated using Voronoi cells and, using the known column heights, the crosstalk between each two columns can be precisely quantified as a function of both their distance and height – later possibly also composition.

Using this quantification from simulation, the crosstalk can be taken into account in the evaluation of experimental images, thereby avoiding errors in the column height results. The improvement in accuracy will be investigated for both uncorrected and aberration corrected STEM of gold nanostructures for different acquisition parameters. Furthermore, a comparison to a statistics based atom counting evaluation will be shown.

IM4.P025
Challenges of HRTEM image contrast simulation of MoS_2/TaS_2 heterostructure

H. Kirmse[1], S. Sadofev[1], S. Blumstengel[1], C. T. Koch[1]

[1]Humboldt University of Berlin, Physik, Berlin, Germany

IntroductionThe 2H modification of MoS_2 performs as a semiconductor and belongs to the materials class of group VI transition metal dichalcogenides (TMDCs) which generate vivid interest of fundamental research. TMDCs exhibit a strong anisotropy of bonding forces. Van der Waals forces act in between covalently bonded atomic triple layers. The stacking sequence in particular of MoS_2 strongly influences the physical properties of the 2D material and is strikingly different from that of the bulk material (1).

Objectives In this work we focus on elucidating the structural perfection within the individual layers as well as on the understanding of the image contrast depending on the TMDC layer orientation.

Materials & methods Pulsed thermal deposition was utilized to grow on an amorphous SiO_2 substrate a heterostructure comprising a ca. 5 nm thick layer of metallic TaS_2 and a ca. 5 nm thick layer of semiconducting MoS_2 atop (2). Cross sectional TEM samples were obtained by conventional preparation comprising mechanical pre-thinning and final Ar^+ ion milling. The structure of the layer stack was investigated by high-resolution TEM (HRTEM) imaging performed using a TEM/STEM JEOL 2200FS operated at an accelerating voltage of 200 kV. Interpretation of HRTEM image contrast demands corresponding simulation due to unknown defocus, TEM specimen thickness, and in-plane orientation. Simulations were performed for a supercell containing a sharp TaS_2/MoS_2 interface utilizing the QSTEM software package (3).

Results HRTEM imaging reveals striking different contrast for the two layers MoS_2 and TaS_2 (see Fig. 1). Within the individual layer the contrast is constant over a lateral distance of more than ten nanometers hinting to single crystalline grains of at least this lateral size. Moreover, a perfect vertical stacking is seen for the MoS_2 layer. The crystal orientation of MoS_2 is identified as $(1\underline{2}10)$ whereas the orientation of TaS_2 cannot be specified since just the (0001) lattice planes are seen edge on. The experimental defocus is uniquely identified to be df = -60 nm from thickness/defocus maps. Against that, a thickness step from 7.5 nm for TaS_2 to 5 nm for MoS_2 has to be introduced to approach the very details of the image contrast. Moreover, the best agreement between experiment and simulation is found only after considering an unintended tilt of the impinging electron beam by about 1.4° (24 mrad) with respect to the $(1\underline{2}10)$ zone axis of MoS_2.

Conclusion The HRTEM image contrast of stacked TMDCs is reproduced. In comparison to single crystalline materials additional parameters like thickness fluctuation, misorientation and unintended beam tilt have to be considered. This makes the setup of a proper supercell and the adaption of suitable simulation parameters a challenge.

References:

(1) Q.H: Wang et al., Nat. Nanotechnol. 7 (2012) 699

(2) N. Mutz et al., arXiv:1811.07663 [cond-mat.mtrl-sci]

(3) C.T. Koch, QSTEM software package, http://qstem.org

This work was funded by the German Research Foundation (DFG) within the collaborative research center 951 HIOS (Projektnummer 182087777).

Fig. 1: HRTEM image of the MoS_2/TaS_2 stack deposited on SiO_2. Inset is taken from Fig. 2.

Fig. 2: Simulations of the HRTEM image contrast for a defocus of df = -60 nm. The TaS_2 layer was rotated off axis by 20. The framed image was found to best match the HRTEM image given in Fig. 1.

Fig. 1

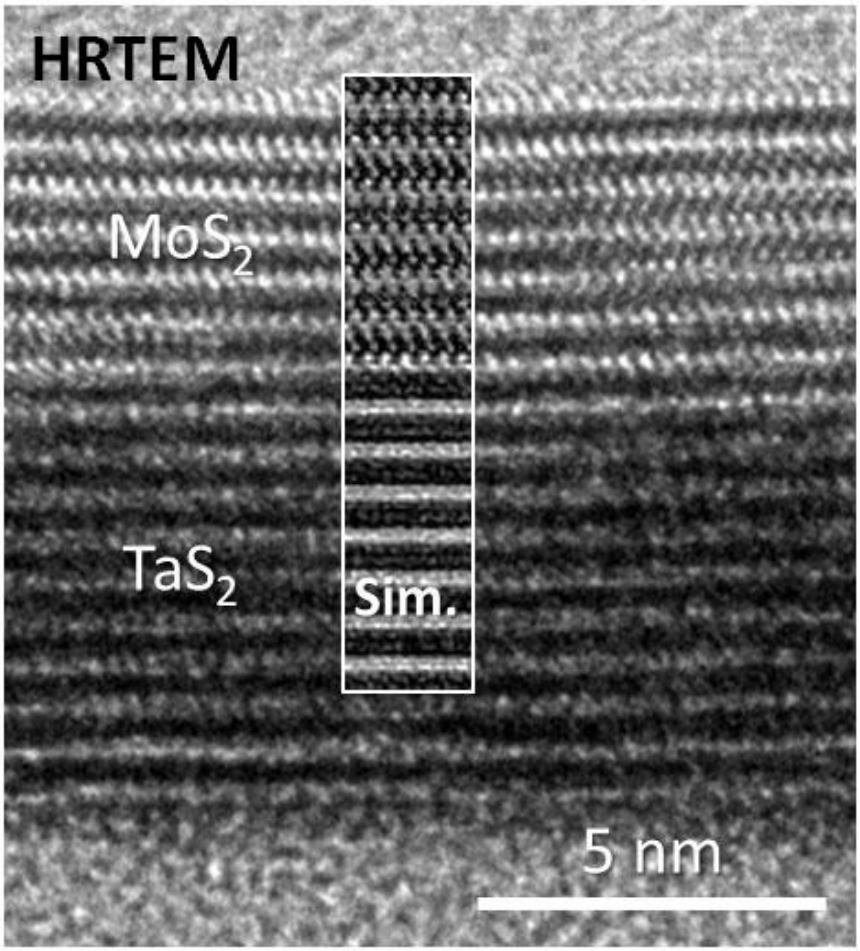
HRTEM
MoS2
TaS2
Sim.
5 nm

Fig. 2

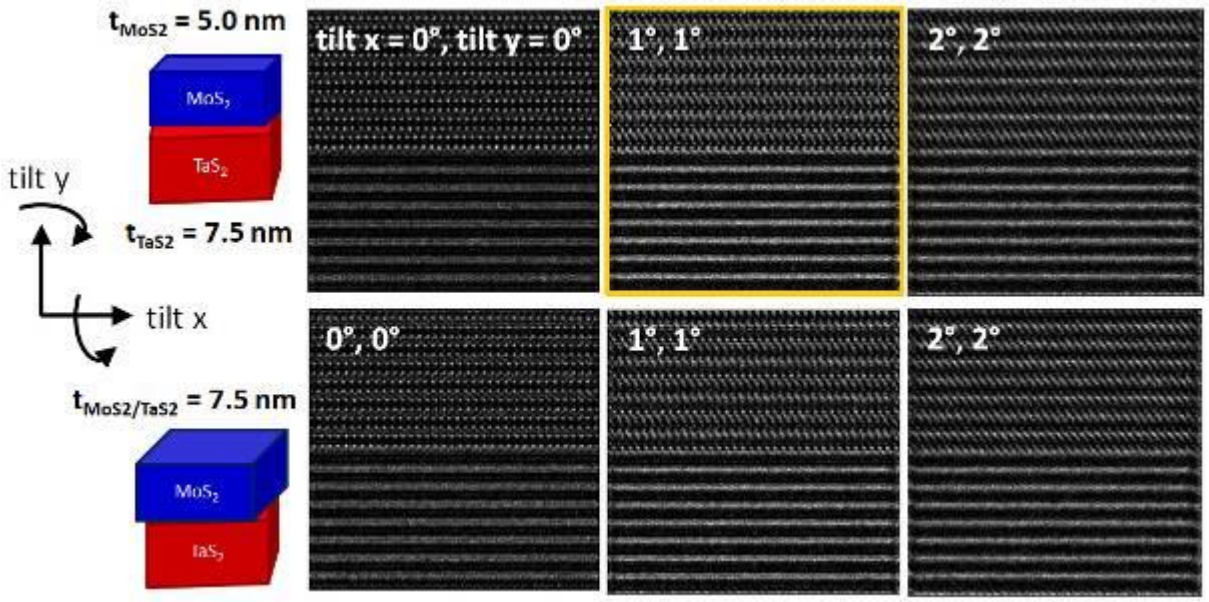
tMoS2 = 5.0 nm
MoS2
TaS2
tTaS2 = 7.5 nm
tilt y
tilt x
tMoS2/TaS2 = 7.5 nm
MoS2
TaS2
tilt x = 0°, tilt y = 0°
1°, 1°
2°, 2°
0°, 0°
1°, 1°
2°, 2°

IM4.P026
Crystallography in the Scanning Electron Microscope

S. Fairman[1], J. Müller[1], C. T. Koch[1]

[1]Humboldt-Universität zu Berlin, Physik, Berlin, Germany

In recent years electron crystallography has been shown as a viable tool for structure determination. Precession electron diffraction and rotation electron diffraction allow experimental diffraction data to be treated as kinematic scattering and advances in computing power in the last few decades have allowed accurate interpretation of dynamical scattering intensities (1). In comparison to X-Ray methods where scattering intensities are much more kinematic, electron diffraction overcomes the need for large single crystals due to the greater interaction strength of electrons (10^5 times more than X-Rays) (2). It also overcomes overlapping reflections problem and provides more reflections due to the curvature of the Ewald sphere. Large angle rocking beam diffraction (LARBED) (3,4) allows the same information available from convergent beam electron diffraction (CBED) over a much larger angular range. It works with dynamical diffraction and works in the case of large unit cell materials. With this method the structure factors are fitted directly to the experimental intensities.

The scanning electron microscope (SEM) provides cost effective, low voltage transmission diffraction for beam sensitive samples such as metal organic frameworks (MOFs) and 2D materials. Importantly, there are no post specimen lenses, giving an undistorted diffraction plane. The large chamber in the SEM allows space for additional hardware to be installed. These advantages along with its ubiquity and ease of use make the development of crystallographic methods in the SEM an important step in electron crystallography.

In this work, a standard Zeiss Gemini SEM 500 equipped with a tilting stage and camera for recording diffraction patterns was used to record tilt series of thin samples at low voltages. With the view toward structure determination, 3D diffraction experiments will be shown on a range of materials.

Shown in Fig.1 (A) is a diffraction pattern of a metal organic framework and Fig.1 (B) is of a less beam sensitive large unit cell material, barium ferrite. Fig.2 (A) shows a diffraction pattern of tungsten disulfide and its 3D reciprocal space reconstruction obtained from a tilt series of many such patterns.

References:

(1) J. M. Zuo, M. Kim, M. O'Keeffe & J. C. H. Spence, Nature 401 (1999) 49

(2) R. Henderson, Q Rev. Biophys. 28, 2 (1995), pp. 171-193

(3) C. T. Koch, Ultramicroscopy 111, 828 (2011).

(4) F. Wang, R.S. Pennington, and C:T. Koch, Phys. Rev. Lett. 117 (2016) 015501

We acknowledge financial support from the German Fesearch Foundation (DFG) (grant numbers KO 2911/12-1(BerlinEM) & Projectnummer 182087777 - SFB951[HIOS])

Fig. 1

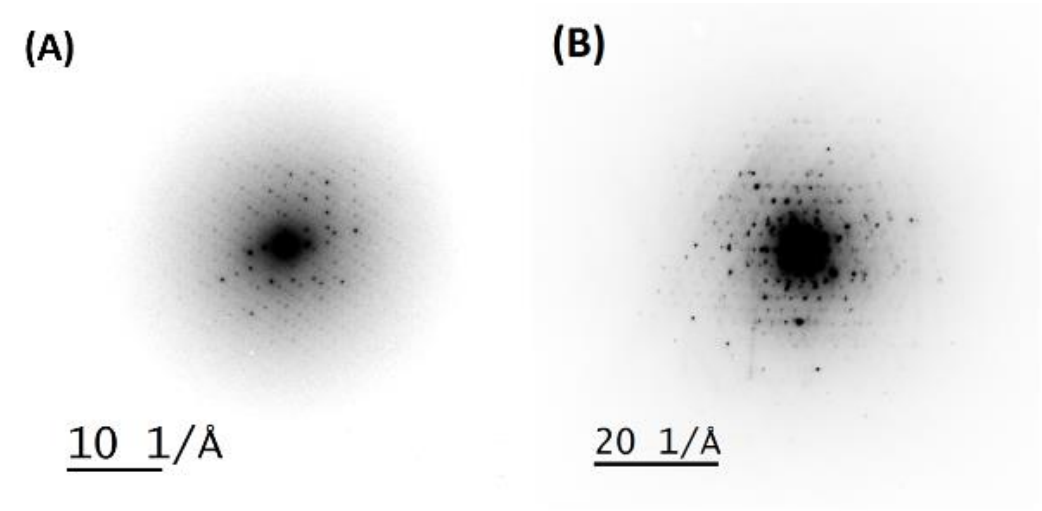

Fig.1: **(A)** Diffraction patterns of a MOF structure and **(B)** a large unit cell material BaFe at 30kV.

Fig. 2

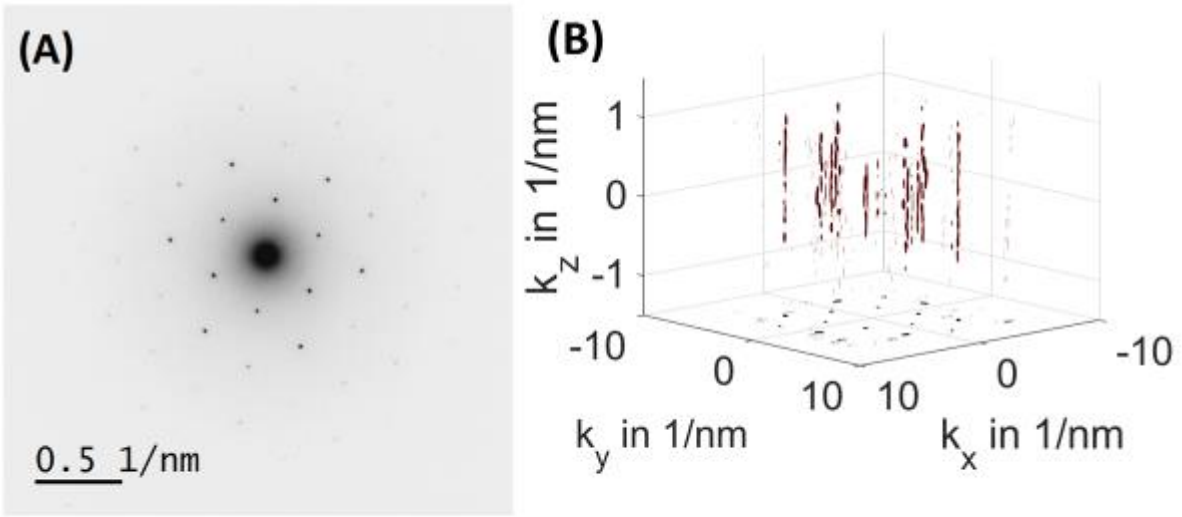

Fig.2: (A) A diffraction pattern of tungsten disulfide (WS2) at 15kV. (B) 3D reconstruction of a tilt series of WS2 showing the extending relrods in the k_z direction.

IM4.P027
Analytical description of diffraction contrast in the two-beam case by modified Bloch waves

W. Mader[1]

[1]University of Bonn, Chemistry, Bonn, Germany

The two-beam intensities of distorted crystals were derived from *modified* Bloch waves (mBW), introduced by Penning & Polder and Kato and applied by Wilkens[1] for the diffraction contrast. In the mBW concept, the excitation error $s(\boldsymbol{r}) = s_0 + u_z(\boldsymbol{r})$ depends on the local orientation of the lattice where $u_z(\boldsymbol{r}) = \mathrm{d}\left(\boldsymbol{g}\cdot\boldsymbol{R}(\boldsymbol{r})\right)/\mathrm{d}_z$ with diffraction vector $\boldsymbol{g}$ and displacement field vector $\boldsymbol{R}(\boldsymbol{r})$. Hence, the excitation amplitudes of the two mBWs 1 and 2 and the eigenvectors vary with $\boldsymbol{r}$. In the differential equations of mBWs the change in the excitation is proportional to the *second* derivative u_{zz} of the displacement field and, hence, is proportional to the *curvature* of the lattice, while in the Bloch-wave formulation scattering is proportional to the lattice tilt u_z.

From the non-specific bright and dark field amplitudes given by Wilkens (1), the intensities for a defect situated at depth z_0 in a foil with thickness $z = t$ are derived to

$$|\psi_n(t)|^2 = \frac{e^{-2\pi\chi t}}{\sqrt{(1+w_0^2)(1+w_t^2)}}\left\{I_n^b + I_{n,0} + I_{n,1} + I_{n,2}\right\} \text{ with}$$

$$I_n^b = \tfrac{1}{2}\{\pm\cos 2\pi P_r + \cosh 2\pi[P_i + (t_{w0} \pm t_{wt})\tau]\},$$

$$I_{n,0} = \pm\tfrac{1}{2}\left\{\cos\left(2\pi P_r(t) + 2\alpha_p\right) - \cos\left(2\pi P_r(t)\right)\right\},$$

$$I_{n,1} = q\sqrt{1-q^2}\left\{-\sinh 2\pi(P_i - P_i(z_0) \pm t_{wt}\tau)\cdot\cos\left(2\pi P_r(z_0) + \alpha_p + \alpha_q\right)\right.$$
$$\left.\pm\sinh 2\pi(P_i(z_0) + t_{w0}\tau)\cdot\cos\left(2\pi(P_r - P_r(z_0)) + \alpha_p - \alpha_q\right)\right\},$$

$$I_{n,2} = q^2\{-\sinh 2\pi(P_i - P_i(z_0) \pm t_{wt}\tau)\cdot\sinh(2\pi P_i(z_0) + t_{w0}\tau)$$
$$\mp\tfrac{1}{2}\cos(2\pi\left(P_r + 2\alpha_p\right)\cdot\mp\tfrac{1}{2}\cos\left(2\pi(P_r - 2P_r(z_0)) - 2\alpha_q\right)\},$$

where the upper signs refer to bright field and the lower to dark field, respectively. The parameters are $P_r \equiv \int_0^t p_r\,\mathrm{d}z$, $P_i \equiv \int_0^t p_i\,\mathrm{d}z$, with $p_r \cong \sigma_r\sqrt{1+w^2}$, $p_i \cong \sigma_i/\sqrt{1+w^2}$, $w \equiv s/\sigma_r$. Here $\sigma \equiv \sigma_r + i\sigma_i$ where $\sigma_r = 1/\xi$ is the excitation number with effective extinction length ξ, $\sigma_i = 1/\xi'$ denotes the effective absorption number. The parameters q, α_p and α_q result from scattering at the lattice defect and are zero for only intraband scattering. Quantities $w_o = w(0)$, $w_t = w(t)$ are normalized excitation errors at the foil surfaces, and a characteristic thickness t_w is given by $w_{0,t}$=$\sinh 2\pi\tau t_{w0,t}$ as function of the excitation errors at the foil surfaces. The coefficient τ of anomalous absorption is defined by $\tau = \sigma_{i,g}/\sqrt{1+w^2}$ with absorption length σ'_g.

The derived mBW intensities reduce to the expressions for the (Bloch-wave-derived) intensities by Katerbau (2) if the local excitation errors w_o and w_t are replaced by w of the perfect crystal and by replacing $P_r \rightarrow \sigma t$; $P_r(z_0) \rightarrow \sigma z_0$, $P_i \rightarrow \tau t$, $P_i(z_0) \rightarrow \tau z_0$, t_{w0} and t_{wt} by t_w. In particular, the background intensity I_n^b on bright field (n = 0) and on dark field (n = 1) images can be used to interpret contrast phenomena according to their physical origin. The contrast fringes round a large misfitting inclusion originate from the cosine term of I_n^b. From perfect crystal regions towards the inclusion the phase factor P_r strongly increases and the cosine term oscillates (Fig. 1). The so-called Ashby-Brown contrast shows an asymmetrical black-white contrast at inclusions. The reason for this contrast are due to boundary conditions for the electron waves at the foil surfaces where the different arguments of the cosh term for t_{w0} and t_{wt} on both sides of the inclusion cause the asymmetry. These contrast phenomena can be simulated using numerical computations, however, without understanding the physical origin behind.

References:

(1) M. Wilkens, phys. stat. sol. 13 (1966) 529

(2) K.-H. Katerbau, Phil. Mag A 43 (1981) 409

Fig. 1: Periodic contrast variations round inclusion, $s_0 = 0$.

Fig. 2: Calculated bright field (lines) and dark field (dotted) contrast across inclusion.

Fig. 1

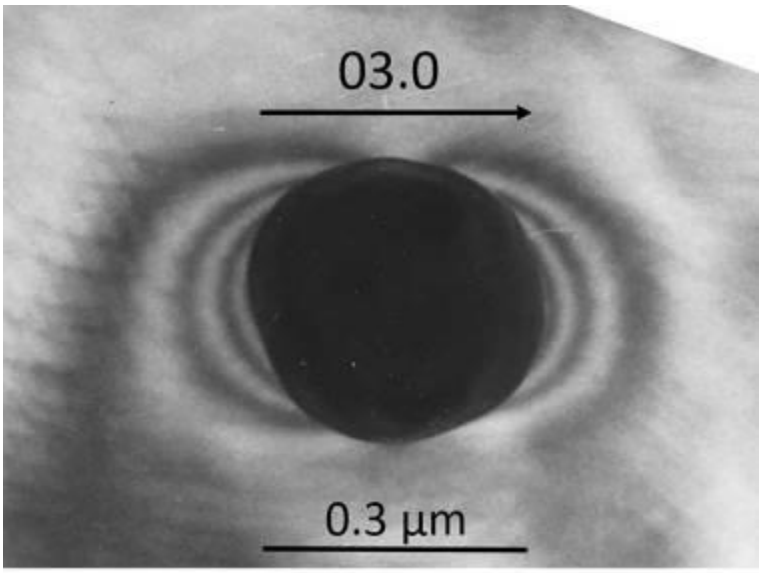
03.0
0.3 µm

Fig. 2

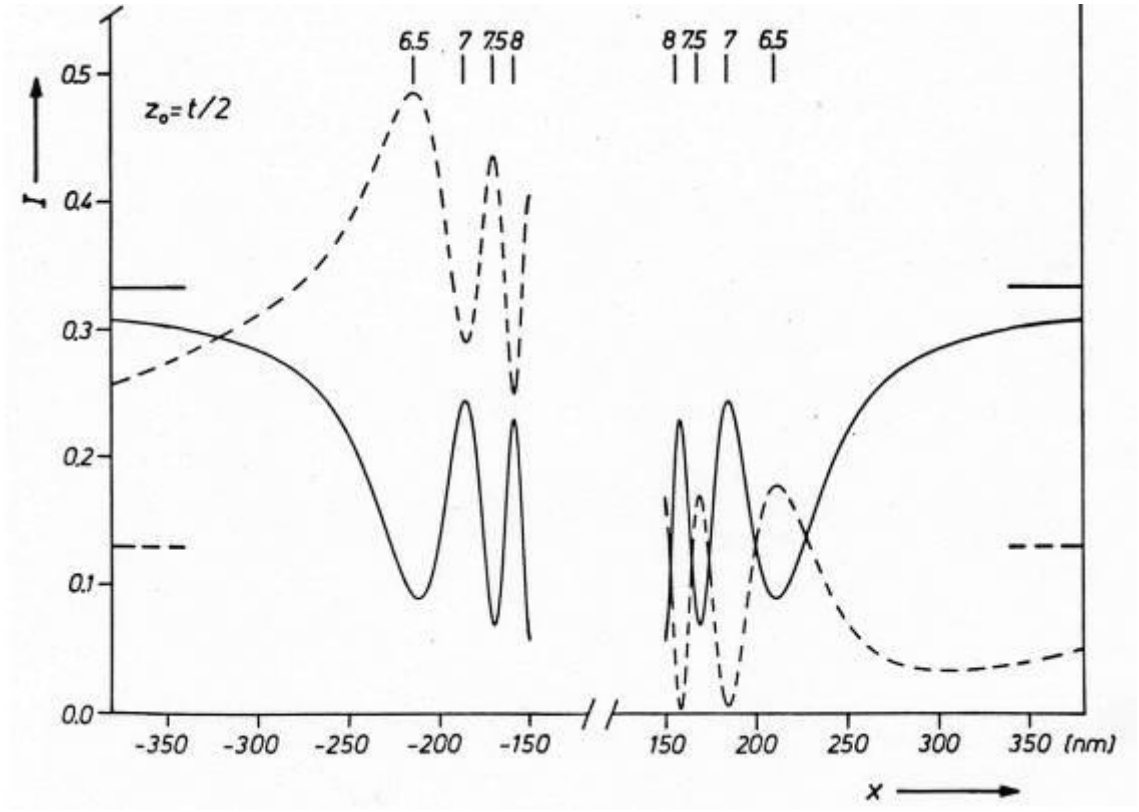
6.5
7
7.5
8
8
7.5
7
6.5
0.5
0.4
0.3
0.2
0.1
0.0
I
$z_o = t/2$
-350
-300
-250
-200
-150
150
200
250
300
350 (nm)
x

IM4.P028
2D materials signature in 3D reciprocal space

T. Gorelik[1], B. Nergis[1], T. Lehnert[1], J. Köster[1], U. Kaiser[1]

[1]University of Ulm, EMMS, Ulm, Germany

2D materials represent an actively developing branch in science, triggered by their exceptional physical properties (1,2). In particular graphene, boron nitride, 2D-TMDs and their few-layer heterostructures are intensively studied by many different imaging and spectroscopic techniques. The in-plane atomic structure of these materials can be imaged at atomic resolution using low-voltage aberration-corrected TEM/STEM (3,4).

Recently, it was reported that 2D materials demonstrate a particular type of 3D structure – out-of-plane corrugation (5). The out-of-plane structural features can hardly be detected in HR-TEM images, being a 2D projection of the tree-dimensional structure. In this respect, 3D electron diffraction (ED) is a powerful tool to gain information on the 3D structural features. Another advantage of ED is that is requires a much less electron dose on the sample, which makes it a promising approach to study the corrugation effects.

For 2D materials, the reciprocal space consists of relrods – lines with continuous intensity distribution oriented orthogonal to the sample plane. The existence of the corrugation in the materials affects the intensity of the relrods as well as their shape.

3D ED data sets are collected in a TITAN-TEM through a sequential stage tilt. In this way, a quasi-continuous sampling of the reciprocal space is achieved. A finer sampling is obtained by employing a combined stage-tilt / beam-tilt approach (6). Different sampling approaches will be compared.

Theoretically, the intensity distribution along the relrods is given by the effective atomic scattering factor of the layer orthogonal to the layer surface. For the case of graphene, the intensity distribution should correspond to the atomic scattering power of carbon. Yet, the experimentally measured profiles show much faster decaying profiles, which we address to the out-of-plane corrugation, in other words - crystallographic mosaicity of the 2D materials. The same reason serves for the effective broadening of the reflections at high stage tilt angles.

Here, the geometry modifications of the relrods caused by the layer corrugation are explained, as well as the methodology of 3D ED data processing is presented, supported by the results obtained for a series of 2D and few-layer materials.

References:

(1) Ferrari, A. C., et al. (2015). Nanoscale, 7, 4598-4810.

(2) A. Dankert, S. Dash, (2017). Nat. Commun. 8, 16098.

(3) M. Linck et al. (2016). Phys. Rev. Lett. 117, 076101.

(4) Sasaki, T., et al. (2014). Ultramicroscopy, 145, 50.

(5) J.C. Meyer et al. (2007). Solid State Communications 143, 101.

(6) Zhang, D. et al. (2010). Z. Kristallogr. 225, 94.

IM5.001 invited
Reversible lithium loading of bilayer graphene studied at atomic resolution

F. Börrnert[1], F. Börrnert[1], M. Kühne[2], S. Fecher[2], M. Ghorbani-Asl[3], J. Biskupek[4], D. Samuelis[2], A. V. Krasheninnikov[3], J. H. Smet[2], U. Kaiser[4]

[1]Max-Planck-Institut für Mikrostrukturphysik, Halle, Germany
[2]Max-Planck-Institut für Festkörperforschung, Stuttgart, Germany
[3]Helmholtz-Zentrum Dresden-Rossendorf, Dresden, Germany
[4]Universität Ulm, Ulm, Germany

In-situ transmission electron microscopy (TEM) is one of the most emblematic characterization techniques today. Not only does it offer the prospect of imaging structural and morphological changes in materials down to the atomic level in real time, but it also allows for chemical analysis at these scales. As such it grants decisive insights into processes occurring in battery materials, the understanding and control of which remains at present a great challenge. Besides guiding the quest for better mass and energy storages, in-situ TEM can be a method of choice to study electrochemically driven phenomena in quasi one-dimensional or two-dimensional (2D) materials at a microscopic level. However, imaging light elements such as Li or C, is severely hampered by their low scattering cross section for impinging electrons and their susceptibility to knock-on damage. Thanks to spherical aberration correction, atomic resolution of carbon nanostructures has nonetheless become customary even at low acceleration voltages. In the case of Li, a similar resolution has so far only been conceivable for atomic columns of a few nm in length corresponding to a few tens of atoms. The additional implementation of chromatic aberration correction now unlocks unprecedented resolving power (1), bound to enhance in situ TEM studies on light atomic nanomaterials.

Graphene is a prime example of such a material, with potential for energy storage applications. Its bulk parent compound – graphite – already finds widespread use as active electrode material in today"s Li-ion technology.

This is because graphite can accommodate up to one Li atom per six C atoms

(LiC6) in the galleries between its constituting graphene sheets, yielding a maximum Li storage capacity of 372 mAh/g. While an intrinsically higher value has been proposed for graphene, today it is mostly its electronic conductivity and its chemical stability that render it useful for Li-ion batteries in the role of a current collecting electrode admixture.

Together with its impermeability, it also qualifies as protective encapsulation for conversion alloying anode materials. Increasing in situ TEM efforts have been devoted towards imaging the lithiation of these, with only a few studies on the graphene sheets themselves.

Here, we investigate the lithiation of single-crystalline bilayer graphene by in-situ spherical and chromatic aberration-corrected low-voltage TEM at true atomic resolution. In contrast to the established phenomenology to be expected for Li-intercalation in this fundamental unit of a graphite intercalation compound (up to C6LiC6), we observe the formation of a high-density crystalline Li phase between the two graphene planes. We support these assertions not only by TEM imaging but also by electron energy loss spectroscopy, as well as by extensive density functional theory calculations (3).

References:

(1) M. Linck et al., Phys. Rev. Lett. 117, 076101 (2016).

(2) M. Kühne et al., Nat. Nanotech. 12, 895 (2017).

(3) M. Kühne et al., Nature 564, 234 (2018).

We acknowledge financial support from the Baden-Württemberg Stiftung gGmbH (project CT 5).

IM5.002
Sub 50 keV helium ions as an imaging probe in transmission microscopy and secondary ion mass spectrometry

M. Mousley[1], S. Eswara[1], J. N. Audinot[1], O. Bouton [1], O. De Castro [1], N. Klingner[2], C. T. Koch[3], G. Hlawacek[2], T. Wirtz[1]

[1]Luxembourg Institute of Science and Technology , Materials Research and Technology , Belvaux, Luxembourg
[2]Helmholtz-Zentrum Dresden-Rossendorf, Institute for Ion Beam Physics and Materials Research, Dresden, Germany
[3]Humboldt-Universität zu Berlin, Structure Research and Electron Microscopy, Berlin, Germany

Transmission imaging with helium ions is expected to offer contrast not possible with electron beams. Whilst MeV helium ion transmission imaging has already been demonstrated1, sub- 50 keV helium ions are more widely available, for example, in helium ion microscope (HIM) machines. These HIM systems can perform high-resolution secondary electron imaging as well as elemental analysis by secondary ion mass spectrometry (SIMS) 2. Despite recent interest in the transmission imaging capabilities of low energy helium3, this method still requires detailed evaluation. Time of flight (TOF) spectroscopy for backscattered helium in a HIM has also been reported4 but transmission TOF energy spectroscopy with sub 50 keV energy helium remains unexplored. This technique should provide information not accessible using solely transmission images.

This work focuses on the contrasts available using sub-50 keV He+ in a transmission-HIM (THIM). Our experiments used an in-house developed THIM utilising a duoplasmatron ion source operated below 50 kV. Powdered crystals of BN, NaCl and MgO were investigated in the THIM, using 10 keV He+ stationary beam illumination. A strong scattering effect has been observed (fig.1B) and may be explained by sample charging, which will require consideration in all future THIM imaging experiments. Scanning THIM (STHIM) results will also be discussed, SE and STHIM images were recorded in parallel for a Cu mesh (fig.1C). As an additional mode, deflector plates can pulse the primary beam, allowing our THIM to record STHIM-TOF spectra (see fig.1D).We will also present selected recent results obtained using our in-house developed SIMS system, attached to a Zeiss Nanofab HIM2. Fig. 2 shows images from a CIGS photovoltaic solar cell active layer, containing Na, In and Cu. HIM-SIMS can efficiently analyse the nanometre scale distribution of Na, the presence of which can reduce the efficiency of the solar cell.

References:

(1) Watt, F. *et al.* Whole cell structural imaging at 20 nanometre resolutions using MeV ions. *Nucl. Instruments Methods Phys. Res. Sect. B Beam Interact. with Mater. Atoms* 306**,** 6–11 (2013).

(2) Dowsett, D. & Wirtz, T. Co-Registered In Situ Secondary Electron and Mass Spectral Imaging on the Helium Ion Microscope Demonstrated Using Lithium Titanate and Magnesium Oxide Nanoparticles. *Anal. Chem.* 89**,** 8957–8965 (2017).

(3) Wang, J. *et al.* Focussed helium ion channeling through Si nanomembranes. *J. Vac. Sci. Technol. B, Nanotechnol. Microelectron. Mater. Process. Meas. Phenom.* 36**,** 021203 (2018).

(4) Klingner, N. *et al.* Nanometer scale elemental analysis in the helium ion microscope using time of flight spectrometry. *Ultramicroscopy* 162**,** 91–97 (2016).

Funding from Luxembourg National Research Fund (FNR) project STHIM (C16/MS/11354626) and EU Horizon 2020 Grant No. 720964.

Fig. 1: A) THIM image of MgO sample on Cu grid, hole width 108 µm bar width 19 µm (scale bar approx. 2.5 mrad), B) a spot pattern from MgO. C) SE and STHIM images of a Cu grid recorded in parallel, hole width approx. 90 µm. D) TOF spectrum of source emission for 10 keV He+.

Fig. 2: HIM-SE image and HIM-SIMS images showing the distributions of Na, In and Cu for an active layer of a CIGS solar cell. SE image recorded using 20keV He+, SIMS images recorded, using 20 keV Ne+ ions, in a Zeiss Nanofab equipped with an in-house developed SIMS system. Field of view is 10 µm.

Fig. 1

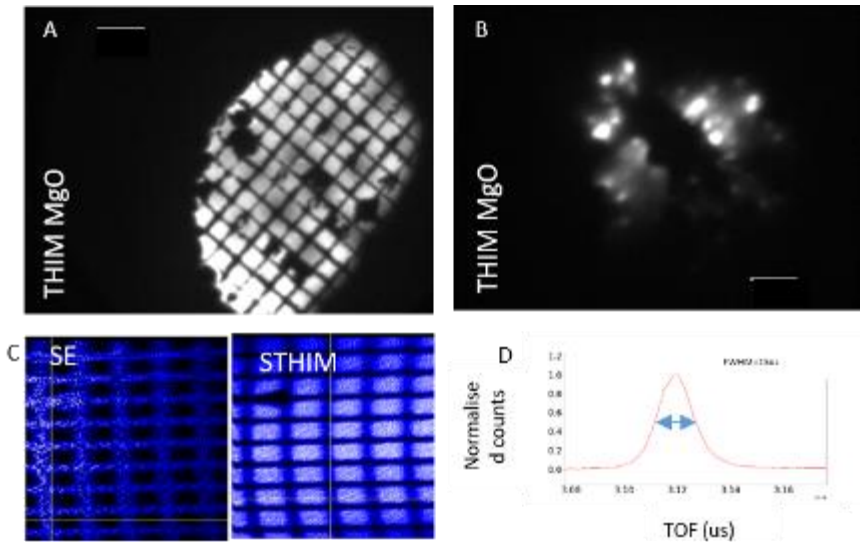
A
THIM MgO
B
THIM MgO
C
SE
STHIM
D
Normalised counts
TOF (us)

Fig. 2

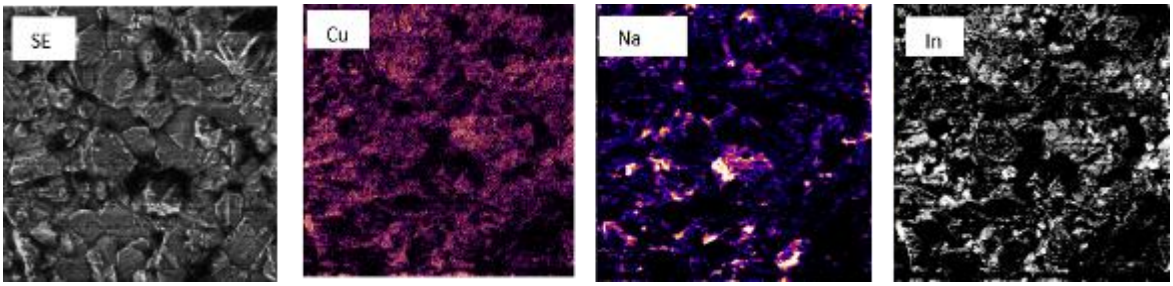
SE
Cu
Na
In

IM5.003
The DELTA – a prototype for Ultra-Low Voltage high resolution SEM and Electron Spectroscopic Imaging

R. R. Schröder[1,2], B. Schindler[3], M. Schnell[3], D. Fischer[4], D. Preikszas[3], I. Wacker[2]

[1]Universitätsklinikum Heidelberg, Cryo Electron Microscopy, Heidelberg, Germany
[2]Universität Heidelberg, Centre for Advanced Materials , Heidelberg, Germany
[3]Carl Zeiss Microscopy GmBH, Oberkochen, Germany
[4]Carl Zeiss SMT GmbH, Oberkochen, Germany

Although low-voltage TEM changed imaging paradigms for very thin and highly conductive samples, increasing ionization and thus increased beam damage create problems for less conductive samples (1).

This may be overcome by reducing electron energy even further and using SEM detection mechanisms instead of TEM or STEM. We explore the possibilities of the DELTA-technology (2) for I. SE and BSE imaging at electron landing energies below 50 eV, well below typical beam damaging energies and II. for electron spectroscopic imaging (SEM-ESI).

To achieve high resolution low energy SEM-ESI, new aberration correction, spectroscopy and detector technologies are needed. In the framework of our DELTA-project a novel SEM prototype combining all this has been developed. Even for electrons at ultra-low energies high resolution imaging (better than 1nm at 50 eV) is possible. As less beam damage is observed at such low electron energies, we utilize increased applicable electron dose for electron spectroscopy. Both, spectra of SE ("work function / electron affinity contrast" (3)) and spectra of BSE can be recorded in a way similar to energy loss imaging and spectroscopy in TEM.

Fig. 1 shows the current DELTA-SEM prototype (a), the main features of its novel electron optical design being the Delta-shaped beam splitter and the electrostatic electron mirror (b). Using an electrostatic energy filter combined with a scintillator electron detector (DELTA-Detector®design) energy-filtered imaging is possible (Fig. 2). Examples of the Delta"s capabilities such as BSE spectral imaging of organic dyes (Ryklin), connectivity of semiconductor material film in OFETS (Zhang), the domain structure of bulk heterojunctions in organic solar cells (Kammerer), and the deduction of workfunction and electron affinity from spectra by Bayesian inference (Eisele) will be explained in more detail in separate contributions (4).

The DELTA prototype offers unique ultra-low electron energies for imaging and electron spectroscopy. With landing energies as low as a few tens of eV it provides unsurpassed surface sensitivity. As shown in Fig. 2, DNA origamis on silicon gain very high contrast, obtained from about 45 carbon atoms in one pixel. Similar sensitivity has been achieved for other light atoms, e.g. when imaging Li-batteries (5). At present we test new detector technologies to further improve SNR at very low electron dose to be equally sensitive for accumulated spectroscopic imaging.

References:

(1) E Majorovits et al, Biophysical J 110 (2016) p776

(2) M Steigerwald et al, Frontiers of Characterization and Metrology for Nanoelectronics (2013)

(3) J Cazaux, Ultramicroscopy 110 (2011) p242

(4) cf. Ryklin et al, W Zhang et al, J Eisele et al, J Kammerer et al, (2019), Proceedings this conference

(5) cf. U Golla et al, Proceedings of M&M 2019

(6) RRS thanks the BMBF for funding the DELTA project (MorphiQuant 3D, FKZ:13GW0044)

Fig. 1: DELTA-SEM. (a) Visible are the electron gun (back), the aberration corrector (front) and the delta-shaped beam splitter (centre, above the sample chamber), cf (b) for schematic representation.

Fig. 2: Energy-filtered secondary electron (SE) (a) and backscattered electron (BSE) (b,c) images of uncoated polymer fibers (about 10 nm in diameter) at 500 eV landing energy (a,b) and DNA origami (12 single DNA-helices, 60 x 90 nm) at 100 eV landing energy (c), both materials on silicon wafer.

Fig. 1

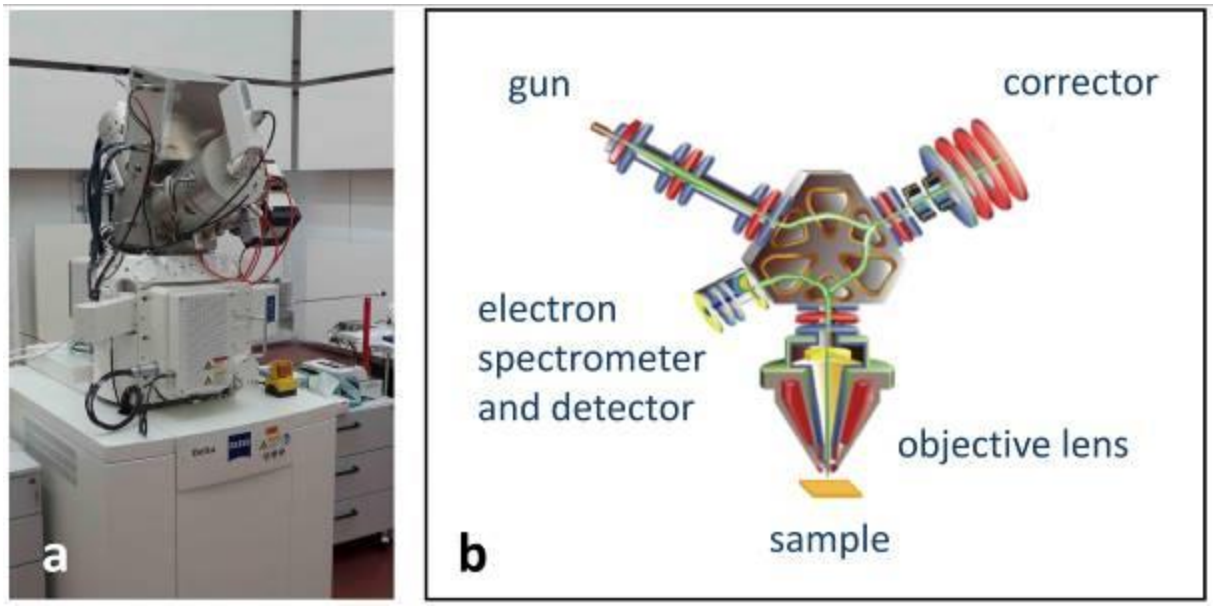
a
gun
corrector
electron
spectrometer
and detector
objective lens
sample
b

Fig. 2

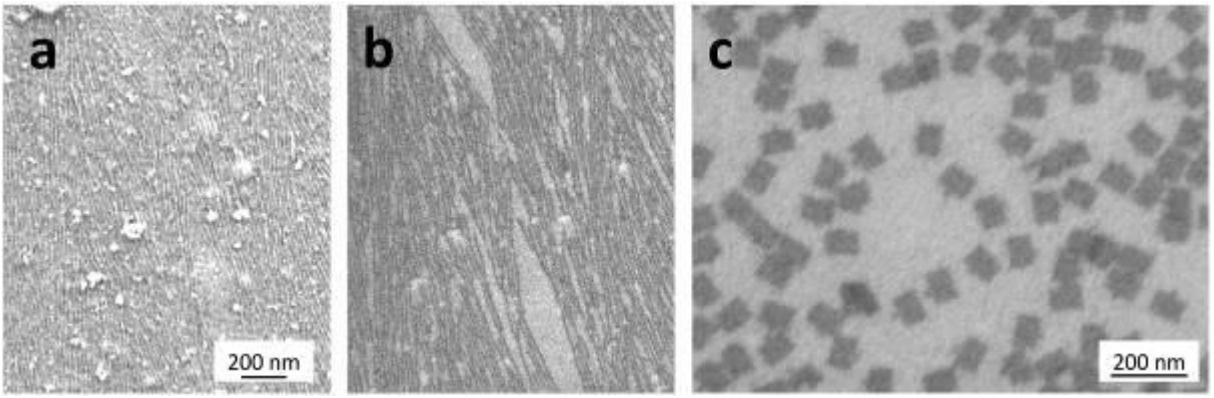
a
200 nm
b
c
200 nm

IM5.004
Features of our newly developed SEM Diffraction Stage with 6-axis sample control and a camera with variable camera length

J. Müller[1], B. Haas[1], S. Shabih[1], C. T. Koch[1]

[1]Humboldt-Universität zu Berlin, Department of Physics, Berlin, Germany

With the availability of fast cameras for electron diffraction, a wide range of diffraction-based techniques has recently been developed for STEM, many of which can be realized also in conventional SEMs or combined FIB/SEM instruments. Due to the low acceleration voltages (0.5kV to 30kV) and their good optics, SEMs are an excellent platform for investigating beam sensitive materials like hybrid inorganic/organic systems. Our diffraction stage can tilt and shift the sample combined with a fast synchronized camera to apply different STEM based methods with SEMs. The system is simpler and more flexible compared to dedicated transmission microscopes, has a larger sample chamber, less operating costs and access to low beam energies reducing knock-on damage. We present our plug and play diffraction sub-stage that can easily be transferred between SEMs in more detail and show a summary of our results.

Our goal is to have a simple system for developing dose-efficient low voltage electron diffractions techniques, such as advanced variants of 4D-STEM to answer questions related to thin bulk and low dimensional samples. With the existing detectors like EDX, the addition of fast electron diffraction and the 6-axis sample control, we have several tools at our hand to map material parameters from nm to cm scale.

Our custom setup consists of a Zeiss GeminiSEM 500 with a hexapod sub-stage, sample holders, a tiny 2.5x2.5x1.1cm³ camera, a linear positioner to move the camera, a cooling unit, a scan generator plus a measurement PC. The hexapod shift ranges (x,y,z) are up to 1.6cm covering an area of 1.6x1.6cm², and the tilt ranges (a,b) are up to 24°. The standard sample holder can fit TEM grids and is mounted to the movable platform of the hexapod. The camera is fiber-coupled and the camera length ranges from 5 to 40mm by moving the camera via software, there are no post-specimen lenses. Our stage has no influence on the chamber vacuum due to the used low outgassing materials. We have full scripting access to our hardware via C++/C# DLLs and developed a scan generator to synchronize the beam position, the camera exposure and the fast beam blanker to get 180fps at 1200x1200 pixels and up to 2000fps at 64x64 pixels. The SEM allows to control the convergence angle and the current up to 20nA allowing for the acquisition of spot patterns, CBED patterns, Ronchigrams and shadow images. We use the open-source Python-based platform Nion Swift as GUI.

We applied our diffraction setup to map layer thickness, orientation, defects, strain, electric fields, unit cell parameters, crystallinity, material composition and other crystallographic information. B.H. presents more results in the material session of this meeting.

With the addition of fast transmission electron diffraction and 6-axis sample control to our SEM, we have a low cost and simply working tool at our hand for investigating thin bulk and low dimensional materials with many exciting diffraction based methods.

We acknowledge financial support by the German Research Foundation (DFG grant nrs. KO 2911/12-1 & KO 2911/13-1, as well as Projektnummer 182087777 - SFB951).

We thank Harald Niebel, Björn Gamm, Markus Boese from Carl Zeiss Microscopy GmbH for help with controlling the SEM and Fardin Gholami, Max Heyl, Katherine Herman from Humboldt-Universität zu Berlin, Abbas Faghani from Free University Berlin for their samples.

Fig. 1

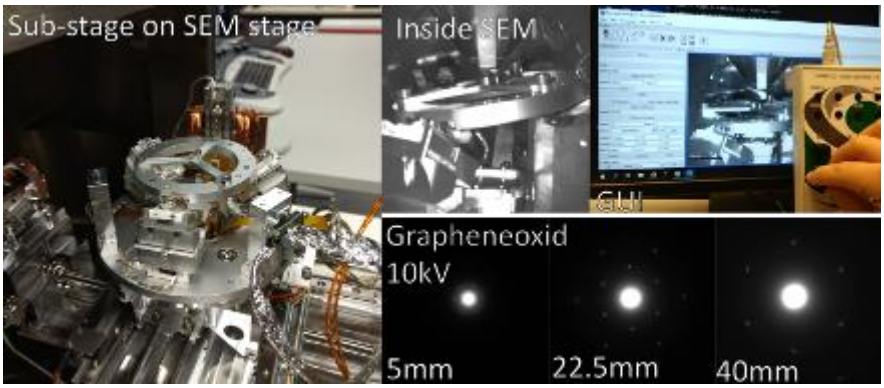
Sub-stage on SEM stage
Inside SEM
GUI
Grapheneoxid
10kV
5mm
22.5mm
40mm

Fig. 2

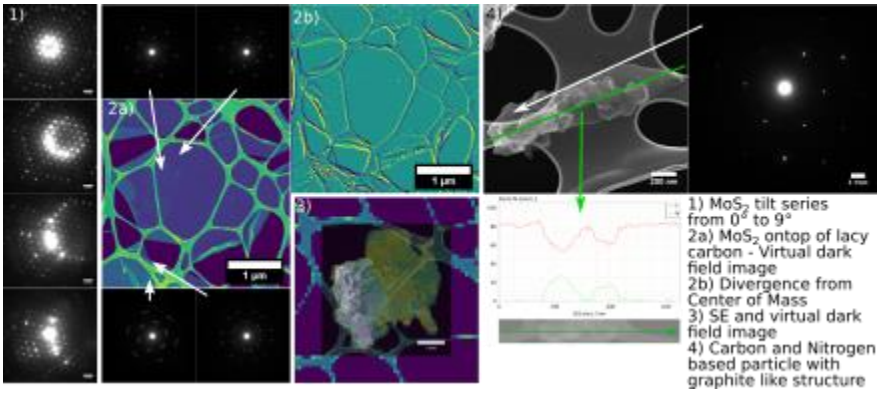
1)
2a)
2b)
3)
4)
1) MoS_2 tilt series from 0° to 9°
2a) MoS_2 ontop of lacy carbon - Virtual dark field image
2b) Divergence from Center of Mass
3) SE and virtual dark field image
4) Carbon and Nitrogen based particle with graphite like structure

IM5.005
Low Energy Nano Diffraction in SEM – Setup and application to *in situ* heating experiments

P. Denninger[1], P. Schweizer[1], C. Dolle[1], E. Spiecker[1]

[1]Friedrich-Alexander-Universität Erlangen-Nürnberg, Lehrstuhl für Mikro- und Nanostrukturforschung, Erlangen, Germany

Low voltage electron microscopy has experienced a revival in recent years due to the advent of 2D materials and renewed interest in soft matter. The major advantages of low energies lie in minimizing knock-on damage and increasing contrast for low-Z materials. While transmission electron microscopy (TEM) traditionally uses high beam energies, a recent push towards lower and lower energies has been made for the investigation of light element-materials, like Carbon Nanotubes and Graphene (1).

On the other hand Scanning Electron Microscopy (SEM) already operates at low voltages (0.5-30kV) by default and can be used in transmission as well. Additional benefits of SEM are the large sample chamber, topographic contrast and large field-of-view. Transmission imaging in SEM has been increasingly explored in recent years, e.g. for the elucidation of the morphology of organic solar cells (2). However, true TEM-like diffraction is still missing in SEM at large.

In this work we introduce a novel diffraction setup in the SEM that is non-invasive, cost-effective and highly flexible. Low Energy Nano Diffraction (LEND) is based on the combination of a fluorescent screen positioned below the sample with a dedicated CMOS camera (Figure 1a). The technique has been implemented and successfully tested for several material systems with a focus on low voltage applications.

Graphene, as an exemplary 2D material, demonstrates the benefits of our diffraction setup. The material can be investigated nondestructively in SEM over an extended period of time due to the low energy electrons, which has been exploited recently for the manipulation of dislocations in bilayer graphene (3). Figure 1b shows a diffraction pattern of monolayer graphene taken with an acceleration voltage of 5 kV. When the electron beam is set on a single spot or scanned over a small sample area a spot-like diffraction pattern is obtained due to the large working distance and small convergence angle in SEM. In addition to the acquisition of single diffraction patterns, our setup also enables diffraction mapping (4D-STEM) enabling, e.g., layer counting and rotation angle determination of multilayer graphene (Figure 1b). Besides 2D materials also soft matter can be analyzed as shown in Figure 1d for the example of a ternary organic solar cell. Using the diffraction information the contrast obtained in low energy STEM can be optimized.

Even hard matter like gold or silicon can be investigated using our diffraction setup provided the specimen is thin enough. By scanning over an area, a cumulative diffraction pattern (ring pattern for polycrystalline gold and spot diffraction pattern for silicon) can be obtained simultaneously to image acquisition (Figure 1c).

The LEND setup can be upgraded to an in situ heating stage for DENS Solution Wildfire Nano-Chips (Figure 2a-b). Our heating stage combines *in situ* heating, imaging and diffraction in SEM (Figure 2b). To showcase the power of this technique solid state dewetting experiments on metal thin films (Figure 2c) and the process of Aluminum Induced Layer Exchange (AIILE) will be shown, where the simultaneous acquisition of real- and reciprocal space information *in situ* is needed to elucidate the interplay of crystallographic and topographic processes.

References:

(1) U. Kaiser et al. Ultramicroscopy, 2011

(2) M. F. G. Klein et al. Journal of Polymer Science, 2012

(3) P. Schweizer et al. Science Advances, 2018

Fig. 1

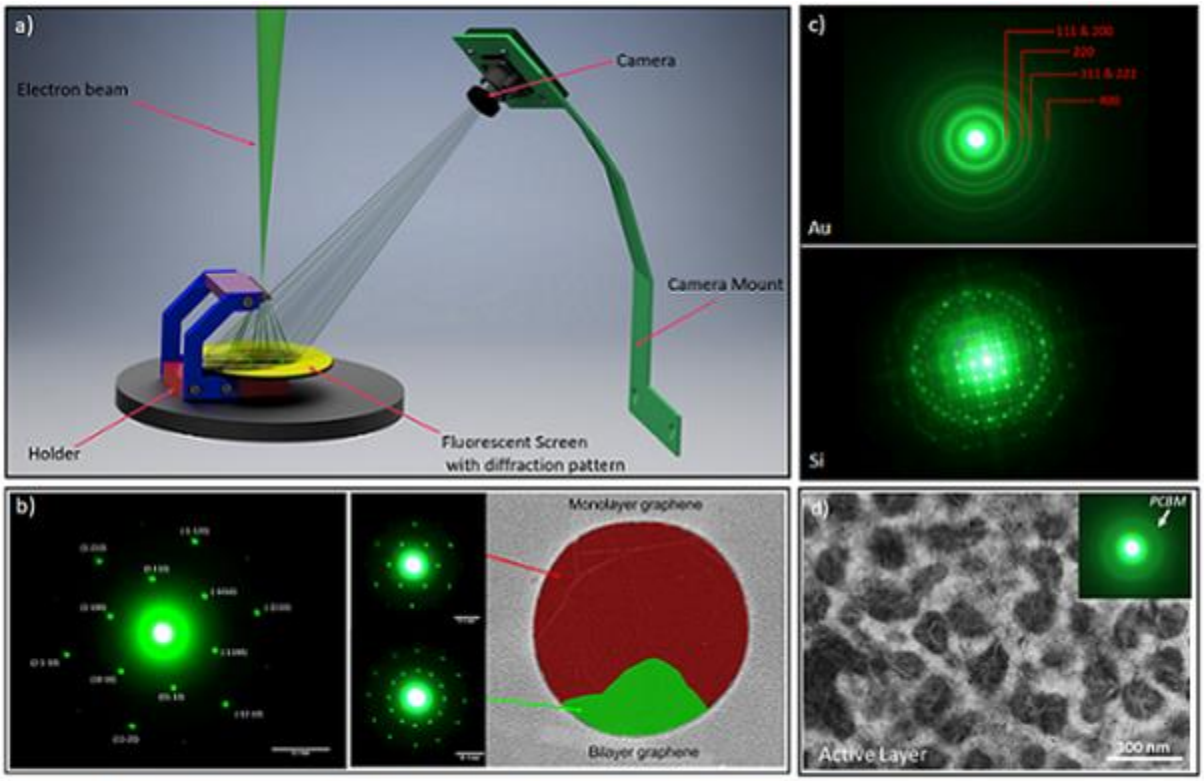

Figure 1: a) Basic principle of LEND, b) Diffraction patterns of graphene (5kV) with rotation analysis, c) Diffraction pattern of Au & Si, d) STEM-image of an organic blend optimized by SEM diffraction

Fig. 2

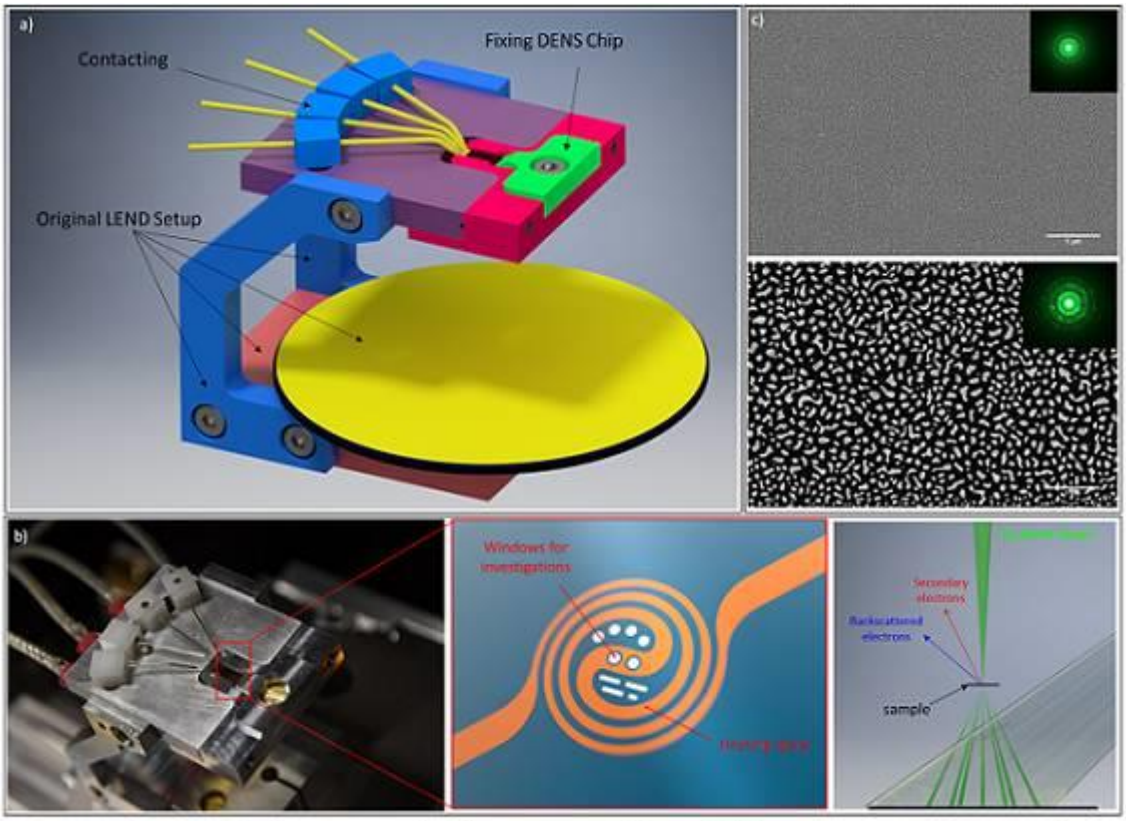

Figure 2: a) 3D model of our custom-built heating stage, b) installed heating stage with DENS Solution Wildfire Nano-Chip, c) solid state dewetting of gold

IM5.006
Differential Electron Scattering Cross-Sections at Low Electron Energies: The Influence of the Screening Parameter

M. Čalkovský[1], E. Müller[1], M. Hugenschmidt[1], D. Gerthsen[1]

[1]Karlsruhe Institute of Technology, Laboratory of Electron Microscopy, Karlsruhe, Germany

The interest in electron microscopy at low electron energies is rising because knock-on damage can be avoided and high contrast is obtained especially for weakly scattering materials. There is also increasing interest in scanning transmission electron microscopy (STEM) performed in a scanning electron microscope equipped with a STEM detector at electron energies ≤ 30keV. To extract quantitative information from STEM images, comparison of experimental data with simulations is essential. Monte Carlo (MC) simulations are well established to calculate high-angle annular dark field (HAADF) STEM intensities IHAADF on a non-atomic level (1). Previous studies at electron energies ≤ 30keV has revealed discrepancies between experimental and simulated I_{HAADF} which are mainly attributed to the differential scattering cross-sections (DSCS) used in MC simulation (2).

In this work we focus on the importance of the screening parameter η in DSCS for MC simulations and on the contribution of η to the Z dependence of I_{HAADF} at electron energies ≤ 30keV. We have studied 9 different materials with different average atomic numbers (3.5-74). Several approaches for η from literature were tested and failed to generally describe the experimental I_{HAADF}. Hence, η was adapted to obtain the best match between experimental I_{HAADF} and MC simulations and the overall Z dependence of I_{HAADF} was derived.

Samples with well-known thickness profiles were obtained by FIB milling wedges from bulk materials (cf. Fig. 1a)). HAADF-STEM images were acquired and intensity line profiles as a function of the sample thickness were extracted (Fig. 1b)). For MC simulations six different approaches for η (3) were tested using the NISTMonte simulation package (4) and simulated I_{HAADF} are compared with measured data.

Fig. 2a) shows the comparison of the measured I_{HAADF} (blue line) as a function of the specimen thickness t and MC simulations for diamond-like carbon (DLC). It is obvious that the simulated curves with different η from literature (3) do not agree with the measured data. Hence, the screening radius was manually adjusted not only for DLC but also for all other investigated single-element materials (Si, Ge, Pd, W) to obtain best possible fit. In Fig. 2b) the best fit for DLC obtained with the screening radius $R = 0.58a_o$ (a_o: Bohr radius) at 10, 20 and 30 keV is shown. The determined screening radii for all investigated single-element materials are plotted as a function of Z in Fig. 2c). The fit curve yields a new expression for the screening radius $R = 1.28\ Z^{-0.44}$. The validity of this equation was tested by comparing experimental and simulated $I_{HAADF}(t)$ of compounds (ZnO, MgO, SrTiO3), which also yields good agreement between experimental and simulated data. With the new screening radius, the overall Z dependence of I_{HAADF} can be calculated by integration of the DSCS over the detection angle range of the STEM detector (3) and is found to be proportional to $Z^{1.58}$.

References:

(1) H. Demers et al., Scanning 33 (2011), p. 135.

(2) T. Volkenandt et al., Microsc. Microanal. 111 (2014) p.20.

(3) I. Kyriakou, J. Appl. Phys. 113 (2013), p. 084303.

(4) N.W.M. Ritchie, Surf. Interface Anal. 37 (2005), p. 1006.

We acknowledge funding of the project by the Deutsche Forschungsgemeinschaft.

Fig. 1

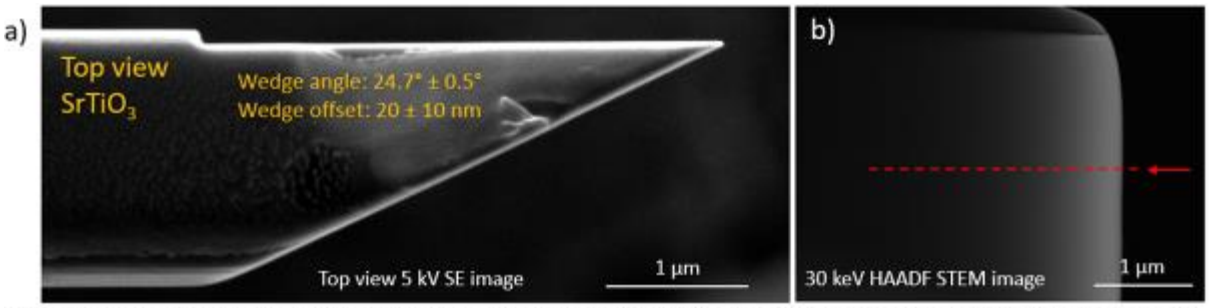

Figure 1. a) 5 keV top-view SE SEM image of the $SrTiO_3$ wedge, enabling the determination of the wedge angle and thickness at the wedge edge. b) 30 keV HAADF-STEM image of the $SrTiO_3$ wedge in side perspective, where the $I_{HAADF}(t)$ line profile was extracted along the dashed line.

Fig. 2

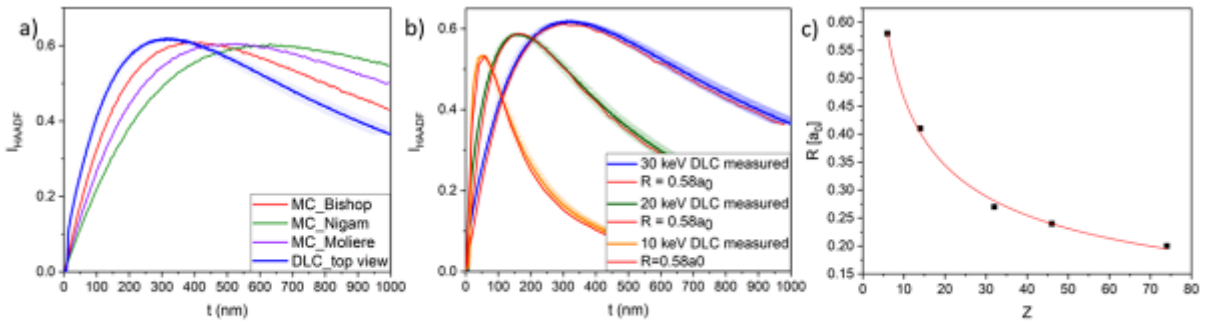

Figure 2. a) Measured I_{HAADF} as a function of sample thickness t and MC simulations with different η for the DLC wedge. b) Comparison of measured and simulated $I_{HAADF}(t)$ with manually adjusted screening radius for DLC at 30, 20, and 10 keV. c) Screening radii for all investigated single-element materials plotted as a function of Z and fit by a power-law function.

IM5.007
Implementation and evaluation of a combined EBIC/FIB setup for failure analysis of oxide devices for operando TEM investigations

O. Recalde[1], A. Zintler[1], U. Kunz[1], Y. Pivak[2], A. Rummel[3], A. Smith[3], L. Molina-Luna[1]

[1]TU Darmstadt, Material Science, Darmstadt, Germany
[2]DENSsolutions, Delft, Netherlands
[3]Kleindiek Nanotechnik, Reutlingen, Germany

Electron beam induced current (EBIC) has proved to be a decisive tool for the analysis of electrical activity in electronic device materials by the study of its minority carriers and defect distribution (1). Here, we propose a novel methodology for local electrical characterization and failure analysis of TEM lamella-based oxide devices. Recent advances in microelectromechanical systems (MEMS) based chips for in situ transmission electron microscopy allow the capability to perform current-voltage measurements while simultaneously analyzing the corresponding structural or electronic structure changes during device operation at high-spatial resolution (2). However, a major key issue for oxide devices is to test electrical performance.

To develop and implement an EBIC-based device testing methodology by using a SEM/FIB microscope, a nanomanipulator testing system and a novel nanochip based TEM sample carrier setup for in situ studies. Preliminary results on Pt/HfO2/TiN stack devices have demonstrated the feasibility of this method.

The devices were fabricated using a focused ion beam (FIB) instrument and an in situ lift-out system. We have implemented an EBIC system on a JEOL JIB-4600F SEM/FIB microscope, including a custom-made amplifier. As previously reported, our in situ TEM setup allows the analysis of the I-V behavior of electron transparent FIB prepared and contacted TEM lamellas (2).

Figure 1 shows the nanochip used to control the biasing and heating environment of a contacted TEM lamella. In situ high-spatial resolution experiments are feasible with this setup. Figure 2 shows an EBIC mapping of current flow (electrical activity) directly on the contacted TEM lamella, where the conductive layers of the device were broken intentionally for testing purposes. The current flow is clearly visible as a brighter contrast on the upper electrode when the stimuli were applied, then after and in the same way the bottom electrode was tested showing the same trend.

These preliminary results demonstrate the feasibility of conducting EBIC on nanochip based sample carriers for in situ transmission electron microscopy at the nanoscale by adjustment of electrical parameters and corresponding EBIC imaging modes. EBIC on SEM/FIB is a first step analysis in order to streamline adequate sample preparation for subsequent studies in an in situ TEM biasing setup.

References:

(1) Chen Li, Jonathan Poplawsky, Yanfa Yan, Stephen J. Pennycook. "Understanding Individual Defects in CdTe Thin-Film Solar Cells via STEM: From atomic structure to electrical activity", Materials Science in Semiconductor Processing, Volume 65, 2017, Pages 64-67.

(2) A. Zintler, U. Kunz, Y. Pivak, S.U. Sarath, S. Vogel, E. Hildebrandt, H.J. Kleebe, L. Alff and L.Molina-Luna. "FIB Based Fabrication of an Operative Pt/HfO2/TiN Device for Resistive Switching inside a Transmission Electron Microscope", Ultramicroscopy, Volume 181, 2017, Pages 144-149.

Fig. 1: a) Overview of a nanochip showing the contact electrodes b) Inset of the contact terminals on the nanochip where the TEM lamella is placed.

Fig. 2: Pt/HfO2/TiN TEM lamella mounted on nanochip a) EBIC analysis on the upper electrode b) EBIC analysis on the bottom electrode.

The authors acknowledge funding from DFG grant MO 3010/3-1 and the European Research Council (ERC) "Horizon 2020" Program under Grant No. 805359-FOXON.

Fig. 1


Electrodes
TEM sample

Fig. 2

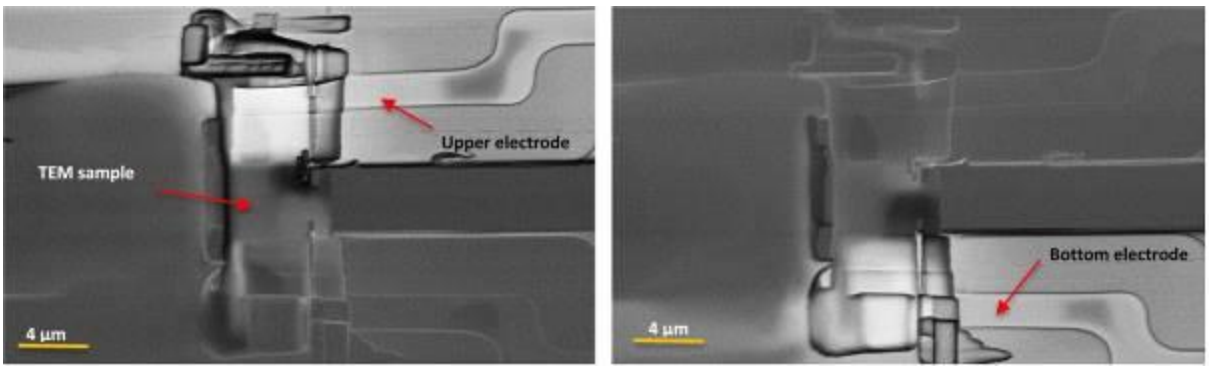
TEM sample
Upper electrode
4 µm
Bottom electrode
4 µm

IM5.LB.P01
Performance of solid-state and scintillation BSE detectors

J. Rozbořil[1], J. Kološová[1], J. Jiruše[1]

[1]TESCAN Brno, Brno, Czech Republic

Scanning electron microscopy (SEM) at low primary electron energies (below 1 keV) is desired for many applications (1): it allows imaging of non-conductive samples, reduces sample damage and increases surface sensitivity.

We compare performance of two different types of detectors for back-scattered electron (BSE) imaging – the proprietary low-energy scintillation detector (2) and state-of-the-art solid-state detector. Both detectors are retractable inside the vacuum chamber for conventional SEM setups and they operate without any deceleration or acceleration of the primary or signal electrons.

The detection limit of the scintillation BSE detector is found to be 200 eV, whereas for the solid-state detector it is 500 eV. The scintillation detector achieves a bit higher sensitivity allowing higher scanning speeds. On the other hand, the solid-state detector offers additional functionalities due to segmentation of the detector. The common four-quadrant segmentation enables to distinguish topographic and compositional contrasts, and other segmentations are also possible. Detectors functionality, image quality, signal-to-noise ratio and acquisition times of the detectors will be compared in detail at different conditions, e.g. see Fig. 1.

We demonstrate that both types of detectors are useful for SEM at low primary electron energies and one should be preferred according to desired application. The scintillation detector exhibits excellent sensitivity for fast imaging and the solid-state detector is advantageous when simultaneous imaging in different contrasts is desired.

References:

(1) D.C. Bell and N. Erdman (Eds.) *Low Voltage Electron microscopy: Principles and Applications*, John Wiley and Sons, 2013

(2) Kolosova, J., Jiruse, J., Fiala, J., & Beranek, J. (2015). Low Energy BSE Imaging with a New Scintillation Detector. *Microscopy and Microanalysis, 21*(S3), 703-704. doi:10.1017/S1431927615004316

Fig. 1: Tin balls at 500 eV imaged by the low-energy scintillation detector (left) and the solid-state detector in compositional mode (right).

Fig. 1

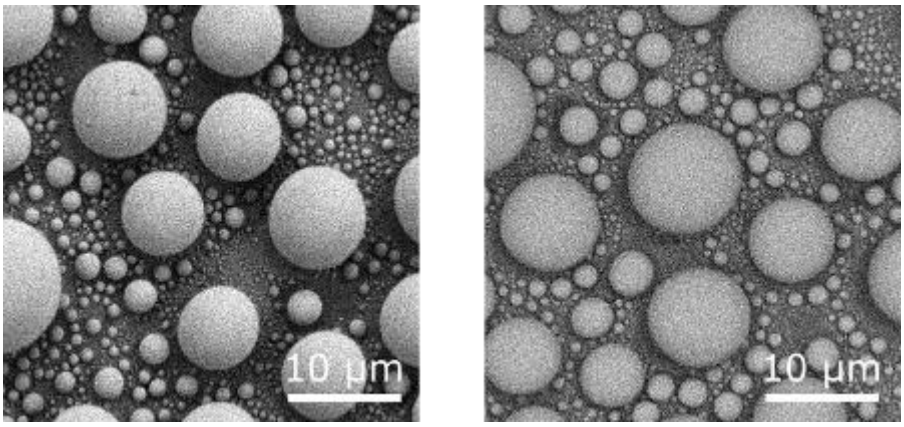

IM5.LB.P02
Advanced sample preparation of graphite used in lithium ion batteries and evaluation of the FIB/SEM data using machine learning

S. Sailer[1], M. Mundszinger[1], U. Kaiser[1]

[1]Ulm University, Electron Microscopy Group of Materials Science, Ulm, Germany

Spheriodized graphite is a widely used anode material in lithium ion batteries (1). As its texture and porosity influences the electrochemical properties of the battery (2), FIB/SEM tomography (slice & view) data of graphite particles is recorded. By segmenting the serial 2D-images, a 3D-reconstruction of the graphite particle is possible and the pore volume can be determined. As the used semi-automatic reconstruction is too time consuming, an investigation process is developed that allows to evaluate the data in an appropriate time scale.

An automatic segmentation method is therefore needed that allows to analyse more than one particle in one tomogram. For this, a homogeneous background is desired, which we realized by embedding the graphite particles.

For the automatic segmentation two different machine learning approaches are investigated. The first methods are trainable classifiers, such as the random forest classifier (3), trained with the interactive software *ilastik (4)*. The second approach is the training of neural networks, such as SegNet[5], with MATLAB. Both, the classifiers and neural networks, can assign each pixel of an image to one of the different classes after training. With the automatically segmented images the pore volume can be determined and a 3D-reconstruction of the particle is possible. By comparing results of the automatic segmentation with a ground truth segmentation[5], the accuracy of the used classifier or network will be determined.

First promising results of the automatic segmentation are shown in figure 1, showing that the automatic segmentation was successful for a single particle. Based on our first results, the optimal automatic segmentation method will be evaluated by comparing different networks and classifiers. We show that the machine learning segmentation techniques speeds up the reconstruction process significantly. Another advantage is that different grains are evaluated at the same time. We will test also different embedding methods in order to receive most homogenous background contrast.

This work is done in the RONDO project (BMBF, 03XP0112E).

References:

(1) C. Pillot, *The rechargeable battery market and main trends 2014-2025*, in: AABC Europe 2016 - Advanced Automotive Battery Conference; Mainz, Germany, 2016.

(2) Y. Ishii et al., *Graphite particles and lithium secondary cell using them as cathode material*, (1998), WO9806679.

(3) L. Breiman, *Random forests,* (2001), *Machine Learning*, vol. 45, pp. 5-32.

(4) C. Sommer et al*., ilastik: Interactive Learning and Segmentation Toolkit;* Eighth IEEEInternational Symposium on Biomedical Imaging (ISBI) Proceedings, (2011), pp.230-223.

(5) V. Badrinarayanan et al., *Segnet: A Deep Convolutional Encoder-Decoder Architecture for Image Segmentation.* IEEE Transactions on Pattern Analysis and Machine Intelligence, (2017), vol. 39, pp. 2481-2495.

Fig. 1: Cross section of a graphite particle (left) and its segmentation performed automatically with the SegNet network (right).

Fig. 1

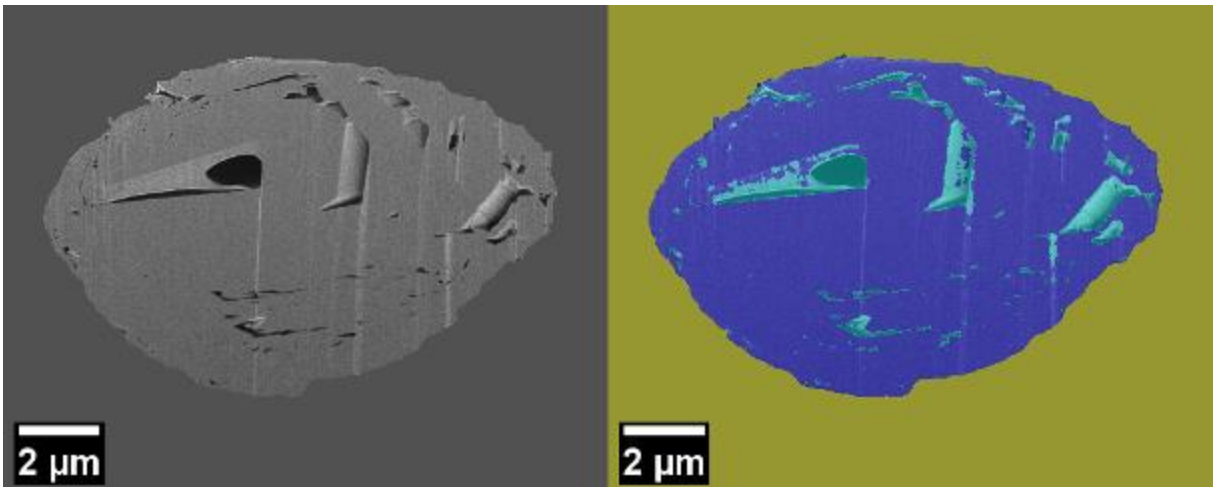

IM5.P001
Investigation of dislocations by STEM in a scanning electron microscope

C. Sun[1], E. Müller[1], M. Meffert[1], D. Gerthsen[1]

[1]Karlsruhe Institute of Technology, Laboratory for Electron Microscopy, Karlsruhe, Germany

Dislocations significantly affect the properties of crystalline solids. Therefore, the characterization of dislocations with respect to their type, density and distribution is highly important. Transmission electron microscopy (TEM) is commonly used for dislocation analysis. Burgers vectors of individual dislocations **b** can be determined by exploiting the **g**·**b**=0 criterion where the sample is oriented in different two-beam conditions **g** and extinction of dislocation contrast is utilized to determine **b**. Based on the reciprocity theorem, bright-field scanning transmission electron microscopy (BF-STEM) can also be applied for defect analysis (1). Up to now BF-STEM defect analyses were restricted to transmission electron microscopes at electron energies of 100 keV and above. However, modern scanning electron microscopes (SEMs) equipped with a STEM detector also facilitate the analysis of TEM samples. Two-beam conditions can be set up by either using a multi-segmented STEM detector (2) or acquiring transmission electron diffraction (TED) patterns in a SEM equipped with an on-axis CCD-camera (3). The latter approach was employed in this study using a Thermo Fisher Helios Nanolab G4 FX equipped with double-tilt TEM specimen holder.

In this work we present systematic analyses of dislocation Burgers vectors and displacement vectors of stacking faults by STEM in a SEM. Fig. (1) shows 30 keV cross-section BF-STEM images of dislocations in an epitaxial [0001] GaN layer which were taken under different two-beam conditions. Two dislocations marked by arrows in Fig. 1(b) show strong contrast under $\mathbf{g}_{(1\text{-}210)}$ two-beam condition (Fig. 1(e)) while their contrast vanish in Figs. 1(a,c) using $\mathbf{g}_{(000\text{-}2)}$ and $\mathbf{g}_{(1\text{-}100)}$. The Burgers vector direction can be determined by $\mathbf{b}=\mathbf{g}_{(000\text{-}2)}\times\mathbf{g}_{(1\text{-}100)}$ yielding a Burgers vector parallel to [11-20] which is compatible with 1/3 Burgers vectors in wurtzite crystal structures. Further details of dislocation line contrast such as double- and single-line contrast can be exploited for Burgers vector determination. In analogy to dark-field (DF)-TEM, DF-STEM without and with excitation error s_g is employed to study the change of dislocation line contrast. Choosing a suitable Bragg reflection, the multi-segmented STEM detector allows to set up conditions where only one Bragg reflection is detected on an annular detector segment. DF-STEM images using $s_g=0$ (Fig. 2(a)) and (**g**,3**g**) weak-beam conditions (Fig. 2(b)) reveal the increase of sharpness of dislocation line contrast under (**g**,3**g**) conditions (4). The reduction dislocation line width can be attributed to the correlation of line width with extinction distance ξ_g and the reduction of ξ_g with increasing s_g.

References:

(1) J.M. Cowley, Appl. Phys. Lett. 15 (1969), p. 58.

(2) C. Sun et al., A new method to orient samples by STEM in a scanning electron microscope, European Microscopy Congress (2016), p. 639.

(3) C. Sun, et. al., Microsc. Microanal. 24 (2018), p. 99.

(4) C. Sun, et. al., Adv. Struct. Chem. Imag. 5:1 (2019), p. 1.

(5) We acknowledge funding by the Deutsche Forschungsgemeinschaft (DFG).

Fig. 1: (a,b,c) 30 keV BF-STEM images of GaN taken with (d) $\mathbf{g}_{(000\text{-}2)}$ (e) $\mathbf{g}_{(1\text{-}210)}$ (f) $\mathbf{g}_{(1\text{-}100)}$ two-beam conditions. ZB indicates the zero-order beam.

Fig. 2: 30 keV DF-STEM GaN images taken with $\mathbf{g}_{(0002)}$ under (a) $s_g=0$ and (b) **g**,3**g** weak-beam conditions.

Fig. 1

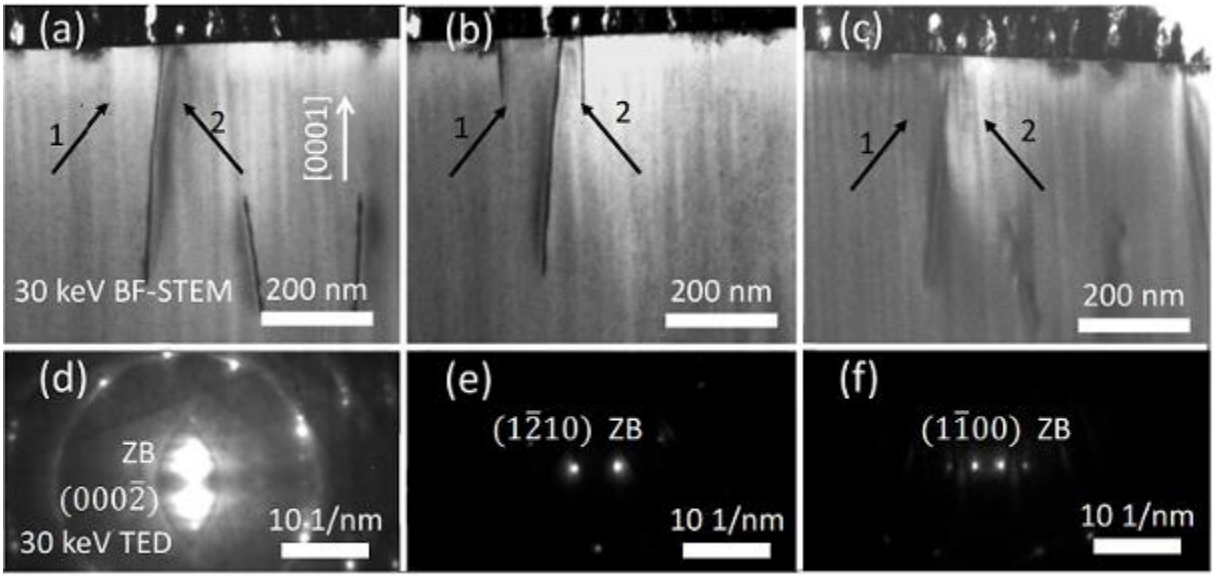
(a)
1
2
[0001]
30 keV BF-STEM
200 nm
(b)
1
2
200 nm
(c)
1
2
200 nm
(d)
ZB
(000$\bar{2}$)
30 keV TED
10 1/nm
(e)
(1$\bar{2}$10) ZB
10 1/nm
(f)
(1$\bar{1}$00) ZB
10 1/nm

Fig. 2

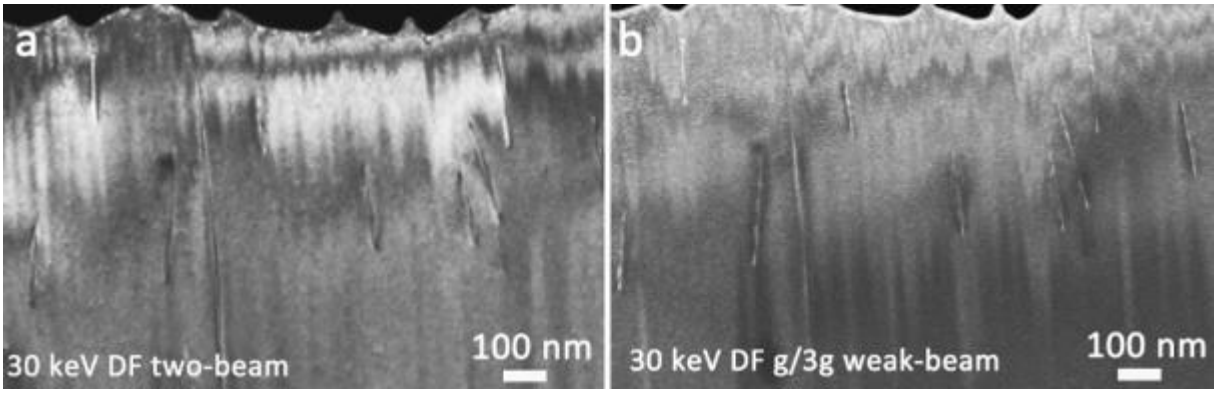
a
30 keV DF two-beam
100 nm
b
30 keV DF g/3g weak-beam
100 nm

IM5.P002
FIB preparation of TEM-lamellas for electron holographic in-situ biasing experiments

U. U. R. Hömpler[1], D. Berger[2], M. Lehmann[1]

[1]Technische Universität Berlin, Institut für Optik und Atomare Physik, Berlin, Germany
[2]Technische Universität Berlin, Zentraleinrichtung Elektronenmikroskopie, Berlin, Germany

For in-operando investigations of semiconductor devices, the specimen must be contacted inside the TEM and electrically operated from the outside. This applied bias provides an additional stimulus, e.g. the step-in potential at the p-n junction can be modified directly (1-3). For measuring the potential distribution within a specimen, electron holography with its access to phase information of the electron wave is used (4,5).

First biasing experiments were carried out by Twitchett et al. (1) and Han et al. (6). Another approach is the combination of FIB prepared TEM-lamellas and MEMS-based chips, which are electrically integrated in a commercially available in-situ heating or biasing TEM-holder (7-10). Here, this approach is pursued with special focus on electron holographic in-situ biasing experiments. Therefore, it is necessary to avoid any electrical bypass of the TEM-lamella. Besides contacting of a TEM-lamella this technique has several benefits: Thinning and cleaning of all four side facets, a constant sample thickness and minimization of amorphous layers.

The procedure is demonstrated on a silicon diode (11). The preparation can be described in four major steps: Fabrication of the TEM-lamella, preparation of the MEMS-based chip, transfer of the TEM-lamella by lift-out, and on-chip thinning of the TEM-lamella. The finally prepared specimen is shown in figure 1. In order to minimize the influence of the electrode"s stray field the reference wave for electron holography passes through one of the windows in the electrodes (12).

The phase profiles (Fig. 2) across the p-n junction with (top) and without (bottom) contribution of the electrode"s electric field show a proportional dependence on the external voltage. To compensate the influence of the MIP and the build-in voltage to the phase shift the holograms with applied voltage are referenced to the holograms without bias. The achieved FIB preparation technique for electrical biasing of TEM-lamellas utilizing electron holography gives access to in-operando investigations on potential related effects in electrically driven specimens e.g. semiconductor devices (13,14).

References:

(1) A.C. Twitchett et al., J. Microsc., 214, 2004

(2) S. Anada et al., J. Appl. Phys., 122, 2017

(3) S. Yazdi et al., Ultramicroscopy, 152, 2015

(4) D. Gabor, Nature, 161, 1948

(5) H. Lichte and M. Lehmann, Advances in Imaging and Electron Physics, 123, 2002

(6) M.-G. Han et al., Appl. Phys. Lett., 92, 2008

(7) U.U.R. Hömpler et al., Proceedings MC2017, Lausanne

(8) D. Berger et al., Proceedings MC2017, Lausanne

(9) M. Duchamp et al., Microsc. Microanal., 20, 2014

(10)] A. Zintler et al., Ultramicroscopy, 181, 2017

(11) D. Cooper et al., J. Appl. Phys., 104, 2008

(12) R. Kraft et al., these proceedings

(13) We thank Dr. David Cooper (CEA, Leti) for providing the semiconductor device.

(14) We kindly acknowledge the support from the DFG within the CRC 787, project A4.

Fig. 1: SEM image of a TEM-lamella with a silicon p-n junction contacted on a MEMS-based chip optimized for electron holography.

Fig. 2: Phase profiles across a silicon p-n junction under reverse (1V to 3V) and forward (1V) bias referenced to an unbiased electron hologram. Top: Phase profiles include the contribution of the electric field of the electrodes and the potential changes within the diode. Bottom: Phase profiles are tilted with respect to the mean of the electric potential in n and p.

Fig. 1

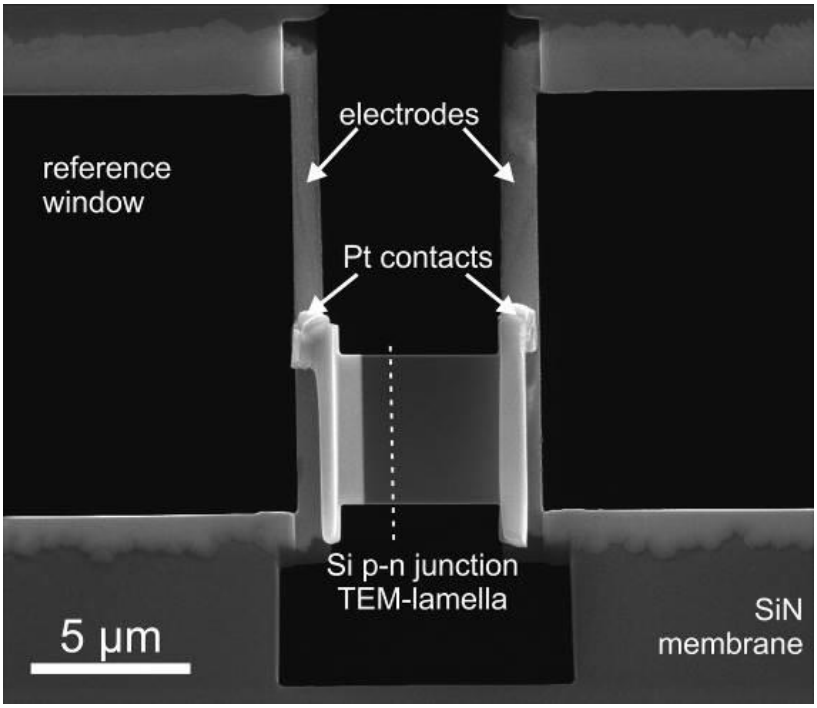

Fig. 2

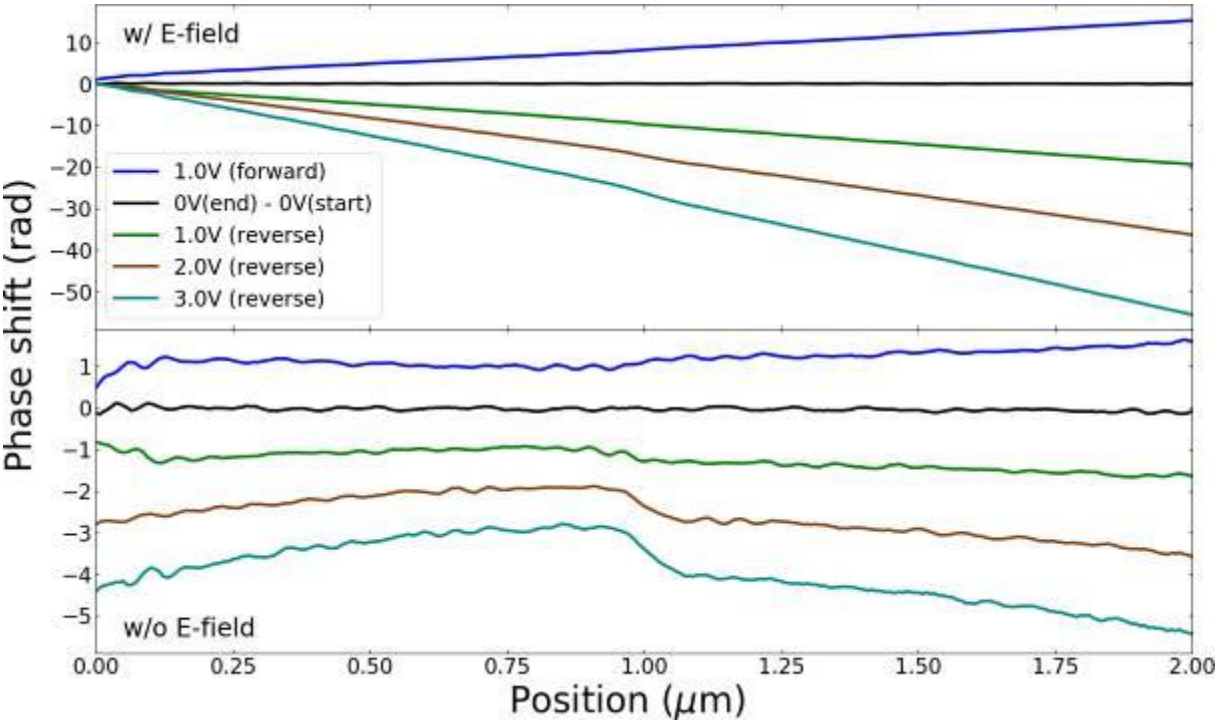

IM5.P003
Beam broadening measured in transmission mode at low electron energies in a scanning electron microscope

M. Hugenschmidt[1], E. Müller[1], D. Gerthsen[1]

[1]Karlsruhe Institute of Technology, Laboratory for Electron Microscopy, Karlsruhe, Germany

In the last years there has been an increasing interest in scanning transmission electron microscopy (STEM) at low primary electron energies $E_0 \leq 30$ keV because low-kV STEM yields high material contrast for weakly scattering materials and reduces knock-on-damage compared to higher E_0. However, the mean free path length decreases with lower E_0. As a result of the increased number of scattering events, beam broadening by plural and multiple scattering is pronounced even for small sample thicknesses and worsens lateral resolution. Beam broadening in the sample cannot be directly imaged but Drees *et al.* (1) proposed a technique to measure the width of the transmitted beam. We use this approach to analyze beam broadening b in materials with known composition (MgO, Si, $SrTiO_3$ and Ge) which cover (average) atomic numbers Z between 10 and 32. A STEM detector in a FEI Strata 400S was used for measuring the transmitted intensity. It is partitioned into several annular segments corresponding to specific scattering angle ranges. The measured STEM intensity is normalized with respect to the intensity of the incident electrons after subtracting the black-level intensity of the inactive detector areas. Specimens with a wedge-shaped thickness profile are essential and were obtained by focused ion-beam milling. The normalized STEM image intensity as a function of the wedge thickness $I(t)$ was measured up to specific angles defined by the number of used detector segments (Fig. 1a). We define b as the beam diameter that contains 68% of the total probe intensity neglecting the width of the primary beam, which is small compared to b. A horizontal line in Fig. 1a indicates the thickness where the measured intensity corresponds to 68% for different scattering angles θ. b is then calculated by $b(t)=t\tan(\theta)$ assuming that the electrons are scattered on average at $t/2$ (Fig. 1b). We note that t is known due to the well-defined thickness profile of the wedge samples. Fig. 2a shows the increase of b over t for all materials at 25 keV. The measured beam broadening is compared with the prediction of Gauvin and Rudinsky (2) by fitting the Hurst exponent H in

$$(b\cdot E_0^{(2H+1)/2})/(Z^{(4H+1)/3}\rho^H A^{-H}) = 0.1167^{1-2H}\,39437^H\,(R/(1-R))^{1/2}t^{1+H} \quad (1)$$

with the fraction $R=0.68$ of electrons contributing to the beam diameter, the atomic mass A and the material density ρ. H was determined to be 0.75 by fitting Eq.(1) to the measured b values. Fig. 2b emphasizes the good description of the complete experimental data set (all materials and 15 keV$\leq E_0 \leq$30 keV). H characterizes different scattering regimes in dependence of the number of scattering events. The determined value $H=0.75$ lies between 0.5 and 1 for diffusion and ballistic regime and is consistent with our definition of the beam diameter containing 68% of the total beam intensity and the analyzed energy and thickness range.

References:

(1) H. Drees *et al.*, Ultramicroscopy, 185 (2018).

(2) R. Gauvin, S. Rudinsky, Ultramicroscopy, 167 (2016).

The authors acknowledge funding by the Deutsche Forschungsgemeinschaft (DFG).

Fig. 1: (a) Normalized STEM intensity for Si at 25 keV as a function of t integrated up to the scattering angles indicated in the legend. (b) Calculation of b in a sample of thickness t.

Fig. 2: (a) Measured and fitted beam broadening for $E_0=25$ keV and different materials as a function of t. (b) Measurements and calculated product $(bE_0^{1.25})/c_{mat}$ for different E_0 and different materials with $c_{mat}=Z^{4/3}\,(\rho/A)^{0.75}$ as a function of t.

Fig. 1

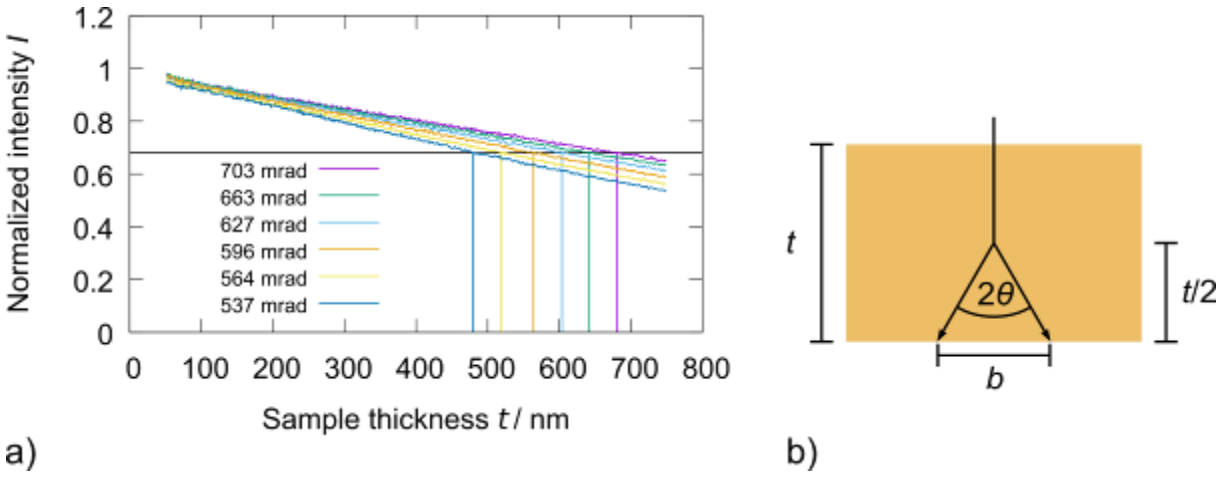
Normalized intensity I
1.2
1
0.8
0.6
0.4
0.2
0
703 mrad
663 mrad
627 mrad
596 mrad
564 mrad
537 mrad
0
100
200
300
400
500
600
700
800
Sample thickness t / nm
a)
t
2θ
t/2
b
b)

Fig. 2

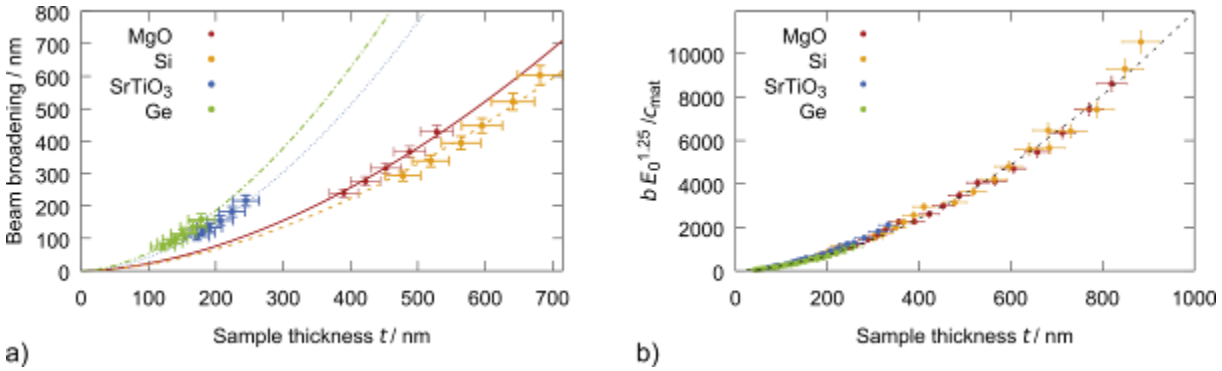
Beam broadening / nm
MgO
Si
SrTiO3
Ge
Sample thickness t / nm
a)
b E0^1.25 /cmat
MgO
Si
SrTiO3
Ge
Sample thickness t / nm
b)

IM5.P004
Latest Developments In Multiple Ion Species Plasma FIB Technology

M. Dutka[1], B. Van Leer[1], A. Prokhodtseva[1], D. Phifer[1]

[1]Thermo Fisher Scientific, Eindhoven, Netherlands

Compared to Ga liquid metal ion source (LMIS) DualBeam FIB-SEMs, Xe inductively couple plasma (ICP) DualBeams are relatively new (1). Until recently, only Ga and Xe source technologies have been commercially available for DualBeams. LMIS Ga FIB technology offers a ion beam that provides high resolution capability for nanoprototyping and offers enough current for S/TEM sample preparation of most samples in less than an hour as well as FIB serial sectioning tomography (SST) of volumes up to 40x40x40 µm /hr (silicon using 30 kV-65 nA) with interslice distances as small as 3 nm (2,3). On the other hand, Xe PFIB technology has a much larger beam current capability allowing researchers to investigate volumes up to 130x130x130 µm /hr (silicon using 30 kV-2.5 µA). Additionally, xenon ions offer the user the ability to prepare gallium-free S/TEM samples or cross-sections (4,5). However, for a number of applications, neither gallium nor xenon may provide the highest quality results because of their intrinsic properties.

In this paper, we present the latest generation of plasma FIB technology supporting multiple ion species as a primary ion beam on Thermo Fisher"s newest DualBeam, the Helios Hydra PFIB. Next to xenon, the Helios Hydra provides researchers with 3 additional ion species –argon, oxygen and nitrogen. A single ion source can deliver all 4 ion species independently with a patented, automated, fast and easy switching capability. Thermo Fisher expects that access to multiple ion species "on -the-fly" will significantly expand the FIB"s application space in addition to providing advantages to various use cases. For example, consider S/TEM sample preparation with Xe+ ions and a final low energy polish of Ar+ ions to improve contrast in HR-STEM.

The Helios Hydra PFIB is designed on an established high-performance platform, the Helios NanoLab, offering state-of-theart SEM performance with sub-nm imaging at 1 keV and up. The multiple ion source technology allows for gas switching between species in less than 10 minutes without any degradation in performance for Xe+ PFIB. The system is fully compatible with the complete line up of automation from Thermo Fisher: AutoTEM 4, Auto Slice&View 4, AutoScript 4, Maps and iFAST.

References:

(1) P. Tesch et al, Proceedings from the 34th International Symposium for Testing and Failure Analysis (2008) p 6.

(2) C.A. Volkert and A.M. Minor, MRS Bulletin 32 (2007), p.389.

(3) J. Mayer et al, MRS Bulletin 32 (2007), p. 400.

(4) L.A. Giannuzzi and N. Smith, Microscopy and Microanalysis 17 (2011), p. 646.

(5) B. Van Leer and R. Passey, Microscopy and Microanalysis 23 (2017), p. 272.

IM5.P005
Depth analysis using soft X-ray spectrometer combined with low acceleration voltage scanning electron microscope

N. Inoue[1], Y. Sakuda[1], Y. Kojima[1], Y. Yamamoto[1], H. Onodera[1]

[1]JEOL, Akishima, Tokyo, Japan

Low acceleration voltage Scanning Electron Microscope (SEM) is widely used as a method to observe the surface of bulk sample. Elemental analysis is possible by using both SEM and X-ray spectrometer such as Energy Dispersive X-ray Spectrometer (EDS) and its application range is wide. In general, EDS is for detecting characteristic X-rays of relatively high energy. Thus, it is difficult to use with low acceleration voltage SEM. In recent years, Soft X-ray Emission Spectrometer (SXES) has been developed for SEM. SXES has attracted attention because it can analyze Al-L emission spectrum of Al metal with the ultrahigh energy resolution of 0.2 eV even in the low acceleration voltage range in SEM (1). Chemically strengthened glass was used in this work. Since this glass can give sufficient strength while having a thickness of 1 mm or less, it is often used as a glass for displays and building materials. In general, chemically strengthened glass is provided by immersing the soda glass in a molten salt having a glass transition temperature or lower and ion exchanging Na^+ contained in the glass to K^+, which generate compressive stress to the surface and increase the strength. Knowing the depth of ion-exchange is important to control the properties of chemically strengthened glasses produced. In this experiment, using SEM-SXES, we tried to analyze the ion exchange depth from the surface of chemically strengthened glass without cross-sectioning or etching with ion gun.

The purpose of this study is to analyze the distribution of K and Na in the depth direction from the surface without sectioning or etching with ion gun.

SEM can easily change the electron beam penetration depth by varying the acceleration voltage. Using the Monte Carlo simulation, the penetration depth of SiO_2 was calculated under the analyzed condition. The depth at an incident voltage of 1.5 kV is 50 nm or less. And at 30 kV it is about 10 μm. The K-L line which is one of the elements attracting attention in the measurement of this chemically strengthened glass is 260 eV. This line can be sufficiently excited even at an incident voltage of 1.5 kV. Therefore, it should be possible to analyze the glass surface from 50 nm to 10 μm in the depth direction by controlling the accelerating voltage without sectioning or etching with ion gun. The depth analysis in the surface normal direction was performed with SXES at incident voltages of 1.5 kV and 5.0 kV. The SXES is able to measure the second order line (130 eV) of K-L which cannot be acquired with EDS. For this time, this K-L second order peak was set as the measurement target.

Fig. 1 shows the changes in peak intensity at the incident voltages of 1.5 kV and 5.0 kV which measured from the surface by SXES. The second order line of LL line of K indicates that the concentration is about 5 times higher at 1.5 kV than at 5.0 kV using the calibration curve method. Fig. 2 shows the simulation results of electron beam penetration depth for SiO_2. The depth is about 400 nm at 5.0 kV and about 50 nm at 1.5 kV. Therefore, the K concentration was found to be lower in the deep region from 50 nm to 400 nm from the surface.

The depth analysis combined with both low acceleration voltage SEM and SXES is a powerful technique to investigate concentration change from the surface to bulk without cross sectioning.

References:

(1) H Takahashi et al 2016 IOP Conf. Ser.: Mater. Sci. Eng. 109 012017

Fig. 1

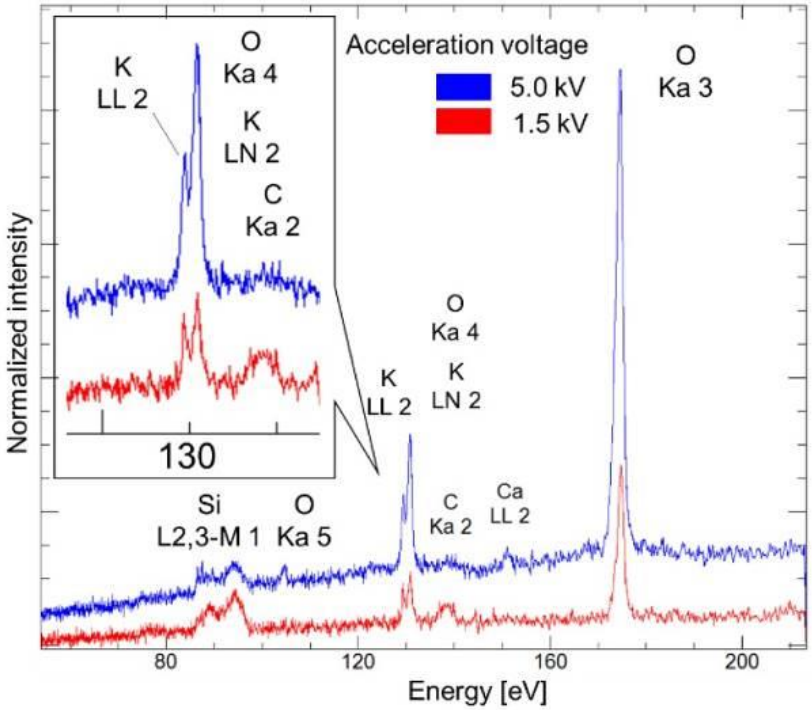

Figure 1. Change in X-ray peak intensity due to difference in incident beam energy measured from the surface normal direction by soft X-ray spectroscopy.

Fig. 2

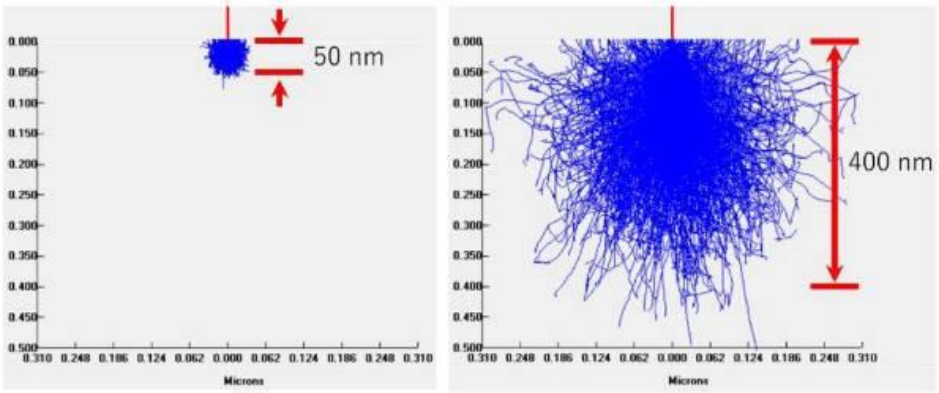

Figure 2. Electron beam penetration depth of SiO_2 calculated by Monte Carlo simulation at different acceleration voltages of (a) 1.5 kV, (b) 5.0 kV

IM5.P006
Tools for 3D Electron Microscopy in Life Sciences - Master Your Versatile Scientific Questions

E. Hummel[1], A. Elli[1]

[1]Zeiss Microscopy, Sector Marketing, Munich, Germany

Scanning electron microscopy (SEM) is a versatile method to obtain high-resolution information on the nanometer scale. While traditionally used for topography measurements, modern SEMs in biomedical research are utilized increasingly to obtain large volume data of biological samples. New developments in hard- and software as well as in electron optics enable an even-larger range of applications. SEM imaging enables scientists to analyze large scale data with full sample and substrate flexibility. The size of the sample carrier is not longer limited to classical EM grids. Even silicon wafers can be equipped with hundreds of sections. Single images are snapshots of a complex three-dimensional situation reduced to a 2D image. To fully understand the sample, volume data are necessarily acquired. Serial section can be used with the Array tomography technique to generate 3D volumes. Apart from using classical Microtomy, SEMs allow to manipulate the samples within the chamber. Two other methods exist to aquire 3D ultrastructural data sets – serial block face imaging using a chamber integrated microtome (3View) and focused ion beam on the Crossbeam system, using a gallium beam to generate 3D data. 3D volumes of pre-selected target areas. In this talk various 3D methods will be presented and discussed. The advantages of every method will be shown elucidating the broad range of possibilities every single method will bring along. Special focus will be set on Focal Charge Compensation – a tool which extend the usability of serial block-face imaging. Different techniques like serial section tomography (Array Tomography), block-face imaging (3View) and focus ion beam scanning electron microscopy (FIB-SEM) gives access into the world in 3D.

As an alternative to sequentially cutting a block tissue into serial sections and subsequently imaging the sections, resin-embedded cells or tissues may be imaged in 3D directly within the SEM chamber in a fully automated workflow: the surface of a specimen block is repetitively cut away with images of the exposed block surface taken after each sectioning event (block-face imaging). Two solutions to cut the sample within the scanning electron microscope are available: either an ultramicrotome inside the SEM chamber (3View) or a focused ion beam FIB-SEM that combines a FE-SEM with a focused ion beam for milling can be used. While 3View provides fastest imaging of 3D volumes with z-resolutions down to 15 nm, FIB-SEM is the best choice for higher z-resolutions down to 3-4 nm. Together with NCMIR, ZEISS developed the Focal Charge Compensation, an accessory of the 3View system which eliminates specimen charging making the 3View universally usable.

In this talk, different applications will demonstrate the strength of the individual 3D methods. Results from cell biology, developmental biology and plant research are shown.

Fig. 1

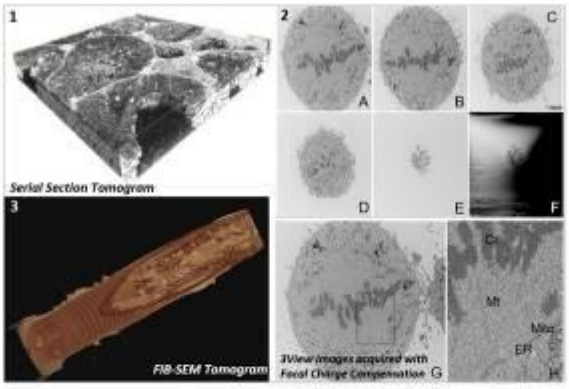

Figure1: 1 shows the 3D reconstruction from serial sections of root nodules at ultrastructural resolution. The alignment, processing, segmentation and visualization of the 2D images into a 3D data set was done by using Dragonfly Pro. In Cell Biology, high resolution imaging of cultured monolayers of cells forms the basis of much fundamental research into cellular structure, function and phenotype. A high ratio of resin to sample means that cell culture monolayers are extremely difficult to image with block-face SEM due to charging effects. Focal Charge Compensation eliminates the charging and thus enables high signal-to-noise 3D imaging of cellular ultrastructure. Figure 1.2 shows single mitotic HeLa cell with the DNA stained and embedded in Durcupan resin. In Figure 1.3 an entire nematode acquired with a FIB/SEM is presented. *C. elegans* was high pressure frozen and freeze substituted in EPON. The 3D data set consists of 10.000 z-sections with 5x5x8 nm pixel size. In this talk you will see movie of this reconstruction revealing the innermost of the worm.

Collection of results created with different 3D methods. (1) Root nodules: Samples provided courtesy of Dr. Janine Sherrier, Dr. Jeff Caplan and Ms. Shannon Modla, University of Delaware, US. (2) Single mitotic HeLa cell: Images courtesy NCMIR, San Diego, USA (3) C. elegans: Courtesy: Anne Steyer, Yannick Schwab (EMBL, Heidelberg, Germany) Sebastian Markert and Christian Stigloher (University Würzburg, Germany).

IM5.P007
Systematic Low-voltage-dependent Study of Contrast and Resolution in C_C / C_S-corrected *SALVE* Images of 2D Materials

Y. Li[1], J. Biskupek[1], Z. Lee[1], T. Lehnert[1], J. Köster[1], U. Kaiser[1]

[1]Ulm University, Electron Microscopy Group of Materials Science, Ulm, Germany

Conventional 200-300 kV TEM investigations on materials with light elements, such as carbon, oxygen and lithium, suffer from the knockon damage caused by electron irradiation. To reduce the damage, acceleration voltages below 80 kV have been more and more applied for beam-sensitive and thin materials such as graphene and single-layer transition metal dichalcogenide (TMD). However, the resolution of TEM is reduced at the same time. Despite nowadays widely used C_S-corrector, the information limit is dominated by the chromatic focus spread at low voltages.

To obtain atomic resolution at low voltages, the C_C- and C_S-corrected Sub-Angstrom-Low-Voltage Electron microscope (SALVE) was established. The aberration-corrector of the SALVE instrument corrects for first-order chromatic aberrations, axial geometric aberrations up to the fifth order, and off-axial geometric aberrations up to the third order. This allows not only to achieve atomic-resolved images of 2D monolayers with high contrast at low voltages, but also to obtain large field of view to get huge structural information in different area in one single exposure.

In this work, we systematically evaluate contrast and resolution in HRTEM images of 2D materials such as graphene and single-layer $MoTe_2$ at 80 kV, 60 kV, 40 kV, 30 kV and 20 kV. All 4k x 4k HRTEM images are acquired under optimized Lentzen conditions and resolution-optimized electron dose. The contrasts are compared quantitatively with corresponding dose-dependent image calculation. Fig. 1 shows the simulated C_C / C_S-corrected HRTEM images for monolayered $MoTe_2$ at 40 kV, 60 kV and 80 kV, as well as the corresponding contrast transfer function (CTF) plots. With the same image spread value, the information limits for the given voltage range 40 – 80 kV are the same judged from the plots in the second row of Fig. 1. In this case, low voltage like 40 kV is preferred over higher voltage 80 kV for achieving better image contrast, demonstrated by the images displayed in the first row.

References:

(1) M. Linck, P. Hartel, S. Uhlemann, F. Kahl, H. Müller, J. Zach, M. Haider, M. Niestadt, M. Bischoff, J. Biskupek, Z. Lee, T. Lehnert, F. Börrnert, H. Rose, U. Kaiser, Phys. Rev. Lett. 117 (2016) 076101.

(2) F. Börrnert, U. Kaiser, Phys. Rev. A. 98 (2018) 023861.

(3) M. Lentzen, Microsc. Microanal. 14 (2008) 16-26.

(4) S. Uhlemann, H. Müller, P. Hartel, J. Zach, M. Haiser, Phys. Rev. Lett. 111 (2013) 046101.

Fig. 1: Simulated C_C / C_S-corrected HRTEM images for monolayered $MoTe_2$ at 40 kV, 60 kV and 80 kV. The corresponding contrast transfer functions are displayed below the images. The dashed lines represent the overall envelope function curves for each accelerating voltage. The simulations utilized the following fixed values: the fifth-order spherical aberration coefficient C_5: 4 mm; image spread: 30 pm; focal spread: 0.5 nm. Defocus and the third-order spherical aberrations C_S are optimized according to (3). Scale-bar: 0.5 nm.

Fig. 1

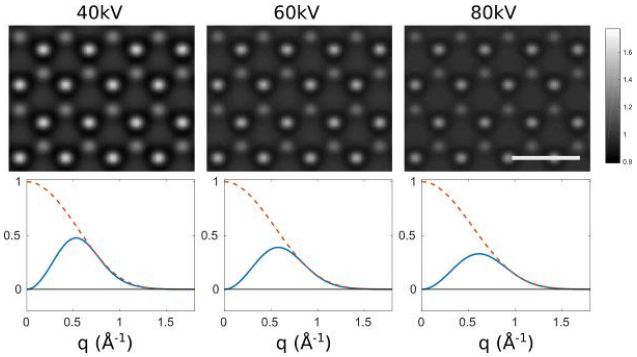

IM5.P008
Simulation of optimal measurement setting and calibration of a novel time-of-flight spectrometer

M. Zouhar[1], B. Daniel[1], T. Radlička[1], M. Oral[1], I. Konvalina[1]

[1]Institute of Scientific Instruments of the CAS, v. v. i., Electron Microscopy, Brno, Czech Republic

We present setting optimal measurement parameters of components of the time-of-flight (ToF) spectrometer (1) via electron tracing in the regions below the sample. The results of the optimization are used to generate a time-to-energy (T2E) conversion table and to consequently convert spectra measured in the time-domain (2).

The goal is to find optimal potentials on the electrodes of the ToF spectrometer which shall be used during measurement and in creation of the T2E conversion table.

A particle tracing library (3, 4) is used to generate data for a given set of values of voltages at the components of the ToF spectrometer for specified outgoing energies up to the landing energy (LE) and angles. The relevant part of the data consists of the triplet the ToF, the angle, and the energy. These values are used to construct a descriptor Q that is optimized to reach the best achievable properties of the spectrometer. Q consists of three interrelated contributions. The first is the signal S, ratio of the counts of the detected and emitted electrons. The second is the resolution R, constructed from a time-spread due to multiple electron trajectories with the same outgoing energy but different angles being detected. The third is the length of the spectrum in the time-domain T, the difference in the ToF corresponding to the LE and some (lower) reference energy. The quantity Q is optimized and the data set of the triplets (ToF, angle, energy) corresponding to the optimal point in the voltage space are used to generate the T2E conversion table.

The methods described above were used to optimize the potentials for LE = 50 eV to obtain the conversion table. A measurement on a graphene based sample was performed, see Figure 1, and the converted results are presented in Figure 2.

References:

(1) B. Daniel, T. Radlička, J. Piňos, E. Mikmeková, I. Konvalina, L. Frank and I. Müllerová, Proceedings of 16th International Seminar Skalský dvůr (2018), p 12-13, ISBN 978-80-87441-23-7.

(2) Companion contribution presented by B. Daniel at this conference

(3) M. Oral 1, O. Číp, L. Slodička, Proceedings of 16th International Seminar Skalský dvůr (2018), p 52-55, ISBN 978-80-87441-23-7.

(4) M. Oral, W. S. M. Werner, T. Radlička, J. Zelinka, D. Pescia, U. Ramsperger, G. Bertolini, Proceedings of SIMDALEE2017, p. 71

(5) O. Y. Ridzel, V. Astašauskas, and W. S. M. Werner, J. Electron Spectrosc. Rel. Phen. (2018)

Fig. 1: A measured time-domain spectrum.

Fig. 2: Spectrum from Fig. 1 converted to energy.

We have presented a method to suitably set up the ToF spectrometer for measurement at a given LE and to generate the T2E conversion table for the setup of the device. We have also shown converted spectra of some early measurements. The next step will be to extract the inelastic mean free path from the energy spectrum. Software based on the BRUCE library (5) will be used for that.

The authors acknowledge funding from the Technology Agency of the Czech Republic (TN01000008, TE01020118).

Fig. 1

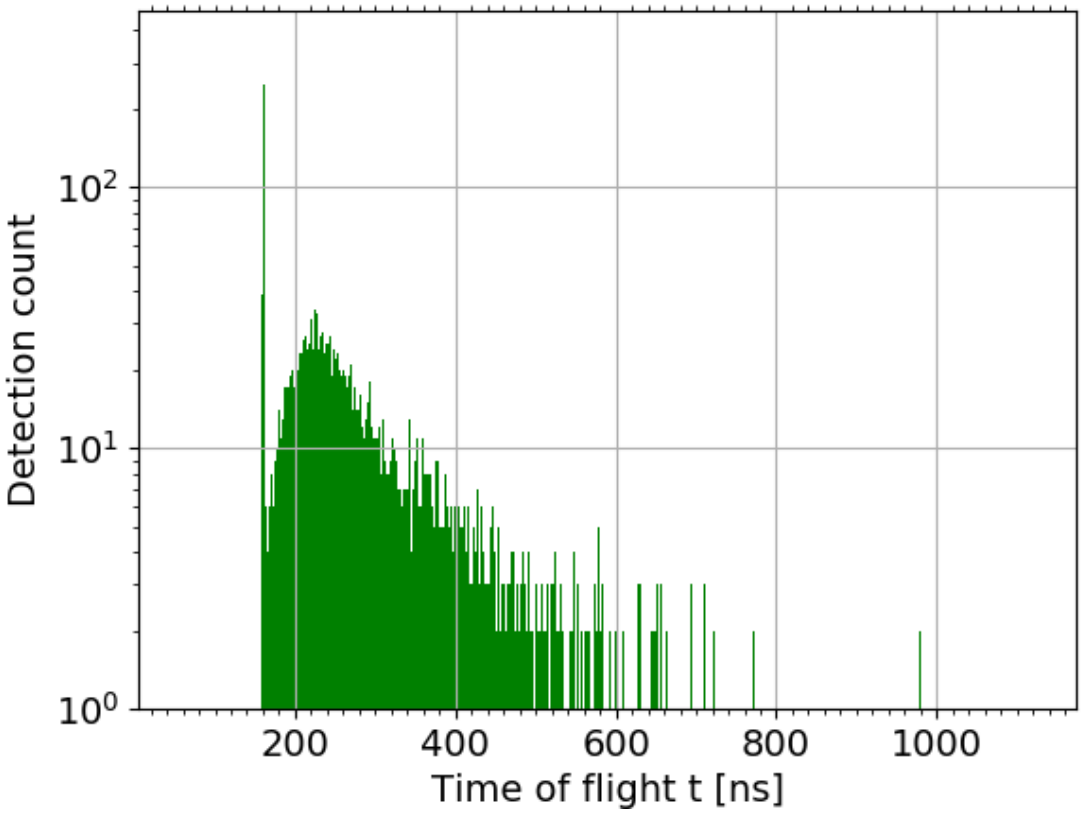
Detection count
10^2
10^1
10^0
200
400
600
800
1000
Time of flight t [ns]

Fig. 2

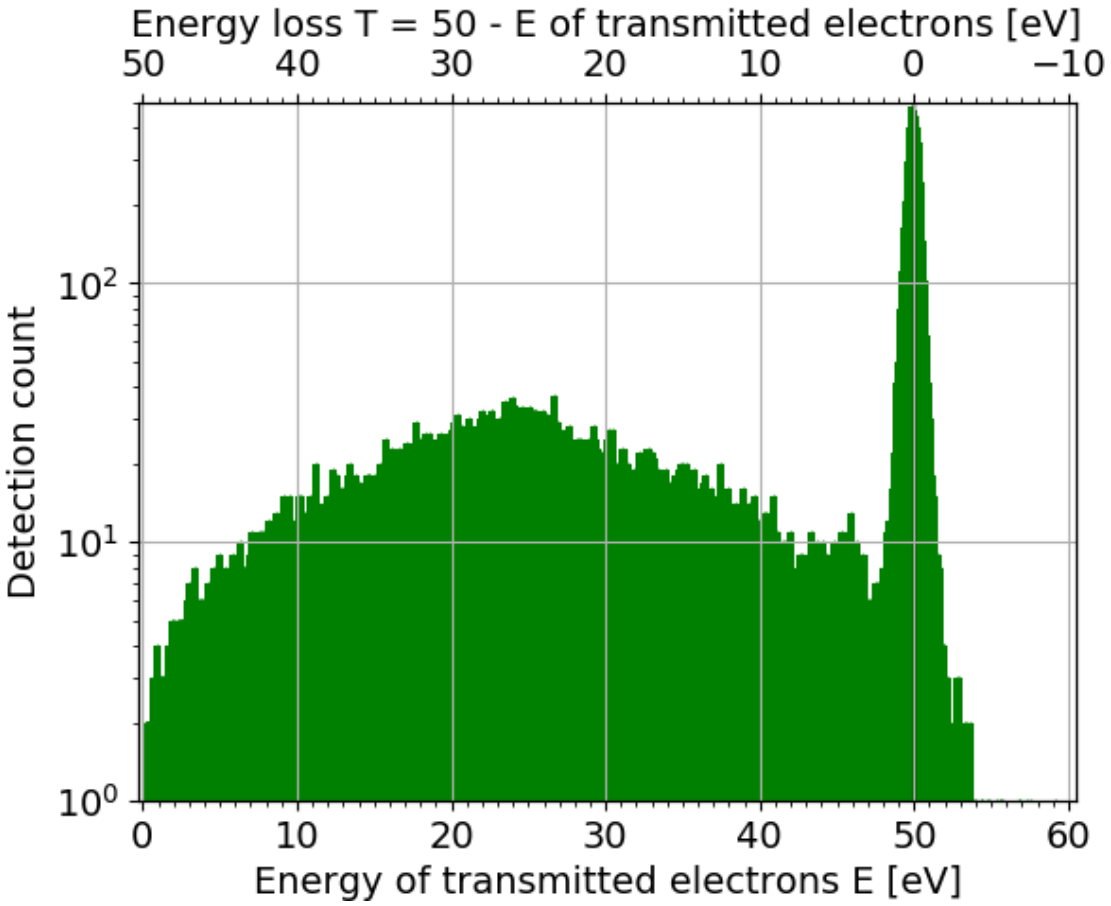
Energy loss T = 50 - E of transmitted electrons [eV]
50
40
30
20
10
0
−10
Detection count
10^2
10^1
10^0
0
10
20
30
40
50
60
Energy of transmitted electrons E [eV]

IM5.P009
Soft X-ray optics fabricated by focused ion beam patterning

C. M. Günther[1], M. Schneider[2], F. Büttner[3], D. Berger[1], S. Eisebitt[2,4]

[1]Technische Universität Berlin, Zentraleinrichtung Elektronenmikroskopie (ZELMI), Berlin, Germany
[2]Max Born Institut, Berlin, Germany
[3]Massachusetts Institute of Technology, Department of Materials Science and Engineering, Massachusetts, United States
[4]Technische Universität Berlin, Institut für Optik und Atomare Physik, Berlin, Germany

FIB-SEM is used for various purposes in specimen preparation, lithography and nanostructuring. All applications require special efforts to ensure reliable processes like high-aspect-ratio milling, defined milling depth or highly automated workflow for repetitive jobs. We highlight two applications from x-ray optics manufacturing whereby the used techniques apply for other tasks as well:

(i) X-ray Fourier-transform holography (FTH)

is a coherent imaging method which can be implemented as a lensless, mask-based approach (1). The key ingredient is a nanostructured optics mask, which is fabricated into a ~1 µm thick, soft x-ray opaque gold film deposited on a transparent silicon nitride membrane. Using a focused-ion beam (FIB), the reference and object apertures defining the holography geometry are fabricated in the gold film (see Fig. 1). The diameter of the reference aperture defines the spatial resolution in x-ray FTH, thus, a high aspect ratio (>10) is required to resolve structures below 50 nm. The goal for object apertures is to mill a blind hole keeping the x-ray transparent membrane intact. The granular structure of the gold layer makes the deterministic fabrication of both kinds of apertures difficult. Optimization steps beyond adapted milling parameters include material development of the holography mask with respect to FIB patterning. Here, the combination of a Cr/Au multilayer replacing the elemental gold in conjunction with reduced ion acceleration voltage allows for more homogenous FIB-milling.

Beyond the fabrication of the FTH apertures, FIB in combination with other lithography methods allows to integrate additional experimental components on the sample itself (2). In Fig. 2 we show a holography sample where a magnetic thin film is integrated with a strip line for the application of electrical current pulses in conjunction with integrated Hall-Voltage measurements.

(ii) In-situ x-ray fluence monitors

Free-electron lasers constitute a new type of x-ray source with unprecedented peak brilliance. However, from the intrinsic underlying SASE generation process originates a stochastic nature, i.e., the pointing and intensity of the pulses varies on a shot-to-shot basis. With a FIB we define curved gratings up to (50 µm)^2 overall size with locally varying angle and period on the order of 100 nm directly in x-ray transparent substrates (see Fig. 3). In x-ray small angle scattering experiments, the curved grating images the incident fluence distribution on the sample onto the detector used to record the primary diffraction pattern from the sample. The position and size of the fluence map generated in addition to the scattering pattern can be adjusted to avoid overlap and optimally use the detector area. In this way, for every single x-ray shot the diffraction signal from the sample can be measured together with the incident fluence distribution giving rise to that signal, allowing for quantitative experiments (3).

As experiments at X-ray free electron lasers are often carried out in a regime where a single shot destroys the sample, a new aspect is sample mass production. The processes presented above are partially automatable (4) allowing to pattern tens to thousands of membranes.

This work is financially supported by EFRE-project "Nano-Werkbank".

References:

(1) S. Eisebitt *et al.* Nature 432, 885-888 (2004).

(2) F. Büttner *et al.* Nat. Nano. 12, 1040 (2017).

(3) M. Schneider *et al.* Nat. Commun. 9**,** 214 (2018).

(4) F. Büttner *et al*. Opt. Express 21(25), 30563 (2013).

Fig. 1: Cross-section through the object (Ø: 1.5 µm) and reference aperture of a FTH mask.

Fig. 2: FTH sample with integrated current-pulse strip line and Hall cross.

Fig. 3: Curved grating milled into a silicon nitride membrane. The period ranges from 300nm to 170nm.

Fig. 1

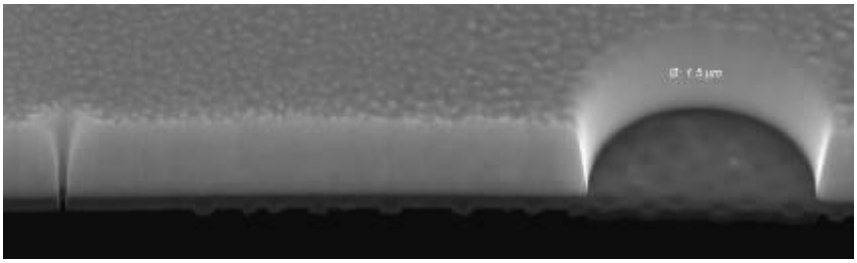

Fig. 2

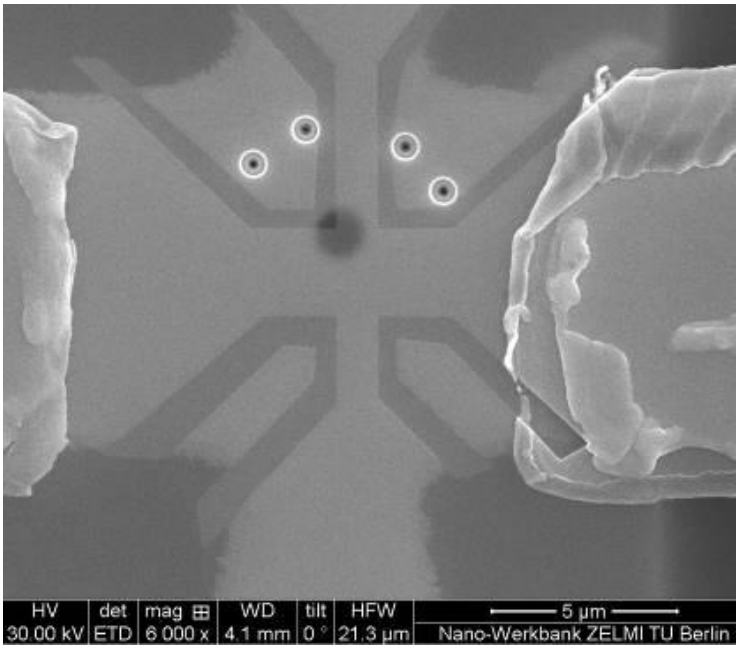

Fig. 3

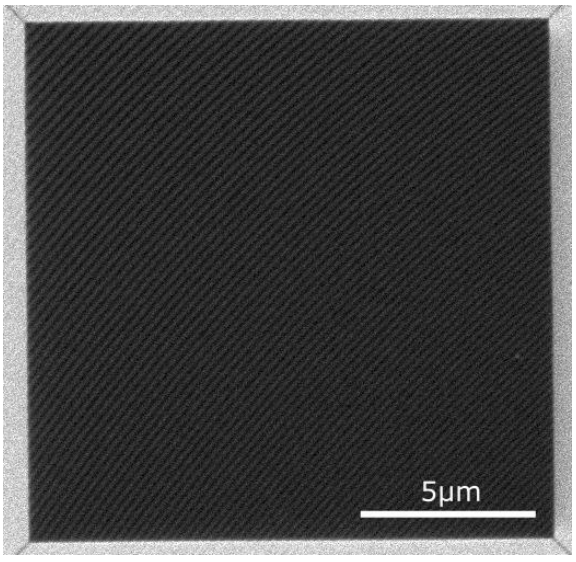

IM5.P010
Focused Ion Beam in Forensic Practice

M. Kotrly[1]

[1]Institute of Criminalistics, Praha, Czech Republic

Techniques of electron microscopy are widely used in the forensic field both for the initial screening and for final expert evaluation. Lately, focused ion beam have been used. Systems are significantly miniaturized and the dual SEM/FIB systems have become common laboratory devices.

Usage of the Ga+ ions represents probably the most widespread FIB technique. In the forensic field, the technique allows to add and remove material ("sections" on the molecular level), imaging in the secondary ions or to carry out ion microanalysis.

The toolmark examination, defectoscopy, metallography and technical diagnostic fields – visualization of deformation changes of materials, their documentation and description and possible detection of causes of deformation. Ion imaging allows good resolution of microstructural grain elements.

In the forensic practice, we most often meet nanocomposites in the form of colour variable pigments – protective elements (e.g. banknotes, documents), car paints, consumer electronics, etc. and in the functional layers of glass (smart glass) – thermoglass, car glass, etc.

Direct phase analysis from the surface does not provide enough information for a qualified comparison of these materials (e.g. to confirm counterfeit identification) and it is necessary to study the individual layers directly in an FIB section.

Study of so called thermogenetic particles which originate under physico-chemical processes with a sharp growth of temperature and pressure (post blast residues, gunshot residues, airbag particles, etc.) is very important as the detection of these particles can prove how a crime was committed. The particles have a specific chemical composition – based on genesis and source. In many cases, detailed structures of the inner particles cannot be identified unambiguously from the surface and often also phases that crystallize in the particles hollows are important. Also morphology of the particles wall structure is important.

Holograms and holographic seals are used more and more often to authorise documents, declare originality of products, etc. It is possible to make a hologram visually very similar to the original one but different in its inner structure. The aim of the analysis is to obtain detailed structural and other information to carry out comparison with the provided reference samples.

If a combination of a handwritten and printed document occurs, which is usually in connection to a will, bill of exchange, contract, etc., it is necessary to prove their originality. Sequence of strokes in case of "additional prints" on the already signed documents is significant for the authentication.

Using the SEM/FIB systems techniques brings new possibilities to the forensic science field and to the exploitation of the evidentiary value of evidence which, in the past, could be examined only with difficulties or was totally unexploitable. The technique was successfully used in the whole range of real cases, e.g. examination of post blast residues, analysis of functional layers of glasses, bill of exchange counterfeits, etc., where conventional techniques could not provide the unambiguous answer.

Microanalytical methods has been supported by the projects VI20152020035, VI20172020050.

IM5.P011
Adding a new imaging capability to an on-axis TKD detector

A. Bastos da Silva Fanta[1], A. Fuller[1], H. Alimadadi[1,2], M. Todeschini[1], D. Goran[3], A. Burrows[1,4]

[1]Technical University of Denmark, DTU Nanolab, Kongens Lyngby, Denmark
[2]Danish Technological Institute,, Aarhus, Denmark
[3]Bruker Nano GmbH, Berlin, Germany
[4]ISS Group Services Ltd, Manchester, United Kingdom

Transmission Kikuchi diffraction (TKD) in the scanning electron microscope has been developing since its emergence less than a decade ago. The recently introduced on-axis detector configuration (1), with its optimized geometry, has significantly increased the signal yield and consequently positively influenced the measurement parameters and speed. Furthermore, a Si diodes based imaging system attached to the detector allows the collection of STEM bright and dark field images. When combined with TKD orientation measurements, the SEM is practically transformed into a low voltage transmission electron microscope. In this perspective, a MEMS based heating system, conventionally developed for TEM in-situ investigation, can now be used in the SEM in combination with TKD to investigate dynamical behaviour of thin films and nano particles (2).

One current existing limitation of in-situ microstructure investigations with on-axis TKD is the simultaneous acquisition of STEM image and orientation measurements. The position of the imaging system, located outside the phosphor screen, requires a movement of the camera to acquire high resolution STEM images and high resolution orientation measurements. This work presents a solution to this limitation by introducing an additional imaging capability to the centre of the screen, which allows acquisition of STEM images and orientation maps without any detector movement.

In this presentation the development of the prototype detector with an additional imaging system will be described and compared to the standard on-axis TKD detector in terms of indexing precision and indexing rate. Furthermore, suggestion of improvement to the prototype design and additional developments ideas will be presented. Finally the combination of on-axis TKD and STEM images at elevated temperature using MEMS based heating system will be demonstrated and the advantages and limits of this new detector configuration discussed.

References:

(1) Fundenberger, J. J.; Bouzy, E.; Goran, D.; Guyon, J.; Yuan, H.; Morawiec, A. Orientation Mapping by Transmission-SEM with an on-Axis Detector. *Ultramicroscopy* 2016, *161*, 17–22.

(2) Fanta, A. B.; Todeschini, M.; Burrows, A.; Jansen, H.; Damsgaard, C. D.; Alimadadi, H.; Wagner, J. B. Elevated Temperature Transmission Kikuchi Diffraction in the SEM. *Mater. Charact.* 2018, *139*, 452–462.

Fig. 1: Illustration of STEM image and TKD orientation measurement acquired with the prototype detector

Fig. 1

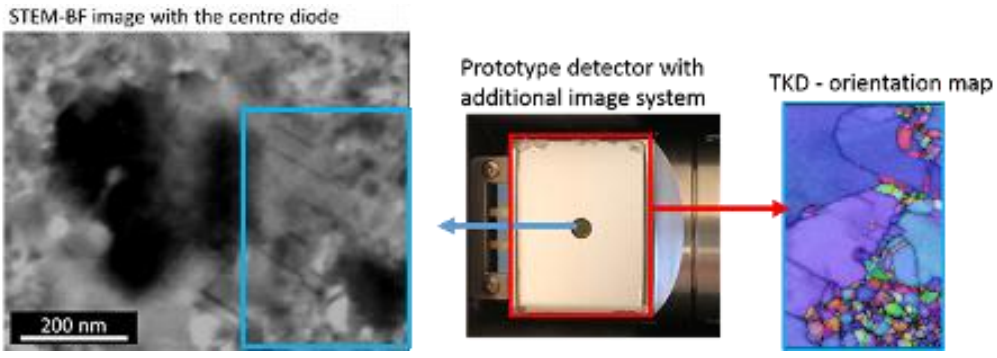

IM5.P012
Very Low Energy Electron Transmission Spectro-Microscopy

B. Daniel[1], M. Zouhar[1], T. Radlička[1], J. Piňos[1], E. Materna Mikmeková[1], I. Konvalina[1], L. Frank[1], I. Müllerová[1]

[1]Institute of Scientific Instruments of the CAS, v. v. i., Brno, Czech Republic

Scanning Low Energy Electron Microscopy (SLEEM) is a technique that combines an ordinary (low voltage) SEM with a biased specimen stage to form a cathode lens. This allows for specimen imaging using electron energies below 50 eV, while retaining resolution on the nanometer scale.

At such low energies, electron interaction with solids is changed and increased drastically in comparison to usual SEM with electron energies of at least several keV. The role of the atomic number for material contrast decreases, interactions of the electrons with the local density of states gain importance. As a result the mechanism of contrast formation in SLEEM is quite different and currently not well understood (1).

For investigation of interaction of low energy electrons with solids with the further goal of improved understanding of SLEEM contrast, a custom ultra high vacuum system has been built: A low voltage SEM with up to 5 keV beam energy was enhanced with a time-of-flight (ToF) spectrometer for energy analysis of electrons transmitted through thin samples. An in-house built 5 axis manipulator with a high voltage biased specimen stage allows precise alignment of the sample and choice of the electron landing energy down to 0 eV. Further capabilities of this system comprise detection of reflected on-axis electrons by magnetic separation, and angular resolution of transmitted electrons using a pixel-based detector. A schematic overview is given in Figure 1.

Due to the short inelastic mean free path at the used electron energies, samples used for ToF measurements need to exhibit a thickness well below 10 nm to allow for sufficient transmitted signal. Additionally the high influence of contamination at low energies puts high demands on the cleanliness of the samples. Since we are already equipped with an easy in-situ cleaning method for graphene (2), this is our material of choice for the first measurements. We intend to extend the range of samples to other layered materials and ultra-thin metal films in the near future.

First results for 25 to 200 eV electrons on graphene show a zero-loss peak with a tail, and a large peak at almost the same ToF for all landing energies, corresponding to less than 5 eV according to preliminary energy conversion. Some candidates for loss features could be found in the tail of the zero-loss peak, but only for low landing energies. These early results served as a motivation for development of an improved optimization technique of the setup of the device (3) as well as almost real-time pre-processing of data. Recent and ongoing updates are expected to increase resolution and allow detection of more subtle features even at higher energies.

References:

(1) I. Müllerová et al, International Journal of Nanotechnology 9.8-9 (2012) 695

(2) L. Frank, E. Mikmeková, M. Lejeune, Applied Surface Science 407 (2017) 105-108

(3) M. Zouhar, B. Daniel, T. Radlička, M. Oral and I. Konvalina: companion poster presented at this conference

The authors acknowledge funding from the Technology Agency of the Czech Republic (TN01000008) and (TE01020118).

This project has received funding from the People Programme (Marie Curie Actions) of the European Union's Seventh Framework Programme FP7/2007-2013/ under REA grant agreement no 606988.

Fig. 1: Schematic image of the system. Colors: Purple: high voltage, Orange: intermediate voltage, Blue: ground, Red: detectors

Fig. 1

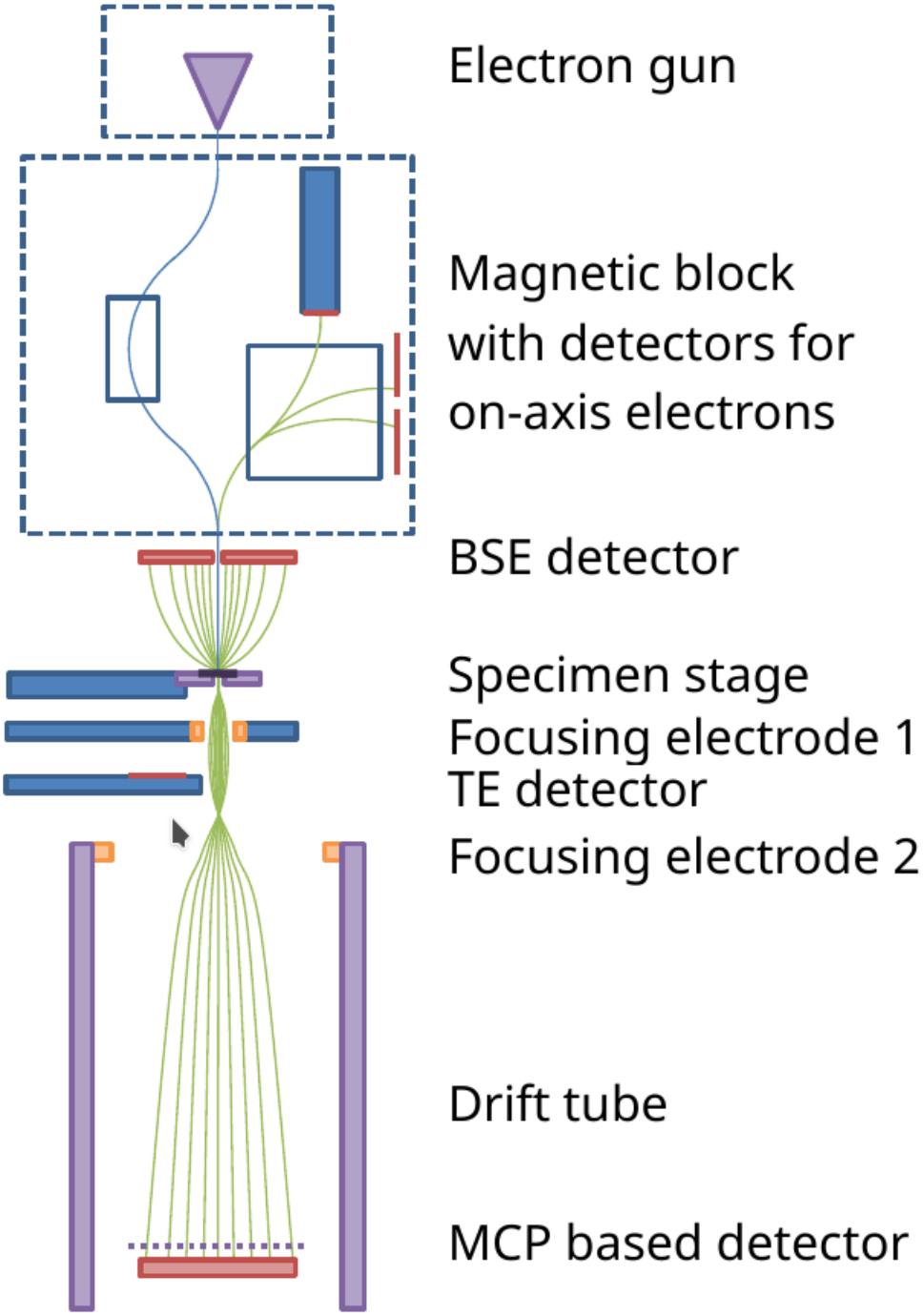
Electron gun
Magnetic block
with detectors for
on-axis electrons
BSE detector
Specimen stage
Focusing electrode 1
TE detector
Focusing electrode 2
Drift tube
MCP based detector

IM6.002 invited
Highly monochromatized EELS for ProBING elementary excitations and their interaction

O. Stéphan[1], M. Kociak[1], A. Gloter[1], L. H. Tizei[1], L. Bocher, X. Li[1], J. D. Blazit[1], M. Tencé[1], A. Zobelli[1], N. Brun[1], M. de Frutos[1], M. Walls[1], C. Colliex[1]

[1] Laboratoire de Physique des Solides, CNRS, UMR8502, Université Paris Sud, Orsay, France

Monochromation obviously improves the energy resolution in EELS but more importantly, it provides access to a wide range of elementary excitations in the low-loss range for primary applications in condensed matter physics and in the field of nano-optics. Its association with high-brightness cold field emission sources and efficient detectors makes it possible to probe the IR-vis-UV range via spatially or momentum-resolved experiments, therefore diversifying the information channels for exploring the physics of these low-energy excitations. As a matter of fact, EELS is bound to become a privileged technique for probing phonons, d-d transitions, charge transfer optical gaps, excitons or plasmons, and their coupling, in complementarity to well established synchrotron-based or optical techniques.

We will review the latest experiments performed with the recently installed Chromatem microscope in Orsay, a NION Hermes STEM for ultra-high energy resolution (down to 5-10 meV) in EELS and equipped with a light injection/detection system and a low-temperature stage. This will include examples of spatially- and or momentum-resolved experiments on individual plamonics nano-objects, plasmonic band-gap materials or correlated oxide thin films or nanostructures.

IM6.003
Surface Plasmon (De)localization in Ordered and Disordered Structures

A. Lubk[1], J. Schultz[1], P. Potapov[1], M. Mayer[2], T. König[2], A. Fery[2], K. Hiekel[3], A. Eychmüller[3]

[1]IFW Dresden, Institute for Solid State Research, Dresden, Germany
[2]IPF Dresden, Dresden, Germany
[3]TU Dresden, Department of Physical Chemistry, Dresden, Germany

Surface plasmons are oscillations of the charge carriers at interfaces between dielectric media of opposing permittivities such as between (noble) metals and air. They strongly couple to electromagnetic (e.g., optical) fields forming a surface plasmon polariton, which leads to interesting phenomena such as wave propagation, strong field confinement (below the optical wavelength) and enhancement. These are exploited in various applications such as wave guides, enhanced optical sensing, or improved solar cells. Accordingly, a key question is how to deliberately enlarge delocalization if strong propagation and transport effects are desired and how to suppress it if strong field enhancement should be achieved.

Strong ballistic propagation of waves occurs in highly dispersive and thus wide bands, which can be created in strongly coupled periodic geometries. Since the pioneering work of P.W. Anderson, it is also well-understood that wave functions have the tendency to localize due to structural disorder, because the interference on the disordered medium mostly randomizes the phases creating constructive interference at well-localized spots only. Here we study whether and how these concepts hold for surface plasmon polaritons by employing state-of-the-art STEM Electron Energy Loss Spectroscopy (to reveal the spatial and spectral distribution at highest resolution) in combination of analytical (to reveal the pertaining physical principles) and numerical (for quantitative comparison) models. STEM-EELS spectrum imaging was carried out at a monochromated Cs-corrected FEI TITAN3 TEM with improved energy resolution (ΔE: 50 meV) (1). Analytical models use a dipole interaction model, bearing resemblance of classical phonon formation physics, and correlation function analysis. For the computational solution we rely on the numerical solvers of Maxwell equations such as Boundary Element methods.

As ordered structure we employ highly periodic chains of highly crystalline Au nanoparticles arranged by wrinkled self-assembly. We show the formation of delocalized plasmon bands from degenerated single particle modes by tracking the evolution of the plasmon mode structure from single particles to long chains beyond 20 NPs (Fig. 1). We show that the emerging surface plasmon bands can be qualitatively understood through a dipole coupling model on a periodic grid, which admits analytical solutions similar to that of a elastically coupled chain of atoms. On the disordered end of the road we employ highly disordered 2D Au networks (Fig. 2). Here we reveal the spatially localized character of the surface plasmons and discuss the spatial and spectral distribution in the context of Anderson localization and transition. Our findings pave the way for plasmon band engineering in complex ordered nanostructures.

References:

(1) Lopatin et al., Ultramicroscopy 184, 2017

(2) We have received funding from the European Research Council (ERC) under the European Union"s Horizon 2020 research and innovation programme (grant agreement No 715620).

Fig. 1

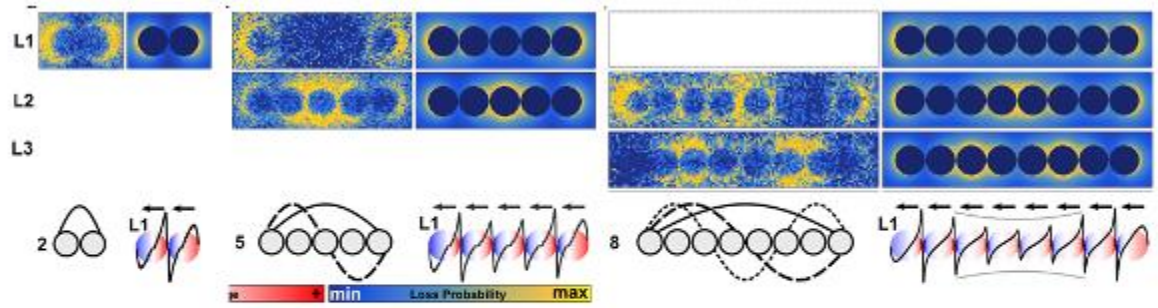

Figure 1: Surface Plasmon hybridization and band formation: Individual NP (diameter: 70 nm) modes hybridize and split up in energy due to interparticle interaction. Accordingly longitudinal modes (Ln) with different node numbers form as revealed by spatially resolved EELS maps and simulations. The lower row displays the dipole fields located on the NPs.

Fig. 2

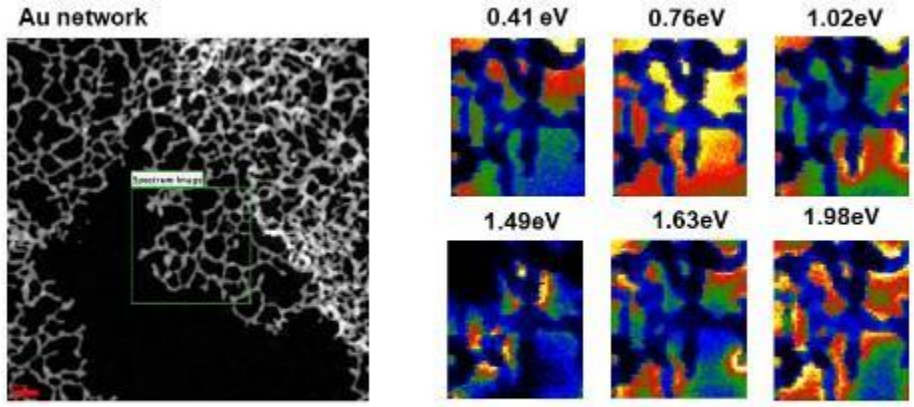

Figure 2: Localized Surface Plasmon modes on a disordered Au network (average grid width: 7 nm): Both energetically and spatially strongly localized modes as revealed by STEM-EELS.

IM6.004
Beam Energy, Sample Geometry dependent Fabry-Pérot Interference in Coherent Cathodoluminescence of Semiconductors in STEM

M. Stöger-Pollach[1], K. Bukvišová[2,1], M. Horák[2]

[1]TU Wien, USTEM, Vienna, Austria
[2]CEITEC, Brno, Czech Republic

Cathodoluminescence has attracted interest in scanning transmission electron microscopy since the advent of commercial available detection systems. Yamamoto and co-workers (1, 2) have already done a detailed study on the light emission of semiconductors under electron beam irradiation. It includes the first hint about the influence of the sample thickness on the emitted spectrum, but a systematic study with respect to sample thickness, beam energy and sample geometry cannot be found anywhere in literature up to now. Beside this influence of the sample thickness, also the beam energy and the presence of interfaces or edges are altering the emitted light spectrum. This has a tremendous impact on the interpretation of CL spectra from semiconducting materials.

In the present study, we compare experimental data from Si and GaAs samples with simulations using Yamamoto's theory of light emission for slab geometry (1). Additionally we study the influence of the lateral dimensions of a sample and the presence of sample edges. This is leading to a completely new picture of CL spectra of semiconductors recorded by employing a (scanning) transmission electron microscope (S/TEM).

As soon as the beam energy surpasses the Cerenkov limit (3) the intensity of coherent CL signal increases and starts to dominate the incoherent signal with respect to beam energy (Fig 1a) and sample thickness (Fig. 1b) related to Fabry-Perot like interference (4).

In a scanning electron microscope (SEM) the situation is completely different, because the sample geometry shows a nearly in infinite thickness (in relation to the wave length of visible light). But back-scattered electrons may also excite Cerenkov radiation which is then collected by a CL system, too. On the other hand, if CL is performed on semiconducting nano-objects, similar artifacts can be expected as long as the beam energy surpasses the Cerenkov limit.

References:

(1) N Yamamoto *et al*, Surf. Int. Analysis 31 (2001) p. 79-86.

(2) N Yamamoto *et al*, J. Electron Micorsc. 45 (1996) p. 64-72.

(3) M Stöger-Pollach, Micron 39 (2008) p. 1092-1110 and M. Horak, M. Stöger-Pollach, Ultramicroscopy 157 (2015) p. 73-78.

(4) M. Stöger-Pollach *et al*, Ultramicroscopy (2019) *accepted*

The authors acknowledge financial support by SINNCE project of the European Union's Horizon 2020 programme under the grant agreement No. 810626.

Fig. 1: a Electron energy dependent CL spectra of 700 nm thick Si (top: simulation, bottom: experiment). b Thickness dependent CL spectra of Silicon recorded with 200 keV electrons.

Fig. 1

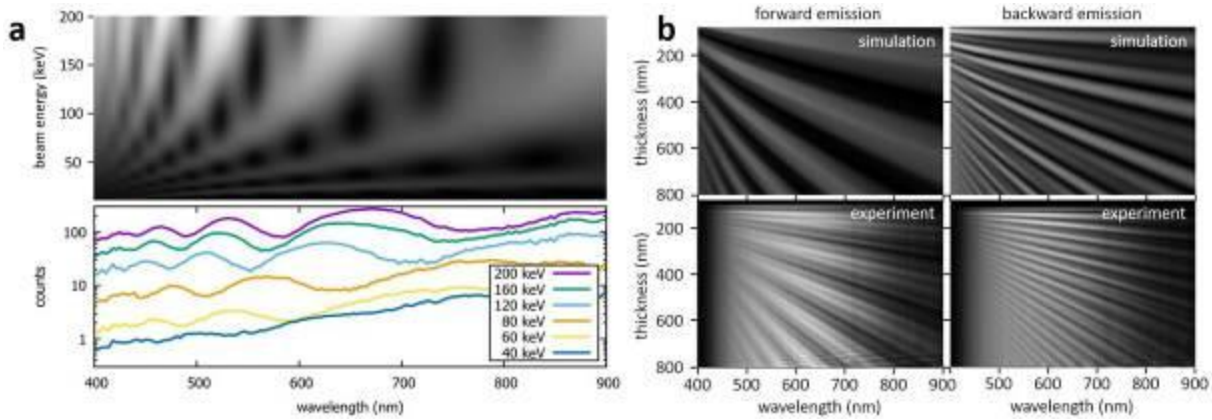
a
beam energy (keV)
200
150
100
50
counts
100
10
1
200 keV
160 keV
120 keV
80 keV
60 keV
40 keV
400
500
600
700
800
900
wavelength (nm)
b
forward emission
backward emission
simulation
simulation
experiment
experiment
thickness (nm)
thickness (nm)
200
400
600
800
400
500
600
700
800
900
wavelength (nm)
wavelength (nm)

IM6.005
Progress in vortex filter EMCD: Experimental evidence and sub-nanometre resolution

T. Schachinger[1,2], S. Löffler[1,2], A. Steiger-Thirsfeld[1], M. Stöger-Pollach[1,2], A. Tavabi[3], F. Venturi[4], V. Grillo[5], M. Horák[6], C. Eisenmenger-Sittner[2], R. Dunin-Borkowski[3], P. Schattschneider[1,2]

[1]TU Wien, USTEM, Vienna, Austria
[2]TU Wien, Institute of Solid-State Physics, Vienna, Austria
[3]Forschungszentrum Jülich, Ernst Ruska-Centre (ER-C), Jülich, Germany
[4]University of Nottingham, Faculty of Engineering, Nottingham, United Kingdom
[5]CNR-Nano, Modena, Italy
[6]Brno University of Technology, CEITEC, Brno, Czech Republic

Soon after the inception of electron energy-loss magnetic chiral dichroism (EMCD) (1), an intimate connection to the orbital angular momentum (OAM) of the probing electron has been put forward (2). In inelastic scattering processes in magnetic materials, a chiral electronic transition transfers OAM in units of from the beam to the probed atom, producing atom-sized electron vortex beams (EVBs) (3).

In this work, new evidence will be given that holographic vortex masks (HVMs), typically used to impart OAM to electrons, can be employed in an imaging STEM-like geometry (Fig.1a), to filter the outgoing inelastically scattered electrons for their OAM content, i.e. to yield an EMCD signal. This approach neither relies on the standard EMCD geometry and the specimen"s role as a beam splitter nor does it require a tedious crystal alignment. The difficulties of this approach were already pointed out in (4). Here, a simplified setup and the improvement of the SNR will be addressed.

Experiments were done on a Titan Holo at the ER-C equipped with a wide-gap polepiece, where a 40 µm phase HVM was inserted in the objective aperture holder. Additional experiments using the setup given in (4) with a 30 µm binary absorption HVM were done on a Tecnai F20. The samples were sputtered 30 nm Fe films on SiNx-membranes and cross-sections of a FeRh layer. Our in-house inelastic multi-slice simulation (IMS) code was used to estimate the EMCD signal and incoherent source size broadening (ISSB) effects.

Fig.1b shows rotationally averaged radial profiles of the energy-filtered EVBs after passing 30 nm Fe and careful astigmatism and defocus control. The difference signal, $IDiff=2\,(I+(r)-I-(r))/(I+(r)+I-(r))$, where $I\pm(r)$ are the respective EVBs" radial profiles for $m=\pm1$, can be reproduced using IMS, showing sub-nanometre spot size. A reversal of $IDiff(r)$ can be observed for the L2-edge, see Fig.1c. Fig.1d and e were taken on a FeRh alloy at 450K. Upon magnetisation reversal, the difference signal changes its sign accordingly. Atomic scale IMS mappings show a significant variation of *IDiff* over the unit cell (Fig.2).

Experiments on different machines and samples show difference signals that fit well to IMS with improved SNR. Signal reversals between the L3 and L2-edges, as well as for parallel and antiparallel magnetisation were observed, hinting at a faint EMCD signal. Sub-nanometre resolution could be achieved and IMS mappings suggest that even atomic resolution should be feasible using Cc corrected machines and improved HVMs.

References:

(1) P. Schattschneider, Nat. 441, 486-488 (2006)

(2) P. Schattschneider, UM 106, 91-95 (2008)

(3) J. Verbeeck et al., Nat. 467, 301-304 (2010)

(4) T. Schachinger et al., UM 179, 15-23 (2017)

(5) Financial support by the ÖAW, HJST (H-294689), FWF (P29687-N36), Horizon 2020 program (Q-SORT, Grant: 766970) and the sample preparation of Arthur Weber is acknowledged.

Fig. 1: a) Experimental setup of vortex filter EMCD. (b) Rot. avg. of m=±1 EVBs at 710eV, 10eV slit, measured at the Titan Holo at 300kV on 30nm Fe and df~0nm, with IDiff curves and the IMS simulation for an ISSB of 0.4nm. (c), the same as (b) but for the L2-edge. (d), the same as (b) but for 50nm FeRh at parallel and (e) anti-parallel lens field, taken at the Tecnai.

Fig. 2: Vortex filter EMCD IMS maps of IDiff over a bcc-Fe unit cell including ISSB, computed for t=30nm and α=7mrad, ß=5mrad, Cs=2.7mm, U=300kV, df=73nm and ISSB=0.1nm. Green circles represent the Fe-atoms.

Fig. 1

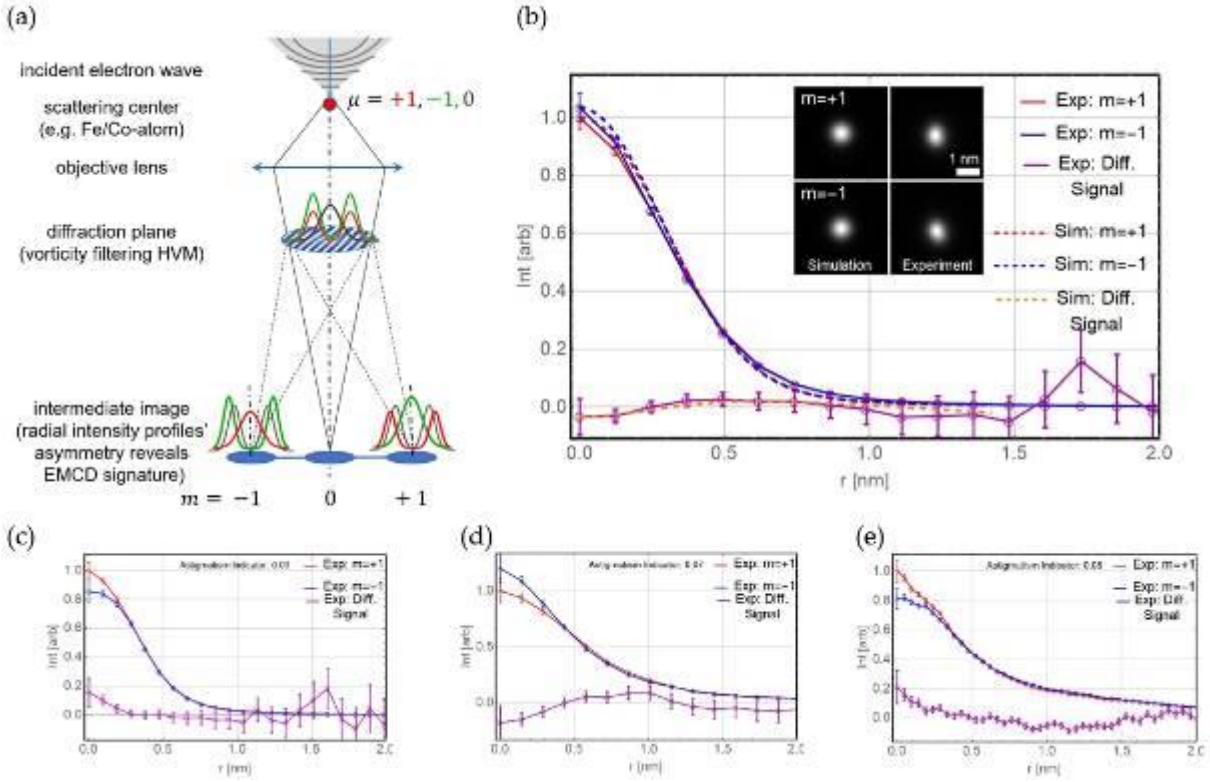

Fig. 2

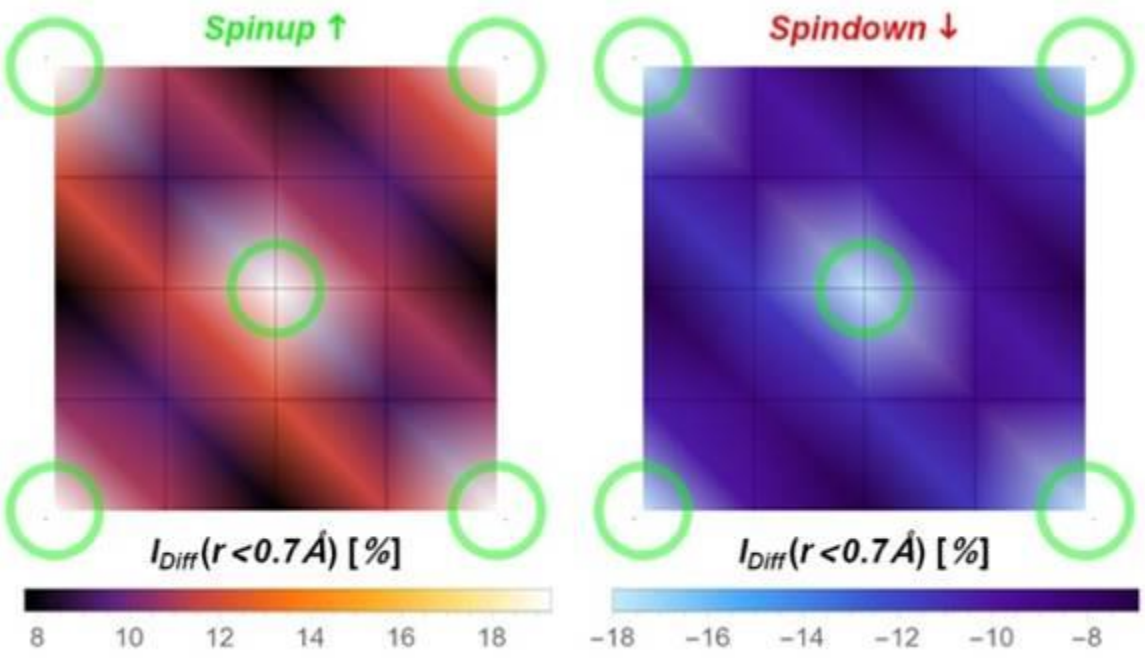

IM6.006
On/off-the-fly methods for optimizing atomically resolved STEM spectrum imaging

Y. Wang[1], M. R. S. Huang[1], U. Salzberger[1], K. Hahn[1], V. Srot[1], W. Sigle[1], P. A. van Aken[1]

[1]Max Planck Institute for Solid State Research, Stuttgart Center for Electron Microscopy, Stuttgart, Germany

Recent advances in instrumentation hardware have made chemical analysis, i.e. electron energy-loss spectroscopy (EELS) and energy-dispersive X-ray spectroscopy (EDXS), at atomic resolution readily possible. However, the acquisition and interpretation of atomically resolved spectra can still be problematic due to, for instance, image distortions or poor signal-to-noise ratio (SNR) spectra, especially for investigating energy-loss near-edge fine structures. To achieve a decent SNR, STEM spectrum imaging (SI) requires much higher electron doses and longer dwell times (pixel exposure times) than for STEM imaging. Consequently, these distortions become more serious in SI data. Instabilities combined with long dwell times may create substantial image distortions, i.e. expansion, compression, and/or shearing of the lattice that limit the interpretability of the results.

In this contribution, we report the development of on/off-the-fly methods for optimizing atomically resolved STEM SI. The first technique is used to post correct (off-the-fly) image distortions in atomically resolved SI and diffraction imaging (1). We demonstrate the correction of linear and nonlinear distortions, the feasibility of this tool for 4D-STEM diffraction imaging, and the application for maximizing the elemental mapping area. In the second technique, by combining multi-frame spectrum imaging and automatic energy-offset correction, we report an on-the-fly SI technique for minimizing image distortions and improving the SNR of EELS spectra (2). The energy-offset correction technique significantly reduces correlated noise (3), as for successive spectra different camera pixels are exposed which precludes amplification of small gain normalization errors. We have implemented these techniques into STEM SI for atomically resolved EELS elemental and fine-structure mapping. Using practical examples, we demonstrate that multi-frame SI and post-alignment can effectively suppress image distortions and improve the final elemental-map quality. The energy-offset correction method reduces the correlated noise and helps to resolve weak features of the near-edge fine structures. The final SI with improved SNR enables the extraction of individual component maps of the Ti-L2,3 near-edge fine structure and of a Ti-O-Ti bonding direction map at atomic resolution in SrTiO3 (Figure 1), which has been theoretically predicted but extremely difficult to detect experimentally due to the poor SNR of the spectrum (4). Combining multi-frame SI and automated energy-offset correction, we demonstrate that these techniques will open new opportunities for atomically-resolved EELS fine-structure mapping. Moreover, this multi-frame SI technique also paves the way for low-electron-dose imaging techniques to reduce damaging of the sample (5), as well as the possibility for atomically resolved imaging and SI at cryogenic temperatures.

References:

(1) Y Wang *et al.,* Microscopy 67 (2018), p.i114.

(2) Y Wang *et al.,* Ultramicroscopy 184 (2018), p. 98.

(3) M Bosman, V J Keast, Ultramicroscopy 108 (2008), p. 837.

(4) M J Neish *et al.,* Phys. Rev. B 88 (2013), p. 115120

(5) L Jones *et al.,* Microscopy 98 (2018) p. i98.

Fig. 1: Fine structure mapping of the Ti-L2,3 and O-K edges in SrTiO3 via multi-frame and energy-offset correction acquisition. (a) Schematic diagram showing the processing of the multi-frame SI. (b) The individual components map of the Ti-L2,3 edges: L3 t2g, L3 eg, L2 t2g, and L2 eg, respectively. (c) Structure of SrTiO3. Oxygen bonding direction maps extracted from multi-frame EELS SIs obtained by MLLS fitting to the O1- and O2 -K edge spectra.

Fig. 1

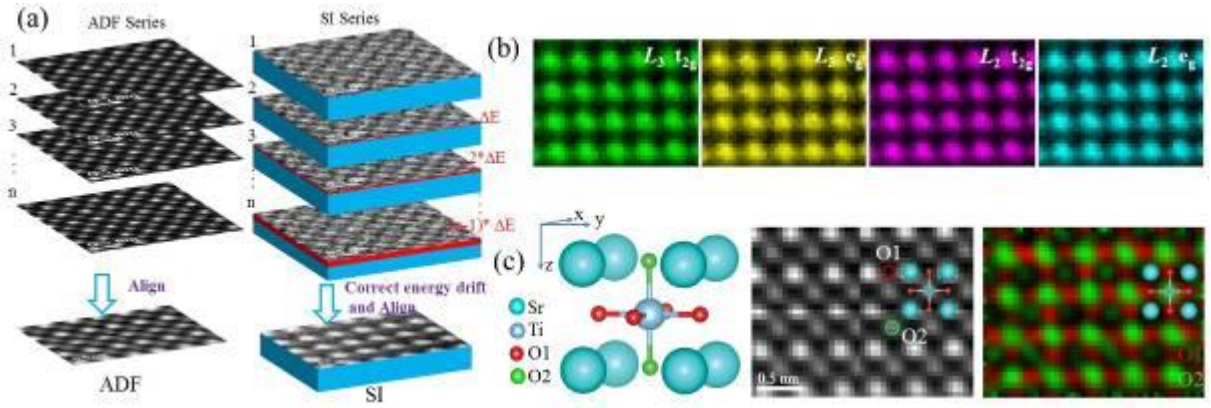
(a)
ADF Series
SI Series
Align
Correct energy drift and Align
ADF
SI
(b)
(c)
Sr
Ti
O1
O2
O1
O2
0.5 nm

IM6.P001
Using STEM EDX Mapping and Mono-EELS To Understand The Reaction Kinetics Of Environmentally Relevant Iron OxideMinerals For Water Remediation

H. Freeman[1], J. P. H. Perez[2,3], N. Hondow[1], L. G. Benning[2,3,4], A. P. Brown[1]

[1]University of Leeds, School of Chemical and Process Engineering, Leeds, United Kingdom
[2]Helmholtz Centre Potsdam - GeoForschungsZentrum, Potsdam, Germany
[3]Free University of Berlin, Department of Earth Sciences, Berlin, Germany
[4]University of Leeds, School of Earth and Environment, Leeds, United Kingdom

Green rust (GR) minerals are redox-active, mixed valent Fe(II)-Fe(III), layered-double hydroxides, which are a promising solution for groundwater remediation as they are able to remove toxic metal contaminants from water by adsorption (1), reduction (2), interlayer intercalation (3) and substitution of structural Fe (4). When adsorbing arsenic (a significant pollutant in groundwater and of concern due to its wide distribution and toxicity), GR should remain stable and not transform into other iron (oxyhydr)oxides (e.g., goethite), which are less effective adsorbents (1,5). To assess the stability of the reacted GR, it is important to know the spatial distribution of the adsorbed material and its effect on the Fe(II):Fe(III) ratio. Possible redox transformations can heavily impact the toxicity and mobility of As in soils and groundwaters.

We have used scanning transmission electron microscopy (STEM) imaging combined with energy dispersive X-ray (EDX) mapping and dual-acquisition monochromated electron energy loss spectroscopy (mono-EELS) to determine the spatial distribution of As species adsorbed on GR and to quantify the Fe(II):Fe(III) ratio for both pure and As-reacted GR.

We have recently established the low fluence conditions required to collect such data; in pure GR, an Fe(II)/Fe(III) ratio of ca. 2 was measured (as expected) at 50 e-Å^{-2} however, above this fluence, the ratio logarithmically decreased and dropped to ca. 0.5 after 1000 e-Å^{-2} (6). This trend was approximately the same for both conventional and cryogenic sample preparation techniques implying that it is the beam alone which causes valence state changes, and not exposure to oxygen during transfer into the TEM or the vacuum of the TEM column. Using these low fluence operating conditions on GR reacted with As(III) and As(V) we measured Fe(II)/Fe(III) ratios of ca. 1.4 and 1.2 respectively. The HAADF-STEM images show different surface morphologies for pure GR, GR+As(III) and GR+As(V). These results, combined with adsorption isotherm results, strengthen previous findings that suggested that As(III) forms monodentate mononuclear (1V) and bidentate binuclear (2C) inner-sphere complexes on the GR particle edges (1,5,7).

References:

(1) J. Jönsson, D.M. Sherman, Sorption of As(III) and As(V) to siderite, green rust (fougerite) and magnetite: Implications for arsenic release in anoxic groundwaters, Chem. Geol. 255 (2008) 173–181.

(2) E.J. O"Loughlin, S.D. Kelly, R.E. Cook, R. Csencsits, K.M. Kemner, Reduction of uranium(VI) by mixed iron(II)/iron(III) hydroxide (green rust): Formation of UO2 nanoparticles, Environ. Sci. Technol. 37 (2003) 721–727.

(3) P. Refait, P. Buaer, A.A. Olowe, J.M.. Genin, The substitution of Fe2+ ions by Ni2+ ions in the green rust compound studied by Mossbauer effect, Hyperfine Interact. 57 (1990) 2061–2066.

(4) I.A.M. Ahmed, S. Shaw, L.G. Benning, Formation of hydroxysulphate and hydroxycarbonate green rusts in the presence of zinc using time-resolved in situ small and wide angle X-ray scattering, Mineral. Mag. 72 (2008) 159–162.

(5) J.P.H. Perez, H.M. Freeman, J.A. Schuessler, L.G. Benning, The interfacial reactivity of arsenic species with green rust sulfate (GRSO4), Sci. Total Environ. 648 (2019) 1161–1170.

(6) H. Freeman, J.P. Perez, N. Hondow, L.G. Benning, A.P. Brown, Beam-induced oxidation of mixed-valent Fe (oxyhydr)oxides (green rust) monitored by STEM-EELS, Micron. In Press, (2019).

(7) Y. Wang, G. Morin, G. Ona-Nguema, F. Juillot, F. Guyot, G. Calas, G.E. Brown, Evidence for different surface speciation of arsenite and arsenate on green rust: An EXAFS and XANES study, Environ. Sci. Technol. 44 (2010) 109–115.

IM6.P002
The influence of x-ray absorption on tomographic reconstruction of spectral data

T. Krekeler[1], M. Ritter[1]

[1]Hamburg University of Technology, Electron Microscopy Unit, Hamburg, Germany

Electron tomography is a well-established method to obtain the 3D *structure* of nanoscale materials. To obtain the 3D *composition* of these materials, EDX tomography is the most common methods to choose, if EFTEM is not available. Due to shadowing and small detector sizes of single EDX detector systems, the technique was limited to small tilt angles or needle shaped specimen. With the introduction of multiple, large area EDX detectors, 3D imaging techniques based on tomographic reconstruction of x-ray data got easier, faster and applicable on other sample geometries.

However, the absorption of x-rays in tomography samples may lead to errors in the tomographic reconstruction as the reconstruction algorithms require images which fulfil the projection requirement (1). While the x-ray absorption in homogenous samples can be corrected, dense sample materials and their spatial orientation relative to the detector may introduce additional absorption effects.

In this work, we investigate x-ray absorption during acquisition of spectrum images at different tilt angles and the effect of the absorption on the tomographic reconstruction using a TEM equipped with four EDX detectors (Talos F200X with SuperX G2 by Thermofisher).

The sample material consists of a thin tungsten layer in hafnia prepared by magnetron sputtering (2). Tungsten acts as strong absorber for soft x-rays while the sputtered hafnia emits both hard (Hf Lα 7.9 keV) and soft x-rays (O Kα 0.52 keV).

A 100 nm thick FIB lamella on a lift-out grid was positioned in the TEM with great care to assure normal orientation of the sample surface to the electron beam and of the tungsten layer to the holder axis (Figure 1) and thereby facilitating the comparison of x-ray data.

Figure 2 shows the experiment setup to examine the absorption of low energy x-rays in the tungsten layer depending on the azimuth and elevation angle (ψ and α) of the EDX detector. The elevation angle of α = 22° is the same for all detectors, as the sample was not tilted. Only detector 1 & 2 were used (azimuth angle ψ = 45° and 135°). Detector 3 & 4 (ψ = 225° and 315°) were ignored because of detector shadowing from the lift-out grid (3).

The absorption of oxygen x-rays depending on the azimuth angle ψ is visualized in figure 3. The image intensities and line profiles show clearly, that the tungsten layer acts as an absorber for low energy oxygen x-rays, while no absorption of hard Hf Lα x-rays is observed.

This effect shows the necessity of careful data acquisition and processing at varying azimuth and elevation angles as absorption may result in errors in quantification or tomographic reconstruction.

References:

(1) P.W. Hawkes, Electron Tomography, Plenum Press, New York, London, 1992.

(2) Vinod et al, Vacuum 155 (2018) 339-344.

(3) Yeoh et al, Microscopy and Microanalysis, 21, 3, 759-764.

Fig. 1: HAADF Image of HfO_2:W:HfO_2 stack with position of EDX Detectors.

Fig. 2: Experiment setup showing attenuation of soft x-rays in the tungsten layer.

Fig. 3: Net intensities of Hf Lα and O Kα detected by EDX Detector 1 & 2. Image intensities and ratio (Hf:O) show strong absorbance of soft x-rays depending on azimuth angle of detector.

Fig. 1

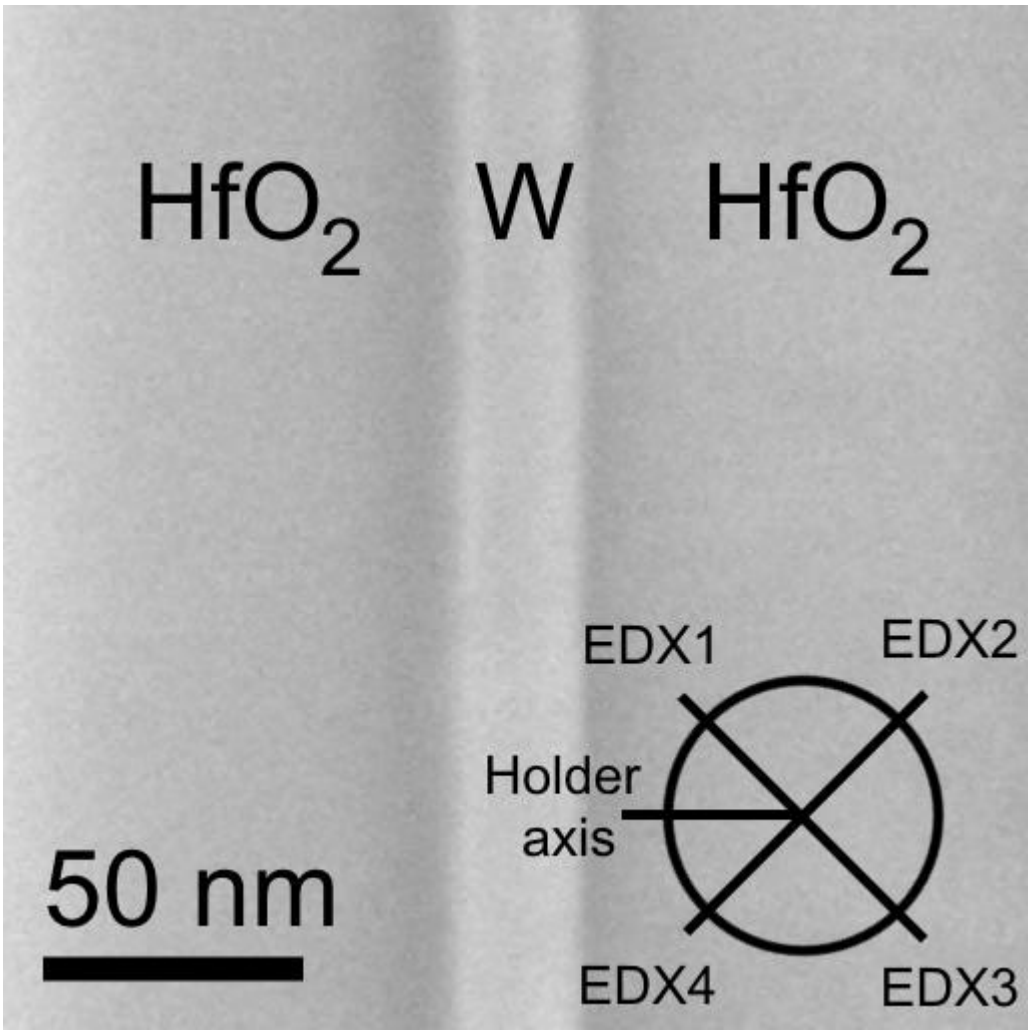
HfO2
W
HfO2
EDX1
EDX2
Holder
axis
50 nm
EDX4
EDX3

Fig. 2

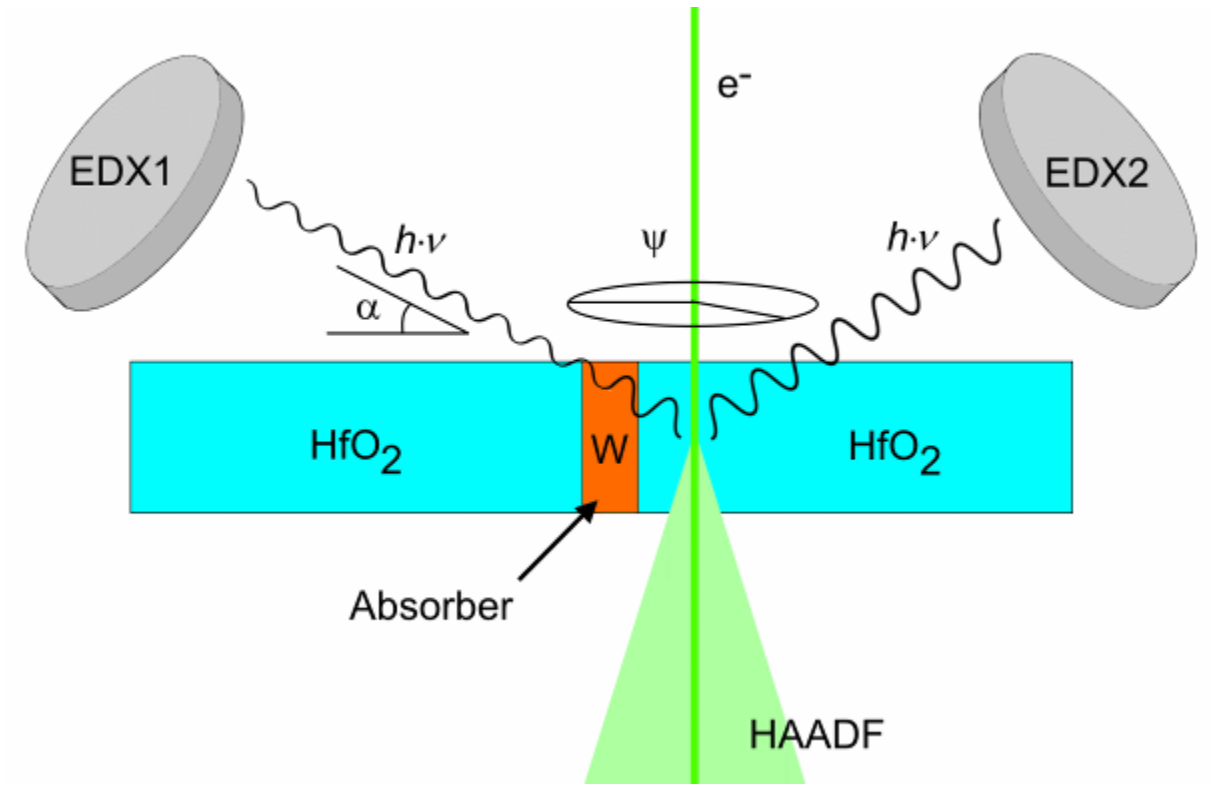
e-
EDX1
EDX2
h·ν
ψ
h·ν
α
HfO2
W
HfO2
Absorber
HAADF

Fig. 3

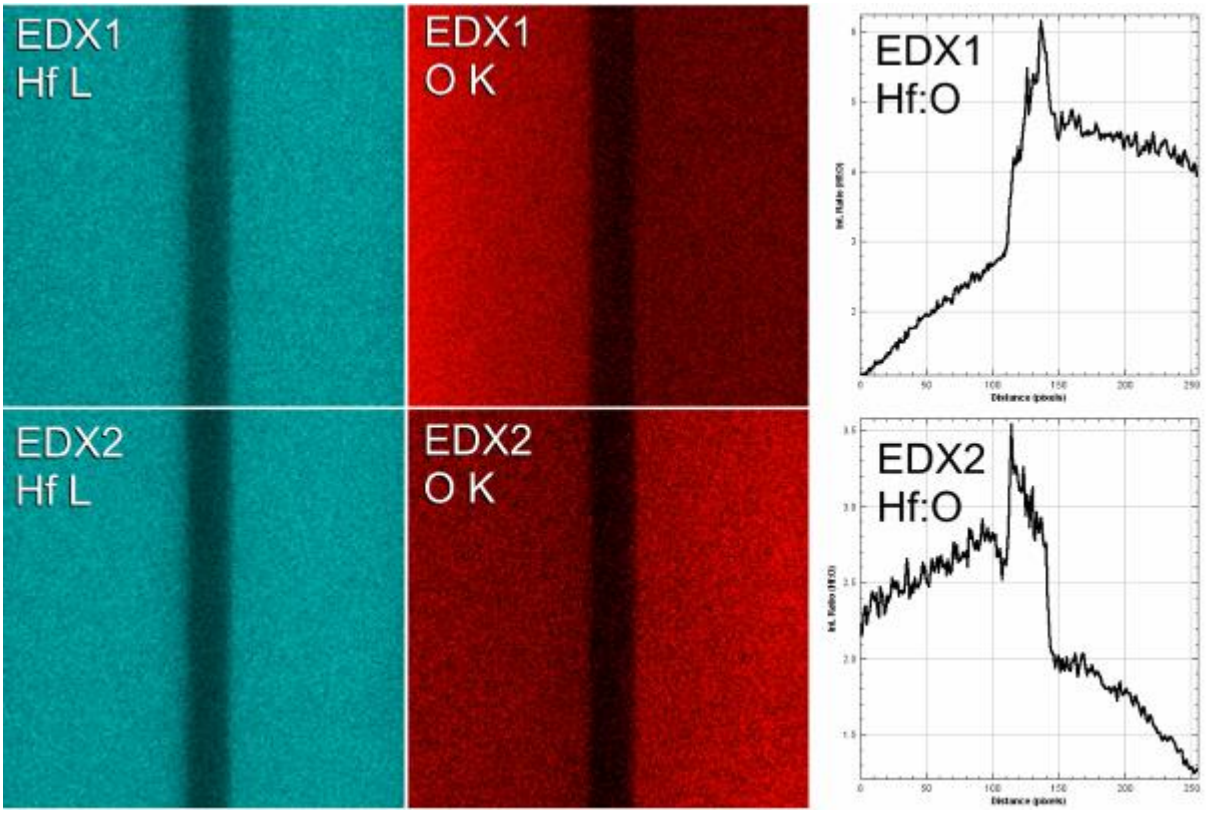

IM6.P003
Including the zero-loss peak and plural scattering in the quantitative analysis of low-loss EELS

A. Eljarrat[1], C. T. Koch[1]

[1]Humboldt University of Berlin, Institute of Physics, Berlin, Germany

Quantitative analysis of image, diffraction or spectroscopic data in transmission electron microscopy (TEM) is many times formulated as an inverse problem in which the observations are related to the material and instrumental properties that produced them. Kramers-Kronig analysis (KKA) is an inverse algorithm obtaining from low-loss electron energy-loss spectroscopy (EELS) the underlying dielectric function. Conventional KKA has a limited range of application as relativistic effects such as Cerenkov loss are not included and the result implicitly relies on our ability to subtract the zero-loss peak (ZLP) tails and suppress plural-scattering effects.

Following our recent development of a relativistic KKA (rKKA) algorithm (1), we present a new version that processes the full raw spectrum at each iteration. This is achieved by including the effect of ZLP and plural-scattering using Fourier-logarithmic deconvolution and its forward analogue, Fourier-exponential convolution operations. As in the previous version, the Kroeger formulation of the surface and bulk full-relativistic double differential cross section (DDCS) is employed. Our objective is to use this algorithm for stand-alone measurement of the dielectric function from low-loss EELS obtained in homogeneous regions of thin-film samples.

This new relativistic algorithm is based on a forward model of the recorded low-loss EELS signal. Hence, it has been designed and thoroughly tested using model-based realistic synthetic data, including; bulk and surface relativistic effects in thin-film samples (1); the effect of ZLP tails and plural-scattering; and detector issues such as noise or gain intensity offset. We have also treated experimental spectra from a variety of semi-conductor materials.

Figures 1 and 2 show rKKA results for AlN and GaN reference spectra from the EELS database (2), respectively. In the top panel (a), light and dark blue areas present the raw and corrected EELS data, respectively. The corrected EELS data has been stripped off the contribution of relativistic effects and the ZLP model, which are presented as a pointed and solid line, respectively. The rKKA algorithm iteratively updates this correction and ZLP model. In both cases, the algorithm converges (typically in a few iterations) to a situation in which the remaining inelastic intensity after subtraction of the correction is well adjusted to the ZLP model. The expected values for AlN and GaN are indicated using a black arrow, these are 6.2 and 3.4 eV, respectively.

Panel (b) compares the dielectric absorption (imaginary part of the dielectric function) of AlN and GaN, obtained from conventional and relativistic KKA algorithms, in blue and red solid lines, with calculated density functional theory (DFT) references (3), in black dashed lines.

In addition to showing the expected results in our synthetic data tests, the relativistic KKA has already shown excellent performance on experimental data. In AlN and GaN the band gap energy region of the materials is revealed after deconvolution of the ZLP model. In both cases an excellent agreement with the reference data is obtained taking into account the spectral broadening and effect of the bulk plasmon (not included in the DFT simulations).

References:

(1) A. Eljarrat and C.T. Koch arXiv: 1811.07575, 2018

(2) www.eelsdb.eu

(3) Yu and Cardona "Fundamentals of Semiconductors", Springer 2010

Fig. 1

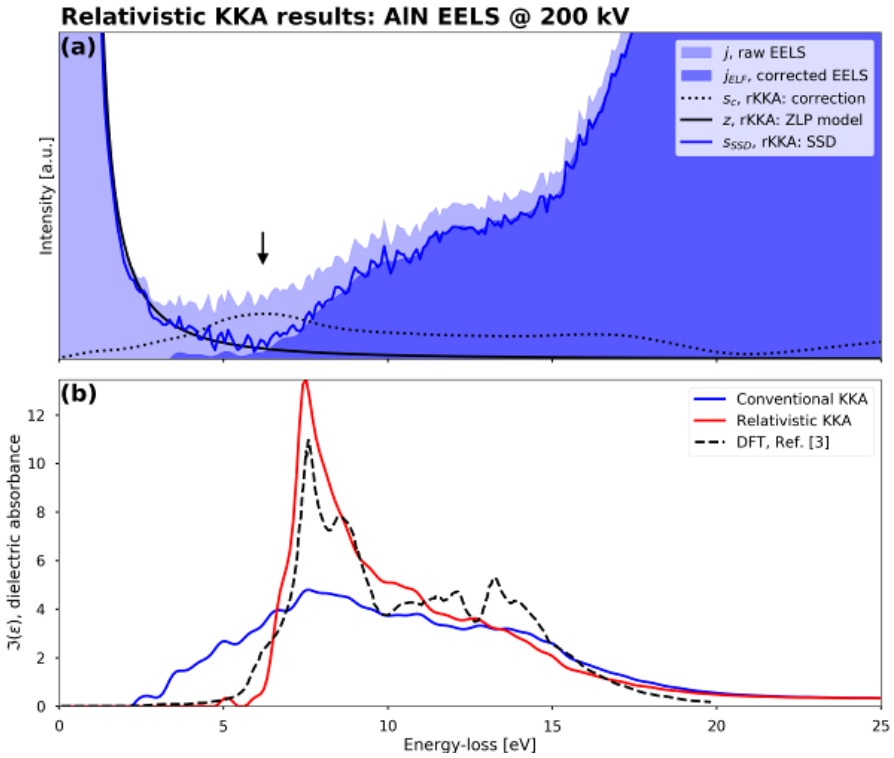
Relativistic KKA results: AlN EELS @ 200 kV
(a)
j, raw EELS
j_{ELF}, corrected EELS
s_c, rKKA: correction
z, rKKA: ZLP model
s_{SSD}, rKKA: SSD
Intensity [a.u.]
(b)
Conventional KKA
Relativistic KKA
DFT, Ref. [3]
ℑ(ε), dielectric absorbance
Energy-loss [eV]

Fig. 2

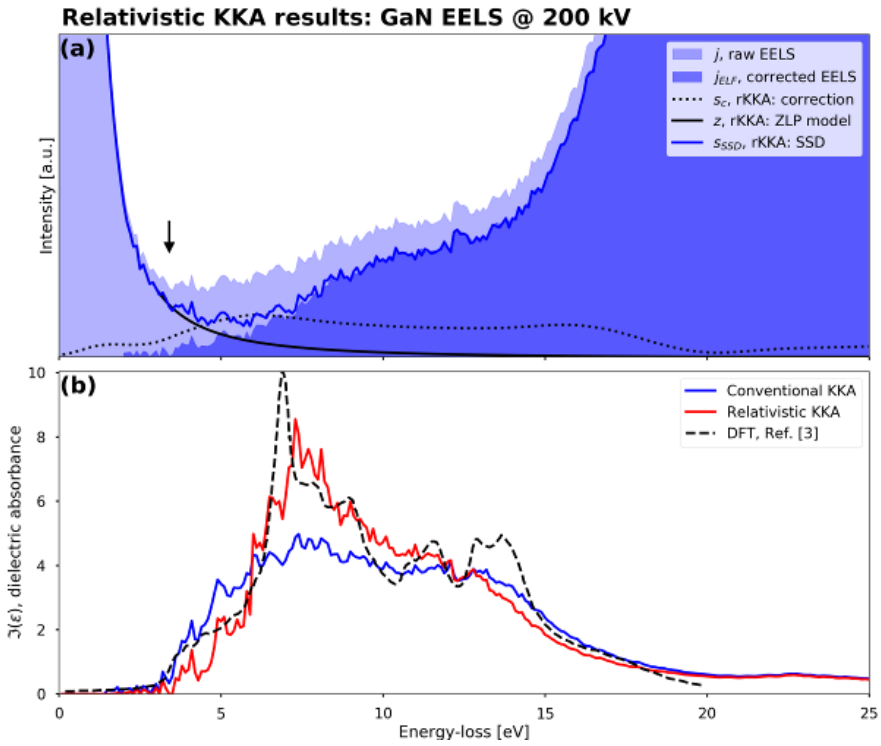
Relativistic KKA results: GaN EELS @ 200 kV
(a)
j, raw EELS
j_{ELF}, corrected EELS
s_c, rKKA: correction
z, rKKA: ZLP model
s_{SSD}, rKKA: SSD
Intensity [a.u.]
(b)
Conventional KKA
Relativistic KKA
DFT, Ref. [3]
ℑ(ε), dielectric absorbance
Energy-loss [eV]

IM6.P004
Investigations of the quantitative analytical depth resolution at metal layers with field emission electron probe microanalysis

J. Nissen[1], D. Berger[1]

[1]Technische Universität Berlin, Center for Electron Microscopy (ZELMI), Berlin, Germany

X-ray element analysis with high spatial resolution is of great importance for many applications in material analysis. Hereby, not only the qualitative resolution, but especially the quantitative resolution, which delivers the exact element composition, is in the focus of interest. So far we investigated the lateral analytical resolution whereby "lateral" indicates the horizontal x-/y- directions. In accordance with many other published results, we measured the best value for the qualitative lateral resolution to be 26 nm at a Si-Au interface (1). To determine the quantitative lateral resolution, different thin metallic layers were analysed in cross-section. For quantitative analysis we use a field emission electron probe microanalyser (FE-EPMA) with the benefits of high spectral resolution and of high signal to noise ratio of the wavelength dispersive X-ray spectrometers (WDX) . Hereby, quantitative lateral resolutions of 140 to 170 nm for Au layers, 150 to 210 nm for Ag layers and 260 to 280 nm for Al layers were proved (2, 3).

The aim of this work, now, is to determine the quantitative depth resolution at thin metallic layers with different thicknesses, generated by vapour deposition onto silicon substrates, and to compare measured, simulated and calculated data. A quantification result of 100.0 +/- 0.5 wt% of the respective layer element and no signal from the substrate indicates that the source volume of the emitted X-rays is completely inside the layer. For comparison the volume of generated X-ray is estimated by Monte Carlo (MC) simulations (casino v2.48) of the electron scattering in the material for electron energies between the primary energy and the critical ionisation energy of the corresponding X-ray line. Furthermore, the quantitative depth resolution is calculated as the ionisation range of electrons (4) whereby the very small self-absorption is neglected.

Figure 1 shows the results of the measurements, simulations and calculations for aluminium and silver layers. The layer thickness is determined from calibrated SEM images of FIB-produced cross-sections. Since the measurements are based on 5 respectively 6 specimen with different layer thickness, the measured depth resolution is specified as a range. The thinnest layer that can be resolved quantitatively in depth is 150 nm thick for Al, measured with 3 kV, as well as for Ag, measured with 5 kV. Regarding the simulated and calculated resolutions, there is a good correspondence with the measured data, except at low keV, where the measured resolution is worse. We have already noticed the same discrepancy for the lateral resolution measurements. The reason for this is not clear yet. Since the effect is the same for the lateral and for depth resolutions, any drift effect can be excluded.

References:

(1) Berger D and Nissen J 2014 *IOP Conf. Ser.: Mater. Sci. Eng.* 55 012002

(2) Berger D and Nissen J 2016 *IOP Conf. Ser.: Mater. Sci. Eng. 109 012001*

(3) Berger D and Nissen J 2018 *IOP Conf. Ser.: Mater. Sci. Eng.* 304 012002

(4) Merlet C and Llovet X 2012 *IOP Conf. Ser.: Mater. Sci. Eng.* 32 012016

Fig. 1: Comparison of simulated, calculated and measured depth resolutions at evaporated

Al layers and Ag layers.

Fig. 1

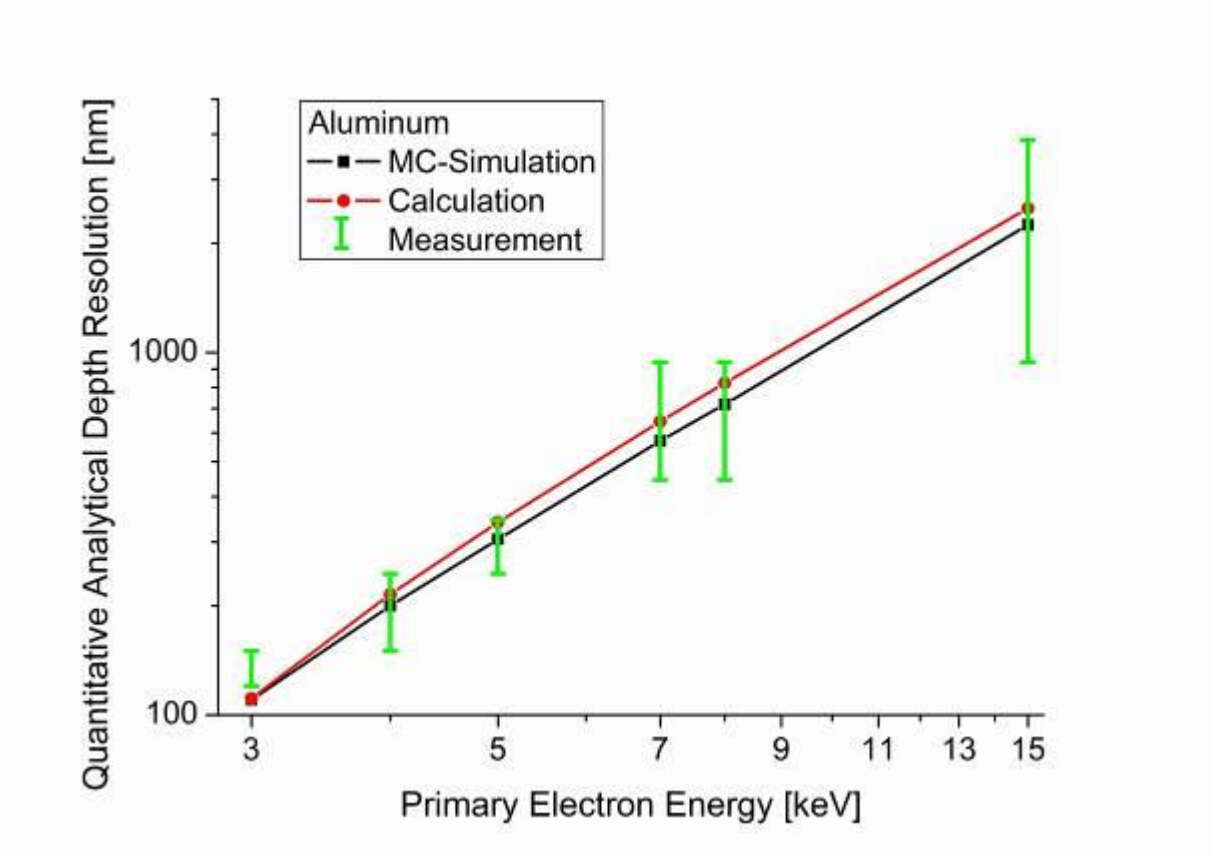
Aluminum
MC-Simulation
Calculation
Measurement
Quantitative Analytical Depth Resolution [nm]
1000
100
3
5
7
9
11
13
15
Primary Electron Energy [keV]

Fig. 2

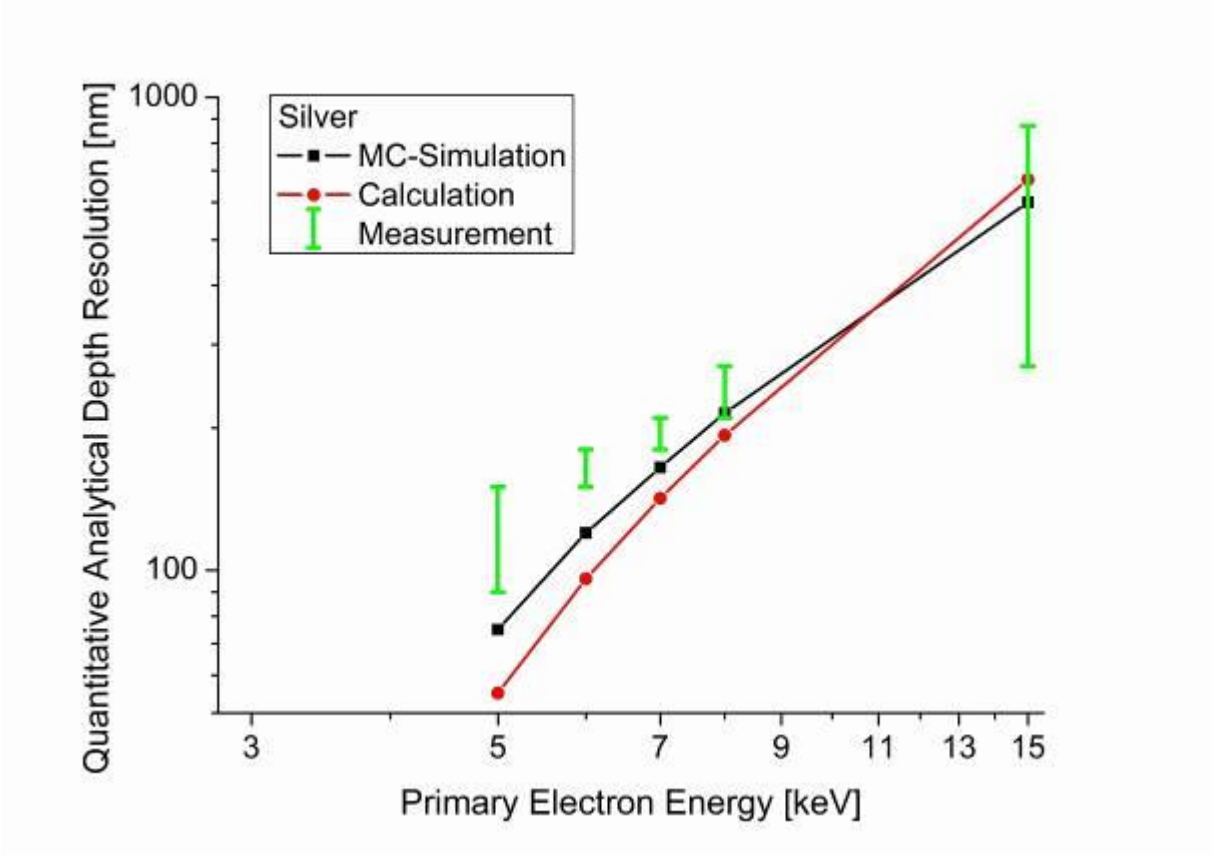
Silver
MC-Simulation
Calculation
Measurement
Quantitative Analytical Depth Resolution [nm]
1000
100
3
5
7
9
11
13
15
Primary Electron Energy [keV]

IM6.P005
Elastic and inelastic contrast in atomic-resolution EFTEM of graphene

M. J. Mohn[1], J. Biskupek[1], U. Kaiser[1]

[1]Universität Ulm, Materialwissenschaftliche Elektronenmikroskopie, Ulm, Germany

In energy-filtered TEM with large energy windows of several eV, chromatic aberrations of the objective lens strongly deteriorate the spatial resolution. Especially in combination with the broad energy distribution of ionization-edge signals, this makes atomic-resolution EFTEM impossible in standard C_S-corrected TEM. With C_C-corrected TEM, however, atomic-resolution EFTEM has been demonstrated, and at 300 kV, lattice fringes were shown with the silicon $L_{2,3}$ edge signal (1). Likewise, the first C_C/C_S-corrected low-voltage TEM "SALVE" (2) allows for atomic-resolution EFTEM even at low acceleration voltages between 20 and 80 kV. Here, we demonstrate its capabilities with experiments at 80 kV, showing lattice contrast in the C-K edge signal from only a single layer of graphene. With our experiments, we investigate the prospects of atomic-resolution EFTEM for beam-sensitive materials. Moreover, we want to analyze the influence of elastic and inelastic scattering in both the low-loss and core-loss regime.

For this purpose, a single layer of graphene is the perfect sample: For one thing, it is ultimately thin, which minimizes effects of multiple scattering. For another thing, the very high stability of graphene is crucial for our experiments. At low acceleration voltages of 80 kV or less, graphene withstands extremely high electron doses and allows for very long exposure time, as compared to other two-dimensional materials. Even with this high stability of graphene, the signal-to-noise ratio in the core-loss filtered images is a big challenge. Despite extremely high electron doses on the order of 10^9 e^-/nm^2, only very low signal is detected on the camera as only one in several thousand primary electrons will contribute to our C-K edge signals (~300 eV energy loss). Therefore, we have to average over multiple unit cells of graphene, in order to evaluate the lattice contrast in the EFTEM images. Our EFTEM experiments were carried out with correction to sufficiently small C_C, and a small positive C_S of a few µm. We have selected energy windows of 20 eV in a GIF Quantum energy filter.

All of our experimental results seem to show the preservation of elastic contrast in the high-resolution EFTEM images. As a consequence, we find that it is possible to obtain both bright- and dark-atom contrast even on the C-K ionization edge. In all cases, at same defocus, the core-loss filtered images showed the same kind of contrast as the zero-loss filtered images (see Figure 1).

This suggests that the image formation is still dominated by phase contrast. Our results pose the question whether "purely inelastic" imaging is possible in energy-filtered TEM at all. We acknowledge helpful discussions with H. Rose (Universität Ulm), M. Linck and H. Müller (CEOS GmbH).

References:

(1) K. W. Urban et al., Phys. Rev. Lett. 110, 185507 (2013)

(2) M. Linck et al., Phys. Rev. Lett. 117, 076101 (2016)

Fig. 1: 80 kV high-resolution EFTEM images of single-layer graphene. (a) Raw signal from the C-K edge with FFT showing graphene reflections (inset, contrast enhanced). (b,c) Dark- and bright-atom contrast signal from the zero-loss signal (ZL, top) and from the C-K ionization edge (bottom), averaged over >100 unit cells.

Fig. 1

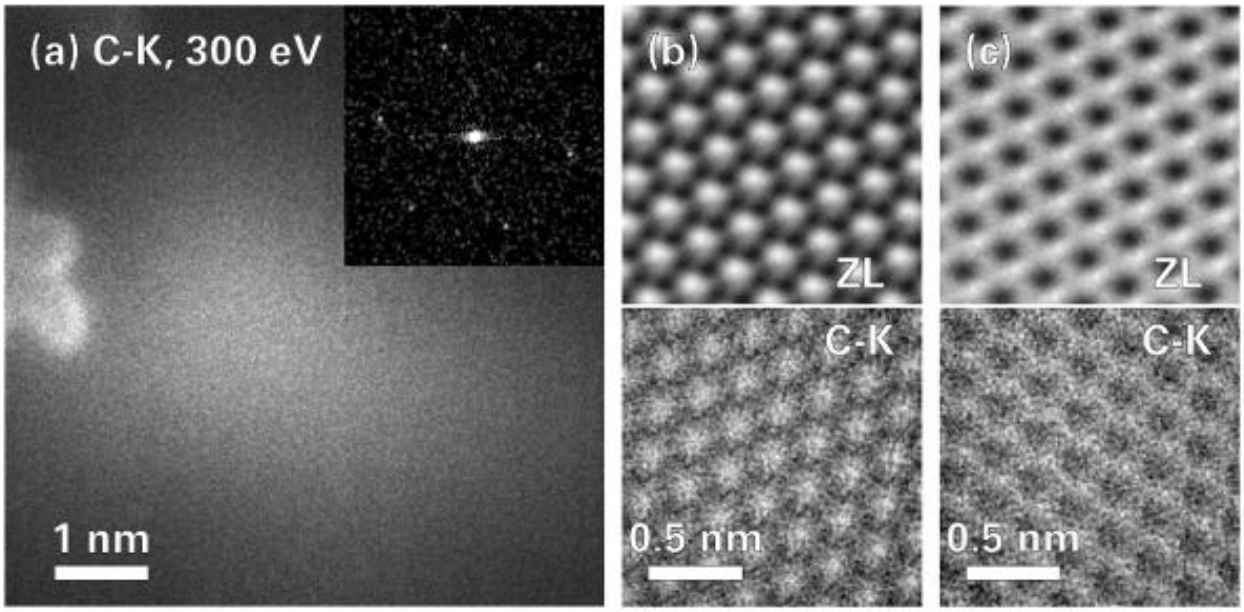

IM6.P006
Characterization of Si surface crystallinity by SEM-SXES

Y. Yamamoto[1], N. Muraya[2], T. Murano[2], H. Takahashi[2]

[1]JEOL Ltd., EP Application Department, EP Business Unit, Akishima, Tokyo, Japan
[2]JEOL Ltd., SA Business Unit, Akishima, Tokyo, Japan

Soft X-ray Emission Spectroscopy (SXES) with high energy resolution is a useful method for chemical state analysis by detecting the variation of energy and spectral shape. Recently, the soft X-ray spectrometer that can be installed on electron microscopes such as Transmission Electron Microscope (TEM) and Scanning Electron Microscope (SEM) has been developed (1). Especially, Field Emission (FE)-SEM can analyze chemical state in a bulk sample using a low voltage electron beam. Moreover, it is possible to change depth of information by changing the incident voltage (2).

Usually, the difference in crystalline state is confirmed by X-ray Photoelectron Spectroscopy (XPS) analysis (3). However, SEM-SXES has also possible to analyze the crystalline state. We have already reported about analyzing Si (c-Si) and amorphous Si (a-Si) by SEM-SXES. And it can be confirmed that the chemical state was altered due to their crystallinity (4).

In this study, using the amorphous Si layer on Si wafer, we attempted to compare both the SEM-SXES analysis using low incident voltages and XPS analysis. And we evaluate crystallinity of silicon surface by SEM-SXES.

The purpose of this study is to confirm the accuracy of SEM-SXES analysis by XPS using Si surface, and to understand the capability of depth analysis by SXES on Si surface crystallinity.

The system for this study is Schottky FE-SEM (JEOL JSM-7900F) combined with the soft X-ray spectrometer (JEOL SS-94000SXES). The detection energy range of SS-9400SXES is from 50eV to 210 eV and energy resolution is 0.3 eV. Samples for this study are; Si wafer of c-Si (Sample A) and Si wafer with a 4-5 nm thickness a-Si layer on the surface (Sample B). And Si wafer with an 8-9 nm thickness a-Si layer on the surface (Sample C). To check the spectrum shape change caused by the a-Si layer close to sample surface, each sample was analyzed by SXES at an incident voltage of 500 eV. Furthermore, we carried out XPS analysis using JEOL JPS-9030, to check the change in crystallinity for each of the Si wafers. Finally, we analyzed Sample C by SXES at incident voltages of 2 keV, 1 keV, and 500 eV for the depth analysis study.

Figure 1 shows X-ray spectra of Si L2, 3-M1, obtained from each sample by SEM-SXES analysis at 500 eV incident voltage. In this case, characteristic X-ray of Si is generated from each sample with a depth of around a 9 nm (Fig.2). Spectral shape of Sample B is observed to be a combination of the spectra from Sample A and Sample C. This is presumed to be due to a 500 eV electron beam which excites both the surface layer of a - Si and the c - Si region inside. This result is consistent with the result of XPS analysis as shown in Fig.3.The result in Fig.4 indicates that the spectrum shape changes with lower incident voltage. This result suggests the possibility of depth analysis of Si surface crystallinity using SXES by changing incident voltage.

These results from the low incident voltage SEM-SXES lead to the possibility of a new evaluation technique for the change in crystallinity of the bulk sample surface.

References:

(1) M. Terauchi et al, *Journal of Electron Microscopy*, Volume 61, (2012), P. 1–8

(2) H. Takahashi et al, Microscopy and Microanalysis 22(S3):422-423 (2016)

(3) Delfino. F, et al., J.Appl.Phys.70-3(1991), 1712

(4) Y. Yamamoto et al., Microscopy and Microanalysis 24(S1):1062-1063(2018)

Fig. 1

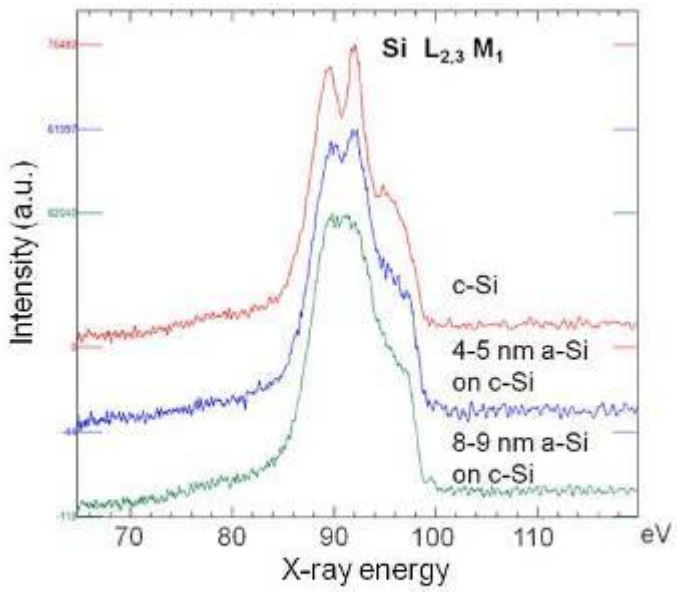

Fig.1. SXES result: Si $L_{2,3}$-M_1 spectra of different thickness amorphous layers on Si, at 500 eV incident voltage

Fig. 2

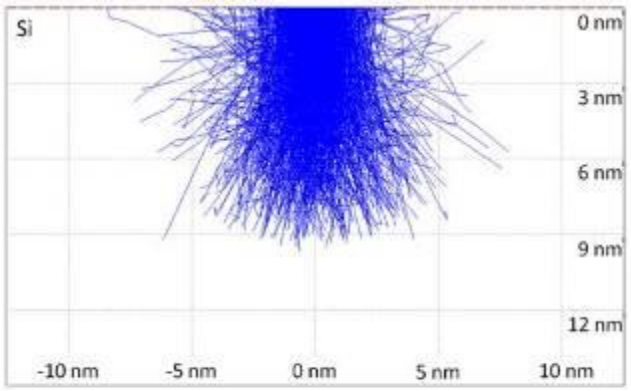

Fig.2. Result of Monte-Carlo Simulation at 500 eV incident voltage for Si bulk sample. (Simulated by Casino)

Fig. 3

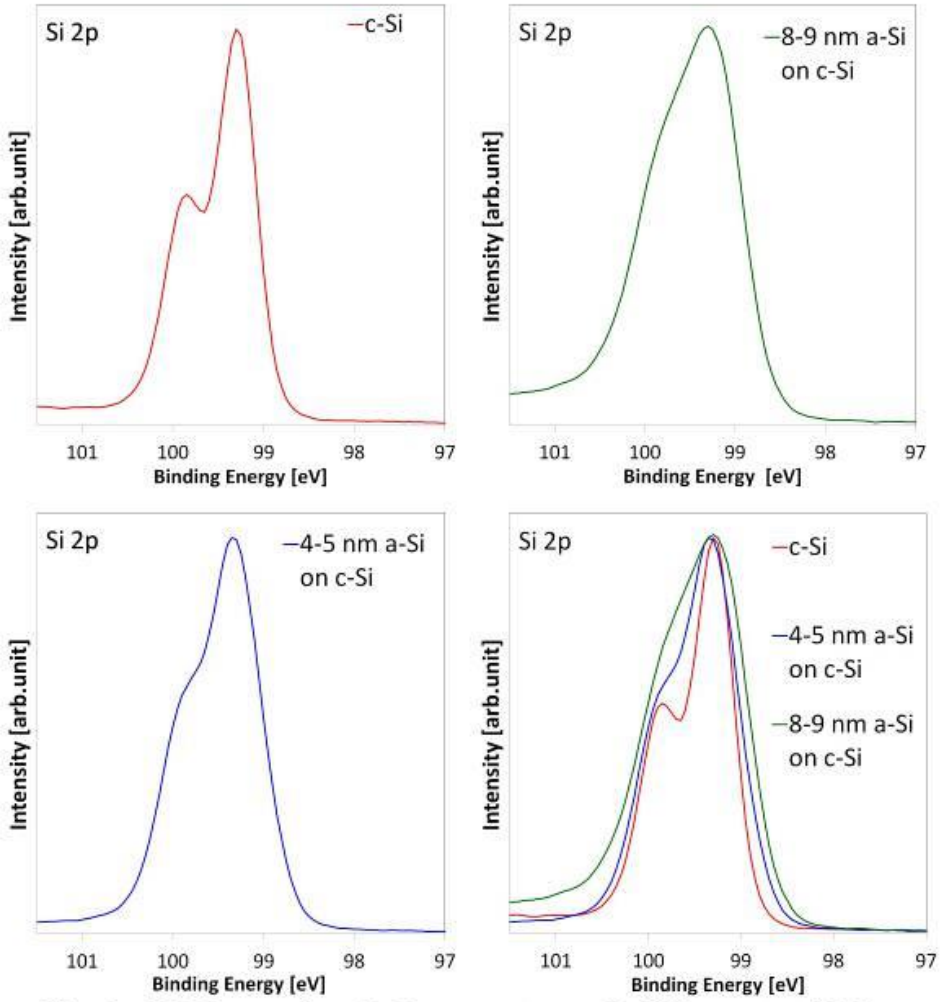

Fig.3. XPS result: Si 2p spectra of different thickness amorphous layers on Si

Fig. 4

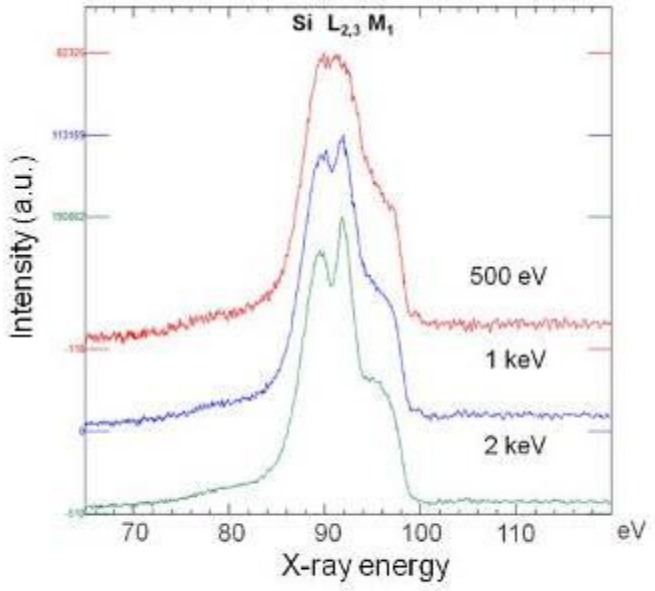

Fig.4. SXES result: Si $L_{2,3}$-M_1 spectra of 8-9 nm a-Si on c-Si, by SXES, at different incident voltage

IM6.P007
The spectrum of electrons backscattered from fluorescent dyes in the DELTA ultra-low voltage scanning electron microscope

D. Ryklin[1], J. Eisele[1], E. R. Curticean[2], I. Wacker[1,2], R. R. Schröder[1,2]

[1]Universität Heidelberg, Centre for Advanced Materials, Heidelberg, Germany
[2]Universitätsklinikum Heidelberg, Cryo Electron Microscopy, Heidelberg, Germany

One application for fluorescent dyes is to label biological structures of interest and, in this way, to enhance or create contrast for fluorescence microscopy. The ability to image and distinguish fluorescent dyes and dye labelled structures in the SEM would allow to *directly* correlate fluorescence and electron microscopic images. That would be a ground-breaking new imaging possibility, for instance, when imaging large volumes in Array Tomography. Obstacles in this way are on the one hand, that fluorescent dyes are sensitive to beam damage in the electron microscope. On the other hand, there is low image contrast between similar organic structures in conventional SEM imaging since the different carbon materials have very similar atomic compositions and densities.

We want to overcome these limitations with the novel DELTA ultra-low voltage SEM (1), which may allow to reduce beam damage by ultra-low beam energies and to achieve image contrast of similar material compositions by spectral data acquisition of secondary electrons (SE) and backscattered electrons (BSE). As a first step, we want to test if we are generally able to find imaging conditions under which we can see significant signal differences in the BSE spectrum of different fluorescent dyes.

We measured BSE spectra of two common fluorescent dyes: 4",6-Diamidin-2-phenylindol (DAPI) and Rhodamin B. Different dye concentrations (5, 0.5, 0.05 mg/mL for DAPI and 10, 1, 0.1 mg/mL for Rhodamin B) were drop-casted on a silicon wafer to be able to compare regions of different thickness of the dried dyes. To roughly correlate their thickness with the SEM measurements, a thickness profile was measured for every droplet with a Dektak profilometer. Imaging magnification at the SEM was low (10kx) in order to reduce contamination and charging effects.

The raw data BSE spectra of DAPI and Rhodamin B (Fig. 1a) show high, systematic noise, most probably induced by instabilities of the detector electronics. To reduce high-frequency noise, a low-pass Fermi filter is applied to the Fourier transform of the data (Fig. 1b). Afterwards, the Rhodamin B spectrum compared to the DAPI spectrum shows both a decreased zero-loss peak and an increased signal above 20eV energy loss (= -180eV BSE energy). Fig. 2a and b show BSE spectra of different layer thickness of DAPI and Rhodamin B, respectively. For DAPI, no significant spectral difference can be observed. For Rhodamin, however, we see with increasing thickness again a decreasing zero-loss peak and an increasing energy-loss signal above 20eV.

We are able to measure spectral differences between DAPI and Rhodamin B. The spectral data may indicate a plasmonic excitation for Rhodamin B at above 20eV, leading to the energy loss of the BSE. The experimental data shows, that the characterization of a fluorescent dye by its BSE spectrum might indeed be possible.

References:

(1) RR Schröder et al., Microsc. Microanal. 24 (Suppl 1), 2018

Fig. 1: Raw data (a) and filtered (b) BSE spectra of DAPI and Rhodamin B (legend: thickness of measured region) at 200 eV primary energy.

Fig. 2: Filtered BSE spectra of different thickness of DAPI (a) and of Rhodamin B (b) at 200 eV primary energy.

Fig. 1

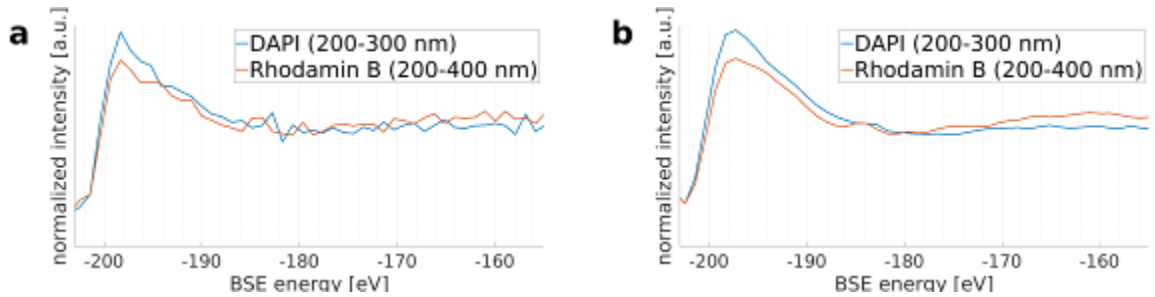
a
DAPI (200-300 nm)
Rhodamin B (200-400 nm)
normalized intensity [a.u.]
-200
-190
-180
-170
-160
BSE energy [eV]
b
DAPI (200-300 nm)
Rhodamin B (200-400 nm)
normalized intensity [a.u.]
-200
-190
-180
-170
-160
BSE energy [eV]

Fig. 2

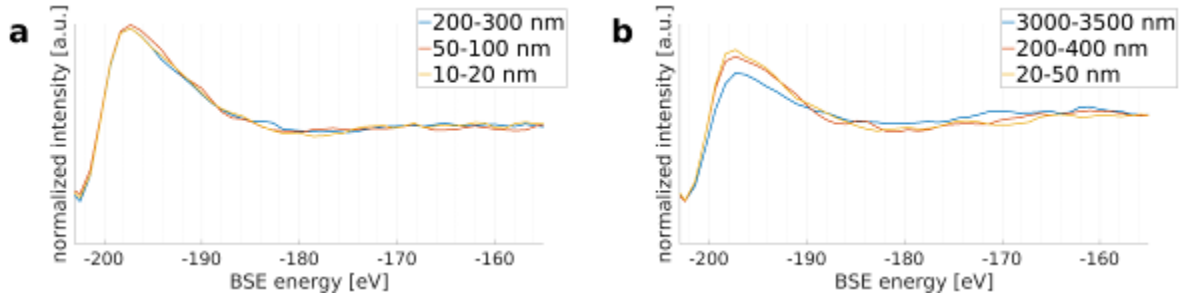
a
200-300 nm
50-100 nm
10-20 nm
normalized intensity [a.u.]
-200
-190
-180
-170
-160
BSE energy [eV]
b
3000-3500 nm
200-400 nm
20-50 nm
normalized intensity [a.u.]
-200
-190
-180
-170
-160
BSE energy [eV]

IM6.P008
Axion plasmonics in topological insulators

J. Schultz[1], J. Krehl[1], P. Potapov[1], F. de Souza Nogueira[1], A. Lubk[1]

[1]IFW Dresden, Institute for Solid State Research, Dresden, Germany

Surface plasmons are self-sustaining resonances occurring at interfaces between media whose permittivities have a different sign. They are associated with strongly enhanced, localized electrical fields, which may be coupled to external optical excitations. Surface plasmons can be used for the sub-wavelength control of electromagnetic fields in various applications. Here, we study the properties of these surface plasmons when they are localized on a surface of a topological insulator, which introduces several fundamental changes to the conventional plasmonic behavior due to the topological surface states.

Surfaces of topological insulators (TI"s) contain conducting states, which leads to negative permittivity on the surface and positive permittivity in the bulk. Consequently topological insulators can in principle sustain surface plasmons if they are embedded in a dielectric environment with positive permittivity. Moreover, the Maxwell equations of a TI contain an additional topological term, a so-called Axion term, effectively coupling electric and magnetic fields, which in turn modifies the surface plasmon resonance. Detailed studies of these topological modifications of surface plasmons are, however, outstanding.

Here we report on analytic developments based on Mie-Theory and axion electrodynamics of topological insulators. The analytic studies suggest, that the modification of the induced magnetic field due to the axion electrodynamics has an appreciable effect on the beam deflection only, whereas energy shifts caused by the axion term are beyond the resolution of spectroscopic techniques. The modification of the dielectric response due to surface states also has an impact on the energy of the surface plasmon modes.

To map the evanescent fields in Bi_2Se_3 and Bi_2Te_3 (two typical topological insulators) with high spatial and spectral resolution, electron energy-loss spectroscopy (EELS) in the scanning transmission electron microscope (STEM) is utilized (see Fig. 1). We probe the z-component of the induced electric field by recording EELS-spectra at different STEM-probe positions (see Fig. 2). The results suggest a shift of the surface plasmon energy due to surface states. To detect the lateral components of the induced electric and magnetic field a completely new setup measuring the deflection of the electron beam (inelastic momentum transfer IMT (1)) needs to be developed. We discuss the application of this novel technique for determining the Axion coupling of electric and magnetic fields (2).

References:

(1) F. S. Nogueira and J. van den Brink, arXiv e-prints, 1808.08825 (2018) (accessed Dec 20, 2018).

(2) J. Krehl et al., Nature Communications 9(1) (2018), p. 4207.

(3) Our studies are funded by ct.qmat

Fig. 1: Experimental Setup of SI and IMT measurements. In the case of SI a EEL spectrum is recorded in the energy dispersive plane by a pixel detector at each STEM-probe position. For IMT measurements an energy selective slit is placed in the energy dispersive plane and an energy filtered diffraction pattern is recorded in the far field at each STEM-probe position.

Fig. 2: Localized Surface Plasmon modes on a Bi_2Te_3 nanorod with 200nm length.

Fig. 1

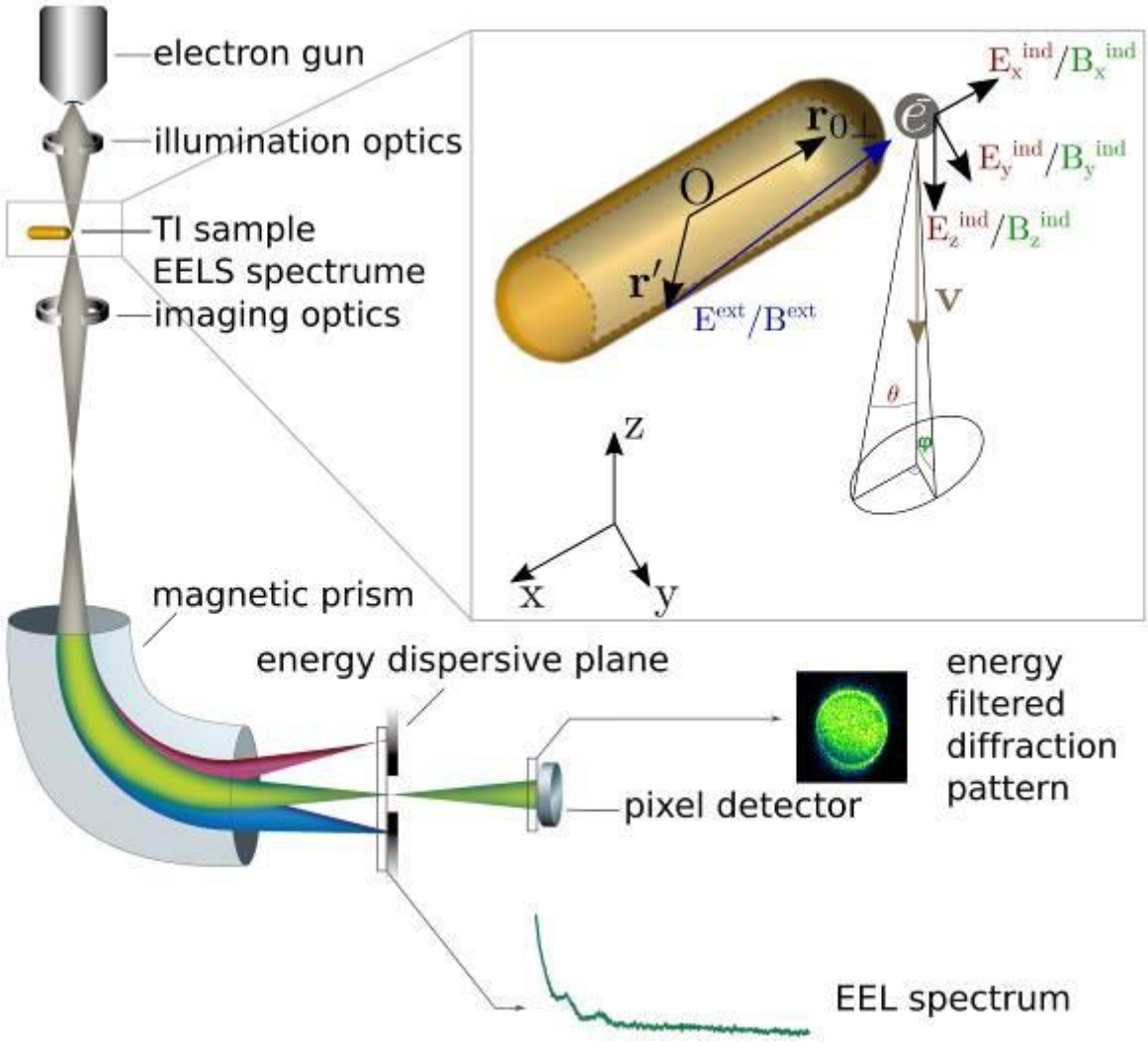
electron gun
illumination optics
TI sample
EELS spectrume
imaging optics
magnetic prism
energy dispersive plane
pixel detector
energy filtered diffraction pattern
EEL spectrum
O
r0⊥
r′
E^ext/B^ext
v
θ
z
x
y

Fig. 2

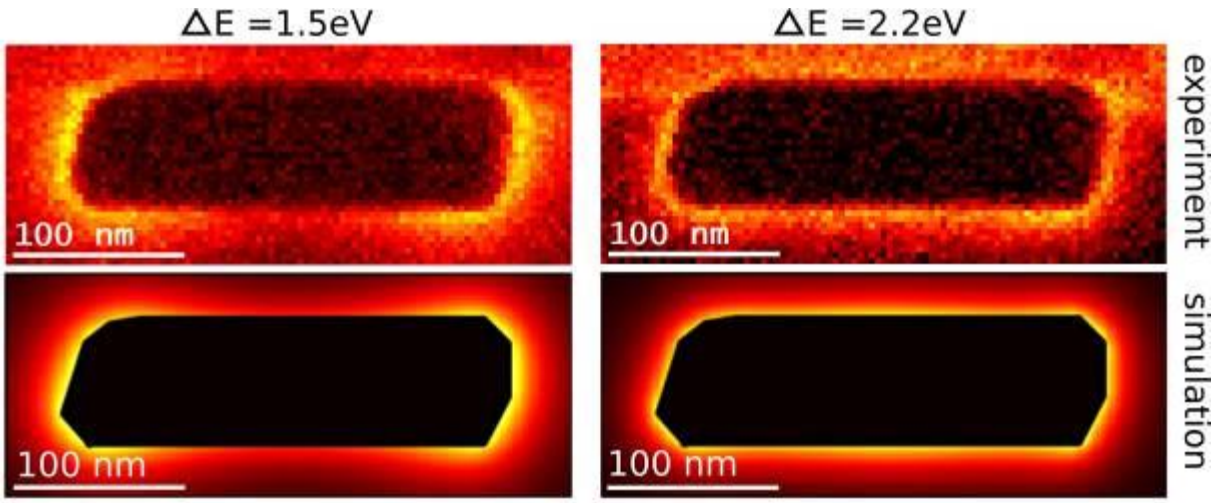
ΔE =1.5eV
ΔE =2.2eV
100 nm
100 nm
100 nm
100 nm
experiment
simulation

IM6.P009
Spatial and Spectral Mapping of Electric Fields of Surface Plasmon Polaritons

J. Krehl[1], G. Guzzinati[2], J. Schultz[1], P. Potapov[1], J. Verbeeck[2], A. Lubk[1]

[1]IFW Dresden, AMEM, Dresden, Germany
[2]EMAT, Antwerpen, Belgium

Surface plasmon polaritons of nanoparticles and -structures exhibit exceptional response characteristics to external fields. Due to the confinement of the electron gas inside they have a discrete spectrum of plasmonic resonances and they can localized electric and magnetic fields of enormous strength. These phenomena make them very interesting for technical applications, such as enhancing photovoltaic elements or optoelectrical transducers. While such nanostructures can be synthesized with a broad range of shapes and materials it is currently not possible to measure the plasmonic fields with sufficient spatial resolution. Energy-filtered transmission electron microscopy combines a high energy resolution with nanometer spatial resolution and high momentum resolution and would be uniquely suited for this.

We therefore proposed to use energy-filtered electron diffraction (Figure 1 left) to measure the lateral field components via the inelastic momentum transfer (IMT) of the plasmon onto the beam electron that excited the plasmon. The lateral momentum transfer by the lateral fields is on the order of some electron volts so the deflection is in the range if microradian. Such small deflections are hard to detect reliably, because the low-angle diffraction mode is prone to making the TEM unstable by putting optical elements to extreme values. We, however, succeeded in demonstrating the technique with a dipole mode of an aluminium nanorod and achieved reasonable agreement with simulations ((1), Figure 2).

In order to acquire range of energies in parallel, instead of only a single energy window, we further propose a spectroscopic setup (Figure 1 right) where one axis of the detector is used for the energy loss and the other for the momentum transfer. This is the known \omega-qsetup, albeit for much smaller momenta than is usual. This ansatz effectively tackles the problem of energy drift during acquisition and allows a direct comparison of different modes and the zero-loss peak for reference. We can report on first results for this approach.

JK and AL have received funding from the European Research Council (ERC) under the Horizon 2020 research and innovation programme of the European Union (grant agreement No 715620). GG acknowledges support from a postdoctoral fellowship grant from the Fonds Wetenschappelijk Onderzoke-Vlaanderen (FWO).

References:

(1) J. Krehl et al "Spectral Field Mapping in Plasmonic Nanostructures with Nanometer Resolution", Nature Communications 9 (2018)

Fig. 1: Energy-filtered setups for low-angle diffraction and spectroscopy.

Fig. 2: Comparison of loss-probability (a and b) and lateral fields (c and d) reconstructed from (upper row) and simulated (lower row) for a 1.05 eV dipole mode of an Aluminium nanorod at 120keV acceleration voltage.

Fig. 1

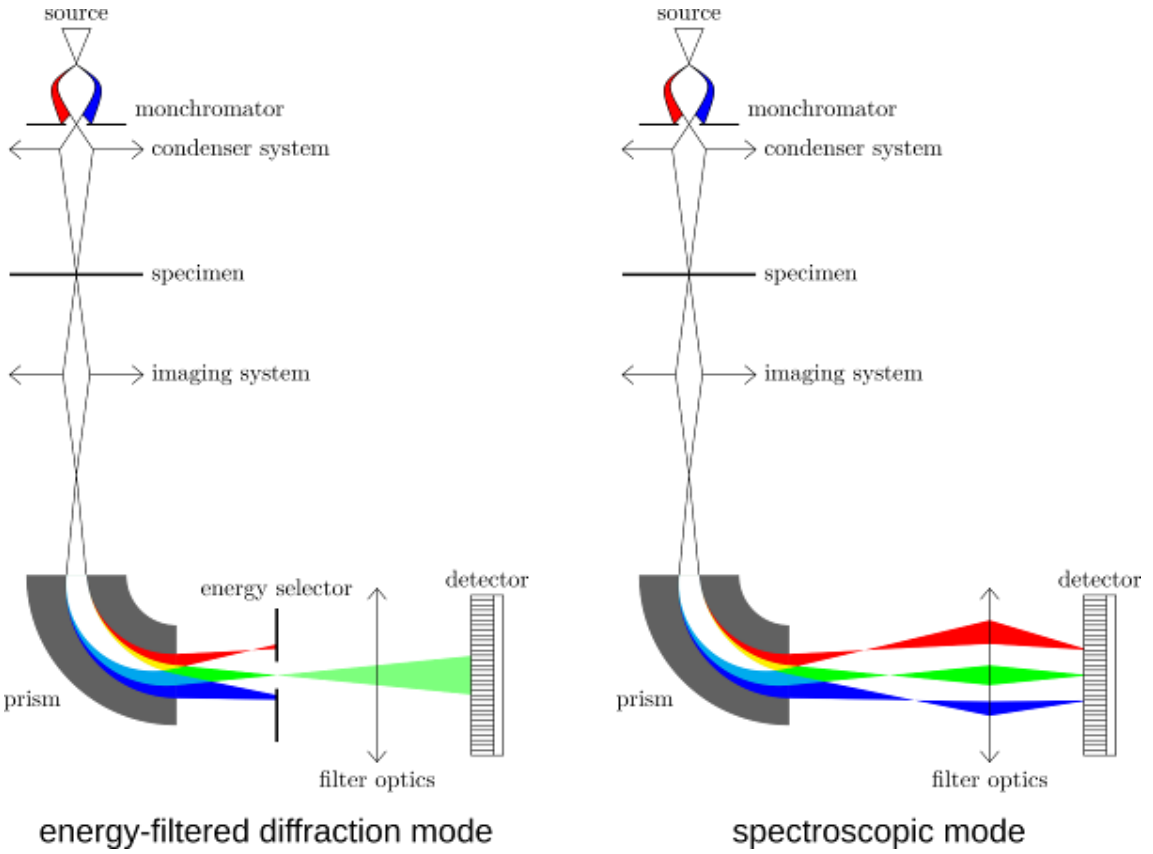
source
monchromator
condenser system
specimen
imaging system
energy selector
detector
prism
filter optics
energy-filtered diffraction mode
source
monchromator
condenser system
specimen
imaging system
detector
prism
filter optics
spectroscopic mode

Fig. 2

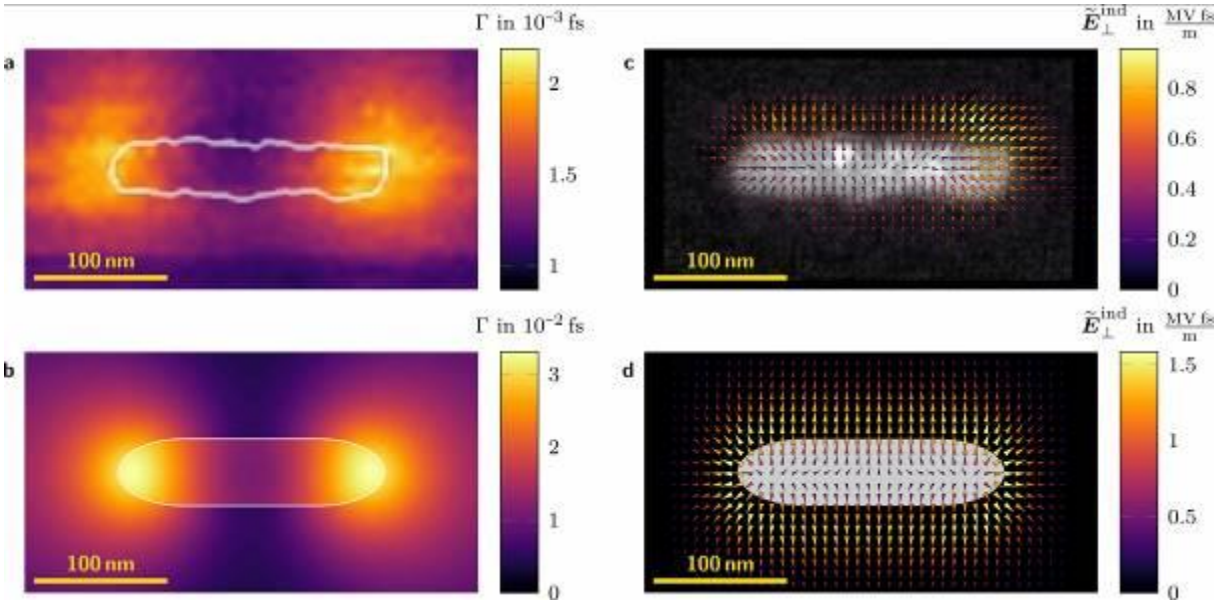
a
Γ in 10^-3 fs
2
1.5
1
100 nm
b
Γ in 10^-2 fs
3
2
1
0
100 nm
c
Ẽ⊥ind in MV fs/m
0.8
0.6
0.4
0.2
0
100 nm
d
Ẽ⊥ind in MV fs/m
1.5
1
0.5
0
100 nm

IM6.P010
Luminescence of Adenine Molecules in Gas Phase Under the Influence of Low Energy Electrons

M. Shafranyosh[1], I. Shafranyosh[1], Y. Svida[1], M. Margitich[1], M. Sukhoviya[1]

[1]Uzhgorod National University, Department of Physics, Uzhgorod, Ukraine

This report presents the results of experimental study of the excitation processes of nucleic acid base adenine by electron impact. This research is a continuation of our previous studies, conducted for other nucleic acid bases - thymine and uracil (1,2).

The experiments were carried out by an optical method that we used earlier (2). The adenine samples (Sigma Aldrich Company, purity 99%) were in form of polycrystalline powder. The gas phase of adenine molecules was formed by heating of adenine polycrystalline powder in a separate metal container. The temperature of the container with adenine powder did not exceed 370 K. Formed gas phase of adenine proceeded by steam pipeline into cell of cubic form. A diaphragm (diameter 1.5 mm) was mounted in one of the outer edges of the cell and was used for input of the electron beam and beam source and the receiver of electron beam (a Faraday Cup) was mounted on the opposite side. Electron beam was formed by five-electrode gun with tungsten cathode. Cell was placed into magnetic field so that its field lines were parallel to the electron beam. The magnetic field was ~ 1.2.10-2T. To remove the radiation from the cell two quartz windows were mounted on its two edges, which are parallel to the electron beam. The experiments were performed at the following conditions: current intensity of the electron beam was within the (5-6) · 10-5A and ΔE½ ~ 0.4 eV (FWHM) energy spread; the pressure in the chamber of the cell ~ 1 · 10-5 Pa.

For the first time the spectra of emission of adenine in the wavelength range from 200 to 500 nm for different energies of exciting electrons were obtained in the study. 7 molecular bands whose maxima are at the following wavelengths: λmλm = 308; 327; 338; 354; 388; 435; 486,1 nm clearly manifested in the spectra. Excitation thresholds of bands are determined and their identification is performed.

References:

(1) Shafranyosh I.I. *et al.* 2012 J. Chem. Phys. http://aip.scitation.org/doi/10.1063/1.4765307

(2) Shafranyosh I.I., *et al.* 2007 Optics and Spectros-copy http://link.springer.com/article/10.1134/S0030400X07040042

IM6.P011
E-beam direction dependent light emission

F. P. Schmidt[1,2], A. Losquin[3], M. Horák[4], J. R. Krenn[2], M. Stöger-Pollach[5]

[1]Fritz-Haber-Institut der Max-Planck-Gesellschaft, Inorganic Chemistry, Berlin, Germany
[2]University of Graz, Institute of Physics, Graz, Austria
[3]University of Bordeaux, Laboratoire Ondes et Matière d'Aquitaine, Bordeaux, France
[4]Brno University of Technology, Central European Institute of Technology, Brno, Czech Republic
[5]TU Wien, University Service Centre for Transmission Electron Microscopy, Vienna, Austria

Nanoscale confinement and localization of light is a key challenge in photonics due to the diffraction limit of light. Coupling photons to charges at metal surfaces allow to beat this limit. This "nanolight" yield promising applications such as sensitive biological and chemical sensors down to the single molecule level, nanolasers or plasmonic solar cells.

Electron beam based techniques, such as electron energy loss spectroscopy (EELS) or more recently cathodoluminescence (CL), have been established as powerful technique in the last decade to study optical nearfields with high spatial resolution (1). Radial breathing modes (RBM), so-called dark modes, have been shown to radiate quite strongly as soon as their size exceeds the quasi-static approximation description (2).

Here we study the influence of the substrate and the angular dependence of the RBM light emission and surprisingly find an energy shift that depends on the e-beam direction. Figure 1a depicts the measurement setup on single silver nanodisks, ranging from 225 to 400 nm in diameter. Each disk is measured four times, giving the CL signals 1-4. The corresponding RBM peak positions are plotted in figure 1b. From this, an energy shift, in addition to but distinguishable from contamination induced shifts, is identified between the different e-beam directions. The experimental results are supported by boundary element simulations (BEM) (3).

CL in a scanning transmission electron microscope is applied. 30 nm thick single silver nanodisks are prepared by electron beam lithography (EBL) on 5 nm SiN_x membrane. By scanning the focused electron beam across the disk, plasmon eigenmodes are excited leading to emission of light, which is collected by 2 separated mirrors, above and below the sample, respectively.

We identified a dependence of the RBM emission wavelength on the direction of the electron beam with respect to the emission direction. While there is only a minor influence of the diameter size, and a negligible dependence on the substrate, the observed shift is related to the electron beam direction relative to the emission direction. This indicates a mode mixing within the particle, which decreases with decreasing thickness of the disk.

References:

(1) M. Kociak, O. Stéphan. Chem. Soc. Rev., 2014,43, 3865.

(2) F.-P. Schmidt, A. Losquin, F. Hofer, A. Hohenau, J. R. Krenn, M. Kociak. ACS Photonics, 2018, 5(3), 861

(3) U. Hohenester, A. Trügler. Comput. Phys. Commun. 2012, 183, 370.

Fig. 1: a) Measurement setup: A single silver nanodisk of 30 nm thickness on a SiN_x substrate of 5 nm is excited by a focused electron beam in the center, while the generated light is collected by 2 mirrors above (1) and below (2) the sample. The measurement is repeated on the same particle with the sample upside down (3, 4). b) RBM peak positions extracted from CL spectra from disks with diameters ranging from 225-400 nm. In average, the RBM peak originating from signal emitted in opposite e-beam direction (1,4; red data points) is red shifted to the RBM peak signal emitted in e-beam direction (2,3; blue) given by the value $\Delta\lambda$. The TEM micrograph shows exemplarily an EBL prepared silver disk, 400 nm in diameter, used in the experiment.

Fig. 1

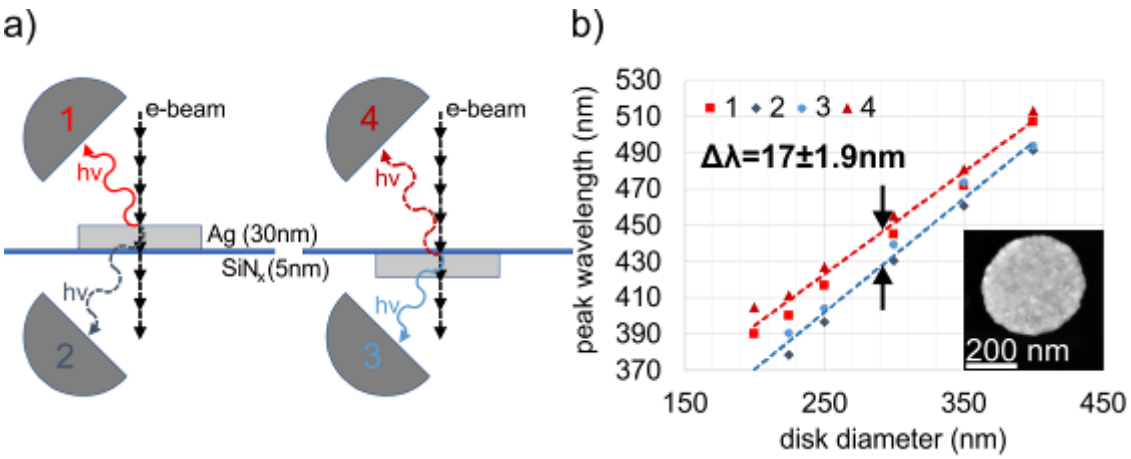
a)
b)
1
2
3
4
e-beam
e-beam
hv
hv
hv
hv
Ag (30nm)
SiNx(5nm)
peak wavelength (nm)
disk diameter (nm)
1 2 3 4
Δλ=17±1.9nm
200 nm
530
510
490
470
450
430
410
390
370
150
250
350
450

IM6.P012
Specifics in EDS spectrum reconstruction at lowest X-ray energies

U. Gernert[1]

[1]Technische Universität Berlin, Center for Electron Microscopy (ZELMI), Berlin, Germany

By continuous development of the silicon drift detector (SDD) and the use of silicon nitride instead of polymeric material for the X-ray entrance window it has become possible to detect X-ray lines even in the energy range below 100 eV. Especially if the high absorption of soft X-ray radiation inside the sample material is reduced by using excitation energies less than 5 keV due to near-surface excitation (1).

At the low-energy level peak overlaps become more frequent because, depending on the atomic number, there exist K-, L-, M- or N-lines with nearly the same energy. Therefore, the exact spectrum reconstruction in the range below 500 eV is important to ensure that the elements of the sample are correctly identified by accurate peak deconvolution. This is also a basic prerequisite for a subsequent semi-quantitative evaluation.

To get proper reconstruction, the resolution of the detector dependent on the considered X-ray energy and the window transmission curve with its absorption edges must be known. But at low X-ray energies additionally the effect of Incomplete Charge Collection (ICC) occurs. Electrons of an electron-whole pairs cloud which is created near the detector surface, get lost. This leads to asymmetric peaks with a broadening on the low-energy side of the peak, resulting in degraded energy resolution and a shift of the total peak to lower energy than theoretically expected (2). To what extent the ICC occurs and at what energies, it depends on the detector construction and the X-ray entrance window properties. So that the various causes of the ICC and their effects on the spectrum could be considered in the spectrum reconstruction algorithms, all the detector and window related parameters must be known and incorporated into the evaluation software.

The investigations to Incomplete Charge Collection were carried out with a 30 mm2 Octane-A Plus SDD from EDAX mounted on a Hitachi SU8030 SEM. The SDD is equipped with an Amptek module, including a low noise preamplifier and an 80 nm silicon nitride window. For the spectra evaluation EDAX Benchmark-EDS was used.

As an example figure 1 shows a spectrum of SiC. Due to Incomplete Charge Collection the C-K-line shows a significant shift to lower energy whereas the Si-L-line is not shifted and located at its tabulated X-ray energy. Different X-ray absorption inside the detector material, caused by the absorption edge jumps of the Si-L-line leeds to different peak shift for low energy lines.

If it is necessary to use X-ray lines at very low energies, an EDS spectra evaluation software is needed, which gives the opportunity to take into account the significantly different peak-shifts of lines between 69 eV (Al-L) and 525 eV (O-K).

References:

(1) U. Gernert, D. Berger, MC 2017, https://nbn-resolving.org/urn:nbn:de:bvb:355-epub-361434, p501ff.

(2) F. Eggert, Abstract preprint personal information, EMAS 2019

Fig.1: Sample SiC; accelerating voltage 3 kV; energy resolution 5 eV per channel; blue: original measured spectrum; red: shift-corrected spectrum

Fig. 1

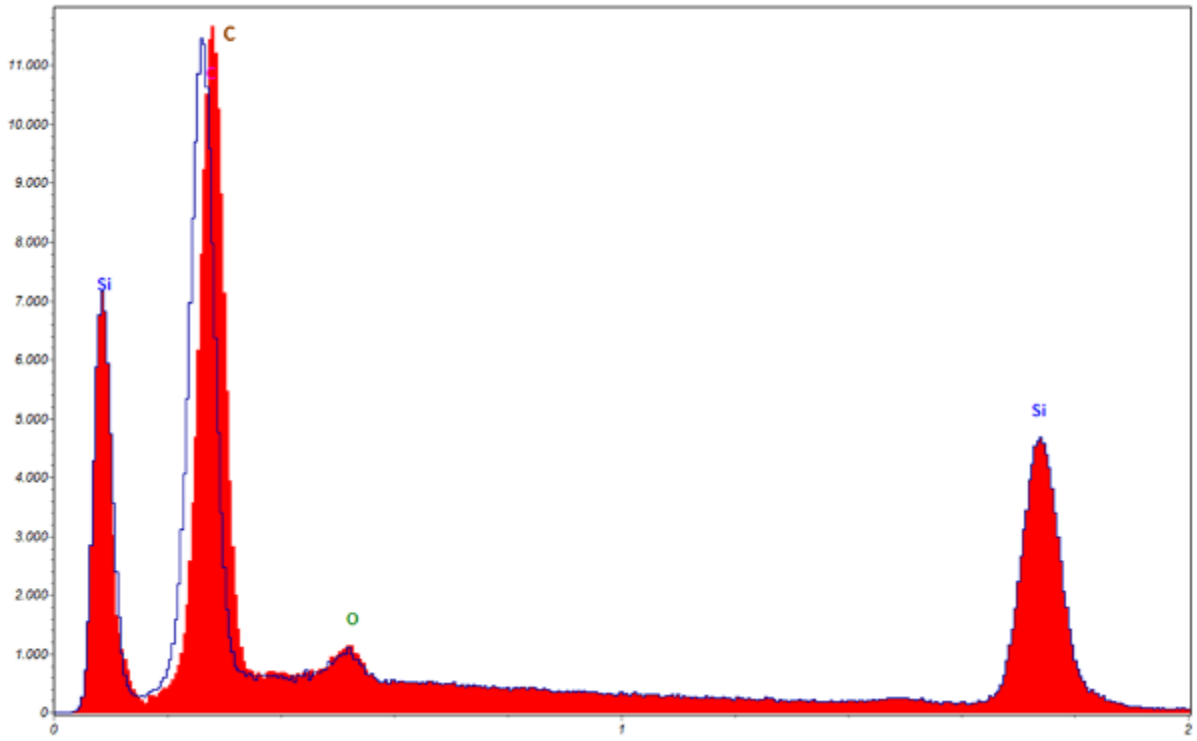
C
Si
O
Si
11.000
10.000
9.000
8.000
7.000
6.000
5.000
4.000
3.000
2.000
1.000
0
0
1
2

IM6.P013
Analytical TEM studies of $LiNi_{0.6}Mn_{0.2}Co_{0.2}O_2$, $LiCoO_2$, and Silicon electrode materials

A. Makvandi[1], M. Peterlechner[1], S. Casino[2], T. Gallasch[2], M. Winter[2,3], G. Wilde[1]

[1]Institute of Materials Physics, University of Münster, Münster, Germany
[2]MEET Battery Research Center, University of Münster, Münster, Germany
[3]Helmholtz-Institute Münster, IEK 12, Forschungszentrum Jülich GmbH, Münster, Germany

The modification of state-of-the-art electrode materials in Li-based batteries by nanostructured coatings is one approach to optimize crucial parameters for application. In general, interfaces determine the local Li-ion transport and finally the electrochemical cell performance. Therefore, it is necessary to study the structure and chemistry of electrodes and electrode/electrolyte interfaces. In this work, the $LiNi_{0.6}Mn_{0.2}Co_{0.2}O_2$ (NMC622) and $LiCoO_2$ (LCO) model electrodes were chosen, and additionally silicon thin film electrodes were studied with a focus on analytical TEM. The objective of the work is to understand surface and interface properties and to be able to map the Li content. Powder materials of LCO and NMC622 were used, and additionally silicon thin film electrodes were made via magnetron sputtering. Cross-sectional TEM samples were prepared by FIB technique. Electron-energy-loss spectroscopy (EELS) and energy dispersive X-ray spectroscopy (EDS) was accomplished in scanning TEM (STEM) mode using a FEI Titan Themis G3 60-300 TEM. Additionally, high-resolution TEM (HR-TEM) was applied. In the case of low-loss EELS spectra of the NMC622, the Li-K edge signal overlaps with adjacent Mn-$M_{2,3}$ and Co-$M_{2,3}$ edge signals. Therefore, the background subtraction was not applied to the Li-K-edge, hindering the direct measurement of the lithium content. In the high-loss EELS spectra, by measuring the intensity ratio (L_3/L_2) of $L_{2,3}$-edge peaks the oxidation state of transition metals (e.g. Ni, Mn, and Co) are measured as the oxidation state of transition metal changes with the lithium content (1). It is therefore possible to estimate the lithium distribution in an indirect way. Based on Figure 1, it is concluded that the analyzed thicknesses do not influence the intensity ratio of the (L_3/L_2) edges. However, a chemical shift due to oxidation can be detected in the case of the Ni-L_3 edge. This is reflected in the elemental composition maps, where the Oxygen and Nickel content is increased in areas close to the surface (see Figure 2). The Nickel is most reactive, making it the element of choice for the tracking of the Li-content. However, the surface oxides must be taken into account for a proper quantification. It is suggested, that measurement artefacts in the thin foil can be reduced, using the Co-edge to map the lithium content.

References:

(1) van Aken, P. & Liebscher, B. Phys Chem Min (2002) 29: 188.

Fig. 1: A series of high-loss EELS spectra acquired from the surface to bulk area with increasing sample thicknesses (from 20 to 50 nm). The L3 edge of Ni is shifted to lower energies in the bulk area of particle, in agreement with Nickel surface oxidation.

Fig. 2: EELS-STEM mapping in a pristine NMC 622 cathode powder: a) HAADF-STEM image and the selected areas for EELS spectrum image (SI) acquisition and spatial drift correction during SI acquisition. b) High-loss EELS spectrum image. (Temperature color scale from blue to red shows increasing concentration). The EELS data of this powder electrode material can be used as a reference for the analysis of sputtered thin films.

Fig. 1

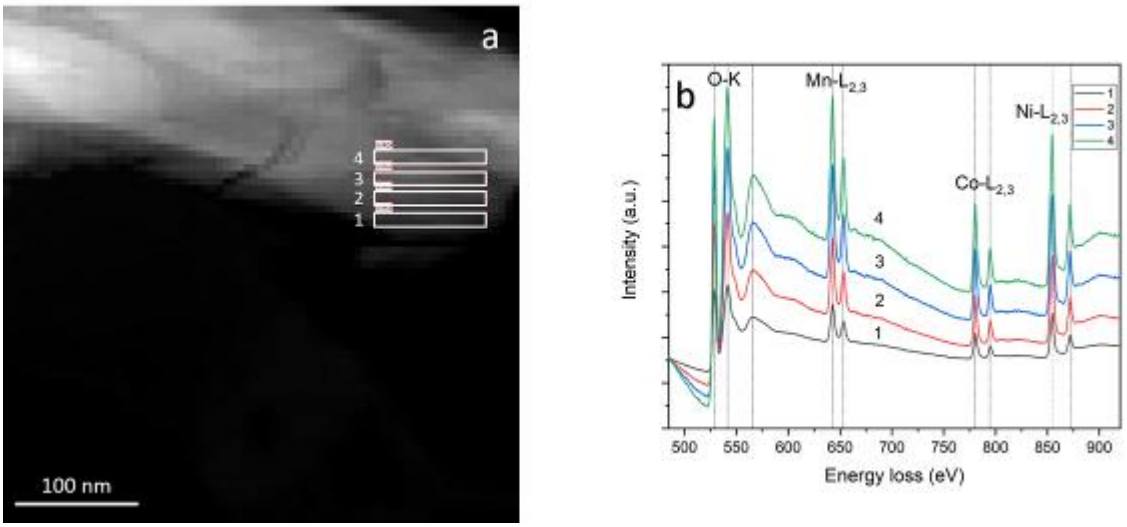
a
4
3
2
1
100 nm
b
O-K
Mn-L2,3
Co-L2,3
Ni-L2,3
1
2
3
4
Intensity (a.u.)
500
550
600
650
700
750
800
850
900
Energy loss (eV)

Fig. 2

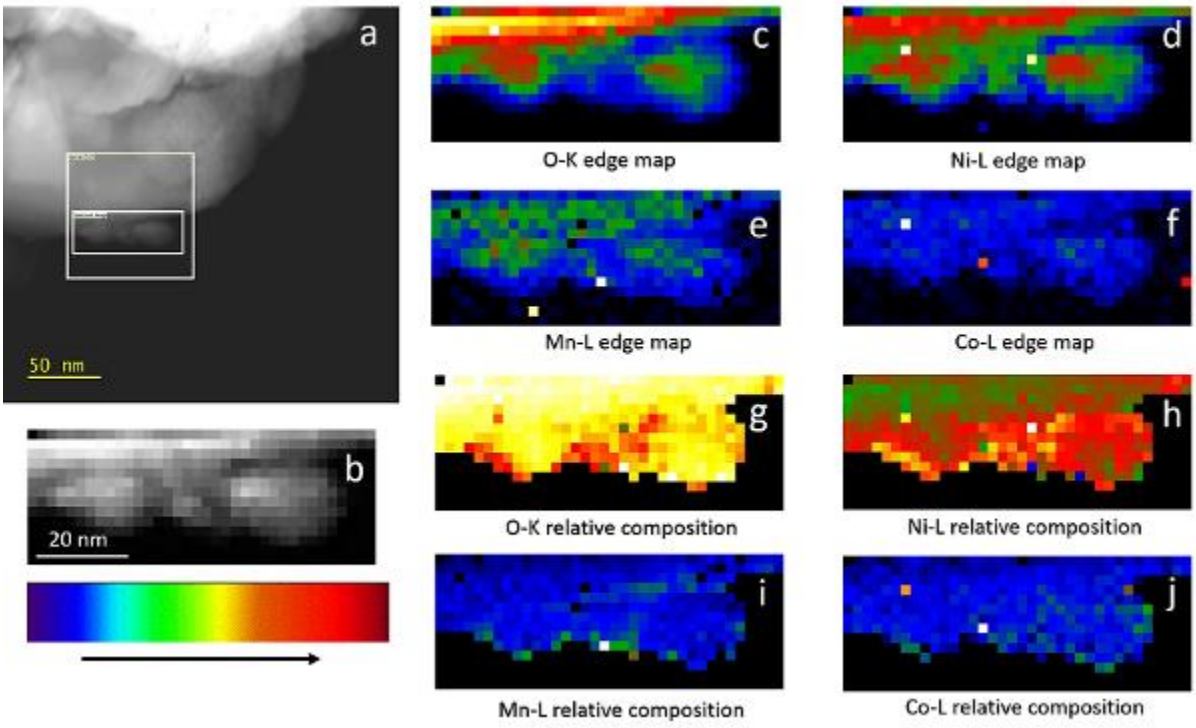
a
50 nm
b
20 nm
c
O-K edge map
d
Ni-L edge map
e
Mn-L edge map
f
Co-L edge map
g
O-K relative composition
h
Ni-L relative composition
i
Mn-L relative composition
j
Co-L relative composition

IM6.P014
A simple procedure for the optimization of classical electron magnetic circular dichroism measurements

S. Schneider[1,2], D. Negi[3], M. J. Stolt[4], S. Jin[4], J. Spiegelberg[3], D. Pohl[1,5], B. Rellinghaus[1,5], S. T. Goennenwein[2,6], K. Nielsch[1,7], J. Rusz[1,3]

[1]IFW Dresden, Institute for Metallic Materials, Dresden, Germany
[2]TU Dresden, Institut für Festkörper- und Materialphysik, Dresden, Germany
[3]Uppsala University, Department of Physics and Astronomy, Uppsala, Sweden
[4]University of Wisconsin-Madison, Department of Chemistry, Madison, United States
[5]TU Dresden, Dresden Center for Nanoanalysis, Dresden, Germany
[6]TU Dresden, Center for Transport and Devices of Emergent Materials, Dresden, Germany
[7]TU Dresden, Institute of Materials Science, Dresden, Germany

Electron magnetic circular dichroism (EMCD) (1), the electron wave analogue of X-ray magnetic circular dichroism (XMCD), allows for the element specific measurement of the spin and orbital magnetic moments with up to nanometer resolution. Despite being in development for more than a decade, the method has not yet reached widespread employment. The most likely reason for that are dynamical diffraction effects, which severely complicate the EMCD detection and often reduce the signal strength.

Therefore, it is necessary to optimize the experimental settings by performing inelastic-scattering calculations in various experimental geometries. To circumvent this step we propose a simple procedure that should help and provide to the experimentalist a set of rules as how to determine the optimal experimental geometry for classical EMCD experiments (2).

In order to test the proposed optimization procedure these rules are applied to measure a dichroic signal in the field-polarized phase of the helimagnet FeGe. To stabilize this phase the classically prepared sample is cooled to 90 K using a liquid nitrogen TEM holder, and the sample is then exposed to the field of the objective lens (B = 2.2 T), resulting in parallel alignment of all magnetic moments with respect to the external magnetic field (cf. Fig. 1 (a)).

By explicitly reviewing the theory of EMCD in two- and three-beam orientations we can identify a pre-factor that scales with the dichroic signal strength. This expression, which is very similar to a structure factor, although the summation is limited to the magnetic atoms of the unit cell only, is introduced as *partial structure factor*. When applied to FeGe the highest *partial structure factor* is found for a two-beam orientation with **G** = {400}, while for a three-beam case with **G** = {200} it is significantly reduced. Explicitly calculating the EMCD signal in the diffraction plane it can be confirmed, that the dichroic signal strength is much more pronounced for the two-beam case (cf. Fig. 1 (b) and (c)). In subsequent experiments a clear EMCD signal can be measured for the two-beam orientation, whereas the dichroic signal is not detectable in the three-beam case (cf. Fig. 2).

By providing the crystal structure and assuming the magnetic structure it is possible to calculate the *partial structure factor* of an arbitrary material, which enables the possibility to choose the optimal experimental orientation for an EMCD experiment. Likewise calculations, simulations and experiments on the field-polarized phase of FeGe confirm the applicability of this easy procedure. Future works on FeGe aim to measure a spatially resolved EMCD signal of the Skyrmion phase to gain further inside into three dimensional spin texture of these magnetic quasiparticles complementary to holographic experiments (3).

References:

(1) Schattschneider et al., Nature 441 (2006), p. 486.

(2) Schneider et al., Physical Review Materials 2 (2018), p. 113801.

(3) Schneider et al., Physical Review Letters 120 (2018), p. 217201.

Fig. 1: (a) Crystallographic unit cell of stoichiometric FeGe in the B20 structure. (b), (c) The calculated diffraction patterns (upper grey scale maps) and EMCD maps (lower colored maps) are shown for each of these cases (scales = 5 mrad).

Fig. 2: EEL spectra measured in two- and three-beam conditions with their respective EMCD signal (difference) in green.

Fig. 1

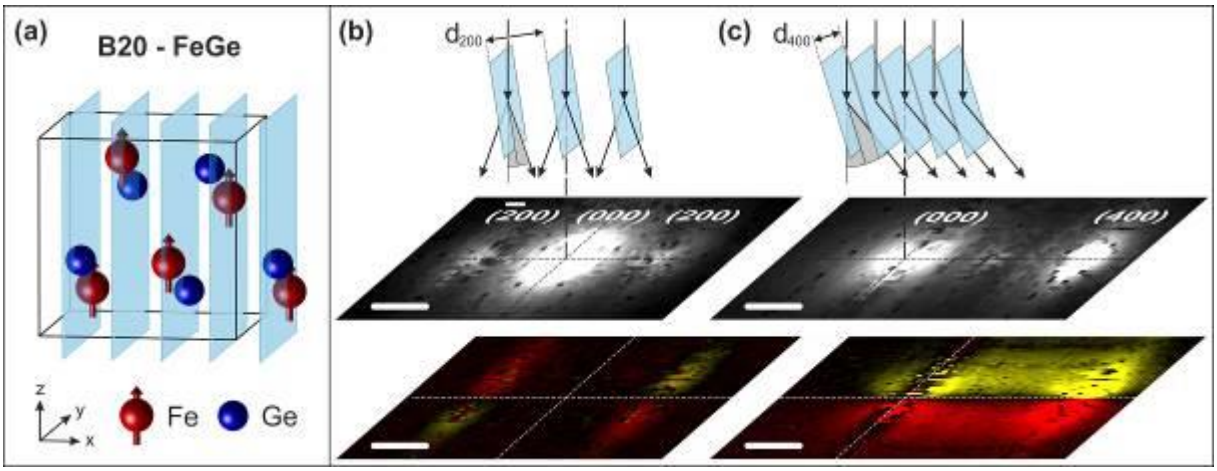
(a)
B20 - FeGe
z
y
x
Fe
Ge
(b)
d_{200}
$\bar{(200)}$
(000)
(200)
(c)
d_{400}
(000)
(400)

Fig. 2

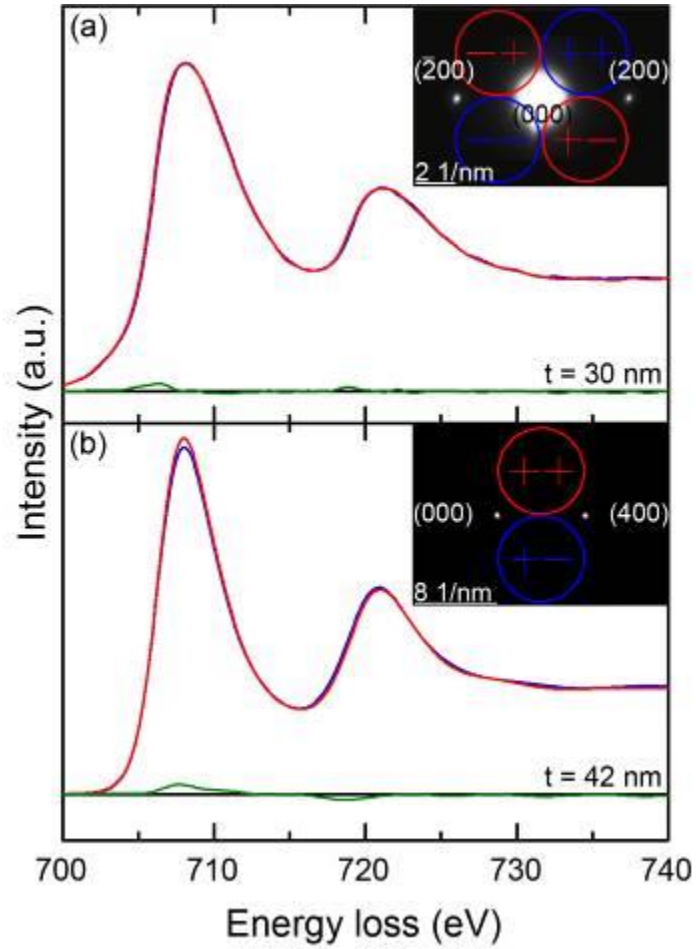
(a)
(200)
(200)
(000)
2 1/nm
t = 30 nm
(b)
(000)
(400)
8 1/nm
t = 42 nm
Intensity (a.u.)
700
710
720
730
740
Energy loss (eV)

IM6.P015
Cryo FIB-SEM TOF SIMS – Analysis of liquid/hydrated specimens

T. Nováček[1]

[1]TESCAN Brno, s.r.o., R&D Applications, Brno, Czech Republic

Secondary Ion Mass Spectrometry (SIMS) is a powerful analytical method for elemental and chemical characterization of various compounds. Its analytical capabilities can be expolited in fields ranging from material science research to life sciences, providing invaluable data on specimen content and spatial distribution of chemical constituents. However, sample navigation and imaging capabilities of dedicated tools are often highly limited.

Integration of SIMS into a FIB-SEM (Focused Ion Beam-Scanning Electron Microscope) system with a cryogenic specimen holder would enable the acquisition of high resolution images by SEM or FIB, and to modify, manipulate and analyze hydrated/liquid or beam-sensitive specimens, biological specimens, polymer solutions or drugs. This significantly facilitates analyses that otherwise require lengthy transfers between single-use instruments *e.g*. for processes in plant physiology (1,2). TOF-SIMS integration also adds another complementary analytical tool to an already versatile instrument equipped with Energy Dispersive Spectroscopy (EDS), Electron Back Scattered Diffraction (EBSD), Raman spectrometry or Scanning Transmission Electron Microscopy (STEM) detectors.

We used a TESCAN LYRA microscope fitted with an Orsay Ga FIB, the PP3010 cryo-SEM preparation system from Quorum Technologies and the Tofwerk c-TOF analyzer. The sample was *Elaphomyces*, amushroom known to accumulate cesium.

A piece of *Elaphomyces* was glued to a holder attached to the cryo-loader and subsequently flash-frozen in liquid nitrogen. From the evacuated loader, the sample was transferred into an evacuated preparation chamber and sputter coated with platinum for conductivity. The holder was then transferred directly onto a cryo-stage in the microscope chamber. This prevents air exposure and keeps ice formation to a minimum. Moreover it keeps the sample hydrated and prevents analyte loss during preparation.

Once sufficient vacuum for FIB-SEM-TOF-SIMS operation was reached, the sample was tilted to the FIB and TOF-SIMS ion optics to ensure the highest possible signal. TOF-SIMS ion optics was tuned to detect positive secondary ions (Cs is more likely to be positively ionized), and FIB scanning was started over an area of 50x50 µm. This yielded a large dataset in which we had 200 frames with 501x501 pixel resolution, each of which contained a mass spectrum up to m/Q = 175. This range is sufficient to capture the Cs signal, as its exact mass is 132.90545 u. The resulting overall spectrum (Fig.1) showed the presence of Cs, while its spatial distribution (Fig.2) did not show any signs of Cs grain formation.

This result confirms the applicability of this instrument configuration – thus expanding the analytical power of TESCAN microscopes.

References:

(1) Kuroda *et al.,* Surface and Interface Analysis, 2013

(2) Aoki *et al.,* Scientific Reports,2016

Fig. 1

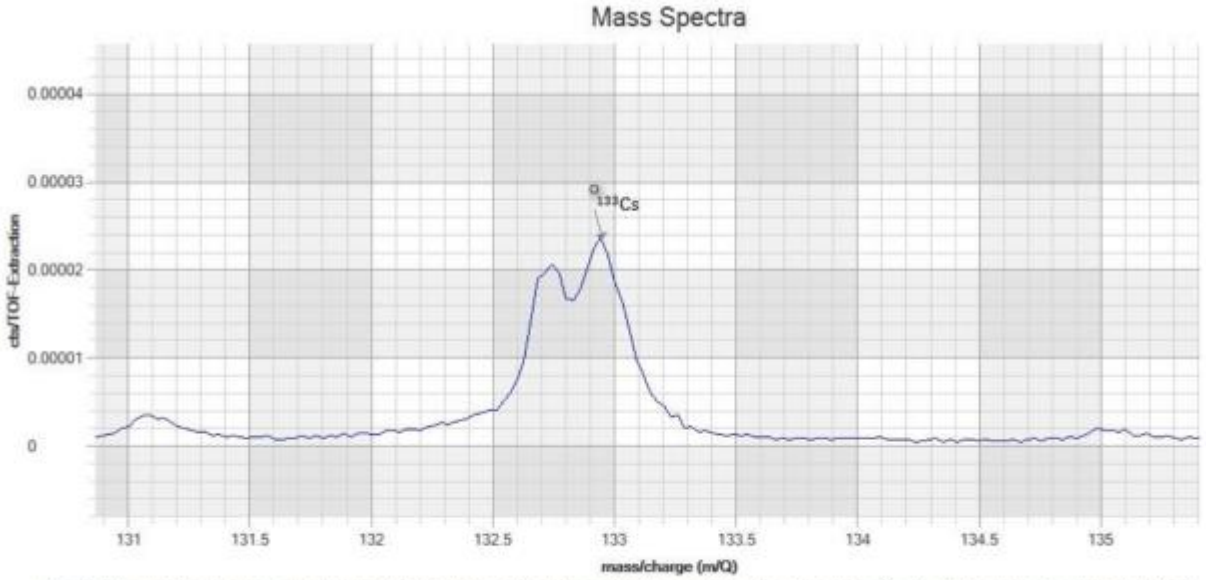

Fig. 1. Excerpt from a mass spectrum of Elaphomyces *showing a double peak; the heavier one is Cs, the lighter one is an unidentified molecular fragment.*

Fig. 2

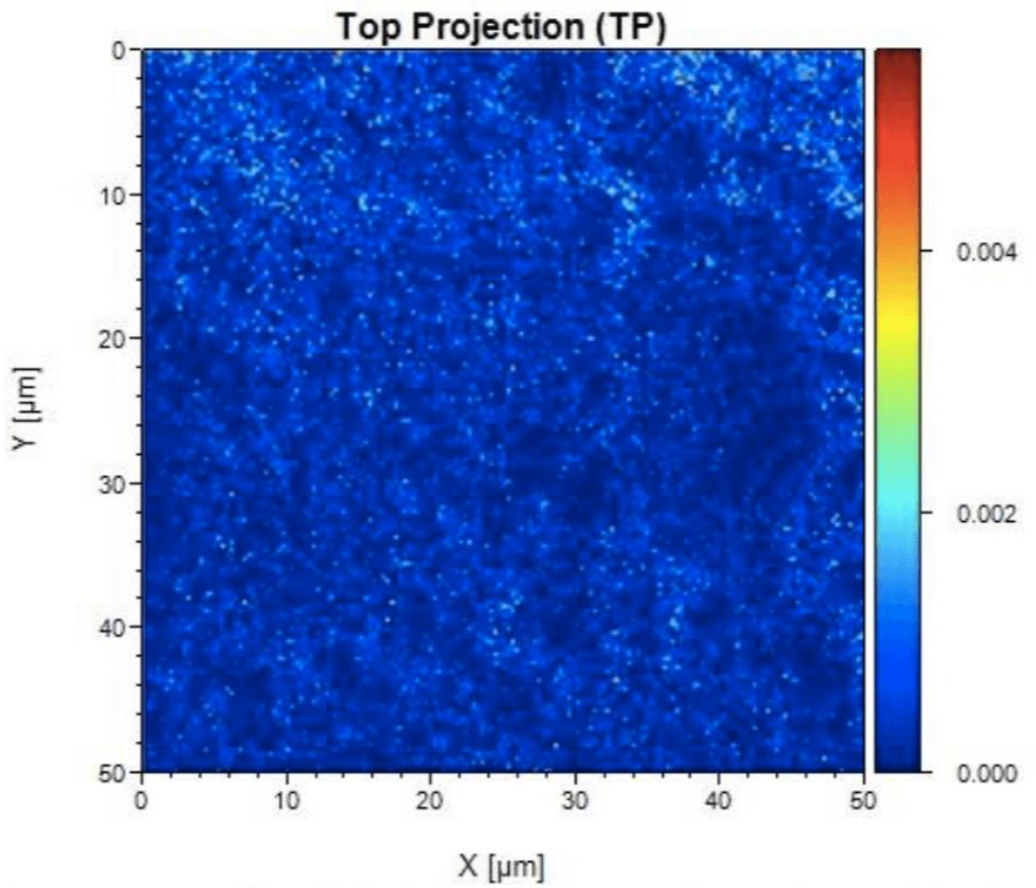

Fig. 2. Top projection of the milled volume of Elaphomyces*, showing the spatial distribution of Cs.*

IM6.P016
Effect of Sample Thickness on Quantitative STEM/EDXS Analysis of Cu(In,Ga)Se2 Solar Cells with ZnO Window Layers

X. Jin[1], R. Schneider[1], D. Hariskos[2], W. Witte[2], M. Powalla[2], D. Gerthsen[1]

[1]Karlsruhe Institute of Technology (KIT), Laboratory for Electron Microscopy, Karlsruhe, Germany
[2]Zentrum für Sonnenenergie- und Wasserstoff-Forschung Baden-Württemberg (ZSW), Stuttgart, Germany

Cu(In,Ga)Se2 (CIGS) thin-film solar cells with ZnO window layers have attracted much attention in the past decades because of their high photovoltaic conversion efficiency. The bandgap energy of the CIGS absorber plays an important role in the solar-cell efficiency, and it is quite sensitive to the stoichiometry of the absorber. Nowadays, scanning transmission electron microscopy (STEM) combined with energy-dispersive X-ray spectroscopy (EDXS) is a powerful technique to analyze the element concentration in materials. However, even for thin TEM samples quantitative STEM/EDXS analyses can suffer from X-ray absorption and fluorescence effects, which are related to the particular composition of the sample and its local thickness t. Due to significant quantification errors only intensities of X-ray lines are usually given in literature (see, e.g. (1)).

In this work, the t effect on quantitative STEM/EDXS analysis of CIGS solar cells with ZnO window layers is investigated, and a correction method is tested. Cross-sectional wedge-shaped TEM samples with a wedge angle of 25˚ (Figs. 1a-b) were prepared by focused-ion-beam milling with an FEI Dual beam Helios G4. The lamellae were attached to Si and Au grids to avoid an artificial increase of the Cu concentration in CIGS due to stray X-rays. STEM/EDXS analyses were performed at 200 kV with an FEI Tecnai Osiris microscope equipped with a ChemiSTEM detector. Recording and quantification of EDXS data were carried out by using the Esprit software of Bruker.

Quantification can be tested by considering first the ZnO window layer with known stoichiometry. The correct stoichiometry is obtained only at the thin edge of the ZnO wedge. Using the thin-film quantification approach, the evaluated O content decreases linearly with increasing t, whereas the Zn content increases (Fig. 1c, t = 0 nm). This behavior is attributed to the t-dependent absorption of the low-energy O X-rays. However, it can be corrected for by considering the local t and ZnO density (5.67 g/cm3) for quantification (Fig. 1c, t = 50-200 nm). We note that the t-dependent absorption of X-rays in ZnO can be exploited to determine the local thickness of the TEM sample. In the CIGS layer, the Ga content remains constant as the t value increases, and the In content at the wedge edge is slightly lower than in thicker regions. However, from the edge to thicker regions, the Se content increases first and then remains constant, whereas the Cu content shows an inverse profile (Fig. 1d). This artifact probably results from the Se evaporation during ion milling, which leads to larger deviations from the bulk composition in thin regions. Up to now, we have not found a good method to correct for this artifact. The concentration of each element in the CIGS layer agrees with the nominal value only when the layer thickness is above ~100 nm. Therefore, it is suggested to choose thicker regions (> 100 nm) of the CIGS layer for EDXS quantification, which can be determined by the thickness analysis of the ZnO window layer mentioned above.

References:

(1) M. Kim, J. Lee, Y. Lee, J. Jeong, K. Lee, J. Vac. Sci. Technol. B 34 (2016) 03H121.

Fig. 1

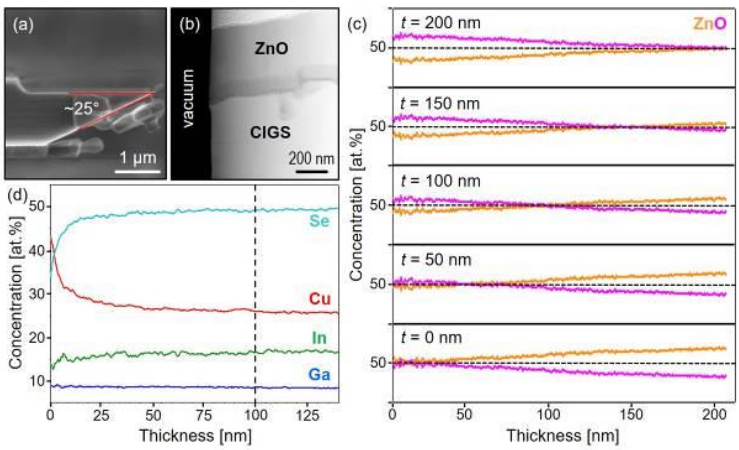

Figure 1. (a) Top view (SE image) and (b) front view (STEM HAADF image) of a cross-sectional wedge-shaped TEM sample of a CIGS solar cell with ZnO window layer, the wedge angle is 25˚; (c) thickness-dependent quantitative EDXS line profile of the ZnO window layer without correction by local thickness and ZnO density (t = 0 nm) and those corrected by different local thicknesses (t = 50, 100, 150 and 200 nm), Zn is denoted in orange and O in purple; (d) thickness-dependent quantitative EDXS line profile of the CIGS absorber, Se is denoted in turquoise, Cu in red, In in green and Ga in blue.

IM6.P017
Imaging Chiral Materials with Photon-Induced Near-Field Electron Microscopy

J. W. Henke[1], T. Harvey[1], O. Kfir[1], C. Ropers[1]

[1]Georg-August-Universität Göttingen, IV. Physicalisches Institut, Göttingen, Germany

Chirality of a physical system describes the absence of symmetry under parity transformation and lies at the heart of many open scientific questions, including the broken symmetry in the biochemistry of life or CP violation, and technologically relevant materials like magnetic skyrmions or metamaterials. Three-dimensional chirality can only be characterized by tomography or with a probe that has controllable helicity. Our aim is to demonstrate the feasibility of employing photon-induced near-field electron microscopy (PINEM) for nano-scale real space imaging of chirality via optical near-fields.

Even though energy-momentum conservation forbids emission or absorption of single photons by electrons in free space, this inelastic electron-light scattering becomes possible in the presence of a surface. This surface allows for a coupling between the electromagnetic field and the electron momentum, because translational symmetry is broken by the surface in this situation (1). The coupling strength of this interaction does not only depend on the incident optical field power, but also on the shape and the optical properties of the surface (2). Since electron beams in electron microscopes can routinely be focused to a spot size on the sub-nanometer scale, mapping of the optical near-fields via the inelastic scattering processes on the same length scales is possible. This technique, called photon-induced near-field electron microscopy (PINEM), can be employed to image plasmonic modes and optical properties with nanometer spatial resolution.

We demonstrate the ability to locally probe chirality on a nanometer scale with PINEM by illuminating a chiral sample with circularly polarised light of different handedness and measuring the difference in coupling strength of the resulting optical near-fields with electrons. The experiments were carried out using FIB-milled spiral gold structures as prototypical chiral samples. As predicted by finite-element simulations (left panel in Fig. 1), a significant difference in the average coupling strength for left- and right-handed circularly polarized illumination of a sample of fixed handedness is observed (right panel in Fig. 1). In addition, spatial variations of the coupling strength over the size of the sample are visible. The dichroism signal, defined as the difference of the two measurements with different handedness of the circularly polarized input light, is opposite for structures of opposite handedness.

PINEM with circular polarized light can be used for characterization of chirality on a nano-scale. This technique offers access to information about chiral materials with nanometer resolution. As it is possible to inelastically scatter nearly all incident electrons with moderate electron-optical field coupling, in the future, this technique could be used for more dose-efficient single-molecule spectroscopy.

References:

(1) B. Barwick et al., Nature 462 (2009) p. 902.

(2) A. Feist et al., Nature 521 (2015) p. 200.

Fig. 1

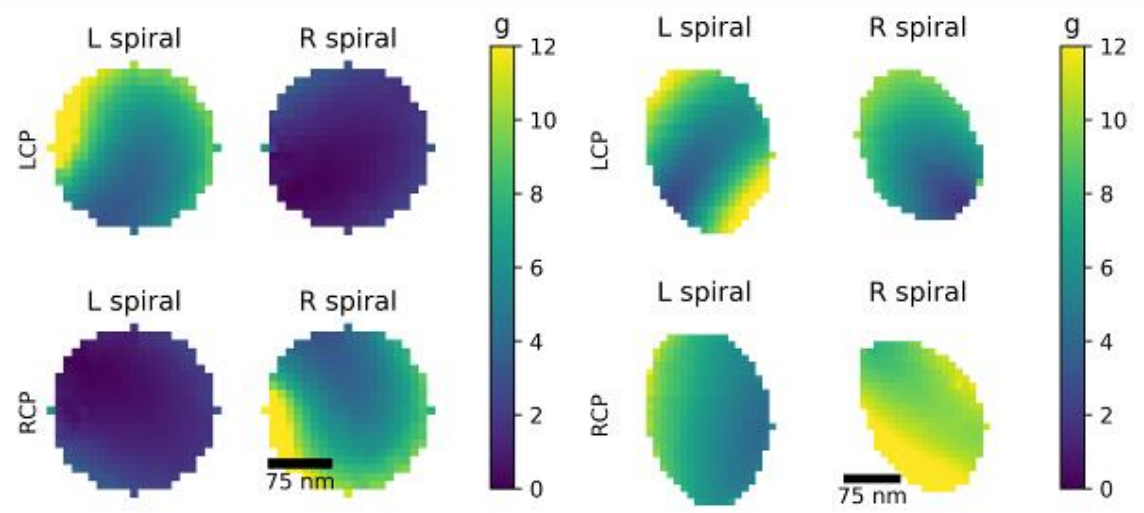

IM6.P018
Segmentation of beam sensitive materials based on machine learning on spatially resolved secondary electron spectra from ultra-low voltage scanning electron microscopy

J. Kammerer[1,2], R. R. Schröder[1,3], I. Wacker[1,3], R. Alkarsifi[4], P. Perkhun[4], O. Margeat[4], J. Ackermann[4], M. Pfannmöller[1]

[1]Heidelberg University, Center for Advanced Materials, Heidelberg, Germany
[2]Karlsruhe Institute of Technology, Light Technology Institute, Karlsruhe, Germany
[3]Heidelberg University Hospital, Bioquant, Heidelberg, Germany
[4]Aix Marseille University, CINaM, Marseille, France

Direct visualization is typically inevitable for the understanding and optimization of nanostructured or hybrid nanomaterials, which facilitates recent developments in materials science. Effective nanoscale phase identification was e.g. demonstrated for organic photovoltaic blends through analytical transmission electron microscopy (ATEM) (1). However, organic semiconductors as well as many other functional materials are susceptible to radiation damage due to the high electron energies in TEM and the projection problem may introduce ambiguities into the investigation of interfaces.

We aim at discriminating a blend of beam-sensitive materials at the nanoscale by analyzing spatially resolved secondary electron (SE) spectra in a prototype ultra-low voltage scanning electron microscope (ULVSEM).

The *cs* and *cc* corrected Zeiss DELTA® (2) ULVSEM allows for lowering the primary electron energies down to 20 eV, while maintaining high resolution. Furthermore, its dedicated energy filter enables generating spatially resolved electron spectra of secondary and backscattered electrons by varying a retarding potential. Unsupervised non-linear manifold learning is used to reveals spectroscopic similarities within the datasets. A polymer: fullerene photovoltaic blend of PTB7:PCBM was investigated as model system at 50 eV primary energy.

Three different phases, which can be assigned to a polymer rich, a fullerene rich and a mixed phase, were identified based on different SE distributions (see fig. 1a/b). A TEM reference measurement according to (1) is provided in fig. 1c where the different phases were identified based on their electron energy loss signals. Deviations of the observed domain sizes are explained by the difference between bulk and surface morphology - the latter being exclusively examined in ULVSEM.

In contrast to previous attempts with spectroscopy in SEM (3), our method relies on nanoresolved SE-spectra and is therefore sensitive towards local variations in the electronic structure. Further advantages arise from the drastically reduced electron energies: (i) alternative contrast mechanisms; (ii) decreased alteration of the materials" electronic structure during the investigation; (iii) minimized signal mixing at interfaces due to reduced interaction volume between electron probe and sample, limited to the first few nanometers. The proposed methodology can easily be transferred to a large variety of beam-sensitive materials and low-contrast material combinations.

References:

(1) Pfannmöller et al., *Nano Lett.*, 11 (8), 2011, p. 3099–3107

(2) Schröder et al., *Microsc. Microanal.,* 24 (S1), 2018, p. 626–627

(3) Masters et al., *Nat. Commun.*, 6, 2015, p. 6928

(4) Funding by the ministry of research, Baden-Württemberg, through the HEiKA materials research centre FunTECH-3D (MWK, 33-753-30-20/3/3), the sds@hd, and from the project "Morphiquant-3D" (BMBF, FKZ 13GW0044) is acknowledged.

Fig. 1: a Unsupervised machine learning reveals three phases (mixed, PCBM and PTB7 rich) from the hyperspectral SE dataset with distinct spectral properties, evident from the averaged cumulative ( ) and differentiated (- -) SE-spectra. b The contrast inversion of the images (circles) and averaged spectra from the normalized dataset for polymer and fullerene rich areas verify a segmentation based on spectral properties. **c** Reference measurement (supervised) from ATEM according to (1).

Fig. 1

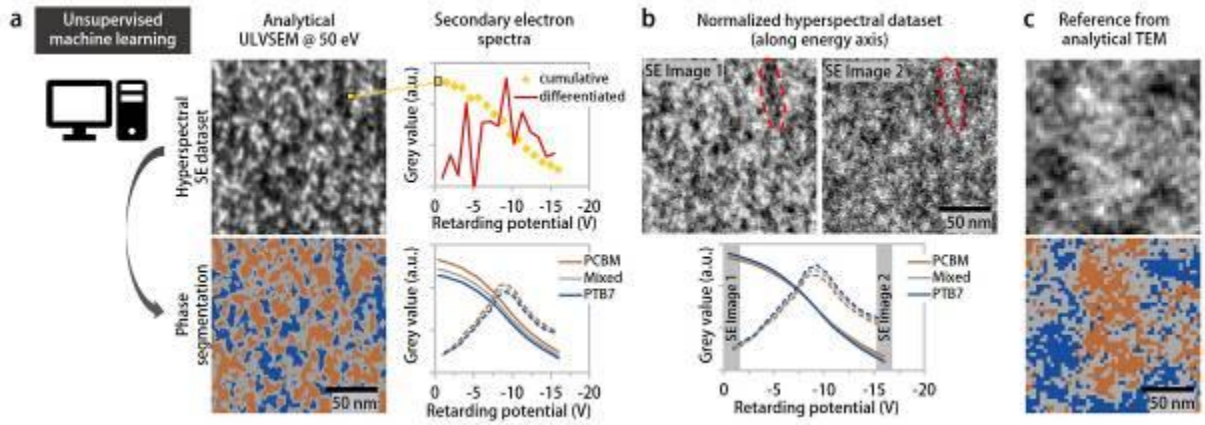
a
Unsupervised machine learning
Analytical ULVSEM @ 50 eV
Secondary electron spectra
Hyperspectral SE dataset
cumulative
differentiated
Grey value (a.u.)
0 -5 -10 -15 -20
Retarding potential (V)
Phase segmentation
PCBM
Mixed
PTB7
50 nm
b
Normalized hyperspectral dataset (along energy axis)
SE Image 1
SE Image 2
50 nm
SE Image 1
SE Image 2
c
Reference from analytical TEM

IM6.P019
EELS study of silicon dioxide based resistive random access memoery devices

K. Patel[1], M. Bosman[1], A. Kenyon[2], A. Shluger[2,3]

[1]Institue of Materials Research and Engineering (IMRE) at the Agency of Science Technology and Research Singapore (A*STAR) / Dept, IMRE, Singapore, Singapore
[2]University College London, 4Department of Electronic and Electrical Engineering, London, United Kingdom
[3]University College London, Physics and Astronomy, London, United Kingdom

We use a combination of transmission electron microscopy (TEM), scanning transmission electron microscopy (STEM) and electron energy loss spectroscopy (EELS) to study SiO1.9 based resistive random-access memory (RRAM) devices. RRAM devices offer a viable replacement for current FLASH memory by offering high switching speeds, reliability, endurance and storage density (1). RRAM devices are typically composed of a metal – insulator – metal structure, where the dielectric layer can be switched between high and low states of resistance. In the initial phase of RRAM operation, a conductive filament is formed across the dielectric layer in a process resembling a soft dielectric breakdown. The resistive switching processes involves the breaking and reforming of the conductive filament *via* application of an electrical field (2).

Devices consisting of Mo (210nm) - SiO1.9 (35nm) – Ti (4nm) – Au (110nm) are studied to determine the forming and breakdown mechanisms. Devices are grown with high interface roughness as this has been shown to improve device performance. Previous studies have shown that this increase in performance is due to an increase number of grain boundaries in the oxide and higher electric fields generated at the rough points at the interface (3). In this study, we see several interesting characteristics of the device using a TEM, STEM and EELS measurements. Firstly, we see many grain boundaries in the SiO1.9, mostly growing from the troughs of the Mo interface in high concentration. The oxide follows the roughness pattern of the Mo electrode giving a patterning effect in the Ti and Au layers (Fig. 1). Furthermore, in a pristine device the Ti layer acts as an oxygen scavenger, becoming heavily oxidized leaving only a very thin layer of metallic Ti between the Au electrode and TiO (Fig. 2). Upon forming the device, EELS analysis shows the diffusion of Ti along the grain boundaries which is subsequently oxidized forming TiO (Fig. 3). Resistivity measurements of amorphous titanium suboxide gives relatively high conductivity compared to TiO2 and SiO1.9 suggesting this is the reason for the final low resistance state (4).

References:

(1) Chang et al "Resistance random access memory", Materials Today, 19(5), 254–264, 2016

(2) A. Mehonic et al., "Electrically tailored resistance switching in silicon oxide," Nanotechnology, vol. 23, no. 45, p. 455201, 2012.

(3) Munde et al., "Intrinsic Resistance Switching in Amorphous Silicon Suboxides: The Role of Columnar Microstructure", *Scientific Reports,* vol 7, Article number: 9274, 2017

(4) Yongfeng et al., "Electrical Properties of Amorphous Titanium Oxide Thin Films for Bolometric Application," Advances in Condensed Matter Physics, vol. 2013, Article ID 365475, 5 pages, 2013.

Fig. 1: STEM images of pristine device showing patterning effect, where the Au-Ti electrode follows the roughness of the Mo electrode

Fig. 2: EELS map of the pristine Ti-SiO1.9 interace. Extracted signals of Ti (a), O contribution from TiO (b) and total O contribution (c). Line profiles indicated by the red markers are plotted for Ti (d) and O (e) showing a thin layer of metallic Ti is present whilst the majority of Ti is oxidized

Fig. 3: EELS map of a positive formed device (a). Extracted signals of Ti (b), O contribution from TiO (c) and O contribution from SiO (d)

Fig. 1

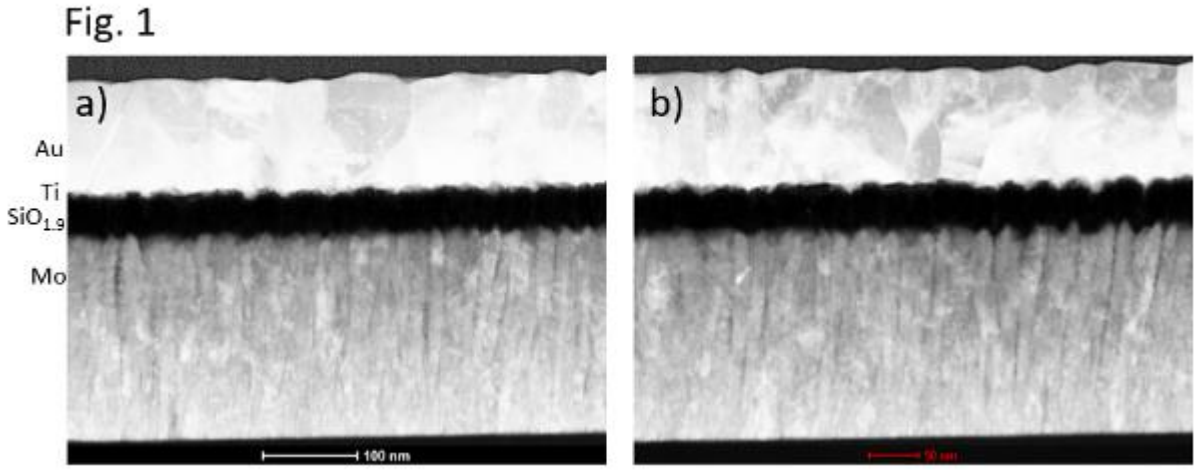

Fig. 2

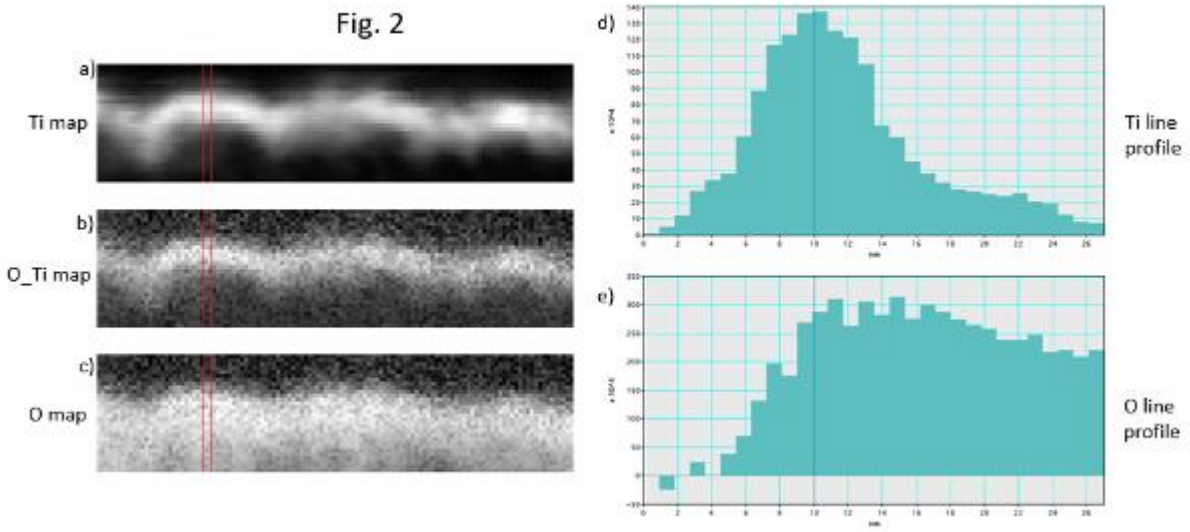

Fig. 3

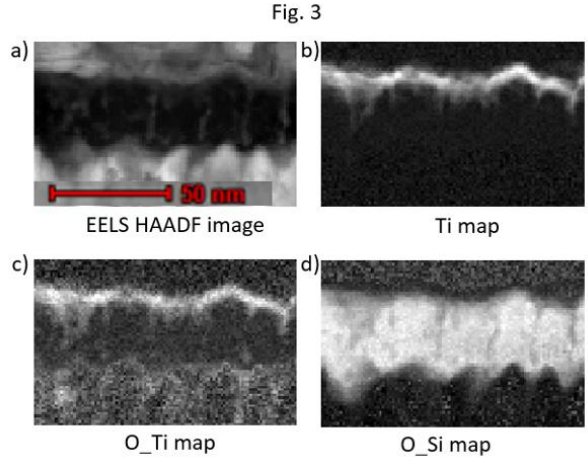

IM7.001 invited
Applications of spectroscopic electron tomography

G. Haberfehlner[1], A. Orthacker[2], G. Kothleitner[1,2]

[1]Institute of Electron Microscopy and Nanoanalysis, Graz University of Technology, Graz, Austria
[2]Graz Centre for Electron Microscopy, Graz, Austria

Electron tomography is a powerful technique for 3D materials characterization at the nano- down to the atomic scale using a (scanning) transmission electron microscope (S/TEM) (1,2). Combining tomography with spectroscopic methods gives access to a wide range of 3D information. In this presentation, we will discuss these possibilities along with applications.

Both electron energy-loss spectroscopy (EELS) and energy-dispersive X-ray spectroscopy (EDXS) allow mapping of chemical variations and gradients, approaching the goal of full 3D elemental quantification. This information can be obtained either by reconstructing elemental maps, or by reconstructing the full spectra, to obtain four-dimensional datasets with spectra for each voxel (3). Using this approach, along with high-resolution STEM studies and diffusion simulations, we were recently able to reveal atomic-scale spinodal decomposition, responsible for the diffusion process forming ordered precipitates in a multicomponent (Al-Mg-Sc-Zr) alloy (4). In these core/shell precipitates, voxel spectroscopy revealed inhomogeneous aluminum concentration within the shell, with a maximum amount of Al at the core/shell interface (Fig. 1a).

When elemental maps are reconstructed in 3D, usually each signal is reconstructed independently. However, image quality of 3D elemental maps can be greatly improved using the correlation between different elemental maps and ADF data by employing variational modelling and multi-channel regularization. For this purpose, we employ a coupled Total Generalized Variation (TGV) regularization (5). This approach allows reconstructing both hard transitions and gradual changes inside a sample, and links different signals. This favors similar interface positions for all reconstructions, significantly improving the quality of 3D elemental maps (Fig. 1b).

Finally, we will also discuss the reconstruction of particle plasmon field from a tomographic series of EELS spectrum images (6.7). Formulating EELS tomography as an inverse problem, we recover the full 3D photonic local density of states (LDOS), which describes nanoscale light-matter interactions around individual or coupled metallic nanoparticles (Fig. 2).

This project has received funding from the European Union's Horizon 2020 research and innovation programme under grant agreement No. 823717 (ESTEEM3). We thank R. Huber, M. Holler and K. Bredies from the Institute of Mathematics, University of Graz, A. Hörl, A. Trügler and U. Hohenester from the Institute of Physics, University of Graz.

References:

(1) Leary and Midgley (2016) MRS Bull. 41:531-536.

(2) Haberfehlner, G. et al. (2015) Nat. Commun. 6, 8779.

(3) Haberfehlner, G. et al. (2014) Nanoscale 6, 14563-14569.

(4) Orthacker. A. et al. (2018) Nat. Mater. 17, 1101-1107.

(5) Huber. R. et al. (2019) Nanoscale, accepted.

(6) Hörl, A., Haberfehlner, G. et al. (2017) Nat. Commun. 8, 37

(7) Haberfehlner, G. et al. (2017) Nano Lett. 17, 6773-6777

Fig. 1: (a) Changes of Al content in a core/shell particle within an Al-Mg-Sc-Zr alloy (4). (b) Reconstruction of HAADF and EDX data using a conventional algorithm (SIRT) and a coupled TGV algorithm (5).

Fig. 2: Reconstruction of the photonic LDOS: (a) Dipole and quadrupole mode around a silver cuboid (6). (b) Bonding mode around laterally coupled silver disks (6). (c) Bonding mode around vertically coupled silver triangles (7).

Fig. 1

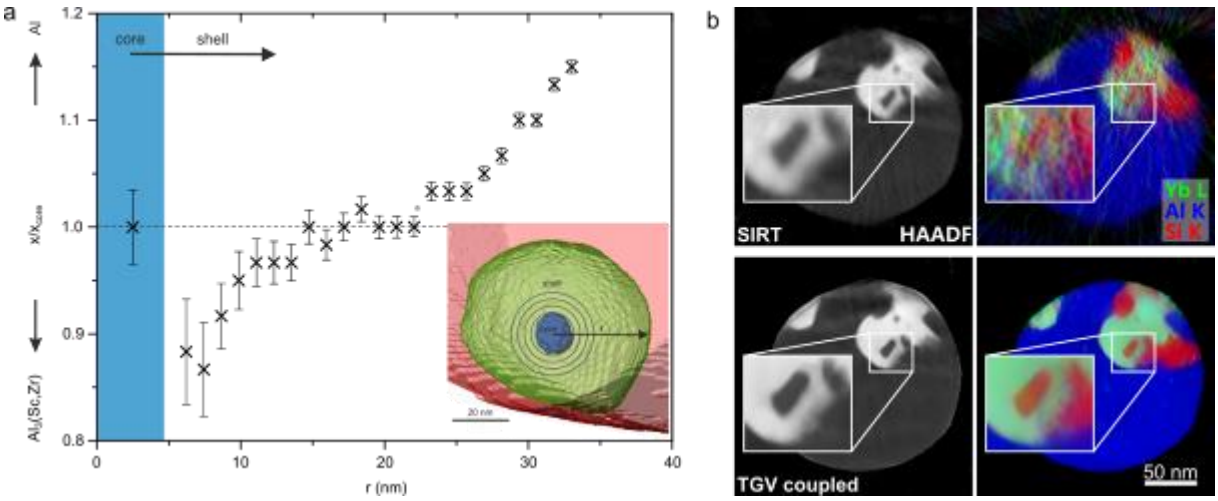
a
b
core
shell
r (nm)
SIRT
HAADF
TGV coupled
50 nm

Fig. 2

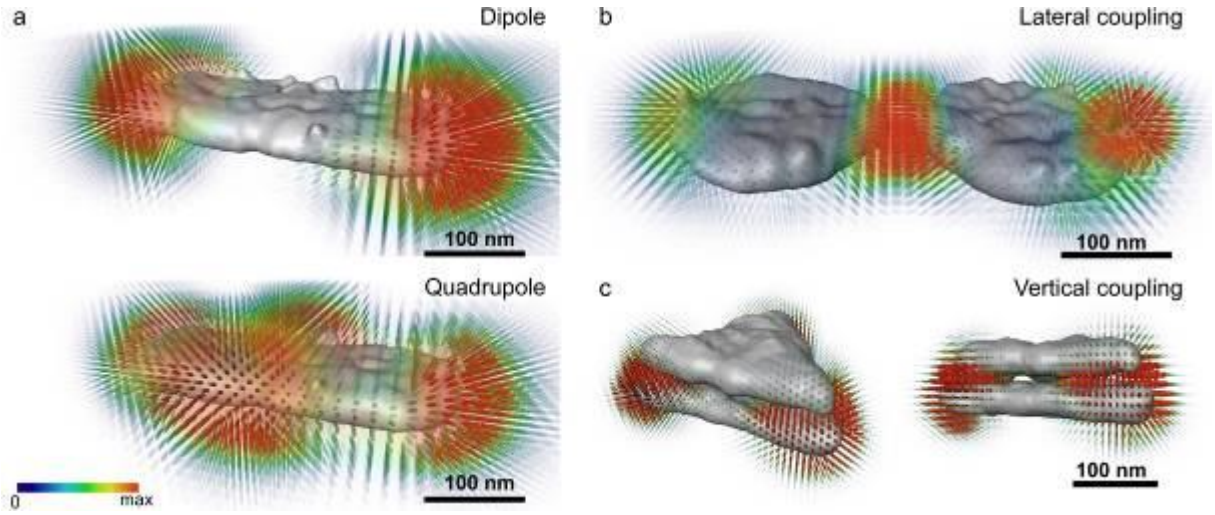
a
Dipole
Quadrupole
b
Lateral coupling
c
Vertical coupling
100 nm
0
max

IM7.003
Holographic Vector Field Electron Tomography – From Holographic Tilt Series to 3D Magnetic Fields and Magnetic Properties of Nanoscale Materials

D. Wolf[1], N. Biziere[2], S. Sturm[1], T. Niermann[3], E. Snoeck[2], C. Gatel[2,4], A. Lubk[1]

[1]IFW Dresden, Dresden, Germany
[2]CEMES CNRS-UPR 8011, Toulouse, France
[3]Technische Universität Berlin, Berlin, Germany
[4]Université de Toulouse, Toulouse, France

The expansion of nanomagnetism into three dimensions as well as the discovery of new magnetic effects in 3D nanomagnets render more complex magnetic configurations possible, many with unprecedented properties (1). The fundamental understanding of nanomagnetism requires a characterization technique that quantitatively maps magnetic structures down to the nanometer scale. Holographic vector field electron tomography (VFET) fulfills this requirement by combining off-axis electron holography (EH) and electron tomography in the transmission electron microscope (TEM). Off-axis EH uses an interferometric setup to measure the phase shift of an electron wave that passed through the sample. The phase shift of ferro-magnetic samples is proportional to projections of both 3D physical quantities electric potential (mainly mean inner potential, MIP) and magnetic flux density (***B***-field). Thus, this linear dependency is an ideal prerequisite to reveal the two 3D physical quantities from a tilt series of 2D phase images by tomographic reconstruction approaches (2). The principle and workflow of holographic VFET is illustrated in Fig. 1. In addition to the comprehensive workflow of recording and reconstructing the 3D data, crucial steps of alignment and image processing, e.g., precise displacement correction of 2D projections and 3D tomograms, phase unwrapping, denoising, etc. need to be addressed.

Fig. 2 shows the 3D reconstruction of the remanent magnetic ***B***-field within a multilayered Co/Cu nanowire (NW) by holographic VFET (3). To this end, two orthogonal holographic tilt series in 280° tilt range and 3° steps were recorded and reconstructed. The 3D structural and chemical distribution is obtained from the MIP tomogram (Fig. 2b), which was computed simultaneously from the electric phase tilt series. The results reveal a complex picture of the 3D magnetization behavior in the NW, for example, the coexistence of vortex and in-plane magnetized states (Fig. 2d). Micromagnetic simulations are conducted that match the experimental ***B***-field tomogram (Fig. 2d), and magnetic parameters of individual layers can be derived. Our highly automated implementation of holographic VFET holds large potential for revealing complex 3D magnetization nanopatterns, currently not possible with other methods at the required spatial resolution within a reasonable amount of time.

References:

(1) A. Fernandez-Pacheco et al., *Nat Commun*, 8 (2017) 15756.

(2) D. Wolf et al., *Chem Mater* 27 (2015) 6771.

(3) D. Wolf et al., (2019) submitted.

(4) D.W, S.S. and A.L. have received funding from the European Research Council (ERC) under the European Union"s Horizon 2020 research and innovation programme (grant agreement No 715620).

Fig. 1: Principle and workflow of holographic VFET.

Fig. 2: Holographic VFET of multilayered Co/Cu nanowire (NW). (a) Idealized NW as intended by template-assisted electrodeposition growth. (b) Volume rendering of the NW's mean inner potential (MIP) displaying Co in red and Cu in bluish/white. The arrow plots indicate field lines of magnetic induction (*B*-field) sliced through eight Co disks. (c) Volume rendering of the NW's B_y component (perp. to the NW axis) of micromagnetic simulation and experiment. (d) Slices through the eight Co disks at positions shown by the arrow plots in (c). The opposite normal B-field components are color-coded in black and green. By tuning the micromagnetic parameters in the simulation, an excellent match with the experiment is achieved.

Fig. 1

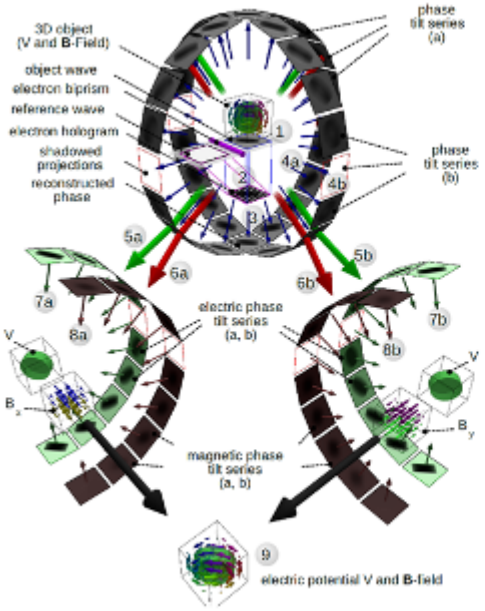

1) **Interaction** of electron waves **with magnetic sample**
2) **Interference** of modulated object wave with unmodulated reference wave by an electrostatic biprism **resulting in an electron hologram**
3) **Reconstruction** of hologram **yielding the amplitude and phase shift** of the object wave
4) **Acquisition of two tilt series** around two tilt axes, X and Y, providing two 360° phase tilt series (4a and 4b). The tilt range could be limited by experimental limitations.

5/6) **Calculation of** half the sum/difference of opposite projections (green/red arrow) resulting in **electric/magnetic phase tilt series**

7) **Reconstruction of 3D electric potential** from electric phase tilt series

8a(b) **Reconstruction of the two magnetic B-field 3D components B_x (B_y)** from the derivative in y (x) - direction of the magnetic phase tilt series a (b)

9) **Computation of 3D B_z component** by solving $\nabla \cdot B - 0$

Fig. 2

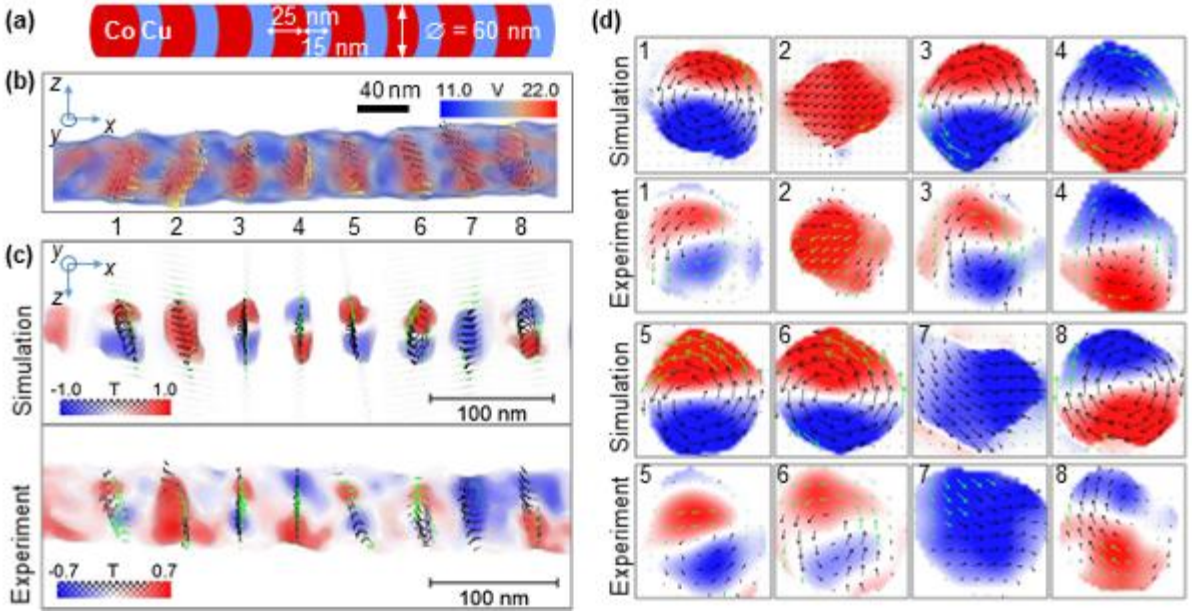

IM7.004
Deep learning based missing wedge artefact removal for electron tomography

J. Rimpeläinen[1], S. Bazrafkan[1], J. Sijbers[1], J. De Beenhouwer[1]

[1]imec - Vision Lab, University of Antwerp, Antwerp, Belgium

High angle annular dark field scanning transmission electron microscopy (HAADF STEM) allows atomic resolution imaging of nanoparticles. From multiple HAADF-STEM projections acquired at different tilt angles, 3D images of the nanoparticle can be constructed using a tomographic reconstruction algorithm. Conventional reconstruction algorithms, such as simultaneous iterative reconstruction technique (SIRT), return a high quality reconstruction only when a large number of equiangular projections is available acquired in a 180 degrees angular range. However, this is not usually the case in electron tomography, where the specimen holder is typically limited to a tilt range of about 140 degrees. Due to this, SIRT reconstructions suffer from severe smearing artifacts.

We demonstrate the use of a deep learning neural network for removal of missing wedge artifacts from SIRT reconstructions of a simulated electron tomography dataset.

The neural network used is a mixed-scale dense convolutional neural network (MSD) (1), which has been previously used for improving the quality of tomographic reconstructions (2).

Deep learning requires a large amount of training data including both imperfect SIRT reconstructions and the corresponding ground truths. Because realistic STEM simulations are very time consuming, we propose a simpler approach for simulating a large number of training samples. This is achieved by constructing a number of different gold nanoparticles using Atomsk software (3) and creating 3D volumes by adding a spherical 3D Gaussian blob at each atom position. From these images parallel beam projections, uniformly angular sampled in a limited angular range of 100 degrees were computed using the ASTRA toolbox (4) and the nanoparticles are reconstructed with SIRT. These low quality reconstructions alongside their corresponding ground truths are used to train the DNN for 55 epochs.

The resulting network is tested using realistic HAADF STEM simulations of a gold nanoparticle consisting of 147 atoms. The 26 projections (pixel size 16 pm) were obtained with a frozen phonon approach using the MULTEM software (5) and were limited in the range of -50 to 50 degrees, resulting in a large missing wedge. Poisson noise was added to obtain a signal to noise ratio of 10. The SIRT reconstruction of this nanoparticle was also computed using ASTRA toolbox (4).

One of the slices of the result, and the comparison to the original SIRT reconstruction can be seen in Figures 1 and 2.

We have demonstrated the use of a DNN for missing wedge artifact removal in electron tomography. We showed that the approach improved quality of the SIRT reconstruction of a more realistic physics based simulation.

References:

(1) D. M. Pelt and J. A. Sethian, Proc. Natl. Acad. Sci. U.S.A, 115(2), 254–259, 2018.

(2) D. M. Pelt, K. J. Batenburg, and J. A. Sethian, J.Imaging, 4(11), p. 128, 2018.

(3) P. Hirel, Comput. Phys. Commun., 197, 212-219, 2015.

(4) W. Van Aarle, W J. Palenstijn, J. De Beenhouwer, T. Altantzis, S. Bals, K. J. Batenburg, and J. Sijbers, Ultramicroscopy, 157, 35–47, 2015.

(5) I. Lobato and D. Van Dyck, Ultramicroscopy, 156, 9-17, 2015.

Fig. 1

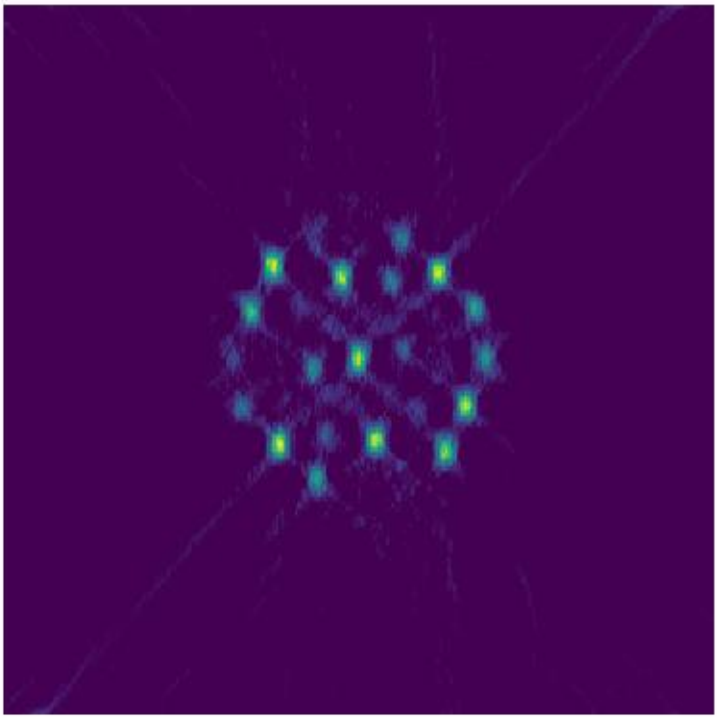

Fig. 2

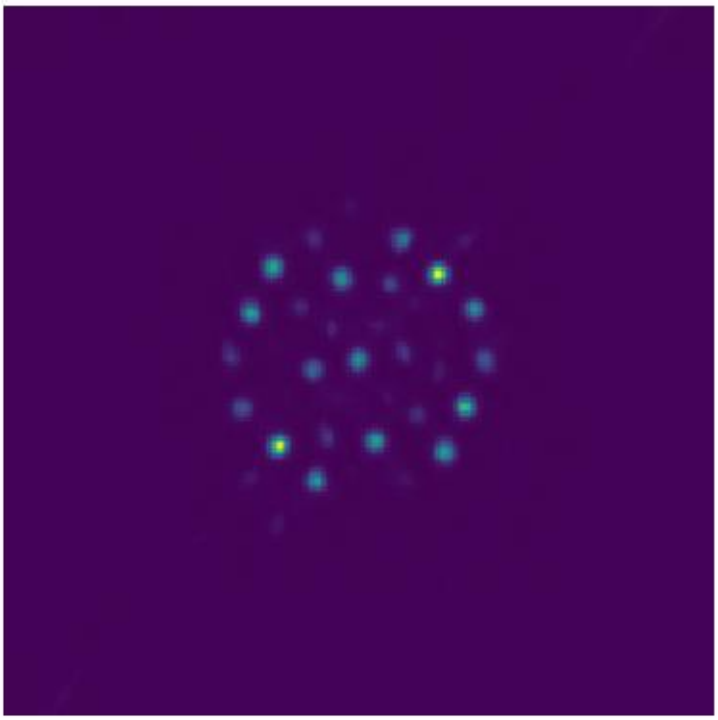

IM7.005
Detection of herpesvirus capsids in transmission electron microscopy images using transfer learning

K. Shaga Devan[1,2], J. von Einem[3], T. Ropinski[1,4], H. A. Kestler[2,4], P. Walther[1], C. Read[5]

[1]Ulm University , Central Facility for Electron Microscopy, Ulm, Germany
[2']Ulm University, Ulm, CÔte D'ivoire
[3]Ulm University Medical Center, Ulm, Germany
[4]Ulm University, Ulm, Germany
[5]Ulm University, Central Facility for Electron Microscopy, Ulm, Germany

The detailed analysis of secondary envelopment of the Human cytomegalovirus (HCMV), a member of the *Herpesvirinae*family, from transmission electron microscopy (TEM) images is an important step towards understanding the mechanisms underlying the formation of infectious virions. As a step towards a software-based quantification of different stages of HCMV virion morphogenesis in TEM, we developed a transfer learning approach based on convolutional neural networks (CNNs) that automatically detects HCMV nucleocapsids in TEM images.

In contrast to existing image analysis techniques that require time-consuming manual definition of structural features, our method automatically learns discriminative features from raw images without the need for extensive pre-processing. For this a constantly growing TEM image database of HCMV infected cells after high-pressure freezing, freeze substitution and Epon embedding was available. From the two investigated transfer learning approaches, namely feature extraction and fine-tuning, the latter enabled us to successfully detect HCMV nucleocapsids in TEM images. Our detection method has outperformed some of the existing image analysis methods based on discriminative textural indicators and radial density profiles for virus detection in TEM images. In summary, we could show that the method of transfer learning can be used for an automated detection of viral capsids in TEM images with high specificity using standard computers. This method is highly adaptable and in future could be easily extended to automatically detect and classify virions of other viruses and even distinguish different virion maturation stages (1).

References:

(1) Devan KS, Walther P, von Einem J, Ropinski T, Kestler HA, Read C. (2019) Detection of herpesvirus capsids in transmission electron microscopy images using transfer learning. Histochem Cell Biol. 151, 101-114.

.

IM7.LB.P01
Femtosecond Laser-Enabled TriBeam for in-situ laser ablation of non-conductive, thermally- and charge sensitive materials

R. Geurts[1], S. Randolph[2], B. Winiarski[3]

[1]ThermoFisher Scientific, R&D, MSD, Eindhoven, Netherlands
[2]ThermoFisher Scientific, R&D, MSD, Hillsboro, United States
[3]ThermoFisher Scientific, R&D, MSD, Brno, Czech Republic

Focused ion beam (FIB) is often used to provide 10"s of micron size cross-sections of many types of materials ready for observation by high resolution scanning electron microscopy (SEM). A few material classes do present some unique challenges to FIB/SEM workflows, these include highly non-conductive materials, thermally sensitive and charge sensitive materials. Non-conductive materials will require some form of charge compensation to enable removal, while thermally and charge sensitive materials may require cooling combined with reduced ion beam currents. As such there is a growing need for additional means of in-situ material removal down to the micron scale. Femtosecond (fs) laser technology has now reached the point of maturity that it can fill this gap.

Materials processed by fs-laser nearly universally demonstrate superior laser cut quality over thermally-ablated surfaces, but neither can produce the final surface quality of FIB. The removal rates are mostly many orders of magnitude greater than that of a FIB or even plasma FIB (PFIB). With increasing trends towards large volume analysis (LVA), there exists an opportunity for fs-lasers. The combination of LVA needs and the athermal nature of fs-laser machining drove the creation of a TriBeam system comprising a SEM/PFIB/fs-laser (1-2). More recent studies have demonstrated that in situ fs-laser machining offers some unanticipated advantages on challenging materials described previously. Here we present in-situ femto-second laser results of various non-conductive, thermally and charge sensitive materials.

Figure 1 shows a collage of different results. A large area cross-sectioning through a soft polymer (nylon 6.6 fabric). A large cross-section through industrial diamond. A large 3D serial sectioning dataset was acquired of a carbon fiber reinforced composite embedded in epoxy. Contrary to (P)FIB no protective layers were used, the final trenches are several hundreds of microns wide and deep, surfaces are clean and hardly show any curtaining. The preparation of the cross-sections of each of the examples was well under 10 minutes. The 3D dataset demonstrated was acquired overnight.

The in-situ ultra-short pulse laser of the tri-beam system enables new workflows, not only for large volume analysis of conductive materials, but also on non-conductive, thermally sensitive and charge sensitive materials which are hard to process by (P)FIB.

References:

(1) Randolph S.J. et al. "In situ femtosecond pulse laser ablation for large volume 3D analysis in scanning electron microscope systems" (2018) Journal of Vacuum Science & Technology B 36, 06JB01 (2018)

(2) Echlin M.P., Mottura et al. "A new TriBeam system for three-dimensional multimodal materials analysis" (2012) Review of Scientific Instruments 83

Fig. 1: A. Nylon Fiber 6.6 Ø=250 µm, B. Cross-section of ~500µm through a carbon fiber composite in epoxy, C. Cross-section of ~350µm through industrial diamond, D. Carbon fiber composite in epoxy in 3D (same as B.).

Fig. 1

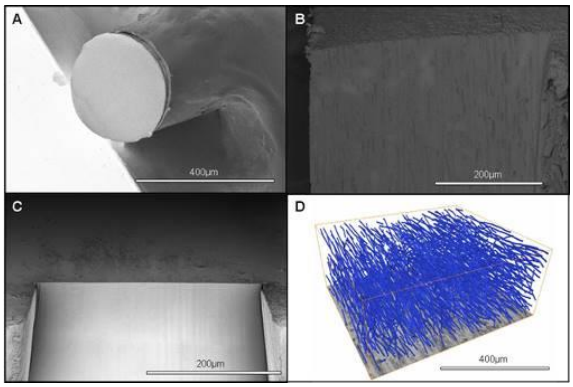

IM7.LB.P02
Three-dimensional observation of internal structure of exhaust gas purification catalyst using electron tomography with improved image processing

H. Ishikawa[1], N. Fujita[2], N. Baba[2]

[1]Toyota Motor Europe, Advanced Technology, Zaventem, Belgium
[2]Kogakuin University, Tokyo, Japan

We aim to improve catalyst activity by controlling the gas transport in exhaust gas catalyst layer. The gas transport phenomena is strongly related to geometric structure in catalyst layer. Catalyst layer has the difference scale pore, primary pore(<10nm) and secondary pore(<200nm), and the gas phenomena is also difference each pore scale. For now, we focus on the primary pore structure and develop "Electron tomography in a wide range and high resolution".

In Electron tomography, we need alignment of the positions and rotation angle before reconstruction. However, it"s difficult to align accurately by marker-based alignment and two-dimensional correlation alignment because this samples are crystalline material and contain a plurality of elements. Therefore, artefacts and distortions occurred in the reconstructed image. In this work, we tried to apply Volume data correlation alignment, which has been developed in Kogakuin University, to this samples.

Composite oxide samples (Aluminium, Cerium and Zirconium) were prepared by coprecipitation method. The sample preparation was performed with a focused ion beam (FIB) on a X-vision210TB (Hitachi). Experiments were performed on a JEM-ARM200F (JEOL), in STEM mode operated at 200KV acceleration voltage. The main process of the Volume data correlation alignment is the cross-correlation calculation between a pair of back-projected ray volume data which are calculated from neighbouring tilt images (Fig. 1). One ray volume data is calculated through a normal Filtered Back-Projection (FBP). The pair of ray volumes mostly cross-correlates at the existing 3-D, so they object position reliably matches at the correct alignment position. 2-D cross-correlation as a function of 2 image shift variables (△x, △y) is extracted from the above calculated 3-D cross-correlation function, where the (△x, △y)-plane is perpendicular to the projection direction inside the 3-D function. The practical procedure is follows: (1) the back-projected ray volume data denoted by Bn(X,Y,Z).(n = order of tilt images). (2) The cross-correlation as a function of (△x, △y) between Bn(X,Y,Z) and Bn+1(X,Y,Z) is calculated using the 3-D FFT and IFFT methods. (3) According to the maximum position of the cross-correlation, the image is translationally shifted. (4) Bn(X,Y,Z) is then replaced with Bn+1(X,Y,Z), and these processes are repeated until the last tilt angle image is achieved. Tilt-axis search is also calculated by cross-correlation. We implement the following method: (1) the series of projection images is divided into two sets in which the even- and odd-numbered images are selected. Each of the 3-D volume reconstruction data is calculated from the selected projection images. (2) The cross-correlation coefficient between the two volume. (3) The processes are repeated by changing Xs (tilt-axis position) and θ (angle of the tilt-axis) which decide the position of the tilt-axis within a particular range of the parameter value.

The reconstruction image was not included the artefacts and distortions except for missing wedge and showed the high resolution (fig.2). As a result of resolution measurement, the reconstruction image showed a resolution of 4.25 nm

We could calculate the error of positions and rotation angle using the volume data correlation alignment. As a result, it"s possible to clear the reconstruction image expect for the artefacts and distortions.

Fig. 1

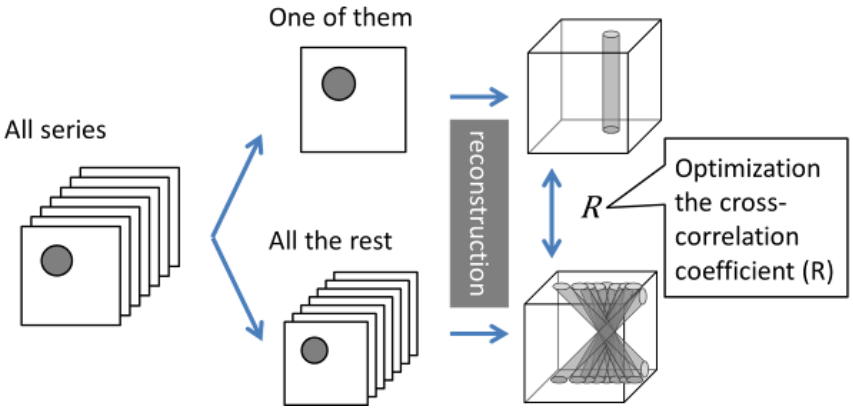
All series
One of them
All the rest
reconstruction
R
Optimization the cross-correlation coefficient (R)

Fig. 2

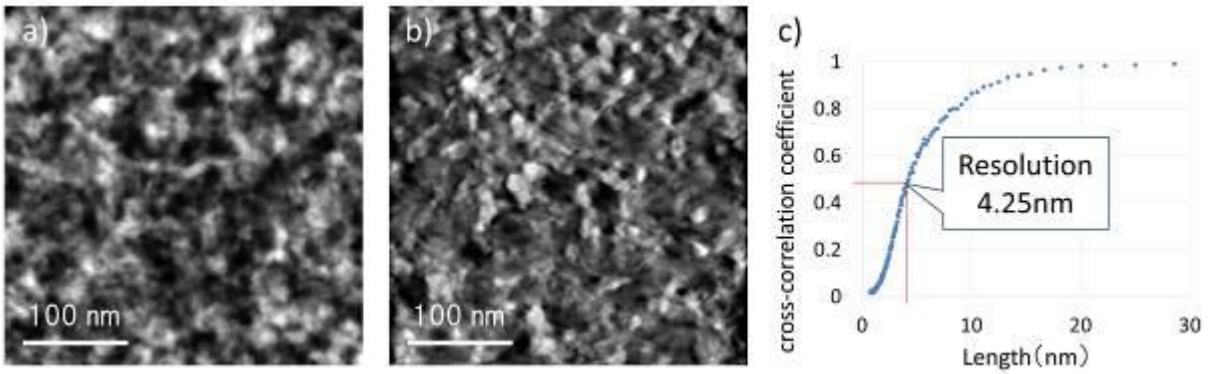
a)
100 nm
b)
100 nm
c)
cross-correlation coefficient
1
0.8
0.6
0.4
0.2
0
0
10
20
30
Length(nm)
Resolution
4.25nm

IM7.P001
3D structure study of colloidal nanocrystals using liquid phase TEM

J. Park[1,2]

[1]Seoul National University, School of Chemical and Biological Engineering, Seoul, South Korea
[2]Institute for Basic Science (IBS), Center for Nanoparticle Research, Seoul, South Korea

Three dimensional (3D) atomic arrangements of materials determine the overlaying free energy landscape, as a result, govern the physical and catalytic properties of materials (1,2). As the material dimension becomes nanometer-scale, the 3D structures of nanocrystals typically deviate from the periodic atomic arrangement of their bulk counterparts due to the dominance of surface dangling bonds, defects, and dislocations (3,4). Such deviations are noticed significant in nanocrystals of less than 4 nm and crystal structures thermodynamically unexpected in a bulk scale are often observed in the small size regime. These unique crystal structures that nanocrystals have can render distinct localized free energy along the surface and make them attractive as heterogeneous catalysts. In addition, populations of synthesized nanocrystals tend to have heterogeneous atomic structures, since uniform thermodynamic control at the level of individual nanocrystals is extremely difficult to accomplish. Thus, understanding of the nanocrystal structures and their unique properties requires precise determination of the positions of the individual atoms in a single nanocrystal level and its reproducibility for the heterogeneous individual nanocrystals.

In this study, we introduce a development of "one-particle reconstruction" in solution phse, based on atomic-resolution 3D SINGLE (structure identification of nanoparticles by graphene liquid cell electron microscopy) (5) and apply it to determine the 3D atomic arrangements of individual Pt nanocrystals in solution.

Our high-resolution 3D density maps and fitted atomic models show face-centered cubic structures of individual Pt nanocrystals with structural degeneracies, including single crystalline, polycrystalline, distorted structures, and a dislocation. Attributed to precise assignment of atomic positions in 3D domain of individual nanocrystals, lattice expansion, internal defects, prominent strains near the surfaces and dislocation plane, and their contribution to the free energy of ligand passivated Pt nanocrystals are directly investigated.

References:

(1) M. A. Pfeifer, G. J. Williams, I. A. Vartanyants, R. Harder and I. K. Robinson, *Nature*, 2006, 442, 63.

(2) V. R. Stamenkovic, B. S. Mun, K. J. J. Mayrhofer, P. N. Ross and N. M. Markovic, *J. Am. Chem. Soc.*, 2006, 128, 8813–8819.

(3) M. Azubel, J. Koivisto, S. Malola, D. Bushnell, G. L. Hura, A. L. Koh, H. Tsunoyama, T. Tsukuda, M. Pettersson, H. Häkkinen and R. D. Kornberg, *Science*, 2014, 345, 909.

(4) T. Nilsson Pingel, M. Jørgensen, A. B. Yankovich, H. Grönbeck and E. Olsson, *Nat. Commun.*, 2018, 9, 2722.

(5) J. Park, H. Elmlund, P. Ercius, J. M. Yuk, D. T. Limmer, Q. Chen, K. Kim, S. H. Han, D. A. Weitz, A. Zettl and A. P. Alivisatos, *Science*, 2015, 349, 290.

IM7.P002
Non-linear dimensionality reduction on low-energy loss spectral imaging data

M. Pfannmöller[1], R. Alkarsifi[2], J. Ackermann[2], O. Margeat[2], R. R. Schröder[1,3]

[1]Heidelberg University, Centre for Advanced Materials, Heidelberg, Germany
[2]Aix Marseille University, CINaM, Marseille, France
[3]Heidelberg University Hospital, Cryo Electron Microscopy, BioQuant, Heidelberg, Germany

Machine learning (ML) in TEM energy-loss (EL) spectroscopy allows correlation of signal properties and physical meaning. In spectral imaging (SI) EL spectra are recorded at nm resolution generating hyperspectral data where noise needs to be separated from sample related signals. For ML typically dimensionality reduction (DR) is performed, facilitating visual inspection and clustering of spectra into material classes. Classical, linear DR algorithms like principal component analysis may fail due to simplified assumptions on the nature of signal generation. Non-linear DR like locally linear embedding (LLE) (1) can separate hyperspectral EL data into distinct classes, even for blends of two organic semiconductors (2). However, embedding coordinates do not provide intuitive inspection of physical meaning, i.e. spectral features.

We show that mapping embedding coordinates from LLE on large SI data sets to original spectral properties enables evaluation of clustering and relating it to materials phase properties.

SI data sets in energy-filtered TEM mode (Zeiss Libra 200 MC) were recorded on 60 nm thin blends of a fullerene derivative (PCBM) and a semiconducting polymer (PTB7). The SI data spans the low EL region to perform analysis on optical properties around π- and σ-plasmons. A reverse computation of LLE into original coordinates was implemented based on the *Modular Toolkit for Data Processing*.

Based on pronounced differences in plasmon excitations in an energy-filtered image with positive contrast of fullerene against polymer phases (Fig 1a) universal differences are visible in average spectra from end members, i.e. strongly enriched phases (Fig 1b). However, segmentation into classes based on hyperspectral details is only possible after non-linear embedding by LLE. LLE allows DR from 84-dimensional space—the number of energy channels—into three major embedding axes (Fig 2a). End member-like spectra are clustered into two clouds apart from a third, intermediate cloud. Two points from the third cloud were selected and reversed to determine spectral representations. Resulting spectra (Fig 2b) differ from the average spectrum of the cloud, but are similar in comparison to end member spectra and do not result from additive overlay of end member phases (Fig 2c).

Conclusions: By reversibly evaluating a non-linear DR algorithm it is possible to identify unknown phases in material systems. For fullerene: polymer blends it reveals details related to close interaction between the two material components, which is essential for establishing valid structure-property relationships.

References:

(1) Saul & Roweis, *J Mach Learn Res*, 4 (2003), 119

(2) Pfannmöller et al., *Nano Lett.*, 11, 2011, p. 3099

(3) Funding by the MWK, Baden-Württemberg, through FunTECH-3D (33-753-30-20/3/3) and from the sds@hd is acknowledged.

Fig. 1: a**:** Energy-filtered TEM image with contrast between fullerene (bright) and polymer (dark) phases based on varying bulk plasmon signals. b: Average low-energy loss hyperspectra from the boxes in a with principal differences.

Fig. 2: a: Clustering of 84-dimensional, hyperspectral data set (Fig 1) into three clouds of end member-like spectra (green and red) and intermediate cloud (blue). b: Average spectrum in comparison to R1 and R2 spectra from the intermediate cloud computed from reversibly evaluating the three-dimensional LL embedding space. **c**: Comparison of R1 and R2 spectra to end members.

Fig. 1

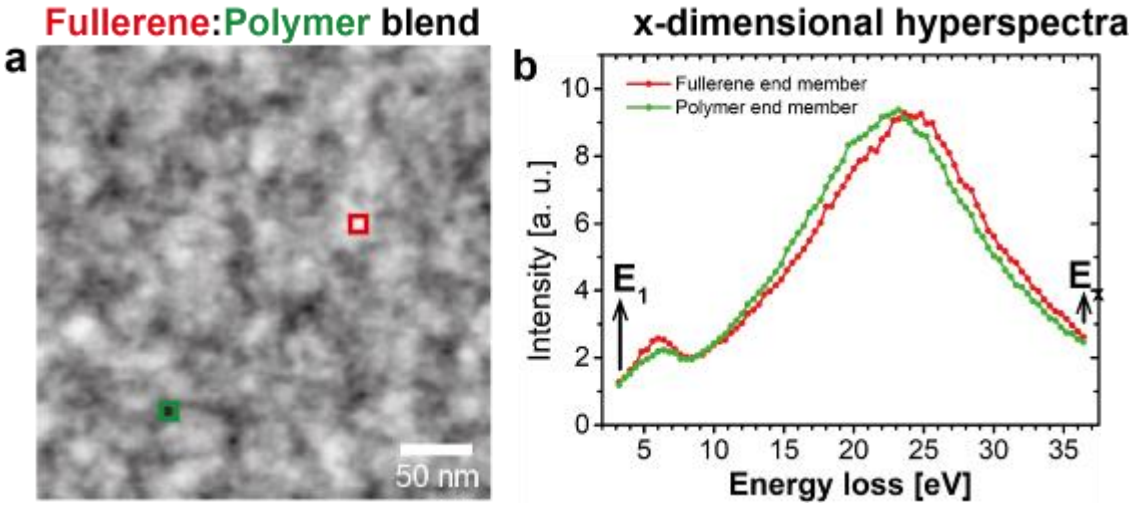
Fullerene:Polymer blend
x-dimensional hyperspectra
a
b
50 nm
Fullerene end member
Polymer end member
Intensity [a. u.]
Energy loss [eV]
E1
Ex

Fig. 2

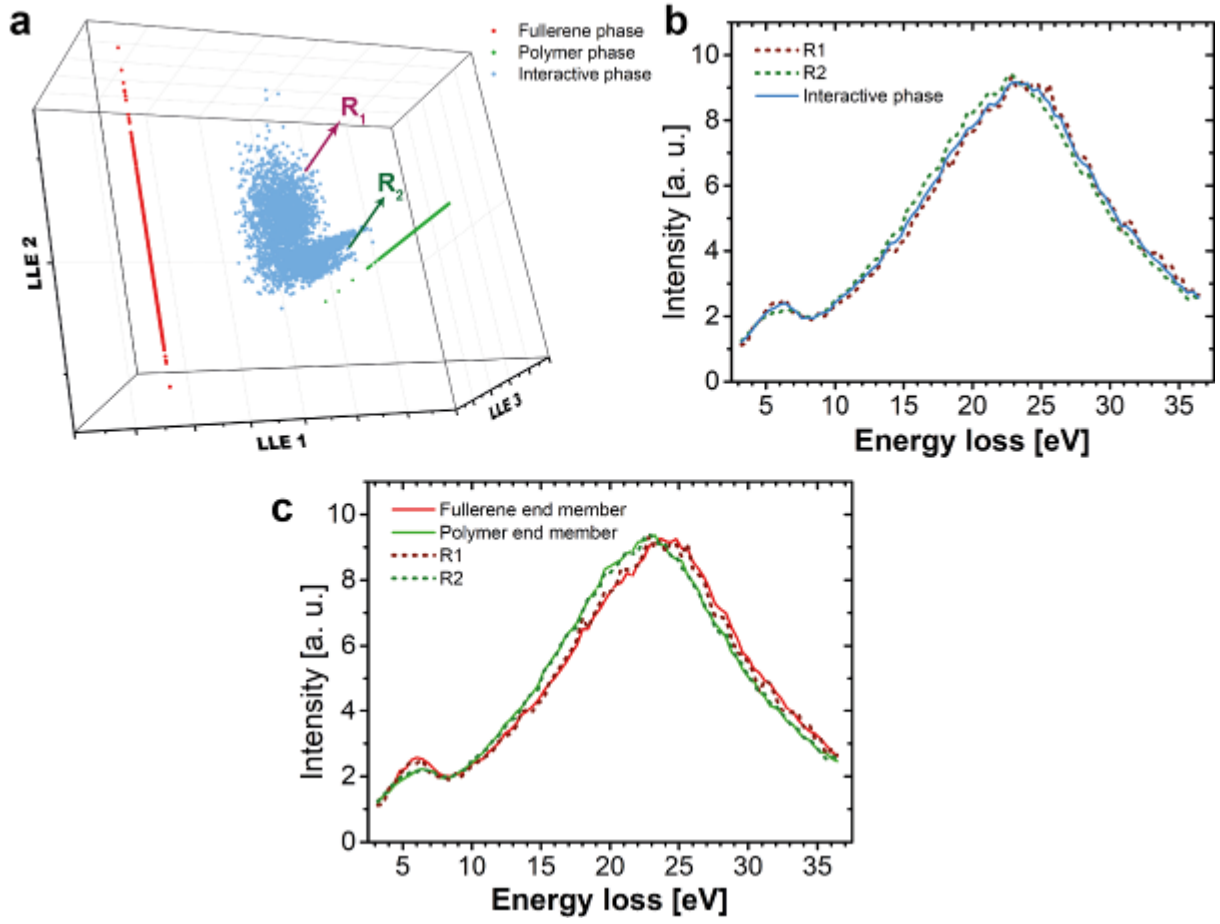
a
b
c
Fullerene phase
Polymer phase
Interactive phase
R1
R2
LLE 1
LLE 2
LLE 3
Intensity [a. u.]
Energy loss [eV]
Fullerene end member
Polymer end member

IM7.P003
Solutions for the challenges of analytic 3D FIB-SEM Tomography

T. Volkenandt[1], F. Pérez-Willard[1]

[1]Carl Zeiss Microscopy GmbH, Oberkochen, Germany

With the development of significantly improved detectors for energy dispersive x-ray spectroscopy (EDS) and electron backscatter diffraction (EBSD), the interest to use them in 3D FIB-SEM tomography workflows rises as well. Especially the improvements in terms of speed and sensitivity motivate researchers to go for larger volumes and higher resolution. However, it is not straight-forward to simply scale up established tomography routines as there are several challenges that may lead to imprecise and misleading results.

With this contribution we highlight and explain existing challenges of 3D FIB-SEM tomography especially concerning accuracy, resolution, speed and integration of analytics. A software solution that addresses these challenges is presented.

In order to facilitate subsequent 3D reconstruction based on the stack of images acquired by FIB-SEM tomography, it is beneficial to sample the volume of interest using isotropic voxels. Depending on the feature size within the sample it may additionally be of interest to keep the isotropic voxels as small as possible to achieve high resolution. For the 2D pixel size of the images, this is no problem, however, achieving an as small slice thickness (Z resolution) consistently is not as easy. Sample drift and thermal effects become significant if isotropic voxel sizes in the order of nm are targeted. In this case it is essential to have a system in place that is capable of measuring slice thickness and sample drift already during the acquisition and react accordingly. Another aspect to consider is the energy of the primary electron beam. To keep the interaction volume of the electrons small enough i.e. in the range of the slice thickness, it is necessary to use low kV. However, if analytics are part of the experiment this often calls for high kV, to excite certain x-ray lines in case of EDS or enable high signal-to-noise patterns on the camera in case of EBSD.

The presented software solution addresses before mentioned and further challenges. Advanced slice thickness tracking together with predictive sample drift measurement is achieved by a pair of angled fiducial lines patterned on the sample surface in advance. These lines show up as notches in the cross-section view. Measuring the distance between the notches during the acquisition in combination with knowing their angle, allows to precisely determine the current slice thickness and drift. This information is used in a closed loop to either speed up or slow down the FIB milling progress and assure consistent image slices. To enable best conditions for imaging and analytic mapping, two sets of beam parameters can be stored and are recalled automatically during the tomography acquisition. Sophisticated algorithms assure perfect beam tuning and sample positioning. Further details about the mentioned techniques will be given in the presentation and substantiated by application examples.

FIB-SEM tomography is a great technique to analyze materials science samples in 3D at high-resolution and combine the investigation also with elemental or crystallographic analysis. However, several challenges arise with respect to accuracy, resolution and speed. In this contribution we present a software solution for FIB-SEM tomography that addresses these challenges and thus assures consistent, high-quality data perfectly suited for subsequent analysis and reconstruction.

IM7.P004
Effect Pigments in Coatings: Evaluating the nanostructure in 2D and 3D by means of electron and X-ray microscopy

L. Berthold[1], C. Patzig[1], C. Thieme[1], S. Reissaus[1], T. Hoeche[1]

[1]Fraunhofer Institute for Microstructure of Materials and Systems, Optical Materials and Technologies, Halle (Saale), Germany

Effect-pigment based coating systems with special optical properties (color, sparkling effects, …) are used to coat numerous consumer products, including cars, architecture or print media.

In order to gain a specific optical impression, it is important to control the size, distribution and orientation of the effect pigments within the polymer matrix of the coating system. Also, the pigments, which typically are of plate-like character with elongations between 5-50 µm and thicknesses of 0.5-1 µm, may be coated with nanoscaled interference layers to enhance optical effects. The control of thickness, homogeneity and element distribution within these layers is of huge importance for the overall optical impression.

The analysis of the 2D pigment distribution and orientation within the coatings can be done via cross section preparation and subsequent light- and scanning electron microscopy analysis (Fig. 1). On the other hand, a 3D pigment analysis within the polymer matrix could so far only be carried out by complex slice-and-view procedures, e.g. in a focused ion beam (FIB) approach, since the resolution of "standard" 3D tomography techniques like X-ray tomography does not yield the resolution needed to analyze pigments with dimensions on the size of a few µm only.

Recently, methodological developments within the field of X-ray microscopy (XRM) enabled to perform 3D tomography with a resolution down to 50 nm. Therefore, detailed 3D investigations of pigment particles in coatings are now possible.

Here, we demonstrate the capabilities of cutting-edge X-ray microscopy for the imaging and determination of 3D orientation distributions of effect pigments in organic coatings.

A Carl Zeiss Xradia 810 Ultra X-Ray microscope was used to analyze the pigment distribution in two model coatings (without and with desorienter particles).

Details of sample preparation using laser micromachining will be shown, as well as 3D data assessable via XRM. Besides a 3D representation of the orientation distribution and visualization of the desorienter particles (Fig. 2), a quantitative description of the orientation distribution is derived and discussed. Additionally, results of a stitching procedure of up to 3 X-ray data sheets will be presented.

Conclusion: Exemplified by model coatings containing effect pigments, the novel capabilities of XRM in terms of unprecedented spatial resolution of relatively large volumes will be demonstrated. The results open the possiblity for the study of particle orientations in systemic applications and the influence of desorienter particles on optical effects. Additionally, the possibility to stitch single data sets to larger unit makes comparatively large 3D volumes of special, pigment-based coating systems accessible.

Fig. 1: Scanning electron microscopy cross section image of a coating system with pigments and desorienter particles

Fig. 2: XRM image of a coating system with pigment particles and desorienter particles

Fig. 1

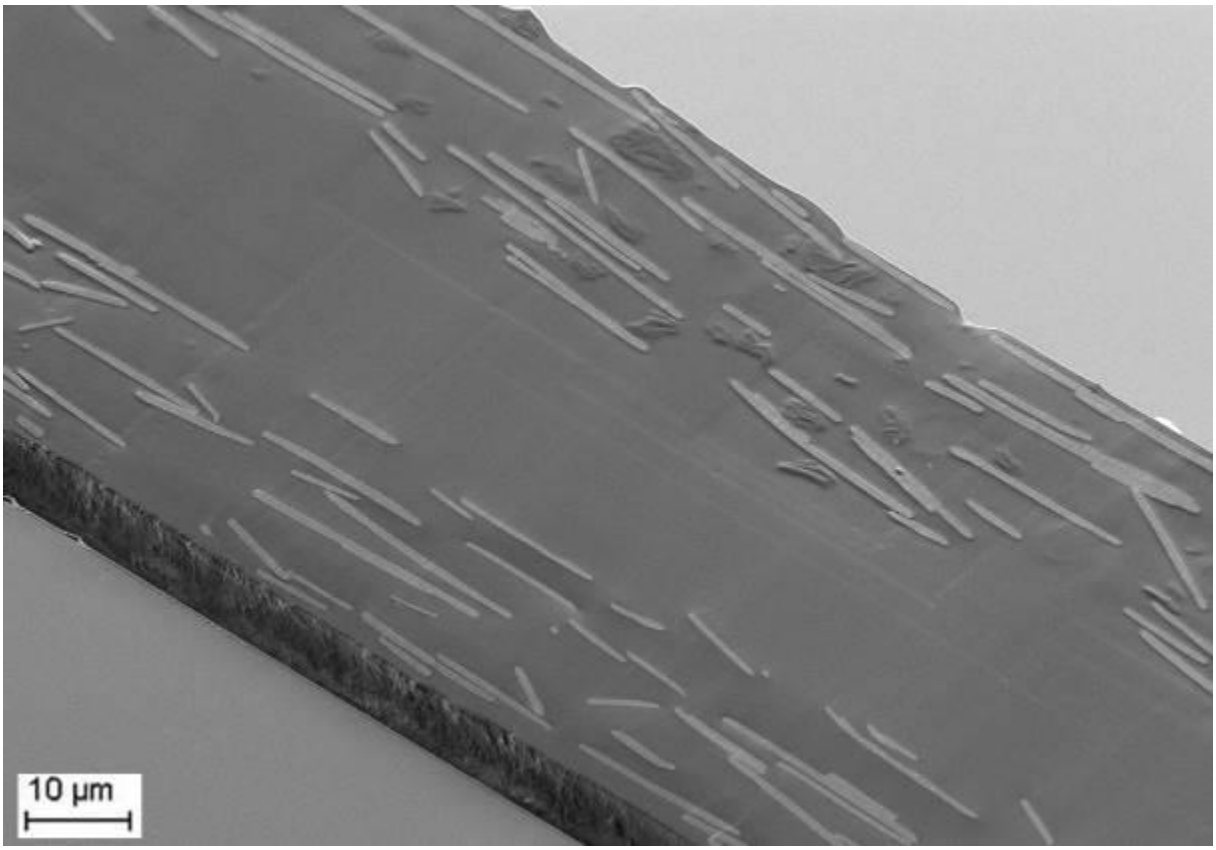

Fig. 2

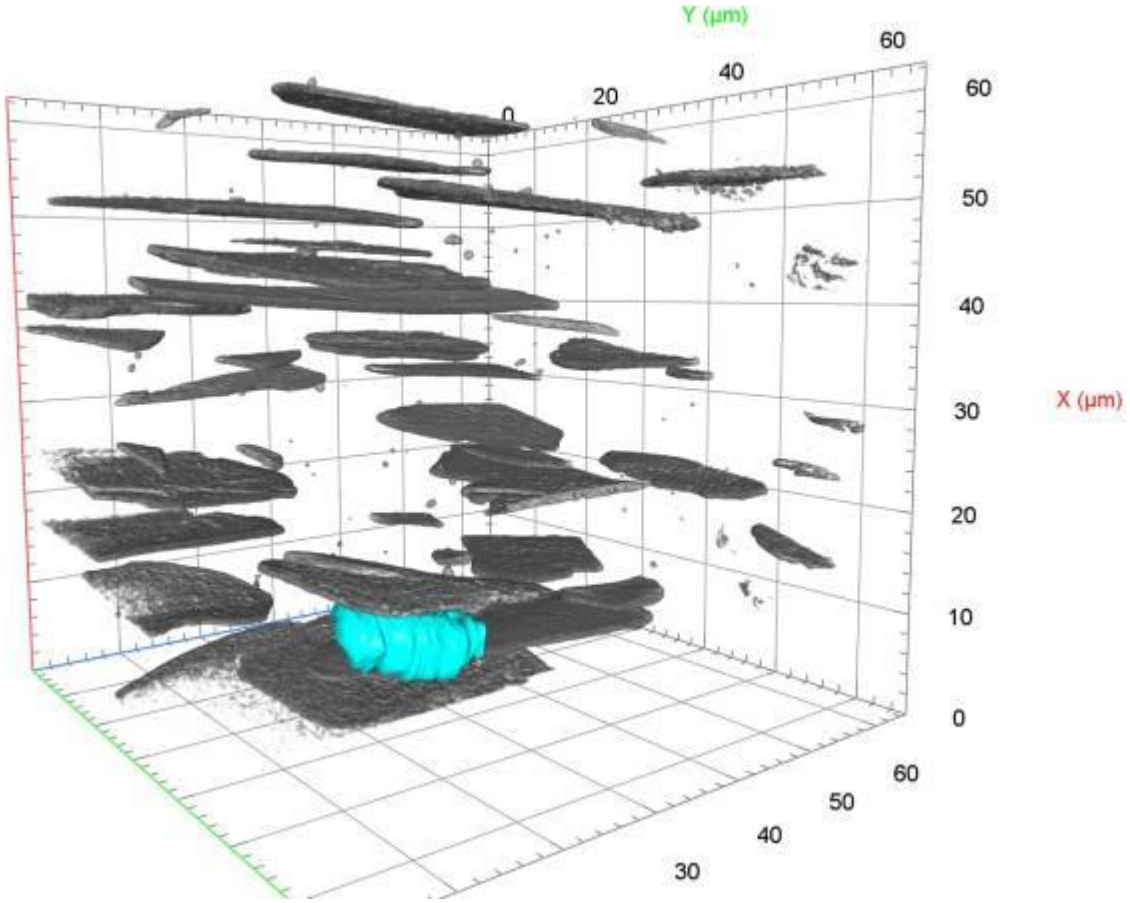

IM7.P005
Component-based quantification of spectrum imaging: philosophy and examples

S. Zhang[1], C. Scheu[1]

[1]Max-Planck-Institut für Eisenforschung GmbH, Düsseldorf, Germany

Spectrum imaging is a modern routine for analytical microscopy, and widely applied to energy dispersive X-ray (EDX), electron energy loss (EELS), and cathodoluminescence spectroscopy. Multivariate analysis is a powerful toolset to exploit the sparsity of hyperspectral datasets. Such dimension reduction is useful for noise cleaning and compact representation of datasets. Nevertheless, most analytical information derived from spectrum imaging is still conventionally analysed on a pixel to pixel basis.

We will first demonstrate how component-based quantification is mathematically equivalent to pixel-based quantification (1). Analysing a handful of spectral components is far more practical and error-proof than going through thousands of spectra from individual pixels. We will present the work flow to quantify EDX spectral components, which is straightforward considering the linear nature of the hyperspectral dataset. The quantification and error analysis of each component are then translated back to individual pixels using our automated routines.

On the other hand, EELS datasets are more nonlinear due to multiple and unspecified scattering events. We will demonstrate here how the dimension reduction to spectral components benefits the supervision necessary for reliable quantification. There are examples to derive linear and even some nonlinear quantities of individual pixels reconstructed from component-based quantification (1).

While the philosophy of component-based quantification can be more widely applied, we will use the feedback from the community to continue the development in routines to evaluate big data and their spectral components. To benefit daily experimental works, our routines are implemented with graphical interfaces for interactive supervision and decision making.

References:

(1) S. Zhang, C. Scheu, Microscopy 67, i133-i141 (2018).

IM7.P006
Diffraction Tomography in Electron Holography to Reach Three-Dimensional Atomic Resolution

J. Krehl[1], D. Wolf[1], A. Lubk[1]

[1]IFW Dresden, AMEM, Dresden, Germany

Electron holography is an important tool of nanoscale analytics, giving direct access to the electric and magnetic potentials down to Angstrom resolution. It has been readily used for atomic scale structure analysis of various thin specimen. In the last decade the limitation that the phase image contains only the projected electromagetic potential was addressed by the development of electron holographic tomography (EHT). Therein multiple projections are combined into a reconstruction of the three-dimensionally resolved, and therefore fully local, potential. The viability and usefulness of this technique has been amply demonstrated in the detailed analysis of e.g. electric potentials in semiconductor devices or magnetic fields in nanomagnets down to the nanometer scale. These tomographic techniques are based on the phase grating approximation (PGA), which is necessary to fulfill the projection requirement, i.e. providing a linear model between the three-dimensional potential distribution and the phase image of the holograms. However, the PGA breaks down when approaching atomic resolution with serious consequences for the tomographic reconstruction (1). We have shown that the main limitation of the PGA is the neglection of propagation effects while the electron wave passes through the sample (2). Therefore, we developed a new approach (3) using the Rytov expansion of the ordinary differential equation for the scattering of high-energy electrons in a linear approximation. This gives us a model which incorporates propagation effects to an extent that is sufficient in the spatial frequency regime relevant in atomic resolution TEM. Furthermore, as the model is linear the reconstruction can be carried out with conventional linear inverse problem solvers, so the reconstruction is only mildly ill-posed, just as the conventional tomographic reconstruction. We demonstrated the feasibility of that approach at a simulated tilt series of a tungsten disulfide nanotube. We recently acquired a holographic tilt series with atomic resolution of a tungsten needle point and report on first reconstructions thereof and discuss ongoing work on the ultimate performance of this reconstruction technique.

JK, DW and AL have received funding from the European Research Council (ERC) under the Horizon 2020 research and innovation programme of the European Union (grant agreement No 715620).

References:

(1) Jonas Krehl and Axel Lubk, "Prospects of linear reconstruction in atomic resolution electron holographic tomography", Ultramicroscopy 2015

(2) Jonas Krehl "Incorporating Fresnel-Propagation into Electron Holographic Tomography" Master Thesis, 2016

(3) Jonas Krehl and Axel Lubk, "Rytov approximation in electron scattering" Physical Review B, 2017

Fig. 1: Electric potential reconstructed with the phase-grating approximation and the Rytov approximation from a simulated tilt series of a W S 2 nanotube.

Fig. 1

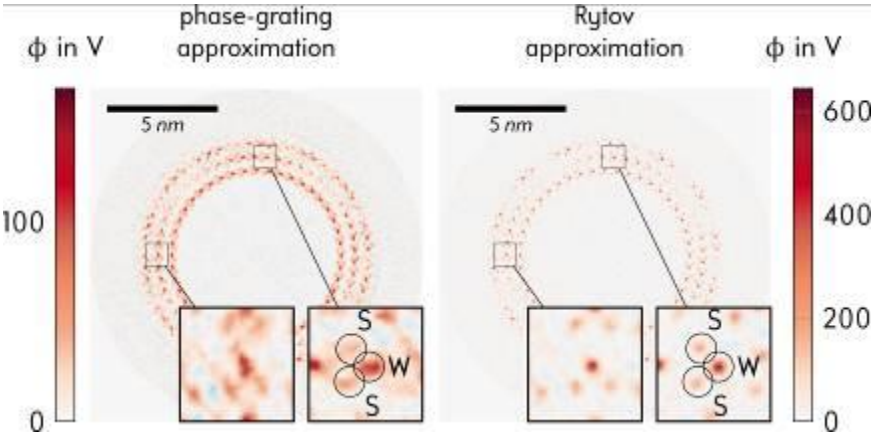

IM7.P007
Three-Dimensional Reconstruction of Combined Tilt- and Focal-Series Scanning Transmission Electron Microscopy data

E. Ortega[1], T. Dahmen[2], N. de Jonge[1,3]

[1]INM - Leibniz Institute for New Materials, Saarbrücken, Germany
[2]German Research Center for Artificial Intelligence (DFKI) , Saarbrücken, Germany
[3]Saarland University, Department of Physics, Saarbrücken, Germany

The primary methods to retrieve three-dimensional (3D) information, from 2D electron microscopy projections, rely on the use of tilt- or focal series combined with algorithms for computed tomography.(1) For tilt series, the quality of the reconstruction depends on the tilting range. The effective length the beam has to travel through the sample can increase by as much as a factor of 2.9 for typical tilt angles of up to 70°, thereby reducing axial resolution.(2) In case of the focal series, the reduced depth of field of aberration corrected scanning transmission electron microscopy (STEM) as well as nonlinear imaging contributions such as shadowing below objects and blurring effects for thick samples, limit the spatial resolution.(3) The combination of both methods was demonstrated to be possible and has the advantage of a limited tilt scheme.(4) In this work, a combined tilt- and focal series (CTFS) approach is optimized to achieve nanoscale 3D information of thin specimens.

The acquisition of high angle angular dark-field (HAADF) STEM images was performed using a JEOL ARM 200CF with both dry- and liquid-phase specimen preparation modalities. Initial studies were conducted on samples drop cast onto carbon grids. Later, liquid cell experiments were carried out using silicon microchips containing a 50 nm-thick silicon nitride (SiN) window containing gold nanoparticles (AuNPs) of 20 nm diameter. CTFS series were acquired at high tilt step increments (5°). On every iteration, the region of interest was realigned and refocused, and a focal series was acquired (Figure 1). For comparison, electron tomography (ET) was performed acquiring a complete stack from -35 to 35° with half a degree steps. 3D reconstructions were obtained using a software package of local design, named Ettention.(5)

The reconstruction from such CTFS sets is not possible with standard algorithms employed for ET. Therefore, a custom Tilt-Focal Algebraic Reconstruction Technique (TF-ART) was employed.(5) To evaluate the performance of the CTFS, the parameters for axial- and lateral resolution were compared between ET and CTFS. Published data from this method shows a reduction of the axial elongation factor (eyz), from 2.8 to 2.2 nm.(6) This improvement and ongoing optimization of parameters and reconstruction settings aims at establishing a new method to acquire 3D STEM data with applications, for example, liquid-phase STEM and other in-situ methods, where the holders" architecture prevents a high tilting range.(7)

References:

(1) Midgley et al., Ultramiscroscopy 96 (2003) p. 413-431

(2) Fernandez, J.J. Micron 43 (2012) p. 1010-1030

(3) de Jonge et al., Microsc. Microanal. 16 (2010) p. 54-63

(4) Dahmen et al., Microsc. Microanal. 20 (2014) p. 548-560

(5) Dahmen et al., Microsc. Microanal. 21 (2015) p. 725-738

(6) Dahmen et al., Microsc. Today 24 (2016) p. 26-31

(7) This work was funded by the German Research Foundation (DFG)

Fig. 1: Schematic overview of the CTFS recording scheme. a) The specimen is rotated in relatively large increments, and a focal series is recorded for every α tilt increment. Imaging is performed point by point with a STEM probe with a convergence semi-angle β. b) Diagram showing different sets of focus series images recorded at various tilt angles.

Fig. 1

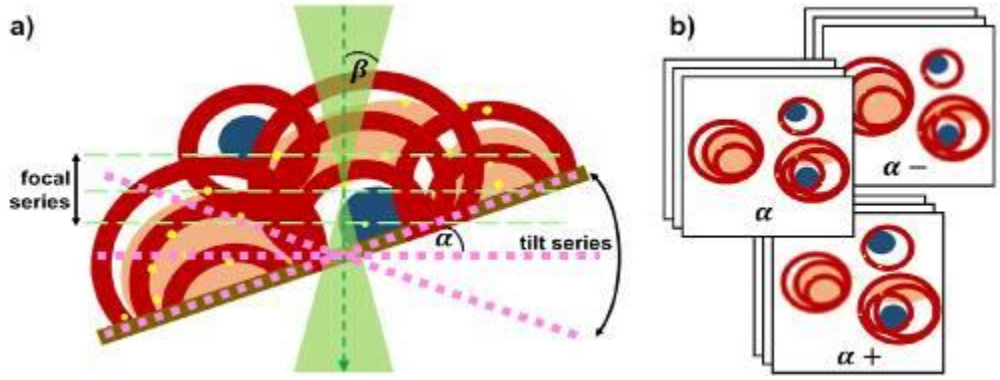

IM7.P008
Correlative FIB/SEM-informed high-resolution X-ray tomography: A case study on a Co-base superalloy oxide scale

J. Rosiwal[1], M. Lenz[1], N. Buchinger[1], J. Wirth[1], S. Englisch[1], M. Weiser[2], B. Apeleo Zubiri[1], S. Virtanen[2], E. Spiecker[1]

[1]Institute of Micro- and Nanostructure Research, FAU Erlangen-Nürnberg, Department of Material Science and Engineering, Erlangen, Germany
[2]Chair for Surface Science and Corrosion, FAU Erlangen-Nürnberg, Department of Material Science and Engineering, Erlangen, Germany

Advances in engineering enabled new applications in high-resolution X-ray tomography (nano-CT), making compact lab-based fully-fledged X-ray microscopes available (1). Modern visualization software allows the complete 3D morphology of the sample to be virtually represented and quantitatively analyzed. However, nano-CT lacks chemical information, leading to difficulties in the exact segmentation of multi-phase microstructures.

To compensate this drawback, we developed a specialized correlative workflow (Fig. 1) combing non-destructive nano-CT with SEM micrographs and EDXS mappings utilizing FIB slice-and-view technique. The sample we chose was the multinary Co-base superalloy ERBOCo-1 (2) which experienced a heat treatment and oxidation at artificial air (20% O2) at 900 °C for 12 hours. To investigate the influence of Aluminum and Chromium on the passivation layer formation inside the oxide scale, a three-dimensional analysis is necessary. The nano-CT of a 15 µm pillar was carried out with a ZEISS Xradia 810 Ultra microscope equipped a Fresnel zone plate in combination with a capillary condenser to achieve a spatial resolution down to 50 nm. A Zernike phase ring was used to provide phase contrast and thus enhance the visibility of porous structures. Using the resulting reconstructed virtual 3D volume, several regions of interest (ROI) were identified and successively exposed by FIB cross-sectional cuts. For each ROI, detailed electron images in SE and BSE contrast were taken alongside EDXS elemental distribution maps.

By direct feature comparison in SEM and nano-CT (Fig. 2a, b) images, segmentation errors due to phase contrast over-enhancements could be corrected. Fig. 1f shows the resulting segmentation of the whole sample. Using EDXS maps, each object could be assigned to an elemental composition, revealing a discontinuous layer of vertically elongated Aluminum-oxides above the γ/γ" microstructure. Two big horizontal porous layers could be identified with porosity fractions of around 2.5 %, which are comparable values to those gained by conventional FIB tomography of another sample from the same oxide scale. We think that correlative SEM/EDXS-informed nano-CT proved its ability to deliver reliable quantitative results and structural information and is a promising method for future research.

References:

(1) L.L. Lavery, J. Gelb, A.P. Merkle, A. Steinbach. X-Ray Microscopy for Hierarchical Multi-Scale Materials. Microscopy Today, 22(03):16–21, 2014.

(2) A. Suzuki, H. Inui, T.M. Pollock, Annu. Rev. Mater. Res. 54, 2015, pp. 345-68

(3) The authors thank the DFG for financial support within the frameworks of the collaborative research center SFB-TR 103 and the project SP648/8 "High-resolution X-ray microscopy for correlative tomography, high-throughput screening and *in situ* mechanical testing of structural and functional materials"

Fig. 1: Correlative workflow schematic **a** bulk oxide scale SEM cross-section **b** (1) Nano-CT tilt series (2) FIB milling (3) SEM/EDXS imaging **c** 3D reconstruction and phase segmentation of analyzed volume **d** Size adjustment of segmented phases **e** Chemical identification of segmented phases **f** Combined 3D visualization of oxide scale layers.

Fig. 2: In-detail comparison of same porous structure in a **a** SEM micrograph of FIB cross-section **b** nano-CT virtual slice showing the high illustration performance of lab-based nano-CT close to its resolution limit of 50 nm. **c** Porosity comparison of two ERBOCo-1 oxide scale samples.

Fig. 1

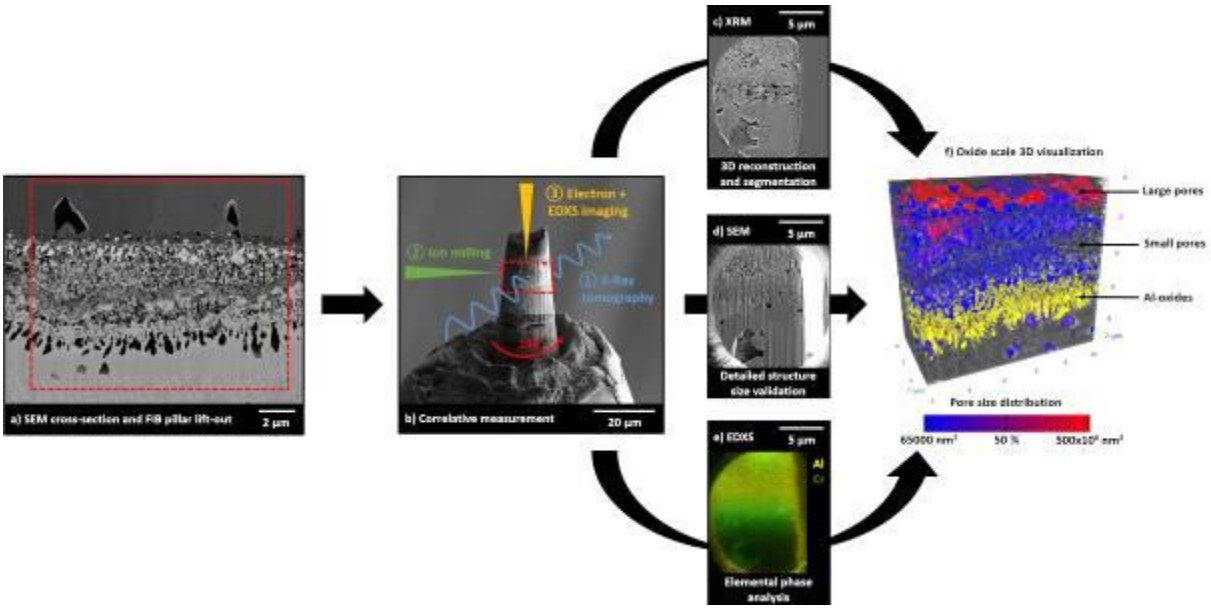
a) SEM cross-section and FIB pillar lift-out
2 µm
b) Correlative measurement
20 µm
c) XRM
5 µm
3D reconstruction and segmentation
d) SEM
5 µm
Detailed structure size validation
e) EDXS
5 µm
Elemental phase analysis
f) Oxide scale 3D visualization
Large pores
Small pores
Al-oxides
Pore size distribution

Fig. 2

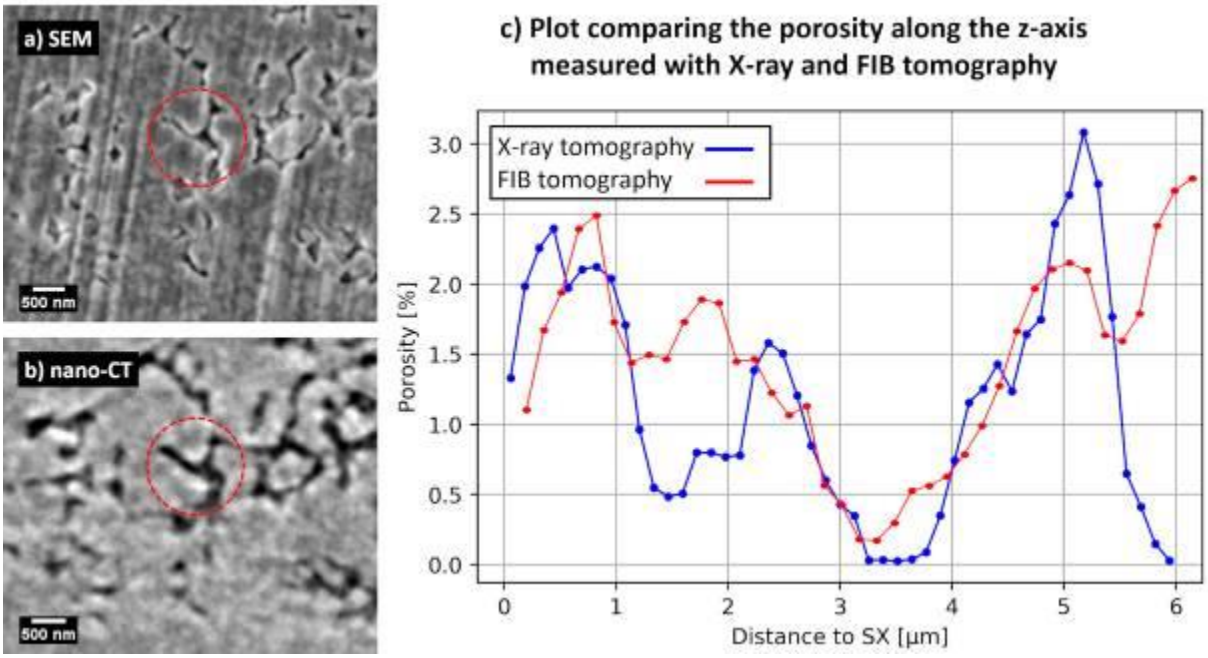
a) SEM
500 nm
b) nano-CT
500 nm
c) Plot comparing the porosity along the z-axis measured with X-ray and FIB tomography
X-ray tomography
FIB tomography
Porosity [%]
Distance to SX [µm]
0.0
0.5
1.0
1.5
2.0
2.5
3.0
0
1
2
3
4
5
6

IM7.P009
User-friendly, admin-friendly robust data storage and sharing platform: the DIADEM project

R. S. Pennington[1], C. T. Koch[1]

[1]Humboldt-Universitaet zu Berlin, Institut fuer Physik, AG SEM, Berlin, Germany

Electron microscopy generates data, often through publicly funded research and as part of larger research projects. Thus, data authenticity, integrity, and understandability are critical concerns, including for raw data generated by the microscope, analysis routines, and processed publication-quality data. Data authenticity requires a chain of custody starting from the microscope and traceable through all users, including analysis and preparations for publication. Thus, data authenticity must have secure archive standards and transfer procedures between institutions - however, not only are local data archives non-standardized, so chains of custody are informal at best, but departing scientists often take their knowledge and data with them. Data integrity requires a dataset to be verifiably complete - not just that the file checksums match, but that the scientific process be fully documented from specimen creation to data acquisition to data analysis to current specimen location. Thus, data integrity requires preserving not just electron micrograph data, but the processes' metadata - however, there exists no standard way to archive neither an electron microscopy dataset nor its metadata, including extended metadata about the scientific process. Data understanding requires tools for investigating existing datasets and incorporating information into ongoing research projects. Thus, data understanding requires the integral dataset be both available and easy to understand; however, electron microscopy datasets that people know exist (e.g. reported in publications) have no clear accessibility standards in either sense.

To address these triple challenges of data authenticity (secure archive standards), integrity (preservation of the whole dataset including its scientific process), and understanding (accessibility), we have developed the DIADEM software package. DIADEM stands for "Decentralized Integrated Archives of Data and Extended Metadata" and/or "Dezentrale integrierte Archive von Daten und erweiterten Metadaten". Its primary objective is to provide an easy-to-use, easy-to-administer secure data archive solution that can still respect local data archive procedures and policies. Its secondary objective is to use the common security procedures of DIADEM nodes to enable site-to-site consensual data exchange of datasets of arbitrary size.

DIADEM is built on open-source and publicly accessible software packages, running atop the Linux operating system and including Python scripts and a RAIDZ2 ZFS multi-disk file system to ensure data integrity.

We have implemented DIADEM as the local data archive for the AG SEM research group at the Humboldt-Universitaet zu Berlin, with a 50TB data archive, secure user-data policies, and the ability to easily link into our in-house multi-GPU computing cluster. For users, the primary interaction is with files - moving files from one location to another causes the DIADEM system to perform an action on those files; a trivial example is data copied from the microscope to a user's archive folder will automatically be filed with date-and-microscope information, and set to be read-only for that user.

We have developed a data archive solution for TEM user groups, designed to be intuitive to use and easy to deploy and secure.

RSP thanks the German Research Foundation (DFG, project PE2500/1-1 "PolaRIS-3D") for funding.

IM7.P010
Three-dimensional measurement of tip shape geometry with SEM

M. Hemmleb[1], J. Langfahl-Klabes[2]

[1]point electronic GmbH, Halle, Germany
[2]PTB, Braunschweig, Germany

For traceable measurements of complex structures, the characterisation of the applied tactile tips is required. Especially advanced measurement tasks, i.e. the recording of the geometry of silicon nanopillars with high aspect ratio, presumes knowledge about the three-dimensional shape. The complete coverage of the tip shape in a 3D measurement data set enables the extraction of 2D profiles in different spatial directions. These profiles can be used for the deconvolution of the data, which were measured with the applied tip. For the characterization of the tip shape, a fast and reliable high-resolution measurement technique is required. SEM imaging fulfils these preconditions very well, but requires some extensions, if height measurements are required. Therefore, we applied a high-resolution SEM (Thermo Fisher Verios G4), which is equipped with a retractable four quadrant (4Q) BSE detector (PNDetector) and an active scanning system for topographic measurements (point electronic). The applied topographic measurement system utilizes the segmented BSE detector, which is inserted below the SEM pole piece. Surface height, e.g. topography, is obtained with a shape-from-shading algorithm that uses the subtle differences in simultaneous BSE signals, as described by the known angular distribution of backscattered electrons. This approach needs no sample tilting and is very computationally efficient and thus allows for live in situ topographic view of the investigated sample. A dedicated calibration standard has been used for this study to ensure height accuracy.
The results show the 3D reconstructed shape of a tactile tip (fig. 1). To avoid scaling errors, the height of the tip was also measured with the 90-degree tilted sample and afterward used for the determination of the correct height scale. As a result, the measurement data of the tip shape were used to extract 2D profiles which are ready for the deconvolution of the tactile measurements.
In summary, the application of topographic SEM measurements is a fast and reliable high-resolution method to determine the shape of tactile tips. Special attention is to pay on the system setup, BSE detector adjustment and the geometric calibration of the scanning system. If these requirements are fulfilled, the quantitative measurement of the tip shape, and derived measures, like profiles, tip angle and diameter is possible in an easy way. In addition, the results show the potential of this method for further applications, i.e. the precise measurement of indenter tips (see fig.2).

Fig. 1: 3D Reconstruction of a silicon microprobe tip.

Fig. 2: 3D Reconstruction of a Berkovich indenter tip.

Fig. 1

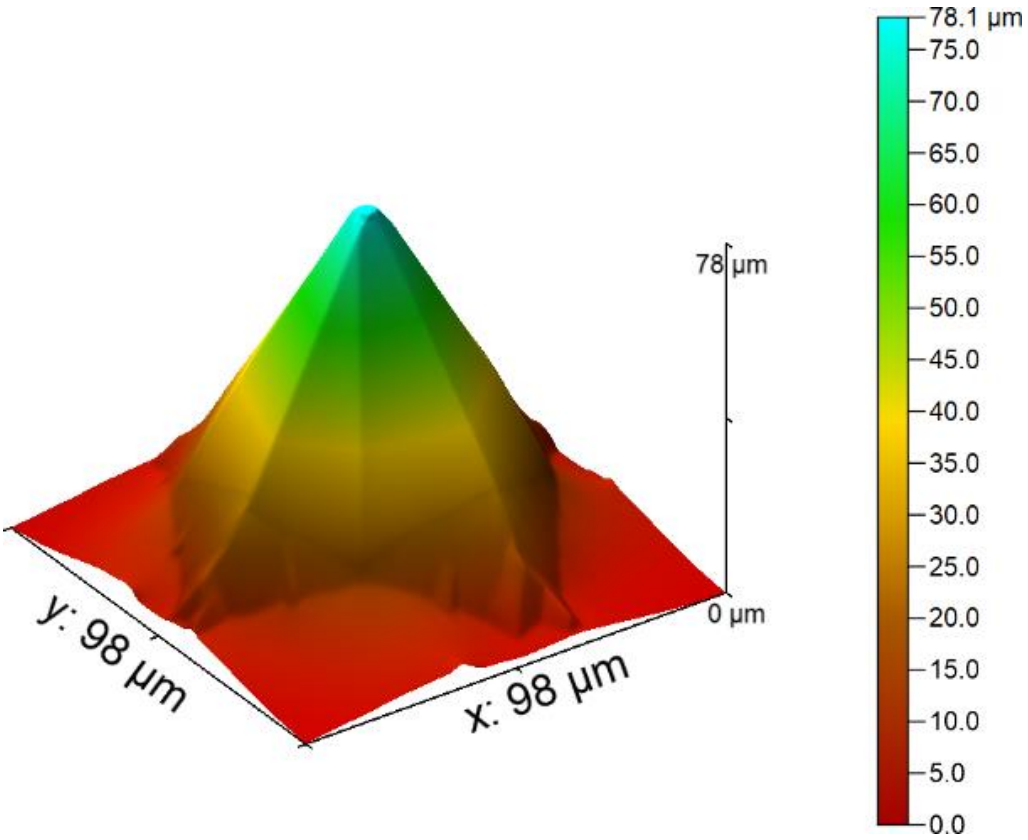
78.1 µm
75.0
70.0
65.0
60.0
55.0
50.0
45.0
40.0
35.0
30.0
25.0
20.0
15.0
10.0
5.0
0.0
78 µm
0 µm
y: 98 µm
x: 98 µm

Fig. 2

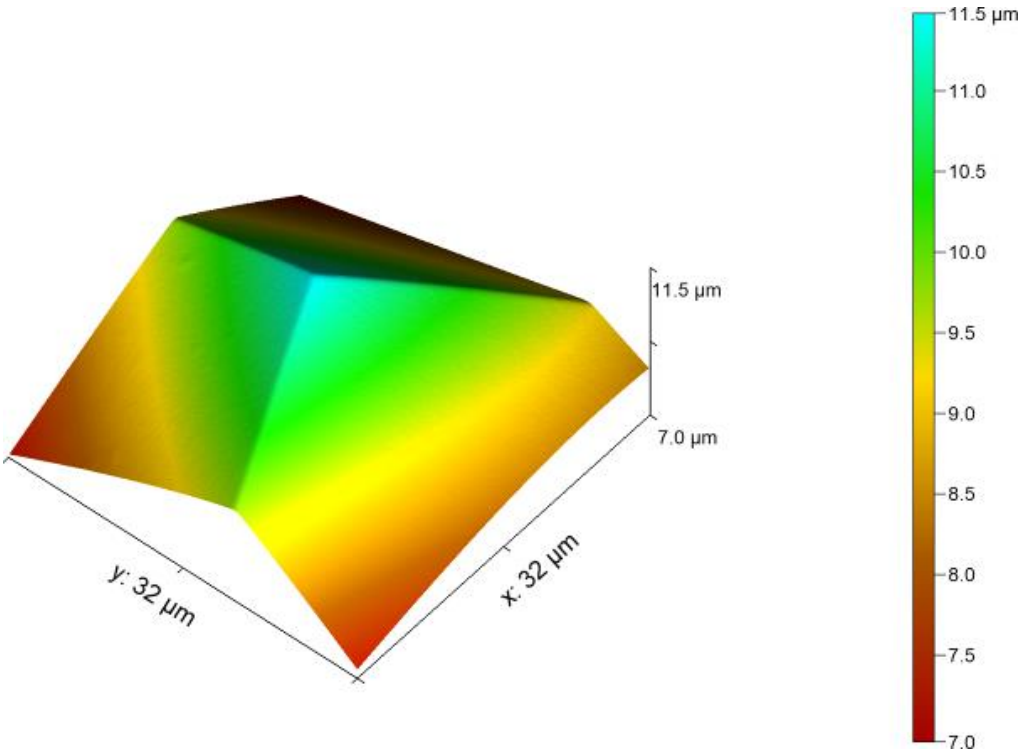
11.5 µm
11.0
10.5
10.0
9.5
9.0
8.5
8.0
7.5
7.0
11.5 µm
7.0 µm
y: 32 µm
x: 32 µm

IM7.P011
Investigation of superlattice defects in magnetite mesocrystals via STEM tomography

S. Sturm[1], D. Wolf[1], J. Brunner[2], E. Sturm[2], A. Lubk[1], B. Büchner[1]

[1]Leibniz-Institut für Festkörper- und Werkstoffforschung Dresden e. V., Dresden, Germany
[2]University of Konstanz, Chemistry, Konstanz, Germany

Mesocrystals are a special sub class of colloidal crystals, exhibiting single crystal like diffraction pattern in small angles as well as single crystal or texture like pattern in wide angles. They are thus formed by assembly of single crystalline building blocks in a long range ordered superlattice with reoccurring specific crystallographic orientation. The growth process as well as the structuration principles of these superlattices, in many aspects bear resemblance to “classical” atomic / molecular crystals, thereby exhibiting a class of possible similar structural defects.

The investigation of superlattice defects helps to deepen our understanding of mesocrystals and their growth process in particular. Moreover, these crystals also represent unique model systems to investigate these processes and structural properties in ways, that are beyond the possibilities for the investigation of “classical” atomic / molecular crystals (e.g. in terms of spatial resolution).

In order to investigate the defect structure of 3D iron oxide self-assembled mesocrystaline materials, we employed electron tomography on specifically picked areas (i.e. surrounding a screw dislocation). This allows to resolve the local three dimensional structure of defects generated within the superlattice during the self-assembly.

For a mesocrystal with fcc superlattice, grown by dislocation driven crystal growth mechanism, the 3D structure of a screw dislocation intersecting the (111) plane has been resolved. Similar to traditional fcc crystals, the screw dislocation dissociates into two Shockley-partials, separated by a stacking fault area within the (11-1) plane.

The further aim is to study the detailed structure of these partials and relate it to the elastic properties of the mesocrystal.

Fig. 1: STEM Tomography of a 3D iron oxide selfassembled mesocrystal with (11-1) planes highlighted in different colors.

Fig. 2: Screw dislocation lattice defect. The superlattice positions of two matching (11-1) planes are overlayed, illustrating the distortion between corresponding layers.

Fig. 1

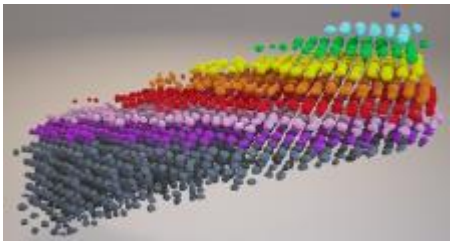

Fig. 2

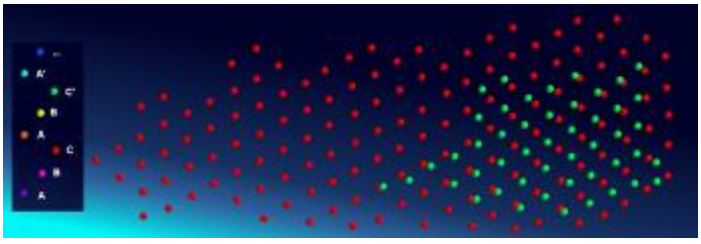

IM7.P012
FIB Tomography of nanoporous gold using an in-column backscatter electron detector

M. Ritter[1]

[1]Hamburg University of Technology, Electron Microscopy Unit, Hamburg, Germany

Focused ion beam (FIB) tomography often is the method of choice to analyze the 3D structure of nanoporous materials. Nanoporous gold (npg) is of interest as a functional material but also as a model system for nanomaterials. It is created by de-alloying, i.e. dissolving silver from gold-silver bulk alloy via electro-corrosion and forms a uniform network structure. 3D transmission electron microscopy provides valuable information about its nanomorphology (1), but a larger volume is needed in order to retrieve statistically relevant data of the ligament network morphology. If the ligament size is tailored to an average much larger than 100 nm, X-ray nanotomography can be used for characterization (2). Due to the small ligament size of approx. 40 nm in our sample, focused ion beam (FIB) tomography had to be applied.

Because of expected "shine-through" effects (3), npg was infiltrated with epoxy resin before FIB tomography was applied in order to lower the influence of this effect. This error source can additionally be decreased by choosing a low energy beam. Newer scanning electron microscopes (SEM) sometimes are equipped with an additional in-column BSE detector (ICD) that is situated at an upper position in the column. In combination with immersion lens mode, this ensures that only the most elastically scattered electrons are collected. The signal is highly sensitive to Z-contrast with almost no topographical information. Also, low energy loss increases the probability of near surface interaction and therefore near surface information.

For FIB tomography of infiltrated nanoporous gold we used a sample with a known average gold fraction of 25 %. The signals of two detector types, in-lens backscatter electron detector (BSD) and in-column backscatter electron detector (ICD) – were recorded and compared. Imaging was performed at 2 kV, from 50 pA. The images were then aligned, median filtered and a threshold was applied with k-means clustering (4) using k = 2 clusters (Fig 1., bar = 500 nm), white representing the gold fraction and black the epoxy resin filler.

The calculated gold fraction after segmentation was too high for both detectors, but could be significantly decreased when using the in-column detector: the gold fraction using ICD was calculated at 38 % and for BSD at 52 %. In Fig. 2 (top) an intensity profile line through FIB slices 1 to 60 at a given pixel position is displayed. The "shine through" effect, which impairs segmentation and leads to overestimation of the gold fraction is more recognizable if the intensity profile line is applied to the image slices that were segmented via thresholding (Fig. 2, bottom). As a conclusion, simple thresholding is not sufficient for accurate segmentation of npg FIB tomography datasets, even when using a dedicated in-column detector.

References:

(1) Krekeler T, *et al.* 2017 *Mater.Res. Lett.* 5 314-321

(2) Larsson E, *et al.* 2019 *J. Synchroton Rad.*26

(3) Prill T, *et al.* 2013 *Scanning* 35 189-195

(4) Lloyd P 1982 *IEEE Trans. Inf. Theory* 28 129-137

The author gratefully acknowledges support by Deutsche Forschungsgemeinschaft (DFG) through the collaborative research centre SFB 986 "Tailor-Made Multi-Scale Material Systems" and Birthe Zandersons for providing the nanoporous gold sample.

Fig. 1

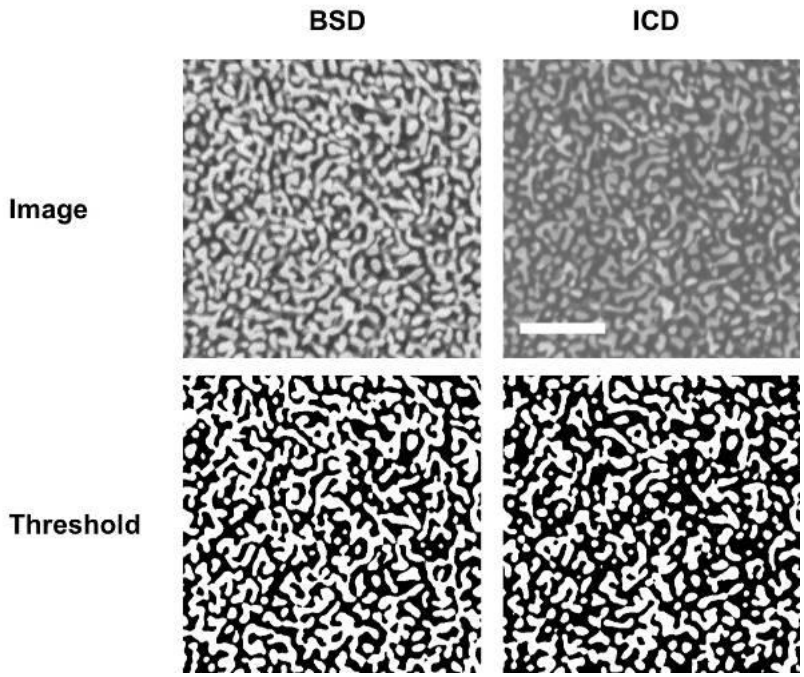
BSD
ICD
Image
Threshold

Fig. 2

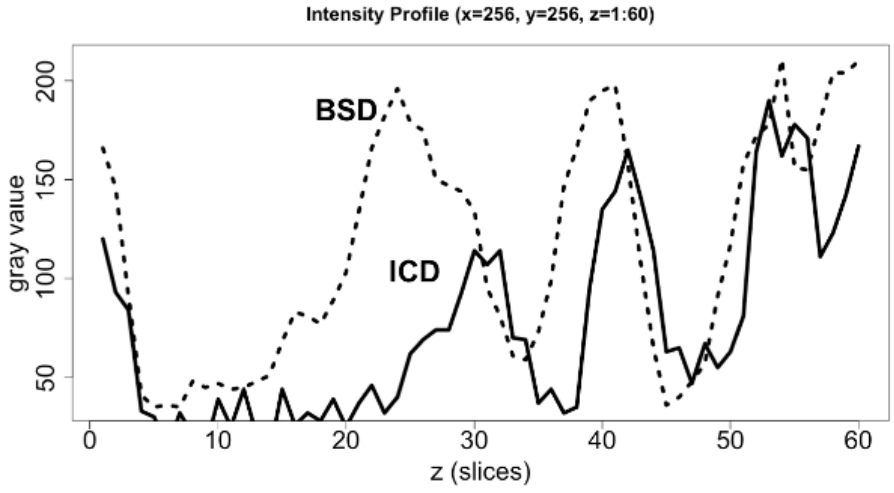
Intensity Profile (x=256, y=256, z=1:60)
BSD
ICD
gray value
z (slices)

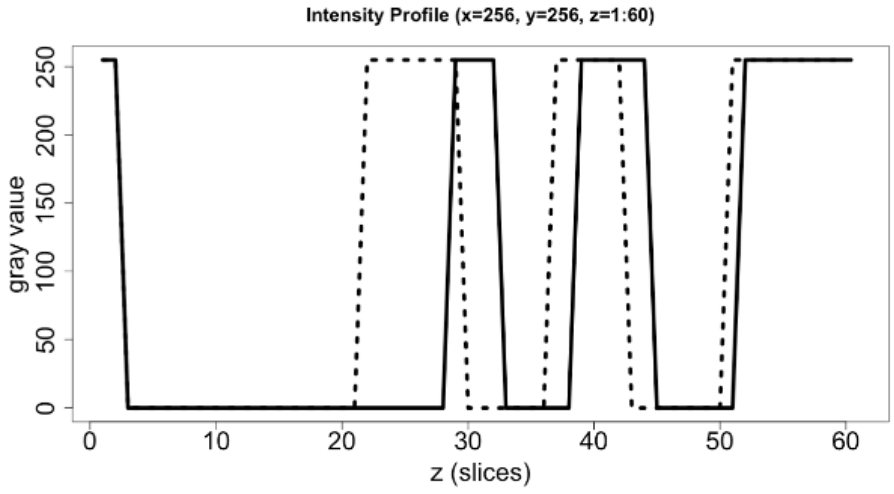
Intensity Profile (x=256, y=256, z=1:60)
gray value
z (slices)

LS1.001 invited
Interpreting cryo-EM maps with atomic models

C. Sachse[1], M. Beckers[2], A. Jakobi[3]

[1]Forschungszentrum Jülich, Ernst-Ruska Centre for Microscopy and Spectroscopy with Electrons , Jülich, Germany
[2]EMBL - European Molecular Biology Laboratory, Heidelberg, Germany
[3]TU Delft, Delft, Netherlands

Despite the impressive boost in productivity of generating high-resolution cryo-EM maps, one of the bottlenecks remains the reliable structural interpretation. Due to the still relatively low resolution between 3 and 5 Å in addition to issues of local resolution variation, molecular flexibility and incomplete binding, it is notoriously difficult and subjective to discriminate signal from noise for critically important densities in order to build and refine atomic models. In order to address this question, we previously published a method to locally sharpen EM densities based on atomic models (Jakobi et al., 2017 eLife; 6:e27131). This method is particularly useful for densities with large local resolution differences. Now that many people have applied this approach, we have seen many examples of large benefits for improving map interpretability in particular in accessory parts of the protein where we see interpretable densities are appearing after local sharpening.

In addition, more recently we worked on an additional way of interpreting densities in the absence of an atomic model where we propose to transform cryo-EM densities into confidence values by means of statistical significance testing combined with false discovery rate control (FDR) (Beckers, et al., 2019 IUCr Journal 6:1). Statistical thresholding and FDR control is a far-reaching concept from statistics, which has been successfully applied to disciplines of neuroimaging and astronomy that belong to a group of image analysis disciplines dealing with noisy image data. In cryo-EM, densities require subjective thresholding and visual inspection of isosurfaces by the structural biologist whenever possible the reference of an atomic model or at least the molecular building blocks. We show that confidence maps are a very useful tool for the interpretation of many types of cryo-EM maps ranging from close-to-atomic resolution 2 to 90 Å in resolution obtained from single-particle reconstruction as well as from subtomogram averaging. Confidence maps represent a conservative way of interpreting molecular structures due to minimized noise. They particularly beneficial for the interpretation of weaker cryo-EM densities in cases of conformational flexibility and lower occupancy of bound molecules and ions in the structure.

LS1.002
Ultrastructure analysis of supramolecular one-dimensional polymers

S. Ehrmann[1,2], R. P. M. Lafleur[3], B. E. W. Meijer[3], R. Haag[2], C. Böttcher[1]

[1]Freie Universität Berlin, Forschungszentrum für Elektronenmikroskopie und Core Facility BioSupraMol, Berlin, Germany
[2]Freie Universität Berlin, Institut für Chemie und Biochemie, Berlin, Germany
[3]Eindhoven University of Technology, Eindhoven, Netherlands

1,3,5-Benztricarboxamide-based amphiphiles (BTA) are known to form one-dimensional, micrometres-long supramolecular aggregates in water, if the balance between hydrophobicity and hydrophilicity is well-chosen.(1) It was recently shown that properties like monomer exchange dynamics of the supramolecular polymers differ significantly among different derivatives.(2,3) In order to gain a better understanding of the structure-function relationship, there is high interest in resolving the ultrastructure of these aggregates towards nanometre scale resolution.

In this work, we aim for an in-depth analysis of the structure of supramolecular polymers of three different BTA-based amphiphiles in homo- and copolymers by means of cryogenic transmission electron microscopy (cryo-TEM) in combination with image processing and image-based helical 3D-reconstruction techniques.(4)

Cryo-TEM images were recorded on a 200 kV Talos Arctica (Thermo Fisher Scientific) with a Falcon 3CE direct electron detector and a phase plate. Image processing and image-based reconstruction was done using the IMAGIC5 software (Image Science Software GmbH, Berlin).

We analysed three different BTAs of which two form one-dimensional polymers and the third spherical micelles in water. The structures differ in size of the hydrophilic headgroups and length of the hydrophobic hydrocarbon chains. From 2D cryo-TEM images, individual fibre motifs were extracted and aligned. Subsequently, multivariate statistical analysis and classification was applied to reveal recurring structural motifs. Following this procedure, a double-helix structure with a regular pitch could be identified for one of the BTA amphiphiles. Intriguingly, we were able to alter the pitch length in either one or the other direction by copolymer formation with different BTA derivatives. In the extreme limit, the pitch length of the helix was infinitely long, *i.e.*, both individual fibers align parallel.

In conclusion, we determined the structural organisation of amphiphiles in one-dimensional polymers in water by cryo-TEM and subsequent image processing. We were able to resolve double-helix structures, as well as parallel pairs of cylindrical fibres. By copolymer formation, transitions between substructures became accessible.

References:

(1) C. M. A. Leenders, L. Albertazzi, T. Mes, M. M. E. Koenigs, A. R. A. Palmans, E. W. Meijer, *Chem. Commun.* 2013, *49*, 1963-1965.

(2) B. N. S. Thota, X. Lou, D. Bochicchio, T. F. E. Paffen, R. P. M. Lafleur, J. L. J. van Dongen, S. Ehrmann, R. Haag, G. M. Pavan, A. R. A. Palmans, E. W. Meijer, *Angew. Chem. Int. Ed.* 2018, *57*, 6843-6847.

(3) X. Lou, R. P. M. Lafleur, C. M. A. Leenders, S. M. C. Schoenmakers, N. M. Matsumoto, M. B. Baker, J. L. J. van Dongen, A. R. A. Palmans, E. W. Meijer, *Nat. Commun.* 2017, *8*, 15420.

(4) C. Böttcher, H. Stark, M. van Heel, *Ultramicroscopy* 1996, *62*, 133-139.

Fig. 1: Left: Cryo-TEM image of a BTA-based supramolecular aggregate. Right: By image processing and image-based reconstruction, a helical ultrastructure of the one-dimensional polymer was identified.

Fig. 1

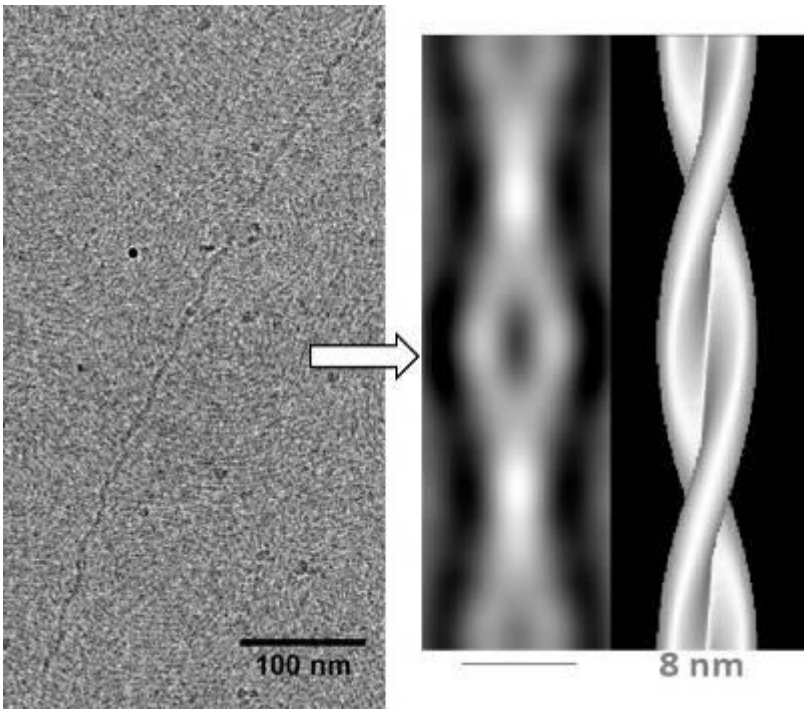

LS1.003
High resolution Cryo-EM fibril structures from systemic amyloidosis

M. Schmidt[1]

[1]Ulm University, Institute of Protein Biochemistry, Ulm, Germany

Systemic AA amyloidosis is a worldwide occurring protein misfolding disease of humans and animals. It arises from the formation of amyloid fibrils from the acute phase protein serum amyloid A. Systemic AL amyloidosis belongs to the most common forms of systemic amyloidosis in industrialized countries. The key pathogenic agents are amyloid fibrils derived from antibody light chains.

For both AA and AL amyloidosis the amyloid fibrils deposited in multiple organs but for AL amyloidosis especially cardiac amyloid is the major risk factor of mortality. Detailed structural studies of amyloid fibrils so far have analyzed *in vitro* amyloid-like fibrils and just recently natural fibrils from organ tissue could be studied in that detail.

Our object of these projects was to investigate these *ex vivo* fibril structures from human (AL and AA amyloid fibrils) and mouse (AA amyloid fibrils) at high resolution and furthermore to create molecular structure models. This allows for a more detailed understanding of the fundamentals of these disorders.

To investigate the molecular basis of these amyloid diseases we purified the fibrils from a mouse and a human patient with systemic AA amyloidosis and from a human patient with AL amyloidosis and analyzed them with electron cryo-microscopy.

Using electron cryo-microscopy, we obtained resolutions of 3.0 Å and 2.7 Å for the murine and human AA fibrils, respectively (Fig. 1). For the human AL fibrils we obtained a resolution of 3.3 Å (Fig. 2).

The two AA fibrils differ in fundamental properties, such as presence of right-hand or left-hand twisted cross-β sheets and overall fold of the fibril proteins. Yet, both proteins adopt highly similar β-arch conformations within the N-terminal ~21 residues. Our data demonstrate the importance of the fibril protein N-terminus for the stability of the analyzed amyloid fibril morphologies.

The resolved AL-fibril core consists of a 91-residue segment presenting an all-beta fold with ten mutagenic changes compared to the germ line. The conformation differs substantially from natively folded light chains: a rotational switch around the intramolecular disulphide bond being the crucial structural rearrangement underlying fibril formation.

References:

(1) Liberta, Loerch, Rennegarbe et al. Nature Communications **10**, Article number: 1104 (2019).

(2) Radamaker, et al. Nature Communications (2019) in press.

Fig. 1: Cryo-EM structure of amyloid fibrils from systemic AA amyloidosis of human and mouse.

Left: Side view of the reconstructed densities. Right: Cross-section of the reconstructions superimposed with a molecular model.

Fig. 2: Cryo-EM structure of an amyloid fibril from systemic AL amyloidosis.

Left: Side view of the reconstructed density. Right: Cross-section of the reconstruction superimposed with a molecular model.

Fig. 1

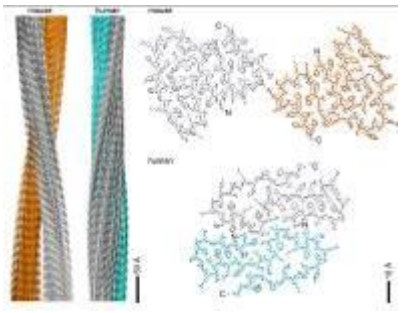

Fig. 2

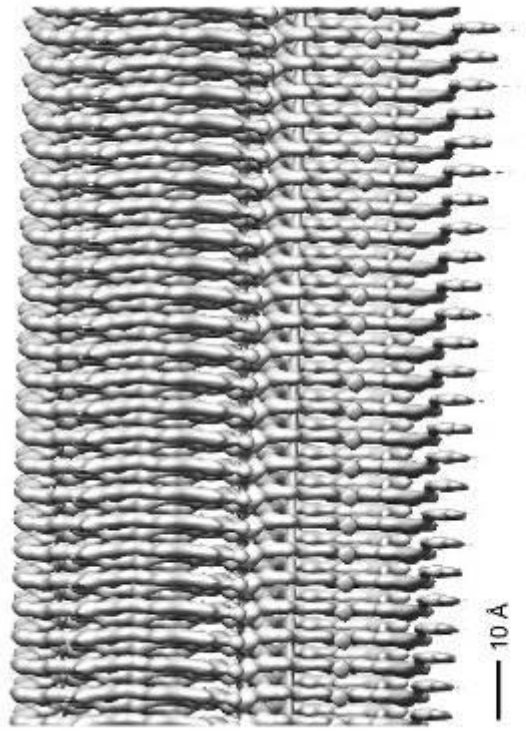

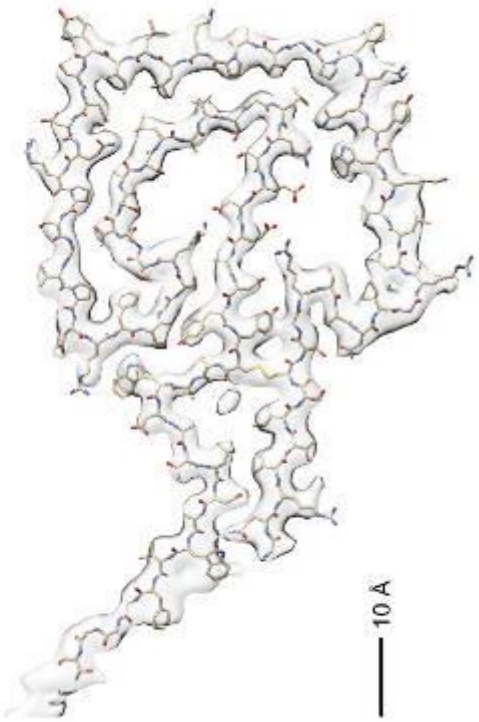

LS1.004 invited
High-resolution cryo-EM of active macromolecular machines: Membrane proteins under turnover condition

A. Möller[1]

[1]MPI of Biophysics Frankfurt, Department of Structural Biology, Frankfurt a. M., Germany

Cryo-electron microscopy (cryo-EM) has the capacity to capture molecular machines in action. Therefore, it is possible to study macromolecular machines under turnover conditions and to immediately observe their conformational dynamics.

Especially for membrane proteins, cryo-EM offers a multitude of advantages over other structural biology techniques as it is gentle on the preserved protein, is tolerant to almost any hydrophobic environment and requires only small sample amounts at low concentration.

In my talk, I will present recent advances from our lab describing the high-resolution structures of a small membrane protein under turnover conditions and will discuss what was required to achieve this.

LS1.005
Structure and Biogenesis of Trypanosomal Mitochondrial Ribosomes

D. Boehringer[1], S. Martin[1], D. Ramrath[1], N. Moritz[2], M. Leibundgut[1], P. Bieri[1], S. Calderaro[2], C. Prange[2], A. Scaiola[1], E. Horn[2], A. Leitner[1], A. Schneider[2], N. Ban[1]

[1]ETH Zurich, Zurich, Switzerland
[2]University of Bern, Bern, Switzerland

Ribosomes are universally conserved ribonucleoprotein assemblies responsible for protein synthesis in which ribosomal RNA (rRNA) was shown to play key functional and architectural roles. Mitochondrial ribosomes from *Trypanosoma brucei,* a unicellular parasite that causes sleeping sickness in humans, are highly divergent featuring the smallest known rRNAs whereas the number of ribosomal proteins is dramatically increased. Using electron microscopy, we determined the atomic structure of mitoribosomes from *Trypanosoma brucei*, which is with 127 ribosomal proteins the most complex ribosomal assembly described to date. Our results reveal the "minimal" set of conserved rRNA regions and protein components shared by all ribosomes. In the trypanosomal mitoribosome the proteins take the role of architectural scaffold from the rRNA, forming a large autonomous outer shell that surrounds the entire particle and that stabilizes and positions the functionally important regions of the rRNA. Structures of ribosomal subunits in different states of assembly reveal how large clusters of biogenesis factors form a rigid scaffold during ribosomal subunit biogenesis that allows the rRNA fold into its native conformation.

LS1.006
Structure of the human MHC-I peptide-loading complex

A. Blees[1], D. Januliene[2], T. Hofmann[3], N. Koller[1], C. Schmidt[3], S. Trowitzsch[1], A. Möller[2], R. Tampé[1]

[1]Goethe University Frankfurt, Frankfurt am Main, Germany
[2]Max Planck Institute of Biophysics, Frankfurt am Main, Germany
[3]Martin Luther University Halle-Wittenberg, Halle, Germany

The peptide-loading complex (PLC) is a transient, multisubunit membrane complex in the endoplasmic reticulum (ER) that is essential for establishing a hierarchical immune response. It coordinates peptide translocation into the ER with loading, editing and release of loaded major histocompatibility complex class I (MHC-I) molecules to the cell surface to evoke a T-cell response against infected or malignant cells (Neefjes et al. 2011, Blum et al. 2013). To decipher the molecular organization and mechanistic events that take place in the PLC, we isolated human PLC from Burkitt's lymphoma cells using an engineered viral inhibitor as bait and determined the structure of native PLC by electron cryo-microscopy (cryo-EM). The intrinsically dynamic nature of this multisubunit complex, composed of the transporter associated with antigen processing (TAP1 and TAP2, jointly referred to as TAP), the oxidoreductase ERp57, the MHC-I heterodimer, and the chaperones tapasin and calreticulin (Hulpke & Tampé 2013, Ortmann et al. 1997), demanded extensive optimization of the cryo-EM sample preparation and sophisticated single particle analysis. The fully assembled PLC was found to be shaped by two editing modules, composed of tapasin, calreticulin, ERp57, and MHC-I, centered around the translocation unit (TAP) in a pseudo-symmetric orientation. Multiple structures of the PLC, captured at distinct assembly states, provide mechanistic insights into MHC-I recruitment and release. Our work defines the molecular symbiosis of an ABC transporter and an ER chaperone network in MHC-I assembly and provides insight into the onset of the adaptive immune response.

References:

(1) Blum, J. S., Wearsch, P. A. & Cresswell, P. Pathways of antigen processing. Annu. Rev. Immunol. 31, 443–473 (2013)

(2) Hulpke, S. & Tampé, R. The MHC I loading complex: a multitasking machinery in adaptive immunity. Trends Biochem. Sci. 38, 412–420 (2013)

(3) Neefjes, J., Jongsma, M. L., Paul, P. & Bakke, O. Towards a systems understanding of MHC class I and MHC class II antigen presentation. Nat. Rev. Immunol. 11, 823–836 (2011)

(4) Ortmann, B. et al. A critical role for tapasin in the assembly and function of multimeric MHC class I-TAP complexes. Science 277, 1306–1309 (1997)

LS1.P001
The Rocking Phase Plate – another step towards improved stability

K. Barragán Sanz[1], S. Irsen[1]

[1]center of advanced european studies and research, Electron Microscopy & Analytics, Bonn, Germany

Phase plates are promising tools for enhancing contrast, especially in cryo-transmission electron microscopy (cryo-TEM). As an alternative to defocusing, contrast of weak phase objects -like most cryo samples- can be improved in close to focus images by inserting a phase plate into the back focal plane of the TEM (1). The phase plate adds an additional phase shift of ideally π/2 to the scattered electrons and thus enhances image contrast. Their advantages for electron tomography and single particle acquisition have been demonstrated recently (2). Nevertheless, phase plates are still no tool for routine application. This is mostly due to difficult handling and limited durability of actual phase plate designs. For more than 15 years, carbon based Zernike phase plates have been the most used type (3). Recently, a new type of hole free phase plates -Volta phase plate- has been made available. The hole free design has reduced ringing artifacts due to the missing hole edge. This is on cost of a variation of the phase shift over time.

Here, we present our experimental results from a rocking phase plate. We use a classical Zernike type phase plate which is based on a thin iridium film instead of carbon. This improves the long term stability of the phase plate. To overcome the ringing artifact problem, we move the phase plate on a circular path during acquisition (see figure 1). This rocking mode virtually smooths the edge of the central hole. Additionally, the diameter of the central hole can be larger compared to classical Zernike phase plates which facilitates the positioning of the phase plate inside the TEM. The rocking mode is possible due to a special, piezo based positioning system, which can position the phase plate with nanometer precision (4).

We were able to show that the rocking mode settings can be used without interference of the phase plate hole edge during image recording. Furthermore, we could not find any resolution loss caused by the moving phase plate. Figure 2 shows a comparison between the phase plate in a) steady and b) rocking mode. No cutoff can be detected in the power spectra of the rocking phase plate in comparison to the power spectrum calculated from a micrograph recorded with a not moving phase plate.

In conclusion, the rocking mode could be an alternative method to acquire phase plate data. Currently, we are recording high-resolution single particle datasets to demonstrate up to which resolution the rocking phase plate can be used.

References:

(1) Danev, R., Nagayama, K. (2001) *Journal of the Physical Society of Japan* 70(3), 696–702

(2) Fan, X., Zhao, L., Liu, C., Zhang, J.-C., Fan, K., Yan, X., et al. (2017) *Structure* 25(10), 1623–1630

(3) Nagayama, K., Danev, R. (2008) *Philos Trans R Soc Lond B Biol Sci.* 363(1500), 2153–2162

(4) Kurth, P., Pattai, S., Rudolph, D., Overbuschmann, J., Wamser, J., Irsen, S. (2014) *Microscopy and Microanalysis* 20(S3), 220–221

Fig. 1: Illustration of the phase plate rocking mode.

Fig. 2: Power spectra of TEM-micrographs in a) steady mode and b) rocking mode.

Fig. 1

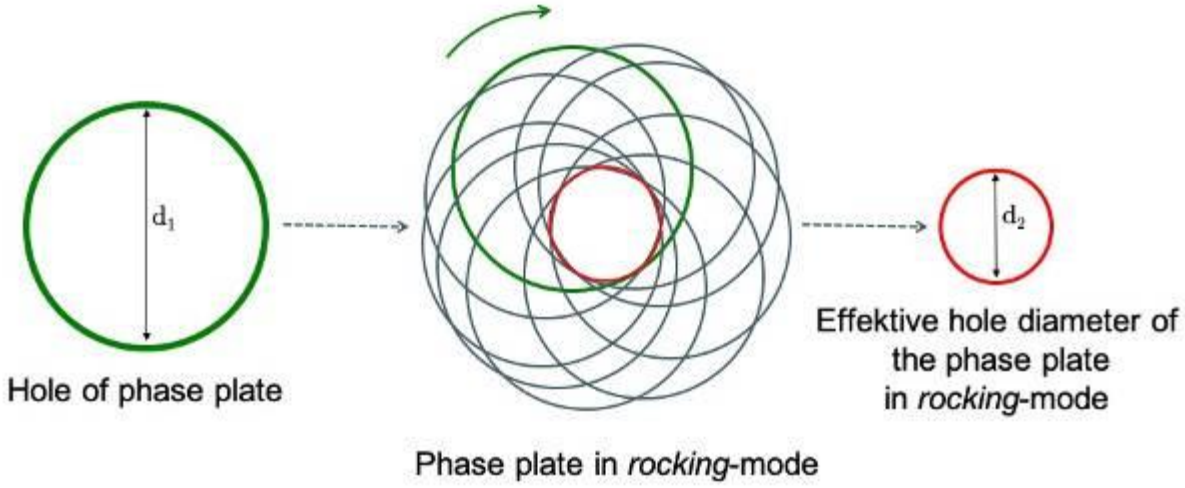
d1
d2
Hole of phase plate
Phase plate in *rocking*-mode
Effektive hole diameter of
the phase plate
in *rocking*-mode

Fig. 2

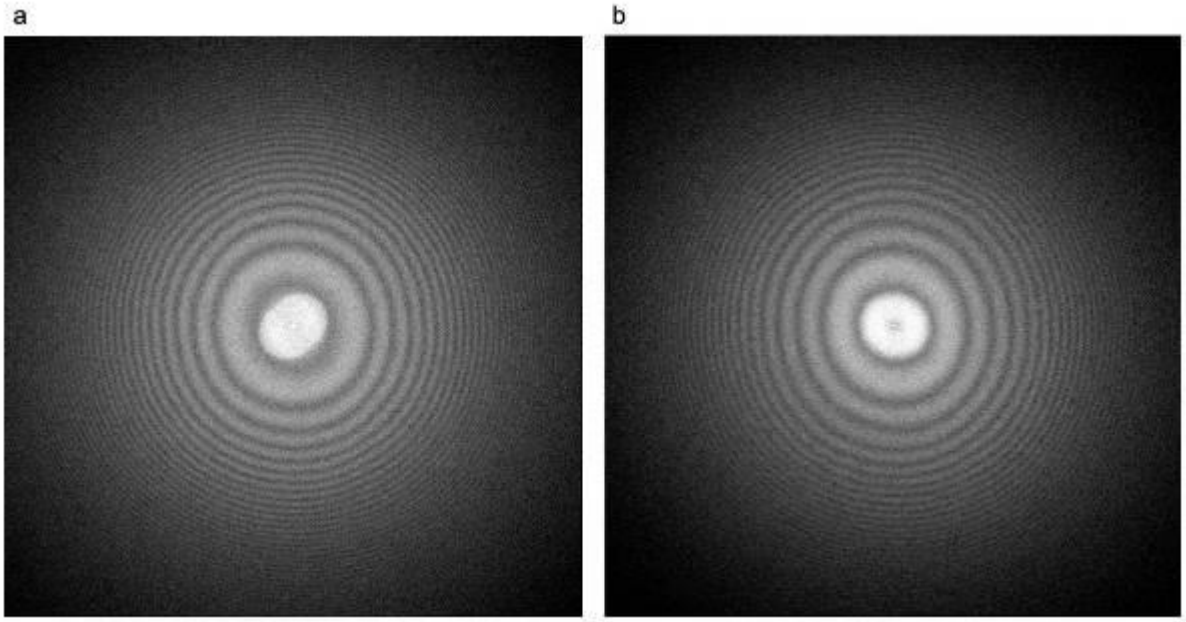
a
b

LS1.P002
Dissecting structural heterogeneity of the bacterial transcription machinery

T. Hilal[1], N. Said[2], Y. Huang[2], U. Homberg[3], S. Prohaska[3], C. Böttcher[1], M. Wahl[2]

[1]Freie Universität Berlin, Electron microscopy, Berlin, Germany
[2]Freie Universität Berlin, Biochemistry, Berlin, Germany
[3]Zuse Institut Berlin, Visual Data Analysis, Berlin, Germany

Genetic information is stored as DNA in all kingdoms of life and converted into RNA by RNA polymerases (RNAP) in a process called transcription, which can be divided into initiation, elongation and termination. The prokaryotic RNAP has a conserved core subunit composition (α^2, β, β", ω) (1). Regulation of the enzymatic activity of RNAP is achieved by interaction with transcription modulating factors like Nus proteins (NusA, B, E, G) upon encounter of signal sequences in the DNA template (2) or secondary structure elements in the nascent RNA (3).

Following up on our previous studies of the bacterial transcription elongation (4,5), we strive to elucidate transcription elongation and termination by the RNAP in more detail. In particular we are interested in the structural basis for the regulation of RNAP during late elongation steps and termination.

Complexes of the elongating *Escherichia coli* RNAP and elongation factors were reconstituted *in vitro* from recombinantly expressed proteins and synthetic RNA/DNA. After complex preparation, a final gel filtration step is conducted to maximize compositional homogeneity. Complementary transcription assays are routinely applied to confirm activity of the purified complexes. Using standard techniques, freshly prepared complexes are vitrified in liquid ethane, visualized by cryo-TEM and subjected to single particle analysis (SPA). To omit preferred particle orientation of RNAP, n-octylglucoside is added to the samples just before grid preparation.

Data collection is achieved in-house on our FEI Talos Arctica equipped with a Falcon3EC at 200 kV. Our workflow encompasses on-the-fly pre-processing and archiving of raw movies, transfer of aligned images to ubiquitously accessible network storage and virtually instant data analysis.

Due to the numerous components the investigated complexes are composed of, structural heterogeneity is unavoidable. We use extensive *in silico* sorting by multi-particle refinement (6) to seperate the individual states.

Despite the clean appearance of the gel filtration chromatograms, initial structure determination by SPA revealed substantial heterogeneity of the samples. Careful inspection of the density map illustrates that the core of RNAP is seemingly invariant, however, density of the factors is often fragmented. These regions were further used to guide the sorting procedure.

Intriguingly, all investigated polymerase complexes were separated into multiple meaningful classes. It turns out that the RNAP associated with factors is a flexible molecular machine, explaining why previous attempts for crystallization of such samples mostly failed.

The resolutions achieved with our setup allow unambiguous fitting of known structures and secondary structure-based modelling. Due to the use of detergent we have to image in rather thick ice. The lack of an energy filter plus the limited penetration depth of 200 kV electrons thus limits our resolution to 5-6Å.

Structural investigation of the bacterial RNAP can be accomplished with little limitations at 200 kV. We could dissect biochemically homogeneous samples into conformationally distinct states, gaining new insights into transcription elongation and termination.

References:

(1) Darst, S. A., *Curr. Opin. Struct. Biol.* 11 (2001)

(2) Cabello, C. M. *et al.*, *Science* 344 (2014)

(3) Komissarova, N. *et al.*, *Mol. Cell* 31 (2008)

(4) Said, N. *et al. Nat. Microbiol.* 2 (2017)

(5) Krupp, F. *et al. Mol. Cell* (2019)

(6) Loerke, J. *et al.*, *Methods Enzymol.* 483 (2010)

LS2.001 invited
In situ structural studies of positive-sense RNA virus replication using cryo-electron tomography

L. A. Carlson[1]

[1]Umeå University, Department of Medical Biochemistry and Biophysics, Umeå, Sweden

Viruses of the positive-sense RNA ((+)ssRNA) type are a major class of human pathogens causing diseases ranging from common cold to Hepatitis C and arthropod-borne fevers. The extracellular stage of these pathogens, the virus particles, has been studied in great detail often resulting in 3D structures at atomic resolution. The intracellular stage of (+)ssRNA viruses, their membrane-bound genome replication complexes, has been more recalcitrant to structural studies. Here, I will present our preliminary studies of replication complexes of (+)ssRNA viruses using focussed ion beam milling and cryo-electron tomography of infected cells and tissues.

LS2.003
Zika Virus Infection and Ultrastructural Changes in Glioblastoma Cell Lines

M. Schneider[1,2], R. Groß[3], T. Hein[4], P. Sander[4], A. Pala[1], J. Münch[3], R. Wirtz[1], P. Walther[2]

[1]University Hospital Ulm, Department of Neurosurgery, Günzburg, Germany
[2]Ulm University, Central Unit for Electron Microscopy, Ulm, Germany
[3]Ulm University, Department of Molecular Virology, Ulm, Germany
[4]University Hospital Ulm, Division of Experimental Anesthesiology, Ulm, Germany

Zika virus (ZIKV) is an enveloped flavivirus with a positive-sense, single-stranded RNA genome, transmitted by Aedes mosquitoes. Following receptor binding, virus endocytosis and vesicle acidification, the 10.7 kb RNA genome is released into the host cell cytoplasm. Background. Due to its neurotropism and specificity for glioblastoma stem cells1, ZIKV is currently considered as an agent for virotherapy of glioblastoma (GBM). We here studied ZIKV viremia in different cell lines derived from GBM patients using advanced STEM tomography of cryofixed material.

GBM cell lines were established from fresh tumor tissue and characterized by a panel of CD cluster antibodies2. For Zika virus infection, we used the Brazilian strain ZIKV_FB-GWUH-2016, isolated from a fetus with microcephaly 3. Cell lines grown to 70% confluence, to which virus diluted in growth medium was added at a multiplicity of infection of 1. Cells were pre-fixed 48h after infection in the biosafety level 2 laboratory and cryofixed within the next hour.

All cell lines expressed CD24, CD31, CD146 and CXCR4, the receptor for CXCL12, an important growth factor for proliferation and invasion. On the ultrastructural level, these GBM cell lines presented with an elaborate profile of actin filament bundles in close vicinity to the attachment sites. Mitochondria showed an extended network and rough endoplasmic reticulum (rER) was abundant. Nuclear Cajal bodies were prominent. Upon Zika virus infection, dramatic alterations in host endomembranes were observed. Viral particle assembly was identified in the ER, a novel structure with about 50nm in diameter and an electron dense lipid bilayer membrane appeared to originate from the Golgi by budding and resembled empty virus particles. Close to the plasma membrane, the most mature virus particles were detected, then accumulating not randomly but perfectly lined up in individual cisternae of the Golgi. These tube-like endomembranes eventually fused with the plasma membrane for release. In most sensitive GBM cell lines, we monitored paraptotic-like cell death by volume-enlarged ER, and swollen mitochondria already at 48h after infection. However, increased mitophagy and autophagolysosome formation were absent. No nuclear fragmentation was observed.

Zika virus infektion in GBM cell lines occurs in the ER and maturation of virus particles appeared to be restricted to the Golgi and proceed towards the cell surface for virus particle release. The highly active virus production phase appeared to be followed by extensive organelle swelling and eventual rupture of the cell membrane, resembling a paraptotic cell death. Current studies are under way to prove immunogenicity of GBM undergoing Zika virus induced cell lysis.

References:

(1) Zhou, Z. et al. Zika virus has oncolytic activity against glioblastoma stem cells. 2017. J Exp Med. 2017 Oct 2; 214(10): 2843–2857. doi: 10.1084/jem.20171093

(2) Sander, P., Mostafa, H., Soboh, A., Schneider, J. M., Pala, A., Baron, A.-K. Schneider, M. (2017). Vacquinol-1 inducible cell death in glioblastoma multiforme is counter regulated by TRPM7 activity induced by exogenous ATP. Oncotarget, 8(21), 35124–35137

(3) Driggers, et al. Zika Virus Infection with Prolonged Maternal Viremia and Fetal Brain Abnormalities. (2016) N Engl J Med 2016; 374:2142-2151doi: 10.1056/NEJMoa1601824.

Fig. 1

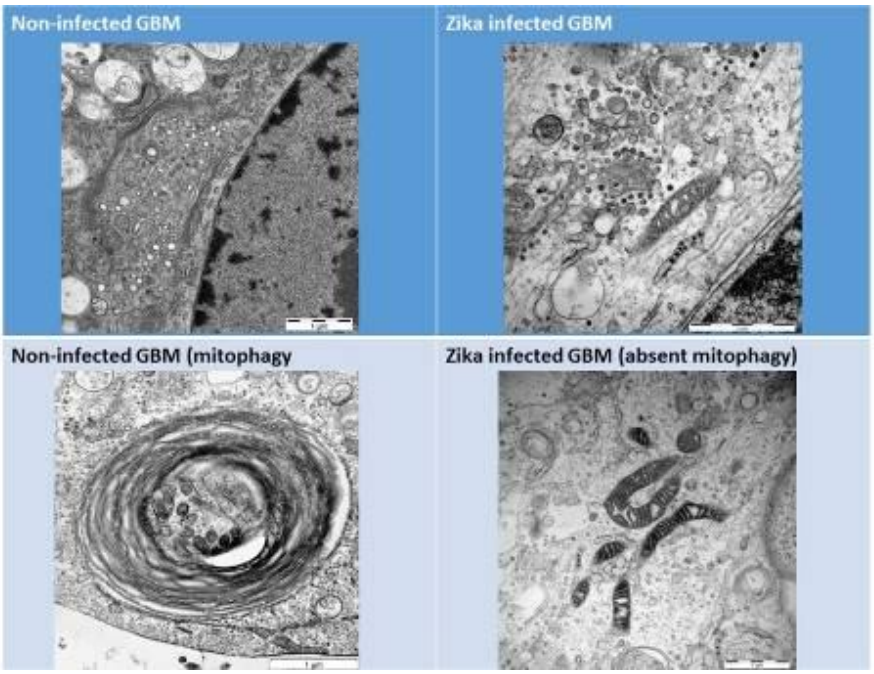
Non-infected GBM
Zika infected GBM
Non-infected GBM (mitophagy
Zika infected GBM (absent mitophagy)

LS2.004
Dissecting herpesvirus secondary envelopment by STEM tomography

C. Read[1,2], M. Schauflinger[1,2], P. Walther[1], J. von Einem[2]

[1]Ulm University, Central Facility for Electron Microscopy, Ulm, Germany
[2]Ulm University Medical Center, Institute of Virology, Ulm, Germany

The Human cytomegalovirus (HCMV) is a member of the *Herpesviridae* family. Formation of infectious virions requires a process called secondary envelopment in which virus capsids in the cytoplasm bud into cellular vesicles to acquire their final envelope. This process is still not fully understood.

It is known that the viral tegument protein pUL71 plays an important role in secondary envelopment (1). Lack of pUL71 results in a complex ultrastructural phenotype including a clear defect in secondary envelopment which is manifested by an increased number of budding cytoplasmic capsids. Recently, we could show by mutational analysis combined with quantitative TEM that a mutant virus expressing C-terminally truncated pUL71 (TB71del348-351) and a virus with a mutated C-terminal tetra-lysine motif (TB71mutK348-351A) exhibit a defect in secondary envelopment as it is described for a virus lacking pUL71. Interestingly, not all morphological alterations that define the ultrastructural phenotype of a virus lacking the complete pUL71, such as enlarged multivesicular bodies and enlarged vesicles showing multiple budding events, were found in cells infected with the C-terminally mutated viruses. This and especially the increased number of budding capsids in TB71mutK348-351A infected cells greatly facilitates the study of secondary envelopment by three-dimensional electron microscopy.

Scanning transmission electron microscopy (STEM) tomography of these cells after high-pressure freezing, freeze substitution and Epon embedding provided evidence for a progressive tegument formation that is associated with advancing secondary envelopment, suggesting that tegumentation and secondary envelopment are intertwined processes. Furthermore, three-dimensional measurements of the tegument thickness in different stages of secondary envelopment could show that the tegument layer exhibits the same thickness at the start of the envelopment process as it does after its completion. This indicates that there must be a structural component in the viral tegument that determines a distinct distance between capsid and viral envelope throughout the entire envelopment process. Third, three-dimensional visualization showed for the first time that secondary envelopment culminates in formation of a narrow bud neck with a minimal measured diameter of 9.1 nm.

In conclusion, ultrastructural visualization and quantitative analysis of secondary envelopment in this system greatly contribute to our understanding of the complex process of secondary envelopment.

References:

(1) Schauflinger et al., 2011, doi: 10.1128/JVI.01540-10

Fig. 1

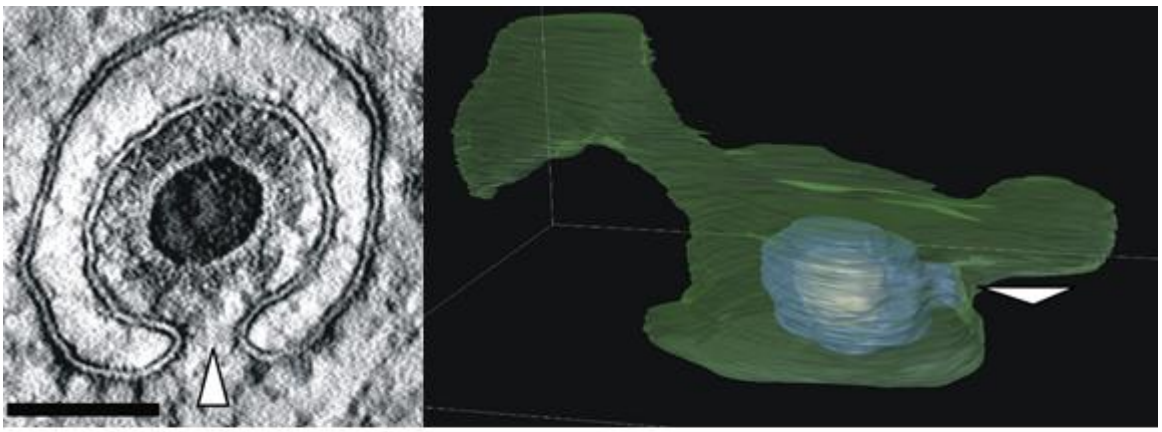

Fig. 1: Secondary envelopment culminates in formation of a bud neck (white arrowhead). Left: Virtual section of a representative budding HCMV capsid based on STEM tomography. Scale bar: 100 nm. Right: Three-dimensional visualization of the capsid. Green semi-transparent: vesicle membrane, orange: capsid, blue: tegument.

LS2.005
Functionalized Bacteriophage Capsids as Inhibitors of Viral Infection

K. Ludwig[1], S. Klenk[2,3], D. Lauster[4], S. Nojoumi[5], S. Behren[2,3], S. Saenger[6], S. Franz[6], K. Zscheppang[7], U. Hoffmann[8], M. Bardua[8], A. Hamann[8], T. Wolff[6], A. Hocke[7], S. Hippenstiel[7], S. De Carlo[9], J. Neudecker[10], N. Budisa[5], R. Netz[11], S. Liese[11], A. Herrmann[4], C. P. R. Hackenberger[2,3], C. Böttcher[1]

[1]Freie Universität Berlin, Forschungszentrum für Elektronenmikroskopie und Gerätezentrum BioSupraMol, Berlin, Germany
[2]Leibniz-Forschungsinstitut für Molekulare Pharmakologie (FMP), Berlin, Germany
[3]Humboldt-Universität zu Berlin, Institut für Chemie, Berlin, Germany
[4]Humboldt-Universität zu Berlin, Institut für Biologie, Molekulare Biophysik, IRI Life Sciences, Berlin, Germany
[5]Technische Universität Berlin, Institut für Chemie, Biokatalyse, Berlin, Germany
[6]Robert-Koch-Institut, FG 17 Influenzaviren und weitere Viren des Respirationstraktes, Berlin, Germany
[7]Charité – Universitätsmedizin Berlin, Medizinische Klinik mit Schwerpunkt Infektiologie und Pneumologie, Berlin, Germany
[8]Deutsches Rheuma-Forschungszentrum Berlin, ein Leibniz-Institut, Experimentelle Rheumatologie, Berlin, Germany
[9]Thermo Fisher Scientific, Eindhoven, Netherlands
[10]Charité – Universitätsmedizin Berlin, Chirurgische Klinik, Campus Mitte/Campus Virchow Klinikum, Berlin, Germany
[11]Freie Universität Berlin, Fachbereich Physik, Theoretische Biophysik und Physik weicher Materie, Berlin, Germany

The attack of various human pathogens starts with their non-covalent attachment to a host cell. The beginning of an infection with the clinically highly relevant Influenza A virus (IAV) can be regarded as an prime example: The spike protein hemagglutinin (HA) of IAV binds to terminal sialic acid (Sia) residues of the cell glycocalyx (1). The affinity per HA binding site to monomeric Sia ligands is only in the millimolar range (2). However, HA as a trimer has three binding sites for Sia and is densely packed on the virus surface, resulting in a strong multivalent binding to the abundantly sialylated surface of the host cell (3). This offers an alternative antiviral strategy: Synthetic multivalent binders could competitively inhibit the binding of the virus (4).

It is still challenging to find biocompatible scaffolds that allow a spatially defined presentation of Sia ligands. Bacteriophage capsids as monodisperse rigid protein scaffolds meet this requirement. Moreover, the incorporation of bioorthogonal amino acids allows a site-specific conjugation of a defined number of ligands. The resulting objectives are (i) to find the suitable bacteriophage capsid, (ii) to realize an arrangement of ligands matching the geometry of the corresponding binding sites of viral spike proteins, (iii) to optimize these ligands with respect to distance, linker length and flexibility and (iv) to test the capacity of the constructs for binding and inhibition, respectively.

We used complementary experimental and theoretical approaches: A virtual screen based on the fixed geometry of the capsid surface predicted linker lengths. Several sialic acid azides were synthesized and conjugated by bioorthogonal CuAAC reaction to the capsids. These functionalized capsids were tested in various HA binding and infection inhibition assays. The underlying binding modes were modeled and simulated by computational methods. Electron cryo-microscopy (cryo-TEM) and cryo-electron tomography (cryo-ET) were the methods of choice when it came to the visualization of binding events.

We identified bacteriophages Qβ as the most suitable candidate to present Sia matching the binding sites of HA. The analysis by cryo-TEM revealed that IAV were densely decorated by sialyated Qβ capsids. Reconstructions of cryo-ET series indicated clearly that very high quantities of Qβ were directly bound to the HA spikes. A final 3D model created by interactive segmentation revealed that single capsids typically interact with only an individual, trimeric HA. To determine whether individual HA trimers can already bind to capsides, we performed cryo-TEM of the capsides incubated with isolated HA ectodomains. The binding of the HA ectodomains in a largely perpendicular orientation to the capsids suggest that binding to an HA trimer engages more than one valency of the sialylated capsid surface. HA binding and infection inhibition tests *in vitro* and *in vivo* confirmed that the sialyated Qβ is a highly potent IAV inhibitor (5).

Our study demonstrates that structurally defined, functionalized Qβ-capsids can serve as highly efficient and specific IAV inhibitors and may ultimately have a therapeutic potential.

References:

(1) Weis, W. et al. *Nature* 1988 333**,** 426

(2) Sauter, N.K. et al. *Biochemistry* 1989 28**,** 8388

(3) Mammen, M. et al. *Angew. Chem. Int. Ed.* 1998 37**,** 2754

(4) Fasting, C. et al. *Angew. Chem. Int. Ed.* 2012 51**,** 10472

(5) Klenk et al. *submitted (in revision)*

LS2.006
Cell biology of Microvillus Inclusion Disease – a fatal hereditary enteropathy

G. F. Vogel[1,2,3], A. R. Janecke[2], T. Müller[2], K. M. C. Klee[3], I. M. Krainer[3], P. A. Filipek[3], C. Posovszky[4], J. M. van Rijn[5], K. Gutleben[1], B. Witting[1], J. R. Goldenring[6], S. Middendorp[5], E. Cutz[7], L. A. Huber[3], M. W. Hess[1]

[1]Medical University of Innsbruck, Division of Histology and Embryology, Innsbruck, Austria
[2]Medical University of Innsbruck, Department of Paediatrics I, Innsbruck, Austria
[3]Medical University of Innsbruck, Division of Cell Biology - Biocenter, Innsbruck, Austria
[4]University Medical Center, Ulm, Germany
[5]University Medical Centre (UMC), Utrecht, Netherlands
[6]Vanderbilt School of Medicine, Nashville, United States
[7]The Hospital for Sick Children, Toronto, Canada

The yet incurable intestinal disorder MVID presents soon after birth (1). Infants suffer from intractable diarrhea, sodium loss and nutrient malabsorption. Parenteral nutrition and/or small bowel transplantation are the only treatments available. Figure 1 shows the ultrastructural hallmarks of affected enterocytes in the small intestine of MVID patients compared to those of healthy controls: (i) erosion of brush border microvilli (apical microvilli highlighted in green), (ii) ectopic intra-/intercellular microvilli (green), forming microvillus inclusions or lateral microvilli, and (iii) subapical clusters of PAS-positive vesicles (orange), interpreted as abnormal recycling endosomes (5). Our team was the first to identify mutated Myosin 5b, Syntaxin3 or Syntaxin binding protein 2 (Myo5b, Stx3, STXBP2/Munc18-2) as cause of MVID (2-4). (Notably, still unsolved MVID cases indicate that other genes might be involved as well.)

To unravel the complex phenotype and pathophysiology of this rare disease we analysed patients' biopsies (*bx*: (3-5)), gut organoids (*org.*: (3)), cell models (knock-in/out *CaCo2*: (3-6)) and organoid-derived monolayers (*org.-mono*: (4)) by microscopy, complemented by genetics and biochemistry. The EM-preparation protocols were described in detail previously: (a) modified variable pH-fixation (5,7) with 4% FA (formaldehyde) > postfixation with glutaraldehyde > standard Epon embedding (*for bx, org.-mono*); (b) FA-pH-shift > Tokuyasu-immuno-EM (*for bx, CaCo2*); (c) variable pH-FA-fixation > high-pressure freezing/freeze-substitution (HPF/FS) > Epon (*for bx*); (d) HPF/FS > Epon ((6); *for CaCo2, org.);* (e) HPF/FS > pre-embedding immuno-EM ((8); *for CaCo2, org.-mono*). For details on PAS-cytochemistry, immuno-EM, thin/semi-thick section EM/tomography, see (5).

Disrupted cargo vesicle traffic and mistargeting of pivotal apical transporter proteins appears as the primary defect in MVID, causing loss of epithelial polarity and facultative brush border atrophy, which in turn account for sodium loss diarrhea and malabsorption (2,4-6). The here presented combination of complementary preparation protocols proved highly suitable for state-of the-art EM of even minute amounts of valuable, unique pathological samples.

References:

(1) Cutz E et al 1989 Microvillus inclusion disease: an inherited defect of brush-border assembly and differentiation. *N Engl J Med* 320:646

(2) Muller T et al 2008 MYO5B mutations cause microvillus inclusion disease and disrupt epithelial cell polarity. *Nat Genet* 40:1163

(3) Wiegerinck CL et al 2014 Loss of syntaxin 3 causes variant microvillus inclusion disease. *Gastroenterology* 147:65

(4) Vogel GF et al 2017 Disrupted apical exocytosis of cargo vesicles causes enteropathy in FHL5 patients with Munc18-2 mutations. *JCI.Insight.94564*

(5) Vogel GF et al 2017 Abnormal Rab11-Rab8-vesicles cluster in enterocytes of patients with microvillus inclusion disease. *Traffic* 18:453

(6) Vogel GF et al 2015 Cargo-selective apical exocytosis in epithelial cells is conducted by Myo5B, Slp4a, Vamp7, and Syntaxin 3. *J Cell Biol* 211:587

(7) Berod A et al 1981 Importance of fixation in immunohistochemistry: use of formaldehyde solutions at variable pH for the localization of tyrosine hydroxylase. *J Histochem Cytochem* 29:844

(8) Hess MW et al 2018 Combining high-pressure freezing with pre-embedding immunogold electron microscopy and tomography. *Traffic* 19:639

Fig. 1

healthy enterocyte

Microvillus Inclusion Disease

LS2.LB.P01
Biophysical Characterisation of Mycobacterial Aerosols from Nectrotic Neutrophils

E. Pfrommer[1,2,3], U. E. Schaible[1], K. Schepanski[3], G. Gabriel[2], R. Reimer[2], C. Dreier[2], T. Dallenga[1], R. Scherließ[4], T. Gutsmann[5]

[1]Research Center Borstel, Leibniz Lung Center, Cellular Microbiology, Borstel, Germany
[2]Heinrich Pette Institut, Leibniz Institute for Experimantel Virology, Viral Zoonosis, Hamburg, Germany
[3]Tropos Institute, Leibniz Institute for Tropospheric Reseaerch , Modelling of Atmospheric Processes, Leipzig, Germany
[4]Christian Albrechts University,, Biophysics, Kiel, Germany
[5]Research Center Borstel, Leibniz Lung Center, Biophysics, Borstel, Germany

The tuberculosis (TB) agent, *Mycobacterium tuberculosis* (M. *tuberculosis*), is primarily transmitted through air, but little is known about mycobacteria containing aerosols. Airborne transmission is defined as transmission of pathogens through the air, from infected to sentinel host and is mainly influenced by two factors. First, the aerobiology of pathogen containing aerosols, which allows its airborne transmission and is defined by size and other physicochemical characteristics of the aerosol (Fernstrom and Goldblatt, 2013). Second, the pathogen induced pathology, which is based on its virulence and enables the release of pathogens as aerosol droplets from the lung (Jones and Brosseau, 2015). A better understanding of physicochemical properties and airborne transmission modalities of pathogen containing aerosol particles and the required pathology will enable us to better define risks of infection, to improve protocols to protect risk groups like care takers or house hold contacts and, ultimately, to develop treatments to prevent pathogen shedding.

Even though it is well established that influenza A virus and *Mycobacterium tuberculosis* can transmit through the air, little is known about the actual composition of pathogen containing aerosols. We therefore propose a method which allows the imaging of aerosols by Transmission Electron Microscopy and Atomic Force Microscopy and gives us an unique insight into aerosol composition using the Andersen Impinger (Andersen, 1958).

Analysis of those mycobacterial aerosol particles indicate that the average aerodynamic diameter and mass density would allow distant airborne transmission. Even so, at higher humidity"s when the hygroscopic property of the mycobacteria enhanced the volume and mass of the aerosol nuclei. By aerosolizing mycobacteria infected necrotic neutrophils to mimic aerosol formation in active TB patients, we observed similar aerosol particle sizes and viability rates as found with free mycobacteria but also an additional population of large aggregates of viable mycobacteria, which were lacking in aerosols from intact neutrophils. Those showed on average a larger particle size distribution but reduced viability.

Taken together, necrosis induction in infected neutrophils led to aerosol particle sizes similar to those with free mycobacteria but also to larger aggregates of viable bacteria. Therefore, mycobacterial tenancy is promoted by infected neutrophil necrosis and allows primarily transmission over short distances between close contacts.

References:

(1) Fernstrom, A. & Goldblatt, M. Airobiology and Its Role in the Transmission of Infectious Diseases. *J. Pathog.*2013**,** 13 (2012).

(2) Jones, R. M. & Brosseau, L. M. Aerosol Transmission of Infectious Disease. *J. Occup. Environ. Med.*57**,** 501–508 (2015).

(3) Andersen A (US ACC. New Sampler for the Collection, Sizing, and Enumeration of Viable Airborne Particles. 1958;(904).

LS2.LB.P02
Persistent virus infection in mosquito derived cells.

K. Franzke[1], M. Leggewie[2,3,4], V. B. Sreenu[3], S. Jansen[2,4], A. Heitmann[2,4], S. R. Welch[3], B. Brennan[3], R. M. Elliot[3], E. Tannich[2], S. C. Becker[5], E. Schnettler[2,3,4]

[1]Friedrich-Loeffler-Institute, Infectiology, Greifswald, Germany
[2]Bernhard Nocht Institute for Tropical Medicine, Hamburg, Germany
[3]MRC – University of Glasgow Centre of Virus Research, Glasgow, United Kingdom
[4]German Centre for Infection research, Hamburg-Lübeck-Borstel-Riems, Germany
[5]University of Veterinary Medicine Hannover, Hannover, Germany

Many insect cell lines are persistently infected with insect-specific viruses (ISV) often not recognized by the scientific community. The previously reported ISVs infect and replicate only in insects and belong to different virus families, like Birnaviridae, Flaviviridae or Phenuiviridae. The initial infections often result from persistent infections of the mosquito eggs/ embryos that had been used for the production of the corresponding insect cell lines; however cross-contaminations between cell lines are also possible. From the point of view that recent findings showing the possibility of interference between arbovirus and ISV infection it is important to be aware of ISV infections in cell lines.

A combination of small RNA sequencing, transmission electron microscopy and PCR is used to investigate persistent virus infection in commonly used aedine cell lines.

We describe the detection of Entomobirnavirus, Culex Y virus (CYV) in Aag2, U4.4 and C7-10 cells. In contrast to U4.4 and C7-10, CYV infection in Aag2 cells is hypothesized to be a cross-contamination as CYV-free Aag2 cells exist. Interestingly, the magnitude of PCR-positivity is variable among cell passages and leads to irregular detection via electron microscopy. Besides, other ISVs belonging to different virus families were detected as well using the small RNA sequencing and PCR approach in mosquito-derived cells.

Taken together, these results show that most of the common used mosquito cells harbor at least one persistent infection with an ISV and are often persistently infected with several different viruses.

LS2.LB.P03
Knockdown of the lipid droplet coat protein PLIN2 causes ultrastructural alterations that correlate with impaired infectious HCV particle production.

V. Nguyen-Dinh[1], S. Lassen[2], C. Grüttner[2], E. Herker[1]

[1]Philipps-University Marburg, Institute for Virology , Marburg, Germany
[2]Heinrich Pette Institute, Leibniz Institute for Experimental Virology, Hamburg, Germany

Chronic hepatitis C virus (HCV) infection remains a widespread public health concern and number of people infected with HCV still increases worldwide. In hepatocytes, perilipin 2 (PLIN2/ADRP) is the major coat protein of lipid droplets, an organelle that HCV utilizes as platform for virion assembly. PLIN2 knockdown in hepatocytes did not cause a general defect in lipid droplet homeostasis, but severely impaired HCV particle production. Here, we investigated lipid droplets and surrounding membrane structures after knockdown of PLIN2 in HCV-infected or uninfected cells by using advanced techniques in light and electron microscopy. Correlative light and electron microscopy (CLEM) images showed double-membrane sacs attached to lipid droplets in cells lacking PLIN2 indicating perturbed organelle interaction. These double-membrane sacs were linked or generated from the endoplasmic reticulum (ER) membrane, with the inner membranes tightly connected or in some areas even fused with the phospholipid monolayer of lipid droplets. Interestingly, in HCV infected cells, these double-membrane sacs contained not only lipid droplets but also the membrane vesicles formed as replication complexes during HCV infection. Strikingly, lipid droplet access of HCV core and NS5A proteins was restricted in PLIN2-deficient cells and correlated with reduced formation of intracellular HCV particles that were less infectious and of higher density indicating defects in maturation. Therefore, we describe PLIN2 as a host factor mediating proper lipid droplet–membrane interaction that is required for formation of functional HCV particles.

LS2.P001
The role of the electron microscope in the study of the immune escape mechanism of malignant cells

A. Helmy[1], O. Hammam[1]

[1]Theodor Bilhars Research Institute, Electron Microscope, Cairo, Egypt

Tumor cells have many immune escape mechanisms, one of them is apoptosis resistance .This electron microscope study tried to clarify this role.

A trial to develop targeted therapy that will sensitize the tumor cells to apoptosis.

In this study, expression of TGF-beta-1 protein and TGF-beta-R-1 receptor in urine and peripheral blood mononuclear cells (PBMNCs) were examined by the light and electron microscopy using immunocytochemical and immunoelectronmicroscopic techniques. Samples were obtained from 20 healthy controls (Group 1) and 120 patients who were classified according to the cytopathologic examination of their urine into 2 main subgroups chronic cystitis (bilharzial and nonbilharzial, Group 2, n = 30) and bladder cancer (transitiona cell carcinoma and squamous cell carcinoma, Group 3, n = 90), whether associated with bilharzial infection or not associated.

PBMNCs stained by both immunocytochemical and immunoelectronmicroscopic techniques showed significant increase in the percentage of positive cases expressing both TGFbeta-1 protein and TGF-beta-R-1 receptors in bladder cancer in comparison with the control ($P < .01$ and $P < .05$, respectively) and with chronic cystitis ($P < .05$). By light and electron microscopic examination, 82 out of 90 bladder cancer cases (91.1%) revealed remarkable apoptotic changes represented by cell shrinkage, surface blebs, nuclear chromatin condensation, and vacuolated cytoplasm. Urine examination of the exfoliated necrotic malignant epithelial (urothelial) cells in paraffin sections stained by both immunocytochemical and immunoelectronmicroscopic techniques revealed a statistically significant decrease in the percentage of positive cases expressing TGF-beta-R1 receptor in bladder cancer in comparison with either chronic cystitis cases or controls ($P < .01$), while TGF-beta-1 protein was significantly increased ($P < .01$).

This work helps in better understand one of the escape mechanisms of tumor cells that may facilitate the reverse of tumor escape from the immune system. It also draws attention to TGF-beta-1 protein that can be used as attractive target for anticancer therapy, and the absence of TGF-beta-R1 can be considered a marker for malignant transformation.

Fig. 1: TEM photomicrograph of immunoperoxidase-labeled PBMNC of patient with bladder cancer showing patchy distribution of TGF-beta-R-1 alongside the cell membrane (uncontrasted section; **×** 1800)

Fig. 2: PBMNCs in patient with bladder cancer, showing clumped nuclear chromatin (N) and vacuolated cytoplasm (× 2300).

Fig. 3: TEM photomicrograph of immunoperoxidase-labeled normal PBMNC showing patchy distribution of TGF-beta-R-1 alongside the cell membrane (uncontrasted section; × 1800)

Fig. 4: TEM photomicrograph of exfoliated epithelial (urothelial) cell in urine of patient with cystitis showing even distribution of the +ve immunoelectron labeling for TGF-beta-R-1 circumscribing the cell membrane

Fig. 1

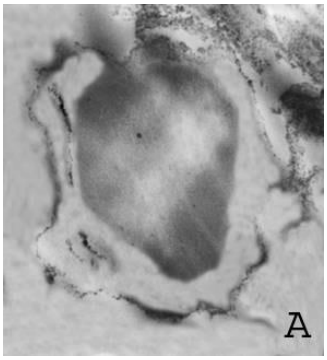

Fig. 2

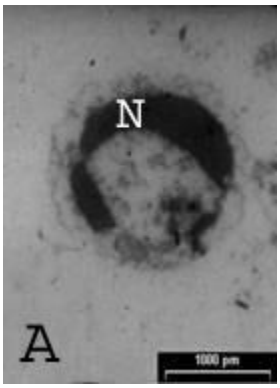

Fig. 3

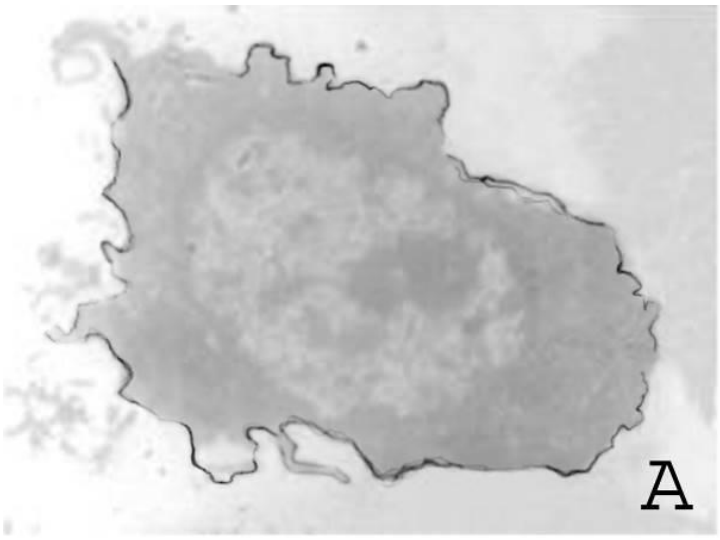

Fig. 4

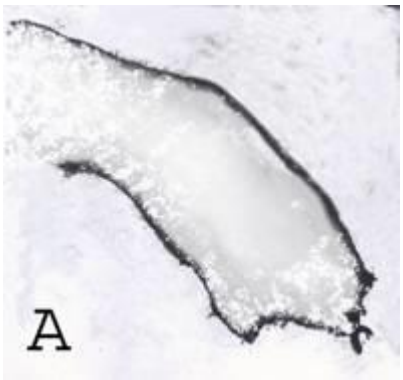

LS2.P002
Ultrastructural Study Of Platelets Changes During And After Liver Surgery In Pigs

A. Helmy[1]

[1]Theodor Bilhars Research Institute, Electron Microscope, Cairo, Egypt

The mechanisms leading to the hemostatic and platelet changes of acute liver injury are poorly understood. Liver transplantation is the main line of treatment for end stage liver diseases and that requires a reduction of blood loss during the operation .

To evaluate platelet changes during and after major hepatic resection to avoid the blood loss during the operation.

The study was done on 20 healthy adult pigs prepared for hepatic resection. Peripheral blood samples (15 ml.) were collected as such: one before the operation, 2 during the operation (one after hepatic mobilization and the other after resection), 2 after the operation (one after 7days and the other after 14 days). Platelet count and markers of platelets activation [platelet factor 4(PF 4) and B-thrmboglobulin(B-TG) were measured in all samples. Separated platelets from peripheral blood and those in the resected liver were examined by transmission electron microscope (TEM).

Our results showed that after hepatic mobilization and resection platelet count significantly dropped ($p<0.05$) & ($p<0.01$) respectively while PF 4 and B-TG significantly elevated ($p<0.05$) & ($p<0.01$) respectively. On 7 th day platelet count elevated but remained lower than normal level while PF 4 and B-TG returned to normal level detected before the operation. On 14th day Peripheral Platelet count returned to normal level with significant elevation of PF 4 and B-TG($p<0.05$)**.** EM analysis of platelets in peripheral blood and in the liver during the operation after hepatic mobilization and resection has revealed evident platelets activation in the form of loss of platelets normal discoid shape and transformed to a spiny sphere with long, thin filopodia. Alpha granules have been evacuated from their contents. These changes disappeared on 7th day and then the long thin filopodia

Liver surgical intervention causes significant drop in peripheral platelet count and an increase in platelet activation. which was detected by significant elevation of plasma levels of PF4&βT-G and confirmed by EM.So our results showed the necessity of proper systemic coagulant therapy beside the platelets transfusion at the end of major hepatic surgery and must be continued for one weak.

Fig. 1: Ultrastructure of activated platelet in peripheral blood after hepatic mobilization during the operation with long thin filopodia.(Magnification X 16,000)

Fig. 2: Ultrastructure of degranulated platelet in peripheral blood after the resection during the operation showing loss of its normal shape with long thin filopodia extending several Ums.(Magnification X20,000)

Fig. 1

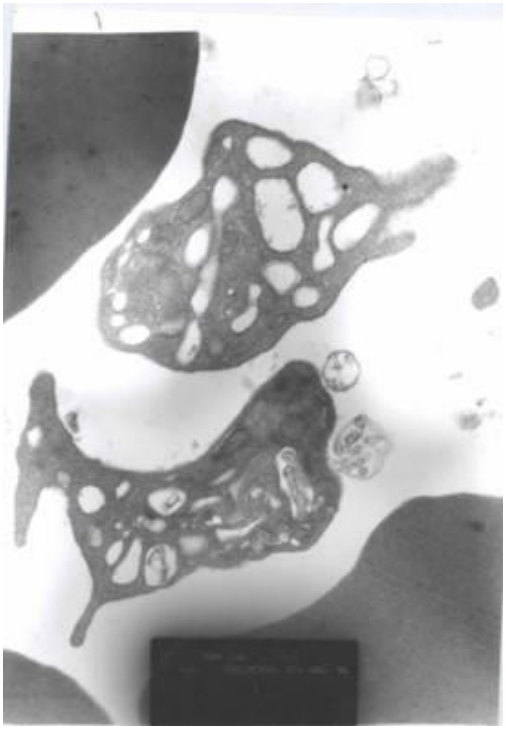

Fig. 2

LS2.P003
The Role Of Electron Microscope In Detecting the Cause Of Neutopenia In Hepatitis C Patients

A. Helmy[1]

[1]Theodor Bilhars Research Institute, Electron Microscope, Cairo, Egypt

Hepatitis C Virus (HCV) patients frequently manifest with neutropenia. Dysregulation of neutrophil apoptosis has been implicated in pathogenesis of Hepatitis C patients.

To explore neutrophil apoptosis and the factors relevant to its pathogenesis to determine its implication in shortened neutrophil survival in HCV patients thus contributing to the neutropenia they suffer from.

This study was carried out on 70 subjects divided into:- Group I (30 chronic HCV patients without neutropenia),Group II (30 chronic HCV patients with neutropenia) and 10 normal controls matched for age and sex. Neutrophils were separated using percoll density for detection of apoptosis by flow cytometry using Annexin V-FITC/propidium iodide dye to discriminate between normal, apoptotic and necrotic cells. Late apoptosis was tested by detection of DNA fragmentation using terminal deoxynucleotidyl transferase mediated deoxyuridine triphosphate nick end labeling test (TUNEL). soluble Fas (sFas)expression of neutrophils was determined in the serum by ELISA. The morphological features of apoptosis was examined by the electron microscope.

The results showed that the level of An+ve/PI-ve cells were decreased in the 2 patient groups versus the control group while in group II An+ve/PI+ve cells were significantly decreased and An-ve/PI+ve cells were significantly increased. The number of TUNEL positive cells were significantly increased in group I in comparison to both the control and group II. s Fas was significantly more increased in neutropenic group than in the other two groups. EM detected apoptotic cells in all neutropenic patients and in 35 % of non neutropenic patients.

Our study points to the significance of sFas and EM examination in detecting apoptosis in such patients, while annexin V and TUNEL tests suggest factors other than apoptosis influencing neutrophil.

Fig. 1: PMN cells in HCV patients showing(A)early apoptotic morphology represented by the intense perinuclear chromatin aggregation with normal cytoplasmic integrity (B)Fragmented nucleus (C) Late apoptotic morphology with vacuolated cytoplasm and fragmented nucleus (D) The cell is filled with numerous apoptotic bodies (each part of the fragmented nucleus became surrounded by part of the cytoplasm) with intact. cell membrane E) The cell releasing the apoptotic bodies (X 8000).(F) High magnification of the released apoptotic bodies from the cells (Arrow) (X 20000).

Fig. 1

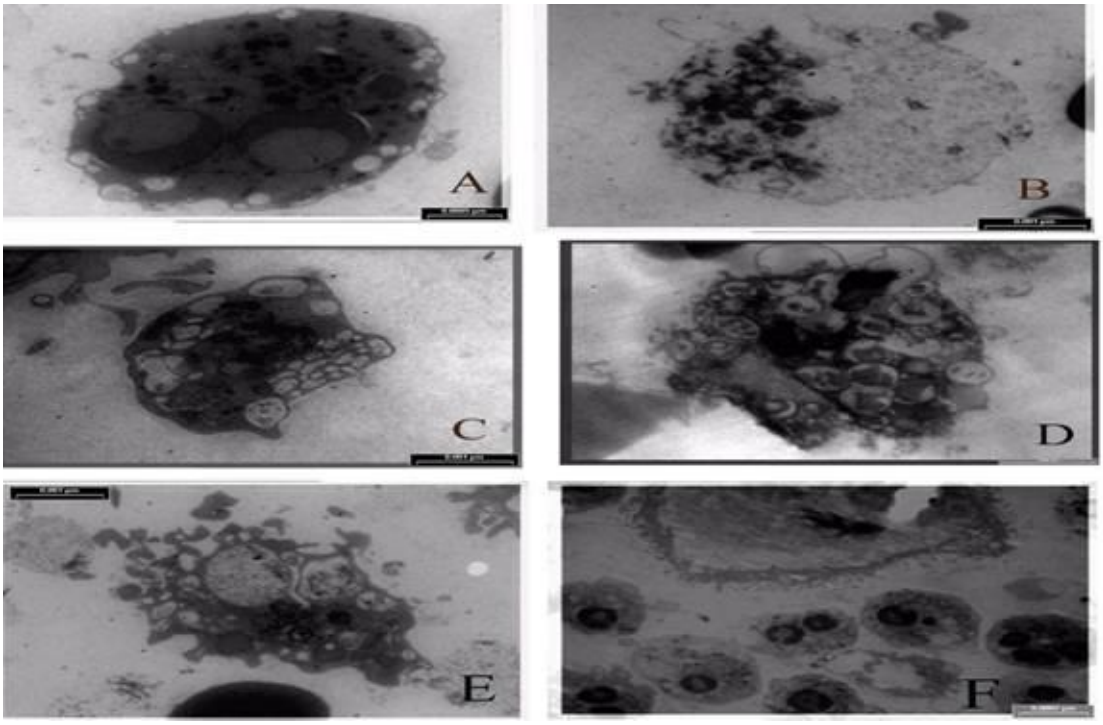

LS2.P004
A new method to enrich particles at the surface of grids for diagnostic electron microscopy of viruses

T. Hoffmann[1], M. Laue[1]

[1]Robert Koch Institute, Advanced Light and Electron Microscopy, Berlin, Germany

Diagnostic electron microscopy is used for detecting viruses and small microorganisms. While it is still used routinely in veterinary medicine, because specific tests are not available for the entire spectrum of host/pathogen combinations, in human medicine it serves as a supporting method in emergencies, such as outbreaks or life threatening diseases of unknown etiology (1). A drawback of diagnostic negative staining electron microscopy is that the method needs concentrated sample suspension for a reliable detection. To reduce the detection limit, ultracentrifugation of particles directly on the grid surface, by using the Beckman Airfuge, is the gold standard (2). However, major disadvantages of the technique are the relatively high price of the centrifuge, including the consumables, and the limited volume that can be processed (i.e. 80 µl). Recently, Beniac et al. (3) presented an alternative particle enrichment method using particle filtration with a syringe pumping system which allowed the detection of a low number of virus particles in a large volume. As a simplified alternative, we developed a filtration method which consists of a molecular centrifugation filter (30 kDa) in which a grid was placed on a support (Clipring of a Gatan cryo-holder) before the sample suspension was added and centrifuged through the filter. After centrifugation the grid was removed and stained with heavy metals. Moreover, the residual liquid resting above the filter was added to another grid for adsorption and then was stained (Figure 1). To validate the performance of the method, enrichment of three different virus suspensions, representing three different size classes, was compared with the performance of the Airfuge method. The results showed that both enrichment methods work equally well. Further experiments demonstrated that the particle density on the grid is only depending on the number of particles present in the sample suspension used for filtration. The combinatory use of two grids per filtration (grid 1 and grid 2; Figure 1) was necessary because larger viruses tended to enrich rather on the grid positioned on the filter than in the residual suspension above the filter while with the smaller viruses (<= 100 nm) it was reversed. Our contribution will show further aspects, like e.g. the staining quality, and provide an estimate for its detection limit. Finally, possible extensions of the method will be discussed.

References:

(1) Goldsmith, C.S. & Miller, S.E. (2009) Clinical Microbiology Reviews 22:552-563.

(2) Laue, M. & Bannert, N. (2010) J Appl Microbiol 109:1159-1168.

(3) Beniac, D. et al. (2014) Viruses 6:3458-3471.

Fig. 1: Schematic representation of the new particle enrichment method which uses filtration through a molecular filter driven by centrifugation. (1) Grid 1 is placed on the filter by using a clipring of a cryo-holder and covered with the sample suspension. The lower reservoir is pre-loaded with a distinct volume of water in order to generate a defined residual suspension volume above the filter. (2) After centrifugation with a desktop centrifuge, grid 1 is removed, washed and contrasted with heavy metals. (3) The upper reservoir is removed and 10 µl of the residual volume above the filter is added to grid 2. After 10 min of incubation, the grid is washed and contrasted with heavy metals.

Fig. 1

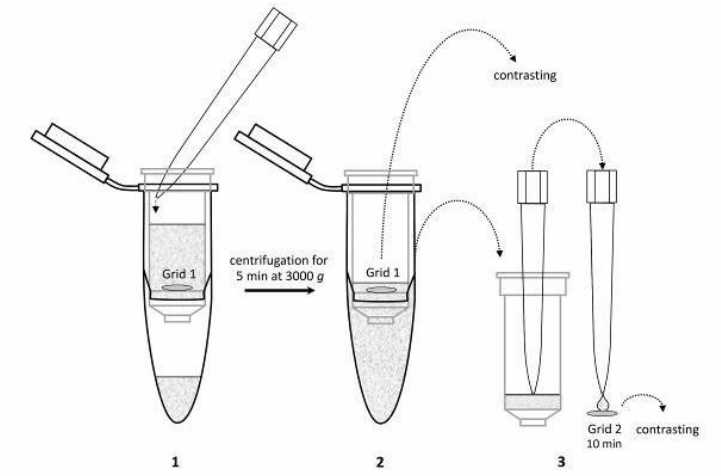

LS2.P005
Diagnostic electron microscopy of viruses with low-voltage electron microscopes

L. Möller[1], G. Holland[1], M. Laue[1]

[1]Robert Koch Institute, Advanced Light and Electron Microscopy, Berlin, Germany

Diagnostic electron microscopy (EM) of viruses is rather applied in particular situations such as outbreaks and not in routine diagnostics. However, it has a couple of advantages which renders this method indispensable, especially in emergency situations (1). One reason for the selected application of diagnostic EM is that transmission electron microscopes are expensive and need a particular lab environment and a particular technical expertise for operation. Recently, a new low-voltage transmission electron microscope was released (LVEM25, Delongh; MiniTEM, Vironova) which requires only few standard lab space and only basic knowledge of EM.

In our contribution we compare high voltage with low voltage electron microscopes, including scanning electron microscopes, regarding their performance for diagnostic EM of viruses.

Different viruses were propagated in suitable host cells according to standard procedures. Rotavirus was obtained from a stool sample. Negative staining and ultrathin section EM was performed according our standard protocols (2). Five different microscopes were used in our comparative study: Tecnai Spirit (ThermoFisher, 120 kV), JEM-2100 (Jeol, 200 kV), LVEM25 (Delongh, 25 kV), MiniTEM (Vironova, 25 kV; same EM hardware than the LVEM25 but without STEM unit), TeneoVS (ThermoFisher, 30 kV).

DEM of viruses using negatively stained samples or thin sections was possible with all microscopes tested (Fig. 1, 2). Image quality differed, especially at higher resolution, among the different microscopes, which is related to their optical resolution limits. Transmission electron microscopes operated at high voltage gave the best image quality. Microscopy with the LVEM25 and the MiniTEM sometimes suffered from image distortions at the periphery of the field of view, most probably because microscopes operate with electrostatic lenses. The lower voltage in low voltage EM restricts imaging to thin samples. In our study poxvirus particles (roughly 200 nm thick) could be imaged at a suitable quality. However, some blurring, perhaps caused by inelastic scattering, was obvious. Thin sections could be imaged at low voltages without additional contrasting of sections (Fig. 1). By using the scanning-transmission microscopy (STEM) option of the LVEM25 at 15 kV, the thickness limitation could be shifted to larger particle sizes and even bacteria could be visualized at sufficient quality. Scanning EM using a STEM-detector at 30 kV also allowed imaging and diagnosis of viruses in negatively stained samples (Fig. 2) or thin sections. To get better resolution, slower scanning was necessary which increased the time to inspect the samples slightly.

Low voltage EM using bright field transmission EM or STEM is a suitable alternative for performing DEM of viruses.

References:

(1) Gentile, M. & Gelderblom, H.R. (2014) New Microbiologica 37:403-422.

(2) Laue, M. (2010) Meth Cell Biol 96:1-20

Fig. 1: Low voltage MiniTEM (25 kV). Thin section (without additional section staining) through an insect cell infected with a flavivirus which is localized within the dilated cisternae of the ER. Bar = 500 nm.

Fig. 2: Teneo STEM (30 kV): Negative staining of a stool sample showing a single rotavirus particle. Bar = 100 nm.

Fig. 1

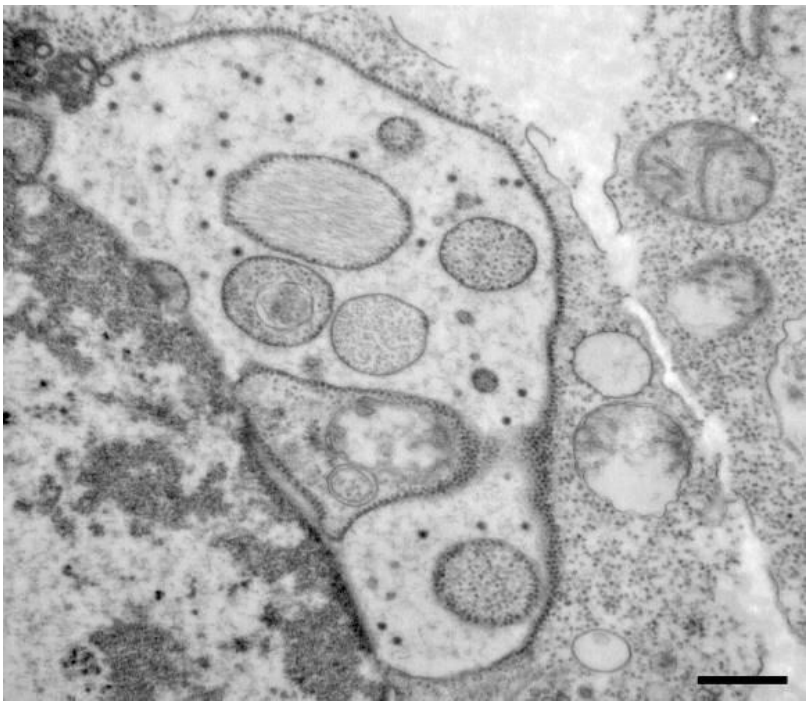

Fig. 2

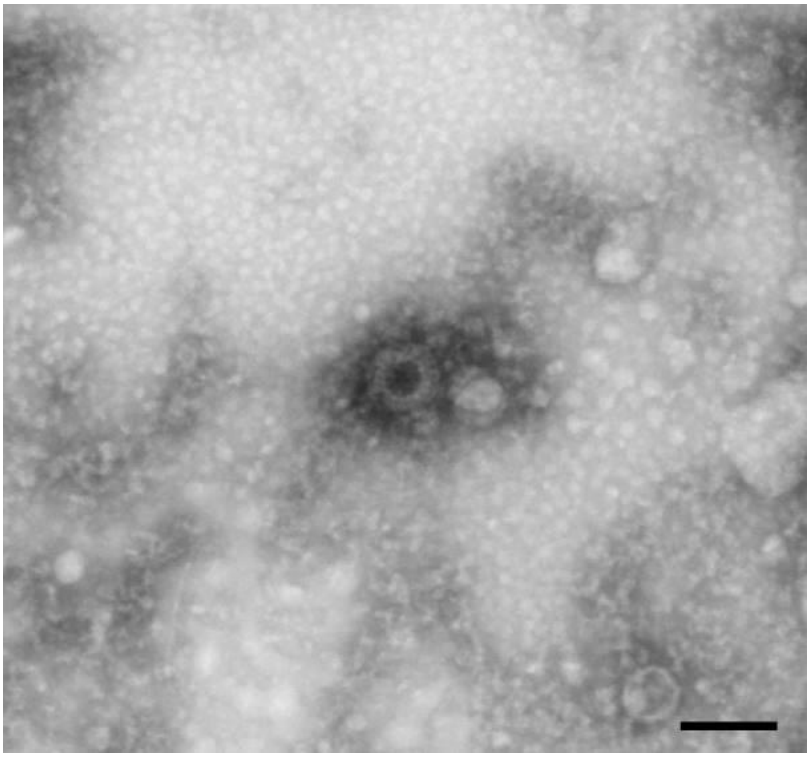

LS2.P006
T-DNA-induced plant tumors and plant galls with bacteria compared with human and animal tumors: structures, prevention and therapy

C. I. Ullrich[1], R. Aloni[2], R. G. Kleespies[1], T. Efferth[3]

[1]Julius Kühn-Institut, Institute for Biological Control, Darmstadt, Germany
[2]Tel Aviv University, School of Plant Sciences & Food Security, Tel Aviv, Israel
[3]Johannes Gutenberg University, Department of Pharmaceutical Biology, Institute of Pharmacy & Biochemistry, Mainz, Germany

Human tumors are still a major threat to human health while plant tumors negatively affect agricultural yields. Treatment of plant and human tumors is unsatisfactory yet, and novel therapy options are urgently needed.

Striking structural similarities of plant crown gall tumors with animal and human tumors, predominantly strong vascularization, suggested to compare their structural and functional characteristics and possible therapy.

Plant gall tissue sections were stained with toluidine blue, aniline blue, lacmoid, and acid fuchsin, and were analyzed by fluorescence and confocal laser scanning microscopy.

Plant tumors and galls develop upon infection by bacteria (*e.g. Agrobacterium tumefaciens* and *A. vitis* which harbor oncogenic T-DNA) and by insects (*e.g.* gall wasps, aphids). Plant tumors are benign, *i.e.* they usually do not produce metastases, nor ultimately kill their host, but they can lead to considerable economic damage up to 80%, due to reduced crop yields of cultivated plants. Human tumors develop by biological carcinogenesis (*i.e.* viruses and other infectious agents), chemical carcinogenesis (anthropogenic and non-anthropogenic environmental toxic xenobiotics) and physical carcinogenesis (radioactivity, UV-radiation). The majority of human tumors is malignant with lethal outcome. Although some treatments for both plant and human tumors are available (antibiotics and apathogenic bacterial strains for plant tumors, cytostatic drugs for human tumors), treatment successes are non-satisfactory, because of drug resistance and the severe adverse side effects.

In human beings, attacks by microbes or herbivores are repelled by cellular immunity (*i.e.* innate and acquired immune systems). Plants instead display chemical defense mechanisms, whereby constitutively expressed phytoanticipin compounds compare to the innate human immune system, whereas the acquired human immune system compares to phytoalexins, which are induced by appropriate biotic or abiotic stressors. Some chemical weapons of this armory of secondary metabolites are also active against plant galls. There is a mutual co-evolution between plant defense and animals/human beings, which was sometimes referred to as *animal plant warfare*. As a consequence, hepatic phase I-III metabolization and excretion were developed in animals and human beings to detoxify harmful phytochemicals. On the other hand, plants invented "pro-drugs" during evolution, which are activated and converted to toxins in animals by this hepatic biotransformation system. Recent efforts focus on phytochemicals that specifically target tumor-related mechanisms and proteins in human beings. These can be:

1. angiogenic or metastatic inhibitors, stimulators of the immune system to improve anti-tumor immunity,
2. specific cell death or cancer stem cell inhibitors,
3. inhibitors of DNA damage and epigenomic deregulation,
4. specific inhibitors of driver genes of carcinogenesis (*e.g.* oncogenes),
5. inhibitors of multidrug resistance (*i.e.* ABC transporter efflux inhibitors).

The present synopsis reveals how a multidisciplinary approach may contribute to the elucidation of animal and human as well as plant tumors with respect to structures, physiology, biochemistry and pathogenicity, and may provide innovative tools for therapy, derived from medicine, pharmacology, plant biology and plant protection disciplines.

LS2.P007
Pathological changes and ultrastructural characterization of *Kudoa pagrusi* (Myxosporea: Multivalvulida) infecting the common sea bream fish *Pagrus pagrus* (Perciformes: Sparidae) from the Red Sea, Egypt

F. Abdel-Ghaffar[1], S. Al-Quraishy[1], R. Abdel-Gaber[1], H. Mehlhorn[1]

[1]Faculty of Science, Cairo University, Zoology, Cairo, Egypt

The Gulf of Suez, Egypt has an abundance and diversity of fish fauna which represent a very important region of fish production and commercial fishing. Among the variety of fish species, *Pagrus pagrus*, is popularly known as the common sea bream fish and accounts for one of the largest productions of industrial fishing. Fish parasites are one of the most important problems facing fish production. Myxozoan parasites represent the most dangerous infection leads to large loss of fishes in Egypt.

The present study is a part of a continuous investigation of myxosporean parasites-infecting fish of the Red Sea and host-parasite relationship applying light and electron microscopy.

In the present study, 100 samples of different sizes of the common sea bream fish *Pagrus pagrus* were collected from the Egyptian water along the Gulf of Suez, Red Sea, Egypt and examined for the prevalence of myxosporidian parasites in general and their pathological effect on their hosts. Fish samples were externally thoroughly examined, dissected, all internal organs and body fluids were removed and examined.

A total of 60 out of 100 fish specimens collected were found to be infected with *Kudoa pagrusi*. Most of infections were intensive and appeared as macroscopic clusters of ovoid to ellipsoidal plasmodia restricted and damaged the cardiac muscles. None of the other organs was found to be infected. Histological studies elaborated tissue distortion at the sites of infection and the adjacent tissue layers. The development of plasmodia reduced the functional area of the heart muscles. Each plasmodium measured 1.2-2.5 (1.53 ± 0.2) mm × 0.63-0.80 (0.65 ± 0.2) mm. Mature spores are quadratic in shape in the apical view showing four equal valves and four symmetrical polar capsules. Fresh spores were 5.0-7.1 (5.7 ± 0.2) µm long × 5.4-8.5 (6.1 ± 0.3) µm wide. Ultrastructural analysis showed that the plasmodia were surrounded by single-unit membrane with numerous projections and pinocytotic channels extended toward the host cell. The generative cells and the different developmental stages were arranged at the periphery of the plasmodia while immature and mature spores were centrally arranged. On the basis of spore morphology, the present species was identified as *Kudoa pagrusi*. Molecular analysis based on small subunit ribosomal DNA (SSU rDNA) sequences revealed that the highest percentage of identity was observed with *K. scomberomori* and followed by *K. shiomitsui*, *K. hypoepicarclialis*, *K. amamiensis*, and *K. kenti*. The kudoid spores showed morphometric variations to some extent but had essentially identical nucleotide sequences of the SSU rDNA gene sequences closest to those of *K. scomberomori* and *K. shiomitsui* recorded from elasmobranchs in the Indo-Pacific Ocean.

A noval myxosporean, *Kudoa pagrusi*, is described from the common sea bream fish. In addition, this study showed host specificity for this parasite species causing extensive post mortem myoliquefaction in hosts" muscles and render fish unsuitable for consumption.

LS2.P008
Improved Whole Thin Section Preparation for Large-Scale Digitization of Diagnostic Tissue using Transmission Electron Microscopy

C. Dittmayer[1], H. H. Goebel[1,2], W. Stenzel[1]

[1]Charité Universitätsmedizin Berlin, Institut für Neuropathologie, Berlin, Germany
[2]Johannes-Guttenberg Universität, Institut für Neuropathologie, Mainz, Germany

Diagnostic ultrastructural examination of human tissue such as muscle tissue requires thorough screening to detect pathological changes such as small nemaline rods and alterations of the myofibrils and the cytoskeleton. Transmission electron microscopy (TEM) allows the detection of these changes and therefore plays a crucial role in research and diagnostics. For routine use, standard examination using single images usually is sufficient, but requires high quality samples with low amount of artifacts such as wrinkles and stain precipitates, ideally without grid bars that may mask important areas within the tissue. However, large-scale digitization of thin section areas using TEM provides additional benefits by preserving the correlation of microanatomy and ultrastructure, allowing decentralized examination and improved software-assisted analysis as compared to single images. For large-scale digitization of thin section areas as well as improved standard examination using single images, we improved the workflow in preparation and data processing of diagnostic tissue samples.

Muscle tissue was fixed in 2.5% glutaraldehyde, osmicated, dehydrated using acetone series and embedded using renlam. Thin sections were cut using an Ultracut E and collected onto hydrophilized pioloform-coated slot grids. The thin sections were then incubated using 1% EDTA for 3.5 min, stained with 5% aqueous uranyl acetate for 8 min. and with Reynolds lead citrate for 3.5 min. Large-scale digitization was performed using a Zeiss TEM 906 by taking 300 to 1000 overlapping single images automatically. The single images were stitched together using Fiji/TrakEM2 software.

Thin sections of diagnostic muscle tissue were reliably prepared with a drastically reduced amount of artifacts such as wrinkles and stain precipitates as compared to standard protocols (fig.1). Hydrophilization of pioloform-coated bar-free slot grids allowed the collection of whole thin sections without wrinkle formation. Therefore, staining artifacts were reduced drastically. Furthermore, staining artifacts were also reduced by using EDTA-treatment and the use of aqueous uranyl acetate instead of alcoholic uranyl acetate. Therefore, our preparation improved large-scale digitization as well as standard examination. Muscle tissue was digitized in a magnification range of 4646x-10.000x using automated image acquisition, requiring a total time of about 50 min. for 300 images.

In summary, we demonstrate a reliable preparation workflow for improved large-scale digitization as well as standard examination of diagnostic tissue. This approach provides benefits especially for research projects, allowing more precise ultrastructural characterization of e.g. new pathological entities. In addition, new and powerful developments in high-throughput TEM-imaging with 40x faster digitization could allow the use of thin section digitization as a routine technique to examine diagnostic tissues.

Fig.1. A thin section area measuring about 135x135 µm was digitized using 289 automatically acquired TEM-images at 10.000x. (A) The overview shows a nemaline myopathy. (B) Zoom-in into a muscle fiber containing many electron dense nemaline rods using the same dataset as shown in A. Individual thin filaments are resolved (inset). Note the absence of preparation artifacts such as wrinkles, stain precipitates and other sorts of thin section contamination.

Fig. 1

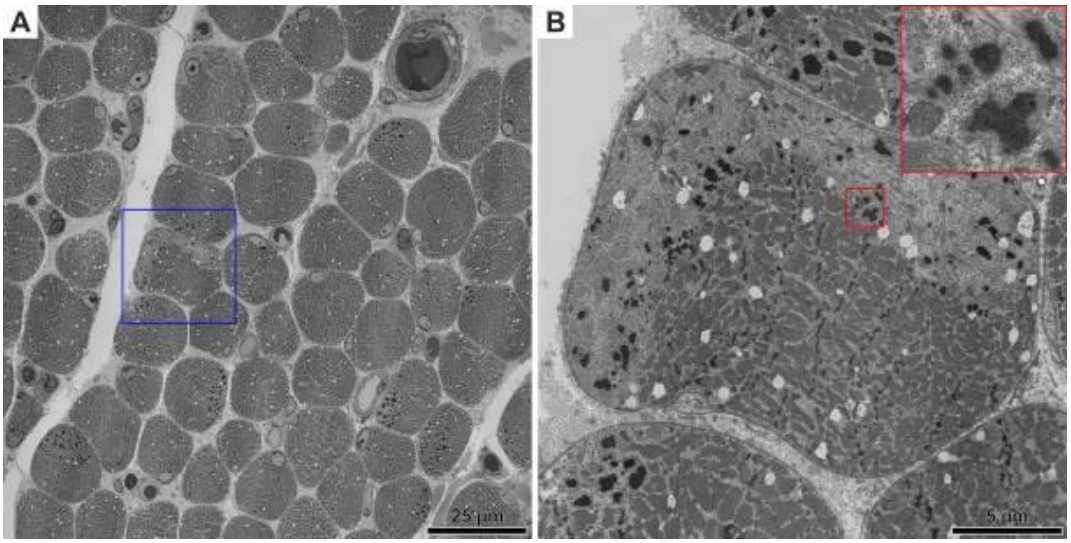

LS2.P009
Exploration of virosphere diversity by electron microscopy

K. R. Richert-Pöggeler[1], K. Franzke[2], K. Hipp[2,3], R. G. Kleespies[4]

[1]Federal Research Center for Cultivated Plants, Julius Kühn Institute, Institute for Epidemiology and Pathogen Diagnostics, Braunschweig, Germany
[2]Institut für Infektologie (IMED), Bundesforschungsinstitut für Tiergesundheit, Friedrich Loeffler Institut, Greifswald-Insel Riems, Germany
[3]Max Planck Institute for Developmental Biology, Electron Microscopy Facility, Tübingen, Germany
[4]Federal Research Centre for Cultivated Plants, Julius Kühn-Institute, Institute for Biological Control, Darmstadt, Germany

Since the recognition of viruses as the causative agents of disease in the last decades of the nineteenth century, scientists have striven to elucidate their structure.

This presentation will give a review on the versatility of electron microscopy as a universal means of virus detection, and its development from descriptive tool to the most powerful technique available to virologists today.

All kind of aspects in electron microscopy were extracted from literature and will be compiled in a figure with important milestones, beginning from 1886 up to date. Biological and chemical as well as physical aspects are considered equally. A decision tree for routine virus diagnosis using transmission electron microscopy will be established.

An overview on the exploration of the virosphere by electron microscopy reveals the rapid and very important development of technologies. Several techniques play a key role in virus diagnostics:

1. Studying the biology of viruses and the etiology of virus disease is crucial to the prevention of viral disease, efficient and reliable virus diagnosis, and virus control.
2. Using the most up-to-date electron cryomicroscopy methods, such investigations are now close to atomic resolution specific inhibitors of driver genes of carcinogenesis (*e.g.* oncogenes).
3. In combination with bioinformatics, the transition from 2D imaging to 3D remodeling allows structural and functional analyses that extend and augment our knowledge of the astonishing diversity in virus structure and lifestyle.
4. In combination with confocal laser scanning microscopy, electron microscopy enables live imaging of cells and tissues with high-resolution analysis.

Electron microscopy plays a pivotal role in the study of viruses, from structural analysis to the biological relevance of the viral metagenome (virome).

LS2.P010
Osteopontin and its spatiotemporal relationship with neuroglial cells in the striatum of rats treated with mitochondrial toxin 3-nitropropionic acid: possible involvement in phagocytosis

H. L. Kim[1], T. R. Riew[2], S. Kim[2], X. Jin[2], M. Y. Lee[2]

[1]The Catholic University of Korea, College of Medicine, Integrative Research Support Center, Laboratory of Electron Microscopy, Seoul, South Korea
[2]Catholic University of Korea, College of Medicine, Department of Anatomy, Catholic Neuroscience Institute, Seoul, South Korea

Osteopontin (OPN, SPP1) is upregulated in response to acute brain injury, and based on its immunoreactivity, two distinct forms have been identified: intracellular OPN within brain macrophages, and small granular extracellular OPN, identified as OPN-coated degenerated neurites. This study investigates the spatiotemporal relationship between extracellular OPN deposition and astroglial and microglial reactions elicited by 3-nitropropionic acid (3-NP).

Male Sprague-Dawley rats were intraperitoneally injected with mitochondrial toxin 3-NP and euthanized at 3, 7, 14, and 28 days. Quantitative and qualitative light and electron microscopic techniques were used to assess the relationship of OPN with neuroglial cells. Statistical significance was determined by Student"s t-test, or one-way analysis of variance followed by Tukey"s multiple comparisons test.

Extracellular OPN was synthesized and secreted by amoeboid-like brain macrophages in the lesion core, but not by reactive astrocytes and activated microglia with a stellate shape in the peri-lesional area. Extracellular OPN accumulation was detected only in the lesion core away from reactive astrocytes in the peri-lesional area at day 3, but had direct contact with, and even overlapped with astroglial processes at day 7. The distance between the OPN-positive area and the astrocytic scar significantly decreased from days 3 to 7. By days 14 and 28 post-lesion, when the glial scar was fully formed, extracellular OPN distribution mostly overlapped with the astrocytic scar. Three-dimensional reconstructions and quantitative image analysis revealed numerous granular OPN dots inside the cytoplasm of reactive astrocytes and brain macrophages. Reactive astrocytes showed prominent expression of the lysosomal marker lysosomal-associated membrane protein 1, and ultrastructural analysis confirmed OPN-coated degenerating neurites inside astrocytes, suggesting phagocytosis of extracellular OPN dots by reactive astrocytes after injury.

Extracellular OPN accumulation corresponded to OPN-coated degenerated neurites, which were closely associated with, or completely engulfed by the reactive astrocytes forming the astroglial scar in 3-NP lesioned striatum, suggesting that OPN may cause astrocytes to migrate towards these degenerated neurites in the lesion core to establish physical contact with, and possibly, to phagocytose them. Our results provide novel insights essential to understanding the recovery and repair of the central nervous system tissue.

References:

(1) Riew et al. Sci Rep. 2017 Mar 27;7:45173.

(2) Kim et al. Acta Histochem Cytochem. 2015 Oct 29;48(5):135-43.

(3) Shin et al. J Neurotrauma. 2012 May 1;29(7):1530-8.

(4) Shin et al. Glia. 2011 Mar;59(3):413-23.

Key Words: Osteopontin, 3-NP, Acute brain injury, Astrocyte, Microglia, Glial scar, Phagocytosis

This research was supported by the grants from the National Research Foundation of Korea (NRF) grant number NRF-2017R1A2B4002922).

LS2.P011
Scanning electron microscope analysis of paraffin embedded samples

E. R. Curticean[1], I. Wacker[2], R. R. Schröder[2,1]

[1]Universitätsklinikum Heidelberg, Cryo Electron Microscopy, Heidelberg, Germany
[2]Universität Heidelberg, Centre for Advanced Materials, Heidelberg, Germany

Light microscopic (LM) analyzes of paraffin-embedded samples are commonly used for diagnostic purposes or histochemical studies in pathology. For decades, the paraffin block has been seen as a routine sample for evaluation of cell or tissue alterations. There is a huge biobank of paraffin samples available for scientific labs and universities all over the world (1). However, for better understanding and characterization of disease, we may need to unveil details in such paraffin samples at the nanoscale level. For this, a possible advantage of high-resolution scanning electron microscopy (SEM) over LM needs to be examined.

We aim for a correlative workflow by optimizing preparation of paraffin samples for EM examinations. Stained or immunolabelled paraffin samples are further processed to gather additional information necessary for a better and more comprehensive diagnosis.

A histological paraffin block of human heart muscle was processed by two different approaches: 1. A small piece of the sample was re-embedded into a smaller paraffin block for semithin sectioning (300nm-500nm) using a histo diamond knife (Diatome). Sections were placed on silanized silicon wafers, dewaxed, post stained with reduced Ossolution, uranyl acetate and lead citrate and imaged in an Ultra 55 Zeiss SEM. 2. A piece of the sample was dewaxed, fixed in glutaraldehyde, postfixed with reduced Os, block stained overnight with uranyl acetate, dehydrated either in graded ethanol and embedded in Epon, or in graded acetone at -20°C and embedded in LR Gold resin (2). Ultrathin sections were placed on silicon wafers, post stained with uranyl acetate and lead citrate and then imaged as above.

Nuclei visualized in the LM by DAPI staining of dewaxed slices (fig 1A) can also be identified in the SEM (fig 1B, circle), but more structural detail is hard to see. Ultrathin sections of resin-embedded samples (fig 2) show some higher resolution details of muscle filaments, e.g. Z-discs (arrows) and remains of mitochondria; nevertheless, as expected, membranes are not visible.

Although dewaxing of semi-thin sections is much faster than dewaxing and re-embedding of tissue pieces the imaging results are not satisfactory. The crosslinking of classical paraffin embedding is too weak and membrane lipids are extracted by treatment with Xylene as an intermedium. Furthermore, the surface tension of the sample seems to pull everything down making the slices ,,collapse"" during the dewaxing process. We can recognize some cellular structures but information at the ultrastructural level is not obtained. The second method produced better results. Structures with high protein content are retained and visible, but membranes and part of the extracellular matrix are damaged.

References:

(1) L Cheng, DG Bostwick, (Eds.), Essentials of Anatomic Pathology, Humana Press, 2002

(2) MA Berryman, RD Rodewald, J Histochem Cytochem (1990) 38: 159

(3) We thank the BMBF for NanoPatho grant FKZ 13N14476

Fig. 1: 300 nm thick slices of paraffin embedded sample of human heart muscle, DAPI stained and imaged in Axio Imager (A) or Ultra SEM at 1,5 kV after post staining (B)

Fig. 2: 80 nm thick slices of sample embedded in Epon (A) or LR Gold (B), post stained and imaged using the SE2 detector of the Ultra SEM

Fig. 1

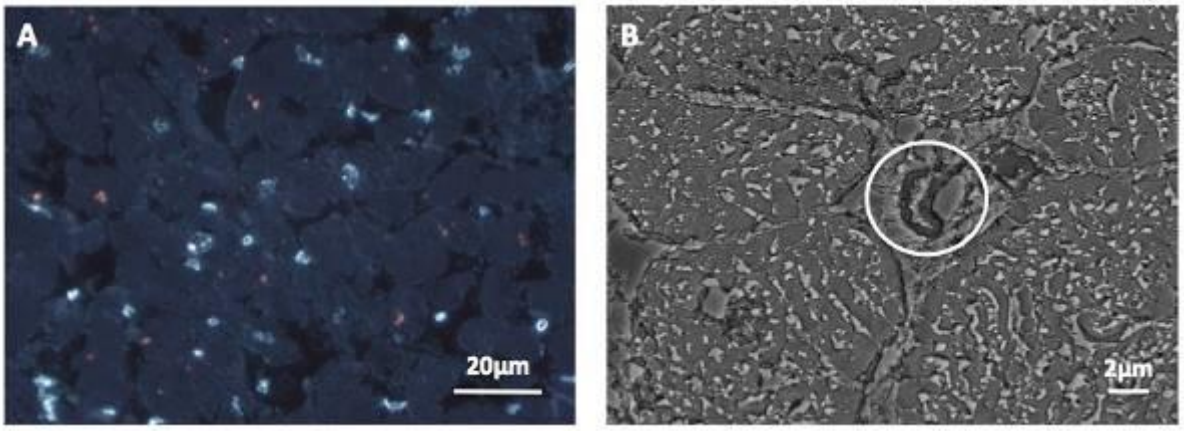

Fig. 2

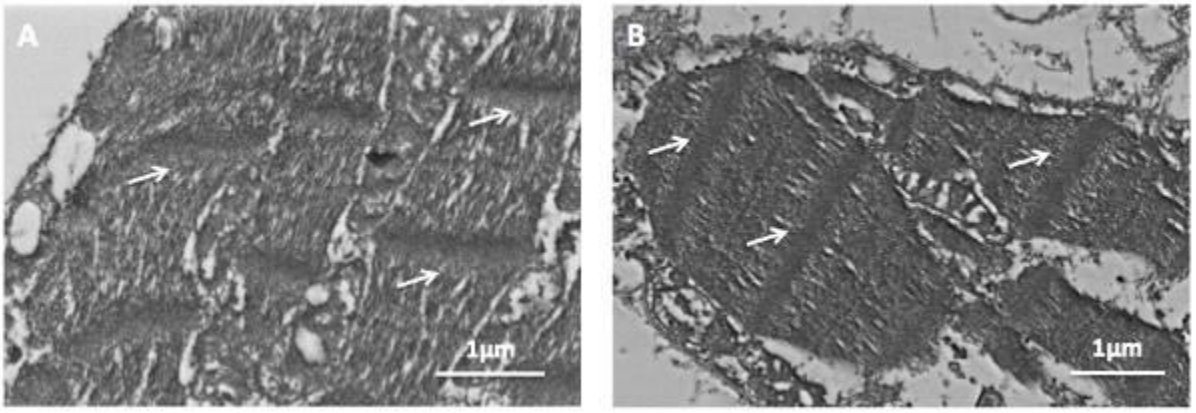

LS2.P012
Bile acid stress response of *Clostridioides difficile* and its effects on host-pathogen interaction.

N. G. Metzendorf[1], R. Schlüter[2], S. Dittmann[1], K. Riedel[1], S. Sievers[1]

[1]University Greifswald, Institute of Microbiology, Greifswald, Germany
[2]University Greifswald, Imaging Center of the Department of Biology, Greifswald, Germany

Clostridioides difficile is an intestinal human pathogen that infects the gut of individuals with a depleted microbiota. During infection the composition of the intestinal bile acid cocktail plays an important role. However, the specific response of vegetative *C. difficile* cells to bile acids is largely unknown on the molecular level and in terms of host-pathogen interaction.

Identification of systemic responses to long term bile acid stress and its effects on host-pathogen interactions.

Proteome signatures of *C. difficile* cells exposed to long-term (LT) stress were obtained by LC-MS/MS. The four main bile acids cholic acid (CA), chenodeoxycholic acid (CDCA), deoxycholic acid (DCA) and lithocholic acid (LCA) were tested. Bacterial morphology was determined and quantified on the basis of transmission electron micrographs. Co-cultivation experiments of bile acid stressed *C. difficile* with intestinal endothelial cells (CaCo-2 cells) were performed and analyzed by scanning electron microscopy and fluorescence microscopy.

LT stress caused a significant and bile acid specific change in global protein signatures. The major structural flagellum protein FliC was dramatically decreased in the presence of LCA compared to control conditions, while DCA and CDCA resulted in moderate down-regulation of FliC, and CA did not affect FliC expression at all. These findings were validated by electron microscopy: while CA treatment did not alter the number of flagella, DCA- and CDCA-stressed *C. difficile* had fewer and LCA-treated bacteria were almost devoid of flagella compared to controls. Co-cultivation experiments showed that bacteria with flagella were in direct interaction with the host.

In our study, we found a differential impact of bile acids on the formation of flagella in *C. difficile* and the expression of FliC, the major flagella protein. This raises the question which regulatory mechanism leads to the absence of flagella during LCA stress and the ineffectiveness of CA. Furthermore, we observed that flagella are needed for direct interaction of pathogen with its host. Dingle *et al*. (2011) reported that lack of flagella, especially the immunogenic FliC, causes non-motility but enhanced adherence and virulence of *C. difficile* in hamster. In conclusion, our results indicate that bile acid stress differentially impacts the status of flagella in *C. difficile* and that loss of flagella could be the main reason for the altered interaction of *C. difficile* and intestinal endothelial cells.

LS2.P013
Rapid fluorescent assays for *in situ* enumeration of microorganisms

L. Mezule[1]

[1]Riga Technical University, Water Research Laboratory, Riga, Latvia

Many microorganisms in the environment and engineered systems are constantly fighting with various stress inducing factors. This further induces microbial starvation, dormancy or or cell entrance into a viable but non-culturable (VBNC) state where they cannot be detected and enumerated with traditional culture based assays that require microbial growth and subsequent formation of a colony. In many of the engineered systems, e.g., water supply, hospital appliances, these organisms can cause serious health hazards. One of the current alternatives are molecular based *in situ* analyses which include epifluorescence staining of the samples without prior cultivation. Despite wide scale availability of various fluorescent stains, these techniques are often inappropriate for the analyses of environmental and surface material samples due to high cell variability, presence of various inhibitors that can induce autofluorescence or incompatibility with sample pre-processing approaches, e.g., immobilization, fixation or permeabilization.

The objective of this research is to develop protocols for rapid and simple *in situ* enumeration of microorganisms in their natural environments.

Current research activities of RTU Water research laboratory have been linked with designing viability staining and fluorescent *in situ* hybridization (FISH) protocols or combination of both for enumeration of total and viable *Escherichia coli,* bacterial spores, *Clostridium*, methanogenic archaea and many more. FISH alone is rapid and robust enough to be employed on a routine basis, however, it`s wide scale application is usually based on the necessity to design a customized protocol for each specific microorganism (group) in a specific matrix. For visualization an epifluorescence microscope (Leica DM6000B) equipped with various filter sets and x100 immersion oil objective was used. Image processing and combination of various fluorescence channels was performed with ImagePro Premier software.

Fluorescent structures, e.g., formazan crystals as markers of respiratory activity (Fig 1) or enzymatically active cells, can be discriminated from nonviable ones. At the same time simultaneous use of multiple probes in FISH allowed to discriminate among various microbial groups in biogas reactors (Fig 2). Use of analytical software allowed to set certain fluorescence thresholds to minimize the impact of autofluorescence and nonspecific binding that seemed to be as one of the biggest drawbacks of FISH.

In conclusion, the results showed that most of these protocols can be validated in environmental systems and yield as a good indicator for overall population quality.

Fig. 1

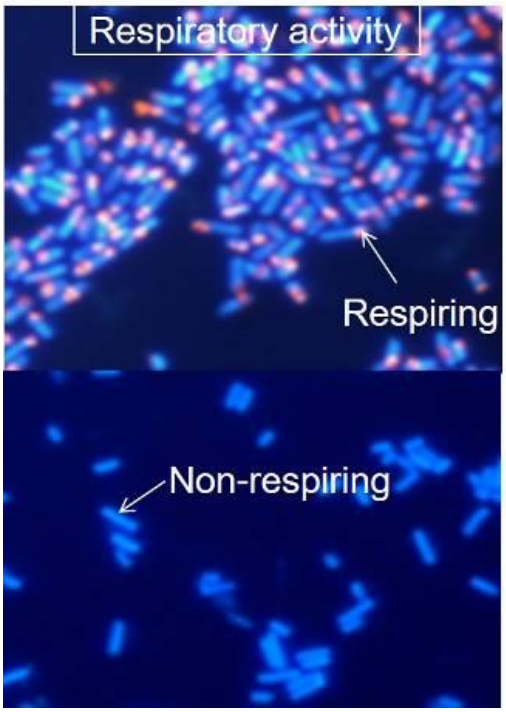

Fig. 2

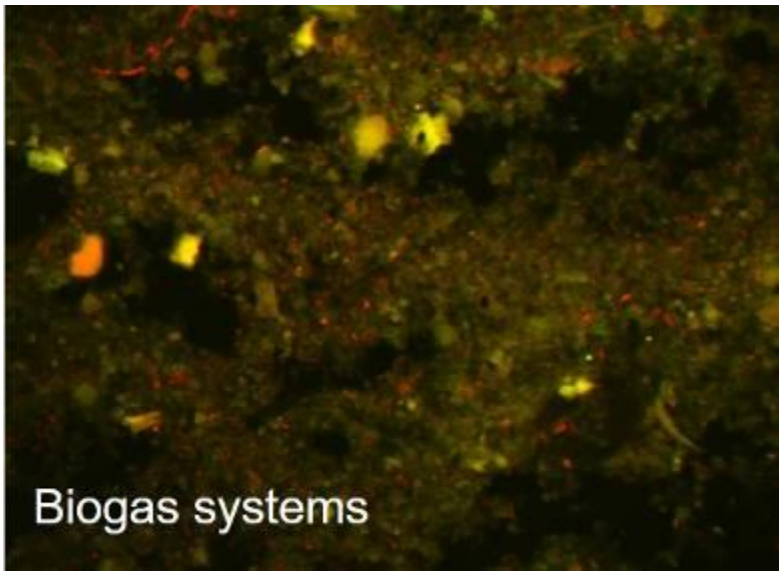

LS2.P014
Developmental Biology of *Ascosphaera torchioi*, a Causing Agent of Chalk Brood Disease in the Larvae of *Osmia lignaria*, as Investigated with Transmission Electron Microscopy, and its Implication for Phylogenetic Placement

N. N. Youssef[1], A. H. Vollmer[2]

[1]Utah State University, Biology, Logan, United States
[2]Utah State University, Nutrition, Dietetics and Food Sciences, Logan, United States

All species of the genus *Ascosphaera* are found in association with nests of bees (Apoidea: Anthophila). Some of these species are pathogenic to bee larvae, causing chalk brood disease; most are saprophytes growing on larval feces, pollen, honey and nesting material. The most pathogenic species, *A. aphis* (Maasen), *A. aggregata* (Skou), and *A. torchioi* (Youssef and McManus), are those associated with honey bees, leaf cutting bees, and blue orchard bees. *Ascosphaera* fungi are characterized by having unique fruiting bodies called ascomata. In the double-walled ascomata, ascospores develop, mature and cluster forming spore balls. Earlier taxonomic studies were based on morphological characters, such as measurement of length and width of ascospores, size and shape of ascomata, and spore balls. Morphology-based taxonomy can be difficult though since these characters can overlap among species. Furthermore, many species are fastidious or even impossible to grow in the laboratory. Recently, molecular approaches have been used to circumvent these problems.

A recent phylogenetic study by Klinger et al. (J Invert Pathol 112:41-46) showed that *A. torchioi* was in a separate clade that was the most basal, with strong genetic similarities to *Eremascus albums*, which has been considered to be a primitive form from which ascomycetous yeast have evolved. Since there are large morphological similarities between *A. aggregata* and *A. torchioi*, we decided to study the *in vivo* developmental biology of *A. torchioi* on the ultrastructural level to determine that the similarities are not only on the morphological, but also on the developmental level, and to answer the question if phylogeny alone can be used for determining relatedness.

Artificial provisions made of sterilized pollen and honey were placed in gelatin capsules placed in a holder. Each provision was inoculated with a drop of sterile water containing a suspension of spores that were collected aseptically from cadavers of *Osmia lignaria* larvae that exhibited the characteristics of chalk brood disease. Eggs of *O. lignaria* collected from natural nests were placed on inoculated artificial provision and kept in an environmental chamber and monitored for larval development. Infected larvae were removed on days 1, 2, 7, 9, 17, and 25 after inoculation and prepared for routine light and transmission election microscopy.

A. torchioi differs from *A. aggregata* by having much larger spores and by having residual bodies that were present within and between the spore balls and also on the inner wall of the ascomata. But similar to *A. aggregata*, the spores of *A. torchioi* germinated in the gut lumen and grew rapidly in the lumen, penetrated the gut wall, spread in the hemocoel and finally occupied it; at this stage death of the larvae commenced. Sexual development was limited to the outer region of the mycelial mat. Formation of the nutriocytes, the ascogonium and how the spores were formed in it, were like those that were described for *A. aggregata*. The same was observed for the process of sporogenesis including ascus division, formation of immature and mature spores and the formation of the spore balls. All these steps of sexual development were studied in detail.

The compelling similarities of the developmental biology between *A. aggregata* and *A. torchioi* allow us to question how their relatedness is presented in recent phylogenetic studies.

LS2.P015
Mechanisms of the urinary concentration defect in TAZ null mice

K. H. Han[1], S. J. Lee[1], Y. S. Chung[1], S. J. Lee[1], E. S. Hwang[2]

[1]Ewha Womans University, Department of Anatomy, Seoul, South Korea
[2]Ewha Womans University, Division of Life and Pharmaceutical Sciences, Seoul, South Korea

TAZ (transcriptional coactivator with PDZ-binding motif, also called WWTR1) shares homology with YAP (Yes-associated protein) and is involved in a variety of cell differentiation. Mice lacking TAZ exhibit multiple renal cysts and urinary concentration defects.

The purpose of this was to examine the effects of TAZ deletion on the loop of Henle, a critical structural composition in urine concentration mechanism. Kidney tissues from wild and TAZ null mice were processed for light and electron microscopic immunohistochemistry. Quantitative image analyses were performed using the AnalySIS software.

TAZ null mice exhibited severe hydronephrosis and low urine osmolality. Histologic analysis demonstrated multiple renal cysts and atrophy of medulla. To identify different parts of the medullary tubule segments, antibodies for AQP1, CLC-K1, and AQP2 were used. The relative area/number of AQP1-positive descending thin limb and CLC-K1-positive ascending thin limb dramatically decreased in TAZ null mice. The area/number of AQP2-positive medullary collecting duct did not significantly change in TAZ null mice. Electron microscopy demonstrated interesting structural abnormalities in the loop of Henle (e.g. thick limb cells in deep inner medulla) in TAZ null mice.

These results suggest that TAZ may play an important role in the differentiation of the loop of Henle in renal medulla.

This work was supported by funds from the National Research Foundation of Korea (NRF-2013R1A1A2058028 & 2017R1D1A1B03030573).

LS2.P016
The ultrastructure of *Anisakis* spp. L3 larva

J. Hrabar[1], A. Vrbatović[1], I. Mladineo[1]

[1]Institute of Oceanography and Fisheries, Laboratory of Aquaculture, Split, Croatia

Genus *Anisakis* Dujardin, 1845 comprises nine species of marine parasitic nematodes, which utilize marine mammals as definitive hosts, and fish and cephalopods as paratenic hosts. Some of the members of this genus are the causative agent of the disease anisakiasis, contracted by consumption of raw or undercooked sea food contaminated with live third stage larvae (L3). Due to increasing trend of consuming raw or undercooked food, more cases of anisakiasis are reported each year, listing this zoonosis as an emerging public health concern. Despite their cosmopolitan distribution and high abundance, and extensive research being conducted, much remains unknown about their biology, especially their morphology at ultrastructural level. Our study presents the comprehensive ultrastructure of *Anisakis* spp. L3 larvae throughout the nematode body. Live L3 were cut into 1mm pieces representing different body regions and fixed by high pressure freezing/freeze substitution (HPF/FS). Fixed samples were then resin embedded, cut to ultrathin sections, double contrasted and inspected under 80 kV microscope. Muscle layer, located below multi-layered cuticle, is composed of elongated cells with large pale areas in non-contractile part indicative of glycogen storage. Epithelial cells of alimentary tract, except for oesophagus, are lined with microvilli and contain many different vesicles and multivesicular bodies. Single-celled excretory gland is composed of tightly packed vesicles of different size, surrounding large nucleus, which open into one main and several minor collecting ducts. All nuclei appeared rich in euchromatin with a single nucleolus, except for excretory gland nucleus that contains many nucleoli. In the hind part of the worm, several exosomal vesicles were found, containing same amorphous matter lining the cuticle from the outside. Presence of countless different vesicles and their localisation in intestinal cells and excretory gland, rich rough endoplasmic reticulum and euchromatin suggests active synthesis of secreted products, which aid the infective larvae in invading host tissue.

LS2.P017
Electron microscopy of ciliogenesis in multiciliary cells – studying the tracheal epithelium of the chicken embryo as a model system

M. Frank[1], A. Reinke[1]

[1]University Medicine Rostock, Medical Biology and Electron Miciroscopy Centre, Rostock, Germany

Multiciliary cells with multiple motile cilia are present in various epithelia including the tracheal epithelium lining the upper airways. The proper generation and function of these cilia is critical for transport and efficient clearance of mucus. Ciliogenesis occurs during final differentiation of the multiciliary cells in the epithelium with the generation of hundreds of basal bodies that dock on the apical membrane and emerge nascent cilia. Recently, molecular mechanisms that govern basal body formation have been revealed, yet many details of this developmental process remain largely unknown. Impaired differentiation of multiciliary cells or the lack of motile cilia cause distinct pathological conditions in humans, for example primary ciliary dyskinesia (PCD) and reduced generation of multiple motile cilia (RGMC).

The chicken embryo offers the possibility to obtain a highly precise developmental staging due to the well controlled incubation conditions of the fertilized eggs. We have used this model system to examine ciliogenesis which starts following embryonic day 15 (E15) in the chicken in more detail. Electron microscopy is essential to identify and analyze the structures of nascent basal bodies and cilia during this process. Here, we have used a combined approach with scanning (SEM) and transmission electron microscopy (TEM).

Tracheal epithelia of E14 to E18 chicken embryos were fixed and processed for SEM and TEM using critical point drying and embedding in epoxy resin to obtain thin sections, respectively. Anterior and distal (posterior) parts of the epithelium were examined for cilia formation. Electron mircoscopy was supplemented with immunofluorescence analysis of ciliary markers, e.g. acetylated tubulin on sections of paraffin embedded material.

SEM analysis shows that at E14 most epithelial cells presented with primary cilia only preceding a massive phase of ciliary sprouting in a rather short time interval between E15,5 and E17 in line with earlier TEM studies and histological observations. While we do not find an obvious anterior to posterior developmental gradient in ciliogenesis along the tracheal epithelium, appearance of ciliated cells frequently occurs in distinct patches and stripe-like patterns. This suggests specific signals from underlying cells or tissues that are no longer obvious in later developmental stages. Complementary TEM analysis allowed to monitor centriole formation that occurred either via deuterosome dependent or mother centriole dependent amplification starting at E15. While few nascent cilia are hit on the TEM thin sections at these early stages, cilia and docking of basal bodies are frequently observed during more advanced stages e.g. at E17 and at E18.

Combination of scanning and transmission electron microscopy is a valuable approach to study structural-functional implications during ciliogenesis. Parallel observation of the appearance of cilia at the cell surface with SEM and structural analysis of the generation of centrioles and the docking of basal bodies within the cell using TEM may further help to identify relevant signals that regulate the differentiation of multiciliary cells.

LS3.003
High-resolution volume EM imaging of Myelin

A. Steyer[1], T. Ruhwedel[1], W. Möbius[1]

[1]Max Planck Institute of Experimental Medicine, Neurogenetics, Göttingen, Germany

Transmission electron microscopy has been widely used to answer a variety of questions in the field of neuroscience. To understand complex structures and morphological changes happening in different mouse mutants volume EM methods such as focused ion beam-scanning electron microscopy (FIB-SEM) as well as array tomography are used. Taking advantage of for example close to isotropic x/y/z-pixel (FIB-SEM) size as well as larger imaging regions (array tomography) those tools have started to elucidate so far not understood questions. We have been investigating different myelin mouse mutants using both techniques to get a better understanding of morphological changes happening to the axon, the myelin and the surrounding cells. A sample preparation protocol has been established combining high quality ultrastructural preservation (samples close to native state) and the most suitable contrast. We have also set up a workflow to look at high-pressure frozen mouse brain in the Cryo-FIB-SEM, allowing direct visualization of the native structures without any chemicals or stains in 3D. Volume visualization tools like IMOD have been used to illustrate the complex structures, such as Myelin outfoldings in three dimensions.

LS3.004
The megapinosome, 3D insights into a novel endocytotic structure with STEM tomography

A. Bauer[1], P. Walther[1]

[1]Ulm University, Central Facility for Electron Microscopy, Ulm, Germany

Megapinosomes are large endocytotic compartments that we found on M2 macrophages. They are very different from classical macropinosomes (1). They consist of a large (µm) vesicle filled with a membrane surrounded trabecular meshwork that is in connection with the cytosol.

To unravel the 3D structure and the dynamics of the megapinosome and the connected structures. For this purpose we used BSA-gold as a fluid-phase endocytotic tracer and analyzed the samples with electron tomography.

Human monocyte-derived M2 macrophages were incubated with BSA-gold (10 nm) for 5 min and then high pressure frozen, freeze substituted, embedded in epon and sectioned (section thickness about 600 nm) and tomographically recorded with a 200 kV scanning transmission electron microscope (JEOL 2100F). The 3D structure of the megapinosome complex and the other endocytotic structures were segmented.

Tomograms of 10 cells were selected and segmented. Structures were identified as endocytotic when they contained BSA-gold. These structures were then subclassified into canonical endocytotic structures or megapinosomal structures. Megapinosomes were identified by the presence of a trabecular meshwork (Fig. a). All structures that were connected with the megapinosomes are classified as megapinosom complex and segmented in blue. The most prominent stuctures of this complex are tubules with a diameter of about 165 nm that can branch and reach a length of several µm, and curved cisternae with a rather constant diameter of 30 nm (Figs. a and b). Similar structures have been described by Griffiths (2). The other endocytotic structures such as endosomes are labeled in brown.

When we compare our fast frozen and three dimensionally imaged data with classical chemically fixed and two dimensionally imaged electron microscopy, the cells show less spherical but more tubular structures, as already pointed out by Doherty (3), Warren (4) and Hopkins (5). We, therefore, conclude that cryo fixation and 3D imaging greatly changes the view of cellular compartments; they look very different to text book illustrations that usually rely on chemically fixed samples.

References:

(1) Bauer A, Subramanian N, Villinger C, Frascaroli G, Mertens T, Walther P. Histochem Cell Biol. (2016) 145, 617-627.

(2) Griffiths G (1992) in Endocytosis (P. J. Courtoy, Ed) Springer Verlag Berlin Heidelberg.

(3) Doherty G J, McMahon H T. Annu. Rev. Biochem. (2009) 78, 857-902.

(4) Warren G. Nature (1990) 346, 318-319.

(5) Hopkins C R, Gibson A, Shipman, Miller K. Nature (1990) 346, 335-339.

Fig. 1 is a virtual section of a tomogram showing the trabecular meshwork, the cisternae, the tubules and the endosomes. Fig. b is the segmentation of the 600 nm thick section. Megapinosom complex in blue, canonical endosomes in brown. The megapinosomes are way bigger than the canonical endosomes.

Fig. 1

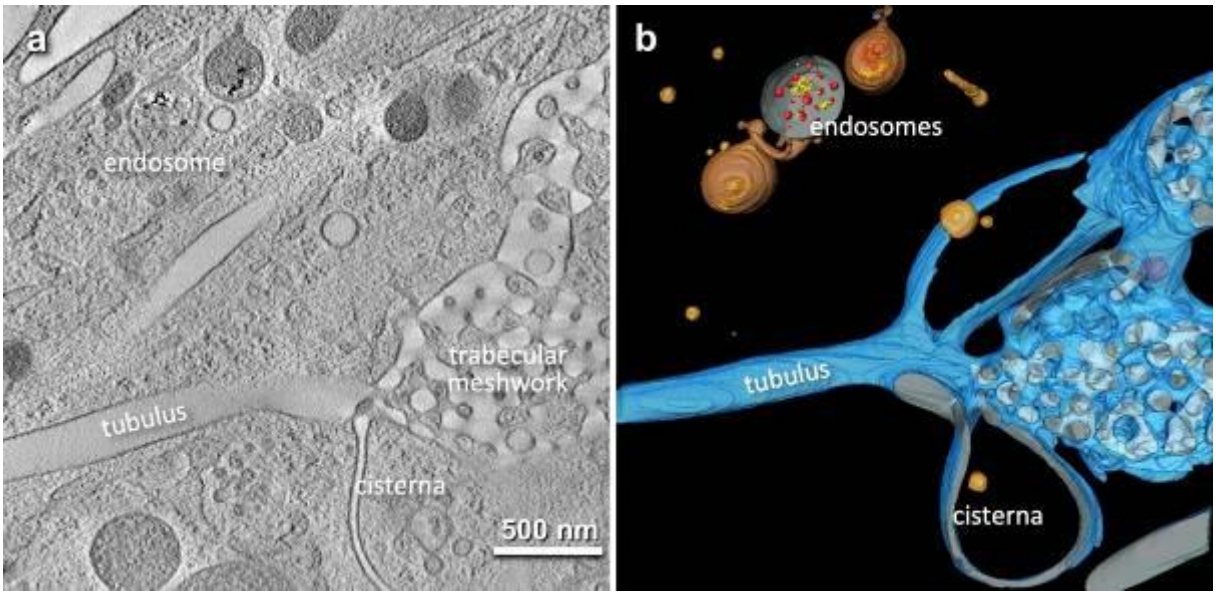
a
endosome
trabecular meshwork
tubulus
cisterna
500 nm
b
endosomes
tubulus
cisterna

LS3.005
Large volume FIB-SEM tomography of neovascular tissue in the rat eye

A. Biesemeier[1,2], S. Liu[2], A. Tschulakow[2,3], U. Schraermeyer[2,3], B. Schröppel[1], C. J. Burkhardt[1]

[1]NMI Natural and Medical Sciences Institute , Applied Materials Science, Reutlingen, Germany
[2]Center for Ophthalmology Tuebingen, Division for experimental vitreoretinal surgery, Tuebingen, Germany
[3]STZ OcuTox, Preclinical Drug Assessment, Hechingen, Germany

High resolution large volume tomography of pathological tissue can reveal subcellular features of a disease in correlation to their macroscopic environment within the tissue. In wet age-related macular degeneration (AMD), a major blinding disease, neovascularisation leads to edema and bleeding into the retina, the reason for that is still not fully understood.

In this work, newly formed blood vessels were investigated in direct neighbourhood to their parent vasculature in a volume of 40 µm^3 and with a voxel size of 15 nm^3 with FIB-SEM tomography. The neovascular architecture, e.g. endothelial substructure, shall be analysed and compared to the resident blood vessels. Volume analyses facilitate the investigation of matrix production in CNV.

A rat model for choroidal neovascularisation (CNV), based on VEGF overexpression in the retinal pigment epithelium (RPE), was used to investigate the ultrastructure of pathological angiogenesis as it also occurs in wet AMD (Julien et al., Mol Vis. 2008 Jul 30;14:1358-72; Liu et al., IOVS *ARVO Meeting Abstracts* 2269 - B0223, (2017)). Eyes were fixed with 5% glutaraldehyde, stained with osmium tetroxide and uranylacetate, dehydrated and embedded in EPON according to standard procedures. The tissue block was made conductive with 10 nm sputtered gold and silver lacquer. Focused ion beam scanning EM tomography was performed on a ZEISS Crossbeam 550 (resolution < 1.5 nm at 1.8 kV; voxel size 15 nm^3) using the ATLAS 5 system for milling and image acquisition with the InLens EsB detector. Segmentation and reconstruction of individual features were performed with Amira (Thermo Fisher) and Fiji/TrakEM (Cardona et al PLoS ONE 7(6):e38011) software tools.

The area of interest comprised neovascular tissue in the retina-choroid interface including deeper choroidal vessels, the choriocapillaris, Bruch"s membrane and the CNV area with several newly formed vessels and multi-layered RPE (figure 1). Due to the high resolution even single collagen and elastin fibers in the vascular bed can be visualized and correlated to pathology.

3D FIB-SEM tomography is a valid tool to investigate larger volumes of biological tissue samples with high voxel resolution. In this work, 3D reconstruction of extracellular matrix in the vascular bed of plastic embedded retina tissue was performed allowing suggestions of the involvement of Bruch"s membrane reassembly in AMD.

Fig. 1: 3D reconstruction of the main features of choroidal neovascularisation (CNV) in the rat (a) and a high magnification detail of the choroid-RPE interface in this area (b). Above choriocapillaris (CC, yellow), the mesh like elastic layer (el, red) and collagen fibers (c) of Bruch"s membrane, a multi-layered retinal pigment epithelium (RPE) with characteristic melanisation (m) and newly formed CNV blood vessels (green with erythrocyte (ery)) can be observed. The 15 nm^3 voxel size of the single images even allow analysing the extracellular matrix components of Bruch"s membrane with high resolution and in correlation with the surrounding structures.

Fig. 1

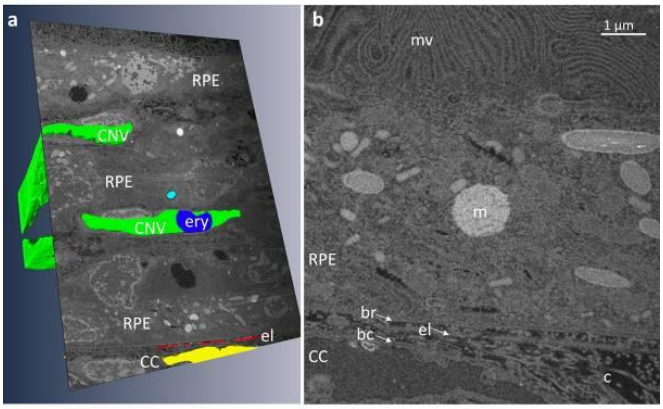

LS3.P001
Reducing the Influence of Electron Irradiation on Sensitive Material with High Speed Large Area Scanning Routines

M. Schmid[1], A. Liebel[1], F. Michael[1], G. Moldovan[2], H. Soltau[1]

[1]PNDetector, Munich, Germany
[2]point electronic GmbH, Halle (Saale), Germany

When examining beam sensitive samples, the overall goal is to minimize the influence of the electron beam on the specimen in order to reduce irreversible beam damage as well as charging effects which can obscure images by distortion or artificial contrast. In case of BSE imaging, this can lead to misinterpretations in compositional contrast. The standard procedure to reduce charging is to lower the beam energy or current or to use low vacuum modes. However, next to these, the method of scanning the sample can help to further reduce charging and sample damage. First, we show how faster scan speeds reduce electron-sample interaction, and second, how large area scans with high pixel counts can help to further improve results.

As sketched in fig. 1(c), the shorter the pixel dwell time (tdwell) the less charge builds up and the faster the pixel will be discharged. Fig. 1(a-b) shows a comparison of two images of silver flakes in an organic matrix taken at the same settings except scan speed and frame averaging. Fig. 1(a) is taken with tdwell = 400 ns while fig. 1(b) is taken with tdwell = 40 ns and 10 frame averaging, which results in the same electron dose. The artificial contrast between the silver flakes in the highlighted section 1 and 2 is reduced as well as the overall charging of the organic matrix. Focusing again on the charging of a single pixel, fig. 1(d) sketches two cases for repeated scans. Either the pixel discharges until the beam passes it again or charges will be accumulated. To avoid this charge accumulation the time between beam passes needs to be elongated.

At this point the observation of large areas comes into account. By enlarging the scan area and the pixel count by the same factor, the pixel size is kept constant but the time between two passes of the electron beam can be significantly increased. Fig. 2(a) shows a 1 Mpixel cutout of a 100 Mpixel image taken again at tdwell = 40 ns with 10 frame average. Compared to the image in fig 1(b), where the beam passes each pixel roughly every 6 ms (including flyback times, etc.) this time increases to about 6 s in the case of the 100 Mpixel image. This gives each pixel a 1000 times longer period to discharge, resulting in a further reduction of charging. Fig 2(c) shows a comparison of the artificial Z-contrast of two silver flakes in the highlighted areas of fig. 1(a-b) and fig. 2(a), nearly vanishing in the latter case.

We propose to use such large area scans instead of the commonly used method of stitching several smaller images for applications such as Serial Block Face Imaging where large area beam sensitive samples are investigated. This not only reduces sample charging or damage but also simplifies and accelerates the data processing. Figure 3 shows such a 100 Mpixel BSE image of a Serial Block Face sample. Further examples from this field will be presented.

Fig. 1: (a-b) 1 Mpixel BSE image of silver flakes in an organic matrix @ 3 keV. (a) tdwell = 400 ns, single frame, (b) tdwell = 40 ns, 10 frame average; (c-d) Schematic illustration of the charging of a single pixel for (a) single beam pass and (b) continuous scanning.

Fig. 2: Same specimen as in figure 1 imaged with (b) 100 Mpixel and (a) 1 Mpixel coutout of this image. (c) Comparison of the artificial contrast between two silver flakes highlighted in fig. 1(a-b) and fig. 2(a)

Fig. 3: (b) 400 Mpixel BSE image of a Serial Block Face sample (zebrafish) and (a) 1 Mpixel cutout of this image imaged @ 3 keV.

Fig. 1

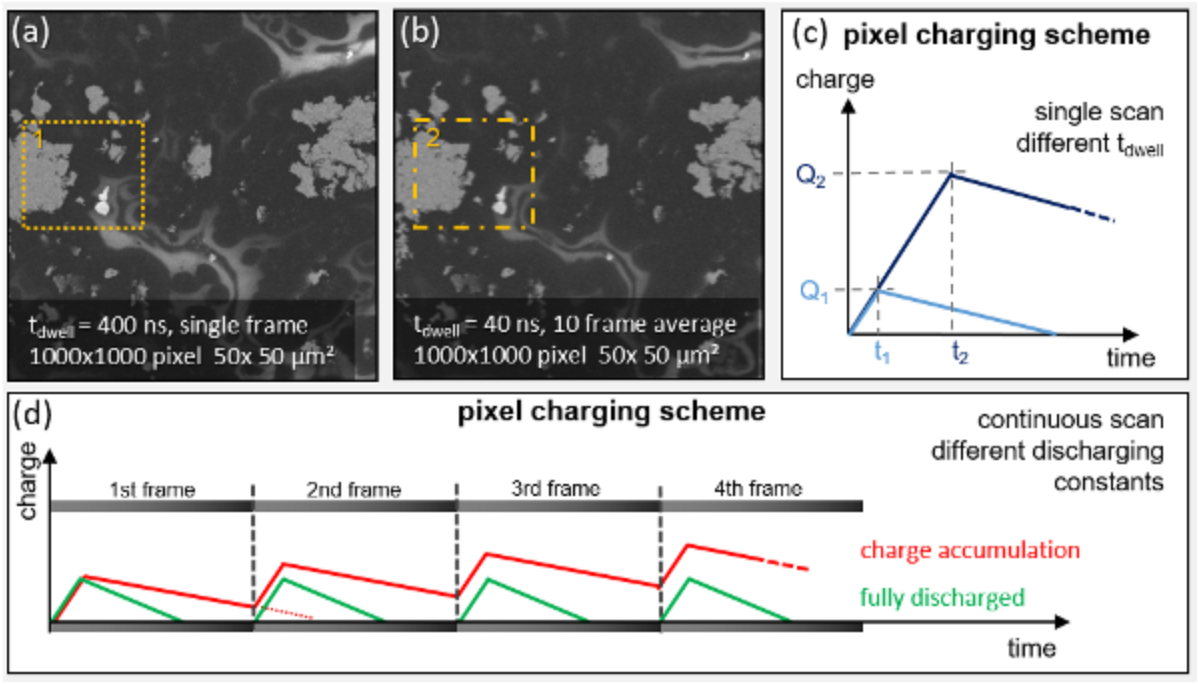
(a)
1
t_{dwell} = 400 ns, single frame
1000x1000 pixel 50x 50 µm²
(b)
2
t_{dwell} = 40 ns, 10 frame average
1000x1000 pixel 50x 50 µm²
(c) pixel charging scheme
charge
single scan
different t_{dwell}
Q_2
Q_1
t_1
t_2
time
(d)
pixel charging scheme
continuous scan
different discharging
constants
charge
1st frame
2nd frame
3rd frame
4th frame
charge accumulation
fully discharged
time

Fig. 2

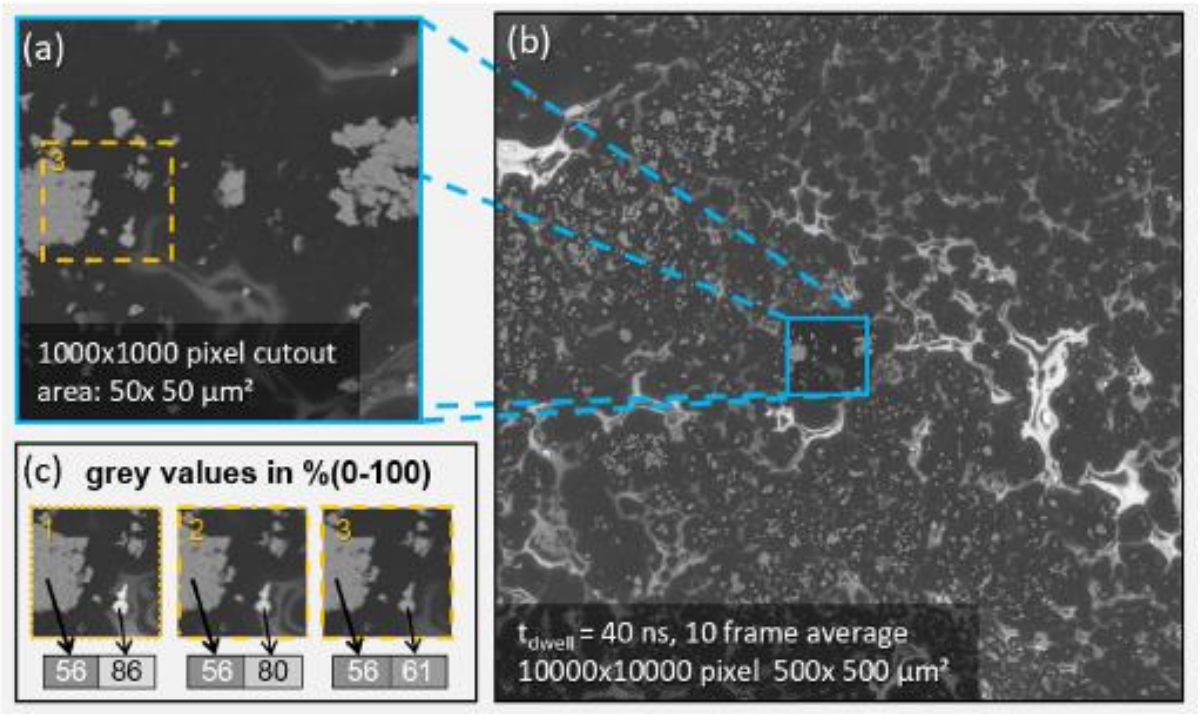
(a)
3
1000x1000 pixel cutout
area: 50x 50 µm²
(b)
t_{dwell} = 40 ns, 10 frame average
10000x10000 pixel 500x 500 µm²
(c) grey values in %(0-100)
1
2
3
56 86
56 80
56 61

Fig. 3

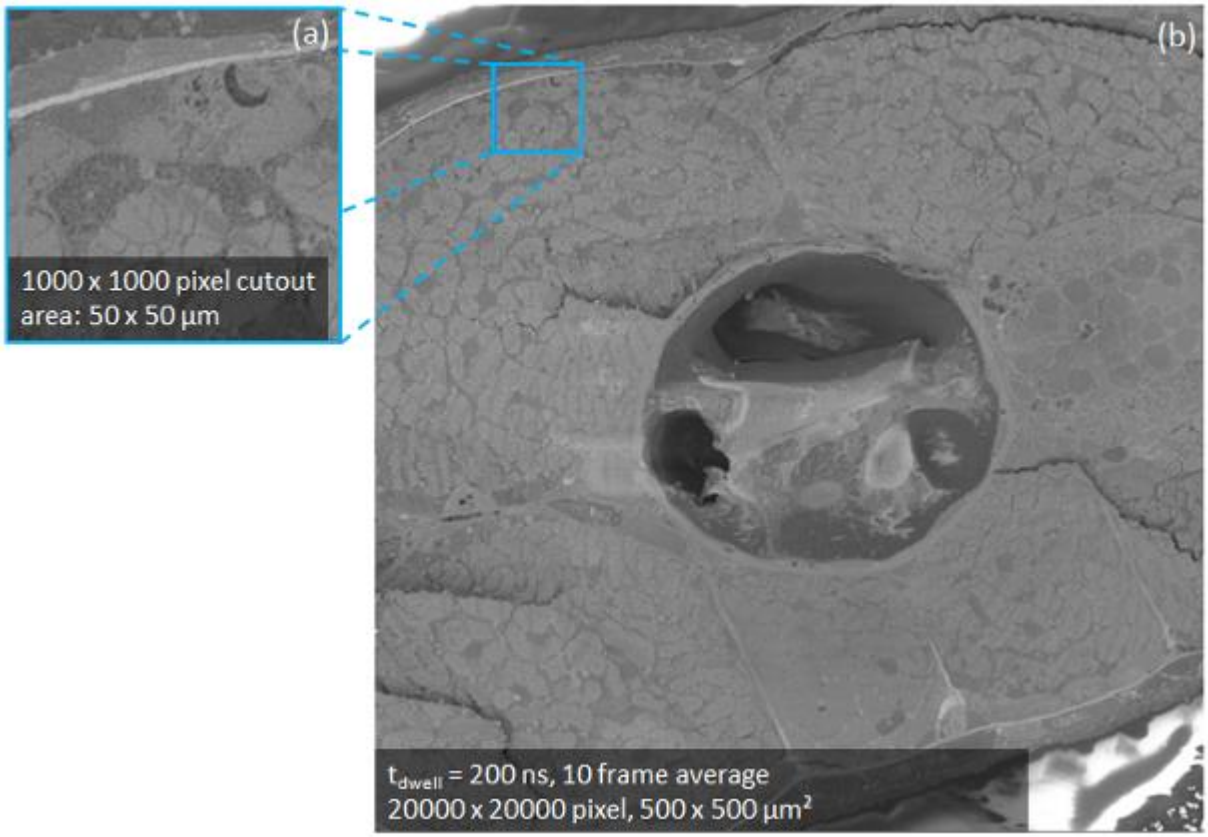
(a)
1000 x 1000 pixel cutout
area: 50 x 50 µm
(b)
t_{dwell} = 200 ns, 10 frame average
20000 x 20000 pixel, 500 x 500 µm²

LS3.P002
Workflow for Focused Ion Beam Tomography of large Volumes

A. Rüttgers[1], K. Schulz[1], S. Irsen[1]

[1]Center of Advanced European Studies and Research, Electron Microscopy & Analytics, Bonn, Germany

Over last years, new tools for generating volume electron microscopy data have been developed (1). These mainly scanning electron microscope based methods somehow replaced serial-section transmission electron microscopy (ssTEM) based methods (2). From these SEM based methods, Focused Ion Beam Scanning Electron Microscopy (FIB-SEM) is best suited to acquire volume data with an isotropic resolution in xyz below 10 nm (3). Problems like cutting artifacts, e.g. compression or wrinkles in serial-section based techniques or charging problems in serial blockface SEM do not apply for FIB-SEM. The drawback of FIB-SEM tomography is the limited tissue volume that can be processed within the typical period, FIB instrument run at stable conditions. Enormous efforts have been made to overcome these limitations by developing custom made instruments which can run over weeks acquiring 3d volumes with volumes >1 $e^6 \mu m^3$(4).

We improved the sample preparation procedure and data acquisition workflow for FIB-SEM-tomography using only standard equipment. We developed a new holder for an easy transfer of the sample from the ultramicrotome into the FIB. We optimized the sample staining protocol to reduce the needed pixel dwell time needed to generate sufficient image contrast. Finally, we optimized the acquisition protocol of the FIB tomography software to run stable up to 100 h. Using these modified setting, we were able to produce tomograms of avian retina tissue up to a volume of 120 x 30 x 30 µm.

References:

(1) Briggman, K. L., Bock, D. D. *Curr. Opin. Neurobiol.* 22**,**154–161 (2012).

(2) Tasdizen, T. *et al.Journal of Neuroscience Methods* 193**,**132–144 (2010).

(3) Kremer, A. *et al.Journal of microscopy* 259**,**80–96 (2015).

(4) Xu, C. S. *et al*. *Elife* 6**,**185 (2017).

LS4.001 invited
Integrated 3D tomography and computational modeling to study forces in metaphase spindles

S. Redemann[1]

[1]University of Virginia, Charlottesville, United States

The faithful segregation of chromosomes during mitosis is a fundamental and important process. Errors in mitosis have severe implications and are often detrimental to development, health and survival of the organism. We know that microtubules, in particular kinetochore microtubules, exert forces on chromosomes to initially position them on the metaphase plate and consequently divide them to the two daughter cells. The forces generated by microtubules are in balance during metaphase resulting in a mechanical steady-state and a stable long-lived spindle shape and length. Previous studies have identified the proteins involved in metaphase spindle assembly. Yet, we do not understand how those proteins lead to force generation through interactions of microtubules, motor proteins and chromosomes in submicron scale, and the collective effect of these forces on spindle shape function at larger scales. One major barrier in answering this question is the limitation of light microscopy in visualizing details of spindle microstructure in submicron resolutions. We have developed a novel approach of visualizing entire spindles in 3D by electron tomography and automatic microtubule segmentation. Using this approach, we can resolve single microtubules, which provides a unique perspective and offers a plethora of completely new information about the microstructure of spindles. Specifically, we can resolve chromosome surfaces, identify microtubules that are in contact with chromosomes (kinetochore microtubules), determine microtubules" nucleation profile, length distribution and local curvature. We combine electron tomography, light microcopy, biophysical modeling and large-scale simulations to develop a detailed and unprecedented understanding of force generation inside the spindle from individual microtubules to the mitotic spindle composed of thousands of microtubules.

LS4.002 invited
Archaeal life investigated by electron cryo-tomography

B. Daum[1]

[1]University of Exeter, Exeter, United Kingdom

Archaea form the third domain in the tree of life and represent our closest prokaryotic ancestors. They are ubiquitous microorganisms that thrive in diverse habitats all around the globe, ranging from extremely harsh environments to the human microbiome. Despite growing recognition of their importance in earth"s ecology and human health, many aspects of the archaeal cell biology are completely unknown. Using state-of-the-art electron cryo-tomography in combination with single particle analysis, we are investigating various aspects of archaeal life, including cell morphology, the structure of molecular machines, the architecture of their cell walls (S-layers), viral infection cycles and parasite-host interactions. Our work sheds new light on the unique and fascinating workings of archaeal life, often revealing unforeseen and striking surprises.

LS4.003
Cryo-electron tomography reveals pH-dependent structural rearrangements of Ebola Virus-Like Particles

S. Winter[1], A. Kolovou [1], P. Chlanda[1]

[1]Center for Integrated Infectious Disease Research - Virology, Heidelberg University Hospital, Heidelberg, Germany

Ebola virus (EBOV) is an enveloped negative stranded RNA virus that has caused severe disease outbreaks in Western and Central African countries. EBOV particles are filamentous in shape and up to several microns long. The filamentous morphology is determined by the viral major matrix protein VP40 that forms a helical scaffold underneath the viral membrane and encapsulates the viral genome containing nucleocapsid. A prerequisite for virus replication is the entry into host cells to access the host cell machinery required for the formation of progeny virions. The Ebola virions are macropinocytosed and trafficked to the late endosome, where low pH activated host cell proteases cleave off the glycosylated mucin-like domain of the Ebola glycoprotein (GP), thereby exposing a fusion peptide and receptor-binding domain. The cleaved GP then binds to the endosomal cholesterol transporter NPC1 and membrane fusion takes place. Although a general entry mechanism has been proposed for EBOV, it is currently unknown how the long filamentous virions disassemble and deliver their genome into the cytoplasm.

We aim to structurally characterize Ebola-virus like particles (VLPs) *in vitro* by cryo-electron tomography (cryo-ET) and analyze potential structural differences between particles at neutral pH and at low pH mimicking the endosome luminal environment. Sub-tomogram averaging (STA) of the VP40 helical layer underneath the membrane at neutral pH and at low pH will be employed to further characterize structural changes.

Ebola VLPs were produced by overexpressing Ebola structural proteins in 293T cells and subsequent purification of particles from the surrounding medium by differential centrifugation. The VLPs were incubated at neutral and low pH for 30 min at 37°C prior to plunge-freezing and acquiring cryo-electron tomograms to analyze overall structural changes. The subtomogram averaging (STA) of VP40 layers was performed in Dynamo.

Ebola VLPs resolved by cryo-ET at neutral pH have a characteristic filamentous morphology with an average diameter of 90 nm. The observed structural features of the VLPs are in agreement with those previously published in cryo-ET studies on Ebola virions. STA of the VP40 layer at neutral pH revealed the helical arrangement of VP40 dimers lining the inner leaflet of the membrane. In contrast, VLPs incubated at low pH were more variable in diameter and some of the particles lost the filamentous morphology. The majority of VLPs subjected to low pH had a detached VP40 layer and contained luminal aggregates, presumably composed of disassembled VP40.

In vitro, VLPs at low pH partially loose the Ebola-characteristic filamentous morphology as a result of VP40 layer detachment from the VLP envelope. We propose that VP40 layer disassembly is a critical intermediate step of viral entry that occurs prior or concomitant with membrane fusion. How the particle"s lumen gets acidified remains to be elucidated and could reveal a yet unknown factor important in Ebola virus disassembly.

"Morphology of Ebola-VLPs at pH 7.4. Cryo-ET slices depicting A) filamentous VLPs and higher magnification images showing B) a top view of a particle showing VP40 striations and trimeric GP-spikes, C) a loosely coiled nucleocapsid inside a particle (indicated by a white arrow), D) an isolated condensed nucleocapsid outside the VLPs with protruding densities formed by VP24 and VP35 and E) trimeric GP-spikes (white arrows). Scalebars from A-E in nm: 500, 100, 100, 20, 20."

Fig. 1

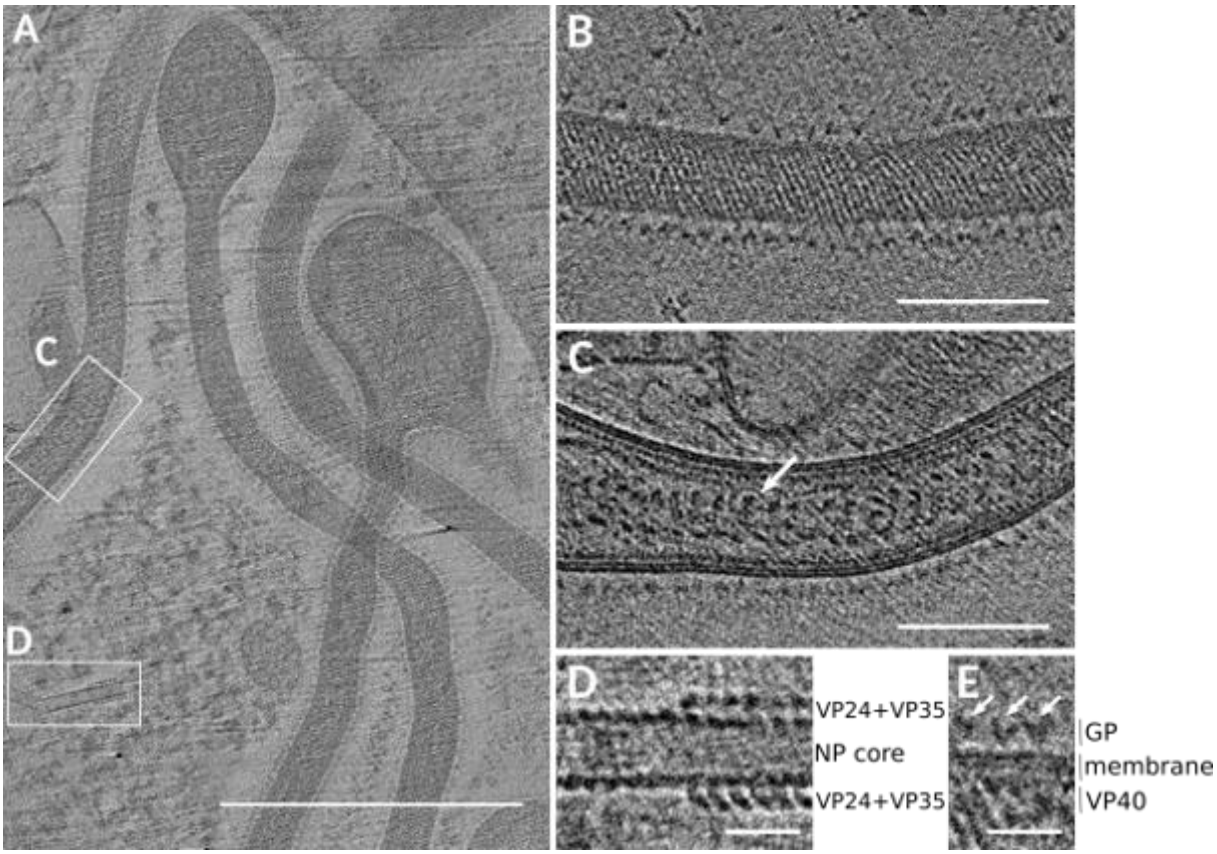

LS4.004
Ultrastructure of k-fibers in 3D-reconstructed mammalian spindles in mitosis

R. Kiewisz[1], N. Lindow[2], C. H. Yu[3], D. J. Needleman[3], T. Müller-Reichert[1]

[1]TU Dresden, CFCI, Dresden, Germany
[2]Zuse-Institut Berlin, Image Analysis in Biology and Materials Science, Berlin, Germany
[3]Harvard University, Department of Molecular and Cellular Biology, Cambridge, Germany

Mitosis is an important biological process to ensure faithful partitioning of chromosomes to form daughter cells. For this partitioning, microtubules (MTs) are arranged in bipolar mitotic spindles. These dynamic biopolymers are composed of α/β-tubulin heterodimers. MTs in spindles are classified according to their plus ends interacting with different cellular target sites. One of those MT classes is kinetochore microtubules (KMTs). KMTs physically connect chromosomes and spindle poles via a specialized structure called the kinetochore. In budding yeast, only a single KMT is connected to each kinetochore. In contrast, multiple KMTs bind to each mammalian kinetochore, forming so-called k-fibers. The ultrastructure of these k-fibers is currently not well documented. Therefore, we set out to characterize this connection in mammalian cells. For the first time, we were able to visualize all MTs in full reconstructions of mammalian mitotic spindles and quantitively analyze the ultrastructure of each k-fiber. This allowed us to answer the questions of how are these k-fibers organized, and what is the length distribution of MTs in k-fibers?

For this project, we used HeLa cells in culture. Cells were enriched in mitotic stages applying a shake-off technique and seeded on Sapphire discs in custom-made dishes. To ensure proper ultrastructural preservation, high-pressure freezing using the Leica ICE was applied. All cryo-immobilized specimens were freeze-substituted in 1% OsO4 and 0.1% UA saturated with Safranin for correlative light and electron microscopy (CLEM). Followed by infiltration and embedding in Epon/Araldite, Safranin staining allowed us to screen for embedded cells at specific mitotic stages (i.e. either metaphase or anaphase). For selected cells, semi-thick (300 nm) serial sections were imaged for electron tomography (TECNAI F30 transmission electron microscope, operating at 300 kV). Calculation of the tomograms was achieved using the IMOD software package (Boulder Laboratory for 3D Electron Microscopy of Cells, USA). The ZIBAmira software (Zuse Institute Berlin, Germany) was then used for MT segmentation and the joining of individual tomograms.

As a first step, we analyzed the structure of k-fibers at metaphase in two reconstructed spindles with an inter-kinetochore distance of 1 µm (± 0.2 µm). For this purpose, we classified all MTs based on their site of plus-end interaction. In our reconstructions, MTs associated with their plus ends to kinetochores were classified as KMTs. We found that 15.7% (775 of 4885) of all MTs were KMTs with an average length of 3.2 µm (± 1.5 µm). For each kinetochore (n=98), we counted 8 ± 1.7 attached KMTs. The minus-ends of KMTs (n=775) were found within an average distance of 2.5 µm (± 1.4 µm) to the center of the centrioles. Unexpectedly, we also observed short KMTs attached to the kinetochores, which were not directly associated with the centrosomes. In fact, only 47.1% of the KMTs were directly contacted to one of the spindle poles. As next steps, we will analyze k-fiber organization in prometaphase and during anaphase.

Applying semi-thick serial-section electron tomography, this approach allowed us for the first time to reconstruct full mitotic spindles in mammalian cells in 3D. Our long-term goal is then to develop a detailed biophysical model of mammalian spindle organization and chromosome segregation.

LS4.005
Soft X-ray tomography for 3D nanoparticle characterization in the cellular ultrastructure

D. Drescher[1], T. Büchner[1], G. P. Szekeres[1,2], V. Živanović[1,2], P. Guttmann[3], S. Werner[3], G. Schneider[3], J. Kneipp[1,2]

[1]Humboldt-Universität zu Berlin, Department of Chemistry, Berlin, Germany
[2]Humboldt-Universität zu Berlin, School of Analytical Sciences Adlershof, Berlin, Germany
[3]Helmholtz-Zentrum Berlin für Materialien und Energie GmbH, Research group X-ray microscopy, Berlin, Germany

Understanding the interactions of nanomaterials with eukaryotic cells is of high interest due to their omnipresence in medicine, nanotechnology, and the environment. In most cases, the quantity of particle uptake at the cellular level can be critical, for example in theranostics. Furthermore, the structure of the cell organelles and the morphology of the particle aggregates are important parameters in processing of the nanostructures by the cells and cytotoxic effects.

From X-ray tomograms, nanoparticles of different materials will be localized and characterized in the cellular ultrastructure. During cellular uptake and processing, particles can accumulate in the endosomes due to the different environment and can form aggregate structures that are specific for the individual cell type and nanomaterial. The size and 3D morphology of aggregates must be characterized to understand the endo/lysosomal processes and the interaction with the biological matrix.

For soft X-ray tomography (SXT) using synchrotron radiation, whole vitrified cells of up to 10 µm thickness are visualized in the X-ray water window at 510 eV photon energy employing the natural contrast due to the stronger absorption of soft X-rays in organic material or by nanoparticles as compared to vitreous ice. (G. Schneider *et al.*, Nat. Methods 2010; D. Drescher *et al*., Adv. Funct. Mater. 2014) SXT data were obtained at the electron storage ring BESSY II (HZB, Germany) from cells containing gold or silver particles that are commonly applied as nanosensors or drug-carriers. High resolution 2D projection images and 3D tomographic reconstructions are used to directly visualize the size and 3D morphology of the intracellular particle aggregates.

The X-ray tomograms indicate that the aggregates of gold nanoparticles that are formed in the endolysosomal system after incubation of the cells differ in size, shape, and density. The dependence on incubation time, cell type and on the influence of pre-aggregation of primary nanoparticles will be shown. The SXT data allow a 3D volume rendering of both cellular organelles and the aggregates of different sizes to better understand particle-cell interactions. In addition to the localization and characterization, SXT is applied for the quantitative analysis of the average particle properties, the statistical distributions for the level of uptake and the size of aggregates inside the cells. The intracellular organization of silver nanoparticles is correlated with the biomolecules adsorbed to the particle surface in endosomes using *in situ* vibrational spectroscopic probing. The X-ray tomograms prove the presence of 2D ring-like nanostructures in the intact cells that was correlated with a specific biomolecule corona (D. Drescher *et al.*, Nanoscale 2013).

Our data provide information about the localization and assembly of the nanoparticles inside endosomes. The possibility to detect different aggregate morphologies within subcellular structures of eukaryotic cells highlights the resolution level presently attainable with cryo-SXT. The detailed, 3D information about particle distribution in cellular substructures from SXT in combination with the chemical characterization of the particle environment obtained by vibrational spectroscopy will help to better understandinteractions of nanoparticles with biomolecules and cells, including optical nanoprobes or theranostic tools.

LS4.006
Electron crystallography complements X-ray crystallography

J. T. C. Wennmacher[1], T. Gruene[1,2], J. A. Van Bokhoven[1]

[1]Paul Scherrer Institute/ ETH Zurich, Laboratory for Catalysis and Sustainable Chemistry, Villigen PSI, Switzerland
[2]University of Vienna, Faculty of Chemistry, Vienna, Austria

A method to elucidate the atomic structure of individual submicrometer-sized crystals would have an enormous impact on both research and industry. This crystal-size remains inaccessible for conventional X-ray crystallography due to the bigger inelastic scattering cross section of X-rays, that destroys the crystalline structure. Therefore, electron diffraction has been applied to this problem. Electrons can locate the crystals in imaging mode and cause less beam damage in the crystal per elastic scattering event. Many different methods have been developed recently to obtain atomic models by electron diffraction of submicrometer-sized crystals. Although the dynamical scattering of electrons causes worse structural model statistics, the reliability of the atomic coordinates remains high.

Thus, we wanted to prove that a complementation of X-ray crystallography with three-dimensional electron diffraction is feasible.

The newest detector technology (Eiger 1M X detector) was mounted to a FEI 30 electron transmission microscope and thus a custom-made electron diffractometer was developed. While capable of counting single electrons, the detector was critical for the fast data collection of organic molecules at room temperature. The analysis was executed by the freely available X-ray crystallography software XDS and SHELX. With real-life examples where conventional x-ray crystallography would fail to obtain an atomic molecular model, the limits of this method were tested.

In one case, the atomic structure of the active pharmaceutical ingredient (api), paracetamol, was determined out of the powder of the cold medicine grippostad (Fig. 1). The atomic molecular model revealed the position of individual hydrogen atoms bound to carbon atoms. Unlike X-ray diffraction, the data showed the real inter-nucleic C-H bond distance. The other case was resembled by submicrometer-sized needles of a salt of a new methylene blue derivative. This dye is representative of a typical organic molecule in synthetic chemistry. Initially, crystals could not be grown large enough to obtain a structure by synchrotron radiation (Fig. 2). Electron crystallography yielded an atomic model within four hours starting from the sample preparation (Fig. 3). Accordingly, time investment for a standard X-ray crystallographic experiment would be the same. Though model statistics accounted for an unreliable model, bond lengths of the structure were in high agreement with the X-ray crystallographic structure obtained when bigger crystals of the compound were available. Interestingly, a disorder of a BF4- anion, that accompany the dye molecule, could be identified and refined.

These results confirm that electron crystallography can extend X-ray crystallography to previously inaccessible atomic structures of submicrometer-sized crystals. The experimental set-up for data collection is simple and can be established at any research institution in the world.

References:

(1) Gruene et al., Angew.Chem.Int.Ed. 2018, 57, 16313–16317

Fig. 1: a) Drugs in powder form b) The powder grains are too small for single-crystal X-ray analysis. c) The diffraction achieves atomic resolution. d) High data quality localises some hydrogen atoms (encircled).

Fig. 2: STEM micrographs of the methylene blue needle (contrast inverted for better visibility).

Fig. 3: Processing pipeline allows structure solution in 4h only.

Fig. 1

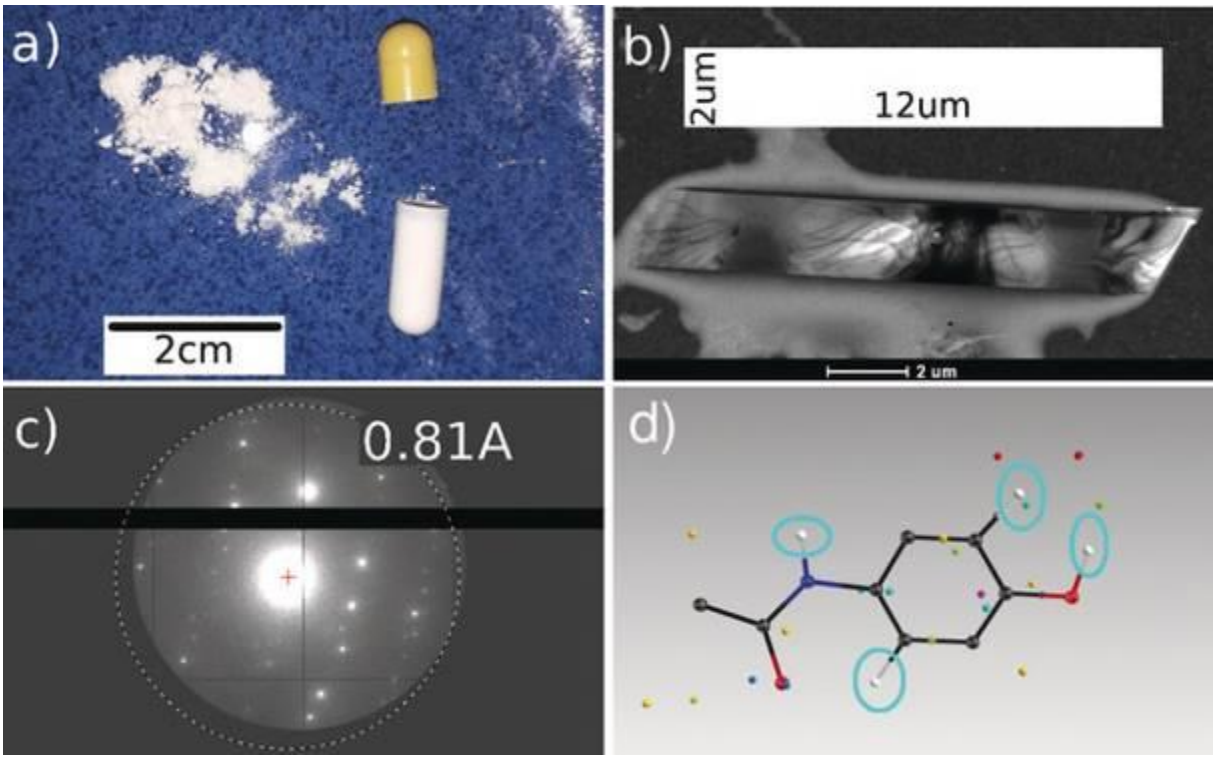

Fig. 2

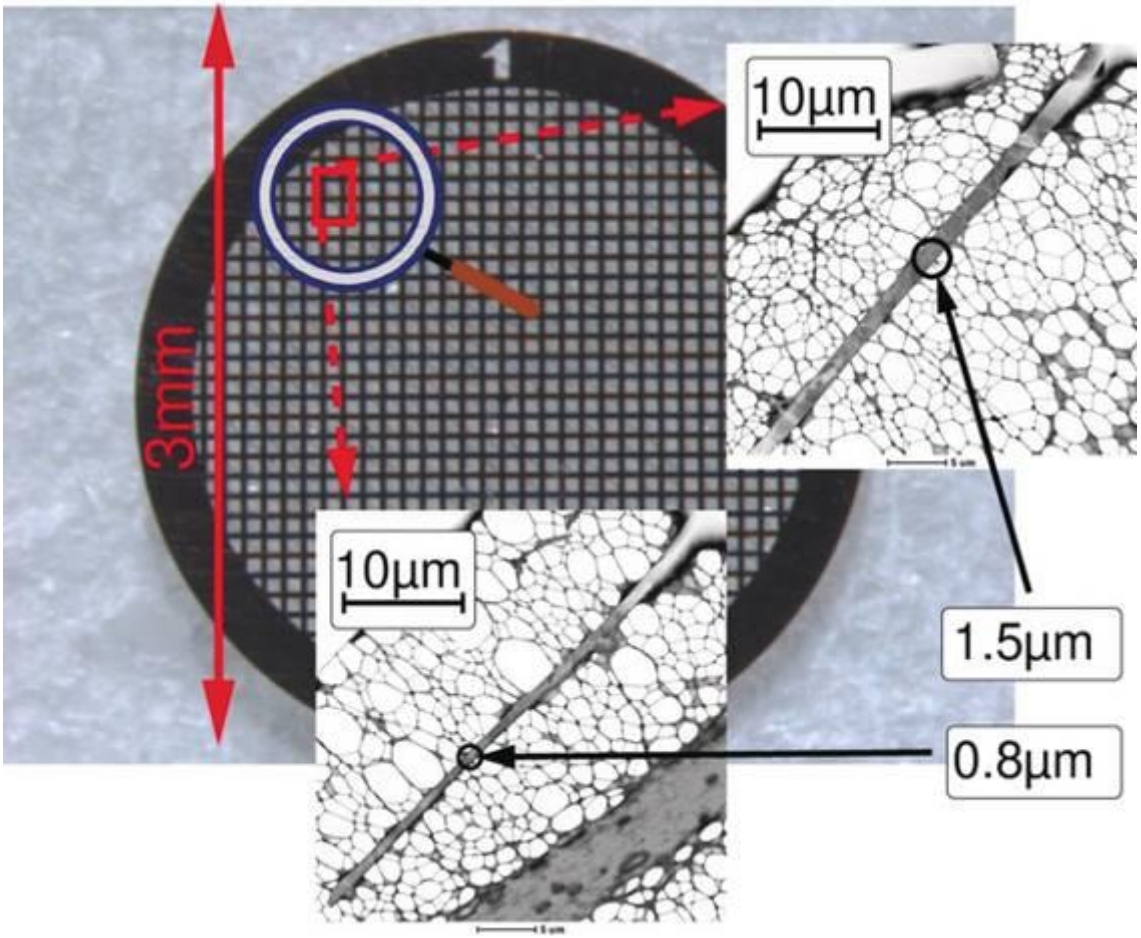

Fig. 3

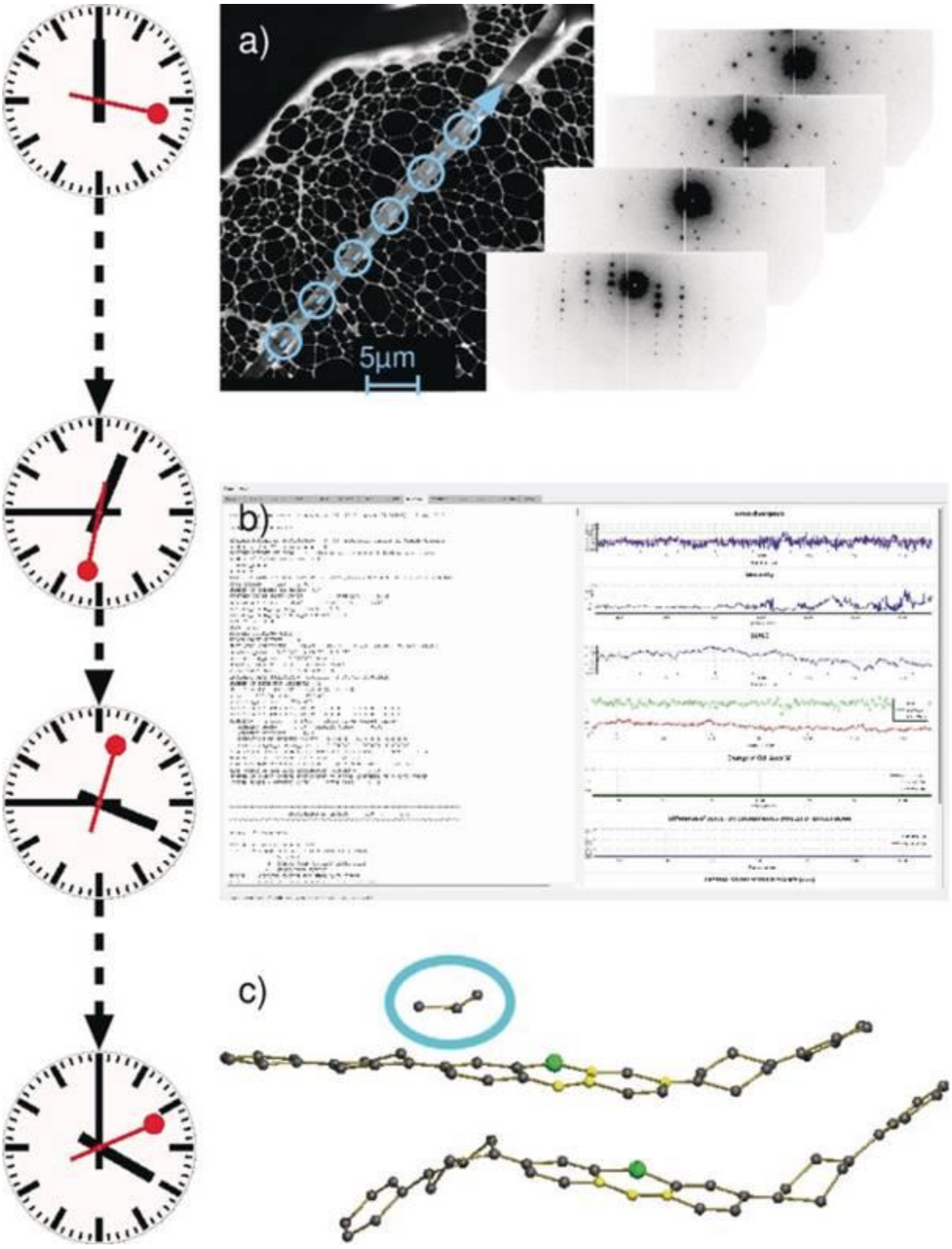

LS4.LB.P01
Location and Identification of Macromolecular Complexes Within Cellular Environments by High-Resolution Template Matchin

N. Grigorieff[1], L. Xue[2], T. Grant[1], J. P. Rickgauer[1], W. Hagen[2], J. Mahamid[2]

[1]Howard Hughes Medical Institute, Janelia Research Campus, Ashburn, Virginia, United States
[2]European Molecular Biology Laboratory, Structural and Computational Biology Unit, Heidelberg, Germany

The development of electron cryo-microscopy (cryo-EM) to visualize isolated macromolecules and assemblies has accelerated in the last five years with the introduction of direct detectors. However, a full understanding of molecular mechanisms requires cellular context to provide a spatial understanding of local environments and to preserve transient interactions. Cellular context can be visualized by electron tomography (ET), currently limited to about 2 nm resolution unless averaging techniques are applied (1). At this resolution, it can be difficult to reliably locate and identify densities in crowded environments.

We have developed a template matching approach (2) that can identify and precisely locate molecules of known structure within cellular environments. The templates are used to match the high-resolution signature of the molecules in 2D images of untilted samples. In our original work (2), we applied this "high-resolution template matching" (HRTM) approach to images of isolated (single) particles and viruses as a proof of principle; however, detection inside cells was not demonstrated. In the present work, we compare the performance of HRTM with the more traditional template matching in ET when applied to images of cells.

We collected images of *Mycoplasma pneumonia*, bacteria sufficiently thin (150 – 300 nm) to be electron transparent. The images were taken of untilted samples using conditions typical for high-resolution single-particle cryo-EM, followed by tilt series from the same areas using standard ET settings and 3D reconstruction. Using atomic models of the 30S and 50S ribosomal subunits, we identified subunits in the untilted images using HRTM (implemented in *cis*TEM (3)), and in the tomograms using established template matching procedures. We compared the 3D coordinates from both methods, identifying corresponding subunits and coordinate deviations.

Our data show about 80% coincidence of 50S subunits located and identified using HRTM and ET. The standard deviation between subunit coordinates was about 4 nm in the image plane and 25 nm perpendicular to it. For the 30S subunit, we observed a lower coincidence of about 50%, and 3x larger standard deviations.

The lower coincidence of 30S subunits identified by the two methods, compared to that of the 50S subunit, is likely due to a) its smaller molecular mass (0.7 MDa vs. 1.3 MDa) and b) its larger conformational variability. To improve detectability of smaller, more variable complexes inside cells using HRTM, we will include multiple conformations in the template search, investigate the use of tilt pairs and improve detection by matching peak profiles and adding conditional matching based on detected nearby 50S subunits.

References:

(1) Beck M & Baumeister W (2016) Cryo-electron tomography: Can it reveal the molecular sociology of cells in atomic detail? *Trends Cell Biol.* 26:825.

(2) Rickgauer JP, Grigorieff N & Denk W (2017) Single-protein detection in crowded molecular environments in cryo-EM images. *eLife* 6:e25648.

(3) Grant T, Rohou A & Grigorieff N (2018) *cis*TEM, User-friendly software for single-particle image processing. *eLife* 7:e35383.

LS4.P001
Spatial arrangement of the thylakoid network in *Arabidopsis thaliana* mutants with galactolipid deficiency

L. Kowalewska[1], R. Mazur[2], J. Szach[1], K. Gieczewska[1], J. Wojtowicz[1], K. Bednarska[1], M. Garstka[2], A. Mostowska[1]

[1]University of Warsaw, Department of Plant Anatomy and Cytology, Warsaw, Poland
[2]University of Warsaw, Department of Metabolic Regulation, Warsaw, Poland

Thylakoid network is an intricate spatial membrane arrangement present inside chloroplasts. As an assembly of proteins, polar lipids, and pigments thylakoids form a platform where photochemical reactions take place. Proper organization of the thylakoid network, as well as its potential to dynamic rearrangement, play a crucial role in the photosynthesis regulation. Although monogalactosyldiacylglycerol (MGDG) and digalactosylidacylglycerol (DGDG) are the main components of the thylakoid membrane matrix their structural role in the formation of thylakoid spatial arrangement is still largely unknown.

The main objective of this work was to clarify the structural role of two galactolipids, MGDG and DGDG, in the formation of the thylakoid network spatial arrangement.

In our study, *Arabidopsis thaliana* mutants with decreased MGDG (*mgd1-2*) or DGDG (*dgd1-2*) levels were used. Visualization of thylakoid network 3D structure was performed using both Electron Tomography (chemically fixed leaf samples) and Confocal Scanning Laser Microscopy (single layers of living mesophyll cells) followed by segmentation and 3D modeling (3DMOD and IMARIS, respectively). Additionally, different thylakoid structural parameters were calculated from TEM sections as well as from 3D CLSM models. Structural results were correlated with the photosynthetic apparatus composition and efficiency examined by 77 K fluorescence, circular dichroism, chl in vivo fluorescence (Dual-PAM), chromatography analysis, CN-PAGE, BN-PAGE, SDS-PAGE and immunoblot detection.

Galactolipid deficiency was structurally reflected in the formation of smaller grana, an increase of grana stacking repeat distance value and significant changes in the spatial organization of the thylakoid network compared to wt plants. The decrease of MGDG level impaired the formation of the typical helical grana structure and resulted in "helical-dichotomic" arrangement. DGDG deficiency changed the shape of the whole thylakoid network from lens-like into a flattened one. Structural aberrations visible in both mutants were accompanied by altered carotenoid and chlorophyll-protein complexes composition.

Our study indicated the important role of both neutral galactolipids in the formation of the proper spatial arrangement of the thylakoid network. Structural aberrations visible at different levels of thylakoid network organization eventually led to the decreased photosynthetic efficiency in both, MGDG- and DGDG-deficient plants.

Presented work was supported by the National Science Centre, grant 2014/13/B/NZ3/00413. Tomography was performed in the Laboratory of Electron Microscopy, Nencki Institute of Experimental Biology on TEM JEM 1400 (JEOL Co., Japan) equipped with tomographic holder and 11 Mpx TEM Camera MORADA G2 (EMSIS GmbH, Germany)

LS4.P002
Formation and transformation of the paracrystalline prolamellar body structure in *Arabidopsis thaliana* plants with lipid deficits

M. Bykowski[1], R. Mazur[2], J. Szach[1], A. Mostowska[1], L. Kowalewska[1]

[1]University of Warsaw, Department of Plant Anatomy and Cytology, Warsaw, Poland
[2]University of Warsaw, Department of Metabolic Regulation, Warsaw, Poland

Chloroplast biogenesis is a process coordinated with seedling development. In early stages of seed germination, in the absence of light, proplastid differentiates into etioplast. Etioplast contains an internal membrane network forming the characteristic paracrystalline structure of interconnected tubules – prolamellar body (PLB). Although the importance of pigment-protein complexes (Pchlide:LPOR:NADPH) in the maintenance of PLB paracrystallinity was elucidated before, the role of lipid matrix components in PLB formation is still elusive. There are three main polar and non-polar lipid groups present in plastid membranes: galactolipids, carotenoids, and chlorophylls. Galactolipids, mainly monogalactosyldiacylglycerol (MGDG), form the lipid bilayer while chlorophylls and their precursors are bound to thylakoid protein complexes; carotenoids are localized both directly in lipid matrix as well as a part of pigment-protein complexes.

The main objective of this work was to elucidate the structural role of selected polar and non-polar lipids on the formation of the spatial PLB structure.

Studies were performed on etiolated seedlings of *Arabidopsis thaliana* mutants with lipid deficits: *aba1-6*, *pif1*, *mgd1-2, chl1-2,* and *lut5-1*. Moreover, subsequent stages of PLB transformation on light were tracked in cotyledons of Col-0 Arabidopsis ecotype. PLB visualization was performed using Electron Tomography (chemically fixed cotyledon samples) followed by segmentation and 3D modeling (IMARIS). PLB structural parameters were calculated using IMARIS and ImageJ software. Additionally, the arrangement of pigment-protein complexes was analyzed using low-temperature fluorescence (77K).

We presented a detailed spatial analysis of light-induced PLB transformation of etiolated Arabidopsis cotyledons during the first four hours of illumination. Additionally, we presented an influence of organic carbon source in nutrition media on the PLB structure as well as on free/bound Pchlide ratio. We compared the spatial structure and calculated structural parameters of PLBs present in etioplasts of mutants with disturbed lipid levels. For instance, MGDG deficit was structurally reflected in a decrease of PLB compactness, while over accumulation of Pchlide gave a reverse effect. Moreover, disturbed levels of xanthophylls influenced the possibility of regular PLB formation.

Our study revealed the important role of a particular level of xanthophylls and protochlorophyllide in the formation of paracrystalline PLB. PLB transformation process presented in this study for wt Arabidopsis plants established a good platform for future studies on the role of lipid components on the formation of photosynthetically active thylakoid network.

Presented work was supported by the National Science Centre, grant 2014/13/B/NZ3/00413. Tomography was performed in the Laboratory of Electron Microscopy, Nencki Institute of Experimental Biology on TEM JEM 1400 (JEOL Co., Japan) equipped with tomographic holder and 11 Mpx TEM Camera MORADA G2 (EMSIS GmbH, Germany)

LS4.P003
Structures involved in endocytosis revisited with electron microscopy.

T. Bergner[1], E. Herdoiza Padilla[2], C. Riedel[2], C. Read[3], P. Walther[1]

[1]Ulm University , Central Facility for Electron Microscopy, Ulm, Germany
[2]Ulm University, Institute of Microbiology and Biotechnology, Ulm, Germany
[3]Ulm University, Central Facility for Electron Microscopy, Ulm, Germany

Endocytotic uptake was investigated with scanning (SEM) and transmission (TEM) electron microscopic approaches in order to characterize the involved structures.

The aim of the study was to investigate the role of actin dependent endocytosis and the involved cellular structures. To achieve this, different electron microscopic techniques were applied.

Macrophages were derived from THP-1 monocytes by activation with PMA and incubated with latex beads coated with human serum. Samples were prepared for scanning electron microscopy by standard methods (chemical fixation, critical point drying and platinum coating) as well as for transmission electron microscopy by high pressure freezing, freeze substitution, embedding and cross sectioning (section thickness 70 nm) (1). Experiments were performed with untreated cells and with cells treated with the mycotoxin cytochalasin D, an inhibitor of actin polymerization, in order to investigate actin dependent endocytotic structures.

Latex beads were taken up in large quantities by untreated macrophages. All stages of engulfment of the beads were clearly visualized by scanning electron microscopy. Initial contact to the beads was made by filopodia like structures, followed by membrane ruffles building phagocytotic cups which finally fully engulfed the beads in the further course of phagocytosis. Cytochalasin D treated cells, however, displayed a significant reduction of such phagocytotic activity and membranes engulfing the latex beads were hardly observed. Cross sections of the untreated macrophages analyzed by TEM showed high amounts of latex beads within the cells. In cross sections of cytochalasin D treated cells we could find beads only on the cell surface, but not within the cells.

The results suggest that the cytochalasin D treatment leads to the inability of taking up the latex beads, due to the inhibited actin polymerization. This confirms the important role of the actin dependent formation of filopodia and membrane ruffles during phagocytotic uptake. For the future novel electron microscopic methods need to be developed to unravel all structures involved in endocytosis.

References**:**

(1) Villinger C, Schauflinger M, Gregorius H, Kranz C, Höhn K, Nafeey S, Walther P (2014) Methods Mol Biol 1117, 617–638

Fig. 1: (A) SEM images of untreated macrophages engulfing latex-beads on the surface. The latex bead in the insert is already covered with filopodia like structures; this seems to be the first step of endocytotic uptake. In the main image, many beads are covered with membranes building phagocytotic cups. (B) SEM image of a cytochalasin D treated macrophage with smoother surface structures; the beads stick on the surface but no endocytotic activity, especially no phagocytotic cups, are visible.

Fig. 2: (A) TEM image of an untreated cross sectioned macrophage, which displays a high number of latex beads inside the cell. (B) Latex beads on the surface but not inside of a cytochalasin D treated cell.

Fig. 1

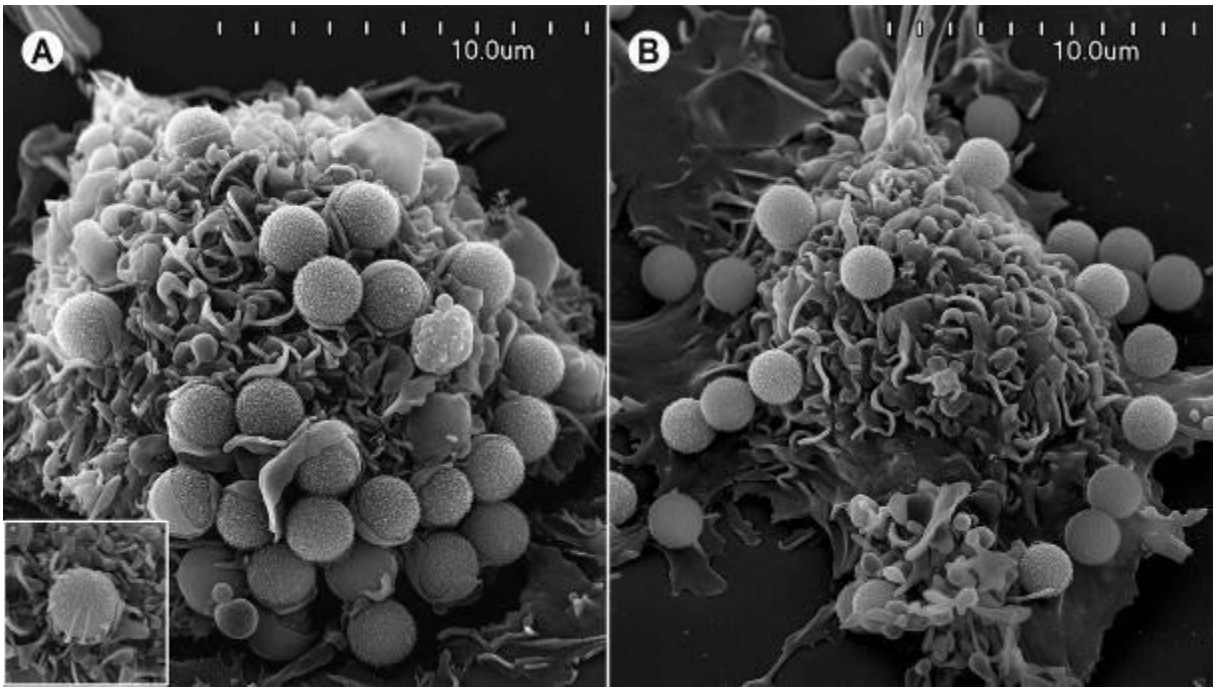

Fig. 2

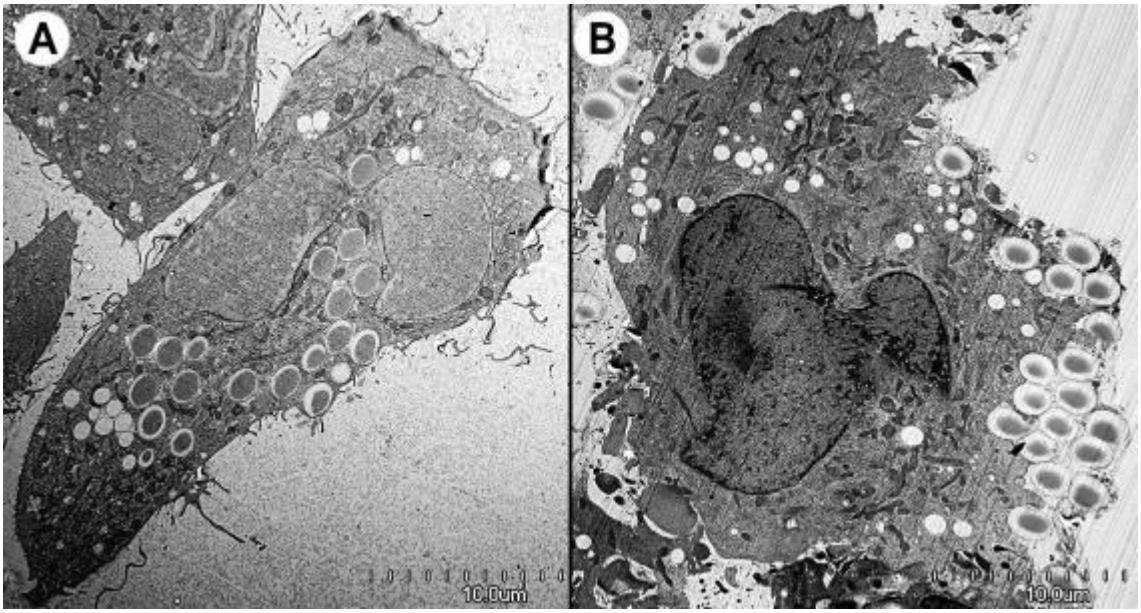

LS4.P004
Imaging of Vitrified Biological Specimens by Confocal Fluorescence Microscopy and FIB/SEM Tomography under cryo conditions

A. Elli[1], Y. Niyaz[1], A. Schertel[1]

[1]Carl Zeiss Microscopy GmbH, Jena, Germany

The investigation of vitrified biological specimens enables the visualization of cellular ultrastructure in a near-to-native fully hydrated state, unadulterated by harmful preparation methods. With light and electron microscopy in combination functional and structural information from the sample can be extracted. Here, we focus on two recent cryo imaging modalities and discuss their impact on cryo correlative workflows. First, we present confocal cryo fluorescence microscopy, utilizing the Airyscan detector with improved signal to noise ratio (SNR) and resolution. Second, we show volume imaging of different biological specimens by focused ion beam scanning electron microscopy (FIB/SEM) under cryo conditions.

Confocal laser scanning microscopes (LSM) are renowned for their optical sectioning capability. In cryo fluorescence microscopy, the situation is aggravated by the fact that currently no immersion optics are readily available and consequently only numerical apertures below NA 1 are possible. We combined the Airyscan detector together with a cryo correlative stage for fluorescent imaging of vitrified samples. The Airyscan detection module allows the spatially resolved detection of fluorescence light otherwise rejected by the pinhole in a standard confocal system. We demonstrate that even without immersion optics, Airyscan achieves a significant increase in resolution and SNR compared to standard confocal images.

FIB/SEM tomography enables the acquisition of large three-dimensional volumetric data from biological specimens by sequentially removing material with the ion beam and imaging the exposed block faces with the electron beam. This imaging method can be applied to frozen hydrated specimens, as recently demonstrated in (*J Struct Biol. 2013 Nov; 184(2):355 60. doi: 10.1016/j.jsb.2013.09.024*). In contrast to Cryo TEM Tomography (cryo ET), FIB/SEM tomography allows easy mapping of large multicellular specimens in the near native state and is particularly suited to analyse samples that require vitrification. The trade-off compared to cryo ET is a somewhat lower resolution comparable with resin-embedded samples. FIB/SEM volume imaging however elegantly extends cellular cryo ET by providing much larger volume access at significantly reduced preparative labour and can thus add necessary contextual information that broadens the view possible with cryo ET.

Both methods by themselves promise significant advantages for biomedical research by enabling the investigation of biological specimens in the near native fully hydrated state. Yet correlating both imaging modalities, LSM and FIB/SEM of vitrified samples, has the potential to provide even deeper insights into biological context. Our new software module, ZEN Connect, allows the user to perform one concise workflow between a LSM and FIB/SEM instrument by keeping the various images organized spatially and at scale in one comprehensive project.

The correlation between cryo light and electron microscopy data will greatly benefit from the ever-increasing resolution in fluorescence imaging. Cryo Airyscan is the next step into that direction delivering three-dimensional optical sectioning data that enables reliable targeting of cellular structures in a FIB/SEM microscope. Once identified, the structural context of the target location either is explored by volume imaging or can be processed further as a cryo lamella for subsequent cryo TEM Tomography.

LS4.P005
Optimized Workflow for Fabrication of Thin Lamellae for Cryo-Electron Tomography Using a TESCAN S8000G

S. Záchej[1], T. Heuser[2], Z. Hovádková[1], J. Havránková[1]

[1]TESCAN ORSAY HOLDING, Brno, Czech Republic
[2]Vienna Biocenter, EM Facility, Vienna, Austria

Cryo-electron tomography (Cryo-ET) provides an insight into the structural details of frozen specimens, such as eukaryotic cells. The principal limitation of the method is a size of the specimen, which often exceeds accessibility of a transmission electron microscopy (TEM). A conventional thinning technique, known as cryo-sectioning, suffers from artefacts caused by knife marks or compression (1). In-situ fabrication of a transparent lamellae from bulk samples using a focused ion beam (FIB) has become an adequate alternative with a continuous control of the preparation process.

The goal of the work was to design a reliable workflow for thin lamellae preparation from eukaryotic cell by using a FIB-SEM instrument. An enhancement was needed for a reliable platinum deposition using the electron beam in cryogenic conditions, geometry of FIB thinning and surface polishing. The last intention was to build a reproducible tool for users of all experience levels by an automation of the workflow.

We used *Saccharomyces cerevisiae* grown on carbon-coated TEM grids. Samples were plunge-frozen in liquid ethane using a Leica GP2 and mounted on a pre-tilted holder, which allows for parallel FIB processing. Then, the non-conductive sample was sputter-coated and loaded to a TESCAN S8000G FIB-SEM (2), equipped with a cryo-stage. Non-homogeneous surface of the frozen cells leads to an unequal sputtering of the underlaying material by impinging ions, thus cause curtaining of the polished surface. To minimize this effect, a protective Pt layer (approx. 1 µm thick) was deposited on the sample surface by an electron-beam deposition.

The FIB was used to open parallel windows into the cell in two phases. In the first step, a major portion of the material was rapidly removed using a high-current ion beam. The second step comprised thinning of the remaining wedge by a low-current ion beam (approx. 50 pA) to avoid a heat damage. Finally, the sample is transferred to the cryo-TEM.

We successfully prepared approx. 200 nm thin artefact-free lamella from a single cell using the optimized cryo-FIB-SEM workflow. The pre-tilted sample holder was redesigned to minimize the stage positioning. The electron-beam deposition of the Pt was modified to work in cryogenic conditions. The protective layer was conductive, compact and served well as a mask during the final polishing. The milling geometry and polishing steps were optimized to avoid a FIB-induced heat damage and to reach minimum thickness of the lamellae. Presets for the deposition, milling and polishing were implemented into a semi-automated procedure in a vector-based scanning generator DrawBeam.

The presented automated workflow of the lamellae fabrication can be routinely used for processing various samples, such as eukaryotic cells or prokaryotic species. Moreover, the in-situ method can be integrated into a complex correlative approach with a light microscopy to provide unique results in the field of structural biology.

References:

(1) A.Al-Amoudi, D. Studer and J. Dubochet, Journal of Structural Biology, Vol. 150 (2005), p. 109-121

(2) Sytar, P., Jiruse, J., & Zavodny, A. (2017), Microscopy and Microanalysis, 23(S1), 38-39

Fig. 1: Top left – Selected region of interest; Top right – FIB view after Pt deposition; Bottom left – The lamella before final polishing; Bottom right – overview in the cryo-TEM (200 keV).

Fig. 1

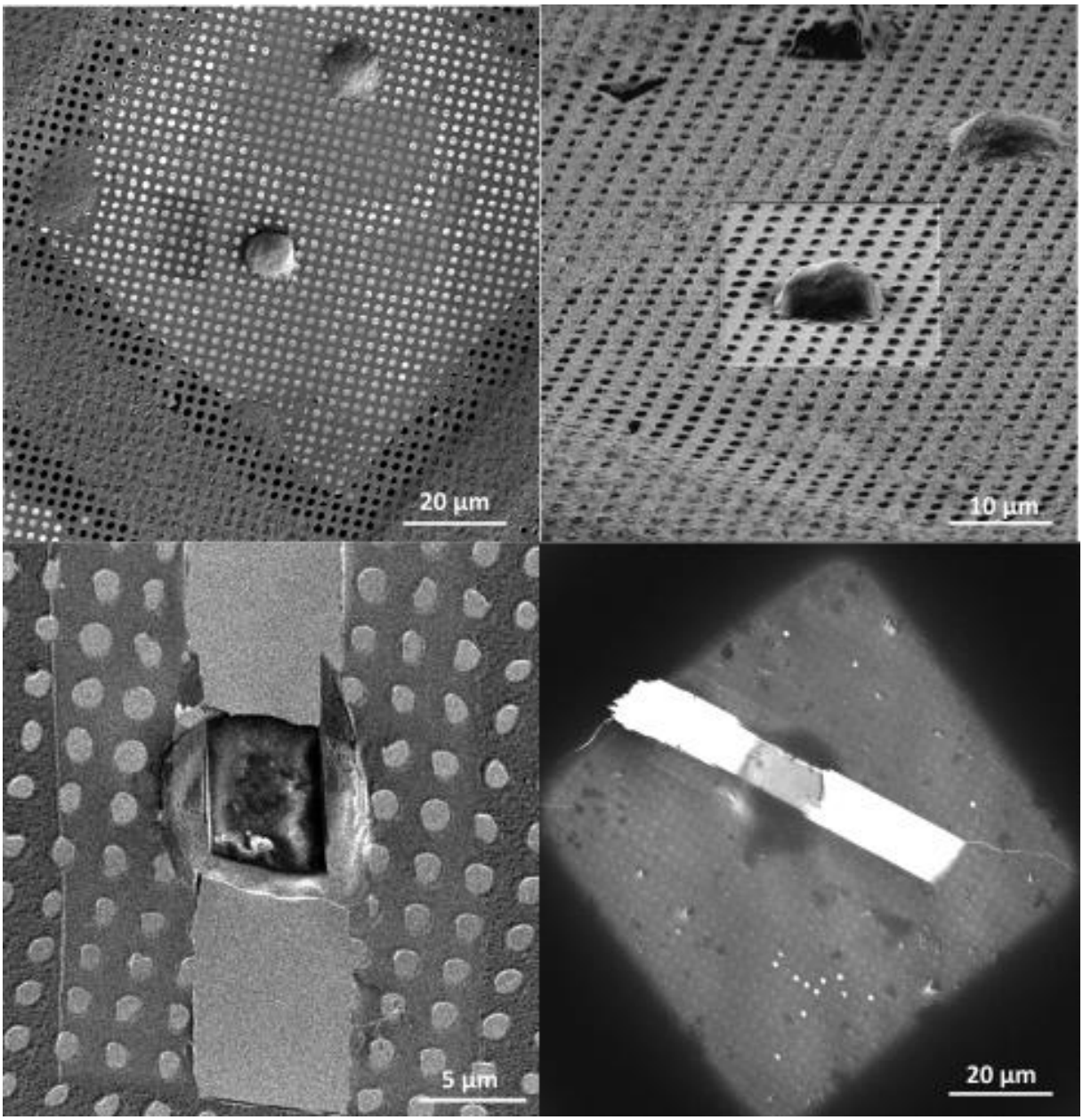

LS4.P006
Shape and structure of archaeal cells, as seen by electron tomography

R. Rachel[1], V. Heinz[2], A. Bellack[3], R. Reichelt[3]

[1]University of Regensburg, Centre for Electron Microscopy, Regensburg, Germany
[2]University of Regensburg, Biophysic II, Regensburg, Germany
[3]University of Regensburg, Microbiology, Regensburg, Germany

Various archaeal cells serve as model system for studies of archaeal molecular cell biology. One example is the euryarchaeon *Pyrococcos furious*, a motile cell expressing numerous archaella. Another archaeon studied in our lab is *Methanocaldococcus villosus*, a hyperthermophilic methanogen with exceptional motility. These cells are described as 'slightly irregular' cocci, up to 1500 nm in diameter. They are regarded as round but a detailed analysis is lacking.

Cells are analysed by electron tomographic methods (Rachel et al, 2010). Using electron cryo-tomography and sub-tomogram averaging, we presented a model of the *Pyrococcus furiosus* archaeallar motor in 3D (Daum et al. 2017). In on-going studies, cells are not concentrated by centrifugation, but by gentle filtration, then cryo-immobilized by high-pressure freezing, followed by freeze-substitution and resin embedding. Parallel beam STEM tomography combined with dual-axis tilting of 600 nm sections enables us to eliminate the focus gradient at high tilt, by increasing the depth of focus. We extend our studies towards naturally occurring lab mutants.

The tomography datasets help us to visualize the cells with minimal distortion, using the improved sample preparation protocol. The natural shape of the cells is trapped in an undisturbed way, before their structure is analysed at a resolution of about 5 nm. We unravelled yet undescribed features, like kinks and sharp bends in the archaeal cell wall, features pointing to novel types of cytoskeleton and to unique mechanisms of cell shape determination.

Combined ultrastructural and biochemical analyses are necessary in order to fully understand the complexity of coccoid archaeal cells. We will complement our studies using electron cryo-tomography, in the near future.

References:

(1) Daum et al, 2017: eLife 6: 27470

(2) Rachel et al, 2010: Meth Cell Biol 96: 47-69

Fig. 1: IMOD screenshot of a 3D reconstruction of a ca. 600 nm thick section of a cell of Pyrococcus furiosus, obtained by STEM tomography.

A, XZ plane; B, XY plane; C, YZ plane. The marked areas point to cell compartments in which the archaella are anchored. Black arrow: archaella (diameter: 11 nm). Bar: 200 nm

Fig. 1

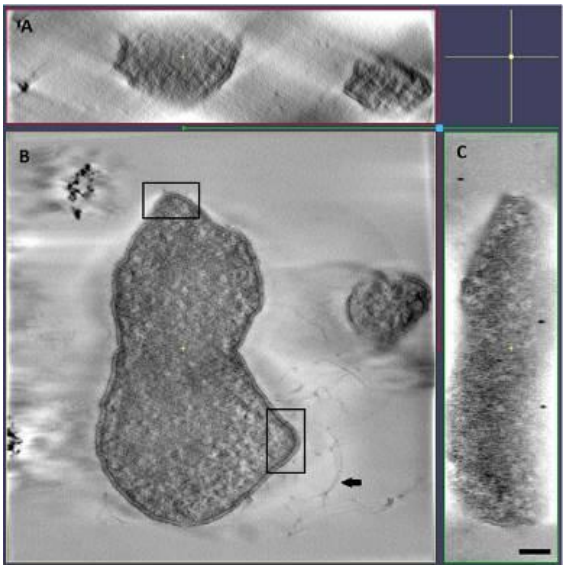

LS5.001 invited
Imaging across scales to understand membrane remodeling at the cell surface

O. Avinoam[1]

[1]Weizman Institute, Rehovot, Israel

Biological membranes are universally conserved as they form the basis for cellularization and subcellular compartmentalization. Membrane remodeling is essential to life because membranes must be able to bend, divide and fuse to allow cells and organelles to multiply, change shape, or mix material and information. To understand membrane remodeling at the molecular level we need to obtain a comprehensive and dynamic view of the changes in membrane architecture, and resolve the spatial and temporal organization of the protein machinery mediating these changes. Accomplishing this goal requires imaging membranes and proteins across different scales, and correlating information from multiple imaging modalities. I will show how correlative light and electron microscopy (CLEM) can be used to gain novel insights into the molecular mechanism of membrane remodeling in the context of three biological processes: Endocytosis, Exocytosis and Cell-to-Cell Fusion.

LS5.002 invited
Correlative cryo-microscopy: bridging across scales to study cellular systems

A. Sartori-Rupp[1]

[1]Institut Pasteur, Paris, France

The investigation of the structure-function relationship of molecules and of molecular machineries directly in the intracellular environment is one of the ultimate goals of functional studies in biology. "Zooming in' continuously from the whole cell into its supramolecular architecture on the same sample can currently not be performed using only one instrument but makes the use of different microscopes, techniques and sample preparation necessary. Techniques based on Fluorescent Light Microscopy (FLM) offer the possibility to image and locate fluorescently labelled molecules in living cells and to follow and record dynamical processes. Transmission Electron Microscopy (EM) and Electron Tomography (ET) allow to visualise all structures (labelled and unlabelled) directly in the cellular environment with greater spatial resolution. The advantages of the two microscopy methods can be combined by a correlative light-electron microscopy approach in which the fluorescently labelled structures are targeted in the light microscope and then relocated and imaged in 2 and 3D in the electron microscope.

Conventional EM on biological samples involves the use of chemical fixatives, dehydration, plastic embedding and the use of heavy metal salts, altering the structures of interest and leading to a considerable loss in resolution. To better preserve the structural integrity of the biological material more sophisticated preparation techniques and investigation methods have to be utilised, namely cryo-preparation and cryo-Electron Microscopy (cryo-EM) / cryo-Electron Tomography (cryo-ET) (1, 2). The biological samples are preserved in vitreous (non-crystalline) ice in a close-to-native state and kept frozen at liquid nitrogen temperature throughout the entire imaging process.

In the case of large pleomorphic objects, such as organelles or cells, Cryo-ET is a powerful tool to perform three-dimensional structural studies of such objects with a resolution of a few nanometers. However, the low contrast of unstained biological material embedded in amorphous ice and the need to minimise the exposure of these radiation-sensitive samples to the electron beam result in a poor signal-to-noise ratio. This poses problems not only in the visualisation and interpretation of the images and of the tomograms, but also in surveying the sample and in finding regions which contain the features of interest.

In this context novel correlative light and cryo-electron microscopy approaches have emerged, which guide the search for the structures of interest by (cryo)-FLM and allow to "zoom in" with cryo-EM (3, 4). Specific features highlighted by fluorescent labels are identified and located by FLM on the frozen-hydrated samples at modest magnifications. Their coordinates are then transferred to the EM such that they can be addressed with negligible pre-irradiation and three dimensional images (tomograms) of the structures identified by fluorescent labelling can be obtained. These methods have been tested and applied to different cellular systems, providing an unprecedented insight into cells structure in an unperturbed environment.

Specifically, we developed correlative light and cryo-EM strategies in order to target defined structures/events that can be altered by conventional EM sample preparation (Fig.1). In particular we apply our approaches to the study of Tunnelling NanoTubes (TNTs), which are long, actin-rich, fragile membranous cell protrusions that form suspended bridges between distant cells (5, 6). In recent years these novel structures have emerged as an important mean of cell-to-cell communication, mediating the bi- and unidirectional transfer of various cargoes, including organelles pathogens, ions, proteins and genetic material, both in vitro and in vivo. To better preserve TNTs" structure, we have set-up a workflow for correlative light- and cryo-ET that has allowed us to elucidate at high resolution the ultrastructural organization of TNTs in neuronal cells preserved in a close to native state (Fig.2).

References:

(1) R. Danev et al., *Trends Biochem Sci.* (2019) May 8 [Epub ahead of print]

(2) F. K. M. Schur, *Curr. Opin. in Struct. Biol.* 58 (2019), 1-9.

(3) A. Sartori et al., *J. Struct. Biol. 160* (2007), 135.

(4) M. Schorb et al., *J. Struct. Biol.* 197 (2017), 83-93.

(5) A. Rustom et al., *Science* 303 (2004), 1007-1010.

(6) A. Sartori-Rupp et al., *Nat. Comm.* 21 (2019), 342.

Fig. 1

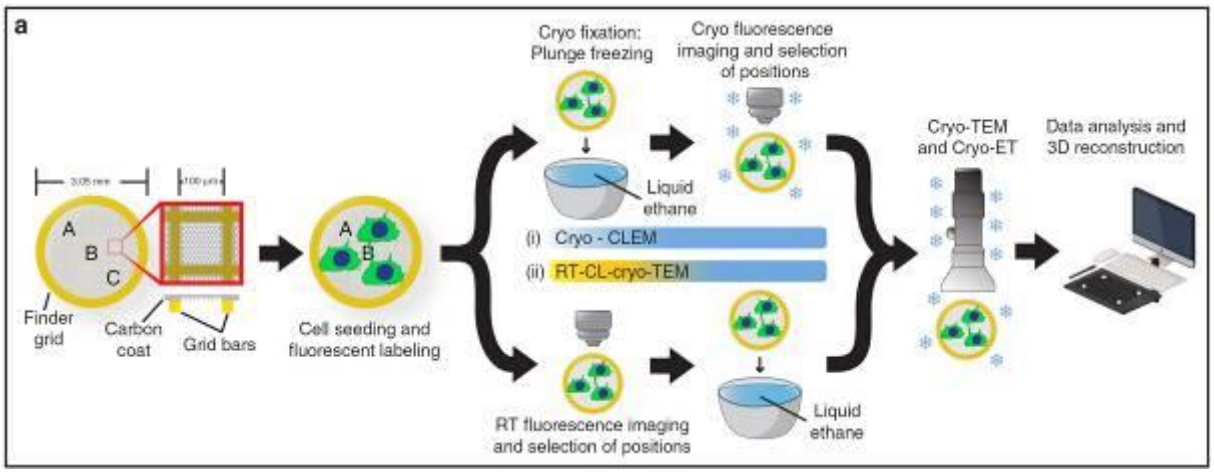
a
Cryo fixation:
Plunge freezing
Cryo fluorescence
imaging and selection
of positions
Liquid
ethane
(i) Cryo - CLEM
(ii) RT-CL-cryo-TEM
Cryo-TEM
and Cryo-ET
Data analysis and
3D reconstruction
A
B
C
Finder
grid
Carbon
coat
Grid bars
Cell seeding and
fluorescent labeling
RT fluorescence imaging
and selection of positions
Liquid
ethane

Fig. 2

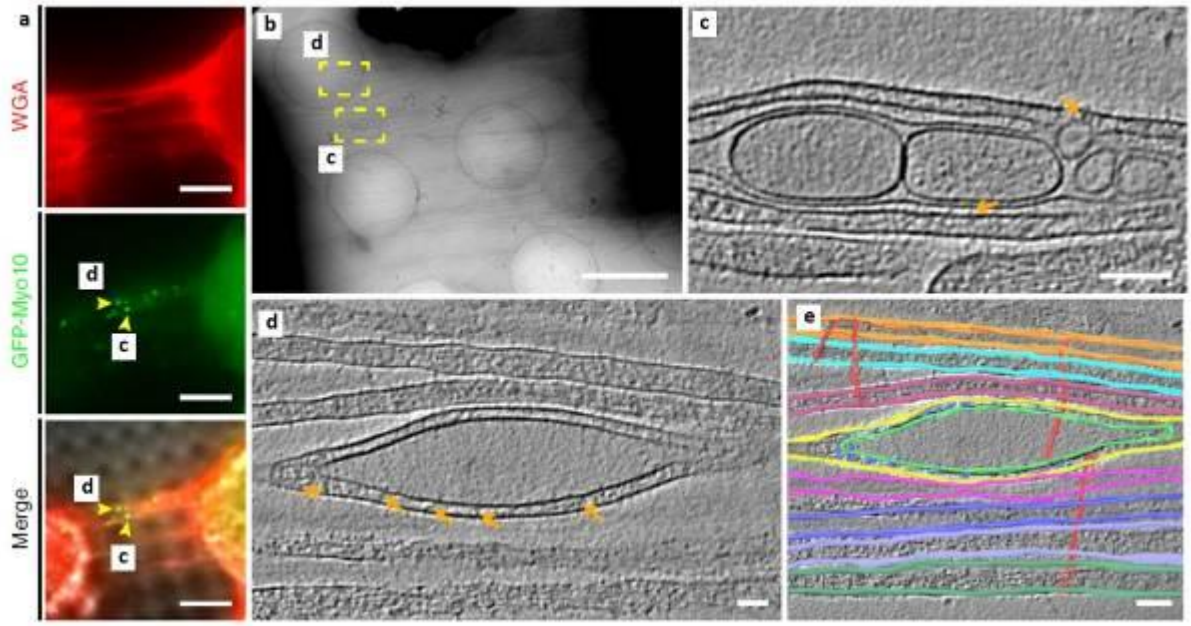
a
WGA
GFP-Myo10
Merge
b
c
d
e

LS5.003
Influenza A virus entry and IFITM3 induced inhibition of membrane fusion studied by cryo-CLEM

S. Klein[1], A. Kolovou[1], P. Chlanda[1]

[1]Heidelberg University Hospital, Center for Integrated Infectious Diseases Research - Virology, Heidelberg, Germany

Influenza A virus (IAV) is an important human pathogen assembling into pleomorphic, enveloped virions that enter the host cell by endocytosis. The low pH in late endosomes triggers structural changes in the viral glycoprotein hemagglutinin, facilitating viral and endosomal membrane fusion that leads to the release of the ribonucleoproteins. Viral membrane fusion is inhibited by the host protein Interferon-induced transmembrane protein 3 (IFITM3) as part of the cell induced anti-viral response. It has been proposed that IFITM3 is able to block IAV membrane fusion in late endosomes at the stage of hemifusion, however, IFITM3 inhibition of membrane fusion has neither been studied at the molecular level nor has it been structurally examined in the context of the cell.

The aim of this project is to establish a correlative light and electron microscopy (CLEM) workflow combining cryo-light microscopy (cLM), cryo focused ion beam milling (cFIB) and cryo electron tomography (cET). Using this workflow, we will structurally characterize IAV entry, as well as IFITM3 induced inhibition of IAV membrane fusion in human cells.

To localize viral entry events in the host cell, IAV virions or virus like particles (VLP) were fluorescently labelled by membrane dyes or by M1-pHluorin (pH sensitive GFP variant) that is incorporated into the VLP during particle assembly. Purified labelled virions were mixed with FluoSpheres and plunge frozen on carbon coated grids. The frozen grids were mapped by cLM. The signal of the spheres was used for correlation with the cTEM map to localize virions for tomogram acquisition.

Human A549 lung cells expressing fluorescently tagged IFITM3 were grown on gold carbon coated grids and labelled with endosomal and lipid droplet (LD) markers. After plunge freezing, grids were mapped by the cLM and cells of interest were selected for cFIB-milling. To achieve high precision correlation in the context of the cell, the signal of LDs was used since they are easily identifiable in tomograms.

cET revealed that VLPs containing M1-pHluorin have a similar morphology as wild-type VLPs. Filamentous VLPs showed an intact M1 layer beneath the membrane with an additional density on the luminal side, presumably corresponding to pHluorin. Furthermore, cCLEM allowed us to localize the fluorescent VLPs with a correlation precision of 200 nm (Fig. 1). A549 cells labelled with endosomal markers show a strong fluorescence signal when imaged by cLM, allowing us to target the cells of interest for cFIB milling. Membranous structures observed by cEM in the lamella will be further studied by cET.

We established a CLEM workflow that will allow us to follow and structurally characterize different steps of IAV viral entry and to elucidate the IFITM3 inhibition of membrane fusion inside the cell by *in situ* cET. Labelled VLPs containing M1-pHluorin are structurally similar to wild-type VLPs and IAV infectious virions and thus, provide a powerful tool to study IAV-cell interactions by CLEM applications.

Fig. 1: CLEM of purified VLPs, labelled with M1-pHluorin using FluoSpheres as fiducial markers. After plunge freezing, grids were mapped and correlated by cLM and cTEM. VLP signal was located and tomograms were acquired. A) Section of the correlated map with VLPs in green and FluoSphere in cyan. B) Enlarged section with VLP signal. C) Reconstructed tomogram acquired at the indicated area.

Fig. 1

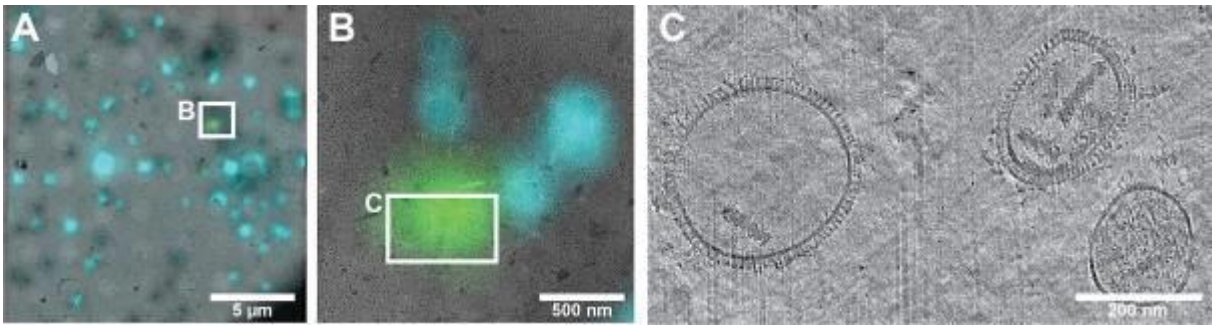

LS5.004
Correlative light and electron microscopy of hRPE cells

K. Bürger[1,2], K. N. Schmidt[2], R. Rachel[1], R. Witzgall[2]

[1]University of Regensburg, Centre for Electron Microscopy, Regensburg, Germany
[2]University of Regensburg, Molecular and Cellular Anatomy, Regensburg, Germany

Various cell lines serve as model system for studies of eukaryotic cell biology. One example is the human retinal pigment epithel (hRPE) cell line. These cells express singular organelle on the cell surface, the so-called primary cilium. They can be genetically modified such that they express proteins carrying a fluorescently labelled tag. Such cell lines can be used as model systems by using correlative light and electron microscopy studies, enabling the localization of tagged proteins by fluorescent light and electron microscopy (Kukulski et al 2011).

Cells were genetically manipulated to express fusion proteins tagged with GFP, Cherry, or other fluorescent proteins. After cultivation on sapphire discs, cells were either cryo-immobilized using high-pressure freezing followed by freeze-substitution, or chemically fixed followed by a specifically adapted progressive lowering of temperature (PLT) method, and finally embedded in Lowicryl HM20. 300, 600 or 900 nm sections on carbon-coated 100-mesh finder grids were first visualized by fluorescent light microscopy, with careful documentation of suitably labelled cells. The same grids with the sections are further processed (adding fiducials and carbon coat), then inserted into an EM equipped for electron tomography (200kV FEG-STEM, JEM2100F) and analysed by STEM tomography (Hohmann-Marriott et al 2009). 3D reconstruction was performed using IMOD (Mastronarde and Held 2017). The fluorescent images and the tomography data were combined using Icy.

The CLEM datasets helped us to obtain insight into the distribution of the proteins inside the cells with both modalities, fluorescence light microscopy and electron tomography. In many cases, the fluorescence signal in samples embedded in Lowicryl HM20 turned out to be sufficiently high. Due to the thickness of the sections (300, up to 900 nm), focus series in fluorescence mode were necessary to be recorded. The mechanical forces during handling for light microscopy and tomography resulted in some loss of section integrity. The information from tomographic datasets was highly valuable for interpretation of the distribution of the fluorescently tagged proteins.

Combined ultrastructural and biochemical analyses are necessary in order to fully understand the distribution of the tagged proteins inside the hRPE cells. We will complement our studies using other modifications of sample preparation (pre- vs. postembedding) in the near future.

References:

(1) Kukulski et al, 2011: J Cell Biol 192: 111-119

(2) Hohmannn-Marriott et al, 2009: Nature Meth 6: 729-731

(3) Mastronarde and Held, 2017: J Struct Biol 197: 102-113

Fig. 1: IMOD screenshot of a 3D reconstruction of a 300 nm thick Lowicryl HM20 section of a hRPE cell, obtained by TEM tomography. For illustration purposes, areas in which a red fluorescence of the tagged protein was visible are highlighted in red. Cy, cytoplasm; M, mitochondrium; rER: rough endoplasmic reticulum. Bar: 500 nm

Fig. 1

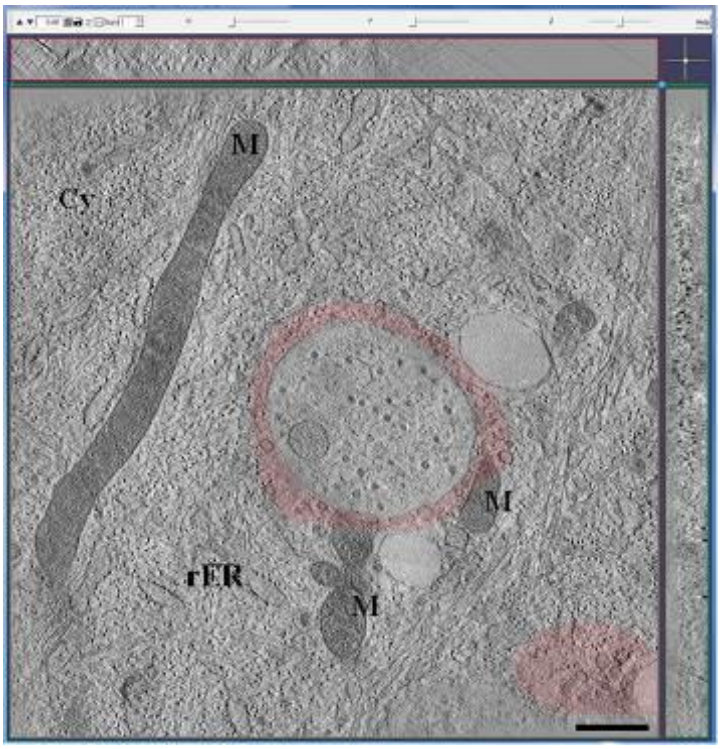

LS5.005
Correlia: an ImageJ-based tool for the co-registration of multi-modal correlative microscopy data

M. Schmidt[1], F. Rohde[1], U. D. Braumann[2,3]

[1]Helmholtz-Centre for Environmental Research (UFZ) GmbH, Isotope Biogeochemistry, Leipzig, Germany
[2]Fraunhofer Institute for Cell Therapy and Immunology, Imaging and image evaluation, Leipzig, Germany
[3]Hochschule für Technik, Wirtschaft und Kultur Leipzig, Fakultät Elektrotechnik und Informationstechnik , Leipzig, Germany

The correlation of different microscopic imaging techniques with microanalytical methods is a means to understand biological processes on a sub-cellular level. For that micrographs and chemical maps with large differences in spatial resolution and field-of-view as well as highly multi-modal content will have to be registered.
We developed the ImageJ plug-in Correlia that provides an environment for handling 2D correlative microscopy data. Several linear as well as non-linear registration methods using feature, tile or area-based similarity measures can flexibly be cascaded to align micrographs. The registration of data-sets containing light- and electron-micrographs as well as chemical maps acquired by secondary-ion mass spectroscopy and energy-dispersive X-ray spectroscopy are demonstrated.
Correlia is an open-source tool developed particularly for the registration and analysis of highly multi-modal 2D correlative microscopy data. It enables multiple users to organise their data in projects and extract overlays of arbitrary combinations of micrographs.

Fig. 1

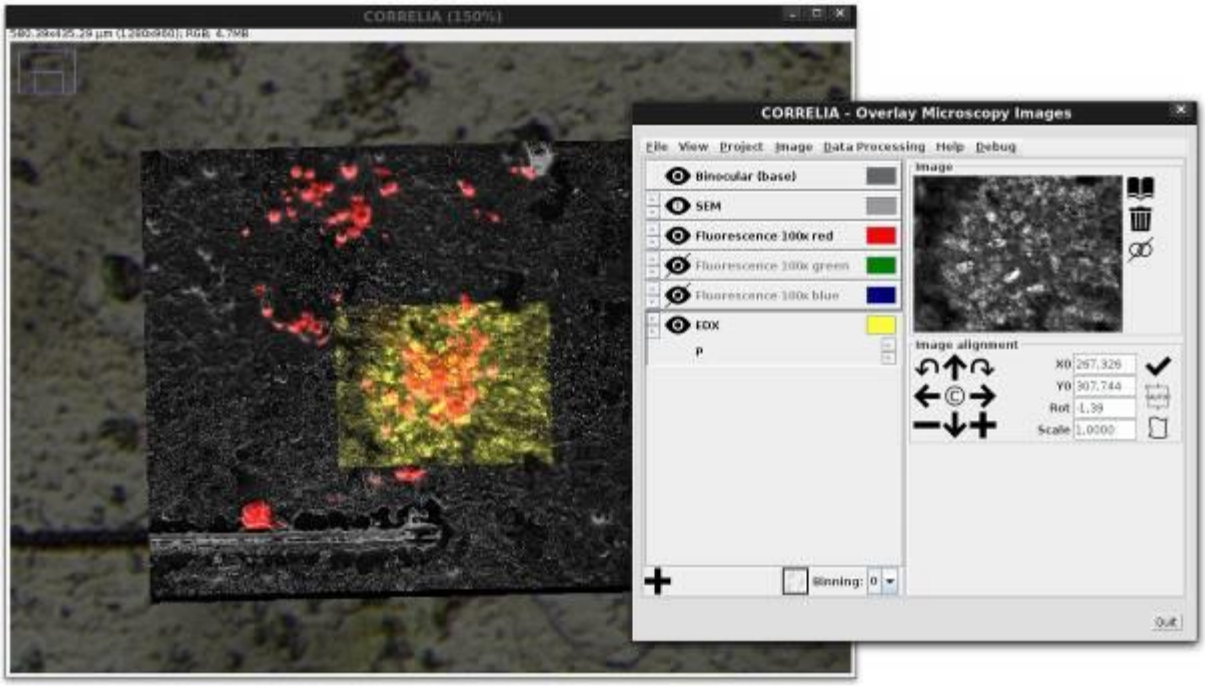

LS5.006
Adapting Correlative Light and Electron Microscopy Approaches to Specific Scientific Questions

E. M. Telley-Tranfield[1]

[1]Instituto Gulbenkian de Ciência, Electron Microscopy Facility, Oeiras, Portugal

Correlative Light and Electron Microscopy (CLEM) combines the dynamic data collection potential of light microscopy (LM) with the high-resolution contextual information from electron microscopy (EM). However, there are many possible combinations of LM and EM in a multitude of different workflows. Each combination provides different levels of biological information and correlation between the two techniques.

A new COST Action called COMULIS aims at fueling collaborations in the field of correlated multimodal imaging (including CLEM), promoting and disseminating the benefits of correlated multimodal imaging through showcase pipelines, and laying the groundwork for its technological advancement and implementation as a versatile tool in preclinical and biological research. I will begin by presenting the on-going and future activities of this open network, as well as the way interested members of the community can join the action.

I will then briefly describe two collaborative CLEM research projects that the Electron Microscopy Facility at the Instituto Gulbenkian de Ciência has been involved in. The goal in each project is to address a specific biological question using CLEM through precise localization of either a protein or a cell using both light and electron microscopy. However, the workflow differs from project to project because of the need to optimize the localization of the signal in LM and find the corresponding area in EM in different model organisms. I will show how we have optimized these two CLEM protocols to address the scientific question under investigation within the constraints of each research project.

LS5.P001
Correlative Probe and Scanning Electron Microscopy in Surface Imaging and Analysis

X. Liu[1], J. Neuman[2], Z. Nováček[2]

[1]Carl Zeiss Microscopy GmbH, Oberkochen, Germany
[2]NenoVision s.r.o., Brno, Czech Republic

Scanning Electron Microscope (SEM) is a one of the most versatile and powerful techniques in inspecting and analyzing the surface microstructures and chemical compositions of sample by utilizing a focused electron beam to scan over the object surface under vacuum condition. However, it is nearly impossible to avoid the electron beam induced both hydro-carbon contamination deposition and sample damage even with the frontier advanced low energy SEM technology for the examination of soft and beam sensitive materials like graphene, polymer membranes, hydrogels, and biological samples etc. Atomic force microscopy (AFM) with not only the outstanding imaging resolution down to atomic level but also the accurate metrology in critical dimensions, 3D roughness (surface, edge and sidewall) is a key nondestructive analytical technique for characterization of surface topography, chemical, electrical, mechanical, magnetic properties of materials under different environments. Integration of AFM into the SEM as an in-situ smart correlative microscope can on one hand avert the limitation of both instruments, and on the other extend the application boundaries and imaging capabilities. The integration of an in-situ AFM into a SEM has been already reported in the past, However the image acquisition was somehow independent which brings challenges in direct synchronizing imaging and correlation due to different scanning systems, resolutions limitation at larger working distance etc (1). We present a new technique for a real time correlative microimaging which enables direct comparison of the images acquired simultaneously by SEM and AFM. The Correlative Probe and Electron Microscopy (CPEM) technology is based on a different principle than other conventional approaches to simply combine the Scanning Probe Microscopy (SPM) into SEM techniques (2). Using CPEM technology, the electron beam of a SEM is focused close to the tip of a compatible SPM, while scanning is done by piezo scanner with the sample. During the measurement, the small offset distance between the tip and electron beam keeps constant. Simultaneous sampling of SPM and SEM signals enables simultaneous imaging of the same region of interest location with SEM and SPM. This constant offset can be simply subtracted during the post-processing. Acquired images can be correlated very easily due to their identical coordination system. Images can be directly correlated without any further data processing, where each pixel is represented by the X, Y, Z coordinates given by SPM and color (mask) corresponding to the signal from SEM. CPEM can accommodate more signals from different SEM detectors or related techniques like electron beam-induced current and cathodoluminescence. Each signal is then represented by the unique mask and can be used for the further image analysis and correlation.

References:

(1) M. Vaupel, A. Dutschke, U.Wurstbauer, F. Hitzel, A. Pasupathy, Topography, complex refractive index, and conductivity of graphene layers measured by correlation of optical interference contrast, atomic force, and back scattered electron microscopy, J. Appl. Phys. 114, 183107 (2013)

(2) NenoVision s.r.o., LiteScope™, NenoVision, 2018, www.nenovision.com

Fig. 1: The compacted LiteScope SPM module (left), plugged into the stage of ZEISS Gemini SEM (right)

Fig. 2: The secondary electron image (left top) and AFM topography image (left down) of a graphene sample, the correlative image of viewing by the CPEM (right).

Fig. 1

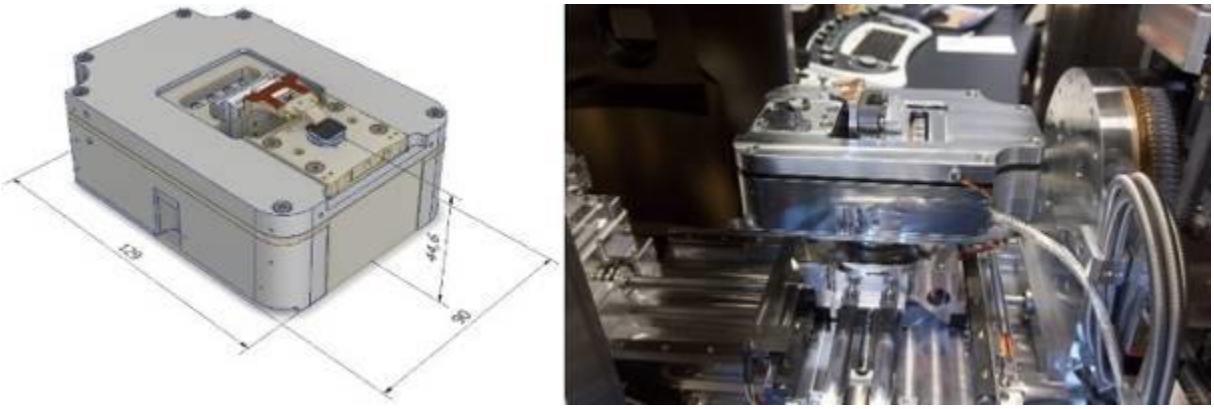

Fig. 2

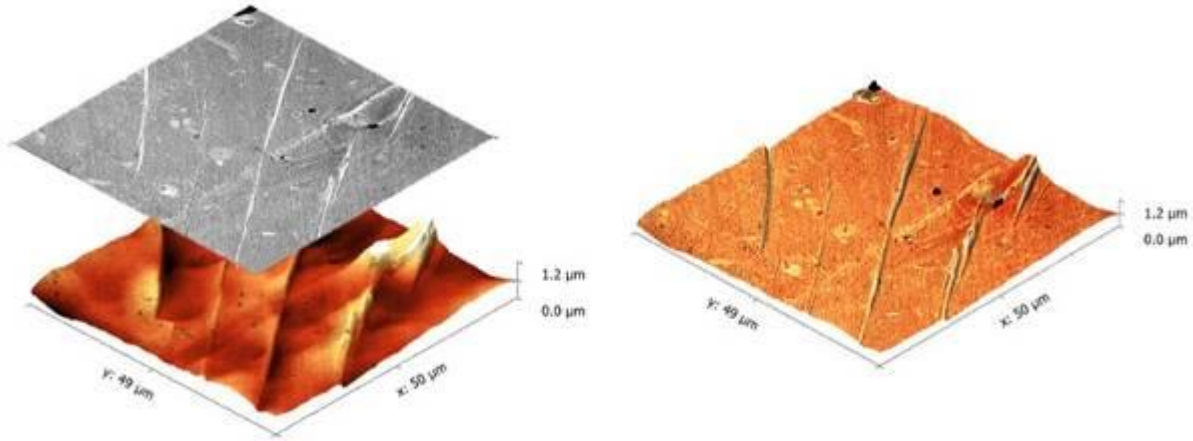

LS5.P002
A correlative workflow including light, X-ray, and electron microscopy to target small cell populations in tissues

S. Kretschmar[1], C. Golfieri[2], T. Santos-Ferreira[3], M. Löffler[4], M. Ader[3], M. Karl[2], T. Kurth[1]

[1]TU Dresden, Center for Molecular and Cellular Bioengineering (CMCB), Technology Platform, EM and Histology Facility, Dresden, Germany
[2]German Center for Neurodegenerative Diseases Dresden (DZNE) and TU Dresden, Center for Regenerative Therapies Dresden, Dresden, Germany
[3]TU Dresden, Center for Regenerative Therapies Dresden, Dresden, Germany
[4]TU Dresden, Center for Advancing Electronics Dresden (cfaed), Dresden Center for Nanoanalysis (DCN), Dresden, Germany

Before the ultrastructural analysis of tissues, semithin sections (1 mm) are stained for light microscopy and used to check quality, orientation of the sample, and to identify regions of interest (ROI) for ultrathin sectioning (50-100 nm) and subsequent transmission electron microscopy (TEM). Small ROIs such as disseminated cells or small cell populations that are either rare or distributed in an unpredictable manner pose a serious challenge and may be extremely difficult to find at the ultrastructural level. A typical example are transplanted cells in tissues. Transplantation of stem cell derived photoreceptors into eyes of patients suffering from retinal degenerative diseases such as age-related macular degeneration (AMD) or retinitis pigmentosa (RP), for example, offers a potential future therapeutic approach, and is studied intensively in pre-clinical animal models, such as mice. Here, the transplanted cells are distributed quite randomly in the subretinal space, inbetween retina and retinal pigmented epithelium (RPE), either as individual cells or cell clusters. For EM, the mouse eyes have to be dissected into very small pieces (below 0.5 mm) each of which carries an unknown number of transplanted cells in unknown positions. Using the conventional approach, a series of iterative semithin sectioning, staining, and LM imaging, with intervals of 10-20 mm to prevent the loss of small ROIs, is performed, which is extremely time consuming and potentially nerve-wrecking.

Here, we present an alternative work-flow that involves X-ray microscopy prior to light and electron microscopy which enables us to systematically identify several ROIs potentially containing cell transplants in a single retina block (Figure 1). After embedding, several blocks were mounted and scanned with the Zeiss/X-Radia 520 X-ray microscope (2-3 hrs scan time per block), data were collected as a series of 2D images (TIFF-stack, spacing 1.8-2.1 mm), where the relative positions of different ROIs relative to the block surface can be determined. This information can be used to target the different ROIs with the ultramicrotome for subsequent 2D-EM-inspection and potential 3D-EM imaging using serial section TEM or by serial block-face SEM. This way, ROIs can be effectively selected and studied with much less effort and within a reasonable amount of time. In addition, the 3D low resolution data help to interpret the 2D EM data, and allow to exclude blocks not containing any donor cells from the ultrastructural analysis.

Fig. 1: Workflow for correlative X-ray, light and electron microscopy. **A** Sample preparation including primary fixation with aldehydes (GA/PFA), postfixation and contrasting with osmiumtetroxide (OsO4), thiocarbohydrazide (TCH), and uranyl acetate (UA), dehydration, and embedding in epoxy resin. **B** Several samples can be mounted and imaged together overnight with a X-ray microscope, followed by reconstruction and storage of data as TIFF-stacks (virtual histology). Regions of interest (ROI) are selected, their positions in the blocks are determined, and finally the samples are remounted on dummy blocks for sectioning. **C** Semithin sections are stained for light microscopy and used together with X-ray image stacks to precisely determine the plane of the ROI, which is then further analysed on ultrathin sections in the TEM. Ultimately, the samples may be further analysed in 3D by serial section TEM or by serial block-face SEM.

Fig. 1

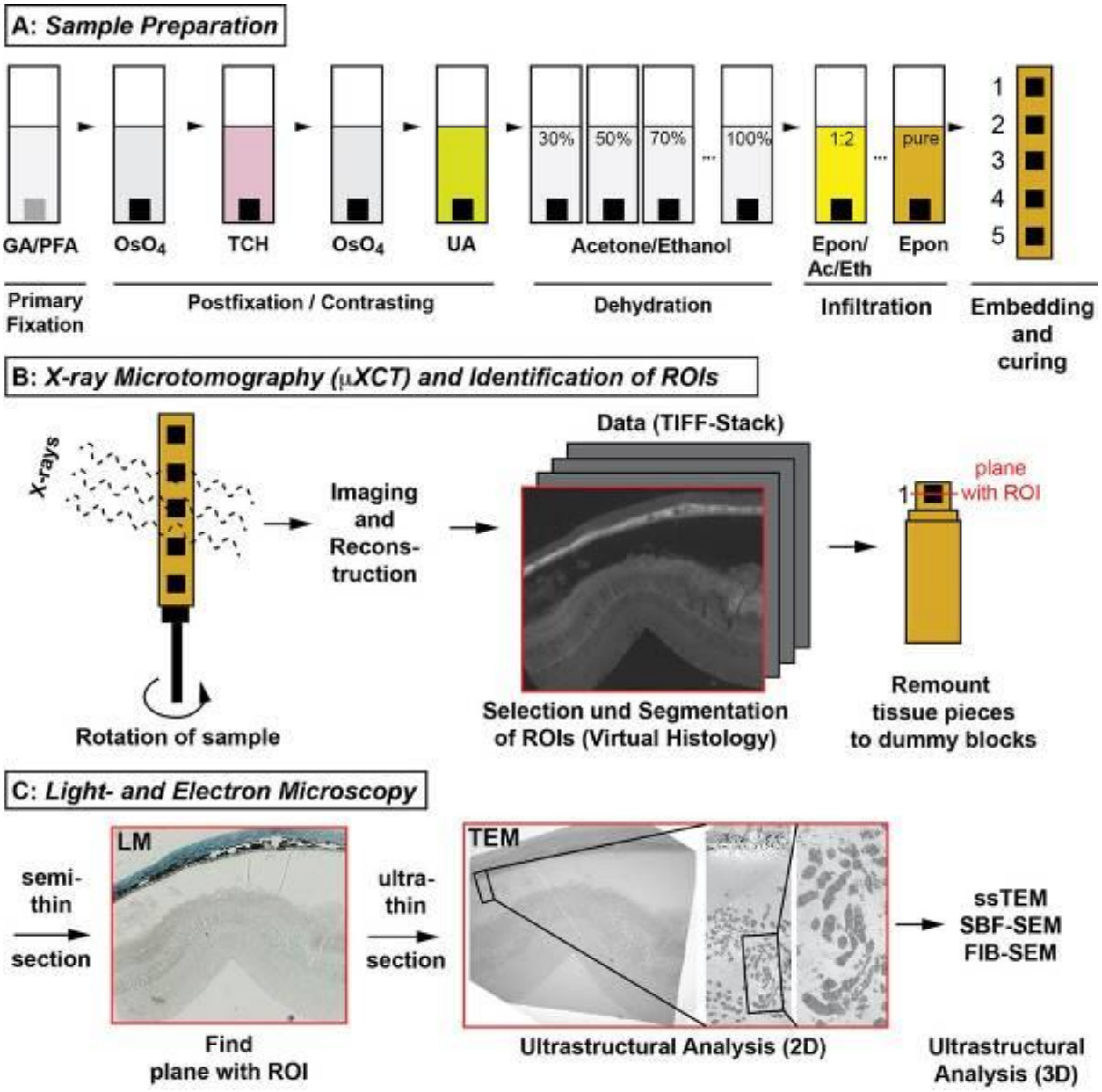
A: Sample Preparation
GA/PFA
OsO4
TCH
OsO4
UA
30%
50%
70%
100%
Acetone/Ethanol
1:2
pure
Epon/ Ac/Eth
Epon
1
2
3
4
5
Primary Fixation
Postfixation / Contrasting
Dehydration
Infiltration
Embedding and curing
B: X-ray Microtomography (µXCT) and Identification of ROIs
X-rays
Rotation of sample
Imaging and Recons-truction
Data (TIFF-Stack)
Selection und Segmentation of ROIs (Virtual Histology)
plane with ROI
Remount tissue pieces to dummy blocks
C: Light- and Electron Microscopy
semi-thin section
LM
Find plane with ROI
ultra-thin section
TEM
Ultrastructural Analysis (2D)
ssTEM
SBF-SEM
FIB-SEM
Ultrastructural Analysis (3D)

LS5.P003
Comparison of electron and fluorescence microscopy techniques with regard to the analysis of thylakoid architecture in *Synechocystis sp.* PCC 6803

M. Ostermeier[1], M. Bramkamp[2], A. Klingl[3], J. Nickelsen[1]

[1]LMU München, Biologie I, Planegg-Martinsried, Germany

Thylakoids are specialised organell-like structures in cyanobacteria and chloroplasts where chlorophyll accumulates and photosynthesis takes place. In *Synechocystis sp*. PCC 6803 they are set in several layers at the edge of the cell and shaped towards convergence zones close to the plasma membrane where the assembly of photosystem II takes place.

To highlight this, a special marker called CurT was used. CurT is a homolog of the CURVATURE THYLAKOID1 protein family found in *Arabidopsis thaliana* (1). In *Synechocystis sp*. PCC 6803 it is significantly responsible for shaping thylakoids toward these converging zones (3).

These structures can now be observed using electron microscopy as well as fluorescence microscopy and in both techniques there are advantages and disadvantages.

The main focus of this work was to figure out similarities as well as differences in the analysis of thylakoid architecture by use of electron microscopy on the one hand and fluorescence microscopy on the other hand.

All work was done on *Synechocystis sp.* PCC 6803. Beside the wild type a CurT knockout mutant was used. Preparation of the cells for electron microscopy like high pressure freezing and immunogold labeling and fluorescence microscopy like immunofluorescence labeling was performed as described priviously (2,4).

Specific changes in thylakoid architecture could be observed in the wild type in comparison to the CurT knockout mutant. The information of both kind of micrographs was also different.

With electron microscopy it was possible to see the bilayer of the thylakoids in detail. Furthermore phycobilisomes, which act as antenna complexes in cyanobacteria, and the amount of single thylakoid layers as well as their specific position could be observed. Using an immunogold staining it was possible to see specific proteins on an ultra thin section through the cell.

Fluorescence microscopy on the other hand benefits from the autofluorescence of chlorophyll to observe single cells in vivo. Beside of a life-death-discrimination it was possible to differ between regions of high and regions of low photosynthetic activity. Using a second fluorescent protein, either genetically tagged (still in vivo) or via immunofluorescence (not in vivo), regions with highly accumulated proteins of interest could be analysed.

With the current studies, we can draw a more detailed image of the thylakoid architecture in *Synechocystis sp.* PCC 6803. Furthermore we can conclude that converging zones are not essential for growth and even thylakoids in the middle of the cell contain photosystem II and chlorophyll.

References:

(1) Armbruster U., Labs M., Pribil M., Viola S., Xu W., Scharfenberg M., Hertle A.P., Rojahn U., Jensen P. E., Rappaport F., Joliot P., Dormann P., Wanner G. and Leister D. (2013) Plant Cell, Vol. 25: 2661–2678.

(2) Dahl R. and Staehelin L. A. (1989) JOURNAL OF ELECTRON MICROSCOPY TECHNIQUE 13:165-174.

(3) Heinz S., Rast A., Shao L., Gutu A., Gugel I. L., Heyno E. Labs M., Rengstl B., ViolaS., Nowaczyk M. M., Leister D. and Nickelsen J. (2016b) The Plant Cell, Vol. 28: 2238–2260.

(4) Rast A., Rengstl B., Heinz S., Klingl A. and Nickelsen J. (2016) Frontiers in Plant Science, Vol. 7, Article 605.

LS5.P004
Subcellular Compartments as Fiducials for cryoFM and 3D cryoFIB-SEM Correlation

N. Scher[1], O. Avinoam[1]

[1]Weizmann Institude of Science, Biomolecular Sciences, Rehovot, Israel

Over the last decade, biological imaging of cells and tissues has improved significantly. Development in both electron and light microscopy allows imaging of large volumes at high-resolution. In addition, information gained from these imaging modalities can be correlated to target specific, rare and dynamic molecular events, which is essential for understanding biological processes. Dual-beam instruments, mounted with scanning electron microscope and focused ion beam (FIB-SEM) are more commonly used for volume imaging in the life sciences because they combine the advantage of high-resolution imaging in all three axes (5 nm3 voxel size), with a wide field of view. However, correlative light and electron microscopy (CLEM) workflows are more challenging, mostly owing to difficulties in correlating information from fluorescence microscopy (FM) in 3D. However, very well resolved cellular compartments under cryo-SEM, such as lipid droplets, could potentially be used as fiducials for 3-dimentional CLEM workflow. Moreover, cryoFIB-SEM imaging has not been thoroughly explored as an imaging modality. Here, we demonstrate a new 3-dimentional CLEM approach which relies on in-situ fiducial markers for FM and EM. Our approach relies on cryo-immobilization followed by FM to target specific subcellular compartments as well as fluorescently labeled lipid droplets. This approach can be used to overlay high-resolution 3D information of cryo-fixed specimens with information from a larger volume of FM information, thus give a better understanding of the cellular ultrastructure with respect to specific biological processes. Moreover, this workflow can be applied in ambient- or cryo-imaging conditions and with different, specimen-specific in-situ fiducial markers.

LS5.P005
Correlative light- and electron microscopy of graphene-covered whole cells facilitates analysis of the spatial relation between ErbB2 membrane proteins and actin filaments

I. N. Dahmke[1], F. Lautenschläger[1,2], N. de Jonge[1,2]

[1]INM-Leibniz Institute for New Materials, Innovative Electron Microscopy, Saarbrücken, Germany
[2]Saarland University, Physics, Saarbrücken, Germany

Growth factor receptors such as the epidermal growth factor receptor 2 (ErbB2) play a central role in cancer cell invasiveness and development of metastasis (1, 2). As such, they are closely linked to cytoskeletal reorganization to enhance cell motility (3). Techniques for the analysis of membrane proteins at the single-molecule level in relation to the cytoskeleton are limited. Conventional electron microscopy (EM) provides the necessary spatial resolution, but during sample preparation the spatial context is usually lost. This limitation was overcome by covering hydrated whole cells with graphene films and thus, enabling high resolution EM while preserving the relation to the cellular ultrastructure (4).

We used graphene liquid-enclosures of breast cancer cells to enable fluorescence microscopy (FM) and high-resolution scanning transmission EM (STEM) of single cells to study the spatial correlation between actin filaments and ErbB2. Hereby, we focused on the analysis of so-called membrane ruffles (5) that show a high content of actin filaments serving as centres for actin reorganization.

Breast cancer cells (SKBR3) were grown on silicon microchips and labelled with fluorescently marked actin (BacMam-GFP-Actin) and quantum dot (QD) nanoparticles attached to specific anti-ErbB2 Affibodies. Next, the samples were covered with graphene (Trivial Transfer Graphene™) applying a method described ealier (3) and subjected to FM. Cellular regions expressing a high number of ErbB2 molecules emitted a red fluorescence (655 nm), whereas actin fibers appeared in green (520 nm). Then, we performed high resolution imaging with STEM at 200 keV beam energy and analysed the distribution of QDs in the micrographs using the pair correlation function.

Correlative light- and electron microscopy (CLEM) of graphene-covered SKBR3 cells with labelled ErbB2 and actin revealed that about 30 % of the cells exhibited an overlay of both fluorescence signals. We found a distinct distribution pattern of ErbB2 molecules on the ruffled regions in these cells compared to cells that were predominantly ErbB2 positive. This finding indicates a complex interaction of ErbB2 signalling and actin filaments.

The graphene-enclosure of hydrated whole cells facilitated CLEM and allowed for the analysis of membrane protein distribution patterns in single cells in relation to the underlying cytoskeleton. We anticipate that the method may become useful in the near future to examine the effects of cancer therapies targeting membrane proteins on the cytoskeleton of metastatic cells.

References:

(1) JC Feldner, BH Brandt, Exp. Cell Res. 272, 39 (2002).

(2) I Chung et al., Nat. Commun. 7:12742 (2016)

(3) BH Brandt et al. FASEB J. 13, 1939-1949 (1999).

(4) IN Dahmke et al., ACS Nano, 11, 11, 11108-11117 (2017).

(5) D Peckys, U Korf and N de Jonge, Sci Adv 1 (2015), p. e1500165.

(6) We thank P Blach and T Trampert for assistance; F Weinberg and D Peckys for discussions and E Arzt for his support through INM. Research was supported by the Leibniz Competition 2018.

Fig. 1: a) STEM image of SKBR3 cells (1,000×). b) Corresponding fluorescence image with ErbB2 (red) and actin (green). c) STEM image marked in a (30,000×). d) STEM image marked in c showing QD-labeled ErbB2 proteins in yellow (100,000×). e) Pair correlation functions of cells with ErbB2 and actin overlay (green) compared to ErbB2 dominant cells (violett).

Fig. 1

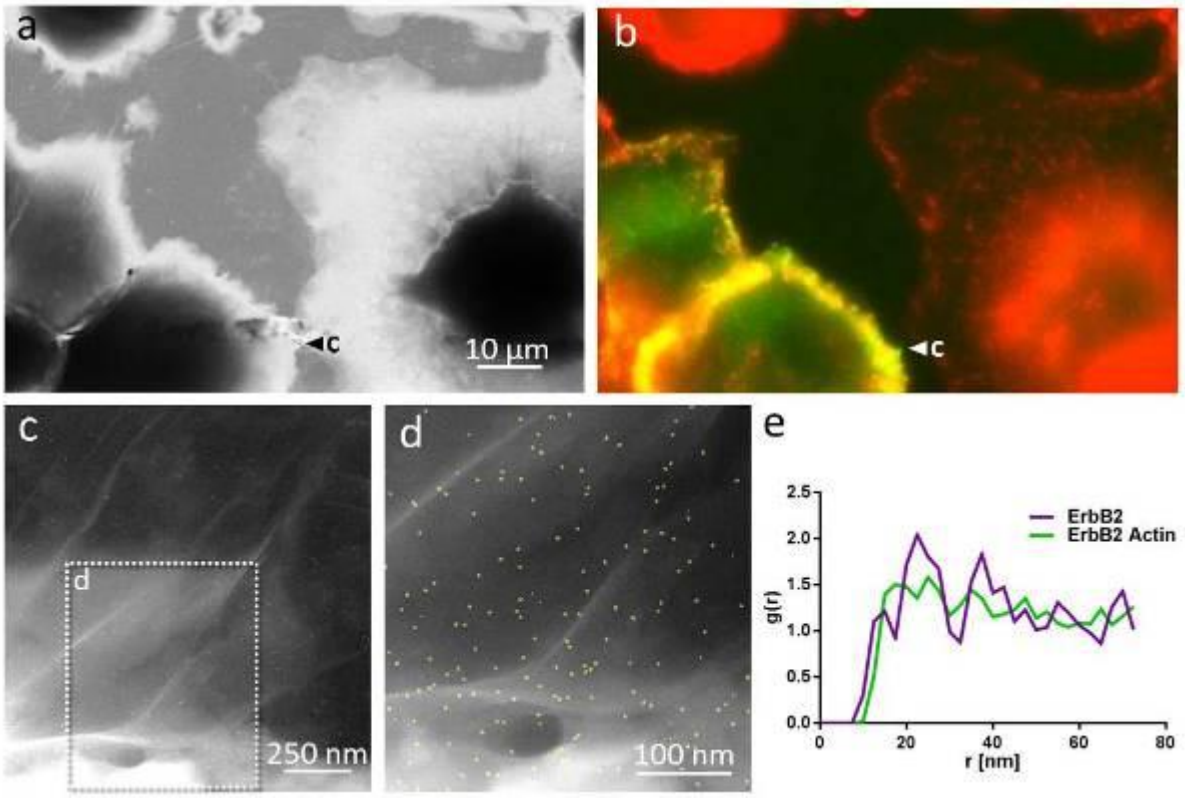
a
c
10 µm
b
c
c
d
250 nm
d
100 nm
e
ErbB2
ErbB2 Actin
g(r)
r [nm]
0.0
0.5
1.0
1.5
2.0
2.5
0
20
40
60
80

LS5.P006
Cryo-Fluorescence Imaging workflows and Instrumentation for CLEM, ET and Particle EM

M. Schwertner[1], A. Kamp[1], M. van Nugteren[1], H. Vader[1], D. Stacey[1]

[1]Linkam Scientific Instruments Ltd., Tadworth, United Kingdom

Keywords: Cryo-fluorescence imaging, Cryo-EM, Cryo-ET, cryo-CLEM, cryo-particle EM, cryo sample preparation.

Cryo-Electron Microscopy (Cryo-EM) and Cryo-Electron Tomography (Cryo-ET) are increasingly used because cryo sample preparation is considered the "gold-standard" for preserving the ultra-structure of the sample in a near-native state

Cryo-EM is often combined with light microscopy (LM), in particular Fluorescence Microscopy (FM). Although LM/FM have lower resolution compared to EM one can make use of well-established fluorescence labelling techniques, such as GFP, in order to identify and pinpoint biological, genetic or chemical events inside the sample.

Using CLEM (1), EM techniques and Light microscopy can be combined to have highly specific biological fluorescence labelling as well as the superior resolution of EM. CLEM also reduces a major issue in EM: beam damage. Because LM is very gentle, a navigation map can be obtained via LM and later used for EM sample navigation without beam-damage (2). For cryo-EM, Light microscopy can also serve to pre-screen sample quality, saving time because only the best samples are taken to cryo-EM. To bridge the resolution gap between EM and LM during CLEM, one can also use Super-Resolution techniques (3) in cryo-mode (4). Even without combining it with EM, super-resolution light microscopy is attractive under cryo-conditions due to significantly reduced bleaching of the fluorescence (4).

Apart from dedicated cryo-sample preparation, such as plunge-freezing (PF) or High-Pressure Freezing (HPF), special tools and instruments are needed to transfer the samples between the EM/LM instruments, to keep the cryo-samples vitrified below -140 DegC and to avoid ice-contamination caused by humidity condensing on the cryo-samples during imaging sessions. We have developed our cryo-stage CMS196 (see fig. 1 for overall instrument and fig. 2 for the sample chamber) for convenient imaging of frozen-hydrated samples over extended time. In this talk we will introduce cryo-workflow paths for sample preparation and cryo-light microscopy and show recent improvements on sample handling and imaging stability with applications in cryo-CLEM, particle EM, cryo-fluorescence and cryo-super-resolution.

References:

(1) T. Mueller-Reichert, P. Verkade (Editors), "Correlative Light and Electron MIcroscopy: Volume 111 (Methods in Cell Biology)", Sep 2012, Academic Press

(2) L.F. van Driel et al. / European Journal of Cell Biology 88 (2009) 669–684

(3) https://www.nobelprize.org/prizes/chemistry/2014/press-release/

(4) F. Moser et al., "Cryo-SOFI enabling low-dose super-resolution correlative light and electron cryo-microscopy",

PNAS 2019, www.pnas.org/cgi/doi/10.1073/pnas.1810690116

Fig 1: CMS196M cryo-stage

Fig 2: Detail of revised cryo-sample chamber layout with improved imaging stability

Fig. 1

Fig. 2

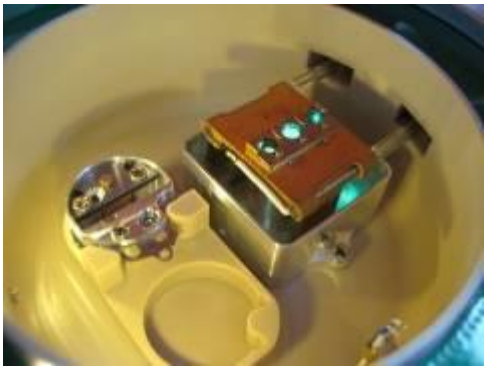

LS5.P007
Multiscale Multimodal Multicolor Microscopy

B. Giepmans[1]

[1]UMC Groningen, BSCS, Groningen, Netherlands

Correlative light microscopy and electron microscopy (CLEM) is a key approach to study structure-function relationships in cell biology. CLEM allows a biological process and building block (molecule, organelle, cell) to be identified and dynamically studied using fluorescent markers followed by high-resolution analysis of the ultrastructural context with EM. In the past decades sample preparation steps, technical approaches, probes, microscopes and image analysis have been optimized to make CLEM a routine approach applied by many labs to date (1). I will focus on additional modalities for identification of molecules in "cellular microscopy" at nanometer range precision, either detecting targeted probes or endogenous fingerprints, currently being explored in our lab (2).

Energy dispersive X-ray analysis (EDX)*:* Development in EDX detectors and computer software nowadays allows (semi)routine EDX *imaging* of 1kx1k pixel areas to fingerprint biomolecules and probes in the context of ultrastructure (Fig.1) (4).

Electron energy loss spectroscopy (EELS)*:* Similarly, EELS TEM allows detection of particles enriched in certain elements targeted for labelling, such as Quantum dots (6). Recently, Tsien and co-workers used lanthanides-enriched molecules that can be deposited using specific probes to perform two-color EELS to discriminate targeted molecules and biostructures of interest (7).

Nowadays, life science microscopists will increasingly explore the use of the electron beam or ion beam to generate signals that fingerprint or identify biomolecules and structures either directly, or indirectly using to-be-developed probes and bypassing the diffraction limit of light microscopy (Fig.1). This will lead to multidimensional EM with a pleiotropy of signals and molecules detected at nm-scale precision and reveal many current secrets underlying the regulation of life.

Our work is supported by the Netherlands organization for scientific research (ZonMW 91111.006; STW Microscopy Valley 12718; TTW15315. This abstract has been reformatted from (8).

References:

(1) de Boer et al. (2015) Nat. Methods 6, 503

(2) Pirozzi et al. (2018) Hist. Cell Biol. 150,509

(3) Scotuzzi et al. (2017) Sci. Rep. 45970

(4) Nisman et al. (2004) J. Histochem. Cytochem. 1, 13

(5) Adams et al. (2016) Cell. Chem. Biol. 11, 1417

(6) Ando et al. (2018) Journal of Physics D: Applied Physics 51 (44) p7,8

Fig. 1: "ColorEM" using elemental analysis by energy dispersive X-ray imaging. ColorEM: label-free (P), paint (Os) and labeling DNA (Au) and peptides (Cd) is compatible. (a) Part of an islet of Langerhans immuno-labeled for structures in DNA (10 nm gold) and insulin (QD). (b) Overlay image of Au (red), Cd (green), Os (yellow) and P (blue) allows identification of G4 structures (gold labels) and insulin (Cd). Note the localization of Au to heterochromatin enriched in P, whereas the Cd signal is enclosed within a combination of Os rings and P that likely identifies phospholipid membranes of the vesicles. Large scale data and full resolution data is available via www.nanotomy.org; Partially reproduced and modified from (6).

Fig. 1

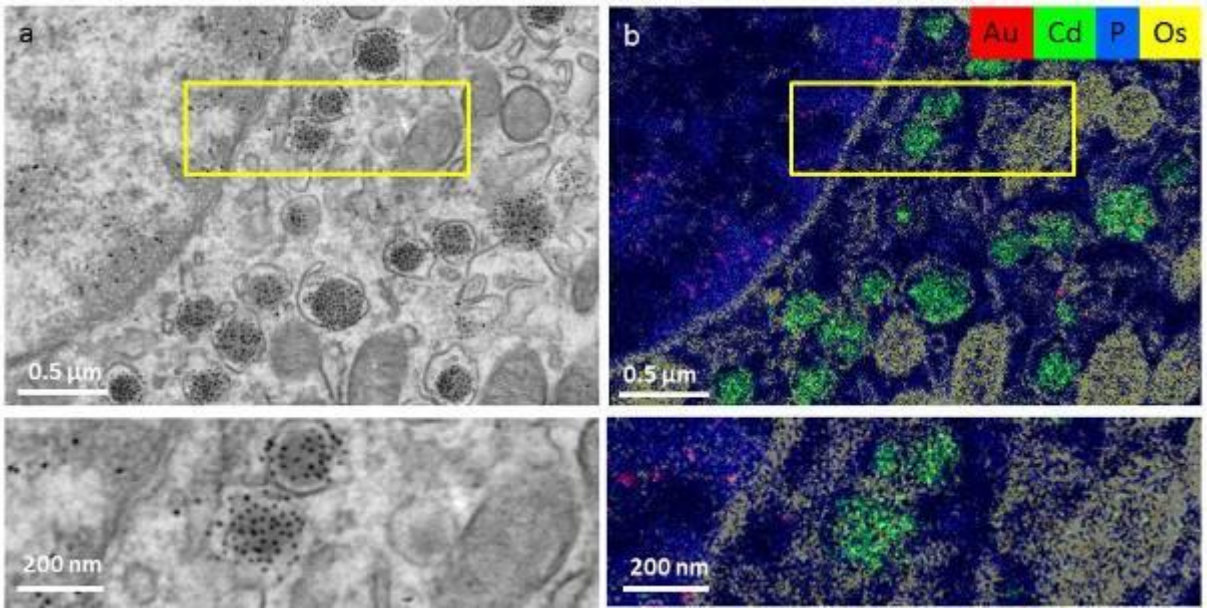

LS5.P008
Connect the microscopic world - Discover New Insights by Connecting Information across Dimensions with ZEN Connect

A. Elli[1], E. Hummel[1]

[1]Carl Zeiss Microscopy GmbH, Jena, Germany

Connected and correlative microscopy becomes increasingly important in all fields of microscopy. Multiple tools are involved during the correlative workflow ranging from light microscopes for large field of view imaging to light microscopes with highest resolution and finally to field emission electron microscopes showing the ultrastructure of a sample. The combination of various imaging tools reveals new insights into biological interdependencies. So far coordinate transfer between different imaging sources is of focus to connect different imaging modalities. The software module ZEN Connect enables to fulfill this task in an easy way - and allows full sample and tool flexibility.

ZEN Connect offers the possibility to combine multiple perspectives of a sample – across scales, across acquisition modes and across different contrast techniques – to provide answers to some of the most challenging scientific questions. The software module can now bring the entire breadth of imaging technologies together. Starting from low resolution imaging using for example a digital camera or a widefield microscope and from there to the LSM/Airyscan system with the aim to further improve resolution and enlighten new functional and structural aspects of the sample, all acquired data are shown in one joined project. Sample regions are relocated in different microscopes easily and the resulting data can be overlaid and stored together in one place. This approach makes it easy to gain insights into the whole experiment and removes the difficulty associated with multiple storage locations and instruments. ZEN Connect enables scientists to keep overview about their experimental data. As a result, you gain efficiency and effectiveness with intuitive data management, simplified workflows and limitless navigation. In this talk multiple correlative workflows will be presented and results from different application areas will be shown. One example is shown below. The figure shows an overview image of a mouse brain tissue section acquired with an Axio Scan Z1. A region of interest was identified and localized with ZEN Connect on a LSM 800 with Airyscan. Neuronal structures like spines which are not detectable with standard detectors were uncovered. Neurons in green and a neuronal protein in red.

Fig. 1

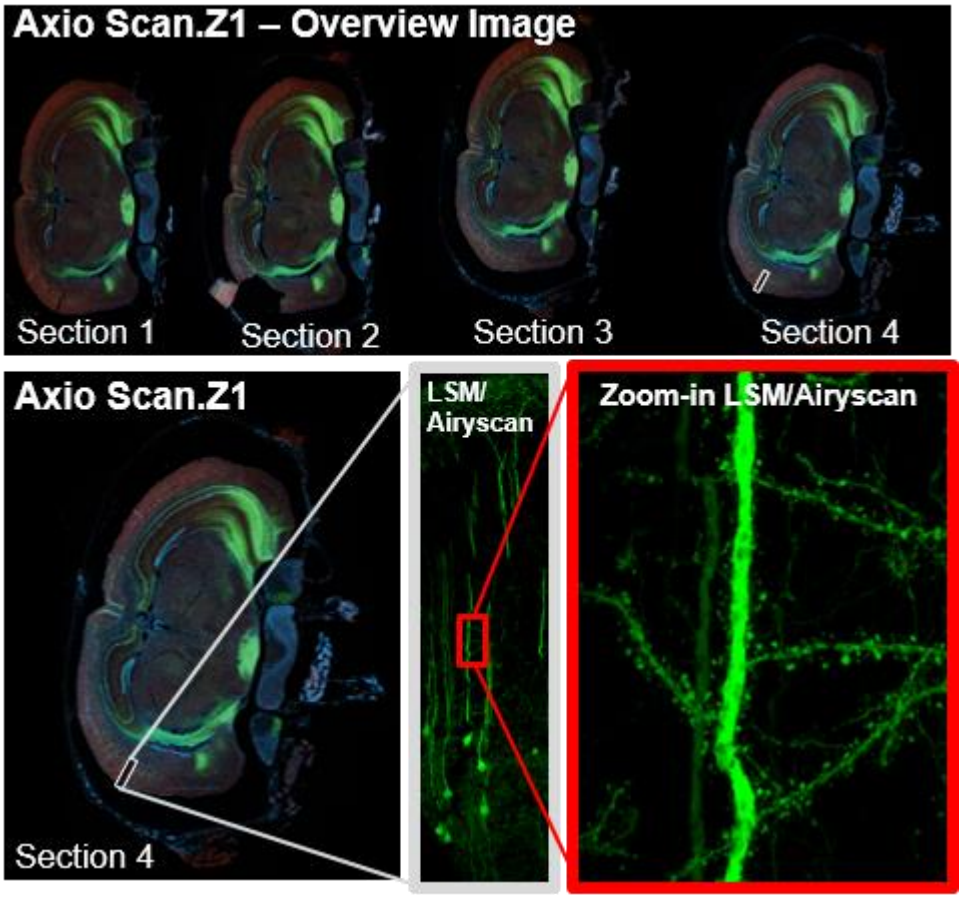

LS6.001 invited
Preservation of Fluorescence associated with Self-labeling Protein Tags in Epoxy Resin for Correlative Light and Electron Microscopy at High Resolution

A. Müller[1,2,3], M. Neukam[1,2,3], A. Ivanova[1,2,3], A. Sönmez[1,2,3], C. Münster[1,2,3], S. Kretschmar[4,5], Y. Kalaidzidis[6,7], T. Kurth[4,5], J. M. Verbavatz[6,8], M. Solimena[1,2,3,6]

[1]Paul Langerhans Institute Dresden of the Helmholtz Center Munich at the University Hospital Carl Gustav Carus and Faculty of Medicine of the TU Dresden, Dresden, Germany
[2]TU Dresden, Molecular Diabetology, Dresden, Germany
[3]German Center for Diabetes Research , Neuherberg, Germany
[4]TU Dresden, Center for Regenerative Therapies Dresden (CRTD, Dresden, Germany
[5]Biotechnology Center of the TU Dresden , Dresden, Germany
[6]Max Planck Institute of Molecular Cell Biology and Genetics , Dresden, Germany
[7]Moscow State University, Faculty of Bioengineering and Bioinformatics, Moscow, Germany
[8]Université Paris Diderot, Institut Jacques Monod, Paris, Germany

Correlative light and electron microscopy (CLEM) approaches can be divided in pre-embedding and post-embedding CLEM depending on the time-point when fluorescence light imaging (FLM) is performed. The goal of post-embedding CLEM is the preservation of fluorescence in the section, which can then be used for both FLM and electron microscopy (EM). This allows for greater precision of correlation and higher-throughput compared to pre-embedding analysis. In the field of EM it is commonly assumed that the initial fluorescence of the sample (mostly based on self-fluorescent protein tags) cannot be preserved in epoxy resins, which have been the most widely used embedding media for EM. Recently developed protein tags such as SNAP and CLIP are not self-fluorescent but bind specific fluorescent substrates based on organic fluorophores.

Our goal was to test the preservation of fluorescence directly associated with protein tags (SNAP or CLIP) in epoxy resins for CLEM combining super resolution microscopy and EM. If so, this approach could then be used to investigate the life-cycle insulin secretory granules (SGs) and their intracellular degradation.

We labeled insulin SGs of different age in beta cells of isolated pancreatic islets from SOFIA (Study of insulin aging) mice, in which an insulin2-SNAP allele had been knocked-in in the Ins2 locus. After labeling the islets were fixed by high pressure freezing (HPF), followed by freeze substitution (FS) and Epon embedding. Combining structured illumination microscopy and transmission electron microscopy (TEM) for correlative light and electron microscopy (CLEM) we precisely tracked age-distinct insulin SGs in Epon sections of SOFIA mouse pancreatic islet beta cells. We furthermore performed electron tomography to investigate the interaction of age-defined insulin SGs with microtubules. This protocol was also applied to insulinoma cells transfected with different proteins fused with SNAP- or CLIP tags and also combined with initial chemical fixation.

We could show for the first time the preservation of fluorescence directly associated with protein tags in epoxy resin. This allowed for CLEM of age-distinct insulin SGs in SOFIA mouse islets fixed by (HPF) and embedded in Epon epoxy resin, providing optimal ultrastructural preservation and contrast1. With this novel approach we could formally demonstrate that the characteristic translucent halo surrounding the insulin SG core is an artifact of chemical fixation leading to overestimation of the SG size. Morphometric analysis further revealed a significantly smaller diameter of 2-day-old insulin SGs compared with the whole SG population. By using the CLIP tag fused to the autophagosomal marker LC3 together with hIns-SNAP we could perform dual color CLEM to image intracellular degradation of SGs by autophagy. To demonstrate the robustness of our method we successfully performed CLEM with cytosolic, nuclear, membrane- and cytoskeleton-associated proteins tagged with SNAP or CLIP, even after chemical fixation and Epon embedding.

Further exploitation of this approach for morphometric analysis of labeled and unlabeled SGs will provide quantitative information about the life cycle of insulin SGs in different metabolic conditions. CLEM in Epon sections after HPF will allow for investigating the interaction of insulin SGs with the cytoskeleton at nanometer-resolution. Preservation of fluorescence in epoxy resin after HPF or after chemical fixation is a major simplification of post-embedding CLEM due to the simple embedding procedure, superior sectioning properties and lesser toxicity compared to acrylic resins.

References:

(1) Müller, A. *et al.* A Global Approach for Quantitative Super Resolution and Electron Microscopy on Cryo and Epoxy Sections Using Self-labeling Protein Tags. *Sci. Rep.* 7**,** 23 (2017).

LS6.002
Immunolocalization of two capsid proteins of therapeutic staphylococcal phages in Transmission Electron Microcope

Z. Kazmierczak[1], S. Nowak[2], M. Mazurkiewicz-Kania[2], K. Dąbrowska[1]

[1]Polish Academy of Science, Wroclaw, Poland
[2]University of Wroclaw, Wroclaw, Poland

Immunolocalization, based on the detection of specific antigens, were used to determine the localization of phage structural proteins. The IgG subtype of antibodies, produced in mice after selected protein immunization, are used in reaction between specific serum and whole phage particles. It enables to indicate precise location of phage protein in the capsid (haed or collar or tail or fibers).

In this studies, two proteins of therapeutic phages A3R and 676Z infect *Staphylococcus aureus* strain pathogenic to humans were examined. Genomes of A3R and 676Z were sequenced in 2014. All these phages were described morphologically, but gene functions were only proposed by annotations. Here we demonstrate structural function of two selected proteins in these two bacteriophages. Proteins were localized in phage capsid by immuno-EM.

The goal of the study was to determine and visualize the localization of two proteins Mcp and ORF096, identical in both phages A3R and 676Z. The results were described in PhD dissertation (Ref.1).

We have selected genes encoding hypothetical structural capsid proteins. These were: AFN38122.1 (Mcp) and AFN38152.1 (ORF096), in phage A3R and their homologues in 676Z. We cloned and expressed the genes and produced proteins for immunization and further investigation of their potential structural function.

C57Bl6/J mice were immunized with highly purified proteins. Staphylococcal proteins: Mcp and ORF096 were given subcutaneously in day 0, 20, 40. Control mice were injected with PBS. After 45 days blood samples were collected and levels of IgG antibody were measured by ELISA immunoassay. Bacteriophages A3R, 676Z were multiplied, purified and concentrated. Phages were incubated with anti-recombinant protein serum conjugated with gold nanoparticles (5nm in diameter goat anti-mouse gold, Sigma), deposited on a girds, fixed and stained. Images of phage particles were recorded by transmission electron microscope techniques (TEM).

The reaction between protein Mcp specific antibodies and whole phage particles (A3R or 676Z) revealed that this protein is localized on phage head. In the reaction between serum specific to ORF096 protein and phages showed that this protein is localized on baseplate on both phages.

References:

(1) Kaźmierczak Z., Identification of adhesive structural proteins of phages T4, A3/R, 676/Z and their effect on mammalian cells (2018).

Fig. 1: The localization of Mcp protein on studied phage.

Fig. 2: The localization of ORF096 protein on studied phage.

These data demonstrate that proteins Mcp and ORF096 are present on capsids of both staphylococcal bacteriophages A3R and 676Z. Mcp which was annotates as hypothetical major capsid protein, localizes on heads of these staphylococcal phages. The base plate of A3R and 676Z phages is co-built by ORF096 protein.

This work was supported by the National Science Centre in Poland grant UMO-2012/05/E/NZ6/03314 and UMO-2018/29/B/NZ6/01659.

Fig. 1

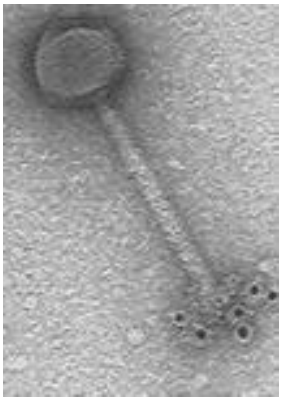

Fig. 2

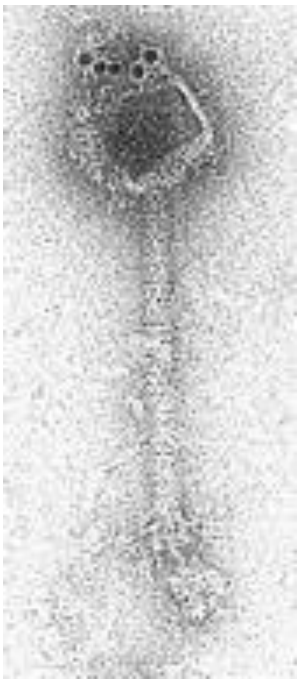

LS6.003
Immunogold detection of synaptic membrane proteins on grid-glued replica pairs

J. Montanaro-Punzengruber[1], R. Shigemoto[1]

[1]Institute for Science and Technology, Austria, Shigemoto Group, Klosterneuburg, Austria

In freeze-fracture replica immunolabelling (FRIL), lightly fixed tissue or cells are high pressure frozen and then fractured at lipid bilayers revealing P-face (protoplasmic side) and E-face (extracellular side) membrane leaflets. Coating these exposed faces with a thin carbon layer captures membrane proteins, which are retained in the carbon replica, even after the remaining tissue is removed with detergent. These fine carbon replicas are floated in drops of antibody and wash solutions and finally with gold-conjugated secondary antibodies, then examined by TEM or SEM to identify and localize specific proteins of interest. FRIL has two distinct advantages over the traditional immunolabelling methods; firstly the whole synaptic active zone can be revealed by the fracture, and secondly, the membrane protein epitopes are exposed and detectable with a high sensitivity by immunogold labeling. Thus, both two-dimensional localization and quantitation of membrane proteins at the synaptic membrane are feasible. One challenge of the FRIL technique is the fragility of the replicas. Fragmented replicas often make interpretation difficult as protein localization must be mapped to histological context to discern regions of interest. In addition, the fracture plane captures the membrane proteins to either P-face or E-face sides of the membrane. Thus, immunolabelling on a single replica will only reveal membrane proteins allocated to either P- or E- face of individual synapses, while those allocated to the corresponding E- or P-face must be detected on the complementary replica. Thus, a count of gold particles on mirrored replica pairs, with appropriate synapse matching, allows a total count of the gold-labelled protein, providing a full and more accurate picture of membrane protein distribution at the synapse. Until now, such work required considerable technical skill. Here we describe a new modification of the original FRIL technique. After freeze-fracture and carbon shadowing, we keep double replica pairs intact by gluing them to EM grids using a UV-cured glue. This procedure is more technically robust as the grid-supported replica can be handled easily and is tolerant to rigorous washing. In double replicas pairs, we can identify reference areas for orientation, finding both sides of matched synapses. In the future, we will use antibodies to intracellular and extracellular epitopes of the same molecule, to estimate total protein numbers and their distribution. We will describe this "grid-glue FRIL technique" in detail using, as an example, NR1 receptor quantitation on mouse hippocampus replicas.

We acknowledge the funding support for this project from ERC694539 to Ryuichi Shigemoto

LS6.004
Subcellular organization of presynaptic Ca2+ channels at hippocampal mossy fiber synapses

î Kulik[1,2]

[1]University of Freiburg, Institute of Physiology, Freiburg, Germany
[2]University of Freiburg, Centre for Biological Signalling Studies, Freiburg, Germany

By connecting the gyrus dentatus with the hippocampus proper, the axons of granule cells, the mossy fibers (MFs), represent an important element of the trisynaptic pathway of the hippocampal proper. Large MF boutons (MFBs) innervate thorny excrescences of CA3 pyramidal cells (PCs), dendrites of stratum lucidum interneurons (SLINs) and hilar interneurons (HIs).

The highly specialized function of MF synaptic specializations depends on the fine control of transmitter release that requires a well-regulated local Ca^{2+} signaling initiated by the opening of high voltage-activated Ca^{2+} (Ca_v) channels. Therefore, we aimed to determine the ultrastructural organization, density and distribution patterns of $Ca_v2.1$ (PQ-type) and $Ca_v2.2$ (N-type) Ca^{2+} channels over the active zone (AZ) of MFBs.

We used quantitative SDS-digested freeze-fracture replica immunoelectron microscopy together with automatized computational cluster analysis and smoothed distance transform analysis of $Ca_v2.1$ and $Ca_v2.2$ immunogold labeling.

Detailed analysis of particle distribution revealed that (i) both $Ca_v2.1$ and $Ca_v2.2$ channels are organized in clusters in MFBs, (ii) AZs of MFs showed a significantly higher density of $Ca_v2.1$ channels than that of $Ca_v2.2$, (iii) clusters of $Ca_v2.1$ are scattered over the entire AZ, (iv) clusters of $Ca_v2.2$ preferentially localized to the periphery of presynaptic membrane specializations at MFB synapses.

Our data demonstrate a similar nano-architecture but distinct density and distribution patterns of $Ca_v2.1$ and $Ca_v2.2$ channels at three different hippocampal MFB synapses. This suggests differential contribution of $Ca_v2.1$ and $Ca_v2.2$ to the precise timing of presynaptic Ca^{2+} inflow and transmitter release that is relevant for the temporal encoding of information in the hippocampus.

LS6.P001
Immunogold labeling of allergens on fine dust filters for SEM investigation.

J. Rattenberger[1], M. Nachtnebel[1], B. Fuehrer[2], C. Kirchnawy[2], L. Kaufmann[2], C. Hartl[2], H. Schroettner[1,3], G. Ettenberger-Bornberg[2]

[1]Graz Centre for Electron Microscopy - ZFE, Graz, Austria
[2]OFI Technologie & Innovation GmbH, Vienna, Austria
[3]Graz University of Technology, Institute of Electron Microscopy and Nanoanalysis - FELMI, Graz, Austria

In the last decades, the number of persons with allergies against at least one of the major allergens has been steadily increasing (1). As people spend most of their time in indoor environments, an allergy-free environment would promote their health situation. Accordingly filtering the relevant aerosols with suitable systems would be beneficial for many situations. State of the art filter tests characterize filters by applying standardized dusts or liquids (2) thus providing no predicate about the filter capacity concerning bioactive aerosols. To overcome this issue an innovative filter testing system is going to be established. In order to operate such a system in a realistic scenario, the missing link is detailed knowledge about the particle distribution to understand where allergic proteins can be found.

Immunogold labeling is a powerful preparation technique giving information about the exact position of specific proteins on the sample. We aim to obtain information about the location of different pollen allergens on particles collected on fine dust filters. Thus, a quite large area has to be investigated to obtain a statistically evaluable dataset and the analysis with the SEM is a more sensible choice to keep the examination time reasonable. Therefore, we had to find a labeling protocol, which enables the direct labeling of the allergen of interest on given fine dust filters. Initial tests with various TEM and/or SEM labeling protocols have shown, that especially due to the hygroscopic properties of the filters no suitable results were able to be obtained. To overcome this issue, an iterative sample preparation process was used to finally obtain a slightly unconventional but successful protocol. On the one hand, the fixation step was combined with the blocking step and on the other hand, the labeling was accomplished in a single step. The latter step was possible by conjugating the used monoclonal primary antibodies with gold nanoparticles. With this protocol we were able to show, that e.g. the labeling of the main ragweed allergen Amb a1 (*Ambrosia artemisiifolia*) has become possible, see Fig. 1. Additionally, to obtain information about the precise particle size, operation settings were ascertained to enable the direct investigation inside an ESEM. We used a rather low acceleration voltage, to enable a more surface sensitive imaging but still having decent BSE contrast to locate the gold nanoparticles. Particle size matters because researchers of the OFI found in previous analyses that pollen allergens are present on fine dust filters although the absence of pollen themselves.

References:

(1) G. D'Amato *et al.*, "Allergenic pollen and pollen allergy in Europe," *Allergy Eur. J. Allergy Clin. Immunol.*, vol. 62, no. 9, pp. 976–990, 2007.

(2) S. Kenneth and G. Chase, *Filters and Filtration Handbook*, Elsevier Science BV, 2007.

The authors thank the Austrian Research Promotion Agency FFG (project 856321) for funding and the environmental protection department (MA22) of Vienna for providing materials.

Fig. 1: BSE images of particles on fine dust filters after applying the labeling protocol against Amb a1 (main Ragweed allergen) with a) the negative control (milled grass and birch pollen), b) the positive control (milled ragweed pollen) and c) particles at a used PM10 filter (arrows mark gold particle positions).

Fig. 1

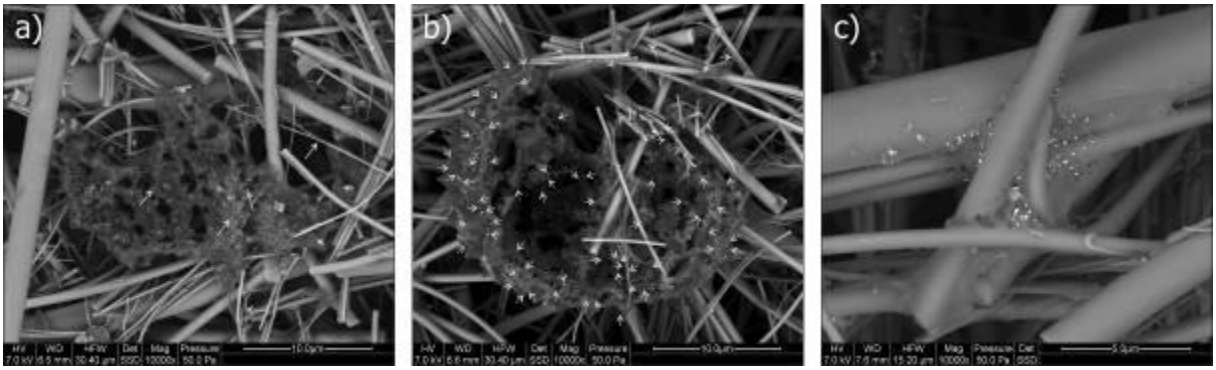

LS6.P002
Nanopatterning glass surface for localization of embryonic stem cells

Z. Hovádková[1,2], J. Pospíšil[3,4], M. Hrabovský[1], R. Váňa[1], J. Jaroš[3,4], J. Damborský[5], K. Pauruch[6], A. Hampl[3,4]

[1]Tescan Brno, R&D Application, Brno, Czech Republic
[2]Brno university of technology, Physical engineering and nanotechnology, Brno, Czech Republic
[3]Masaryk university, Department of histology and embryology, Brno, Czech Republic
[4]St. Anne's Hospital, International clinical research centre, Brno, Czech Republic
[5]Masaryk university, Department of Experimental Biology and Research Centre for Toxic Compounds in the Environment, Loschmidt laboratories, Brno, Czech Republic
[6]Masaryk university, Department of chemistry, Brno, Czech Republic

Nowadays the embryonic stem cells (ESCs) are essential source for the cell-based research due to their ability to differentiate into cells of all tissues in human body and their self-renewal capacity. To fulfil their application potential, understanding their biological activity including interactions with their neighboring cells and microenvironment is very important and for observation of their properties precise localization is a necessity (1). A technique chosen for this research was electron beam lithography (EBL) which enables us patterning large object with a good accuracy.

The scope of this project was to investigate functional nanopatterns where cells can grow and to find out whether cell behavior is dependent on the nanopattern (density, shape of the objects etc.).

In this experiment we used Ø12 mm cover glasses with thickness 1.5H. The surface was modified by coating 20nm indium tin oxide (ITO) film and then covered by repulsive layer to decrease the cell response to non-modified surface and to increase specificity of adhesion protein binding to structures. We spin coated the adhesion promotor AR 300-80 followed by coating 200nm layer of positive resist CSAR 62. It is proven the promotor helps the adhesion of the resist and its uniformity. The patterning was done using electron microscope Tescan MIRA 3. We exposed the patterns utilizing the EBL technique for its ability to create large patterned surfaces with a good accuracy within relatively short amount of time. To reach the best results the parameters were optimized, so the applied beam current was 330 pA, the step size 12.2 nm, the write field size 100 µm and the working distance 9 mm. The dose parameters were different in dependence of the pattern - the density and shape of the objects but the maximal dose was 92 µC/cm2. After the exposition the samples were developed in the amyl acetate for 1 minute, washed in the isopropyl alcohol (IPA) and dried in the nitrogen flow. On the top of the glass there was a thin layer (20 nm) of platinum sputtered and the lift-out was done within the NEP. To avoid tearing off the platinum patterns the tantalum film was added under the platinum layer. Tantalum was chosen as an adhesion layer for its nontoxic and transparent properties. The lasts steps were adding protein supporting the cell adhesion to the platinum objects and seeding the cells.

Firstly, we observed the adhesion of the protein to the lines with wide ≈100 nm. It was shown even the lines are really thin the protein can be observed and is attached. The next part of the experiment was to optimize the dose of the electrons in the EBL and the lift-out time and temperature in dependence of the density of nanolines. The last step was to observe the cells and their behavior. We analyzed the cells cultivated on bio-functionalized nanopattern for four hours by SEM and compared the results with the cells seeded on Martigel, where the cell spreading was greater.

Finding out the relationship between the shape of the nanolines and the cell behavior is still under research. These results may lead to better understanding of cell properties and biomolecule distribution in cell membrane.

References:

(1) Ebryonic stem cells, Junying Yu and James A. Thompson

This work was supported by Grant Agency of Masaryk University (MUNI/A/1369/2016, MUNI/A/1298/2017) and European Regional Development Fund-Project FNUSA-ICRC (No.CZ.1.05/1.1.00/02.0123).

LS6.P003
Enhanced Biomarkers Immunoplasmon Sensing using Super-localization Fluorescence-free Nanoscopy

S. Lee[1], S. H. Kang[1]

[1]Kyung Hee University, Applied Chemistry, Yongin, South Korea

Nanoscopy based on single-molecule localization offers a practical way to explore plasmonic interactions with nanometer resolution. So far, two fields have dominated the attention of sub-diffraction photonics research: fluorescence-free and fluorescence nanoscopy. Fluorescence-free nanoscopy prevents more sensitive and selective immunodetection due to photostability. We have developed high sensitive and precise immunoplasmonic sensors by 3D as well as 2D antibody-antigen binding on nanoarray chip using superlocalization fluorescence-free nanoscopy based on wavelength-dependent plasmon scattering. Here, the silver nanoparticle (nanotag) conjugated with biomarker was immunoreacted on 100 nm gold nanosubstrate. superlocalization on nanoscale by the least-cubic algorithm of biomarker was performed using three dimensional (3D) fluorescence-free nanoscopy. The accurate localization of the nanoparticle for detection (i.e., silver and gold) after reaction provided important information to reduce the error in data interpretation as well as the presence or absence of reaction. This results demonstrated the possibility for detection of extremely low concentration detection of various disease-related biomolecules at the single-molecule level.

References:

(1) Analytical Chemistry, 2018, 90, 5100−5107.

(2) Biosensors and Bioelectronics, 2017, 87, 842–849.

LS6.P004
Three-Dimensional Orientation of Anisotropic Plasmonic Aggregates at Intracellular Nuclear Indentation Sites by Integrated Light Sheet Super-Resolution Microscopy

S. K. Chakkarapani[1], S. Lee[1], S. Park[2], S. H. Kang[1]

[1]Kyung Hee University, Applied Chemistry, Yongin, South Korea
[2]Seoul National University, Advanced Institutes of Convergence Technology, Suwon, South Korea

Three-dimensional (3D) orientations of individual anisotropic plasmonic nanoparticles in aggregates were observed in real time by integrated light sheet super-resolution microscopy (iLSRM). Asymmetric light scattering of a gold nanorod (AuNR) was used to trigger signals based on the polarizer angle. Controlled photoswitching was achieved by turning the polarizer and obtaining a series of images at different polarization directions. 3D subdiffraction limited super-resolution images were obtained by super-localization of scattering signals as a function of the anisotropic optical properties of AuNRs. Varying the polarizer angle allowed resolution of the orientation of individual AuNRs. 3D images of individual nanoparticles were resolved in aggregated regions, resulting in as low as 64 nm axial resolution and 28 nm spatial resolution. The proposed imaging setup and localization approach demonstrates a convenient method for imaging under a noisy environment where the majority of scattering noise comes from cellular components. This integrated 3D iLSRM and localization technique was shown to be reliable and useful in the field of 3D nonfluorescence superresolution imaging.

Keywords: integrated 3D nanoscopy, gold nanorod, anisotropy, superlocalization, polarization Plasmonic

LS7.001 invited
Image Quality in SBF-SEM: Obstacles and Approaches

R. Reimer[1]

[1]HPI Hamburg, Strukturelle Zellbiologie der Viren, Hamburg, Germany

Serial Block Face Scanning Electron Microscopy (SBF-SEM) was initially developed to depict relatively large tissue volumes. Meanwhile this technique is being applied routinely in many labs with great results. Preparation techniques and imaging conditions have also been standardized for common large volume imaging. In contrast, achieving a higher (subcellular) resolution is often hindered by physical problems like noise, charging, beam damage, but also by preparation artefacts. We refined the preparation chain and adapted the imaging conditions accordingly for our SBF-SEM to get the highest resolution possible. The application of correlative (live-cell) light microscopy, cryo-preparation and charge-suppression by positive sample biasing adds value to the datasets and opens up new prospects in cell biology and infection research.

LS7.002 invited
Single protein visualization in whole cells: an introduction to sample preparation and imaging by liquid-phase electron microscopy

D. Peckys[1], D. Alansary[1], B. Niemeyer[1], N. de Jonge[2]

[1]Saarland University, Biophysics, Homburg, Germany
[2]INM – Leibniz Institute for New Materials, Innovative Electron Microscopy, Saarbruecken, Germany

The spatial organization of membrane proteins provides information that helps understanding their functioning, and that knowledge can be used for achieving progress in drug development. However, obtaining quantitative data in single molecule studies is difficult especially when endogenous proteins are to be studied and without disruption of the plasma membrane environment.

We have developed liquid-phase electron microscopy (LPEM) to study membrane proteins at the single-molecule and single-cell level in whole cells in hydrated state based on specific protein labeling with nanoparticles. The achieved resolution is sufficient to resolve protein complexes. Three different approaches are now available: 1) a liquid flow holder for scanning transmission electron microscopy (STEM) (1), 2) environmental scanning electron microscopy (ESEM) with a STEM detector (2), and 3) STEM of a wet sample covered with a sheet of graphene (3). The images are processed with an automated batch analysis, yielding the spatial information for each detected protein label. Data of thousands of label positions are statistically analyzed by using the pair correlation function, and cluster detection algorithms. The total time from the sample preparation, being the fastest part with only 3 – 5 work hours, until the results of the data analysis can be as short as 2 – 3 days. We thereby obtain information if a protein interacts and forms dimers or higher oligomers.

Using these analytical tools, we have studied the activation state, represented by dimerization, of growth factors such as EGFR and HER2, playing crucial roles in many cancer types, and the effects of state-of-the-art drugs against them (2). LPEM was also used to study the stoichiometry of ion channels, for instance of anoctamin1, a Ca2+-activated chloride channels, and of ORAI1, a Ca2+ channel with an essential role for intracellular Ca2+ homeostasis.

LPEM opens a new way to view and to analyze the distribution and interaction of membrane proteins, with a resolution not achievable by any light microscopy based method. Key advantages compared to conventional electron microscopy are the relatively fast sample preparation, and the capability to examine the target protein in its native environment, i.e. within the intact plasma membrane of the hydrated cell.

References:

(1) de Jonge N, Peckys DB, Kremers GJ, Piston DW. (2009) Proc Natl Acad Sci 106: 2159-64

(2) Peckys DB, Korf U, Wiemann S, de Jonge N. (2017) Mol Biol Cell 28: 3193-202

(3) Dahmke IN et al. (2017) ACS Nano 11: 11108-17

The authors thank E. Arzt for his support through INM and the DFB through SFB1027.

Fig. 1: STEM image of automatically detected QD-labeled ORAI1 proteins (yellow) after activation (false colored). The inset shows the pair correlation function $g(r)$ of all detected labels (N=4977) indicating dimerization at a distance r=20 nm and the presence of larger clusters (30 – 700 nm).

Fig. 1

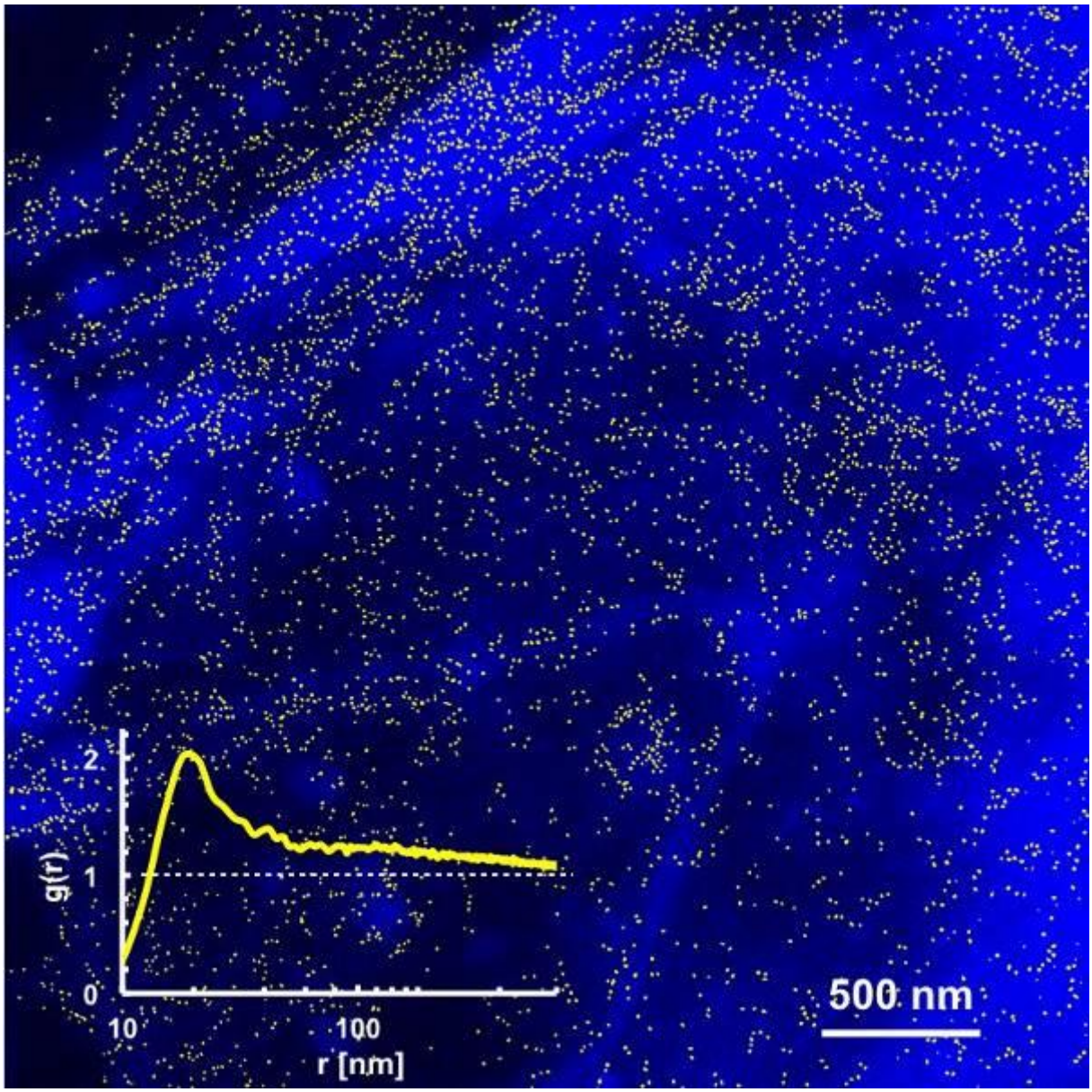

LS7.003
Large-area observation with silicon nitride sample supporting-film and montage system in TEM

Y. Konyuba[1], Y. Ikeda[1], T. Haruta[1], T. Fukuda[1], C. Hamamoto[1]

[1]JEOL Ltd., EM business unit, Tokyo, Japan

In recent years, to clarify a sample structure with a wide scale range (from nanometer to sub-milimeter) simultaneously, new approach of sample preparation and large field-of-view observation of the prepared sample are requested (1). The acquisition and handling for large volume data are realized and becoming easier using modern digital imaging devices and software. However, to observe a large field of view, it still requires improvement of a sample preparation technique and jigs for them. When we observe a large area of a sample on sample-supporting films with a conventional grid, sample information behind the grid bars is lost. In this way, the observation-area of TEM is confined to the grid size. However, in a grid with large hole, the wide sample supporting film, made of plastics, breaks easily, resulting in low success rate of sample preparation. Furthermore, it is often difficult to acquire large sample area on a supporting film with no wrinkles and deflections, because they are made by scooping a floating film and often to have the winkles and deflections.

To solve the above problems, we have fabricated a chip with a large silicon nitride (SiN) window (Fig. 1a) via MEMS process, for mounting large sample area (2). The SiN window chip has been fabricated to be 1 × 2 mm^2-sized and 30 nm-thick. Conventional sample preparation method (mounting and staining ultrathin sections) is applicable to the SiN window chip, since the chip is chemically stable. For image observation, this chip is embedded in an exchangeable retainer made for a common TEM holder. In TEM observation, Z-adjustment of sample requires so little, as the SiN window has little height difference (Fig. 1b).

In this paper, we report a couple of experimental results using the SiN window chip. The large field image of a sample was taken with an auto montage system (JEOL: Limitless panorama). Figure 2 shows the TEM montage image of a whole *Drosophila* embryo. The microscope we used was a 120 kV transmission electron microscope (JEOL: JEM-1400Flash), which was equipped with a sCMOS camera (JEOL: Matataki Flash). Figure 2a shows a TEM image of large-area, sized 680 × 250 μm^2 with several hundred million pixels, which was reconstructed from 184 (23 × 8) TEM images.

Now, we currently plan to fabricate a chip with a larger SiN window or multiple SiN windows. Plus, we will report on extended travel range of specimen stage with a special holder, which can be compatible with standard sample driving mechanism (3).

References:

(1) Bloss, Erik B., et al. "Single excitatory axons form clustered synapses onto CA1 pyramidal cell dendrites."*Nature neuroscience* 21.3 (2018): 353.

(2) Konyuba, Yuji, et al. "Fabrication and characterization of sample-supporting film made of silicon nitride for large-area observation in transmission electron microscopy."*Microscopy* 67.6 (2018): 367-370.

(3) Haruta, Tomohiro, et al. "Development of novel correlative light and electron microscopy linkage system using silicon nitride film."*Microscopy* (2019): in press.

Fig. 1: a) Appearance of SiN window chip. b) Height profile of SiN window, measured by scanning white-light interferometer.

Fig. 2: Large-area TEM image of *Drosophila* embryo. (a) Image for large-area observation with auto montage system. White square includes pole cell. (b) Magnified image of an area at the white square in (a), which shows the pole cell. (c) Zoom view of the white square area in (b).

Fig. 1

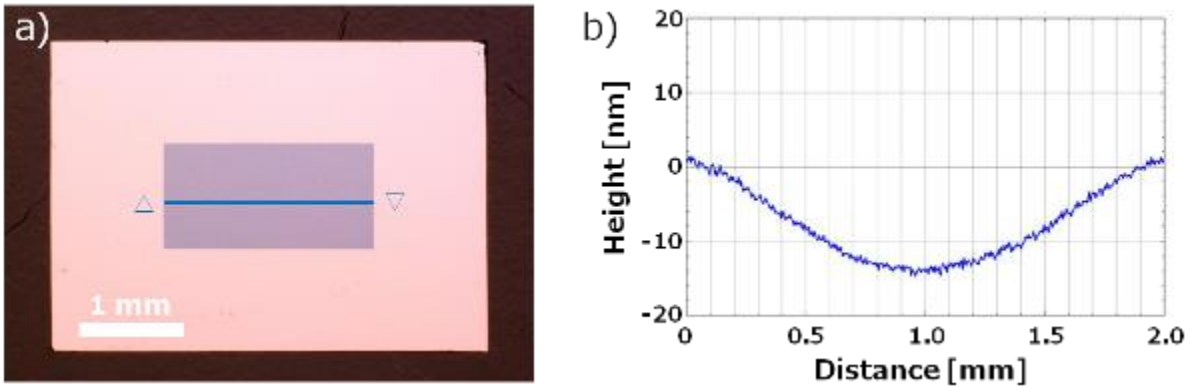
a)
1 mm
b)
Height [nm]
20
10
0
-10
-20
0
0.5
1.0
1.5
2.0
Distance [mm]

Fig. 2

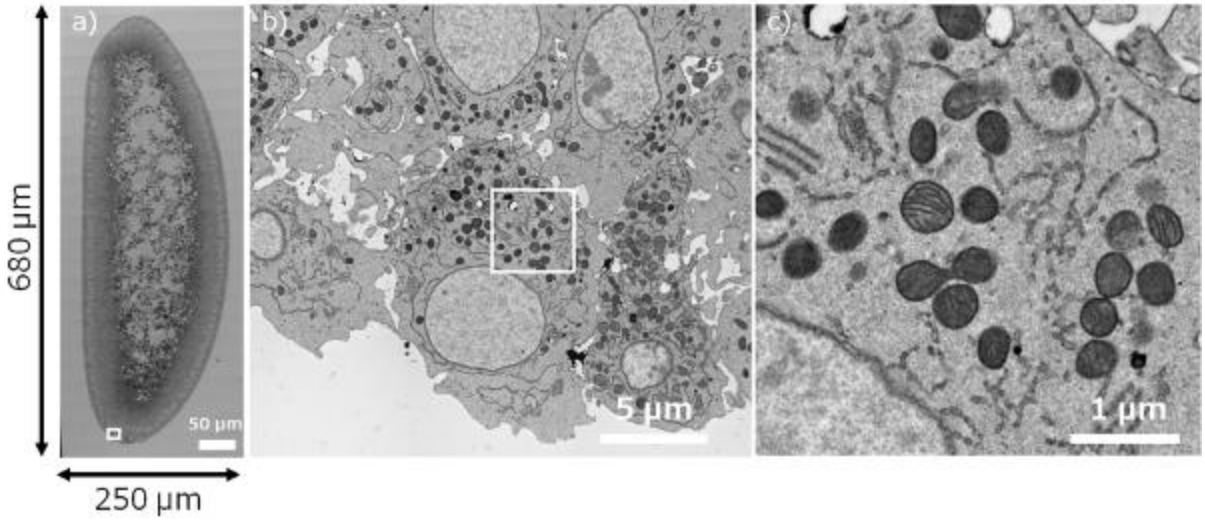
a)
b)
c)
680 µm
250 µm
50 µm
5 µm
1 µm

LS7.004
Contrast generation for array tomography samples – exploring alternative heavy metal stains

I. Wacker[1], E. R. Curticean[2], R. R. Schröder[1,2]

[1]Universität Heidelberg, Centre for Advanced Materials, Heidelberg, Germany
[2]Universitätsklinikum Heidelberg, Cryo Electron Microscopy, Heidelberg, Germany

For blockface-based volume EM approaches (1) serial blockface or focused ion beam SEM contrast generation relies on high amounts of heavy metals in the sample block. Array tomography (2), however, where serial sections are imaged, gives a second opportunity to introduce contrast: Sections may be post stained with a variety of heavy metals. In addition to the most commonly used uranyl and lead (Pb) stains a number of Lanthanoid stains have been introduced recently (3,4).

Our aim was to check the staining efficiency of Lanthanoids for different tissues, fixation and embedding procedures. First observations lead us on to test how much heavy metal is needed *en bloc*to allow retrieval of a good signal through post stain.

Mousemuscle and liver, bacteria, and cress roots were chemically fixed. Reduced Os and uranylacetate (UAc) were used for staining *en bloc*. Their concentrations were varied in several steps from 1% Os down to 0.01% and from 2% UAc down to 0.1%. Samples were embedded in Epon or HM20. Metals tested for post staining were UAc, Pb, a Gd/Sa mix (3) - available as UAR-EMS, Hf (4), and Uranyless, a non-disclosed Lanthanoid mix. Single, double, and triple post staining procedures were compared.

For samples with high amounts of heavy metal (e.g. 0.5-1% Os plus 2% UAc) in the block Lanthanoids are a valid alternative to UAc for all tissue types tested. In samples without any heavy metal in the block, the protein filaments in muscle cannot be visualized by post staining with UAR-EMS nor Pb (Fig. 1A), but are easily seen after double staining with Uac and Pb (Fig. 1 B). On sections from blocks with as little as 0.1% Os and 0.1% UAc (Fig 2) comparable signals could be retrieved by double (not shown) and triple (Fig 2D) staining procedures. Remarkable is the fact that here the Gd/Sa mix (Fig 2B) shows a much better distinction of membranes from protein than Uac (Fig 2A) or Pb (Fig 2C) alone.

Our observations indicate that lanthanoids need other metal pre-stains as seeds for binding. Since one of the bottlenecks in volume EM is segmentation, we are currently trying to establish "contrast metrics", i.e. measure electron density of e.g. membranes vs the surrounding "soup of proteins". Possibly, clever combinations of stains or varying their sequence may influence whether we just gain an overall darker image (with more scattering elements) or rather a selective highlighting of certain structures. In that context we are also exploring the use of lanthanoids for staining *en bloc*, with the potential to reduce concentrations of fluorescence quenchers such as Os even further to enable correlative approaches.

References:

(1) CJ Peddie, LM Collinson, Micron 61 (2014), 9

(2) I Wacker, RR Schröder, J Microscopy 252 (2013), 93

(3) M Nakakoshi, J El Microscopy 60 (2011), 401

(4) K Ikeda *et al*, Microsc. Res. Tech. 74 (2011), 825

(5) We thank the BMBF for grant NanoPatho, FKZ 13N14476

Fig. 1: Comparison conventional post stain vs lanthanide mix: Muscle tissue embedded in HM20 without any heavy metal *en bloc*, sections stained with 2% aqueous uranyl acetate (A) or UAR-EMS (B), both followed by Reynold"s lead citrate

Fig. 2: Contrast of membranes vs protein: Muscle tissue embedded in Epon with 0.1% reduced Os and 0.1 % uranylacetate *en bloc*, sections stained with 2% aqueous uranyl acetate (A), UAR-EMS (B), Reynold"s lead citrate (C), or a combination of all three in the order indicated

Fig. 1

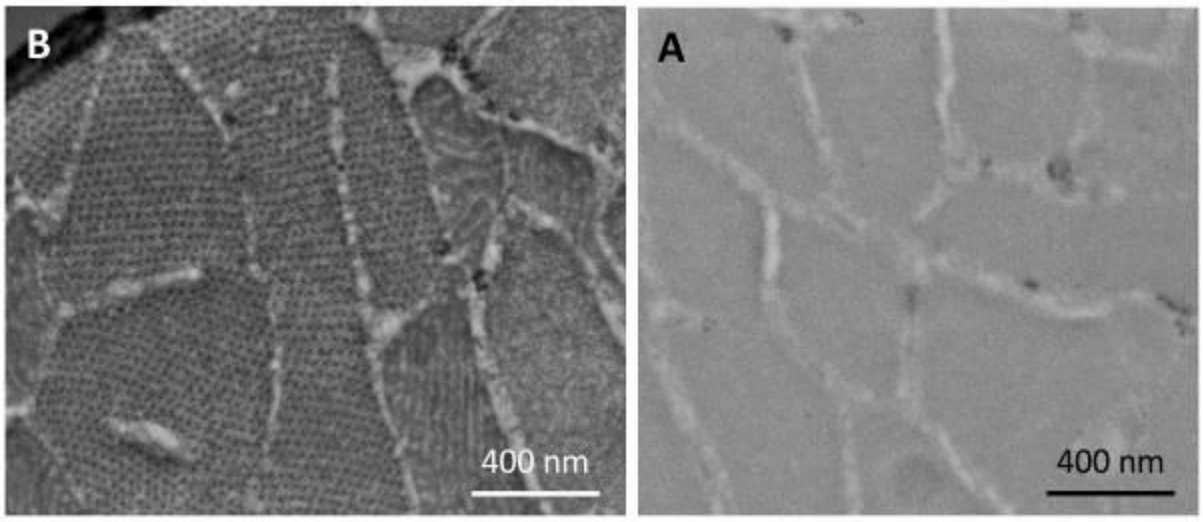
B
400 nm
A
400 nm

Fig. 2

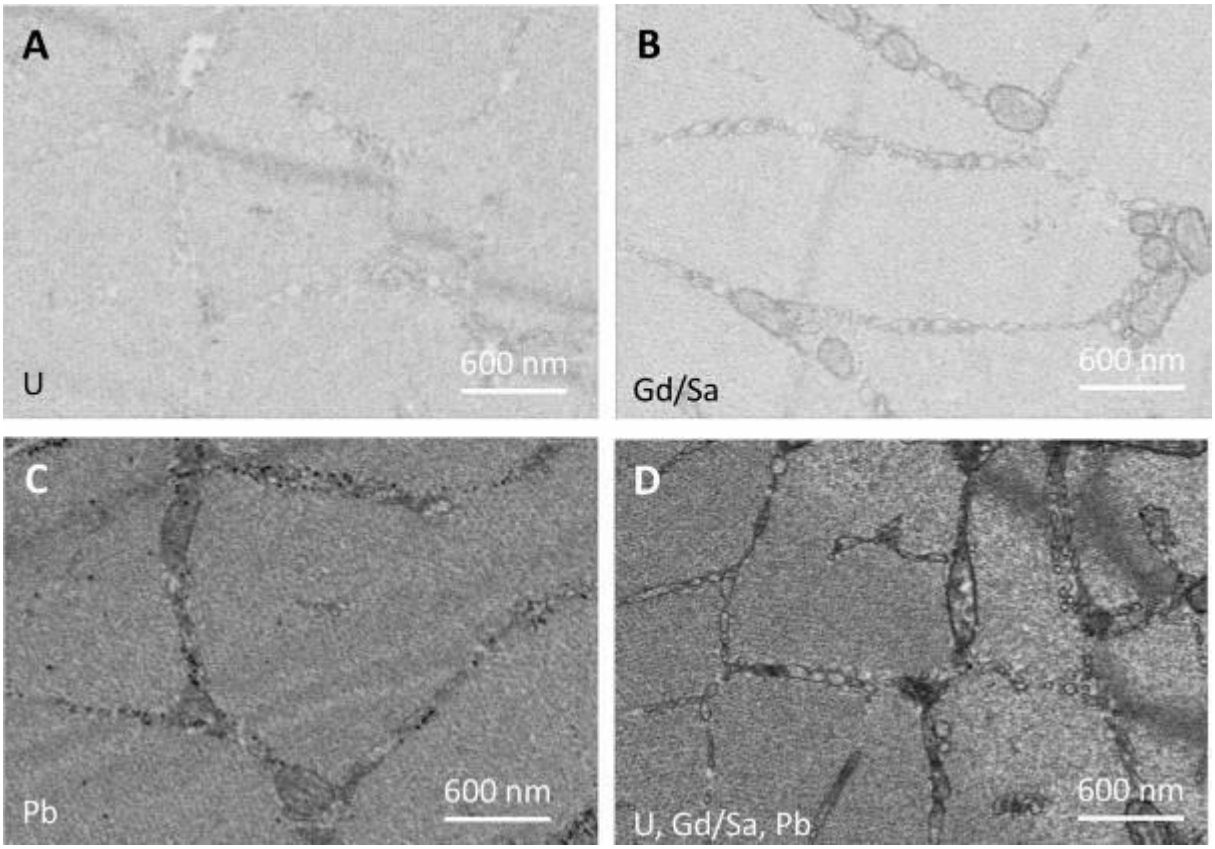
A
U
600 nm
B
Gd/Sa
600 nm
C
Pb
600 nm
D
U, Gd/Sa, Pb
600 nm

LS7.005
Directed freeze-fracturing of microbial biofilm for ultrastructural analysis by scanning electron microscopy

G. Holland[1], F. Fuchs[2], M. Cortesao[2], R. Moeller[2], M. Laue[1]

[1]Robert Koch Institute, Advanced Light and Electron Microscopy, Berlin, Germany
[2]German Aerospace Center (DLR), Radiation Biology Department, Institute of Aerospace Medicine, Cologne, Germany

To analyze the internal architecture of microbial biofilm at different scales we sought for a technique which allows the dissection of larger parts of the biofilm at distinct pre-selected locations. SEM provides both a large field of view and a sufficiently high resolution to reveal smallest ultrastructural details. We first tried a published protocol which uses sectioning with a razor blade of the chemically fixed biofilm (1), but realized that our biofilm, which grows on a filter substrate, is partially destroyed by the sectioning. This result prompted us to adapt existing freeze-fracturing protocols (2) to our needs.

The adapted protocol (3) uses chemical fixation with osmium tetroxide to stabilize the biofilm which was grown on porous filter substrates placed on agar. Fixed biofilm was dehydrated in a graded series of ethanol before regions of interest (max. 5 x 5 mm) were extracted with a razor blade. Extracted biofilm regions were placed on almost closed tips of a fine bend forceps and frozen in liquid nitrogen. By releasing the tips of the forceps the spring force introduced a straight fracture usually at the position which was originally located in the middle between the two tips. Fractured biofilm pieces were thawed in ethanol, dried by critical-point drying (CPD 300, Leica Microsystems), mounted on stubs and sputter-coated with gold/palladium. SEM was done with a field-emission SEM (Gemini 1530, Zeiss) at 3 kV and 5 mm working distance using the in-lens secondary electron detector and an Everhart-Thornley detector (signal mixing of 50:50).

So far we have studied biofilm of *Bacillus subtilis* (3) and of *Aspergillus niger* by using the adapted freeze-fracture method. The method revealed not only the overall morphology of the biofilm (Fig. 1, 3) but also ultrastructural details, like the extracelluar matrix (Fig. 2) or spore formation. It is of particular note that the fracturing process not only proceeded along surfaces but also produced fractures through cells and extracellular structures, which gave insight in the intracellular/internal ultrastructure (Fig. 2, 3).

The directed freeze-fracture method allows the reproducible ultrastructural analysis of larger biofilm structures grown on filter substrates from macro- to nanoscale and therefore complements cryo-preparation methods which are restricted to rather tiny biofilm structures for ice crystal-free freezing (4, 5).

References:

(1) Serra, D.O. et al. (2013) MBio 4:e00103–e00113.

(2) Moore, J.A; Payne, S.A. (2012) Meth Mol Biol 835:107-119.

(3) Fuchs, F. et al. (2018) J Microbiol Meth 152:165-172.

(4) Schaudinn et al. (2019) J Microscopy https://doi.org/10.1111/jmi.12788.

(5) Hrubanova, K. (2018) Micron 110:28–35.

Fig. 1: Overview of a freeze-fracture through a biofilm of *Bacillus subtilis*. Scale bar = 20 µm.

Fig. 2: Detail of the surface of a fracture through a *Bacillus subtilis* biofilm which shows intact and fractured bacteria as well as extracellular matrix (arrows) between the cells. Scale bar = 1 µm.

Fig. 3: Overview of a freeze-fracture through a biofilm of *Aspergillus niger*. The conidiophores extend from a dense basal mycelium. Note that some of the conidiophores are fractured. Scale bar = 100 µm.

Fig. 1

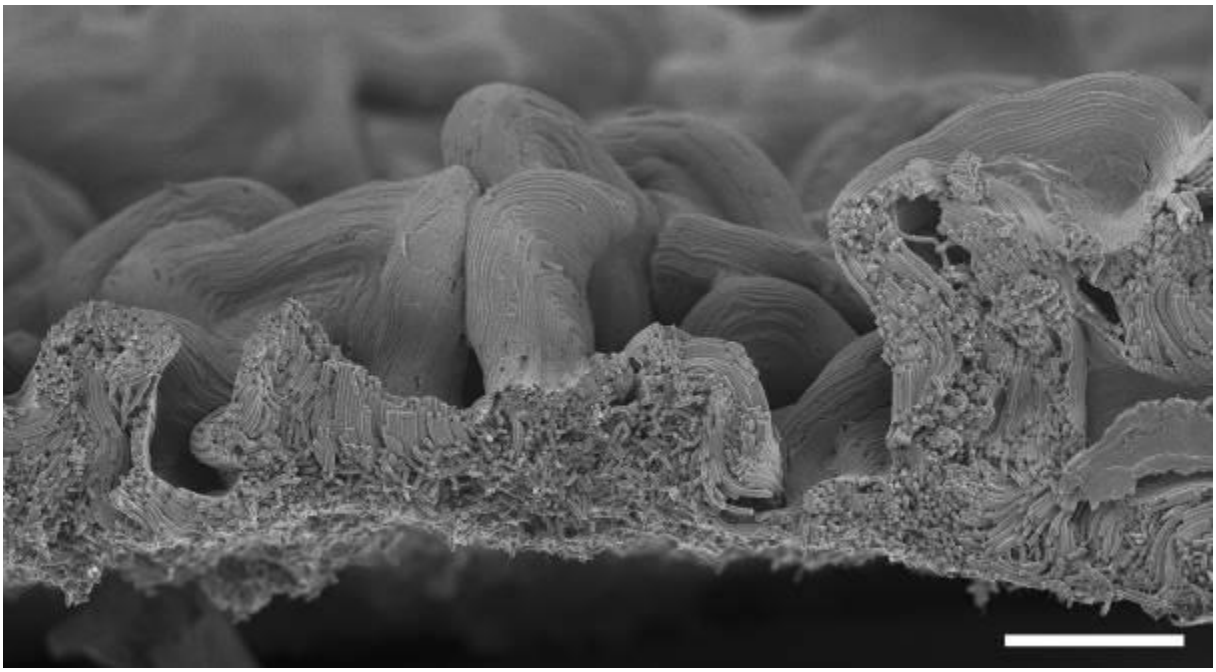

Fig. 2

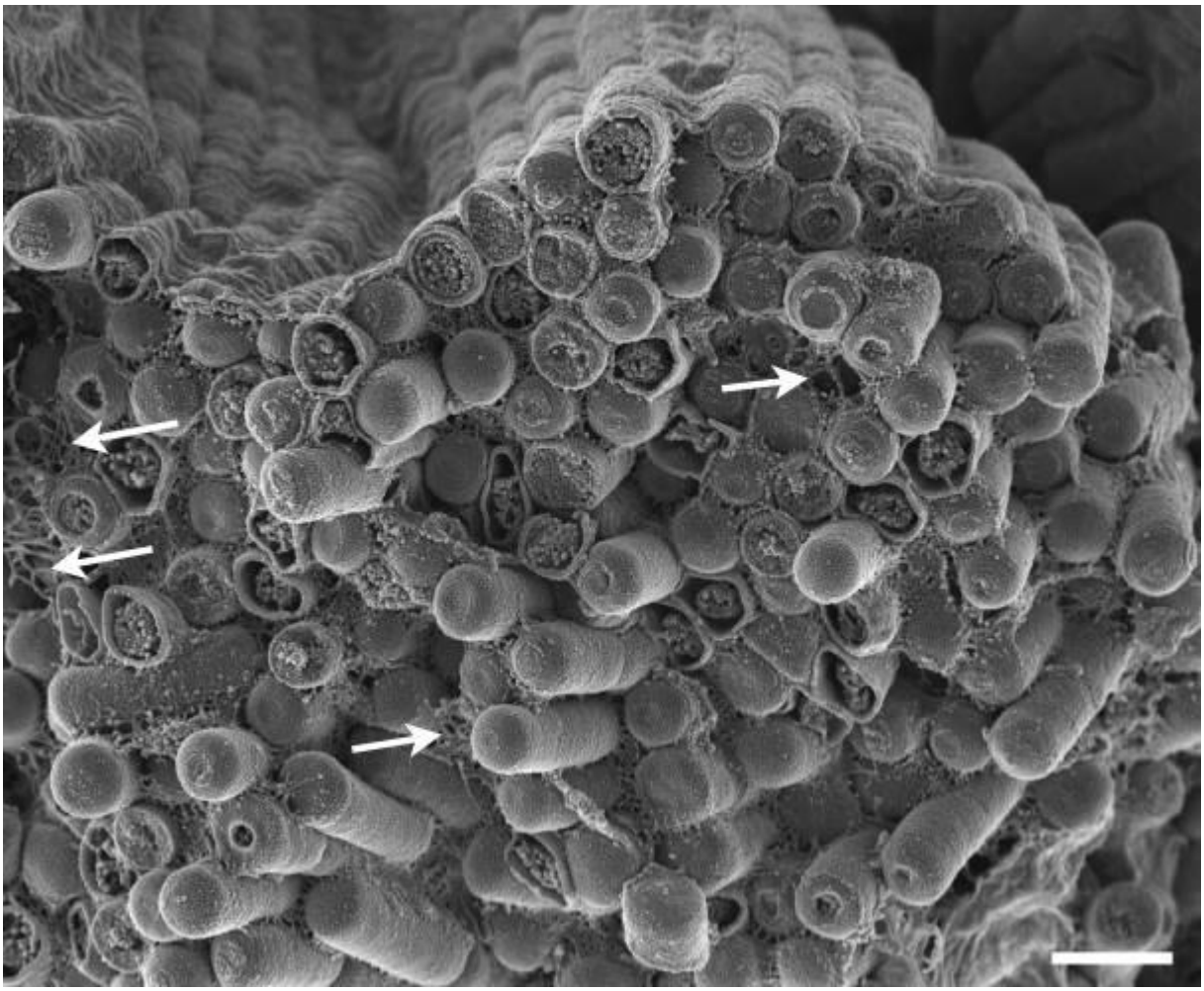

Fig. 3

LS7.006
Scanning Electron Microscopy and Raman Spectroscopy of *Candida parapsilosis* and *Staphylococcus epidermidis* Biofilms

K. Hrubanova[1], J. Nebesarova[2], F. Ruzicka[3], Z. Pilat[1], O. Samek[1], V. Krzyzanek[1]

[1]Institute of Scientific Instruments of the CAS, v. v. i., Brno, Czech Republic
[2]Biology Centre of the Czech Academy of Sciences, Ceske Budejovice, Czech Republic
[3]Masaryk University and St. Anne's Faculty Hospital, Department of Microbiology, Brno, Czech Republic

Biofilm forming microbial species *Candida parapsilosis* and *Staphylococcus epidermidis* have been recently linked to serious infections. Life in biofilm is favorable for microbes, bringing advantages such as enhanced persistence and resistance to environmental threats, i.e., antimicrobial agents, toxic substances, thermal and oxidative stress. Understanding the biofilm structure can contribute to the underlying biochemical mechanisms. This will help to develop a more efficient treatment strategy for biofilm infections.

Main aim was to employ the scanning electron microscope (SEM) morphological examination to study the extracellular matrix (ECM) content and distribution in the biofilm (Fig. 1) with chemical characterization by Raman microspectroscopy, where the central objective was to identify the main components of the biofilm (Fig. 2). We compered the Raman spectra from the freshly inoculated substrate, containing only the microbial cells, but no ECM, with relatively fresh (6h old) biofilm containing also ECM.

We studied microbial biofilms by SEM, which allowed us to visualize the distribution of cells inside the ECM. We compared classical with cryogenic SEM, which employs physical sample preparation based on plunging the sample into liquid cryogen, as well as high-pressure freezing (HPF). For imaging the biofilm interior, we applied the freeze-fracture technique (FFT). we showed that the different means of sample preparation have a fundamental influence on the biofilm structure. We complemented the SEM observations with Raman spectroscopic analysis, which allowed us to assess the time-dependent chemical composition changes of the biofilm *in vivo*. We identified the individual spectral peaks of the biomolecules in the biofilm to follow the temporal development of the chemical composition.

We showed that the combination of Raman spectroscopy with selected SEM techniques can provide a deeper insight into the chemistry and composition of biofilms. The influence of variations in the amount of extracellular material during the different stages of biofilm growth was studied by a combination of SEM and Raman spectroscopy (1).

References:

(1) Hrubanova, K.; Krzyzanek, V.; Nebesarova, J.; Ruzicka, F.; Pilat, Z.; Samek, O.; Monitoring Candida parapsilosis and Staphylococcus epidermidis Biofilms by a Combination of Scanning Electron Microscopy and Raman Spectroscopy. *Sensors* 2018, 18(12), 4089.

The research was supported by the Czech Science Foundation (project 17-15451S) and the Technology Agency of the Czech Republic (project TN01000008); the infrastructure by the Czech Academy of Sciences (project RVO:68081731) and the Ministry of Education, Youth and Sports of the Czech Republic (LM2015062 Czech-BioImaging).

Fig. 1: SEM micrographs show the bacterial and yeast biofilm structure: A and C *S. epidermidis*; B and D *C. parapsilosis*. In the upper line, images of biofilm interior prepared by HPF/FFT, in the bottom line images of biofilm surfaces prepared by combined preparation, SEM parameters: 2 keV, WD 6 mm. Marks: Stars ECM, squares cells, round upper side of biofilm layer.

Fig. 2: Raman spectra of biofilms. A: *C parapsilosis*; B: *S epidermidis*. Comparison of the fresh substrates containing no ECM (0h, blue) with 6 hours old biofilm, showing the ECM production (6h, red). The Raman peaks associated with biomolecules are numbered. The spectra from 6 measurements.

Fig. 1

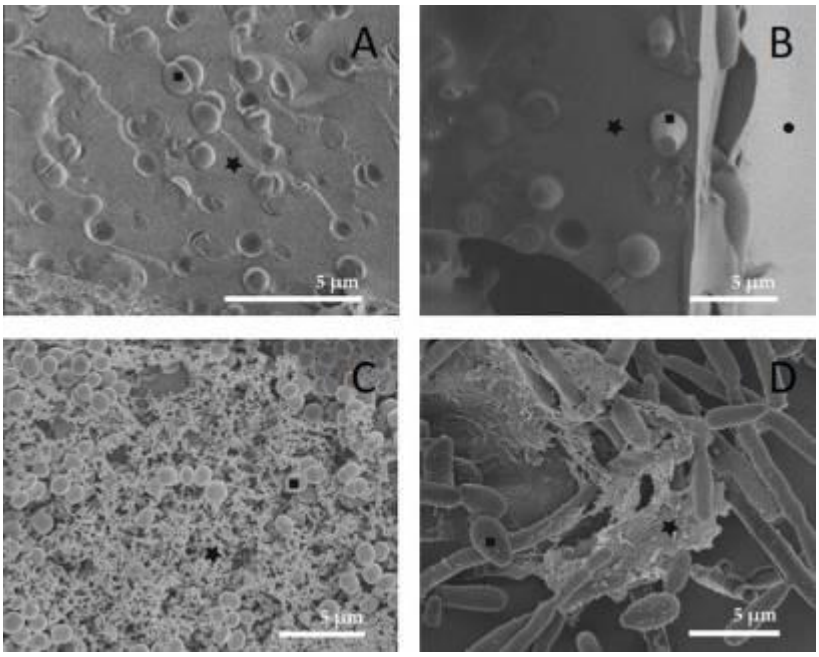
A
5 µm
B
5 µm
C
5 µm
D
5 µm

Fig. 2

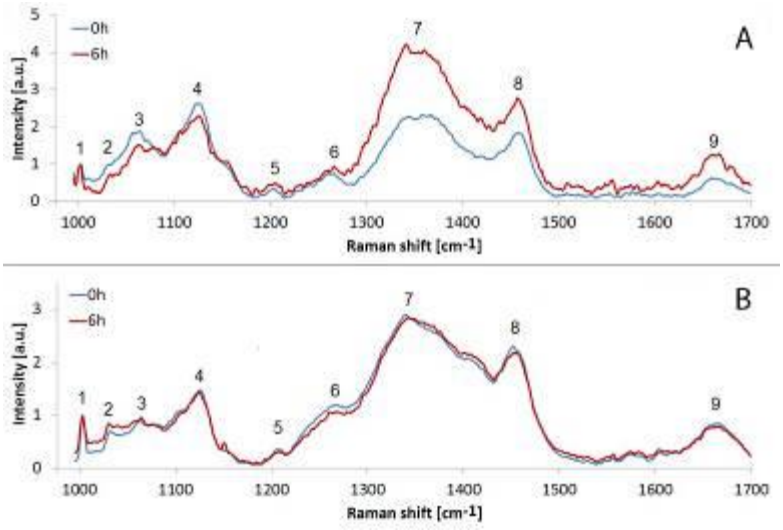
0h
6h
A
Intensity [a.u.]
Raman shift [cm-1]
1
2
3
4
5
6
7
8
9
B

LS7.LB.P01
Genome-informed microscopy: CLEM for studying viral infections of uncultivated archaea

I. Monsees[1], V. Turzynski [1], J. Rahlff[1], A. Klingl[2], A. Probst[1]

[1]Universität Duisburg-Essen, GAME, Essen, Germany
[2]LMU München, Biologie I - Botanik, München, Germany

Metagenomic approaches provide great amount of information about novel microbial organisms and their viruses and enable researchers to build hypothesizes about microbial interactions in actual ecosystems. Interactions of microbes and viruses are predicted from datasets based on, e.g., matching spacers of CRISPR Cas systems to viral genomes. However, linking these predictions to actual cell morphology of the host remains an unresolved problem in environmental microbiology. In contrast, modern electron microscopy techniques are providing a sub nanometer resolution, but they are missing the link to the genomic information. By correlating fluorescence images of virus infections of archaeal biofilms with electron microscopy, we provide a method to verify bioinformatically driven hypotheses *in situ*.

The aim of this work was to use correlative microscopy to analyze viral infections of uncultivated archaea in samples taken from the natural ecosystem. Therefore we have chosen biofilm flocks from the Mühlbacher Schwefelquelle, Isling (MSI) in Germany as the model system (Probst, Weinmaier et al. 2014). A novel viral genome infecting the dominating archaeal species was previously bioinformatically predicted and its viral nature was proven using genomeFISH coupled to fluorescence microscopy (Barrero-Canosa, Moraru et al. 2017).

To correlate the results of genomeFISH to electron microscopic images, glass slides with a coordinate system engraved on the surface were used. The flocks are examined for viral infections in fluorescence microscopy (FM). The shape and the coordinates of the flocks are documented and their position is verified in the light microscope after sample preparation for SEM by critical point drying.

We successfully correlated FM with SEM to examine virus infections in environmental samples. GenomeFISH was used to spot viral infections within the biofilms. In FM a variety of signals was observable leading to the hypothesis that different infection stages of the cells can be distinguished. During SEM image acquisition it was possible to reidentify the flocks imaged in FM. Spots with viral infections were examined for similarities and unique appearances compared to spots with low or no viral signal. Morphologies belonging to different steps of viral infections were identified.

The work is a proof of principle study to show that genomic information can be used to design probes for genomeFISH, which can in turn be correlated to scanning electron microscopy for samples taken from the environment. Our results enable the conclusion that the studied archaea are regularly infected in the ecosystem and undergo strong morphological changes during the infection cycle. These results have ultimate implications on ecosystem understanding of the subsurface and indicate that viruses impact autotrophic and heterotrophic carbon cycling.

References:

(1) Barrero-Canosa, J., et al. (2017). Environmental Microbiology 19(1): 70-82.

(2) Probst, A. J., et al. (2014). Nature Communications 5: 5497.

LS7.LB.P02
Rapid automated freeze substitution under agitation: better samples within shorter time

S. Reipert[1], H. Goldammer[1], E. Hollergschwandtner[1], D. Gruber[1], C. Richardson[2], M. W. Goldberg[2], T. Hawkins[2], W. A. Kaufmann[3], J. M. Volland[4], M. Stöger-Pollach[5], J. Neumüller[6], U. Kaindl[6], T. Schwaha[7], M. Eckhard[1], S. Antreich[1], Y. D. Stierhof[8]

[1]University of Vienna, Core Facility Cell Imaging and Ultrastructure Research (CIUS), Vienna, Austria
[2]Durham University, Department of Biosciences, Durham, United Kingdom
[3]Institute of Science and Technology-Austria, Electron Microscopy Facility, Klosterneuburg, Austria
[4]University of Vienna, Department of Limnology and Oceanography, Vienna, Austria
[5]Vienna University of Technology, University Service Center for TEM (USTEM), Vienna, Austria
[6]Medical University of Vienna, Center of Anatomy and Cell Biology, Vienna, Austria
[7]University of Vienna, Department of Integrative Zoology, Vienna, Austria
[8]University of Tübingen, Center for Plant Molecular Biology (ZMBP), Tübingen, Germany

Whether explored in its own by electron microscopy or in correlation with other microscopic or analytical techniques, studies of the ultrastructure of cells and tissues require a high quality in sample preservation. Cryopreparation is a means to achieve this goal. It comprises ultrarapid freezing of native samples at ambient or high-pressure followed by freeze substitution (FS) in an automated FS system (AFS) to replace frozen cell water molecules of the sample by organic solvents and additives at temperatures below the onset of destructive water recrystallization.

Until recently, FS was a time-consuming process. In 2011, McDonald and Webb demonstrated that sample agitation during FS dramatically reduces the necessary time. As a proof of concept, they performed FS within 3 hours or less in dry ice-filled buckets placed on laboratory shakers (1).

To agitate samples in an AFS, we introduced a magnetic force-driven agitation module into the cryochamber that allowed shortening of the protocol from days to a couple of hours (2). Applied to symbiotic algae in *Paramecium* sp. it resulted in superior preservation, which encourages rethinking of the symbiont/ host interaction (3). It also led to the discovery of optically active mesostructures in the ovisac of *Artemia franciscana* (4). Moreover, aldehyde-fixed ciliates *Zoothamnium niveum* harboring bacterial endosymbionts were processed by a hybrid approach for NanoSIMS by Volland et al., who plunge-froze and freeze-substituted them by using an agitation module (5). The resin-embedded samples were used for correlating TEM studies with the localization of carbon isotopes.

For dissemination, we started low-cost manufacturing of agitation modules for two of the most widely-used FS units, the AFS(1) and AFS2 from Leica Microsystems. To test them, several labs independently used the modules on a wide variety of species. We demonstrate that automated processing with sample agitation saves time, increases flexibility with respect to sample requirements and protocols, and produces data of at least as good quality as other approaches (6). Conclusively, the method has the potential to replace lengthy FS under static condition that is experienced as a time consuming bottleneck for cryopreparation.

References:

(1) McDonald KL, Webb RI (2011). Freeze substitution in 3 hours or less. J Microsc. 243(3):227-233.

(2) Goldammer H, Reipert S (2015). Freeze Substitution Device. University of Vienna, Austrian Patent No. AT515423 and German Utility Model DE 21 2015 000 100.

(3) Goldammer H et al. (2016). Automatized freeze substitution of algae accelerated by a novel agitation module. Protist. 167(4):369-376.

(4) Hollergschwandtner E et al. (2017). Novel mesostructured inclusions in the epidermal lining of Artemia franciscana ovisacs show optical activity. PeerJ. 5:e3923.

(5) Volland JM et al. (2018). NanoSIMS and tissue autoradiography reveal symbiont carbon fixation and organic carbon transfer to giant ciliate host.ISME J. 12(3):714-727.

(6) Reipert S et al. (2018). Agitation Modules: Flexible Means to Accelerate Automated Freeze Substitution. J Histochem Cytochem. 66(12):903-921.

LS7.P001
Cross-sectioning of nano- and micro- fibrous polymeric materials

O. Židek[1], A. Kotzianová[1], J. Klemeš[1], M. Pokorný[1], V. Velebný[1]

[1]Contipro a.s., Dolní Dobrouč, Czech Republic

Nowadays, the ion beam slope cutting method is used mainly for materials made of metals, but rarely in the field of polymeric nano- and micro- fibrous materials. However, it is one of the few methods that allows us to look inside such fibres as it is impossible to create a cross-section of a nano- or micro- fibre using conventional approaches (scissor cut or scalpel cut even after freezing, figure 1a, 2a) without destroying its morphology. The whole process of slope cutting polymer is quite complex and require a proper setting. Although the whole process is time-consuming, it's a unique way to look under the surface of nano- and micro- fibre.

We want to prepare cross-sections of nano- and micro- fibrous polymeric materials without artefacts.

Ion beam slope cutter (IBM, Leica), scanning electron microscope (SEM, ZEISS), optical microscope (OM, Keyence) and sputter coater (SC, Leica) were used to prepare and analyse cross sections of nano- and micro- fibrous polymeric materials. The ion beam slope cutter consists of three ion guns. The sample, placed on a special stage, is cut (up to 100 µm) by accelerated ions. The stage could be cooled up to -180 °C. One, two or all guns could be used for cutting. All cut samples where coated in SC before imaging by SEM.

We found, that the final cut appearance is highly influenced by set temperature, cutting time, accelerating voltage, current and number of used guns. Different values of all these parameters have significant effects on the result. Various settings of the ion beam cutting process were tested and the ideal parameters were determined for slope cutting of polymeric nano- and micro- fibres. Using all three guns, the accelerating value of 5 kV, current of 2 mA, temperature of -120°C and cutting time of 180 minutes, we were able to cut sample by 100 nm to 100 µm without any significant destruction in their morphology (figure 1 b, 2b). Prepared cross-section were image by SEM or OM, according to their diameter.

We determined the ideal parameters of the ion beam slope cutting method for cross-sectioning nano- and micro-fibrous polymeric materials. This method, usually used for metals, allowed us to image and to study the inner structure of fibres with dimension in nano- and micro- scale.

Fig. 1

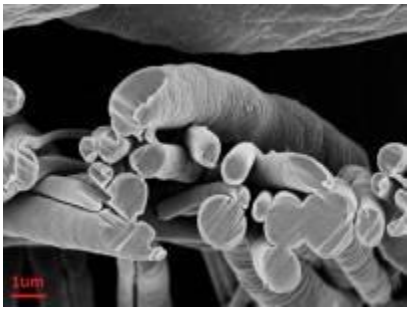

Fig. 2

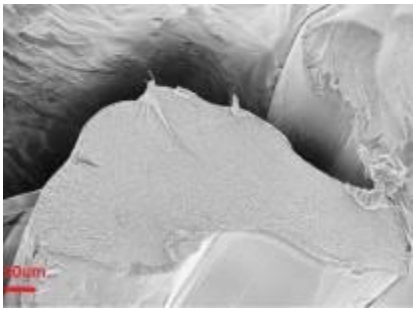

LS7.P002
Development of a cryofixation and freeze substitution protocol for highly pathogenic microorganisms

A. Kauter[1], M. Laue[1]

[1]Robert Koch Institute, Advanced Light and Electron Microscopy, Berlin, Germany

Cryopreparation methods are well-established in electron microscopy of biomedical samples. Examinations of highly pathogenic microorganisms, such as Ebolavirus or Anthrax bacteria, must be performed in special laboratories which prevent the escape of active microorganisms. Usually, all processes, which involve handling of microorganisms must be performed in a biosafety level cabinet. Moreover, hazardous materials or procedures, which could interfere with the protection of lab workers and the environment must be excluded. These limitations impair the application of cryopreparation methods for studying highly pathogenic organisms.

The aim of our project was to explore, whether metal-mirror cryofixation (= impact cryofixation or slam-freezing) followed by freeze-substitution allows to preserve and to inactivate pathogenic microorganisms, or not. With an adequate inactivation during freeze-substitution, samples could leave the laboratory of higher biosafety level and following preparations and investigations, including electron microscopy, could be performed under standard lab conditions. Imapct cryofixation is performed with rather small and simple machines that uses liquid nitrogen for cooling, a copper metal-mirror and a plunger for slamming the samples against the cooled metal-mirror.

We used an impact cryofixation device according to Sitte (1) and performed freeze-substitution in an AFS2. To test the suitability of the approach we chose the soil bacterium *Bacillus subtilis* and the hospital pathogen *Acinetobacter baumannii* as model systems. Freeze-substitution was done by varying composition of different fixatives in acetone. The inactivation of bacteria by freeze-substitution was validated by recultivation after freeze-substitution. Samples were embedded in LR White, sectioned with an ultramicrotome and analyzed with a transmission electron microscope.

Various freezing parameters, such as sample support, mounting of samples and machine settings, were tested. As support, thin polyester filter membranes with pores (0.2 µm) were found suitable, because bacteria could be concentrated on the filters from suspensions by using a simple filtration approach (2). A set of machine settings was found which gave sufficient and reproducible ultrastructural preservation of bacteria (Figure 1, 2). Recultivation showed that freeze-substitution with osmium tetroxide, uranyl acetate in acetone resulted in complete inactivation for both organisms tested.

Impact cryofixation followed by freeze-substitution allow ultrastructural preservation and inactivation of bacteria. It is likely that similar results can be achieved for highly pathogenic bacteria. Further investigations will test if the method can be extended to virus-infected cells.

References:

(1) Sitte, H. et al. (1987) In: *Cryotechniques in Biological Electron Microscopy.* p.87-113.

(2) Schaudinn, C. et al. (2019) *J Microscopy.* doi.org/10.1111/jmi.12788

Fig. 1: Impact cryofixation of *Bacillus subtilis* bacteria concentrated on a polyester filter membrane. Transmission electron microscopy of an ultrathin cross-section through the filter membrane shows a dense layer of bacteria above the porous filter membrane. Scale bar 10 µm.

Fig. 2: Transmission electron microscopy of an ultrathin cross-section through a single bacterium shows sufficient freezing quality and ultrastructural detail. Scale bar 200 nm.

Fig. 1

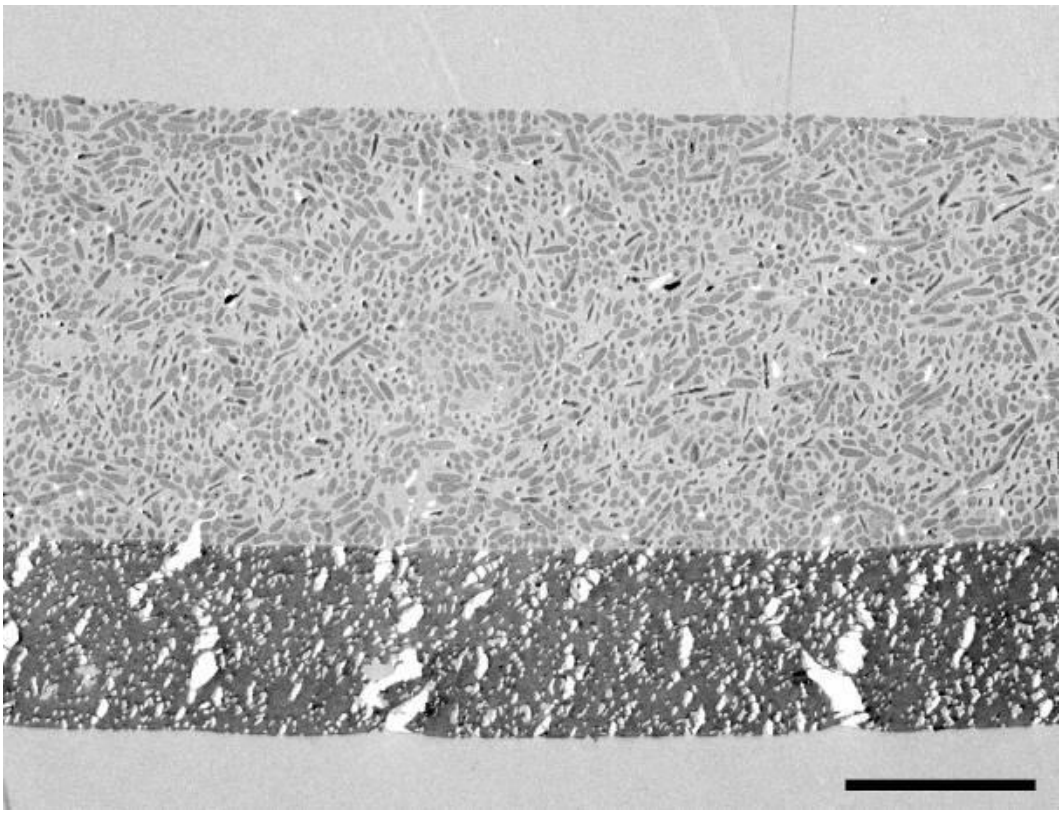

Fig. 2

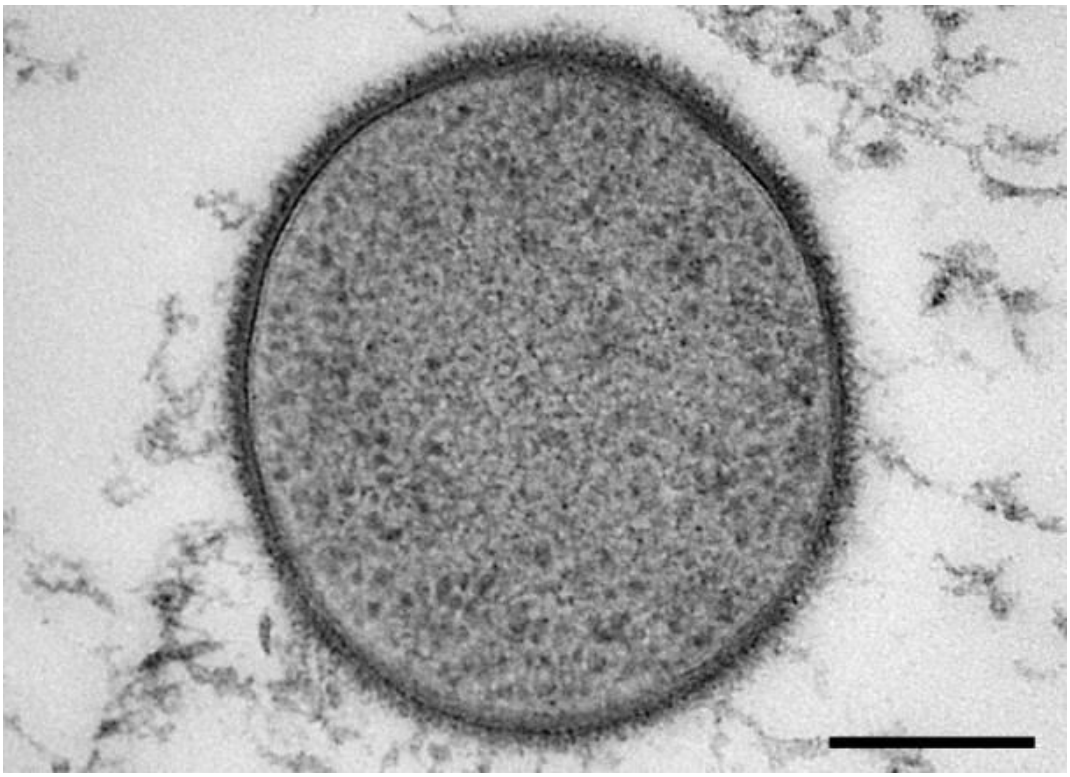

LS7.P003
Applications of Micro Robotics in a FIB-SEM

M. Ross-Messemer[1], F. Aue[1]

[1]Carl Zeiss AG, Central Research and Technology, Oberkochen, Germany

One major goal in FIB-SEM development is the automatization of processes to save time while investigating the current sample. Machine Learning algorithms promises to solve such complex processes, which normally can only be fulfilled by a numerous of manual interactions.

Our developed MatLab™ routines used the opportunity for fully remote control of all used equipment in our FIB-SEM NEON40.

We investigated a special mounted micro-robotic approach using a Kleindiek MM3A™ micromanipulation system combined with a rotip and a microgripper. With this system we learned the basic tasks, which are necessary to produce successful processes for the FIB-SEM community.

Results of automated processes will be presented. Strategies for driving the micromanipulation system using the installed detectors and sample manipulation systems in our NEON 40 will be explained.

The implementation of robotic approaches in a FIB-SEM environment simplifies and reduces the time for microscopic tasks. Additionally a damage of the investigated sample is nearly impossible.

LS7.P004
New serial sectioning workflow for multi-beam SEM applications

C. Tröger [1], K. Schulz[1], S. Irsen[1]

[1]center of advanced european studies and research, Electron Microscopy & Analytics, Bonn, Germany

The nervous system of most species is densely packed with neuronal axons, dendrites and synapses. Knowing their connections is an important step in improving the understanding of neuronal functions. The typical size range of these structures is in the range of 40 – 50 nm (1). This requires electron microscopy (EM) for imaging at nm resolution. Various techniques are used to record 3D volumes of neuronal tissue using EM (2). Especially for larger volumes the experiment time is a limiting factor in most of these techniques (3). Recent developments of multi-beam scanning electron microscopes (mSEM) (4) reduces the experiment time dramatically. Creating datasets of mm^3 to cm^3 volumes with a lateral resolution below 10 nm comes in a range of month instead of years of instrument time. Due to the instrument design, the sample stage is at a voltage of 30 kV. This creates new challenges for sample preparation. Serial sections on Kapton tape (ATUMtome) is a great technique for collecting up to thousands of sections (2). The drawback of this technique is the bad conductivity of the Kapton tape which can be the reason for charging artifacts of the mSEM data. New conducting tapes are available but not yet satisfying (5). We use conductive wafers (Si and ITO coated glass) as substrates for serial sections a promising conductive alternative compared to tape. The advantages are imaging conditions without tape-related issues. Furthermore, a higher packing density of the collected sections on the rigid and flat wafer surface allows less complicated staining procedures and facilitates loading into various microscopes which is advantageous for correlative approaches.

Here, we present our workflow for serial sectioning of tissue for mSEM applications. We modified an ultramicrotome for optimized collection of serial sections on wafer pieces. With our workflow it is possible to collect up to hundreds of wrinkle- and chatter-free sections in a short time.

References:

(1) Harris, K. M., Stevens, J. K. (1989) *J Neurosci* 9, 2982-2

(2) Christopher, J. P., Lucy, M. C. (2014) *Micron* 61, 9-19

(3) Emmons, S. W. (2015) *Philos Trans B* 370, 20140309 – 20140309

(4) Pereira, A. F., Hageman, D. J., Garbowski, T., Riedesel, C., Knothe, U., Zeidler, D., & Knothe Tate, M. L. (2016) *PLoS Computational Biology* 12(11)

(5) Kubota, Y., Sohn, J., Hatada, S., Schurr, M., Straehle, J., Gour, A., et al. (2018) *Nature Comm* 9(1), 437

LS7.P005
Revival of Ultra-Rapid Freezing and High Vacuum Drying (URFD) as a Preparation Method for Electron Microscopy and AFM

M. Dürrenberger[1], S. Erpel[1]

[1]UNI Basel, Swiss Nanoscience Institute, Nano Imaging Lab, Basel, Switzerland

Freeze drying was a widely spread preparation method for microscopy in the 1970ies and 1980ies. It has been given up as soon as ultra-rapid freezing with objects embedded in amorphous ice came up as a standard preparation method. The reason for this was the credo, that an additional step like sublimating the ice would only introduce preparation artefacts. A bad contrast caused by the tiny difference in density of water and density of proteins in water (cells, molecules) was compensated by all kinds of image processing.

We developed again a preparation line starting with ultra-rapid freezing according to Dubochet, followed by sublimating the amorphous ice at a vacuum of 10^{-5} mBar at 172° Kelvin. We also tested the use of a liquid-salt volatile buffer (TAM) before freezing. We developed this preparation line for SEM, TEM and AFM.

Freezing is performed by plunging objects in liquid propane at 82° Kelvin with a speed of about 4 m/s in a home-made machine. The sublimation of amorphous ice is done in a Turbo Freeze Dryer from Quorum, Type 775X using all kinds of modified sample holders. TAM buffer (Triethylammonium Acetate Buffer) is bought from Sigma.

The sublimation procedure was always the same: for 5h at 10^{-5}mBar at 172° Kelvin, 2h at 10^{-5}mBar at 192° Kelvin, 2h at 10^{-5}mBar at 212° Kelvin, 2h at 10^{-5}mBar at 232° Kelvin, 2h at 10^{-5}mBar at 252° Kelvin, 2h at 10^{-5}mBar at 272° Kelvin followed by warming to room temperature until harvesting. For TEM, carbon coated TEM Grids were used and the grids were inspected unstained. For SEM, 13 mm diameter cover glasses, coated with polylysine were used. A 10 nm sputtered layer of gold or platinum was aded to maintain electrical conductivity. For AFM, polylysine coated 22 x 22 mm cover glasses were applied with no further treatment.

Figure 1 shows a HeLa cell surface after classical critical point drying (aldehyde fixation, dehydration in Ethanol, critical point drying in liquid CO_2)

Figure 2 shows the same HeLa cell line dipped in TAM and then ultra-rapid frozen and high vacuum dried.

Both samples were sputtered with 10nm gold and imaged in a FE-SEM. Mag. 20"000x, side length 15µm.

Ultra-rapid freezing and drying of samples is a valuable method to look at several different samples in different Microscopies. For SEM, cells on glass show a better surface structure preservation compared with critical point drying. Other samples have not yet been tested.

Hemocyanin and functionalized nanoparticles could be imaged in the TEM with a preservation level that could not be performed with negative staining. Other samples have not yet been tested.

All kinds of functionalized nanoparticle were imaged by AFM. The quality of preparation allowed the distinction of individual functional molecules on the surface of nanoparticles

Fig. 1

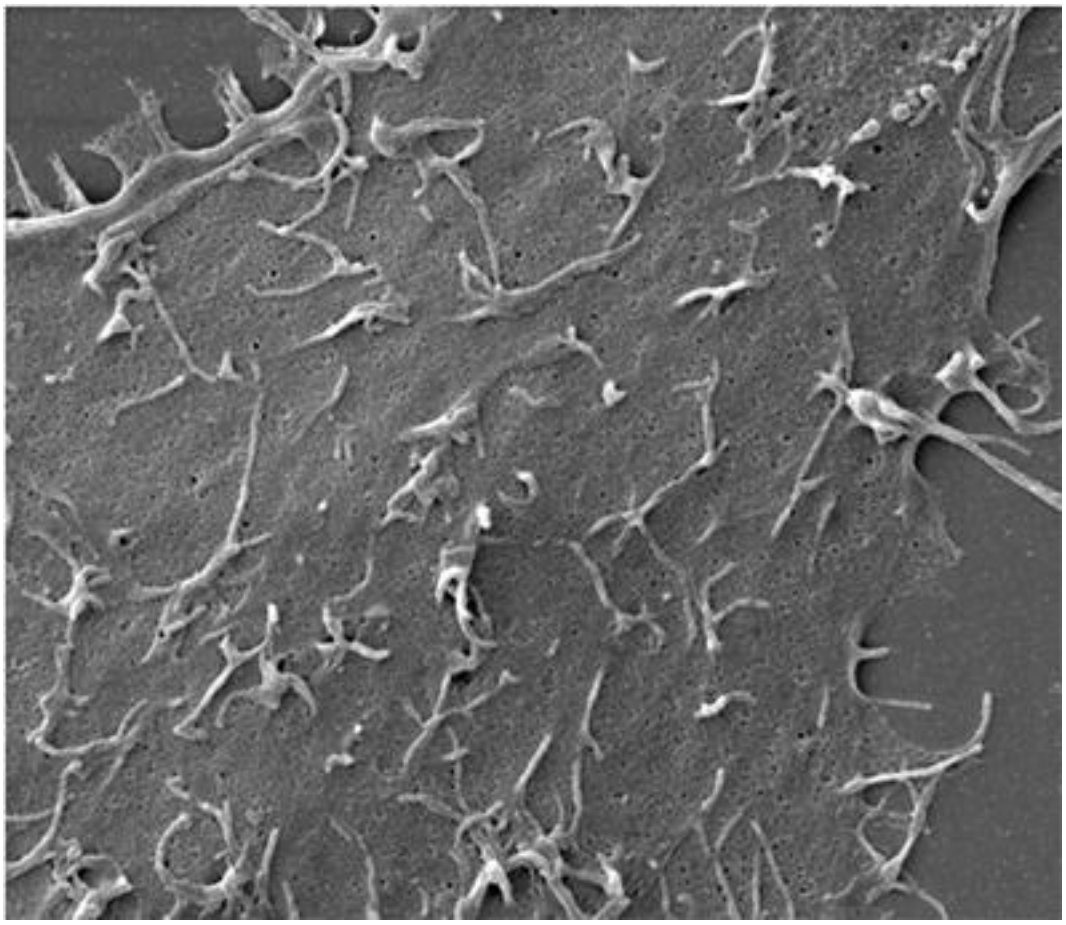

Fig. 2

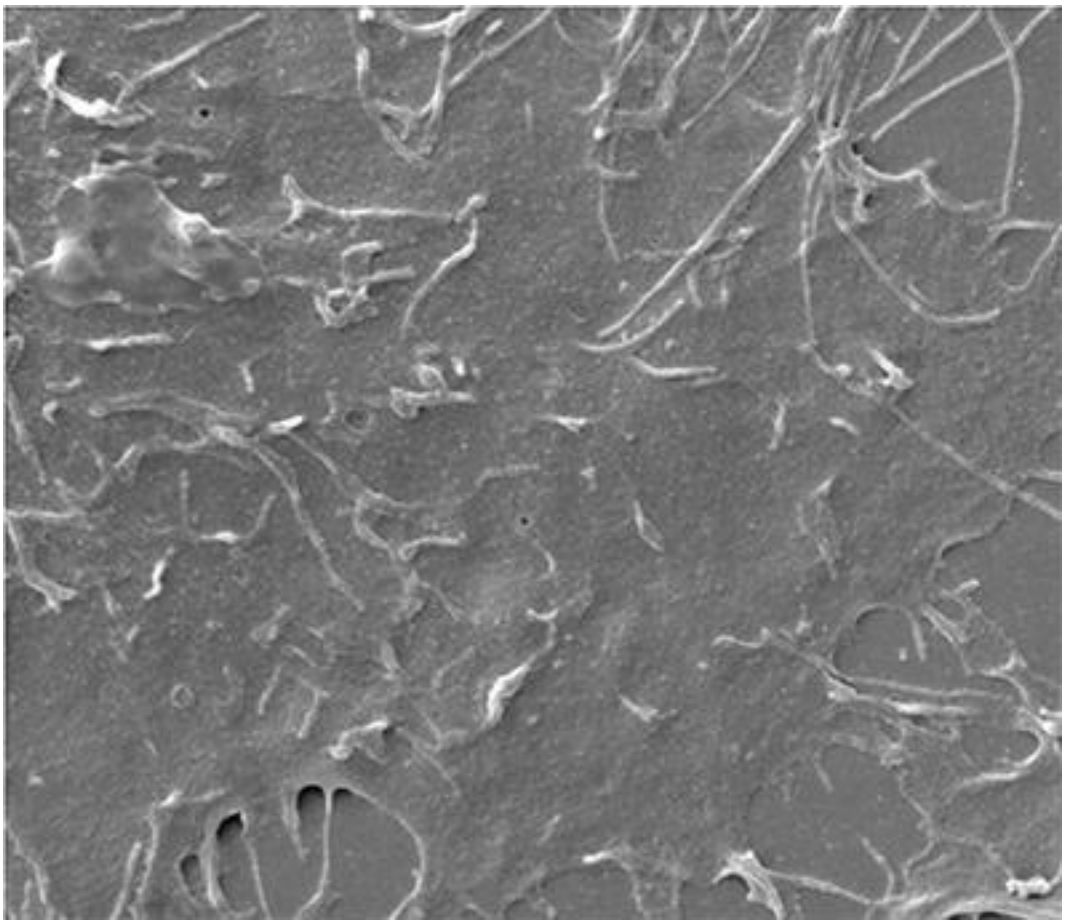

LS7.P006
New modifications of the specimen preparation protocol for serial block-face scanning electron microscopy.

J. Nebesářová[1,2], E. Ďurinová[1,2], J. Langhans[1], M. Vancová[1,2]

[1]Biology Centre of CAS, Laboratory of Electron Microscopy, Ceske Budejovice, Czech Republic
[2]University of South Bohemia, Faculty of Science, Ceske Budejovice, Czech Republic

Preparation of biological specimens for serial block-face scanning electron microscopy (SBF SEM) is based on protocols standardly used for transmission electron microscopy. Protocols suggested by Denk and Horstman (2004) or Deerinck et al. (2010) are currently the most commonly used. They include an intensive osmium treatment and en bloc staining with heavy metals which are performed prior to embedding. Specimens must be also precisely trimmed before their cutting in SEM chamber. These requirements make specimen preparation for SBF SEM laborious and time-consuming and limit the use of this method.

The aim of this study was to modify selected steps of the specimen preparation protocol to make them shorter and easier. We tested different combinations of staining procedures in terms of homogeneity of the staining agent distribution in the sample and its charging under an electron beam during the SEM examination. Further we measured the electric conductivity and the hardness of different variants of resins, compared the influence of different trimming tools on the smoothness of the resin block sides and exposed face from which the ultrathin sections were cut. Measurements of electrical conductivity of polymerized resin blocks proved, that all tested resins - epoxy, methacrylate and melatonin - exhibit negligible electric conductivity, even in the case of an addition of conductive nanoparticles in the resin. This explains, why small areas of pure resin in the specimen, e.g. lumen of blood vessel, can cause the heavy charging of the specimen during its examination in the SBF SEM.

We used desktop milling machine controlled by a computer (Figs. 1,2) in combination with minimal resin embedding procedure (Schieber et al., 2017) to reduce the trimming time. This approach allowed us to shorten the time needed for one sample trimming to about 10 minutes. Suggested modifications facilitate and accelerate the specimen preparation of biological objects for SBF SEM without significantly affecting of the resulting image quality.

This study was supported by the Technology Agency of the Czech Republic (TE01020118) and *by the MEYS CR (LM2015062 Czech-BioImaging).*

References:

(1) Denk W, Horstmann H, 2004: *PLoS Biol*., 2, 1900–1909

(2) Deerinck TJ, Bushong EA, Thor A, Ellisman MH, 2010: *Microscopy*, 6–8. http://ncmir.ucsd.edu/sbfsem-protocol.pdf.

(3) Schieber NL, Machado P, Markert SM, Stigloher C, Achwab Y, Steyer AM, 2017: Methods Cell Biol, 140, 69-83.

Fig. 1: The milling cutter.

Fig. 2: The pyramid with a piece of mouse brain tissue embedding in epoxy resin (EMbed 812pon, EMS) trimmed using the milling cutter.

Fig. 1

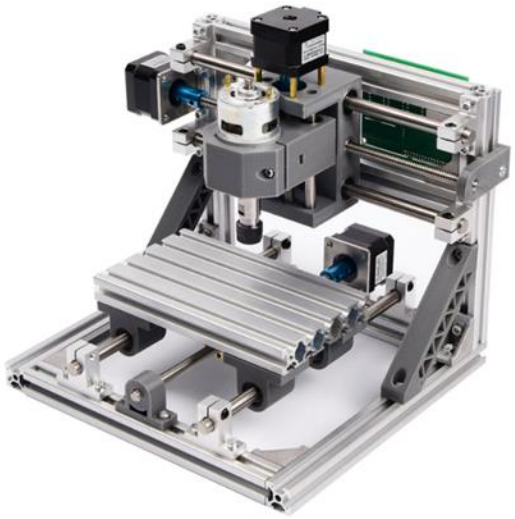

Fig. 2

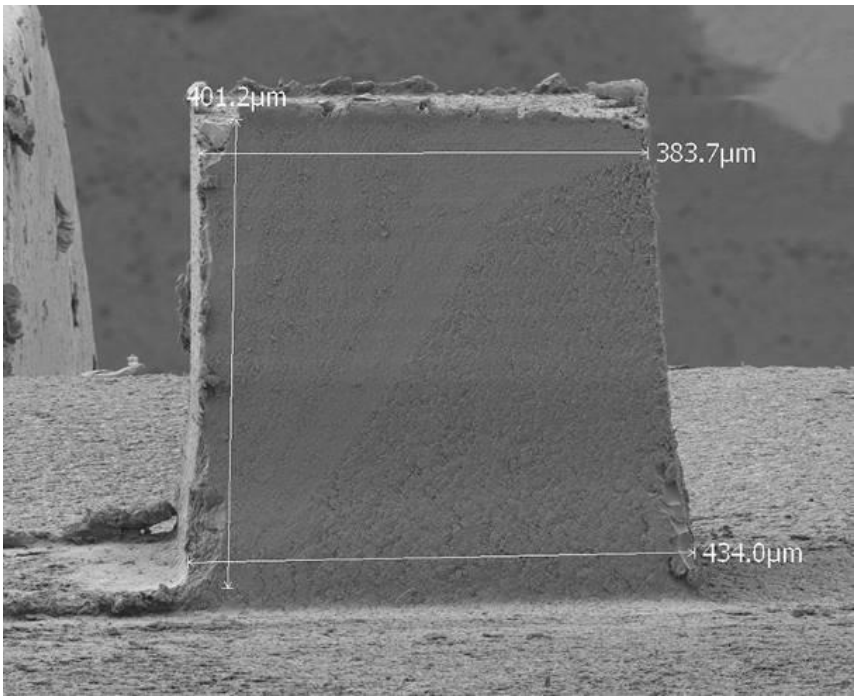

LS7.P007
Calcium accumulation after exuviae ingestion in the hepatopancreas of *Porcellio scaber* and the preservation of exosomes in high pressure frozen samples.

U. Rupp[1], A. Ziegler[1]

[1]Ulm University, Central Facility For Electron Microscopy, Ulm, Germany

The hepatopancreas of isopods serves for food digestion, storage of lipids and carbohydrates, storage of essential metals as well as accumulation and detoxification of xenobiotic metals. Metal is accumulated in lysosomal metal granules - also called cuprosomes - in the two major cell types (S and B) (1). A recent µCT study on mineral shifts in moulting *Porcellio scaber* has shown that mineral is present within the hepatopancreas, however, only when the animal has ingested the exuviae after moult (2). This indicates uptake of exuvial mineral by the hepatopancreas, with the potential to experimentally reveal the pathway for mineral uptake.

The aim of this study was i) to improve preservation of the ultrastructure and mineral content of the hepatopancreas cells, ii) to reveal any contribution of the metal containing granules for the uptake of calcium from the ingested exuviae and iii) to reveal mineral distributions within the cytosol and organelles other than the metal containing granules.

We used *P. scaber* at the postmoult stage that have ingested their exuviae after moult, those that have not ingested their exuviae as a negative control, and as a second control animals at the intermoult stage. For preservation of ultrastructure and mineral, samples were high pressure frozen and freeze substituted. To minimize loss of mineral ultramicrotomy of EPON embedded samples was performed using an oscillating diamond knife (Diatome Ultra Sonic) and propane-1,3-diol as floatation medium. For elemental and structural analysis, we applied EDX, EFTEM, TEM multi-image acquisition and STEM Tomography.

The cryofixed samples reveal multivesicular bodies in both cells types and numerous extracellular vesicles (exosomes) that are not present in chemically fixed samples. In animals that have ingested both exuviae we found a significant higher calcium concentration in the metal granules of S cells in comparison to control animals. In B cells the calcium concentration was much lower and independent of moulting stage and treatment. We also observe intracellular seams and small granules of calcium and phosphorus along the microvilli and along the lateral plasma membranes of S-cells. Similar mineral granules occur between cells and within the basal lamina. In intermoult animals such mineral seams and granules are less abundant and absent in control postmoult animals.

The results suggest that calcium uptake from the ingested exuviae takes place across the apical plasma membrane of the S-cells and calcium accumulation within lysosomal metal granules suggesting reutilization of exuvial calcium for cuticle mineralization. Transport into the hemolymph occurs in form of calcium phosphate via the basolateral membrane and the basal lamina. Supported by the DFG ZI 368/11-1.

References:

(1) Prosi F. and Dallinger R. 1988. *Cell Biol. and Toxicol.* 4: 81–96.

(2) Ziegler A. Neues F. Janáček J. Beckmann F. Epple. M. 2017. *Arthropod Struct. and Dev.* 46: 63–76.

Fig. 1: STEM micrograph of a hepatopancreas cell with metal granules and EDX element distribution.

Fig. 2: EFTEM element analysis of submicrovillar mineral. A: Zero loss image. B: ESI of resulting calcium signal after energy filtering. C. High resolution image of mineral. The yellow circle marks the area analysed by PEELS in spot mode. D. Image of EELS spectrum; arrows mark the Ca L3 and L2 edges. E, F. PEELS spectra for Ca and P.

Fig. 1

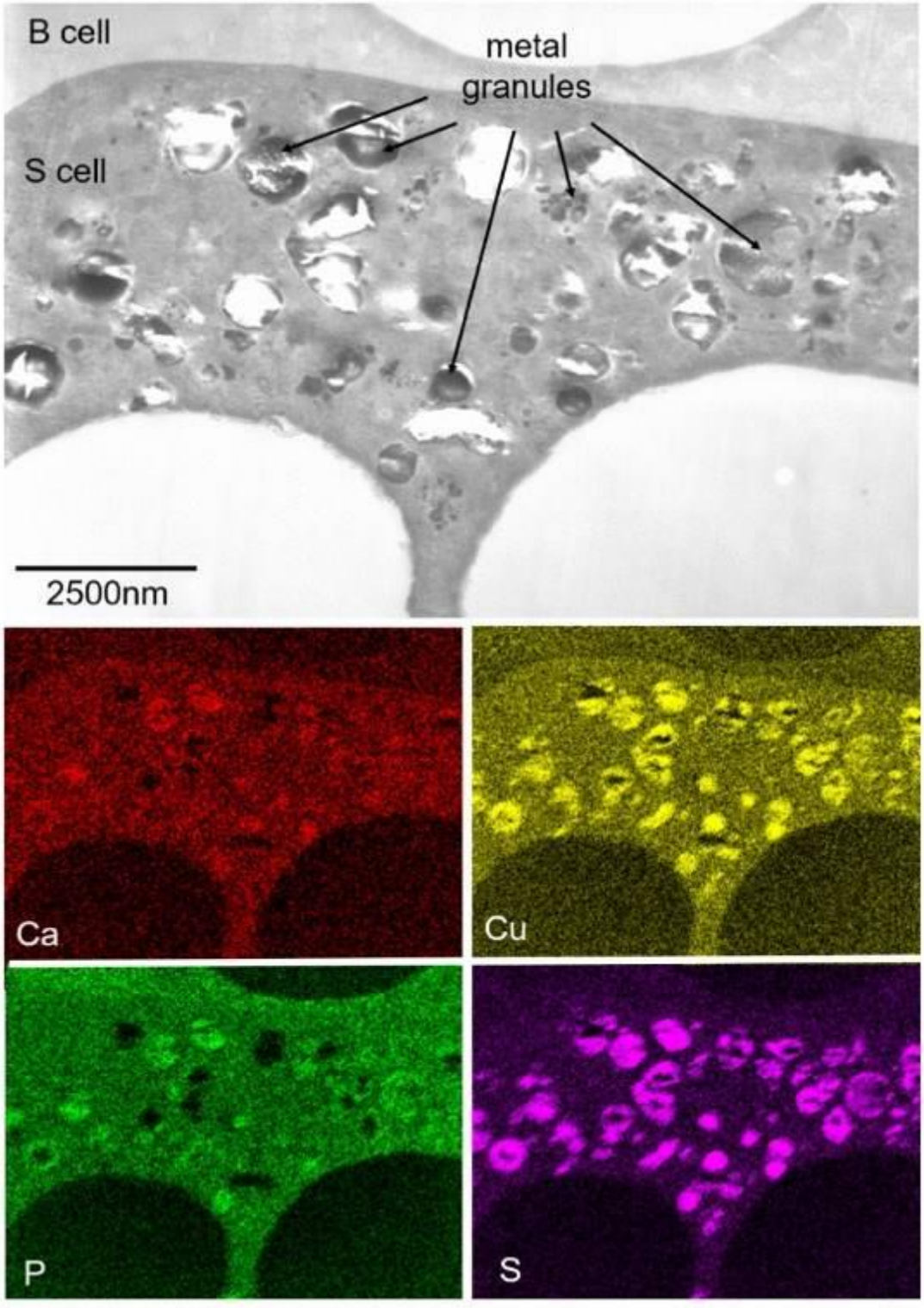

Fig. 2

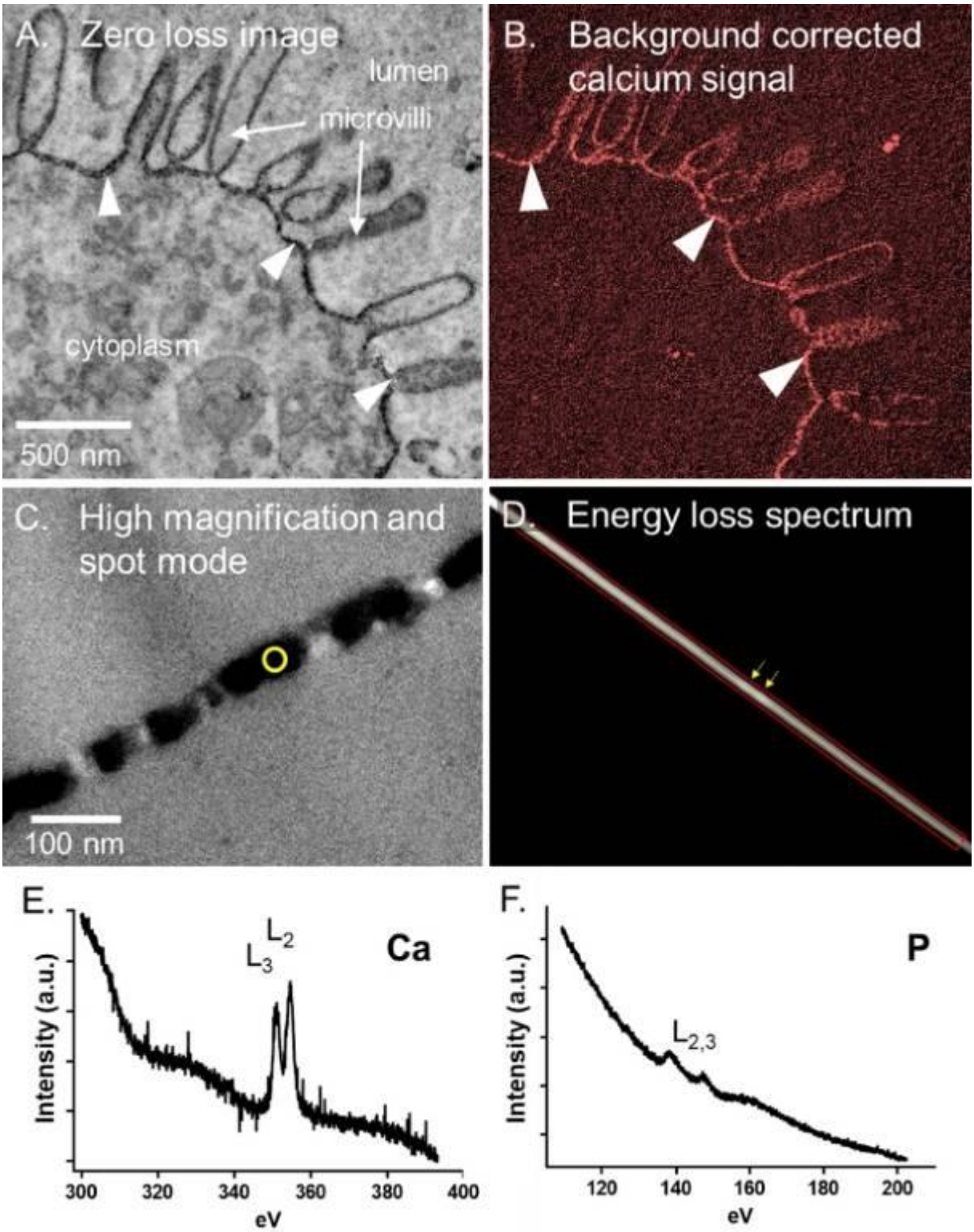
A. Zero loss image
lumen
microvilli
cytoplasm
500 nm
B. Background corrected calcium signal
C. High magnification and spot mode
100 nm
D. Energy loss spectrum
E.
Ca
L2
L3
Intensity (a.u.)
300
320
340
360
380
400
eV
F.
P
L2,3
Intensity (a.u.)
120
140
160
180
200
eV

LS7.P008
Topographical sample supports recover the missing wedge in TEM

J. T. C. Wennmacher[1], T. Gruene[1,2], J. A. Van Bokhoven[1]

[1]Paul Scherrer Institute/ ETH Zurich, Laboratory for Catalysis and Sustainable Chemistry, Villigen PSI, Switzerland
[2]University of Vienna, Faculty of Chemistry, Vienna, Austria

A TEM sample support is an engineered compromise between mechanical stability and electron transparency. So metal grids holding electron-transparent films that carry the objects of interest are deployed in TEM studies. The compromise comes with the cost of electron transparency at high tilt angles parallel to the optical axis of the TEM. Hence conventional TEM Grids possess space, that cannot be sampled by electrons. In real and reciprocal space this region is resembled by a wedge and the so called "Missing Wedge problem" is challenging the field of TEM since ever. The problem arises from nano-sized objects, which very often attach to the thin film of TEM grids in a preferred orientation. Here the missing wedge leaves a preferred site common to all objects unsampled. The information cannot be recovered even if data of many objects are merged. This leads to incomplete three-dimensional information of the reconstructed object, rendering its true information content two-dimensional. As a result distorted electron density in three-dimensional reconstructions is yielded. For 3D electron crystallography this means a low reliability of the atomic models obtained.

Here we designed two types of topographical sample supports that fight preferred orientation and thus lead to complete structures for electron crystallography.

One support can be obtained by simply brushing with a faint haired paintbrush across the surface of a continuous carbon film TEM grid. Another approach utilizes a network of nylon nanofibres. The fibrous tissue can be obtained by electro-spinning of a nylon solution on a TEM grid. Nanocrystals of the zeolite ZSM-5 were chosen as an example for objects with a preferred orientation. Here their crystallographic b axis was preferably oriented parallel to the optical axis of the microscope.

The first approach folded electron transparent carbon coils out of the continuous carbon film. ZSM-5 nanocrystals were found in manyfold orientations attached to these micrometer-sized coils. Merging the crystallographic data of just three crystals, achieved 100% completeness, thus demonstrating the randomness of their orientation toward the optical axis of the microscope. The second approach resembled by the three-dimensional network of nylon nanofibres matched the dimension of its topology to the dimension of the attached nanocrystals. The random orientation of the fibres was transferred to the attached crystals. Data completeness was achieved after the crystallographic data of 4 crystals were merged. Density and thickness of the fibres could be controlled by the electron spinning process and were adjustable to the objects considered. The nylon network was suitable for objects residing in liquids also.

Two simple approaches can randomise the orientation of preferably oriented objects of submicrometer-size. This randomisation overcomes the "Missing Wedge problem" in TEM studies and probably other radiation transmission studies.

References:

(1) Wennmacher et al., under resubmission

Fig. 1: Conventional sample support leads to incomplete data. When the crystal is centred between grid bars, the maximum rotation range is about 140◦, 78% data completeness respectively.

Fig. 2: Cartoon illustrating the randomized orientation of ZSM-5 crystals attached to the wrapped foil.

Fig. 3: Cartoon illustrating the randomized orientation of ZSM-5 crystals attached to the nylon fibres.

Fig. 1

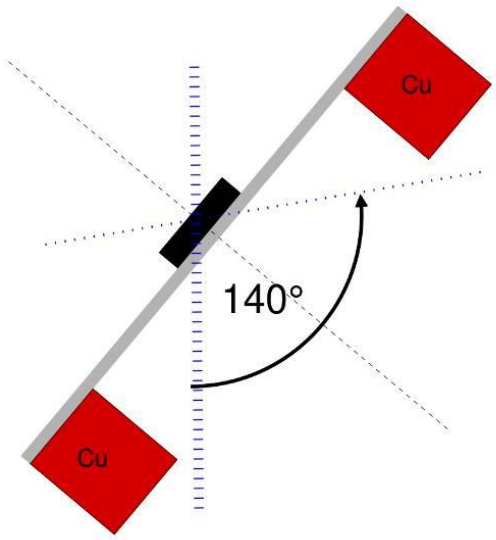

Fig. 2

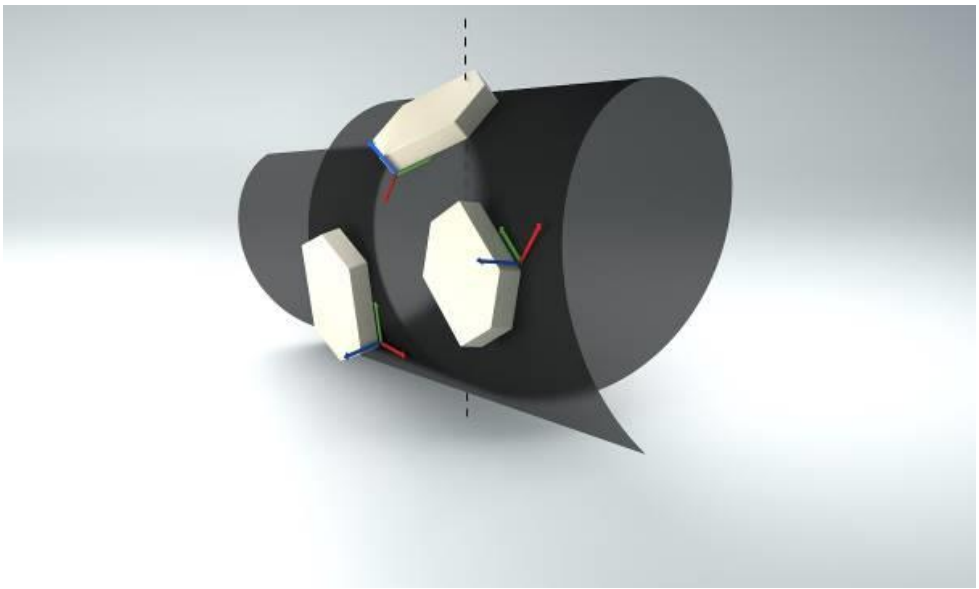

Fig. 3